ISSN 1028-8546

Volume XVI, Number 2
Series: En
June, 2010

Azerbaijan Journal of Physics

Fizika

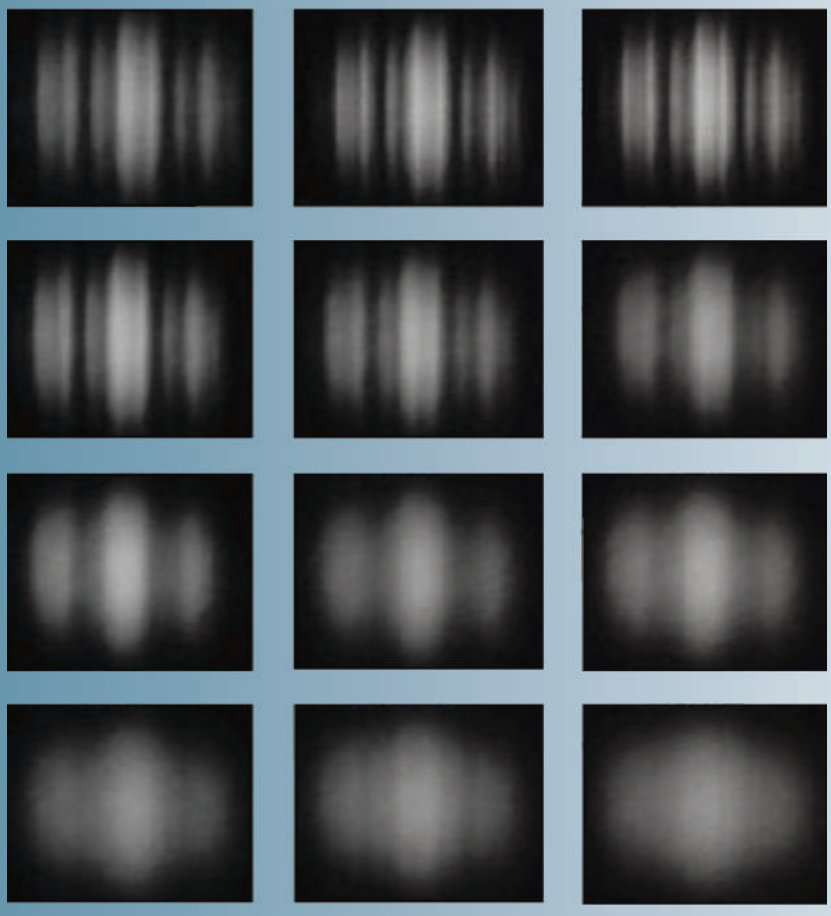

www.elm.az/physics

G.M. Abdullayev Institute of Physics
Azerbaijan National Academy of Sciences
Department of Physical, Mathematical and Technical Sciences

Published from 1995

ISSN 1028-8546
vol. XVI, Number 2, 2010
Series: En

Azerbaijan Journal of Physics

Fizika

G.M.Abdullayev Institute of Physics
Azerbaijan National Academy of Sciences
Department of Physical, Mathematical and Technical Sciences

PUBLISHING OFFICE

33 H.Javid ave, AZ-1143, Baku
ANAS, G.M.Abdullayev Institute of Physics

Tel.: (99412) 439-51-63, 439-32-23
Fax: (99412) 447-04-56
E-mail: joph@physics.ab.az
Internet: www.elm.az/physics

It is authorized for printing: 02.20.2010

Published at "**ŞƏRQ-QƏRB**"

17 Ashug Alesger str., Baku

Typographer : Aziz Gulaliyev

Sent for printing on: __.06. 2010
Printing approved on: __.06. 2010
Physical binding:_____
Number of copies:_____200
Order:_____

SPECIAL FUNCTIONS AND DIFFERENCE EQUATIONS

NATIG M. ATAKISHIYEV
Instituto de Matematicas, Unidad Cuernavaca
Universidad Nacional Autonoma de Mexico
A.P. 273-3, Admon.3, 62210 Cuernavaca
Morelos, Mexico

We give an overview of the general properties of special functions of mathematical physics. The main goal is to call attention to the importance of *difference equations* as a fundamental tool for constructing various generalizations of the classical special functions. Some explicit methods for solving difference equations are discussed. As a particular example we consider in detail a difference equation for *Kravchuk functions*. Another generalization of the classical Hermite polynomials, the so-called *continuous q-Hermite polynomials of Rogers*, which are governed by a *q*-difference equation, is also discussed.

Finally, we brieffy touch upon transformation properties of some special functions with respect to the *integral and finite (discrete) Fourier transforms*.

1. INTRODUCTION

The aim of this mini-review is simply to call attention of physicists to *difference equations* as a useful constructive device for solving various problems in mathematical physics. By no means I am intend to cover the whole theory of difference equations [1], but have chosen a path which I myself have followed and found interesting. The main purpose is to convince the reader that *"the subject is one of simplicity and elegance"*. This short quotation is from the book on differential equations by S.L.Ross [2], but I believe that it fits to the case of *difference equations* as well.

One of the most important advantages of introducing difference equations into our regular mathematical apparatus is that in this way one can essentially enlarge the family of special functions, already thoroughly studied and, therefore, well known to us. We discuss some methods for solving difference equations. As a particular example we consider in detail a difference equation for the *Kravchuk functions*. We also discuss transformation properties of some special functions with respect to the *classical Fourier integral transform*. We show that even *q*-generalizations of well-known orthogonal polynomial families transform *in a simple way* under the Fourier integral transform and, consequently, under the fi*nite Fourier transform*.

The layout of the exposition is as follows. Section 2 collects some background facts about classical hypergeometric polynomials of Jacobi, Laguerre and Hermite. Section 3 contains a detailed discussion of main properties of the classical Hermite polynomials. In section 4 we start out by defining difference operators and then construct a finite model of the linear harmonic oscillator in quantum mechanics in terms of Kravchuk polynomials. Section 5 is devoted to another generalization of the classical Hermite polynomials, to the continuous *q*-Hermite polynomials of Rogers. In this section we also show that the continuous *q*-Hermite polynomials of Rogers exhibit remarkably simple transformation properties with respect to the classical Fourier integral transform. Finally, in section 6 we discuss the finite Fourier transform and *q*-extended eigenvectors of this transform in terms of the continuous *q*-Hermite polynomials of Rogers.

Throughout this exposition we employ standard notations of the theory of special functions (see, for example, [3] or [4]).

2. CLASSICAL SPECIAL FUNCTIONS

Classical special functions of mathematical physics arise in solving many theoretical and applied problems in various branches of natural sciences. They form a fundamental part of our mathematical language, helping us to express precisely our knowledge about the world, in which we live. Their importance is therefore difficult to overestimate. The well-known examples of special functions are the *classical Jacobi, Laguerre and Hermite polynomials*. They satisfy the second-order linear differential equation of Sturm-Liouville type

$$\sigma(x)y''(x) + \tau(x)y'(x) + \lambda y(x) = 0 \qquad (2.1)$$

where primes denote differentiation with respect to the independent variable x, $\sigma(x)$ and $\tau(x)$ are polynomials of at most second and first degree in x, respectively, and λ is a constant. Observe that the generic case of equation (2.1) with

$$\sigma(x) := ax^2 + bx + c \equiv a(x - x_1)(x - x_2), \quad x_1 \neq x_2,$$

is reduced to the differential equation

$$x(x-1)y''(x) + [(\alpha + \beta + 1)x - \gamma]y'(x) + \alpha\beta y(x) = 0 \qquad (2.2)$$

for the *Gaussian hypergeometric function* ${}_2F_1(\alpha; \beta; \gamma; x)$ upon making the linear change of the variable

$$x \Rightarrow (x_2 - x_1)x + x_1$$

x_1 and x_2 are distinct zeroes of $\sigma(x)$. The explicit form of the Gaussian hypergeometric function ${}_2F_1(\alpha; \beta; \gamma; x)$ is given by a power series[1] in the variable x, namely

$${}_2F_1(\alpha;\beta;\gamma;x) = \sum_{k=0}^{\infty} \frac{(\alpha)_k (\beta)_k}{(\gamma)_k} \frac{x^k}{k!} \qquad (2.3)$$

[1] We recall that geometric series $S_N(x)$ is define as $S_N(x) = 1 + x + x^2 + \cdots + x^{N-1} = \frac{1-x^N}{1-x}$

where $(\alpha)_k := \frac{\Gamma(\alpha+k)}{\Gamma(\alpha)}$, $k = 0; 1\ldots..$, is the shifted factorial:

$$(z)_k = \begin{cases} 1, & k = 0 \\ z(z+1)\ldots..(z+k-1), & k = 1,2,3\ldots.. \end{cases}$$

It is to be emphasized that if $z = -n$ and n is a nonnegative integer number, then the shifted factorial

$$(-n)_k = \begin{cases} (-1)^k n!/(n-k)!, & 0 \le k \le n \\ 0, & k > n, \end{cases} \tag{2.4}$$

which is a direct consequence of the properties of the gamma function $\Gamma(z)$.

Remark 1. Probably the most frequently used among all special functions is the *gamma function* $\Gamma(z)$ *(or Euler's integral of the second kind)*. The gamma function is defined for $x > 0$ by the integral

$$\Gamma(x) := \int_0^\infty e^{-t} t^{x-1}\, dt.$$

From this definition it follows that

$$\Gamma(x+1) = \int_0^\infty e^{-t} t^{x-1} dt = -e^{-t} t^x \Big|_0^\infty + \int_0^\infty e^{-t}\, t^{x-1} dx = x\Gamma(x).$$

Thus integration by parts in the integral representation for the $\Gamma(x + 1)$ reveals one of the fundamental properties of the *gamma function*, that is, the *recurrence formula (or functional equation)* $\Gamma(x + 1) = x\Gamma(x)$. This relation in turn means that $\Gamma(x)$ can be analytically continued to a meromorphic function $\Gamma(z)$ on the complex z-plane and

$$\Gamma(z + 1) = z\Gamma(z) :$$

As a meromorphic function of z, the function $\Gamma(z)$ has simple poles at the points $z = -l$ (for $l = 0; 1; 2; \ldots.$), to which correspond the residues $(-1)^l/l!$. Therefore $(-n)_k = \Gamma(k-n)/\Gamma(-n)$, from which expression (2.4) immediately follows. We close this remark about the properties of the function $\Gamma(z)$ by the observation that it is evident from (2.4) that the hypergeometric function ${}_2F_1(-n; \beta; \gamma; x)$ represents in fact a terminating series in x,

$$2F1(-n;\beta;\gamma;\, x) = \sum_{k=0}^{n} \frac{(-n)_k (\beta)_k}{(\gamma)_k} \frac{x^k}{k!},$$

that is, ${}_2F_1(-n; \beta; \gamma, x)$ is *a polynomial of degree n in the variable x*.

The standard way of solving the equation (2.1) is to look for its solutions in the form of power series in the independent variable x. Indeed, if x_1 is a root of the equation $\sigma(x) = 0$, then the equation (2.1) has a particular solution of the form

$$y(x) = \textstyle\sum_{k=0}^{\infty} c_k\, (x - x_1)^k, \tag{2.5}$$

where the coefficients c_k satisfy the two-term recurrence relation

$$\begin{aligned} &(k+1)[\tau(x_1) + k\sigma'(x_1)]c_{k+1} + \\ &+\left\{\lambda + k\left[\tau'(x_1) + \tfrac{k-1}{2}\sigma''(x_1)\right]\right\} c_k = 0 \end{aligned} \tag{2.6}$$

To prove that it is more convenient to rewrite the equation (2.1) in the *self-adjoint form*

$$[\sigma(x)\rho(x)y'(x)]' + \lambda\rho(x)y(x) = 0,$$

$$[\sigma(x)\rho(x)]' = \tau(x)\, \rho(x), \tag{2.7}$$

where the second line is the first-order differential equation for *defining a function* $\rho(x)$. Now the proof that (2.5) and (2.6) represent a solution to (2.1) follows from the identity

$$\begin{aligned} &\rho^{-1}(x)\frac{d}{dx}\left[\sigma(x)\rho(x)\frac{d}{dx}(x-x_1)^k\right] \\ &= k\left[\tau'(x_1) + \frac{k-1}{2}\sigma''(x_1)\right](x-x_1)^k + \\ &+k[\tau(x_1) + (k-1)\sigma'(x_1)](x-x_1)^{k-1} + (k-1)\sigma(x_1)(x-x_1)^{k-2}, \end{aligned} \tag{2.8}$$

which is valid for *any arbitrary value* x_1 of the independent variable x (*not necessarily a zero of* $\sigma(x)$). This identity is readily verified by using the second line in (2.7) and taking into account that

$$\sigma(x) = \sigma(x_1) + (x-x_1)\sigma'(x_1) + \frac{1}{2}(x-x_1)^2\sigma''(x_1),$$

$$\tau(x) = \tau(x_1) + (x-x_1)\tau(x_1).$$

Upon inspection of the identity (2.8) it becomes immediately apparent that the series (2.5) is a solution of the equation (2.1), rovided that the coefficients c_k satisfy the three-term recurrence relation

$$\begin{aligned} &\left\{\lambda + k\left[\tau'(x_1) + \tfrac{k-1}{2}\sigma''(x_1)\right]\right\} c_k + (k+1)[\tau(x_1) + k\sigma'(x_1)]c_{k+1} + \\ &+(k+1)(k+2)\sigma(x_1)c_{k+2} = 0. \end{aligned} \tag{2.9}$$

One may simplify this recurrence relation by choosing x_1 as a root of the equation $\sigma(x) = 0$; then equation (2.9) evidently reduces to the desired two-term recurrence relation (2.6). Moreover, as is clear from the same identity (2.9), the series (2.5) will satisfy the equation (2.1) even in the event when $\sigma(x)$ has no zeros (that is, $\sigma(x)$ is a constant), provided that

$$(k+1)(k+2)\sigma c_{k+2} + \left(\lambda + k\tau'(x_1)\right)c_k = 0, \qquad k=0, 1, 2, \ldots\ldots,$$

and x_1 is a root of the equation $\tau(x) = 0$.

It is worth pointing out that the differential equation (1.2) for the Gaussian hypergeometric function (2.3) has $\sigma(x) = x(x - 1)$, $\tau(x) = (\alpha + \beta + 1)\, x - \gamma$, $\lambda = \alpha\beta$. Consequently, the two-term recurrence relation (2.6) for this particular case takes the form

$$c_{k+1} = \frac{(k+\alpha)(k+\beta)}{(k+\gamma)(k+1)} c_k, \qquad k = 0, 1, 2, \ldots\ldots,$$

which confirms that the Gaussian hypergeometric function ${}_2F_1(\alpha; \beta; \gamma; x)$ is a solution of the differential equation (2.2).

EXAMPLES:

1. The *Jacobi polynomials* $P_n^{(\alpha,\beta)}(x)$ are explicitly given by

$$P_n^{(\alpha,\beta)}(x) := \frac{(\alpha+1)_n}{n!}\ {}_2F_1\left(-n, n+\alpha+\beta+1; \alpha+1; \frac{1-x}{2}\right);$$

whereas the *Legendre (or spherical) polynomials*

$$P_n(x) := {}_2F_1\left(-n, n+1; 1; \frac{1-x}{2}\right)$$

are particular case of the Jacobi polynomials $F_n^{(\alpha,\beta)}(x)$ with $\alpha = \beta = 0$

2. The *Laguerre polynomials* $L_n^{(\alpha)}(x)$ are defined as

$$L_n^{(\alpha)}(x) := \frac{(\alpha+1)_n}{n!}\ {}_1F_1(-n, \alpha+1; x).$$

3. The *Hermite polynomials* $H_n(x)$ are defined as

$$H_n(x) := (2x)^n\ {}_2F_0\left(-\frac{n}{2}, \frac{1-n}{2}; -\frac{1}{x^2}\right). \qquad (2.10)$$

3. HERMITE POLYNOMIALS

The Hermite polynomials $H_n(x)$ are of the particular importance for our exposition, therefore we consider them in this section in detail. The Hermite polynomials are generated by the second-order differential equation

$$\frac{1}{2}\left(x^2 - \frac{d^2}{dx^2}\right) f_n(x) = \lambda_n f_n(x). \qquad (3.1)$$

This equation is not of the hypergeometric type (2.2), but it can be reduced to it in the following way. Since we are aiming at *square-integrable solutions* of equation (3.1), let us first define asymptotical behavior of $fn(x)$ in the limit as $x \to \pm\infty$. Assume that $fn(x)$ behaves like $e^{\alpha x^\beta}$ at infinity (where α and β are some constants); then from (3.1) it follows that

$$\frac{1}{2}\left\{x^2 - \alpha\beta\left[\alpha\beta x^{2(\beta-1)} + (\beta-1)x^{\beta-2}\right]\right\} e^{\alpha x^\beta} = \lambda_n e^{\alpha x^\beta}.$$

So to cancel on the left side the first two leading terms at infinity, one should require that $(\alpha\beta)^2 = 1$ and $\beta = 2$; thus $\beta = 2$ and $\alpha = \pm 1/2$. One must discard the case with $\alpha = 1/2$ (because it contradicts the requirement of the square-integrability) and then looks for solutions of (3.1) in the form

$$f_n(x) = u_n(x) e^{-x^2/2}.$$

This means that the functions $u_n(x)$ are solutions of the second-order differential equation

$$\left[\frac{d^2}{dx^2} - 2x\frac{d}{dx} + (2\lambda_n - 1)\right] u_n(x) = 0 \qquad (3.2)$$

When $\lambda_n = n + 1/2$ equation (3.2) represents the standard second-order differential equation

$$\left(\frac{d^2}{dx^2} - 2x\frac{d}{dx} + 2n\right) H_n(x) = 0. \qquad (3.3)$$

for the Hermite polynomials $Hn(x)$. The reader is left with the easy task of verifying that (3.3) is the equivalent of the second-order differential equation for the hypergeometric ${}_2F_0$-polynomial in the independent variable $-1/x^2$ associated with the parameters $\alpha = -n/2$ and $\beta = (1 - n)/2$. Thus one arrives at the explicit hypergeometric representation (2.10) for the Hermite polynomials $H_n(x)$.

Solutions of differential equation (3.1) with the spectral parameter $\lambda_n = n + 1/2$ are of the form

$$f_n(x) = H_n(x) e^{-x^2/2}, \quad n = 0, 1, 2, \ldots, \qquad (3.4)$$

and they are called *Hermite functions* in the mathematical literature. They are interpreted (after being appropriately normalized) as the wave functions of the linear harmonic oscillator in quantum mechanics [5].

The main properties of the Hermite polynomials are listed below.

Explicit formula:

$$H_n(x) = (2x)^n\ {}_2F_0\left(-\frac{n}{2}, \frac{1-n}{2}; -\frac{1}{x^2}\right) = n! \sum_{k=0}^{[\frac{n}{2}]} \frac{(-1)^k}{k!\,(n-2k)!} (2x)^{n-2k};$$

Three-term recurrence relation:

$$2xH_n(x) = H_{n+1}(x) + 2nH_{n-1}(x), \quad H_0(x) = 1, \ n = 0, 1, 2, \ldots\ldots;$$

Differentiation formula:

$$H_n'(x) = 2nH_{n-1}(x);$$

Second-order differential equation:

$$\left(\frac{d^2}{dx^2} - 2x\frac{d}{dx} + 2n\right) H_n(x) = 0;$$

Rodrigues formula:

$$H_n(x) = (-1)^n e^{x^2} \left(\frac{d}{dx}\right)^n e^{-x^2}, \qquad n = 0, 1, 2, \ldots;$$

Orthogonality on the whole real line $x \in \mathcal{R}$:

$$\frac{1}{\sqrt{\pi}} \int_{\mathcal{R}} H_m(x) H_n(x) e^{-x^2} dx = 2^n n!\, \delta_{m,n};$$

Eigenfunctions of the Fourier integral transform:

$$\frac{1}{\sqrt{2\pi}} \int_{\mathcal{R}} e^{ixy} H_n(y) e^{-y^2/2} dy = i^n H_n(x) e^{-x^2/2};$$

Completeness of the Hermite functions $H_n(x)e^{-x^2/2}$, $n = 0; 1; 2; \ldots\ldots;$ in the Hilbert space of square-integrable functions $L_2(\mathcal{R}, dx)$;

Linear generating function:

$$exp(2xt - t^2) = \sum_{n=0}^{\infty} \frac{t^n}{n!} H_n(x). \qquad (3.5)$$

Remark 2. It is worth noting that *the real beauty* of the above linear generating function is that it actually *encodes*

all information about the three-term recurrence relation, the Rodrigues formula, the differentiation formula, the second-order differential equation, and so on.

4. DIFFERENCE OPERATORS AND FINITE OSCILLATOR

A notion of *difference operators* appears in non-relativistic quantum mechanics at its early stage. Indeed, consider a quantum-mechanical system of N particles with positions in three-dimensional space, that are characterized by the radius vector $\vec{r}_n$, $1 \leq n \leq N$ [5]. Then an infinitely small *displacement (or translation)* in this space over a distance $\delta\vec{r}$ signifies a transformation under which the radius vectors $\vec{r}_n$ of all the particles receive the same increment $\delta\vec{r}$: $\vec{r}_n \Rightarrow \vec{r}_n + \delta\vec{r}$. The *operator of a parallel displacement* over any finite (not only infinitesimal) distance $\vec{a}$ can be expressed in terms of the momentum operator . By the definition of this operator $\hat{T}_{\vec{a}}$ we must have

$$\hat{T}_{\vec{a}}\,\psi(\vec{r}) = \psi(\vec{r}+\vec{a}). \tag{4.1}$$

Expanding the function $\psi(\vec{r}+\vec{a})$ in a Taylor series gives

$$\psi(\vec{r}+\vec{a}) = \psi(\vec{r}) + \vec{a}\,\frac{\partial\psi(\vec{r})}{\partial\vec{r}} + \cdots, \tag{4.2}$$

or, in terms of the momentum $\vec{p}$,

$$\psi(\vec{r}+\vec{a}) = \left[1 + \tfrac{i}{\hbar}\vec{a}\vec{p} + \tfrac{1}{2}\left(\tfrac{i}{\hbar}\vec{a}\vec{p}\right)^2 + \cdots.\right]\psi(\vec{r}). \tag{4.3}$$

The expression in the rectangular brackets on the right side of (4.3), $\hat{T}_{\vec{a}} := \exp\left(\frac{i}{\hbar}\vec{a}\vec{p}\right)$ is the required operator of the f*inite displacements*. From (4.2) or (4.3) it is also evident, that the momentum operator $\vec{p}$ itself (multiplied by the constant factor represents the *operator of infinitesimal displacements*, or, in the terminology of group theory, it is the *generator of displacements*.

Once the action of the simple difference operator $\exp(a\partial_x)$ is clear from (4.1),

$$\exp(a\partial_x)\,f(x) = f(x+a), \qquad \partial_x \equiv \frac{d}{dx},$$

one may try and solve a difference equation of the form

$$\left[\alpha_l(x)e^{-\partial_x} + e^{\partial_x}\alpha_l(x)\right]f_n(x;l) = \lambda_n(l)f_n(x;l), \tag{4.4}$$

where $\alpha_1(x) := \sqrt{(x+l)(l+1-x)}$ and $-l \leq x \leq l$. Observe that in view of the relation $\alpha_l(-x) = \alpha_l(x+1)$, the equation (4.4) is invariant with respect to the change of the sign of x.

As usually, one starts with a *"ground state"* $f_0(x; l)$, which defines *asymptotical* behavior of solutions $f_n(x; l)$ at the ends of the interval $[-l; l]$ (compare that with the case of the Hermite functions). Since

$$\begin{aligned} e^{\partial^x}\Gamma(x+\alpha) &= \Gamma(x+\alpha+1) = (x+\alpha)\Gamma(x+\alpha), \\ e^{\partial^x}\Gamma(\alpha-x) &= \Gamma(\alpha-x-1) = (\alpha-x-1)^{-1}\Gamma(\alpha-x), \end{aligned} \tag{4.5}$$

and the action of the second difference operator $e^{-\partial_x}$ on the same gamma functions is readily obtained from (3.5) by reversing the sign of the variable x, one can look for a "ground state" of the form

$$f_0(x;l) = \Gamma^{\beta}(x+\alpha)\Gamma^{\beta}(\alpha-x), \tag{4.6}$$

where a and β are some constants to be found. Substituting (4.6) into the left side of (4.4) gives

$$\begin{aligned} \alpha_l(x)f_0(x-1;l) + \alpha_l(x+1)f_0(x+1;l) = \Big\{\alpha_l(x)\left[\tfrac{\alpha-x}{x+\alpha-1}\right]^{\beta} + \\ +\alpha 1x+1x+a\alpha-x-1\beta f0x;\, l \end{aligned} \tag{4.7}$$

The equation (4.4) for $f0(x; l)$ will hold if the expression in the curly braces in (4.7) turns out to be a constant. So one chooses $a = l + 1$ and $\beta = -1/2$, and then this expression becomes $x + l + l - x = 2l$. Hence,

$$f_0(x;l) = [\Gamma(x+l+1)\Gamma(l+1-x)]^{-1/2} \tag{4.8}$$

and the corresponding eigenvalue $\lambda_0(l)$ is equal to $2l$.

Remark 3. Observe that there is actually another possibility for the $f0(x; l)$ when $a = l + 1$, $\beta = 1/2$ and $\lambda_0(l) = 2(l+1)$. But this solution with the positive value of β is discarded because when l it reduces to the function $e^{x^2}/2$, which is not square-integrable on the real line $x \in \mathfrak{R}$ (compare this reasoning with the selection of solutions of the differential equation (3.1)). We recall in this connection that the gamma function (x) asymptotically behaves like $\sqrt{\frac{2\pi}{x}}\left(\frac{x}{e}\right)^x$ in the limit as $x \to \infty$.

Having defined $f_0(x; l)$, one may find all $2l$ linearly independent *"excited states"* with $n = 1, 2, \ldots, 2l$ in the following way. Let us assume that $f_n(x; l) = u_n(x; l)\, f_0(x; l)$ and then evaluate

$$\begin{aligned} &\left[\alpha_l(x)e^{-\partial_x} + \alpha_l(x+1)e^{\partial_x}\right]f_n(x;l) = \\ &= \left[\alpha_l(x)f_0(x-1;l)e^{\partial_x} + \alpha_1(x+1)f_0(x+1;l)e^{\partial_x}\right]u_n(x;l) = \\ &= f_0(x;l)\left[(x+l)e^{-\partial_x} + (l-x)e^{\partial_x}\right]u_n(x;l), \end{aligned} \tag{4.9}$$

where at the last step we employed the functional relations

$$f_0(x-1;l) = \tfrac{x=1}{\alpha_1(x)}f_0(x;l), \quad f_0(x+1;l) = \tfrac{l-x}{\alpha_l(x)}f_0(x;l),$$

for the "ground state" $f_0(x; l)$, which are easy consequences of the definition (4.8).

From difference equation (4.9) it is clear that the *Kravchuk polynomials* $n_n(x) = k_n^{1/2}(x+l;2l)$ (see below) are eigenfunctions of the operator $(x+l)e^{-\partial_x} + (l-x)e^{\partial_x}$ with the eigenvalues $\lambda_n(l) = 2(l-n)$. This means that we have explicitly constructed solutions of the difference equation (4.4) of the form

$$f_n(x;l) = d_n^{-1}\,\tfrac{k_n^{(1/2)}(x+l;2l)}{\sqrt{\Gamma(x+l+1)\Gamma(l+1-x)}}, \qquad 0 \leq n \leq 2l \tag{4.10}$$

which are associated with the eigenvalues $\lambda_n(l) = 2(l-n)$. The normalization constant $d_n = 2^{l-n}/[n!\,(2l-n)!]^{1/2}$ in (4.10) is chosen in such a way, that the eigenfunctions $f_n(x; l)$ satisfy the *discrete orthogonality relation*

$$\sum_{k=-1}^{l} f_m(k;l) f_n(k;l) = \delta_{m,n}. \qquad (4.11)$$

The reason for picking up this particular example of difference equation (4.4) is that it actually represents a *finite (or discrete) model* of the linear harmonic oscillator in quantum mechanics. We recall in this connection that the quantum-mechanical analogue of Newton's equation is $m\frac{dv}{dt} = -\frac{dU}{dx}$, where m is the mass $v = \frac{dx}{dt} = i\hbar^{-1}[\hat{H}, x]$ is the velocity operator, and $\hat{H} = p^2/2m + U(x)$ is the Hamiltonian [5]. For the linear harmonic oscillator, *i.e.*, when we have $U(x) = m\omega^2 x^2/2$, this equation takes the form

$$\left[\hat{H}, [\hat{H}, x]\right] = (\hbar\omega)^2 x. \qquad (4.12)$$

Now it is easy to check that the difference operator (compare with equation (4.4))

$$\hat{D}_l := \frac{1}{2}\left[\alpha_l(x) e^{-\partial x} + e^{\partial_x}\alpha_l(x)\right] \qquad (4.13)$$

satisfies the same commutation relation

$$\left[\hat{D}_l, [\hat{D}_l, x]\right] = x \qquad (4.14)$$

with the independent variable x as $\hat{H}/\hbar\omega$ in (4.12).

The main properties of the *Kravchuk polynomials* $k_n^{(p)}(x;N)$ are the following.
They are defined as:

$$k_n^{(p)}(x;N) = C_N^n (-p)^n \, {}_2F_1\,(-n; -x; -N; 1/p), \quad \text{n=1, 2, ……N,}$$

where $0<p<1$ and $C_N^n := N!/n!(N-n)!$ is the binomial coefficient;
They satisfy three-term recurrence relation:

$$[x - pN + (2p-1)n]k_n^{(p)}(x;N) = (n+1)k_{n+1}^{(p)}(x;N) + \\ + p(1-p)(N+1-n)k_{n-1}^{(p)}(x;N),$$

$$k_{-1}^{(p)}(x;N) = 0 \qquad k_0^{(p)}(x;N) = 1$$

They possess the symmetry property:

$$k_n^{(p)}(x;N) = (-1)^n k_n^{(1-p)}(N-x;N);$$

Limit relation as $N\to\infty$

$$\lim_{N\to\infty}\left[k_p^{(p)}(pN + x\sqrt{2p(1-p)N}; N)/(C_N^n)^{1/2}\right] = \sqrt{\frac{[p(1-p)]^n}{2^n n!}}\, H_n(x);$$

Difference equation:

$$\left[p(N-x)e^{\partial_x} + x(1-p)e^{-\partial_x}\right]k_n^{(p)}(x;N) = \\ = [x(1-2p) + pN - n]k_n^{(p)}(x;N);$$

Discrete orthogonality relation:

$$\sum_{j=0}^{N} p^j (1-p)^{N-j} C_N^j \, k_m^{(p)}(j;N) k_n^{(p)}(j;N) = [p(1-p)]^n C_N^n \delta_{m,n};$$

Generating function:

$$\left(1 - \frac{1-p}{p}t\right)^x (1+t)^{N-x} = \sum_{n=0}^{N} (-t/p)^n \, k_n^{(p)}(x;N).$$

5. CONTINUOUS *Q*-HERMITE POLYNOMIALS OF ROGERS

The continuous q-Hermite polynomials $H_n(x|\,q)$ of Rogers are those q-extensions of the ordinary Hermite polynomials $H_n(x)$, which are generated by the three-term recurrence relation

$$H_{n+1}(x|q) = 2xH_n(x|q) - (1-q^n)H_{n-1}(x|q), \\ 0<q<1, \qquad H_0(x|q) = 1, \quad n = 0, 1, 2, \ldots \qquad (5.1)$$

Recall that

$$H_{n+1}(x) = 2xH_n(x) - 2nH_{n-1}(x), \qquad H_0(x) = 1, \qquad n = 0, 1, 2, \ldots$$

The explicit form of $H_n(x|\,q)$ is exhibited by their Fourier expansion

$$H_n(x|q) = \sum_{k=0}^{n} \begin{bmatrix} n \\ k \end{bmatrix}_q e^{i(n-2)\theta}, \qquad x = \cos\theta, \qquad (5.2)$$

where $\begin{bmatrix} n \\ k \end{bmatrix}_q$ is the q-binomial coefficient,

$$\begin{bmatrix} n \\ k \end{bmatrix}_q := \frac{(q;q)_n}{(q;q)_k\,(q;q)_{n-k}} = \begin{bmatrix} n \\ n-k \end{bmatrix}_q, \qquad (5.3)$$

and $(a;\,q)_n$ is the *q-shifted factorial*,

$$(\alpha;q)_0 = 1, \qquad (\alpha;\,q)_n \prod_{k=0}^{n-1}(1-aq^k), \qquad n = 1, 2, 3, \ldots \quad (5.4)$$

Observe that if the parameter a in (5.4) is equal to q^{-N} with $N = 0;\, 1;\, 2;$ ....., then (compare that with the formula (3.4) for the shifted factorial $(-n)_k$)

$$(q^{-N};q)_n = \begin{cases} (-1)^n \; q^{n(n-1-2N)/2}, & 0 \le n \le N, \\ 0, & n > N. \end{cases} \qquad (5.5)$$

This circumstance enables one to write another explicit formula for the continuous q-Hermite polynomials $H_n(x|\,q)$ of Rogers in terms of the *basic hypergeometric polynomials* :

$$H_n(x|q) = e^{in\theta} \, {}_2\phi_0(q^{-n}, 0; q; q^n e^{-2i\theta}) = \\ = e^{in\theta} \sum_{k=0}^{n-1} \frac{(q^{-n};q)_k}{(q;q)_k} (-1)^k q^{k[n+(1-k)/2]} e^{-2ik\theta}. \qquad (5.6)$$

Although the continuous q-Hermite polynomials were introduced by Rogers back in 1894 in [6], their orthogonality property on the finite interval $x\in[-1;\,1]$

$$\frac{1}{2\pi}\int_{-1}^{1} H_m(x|q) H_n(x|q) \frac{\omega(x|q)}{\sqrt{1-x^2}} dx = \frac{\delta_{mn}}{(q^{n+1};q)_\infty} \qquad (5.7)$$

was established by Szegö only in 1926 [7]. The weight function in the orthogonality relation (5.7) can be expressed in terms of the classical theta-function

$$\vartheta_1(z,q) := 2q^{\frac{1}{4}} \sum_{n=0}^{\infty} (-1)^n \, q^{n(n+1)} \sin(2n+1)\, z = \\ = \frac{q^{\frac{1}{4}}}{2\sin z}(q^2;q^2)_\infty (e^{2iz};q^2)_\infty (e^{-2iz};q^2)_\infty, \quad |q| < 1, \quad (5.8)$$

in the following way

$$\frac{\omega(x|q)}{\sqrt{1-x^2}} = \frac{2}{q^{1/8}(q;q)_\infty}\vartheta_1(\theta, q^{1/2}), \qquad x = \cos\theta.$$

The linear generating function for the polynomials $H_n(x|\,q)$ is of the form

$$\sum_{n=0}^{\infty}\frac{t^n}{(q;q)_n}H_x(x|q) = e_q\left(te^{i\theta}\right)e_q\left(te^{-i\theta}\right), \qquad x = \cos\theta \quad (5.9)$$

where $e_q(z)$ is the q-exponential function, defined as

$$e_q(z) := \sum_{n=0}^{\infty}\frac{z^n}{(q;q)_n} = \frac{1}{(z;q)_\infty}. \qquad (5.10)$$

Remark 4. We emphasize that it is not hard to derive (5.9) exactly in the same way as its classical counterpart (3.5). Indeed, one just substitutes the explicit form (5.2) of the polynomials $H_n(x|\,q)$ into the left side of (5.9) and then uses (5.3) to show that

$$\begin{aligned}\sum_{n=0}^{\infty}\frac{t^n}{(q;q)_n}H_n\left(x\,\middle|q\right) &= \sum_{n=0}^{\infty}\left(te^{i\theta}\right)^n\sum_{k=0}^{n}\frac{e^{-2ik\theta}}{(q;q)_k(q;q)_{n-k}}\\ &= \sum_{k=0}^{\infty}\frac{e^{-2ik\theta}}{(q;q)_k}\sum_{n=k}^{\infty}\frac{\left(te^{i\theta}\right)^n}{(q;q)_{n-k}}\\ &= \sum_{k=0}^{\infty}\frac{e^{-2ik\theta}}{(q;q)_k}\sum_{m=0}^{\infty}\frac{\left(te^{i\theta}\right)^{m+k}}{(q;q)_m}\\ &= \sum_{k=0}^{\infty}\frac{\left(te^{-i\theta}\right)^k}{(q;q)_k}\sum_{m=0}^{\infty}\frac{\left(te^{i\theta}\right)^m}{(q;q)_m}\\ &= e_q\left(te^{i\theta}\right)e_q\left(te^{-i\theta}\right),\end{aligned}$$

upon employing an evident summation formula $\sum_{k=0}^{\infty}\sum_{k=0}^{n}f(n,k) = \sum_{k=0}^{\infty}\sum_{n=k}^{\infty}f(n,k)$ for an arbitrary function $f(n,k)$.

In the limit as the deformation parameter q tends to 1, the q-Hermite polynomials $H_n(x|\,q)$ reduce to the ordinary Hermite polynomials $H_n(x)$:

$$\lim_{q\to 1^-}\frac{H_n\left(\sqrt{\frac{1-q}{2}}x|q\right)}{\left(\sqrt{\frac{1-q}{2}}\right)^n} = H_n(x). \qquad (5.11)$$

It should be also recalled that to consider the continuous q-Hermite polynomials $Hn(x|\,q)$ for the values of the parameter q in the interval $[1;\infty)$, it is customary to introduce the so-called continuous q^{-1}-Hermite polynomials

$$h_n(x|q) := i^{-n}H_n(ix|q^{-1}). \qquad (5.12)$$

In view of the inversion formula·

$$\begin{bmatrix}n\\k\end{bmatrix}_{q^{-1}} = q^{k(k-n)}\begin{bmatrix}n\\k\end{bmatrix}_q$$

for the q-binomial coefficient (5.3), from (5.2) one readily deduces that

$$h_n(\sin h\,\chi|q) = \sum_{k=0}^{n}(-1)^k\,q^{k(k-n)}\begin{bmatrix}n\\k\end{bmatrix}_q e^{(n-2k)\chi} \qquad (5.13)$$

It is important to observe that in order to be able to formulate adequately transformation properties of the q-Hermite and q^{-1}-Hermite polynomials $H_n(x|\,q)$ and $h_n(x|\,q)$ with respect to the Fourier transforms one has to employ the following nonconventional parametrization for their argument x:

$$\begin{aligned}x = \cos\theta = \sin ks, \qquad \theta = \frac{\pi}{2} - ks, \qquad 0 < q < 1;\\ x = \sin h\,\chi = \sin h\,ks, \quad \chi = ks, \quad 1 < q < \infty \end{aligned} \qquad (5.14)$$

In both cases above $k := \sqrt{lnq^{-1/2}}$, equivalently, $q := e^{-2k^2}$. Thus, formulas (5.2) and (5.13) are representable as expansions

$$H_n(\sin ks|q) = i^n\sum_{k=0}^{n}(-1)^k\begin{bmatrix}n\\k\end{bmatrix}_q e^{i(2k-n)ks} \qquad (5.15)$$

$$h_n(\sin ks|q) = \sum_{k=0}^{n}(-1)^k\begin{bmatrix}n\\k\end{bmatrix}_q q^{k(k-n)}e^{(n-2k)ks} \qquad (5.16)$$

which were key relations in establishing that the Fourier integral transform interrelates q-Hermite and q^{-1}-Hermite polynomials. This integral transform has the form [9]:

$$\frac{1}{\sqrt{2\pi}}\int_{\mathcal{R}} e^{ixy-\frac{x^2}{2}}H_n(\sin kx|q)dx = i^n\,q^{n^2/4}h_n(\sin h\,ky|q)e^{-y^2/2} \qquad (5.17)$$

A more detailed discussion of this remarkable transformation property of the continuous q-Hermite polynomials of Rogers with respect to the Fourier integral transform can be found in [10].

Finally, the continuous q-Hermite polynomials $Hn(\sin ks|\,q)$ satisfy the q-difference equation

$$\left[e^{iks}e^{-ik\partial_x} + e^{-iks}e^{ik\partial_x}\right]H_n(\sin ks|\,q) = 2q^{-n/2}\cos ksH_n(\sin ks|\,q) \qquad (5.18)$$

where $\partial_x = \frac{d}{dx}$ and $e^{\pm ik\,d_s}$ are shift operators $e^{\pm ik\,d_s}f(s) = f(s \pm ik)$. We recall that this simple q-difference equation for the continuous q-Hermite polynomials $H_n(\sin ks|q)$ is a direct consequence of Rogers' linear generating function (5.9). But it is not difficult to verify the validity of this q-difference equation by using an explicit form of the polynomials $Hn(\sin kx|q)$.

In the case when the parameter q lies in the interval $[1;\infty)$, the q-difference equation (5.18) takes the form

$$\left[e^{iks}e^{-ik\partial_s} + e^{-iks}e^{ik\partial_s}\right]H_n(\sin ks|q) = 2q^{-n/2}\cos ksH_n(\sin ks|q) \qquad (5.18)$$

Valuable background material about these two difference equations (5.18) and (5.19) for the continuous q-Hermite and $q¡1$-Hermite polynomials, respectively, can be found in [11] and [12].

Thus, the main properties of the *continuous q-Hermite polynomials of Rogers* are:

Explicit formula

$$H_n(x|q) = e^{in\theta}\,{}_2\phi_0\left(q^{-n},0;q\,;q^ne^{-2i\theta}\right) = \sum_{k=0}^{n}\begin{bmatrix}n\\k\end{bmatrix}_q e^{i(n-2k)\theta}, \qquad x = \cos\theta;$$

Three-term recurrence relation

$$H_{n+1}(x|q) = 2xH_n(x|q) - (1-q^n)H_{n-1}(x|q),$$

$0 < q < 1, \qquad H_0(x|q) = 1, \qquad n = 0, 1, 2, \ldots;$

Orthogonality property on the finite interval $x \in [-1;\,1]$

$$\frac{1}{2\pi}\int_{-1}^{1} H_m(x|q)H_n(x|q)\frac{\omega(x|q)}{\sqrt{1-x^2}}dx = \frac{\delta_{mn}}{(q^{n+1};q)_\infty},$$

$$\frac{\omega(x|q)}{\sqrt{1-x^2}} = \frac{2}{q^{1/8}(q;q)_\infty}\vartheta_1(\theta, q^{1/2}), \qquad x = \cos\theta;$$

Linear generating function

$$\sum_{n=0}^{\infty}\frac{t^n}{(q;q)_n}H_n(x|q) = e_q(te^{i\theta})e_q(te^{-i\theta}) \qquad x=\cos\theta;$$

Limit relation

$$\lim_{q\to 1^-}\frac{H_n\left(\sqrt{\frac{1-q}{2}}x|q\right)}{\left(\sqrt{\frac{1-q}{2}}\right)^n} = H_n(x);$$

q-difference equation

$$\left[e^{iks}e^{-ik\partial_s} + e^{-iks}e^{ik\partial_s}\right]H_n(\sin ks|q) = 2q^{-n/2}\cos ksH_n(\sin ks|q);$$

Fourier integral transform

$$\frac{1}{\sqrt{2\pi}}\int_{\mathcal{R}} e^{ixy-\frac{x^2}{2}}H_n(\sin kx|q)dx = i^n q^{n^2/4}h_n(\sin kx|q)dx = \\ = i^n q^{-n/2}h_n(\sin ky|q)e^{-y^2/2}.$$

6 FINITE FOURIER TRANSFORM

We recall that the *finite (discrete) Fourier transform (FFT)* is defined as an action of the operator (or the equivalent $N \times N$ unitary symmetric matrix $\boldsymbol{\Phi}^{(N)} = \left\|\boldsymbol{\Phi}_{m,m'}\right\|$ with elements (see, for example, [13])

$$\Phi^{(N)}_{m,m'} = \frac{1}{\sqrt{N}}exp\left(\frac{2\pi i}{N}mm'\right) = \frac{1}{\sqrt{N}}q^{mm'},$$
$$q := e^{\frac{2\pi i}{N}}, \qquad m, m' \in \{o, 1, \dots\dots, N-1\}. \qquad (6.1)$$

Its eigenvectors $\boldsymbol{f}(n)$ with components $\left\{f_k^{(n)}\right\}_{k=0}^{N-1}$ are solutions of the standard equations

$$\sum_{m=0}^{N-1}\Phi^{(N)}_{m,m'}f^{(n)}_{m'} = \lambda_n f^{(n)}_m, \qquad n \in \{0, 1, \dots..N-1\}. \qquad (6.2)$$

Since the fourth power of $\Phi^{(N)}$ is the identity operator (or matrix), the only four distinct eigenvalues among λ_n are ±1 and ±i. Observe that the relations (6.2) can be regarded as a discrete analogue of the continuous case where the Hermite functions $H_n(x)e^{-x^2/2}$ are constant multiples of their Fourier transform.

The finite Fourier transform (6.1) appears in various mathematical problems and has been studied in detail. In particular, Schur was the first who determined the eigenvalues of $\boldsymbol{\Phi}^{(N)}$ in order to compute the trace of $\boldsymbol{\Phi}^{(N)}$ or the quadratic Gauss sum.

The finite Fourier transform (6.1) has deep roots in classical pure mathematics and we briefly recall here only one aspect of this close connection [14].

It is easy to evaluate a sum of the first N terms of the geometric series, $S_N^{(n)}(x) := \sum_{k=0}^{N-1}x^k$, since the characteristic
form of this series allows one to represent $S_N(x)$ in two different ways: as $S_N(x) = S_{N-1}(x) + x^{N-1}$ or $S_N(x) = 1 + xS_{N-1}(x)$. By equating then these two expressions, we deduce that

$$S_N(x) = \frac{1-x^N}{1-x}.$$

But if one tries to deal with the sequence $\left\{x^{k^n}\right\}_{k=0}^{\infty}$, where n is an integer greater than one, then the task of evaluating the sum $S_N^n(x) := \sum_{k=0}^{N-1}x^{k^n}$ becomes considerably more difficult.

For simplicity let us discuss here how one can treat the case $n = 2$. The trace of the matrix $\Phi_{jk}^{(N)}$ is equal to

$$tr\,\Phi_{jk}^{(N)} := \sum_{k=0}^{N-1}\Phi_{kk}^{(N)} = \frac{1}{\sqrt{N}}\sum_{k=0}^{N-1}exp\left(\frac{2\pi i}{N}k^2\right) = \frac{1}{\sqrt{N}}S_N^{(2)}(e^{2\pi i/N}). \quad (6.3)$$

On the other hand, if we know N eigenvalues λ_J of the matrix $\Phi_{jk}^{(N)}$, then the trace of $\Phi_{jk}^{(N)}$ is equal to the sum $\sum_{k=}^{N-1}\lambda_j$ of these eigenvalues. So in this way one expresses the quadratic sum $S_N^{(2)}(e^{2\pi i/N})$ through the eigenvalues λ_j of the FFT matrix $\Phi_{jk}^{(N)}$.

Gauss had studied and solved the problem of the eigenvalues of the finite Fourier transform. He established that

$$S_N^{(2)}\left(e^{\frac{2\pi i}{N}}\right) = \begin{cases}\sqrt{N}, & if \quad N \equiv 1(mod\ 4),\\ i\sqrt{N}, & if \quad N \equiv\ 3(mod\ 4),\end{cases} \qquad (6.4)$$

when N is an odd positive integer and $S(2)$ for all even positive integer values of N. Observe that formulas (6.3) and (6.4) provide a lucid illustration of how is convenient to express some properties of the FFT interms of basic notions of number theory.

Later Dirichlet, Cauchy, Kronecker, and Schur have essentially contributed into a better understanding of this intimate connection between quadratic Gauss sums and the finite Fourier transform.

Mehta studied the eigenvalue problem (6.2) and found analytically a set of eigenvectors $f^{(l)}(j) = F_{jl}^{(N)}$ of the finite Fourier transform (6.1) of the form [15]

$$F_{jk}^{(N)} := \sum_{n=-\infty}^{\infty}e^{-\frac{\pi}{N}(nN+j)^2}N_k\sqrt{\frac{2\pi}{N}}(nN+j), \qquad (6.5)$$

where $H_k(x)$ is the ordinary Hermite polynomial of degree k in the variable x. These Mehta eigenvectors $F_{jl}^{(N)}$ correspond to the eigenvalues , $\lambda_l = i^l$, that is,

$$\sum_{i=0}^{N-1}\Phi_{jl}^{(N)}F_{lk}^{(N)} = i^k F_{jk}^{(N)}, \qquad 0 \le j, k \le N-1 \qquad (6.6)$$

The eigenfunctions (6.5) are real and naturally periodic with period N. So Mehta in fact explicitly constructed the discrete analogue of the well-known continuum case where the Hermite functions $H_k(x)\exp(-x^2/2)$ are constant multiples of their own Fourier transforms.

Once the Fourier integral transform (5.17) is known, it is natural to look for its finite analogue. We recall that in the proof of (6.6) for Mehta's eigenvectors $F^{(N)}$ of the FFT it was essential to use the simple transformation property of the Hermite functions $H_k(x)\exp(-x^2/2)$ under the Fourier integral transform.

So in [16] it was shown that one can actually employ Mehta's technique to prove that the q-extensions of Mehta's eigenvectors $F^{(N)}$ of the form

$$F_{mn}^{(N)}(q) := \sum_{k=-\infty}^{\infty} exp\left[-\frac{1}{2}(x_k(m))^2\right] H_n(sinkx_k(m)|q), \quad (6.7)$$

$$F_{mn}^{(N)}(q^{-1}) := i^n \sum_{k=-\infty}^{\infty} exp\left[-\frac{1}{2}(x_k(m))^2\right] h_n(\sin h\, kx_k(m)|q), \quad (6.8)$$

given by the continuous q-Hermite polynomials $H_n(x|q)$ of Rogers at the points

$$x_k^{(N)}(m) := \sqrt{\frac{2\pi}{N}}(kN+m),$$

also enjoy simple transformation properties with respect to the FFT (6.1). Thus, the FFT (6.1) interrelates two q-extensions of the Mehta eigenvectors (6.5),

$$\sum_{m=0}^{N-1} \Phi_{jm}^{(N)} F_{mk}^{(N)}(q^{-1}) = e^{\frac{k^2}{4}} F_{jk}^{(N)}(q). \quad (6.9)$$

defined by (6.7) and (6.8), respectively.

Similarly, one may begin with the Fourier expansion for the q-extended Mehta eigenvectors $F^{(N)}(q)$ in order to verify that

$$\sum_{m=0}^{N-1} \Phi_{jm}^{(N)} F_{mk}^{(N)}(q) = q^{k^2/4} F_{jk}^{(N)}(q). \quad (6.10)$$

Since the parameters q and N are *independent* here, from (6.7) and (6.8) one readily verifies, that the Mehta eigenvectors (6.5) are regained in the limit as $q \to 1^-$,

$$\lim_{q\to 1^-}\left[k^{-n} F_{jk}^{(N)}(q)\right] = F_{jk}^{(N)} = i^{-n} \lim_{q\to 1^-}\left[k^{-n} F_{jk}^{(N)}(q^{-1})\right],$$

and both relations (6.7) and (6.8) reduce to (6.6). Also, the continuous limit as $N \to 1$ returns the Fourier integral transform (5.17) and its inverse, respectively.

Once the FFT (6.9) and (6.10) are known, it is not difficult to explicitly determine eigenvectors of the FFT (6.1)
in terms of the two q-extensions (6.7) and (6.8) of the Mehta eigenvectors (6.5). The details are given more completely in [17].

ACKNOWLEDGMENTS

Discussions with Shakir Nagiyev and Elchin Jafarov are gratefully acknowledged.

[1]. *A.F.Nikiforov, S.K.Suslov and V.B.Uvarov*, Classical Orthogonal Polynomials of a Discrete Variable, Springer, Verlag, Berlin, Heidelberg, 1991.

[2]. *S.L.Ross*, Differential Equations, Xerox College Publishing, Lexington, Massachusetts, 1974.

[3]. *G.Gasper and M.Rahman*, Basic Hypergeometric Functions, Second Edition, Cambridge University Press, Cambridge, 2004.

[4]. *G.E.Andrews, R.Askey and R.Roy*, Special Functions, Cambridge University Press, Cambridge, 1999.

[5]. *L.D.Landau and E.M.Lifshitz*, Quantum Mechanics (Non-relativistic Theory), Pergamon Press, Oxford, 1991.

[6]. *L.J.Rogers*, Second memoir on the expansion of certain infinite products, Proc. Lond. Math. Soc., 25, 318{43,1894.

[7]. *G. Szegő*. Ein Beitrag zur Theorie der Thetafunktionen, Sitzangsberichte der Preussischen Akademie der Wissenschaften, Phys.-Math. Klasse, 19, 242{252, 1926; reprinted in Collected Papers (R.Askey, ed.), 1, 795{805,BirkhÄauser, Boston, MA, 1982.

[8]. *R.Askey*, Continuous q-Hermite polynomials when q > 1, In q-Series and Partitions, Ed. by D. Stanton, The IMA Volumes in Mathematics and Its Applications, 18, 151{158, Springer-Verlag, New York, 1980.

[9]. *N.M.Atakishiyev and Sh.M.Nagiyev*, On the wave functions of a covariant linear oscillator, Theor. Math. Phys.,98, 162{166, 1994.

[10]. *N.M.Atakishiyev*, Fourier{Gauss transforms of some q-special functions, CRM Proceedings and Lecture Notes, 25, 13{21, American Mathematical Society, Providence, Rhode Island, 2000.

[11]. *M.K.Atakishiyeva and N.M.Atakishiyev*, Fourier-Gauss transforms of bilinear generating functions for the continuous q-Hermite polynomials, Physics of Atomic Nuclei, 64, 2086{2092, 2001.

[12]. *M.N.Atakishiyev and A.U.Klimyk*, On factorization of q-difference equation for continuous q-Hermite polynomials, J. Phys. A: Math. Theor., 40, 9311{9317, 2007.

[13]. *A.Terras*, Fourier Analysis on Finite Groups and Applications, Cambridge University Press, Cambridge, 1999.

[14]. *N.M.Atakishiyev*, On q-extensions of Mehta's eigenvectors of the finite Fourier transform, Int. J. Mod. Phys. A,21, 4993{5006, 2006.

[15]. *M.L.Mehta*, Eigenvalues and eigenvectors of the finite Fourier transform, J. Math. Phys., 28, 781{785, 1987.

[16]. *N.M.Atakishiyev, D.Galetti and J.P.Rueda*, On relations between certain q-polynomial families, generated by the finite Fourier transform, International Journal of Pure and Applied Mathematics, 26, 275{284, 2006.

[17]. *N.M.Atakishiyev, J.P.Rueda and K.B.Wolf*, On q-extended eigenvectors of the integral and finite Fourier transforms, J. Phys. A: Math. Theor., 40, 12701{12707, 2007.

ABOUT THE MECHANISM OF THALLIUM IMPURITY INFLUENCE ON ELECTRIC PROPERTIES OF THE PbTe

G.A.AHMEDOVA, D.Sh.ABDINOV
Institute of Physics of Azerbaijan National Academy of Sciences,
Baku, Az-1143, H.Javid ave., 33, Baku, Azerbaijan
gulgun_ahmed@yahoo.com

It is found out, that values of the electric parameters of PbTe single crystals samples and dependence character of these parameters on temperature and concentration of Tl impurity, as well as on the type of the conductivity of crystals (a sign α and R) are essentially determined by their prefiring temperature. It is explained, by the fact that with growth of the annealing temperature, concentration of the double charged vacancies in the tellurium sub lattice, rises increasing a probability of formation of electroneutral or singly charged complexes of impurity atom-vacancy type.

1. INTRODUCTION

Thallium impurities in lead chalcogenide , including in PbTe are deep acceptors [1-5]. Thus, it is found out that up to certain concentration of the thallium (for PbTe up to 9×10^{19} cm^3) [2, 5] Hall concentration of the holes (*p)* at 77 K increases proportionally N_{Tl} , and each Tl atom creates one hole in the valent zone. In the field of the high concentration of the thallium, function $p(N_{Tl})$ at T=77 K shows the saturation tendency, and limiting concentration of the holes (~ $1{,}2\times10^{20}$-5×10^{19} cm^3) a few times lower solubility Tl in lead chalcogenide. Such dependence p from N_{Tl} are explained by self-compensation acceptor actions of the thallium with intrinsic defects in these compounds [5, 7].

Concentration of the structural defects depends on real structure (poly-or single crystallizing) of the sample, as well as, a mode of their thermal processing [8, 9]. Data [5, 7] were received in the polycrystalline samples of the PbTe received by a metal-ceramic method and subjected homogenizing at the temperature 650 ^{0}C within 100 hours.

Therefore, for reception information of the Tl impurity action mechanism on electric properties PbTe, in the current work, investigated PbTe single crystals samples with impurity Tl, past preliminary thermal processing at the temperatures 473, 573, 673, 873 K.

2. EXPERIMENTAL

The PbTe single crystals with various concentration of the Tl were grown by the Bridgman method from the stoichiometric melt. The technological parameters for the synthesis and growing of the PbTe single crystals are presented in [10].The samples were single crystalline, which was confirmed by the X-ray method.

The samples for research as a rectangular parallelepiped with the geometrical sizes 3x5x12 mm were cut out from single crystal ingots on electro erosive installation. The electrical parameters were measured using the dc probe method along the large face (length) of the sample.

The samples were annealed in spectrally pure argon atmosphere for 120 hours.

3. RESULTS AND DISCUSSION

Results of the measurements thermal processing influence on electroconductivity *(σ)*, thermopower *(α)* and the Hall *(R)* factors of pure PbTe single crystal samples, are presented on fig. 1. It is seen, that σ dependence on temperature for samples both an unannealed and annealed at 473, 573 K at low temperatures possess semiconductor character. Thus with growth of temperature of annealing, a temperature interval in which semi-conductor character σ *(T)* is observed is narrowed. The samples that past heat treatment at 673 and 873 K σ *(T)* possess metal character (fig. 2). A sign of α is a positive for the samples which σ *(T)* possessing semiconductor character at low temperatures and with increasing of the temperature absolute value of α increases. The sign of thermopower factor of the samples that past heat treatment at 673K, up to ~ 230 K is negative, and higher than this temperature is positive. The samples annealed at 873 K possess *n-type* conductivity whole temperatures interval and in this case absolute value of α with increasing of temperature rises. The similar (as in a case α) results are observed as well as on Hall factor. These results testify that values and character of temperature dependence of electric parameters, as well as, type of conductivity of the PbTe single crystal samples are essentially determined by heat treatment temperature which they passed. Interesting results are received also influence of thallium on the electric properties of PbTe single crystals that past heat treatments at various temperatures.

In fig.3 presented dependences of concentration of the current carriers *(a)* and electroconductivity *(b)* from concentration of the thallium, for the samples which annealed at various temperatures. It is seen, that in these cases dependences characters of $n\ (N_{Tl})$ and $\sigma(N_{Tl})$ are different for the samples annealed at various temperatures. In the unannealed samples up to concentration $N_{Tl}=0{,}01$ at. % Hall concentration and electroconductivity increase proportionally N_{Tl} at 77 K.

In the field of the high concentration of the thallium, function $n\ (N_{Tl})$ and $\sigma\ (N_{Tl})$ at 77 K display tendency to saturation. Such dependences are completely according to results of the works [5-7, 11-13] and can be explained by the phenomenon of self-compensation acceptor actions of

the thallium with intrinsic defects in PbTe suggested in these works.

With increasing temperature of annealing, σ increases and n reduces at low concentration of Tl (up to ~ 0,01 at. %), and after temperatures of annealing 673 and 873 K when contents Tl more 0,01 at. % with increasing concentration of the last
σ and n decrease.

Factors α and R for the samples with an impurity of the thallium that annealed at 673 and 873 K have negative sign at 77 K. Thus, the sign α and R for the samples annealed at 673 K, higher than 165-230 K and 260-230 K temperature (depending on concentration Tl) changing to positive, varies to positive, and in a case annealing at 873 K the sign of α and R are negative in all the investigated interval of temperatures.

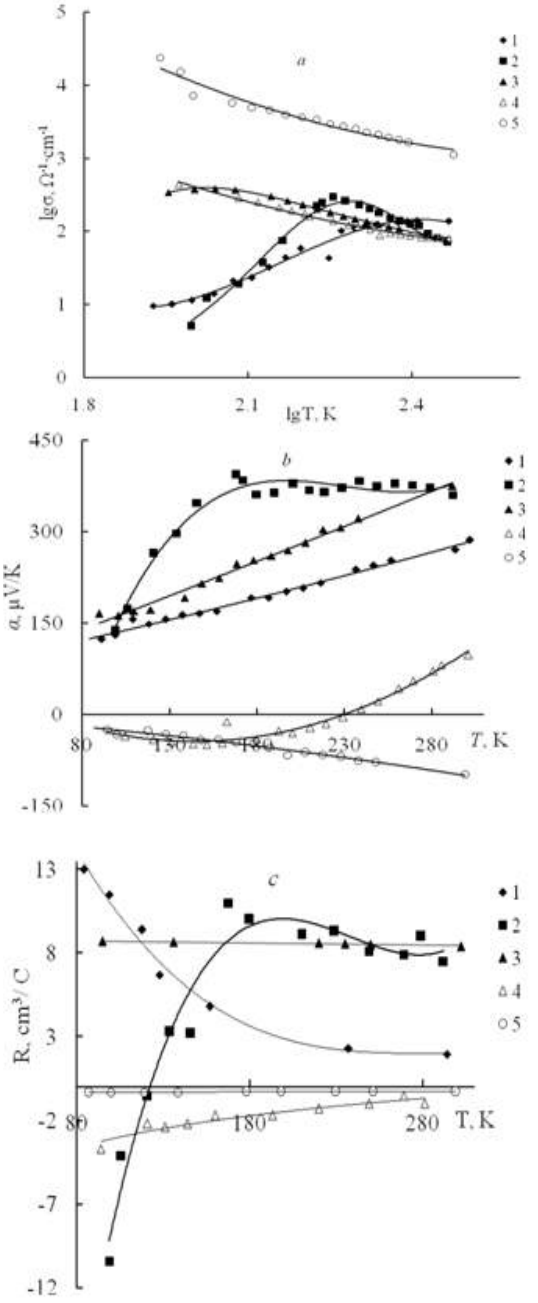

Fig.1. Temperature dependence of electrical conductivity (*a*), thermo-e.m.f (*b*) and Hall factor (*c*) of PbTe single crystals. Curves 1-5 refers to the sample unannealed and samples annealed at 473, 573,673, 873 K respectively.

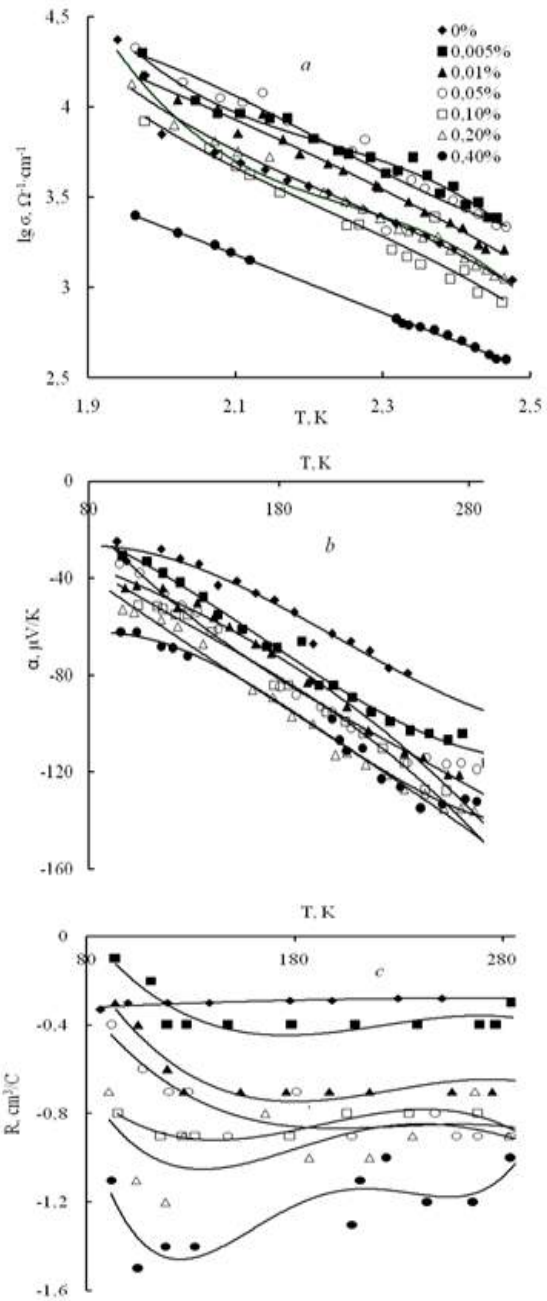

Fig.2.Temperature dependence of electrical conductivity (*a*), thermo-e.m.f (*b*) and Hall factor (*c*) of samples PbTe single crystals doped by Tl, annealed at 873K.

σ *(T)* dependence for all samples PbTe with Tl impurity annealed above than 473 K has metal character.

The reduction of σ and n with growth of concentration Tl in the samples annealed at 673 and 873 K cannot be explained only self-compensation of Tl impurity. Therefore, for an explanation of the received results, the following mechanism is supposed. While heat treatment of the samples, with parallel removal of the deformation defects arising at growth PbTe single crystals, occurs also a new vacancies formation in the tellurium sub lattice [8, 9].

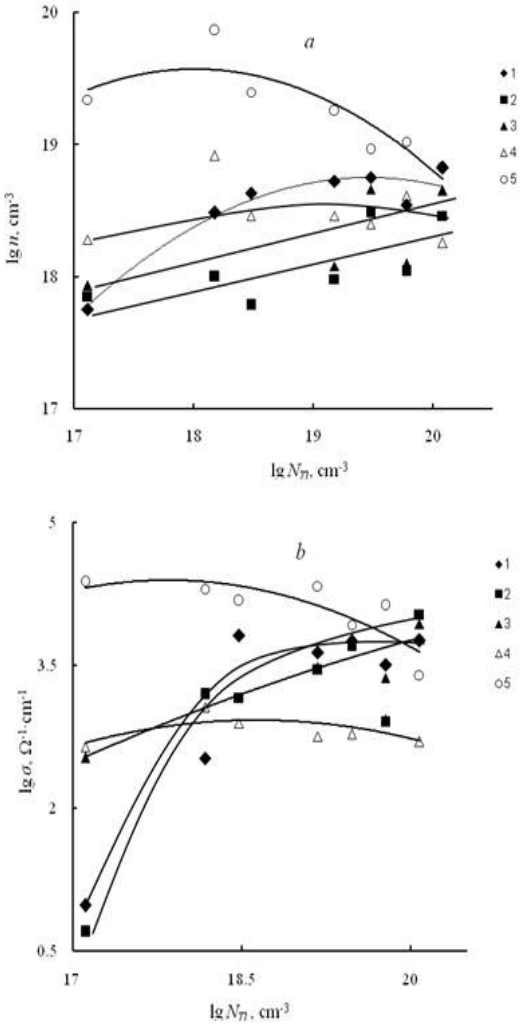

Fig.3. Dependence of concentration of charge carriers *(a)* and electrical conductivity *(b)* on concentration of thallium in PbTe single crystals at ~ 77 K. Curves 1-5 refers to the sample unannealed and samples annealed at 473, 573,673, 873 K respectively.

With growth of annealing temperature, this process, i.e. process of occurrence of vacancies in the tellurium sub lattice amplifies. It carries increase of concentration of vacancies in Te sub lattice with increasing of annealing temperature. With increasing concentration of vacancies in tellurium sub lattice, concentration of the electrons in the sample increases also. Therefore, with heat treatment, value both σ and n increases, $\sigma(T)$ get metal character, and α and R signs become negative at low temperatures. On the other hand, with increasing concentration of vacancies, the probability of the formation electro-neutral (two thallium atoms with one vacancy) or single charged (one thallium atom with one vacancy) impurity atom - vacancy type complexes increases also. Both processes will be accompanied by reduction concentration of electrons in the sample and reduction value of σ at the given temperature. Thus, probably there is also self-compensation of Tl impurity. However, apparently, process of formation electro neutral or single charged complexes impurity - vacancy prevails of process of self-compensation.

4. CONCLUSIONS

It is found out, that values of the electric parameters of PbTe single crystals samples and dependence character of these parameters on temperature and concentration of Tl impurity, as well as on the type of the conductivity of crystals (a sign α and R) are essentially determined by their prefiring temperature. It is explained, by the fact that with growth of the annealing temperature, concentration of the double charged vacancies in the tellurium sub lattice, rises increasing a probability of formation of electroneutral or singly charged complexes of impurity atom-vacancy type.

[1]. *A. N. Veys, A.S.Nemov, V. A.Polovkin and Yu.Ukhanov*, Fiz. Tekh. Poluprovodn. 11(5), 669 (1977)

[2]. *A. N. Veys, V.I.Kaydanov, A.S.Nemov, S.N. Yemelin, A.Ya Ksendzov, and Yu.K.Shalabutov*, Fiz. Tekh.Poluprovodn. 13(1), 185 (1979)

[3]. *V.I.Kaydanov, R.B.Melnik and A.S.Nemov*, Fiz. Tekh.Poluprovodn. 13(5), 1011 (1979)

[4]. *V.I.Kaydanov, A.S.Nemov and Yu. I. Ravich*, Fiz. Tekh. Poluprovodn. 26(2), 201, (1992)

[5]. *A.S.Nemov , Yu. I. Ravich*, Usp. Fiz. Nauk 168 (8), 817 (1998)

[6]. *L.I. Bitinskiy, V.I.Kaydanov, R.B.Melnik, A.S.Nemov and Yu. I. Ravich*, Fiz. Tekh. Poluprovodn. 14(1), 74, (1980)

[7]. *V.I.Kaydanov, A.S.Nemov and Yu. I. Ravich*, Fiz. Tekh. Poluprovodn. 28(3), 369, (1994)

[8]. *S. S. Gorelik and M. Ya. Dashevskii, Materials Science of Semiconductors and Insulators* (Moscow, Metallurgiya, 1988) [in Russian].

[9]. *G. A. Akhmedova, G. Z. Bagieva, Z. F. Agaev, and D. Sh. Abdinov*, Fiz. Tekh. Poluprovodn. 43(11), 1456 (2009)

[10]. *Z. F. Agaev, E.M.Allahverdiyev, Q.M.Murtuzov and D. Sh. Abdinov*, Neorgan.mat. 39(5), 543 (2003)

[11]. *M.K. Jitinskaya, V.I. Kaydanov, S.A.Nemov and L.A.Afanasyeva*, Fiz. Tekh. Poluprovodn. 22(11), 2043 (1988)

[12]. *L.I.Bitenskiy, V.I. Kaydanov, R.B.Melnik, S.A.Nemov and Yu.I.Ravich*, Fiz. Tekh. Poluprovodn. 15(5), 981 (1981)

[13]. *L.I.Bitenskiy, V.I. Kaydanov, V.P. Makeenko, R.B.Melnik and S.A.Nemov*, Fiz. Tekh. Poluprovodn. 18(3), 489 (1984)

$A^{III}_2B^{VI}_3$ THIN FILMS PREPARATION by Sol-Gel TECHNIQUE

MAHARRAM Z. ZARBALIYEV
Institute of Physics, National Academy of Sciences,
Azerbaijan, AZ1143, Baku, Azerbaijan
Department of Physics Harran University,
63400, Sanliurfa, Turkey
Adress: e-mail: mzarbaliyev@gmail.com
Tel: +90 539 4301733

In this work describe the preparation attempting of $A^{III}_2B^{VI}_3$ (In_2Se_3 and Ga_2Se_3) semiconductor compounds thin films on glass substrate by sol-gel method. The samples were characterized by X-ray diffraction analyses (XRD), UV-Visible spectrometer. XRD study and optical absorption spectrums show that fabricated thin films formed mainly as an In_2Se_3 and Ga_2Se_3 crystal structure. The band gap energy value estimating from optical absorption spectrums for the In_2Se_3 thin films were about E_g ~1.24 eV and the Ga_2Se_3 thin films were about E_g ~2.56 eV.

1. INTRODUCTION

The research of cheep methods on solar energy convertors are not decrease today and on this sense investigating on preparation and mass-fabrication of semiconductor devices where used $A^{III}_2B^{VI}_3$ compounds are becomes even more important**.** The using of these materials in new technologies increases the specified importance even more. For example to it is informed that In_2Se_3 thin films can be used for optoelectronic applications and nonvolatile memory devices [1]. The Ga_2Se_3 compound used as substrate-compatible heteroepitaxial thin films[2,3,4] and it is informed on behavior of a natural subnano scale quantum wire properties[2]. On the other hand it is attractive that the preparation of $A^{III}_2B^{VI}_3$ compounds thin films by simple method will by lay the new way to preparation on ternary $M^IA^{III}B_2^{VI}$ (M=Cu, Ag ; A=In, Ga ; B=Se, S) compounds thin films which already very important materials for solar energy conversation. The many of current papers confirmed high efficiency solar energy conversation of the up stated ternary thin films prepared using different complicated technologies which were very expensive.

Preparation of the $A^{III}_2B^{VI}_3$ compounds thin films using by sol-gel method a can be appreciated that more suitable for solar energy conversation.

Sol-gel principles

The Sol-Gel prosessing as a interdissiplinary science branch are include on investigation of percolation theory, condensation mechanizm and conditions in chemistry which has mainly found application in ceramic processesings. Further distribution of this method is observed on to wide investigation areas as a powdwrs, thin films and so on. Process of the preparation a thin films by sol-gel method consists of two stages. The first step is receiving of a demanded solution which contain the ions of chosen material and the second step the derivation of thin films of material from the specified solution on the necessary substrates. Further it is carried out prosess drying and gelation with formation of chemical compound. Further a description of the above-stated steps on receiving of In_2Se_3 and Ga_2Se_3 thin films is resulted.

2. EXPERIMENTAL

The In_2Se_3 and Ga_2Se_3 thin film samples were prepared as deep coating technique by withdrawing from correspondent solution extract. Thin films preparation by sol-gel method mainly depends on solution pH parameter, viscosity of solution, and a withdrawal rate. Drying and gelation process of thin films were formed in a vertical displaced bake, where a temperature gradient changed from room to desired temperature. The XRD spectra were obtained using a Rigaku Ultima III unit (CuKα, 40 kV, 30 mA, 1.54 Å) difractometer. Perkin Elmer 45 UV-VIS dual beam spectrometer was used to get optical transmission and/or absorption spectra of the samples where the incident light fall down to the sample at normal angle and not polarized at the measurement wavelength diapason between 300 ÷ 900 nm ranges.

Solution preparation

The In_2Se_3 and Ga_2Se_3 solutions prepared as two part solutions which after were stirring together. For In_2Se_3 solutions the SeO_2 was weighted to correspond on molar weight and dissolved in HCl or $SeCl_4$ weighted and dissolved in ethanol (C_2H_5OH) for Se ions, and stirred about one hour at room temperature. Another solution prepared for In ions where also weighted from $InCl_3$ or Indium hydrate pent nitrate ($In(NO_3)_3{\cdot}5H_2O$) corresponding to molar weight. These materials was dissolved in Glacial Acetic Acid (CH_3COOH) and stirred 1 hour at room temperature. Further the second solution was subsequently added to first solution drop by drop. Result solutions was stirred more than 2 hour and the pH of result solutions regulated by adding ethanolamine (C_2H_7NO). The pH parameter was about 4.0 for all the solutions. Several drops Glycerol was added as stabilizer of solutions. The viscosity of solutions was measured by viscometer and estimated as ~ 6.5 mPa/s.

The Ga_2Se_3 solution also was prepared by mixing the following two solutions. The Gallium(III) acetylacetonate ($C_5H_8O_2$)3Ga was weighed to correspond Ga_2Se_3 molar weight using Ga ions and dissolved in Acetylacetone ($C_3H_6O_2$) at room temperature for 12 hour. Further added Methanol (CH_3OH) several times to dissolve the Gallium (III) acetylacetonate - ($C_5H_8O_2$)3Ga. Selenium ions were prepared from $SeCl_3$. The $SeCl_3$ was weighed following the Ga_2Se_3 demanded molar weight and dissolved by

Ethanol (C_2H_5OH) as the event of In_2Se_3. This solution can be prepared instantly when the Ga ion solutions are ready. This way mixing of the above two solutions would be easy and simple. The Se ion solution was added drop by drop to Ga ion solution and stirred. After complete mixing it was the solution mixed more than 3 hours under the required pH. The pH regulation was done adding Triethylamine ($C_6H_{15}N$) solution which before diluted in Ethanol 5-10 drop per minute with 15 minutes. Resulting solutions had pH between 1.88 and 2.05 values. The viscosity of the solutions was measured viscometer and estimated as ~6.1 mPa/s.

The thin films samples prepared from solutions which aged more than 2 months and new prepared samples was showed the identical XRD spectrums.

Samples preparation

The In_2Se_3 and Ga_2Se_3 thin films prepared as deposition on glass or quartz substrate with a drawing rate of 15-20 cm per minute were samples withdrawn from the solution to a vertical located furnace. In this technique there is no restriction on the size of the substrate and substrates were ~ 15x60 mm size. The furnace had a size of 120 cm along to sample moving direction and a temperature gradient in furnace changing from room temperature up to a desired temperature.

The In_2Se_3 thin film samples were prepared at between 300°C ÷ 600°C temperatures by 20°C interval. Identically the Ga_2Se_3 thin film samples were prepared 450°C ÷ 550°C temperatures by 20°C interval steps. After crystal forming procedure in vertical furnace, which can be named "drying" of the samples, these thin films were annealed in horizontal furnace which temperature arising regulated as the terms steps.

Several thicknesses of the In_2Se_3 and Ga_2Se_3 thin films were regulated by the layer to layer coating at crystal formation temperature.

3. RESULT AND DISCUSSIONS

The XRD spectra of the In_2Se_3 thin film samples are revealed in Fig.1. Only three characteristic spectrums are resulted in Fig1 as **a**, **b** and **c** for α-In_2Se_3, β-In_2Se_3 and γ-In_2Se_3 phases which formed nearly temperatures 400°C, 500°C and 600°C accordingly.

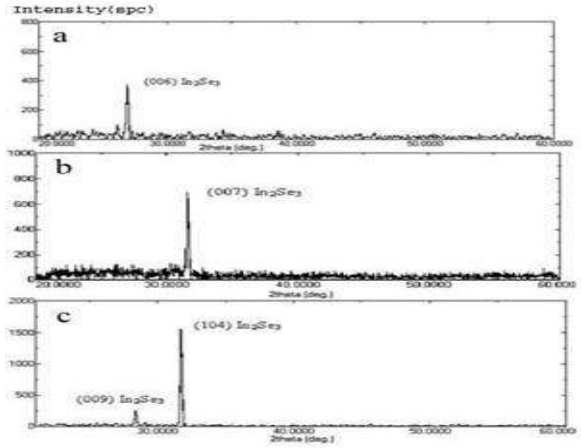

Fig1. X-ray diffraction spectrums of In_2Se_3 thin films prepared by sol-gel method.

As seen in **a** spectra in Fig.2, the Ga_2Se_3 thin film crystal formation condition begins at 470°C, so the spectra **b**, **c** and **d** show that the crystal state remains even at 550°C. It is seen from Fig2 that the maximum of XRD spectra peak intensity was observed at temperature 500°C. It is known, that the Ga_2Se_3 compound also has three phases which are named α, β, and γ phases. The β phase shows a superstructure with ordered vacancies [5,6]. As follows from the spectra in Fig.2 that investigating peaks coincide with XRD analysis database peaks of JCPDS 44-1012 [7]. The peak positions according to JCPDS 44-1012 data indicate the β-Ga_2Se_3 crystal phase, and the crystal structure for this phase is denoted as monoclinic structure.

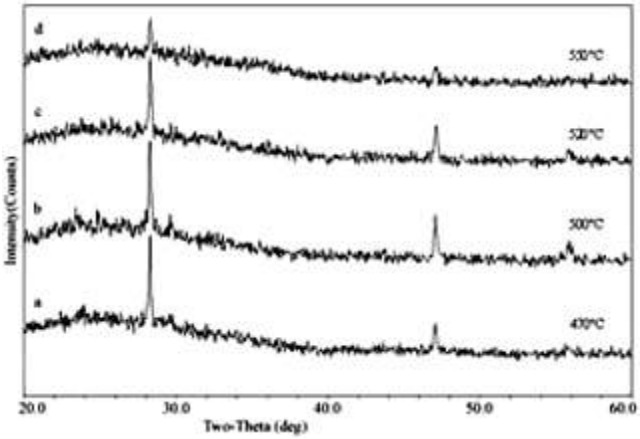

Fig.2. X-ray diffraction spectrums of Ga_2Se_3 thin films prepared by sol-gel method.

The estimated average crystallite size, *D*, was obtained from XRD peaks at scan rate of 3°/min based on Scherrer's equation: $D = 0.9\,\lambda/(\beta \cos\theta)$, where λ is the wavelength of the X-rays, which is 0.15406 nm for Cu Kα irradiation, θ the diffraction angle, and β is the full width at half maximum (FWHM). The calculated grain size for the sample that annealed at 500°C was approximately 260 nm.

Many factors can affect the intensity of the specified XRD analysis spectrum. Therefore, the time increase up to temperature of formation, endurance annealing and especially time of cooling up to room temperature can have influence on the intensity of the specified peaks.

The transmission and absorption spectrums of In_2Se_3 and Ga_2Se_3 thin film samples near the fundamental absorption edge were investigated.

It will be pertinently note that estimation of band gap energy for In_2Se_3 thin film samples are considered as a miscellaneous. In this work are presented the experimental results on absorption spectrums and band gap estimating for In_2Se_3 thin film samples which depicted in Fig3 at room temperature. In inserted figure depicted the $(\alpha h\nu)^2$ dependence to hν of In_2Se_3 thin film samples prepared by sol-gel method. Estimating band gap energy E_g is corresponds to ~ 1.2 eV. This is show the agreement with literature [8,9,10].

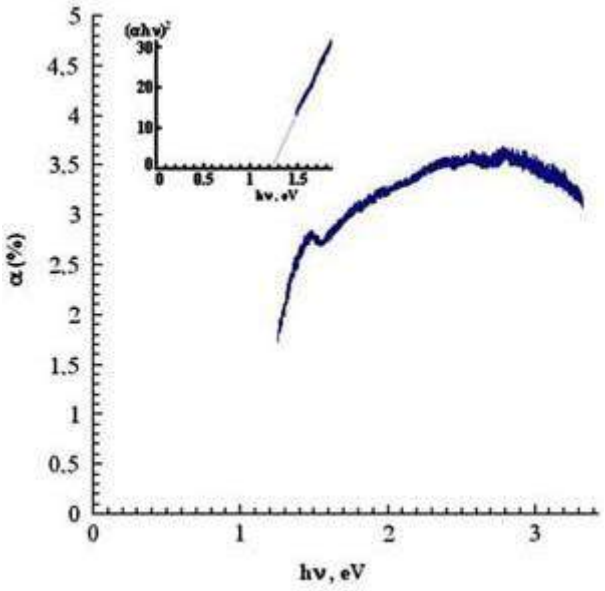

Fig.3. Optical absorption spectrum and energy band gap estimation (inserted fugure show the $(\alpha h\nu)^2$ dependence to hν) for In_2Se_3 thin films prepared by sol-gel method

In Fig.4 reveals the optical absorption spectrum of the Ga_2Se_3 thin film samples in the 350 ÷ 550 nm wavelength regions at room temperature. As seen from spectrum, the fundamental absorption edge beginning nearly at ~ 485 nm and increase by decreasing of the wavelength. As it was reviewed in [6], the β phase of Ga_2Se_3 thin film crystals have allowed direct optical transitions near fundamental absorption edge. In this case also for spectral dependence of absorption coefficient can be applicable a formula $(\alpha h\nu)^2 = A(h\nu - E_g)$, where A is a constant and E_g is band gap of semiconductor. Construction of graph $(\alpha h\nu)^2$ to hν according to a formula is given in inserted figure Fig.4. Energy value for E_g can be obtained by mental continuation of linear part this curve to abscise axis crossing. The estimated value of E_g with same accuracy corresponds to 2.56 eV for Ga_2Se_3 thin film samples. This is good agreement with the existing literature β phase of Ga_2Se_3 thin films [5, 6].

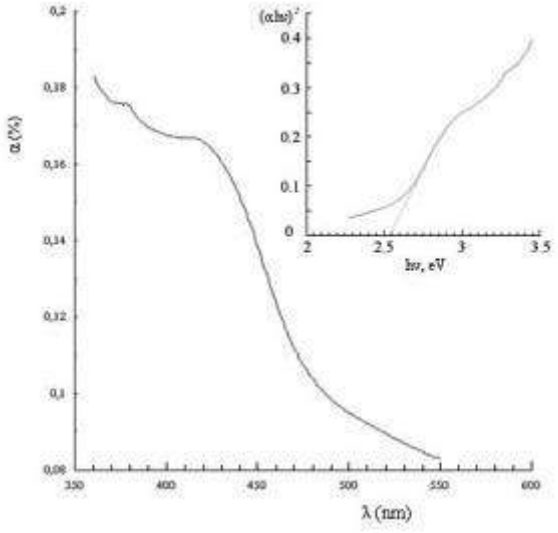

Fig.4. Optical absorption spectrum and energy band gap estimation (inserted fugure show the $(\alpha h\nu)^2$ dependence to hν) for Ga_2Se_3 thin films prepared by sol-gel method

CONCLUSION

The In_2Se_3 and Ga_2Se_3 thin film samples prepared by Sol-Gel method and had a crystal structure which was monoclinic. The XRD database showed that the peak positions correspond to the β-Ga_2Se_3 crystal phase. Thin film structure as well as reproducibility during so called solution age more than 2 months. Estimated value of the band gap energy for In_2Se_3 thin films samples was about E_g ~1.2 eV and for Ga_2Se_3 thin film samples about E_g ~2.56 eV at room temperature. The thin films of In_2Se_3 and Ga_2Se_3 semiconductors prepared by Sol-gel method were comparable with other methods used to produce semiconductor thin films.

[1]. *Heon Lee, Young Keun Kim, Donghwan Kim and Dae-Hwan Kang*, IEEE Transactions on Magnetics, 2005, v.41, n2, p.1034-1036

[2]. *N.Ishikawa, T. Nakayama* Physica: E, 2003, v.17, p.185-186

[3]. *C.J.Brinker, G.S.Frye, A.J. Hurd and Ashliy* Thin Solid Films, 1991, v.201, p.97-108

[4]. *S.M.Souza, C.E.M.Campos, J.C.de Lima, T.A.Grandi, P.S. Pizani* Solid State Communications, 2006, v.139, p.70-75

[5]. *M.A.Afifi, A.E.Bekheet, H.T.El-Sahir, I.T. Zedan* Physica B, v. 325, 2003, p.308-318

[6]. *M.Rusu, S.Wiesner, S.Lider, E.Strub, J.Röhrich, R.Würtz, W.Fritsch, W.Bohne, Th.Schedel-Niedrig, M.Ch Lux-Steiner., Ch.Giesen and M.Heuken* Journal of Physics: Condensed Matter, 2003, v.15, p.8185-8193

[7]. *D. Lübers, V. Leute* Solid State Chemistry, 1982, v.43 p.339

[8]. *G.A.Gibson, A.Chaiken, K.Nauka, C.C.Yang, R.Davidson, A.Holden, R.Bicknell, B.S.Yeh, J.Chen, H.Liao, S.Subramanian, D.Shut, J.Jasinski, Z.Liliental-Weber* Applied Physics Letter , 2005, v.86, 051902 (3 pages) (published on line 25 January 2005)

[9]. *H.T.El-Sahir, A.E. Bekheet* Journal of Physics D: Applied Physics 25:1122

[10]. *M.Parlak, C.Ercelebi, Z.Salayeva, K.Allakhverdiev* Thin Solid Films, 1995, 258:86

INTERLAYER EXCHANGE COUPLING IN ULTRATHIN Py/Cr/Py TRILAYERS

B. AKTAŞ, R. TOPKAYA, M. ERKOVAN, A. ÖZTÜRK, O. ÖZTÜRK
Gebze Institute of Technology, Department of Physiscs,
P.K. 141, 41400 Gebze-Kocaeli, Turkey

M. ÖZDEMIR
Marmara University, Faculty of Science and Letters,
Department of Physics, Istanbul, Turkey

Magnetic properties of ultrathin Py/Cr/Py trilayers have been investigated as a function of Cr spacer layer thickness by using ferromagnetic resonance (FMR) and vibrating sample magnetometer (VSM) techniques. The Cr spacer layer thickness was increased from 4Å to 40Å with 1Å steps to determine the dependence of interlayer exchange coupling between ferromagnetic layers on the spacer layer thickness. Two strong and well resolved peaks were observed which correspond to a strong (acoustic) and weak (optic) modes of magnetization precession in the effective dc field due to the exciting external microwave field as the external dc field orientation comes close to the film normal. The separation of the two modes in the field axis depends on the thickness of Cr spacer layer. An interchange in the relative positions of the acoustic and optic modes has been observed for a particular thickness of Cr spacer layer as well. It was found that the relative position of the peaks depends on the nature (sign) of the interlayer exchange coupling between ferromagnetic layers through Cr spacer layer. In Py/Cr/Py trilayers, strength of the interlayer exchange coupling constant oscillates and changes its sign with Cr spacer layer thickness with a period of about 11Å.

1. INTRODUCTION

Magnetic multilayers consisting of ferromagnetic and nonmagnetic films have attracted considerable attention from researchers since the observation of GMR [1, 2] and TMR [3, 4] effects due to their applications in the magnetoelectronics such as data storage and information processing etc. The GMR effect and spin transfer phenomenon are mainly determined by magnetic, electrical and geometric properties of super structured thin films. Interlayer exchange coupling between ferromagnetic layers across nonmagnetic spacer layer was discovered by P. Grünberg in Fe/Cr/Fe multilayer structures by means of light scattering from spin waves [5]. S. S. P. Parkin showed that interlayer exchange coupling oscillates in NiCo/Ru/NiCo multilayers [6]. Evaluating numerous experiments in Fe/TM/Fe and Co/TM/Co (TM: Transition Metal) multilayer structures [7–9], S. S. P. Parkin concluded that the oscillation is a common property of all transitions metals [10].

Magnetic anisotropy and interlayer exchange coupling parameters play the most important role in GMR effect for sensor applications. The exchange interactions between ferromagnetic layers through a nonmagnetic metallic spacer must be anti-ferromagnetic in order to have significant GMR effect. Oscillatory interlayer exchange coupling between ferromagnetic layers was explained by Ruderman–Kittel–Kasuya–Yosida (RKKY) interaction [11-13] which is an indirect exchange interaction of localized spins in magnetic layers mediated conducting electrons of nonmagnetic spacer. As the need for ultra high density data recording is increased, the size of the film used in spintronic applications has to be decreased [14]. Therefore, the accurate magnetic characterization is one of the major issues related to magnetic multilayer structures. So far numerous superlattice structures made of ferromagnetic and nonmagnetic metallic thin layers have been investigated by using different characterization techniques [15-17].

The FMR was proven to be one of the well established and useful techniques [18-34] to investigate magnetic materials and to determine magnetic properties, such as magnetic anisotropy, magnetic moment and magnetic damping etc. In this study, interlayer exchange coupling between ferromagnetic layers separated by non-magnetic spacer has been studied by the conventional FMR and VSM techniques. Although there are many more useful magnetic multilayer structures for GMR applications, we have chosen Py/Cr/Py trilayers as prototype system in order to show the usefulness of FMR technique for investigating the magnetic properties as a function of nonmagnetic spacer thickness. Since Py is one of the magnetically soft materials with relatively weak magnetic damping, it gives quite well defined FMR signal with narrow resonance line. Thus, relatively sharp peaks for different FMR excitation modes allow us to deduce magnetic parameters by fitting the theoretical values to the experimental data.

2. SAMPLE PREPERATION

Cr(50 Å)/ Py(30 Å)/Cr(t)/Py(20 Å)/Cr(100Å) multilayers were grown onto naturally oxidized p-type single crystal Si(100) substrate by magnetron sputtering where t denotes the thickness of Cr spacer layer and ranges from 4 Å to 40 Å with 1Å steps. The substrates were cleaned in ultrasonic bath by using methanol and ethanol consecutively before transferring into the UHV conditions. Then they were annealed up to 600 ^{o}C for 30 minutes in UHV to minimize the surface deficiencies. The water-cooled 3" diameter target provides the thickness homogeneity.

High purity Permalloy, $Ni_{80}Fe_{20}$ (Py) and Cr targets were sputtered by rf (20 Watt) and dc (30 watt) power supplies, respectively. These powers allow the slowest deposition rates with optimum pressure to get an ideal surface morphology.

Although the base pressure in the preparation chamber is $1x10^{-8}$ mbar, the pressure during the sputtering was $1.6x10^{-3}$ mbar. The distance between the target and the substrate was 100 mm, allowing 1Å deposition sensitivity by decreasing deposition rate.

A water-cooled Matek TM 350 QCM thickness monitor was used to measure the film deposition rate *in*

situ. At the beginning of film growth, the QCM was calibrated for Py and Cr deposition rates. The calibration of QCM thickness monitor was complemented by monitoring the attenuation of the substrate photoemission signal (by XPS) from the deposited films. For thickness determination we monitored the Si*2p* attenuation as a function of chromium exposure by using XPS signals. Converting this to a Cr thickness, the electron mean free path was calculated by using the TPP formula developed by Tanuma, Powell, and Penn [32]. Since Py has two components, the Veeco Dektak 8 profile-meter was used to calibrate thickness additionally to confirm the results of the photoemission attenuation.

The prepared trilayers were covered by a 100 Å Cr cap layer to prevent oxidation of trilayer structures. We have investigated the suitable thickness of magnetic layers to observe measurable exchange coupling between ferromagnetic layers through a metallic Cr spacer. The metallic films have poli-crystalline structures. Small samples of 1x1.5 mm in lateral size were cut from the deposited films for the FMR measurements.

3. EXPERIMENTAL RESULTS

The FMR measurements were carried out by using a Bruker EMX model X-band ESR spectrometer at microwave frequency of 9.5 GHz. The measurements were carried out as a function of the angle of the external dc field with respect to the film normal at room temperature. The sample sketch, relative orientation of the equilibrium magnetization vector **M**, the applied dc magnetic field vector **H** and the experimental coordinate system are shown in Fig. 1(a). The picture of the prepared trilayer structure is shown in Fig. 1(b). The magnetic field component of microwave is always kept perpendicular to the dc field during the sample rotation. The applied microwave field remains always in sample plane for conventional geometry and power is kept small enough to avoid saturation, as well.

The magnetization measurements were performed by using Vibrating Sample Magnetometer (VSM, Quantum Design PPMS 9T) at room temperature for both in plane geometry (IPG; field parallel to the sample plane) and out of plane geometry (OPG; field perpendicular to the sample plane).

FMR spectra are very sensitive to the relative orientation of the external dc field. The spectra also strongly depend on both ferromagnetic and nonmagnetic Cr spacer layer thickness. After a few quick trials it has been seen that the thicknesses and/or magnetic anisotropies of two ferromagnetic layers should be different from each other to observe the influence of exchange interactions on FMR spectra. Therefore, the thicknesses of bottom and upper Py layers were chosen as 20Å and 30Å, respectively. The samples were labeled as Sx, where x is the Cr spacer thickness in Å.

Fig.2 shows two representative FMR spectra (solid circle) for the external field applied parallel and/or perpendicular to the Py(30 Å)/Cr(7 Å)/Py(20 Å) trilayer. This figure also shows simulated spectra (continuous lines) obtained using the theoretical model described below. There are two excited FMR modes for OPG case. However when the field is applied parallel to the sample plane (IPG), a single FMR mode takes place.

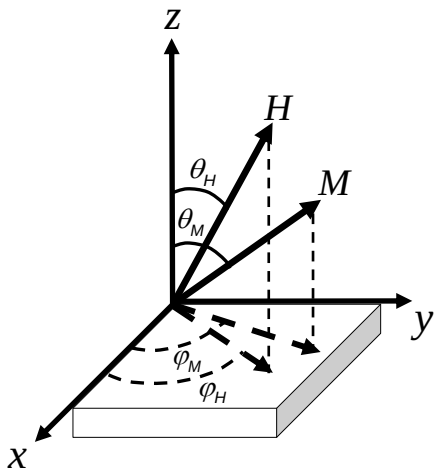

Fig.1. Relative orientations of the external dc magnetic field and magnetization vectors with respect to the sample plane

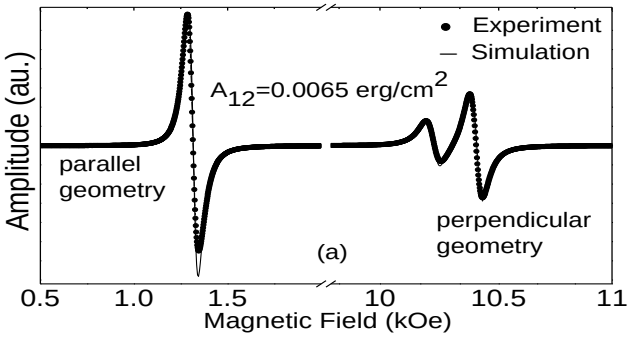

Fig.2. Experimental and simulated FMR spectra of Py(20 Å)/Cr(7Å)/Py(30Å) trilayer film for the external field parallel and perpendicular to the sample plane.

The FMR spectra in Fig.3 are two selected examples to show the effect of spacer thickness. The two well-resolved FMR modes were observed for both samples S4 and S10 at OPG case. As can be seen in the Fig. 3 (a3, b3), the relative intensities of the two modes (optic and acoustic modes) are different from each other. The weaker mode (named as optic mode) appeared at lower field side of the strong mode (main or acoustic mode) for sample S4 shifts to higher field side for the sample S10.

The angular variations of resonance fields for two different samples are given in Fig.4. Theoretical resonance field values have been obtained by using the theoretical model described below. The resonance field values for both samples are almost same for a broad range of angle. However there are noticeable differences where the field is applied very close to the film normal, that is, the resonance field values for S4 is higher compared to that for S10. This means that the thicker spacer weakens the magnetic coupling between the ferromagnetic layers to allow more freedom for them to act as independent ultrathin magnetic layers. However, when the spacer becomes thinner, both layers are more strongly coupled and act almost as a single thicker layer. Since the uniaxial perpendicular anisotropy for thinner film is generally higher compared to that for thicker layer the resonance for OPG case is expected to occurs at lower field for S4. The

strong angular dependence is due to mainly shape anisotropy (demagnetizing field).

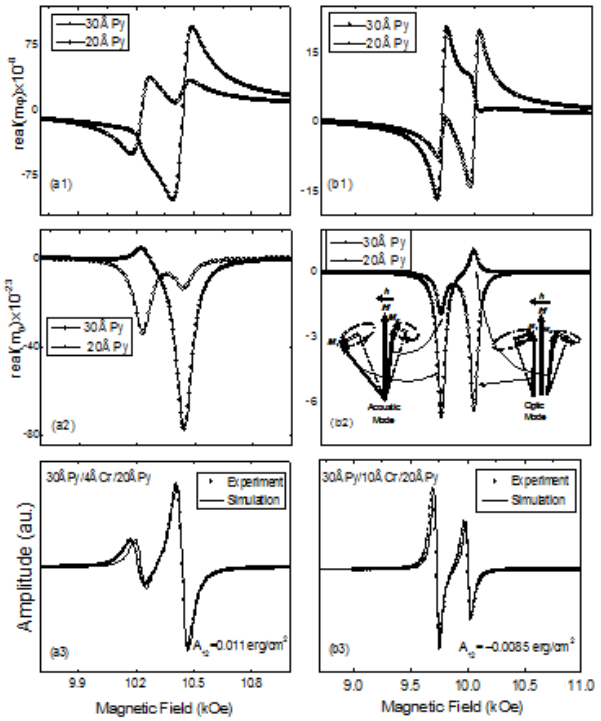

Fig.3. FMR curves for ferromagnetically (on the left) and antiferromagnetically (on the right) exchange coupled two samples. The real values of azimuth (a1 and b1) and polar (a2 and b2) components of ac magnetizations for each layer are given as a function of the external dc magnetic field to show relative phase of the dynamic components of the magnetization for the acoustical and the optical modes. The field-derivative FMR absorption curves for S4 and S10 given in a3 and b3 respectively.

Two strong and well resolved peaks were observed for the two main modes of FMR excitation as the field orientation comes close to the film normal for most of the Cr thickness (except 11 Å , 22 Å and 33 Å). However these two modes come closer and overlap giving rise to a single peak as the field orients close to film plane. The relative position and separation of the two modes in the field axis depend on the thickness of the Cr spacer. An interchange in the relative positions of the strong and the weak modes for a particular thickness of Cr has been observed for OPG case.

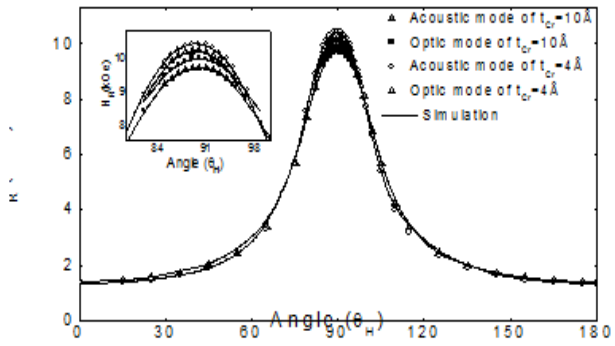

Fig.4. Dependence of the experimental and simulated resonance field values as a function of θ_H for the samples S4 and S10. The inset shows a small region of the curves for the field oriented very close to the film normal.

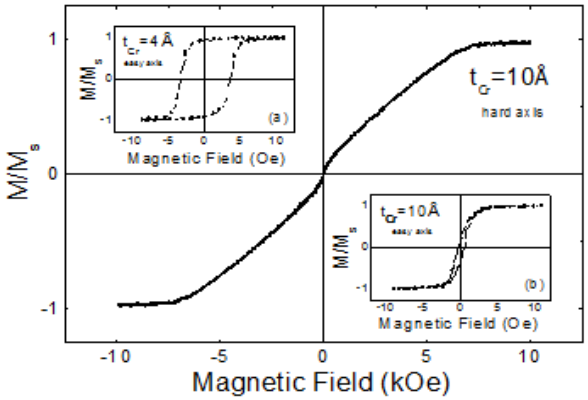

Fig.5. Hysteresis curve recorded at room temperature of sample S10 for the external magnetic field applied along the hard magnetization axis (perpendicular to the film plane). The hysteresis curves for the easy directions (in the film plane) of the magnetizations for S4 and S10 are given in the insets a and b, respectively.

Fig.5 shows magnetic hysteresis curves of the samples S4 and S10 for both IPG and OPG cases. For OPG, the magnetization of the sample S10 saturates at about 7 kOe that corresponds to the effective uniaxial anisotropy containing demagnetizing field and induced perpendicular axial anisotropy field. The sudden jump in the field range of 0-100 Oe for OPG case can be attributed to a small misorientation of the external field, since the projection of the field onto the sample plane can saturates magnetization. Thus detection coils can detect a significant dc signal due to M saturated in sample plane. For IPG case, the hysteresis curves have been given as insets in Fig.5 for both samples S4 and S10. As seen in these insets, the magnetization saturates at very low field even below 10 Oe for the two samples. The hysteresis for sample S4 is wide, square-like at IPG case and its remanence is very close to saturation value. However for sample S10, the remanence value at IPG case is almost one fifth of saturation magnetization value and the magnetization gradually goes to saturation compared to that for S4. Similar behaviour has been reported in the literature for Py/Cr/Py multilayers [33]. This could be considered as a sign for antiferromagnetic interactions between the ferromagnetic layers through the non-magnetic spacer for sample S10 thickness is about 11 Å.

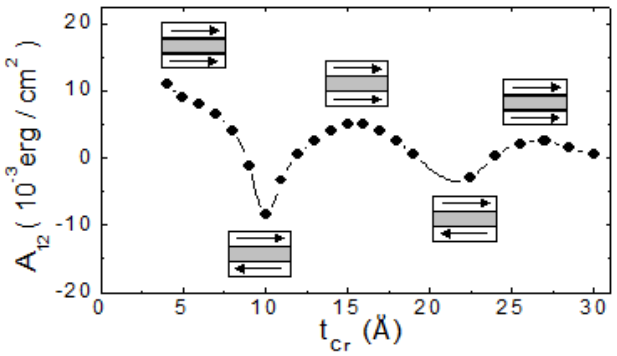

Fig.6. Effective interlayer exchange coupling parameter, A_{12}, obtained from the fitting as a function of non- magnetic spacer (Cr) thickness. The sign of exchange parameter changes with the spacer thickness and causes parallel or antiparallel alignment of the magnetization of neighboring layers as shown by arrows for some spacer thicknesses.

4. DISCUSSION OF THE RESULTS

We have developed a general computer program for the structure consisting of magnetically exchange coupled N layers to fit theoretical FMR spectra to the experimental FMR spectra by using the developed theoretical model. The damping parameter has very minor effects on the resonance field value, but it basically determines the resonance line shape. Although the model and computer program are suitable for both the Gilbert and Bloch type dampings, we have used only the Gilbert type damping to get satisfactory fit between the experimental and the simulated line shape of field derivative FMR spectra for general directions of external dc field. For magnetically homogeneous films one can successfully fit the data by using only the Gilbert type damping term. However if there is a magnetic inhomogeneity, the Bloch type damping term can be included as well.

The experimental FMR spectra could be fitted using the Zeeman, the demagnetizing and the uniaxial anisotropy energies (the uniaxial axis is along the film normal). The induced uniaxial energy strictly depends on the magnetic layer thickness. Especially for ultra thin films this term sometimes can become comparable to the demagnetizing energy. As the magnetic layer becomes thinner than 5Å, the magnetization does not saturate easily, and this is why we used thicker magnetic layers in order to saturate magnetization to a constant value that we assumed in the development of the theory.

Since the angular dependencies of perpendicular anisotropy and the demagnetizing energy are determined by the saturation magnetization, it is very difficult to extract induced perpendicular anisotropy by using FMR data only. Actually the FMR intensity is linearly proportional to the saturation magnetization. Thus one can use reference sample to calibrate the spectrometer signal for exact magnetization measurements. But it seems to be more convenient to have magnetization values obtained by using dc magnetization measurement techniques.

As can be seen in Figs.2, 3 and 4 there is a good agreement between the experimental and the calculated FMR spectra. A careful analysis shows that the position of the resonance peaks are determined by the saturation magnetization M_s, the effective anisotropy and the exchange coupling of the magnetic layers. In fact, in the case of magnetically equivalent layers, the ferromagnetic exchange interaction has no effect on the resonance field, that is, a single resonance peak is observed due to simultaneous excitations of precession of magnetization in all layers. However when magnetic properties of individual magnetic layers slightly differ from each other, then, the exchange coupling between successive ferromagnetic layers starts to play an important role on the FMR curve. Thus, as the external dc field is scanned in a constant microwave frequency, the magnetization vector in one of the layers comes close to resonance condition in a particular field value while the other layer is still far from resonance for non-exchange coupled case; that is, the directions of dynamic magnetizations of neighboring layers become different from each other. Now when exchange coupling is switched on, it tries to make magnetization vector in non resonating layer parallel to that of resonating layer. Thus, additional inertia torque due to the magnetic field produced by the other layer arises and this torque has to be balanced by changing the resonance field. Similarly as the field scan is continued beyond the first resonance value, then, it reaches to the value that would correspond to resonance value for non-coupled second layer. Again due to exchange coupling with the first layer, the resonance field differs from that of non-coupled layer.

For ferromagnetic (antiferromagnetic) coupling the optical mode occurs at lower (higher) field side of the main (acoustic) mode. The separation between the optic mode and acoustic mode in the field axis is determined by orientation of the external field, the saturation magnetization, the anisotropy field and the exchange coupling parameter. In fact, the separation between the modes generally increases with absolute value of exchange parameter. That is, if interlayer exchange coupling strength increases, the optic mode moves away the acoustic mode, and the relative intensities and the separation between the modes increase. On the other hand, if interlayer exchange coupling strength decreases, the optic mode comes close to the acoustic mode, and the relative intensities and the separation between the modes decrease.

As a result of exchange coupling of magnetically non equivalent neighboring layers, two resonance modes are observed in FMR curves for OPG case. Fig.3 also shows the calculated real values of azimuthal (a1 and b1) and polar (a2 and b2) components (transverse components) of ac magnetizations for each layer of the samples S4 and S10 which are given as a function of the external dc magnetic field. These components also allow us to get the relative phase of the dynamic components of ac magnetization as a function of the external dc field. As can be seen in the Fig. 3 (a1 and a2) and (b1 and b2), the real values of azimuthal and polar components of ac magnetizations for the two samples are different from each other. This means that the magnetization vector makes an elliptical (rather than circular) precession about the dc magnetization (and the effective dc field) component.

The magnetization of each layer contributes to the resonance absorption for each FMR mode. Since the excitation amplitude and the phase of precession of dc magnetizations of neighboring layers continuously changes with the dc field, the phase difference becomes either zero or π at the exact resonance field values of the two modes. The mode for the first case (in phase) is called as acoustic mode while the other is called as optical mode to make analogy with phonon spectra. While the relative contributions from the different modes continuously change (evolve) with the external dc magnetic field, one of the layers makes dominant contribution to the FMR signal amplitude (ac susceptibility) for each mode about the resonance field.

Since the average magnetic susceptibility is proportional to the vector sum of transfer components of ac magnetization, the intensity of the acoustical mode is always higher than that of optical mode at exact resonance fields. The relative positions of the modes depend on the sign of exchange coupling parameters A_{12} and B_{12} as well. As mentioned before, these parameters represent the exchange field on a magnetic layer due to

the neighboring layer. This field depends on the relative orientation of the magnetization. For independent determination of these parameters one needs to control the relative orientations of M_1 and M_2. Unfortunately, since the demagnetizing energies of neighboring layers are close to each other and the Zeeman energy is too large compared to the exchange energy, the magnetization vectors of neighboring layers remain almost always parallel to each others at the FMR resonance field. So the effective exchange field on one of the magnetic layer due to the other magnetic layer does not depend on the external field direction. Therefore it is not practical to get additional information for different angles to deduce both exchange coupling terms independently. If we had been able to rotate the magnetization of individual magnetic layers with respect to each other, then, we would have determined both parameters independently. But we do not have possibility to fix the magnetization of the one layer and sweep the external field gradually to rotate the magnetization of second layer in order to determine A_{12} and B_{12} independently. Therefore we have used only the bilinear term, that is, A_{12} in the simulations. Maybe in the future, we can achieve this with different multilayer structures.

The deduced interlayer exchange coupling parameter, A_{12} is plotted in Fig.6 as a function of non magnetic spacer (Cr) thickness. It should be remembered that both the bilinear and the biquadratic exchange energies are represented by a deduced effective parameter, (A_{12}). As can be seen from this figure, the exchange parameter qualitatively exhibits oscillatory behavior. The absolute value decreases with increasing spacer thickness. However interlayer exchange coupling constant changes its sign and oscillates with a period of about 11Å. This result is consistent with the theory given by A. Fert *et al.* [36]. The deduced value of exchange parameter for Py(20 Å)/Cr(10Å)/Py(30Å) trilayer film is nearly half of the values given for $(Py/Cr(12\ Å))_{40}$ multilayer system prepared by electron beam deposition system [33]. However the deduced value in our case is still almost 20 times less than that found for Fe/Cr superlattice in the literature [34]. The period of the oscillation of the interlayer exchange coupling is very close to that for $(Py/Cr(12\ Å))_{40}$, but is significantly smaller than that given for Fe/Cr multilayers [7]. The smaller oscillation period was attributed to interface roughness or interdiffusion between the two interfaces of the trilayer [33].

5. CONCLUSIONS

Ultrathin Py/Cr/Py trilayer films grown on Si (100) substrate by magnetron sputtering technique under UHV conditions have been studied by VSM and FMR techniques. In the present study we have investigated the dependence of the interlayer exchange coupling on Cr spacer layer thickness in interval from 4 Å to 40 Å. The computer program was written to deduce the interlayer exchange parameter for magnetically exchange coupled magnetic multilayers and it was applied to the Py/Cr/Py trilayers.

The deduced magnetic parameters strictly depend on the layer thicknesses as well. Actual line shapes, resonance positions, the relative intensities of the different FMR modes and angular dependence of these modes are successfully simulated by using only single set of parameters like M_s, K_p, A_{12} and α with the written program. Particular parameters have dominant effect on some particular aspects of the FMR spectra. For instance the angular dependence of the resonance field is mainly determined by M_s and the perpendicular anisotropy. But relative position and especially relative mode intensities are well accounted for the interlayer exchange coupling. The damping parameter determines the line shapes. The angular dependence allows us to get more accurate parameters and sufficiently good fitting by using as many data as we need since we have freedom to do experiment for any direction of external static magnetic field. It was understood that the FMR is a very sensitive and powerful technique to study magnetic properties of single and/or layered ferromagnetic thin (even at nano-meter range) films separated by a very thin non-magnetic spacer layer.
As a result of fitting the theoretical values to the experimental data, it has been seen that the interlayer exchange coupling constant has qualitatively oscillatory behavior with respect to the nonmagnetic spacer thickness. The oscillation period was found to be about 11Å for Py/Cr/Py trilayers. The value of this parameter reduces with increase of Cr thickness and it becomes undetermined beyond 30Å. If magnetic properties of different layers are very close to each other, two modes comes close to each other and additionally if damping parameter is relatively larger (broad peaks), then, these two peaks overlap and give a distorted single line. In this case, accuracy of exchange parameter decreases.

ACKNOWLEDGEMENTS

This work was partly supported by the Ministry of Industry and Trade of TURKEY (Project No: 00185.STZ.2007-2), State Planning Organization of Turkey (DPT-Project No: 2009K120730) and Marmara University (BAPKO Project No: FEN-KPS–100105–0073). We gratefully acknowledge that all samples used in this study grown at Nanotechnology Center of Gebze Institute of Technology.

[1]. *M. N. Baibich, J. M. Broto, A. Fert, F. Nguyen Van Dau, F. Petroff, P. Eitenne, G. Creuzet, A.Friederich, and J. Chazelas*, Phys. Rev. Lett. 61, 2472 (1988).

[2]. *G. Binasch, P. Grünberg, F. Saurenbach, W.Zinn*, Phys. Rev. B 39, 4828 (1989).

[3]. *T. Miyazaki, N. Tezuka*, J. Magn. Magn. Mater. 139, L231 (1995).

[4]. *J. S. Moodera, L. R. Kinder, T. M. Wong, R.Meservey*, Phys. Rev. Lett. 74, 16 (1995).

[5]. *P. Grünberg, R. Schreiber, Y. Pang, M.B.Brodsky, H. Sowers*, Phys. Rev. Lett. 57, 2442 (1986).

[6]. *S. S. P. Parkin, D. Mauri*, Phys. Rev. B 44, 7131 (1991).
[7]. *S. S. P. Parkin, N.More, K. P. Roche*, Phys. Rev. Lett. 64, 2304 (1990).
[8]. *S. S. P. Parkin, R. F. C. Farrow, R. F. Marks, A.Cebollada, G. R. Harp, R. J. Savoy*, Phys. Rev. Lett. 72, 3718 (1994).
[9]. *S.S.P. Parkin, R. Bhadra, and K.P. Roche*, Phys. Rev. Lett. 66, 2552 (1991).
[10]. *S. S. P. Parkin*, Phys. Rev. Lett. 67, 3598 (1991).
[11]. *M. A. Ruderman, C. Kittel*, Phys. Rev. 96, 99 (1954).
[12]. *T. Kasuya*, Prog. Theor. Phys. 12, 45 (1956).
[13]. *K. Yosida*, Phys. Rev. 106, 893 (1957).
[14]. *Stuart Parkin, Xin Jiang, Christian Kaiser, Alex Panchula, Kevin Roche, Mahesh Samant*, Proceedings of the IEEE, vol. 91, no.5, MAY 2003.
[15]. *B.Heinrich, Z. Celinski, J. F. Cochran, W.B.Muir, J. Rudd, Q. M. Zhong, A. S. Arrott, K. Myrtle, J.Kirschner*; Phys. Rev. Lett. 64, 673 (1990).
[16]. *J. J. de Vries, W. J. M. De Jonge, M. T. Jhonson, J. aan de Stegge, A. Reinders*, J. Appl. Phys. 75, 6440 (1994).
[17]. *M. Belmeguenai, T. Martin, G. Woltersdorf, G.Bayreuther, V. Baltz, A. K. Suszka, B.J. Hickey*, J. Phys.: Condens. Matter. 20, 345206 (2008).
[18]. *Zhenyong Zhang*, "Ferromagnetic Resonance Study in Exchange Coupled Magnetic/Non-magnetic Multilayer Structures", Ph.D. Thesis, The Ohio State University (1994).
[19]. *Philip E. Wigen, Zhenyong Zhang*, Brazilian Journal of Physics, 22, 267 (1992).
[20]. *Z. Zang, L. Zhou, P. E. Wigen, K. Ounadjela*, Phys. Rev. Lett. 73, 336 (1994).
[21]. *B.Z Rameev, A. Gupta, F. Yıldız, L.R. Tagirova, B.Aktas*, J. Magn. Magn. Mater. 300, e526-e529 (2006).
[22]. *N. Akdogan, B.Z Rameev, L. Dorosinsky, H. Sozeri, R. Khaibullin, B. Aktas, L. Tagirov, A. Westphalen, H. Zabel*, J. Phys. Con. Mat. 17 (34) L359-L366 AUG 31 (2005).
[23]. *S. Kazan, A. Cemil Başaran, B. Aktaş, M. Özdemir, Y.Öner*, Physica B 403, 1117 (2008).
[24]. *B. Heinrich, G. Woltersdorf, R. Urban, B. Aktaş, L.R.Tagirov, F. Yıldız, K. Özdoğan, M. Özdemir, O. Yalçın, B. Z. Rameev*, J. Appl. Phys. 102, 013912 (2007).
A. *R. Köymen, L. R. Tagirov, R. T. Gilmutdinov, C.Topacli, C. Birlikseven, H. Z. Durusoy, B. Aktaş*, IEEE Transactions on Magnetics, 34, 846 (1998).
B. *Aktaş*, Thin Solid Films 307, 250 (1997).
C. *Aktaş, M. Özdemir*, Physica B, 193, 125 (1994).
[25]. *B. Aktaş, Y. Öner, E. A. Harris*, Phys, Rev. B 39, 528 (1989).
[26]. *G. D. Fuchs, J. C. Sankey, V. S. Pribiag, L. Qian, P.M. Braganca, A. G. F. Garcia, E. M. Ryan, Zhi-Pan Li, O. Ozatay, D. C. Ralph, R. A. Buhrman*, Appl. Phys. Lett. 91, 062507 (2007).
[27]. *M. Farle*, Rep. Prog. Phys. 61, 755 (1998).
[28]. *Z. Celinski, K. B. Urquhart, B. Heinrich*, J. Magn. Magn. Mater. 166, 6 (1997).
[29]. *J. J. Krebs, P. Lubitz, A. Chaiken and G. A. Prinz*, J. Appl. Phys. 67, 5920 (1990).
[30]. *Chubing Peng, Chen Dai and Daosheng Dai*, J. Appl. Phys. 72, 4250 (1992).
[31]. *S. M. Rezende, C. Chesman, M. A. Lucena, A.Azevedo, F. M. de Aguiar and S. S. P. Parkin*, J. Appl. Phys. 84, 958 (1998).
[32]. *S. Tanuma, C.S. Powell, and D.R. Penn*, Surf. Sci. 192, L849 (1987).
[33]. *A .Fert, A. Barthelemy, P. Lequien, R. Loloee, D.K.Lottis, D. H. Mosca, F. Petroff, W. P. Pratt, and P. A. Schroeder*, J. Magn. Magn. Mater. 104, 1712 (1992)

ELECTRONIC BAND STRUCTURE AND OPTICAL PROPERTIES OF Sb_2S_3 AND Sb_2Se_3: AB INITIO CALCULATION

HUSNU KOC, AMIRULLAH M. MAMEDOV
Physics Department, Cukurova University, Adana, Turkey
hkoc@student.cu.edu.tr; mamedov@cu.edu.tr

The electronic band structures, density of states (DOS) and optical properties of V_2-VI_3 -type binary compounds, Sb_2S_3 and Sb_2Se_3, are investigated using the density functional theory and pseudopotential theory under the local density approximation (LDA). The obtained electronic band structure show that Sb_2S_3 and Sb_2Se_3 crystals have the indirect forbidden gap of 0.7278 eV and 0.62 eV, respectively. The structural optimization for Sb_2S_3 and Sb_2Se_3 have been performed using the LDA. The valance band in our calculations is composed of the 3s and 3p states of the S atom and 4s and 4p states of the Se atom, 5s and 5p states of Sb, while the conduction band consists of the 5p states of the Sb, S and Se atoms. The result of Sb_2S_3 and Sb_2Se_3 have been compared with the experimental results and have been found to be in good agreement with these results. The linear photon-energy dependent dielectric functions and some optical properties such as the energy-loss function, the effective number of valance electrons and the effective optical dielectric constant are calculated.

1.INTRODUCTION

Sb_2S_3 and Sb_2Se_3, a member of compounds with the general formula V_2-VI_3 (V=Bi, Sb and VI=S, Se) are layer structured semiconductors with orthorhombic crystal structure (space group Pnma; No:62), in which each Sb-atom and each Se/S-atom is bound to three atoms of the opposite kind that are then held together in the crystal by weak secondary bond [1,2]. These crystal have 4 Sb_2B_3 (B=S, Se) molecules in a unit cell. Therefore, these compounds have a complex structure with 56 valance electrons per unit cell. In the last few years, Sb_2Se_3 has received a great deal of attention due to its switching effects [3] and its excellent photovoltaic properties and high thermoelectric power [4], which make it possess promising applications in solar selective and decorative coating, optical and thermoelectric cooling devices [5]. On the other hand, Sb_2S_3 has attracted attention for its applications as a target material for television cameras [6,7], as well as in microwave [8], switching [9], and optoelectronic devices [10-12].

Kuganathan et al [13] used density functional methods as embedded in the SIESTA code, to test the proposed model theoretically and investigate the perturbations on the molecular and electronic structure of the crystal and the SWNT (single walled carbon nanotubes) and the energy of formation of the Sb_2Se_3 @ SWNT composite. Caracas et al [14] computed the valance electron density, the electron band structure and the corresponding electronic density-of-states (DOS) of A_2B_3 (A=Bi, Sb and B=S, Se) compounds using the density functional theory. As far as we know, no ab initio general potential calculations of the optical properties of Sb_2S_3 and Sb_2Se_3 have been reported in detail.

In the present work, we have investigated the electronic band structure, the total density of states (DOS), structure optimization and photon energy-dependent optical properties of the Sb_2S_3 and Sb_2Se_3 crystals using a pseudopotential method based on the density functional theory (DFT) in the local density approximation (LDA) [15].

Table 1. Structure parameters of Sb_2S_3 and Sb_2Se_3 materials

Material		a (Å)	b (Å)	c (Å)	Space Group
Sb_2S_3	Present (LDA)	11.71	4.08	11.87	
Sb_2S_3 [23]	Experiment.	11.31	3.84	11.23	
Sb_2S_3 [24]	Experiment.	11.30	3.83	11.22	D_{2h}^{16}
Sb_2S_3 [25]	Experiment.	11.27	3.84	11.29	
Sb_2Se_3	Present (LDA)	12.22	4.14	11.98	
Sb_2Se_3 [13]	Theory (GGA)	11.91	3.98	11.70	
Sb_2Se_3 [2]	Experiment.	11.79	3.98	11.64	D_{2h}^{16}
Sb_2Se_3 [26]	Experiment.	11.78	3.99	11.63	
Sb_2Se_3 [27]	Experiment.	11.77	3.96	11.62	

2. COMPUTATIONAL DETAILS

SIESTA (The Spanish Initiative for Electronic Simulations with Thousands of Atoms) code [16-18] was utilized in this study to calculate the energies and optical responses. It solves the quantum mechanical equation for the electron within DFT approach in the LDA parameterized by Ceperley and Alder [19]. The interactions between electrons and core ions are stimulated with seperable Troullier –Martins [20] norm-conserving pseudopotential. The basis set is based on the finite range pseudoatomic orbitals (PAO's) of the Sankey-Nicklewsky type [21], generalized to include multiple-zeta decays.

We have generated atomic pseudopotentials separately for Sb, S and Se by using the $5s^25p^3$, $3s^23p^4$ and $4s^24p^4$ atomic configurations, respectively. The cut-off radii for the present atomic pseudopotentials are taken as 2.35, 1.7 and 1.85 a.u. for the s, p, d and f channels of Sb, S and Se, respectively.

SIESTA calculates the self-consistent potantial on a grid in real space. The fineness of this grid is determined in terms of an energy cut-off E_c in analogy to the energy cut-off when the basis set involves plane waves. Here by using a double-zeta plus polarization (DZP) orbitals basis and the cut-off energies between 50 and 450 Ry with various basis sets, we found an optimal value of around 350 Ry for Sb_2S_3 and Sb_2Se_3. For the final computations, 10 k-points for Sb_2S_3 and 36 k-points for Sb_2Se_3 were found to be adequate for obtaining the total energy with an accuracy of about 1meV/atoms.

3. RESULTS AND DISCUSSION

3.1. STRUCTURAL OPTIMIZATION

All physical properties are related to the total energy. For instance, the equilibrium lattice constant of a crystal is the lattice constant that minimizes the total energy. If the total energy is calculated, any physical property related to the total energy can be determined. Firstly, the equilibrium lattice parameters were computed by minimizing the crystal's total energy calculated for the different values of lattice constant by means of Murnaghan's equation of states (EOS) [22] and the result are shown in Table 1 along with the experimental and theorical values. The lattice parameters for Sb_2S_3 and Sb_2Se_3 are found to be a= 11.71, b=4.08, c=11.87 and a= 12.22, b=4.14, c=11.987 for orthorhombic structures, respectively and it are in a good agreement with the experimental and theory. In all our calculations we have used the computed lattice parameters (Table).

3.2. ELECTRONIC BAND STRUCTURE

For a better understanding of the electronic and optical properties of Sb_2Se_3 and Sb_2Se_3, the investigation of the electronic band structure would be useful. We first describe our calculated electronic structures along high symmetry directions in the first Brillouin zone (BZ) of the orthorhombic system. The energy band structures calculated using LDA for Sb_2Se_3 and Sb_2Se_3 are shown in Fig. 1. As can be seen in Fig.1a, the Sb_2S_3 crystal has an indirect forbidden gap with the value 0.7278 eV .

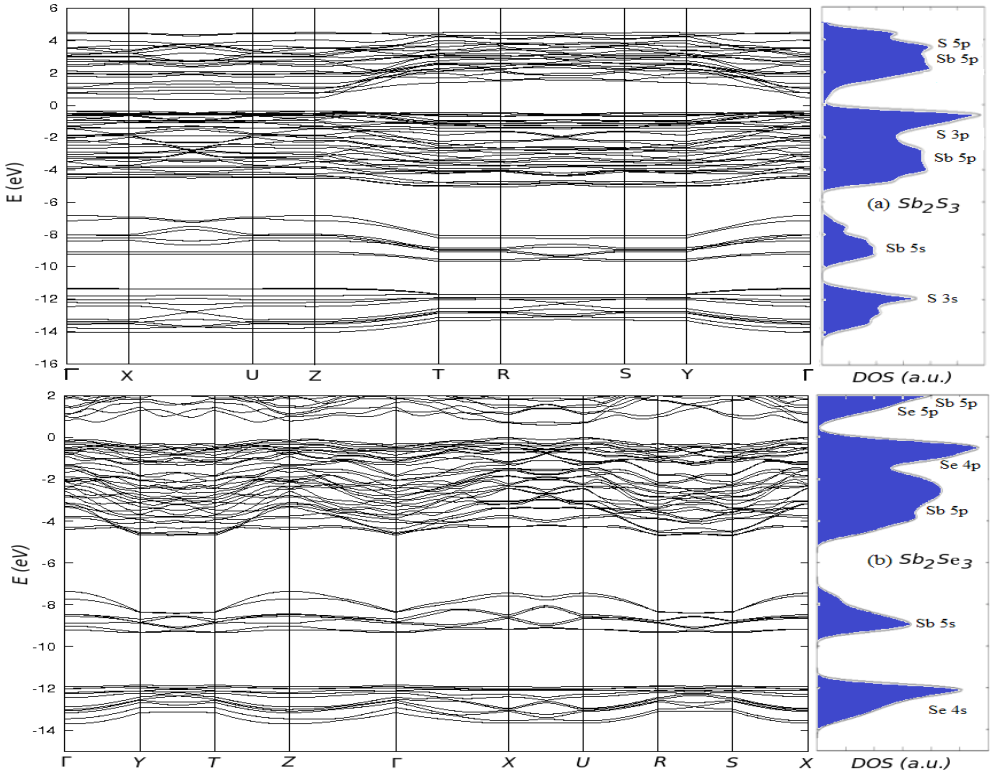

Fig. 1. Energy band structure a nd DOS (density of states) for Sb_2S_3 and Sb_2Se_3.

The top of the valance band positioned at the Γ point of BZ, and the bottom of the conduction band is located at the nearly midway between the X and U point of BZ.

The calculated band structure of Sb_2Se_3 are given in Fig. 1b. As can be seen from the figure, the band gaphas the same character with that of Sb_2S_3, that is, it is an indirect gap. The top of the valance band positioned at the X point of BZ, the bottom of the conduction band is located at the nearly midway between the X and U point of BZ. The indirect and direct band gap values of Sb_2Se_3 crystal are, 0.62 eV and 0.71 eV, respectively.

In the rightmost panels of Fig. 1, the density of states (DOS) are presented. The valance band in our calculations is composed of the 3s and 3p states of the S atom, 4s and 4p states of the Se atom and 5s and 5p states of Sb but on the top of valance band the weight of S 3p and Se 4p states is more than the weight of Sb 5p states, while the conduction band consists of the 5p states of the Sb, S and Se atoms.

Finally, the band gap values obtained are less than the estimated experimental results of 1.13 eV [28], 1-1.13 eV [29,30] for Sb_2Se_3 and 1.56 eV [28], 1.63-1.72 eV [31] for Sb_2S_3. For all crystal structures considered, the

band gap values are underestimated than the experimental values. It is an expected case because of the use pseudopotential method.

3.2. OPTICAL PROPERTIES OF Sb_2S_3 and Sb_2Se_3

It is well known that the effect of the electric field vector, $\mathbf{E}(\omega)$, of the incoming light is to polarize the material. At the level of linear response this polarization can be calculated using the following relation [32]:

$$P^i(\omega) = \chi_{ij}^{(1)}(-\omega,\omega).E^j(\omega), \quad (1)$$

Where $\chi_{ij}^{(1)}$ is the linear optical susceptibility tensor and it is given by [33]

$$\chi_{ij}^{(1)}(-\omega,\omega) = \frac{e^2}{\hbar\Omega}\sum_{nm\vec{k}} f_{nm}(\vec{k})\frac{r_{nm}^i(\vec{k})r_{mn}^i(\vec{k})}{\omega_{mn}(\vec{k})-\omega} = \frac{\varepsilon_{ij}(\omega)-\delta_{ij}}{4\pi} \quad (2)$$

where n,m denote energy bands, $f_{mn}(\vec{k}) \equiv f_m(\vec{k}) - f_n(\vec{k})$ is the fermi occupation factor, Ω is the normalization volume. $\omega_{mn}(\vec{k}) \equiv \omega_m(\vec{k}) - \omega(\vec{k})$ are the frequency differences, $\hbar\omega_n(\vec{k})$ is the energy of band n at wavevector **k.** The $\vec{r}_{nm}$ are the matrix elements of the position operator [33].

As can be seen from equation (2), the dielectric function $\varepsilon_{ij}(\omega) = 1 + 4\pi\chi_{ij}^{(1)}(-\omega,\omega)$ and the imaginary part of $\varepsilon_{ij}(\omega)$, $\varepsilon_2^{ij}(\omega)$, is given by

$$\varepsilon_2^{ij}(w) = \frac{e^2}{\hbar\pi}\sum_{nm}\int d\vec{k} fnm(\vec{k})\frac{v_{nm}^i(\vec{k})v_{nm}^j(\vec{k})}{\omega_{mn}^2}\delta(\omega-\omega_{mn}(\vec{k})). \quad (3)$$

The real part of $\varepsilon_{ij}(\omega), \varepsilon_1^{ij}(\omega)$, can be obtained by using the Kramers-Kroning transformation [33]. Because the Kohn-Sham equations determine the ground state properties, the unoccupied conduction bands as calculated have no physical significance. If they are used as single-particle states in a calculation of optical properties for semiconductors, a band gap problem comes into included in calculations of response. In order to take into account self-energy effects, in the present work, we used the 'scissors approximation' [32].

The known sum rules [34] can be used to determine some quantitative parameters, particularly the effective number of the valence electrons per unit cell N_{eff}, as well as the effective optical dielectric constant ε_{eff}, which make a contribution to the optical constants of a crystal at the energy E_0. One can obtain an estimate of the distribution of oscillator strengths for both intraband and interband transitions by computing the $N_{eff}(E_0)$ defined according to

$$N_{eff}(E) = \frac{2m\varepsilon_0}{\pi\hbar^2 e^2 Na}\int_0^\infty \varepsilon_2(E)EdE, \quad (4)$$

Where N_a is the density of atoms in a crystal, e and m are the charge and mass of the electron, respectively and $N_{eff}(E_0)$ is the effective number of electrons contributing to optical transitions below an energy of E_0.

Further information on the role of the core and semi-core bands may be obtained by computing the contribution which the various bands make to the static dielectric constant, ε_0. According to the Kramers-Kronig relations, one has

$$\varepsilon_0(E) - 1 = \frac{2}{\pi}\int_0^\infty \varepsilon_2(E)E^{-1}dE. \quad (5)$$

One can therefore define an 'effective' dielectric constant, which represents a different mean of the interband transitions from that represented by the sum rule, equation (5), according to the relation

$$\varepsilon_{eff}(E) - 1 = \frac{2}{\pi}\int_0^{E_0} \varepsilon_2(E)E^{-1}dE. \quad (6)$$

The physical meaning of ε_{eff} is quite clear: ε_{eff} is the effective optical dielectric constant governed by the interband transitions in the energy range from zero to E_0, i.e. by the polarizition of the electron shells.

In order to calculate the optical response by using the calculated band structure, we have chosen a photon-energy range of 0-25 eV and have seen that a 0-17 eV photon-energy range is sufficient for most optical functions.

The Sb_2S_3 and Sb_2Se_3 single crystals have an orthorhombic structure that is optically a biaxial system. For this reason, the linear dielectric tensor of the Sb_2S_3 and Sb_2Se_3 crystals have three independent components that are the diagonal elements of the linear dielectric tensor.

We first calculated the real and imaginary parts of z-components of the frequency-dependent linear dielectric function and these are shown in Fig. 2. The ε_1^z is equal to zero at about 4.12 eV, 9.61 eV, 13.37 eV and 20.1 eV in Fig. 2a for Sb_2S_3, while the ε_1^z is equal to zero at about 2.95 eV, 8.91 eV, 13.06 eV and 19.89 in Fig. 2b for Sb_2Se_3 crystal. The peaks of the ε_2^z correspond to the optical transitions from the valence band to the conduction band and are in agreement with the previous results. In general, there are various contributions to the dielectric function, but Fig. 2 shows only the contribution of the electronic polarizability to the dielectric function. Fig. 2 shows also that except for a narrow photon-energy region, between 0.5 eV and 2 eV, the ε_1^z increase with increasing photon energy, which is the normal dispersion. In the range between 2.0 eVenergy and 5.0 eV ε_1^z decrease with increasing photon-energy, which is the characteristics of an anomalous dispersion. Furthermore as can be seen from Fig.2, the photon –energy range up to 1.5 eV is characterized by high transparency, no absorbtion and a small reflectivity. The 1.9-5.0 eV photon energy range is characterized by strong absorption and appreciable reflectivity. We also calculated all optical

functions along x- and y- directions. They show the different structures in the same energy region like for the z- direction, but these singularities have the similarly quantum-chemical mechanism.

The calculated energy-loss functions, $L(\omega)$, are also presented in Fig. 2a and Fig. 2b. In this figure, correspond to the energy-loss functions along the z-directions. The function $L(\omega)$ describes the energy loss of fast electrons traversing the material. The sharp maxima in the energy-loss function are associated with the existence of plasma oscillations [35]. The curves of L_z in Fig. 2 have a maximum near 20.30 eV for Sb_2S_3, and 20.83 for Sb_2Se_3.

The effective optical dielectric constant, ε_{eff}, shown in Fig. 3, reaches a saturation value at about 20 eV. The photon-energy dependence of ε_{eff} can be separated into two regions. The first is characterized by a rapid rise and it extends up to 12 eV In the second region the value of ε_{eff} rises more smoothly and slowly and tends to saturation at the energy 20 eV. This means that the greatest conribution to ε_{eff} arises from interband transitions between 2 eV and 17 eV.

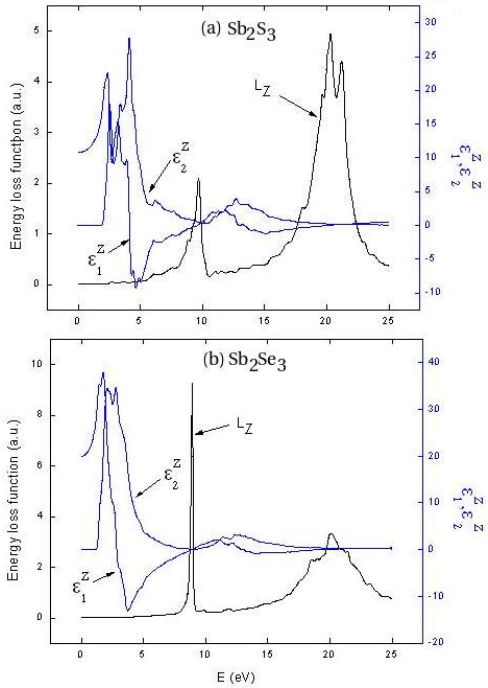

Fig. 2. Energy spectra of dielectric function $\varepsilon = \varepsilon_1 - i\varepsilon_2$ and energy-loss function (L) along the z-axes for Sb_2S_3 and Sb_2Se_3.

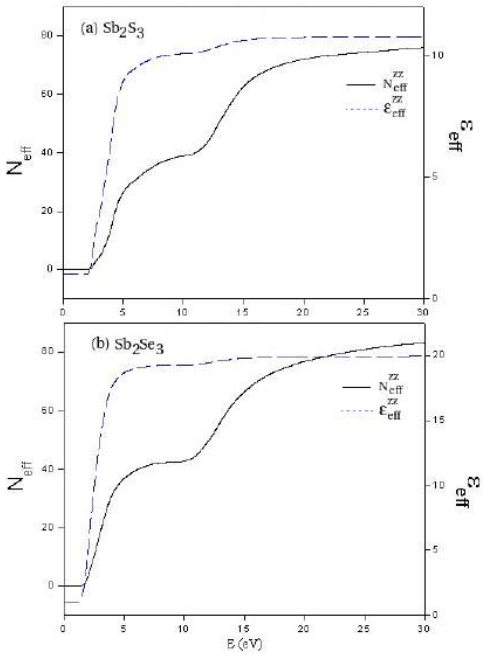

Fig. 3. Energy spectra of N_{eff} and ε_{eff} along the z- axes

4. CONCLUSIONS

In present work, we have made a detailed investigation of the electronic structure and frequency-dependent linear optical properties of the Sb_2S_3 and Sb_2Se_3 crystals using the density functional methods. The task of this work was to apply the density-functional methods to a complex crystal like the Sb_2S_3 and Sb_2Se_3. It is seen that Sb_2S_3 and Sb_2Se_3 crystals have the indirect forbidden gap. The obtained band gap values are in agreement with the previous results. The total DOS calculation shows that the valance band is composed of the 3s and 3p states of the S atom and 4s and 4p states of the Se atom, 5s and 5p states of Sb, while the conduction band consists of the 5p states of the Sb, S and Se atoms. we have photon-energy dependent dielectric functions and some optical properties such as the energy-loss function, the effective number of valance electrons and the effective optical dielectric constant along the all main axes. The results of the structural optimization implemented using the LDA are in good agreement with the experimental results. To our knowledge, this is the first detailed study of the optical properties of the Sb_2S_3 and Sb_2Se_3

[1]. *O. Madelung,* Semiconductory Other than Group IV Elements and III-V Compounds, Springer, Germany, 1992, p.50.

[2]. *E.A. El-Sayad, A.M. Moustafa, S.Y. Marzouk*, Physica B 2009, 404, 1119-1127.

[3]. *J. Black, E.M. Conwell, L. Sigle, C.W. Spencer*, J. Phys. Chem. Solids 1957, 2, 240.

[4]. *N.S. Platakis, H.C. Gatos,* Phys. Status Solidi A Appl. Res. 1972, 13, K1.

[5]. *K.Y. Rajapure, C.D. Lokhande, C.H. Bhosele*, Thin Solid Films 1997, 311, 114.

[6]. *S.V. Forgue, R.R. Goodrich, A.D. Cope*, RCA Rev. 1951, 12, 335.

[7]. *C. Ghash, B.P. Varma*, Thin Solid Films 1979, 60, 61.

[8]. *J. Grigas, J. Meshkauskov, A. Orhiukas*, Phys. Status Solidi A Appl. Res. 1976, 37, K39.

[9]. *M.S. Ablova, A.A. Andreev, T.T. Dedegkaev, B.T. Melekh, A.B. Pevtsov, N.S. Shendel, L.N. Shumilova*, Soviet Phys. Semicond.-USSR 1976, 10, 629.

[10]. *M.J. Chockalingam, N. Nagaraja Rao, K.Rangarajan, C.V. Surganarayana*, J. Phys. D. Apply. 1930,3,1641.

[11]. *E. Montrimas, A. Pazera*, Thin Solid Films 1976, 34, 65.

[12]. *J. George, M.K. Radhakrishnan*, Solid States Comm. 1980, 33, 987.

[13]. *N. Kuganathan*, E-Journal of Chemistry 2009, 6, 5147-5152.

[14]. *R. Caracas, X. Conze*, Phys. Chem. Minerals 2005, 32, 295-300.

[15]. *W. Kohn and L. J. Sham*, Phys. Rev. 1965, 140, A1133.

[16]. <www.uam.es / siesta>

[17]. *P. Ordejon, E. Artacho, J. M. Soler*, Phys. Rev. B (Rapid Common) 1996, 53, R10441.

[18]. *J. M. Soler, E. Artaeho, J. D. Gole, A. Garsia, J. Junguera, P. Ordejon, D. Sanchez-portal*, J. Phys: Condens Matter 2002, 14, 2745.

[19]. *D. M. Ceperley, M. J. Alder*, Phys, Rev. Lett. 1980, 45, 566.

[20]. *N. Troullier, J. L. Martins*, Phys. Rev. B 1991, 43, 1993.

[21]. [*O. F. Sankey, D.J Niklewski*, Phys. Rev B 1989, 40, 3979.

[22]. *F. D. Murnaghan*, Proc. Nat. Acad. Sci. USA 1944, 30, 5390.

[23]. *A. Kyono, M. Kimata, M. Matsuhisa, Y. Migashita, K. Okamoto*, Phys. Chem. Minerals 2002, 29, 254-260.

[24]. *By D.O. Micke, J.T. Mcmullan*, Z. Kristallogr. 1975, 142, 447-449.

[25]. *A.M. Salem, M.S. Selim*, J. Phys. D: Appl. Phys. 2001, 34, 12-17.

[26]. *X. Zheng, Y. Xie, L. Zhu, X. Jiang, Y. Jia, W. Song, Y. Sun*, Inorganic Chemistry 2002, 41, 455-461.

[27]. *Z. Hurych, D. Davis, D. Buczek, C. Wood*, Phys. Rev. B 1974, 9, 4392-4404.

[28]. *G.-Y. Chen, B. Dneg, G.-B. Cai, T.-K. Zhang, W.-F. Dong, W.-X. Zhang, A.-W. Xu*, J. Phys. Chem. C 2008, 112, 672-679.

[29]. *O. Madelung*, Semiconductors Other than Group IV elements and III-V Compounds, in: R. Poerschke (ed), Data in Science and Tecnology, Springer, Berlin, 1992, p50.

[30]. *R.S. Mane, C.D. Loklande*, Mater. Chem. Phys. 2000, 65, 1.

[31]. *A.F. Skubenko, C.V. Laptii*, Soviet Phys. Solid State 1964, 4, 327.

[32]. *Z.H. Levine, D.C. Allan* . Phys Rev, Lett. 1989, 63, 1719.

[33]. *H.R. Philipp, H. Ehrenreich*, Phys. Rev. 1963, 129, 1550.

[34]. *O.V. Kovalev*, Representations of the Crystallographic Space Groups. Irreducible Representations Induced Representations and Corepresentations, Amsterdam: Gordon and Breach (1965).

[35]. *L. Marton*, Rev. Mod. Phys. 1956, 28, 172.

A NEW METHOD AND COMPUTER CONTROLLED SYSTEM FOR MEASURING THE Z PARAMETERS OF SEMICONDUCTORS IN REAL MODULES

RASIT AHISKA
Gazi University, Faculty of Technology, Electronic and Computer Engineering Department, Ankara, TURKEY
ahiska@gazi.edu.tr

Determination the z figure of merit of thermoelectric (TE) semiconductor materials is of essence in production of TE modules. In order to determine the z figure of merit of TE materials, various methods, apparatuses and software have been developed. All of these methods foresee the assignment of the z figure of merit when the semiconductor is free; that is, before being employed in the module. However, TE modules are systems composed not only of semiconductor materials but also ceramic, copper plates, and soldering. All these components affect the performance of the module directly. Not only the current applied, temperature or geometric factors but also changes in characteristics of other components in the module affect on the parameters of semiconductor in an operation module. Hence parameters of semiconductor in an operating module are different from those in free material. That is why calculations of performances of TE modules based on the z figure of merit of semiconductor not in use lack accuracy. In this study, a computer controlled test system composed of hardware and software, Thermoelectric Performance Analysis System (TEPAS) based on a new method taking inputs of easily measurable parameters like temperature, current and voltage, is employed in calculation of thermal conductivity, κ, Seebeck coefficient,α, specific resistivity, ρ, and quality parameter, z, of semiconductor in standard TE modules of MELCOR Inc. CP 1.0-127-05L, CP 1.4-127-10L and CP 1.4-71-06L (TEC1-07106). Comparisons between these parameters with direct measurements have revealed the advantage of new method and TEPAS. With new method and TEPAS the z figure of merit of 15 TE modules are investigated.

1. INTRODUCTION

There exist traditional methods, apparatuses and software to analyze performances of TE modules [1,2]. The traditional methods take the parameters of the semiconductor material as constant or temperature-dependent only. However, since the parameters attained are not valid under real conditions, evaluation of output parameters of a TE module with these methods is misleading [3]. In order to determine output parameters of thermoelectric modules and semiconductors, a new method depending on measurement of temperature, current and voltage has been developed.

In this study, a computer controlled, USB based, portable TE performance analysis system composed of hardware and software have been realized to provide an application to the developed method. By TEPAS CP 1.0-127-05L, CP 1.4-127-10L and CP 1.4-127-06L (TEC1-07106) model standard TE modules of Melcor Inc. have been employed in experimental studies [4]. Thermal conductivity, κ, Seebeck coefficient, α, specific resistivity, ρ, and coefficient of performance, z, of TE semiconductor material of 15 modules calculated with traditional methods and the analytic formulas acquired with the new method have been compared with results of TEPAS and other experimental results, and the advantage of the new method and the testing mechanism have been depicted.

2. NEW METHOD

The parameters employed in the new method are current pulled by the module (I), voltage across the terminals of it (V), thermoemf it produces (E) and temperature of any of it surfaces (T_H or T_C). Effects of all internal and external factors on performance of TE module are taken into account in the new method as it employs the parameters, V_{max}, I_{max} and E_{max} in calculations; since, these parameters are attained via direct measurement while the module is operating.

For an unloaded working TE module, total thermal load, $Q_L = 0$, and energy absorbed by the cold side of the module, $Q_C = 0$. Under this condition, temperature of the cold side and the temperature difference between the two sides of the module occur to be T_{Cmin} and ΔT_{max}, respectively. Furthermore, $I = I_{max}$, $V = V_{max}$, and $E = E_{max}$. The equations acquired with the new method are presented in equation (1) - (2) below [4].

$$V_{min} = \frac{2NI_{max}\rho}{G};$$

$$E_{max} = 2N\alpha\Delta T_{max};$$

$$V_{min} = V_{max} - E_{max} \quad (1)$$

$$\rho = \frac{GV_{min}}{2NI_{max}};$$

$$\alpha = \frac{V_{max}}{2NT_H};$$

$$k = \frac{0.5I_{max}V_{min}V_{max}}{2NGE_{max}T_H};$$

$$z = \frac{E_{max}V_{max}}{0.5V_{min}^2 T_H} \quad (2)$$

Here, G = a / h (Area / Length of TE Element (cm)) is the geometric factor of the thermoelement, and N is the number of thermoelements in a single module. V_{max} and E_{max} in the above equations characterize TE semiconductors and do not depend on geometric properties of the semiconductor. In order to benefit from (1) – (2), both experimental parameters I_{max}, V_{max}, and

E_{max}, and one of the temperatures T_C or T_H have to be measured directly. According to these equations in place of parameters of TE material such as thermal conductivity, κ, Seebeck coefficient,α, and specific resistivity, ρ, experimental parameters such as I_{max}, V_{max} and E_{max} have been employed.

3. SYSTEM DESIGNED

Computer controlled TEPAS, with its hardware and software, has been designed and realized for performance analysis and acquisition of parameters of operating TE modules and systems. In figure 1 below, internal and external views of TEPAS are demonstrated. On the system, there exist TE module power outputs, inputs for thermocouples, USB ports for computer connections, connections for control of the cooling system, 220V power supply inputs, and switch for opening and closing the system.

With TEPAS, it is possible to measure current through and voltage across TE modules and temperature measurements with thermocouples on 8 channels. Since power to TE module to be tested is supplied by TEPAS, current and voltage of the module have been measured with SMPS inside the system. For transferring measurement data to the computer and control signals to the system USB based DA&C modules have been employed.

In order to conduct experimental studies with TEPAS and to test TE modules, a special TE system has been set up. This configuration consists of 3 main parts: TE module setup, cooling system (CS) and heating system (HS). In figure 2, below, basic structure of TE system setup and its connections to TEPAS have been demonstrated.

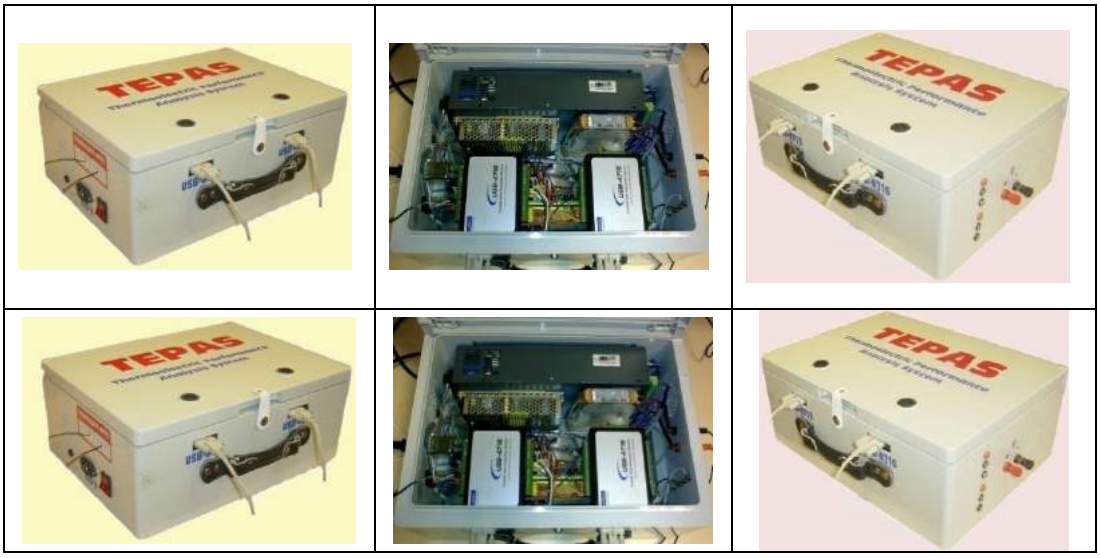

Figure 1. General view of TEPAS

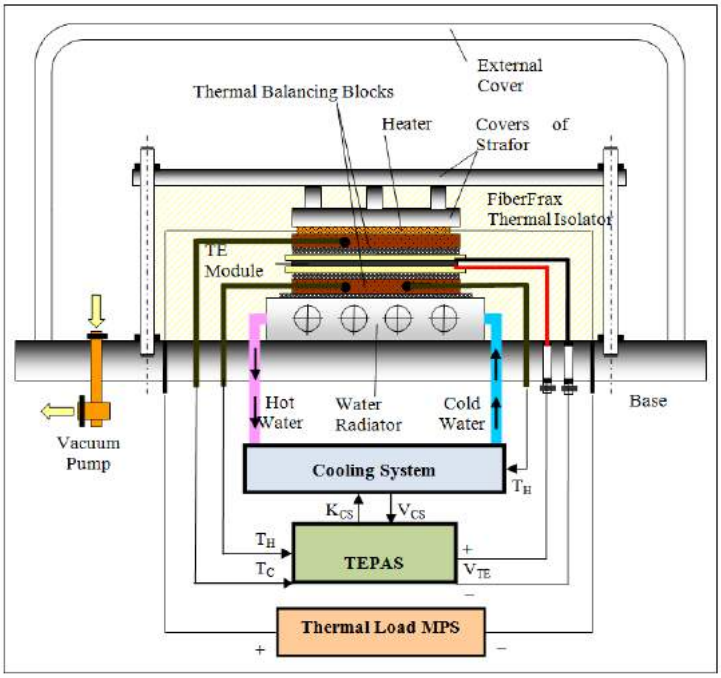

Figure 2. TEPAS testing setup

Table 1

Catalog ,N	G, cm	$E_{max,}$ V	$\alpha,10^{-4}$ VK^{-1}	α_T10^{-4} VK^{-1}	α_E10^{-4} VK^{-1}	$\rho,10^{-3}$ Ωcm	ρ_T10^{-3} Ωcm	ρ_E10^{-3} Ωcm	$k,10^{-2}$ WK^{-1}	k_T10^{-2} WK^{-1}	k_E10^{-2} WK^{-1}	$z,10^{-3}$ K^{-1}	$z_T,10^{-3}$ K^{-1}	$z_E,10^{-3}$ K^{-1}
CP0.85-127-06L	0,042	3,35	2,02	2,1		1,01	0,7		1,51	2,3		2,68	2,41	
CP1.0-127-08L	0,05	3,40	2,02	2,2		1,01	0,9		1,51	1,7		2,68	2,47	
CP1.0-127-06L	0,061	3,40	2,02	2,2		1,01	0,9		1,51	1,7		2,68	2,47	
CP2-31-06L	0,282	0,83	2,02	0,5		1,01	0,9		1,51	1,7		2,68	2,47	
CP1.4-71-045L	0,171	1,85	2,02	1,2		1,01	0,9		1,51	1,8		2,68	2,35	
CP1.4-127-06L	0,118	3,40	2,02	2,2		1,01	0,7		1,51	2,4		2,68	2,47	
CP1.4-127-045L	0,171	3,30	2,02	2,1		1,01	0,9		1,51	1,8		2,68	2,35	
CP2-127-10L	0,184	3,40	2,02	2,2		1,01	1,1		1,51	1,5		2,68	2,47	
CP2-127-06L	0,282	3,45	2,02	2,2		1,01	0,9		1,51	1,7		2,68	2,53	
CP1.4-71-06L	0,118	1,90	2,02	2,2	1,23	1,01	0,9	0,4	1,51	1,8	1,8	2,68	2,47	1,7/2,1
CP1.0-127-05L	0,079	3,40	2,02	2,2	1,8	1,01	0,9	1,1	1,51	1,7	1,6	2,68	2,47	2,2/1,84
CP1.4-127-10L	0,077	3,45	2,02	2,2	2,0	1,01	0,9	1	1,51	1,7	2,7	2,68	2,53	1,7/1,5
1MC06-032-05	0,024	1,77	2,02	1,1		1,01	0,8		1,51	1,7		2,68	2,52	
1MC06-032-15	0,024	1,84	2,02	1,2		1,01	0,8		1,51	1,8		2,68	2,57	
1MC06-008-15	0,024	0,69	2,02	0,3		1,01	1,4		1,51	2,4		2,68	2,57	

($E = 2\alpha N$, $\alpha = E / 2N$; $R = 2 \rho N / G$, $\rho = RG / 2N$; $K = 2kNG$, $k = K / 2NG$).

4. RESULTS AND DISCUSSIONS

In table 1 below, results acquired at T_H = 300 K are presented.

Here, entries without T index are attained traditional method, entries with T index are calculated by new method, and entries with E index are measured with TEPAS or directly with Z-meter. Module codes starting with CP and 1MC are modules of Melcor and RTM, respectively [5]. Measurement on only CP 1.0-127-05L, CP 1.4-127-10L and CP 1.4-71-06L (TEC1-07106) modules are taken directly with TEPAS. According to table 1, on CP modules direct measurements with TEPAS have I_{max} - 0.6%; V_{max} - 3.3%; ΔT_{max} - 1.9% average precision, and calculations have z - 4.6% error percentages.

5. CONCLUSIONS

Error percentages in α, ρ, k and z measured with TEPAS and the new method are found to be very little compared to other methods and apparatuses. It is demonstrated that α, ρ, k and z parameters linearly depends on E and thermoemf is the key parameter, and with TEPAS based on the new method all parameters can be directly measured. In conclusion thanks to new TE performance analysis system, α, ρ, k and z parameters of semiconductors in TE module can be measured fast, with high reliability and practically. TEPAS can be employed not in testing of TE modules or semiconductors but also in mass production of these as a quality controller.

[1]. *Harman T C* 1958 Special techniques for measurement of thermoelectric properties J. Appl. Phys. 29 1373-1379.

[2]. *Heylen A E* D 1975 Figure of merit determination of thermoelectric modules Energy Conversion 15 65-70.

[3]. *Ahıska R, and Ahıska, K.*, 2010 New method for investigation of parameters of real thermoelectric modules Energy Conversion and Management 51 338–345

[4]. http://www.melcor.com homepage of Melcor

[5]. *G. Gromov, D. Kondratiev, A. Rogov, L. Yershova* 2009 Z-meter: Easy-to-use Application and Theory,http://www.rmtltd.ru

DROPLET PHASE OF POINT ION SOURCES FOR NANOTECHNOLOGY PURPOSES

I.S. GASANOV, I.I. GURBANOV, I.A. NASIBOV, F.F. EFENDIYEVA
Institute of Physics of NAS, G. Javid pr., 33, Baku, AZ1143 Azerbaijan
ilkhamg@mail.ru

Detailed research of disperse phase characteristics in a point (liquid metal) source of indium, tin and eutectic alloy $Ni_{81}B_{11}Al_8$ ions is carried out. Ion emission of a source is characterized by high stability up to the certain value of a beam current (I~40 μA for Sn and In). At the further increase in a current, there is an electric dispersion of a working liquid and excitation of capillary instability on its surface. Generated nanoparticles have the dimensions of 2-20 nanometers (Sn) and a specific charge about $5 \cdot 10^4$ C/kg. The majority of particles have the minimal dimension. Presumably charged nanoparticles of minimal sizes are structural elements of a liquid phase. Similar researches are carried out for obtaining of germanium nanoparticles in a source modification with a porous electrode.

An ion phase of point sources generally was used in technology up to now. Opportunities of a drop phase use of these sources in nanotechnology for a creation of various quantum structures and nanosensors are discussed.

I. INTRODUCTION

In detail investigated point (liquid metal) ion sources have a number of high parameters, and have found an application in technology of focused ion beams (FIB).

Due to the small size of the liquid emitter, the initial density of an ion current is estimated at a level of $\sim 10^8$ A/cm^2 which is higher for some orders of magnitude than at best plasma sources [1, 2]. The thermal velocity spread of ions in point sources is lower than at plasma sources and makes some electron-volts. The specified factors allow for example obtaining the focused beams of gallium ions with high brightness and the dimension of a spot of 5 nanometers [3].

In the certain modes of an action point sources generate charged nanoparticles and this is accompanied simultaneously by an excitation of oscillations of an ion current [4].

Emission features of a disperse phase are less investigated in details and as a consequence streams of accelerated nanoparticles in point sources are not used practically in technology though the dimensions of particles cause the assumption of their application for creation of nano-objects.

The features of generation of the charged droplets with the nanometer dimension in a point source and opportunities for their practical application presented in this work.

II. EXPERIMENTAL SETUP

Experiments carried out with a compact source of container type (Fig. 1), indium, tin and eutectic alloy $Ni_{81}B_{11}Al_8$ were used as working substances [5].

The graphite container was warmed up by electron bombardment from the back side up to fusion temperature of working substance. For stable ion emission the reliable wetting of a needle by a liquid required. The iron needle was used with tin, nickel - with indium and tungsten - with eutectic alloy.

The extractor was positioned at a distance no more than 1 mm from a needle, the straightened voltage up to 10 κV applied between them. The constant and variable components of an ion current were measured in a collector and extractor circuits. Spectra of fluctuations of an ion current were registered by spectrum analyzer S4-25 and oscillograph S8-1.

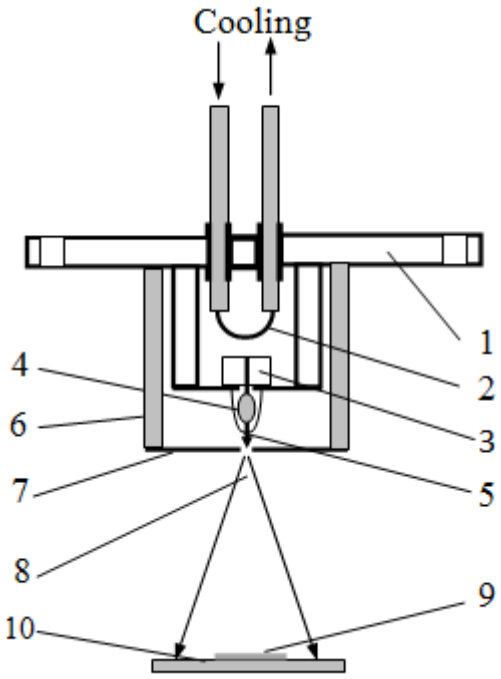

Fig. 1. The scheme of point ion source: 1-flange; 2-cathode; 3-container; 4-working substance; 5-needle; 6-insulator; 7-extractor; 8- ion beam; 9-substrate; 10-collector

The mass analyzer with the crossed electromagnetic fields and a two-coordinate recorder were used for definition of a beam compose, thus the analyzer positioned between an extractor and a collector.

The dimensions of deposited nanoparticles and their histograms were determined by transmission electron microscope Tesla and atom force microscope AFM NE.

The source was mounted on the vacuum installation VUP-4 with limiting pressure of $5 \cdot 10^{-6}$ torr.

III. RESULTS AND DISCUSSION

Ion emission appears in the given source at a voltage of 5÷6 κV between a needle and an extractor. As it has been established earlier [6] the stable emission of ions is disrupted at a current of a beam around 40 μA

(Sn). An excitation of fluctuations of an ion current with frequency of 15÷20 MHz and a generation of metal droplets occurs simultaneously. The spectrum of fluctuations is discrete, more intensive and low-frequency modes appear with increase in a current, and the earlier excited modes are kept. At a limiting current of 120 μA, the frequency of fluctuations is equal to 2 MHz. Amplitude of fluctuations in a circuit of an extractor is considerably higher than in a circuit of a collector, as a collector is shielded by the extractor (Fig. 1). However the level of modulation of an ion current is insignificant and did not exceed 7 % (Fig. 2). At excitation of fluctuations, the volt-ampere characteristic of a source does not find out any sharp breaks.

At an excitation of fluctuations of a current, a stream of liquid droplets appears in compose of a beam and this stream extends along an axis with a small angle of a divergence (Fig. 3). The specific charge of the majority of particles is equal to $5 \cdot 10^4$ C/kg, at increase in a current of a beam, the specific charge of particles decreases so larger drops are generated on the average [7, 8].

The spectrum of the particles is continuous in a range of 2-20 nanometers, the range of the dimensions extends up to 40 nanometers with increase in a current, there are separate particles with the dimensions up to hundreds nanometers (Fig. 4). The number of the least dimension particles exceeds by three orders of the magnitude the number of the greatest dimension particles. Calculations show that at the noted specific charge of nanoparticles, one elementary charge account for every 16 atoms on the average. At obtaining of the three-dimensional image of a surface with the deposited particles the polished substrate from stainless steel was on distance of 70 mm from a needle, the time of an exposition is 12 s at the common current of an ion beam of 65 μA. The characteristic dimension of particles makes few nanometers on coordinate z [9].

Radial distributions of ion current density have been measured in two modes of a source - stable and modulated - (Fig. 5). Small reduction of a current density in the central area of a beam at excitation of fluctuations (Fig. 5, curve 2) attracts attention. Despite of small reduction value of the current density, the similar form of radial distribution generated stably and was observed by other authors also.

At use of eutectic alloy $Ni_{81}B_{11}Al_8$ as a working substance fluctuations of an ion current and, accordingly, a generation of nanoparticles was not observed up to a limiting current of 150 μA in a wide range of frequencies up to 1 GHz.

Conditions of an excitation and a character of fluctuations of an ion current allow to conclude, that at abruption of metal droplets from a top of the extended Taylor`s cone [10] capillary instability develops on a surface of a liquid.

From expression for wave length of a capillary instability [11], it is possible to obtain values of wave lengths, for example, at limiting observable frequencies:

$$\lambda_1 = \sqrt[3]{\frac{8\pi\sigma}{\rho f^2}} = 1.3\ \mu m\,, \qquad (1)$$

where σ is coefficient of a superficial tension, ρ is density of a liquid, at f=30 MHz and λ_2 = 7,9 micrometers at f=2 MHz.

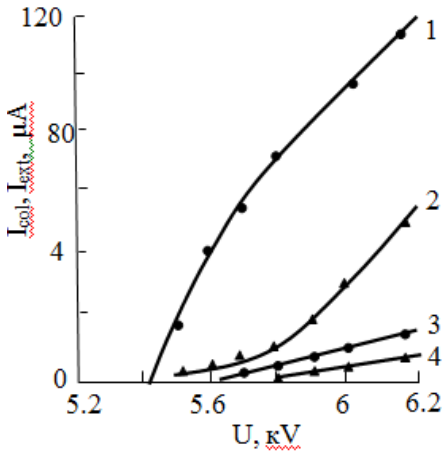

Fig. 2. Dependence of current components in collector and extractor circuits from extracting voltage (In): 1 – I_{col}, 2 – I_{ext}, 3 – $\tilde{I}_{ext}$, 4 – $\tilde{I}_{col}$

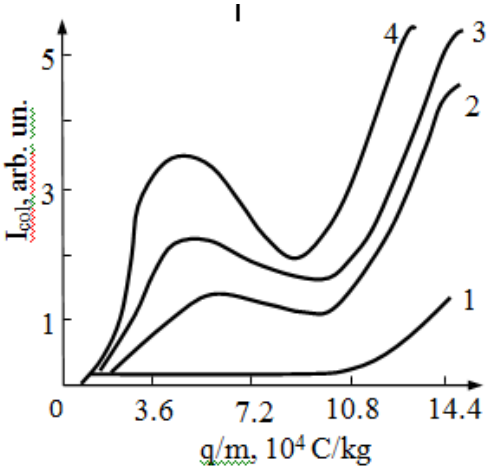

Fig. 3. Area of mass spectra of an ion beam corresponding to nanodroplet phase (Sn): 1-I_b=28 μA; 2-40 μA; 3-68 μA; 4-95 μA

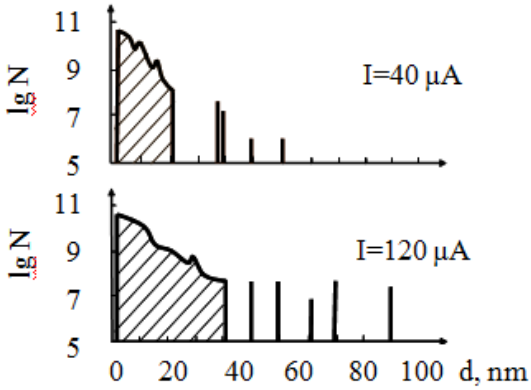

Fig. 4. Histograms of the tin nanoparticle dimensions obtained by means of an electron microscope.

Last dimension corresponding to indignations of the greatest wave length well agreed with direct measurements of the size of Taylor`s cone by shadow

photo. As the thickness of a liquid film is small at the basis of Taylor`s cone fluctuations are suppressed here. So the system of standing capillary waves develops and for this reason the spectrum of fluctuations is discrete.

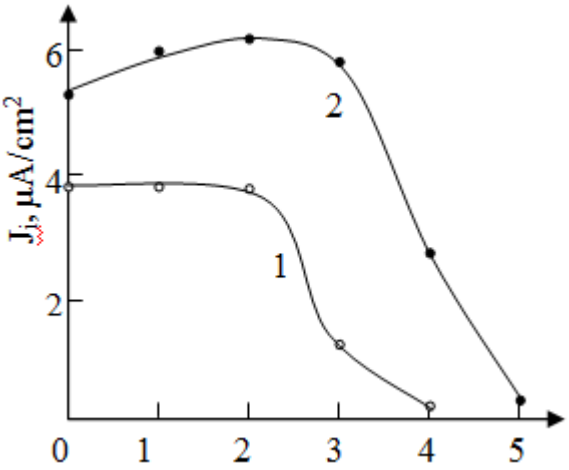

Fig. 5. Radial distribution of ion current density: 1 - beam current I_b = 38 μA, 2 – I_b= 65 μA.

Apparently the sizes of the majority generated nanoparticles are less than length of capillary waves so torn off droplets are not formed by a capillary wave. It is possible to assume that the charged particles are formed inside of a liquid and entirely come off at the certain value of an electric field at the surface. Charged nanoparticles of minimal sizes are probably structural elements of phase transformations [12], by theoretical estimations the dimension of such elements should be of 3.2 nanometers for tin which is close to dimension measured in our experiments (Fig. 4).

In a source on the basis of alloy $Ni_{81}B_{11}Al_8$, the abruption of liquid drops do not occur and capillary instability is not excited because of high viscosity of nickel.

The experimental facts mentioned above testify that the emission of ions and charged nanoparticles occurs independently in point sources so a generation of a disperse phase does not render appreciable influence on ion emission. If to start with existing model of field emission [13], according to which ions and nanoparticles are taken from the same areas, it is difficult to explain a registered low level of a modulation of an ion current (Fig. 2). At abruption of nanodroplets deformation of an emission zone should modulate essentially an ion current that does not prove by experiment.

Therefore it is necessary to assume that the dimension of the ion emission area considerably exceeds the dimension of the nanoparticle emission area. In the center of an emission zone where the greatest value of field intensity is realized the ledge of a liquid is formed from which charged nanoparticles are extracted. In this case an emission of fine dispersive phase will not lead to appreciable modulation of an ion current. Nanoparticles extend along an axis of a beam, and shield the central area of the emitter in the certain degree. As a result the ion current density decreases in the center of a beam (Fig. 5).

Proceeding from the given model, it is possible to estimate the lower limit of the diameter of emission area in the assumption, that $d_i >> d_n$, where d_i and d_n are the dimensions of emission area of ions and nanoparticles accordingly [14]. If d_n to accept equal to the average dimension of nanoparticles of 10 nanometers (Sn), we shall obtain the dimension for d_i: $d_i = 10d_n = 100$ nanometers. In that case at I_i= 10 ÷ 100 μA for initial density of an ion current, value of $j_i = 1.25 \cdot 10^5 \div 1.25 \cdot 10^6$ A/cm^2 will turn out, which is less on 2 orders of the magnitude than the value obtained in existing models of a field emission.

An obtaining of nanoparticles from conductive and magnetic materials by point sources does not represent difficulties. Obtaining nanoparticles of semiconductor substances particularly represents the big interest for formation of surface quantum structures. However the majority of pure semiconductors and their compounds have a high pressure ($p_s > 10^{-2}$ torr) of saturated vapors at the fusion temperature. At such pressure the gas discharge between a needle and an extractor will be ignited and process of field emission disrupted.

For obtaining of an ion emission from liquid semiconductors a modification of an ion source with a porous electrode [15-17] has been offered. The exhaust outlet of the container closed up by point electrode from porous tungsten. At the fusion the working substance flows into pores of an electrode and does not allow vapors of working substance to leave the container to vacuum. The source works at rather higher temperature of the container in order pressure difference allow a liquid go through pores. Emission of ions and nanoparticles of germanium has been obtained in our last experiments with the modified source in which it is used point porous electrode. The electrode has been made from pressed and sintered tungsten. Tightness of the container with working substance is rather important as under pressure of vapors the liquid gets into pores even if it does not moisten tungsten.

IV. CONCLUSION

Proceeding from data about parameters and features of a charged nanoparticle generation in point sources it is possible to offer some variants of their application in nanotechnology.

It is possible to obtain films of various materials of nanodimensional thickness by deposition nanoparticles on a surface. It is possible to accompany a deposition of particles with process of bombardment of a surface by fast ions of the same material which improves quality of a film. This technology is known as secondary ion deposition (SID).

Nanoparticles can be deposited on demanded regions of preliminary prepared surface and form various quantum structures by scanning of a charged nanoparticles stream. Structures can be formed also in another way: first to deposit particles on a surface, and

then to redistribute them on the necessary coordinates by probe microscope.

The accelerated droplets of a desirable material can be deposited on ledges of cantilevers of atom force microscopes for creation nanodimensional points.

Nanodispersive component of point sources can be used for diagnostics of structural elements in a liquid phase of various materials.

By means of point sources it is possible to create quantum holes and wires on a surface. It can be realized in the nonconventional way, without use of difficult optics for the focusing of beams. The conductive object positioned horizontally near to a point, for example on distance of 100 nanometers. After achievement of ion emission the deepening object of nanometer dimension will be etched opposite to a point on a surface as the ion beam will not have time to diverge on such distance. A nanowire will be etched if an object transported slowly in a horizontal direction. If work in a mode of nanoparticle generation, quantum holes and wires can be filled by droplets of working substance and potential barriers prepared under corresponding conditions.

It is obvious, that the specified technological opportunities required detailed experimental testing.

ACKNOWLEDGEMENT

The present investigation has been executed at the support of the fund STCU (the grant No. 4520).

[1]. *I.Brodie and J.Muray*, The Physics of Microfabrication. New-York: Plenum Press; (1982).

[2]. *D.R. Kingham and L.W.Swanson*, Vacuum. 43, 945 (1984).

[3]. URL of companies: FEI <http: // www.fei.com>; JEOL <http: // www.jeol.com>.

[4]. *V.G.Dudnikov and A.L.Shabalin*, Jour. Tech. Phys. 55, 4, 778 (1985) (in Russian).

[5]. *M.D.Gabovich, I.S.Gasanov and I.M.Protsenko*, Jour. Tech. Phys . 58, 12, 2370 (1988) (in Russian)

[6]. *V.E.Badan and I.S.Gasanov*, Letters to Jour. Tech. Phys. 15, 17, 52 (1989) (in Russian).

[7]. *I.S.Gasanov*, Letters to Jour. Tech. Phys. 25, 17, 28 (1999) (in Russian).

[8]. *I.S.Gasanov, E.J.Salaev and I.I.Gurbanov*, Applied Physics. 2, 49 (2005) (in Russian).

[9]. *I.S.Gasanov and I.I.Gurbanov*, Letters to Jour. Tech. Phys. 34, 12, 47 (2008) (in Russian).

[10]. *G.Taylor*, Proc. Roy. Soc. A; 280, 397 (1964).9.

[11]. *L.D.Landau and E.M.Livshits*, Hydrodynamics. Moscow: Science; (1986) (in Russian).

[12]. *V.I.Stafeev*, Phys. Tech. of Semiconductors. 21, 4, 733, (1987) (in Russian).

[13]. *V.V.Vladimiriov, V.E.Badan, V.N.Gorshkov et al.* J.Vac. Sci. Technol., B, 9, 5, 2587 (1991).

[14]. *I.S.Gasanov and I.I.Gurbanov*, Applied Physics; 1, 57 (2010) (in Russian).

[15]. *I.Ishikawa and T.Takagi*, J. Appl. Phys.; 56, 3056 (1984).

[16]. *I.Ishikawa*, NIM. B40/41, 1041 (1989).

[17]. *I.S.Gasanov, I.I.Gurbanov*, JJAP. 47, 8229 (2008).

Ab INITIO LATTICE DYNAMICS OF $TlGaS_2$

D.A. HUSEINOVA[1], F.M. HASHIMZADE[1], G.S. ORUDZHEV[1], M.A. NIZAMETDINOVA[2]
[1] Institute of Physics, Azerbaijan National Academy of Sciences, Baku, Azerbaijan
[2] Azerbaijan University of Architecture and Construction, Baku, Azerbaijan
hashimzade@physics.ab.az

We present first-principles calculation of lattice dynamics of the $TlGaS_2$ ternary semiconductor compounds. Calculations have been performed using open-source code ABINIT on the basis of the density functional perturbation theory within the plane-wave pseudopotential approach. Results on the frequencies of phonon modes in the centre of Brilloin zone agree well with experimental data on Raman scattering, infrared reflectivity in $TlGaSe_2$.

1. INTRODUCTION

Recent years the semiconductor compound $TlGaS_2$ as well as its structural analogue $TlGaSe_2$ and $TlInS_2$ are studied rather intensively. As far as we know, despite the great diversity of experimental data on IR and Raman spectra, calorimetric measurements for the compound $TlGaS_2$, theoretical calculations of lattice dynamics has not been reported in the literature. In this paper we perform such calculations from first principles in the framework of the density functional perturbation theory. We use the norm preserving pseudopotentials and local density approximation taking into account the exchange-correlation corrections. It is known that first-principles calculations of lattice dynamics based on density functional perturbation theory are sufficiently accurate, and employing this method, the phonon dispersions for many crystals are reproduced quite well. In particular, this method was successfully applied to the calculation of lattice dynamics of layered crystal of graphite, which is characterized by weak van der Waals chemical binding between the layers [1].

2. STRUCTURAL DATA AND GROUP-THEORETICAL ANALYSIS OF PHONON SPECTRUM OF $TlGaS_2$

Ternary $TlGaS_2$ compound crystallizes in a monoclinic system with base-centered lattice and space group symmetry C_{2h}^6 at room temperature [2]. The primitive cell contains 8 formula units. The crystal structure consists of layers composed of tetrahedral complexes Ga_4S_{10} linked together by the common atoms of selenium. Univalent thallium ions are in trigonal-prismatic voids between these complexes. Two layers within the unit cell are rotated relative to each other at 90^0 ([3]).

Each layer consists of two atoms of Tl1, Tl2, Ga1, Ga2, S3, S4, S5 and one atom of S1 and S2. A rotation about the second-fold axis accompanied by a shift along *c*-direction transforms each layer into itself. Unit cell parameters and reduced coordinates of atoms inside the unit cell (in units of the corresponding parameters of monoclinic unit cell) taken from [2], and our optimized data are given in tables 1 and 2.

Table 1. Experimental and optimized unit cell parameters of $TlGaS_2$.

a^{exp}(Å)	b^{exp} (Å)	c^{exp} (Å)	β^{exp}	a^{opt} (Å)	b^{opt} (Å)	c^{opt} (Å)	β^{opt}
10.299	10.284	15.175	99.603^0	10.1045	10.1047	16.259	98.876^0

Table 2. Experimental and optimized atomic coordinates of $TlGaS_2$.

Atom	x^{exp}	y^{exp}	z^{exp}	x^{opt}	y^{opt}	z^{opt}
Tl1	0.4640	0.1881	0.1095	0.4609	0.1872	0.0958
Tl2	0.2156	0.0615	0.6127	0.2126	0.0622	0.5994
Ga1	0.3979	0.1891	0.8365	0.3950	0.1890	0.8241
Ga2	0.1454	0.0637	0.3373	0.1420	0.0641	0.3248
Se1	0	0.9314	0.2500	0	0.9329	0.2500
Se2	0	0.4436	0.2500	0	0.4424	0.2500
Se3	0.2073	0.4378	0.0767	0.2111	0.4372	0.0946
Se4	0.2568	0.1888	0.2509	0.2548	0.1877	0.2502
Se5	0.4568	0.3124	0.5722	0.4607	0.3124	0.5910

As one can see from table 2, the optimized parameters *a* and *b* are somewhat reduced, while the value of *c* significantly increased after optimization, with unit-cell volume increased by 3% approximately. Estimates show that the layer thickness and the unit cell size in the direction parallel to the layers decrease, as a result of optimization, approximately in equal measure, i.e. the layer shrinks as a whole but the distance between layers increases dramatically.

The Brillouin zone for base-centered monoclinic lattice $\mathbf{g}_1 = 2\pi\,(a^{-1}, b^{-1}, a^{-1}\tan(\beta-\pi/2))$, $\mathbf{g}_2 = 2\pi\,(-a^{-1}, b^{-1}, -a^{-1}\tan(\beta-\pi/2))$ and $\mathbf{g}_3 = 2\pi\,(0, 0, c^{-1}\sec(\beta-\pi/2))$ is bounded by planes:

$$\pm 1/2\ \mathbf{g}_3;\ \pm 1/2\ \mathbf{g}_1;\ \pm 1/2\ \mathbf{g}_2$$
$$\pm 1/2\ (\mathbf{g}_1 - \mathbf{g}_3);\ \pm 1/2\ (\mathbf{g}_2 + \mathbf{g}_3);\ \pm 1/2\ (\mathbf{g}_1 - \mathbf{g}_2 - \mathbf{g}_3)$$

The coordinates of symmetric points and the matrix of irreducible representations are given in [4]. According to [4], the degeneracy of phonon branches occurs along line V at the boundary of the Brillouin zone (due to the symmetry with respect to time reversal the representations of V1 and V2 are degenerate). Decomposition of the vibrational representation into irreducible ones in the center of the Brillouin zone has the form:

$$\Gamma_{vib} = 23\ A_g + 25\ B_g + 23\ A_u + 25\ B_u$$

Although the group theoretical analysis predicts 48 bands in the Raman spectra and 45 bands in the infrared absorption spectra in all, the experimentally observed number of bands is considerably less. As indicated in [3], many bands are closely spaced, and maybe that makes difficult their experimental detection. If we neglect the interaction between layers, the number of phonon branches is halved. Since the inversion symmetry transforms layers into each other, the rule of alternative prohibition works, i.e. one of the split bands is active in the Raman and the other one is active in the infrared spectrum.

3. METHOD OF CALCULATION

Calculation of the phonon spectrum of $TlGaS_2$ has been performed in the framework of the density perturbation functional theory [6] using the local-density approximation. We used the software package ABINIT [6] and the norm preserving pseudopotentials [7]. The basis of plane waves was truncated at electron kinetic energy of 40 Hartrees. Integration over the Brillouin zone was carried out using a 2×2×2 grid according to the scheme proposed by Monkhorst and Pack [8]. The equilibrium structure was determined by minimizing the total energy with respect to the lattice constants and the internal structural parameters. Dynamic matrix describing the phonon spectrum throughout the Brillouin zone was obtained by Fourier interpolation using the ANADDB program of the ABINIT software package. The calculated phonon spectrum is shown in figure 3.

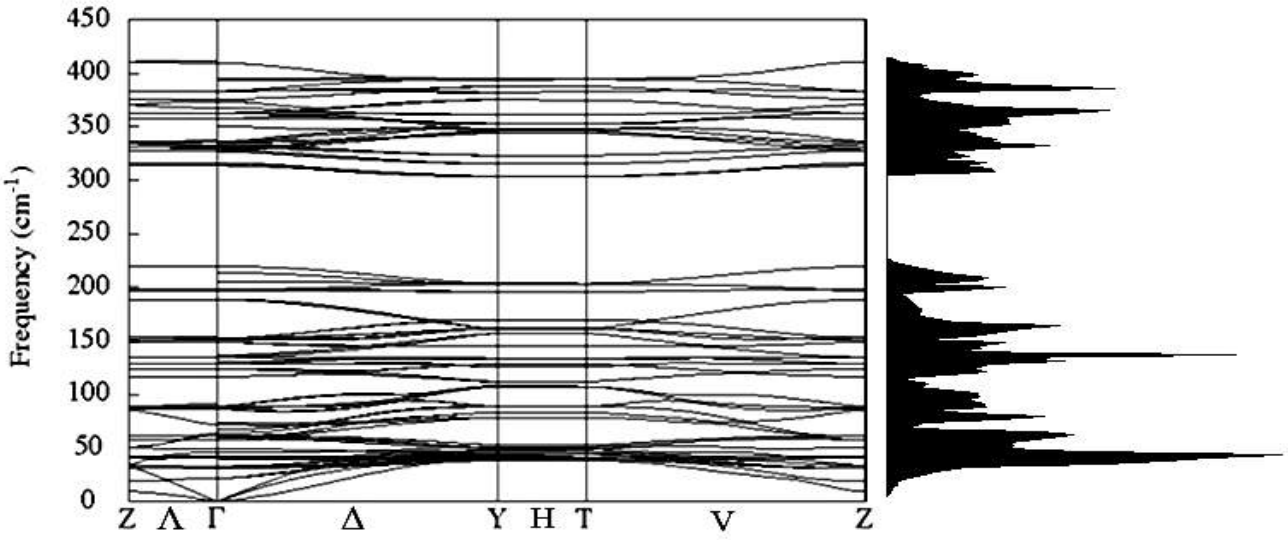

Figure 3. Calculated phonon spectra and phonon density of states (inset to the right side) of $TlGaS_2$.

4. RESULTS AND DISCUSSION

As one can see from figure 3, the dispersion of optical phonon branches along Λ line perpendicular to the layers is weak. In the direction parallel to the layers, all optical modes are split into pairs with nearly identical dispersion, which is, naturally, a consequence of stratification of the crystal structure and of the fact that the crystal unit cell contains two layers. In the direction of V, on the border of the Brillouin zone, these pairs are degenerate due to the symmetry with respect to time reversal. Figure 3 shows also the calculated phonon density of states. It consists of two separate bands.

The tables given below show the frequency of Raman-active (table 3) and IR-active (table 4) modes. Generally speaking, one should compare the results of our calculations with experiments at room temperature. However, taking into account that the resolution at low temperatures is better, and frequencies are not very strongly dependent on temperature, we have used experimental data for low temperatures. Calculations show that the maximum interlayer splitting is less than 10 cm^{-1}, and it indicates a weak coupling between layers. On the other hand, the frequency difference of A-type and B-type modes is also small. As a result, even at low temperatures about 20 frequencies are observed in the Raman spectra, and virtually there is no polarization dependence. Almost all of the observed frequencies in the Raman spectra can be identified.

Table 3 **.** Frequencies (cm^{-1}) of Raman-active modes in $TlGaS_2$

Ag	Bg	[5]	[3]	[9]
21.74	21.74	21	23	22
30.89	30.89	29	29	
31.54	31.55			
41.14	40.24	41	42	44
49.35	45.63	46		52
57.78	57.80			
61.35	61.39			
	71.85	72	70	66
87.42	87.50	77	76	76
	88.89			
116.74		112	112	112
124.17		121	123	122
128.40	128.55	125		
134.80	134.83			
	149.40			143
151.56	151.56			
	152.85	174	173	150
188.85		185	185	182
197.61	197.63			208
	219.74			224
313.89	316.17	314, 319	318	310
328.19	328.19	327	325	322
330.53	331.67			
335.84	335.86			
357.53		348, 352	347	347
362.75	362.80			
367.53				
	375.74			
383.27	383.27	391	390	386
	409.39			

5. CONCLUSION

We have calculated the phonon spectrum of ternary $TlGaS_2$ compound in the framework of the density functional perturbation theory using ABINIT code. The lattice dynamic of monoclinic $TlGaS_2$ shows many interesting features which are related to the layer crystal structure. For example, a weak dispersion of optical phonon branches in the direction perpendicular to the layers, and splitting of all optical modes into pairs with nearly identical dispersion in the direction parallel to the layers, which is a natural consequence of stratification of the crystal structure and of the fact that the crystal unit cell contains two layers. The phonon frequencies in the centre of Brillouin zone are in a good agreement with available experimental data.

Table 4 . Frequencies (cm^{-1}) of IR–active vibrational modes in $TlGaS_2$.

TO	LO [100]	LO[001]	LO [010]
31.06	31.06	31.06	
31.07			31.08
32.52	32.90	32.52	
32.54			32.91
40.31	40.31	40.34	
41.86			41.86
57.05	60.60	57.05	
57.05			60.52
60.89			63.64
61.00	66.78	61.00	
63.68			66.80
72.99	73.00	86.32	
86.35	88.31	88.85	
86.40			88.45
88.85	88.94	91.12	
116.75			116.75
123.50			123.53
128.41	130.59	128.41	
128.50			130.63
134.69	136.95	134.68	
134.71			136.99
149.33	149.34	149.34	
150.64	151.14	150.67	
150.67			152.89
151.20	152.90	153.74	
188.42			188.43
197.01	205.54	197.01	
197.01			205.52
213.74	213.75	219.48	
313.95			314.05
315.75	315.84	316.10	
327.07	327.12	327.86	
327.86			332.15
327.90	334.64	335.42	
332.15			334.63
335.87			350.60
335.88	350.59	336.80	
357.53			357.53
362.71	362.74	362.74	
362.73			362.76
373.56			373.56
375.72	375.72	375.72	
383.28	393.73	383.29	
383.29			394.80
393.73	394.80	411.68	

[1]. S. *Baroni, A. Dal Corso, S. de Gironcoli and P. Giannozzi* 2001 Rev. Mod. Phys. 73 515

[2]. *G.E. Delgadoa, A.J. Mora, F.V. Pe´rez, J. Gonzalez* Physica B 391 (2007)

[3]. *W Henkel, H.D. Hochheimer, C. Carlone, A.Werner, S. Ves and H.G. von Shnering* 1982 Phys.A.Rev. B 26 3211

[4]. *Dzh. A. Guseyinov and M.A. Nizametdinova* 1988 Izv. Akad. Nauk Az SSR, ser. fiz.-tekh. & mat. nauk 5-6 73

[5]. *K.R. Allakhverdiev, M.A. Nizametdinova, R. Sardarly, E.A. Vinogradov, G.N. Zhizhin*, in Proceedings of yhe International Conference on Lattice Dynamics, Paris, 1977, edited by M.Balkanski (Flammarion, Paris, 1978), p.95

[6]. *X. Gonze, J-M. Beuken, R,Caracas, F. Detraux, M. Fuchs, G-M. Rignanese, L. Sindic, M. Verstraete, G. Zerah, F. Jollet, M. Torrent, A. Roy, M. Mikami, Ph. Ghozes, J-Y. Raty and D.C. Allan* 2002 Comput. Mater. Sci. 25 478

[7]. *N .Troullier and J.L. Martins* 1991 Phys.RevB43 1993

[8]. *H. J. Monkhorst and J.D. Pack* 1976Phys Rev B 13 5188

[9]. *N.M.Gasanly, B.N.Mavrin, Kh.E.Sterin, V.I.Tagirov, and Z.D.Khalafov*, Phys.Status Solidi B 86, K49, (1979)

NEW TECHNOLOGIES OF THE NANO-PARTICLE IMMOBILIZATION IN THE POLYMER SOLUTIONS FOR PREPARATION OF THE POLYMER NANOCOMPOSITES

M.A. KURBANOV, G.G. ALIYEV, F.N. TATARDAR, I.S. SULTANAHMEDOVA, A.A. MEHDILI

Institute of Physics, Azerbaijan National Academy of Sciences
Javid av. 33, AZ-1143, Baku, Azerbaijan
e-mail: mkurbanov@physics.ab.az

New technology of nano-particles immobilization in polymer solution based on application of plasma of electric discharge is proposed. Plasma of electric discharge occurs in dielectric-gaseous media-solution-polymer. Under action of electric discharge uniform distribution of nano-particles and their aggregation in polymer solution is realized.

INTRODUCTION

It is known that prevention of the nano-particles mobilization and their uniform distribution in the polymer phase volume are one of the main problems of nanocomposites [1-3]. There are physical and chemical methods of nano-particle immobilization in the polymer solutions at preparation of the polymer nanocomposites [1]. It is necessary to note that applicability of the certain method of prevention of nano-particles essentially depends from properties of polymers and nano-particles. Creation of the active centers in the polymer phase of the nanocomposite is initial stage of the nanocomposite formation. Regions of the cluster formations, i.e. nano-particles mobilization also can be the presence of the active centers of nano-particles stabilization. Mentioned effects are natural processes at preparation of the polymer nanocomposites. However, it is necessary to prevent against of large-scale cluster formation of nano-particles since at sizes of clusters larger than 300 nm, prepared composite will be transformed to the macrocomposite, i.e. it loses its nano-properties.

Aim of current paper is development of the immobilization technology of the nano-particles at preparation of active composites by applying electric discharge plasma and generators of acoustic waves based on piezoelectric cells. Following tasks are solved in order to achieve mentioned aim:

1) Creation of active centers of nano-particles localization by crystallization of the composite under acting plasma of electric discharge and temperature.

2) Development of the immobilization technology of the nano-particles in polymer solutions under influence of the local discharges and acoustic elastic waves.

The system allowing the realization of immobilization process of nano-particles in the polymer solution is presented in fig. 1. polyethylene of high density is used as polymer whereas particles SiO_2, $BaTiO_3$ with sizes 8 and 300 nm respectively are used as nano-particles.

METHOD OF EXPERIMENT

Let us firstly consider the technology of the creation of active centers of cluster formation of nano-particles by realization of crystallization of composites under acting plasma of electric discharge.

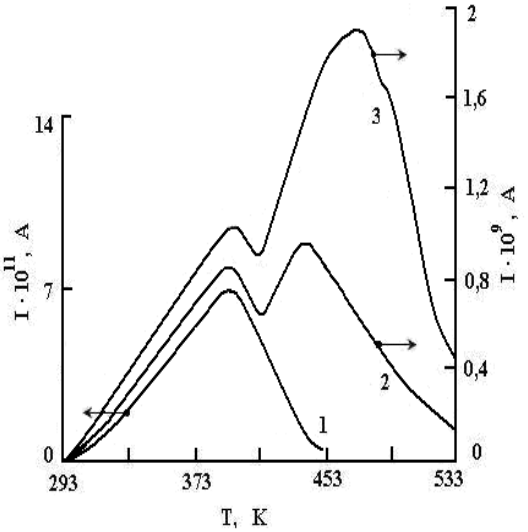

Fig.1. Spectra of the termostimulated depolarized currents of micro-piezocomposite HDPE+50 % NCR–7M for 1-output HDPE; 2-thermocrystallized micro-composite HDPE +50 % vol. NCR–7M; 3-composite crystallized under action of plasma electric discharge.

Method of crystallization at influence of plasma of electric discharge and temperature consists in heating of product till melting temperature, its storage at this temperature during of 5-10 minutes and its subsequent cooling till temperature of crystallization with speed 0.5÷4 K/minute without canceling of action of discharge aiming directed change of chemical (oxidation) and physical (permolecular) structures of polymer matrix. Melting temperature of the composite is determined through the third peak of thermodepolarization current spectrum (fig. 1, curve 2).

Lower limit of the temperature range of crystallization is determined by start of visible increase of deformation of composites. Crystallization duration t_{cr} is going to be limited by saturation of optical density of oxygen containing groups (for example, c=0), which appear in IR spectrum of polymer-piezoceramics composite as a result of action of electrical discharge and changed in range from 15 to 30 minutes. Polyvinyldenfluoride produced by "Plastpolimer" from Sankt-Petersburg is used as thermoplastic polymer matrix and piezoceramics of zirconate-titanate-lead (ZTL) family of rombohedral

structure PZT-5A (NCR-3M) is used as piezoelectric phase.

Following polyolefins are used too: polyethylene of high density and polypropilene. In figure 1, the spectrum of thermostimulated depolarized current is presented. One can determine the upper limit of crystallization temperature of composites (fig. 1, curve 2).

Experimental results show that after crystallization of polymer matrix under action of plasma of electric discharge, new oxygen containing groups C=O, C-O-C, OH appear in its IR spectrum.

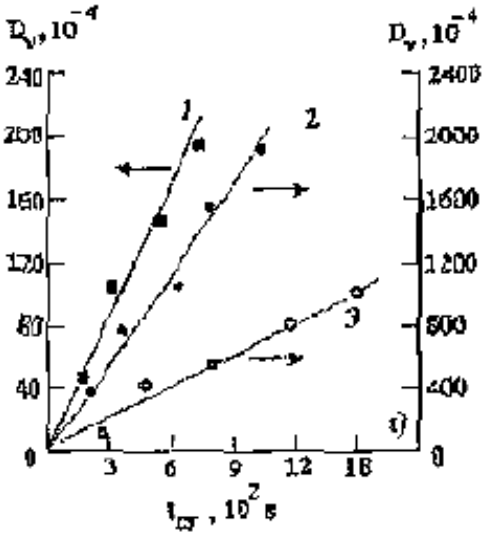

Fig.2. The change of optical density ΔD of IR spectrum.

The change of optical density ΔD of IR spectrum of mentioned above group polymer matrix crystallized under action of plasma electric discharges is presented in fig. 2. One can observe that change of optical density ΔD during of crystallization time up to 15 minutes has linear character. It is necessary to note that intensive oxidation of polymer chains also occurs. Centers of oxidation are nucleuses for cluster formation of nano-particles. Dissolving of polymer in toluol is next stage of the immobilization process. For example, in case of polyethylene of high density this temperature is equal to the temperature of formation of first maximum. Thereafter, nano-particles SiO_2 of range (0,5÷1,0) from volume percentage should be injected to this solution. Now, we will consider processes ensuring immobilization of nano-particles in solution preliminarily crystallized under action of plasma of electric discharge of polymers.

Immobilization of nano-particles in polymer phase of composite is realized by the following stages:

– Injection of dielectrical nano-particles SiO_2 to solution and as far as possible uniformly distribute nano-particles in it;

– Dissolving of used polymers in toluol at temperature determined from spectrum of thermostimulated depolarized current (first maximum, curve 2);

– Obtain the mixture of toluol-polymer and toluol-nano-particles;

– Realize chemical sedimentation of polymer to piezocomposite under action of plasma of electric discharge or acoustic waves.

Let us first consider the process of immobilization of SiO_2 nano-particles in polymer at chemical precipitation.

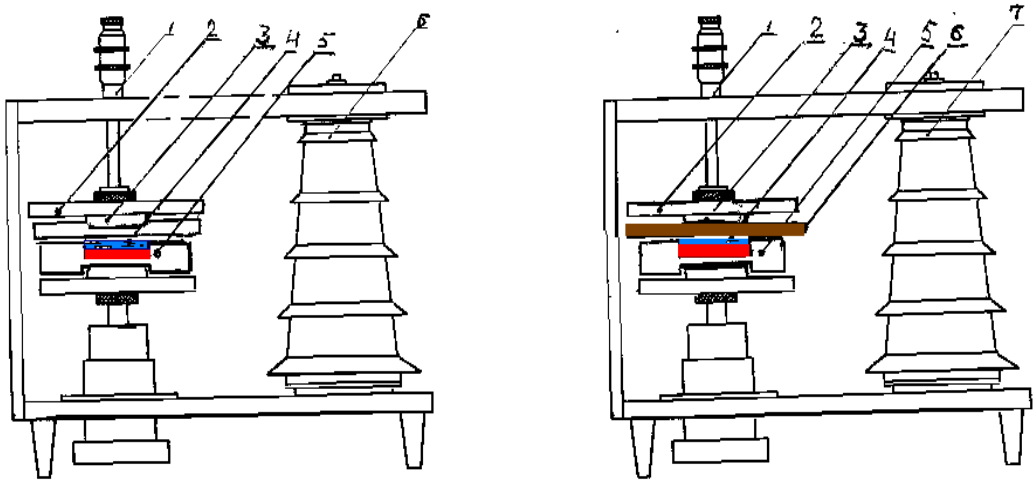

Fig.3. The process of immobilization of SiO_2 dielectric nano-particles

In fig. 3, we present the cell, where the process of immobilization of SiO_2 dielectric nano-particles is realized at chemical precipitation. As one can see from this figure, the structure formed from metal-dielectric-gaseous media-solution-(polymer-nano-particles-toluol)-dielectric and metallic electrode is located under the sinusoidal voltage. At certain value of the applied voltage, an electric discharge appears in this systems gaseous media layer between upper dielectric barrier and solution of polymer and nano-particles. The structure of appeared discharges is shown in fig. 4.

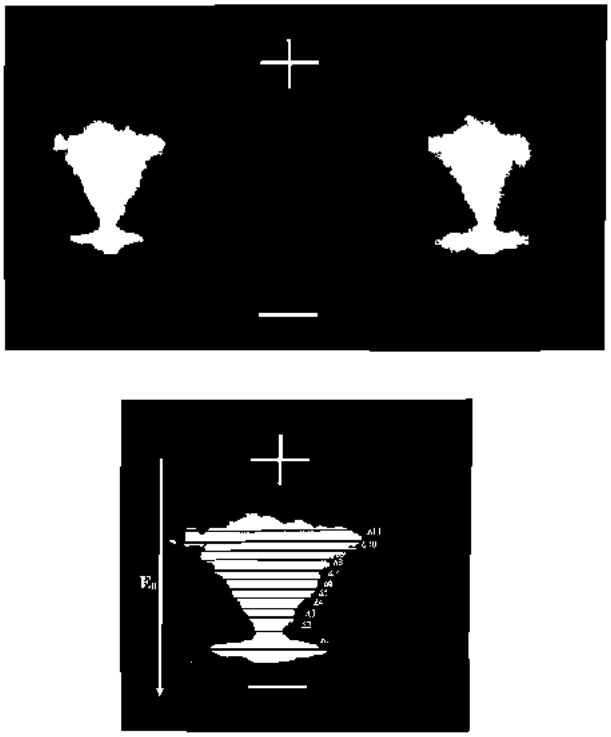

Fig. 4. Micro discharges.

As one can see, the discharge appears in various points of solvent's surface and solution is located under action of strikes of micro-discharges. Changing the distance between dielectric attached to high-voltage electrode and surface of solvent or thickness of air-gap between dielectric's anode and surface of liquid one can regulate the energy parameters of discharges. Selecting operating modes and power parameters of discharge one can provide uniform distribution of nano-particles in polymer solution. During of chemical precipitation, power parameters of discharge will change depending on the change of thickness of air-gap. At the end of chemical precipitation process, all plasma channels of discharge will have direct contact with surface of piezocomposite. Process of plasma treatment and immobilization of SiO_2 nano-particles in plasma phase will finish after this behavior. Creation of acoustic waves in polymer solution having nano-particles is another effective technology. Essential difference of acoustic method of immobilization, proposed by us, lies on that, where acoustic waves have to be created by the help of piezoelectric cell, which has acoustic resistance being equal to acoustic resistance of dissolvent. Used piezoelectric cell has direct contact with polymer solution. At that the conditions of effective influence of acoustic waves to nano-particles in dissolvent will appear. Probability of caption of nano-particles by active centers and formation of small nano-particle clusters will increase.

Thus, process of immobilization and uniform distribution of nano-particles in polymer phase precipitated on surface of piezocomposite electric cell will be realized. Hybrid nano- and micro-piezoelectric composites will be created. Realization of nano-particles immobilization in hybrid composite is determined by analysis of spectrum of thermo-stimulated depolarized (TSD) current. From analysis one can observe that TSD spectra of composites only with micro-piezoelectric nano-particles have two maximums: second maximum corresponds to polymer phase having direct contact with micro-piezoparticles. TSD spectra obtained by hybridization method have one maximum, which is shifted substantially to side of high temperatures. Absence of the first maximum in the TSD spectrum indicates nano-structuring. Indeed, an application of nano-particles to polymer phase restricts thermo oscillations of polymer chains and thermo-relaxation of charge becomes difficult.

Table 1. Piezoelectrical, mechanical, electrophysical and electromechanical parameters of micro-piezocomposite HDPE–50% об. NCR-7M.

Parameters	Piezocomposite	
	HDPE–50% vol. NCR–7M	HDPE–0,4vol. SiO_2-49,6%об. NCR–7M
$\varepsilon_{33}/\varepsilon_0$	100	140
K_{31}	0,15	0,22
K_{33}	0,25	0,38
$d_{31}\cdot10^{12}$, *Kl/N*	50	80
$d_{33}\cdot10^{12}$, *Kl/N*	89	150
Q_m	16	96
$Y\cdot10^{-10}$, *Pa*	1,6	8,6
$tg\delta\cdot10^2$; $E=5\cdot10^3$ *V/m*	0,145	0,06
$(d_{31}Y)^2$, $(Kl/m^2)^2$	0,64	47,5
$K^2_{31}\cdot Q_m$	0,36	4,7
$K^2_{33}/tg\delta$	43	240
$K^2_{31}\cdot Q_m\cdot\varepsilon_{33}/\varepsilon_0$	36	658
Diameter of piezoelectric cell, 10^{-3} *m*	20	20
Thickness of piezoelectric cell, 10^{-6} *m*	250	250
Diameter of piezo-particles, 10^{-6} *m*	160–200	160–200
Diameter of nano-particles, 10^{-9} *m*	50–70	50–70
Structure of pizo-phase	tetragonal	tetragonal
Structure of SiO_2 nano-particles	amorphous	amorphous

Thus, by using TSD spectra one can predict nano-structuring of polymer phase of composite. In table 1, electromechanical parameters of piezocomposite material and nano-structured hybrid piezoelectric composite are presented. Results of research show that electrophysical, mechanical and electromechanical parameters of hybrid composites are noticeable higher than similar parameters of composites polymer-piezoceramics.

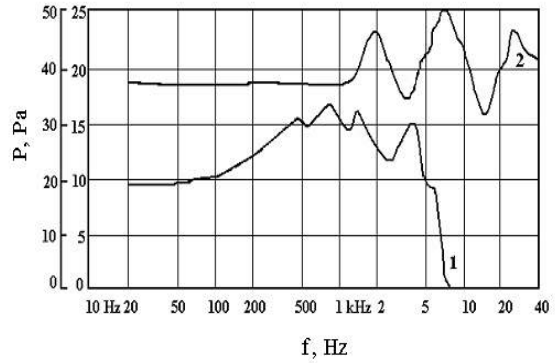

Fig.5. Amplitude-frequency characteristics of output acoustic signal of electroacoustic transducers.

In fig. 5, amplitude-frequency characteristics of output acoustic signal of electroacoustic transducers based on micro-piezocomposite HDPE+50% NCR-7M and hybrid nano- and micro-piezocomposites is HDPE+0,4% SiO_2+ 49,6% NCR-7M are presented in pascal (Pa). One can observe that hybrid piezoelectric cells have larger frequency range and they are bigger by value of output signal.

CONCLUSION

The technology of creation of hybrid piezoelectric composites having higher electromechanical and piezoelectric properties is worked out for first time.

[1]. *V.Y. Topolov, A.Y. Panich, M.A. Kurbanov*, Nano- and micro-scheme engineering, № 1, c. 34-38, (2006).

[2]. *V.V. Ermakin, A.E. Panich, V.G. Smotrakov, M.A. Kurbanov*, Piezoelectric composites based on titanate-Pb-K ceramics, International Conf. "Fundamental problems of functional material sciences, piezoelectric instrument-making and engineering" Piezotexnika–2005, 23–26 august. Rostov, (2005). c. 234-239.

[3]. *Q.M. Zhang, X. Geng*. Journal. Applied Physics, **76**, *10*, 6014 (1994).

THE CHARACTERISTIC STUDY OF InSb EPITAXIAL LAYERS GROWN BY LPE

Sh.O. EMINOV, E.K. HUSEYNOV, A.A.RAJABLI, E.A.MAMEDOVA, T.I.IBRAGIMOV
H.M.Abdullayev Institute of Physics NAS Azerbaijan,
AZ-1143 Baku, H.Javid, 33
e-mail shikhamir@mail.ru

p-InSb epilayers were grown from In-Sb solution using liquid phase epitaxy from In-Sb solution at the n-InSb substrates.The source preparation method, the novel boat for LPE and growth procedures were described. The dependence of hole concentration in the epitaxial layer vs concentration of Cd in the liquids phase was investigated and segregation coefficient of Cd in In-Sb solution Ks~0.3 for concentration range C_L(Cd)~0.001- 1%(ат) was evaluated.
The structural (XRD) and compositional quality (EDS), the surface morphologies of as-grown epilayers were studied and discussed. The effect of mis-orientation of the substrate surface on the morphological evolution of the films was investigated. The features of the surface like terracing , inclusions, meniscus lines were described in sufficient detail.

1. INTRODUCTION

Indium Antimonide (InSb) is a narrow gap semiconductor material from the III-V group used in infrared detectors, including thermal imaging cameras, FLIR systems, and in astronomy for the 3-5 μm spectral range. Many investigation have been accomplished on p on n type photovoltaic detectors which were made by diffusion Zn or Cd into n-type substrates [1-3] or implantation of Be or Zn [4] accompanied with post-implant annealing. Usually two temperature zone method was use for thermal processing (480ºC in higher and 450ºC in lower temperature zone for 10 h). However, in the above detectors, some difficulties arise from the industrial point of view. One difficulty is increasing of leakage current in the current-voltage characteristics due to the diffusion-induced damages. It was reported that long term thermal processing resulted in n to p type conversion (and p to n) [5] due to redistribution of the impurities in the volume of the substrate. Another difficulty is the necessity of controlling the diffusion layer thickness.

On the contrary, only limited number of investigations have been reported on p-n photovoltaic detectors, which can be obtained by using liquid phase epitaxy (LPE) [6-9].

It is purpose of this work to present the results of the study the features of InSb epilayers grown by liquid phase epitaxy in the horizontal graphite boat at the hydrogen ambient.

2. EXPERIMENTAL DETAILS

Fabrication of the epilayers .

a) Substrates. The epilayers were grown on n-type InSb (111) Czochralski growth Te doped ($n\sim10^{15}$-10^{16} $см^{-3}$) mechanically and chemical-mechanically polished wafer with dimensions 14 x20 mm and thickess of 400-500μm. The wafers purchasing from different suppliers, cut along <111> with the miscut angles ± 0,1º either 1º, depending on suppliers, were used as substrates. The growth was carried out on (111)A(In) and (111)B(Sb) faces of the substrates. The detailed description of substrates preparing procedures was done in our recent papers [9]. The reasons for choosing of the B-side of substrate for LPE growth are connected with the followings. In accordance with the structure of external electron orbits of Sb and In atoms as well as with the character of interconnection between them in the InSb crystal lattice, the both (111)A and (111)B faces end up by the bonds with different electronic configuration. Consequently, the work function of electrons from the B face is less than from the A face , and catalytic activity of this plane is higher than that of A plane. For that reason the B face of the substrates of III-V and II-VI compounds with the zinc-blende structures (such as InSb, GaAs and CdZnTe) with (111) orientation is commonly utilizing as the working face for fabrication of devices. It was experimentally observed that undoped InSb single crystal grows more stable in B(111) direction rather than in A(111) direction. Further, the another significant and practical reason of this choice is connected with the chemical wet etching of the substrate. As it was reported at our recent papers [9], due to the polarity of A and B-faces it is not available any chemical etchant which able to dissolve (to etch) the A-side of the substrate uniformly. The etchants such as CP-4, CP-4A as well as the etchants composed on the basis of lactic acid etc., resulted in non-uniform and oxide surface. Only etching of the (111)B-side of InSb substrate in the solution on the basis of tartaric acid is resulted in mirror polished surface without of visible tracks of oxides. At the some time the A-face has shown the etch pits.

b) Solution. Solution was prepared from In (6N) and Sb(6N) and Cd (6N) in ratios as prescribed by the solubility curve at the desired saturation temperature. For Liquidus temperature T_L=425ºC the typical In:Sb ratio (***at.%***) was respectively 75,58 : 24,42.The composition C_L of the Cd impurity in solution was varied from 0,001 to 0,1at% depending on setting concentration of the holes at the layers (C_s) . As it was mentioned below for the avoid the thermal degradation of the substrate the charge consisting of In and Sb and Cd was melted prior to epitaxial growth in the boat without of inserting of the substrate at 460ºC and wasquickly cooled up to ambient temperature after 0,5 h thermal processing.

c) *Growth equipment* LPE growth was carried out in a quartz reactor tube which is resistively heated by a single-zone isothermal furnace. The original horizontal boat with a slider with tunable distance between substrate surface and bottom of the boat developing at our laboratory [10] with solution wells of dimension 15x20x mm and

fabricated from high density graphite was used in the experiments. The graphite boat assembly was annealed at 1000º C at the vacuum furnace accompanied by the annealing at 800ºC at hydrogen ambient. The reactor tube was also subjected to proper chemical cleaning at the mixture of Nitric and Hydrofluoric acids to get rid off various contaminants.

d) *Growth procedure.* In a typical experiments, the previously prepared In-Sb-Cd solution ingot was taken in solution wells of the boat and the freshly prepared substrate was inserted in the slots made on the slider. After purging the system with Nitrogen and changing of that with pure Hydrogen the solution temperature was increased above the growth temperature and baked for sufficiently long time and allowed to homogenize for an optimum period. The growth was initiated by bringing the substrate under the solution at preset temperature (T_L=425ºC) and cooling it at the preset rate of 0,1-0,2 ºC/min. The cooling was stopped at the termination temperature and the growth took place during this interval under controlled conditions. Growth was terminated by removing the substrate from under the melt by pulling the slider. To maintain the best growth conditions the solution was kept during 4-6 hours at the temperature T~440ºC The selected temperature condition and the growth duration let us from the one side to remove the oxide layer from the substrate surface and the oxides containing into the melt solution and maintaining the homogenization of the solution from the other side.

For avoid the thermal degradation of the substrate the solution preparation method was improved by the following way. The charge consisting of In and Sb and Cd was previously melted in the boat at temperature of 460ºC without of inserting the substrate and quickly cooled up to ambient temperature after 0,5 h exposure. The solution ingots prepared by this way consists of In core which uniformly covered by the polycrystalline InSb. Then the substrate was brought into the suitable slot of the boat, after that the epitaxial growth were arranged. The charge prepared by this way quite enough quick (during 30 min) was homogenized by the heating on ΔT_0=10-15ºC higher than T_L.

The three growth modes were used for epitaxy: the supercooling, the ramp cooling and the step cooling. During the first two modes the cooling rate was 0,1ºC/min with the cooling interval of 3÷10ºC. In the step-cooling growth experiments a super-cooling in the range 5-25ºC below the liquidus temperature was employed while the growth duration was from 10 to 30 minutes.

e. *Characterizing of the epilayers*

The surface morphology of the layers was examined using the Leitz-orthoplan microscopes (x 100-1000) in reflection mode.The thickness of the epilayers was determined by measurement of thickness of the decorating of the edge of cleaved part of epilayers with optical microscopes to within ±1 μm.,. The roughness, waviness and dimensions of surface defects were measured with the "Alpha-step 500"profilometer.

The structural quality of the both substrates and grown epilayers were assessed on the basis of the X-ray diffraction patterns (XRD) with the DRON-2 unit and the JEOL JSM-6300SEM scanning electron microscope with energy dispersive X-Ray spectroscopy (EDS) function.

Hall electron mobility and concentration of the carriers in the epilayers were measured using a Bio- Rad Microscience HL5500 Hall system employing Van der Pauw geometry at measuring conditions with magnet field 0,224 Tesla at 77K.

On the basis of these p-n junctions the mesa diodes with specific detectivity $D_\lambda^* \sim 5\times10^{10}$ -1×10^{11} cm $Hz^{1/2}/W$ (λ=5 μm) were fabricated by using photolithography and anodizing in 0.1KOH solution for prevent surface leakage. The Volt-ampere characteristics were measured by standard methodic at 77K . The absolute value of photocurrent was measured with a 500K black body, it's spectrum with IKS-21 spectrophotometer.

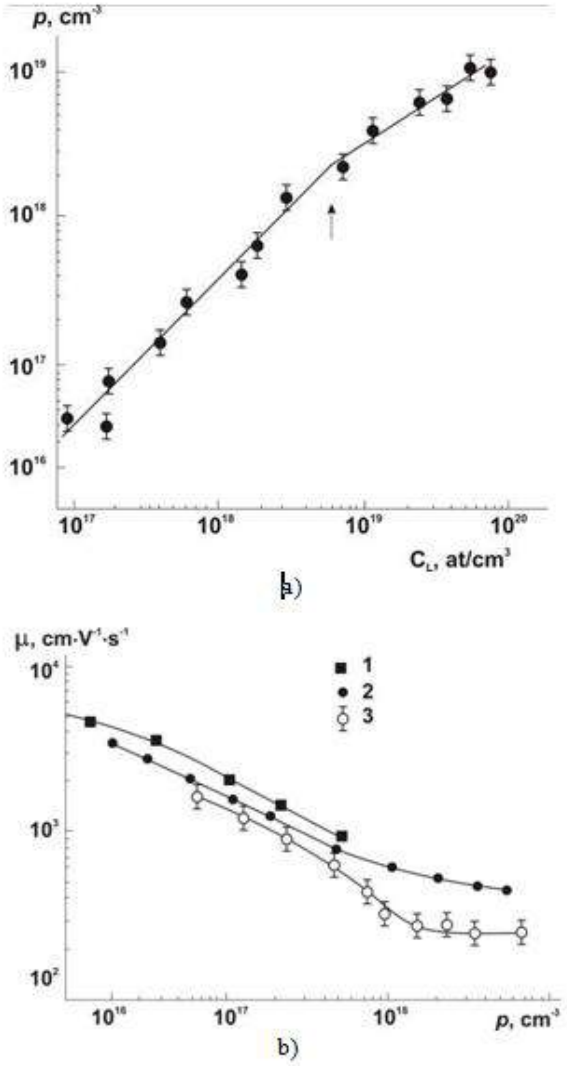

Fig.1 a) Dependence of holes concentration on Cd composition at liquid phase at 77K; b) Dependence of hole mobility on holes concentration (77K).

3. RESULTS AND DISCUSSION

The epitaxial layers of p-type with mirror smooth surface and thickness from 5 to 25 μm were grown.

Electrical properties of epilayers The concentration of holes at 77K were $5x10^{16}$-$5x10^{19}$ depending of impurity level at the liquid phase . The dependence of epy holes concentration vs concentration of Cd in the liquids phase, a s well as the dependence of mobility of holes on concentration are shown in fig.1a and 1b, respectively. On

the basis of this the the of segregation coefficient of Cd in In-Sb solution Ks~0.3 for concentration

The structural and compositional quality of epilayers. The XRD spectra for substrate and for epilayer are shown in Fig 2 and Fig 2 b , respectively . The single sharp XRD peak from (220) planes with a FWHM of ~ 25 arc min observed for both epilayers and substrate substantiates the good quality of the grown homoepitaxial layer of InSb. It was very clear that the structural quality of the epilayer is as good as the substrate

The EDS spectrum of the epilayer is shown in Fig.3 . It was very evident that there four peaks in the spectrum, three of which is originated from In and two different energy states of Sb(SbLa and SbLb). By comparing with intensity of In peak and the strong one of Sb, we could identify the composition of In and Sb to be approximately 1:1.

Surface morphology. The most of the grown epilayers has a mirror smooth surface (Fig.3(a) .However, the surface morphology is strongly affected by the quality of the substrate surface. The typical features like terracing, funnel-shaped voids, inclusions, meniscus lines, etc are presenting on the surface of the epilayers can seen from Fig. 3 (b) and Fig 4 .The description of some of these defects is presented below.

It may be noted that the nature of the substrate surface at the selected routine of epitaxial growth is a critical factor in any epitaxial growth process and can affect the LPE growth in several ways.

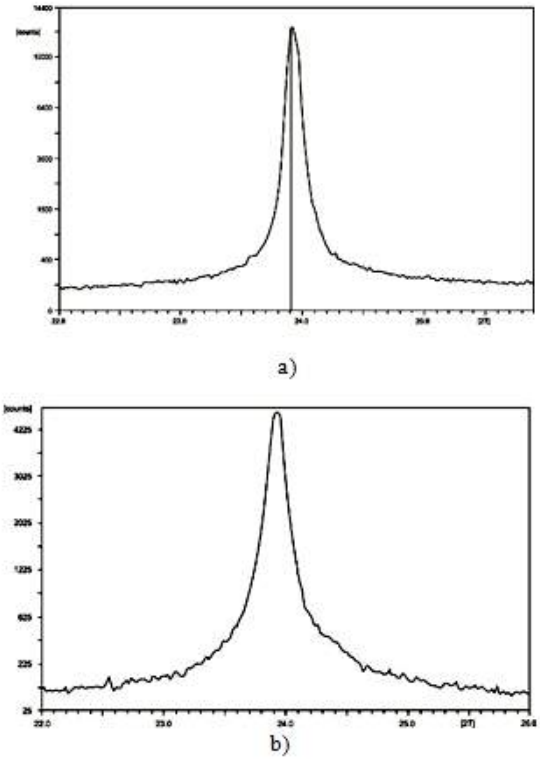

Fig 2 The rocking curves for epitaxial layer (a) and (b)for substrate

Effect of miscut angle. The surface morphology of epilayers grown on the substrate with miscut angle ±0,1 is shown on Fig. 3a , and with miscut angle ±1° at the fig. 3b. In the figures it was very evident that at the second case (Fig.3b) the terrace growth is shown , while the mirror surface without of any roughness is shown at the minor miscut angle.

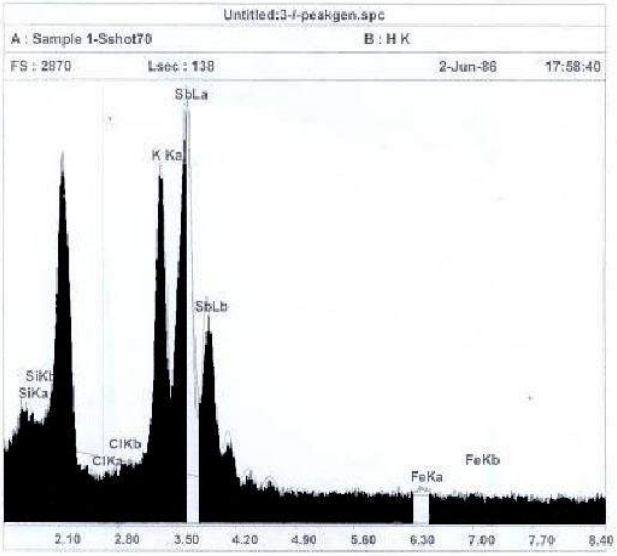

Fig. 3 EDS spectrum of the epilayers

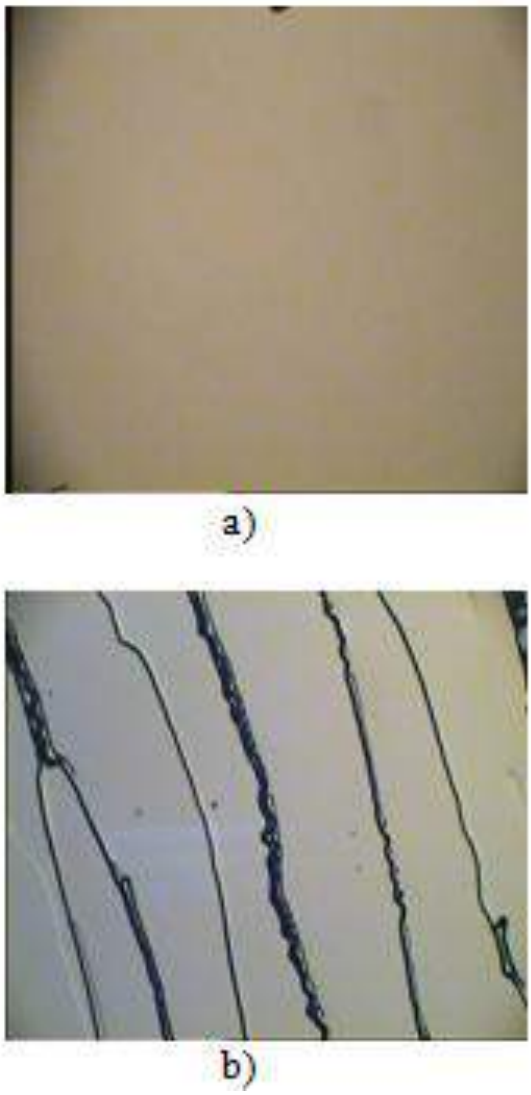

Fig.3 Surface of the epilayers grown on the substrates with different mis-cut angle a) ±0,1 and b) ±1°

The effect of substrate misorientation studies on Si and GAs made by E.Bauser [11] have shown that even within a very small angle of surface misorientation from a low index plane there can be a large effect on layer morphology. As the miscut angle approached 0.1° layers were still close to atomically flat, however misorientation steps became the primary nucleation sites for growth. For miscut angles between 0.1° and 2° the terrace growth mechanism was observed. Terrace growth can be understood by considering that the heights and distances of surface steps are randomly distributed. During growth atoms attach to step ledges . A small step will grow quickly as atoms attach to ledges, but a larger step will require many more atoms to attach. In this way, small steps will catch up with large steps and steps tend to bunch during growth.

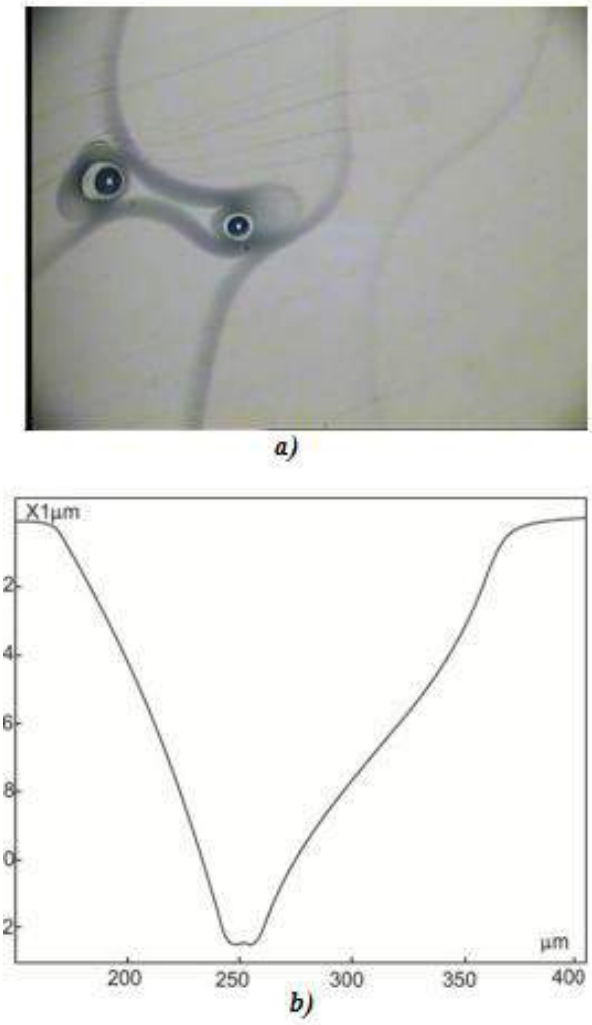

Fig. 4. The micro funnel like defects on the surface of the epilayer ; a-micro-funnel ; b-profile of the defect

Meniscus lines appear to represent the contour of the trailing edge of the liquid as it moved across the crystal during the sliding procedure. Although these are not observable with unaided eye, they may readily be viewed under the microscope. The

Funnel-shape voids at the epilayers The photograph of the funnel-shaped void appearing in the epilayer and the profile of that measured by the Alpha-Step-500 is shown at the Fig. 4 a and 4b, respectively. The craters of these funnels has the form of end epitaxial screw surface and have shape of ring while observed under microscope. The nature of these defects is directly related to the substrate surface preparation. The application of CP-4 and CP-4A type etchant as well as the mixture on the basis of lactic acid prior of epitaxy give rise to the selective etching and forming the etch pits and hillocks on the surface, as well as give rise to the thickness abrupt difference on the centre and on the edge of the substrate due t o very big etching rate.[9] At the first moment of bringing the substrate under the solution the liquid melt is spread along the substrate surface. As the surface tension hindered to penetration of liquid into the narrow and deep pits, the surface on vicinity of these pits hasn't wet. For maintenance of minimum of solution surface layer of liquid locating under this pit is break. and funnel-shaped void is formed into liquid under the pits and meniscus are constituted around of them. In case the neighbors pits are located on distance commensurable with the meniscus diameter the funnels are merged and dumbbell-like voids was formed into the volume of liquid. Epitaxial growing was not occurred on the areas of existence of these voids.

The void on the substrate surface act as obstacles to the growth steps similar as the touring particles such as dust, liquid or solid inclusions, etc. At an obstacle the advancement of a growth step is hindered. The motion of the step has slowed down at the obstacle while the part of the same step at some distance away from this location has not been affected. In Fig. 4a the step behavior at a circular pit (funnel) is observed. It is quite interesting to follow how the steps pass this obstacle. After having reached the obstacle, the steps get deflected and starts to form bends on both sides of the edge of the obstacle. In the down step region, the steps have regained a similar shape as the steps before the obstacle.

4. CONCLUSION

n-InSb epilayers were grown from In-Sb solution using liquid phase epitaxy from In-rich solution at the n-InSb substrates. It may be noted that the nature of the substrate surface at the selected routine of epitaxial growth is a critical factor in any epitaxial growth process and can affect the LPE growth in several ways. The surface morphology strongly affected by mis-orientation of the substrate - at the miscut angle ±1°the terrace growth shown , while the mirror smooth surface without of any roughness is shown at the minor miscut angle.

The features like terracing , inclusions, meniscus lines, etc are presented and a variety of methods devised to overcome such undesirable defects were described in sufficient detail. The dependence of hole concentration in the epitaxial layer vs concentration of Cd in the liquids phase was investigated. On bases of this measurements the volume of segregation coefficient of Cd in In-Sb solution Ks~0.3 for concentration range C_L(Cd)~0.001-1%(ат) was evaluated.

---

[1]. *I. Bloom , Ya. Nemirovsky*, IEEE Trans. Electron Dev.,39 (4) (1992)

[2]. *S. L. Tu, K. F. Huang1 and S. J. Yang*. Jap. J. Appl. Phys., 28 (1989) 1874

[3]. *M. Moradi, M Daraee, M. Hajian et all* Ukr. J. Phys., 55, 4 (2010) 422.

[4]. *P. V. Biryulin, V. I. Turinov et all*. Semiconductors, 38 (2004) 498

[5]. *N.Blaut-Blachev et al*., Inorgan Mater.,13(1977) 629

[6]. *Capper P., Mauk M.G. (editors),* Liquid Phase Epitaxy of Electronics, Optical and Optoelectronic Materials. London: Wiley-Interscience Publishers, 2007.

[7]. *K. Kanzaki et all* Jap. J.Appl.Phys.15,7(1976) 1329

[8]. *N. D.Udashankar and H.L. Bhat Bull*.Mater.Sci. 26,7,(2003) 685

[9]. *Sh. Eminov, E.K.Huseynov et.all.*, Fizika, XIV, 3(2008) 101

[10]. *Sh. Eminov, A.A.Rajabli*, Instruments and Experimental Techniques, 53,2 (2010) 218

[11]. *E. Bauser et all.* Cryst. Growth 27 (1974) 148

STRUCTURAL ORGANIZATION OF SMALL CARDIOACTIVE PEPTIDE

L.I.ISMAILOVA, R.M.ABBASLI, N.A.AKHMEDOV, N.M.QODJAYEV
Baku State University, Institute for Physical Problems,
Z. Khalilov 23, AZ–1148, Baku, Azerbaijan
Abbasli_Rena@mail.ru

Present article is devoted to study the spatial structure and conformational properties of Small Cardioactive Peptide (SCP) Ala1-Pro2-Asn3-Phe4-Leu5-Ala6-Tyr7-Pro8-Arg9-Leu10-NH_2 (APNFLAYPRL amide). The low-energy conformations of decapeptide molecule belonging to ten different forms of the backbone were found. The values of dihedral angles of the backbone and side chains of the amino acid residues constituting this peptide were determined, and the energies of intra- and interresidual interactions were estimated.

1. INTRODUCTION

The problem of spatial organization and conformational properties of peptides is of a key significance for our understanding of molecular mechanisms of recognizing, action and regulation in various biosystems. Small cardioactive peptide (SCP), with a primary structure, including ten amino acid residues Ala1-Pro2-Asn3-Phe4-Leu5-Ala6-Tyr7-Pro8-Arg9-Leu10-NH_2 was extracted from the muscle of Mytilus edulis. The mechanism of action of this APNFLAYPRL amide was examined on identified central neurons of the snail, Helix aspersa, using intracellular recordings [1]. It was found, that C-terminal sequence YPRL amide fragment of this molecule was inactive even at higher concentrations, while LAYPRL amide fragment exhibited activity but with a lower potency. This indicates that hexapeptide is the minimum sequence required for the biological activity of the SCP and for interaction with the SCP-like peptide receptor. However, the activity of all APNFLAYPRL amide is very higher [1].

The diversity of biological functions of this decapeptide is undoubtedly connected to its conformational possibilities. In order to elucidate the mechanism of action of the APNFLAYPRL amide the investigation of the structure-function relationship is necessary. It is important to know conformational possibilities of this molecule, i.e. the full complement of low-energy conformational states, and the potentially and physiologically active conformations of this decapeptide.

2. METHOD

The theoretical conformational analysis based on the proposed previously and repeatedly approbated approach [2-5] was used to study the structural organization of the cardioactive decapeptide and to determine all the energetically preferable conformations for this molecule, which may hence be the potential physiologically active conformations. The calculations were carried out on mechanical models of electrostatic (U_{el}), torsional (U_{tors}) interactions and the energies of hydrogen bonds (U_{hb}).

The nonvalent interactions were calculated by the Lennard-Jones potential with the parameters proposed by Momany and Scheraga [6]. The contribution of electrostatic interactions was taken into account in a monopole approximation with the partial charges of atoms as suggested by Momany and Scheraga [6]. The effective dielectric constant ε in water environment, values of valent angles, and length of valent bonds, the potentials and barriers for the torsional interaction calculation were taken from the research [2]. Hydrogen bonding energy was calculated based on Morse potential. Dissociation energy of the hydrogen bond is taken to be 6.3kJ/mol at NH…OC distance r_0=1.8Å [6]. A procedure for the minimization fragments global energy was conducted by the method of conjugate gradients using the program described [7]. The nomenclature and conventions used for torsion angles are those of IUPAC-IUB Commission [8].

The conformational state of amino acid residue has been determinate by B, R, L, P forms of the main chain of a residue. We designated the conformational state of any amino acid residue using the indentifiers X_{ij} where X defines the low-energy regions of the φ–ψ conformational map: R (φ,ψ=(–180°)–0°); B (φ=(–180°)–0°; ψ=0°–180°); L (φ,ψ=0°–180°); P (φ=0°–180°; ψ=(–180°)–0°); i, j,…=11(equal to 11, 12, 13,… 21,…,etc.) account for the positions of side chain of the residue $\chi_1,\chi_2,\ldots$, with the index 1 corresponding to the angle χ=0°–120°; index 2, to the angle χ=120° to (–120°) and index 3, to the angle χ=(–120°)–0°.

The number of possible conformations within each form depends on the nature of a residue. In should be noted that all backbone forms and peptide chain types are initially presumed to be equivalent. In order to abridge the number of conformations we used the approach to peptide structure calculation based on the fragmental analysis with using the universal sets of low-energy conformation states of the free amino acids and tested on numerous peptides, as for example in articles [3-5].

3. RESULTS AND DISCUSSION

Taking into account the specific features of the amino acid sequence we chose the following scheme of conformational analysis of the decapeptide molecule: the pentapeptide Ala1-Pro2-Asn3-Phe4-Leu5, the tetrapeptide Tyr7-Pro8-Arg9-Leu10-NH_2, the hexapeptide Leu5-Ala6-Tyr7-Pro8-Arg9-Leu10-NH_2 and the decapeptide Ala1-Pro2-Asn3-Phe4-Leu5-Ala6-Tyr7-Pro8-Arg9-Leu10-NH_2. At the first stage, on the basis of the low-energy conformations of the monopeptides, we studied the conformational possibilities of N-terminal pentapeptide fragment and C-terminal tetrapeptide. From the results of the calculations of the tetrapeptide fragment and on the basis of the low-energy conformations of two monopeptides Leu5 and Ala6 we carried out a theoretical conformational analysis of

hexapeptide molecule. At the final stage calculation of this hexapeptide and N-terminal pentapeptide enabled us to evaluate the conformational properties of the whole decapeptide molecule. The SCP-amide was included 170 atoms and 49 variables of the dihedral angles of rotation of the main and side chaines.

Fragment Ala1-Pro2-Asn3-Phe4-Leu5

The spatial structure of the N-terminal pentapeptide fragment was studied on the basis of stable conformations of methylamides of N-acetyl-L-alanine, L-proline, L-asparagin, L-phenylalanine and L-leucine. It was found that exhibit 8 backbone forms (from 16 possible for pentapeptide forms of the main chain). Six forms of the backbone fall into the range 0-20 kJ/mol, from which big number of low-energy conformations possessed the forms of the main chain BRRRR and BBRRR with folded forms of the C-terminal fragments.

The global conformation of the pentapeptide fragment is $B_2BR_{11}R_{11}R_{2122}$ (U_{rel}=0 kJ/mol). The folded form of the backbone ensures the neighborhood of the main chain and side chains of this fragment. We included in the subsequent calculation of the whole decapeptide molecule all the low-energy forms of the pentapeptide.

Fragment Tyr7-Pro8-Arg9-Leu10-NH2

On the following stage of the calculation the conformational properties of the C-terminal tetrapeptide fragment were evaluated. The spatial structure of this tetrapeptide was studied on the basis of stable conformations of methylamides of N-acetyl-L-tyrosine, L-proline, L-arginin, and L-leucine. For the residue Tyr7, preceeding before Pro, was considered only one B form of the main chain, but the following amino acids were taken into account by B and R forms of main chain. Over 90 variants were formed, minimized with a variation of all variable dihedral angles. The results of the calculation of this fragment are given in table 1, showing energy distribution both in respect of the conformations and forms of the main chain, from which follows that the conformations with completely extended BBBB and folded BRRR main chains have low-energy.

Table 1.

The energies (kJ/mol) of favorable conformations of Tyr7-Pro8-Arg9-Leu10-NH_2 fragment

№	Conformation	U_{nv}	U_{el}	U_{tors}	U_{tot}	U_{rel}
1	B_{11} $RB_{2222}R_{1122}$	-58.0	2.5	15.1	-40.3	18.5
2	B_{21} $BR_{3322}R_{1222}$	-62.2	-2.5	14.7	-49.6	9.2
3	B_{11} $BB_{1222}B_{2122}$	-56.3	-2.1	-5.0	-53.3	5.5
4	B_{11} $RR_{2222}R_{3222}$	-72.7	-0.8	15.1	-58.8	0

The fragment Tyr7-Pro8-Arg9-Leu10-NH2 comprises the amino acids with quite large and labile side chains, which form effective di-, tri- and tetrapeptide interactions in practically all tetrapeptide forms, particularly in conformation $B_{11}RR_{2222}R_{3222}$ (U_{rel}=0 kJ/mol). Nearly, 5.5 kJ/mol loses conformation $B_{11}BB_{1222}B_{2122}$ (U_{rel}=5.5 kJ/mol) with completely extended form of the main chain (see table 1). Truth a number of low-energy conformations for it (20) more, than for the folded form of the main chain (11). We included all the low-energy forms of the tetrapeptide fragment in the subsequent calculation of the hexapeptide fragment.

Fragment Leu5-Ala6-Tyr6-Pro8-Arg9-Leu10-NH2

The starting conformations of C-terminal hexapeptid fragment were constructed from stable conformations of the C-terminal tetrapeptid and two forms of monopeptides N-acetyl-L-leucine and L-alanin. Over 200 variants were formed, minimized with a variation of all dihedral angles. The results of calculation of this hexapeptide showing energy differentiation of the conformations and forms are given in table 2.

The calculation revealed a significant energy differentiation between the conformations of this fragment, since the majority of conformations fell into the energy range of 0–20 kJ/mol. However, only five forms from 16 possible forms of the main chain lie in this energy interval. The global conformation $B_{2222}RB_{11}BB_{1222}B_{2122}$ (U_{rel}=0 kJ/mol) has energy contributions: U_{nv}=(–107.5) kJ/mol; U_{el}=8.4 kJ/mol; U_{tors}=10.1 kJ/mol. The form of the main chain in this conformation ensures for closely spaced amino acids Leu5 and Tyr7 with Pro8 and Arg9.

Only 4.6 kJ/mol loses conformation $B_{2122}RB_{21}RR_{1222}R_{3222}$ with the folded form of the main chain. They are stimulated by interactions of the residues Leu5 with Tyr7, Tyr7 with Pro8, Arg9 and Leu10. For the form of the main chain BRBRRR only three conformations have a relative energy in the range 4-12 kJ/mol, but energy rest exceeds 24 kJ/mol. All conformations with the energy, not exceeding 24 kJ/mol, were enclosed by us for the calculation of the spatial structure of the whole decapeptide molecule. Here enter low-energy conformations of all possible forms of the main chain for hexapeptide fragment.

Decapeptide molecule Ala1-Pro2-Asn3-Phe4-Leu5-Ala6-Tyr7-Pro8-Arg9-Leu10-NH_2

At the final stage of the analysis, a calculation of the N-terminal pentapeptide Ala1-Leu5 and the C-terminal hexapeptide Leu5-Leu10-NH_2 enabled us to estimate the conformational properties of the decapeptide molecule Ala1-Leu10-NH_2. The starting conformations of this molecule were constructed from the low-energy conformations of the pentapeptide fragment, two forms of the monopeptide Leu5 and the stable conformations of the hexapeptide fragment. Thus, at the last stage a number of structures of SCP amide to be analysed amounted to 100. We carried out all of these structures by minimization over all the dihedral angles.

The relative energy of the conformations of the decapeptide molecule varied within the range 0–67.6 kJ/mol. Table 3 presents the energy distribution of the contributions in the most preferential conformations of the SCP amide. Figures 1(a, b) represents schematically the backbone forms and positions of residues in two low-energy conformations of this molecule.

Table 2.The energies (kJ/mol) of favorable conformations of Leu5-Ala6-Tyr7-Pro8-Arg9 -Leu10-NH_2 fragment

№	Conformation	U_{nv}	U_{el}	U_{tors}	U_{tot}	U_{rel}
1	B_{2122} B B_{11} B B_{1222} B_{2122}	-80.2	7.1	7.6	-65.5	23.9
2	B_{2222} R B_{11} B B_{1222} B_{2122}	-107.5	8.4	10.1	-89.5	0
3	R_{2122} B B_{11} B B_{1222} B_{2122}	-79.0	7.6	6.7	-65.1	24.4
4	R_{3222} R B_{11} B B_{1222} B_{3122}	-89.0	12.2	10.5	-65.9	23.5
5	B_{2122} B B_{21} R R_{1222} R_{3222}	-94.5	8.4	17.2	-68.9	20.6
6	B_{2122} R B_{21} R R_{1222} R_{3222}	-112.6	8.4	19.3	-84.8	4.6
7	R_{2122} B B_{21} R R_{1222} R_{3222}	-93.7	8.8	16.4	-68.5	21.0
8	R_{2122} R B_{21} R R_{1222} R_{3222}	-106.3	9.7	22.7	-73.9	15.5
9	B_{2222} R B_{21} B R_{3322} R_{1222}	-110.0	8.0	21.8	-80.2	9.2
10	R_{2122} R B_{21} B R_{3322} R_{1222}	-92.0	10.9	16.8	-64.3	25.2

Table 3.The energies (kJ/mol) of favorable conformations of SCP molecule

N	Conformation	U_{nv}	U_{el}	U_{tors}	U_{tot}	U_{rel}
1	B_2 $RR_{11}B_{21}B_{2222}R_2B_{11}BB_{1222}B_{2122}$	-207.1	12.6	19.7	-174.7	0
2	$B_2RR_{21}B_{11}R_{3222}R_2B_{11}BB_{1222}B_{3122}$	-203.3	12.6	19.7	-170.9	3.8
3	$B_2RR_{21}B_{11}B_{2222}R_2B_{11}BB_{1222}B_{2122}$	-199.5	20.2	19.3	-160.0	14.7
4	$B_2RB_{21}R_{11}B_{2222}R_2B_{11}BB_{1222}B_{2122}$	-186.5	15.1	18.5	-152.9	21.8
5	$B_2RB_{11}B_{21}B_{2122}R_2B_{21}RR_{2222}R_{3222}$	-200.8	17.2	31.9	-152.0	22.7
6	$B_2RR_{11}R_{21}B_{2222}R_2B_{11}BB_{1222}B_{2122}$	-189.0	20.6	17.6	-151.2	23.5
7	$B_2BR_{11}R_{11}R_{2122}B_2B_{21}RR_{1222}R_{3222}$	-196.6	18.5	29.0	-149.1	25.6
8	$B_2RR_{21}B_{11}R_{2122}B_3B_{21}RR_{1222}R_{3222}$	-190.3	14.7	28.1	-147.8	26.9
9	$B_2RR_{21}B_{11}B_{2122}R_3B_{21}RR_{1222}R_{3222}$	-192.8	18.5	28.1	-146.6	28.1
10	$B_2RB_{21}R_{11}B_{2122}R_2B_{21}RR_{1222}R_{3222}$	-188.6	15.5	27.3	-145.7	29.0

The global conformation of the decapeptide molecule (U_{rel}=0,kJ/mol) is $B_2RR_{11}B_{21}B_{2222}B_2B_{11}BB_{1222}B_{2122}$. The contribution of the stabilizing nonvalent to this conformation is (–207.1) kJ/mol, whereas electrostatic interactions account for 12.6 kJ/mol and torsion, for 19.7 kJ/mol. The main contributions of the interresidual interactions in this conformation were: dipeptide contributions (–71.8) kJ/mol, tripeptide (–62.2) kJ/mol, tetrapeptide (–18.9) kJ/mol, pentapeptide (–23.1) kJ/mol, hexapeptide (–8.0) kJ/mol, heptapeptide (–9.7) kJ/mol, octapeptide (–10.9) kJ/mol and nonapeptide 13.0 kJ/mol.

The spatial location of amino acid, submitted for fig. 1(a), shows that quite large and labile side chaines Arg9 and Tyr7, though and realize interactions with nearly located residues, however completely do not exhaust their own conformational possibilities. This problem was solved by the construction of a series of conformational maps χ_1–χ_2 ,χ_2–χ_3... for the side chains of these residues.

Our calculations showed that in this low energy structure the side chaines of Tyr7 and Arg9 have conformational mobility because of its localization on surface of the molecule. It is substantiated by physiological expediency: such mobility of the aromatic rings is probably necessary for complementary binding with the specific receptors. According to conformational maps, in the position χ_7^1 =60° and χ_9^1 =60° these side chains are oriented to the solvent and ready to realize interactions with the receptor.

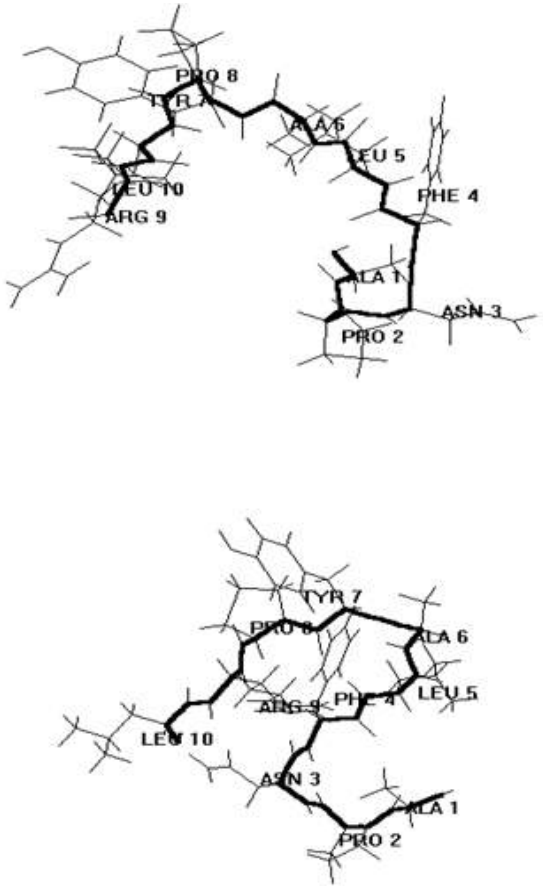

Fig.1. Atomic model of spatial structures of $B_2RR_{11}B_2B_{22}B_2B_1BB_{1222}B_{21}$ (U_{rel}=0 kJ/mol) of SCP(a) and $B_2RR_{21}B_1R_{32}R_2B_1BB_{1222}B_{31}$ (U_{rel}=3.8 kJ/mol) of SCP (b).

The next low-energy conformations of the SCP is $B_2RR_{21}B_{11}R_{3222}R_2B_{11}BB_{1222}B_{3122}$ (U_{rel}=3.8 kJ/mol). Here are the contribution of nonvalent interactions forms (–203.3) kJ/mol, electrostatic12.6 kJ/mol and torsion 19.7 kJ/mol. The form of backbone of this conformation ensures for closely spaced amino acids Phe4, Tyr7, Leu5, Ala1 and Pro2. This density parking of folded part of molecules dispenses Arg9 from strong interactions (fig. 1(b)).

4. CONCLUSION

We have studied in detail the spatial structure and conformational properties of SCP amide. The theoretical conformational analysis of this molecule leads to the such its structural organization and structural organizations of tetra- and hexapeptide fragments. Matching, tinned at calculations results, possible see a necessary picture. The best low-energy conformation of the tetrapeptide Tyr7-Pro8-Arg9-Leu10, which has folded structure, saturated by interresidue interactions, ties their own contacts Tyr7 with Arg9. This structure does not fall into the low energy conformations of the hexapeptide and decapeptide molecules, which show an activity and are involved with SCP-a similar receptor. It is worth noting that low energy structures of the hexapeptide and decapeptide molecules have completely identical conformations. Signifies, for the manifestation of minimum activity needed exactly such move of main chain. The conformational freedom of side chains Tyr7 and Arg9 permits their area in the interaction with the receptor.

Absence given on the nature of the most receptor, on mechanisms of interaction with him, does tinned by us detailed information on spatial structure and conformational possibilities of the cardioactive decapeptide very useful. The results of the conformational analysis of the cardioactive decapeptide APNFLAYPRL amide may be used to clarify the problems of a link between the functions of this molecule and for the goal-directed synthesis of its analogues, which model quite definite conformations of the natural molecule.

[1]. *M.L.Chen, Y. Muneoka and R.J. Walker* Gen. Pharmacol., 1995, v. 26, pp.273-283

[2]. *E.M.Popov* Int. J. Quant. Chem., 1979, v.16, pp.367-373

[3]. *L.I. Ismailova, R.M.Abbasli, N.A.Alhmedov, N.M.Godjaev* , 2005, Bioorg. Chem., v.31, №1, p.31-38 (In Russian)

[4]. *L.I. Ismailova, R.M.Abbasli, N.A.Alhmedov*, Biophysics, 2008, v.53, №1, p. 14-21 (In Russian)

[5]. *L.I. Ismailova, N.A.Alhmedov, R.M.Abbasli* Biophysics, 2007, т.v52, №6, p. 1141-1147 (In Russian)

[6]. *F.A. Momany, R. McGuire, A.W. Burgess and H.A. Scheraga*, J. Phys. Chem., 1975, v.79, pp.2361-2380

[7]. *I.S. Maksumov, L.I. Ismailova, and N.M.Godjaev*, J. Str. Chem. т.24, с.147-148 (In Russian)

[8]. IUPAC-IUB Quantity, Unit and Symbols in Physical Chemistry, Blackwell Scientific Publications, Oxford, 1988, v.39

PREPARATION AND MECHANISM OF CURRENT PASSAGE IN p-GaAs/n-$Cd_{1-x}Zn_xS_{1-y}Se_y$ HETEROJUNCTIONS

A.Sh.ABDINOV, H.M.MAMEDOV, N.M.MEHDIYEV*, V.U.MAMEDOV

Department of Physical Electronics, Faculty of Physics,
Baku State University, 370148, Z.Khalilov str., 23, Baku, Azerbaijan,
**Azerbaijan State Oil Academy*
e-mail: mhhuseyng@yahoo.co.uk

Anisotype heterojunction have been fabricated of n-type $Cd_{1-x}Zn_xS_{1-y}Se_y$ (x=0.9; y=0.8) thin films onto p-GaAs single crystal wafers using an electrochemical deposition method. The *I-V* and *C-V* measurements have been carried out for explanation of current passage mechanism through the junctions. We studied the voltammetric behavior of the $Cd_{1-x}Zn_xS_{1-y}Se_y$ thin films on GaAs substrate from aqueous solutions. The thin films of $Cd_{1-x}Zn_xS_{1-y}Se_y$ were prepared by electrodeposition at different deposition potentials. We investigated the influence of the deposition potential on the electrical and morphological characteristics of electrodeposited thin films. It is established that thermal annealing at $t = 300^0C$ during t=15 min in argon atmosphere reduces the concentration of defects, results in formation of heterojunctions and minimum values of non-ideality factor of *J-V* characteristics.

INTRODUCTION

The A^2B^6 type semiconducting compounds, especially the Cd and Zn chalcogenides have been extensively studied due to their potential applications, in semiconductor device technology and solar cells [1 – 5]. Heterojunction solar cells based cadmium and zinc chalcogenide systems are known to yield respectable efficiencies. Solar cells from cadmium and zinc chalcogenide single crystals are very expensive; therefore the use of polycrystalline metal chalcogenide thin film is a desirable alternative for cost reduction. Thin-film research is extensively carried out as a mean of substantially reducing the cost of photovoltaic systems. The rationale for this is that thin-film products are cheaper to manufacture owing to their reduced material, energy, handling and capital costs. Reduction of cost for the thin film cells is achieved by minimization of the amount of material used, the possibility of inexpensive materials, processing methods and the use of inexpensive mounting arrays. Several methods such as vacuum evaporation, screen-printing, spray pyrolisis, chemical bath deposition and electrodeposition have been employed for the preparation of cadmium chalcogenide thin films.

Electrodeposition is a perspective competitor in thin film preparation because of several advantages such as the possibility for large-scale production, minimum waste of components and easy monitoring of the deposition process [1 – 3]. This technique is generally less expensive than those prepared by the capital-intensive physical methods. The composition of the electrolytes and deposition condition play an important role in determining the quality of the films deposited. The use of additives in aqueous electroplating method is extremely important. The presence of complexing agents in the solution during the electrodeposition process of metal chalcogenide thin films was found to improve the lifetime of the deposition bath as well as the adhesion of the deposited film on the substrate.

On the other hand quaternary $Cd_{1-x}Zn_xS_{1-y}Se_y$ semiconductors seem to be useful materials photosensitive in the visible and ultraviolet wavelength regions [1-7]. This is apparently because the physics of these materials completely is not understood yet. However, single crystals of GaAs are well studied materials; therefore their use at manufacturing of heterojunctions p-GaAs/$Cd_{1-x}Zn_xS_{1-y}Se_y$ will be good way of studying of electrical and photoelectrical properties of films $Cd_{1-x}Zn_xS_{1-y}Se_y$. In addition, films of $Cd_{1-x}Zn_xS_{1-y}Se_y$ grown on CdTe, Si and GaAs substrates have great interest because of their applicability at fabrication of lasers [6] and solar cells [7]. In the present work, anisotype heterojunction of p-GaAs/n-$Cd_{1-x}Zn_xS_{1-y}Se_y$ was fabricated by depositing of $Cd_{1-x}Zn_xS_{1-y}Se_y$ thin films as a window using the electrochemical deposition method onto the p-GaAs single crystals. The dependence of the current - voltage characteristics on the temperature and capacitance-voltage (C-V) measurements were studied for obtaining the information on the junction region of the heterojunctions.

EXPERIMENTAL

Electrodeposition of the $Cd_{0.1}Zn_{0.9}S_{0.2}Se_{0.8}$ films onto the p-GaAs substrates was carried out at room temperature from aqueous solution containing cadmium ($CdCl_2$), zinc ($ZnCl_2$), sodium ($Na_2S_2O_3$) and selenium (SeO_2 or $Na_2Se_2O_3$) salts. The thickness and resistivity of the monocrystalline p-GaAs substrates were 0.4 mm and ρ = 2-4 Ω·cm, respectively. Before the electrodeposition process, the surfaces of GaAs substrates were etched in an aqueous solution of hydrochloric acid (HCl) and KOH-KNO_3 (1:3) composition for 3 min. After etching the silicon wafers were washed for 2 min in pure alcohol and distilled water, which it was maintained at high temperatures (≥ 300°C).

RESULTS AND DISCUSSION

Cyclic voltammetry was used to monitor the electrochemical reactions in solutions of $CdCl_2$, $ZnCl_2$, $Na_2S_2O_3$ and $Na_2Se_2O_3$, then in their combined solution of the same concentration and pH (Figure 1). The cyclic voltammogram was scanned in the potential range 1.2 V to –1.2 V versus graphite (or Ag/AgCl). All voltammetry curves were scanned first in the cathodic direction and positive current indicated a cathodic current. In the case of cadmium chloride solution (Figure 1a), the current rise started at –0.15 V, followed by large reduction wave at –0.7 V. This response was associated with Cd reduction

on GaAs substrate. The deposition reaction was reconfirmed by the reverse scan. The two stripping peaks at positive potential limits, 0.7-0.9 V indicated the oxidation of the cadmium compound. Figure 1b shows the voltammogram recorded for $ZnCl_2$ on GaAs substrate. The forward scan showed a reduction potential starting at about –0.65V. This was due to the reduction process of Zn onto the working electrode. The reduction peak increased towards the more-negative region where hydrogen evolution also occurred.

During the reverse scan, the oxidation wave of zinc could be seen starting at about –0.9 V. The oxidation peak clearly showed that the process was reversible whereby the deposited Zn dissolved upon reversing the potential. The forward scan of $Na_2S_2O_3$ and $Na_2Se_2O_3$ solutions (Figure 1c, curve 1) shows the cathodic current to start flowing at about –0.2-0.4V. The shoulder at –0.65-0.8V might be associated with the reduction of $Na_2S_2O_3$ and $Na_2Se_2O_3$ ions. Figure 1d shows the cyclic voltammogram of the GaAs working electrode in the mixture of $CdCl_2$, $ZnCl_2$, $Na_2S_2O_3$ and $Na_2Se_2O_3$ salt.

The wave around –0.85-0.88V corresponded to the formation of $Cd_{0.1}Zn_{0.9}S_{0.2}Se_{0.8}$ layers and the cathodic current increased gradually up to –0.9V, indicating the growth of layers. Based on the above results, the voltammogram suggested that a deposition on the working electrode can be expected when the potentials above – 0.86 V are applied.

Depending on the deposition time and the individual system, $Cd_{0.1}Zn_{0.9}S_{0.2}Se_{0.8}$ films of thickness up to 0.5 ÷ 1.6 μm was obtained from a solution. In order to fabricate the heterojunctions, an ohmic contact was performed on the side of $Cd_{0.1}Zn_{0.9}S_{0.2}Se_{0.8}$ films by evaporating an In electrode. An ohmic Al electrode, in reticulose form was evaporated on the p-GaAs wafers with an area of ~1cm^2. Thermal annealing of heterojunctions in argon atmosphere was carried out in thermogravimeter TQA-50.

In order to achieve a more direct insight into the surface structural features of the films, atomic force microscopy (AFM) imaging had been performed.

The surface images in an area of 19 μm×19 μm of the thin films deposited at -0.86 V deposition potential is shown in Figure 2. It is established that at deposition potential U <-0.5 V the surface of the films was not very compact.

The films were constituted by nano particles with an irregular size distribution, i.e. a lot of empty spaces could be seen between these particles. AFM images of samples clearly show the conversion of nano particles into spherical grains that were quite uniform over the GaAs substrates, at increasing deposition potential. However, the film consisted of smaller and larger nano particles in deposition potential above –0.9 mV. This might be due to the difference of rate of nucleation and growth. At the right hand side of the image, intensity strip is shown which indicates the height of the surface grain along Z-axis.

AFM picture shows the presence of high hills on top of a homogeneous granular background surface. The height of the hills was found to be decreased as the deposition potential increased up to -0.8V.

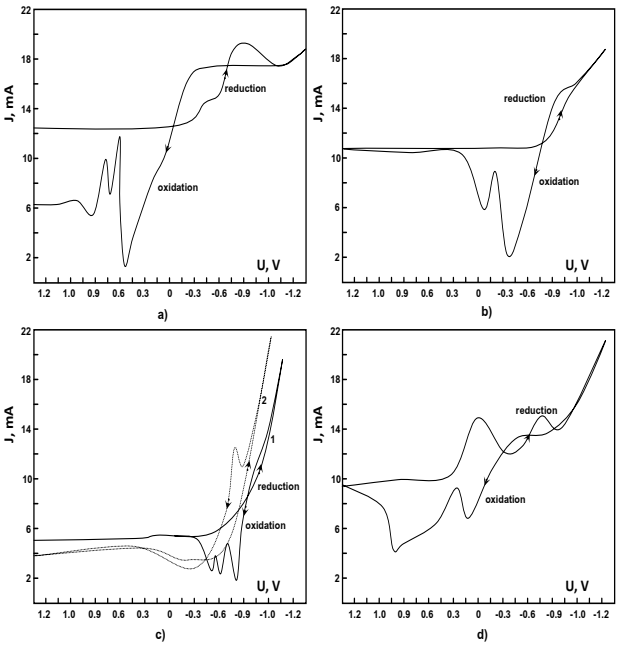

Fig. 1. Cyclic voltammogram for (a) 0.01M $CdCl_2$, (b) 0.09M $ZnCl_2$, (c1) 0.02M $Na_2S_2O_3$, (c2) 0.08M $Na_2Se_2O_3$ and (d) mixture of (a), (b) and (c) solutions at room temperature.

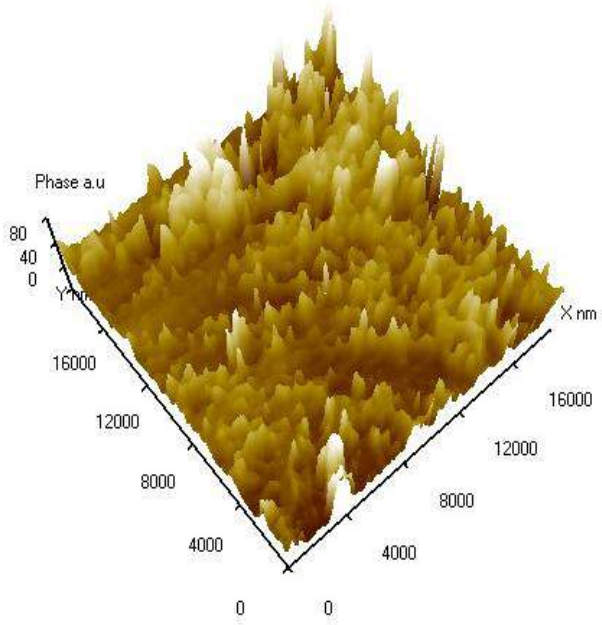

Fig 2. Atomic force microscopy images of $Cd_{0.1}Zn_{0.9}S_{0.2}Se_{0.8}$ thin films at deposition potential of U=-0.86 V

The X-ray diffraction study showed that the as electrodeposited film of $Cd_{0.1}Zn_{0.9}S_{0.2}Se_{0.8}$ is amorphous. The was subjected to a thermal treatment consisting in an annealing at 300^{o}C during 8-15 min in argon atmosphere. After annealing the films become crystalline. The optimal electrical and structural parameters that lead to a film with a high adherence and chemical stability are pointed out. After thermal annealing the XRD data indicated presence of two peaks at 2θ = 35.5° and 53.3° corresponding to orientation along (102) and (201) planes of CdS-ZnSe system. The high intensity of the substrate peak (GaAs) compared to the compound peak shows that the film thickness is low due to insufficient deposition time. As

the deposition time was increased to 30 minutes, additional peak corresponding to (110) plane at $2\theta = 43.9°$ was obtained. The highest peak corresponds to the orientation along (102) plane. The obtained d-spacing values corresponds well the standard Joint Committee on Powder Diffraction Standard data. When the deposition time was increased to 45 minutes, the intensity of the peaks was higher than the substrate indicating more material deposition. The XRD results obtained indicated that the films were polycrystalline in nature. The films deposited for this period was smooth and adhered well towards the substrate. However when the deposition time was increased to 60 minutes and above, the presence of additional peaks, which does not correspond to CdS-ZnSe system, was obtained. This is phenomenon may occur due to co-deposition of elemental materials due to long immersion time in the deposition bath.

Figure 3 illustrates the typical J-V characteristics of p-GaAs/n-$Cd_{1-x}Zn_xS_{1-y}Se_y$ heterojunction at different temperatures.

These curves were definitely of the diode type, with the forward direction corresponding to the positive potential on p-GaAs. The rectifying ratio at 1 V for all the investigated devices was found to be in the range of 500-700 at 300 K. The built-in potential is U_b=0.8 V. It is clearly seen from figure, that with decreasing the temperature the built-in potential strongly increases. It testify that with decreasing of temperature resistivity of films $Cd_{0.1}Zn_{0.9}S_{0.2}Se_{0.8}$ increases so that the significant part of an applied voltage falls on films volume, instead of the junction region. Temperature dependence of J-V characteristics shows, that decreasing of temperature leads to decrease both forward, and reverse current. The forward J-V characteristic of junctions at room temperature and below contains two areas.

In the field of low voltages (U<0.25 V at room temperature) the basic contribution to current brings recombination currents which are described by expression:

$$J = J_{01} exp(eU / \beta kT), \quad (1)$$

where β=1.2-1.8 and $J_{01} = 10^{-10} - 10^{-8} A$. Note, that values of β and J_{01} vary nonmonotonically with changing of temperature and duration thermal annealing in argon atmosphere.

Thermal annealing at t = 300^0C during t=15 min results to minimum values of β and J_{01}. Obviously, it is due to the decrease of defect states on the junction region (formation of heterojunctions), and also re-crystallization of films $Cd_{1-x}Zn_xS_{1-y}Se_y$ at thermal annealing in argon atmosphere.

However in the field of high voltages (U>0.3 V at room temperature) the current is caused by tunneling through the junction and described by the formula:

$$J = J_{02} exp(\alpha U) \quad (3)$$

Where, α=10–12 V^{-1} and does not depend on the temperature.

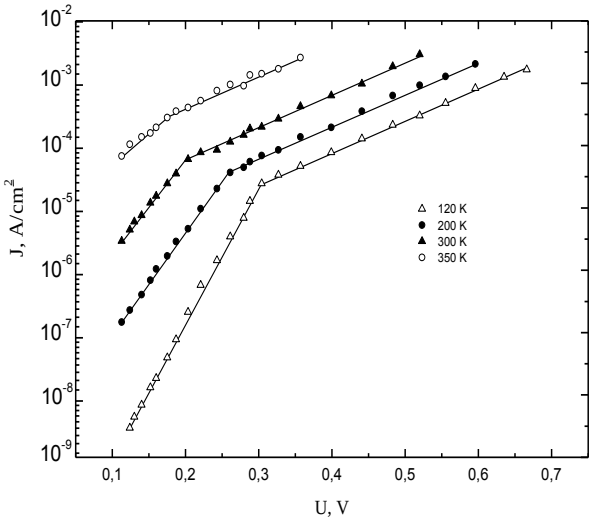

Fig.3. Semilogarithmic plot of forward bias of *J-V* curves for p- GaAs/n-$Cd_{1-x}Zn_xS_{1-y}Se_y$ heterojunctions at different temperatures.

For the definition of contact potential difference, thickness of depletion-layer width and concentration of impurity in surficial region of $Cd_{1-x}Zn_xS_{1-y}Se_y$, the capacitance-voltage characteristics of heterojunctions is investigated. Dependence of barrier capacitance on applied voltage at frequency of 0.5-8 kHz is presented on figure 4. The linearity of dependence C^{-2}=f(U) testifies that investigated heterojunctions p-GaAs/$Cd_{1-x}Zn_xS_{1-y}Se_y$ are abrupt junctions. This characteristic could be discussed in terms of the p-n junction type analysis, which the quasi-Fermi level for electrons is separated from that for holes in the depletion region when a voltage is applied across the junction, i.e. a net current flows across the heterojunctions.

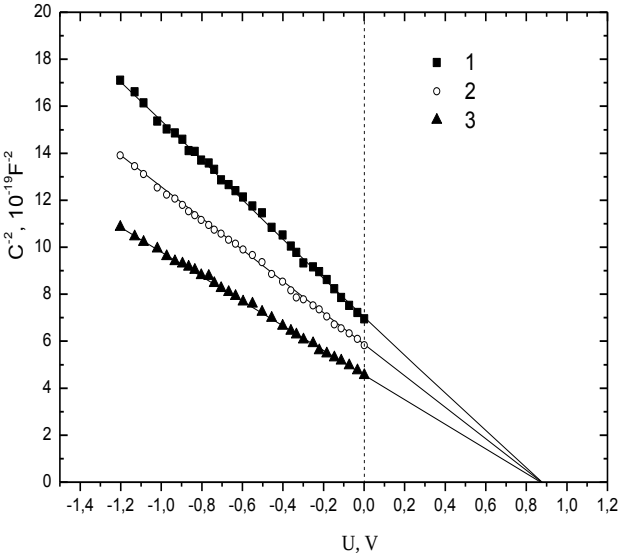

Fig. 4. Capacitance-voltige dependences for heterostructures for p-GaAs/n-$Cd_{1-x}Zn_xS_{1-y}Se_y$ heterojunctions without (1) and after thermal annealing (2, 3). 2- 200^0C for15 min; 3- 300^0C, for 15 min

The total capacitance, C, of the junction can be expressed by the well-known relation:

$$\frac{\partial C^{-2}}{\partial U} = \frac{2}{e\varepsilon_0 S^2}\left(\frac{1}{\varepsilon_2 N_A} + \frac{1}{\varepsilon_1 N_D}\right) \qquad (3)$$

Substituting values of $\varepsilon_1 = 9$, $\varepsilon_2 = 11.5$, $\varepsilon_0 = 8.85\cdot10^{-14}$ F·cm^{-1}, $e = 1.6\cdot10^{-19}$ Kl, $N_A = 3\cdot10^{18}$ cm^{-3}, $S = 0.98$ cm^2 it is found, that concentration of carriers in films $Cd_{1-x}Zn_xS_{1-y}Se_y$ is equal to $N_D = 3\cdot10^{18}$ cm^{-3}.

CONCLUSION

Anisotype heterojunction of p-GaAs/$Cd_{1-x}Zn_xS_{1-y}Se_y$ are fabricated by the electrodeposition method. It is established that thermal annealing at t = 300^0C during t=15 min in argon atmosphere reduces the concentration of defects, results in formation of heterojunctions and minimum values of non-ideality factor of *J-V* characteristics.

[1]. *A.Abdinov, H.Mamedov, S.Amirova*, Japanese Journal of applied physics, 46 (2007) 7359.

[2]. *A.Abdinov, H.Mamedov, and S.Amirova*, Thin Solid Films, 511-512 (2006) 140.

[3]. *A.Abdinov, H.Mamedov, G.Garibov, S. Amirova, N.Ragimova*, Optoelectronics and advanced materials, 1 (2007) 480.

[4]. *Y.Caglar and M.Zor*, Anad. Uni. J. Sci. and Tech., 4 (2003) 53.

[5]. *Y.Feng, K.Teo, M.Li, H.Poon, C. Ong and J. Xia*, Journal of Applied Physics, 74 (1993) 3948.

[6]. *R.Venugopal, D.Reddy and B.Reddy* Materials Chemistry and Physics, 55 (1998) 36.

[7]. *S.Fujita, Sh.Hayash, M.Funato, T. Yoshie, Sh. Fujita*, J. Cryst. Grown, 107 (1991) 674.

PHYSICOCHEMICAL AND THERMODYNAMIC PROPERTIES OF THE $GeSe_2$–A^2B^6 (A^2 = Hg; Cd; B^6 = S, Te) SYSTEMS

M.M.ASADOV, A.D.MIRZOEV

Institute of Chemical Problems, National Academy of Sciences of Azerbaijan,
H.Javid Pr. 29, AZ 1143 Baku, Azerbaijan
E-mail: mirasadov@gmail.com

The phase diagrams of $GeSe_2$–A^2B^6 (A^2 = Hg; Cd; B^6 = S, Te) systems were plotted by the methods of differential thermal and X-ray diffraction analyses, by the measurement of electromotive force (emf), microhardness and density. It is established, that phase equilibriums in the pseudo-binary $GeSe_2$ – CdTe, $GeSe_2$ – HgTe, $GeSe_2$ – HgS, $GeSe_2$ – CdS systems are characterized by formation of the limited solid solutions on basis of basic components and fourfold intermediate phases such as $A_2GeSe_2Te_2$ and $A_4GeS_4Se_2$: $Cd_2GeSe_2Te_2$ (hexagonal system; a = 5.69; c = 11.32 Å), $Cd_4GeS_4Se_2$, $Hg_2GeSe_2Te_2$ (tetragonal system; a = 7.50; c = 36.48 Å), $Hg_2GeS_2Se_2$ (hexagonal system; a = 7.20; c = 36.64 Å), $Hg_4GeS_4Se_2$ (monoclinic system; a = 12.38; b = 7.14; c = 12.40 Å). New dependences of the important physicochemical properties of solid solutions on basis of the $GeSe_2$ crosscuts of $GeSe_2$–A^2B^6 (A^2 = Hg; Cd; B^6 = S, Te) on composition are obtained. Thermodynamic characteristics of $Cd_2GeSe_2Te_2$ and $Hg_2GeSe_2Te_2$ phases were determined.

1. INTRODUCTION

Chalcogen compounds with more electropositive chemical elements are semiconductor materials. Among these materials A^2B^6 compounds possess unique physical properties [1–3]. Chalcogenids usually are receive ed by interaction of metal and chalcogen at heating in sealed and evacuated quartz ampoules. Sulfide HgS exists in two modifications α (zinnober) and β (metazinobarit). Temperature of transition $\alpha \leftrightarrow \beta$ is 345 °C. Compounds β-HgS, HgSe, and HgTe crystallize in a lattice of type blende. HgTe has practically zero forbidden zone. Degree of overlaps of a valent zone and a zone of conductivity for HgTe is 0.001 eV, for HgSe this is 0.07 eV. For α-HgS width of the forbidden zone is 2.0 eV. HgS is a material for photoresistors, a component of light composition on basis CdS. HgSe is used as a material for photoresistors, gauges of measurement of magnetic fields. Selenides are used as laser materials, as components for luminophores and thermoelectric materials. HgTe is a component of materials for receiver's of infra-red and X-ray radiation. Tellurides are used for photo cells, photosensitive layers of electron beam devices, dosimeters. $GeSe_2$ also is the semiconductor with width of the forbidden zone equal to 2.49 eV ($\rho = 10^{12}$ Ω·cm).

Stability of the pseudo-binary $GeSe_2$–CdTe, $GeSe_2$–HgTe, $GeSe_2$–HgS, $GeSe_2$–CdS systems is confirmed by methods of samples' physicochemical analysis and the measurement of electromotive force (e.m.f.) [4,5].

2. EXPERIMENTAL DETAILS

Synthesis of initial binary compounds of the $GeSe_2$–A^2B^6 crosscuts has been carried out by direct fusion of high-purity components taken in stoichiometric ratio, in evacuated up to 10^{-3} MPa quartz ampoules in electric furnace within two days. The heating of ampoules with substances has been gradually carrying out in the furnace up to the fusion temperature of corresponding binary compounds in connection with behavior of exothermic reactions of germanium, cadmium and mercury chalcogenides' formation. At temperatures of chemical reactions' behavior of binary chalcogenides' formation ampoules were being exposed during 4–6 hours [4]. Then temperature in the furnace has been smoothly increasing up to the fusion temperature of corresponding formed binary compound. During production of the $GeSe_2$, CdTe, HgTe and HgS compounds the exposure was made at 740, 1092, 670 and 820 °C correspondingly. The individuality of the obtained $GeSe_2$, CdTe, HgTe and HgS chalcogenide compounds has been controlled by methods of the physicochemical analysis by comparison of the obtained for them characteristics to the reference data.

With the purpose of definition of important parameters of intermediate phases and limited solid solutions of the threefold mutual Cd (Hg), Ge || S (Se), Te systems we investigated physicochemical and thermodynamic properties of the pseudo-binary $GeSe_2$–CdTe, $GeSe_2$–HgTe, $GeSe_2$–HgS, $GeSe_2$–CdS systems.

It is known, that using the e.m.f. measurement method [6,7,8] in establishing phase limits binary systems lies in that the potentials of the one-phase alloy electrodes at a fixed temperature, decrease with increasing content of the less noble component in the alloy whereas the potentials of the two-phase alloy electrodes, are constant and independent of composition within a two-phase region. The potentials vary, however, when passing from one-phase region to another. The temperature dependence of the e.m.f. shows a linear character if no phase transition occurs. When within the temperature range applied to the e.m.f. measurements a phase transition occurs in the alloy electrode, the temperature coefficient of the e.m.f. below and above the transition point will take different values.

An e.m.f. method with a liquid electrolyte is used to determine the partial molar thermodynamic properties of Cd in $GeSe_2$–CdTe and Ge in $GeSe_2$–HgTe quaternary solid alloys. The temperature range for the measurement at 298 and 380 K. The cell arrangement is as follows

Cd (s) / Cd^{2+} (KCl–LiCl) / $GeSe_2$–CdTe (s)
Ge (s) / Ge^{2+} (KCl–LiCl) / $GeSe_2$–HgTe (s)

Under reversible conditions the Gibbs free energy change for the reaction at temperature T is given by

$$\Delta\overline{G}_{Me} = -zFE \qquad (1)$$

were z = 2, Me = Cd, Ge, F the Faraday constant (96486 C mol^{-1}), E the measured electromotive force of the cell (V).

3. RESULTS AND DISCUSSIONS

The phase diagrams of the pseudo-binary $GeSe_2$–A^2B^6 (A^2 = Hg; Cd; B^6 = S, Te) systems were plotted by the methods of differential thermal and X-ray diffraction analyses, by the measurement of electromotive force (e.m.f.), microhardness and density. It was established, that in the $GeSe_2$–CdTe (Fig. 1), $GeSe_2$–HgTe (Fig. 2), $GeSe_2$–HgS, $GeSe_2$–CdS systems phase equilibriums are characterized by formation of limited solid solutions on basis of $GeSe_2$ and A^2B^6 components (Table 1) and quaternary intermediate phases such as $A_2GeSe_2Te_2$.

In these systems intermediate phases of $A_2GeSe_2Te_2$ composition are forming at temperatures 477°C ($Hg_2GeSe_2Te_2$; tetragonal system; a = 7.50; c = 36.48 Å), 647°C ($Cd_2GeSe_2Te_2$; hexagonal system; a = 5.69; c = 11.32 Å), 707°C ($Hg_2GeSe_2S_2$; hexagonal system; a = 7.20; c = 36.64 Å) accordingly. In $GeSe_2$–HgS system at 862°C, the $Hg_4GeSe_2S_4$ intermediate phase (monoclinic system; a = 12.38; b = 7.14; c = 12.40 Å) is also forming. All obtained fourfold compounds are to fuse incongruently.

Dependences of solid solutions' properties on a structure have been determined. Samples were annealed at high temperatures (on 5–10°C lower than eutectic temperature). In the Tables 2–4 concentration dependences of alloys-solid solutions on $GeSe_2$ basis with a rhombic lattice are resulted.

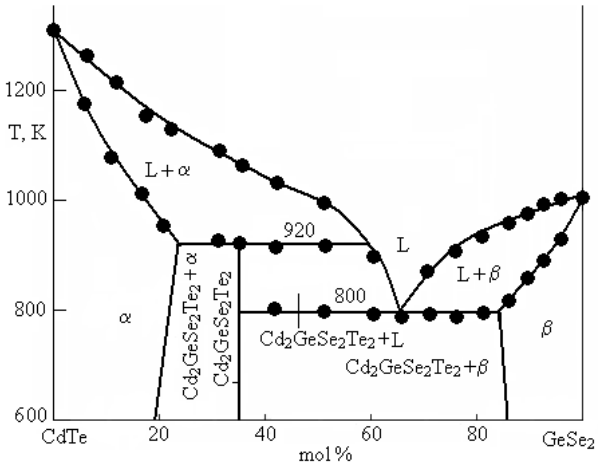

Fig. 1. Phase diagram of the CdTe–$GeSe_2$ system.

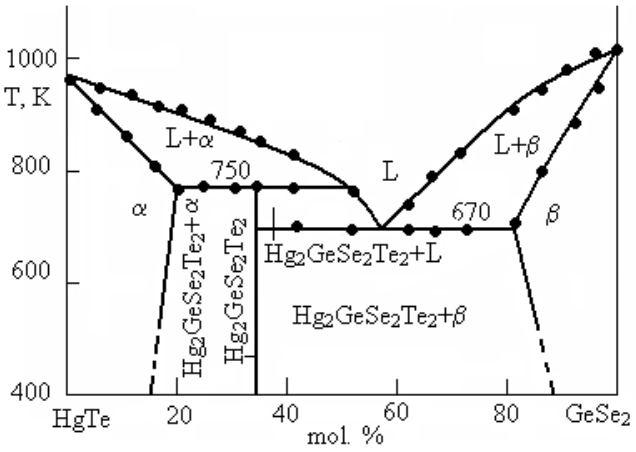

Fig. 2. Phase diagram of the HgTe–$GeSe_2$ system

Table 1 Areas of solid solutions in the systems such as $GeSe_2$ – HgS and $GeSe_2$ – HgTe

Systems	Solubility, mol %	
	On $GeSe_2$ basis	On HgS (HgTe) basis
$GeSe_2$–HgS	18 mol% HgS (600 °C)	5 mol% $GeSe_2$ (600 °C)
$GeSe_2$–HgTe	20 mol% HgTe (477 °C)	20 mol% $GeSe_2$ (477 °C)
$GeSe_2$–CdTe	16 mol% CdTe (647 °C)	22 mol% $GeSe_2$ (647 °C)

Table 2 Physicochemical properties of the $(GeSe_2)_{1-x}$– $(CdTe)_x$ solid solutions

Composition, Mol % CdTe	Structure parameters of a lattice			Microhardness, MPa	Density, q/sm^3
	a/Å	b/Å	c/Å		
0.0	7.037	11.82	16.82	1400	4.68
2.5	7.040	11.83	16.82	1400	4.69
2.5	7.045	11.84	16.84	1420	4.70
2.5	7.050	11.84	16.84	1440	4.72
2.5	7.054	11.86	16.87	1470	4.72
2.5	7.060	11.86	16.88	1500	4.74
2.5	7.066	11.90	16.90	1510	4.76

Table 3 Physicochemical properties of the $(GeSe_2)_{1-x}$ – $(HgTe)_x$ solid solutions

Composition, Mol % HgTe	Structure parameters of a lattice *a*/Å	*b*/Å	*c*/Å	Microhardness, MPa	Density, q/sm^3
0.0	7.037	11.82	16.82	1400	4.68
2.0	7.040	11.83	16.82	1400	4.70
3.0	7.038	11.84	16.84	1420	4.70
5.0	7.037	11.81	16.82	1450	4.72
6.0	7.035	11.81	16.80	1460	4.73
7.0	7.032	11.80	16.80	1470	4.75
8.0	7.030	11.80	16.78	1470	4.76
9.0	7.030	11.78	16.75	1480	4.79
10	7.284	11.76	16.72	1480	4.80

Table 4 Physicochemical properties of the $(GeSe_2)_{1-x}$ – $(HgS)_x$ solid solutions

Composition, Mol % HgTe	Structure parameters of a lattice *a*/Å	*b*/Å	*c*/Å	Microhardness, MPa	Density, q/sm^3
0.0	7.037	11.82	16.82	1400	4.68
2.0	7.037	11.82	16.80	1400	4.70
3.0	7.030	11.81	16.78	1420	4.72
5.0	7.024	11.79	16.76	1450	4.83
7.5	7.020	11.77	16.74	1480	4.90
10	7.012	11.74	16.76	1500	5.06

It is established, that formation of solid solutions on A^2B^6 basis in the $GeSe_2$–A^2B^6 systems is accompanied by an appreciable negative deviation from the Raoult law. For concentration dependences of solid solutions on A^2B^6 basis the following relation don't meet the conditions: $p_{A^2B^6} = x_{A^2B^6} p^*_{A^2B^6}$, where $p^*_{A^2B^6}$ is the steam pressure of pure A^2B^6. For the $(GeSe_2)_{1-x}$–$(A^2B^6)_x$ solid solutions the appreciable deviation from the Raoult law don't appear.

The thermodynamic analysis of chemical reactions has been carrying out with use of Gibbs-Duhem equation. For conditions of $\sum_i \nu_i d\mu_i = 0$ equilibrium which binds the change of chemical potential of components of system at *T = const, p = const.* For simplicity let's consider a $A \leftrightarrow B$ reaction. Then change of Gibbs function is: $dG = \mu_A d\nu_A + \mu_B d\nu_B$. Let's assume, that the infinitesimal $d\xi$ amount of matter *A* turns into *B*; then $\Delta A = -d\xi$ and $\Delta B = d\xi$. This implies:

$$dG = -\mu_A d\xi + \mu_B d\xi = (\mu_B - \mu_A)d\xi \quad (T = const, p = const). \qquad (2)$$

If equation (1) is re-arranged as $(\partial G / \partial \xi)_{p,T} = \mu_B - \mu_A$ it is obvious, that at behavior of $A \leftrightarrow B$ reaction the graph slope of dependence *G* on ξ will define the $\mu_B - \mu_A$ value. It proceeds on the theory that the chemical reaction flows in direction of *G* decrease. When $\mu_A > \mu_B$, reaction flows from *A* to *B* and on the contrary when $\mu_A < \mu_B$, reaction flows from *B* to *A*. At $\mu_A = \mu_B$, the reaction is in equilibrium position. According to the above for $A \leftrightarrow B$ reaction it is possible to set values of condition's quantities for case when chemical equilibrium is occurring.

The thermodynamic potential of $A \leftrightarrow B$ reaction, according to stability condition in a system equilibrium state, is to be minimal. If take into account, that standard chemical potentials are standard mole Gibbs functions then at *T = const, p = const* in an equilibrium state the value of ΔG^0_m is to be minimal. In $\Delta G^0_m = \Delta H^0_m - T\Delta S^0_m$ relation values of ΔH^0_m and ΔS^0_m poorly depend on temperature. Subject to it for the given values of condition's quantities the probability of behavior of $A \leftrightarrow B$ reaction is estimating.

The following equilibrium conditions are generally fair: a) chemical balance; b) reaction is possible; c) reaction is not possible. In agreement with the theory for these cases

$$\left.\begin{array}{l} \Delta G = 0; \Delta H = 0 \\ \Delta G < 0; \Delta H > 0 \\ \Delta G > 0; \Delta H < 0 \end{array}\right\} \qquad (3)$$

From (3) it follows, that at chemical reactions' calculations calculation of ΔG value is required in every case. It specifies that knowledge of chemical potentials of all reaction participants at given values of condition's quantities is necessary. For calculation of condensed phases it is convenient to use Gibbs – Helmholtz equation subject to phases' heat capacities

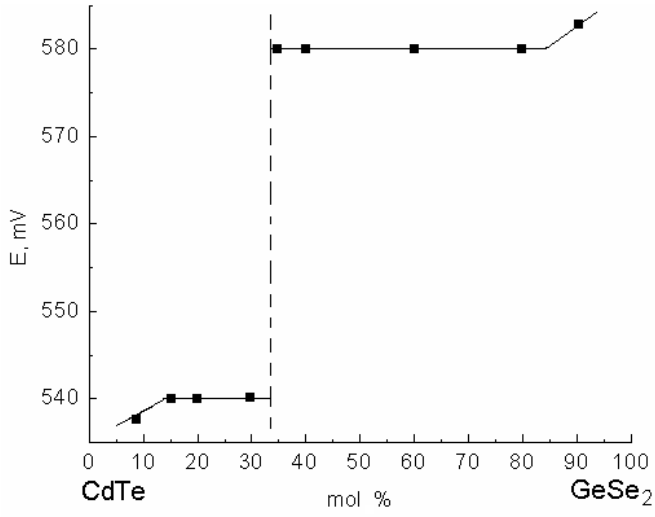

Fig. 3. Dependence of e.m.f. on composition in the CdTe–$GeSe_2$ system at 298 K.

$$\Delta G = \Delta H^0 - T\Delta S^0 + \int_{T^0}^{T} \Delta C_p dT - T\int_{T^0}^{T}\left(\frac{\Delta C_p}{T}\right)dT \quad (4)$$

The reactions flowing in a reversible galvanic cell concentrating relative to the electrodes have been studied by the method of e.m.f. measurement. The annealed alloys of the $GeSe_2$–CdTe, $GeSe_2$–HgTe systems have been used as electrodes. E.m.f. measurements confirm the accuracy of plotted phase diagrams (Fig. 3 and Fig. 4).

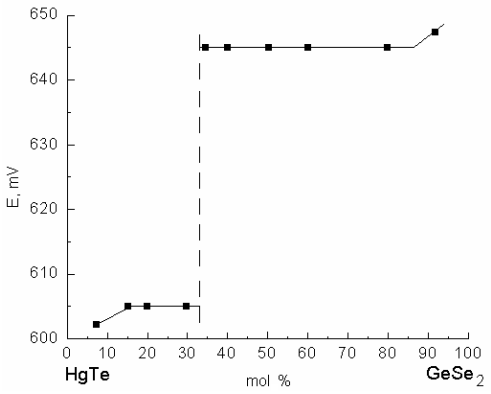

Fig. 4. Dependence of e.m.f. on composition in the HgTe–$GeSe_2$ system at 298 K.

On the base of plotted phase diagrams and measured partial molar thermodynamic properties of Cd in the system $GeSe_2$–CdTe and Ge in $GeSe_2$–HgTe (Table 5), the integral molar thermodynamic properties of fourfold phases have been calculated (Table 6). At this the standard molar thermodynamic properties of binary compounds $GeSe_2$, CdTe, HgTe [2,3] and potential-forming reactions in the pseudo-binary $GeSe_2$–CdTe, $GeSe_2$–HgTe cuts mutual Cd (Hg), Ge || S (Se), Te systems were also used.

4. CONCLUSION

The phase diagrams of the pseudo-binary $GeSe_2$–A^2B^6 (A^2 = Hg; Cd; B^6 = S, Te) systems were plotted by the methods of differential thermal and X-ray diffraction analyses, by the measurement of electromotive force (e.m.f.), microhardness and density. New intermediate quaternary $Cd_2GeSe_2Te_2$, $Cd_4GeS_4Se_2$, $Hg_2GeSe_2Te_2$, $Hg_2GeS_2Se_2$, $Hg_4GeS_4Se_2$ phases and limited solid solutions on the base of binary components $GeSe_2$ and A^2B^6 have been found. Physicochemical and thermodynamic properties of some compositions of intermediate phases have been studied. The standard mole thermodynamic functions of quaternary $Cd_2GeSe_2Te_2$ and $Hg_2GeSe_2Te_2$ phases were determined.

Table 5 The standard partial molar thermodynamic properties of Cd in the system $GeSe_2$–CdTe and Ge in $GeSe_2$–HgTe

Phase	$-\Delta_f \overline{G}_{Me}$ kJ mol^{-1}	$-\Delta_f \overline{H}_{Me}$ kJ mol^{-1}	$\Delta_f \overline{S}_{Me}$ J mol^{-1} K^{-1}
$Cd_2GeSe_2Te_2$	108.5 ± 11.5	82.8 ± 2.9	86.1 ± 18.9
$Hg_2GeSe_2Te_2$	402.2 ± 46.1	324.3 ± 1.6	261.3 ± 45.8

Table 6 The standard molar thermodynamic functions of quaternary phase in the systems $GeSe_2$–CdTe and $GeSe_2$–HgTe

Phase	$-\Delta_f G^0_{298}$ kJ mol^{-1}J	$-\Delta_f H^0_{298}$	$\Delta_f S^0_{298}$ J mol^{-1} K^{-1}
$Cd_2GeSe_2Te_2$	298.3 ± 1.9	276.3 ± 13.3	73.8 ± 32.7
$Hg_2GeSe_2Te_2$	605.8 ± 3.9	545.6 ± 21.2	202.0 ± 30.0

[1]. Physics and Chemistry of II-VI Compounds. Edited by M.Aven and J.S.Prener. GER and Development Center Schenctady, New York, USA. North-Holland Publishing company– Amsterdam. 1967.

[2]. Physico-Chemical Properties of Semiconductor Matters, Handbook, Composite authors (in Russian), Moscow, Nauka, 1978.

[3]. *O.Kubaschewski, C.B.Alcock*, Metallurgical Thermochemistry, Fifth Edition, Pergamon Press, Oxford, New York, Toronto, Sydney, Paris, Frankfurt, 1979.

[4]. *M.M.Asadov, A.C.Mirzoev, O.M.Aliev*, Azerb. Chem. J. 2 (2006) 77–81.

[5]. *A.C.Mirzoev*, Thesis of Institute of Chemical Problems, NASA (in Azerbaijani), Baku, Azerbaijan, 2008

[6]. *M.M.Asadov*, Russ.J.Inorg. Mater. 20 (1984) 38–40.

[7]. *M.M.Asadov*, Russ. J. Inorg. Mater. 20 (1984) 1621–1623.

[8]. *Z.Sztuba, K.Wiglusz, I.Mucha, A.Sroka, W.Gawel*, CALPHAD 32 (2008) 106–110.

AN ALTERNATIVE COMMUNICATION SOURCE: FREE ELECTRON LASER

MEHMET KARA[*], METİN ORBAY[**]

[*] *Bolu Vocational High School, Abant İzzet Baysal University, 14200, Bolu-TURKEY, mkara60@hotmail.com.*

[**] *Department of Physics, Faculty of Art and Sciences, Amasya University, 05189, Amasya-TURKEY, metin.orbay@amasya.edu.tr*

Nowadays, conventional lasers are widely used in communication systems. In this point, Free Electron Laser (FEL) represents a radical alternative to conventional lasers, due to being high power, tunable source and short wavelength, in spite of the considerable cost and complexity.

In this presentation, firstly, the currently operating FELs performance will be summarized. And then, the desired requirements of a communication source will be outlined and compared to the FEL features.

I. INTRODUCTION

The microwave tubes which were the first powerful coherent radiation sources invented in the beginning of the last century. Their development received a strong impetus from radar systems development. Even these days, these tubes are still successful and useful sources of coherent radiation with wavelengths ranging from several meters to about 1 millimeter. As is well known, microwave tubes operating at kilowatt power levels are found in nearly every home, and radar and communications applications also affect daily lives. The significant caused invention of the open led to the development of the conventional laser and an immediate reduction in the attainable wavelength by about four orders of magnitude. The optical cavity with macroscopic dimensions that could store significant optical power at short wavelengths was crucial to the invention of the laser [1].

John Madey and his colleagues constructed a quite exotic new laser called Free Electron Laser (FEL) in the coherent infrared wavelength range [2]. Since that time tremendous progress has been made in the experimental and theoretical aspects of FELs and a bibliography can be founded in Refs.[3,4]. Basically, the FEL uses a beam of relativistic electrons to generate high intensity electromagnetic radiation, much brighter than that produced by a synchrotron source. As seen Figure 1, the basic components of a FEL are the electron beam, the magnetic undulator, and optical mirrors [5].

As seen from Figure 2, the undulator has a sinusoidal magnetic field. In this field, one electron moves along a sinusoidal field and then emits an electromagnetic wave, with a number of periods equal to the number of undulator periods and a wavelength equal to the undulator period, reduced by a relativistic contraction factor inversely proportional to the square of its energy. This makes it easy to shorten the wavelength by increasing the electron beam energy and for *GeV* electron beams one can produce wavelengths of the desired atomic dimensions.

The wavelength λ of the emitted radiation depends on the electron energy E, on the period of the undulator magnet λ_0 and on its magnetic field B,

$$\lambda = (1 / 2) \lambda_0 (1+ K^2)(mc^2 / E)^2$$

where K is called pitch parameter and given by

$$K=eB \lambda_0/(2\pi mc^2).$$

The width of the energy distribution of the radiation on axis is inversely proportional to the number of undulator periods which can easily be of the order of 100 or larger [6].

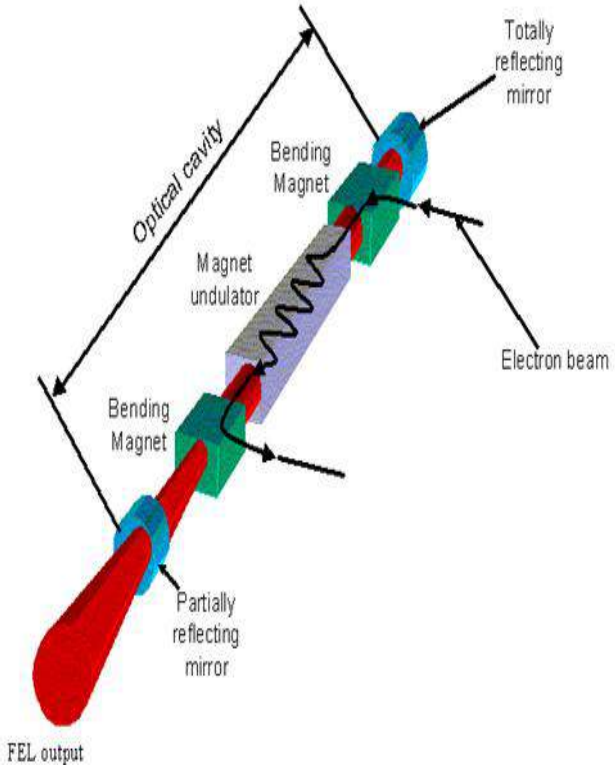

Fig. 1. Schematic representation of a FEL [5].

The radiation is very well collimated, with an opening angle of a few microradians, corresponding to a beam diameter of less than 1mm if one observes it 100m away from the undulator source. The number of photons emitted from one electron within this energy-width and angle is rather low. About one photon per 100 electrons passes through the undulator. In the case of an ensemble

of electrons, the total radiation field generated is the sum of the fields generated by all electrons. When the electrons in a storage ring go through the undulator, there is no correlation between their positions on the scale of the radiation wavelength. As a result the fields they generate superimpose at random, with a partial cancellation. What the beam produces in this case is called "spontaneous radiation", and its intensity is proportional to the number of electrons, N_e. This intensity is then proportional to the number of electrons squared. Since N_e is a billion or more, one obtains a huge gain [6].

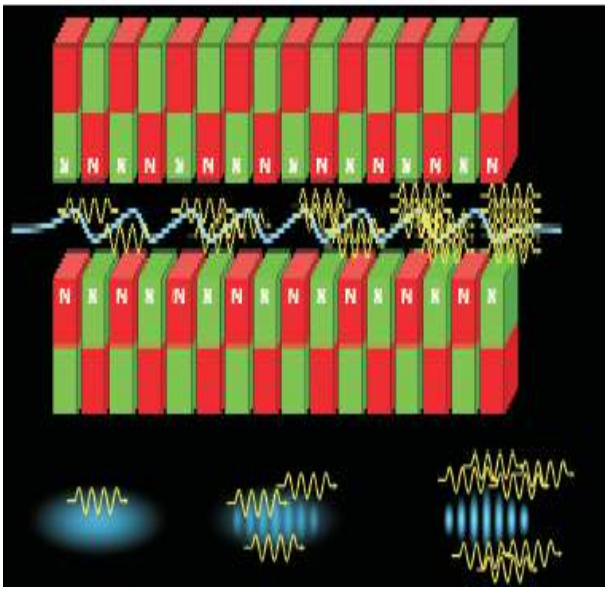

Fig. 2. Schematic representation of the self-amplifying light emission from the beam of electron in the undulator [7].

The beam of relativistic electrons moving through the undulator magnetic field transfers part of its energy to copropagating electromagnetic wave. The electrons enter the undulator with energy γ_i (with an initial power P_i) and leave the undulator with energy γ_f (with final power P_f). Therefore, it is important that energy is transferred from the electron beams to the electromagnetic radiation [4]. The most remarkable properties of this type system is its ability to deliver time structured pulses down to the picoseconds range whilst maintaining exceptional stability, at virtually any wavelength from *the ultraviolet* to *the far infrared* [5]. So, the FEL represents a radical alternative to conventional lasers in despite of the considerable cost and complexity. Because of the most interesting features of FELs, it would be a potentially attractive as an alternative communication device.

II. THE FEL A COMMUNICATION SOURCE

It is known that the capacity of a communication channel in bit per second (*Bps*) is given by

$$C=B\ log_2(1+P_n/P_s),$$

where, P_n and P_s are the average signal and noise powers, respectively, and B is the transmission bandwidth in cycles per seconds (*Cps)* [8]. In connection with this expression, the FEL features and the desired communication source are given in Table 1.

As seen in Table 1, the FEL would hence be obvious to make use in communication devices since a communication FEL beam can be easily modulated for carrying a message. However, at the present time, it is also a rather complex device and this will certainly limit its use. Nevertheless, some applications of FEL may be attractive as radar system [9]. The natural attributes of the FEL may fit this need rather well. The FEL radar system which is also quite feasible could have; short pulse (high resolution), short wavelength (good directivity), frequency agility, high pulse repetition rate. Unfortunately, the FEL is expensive, so only a limited subset of all possible applications can be addressed (see: Refs.[9-12] and references quoted therein) until cheaper FEL is developed. Table 2 summarizes currently operating some FELs in the world (please visit http://sbfel3.ucsb.edu/www/vl_fel.html to the latest developments on FELs).

In Table 2, λ is the typical wavelength, σ_z is the electron micropulse length, E is the electron-beam energy, I is the peak current, N is the number of undulator periods, λ_0 is the undulator wavelength, and K is the undulator parameter. The undulator parameter is $K=eB\lambda_0/2\pi mc^2$, where B is the root-mean square undulator field strength, e is the electron charge magnitude, m is the electron mass, and c is the speed of light [12].

III.CONCLUSION

The FEL is without doubt one of the major inventions of the last century in the field of laser technology. It is obvious that the FEL will be more developed in the future. As the FEL does so, it will play an increasingly important role in communication devices and make communication more clear and disconnected.

Table 1. The FEL features and the desired requirements of a communication source

The most interesting features of FEL are	***The desired communication source can be***
Tunability, High peak power, Flexible pulse structure, Broad wavelength coverage.	Large bandwidth, High average power, High rate of modulator, Low noise.

Table2. Currently operating some FELs [12]

Operating FELs:	**λ (μm)**	**σ_z**	***E*(MeV)**	***I*(A)**	***N***	**λ_0(cm)**	***K***
UCSB (mmFEL)	338	25μs	6	2	42	7.1	0.71
Tokyo(UT-FEL)	43	10ps	13	22	40	4	0.7
Netherlands (FELIX)	40	5ps	25	50	38	6.5	1.5
Bruyeres (ELSA)	20	50ps	18	50	30	3.2	0.8
Frascati (LISA)	15	7ps	25	5	50	4.4	1
Grumman (CIRFEL)	14	5ps	14	150	73	1.36	0.2
Beijing (IHEP)	10	4ps	30	14	50	3	1
Orsay (CLIO)	8	3ps	50	80	48	4	1
Darmstadt (IR-FEL)	5	2ps	40	2.7	80	3.2	1
Vanderbilt (FELI)	3	3ps	43	20	47	2.3	1
Okazaki (UVSOR)	0.3	126ps	500	5	16	11	2
Florida (CROEL)	500	25ps	1.7	0.2	156	0.8	1.2
Rutgers (FEL)	140	25ps	38	1.4	50	20	1
Moscow (Lebedev)	100	20ps	30	0.25	35	3.2	0.75
Tokai (SCARLET)	40	4ns	15	10	62	3.3	1
UCLA (IR-FEL)	10	2ps	20	150	40	1.5	1
Stanford (FIREFLY)	4	2ps	43	40	120	3.56	0.9
Osaka (FELI)	1	2ps	170	100	50	6	1.26
Dortmund (FEL)	0.4	50ps	500	90	17	25	2.1
Harima (HIT)	0.28	100ps	500	3	170	1.8	4.2
CEBAF (UVFEL)	0.15	0.4ps	200	200	48	3	1.5
BNL (DUVFEL)	0.1	0.2ps	310	300	682	2.2	1.54
SLAC (LCLS)	0.0004	0.1ps	7000	2500	723	8.3	4.4

[1]. Free Electron Lasers and Other Advanced Sources of Light: Scientific Research Opportunities, Commission on Physical Sciences, Mathematics, and Applications, National Academy Press, Washington (1994).

[2]. *J. Madey*, J. Appl. Phys., 42 (1970) 1906.

[3]. *E.L. Saldin, E.V. Schneidmiller and M.V. Yurkov*, The Physics of Free Electron Lasers, Springer Verlag, Berlin (2000).

[4]. *G. Dattoli, A. Renieri and A. Torre*, Lectures in Free-Electron Laser Theory and Related Topics, World Scientific, Singapore (1995).

[5]. www.srs.dl.ac.uk/Annual_Reports/AnRep99_00/FEL.gif (Accessed on 7 May 2010).

[6]. *C. Pellegrini and J. Stöhr,* X-Ray Free Electron Lasers: Principles, Properties and Applications, http://ssrl.slac.stanford.edu/stohr/xfels.pdf

[7]. *J. Ullrich*, Free-Electron Lasers: Physics with ultra-short and super-brilliant X-ray pulses;

[8]. http://www.mpi-hd.mpg.de/mpi/fileadmin/files-mpi/Flyer/FEL_en.pdf

[9]. *C.E. Shanon and W. Weaver*, The Mathematical Theory of Communication, University of Illinois Press, Urbana (1972).

[10]. *J. Walsh*, Nucl. Instr. and Math. A 239 (1985) 383.

[11]. *S.H. Gold and G.S. Nusinovich*, Rev.Sci.Instr., 68 (1997) 3945.

[12]. *R.F. Haglund*, Photon-Based Nanoscience and Nanobiotechnology, NATO Science Series II Mathematics Physics and Chemistry, 239 (2006) 175.

[13]. *S. Geisenheyner*, Potential defense applications of free electron lasers, Armada International, 1994.

[14]. http://www.nap.edu/openbook.php?record_id=9182&page=22#p20003398ttt00007 (Accessed on 7 May 2010).

STUDY OF A WELL POTENTIAL WITH ASYMPTOTIC ITERATION METHOD

E. ATESER[1], H. CIFTCI[2]

[1]*Aksaray Üniversitesi, Fen Edebiyat Fakültesi, Fizik Bölümü, 68100, Aksaray/Türkiye*

[2]*Gazi Üniversitesi, Fen Edebiyat Fakültesi, Fizik Bölümü, 06100, Teknikokullar/Ankara/Türkiye*

In this paper, a new well potential for Schrödinger equation have been studied with aysmptotic iteration method and the eigenvalue sets calculated due to the potential parameters such as R, *l* and *γ*.

I. INTRODUCTION

Scientists have been trying to solve Schrödinger equation since it became a key opening the quantum world of the matter. Many methods such as Hill Determinant [1], Super Symmetry [2],WKB [3], Shifted 1/N Expension [4] and etc. were developed and used to solve the equation analytically or numerically.

Recenty, a new method called Asymptotic Iteration (AIM) has been developed by Ciftci et al [5] for solving second order linear, homogeneous differential equations including Shrödinger's by an analytical or numerical way. The authors have also developed the perturbation expansion of the method for various potentials such as quartic and complex cubic unharmonic oscillators and Pöschl- Teller [6]. The method has been applied to many quantum systems as a model or an alternative way of the solution. These studies can be summarized as follows. The construction of the general formulas for the exact solution of Schrödinger equation using Pöschl-Teller potentials including Coulombic and harmonic oscillator terms [7]. Morse [8], Kratzer [9] potentials and many others [10-14].

Single well potentials are useful models to describe the charecteristics of a particle in the existance of a force with one center. One dimensional form of it can be used as a model, viewing the scattering mechanism of low energy electrons by a noble gas atoms and three dimensional form, a nucleus consisting of protons and neutrons in an infinite well [15]. In this work, we have studied such a well potential in three dimension , having a new form as,

$$V(r)=\frac{\gamma(\gamma+1)}{(R-r)^2}$$

and calculated eigenvalue sets due to the potential parameters such as R, *l* and *γ* by using AIM. This potential can be taken as a physical model of a perfect infinite square well potential. It is clear that when r goes to zero, the potential behaves as a constant but when to R, it goes to infinity and thus, there is an infinite barrier at r=R. In preparation of the single well application, the features of AIM are mentioned in section 2. The Section 3 is about Schrödinger equation with the new potential form. Finially, the results for various potential parameters are discussed and convergence rate of the method indicated.

II. THE METHOD

Ciftçi et al [5] developed AIM to solve second order linear, homogeneous differential equation of the form

$$y''(x)=\lambda_0(x)y'(x)+S_0(x)y(x)$$

where $\lambda_0(x)\ and\ S_0(x)$ should be functions which can be derivated continiously. By applying this method, a differential equation having this form can be solved analatically or numerically. In the method, a functianal iteration is done to reduce the second order differential equation to the first order linear but not homogeneous one. The procedure can be summarized as follows. Firstly, the general forms of $\lambda_0(x)\ and\ S_0(x)$ are obtained as

$$S_n=S'_{n-1}+S_0\lambda_{n-1}$$

$$\lambda_n=\lambda'_{n-1}+\lambda_0\lambda_{n-1}+S_{n-1}$$

Secondly, a creteria,

$$\frac{S_n}{\lambda_n}=\frac{S_{n-1}}{\lambda_{n-1}}=\alpha$$

is introduced to solve the equation. This iteration can be done up to a finite number such as 4,5 or etc for the exact solutions. Whereas for a numerical solution, the iteration should be done up to the ratios of the functions should equal to a constant like α. Once α(x) is obtained, the general solution of the differential equation is as follows

$$y(x)=\exp\left[-\int^x\alpha(x')dx'\right]\left\{C_2+C_1\int^x\exp\left[\int^{x'}(\lambda_0(x'')+2\alpha(x''))dx''\right]dx'\right\} \quad (1)$$

Eigenvalues of the equation can also be obtained by the following relation,

$$\lambda_{n+1}S_n-S_{n+1}\lambda_n=0$$

Although, the differention equation can be solved for every r point in an exact solution, an appoximation, a suitable r_0, should be done to solve it numerically.

III. GENERAL FORMULATION OF THE PROBLEM0

Consider the potential given below,

$$V(r)=\frac{\gamma(\gamma+1)}{(R-r)^2}\quad r\in(0,R) \tag{8}$$

Where $\gamma>0$. In this case, the Schrödinger equation is written as,

$$\left[-\frac{d^2}{dr^2}+\frac{\ell(\ell+1)}{r^2}+\frac{\gamma(\gamma+1)}{(R-r)^2}\right]\Psi(r)=E\Psi(r) \tag{9}$$

with the boundary conditions, $\Psi(0)=\Psi(R)=0$. In order to apply AIM to this problem, first of all the asymptotic wavefunction must be obtained and then got a second order differential equation. The wavefunction behaves as

$$\Psi(r\to R)=(R-r)^{\gamma+1} \tag{10}$$

$$\Psi(r\to 0)=(r)^{\ell+1}$$

for the boundary conditions. So the asymptotic wavefunction can be written as

$$\Psi(r)=r^{\ell+1}(R-r)^{\gamma+1}f(r) \tag{11}$$

After substuting this form into Eq.(9), Schrödinger equation turns out of a second order linear and homogeneous differential form as,

$$f''(r)=2\left(\frac{(\gamma+1)}{R-r}-\frac{(\ell+1)}{r}\right)f'(r)$$

$$+\left(-E+\frac{(2\ell+2)(\gamma+1)}{r(R-r)}\right)f(r) \tag{12}$$

If r=zR substitution is used, Eq.(12) can be dimensionless as,

$$f''(z)=2\left(\frac{(\gamma+1)}{1-z}-\frac{(\ell+1)}{z}\right)f'(z)$$
$$+\left(-\varepsilon+\frac{(2\ell+2)(\gamma+1)}{z(1-z)}\right)f(z) \tag{13}$$

where

$$E_{nl}(\gamma,R)=\frac{\varepsilon_{nl}(\gamma)}{R^2} \tag{14}$$

Now, AIM's procedure, equations from (2) to (7), are applied to find eigenvalue sets . In the numerical calculations, z_0 is taken as $z_0=1/2$. ε values for the first four states have been calculated for different l and γ values in Table 1. If one wants to calculate the corresponding energy eigenvalues, one has to use Eq.(14)

Table 1. ε values for the first four states

$z_0=1/2$	γ	ε_0	ε_1	ε_2	ε_3
l=0	1	20.1907	59.6795	118.9	197.859
	2	33.2175	82.7192	151.85	240.709
	3	48.8312	108.516	187.636	286.41
l=1	1	35.6807	84.9446	153.993	242.797
	2	53.967	113.094	191.999.	290.663
	3	74.9652	144.056	232.865	341.412
l=2	1	53.967	113.094	191.999	290.663
	2	77.4838	146.375	235.085	343.575
	3	103.755	182.497	281.054	399.393
l=3	1	74.9652	144.056	232.865	341.412
	2	103.755	182.497	281.054	399.393
	3	135.284	223.791	332.142	460.296

IV. CONCLUSION

In this work, Schrödinger equation has been studied in three dimensions for a new single well potential by using AIM and eigenvalue sets calculated numerically for different potential parameters. If Table 1 is investigated, it is concluded that, there are some degenarete energy levels as $\varepsilon_{n\ell}(\gamma)=\varepsilon_{n\gamma}(\ell)$. Generally, 25 iteration steps have been used to get high accurate results in the numerical calculations. Thus, the results show that, AIM can be applied to this problem for any potential parameter and angular momentum quantum number l. As we know that it is impossible to find a perfect infinite square well in nature, so the potential studied in this work can be considered as a more realistic one. In order to see this correlation, it is enough to look at the limit value of γ ->0 where the potential turns into the infinite square well.

[1]. *M. Znojil J. Math. Phys. 1992, 33, 213.*
[2]. *F. Cooper, A. Khare and U. Sukhatme Phys. Rep. 1995, 251, 267.*
[3]. *Y.P.Varshni J. Phys. A. 1992, 25, 5761.*
[4]. *R. K. Roychoudhury and Y. P. Varshni J. Phys. A 1998, 21, 3025.*
[5]. *H. Ciftci, R. L. Hall and N. Saad J. Phys. A 2003, 36, 11807.*
[6]. *H. Ciftci, R. L. Hall and N. Saad , Phys. Lett. A. 2005 340, 388.*
[7]. *H. Ciftci, R. L. Hall and N. Saad, J. Phys. A: Math. Gen. 2005, 38,1147.*
[8]. *Boztosun., M. Karakoc, F. Yasuk and A. Durmus, , J. Math. Phys., 2006 ,47, 062301*
[9]. *O.Bayrak and I. Boztosun J. Phys. A 2006, 39, 6955.*
[10]. *H. Ciftci, R. L. Hall and N. Saad, Phys. Rev. A. 2005 ,72, 022101.*
[11]. *T. Barakat, K. Abodayeh and A.Mukheimer, J. Phys. A 2005, 38, 1299.*
[12]. *F. M. Fernandez Phys. Lett. A. 2005, 346, 381.*
[13]. *O. Bayrak and I. Boztosun Physica Scripta 2007, 72, 92.*
[14]. *T Barakat, J. Phys. A 2006, 39,823.*
[15]. *S. Gasiorowicz 1974 Quantum Physics (John Wiley and Sons)*

THERMAL CAPACITY AND PHASE TRANSITIONS IN $TlFeTe_2$ CRYSTALS

A.M. ABDULLAYEV, E.M. KERIMOVA, S.S ABDINBEKOV

Institute of Physics
Azerbaijan National Academy of Sciences,
Baku, Az-1143, H.Javid ave., 33, Baku, Azerbaijan

This paper deals with the thermal capacity of $TlFeTe_2$ crystals abstract within 4.2-300K.

Dependence $C_p(T)$ reveals two strongly pronounced anomalies indicating presence of phase transitions. Maximum values of anomalies are at temperatures.

T_{c1}=69.1±0.3 T_{c2}=220±0.3 K. changes energy ΔQ and entropy ΔS of phase transition, factors of thermodynamic potential close to have been T_{c2} defined. Small magnitude $\frac{\Delta S}{R} = 0.12$ specifies that this transition concerns transitions of displacement type. The behaviour of anomalous thermal capacity close to T_{c2} is well described by Landau phase transitions theory.

Ternary compounds $TlFeS_2$ and $TlFeSe_2$ fall in the number of $TlMX_2$-typed compounds (M=Cr; Fe; x=S, Se, Te) having semiconductive and magnetic properties [1-3].

Neutronographic investigations at~16K[1] show that $TlFeS_2$ compound has antifferromagnetic ordering at low temperatures. By NGR [2,3] it is established that magnetic phase transition $TlFeS_2$ is observed within T=170-190K. Study of $TlFeS_2$ and $TlFeSe_2$ thermal capacity [4,5] shows that in behavior of $C_p(T)$ within 4.2-300K anomalies are not observed that is characteristic of magnetic phase transitions.

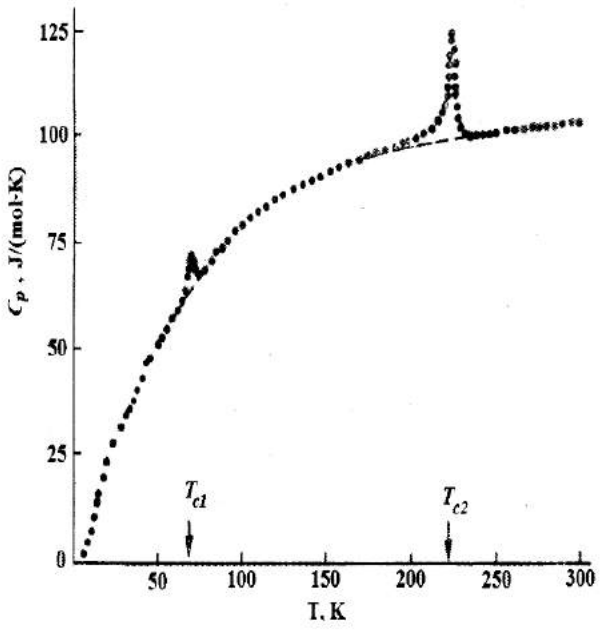

Fig.1 Dependence $C_P(T)$ for $TlFeTe_2$

Complete phase diagram of TlTe-FeTe system is studied [6]. It was established that liquids curve of TlTe-FeTe system consist of crystallization regions of Tl_2Te, $TlFeTe_2$ and FeTe compounds. Simple eutectics of $(TlTe)_{0.4}(FeTe)_{0.6}$ composition is formed between $TlFeTe_2$ and FeTe compounds. This eutectic is melted at 813K.

Temperature dependence of electrical conductivity and Hall coefficient of $TlFeTe_2$ are studied. Forbidden band width of $TlFeTe_2$ band is equal to 0.42 eV. It was shown that scattering of current carriers on acoustic vibrations of lattice taces place at high temperatures ($\mu \sim T^{-3/2}$). Temperature behavior of thermo- e.m.f. in $TlFeTe_2$ is studied. The concentration ($n_p=6.67\cdot10^{17}cm^{-3}$) and effective mass of hole ($m_p=0.074m_0$) are calculated for $TlFeTe_2$ [6].

This paper deals with $TlFeTe_2$ crystal thermal capacity on the base of precious calometric measurements. Thermal capacity has been investigated within 4.2-300K on adiabatic calorimetric installation used earlier in [7]. Relative error to determine thermal capacity at T>10K does not exceed 0.3% but at T<10K does not exceed ~2% of measured value. Polycrystalline samples of $TlFeTe_2$ have been synthesized by melting appropriate components in evacuated quartz ampoules [1].

In Fig.1 investigation results of $TlFeTe_2$ crystal thermal capacity have been given. As it is seen from Fig.1 dependence $C_p(T)$ shows two clearly defined anomalies being indicative of presence of phase transitions. Maximum values of anomalies are at T_{c1}=69.1±0.3; T_{c2}=220±0.2K. Within phase transitions there have been carried out 5 sets of measurements with temperature spacing from 2 up to 0.2K.

By extrapolation $C_p(T)$ (Fig.1, dotted line) within anomalous behavior regular C_{po} and anomalous ΔC_p parts of thermal capacity are separated where $\Delta C_p = C_p - C_{po}$ that allows the characteristics of $TlFeTe_2$ crystal phase transition to be determined and analyzed. Magnitude of anomaly at T_{c1} is 13% of its regular port, but in the vicinity of T_{c2} this magnitude is of the order of 17%.

Changes of energy (ΔQ) and entropy (ΔS) related to phase transition at T_{c2} have been determined by integrating cubic interpolation splines $C_p(T)$ and $\frac{\Delta CP(T)}{T}$ within 188-230K, respectively. Values of ΔQ and ΔS are given in Table. Small magnitude $\frac{\Delta S}{R} = 0.12$ indicates that given transition classifies among the transitions of shift type.

On temperature dependence of $TlFeTe_2$ thermal capacity there have been found out a number of

characteristic peculiarities: small jump at T_{c2} and anomaly nonsymmetric against transition temperature. Phase transition at T_{c2} can be treated as the transition of the second kind.

Within the point of transition at T_{c2} close to the critical point thermodynamic potential can be expanded by degrees of order parameter by the formula [8]:

$$\Phi = \Phi_0 + A\eta^2 + B\eta^4 + D\eta^6$$

Where $A=a(T-T_k)$. Here for phase transition of kind II $B>0$. temperature of transition T_{c2} and stability boundary T_k are identical in this case, i.e. $T_{c2}= T_k$ [8].

In lowsymmetric phase minimization of thermodynamic potential for excessive thermal capacity presents:

$$\Delta C_P = \frac{a^2 T}{2\sqrt{B^2 - 3AD}}. \qquad (1)$$

Transforming this formula one can show [9] that this magnitude $\left(\frac{\Delta C_P}{T}\right)^2$ below T_{c2} is the temperature function of kind:

$$\left(\frac{\Delta C_P}{T}\right)^2 = \frac{4B^2}{a^4} + \frac{12D}{a^3}(T_{C2} - T). \qquad (2)$$

In Fig.2 there has been presented dependence $\left(\frac{\Delta C_P}{T}\right)^{-2}$ on T for $TlFeTe_2$, it is linear within 219.7-221.6K. In the immediate vicinity of transition temperature (T_{c2}-T≤0.4K) the have been observed deviations $\left(\frac{\Delta C_P}{T}\right)^{-2}$ from linear dependence. This fact and excessive thermal capacity at $T> T_{c2}$ appear to be due to the presence of defects in samples [10]. From Fig.2 it is seen that linear temperature dependence $\left(\frac{\Delta C_P}{T}\right)^{-2}$ in carried out down to $T= T_{c2}$-0.4K that indicates the lach of distinct contribution of correlation effects to thermal capacity. From equality (2) we determine two relationships between coefficients of equation (1) which are presented in Table.

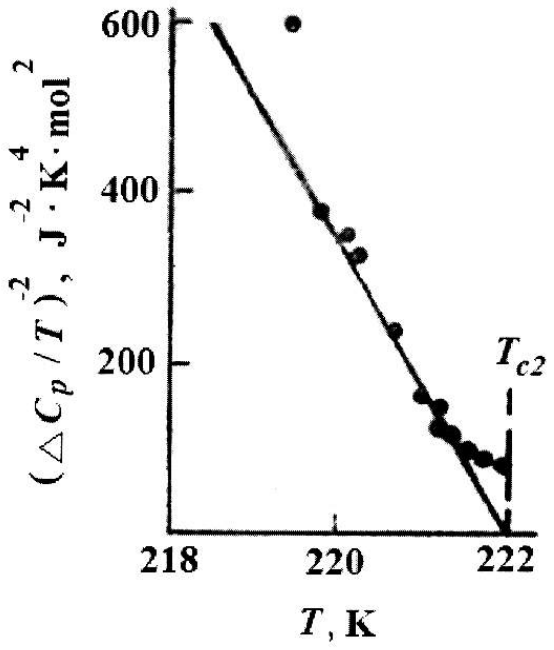

Fig.2. Temperature dependence $\left(\frac{\Delta C_P}{T}\right)^{-2}$ for $TlFeTe_2$

Small magnitude of thermal capacity anomaly related to phase transition at T_{c1} does not allow quantative analysis of excessive thermal capacity within Landau thermodynamic theory to be made as it has been made close to phase transition at T_{c2}.

ΔQ, $\frac{\text{J}}{\text{mol}}$	ΔS, $\frac{\text{J}}{\text{mol}\cdot\text{K}}$	$\frac{\Delta S}{R}$	$\frac{a^2}{B}$, $\frac{\text{J}}{\text{mol}\cdot\text{K}^2}$	$\frac{a^3}{D}$, $\frac{\text{J}^2}{\text{mol}^3\cdot\text{K}^3}$
230±10	1,03±0,01	0,12	0,781	0,071

This on the base of experimental data analysis on $TlFeTe_2$ thermal capacity one can make conclusions, such as follows:

1) to reveal phase transitions at T_{c1}=69.1K and T_{c2}=222.0K

2) small change of entropy is characteristic of them as transitions of shift type.

3) behaviour of anomalous thermal capacity close to of T_{c2} is adequately explained by Landau phase transition theory.

[1]. *G.I.Makovetskii, E.I.Kasinskii* Izv. USSR Akad. Of Sci., nonogranic materials., 1984. Vol.20., №10., pp.1752-1753.

[2]. *H.Sabrousky, M.Rosenberg, D.Welz, P.Deppe, W.Schofer* J.Magn. Magnetic Mater.1986. V. 54-57.p. 1497-1498.

[3]. *G.D.Sultanov, G.D.Guseynov, E.M.Kerimova*, Printed Matters of All-Union Conference on material science of chalcogenide and oxy -semiconductors. Chernovtsi, 1986, p.195.

[4]. *M.A.Aldjanov, N.G.Guseynov, Z.N.Mamedov* FNT., 1986, Vol.12., №11., pp.1224-1226.

[5]. *M.A.Aldjanov, N.G.Guseynov, Z.N.Mamedov M.T.Kasumov*, Dep in VINITI., 1987, №623-B87.

[6]. *E.M.Kerimova, F.M.Seidov, S.V.Mustafaeva, A.B.Magerramov, L.A. Ismailzade,* Investigation of TlTe-FeTe system and electric properties of $TlFeTe_2$ 2000. V.6, №1. P.47-49.

[7]. A.*M.Abdullayev, E.M.Kerimova, A.K.Zamanova* Thermal capacity and phase transitions in $TlInS_2$ and $TlInSe_2$ crystals. Nonorganic materials, 1994, Vol. 30., № 7. pp. 887-890.

[8]. *L.D.Landau, E.M. Lifshits* Theoretical physics T.V. Statistical physics. Part. I, M., Nauka., 1976., p.583.

[9]. *K.S.Alexandrov, I.N.Flerov* Field of thermodynamic theory application for structural phase transitions close to tricritical point. FTT, 1979., V.21, № 2,p.327-336/

[10]. *A.B.Voronel, S.R.Garber, V.M. Mamnitskii*. On quantative characteristics of thermal capacity in points of phase transitions of the second kind. JETF. 1986., Vol 55., № 6., p. 2017-2030.

p-TYPE $(Bi_{0.25}\ Sb_{0.75})_2\ Te_3$ THERMOELECTRIC ELEMENT FABRICATION AND CHARACTERIZATION

G. KAVEI [1],H. RASOULNEJAD [2] AND K. QAHRAMANOV [2]

1-Material and Energy Research Center (MERC), P. O. Box 14155-4777, Tehran, IRAN.

E-mail: g-kavei@merc.ac.ir or ghassem113@yahoo.com

2-Azerbaijan National Academy of Sciences (ANAS), Institute of Physics

33, H.Javid ave., Baku, Azerbaijan, Az-1143.

Bi_2Te_3 based solid solutions, are widely utilized as thermoelectric (TE) materials in Peltier modules, in order to attain higher figure of merit (Z) a fraction of weight at different percentage of Sb is added. The compound Bi-Te-Sb prepared by unidirectional solidification techniques such as melting accompanied with oscillating the melted compound followed by, crystallizing by zone growth method. This work is focused on, the preparation and characterization of the samples with formula Bi_2Te_3 and $(Bi_{0.25}Sb_{0.75})_2Te_3$. $(Bi_{0.25}\ Sb_{0.75})_2\ Te_3$ are known as p-type TE pellet, this compound has a higher Z compared with other solid solutions of the Sb-Bi, which have been tested as p-type pellet. The major aspects of TE such as electrical and thermal conductivities and Seebeck coefficient, which directly affect the figure of merit were measured. X-ray powder diffraction analysis of $(Bi_{0.25}\ Sb_{0.75})_2\ Te_3$ compared with Bi_2Te_3 suggests that the grown crystals are stoichiometric for $(Bi_{0.25}\ Sb_{0.75})_2\ Te_3$. It should also be noted that there is a strong relation between Z, balancing charge carriers and phonons of the compound, but they will not be discussed here. From experimental results $Z \approx 2.7 \times 10^{-3}\ K^{-1}$ was obtained, this is the same value which was reported in the previous work.

INTRODUCTION

Bismuth Telluride compounds are of great interest due to their high potential for technological applications. These compounds are widely used in many fields such as power supply and refrigeration due to their ability to produce significant temperature gradient with the application of current.

In this work, a novel crystal growth process was developed to fabricate Bi_2Te_3-based TE materials. It is possible to obtain a high figure of merit due to careful crystallization and annealing ingots. XRD spectra confirm this state. We have fabricated p-type $(Bi_{1-x}Sb_x)_2Te_3$ crystallized ingots, compared with Bi_2Te_3 XRD spectra and then measured their TE parameters, i.e. electrical conductivity σ, thermal conductivity κ and Seebeck coefficient α. We have defined the figure of merit from a formula, $Z = \frac{\alpha^2\sigma}{\kappa}$ which quoted in the enormous papers and texts.

EXPERIMENTAL

To fabricate p-type $(Bi_{1-x}Sb_x)_2Te_3$ compound with x = 0.75, the elements of Bi, Te and Sb were purified up to 5N purity. The powder mixtures were placed into a quartz tube, and the tube is evacuated below 10^{-5} Torr and the tube was heated to 250 ^oC for degassing from wall of the cylindrical furnace. Then the Nitrogen or Argon gas was admitted into the vacuum system to remove the reacting atmospheric gases such as hydrogen and oxygen. This procedure secured the undesired reactions of the gases with the elements not to be occurred, when the sintering was carried out. The evacuated tubes were at 10^{-4} Torr and sealed. The powder mixture was sintered at 700 ^oC to obtain a melt. The melt in the tube was stirred with 80 oscillations per minute at 700 ^oC, for one hour using a rocking furnace to make a homogeneous melt without segregation. The tube containing the melt was quenched at a 200 ^oC oil tank, and then cooled to room temperature. The solidified ingot was pulverized and filled in a quartz tube (□ 300 mm length and 8 mm diameter). The inside wall of the tube was carbon coated by acetone cracking to prevent adhesion of the compounds and Te diffusion deep into the tube wall. According to above-mentioned process, the tube was evacuated again to 10^{-4} Torr and sealed. The tube was placed in a vertical melting-zone system to crystallize the material at a speed of $13mm.h^{-1}$. The crystallized ingot in the tube was annealed at 300 ^oC for 24 h, then cooled down to room temperature for 5 h. The ingot was taken off the tube ready to characterize. In order to provide a good conductive surface, a solution of $HNO_3 : H_2O = 1:5$ was used in etching and cleaning of the ingot surface.

The microstructural properties of the sample were investigated by X-ray diffraction (XRD). The conventional X-ray diffractometer with a target of $Cu_{K\alpha}$ (λ=1.54056Å) have been employed for analyzing. The TE properties of the crystal were measured along the growth axis at room temperature. Specimens with dimensions 25 mm length and 8mm diameter were cut from the ingot for the measurements of electrical conductivity σ, Seebeck coefficient α, and thermal conductivity κ. To measure the Seebeck coefficient α, special configuration was designed [1]. The technique based on applying heat to one end of the specimen, measuring the temperature gradient by a Al-Ni and Al-Cr (Alumel – Chromel) thermocouples, and the potential gradient at a 10 mm define length of the sample. The Seebeck coefficient (α) of the ingot was determined from $\frac{\Delta V}{\Delta T}$.

The electrical conductivity σ was determined by applying current along the length of the sample. From the formula of $\sigma = \frac{Il}{VA}$ electrical conductivity can be calculated where I is the current, V potential different between two ends of length l on the sample, l is a defined length and A is the cross section of the sample. Repeated measurements were made rapidly with duration shorter than 1s to prevent errors due to the Peltier and Joule

effects. The thermal conductivity κ , was measured by same methods as [24].

Having these measurements the figure of merit (*Z*) at the room temperature was evaluated by the formula $Z = \frac{\alpha^2 \sigma}{\kappa}$.

RESULTS AND DISCUSSION

The preferred orientations of the grains in the crystals were studied by XRD analysis. Fig 1 shows the XRD patterns obtained from powder of the samples. The structure of $(Bi_2Te_3)_{0.25}(Sb_2Te_3)_{0.75}$ is just matched with the Bi_2Te_3 'Sb_2Te_3 and $Sb_{0.405}Te_{0.595}$. The bars (lower part of the XRD pattern in Fig. 1) are characteristic lines of planes for Bi_2Te_3, $Sb_{0.405}Te_{0.595}$, Sb_2Te_3 and Bi_2Te_3 structures respectively, and unit cells of the compounds. From data sheet of XRD system the intensity of (015), (1010),(110), (0015) and (0210) planes attributed to Bi_2Te_3, Sb_2Te_3 and, to the unstoiciometric solution of antimony telluride ($Sb_{0.405}$ $Te_{0.595}$ solid solutions). The compound is formed by substitution of Sb atoms by the Bi sites of the Bi_2Te_3 structure or vice versa. $Sb_{0.405}$ $Te_{0.595}$ solid solution results in anisotropy owing to unstoiciometric correspond to lack of enough Te in the compound. This is due to low vapor point of Te relative to Bi and Sb. The (006) plane is attributed to Bi_2Te_3 and Sb_2Te_3, and finally (0018) and (1019) planes are related to $Sb_{0.405}Te_{0.595}$ and Sb_2Te_3.

Table 1 summarizes data of the TE properties for the ingot. The measured values of the Seebeck coefficient α, thermal conductivity κ and electrical conductivity σ compared with those obtained by [2-4]. In the previous work [4] it was deduced that there may be errors on measurements. However, the XRD characterization was repeated and measurements was carried out with high precision but there were no deviation on the *Z* value. The relationship between the Seebeck coefficient α and the carrier concentration *n* at a given temperature can be expressed as follow:

Table1 Summarized TE properties of the $(Bi_{0.25}\ Sb_{0.75})_2\ Te_3$ ingot

Parameter	Present work	Ref.27	Ref 25	Ref 26
$\alpha(\mu VK^{-1})$	222	216.45	227	215.5
$\sigma(\times 10^3 \Omega.m)^{-1}$	1205	1488	512	621
$\kappa(W/Km)$	2.2	2.58	1.73	1.18
$Z(\times 10^{-3} K^{-1})$	2.7	2.7	1.53	2.44

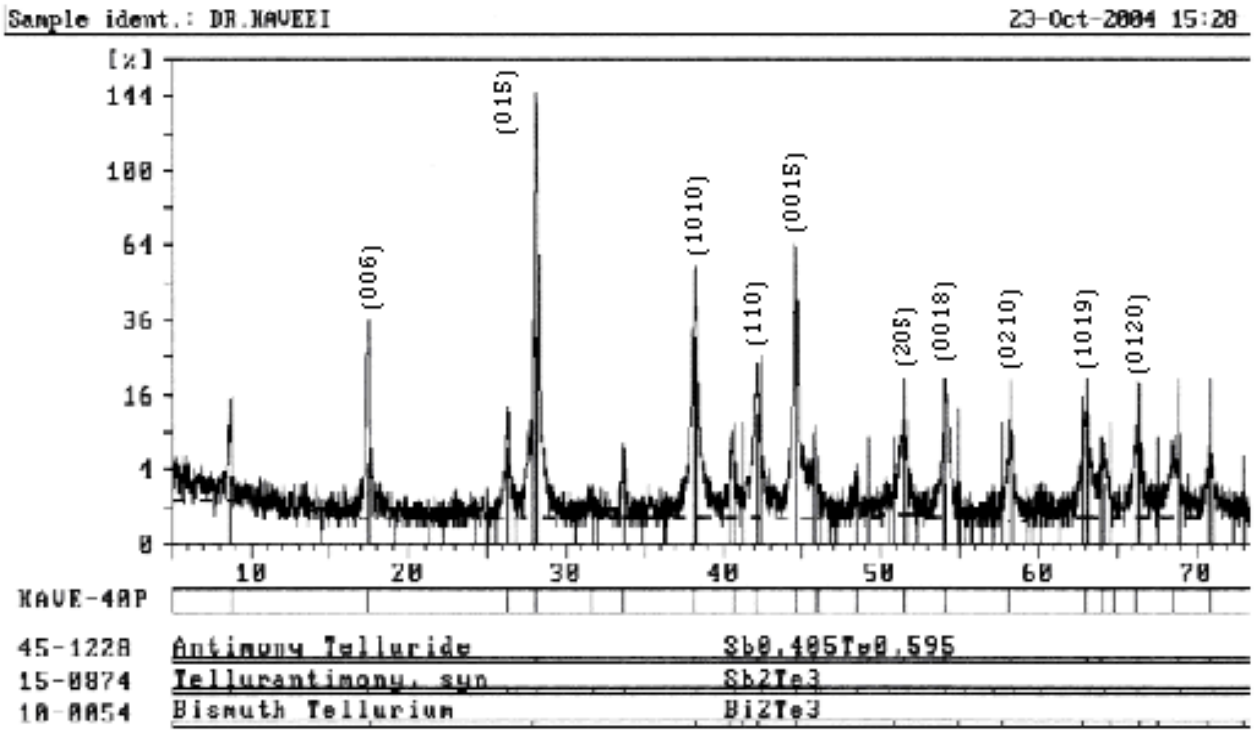

Fig. 1 XRD pattern obtained from powder of p-type $(Bi_{0.25}\ Sb_{0.75})_2\ Te_3$, the bars underneath show patterns of the $Sb_{0.405}Te_{0.595}$, Sb_2Te_3 and Bi_2Te_3 respectively.

CONCLUSION

p-type ($Bi_{0.25}$ $Sb_{0.75}$)$_2$ Te_3 compound was fabricated, and $Z = 2.7x10^{-3}K^{-1}$ has been obtained. The compound has a highest figure of merit compared with recent works. Nevertheless, fractions of Bi and Sb have been examined, The ($Bi_{0.25}$ $Sb_{0.75}$)$_2$ Te_3 has highest figure of merit among them. The discrepancies of the measured values of this work and the previous wok are attributed to the measurements on different position on the ingot. There are reports that the stoichiometry of the compound changes along the ingot if along the ingot the zone melting method is employed for crystallization.

[1]. *R.Taylor*, CRC hand book of thermoelectric Ed. M. D.Rowe., 1995, (CRC Press Boca Raton FL), 165.

[2]. *H. Scherrer and S.Scherrer*, CRC hand book of thermoelectric Ed. Rowe. M. D., 1995 , (CRC Press Boca Raton FL),211.

[3]. *J.Seo and K. Park*, Mater. Res. Bull, 35, 2000, 835.

[4]. *G.Kavei and A.A.Khashachi*, Journal of thermoelectricity, No. 3, 2005, 40-45.

RADIO AND X-RAY EMISSION FROM SUPERNOVA REMNANTS

ASVAROV A.I.[1], NOVRUZOVA H. I.[2], AHMEDOVA S.I.[3]

Institute of Physics of the National Academy of Sciences of Azerbaijan, Baku, Azerbaijan,

asvarov@physics.ab.az, astro@physics.ab.az

In this paper we study the statistical correlation between radio and X-ray emissions from shell-type supernova remnants (SNR). The primary aim of this study is to test the model of radio emission of shell-type SNRs presented by one of the authors. Based on this model of radio emission, by using the Monte Carlo techniques we have simulated statistical relations radio – X-ray luminosities (not surface brightnesses) which then were compared with the observations. X-ray emission is assumed to be thermal. To have a uniform statistical material we used observational data on the SNRs in Magellanic Clouds.

1. INTRODUCTION

Radio emission is the most characteristic property of SNRs, and the specific form of a spectrum $S_\nu \propto \nu^{-\alpha}$ (S_ν - flux density at frequency ν, α is the spectral index of the radio emission) of this radiation is considered as one of methods of identification of SNRs among other morphologically similar structures in space. Last version of the catalogue of galactic SNRs contains 274 objects [1]). It is well established the synchrotron nature of radio emission from SNRs, i.e. the relativistic electrons moving in magnetic fields are responsible for their radio emission. The problem of origin of relativistic electrons and the magnetic fields in the shells of SNRs remains not completely resolved. This problem is tightly connected with the general problem of understanding the physics of SNRs. After the radio the X-ray observations are very important chanel of receiving an information about SNRs. More than half of known SNRs detected in X-rays. Although the mechanisms of emissions in radio and X-rays are different but both of them originate in the shock wave vicinity and depend on the same set of interstellar medium (ISM) and shock parameters. The study of relation between X-ray and radio emissions can be very useful tool for understanding the evolution of SNRs.

The paper is organized as follows: first we analyze the model of radio emission that will be used in this study; in the following paragraph we derive the formulae for the thermal bremsstrahlung emission from the adiabatic SNR describing by the Sedov solution [2]. In Chapter 4 we describe the model and analyze the observational data used in this work. The results and short discussion are presented in the last paragraph.

2. RADIO EMISSION OF SNR

Synchrotron radio emission is one of the main properties of SNRs. Almost all the known SNRs are the sources of synchrotron radio emission. Naturally, much richer observational information on the SNRs is available in the radio range that can be used for explaining the origin of high energy electrons and magnetic fields responsible for the synchrotron emission. DSA mechanism is the most suitable mechanism for explaining the origin of radio-emitting electrons. But in the theory of DSA some principal aspects remain unclear. Modeling of the SNR radio evolution by using the most reliable and common theoretical results of DSA and comparison with observational data can be used for resolving mentioned questions. The model of radio emission of shell-type SNRs using test-particle DSA has been developed in the recent paper of the author [3]. The model is based on the assumptions that electrons are injected into the mechanism directly from the high energy tail of the downstream Maxwellian distribution function, and the magnetic field is the compressed at the shock typical interstellar field.

The model predicts that the radio surface brightness (Σ_R) evolves with diameter as D

$$\Sigma_R \propto n^{2/3} B^{3/2} E_{SN}^{1/2} D^{-(0.3-0.4)} \qquad D < D_b,$$
$$\Sigma_R \propto D^{-(5-6)} \qquad D > D_b \quad (1)$$

The critical diameter D_b corresponds to diameter of the remnant when the shock Mach number becomes $M \le 10$ if evolution occurs without onset of a radiative phase, otherwise D_b is the diameter of the remnant at the moment of onset of a radiative phase. In the first case transition from one branch of a curve to another has smooth character, in the second case - rather sharp

Our model easily explains both very large diameter radio sources such as the Galactic Loops and the candidates for Hypernova radio remnants and the small size radio sources as the remnant of Nova Persei 1901. The model predicts no radio emission from the radiative SNRs and the existence of radio quiet but relatively active SNRs is possible. In our model we used the formulae for radio emissivity presented in [3] without any change.

3. X-RAY EMISSION OF SNRs

X-ray emission in SNR is generally considered to be thermal although X-ray observations of some SNR like SN1006 [4] and several other young SNRs show the spectra are dominated by synchrotron emission. Taking into account the fact that the role of young SNRs in the statistics of SNRs is negligible in the following we will ignore the possible contribution of synchrotron X-ray emission of shell-type SNR.

The volume bremsstrahlung X-ray emissivity of plasma with temperature T is [5]

$$\varepsilon_X = \frac{8}{3}\sqrt{\frac{2\pi}{3}}\frac{e^6}{(m_e c^2)^{3/2}}\frac{n_i\, n_e Z_i^2}{\sqrt{T}}\exp\left(-\frac{E_X}{T}\right) g_{ff}$$
$$(\text{erg cm}^{-3}\,\text{s}^{-1}\text{sr}^{-1}\,\text{Hz}^{-1}), \qquad (2)$$

where n_i, Z_i are the density and mean charge of ions respectively, n_e is the concentration of electrons, $E_X = h\nu_X$ is the energy of X-ray photons, T is the temperature of electrons in units of energy, g_{ff} is Gaunt

factor, the weakly dependent on T function (at $E_X \sim T_e$ and 100 eV< T_e< 10 keV g_{ff} changes in 0.8<g_{ff}<1.2), the remaining parameters has commonly accepted meaning.

X-ray telescopes count photons in certain energy ranges $\Delta E_X = E_{X2} - E_{X1}$. Let us define integral x-ray emissivity as

$$\varepsilon_X(\Delta E_x, R) = \int_{E_{X1}}^{E_{X2}} 4\pi\, \varepsilon_X(E_X, R)\, dE_X \quad (\text{erg s}^{-1}\ \text{cm}^{-3})$$

For our study it is convenient to use the range of energies between E_{X2} =10 keV and E_{X1}=2 keV. This is because in this range the importance of line emission and interstellar absorption are not so important. In addition, observational data from several X-ray telescopes are in this or near range of energies. At lower energies of x-ray photons the interpretation of observations complicated both by strong line emission and interstellar absorption.

For spherical symmetry SNR the X-ray luminosity can be obtained by integrating the emissivity over the volume

$$L_X = 4\pi \int_0^{R_s} \varepsilon_X(\Delta E_X, R)\, R^2\, dR \quad \left(\frac{\text{erg}}{\text{s}}\right),$$

Since we are considering adiabatic SNR in the uniform ISM the Sedov solution we gives us all the parameters necessary for evolution of this integral. Self similar solution allows us to find the values of temperature and density inside the remnant if their values are determined at the boundary of the shock front. From the shock boundary conditions for the case of a strong shock wave the concentration and temperature of plasma directly behind the front of a shock wave are expressed as

$$n_s = n_0 \frac{\gamma+1}{\gamma-1} \qquad (=4n_0) \quad \text{for } \gamma=5/3 \tag{3}$$

$$T_s = \frac{2(\gamma-1)}{(\gamma+1)^2}\mu V_s^2 \quad \left(=\frac{3}{16}\mu V_s^2 \ \text{ for } \gamma=\frac{5}{3}\right) \tag{4}$$

where n_0 - the concentration of particles in the ISM, γ - the specific heats ratio, which equals 5/3 for a monatomic gas, V_s is the speed of the shock wave, μ is the mean mass per particle. Since we are using the self-similar solution of Sedov, it is convenient to express the radial dependence of emissivity in terms of self-similar variable $r = R(t)/R_s(t)$. To do this the radial distribution of density and temperature is expressed as

$$n = n_s \cdot x(r)$$

$$T = \frac{P_s}{n_s}\cdot\frac{y(r)}{x(r)} = T_s \cdot \frac{y(r)}{x(r)}$$

where P_s is the gas pressure directly behind the shock front, which by using (3) and (4) can be written as

$$P_s = \frac{2}{\gamma+1}\mu n_0 V_s^2 \quad \left(=\frac{3}{4}\mu n_0 V_s^2 \ \text{ for } \gamma=\frac{5}{3}\right) \tag{5}$$

Dimensionless concentration and pressure of matter inside the SNR can be found from the exact Sedov solution, which is presented in parametric form (see [2]), but there is a high quality approximate solutions, which greatly simplifies the calculations (e.g. [6]). The boundary conditions are $x(r=1)=y(r=1)=1$. Taking into consideration the last relations after some transformation the expression for the X-ray luminosity of the SNR with a radius R_{pc} (expressed in parsecs) takes the form

$$L_X(\Delta E_x) = 1.793\times10^{33} Z_i^2 n_s^2 \sqrt{T_s}\, R_{pc}^3 \times \int_{r_{in}}^{1} dr\, r^2 x(r)^2 \sqrt{y(r)/x(r)}\ e^{-E_{x1}/T_{keV}} (1 - e^{-(E_{x2}-E_{x1})/T_{keV}}) \tag{6}$$

where E_X ,T are measured in keV. In this expression r_{in} - is the inner radius of SNR, from which self-similar treatment holds. This means that we ignore the X-ray emission from the inner part of the remnant occupied by the ejecta. This assumption is not acceptable for young SNRs, in which reverse shock wave has a significant contribution.

4. OBSERVATION

It is important to note that in this study we are going to use the most uniform and pure observational information. This concerns the X-ray observations. X-ray observations are carried out with the help of the orbital telescopes the lifetime of which is limited and the characteristics of instruments changes during their active life. To convert the count rate to an energy flux and then to luminosity we need additional information both about the changing instrument and observing object and have to chose the model assumptions. When one observes an individual object these problems easily can be taken into account, but when we deal with statistics the problem is complicated due to the fact every object usually was observed during different periods of observations of given instrument or with the help of another telescope with other characteristics. Taking into account this we tried to use observational material as uniform as it possible. We use most raw information, namely, count rates from the X-ray sources. As we will show in the following the use of surface brightness instead of count rates result in additional non-physical dependences due to D^{-2} (or θ^2, θ-angular size of the object) factor. The information given in the paper [7] satisfies our requirements. In figure 1 the correlation between X-ray and radio luminosities are presented. As we can see there is week correlation between them. The trend line in the figure reflects the dependence between X-ray and radio fluxes as $F_R \propto F_X^{0.44}$ the correlation coefficient is 0.3. The correlation as we can see is not so tight as concluded by Berkhuijsen (1986) [8]: $\Sigma_R \propto \Sigma_X^{0.92}$ with r=0.71.

5. THE MODEL

Both X-ray and radio luminosity of SNR depends on the same parameters which can be divided into three groups: parameters characterizing the SN itself (the ejecta mass Mej, the initial kinetic energy of the ejecta E_{SN}, the rms velocity of the ejecta v_0), parameters concerning the ISM (the total pressure P_0, the density of plasma n_{e0}, the magnetic field strength B_0) and free parameters of the model of acceleration. We generate SNRs with constant birthrate. For each remnant all the necessary parameters are chosen randomly from some range different for different parameters. The masses of ejecta are from the range of [0.5-5] masses of the Sun, the energies of explosion belong to the values from 5 10^{50}erg

to 5 10^{51} erg, for the dencity of the ISM we use the tree-phase model of the ISM developed by McKee and Ostriker [9]. The expansion law of the SNR is taken as Sedov law, $R_s \sim t^{2/5}$ [11].

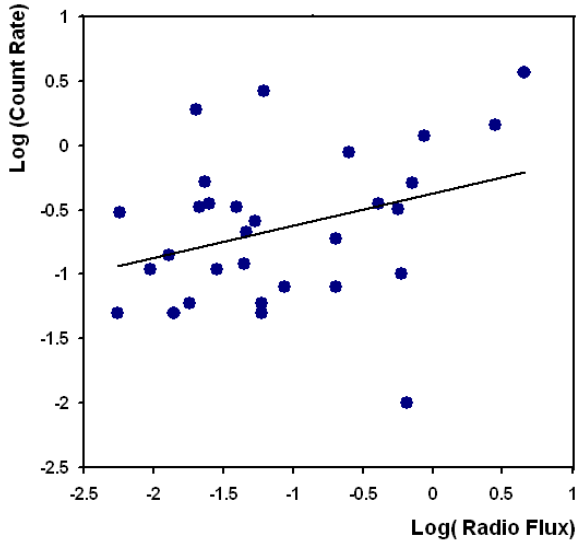

Fig.1. The relation between the ROSAT X-ray count rate and the spectral fluxies at 1.4 GHz for SNR in LMC. The count rates from SNRs in LMC are from [7], radio fluxies are from the work [10] .

The role of different parameters is different. Our model is very useful to check the role of any of the input parameters. To apply our model to the real SNRs, we first have to specify additional new parameters concerning the SNR itself (the ejecta mass *M*ej, the initial kinetic energy of the ejecta E_{SN}, the rms velocity of the ejecta v_0), and the ISM (the total pressure P_0, the density of plasma n_{e0}, the magnetic field strength B_0 The beginning of the model is parameterized by the initial radius R_0 and Mach number M_0 of the shock wave at which the Sedov phase begins. We ignore the ejecta stage because the possible contribution of this part of the remnant to the total emission with time will rapidly decrease. In the following we assume a fully ionized gas with a ratio of specific heats $\gamma = 5/3$ and with a helium abundance relative to hydrogen as $n_{He} = 0.1\ n_H$. The interstellar magnetic field plays very important role in our model. The pressure of the magnetic fields is taken to be proportional to the pressure of the thermal gas.

We have generated SNRs with initial parameters every

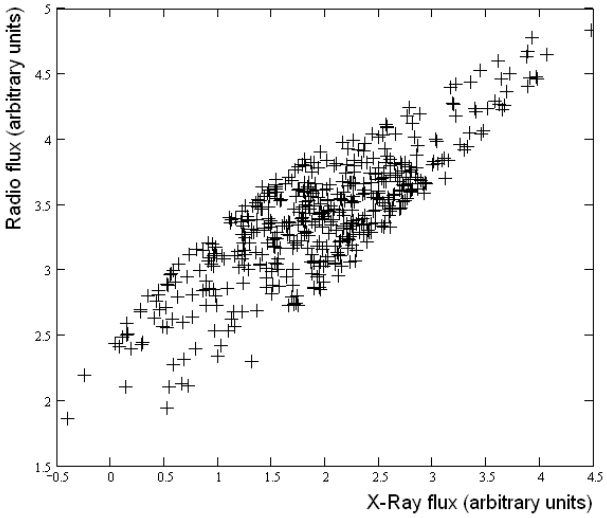

Fig. 2. Monte-Carlo modeled relation between radio and X-ray fluxes. The correlation coefficient r=0.82

In Fig 2 the result of one run is presented as an example. The trend line is for $F_R \propto F_X^{0.49}$ as in the case of observational one though the correlation in model case much tight than in observations.

[1]. *D.A.Green*, 2009, `A Catalogue of Galactic Supernova Remnants (2009 March version)', Astrophysics Group, Cavendish Laboratory, Cambridge, United Kingdom (available at "http://www.mrao.cam.ac.uk/surveys/snrs/").

[2]. *L Sedov*,. 1972, Similarity and Dimensional Methods in Mechanics , M., Nauka

[3]. *A.I. Asvarov* A&A 2006, v. 459, p.519.

[4]. *K.Koyama, R.Petre, E.Gotthelf, et al.,* Nature, 1995, 378, 255

[5]. *V.L.Ginzburg* 1981, Theoretical Physics and astrophysics, M; Nauka, 504 p.

[6]. *D.P.Cox, P.R. Anderson* ApJ, 1982, v 253, p. 268

[7]. *R. M.Williams, Y.-H.Chu, J. R.Dickel, R.Petre, R. C.Smith, M.Tavarez*, 1999, ApJS, 123, 467

[8]. *E.M. Berkhuijsen* A&A 1986, v.166, p. 257.

[9]. *C. F.McKee, J. P. Ostriker* ApJ, 1977, v.218, p.148

[10]. *C. Badenes, Dan Maoz, B.T. Draine* ArXive e-print 1003.3030v1, 2010

[11]. *A.I.Asvarov, H.I. Novruzova* Azerb.Astron J., 2007, v.2, p.42

COPPER-RELATED DEEP ACCEPTOR IN QUENCHED Ge-Si <Cu,Al> CRYSTALS

G.Kh. AZHDAROV[A], Z.M. ZEINALOV[B], Z.A. AGHAMALIYEV[A], Z.M. ZAKHRABEKOVA[A], S.M. BAGIROVA[A]

[a] *Institute of Physics, H Javid ave. 33, Baku, 370143 Azerbaijan*

[b] *Ganja State University, Shakh Ismayil Khatayi 187 ave., Gandja, Azerbaijan.*

email: zangi@physics.ab.az

It is shown by Hall measurements that quenching complexly doped $Ge_{1-x}Si_x$ <Cu, Al> ($0 \le x \le 0{,}20$) crystals from 1050-1080 K leads to the formation of additional electroactive acceptor centers in them. The activation energy of these centers increases linearly with an increase in the silicon content in the crystal and is described by the relation $E_k^x = (52 + 320x)$ meV. Annealing these crystals at 550–570 K removes the additional acceptor levels. It is established that the most likely model for the additional electroactive centers is a pair composed of substituent copper and aluminum atoms (Cu_sAl_s) or interstitial copper and substituent aluminum atoms (Cu_iAl_s). It is shown that the generation of additional deep acceptor levels must be taken into account when using the method of precise doping of $Ge_{1-x}Si_x$ <Al> crystals with copper.

The decay of supersaturated solutions of electroactive impurity in doped semiconductors is used as an effective method for controlling the electronic properties of materials. Copper in both germanium and silicon and in their solid solutions forms multiplet deep impurity centers and significantly affects the electric properties of these semiconductors in a wide temperature range. The three acceptor levels that are observed in these materials are assigned to copper substituents [1]. In germanium these energy levels are E_v+40 meV, E_v+330 meV, and E_c-260 meV. Copper is a rapidly diffusing impurity in Ge, Si, and Ge-Si; therefore, the decay of its supersaturated solution in these crystals under thermal treatment is successfully used to control the impurity concentration in the matrix. However, the tendency of rapidly diffusing deep impurities to the formation of compounds and complexes with different lattice defects under thermal treatment [2-7] may lead to the generation of additional electroactive centers which significantly affect the electric properties of the matrix. Undoubtedly, determining the forming conditions of such centers and their parameters is an important when obtaining materials with specified properties.

It was shown in [5] that the thermal treatment of Ge <Cu> at 970 K with subsequent quenching leads to the formation of an additional deep acceptor level E_v+80 meV. The concentration of this level correlates with that of the substituent copper impurity (Cu_s) in the crystal. This level was assigned in [5] to a complex containing Cu_s atoms. Thereafter, the same complex was found in $Ge_{1-x}Si_x$ <Cu> crystals ($0<x<0{,}15$) subjected to heat treatment at 970-990 K [2]. In [2,5], the most likely model for additional deep acceptors was considered to be a pair composed of Cu_s and a mobile defect, which can be either a vacancy or a copper (Cu_i), carbon, or oxygen interstitial. The effect of thermal treatment at temperatures above 1070 K on the spectrum of impurity states and electric properties of $Ge_{1-x}Si_x$ <Cu,Sb> crystals was studied in [3,4]. No additional level corresponding to the acceptor level E_v+80 meV in germanium with copper impurity was observed in the $Ge_{1-x}Si_x$ <Cu, Sb> samples under study.

In recent years, considerable progress has been made in the growth and controlled doping of Ge-Si crystals with typical shallow impurities (Al, Ga, In, As, Sb) by conservative and nonconservative methods [8-16]. For this reason, one can perform more detailed studies aimed at analyzing the interaction of impurities in complexly doped crystals of Ge-Si solid solutions, which give rise to various electroactive centers.

In this study we used Hall measurements to analyze the effect of thermal treatment in the range 1050-1150 K on the spectrum of impurity states in complexly doped $Ge_{1-x}Si_x$<Cu,Al,Sb> crystals ($0 \le x \le 0{,}20$). The purpose of this study was to determine the possibility and conditions for forming electroactive complexes in Ge and Ge-Si crystals, which were doped with a typical shallow acceptor impurity (aluminum) and rapidly diffusing copper impurity with the formation of complexes.

Ge and Ge-Si crystals with a Si content up to 20 at%, doped simultaneously with aluminum and antimony, were grown by the upgraded Bridgman method using a Ge seed and a feeding silicon ingot (the latter was applied to obtain solid solutions)[8]. Note that antimony was used as an auxiliary shallow donor impurity to control the degree of compensation of acceptor states of the impurities under study [17]. This is necessary for the Hall detection of the additional levels arising in the band gap. The optimal process parameters necessary for obtaining the specified level and ratio of impurity concentrations in the crystals grown were determined by mathematical modeling the impurity distribution in the ingot based on the relations derived in [8,15]. Samples shaped like rectangular parallelepipeds were prepared from disks ~1,5 mm thick; the latter were cut from crystals in the direction parallel to the crystallization front. The macrocomposition of each disk (the content of germanium and silicon atoms) was determined from their specific weight [9]. This technique is rather precise for the Ge-Si system in view of the large difference in the specific weights of Ge and Si (5,33 and 2,33 g/cm^3, respectively). Depending on the concentration ratios of the aluminum and antimony impurities, the samples had either electron or hole conductivity. The samples were subjected to a corresponding treatment and surface cleaning [18] and then doped with copper by the diffusion method at the temperature of maximum solubility of this impurity in crystals of specified composition [4]. After determining the temperature dependence of the Hall coefficient in a range of 65-350 K, the samples were subjected to thermal treatment at 1050-1150 K. The sam-

ples were kept at each temperature for 4 h. The equilibrium state was established for this time interval [2]. Quenching was performed by throwing samples into ethyl alcohol at dry ice's sublimation temperature. The energy positions of the impurity states and their concentrations in thermally processed crystals were derived from the Hall measurements. Note that the advantage of this method is the possibility of fairly exactly determining the concentration and activation energy of impurity levels [5] (except for the closely located ones). The free carrier concentration in the samples was calculated from the temperature dependence of the Hall coefficient using the Hall factors of electrons and holes in Ge and Ge-Si [19].

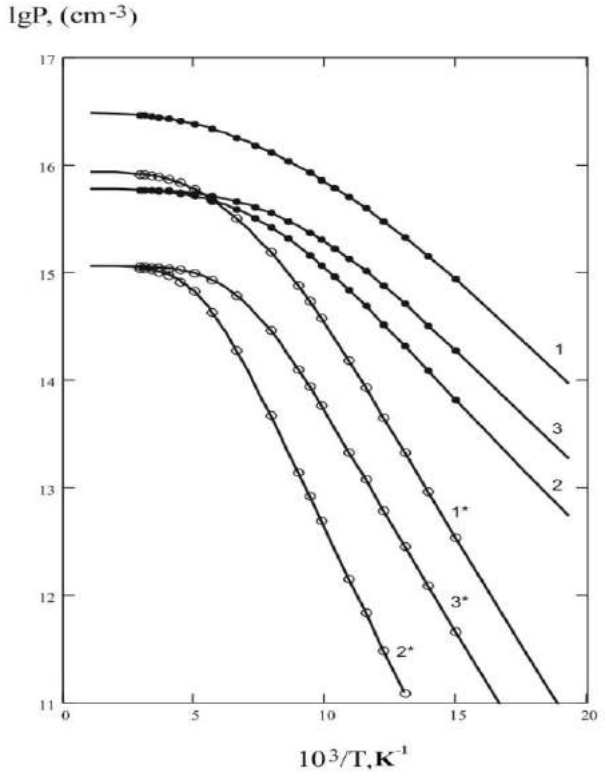

Fig. 1. Temperature dependences of the free-hole concentration for the (1-3) Ge<Cu, Al, Sb> and (1*-3*) $Ge_{0,88}Si_{0,12}$ <Cu, Al, Sb> samples: (1,1*) after doping samples with copper at 1145 and 1170 K, respectively; (2,2*) after heat treatments at 1050 and 1070 K, respectively; and (3,3*) after annealing at 550 K for 20 h. The solid lines are the theoretical results that are in the best agreement with the experimental data; curves 1, 1*, 3, and 3* were calculated taking into account the effect of the partially compensated first Cu_s level: $E_{Cu1}=E_v+40$ meV in Ge and $E_{Cu1}=E_v+72$ meV in $Ge_{0,88}Si_{0,12}$ [18]; curves 2 and 2* were obtained taking into account two active levels: the first Cu_s acceptor level and the additional acceptor center with $E_k=E_v+52$ meV in Ge and $E_k=E_v+91$ meV in $Ge_{0,88}Si_{0,12}$.

Complex-alloyed Ge and Ge-Si samples with aluminum (N_{Al}) and antimony (N_{Sb}) impurity concentrations on the order of 10^{15}-10^{16} cm^{-3} have an electron (at $N_{Sb}>N_{Al}$) or hole (at $N_{Sb}<N_{Al}$) conductivity. After doping samples with copper at 1150-1175 K, the temperature behavior of the free carrier concentration in the samples exhibits corresponding acceptor states of Cu_s [4], depending on the N_{Al} and N_{Sb} values. The temperature dependences of the free electron or hole concentration in these samples are theoretically described well in terms of the equation of electric neutrality using the data of [18] on the activation energy of the corresponding Cu_s levels. The thermal treatment of these crystals in the range of 1050-1150 K showed additional deep acceptor levels (located above the first Cu_s level) to form in the Ge <Cu,Al,Sb> and $Ge_{1-x}Si_x$<Cu,Al,Sb> samples quenched from 1050-1080 K. These levels manifest themselves in crystals with N_{Al} on the order of 10^{16} cm^{-3}, in which the acceptor level of aluminum impurity is significantly or completely compensated. As an example, the figure 1 shows the temperature dependences of the hole concentration p for two such samples: Ge <Cu,Al,Sb> and $Ge_{0,88}Si_{0,12}$ <Cu,Al,Sb>. Before doping with copper, these samples had an electronic conductivity, which was caused by the antimony impurity with an effective concentration $N^*_{Sb}=N_{Sb}-N_{Al}$ of $6{,}5\times10^{15}$ cm^{-3} and $2{,}1\times10^{15}$ cm^{-3} in Ge and $Ge_{0,88}Si_{0,12}$, respectively. Note that the total concentration of the Al and Sb impurities in the samples is on the order of 10^{16} cm^{-3}.

The experimental data in the figure, which correspond to the dependences p(T) after doping samples with copper (curves 1,1*), are quite adequately described within the theory [17] taking into account the activation of the first acceptor copper level (which is partially compensated by the electrons of antimony impurity with a concentration N^*_{Sb}). As can be seen in the figure, a thermal treatment of the Ge <Cu,Al,Sb> and $Ge_{0,88}Si_{0,12}$ <Cu,Al, Sb> samples at 1050 and 1070 K, respectively, increases the slope of the dependence p(T) at low temperatures (curves 2,2*). Such behavior indicates the formation of an additional acceptor level, which is located above the first Cu_s level. To establish the nature of this additional level, we performed experiments on sample annealing, which was performed, as in [2,5], at 550–570 K. The results showed that the additional acceptors decompose at these temperatures and completely disappear during annealing for 20 h. Curves 3 and 3* in the figure are the dependences p(T) in the samples under study after such an annealing. It is noteworthy that the slope of the curve p(T) at low temperatures decrease after the annealing. It can be seen that the behavior of curves 3 and 3* for both samples in the entire temperature range is described fairly well within the theory taking into account the effect of the partially compensated first Cu_s acceptor level with a concentration equal to the copper solubility at the annealing temperature of the sample. Here, as for curves 1 and 1*, the effective concentration of compensating antimony atoms coincides with the initial value of N^*_{Sb} before the doping of samples with copper.

An analysis of the experimental data for the samples with different initial impurity contents showed that the most likely candidates for the additional levels are Cu_sAl_s or Cu_iAl_s pairs. According to the data in the literature [20], the equilibrium concentration of copper interstitials Cu_i in silicon and germanium at different temperatures is of the same order of magnitude as that of site atoms Cu_s. The formation of Cu_sAl_s or Cu_iAl_s acceptor pairs in complexly doped Ge and Ge-Si crystals subjected to heat treatment in the range of 1050-1080 K can be considered as follows. The excess copper concentration, in comparison with the equilibrium one, passes from the lattice to

interstitial sites at the annealing temperature: $Cu_s \rightarrow Cu_i + V$ (V is a vacancy). The copper atoms located in sinks (which are electrically passive) pass from them to interstitial sites: Cu sinks $\rightarrow$ Cu_i. At temperatures of 1050-1080 K, the Al_s substituents located in lattice sites are negatively charged, whereas copper interstitials are positively charged [21]. Mobile positively charged copper atoms migrate through the matrix to interact with negatively charged Al_s, atoms and form $Cu_i + Al_s \rightarrow Cu_iAl_s$ or $Cu_i + (Al_s + V) = Cu_sAl_s$ pairs, which have acceptor properties. The vacancies and remaining Cu_i atoms pass to sinks during quenching: Cu_i, $V \rightarrow$ sinks. The formation of Cu_s-Al_s pairs is confirmed by their fairly high stability up to 1080 K. The pairs formed by impurity atoms occupying lattice sites are known to be more stable than the pairs formed by interstitials and impurity substituents [22]. However, there are also data on the stability of pairs formed by impurity interstitials and atoms in lattice sites in Ge and Ge-Si [2,5].

To determine the activation energy and concentration of additional deep acceptor complexes, curves 2 and 2* in the figure were interpreted within the two level system according to the equation [17]

$$p + N_{Sb}^{**} = \frac{N_{Cu}}{1 + \dfrac{p\gamma_{Cu1}}{N_V \exp(-E_{Cu1}/kT)}} + \frac{N_K}{1 + \dfrac{p\gamma_k}{N_V \exp(-E_K/kT)}} \quad (1)$$

Here, N_v is the effective mass of the density of states in the valence band of the crystal; N_{Cu} and N_k are the concentrations of Cu_s atoms and additional acceptor centers, respectively; E_{Cu1} and E_k are the activation energies of the first copper level and additional acceptors; γ_{Cu1} and γ_K are the degeneracy factors of the first copper level and additional acceptor level; and N_{Sb}^{**} is the effective concentration of compensating antimony atoms in the presence of additional acceptor centers.

The desired parameters E_k and N_k were calculated by fitting the theoretical curves to the experimental data using the least-squares method. In Eq.(1) the degeneracy factor of both acceptor levels was assumed to be 4 [5]. The N_v and E_{Cu1} values were taken from the data in the literature [18]. The Cu_s concentration was derived from curve 3. The solid curves 2 and 2* in the figure correspond to the theoretical curves calculated using the following parameters of the impurities and additional deep acceptor centers: $E_k = E_v + 52$ meV, $E_{Cu1} = E_v + 40$ meV, $N_k = 4{,}20 \times 10^{15}$ cm^{-3}, $N_{Cu} = 1{,}25 \times 10^{16}$ cm^{-3}, $N_{Sb}^{**} = 1{,}07 \times 10^{16}$ cm^{-3} for curve 2 and $E_k = E_v + 91$ meV, $E_{Cu1} = E_v + 72$ meV, $N_k = 3{,}70 \times 10^{15}$ cm^{-3}, $N_{Cu} = 3{,}5 \times 10^{15}$ cm^{-3}, $N_{Sb}^{**} = 5{,}80 \times 10^{15}$ cm^{-3} for curve 2*.

The additional deep acceptor centers are formed in all compositions of $Ge_{1-x}Si_x$ crystals ($0 \le x \le 0{,}20$) studied here. The analysis of the activation energy of these centers in the crystals shows a linear increase in E_k with an increase in the silicon content in the matrix, which is described by the relation:

$$E_k^x = (E_k^0 + 320 \cdot x)\text{meV} = (52 + 320 \cdot x)\text{meV} \quad (2)$$

Note that the increase in the acceptor complex activation energy with increasing silicon content in the $Ge_{1-x}Si_x$ matrix is in agreement with the concepts of the virtual crystal model for solid solutions of binary systems, because the energy of all impurity levels in silicon exceeds that in germanium.

Quenching complexly doped $Ge_{1-x}Si_x$ <Cu,Al,Sb> ($0 \le x \le 0{,}20$) crystals from 1050-1080K leads to the formation of additional acceptor levels in them, which are located above the first impurity Cu_s level. The activation energy of these levels increases linearly with an increase in the silicon content in the crystal. The annealing of the samples at 550-570 K leads to the disappearance of the additional acceptor levels. The most likely model for the additional electroactive centers is Cu_sAl_s or Cu_iAl_s pairs. When using precise doping of $Ge_{1-x}Si_x$ <Al> crystals with copper, it is necessary to take into account the formation of additional deep acceptor levels.

[1]. *A.G. Milnes*, Deep Impurities in Semiconductors (Wiley, New York, 1973; Mir, Moscow, 1977).

[2]. *P.G. Azhdarov*, Neorg. Mater. 36 (5), 526 (2000).

[3]. *I.N. Belokurova, V.D. Degtyarev, and E.D. Skudnova*, Izv. Akad. Nauk SSSR, Neorg. Mater. 22 (1), 145 (1986).

[4]. *G.Kh. Azhdarov, R.Z. Kyazimzade, and V.V. Mir-Bagirov*, Fiz. Tekh. Poluprovodn. 26 (2), 553 (1992) [Sov. Fiz. Semicond. 26 (2), 314 (1992)].

[5]. *Y. Kamiura, F. Hoshimoto, T. Nobusada, and S. Yoneyama*, J. Appl. Phys. 56 (4), 936 (1984).

[6]. *E.V. Skudnova, V.F. Degtyarev, and V.K. Prokofyeva*, Izv. Akad. Nauk SSSR, Neorg. Mater. 24 (2), 198 (1988).

[7]. *A.A. Gvelesiani, V.F. Degtyarev, and E.V. Skudnova*, Izv. Akad. Nauk SSSR, Neorg. Mater. 23 (3), 368 (2007).

[8]. *Z.M. Zakhrabekova, Z.M. Zeinalov, V.K. Kyazimova, and G.Kh. Azhdarov*, Izv. Akad. Nauk SSSR, Neorg. Mater. 43 (1), 5 (2007).

[9]. *G.Kh. Azhdarov, T.Kucukomeroglu, A. Varilci, et al.*, J. Cryst. Growth 226 (4), 437 (2001).

[10]. *Yonenaga*, J. Cryst. Growth 226 (1), 47 (2001).

[11]. *N.V. Abrosimov, S.N. Rossolenko, W. Thieme, et al.*, J. Cryst. Growth 174 (1–4), 182 (1997).

[12]. *C. Marin and A.G. Ostrogorsky*, J. Cryst. Growth 211 (1–4), 378 (2000).

[13]. *A. Barz, P. Dold, U. Kerat, et al.*, J. Vac. Sci. Technol. B, Microelectron. Nanometer Struct. 16 (3), 1627 (1998).
[14]. *K. Nakajima, S. Kodama, S. Miyashita, et al.*, J. Cryst. Growth 205 (3), 270 (1999).
[15]. *G.Kh. Azhdarov, Z.M. Zeinalov, and L.A. Guseinli*, Kristallografiya 54 (1), 137 (2009) [Crystallogr. Rep. 54 (1), 152 (2009)].
[16]. *V.K. Kyazimova, Z.M. Zeynalov, Z.M. Zakhrabekova, and G.Kh. Azhdarov*, Crystallogr. Rep. 51 (Suppl. 1), 192 (2006).
[17]. *J.S. Blakemore*, Semiconductor Statistics, (Macmillian, New York, 1962; Mir, Moscow, 1964).
[18]. *G. Azhdarov, R. Kyazimzade, and M. Hostut*, Solid State Commun. 111, 675 (1999).
[19]. *R.Z. Kyazimzade*, Doctoral Dissertation in Physics and Mathematics (Baku State Univ., Baku, 1998).
[20]. *R.N. Hall and J. H. Racette*, J. Appl. Phys. 33 (2), 379 (1964).
[21]. *Y. Kamiura and F. Hashimoto*, Jpn. J. Appl. Phys. 28 (5), 753 (1989).
[22]. *V.I. Fistul and A.G. Yakovenko*, Doping of Semiconductors (Metallurgiya, Moscow, 1982) [in Russian].

RESEARCH OF SURFACE OF $Pb_{1-X}Mn_XTe$ (Se) EPITAXIAL FILMS IN CORRELATION WITH ELECTROPHYSICAL PROPERTIES

I.R.NURIYEV, R.M.SADIGOV, M.B.HAJIYEV

Institute of Physics named after academician H.M.Abdullayev NAS of Azerbaijan, AZ1143, Baku, 33, H.Javid ave.

e-mail: h.nuriyev@gmail.com

In the present work are investigated the structure and surface morphology of $Pb_{1-x}Mn_xTe$ (Se) epitaxial films in correlation with electrophysical properties. Films are obtained by a molecular beam condensation method, on the newly splited sides of BaF_2. Correlation is established between morphology of a surface and electrophysical parameters of films. It is shown that formation of black clusters on a surface of investigated films is characteristic, according to others chalkogenids A^4B^6.

During last twenty years semimagnetic solid solutions of lead chalkogenids in which atoms of lead are partially replaced with atoms of a transitive element-manganese with uncompensated magnetic moment became a subject of intensive experimental and theoretical researches [1-5]. As a result of introduction of manganese ions in a lattice of lead chalkogenids compound, for example in PbTe and by the formation of solid solution $Pb_{1-x}Mn_xTe$ the lattice parameter insignificant decreases, but width of the forbidden zone strongly increases, and also in a magnetic field the energy spectrum of charge carriers unusually changes. So it is possible to manage properties of structures on their basis with the help of magnetic fields and temperatures.

These researches basically were carried out on massive monocrystals of above mentioned chalkogenids. But for practical applications their epitaxial films possess big prospect.

For creation of various devices of IR technics, multielement matrixes on the basis of films of these semiconductors and their successful application in modern optoelectronics are required films with stabile properties. For this the establishment of growth laws and development of technology of obtaining of structurally-perfect epitaxial films with given structural, electrophysical and photoelectrical parameters are necessary.

In works [6-12] are investigated obtainment features of structurally-perfect, photosensitive epitaxial films $Pb_{1-x}Mn_xTe$(Se) on various substrates.

It is known that morphology of surfaces of crystals plays the important role at manufacturing of various devices their basis. Devices with high parameters are created on homogeneously pure, structurally-perfect, mirror smooth surfaces of crystals [13]. Because of that research of structure and surface morphology represents scientifically-practical interest.

In the present work the structure and surface morphology epitaxial films of solid solutions $Pb_{1-x}Mn_xTe$ (Se) ($x=0.02\div0.03$) obtained by a molecular beam condensation method on the newly splited sides of BaF_2, in correlation with electrophysical properties are investigated.

It is known that properties of epitaxial films are in many cases defined by the substrate parameters. In particular the maximal possible coincidence of lattice parameters and factors of thermal expansion of a substrate and an increased film is desirable. Small distinction in parameters of lattices leads to occurrence of high density of dislocations in a film. By selection of corresponding compositions of materials of a substrate and a film it is possible to obtain the accordant pair having isoperiodic structure. From this point of view for obtaining of structurally perfect $Pb_{1-x}Mn_xTe$ (Se) films suitable for creation devices on their basis, substrates from materials $A^{IV}B^{VI}$ are more convenient and perspective. These substrates are widely applied to creation of lasers and photo diodes on heterostructures from $A^{IV}B^{VI}$ materials.

Substrates from monocrystals of BaF_2 are dielectric, the main advantage is the possibility of realization of an electrical isolation of separate functional elements at creation multi-element structures, and there are satisfactory correlations between their above-stated parameters with an increased film.

Structure and surface morphology are investigated with the three-crystal X-ray spectrometer TRS according to two-crystal dispersion-free scheme (n, -n) [14], electronograph (EMR-100) and raster electron microscope (09IOE-100-005). Structural perfect films are obtained at $T_{sub}=673\div683$ K substrate temperatures and $\upsilon_c=8\div9$ Å/s condensation rates. Rate of the condensation was given by the temperature of the main source $Pb_{1-x}Mn_xTe$ (Se).

Obtained epitaxial films have perfect face centered cubic crystallic structure (Fig.1a).

It is shown that on the surface of these films are observed the black clusters, formed owing to capture of oxygen with excessive atoms of metal in the process of growth and leading to reception of films with small values of mobility of carriers of charge ($\mu_{77K}=(0.5\div0.8)\cdot10^4$ $sm^2/V\cdot s$) (Fig.1b). Application of additional compensating Te and Se vapor sources in the process of growth, had been eliminated observable black clusters, films with homogeneously pure surface and high value of mobility of carriers of a charge ($\mu_{77K}=(2\div3)\cdot10^4$ $sm^2/V\cdot s$) (Fig.1c) are received.

Similar pictures are also obtained at research epitaxial films $Pb_{1-x}Mn_xTe$.

So it is shown that formation of black clusters on a surface, in accordance with other chalkogenids A^4B^6 is characteristic for $Pb_{1-x}Mn_xTe$ (Se) epitaxial films and purity of a surface plays the important role in obtaining of films with high electrophysical parameters.

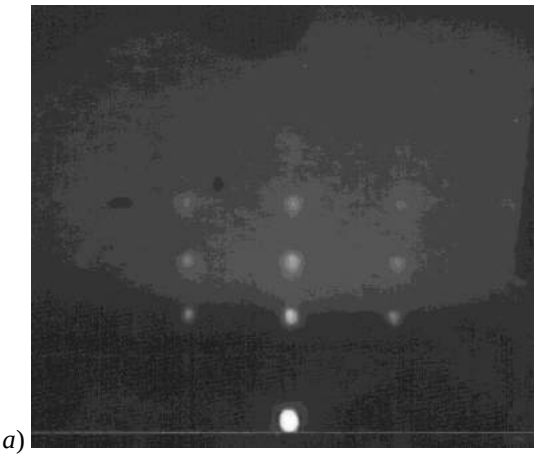

a)

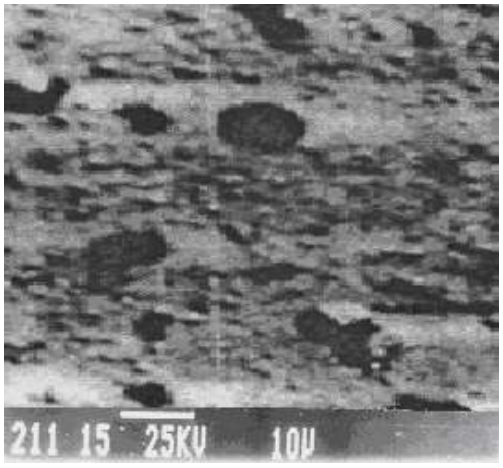

b)

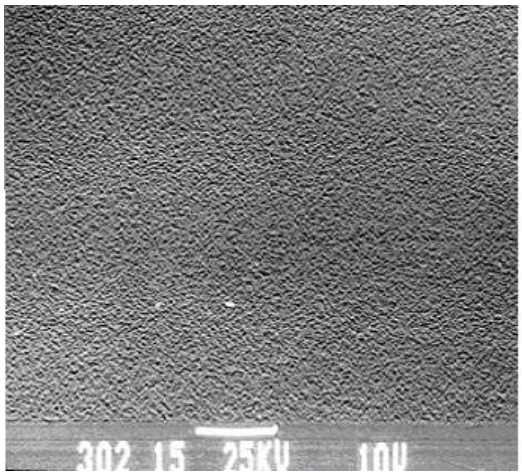

c)

Fig.1. Electronogram (a) and electronomicroscopic pictures (b,c) of $Pb_{1-x}Mn_xSe$ (x=0.02) epitaxial films: b) without additional Se vapor source, c) with additional Se vapor source.

Similar pictures are also obtained at research of $Pb_{1-x}Mn_xTe$ epitaxial films. Films $Pb_{1-x}Mn_xSe$ (x=0.02) grow by a plane (111) and there electronogram is displayed on the basis of a cubic lattice with a=6.11 Å. Dependence of crystal perfection of $Pb_{1-x}Mn_xSe$ (x=0.02) epitaxial films from the temperature of substrates was investigated by the X-ray diffraction method. On Fig.2 is shown the dependence of semiwidth of X-ray diffraction swinging curves ($W_{½}$) from the temperature of substrate BaF_2 at condensation rates υ_c=8÷9 Å/s. Apparently from the figure, with the increase of the substrate temperature the semiwidth of X-ray diffraction swinging curves decreases and at T_{sub}=673÷683 K gets the minimum value $W_{½}=100''$ (Fig.3). This result is also confirmed with the electron microscopic researches. On electron microscopic picture the smooth surface without secondary inclusions (Fig.1c) is observed. At the further increase of the substrate temperature increase of $W_{½}$ is observed.

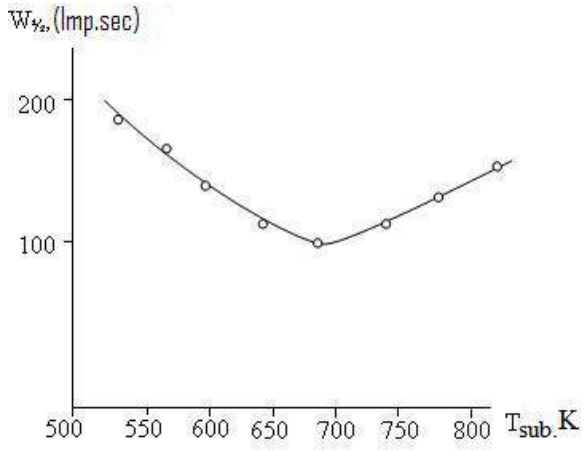

Fig.2. Dependence of swing curve of X-ray diffraction from temperature of substrate of $Pb_{1-x}Mn_xSe$ (x=0.02) epitaxial films.

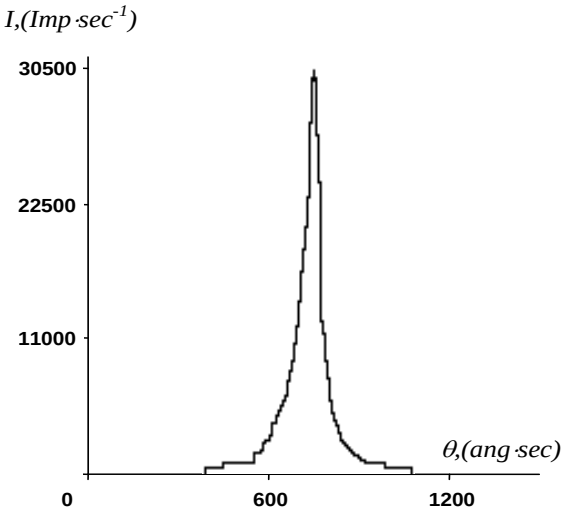

Fig.3. Swing curve of X-ray diffraction of $Pb_{1-x}Mn_xSe$ (x=0.02) epitaxial films.

Thus by the regulation of the temperatures of basic and additional compensating sources is succeeded obtainment of structurally perfect high-resistance epitaxial films $Pb_{1-x}Mn_xTe$ (Se) with n-, p-type conductivity having concentration $(n,p)_{77K}=5\cdot10^{15}\div2\cdot10^{16}$ см$^{-3}$ and mobility $\mu_{n,p}(77K)=(2\div3)\cdot10^4$ sm^2/V·s of charge carriers. Values of mobility of charge carriers also testify the high crystal perfection of the obtained films.

Research of electrophysical properties of films shows that mobility of charge carriers also depends on substrate temperature (T_{sub}) and condensation rate (υ_c). At T_{sub}=683 K substrate temperature value of mobility and concentration are accordingly equal $\mu_{n,p}(77K)=(2\div3)\cdot10^4$ cm^2/V·s, $(n,p)_{77K}=(0.8\div1)\cdot10^{17}$ cm^{-3}.

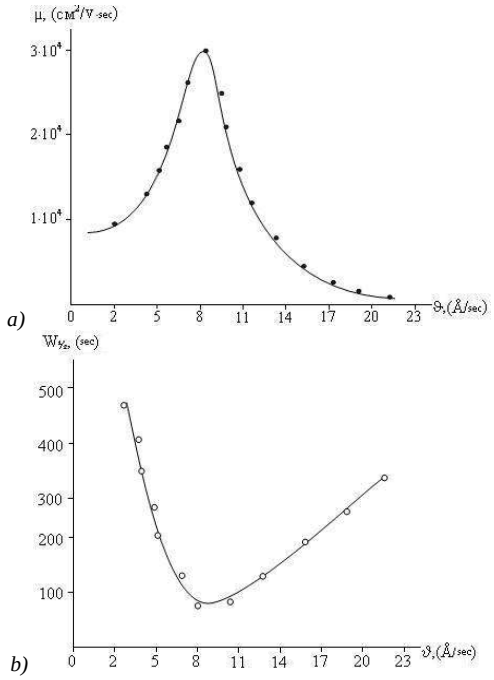

Fig.4. Dependence of mobility of charge carriers (a) and crystal perfection (b) from condensation rate $Pb_{1-x}Mn_xSe$ (x=0.02) epitaxial films.

It is shown that crystal perfection and mobility of charge carriers of $Pb_{1-x}Mn_xSe$ (x=0.02) epitaxial films obtained with application of an additional compensating Se vapor source in the growth process, strongly depends on the condensation rate (Fig.4a,b). Apparently from presented figures the semiwidth values of X-ray diffraction swinging curves, characterising structural perfection of growing films (the minimum value of semiwidth corresponds to the maximum crystal perfection) (Fig.4a) and mobility of charge carriers (Fig.4b) with increase of condensation rate at first grow, and then passing through a maximum decrease. The best results are obtained in epitaxial films growing at condensation rate υ_c=8÷9 Å/s.

These films have perfect crystal structure with cubic face centered lattice in parameter a=6.11 Å, corresponding initial structures of investigated solid solutions.

It is established that formation of black clusters on a surface, in accordance with other chalkogenids A^4B^6 is characteristic for epitaxial films $Pb_{1-x}Mn_xTe$ (Se) and purity of a surface plays the important role in obtaining of films with high electrophysical parameters.

[1]. *D.G.Andrianov, N.M.Pavlov, A.S.Savelev, etc.* // Fiz. Tekh. Poluprovodn., 1980, v.14, #6, pp.1202-1212.

[2]. *I.I.Zasavitskiy, L.N.Kovalchik, B.N.Matsonashvili, etc.* // Fiz. Tekh. Poluprovodn., 1988, v.22, #12, pp.2118-2123.

[3]. *V.G.Guk, E.V Osipova., T.I.Papushina* // Inorganic materials, 1992, v.28, #2, pp.340-343.

[4]. *V.T.Trofimov, G.Z.Abbasov, Q. Sprinholts, Q.Bauer, etc*. // Fiz. Tekh. Poluprovodn., 1993, v.27, #7, pp.1158-1164.

[5]. *E.I.Rogacheva, A.S.Sologubenko, I.M. Krivulkin* // Inorganic materials, 1998, v.34, #6, pp.669-674.

[6]. *I.R.Nuriyev, S.S.Farzaliyev, R.M.Sadigov* // Poverrhnost, 2004, #2, pp.110-112.

[7]. *I.R.Nuriyev, S.S.Farzaliyev, H.D.Djalilova, R.M.Sadigov* // Priklad. Fiz., 2004, #4, pp.89-92.

[8]. *I.R.Nuriyev, M.B.Hajiyev, R.M.Sadigov, A.M. Nazarov* // Priklad. Fiz., 2007, #2, pp.132-135.

[9]. *I.R.Nuriyev, M.B.Hajiyev, R.M. Sadigov* // Fizika, 2007, #4, pp.121-123.

[10]. *I.R.Nuriyev, R.M Sadigov, A.M. Nazarov* // Crystallography, 2008, #2, pp.329-331.

[11]. *I.R.Nuriyev, E.Y.Salayev, M.B.Hajiyev, H.D.Djalilova, R.M.Sadigov, A.M.Nazarov, B.S. Barhalov* // Priklad. Fiz., 2009, #2, pp.127-129.

[12]. *I.R.Nuriyev, M.B.Hajiyev, R.M. Sadigov* // Crystallography, 2009, v.54, #2, pp.356-358.

[13]. *A.M.Afanasyev, P.A.Aleksandrov, R.M. Imamov* // X-ray difractometry diagnostic of submicronic layers. Moscow, Nauka 1989, 151 pp.

[14]. *Z.G. Pipsker* X-ray crystallooptics Moscow, Nauka, 1982, 390 pp.

STRUCTURE, MORPHOLOGY OF THE SURFACE AND ELECTROPHYSICAL PROPERTIES OF EPITAXIAL FILMS OF $PbS_{1-x}Te_x$ AND $PbSe_{1-x}Te_x$

I.R.NURIYEV, S.S.FARZALIYEV

Institute of Physics named after academician H.M.Abdullayev NAS of Azerbaijan, AZ1143, Baku, 33, H.Javid ave.

e-mail: h.nuriyev@gmail.com

The structure and surface morphology of epitaxial films of $PbS_{1-x}Te_x$, $PbSe_{1-x}Te_x$ are investigated in correlation with electrophysical properties. Films are obtained by method of condensation of molecular beam on the newly splited sides of BaF_2. Isoperiodicity of crystal lattices, affinity of values of factors of thermal expansion of a substrate and the grown up films, have given the chance to obtain films with perfect crystal structure. Correlation between morphology of a surface and electrophysical parameters of films is established. It is shown that formation of black congestions on a surface of films according to others chalkogenides A^4B^6, are characteristic for solid solutions $PbS_{1-x}Te_x$, $PbSe_{1-x}Te_x$.

Lead chalkogenids compound and their solid solutions take the important place in the infra-red technics. On the basis of these semiconductors are made various optoelectronics devices and are used in the field of a spectrum 3÷5 mkm [1]. Are developed a number of methods for obtaining structurally-perfect homogeneous epitaxial films of these materials with given thickness, composition and concentration of charge carriers [2].

In works [3-7] films of PbS (Se, Te) are obtained and investigated. In these works as substrates basically are used NaCl, KCl, $LiNbO_3$ and mica. The received films do not possess perfect structure and high values of electophysical parameters that apparently, is related with discrepancy of parameters of crystal lattices of substrates and grown up epitaxial films. Works [8-9] are devoted to research of growth features, structure, photoelectric and optical properties of $PbS_{1-x}Te_x$, $PbSe_{1-x}Te_x$ epitaxial films.

It is known that devices are created on a surface of crystals [10]. Because of that the structure and surface morphology plays the important role in obtaining optoelectronics devices meeting modern requirements.

In the present work the structure and surface morphology of $PbS_{1-x}Te_x$ (x=0.5) epitaxial films, $PbSe_{1-x}Te_x$ (x=0.2) grown up on newly splited sides of BaF_2 (111), in correlation with electrophysical properties are investigated.

As the substrates are chosen monocrystals of BaF_2, because of their optical transparency in a spectral range 3÷12 mkm, good mechanical durability and chemical inertness [11]. This material is dielectric, has CaF_2 type of cubic structure with lattice parameter a=6.19 Å. The coefficient of thermal expansion (CTE) of BaF_2 is close to CTE of $PbS_{0.5}Te_{0.5}$, $PbSe_{0.8}Te_{0.2}$ (a_{BaF_2} =1.8·10^{-5} K^{-1}, $a_{PbS_{1-x}Te_x}$ =2.3·10^{-6} K^{-1}, $a_{PbSe_{1-x}Te_x}$ =2.1·10^{-5} K^{-1} at 300 K).

Epitaxial films with thickness 0.5÷1 mkm are obtainned by the molecular beam condensation method, on standard vacuum unite UVN-71P-3. As a source earlier synthesized solid solutions with a corresponding chemical composition have been used. Isoperiodicity of crystal lattices of a substrate and the grown up films ($a_{BaF_2} = a_{PbSe_{1-x}Te_x} = a_{PbSe_{1-x}Te_x}$ =6.19 Å) and close values of CTE has given the chance to obtain films with perfect crystal structure. Considering partial decomposition of investigated materials in the evaporation process, by the regulation of the condensation rate and application of an additional compensating Te source it was possible to obtain epitaxial films with demanded chemical composition, type of conductivity and perfect structure.

Structural perfectness of films are investigated by the electronograph (EMR-100) and X-ray diffraction method. The surface morphology was investigated by the electron microscope method. Optimum obtainment conditions of structural perfect epitaxial films of the investigated solid solutions are established. It is established that at 675÷680 K substrate temperatures and $\upsilon_к$=8÷9 Å/s condensation rates on the newly splited sides of BaF_2 by a plane (111) grows epitaxial films of $PbS_{1-x}Te_x$ (x=0.5) and $PbSe_{1-x}Te_x$ (x=0.2) repeating substrate orientation. Electron-diffraction pattern (a) and X-ray diffraction swinging curves (b) of epitaxial films of $PbSe_{1-x}Te_x$ (x=0.2) are presented on Fig.1.

The epitaxial films obtained under the above-stated conditions, have perfect crystal structure with cubic face centered lattice, in the parametre corresponding to initial structures of investigated solid solutions. Electron-diffraction pattern and X-ray diffraction swinging curves from these films testify that (Fig.1.a,b). From the calculations of these pictures were defined parameters of a lattice *a* and corresponding structure of the investigated solid solutions. Certain value of parameter of a lattice of solid solutions $PbSe_{1-x}Te_x$ (x=0.2) equal a=6.19 Å practically did not differ from initial which was set by a proportion of components in initial mixture. The semiwidth of X-ray diffraction swinging curves, equal $W_{½}$=100$''$ (Fig.1.b) testifies to high crystal perfection of the obtained films.

However on electron microscopic pictures taken from the surface of these films, are observed microinclusions in the form of black clusters which quantity increase with reduction of condensation rate and increase of substrate temperature (Fig.2a).

According to the literary data [12, 13] these clusters are the oxides, formed owing to capture of oxygen with excessive atoms of metal (Pb) in the growth process. With application of an additional vapor source of Te in the growth process it was possible to obtain films with a pure

smooth surface free from black clusters (Fig.2b).

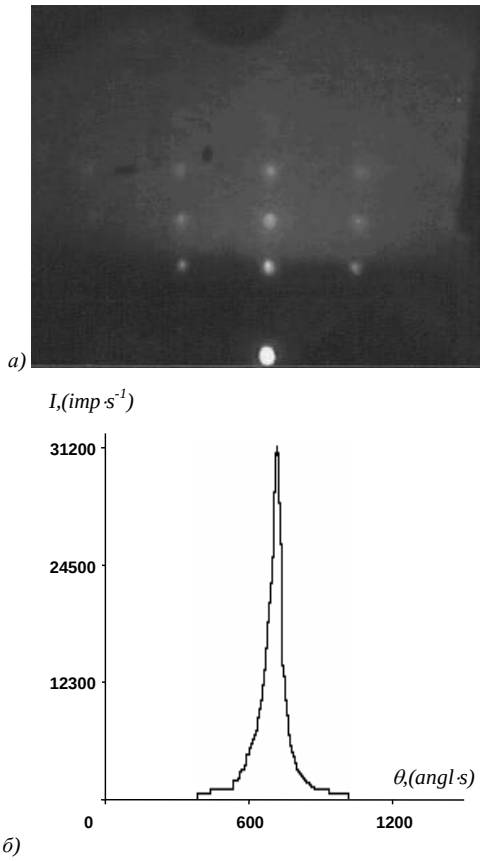

Fig.1. Electron-diffraction pattern (a) and swing curve of X-ray diffraction (b) of $PbSe_{1-x}Te_x$ (x=0.2) epitaxial films.

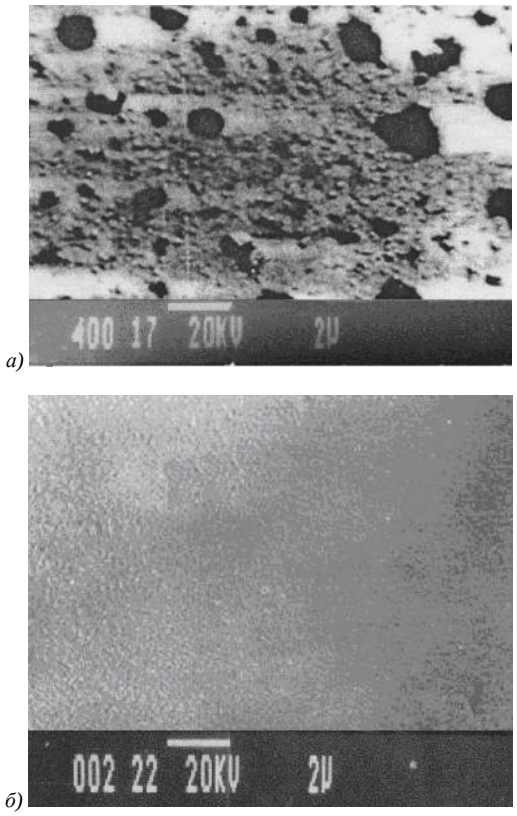

Fig.2. Electron microscopic picture of $PbSe_{1-x}Te_x$ (x=0.2) epitaxial films a) without additional compensation source vapor of Te;b) with additional compensation source vapor of Te.

Use of such a source resulted with disappearance of black stains, (Fig.2.b) and improvement of structure and increase of mobility of charge carriers in the obtained films. Dependence of concentration of charge carriers of epitaxial films $PbSe_{1-x}Te_x$ (x=0.2) from temperature of an additional compensating Te vapor source is presented on Fig.3.

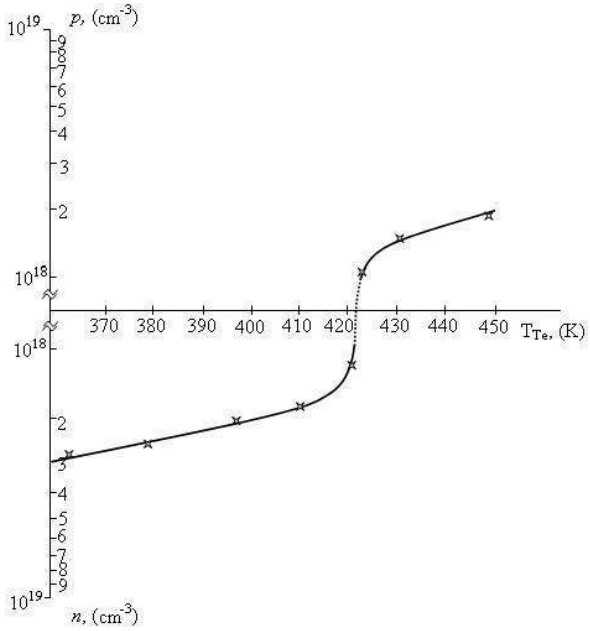

Fig.3. Dependence of concentration of charge carriers from temperature of an additional compensating Te vapor source in $PbSe_{1-x}Te_x$ (x=0.2) epitaxial films.

Apparently from the figure, during the growth of epitaxial films the temperature of an additional compensating Te vapor source varies in the interval 370÷460 K. With the rise of temperature of an additional compensating Te vapor source to 430 K black clusters completely disappear and the obtained films possess a mirror smooth surface (Fig.1.b). The further rise of temperature of an additional Te vapor source above 420 K leads to inversion of type of conductivity; n-type conductivity is replaced with p-type (Fig.3). This fact is explained with the filling of empty seats with Te atoms, which during growth play an acceptor role in semiconductors A^4B^6. In the obtained films concentration of charge carriers makes $(n,\ p_{77K})=(5\cdot10^{16}\div1\cdot10^{17})$ sm^{-3}. Thus, without breaking vacuum, in a uniform work cycle, have been obtained $PbSe_{1-x}Te_x$ (x=0.2) epitaxial films having n-, p-type conductivity, with high crystal perfection. The obtained films with the above-stated parametres give great opportunities for creation of high-sensitivity photodetectors for the infra-red technics on their basis.

The similar picture is also observed on a surface of epitaxial films $PbS_{1-x}Te_x$ (x=0.5).

Research of electrophysical properties has shown that value of mobility of charge carriers of epitaxial films obtained without application and with application of an additional vapor source of Te differs. It was clear that

mobility of charge carriers of epitaxial films obtained without application of additional vapor source of Te has rather small value (μ_{77K}~$(0.5\div1)\cdot10^4$ $sm^2/V\cdot s$), than the mobility of charge carriers of epitaxial films obtained with the application of an additional vapor source of Te (μ_{77K}~$(1.8\div2)\cdot10^4$ $sm^2/V\cdot s$).

Thus, purity of a surface plays the important role in obtaining of $PbSe_{1-x}Te_x$ (x=0.2) epitaxial films with high electrophysical parameters. Apparently black clusters being an additional source of dispersion in the investigated films lead to reduction of mobility of charge carriers.

It is possible to consider established that formation of black clusters according to other A^4B^6 chalkogenids are characteristic for epitaxial films of solid solutions of $PbSe_{1-x}Te_x$ and $PbS_{1-x}Te_x$.

---

[1]. *Sizov F.F.* // Foreign electronics. 1977, v.24, pp.3-48.

[2]. *Matveenko A.V., Medvedev Y.V., Berchenko N.N.* // Foreign electronics, 1982, #11, pp.54-115.

[3]. *Egerton R., Juhazs C.* // Brit.J.Appl.Phys., 1967, v.18, # 7, pp.1009-1001.

[4]. *Poh K.J., Anderson J.C.* // J.Thin Solid Films, 1969, v.3, pp.139-156.

[5]. *Nuriyev I.R., Nabiyev R.N.* // DAN Az.SSR, 1986, v.42, #8, pp.19-23.

[6]. *Nuriyev I.R., Salayev E.Yu., Sharifova A.K.* // Surface, 1987, v.2, pp.123-129.

[7]. *Semiletov S.A., Suleymanov N.A., Nuriyev I.R.* // Crystallography, 1980, v.25, iss.4, pp.876-877.

[8]. *Nuriyev I.R., Farzaliyev S.S., Nazarov A.M.* // News of NAN of Azerbaijan, Baku, 2002, v.XXII, #2, pp.43-45.

[9]. *Nuriyev I.R., Aliyev A.A., Gasanov I.S. and etc.* // Physics, v.XIII, #4, Baku, 2007, pp.118-120.

[10]. *Afanasyev A.M., Aleksandrov P.A., Imamov R.M.* // X-ray difractometry diagnostic of submicronic layers. Moscow, Nauka 1989, 151 pp.

[11]. V*oronkova E.M., Grechushnikov B.N., Distler G.I. and etc.* // Moscow, Nauka 1965, 335 pp.

[12]. *Egerton R.F. and Juhasz C.* Brit.J.Appl.Phys., 1967, v.18, #7, pp.1009-1011.

[13]. *Parker E.K., Williams D.* Thin Solid Films. 1976, v.35, #3, pp.373-395.

THE STRUCTURE OF THE POLYMER COMPOSITES POLYMERIC PHASE - PIEZOELECTRIC CERAMICS AND ITS IMPACT ON THE CHARGE STATE PHASE BOUNDARY

S.N. MUSAEVA, U.V. YUSIFOVA, M.A. KURBANOV, A.F. NURIEV, G.KH. KULIEV, F.F. YAKHYAEV, E.A. KERIMOV, G.G. ALIYEV

Institute of Physics, Azerbaijan National Academy of Sciences

Javid av. 33, AZ-1143, Baku, Azerbaijan

e-mail: mkurbanov@physics.ab.az

Using different methods of studying the structure of polymers is shown that the dispersion of piezoceramic particles is accompanied by amorphization of the polymer phase composites. Increasing the degree of amorphization of the structure of the composites leads to an increase in the charge stabilized at the interface in the process of electro-thermopolarization.

INTRODUCTION

Numerous studies have shown that the main reason for the formation of the electro, piezo-, pyroelectric effects in polymer – segnetopiezoceramic following are the electron–ion and polarization processes:

- accumulation in the process of polarization charges at the interface of polymer–piezoelectric particle [1–3];
- orientation domains piezoelectric phase in the field of boundary charges;
- the emergence of local mechanical fields arising from the orientation of domains and enhances their de-orientation.

Apparently, these effects are directly related to the injection process electro-thermo-polarization charges and their stabilization at the phase boundary. This, in turn, determined by chemical and physical structure of polymer matrix composite. Therefore, research on physical and chemical structures of polymer matrices with their dispersion micro-piezoelectric particles are of great importance in the development of polymer, active composite materials for various purposes. It is natural to assume that the electron-ion, polarization and physical-mechanical processes that are in one phase will affect the development of similar processes in another phase. In this connection, you must have information about the processes taking place both in the dispersion of the polymer phase, and at electrothermopolarization of composites as a whole. The aim of this work is to study the structure of the polymer phase polymer composites - piezoelectric ceramics in the process of grinding piezoceramic particles. As the polymer phase, the investigated composites selected polyolefins (polyethylene high and low density polypropylene) and fluorocarbon polymer polivinilidenftrorid. Samples of the composites prepared by hot pressing. As inorganic dispersants used piezoceramics tetragonal, and rhombohedral mixed structures. We used also piezoceramic fillers. In particular, $CaTiO_3$ and SiO_2. Of the powders of these materials by mechanical mixing to obtain a homogeneous mixture. Then, at certain temperatures and pressures obtained samples of the composite element. Pressing temperature is determined from the melting temperature of the polymer phase. The volume content of inorganic phase composites, depending on their appointments ranged from 5% to 70%. Electrothermopolarization condition of composites optimized experimentally by studying the dependence of physical and thermal properties and piezoelectric composites on the temperature and electric field polarization. As the methods of investigating the structures used are as follows: x–ray analysis, IR–spectroscopy, ESR and derivatography.

METHOD OF EXPERIMENT

However, it could be assumed that the introduction of segnetopiezoparticles leads to a significant change in the actual structure of the polymer, which, in turn, lead to the dominant role of "external residual" polarization due to a significant increase in the concentration of traps. Therefore, in a polymer matrix have been introduced inorganic fillers, leading to amorphization of the matrix, but do not have domain-orientation polarization. As such inorganic fillers used calcium titanate ($CaTiO_3$), having as segnetopiezoceramic PZT perovskite structure, silicon oxide (SiO_2) and rare earth elements. Changes in the structure of polyolefins is apparent in the diffraction pattern, IR - spectra derivatogram ESR - spectra before and after the dispersion of various inorganic fillers.

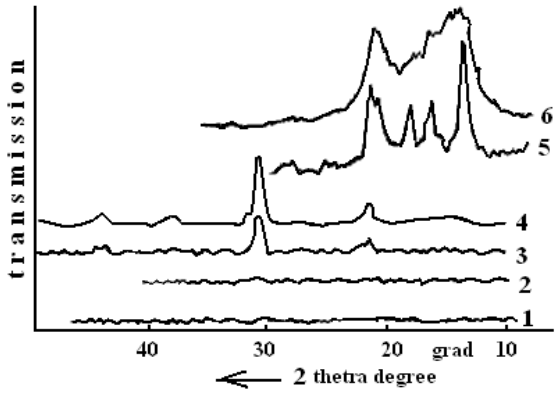

Fig. 1. The diffraction patterns of PP and composites on its basis and PZT-4. 1. PP + PZT–4, Φ=50 %; 2. PP + $CaTiO_3$, Φ=40 %; 3. PP + $CaTiO_3$, Φ=10 %; 4. PP + PZT-4, Φ=10 %; 5. PP – slowly cooled; 6. PP – hardened.

Figure 1 shows diffraction ghosts source of polypropylene and a composite with segnetopiezoelectric of PZT–4 or $CaTiO_3$. It is evident that the temperature - time regime of crystallization of PP significantly affects its diffraction pattern. With rapid cooling, in the formation of spheruliteless structure is the structural

transformation of isotactic form of the unit cell, obtained for the spherulitic polypropylene, in the smectic, ie the defective modification (diffraction 5 and 6). In the presence of the filler PZT–4 or $CaTiO_3$ deficiency PP increases, and with increasing volume content as PZT–4 and $CaTiO_3$ from 10% to 50% vol. is almost complete amorphization of PP (diffraction pattern 1–4). Similar results were obtained for all the investigated composites, in particular, for composites based on PP and segnetopiezoceramic mixed (P_E + T) structure – PZT–2 or silicon oxide (Fig. 2) and composites based on HPPE with piezoceramic tetragonal structure of PZT–5H (Fig. 3). Comparison of diffraction pattern polyolefin matrix (PP and HPPE), dispersive different in structure segnetopiezoceramic (PZT–4, PZT 2, PZT–7, etc.), or fillers that do not have a domain - the orientation of the polarization (SiO_2, $CaTiO_3$) show that the amorphization and defect occur with the introduction of polymer each of these inorganic fillers.

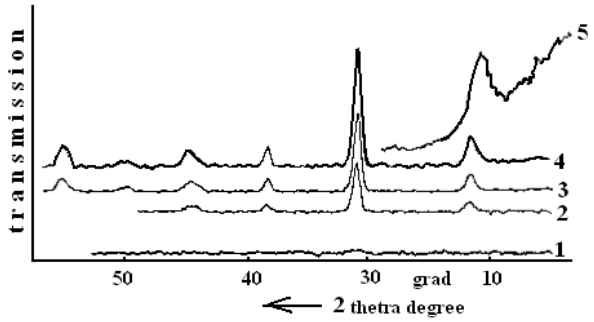

Fig. 2. The diffraction patterns of PP source and containing segnetopiezoelectric PZT-2. 1- PP +40% vol. PZT - 2; 2-PP +10% vol. SiO_2; 3 -PP +10% vol. PZT–2; 4-PP +5% vol. PZT–2; 5-Hardened polypropylene.

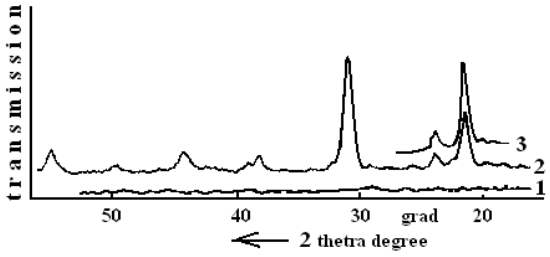

Fig. 3. Diffraction patterns of HPPE source and containing PZT - 5H. 1-HPPE +40% reported PZT-5H; 2-HPPE +40% vol. PZT-5H; 3- HPPE-hardened.

The dispersion of HPPE and PP segnetopiezo-ceramic (PZT–2, PZT–4) or $CaTiO_3$ leads to the ESR - signals. In the spectrum there is a broad line (g = 2,00 and the ΔH = 250–300 Hz) (Fig. 4, signal 1) and narrow lines (Fig. 4, signal 2, 3 and Fig. 5 a, b, c) with widths of 5–15 Hz, due, probably, the oxidation of the polymer (peroxide radicals). Attention is drawn to the fact that, for composites based on polyethylene using each of these fillers is observed, mainly, one line with ΔH = 10–15 Hz, while for the composites based on polypropylene - a few narrow lines of low intensity (Fig. 5 , b) with ΔH = 5–6Hz.

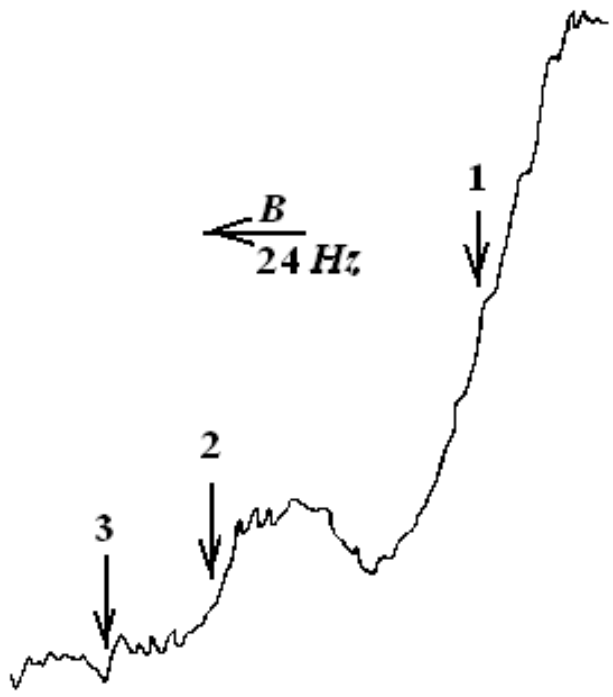

Fig. 4. The ESR spectra for the PP filled with segnetopiezoelect-ric PZT - 4.

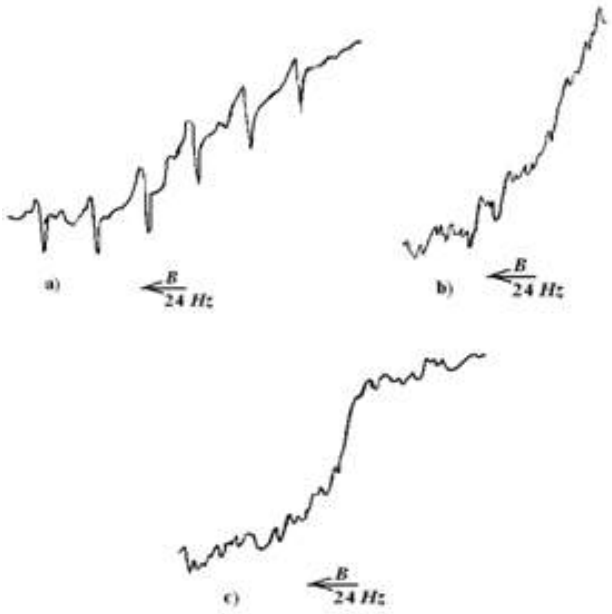

Fig. 5. The ESR spectrum of composites: a – HPPE+ 10% vol. PZT-4; signal-center line. Side six lines belong to the standard; b – PP+10% vol. PZT-4; c - HPPE +15% vol. PZT-2.

Amorphization and the appearance of the ESR - signals in the composites showed rupture of chemical bonds of polymer chains. The formation of free radicals leads to oxidative stress as evidenced by the change – IR spectra. In IR –absorption spectrum of HPPE (Fig. 6) there is a new broad band at 450–700 cm^{-1} with a maximum at 560–600 cm^{-1}. There is also the splitting of the band 720 cm^{-1} in two: 715–718 cm^{-1} and 725–730 cm^{-1}. It is known that the band 720 cm^{-1} due to vibrations of

CH_2 in amorphous and in crystalline regions, and the band 715 and 723 cm^{-1} - in the amorphous band at 730 cm^{-1} crystal phases of polyethylene. The observed splitting of evidence of the destruction of crystalline sites and increasing the proportion of amorphous phase and, consequently, an increase of defects and inhomogeneities of the structure, which can be injected to stabilize the polarization charges. Increased percentage of amorphous phase in the composites with increasing volume content of fillers confirmed derivatogram. Fig. 7 shows derivatograms polypropylene and composites based on it with different content segnetopiezoceramic PZT–4. As can be seen from the figure, with increasing volume content of PZT–4 the value of the endothermic peak at ≈ 423 K corresponding to the melting temperature phase decreases until its complete disappearance in the content of PZT–4 40% vol.

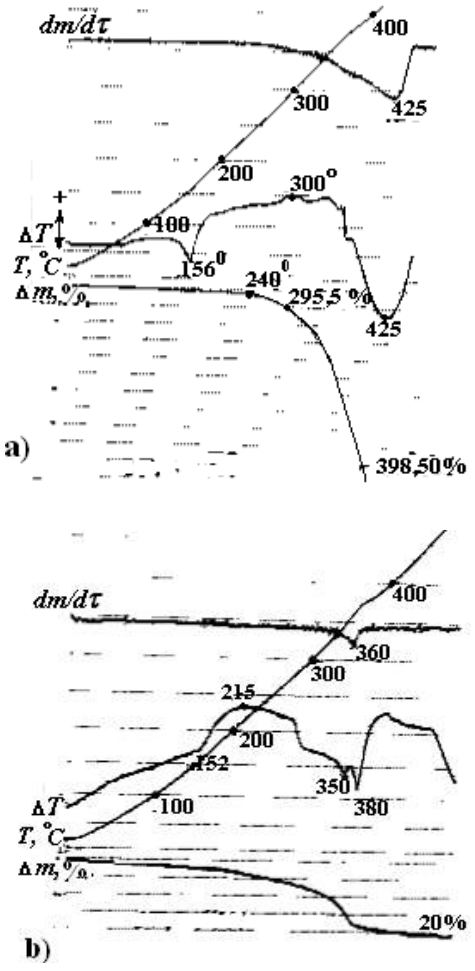

Fig. 6. Derivatogram polymer composites: a - PP; b – PP+50% vol. PZT-4.

Places destruction of the crystallites formed free radicals and polar groups are active traps for injected and migrating to macro–condition space charges and can create internal and external polarization at electro–thermal processing. If these traps could ensure the stability of the polarization and, consequently, the effective charge, regardless of the type of filler (or may not have a domain - the orientational polarization) in the composites would form a stable electricity, piezoelectric and pyroelectrical state. At the same time of the investigated composites only dispersed PZT–ceramics, having a domain-orientation polarization, characterized by the formation of electrets with high surface density and stability of the charge. Electrets based on polyolefins and inorganic fillers $CaTiO_3$, oxides of silicon and rare earth elements is extremely unstable and of no practical significance. It follows that the main factor in the formation of a stable electro, piezo- and pyroelectric states composites based on pyroelectrical polyolefins is domain-orientation polarization. Of course, in forming a stable electro, piezoelectric and polymer composites pyroelectrical states – segnetopiezoelectrical contributes stabilized on various traps injected charge (outside the remanent polarization, and to some extent, space–charge polarization). After all, the sign of the effective charge of many polarized composites corresponds gomocharge and in the presence of domain-orientation polarization of the electret, piezo- and pyroelectric characteristics of them will depend on the size and stability of trapped injected charge.

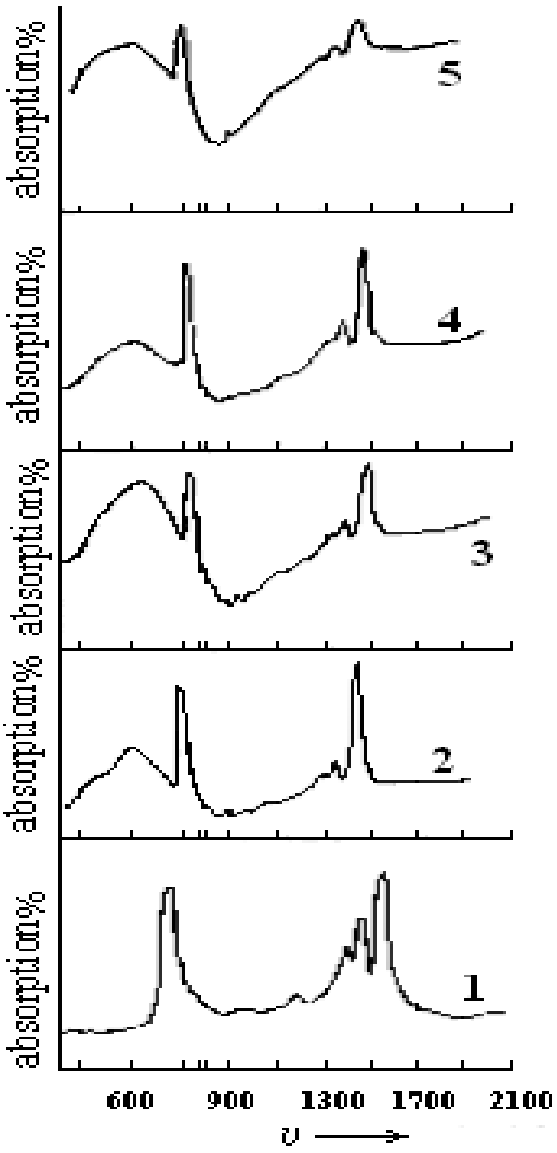

Fig. 7. Spectrum - IR absorption of the composites: 1-HPPE; 2-HPPE+5% vol. PZT - 2; 3-HPPE+10% vol. $CaTiO_3$; 4-HPPE+5% vol. PZT–4; 5-HPPE+10% vol. PZT–4.

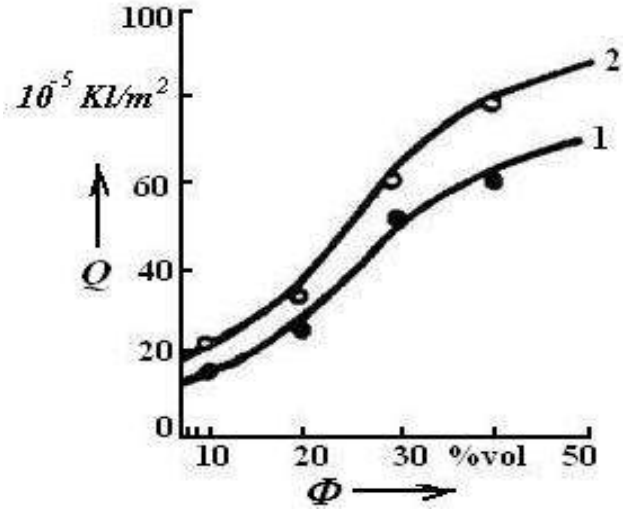

Fig. 8. The dependence of the boundary charge of the composite PP - PZT-4 from the bulk PZT-4. 1- spheruliteless; 2- spherulitic.

Comparison of studies on structural changes of the polymer phase and magnitude of the boundary of the charge depending on the volume content of inorganic particles (Fig. 8) shows that the effects of violations of the crystalline phase and the accumulation of charges at the interface is clearly linked: with increasing degree of amorphization of the polymer matrix increases the charge stabilized at the interface.

The experiments also show that changes in temperature regimes of crystallization time (slow and fast cooling) affect the degree of amorphization during grinding of the polymer matrix piezoceramic particles (Fig. 8, curves 1 and 2).

CONCLUSION

Thus, analysis of the diffraction, ESR, IR spectra and derivatogram indicates a strong change in the structure of polyolefins in compositions with segnotopiezo filler based on PZT or fillers with no spontaneous polarization. The results can be generally summarized as follows:

1) The fillers in HPPE and PP matrices, mostly, are in the form of polydisperse particulate precursors and chemical interaction of fillers with polymer matrix weak;

2) There is a strong destruction of the crystalline parts of polymers (breaking of various chemical bonds), an increase in the proportion of amorphous or defective parts;

3) Changes molecular structure, free radicals are formed and there is a chemical change in the structure of the polymer - for free radical oxidation process.

[1]. *M.A. Kurbanov, S.A. Abasov, S.I. Veliyev*. The structural changes in polyethylene under conditions of electric discharges. Izv. An. Azerb. SSSR, 1981, № 2, p. 87–90.

[2]. *M.A. Kurbanov, S.N. Musaeva, E.A. Kerimov*. Character of distribution of local levels in the quasi-forbidden band of polymer phase of polymer–piezoelectric composites. Institute of Physics, Azerbaijan National Academy of Sciences, J. Physics 2004, X, № 1-2.

[3]. *M.A. Kurbanov, A.E. Panich, G.G. Aliev, B.M. Izzatov, G.Kh. Kulieva*. On the regularities of electrical characteristics of the istics piezocomposites at electrothermopolarization. International conference "Physics–2005". Baku Discharges, 2005, 7-9 June. p.521-522.

DIRECT ELLIPSOMETRY TASK FOR ZnS/GaAs, ZnSe/GaAs AND $CuGaS_2$/GaP THIN FILM/SUBSTRATE SYSTEMS

XURAMAN N. XALILOVA, DURDANA I. HUSEYNOVA, SADIG V. HAMIDOV, VUSALA N. JAFAROVA, ZAKIR A. JAHANGIRLI, HUSEYN S. ORUDZHEV, NAZIM T. MAMEDOV

Institute of Physics, Azerbaijan National Academy of Sciences, AZ 1143, H.Javid ave.33, Baku

In this work ellipsometric approach has been developed for ZnS/GaAs, ZnSe/GaAs and $CuGaS_2$/GaP film/substrate systems to solve direct ellipsometry task. The proposed approach allows to finding through ellipsometric parameters the lattice mismatch effect on optical indicatrix of the considered stressed film.

INTRODUCTION

In recent two decades ellipsometric approach has gained a worldwide recognition as the most correct approach for description of light wave. Applications of are nowadays very numerous and are spread out from *in-sity* control in planar technologies to precise determination of optical function of solids. Ellipsometry is well known as one of the powerful methods to control thin film and surface parameters [1-7]. A huge variety of problems which are or could be solved by ellipsometric study is very persuative and has provoked our present trial to explore a possibility of ellipsometric investigation of the photoelastic effect which should take place in thin film/substrate systems because of lattice mismatch.

In this work ellipsometric approach have been developed for ZnS/GaAs, ZnSe/GaAs and $CuGaS_2$/GaP film/substrate systems to solve direct ellipsometry task. The proposed approach allows to finding through ellipsometric parameters the lattice mismatch effect on optical indicatrix of the considered stressed film.

1. PHOTOELASTIC EFFECT IN STRESSED FILM

The photoelastic effect due to stress (t) or deformation (r) which corresponds to this stress is written in matrix form as

$\Delta\eta_{ij}=\pi_{ijkl}t_{kl}=p_{ijkl}r_{kl}$, in tensor form, $\Delta\eta_m=\pi_{mn}t_n=p_{mn}r_n$ where $\pi_{mn}=\pi_{ijkl}$, n=1,2,3 ; $\pi_{mn}=2\pi_{ijkl}$, n=4,5,6 and $=p_{ijkl}$, n=1,2,3 ; $p_{mn}=2p_{ijkl}$, n=4,5,6. Here Δ is the change of the polarization constant η_m due to stress or deformation, π_{mn} and p_{mn} are the piezooptic and photoelastic coefficients, correspondingly; t_n and r_n are the stress and deformation, correspondingly.

To write down the equation of the photoelastic effect in the stressed film it is necessary to know symmetries of the film and substrate, as well as their orientation. For the sake of certainty let us consider ZnS $(\bar{4}3m)$ /GaAs($\bar{4}3m$) and $CuGaS_2$($\bar{4}2m$) /GaAs($\bar{4}3m$) [9] systems with interface surface perpendicular to [001] direction (z-direction) in both cases.

1.1 ZnS/GaAs SYSTEM

Before stress, in a coordinate system where z is directed perpendicular to the interface and x and y axes lie in the plane of interface, the equation for polarization constants in the film can be written as

$$\eta\,(x^2+y^2+z^2)=1 \qquad (1)$$

After the stress, t, due to the lattice mismatch is applied along x and y directions we have

$$\begin{bmatrix} & t & t & 0 & 0 & 0 & 0 \\ \Delta\eta_1 & \pi_{11} & \pi_{12} & \pi_{12} & 0 & 0 & 0 \\ \Delta\eta_2 & \pi_{12} & \pi_{11} & \pi_{12} & 0 & 0 & 0 \\ \Delta\eta_3 & \pi_{12} & \pi_{12} & \pi_{11} & 0 & 0 & 0 \\ \Delta\eta_4 & 0 & 0 & 0 & \pi_{44} & 0 & 0 \\ \Delta\eta_5 & 0 & 0 & 0 & 0 & \pi_{44} & 0 \\ \Delta\eta_6 & 0 & 0 & 0 & 0 & 0 & \pi_{44} \end{bmatrix} \qquad (2)$$

and

$$[\eta+(\pi_{11}+\pi_{12})t]x^2+[\eta+(\pi_{12}+\pi_{11})t]y^2+[\eta+(2\pi_{12})t]z^2=1 \qquad (3)$$

Taking into account the relationship for r_0 [8] and that η equals $1/N^2$ (N is the refractive index) and supposing that everywhere $\Delta\eta<<\eta$, we have for optical indicatrix that

$$\frac{x^2+y^2}{N^2\left(1-N^2\frac{(p_{11}+p_{12})r}{2}\right)^2}+\frac{z^2}{N^2\left(1-N^2p_{12}r\right)^2}=1 \qquad (4)$$

i.e., initially optically isotropic film turned into optically uniaxial film with optical axis **C** along the normal to the interface. The ordinary and extraordinary refractive indexes of the last film are

$$N_0=N\left(1-N^2\frac{(p_{11}+p_{12})r}{2}\right) \qquad (5)$$

and

$$N_e=N\left(1-N^2p_{12}r\right) \qquad (5^*),$$

respectively.

1.2 $CuGaS_2$/GaP system

CuGaSe film is a uniaxial film, and the equation for polarization constants before stress can be written as $\eta_o(x^2+y^2)+\eta_e z^2=1$.

Stress induced by the lattice mismatch along x and y and the $\Delta\eta_i$ are related as

$$\begin{bmatrix} & t & t & 0 & 0 & 0 & 0 \\ \Delta\eta_1 & \pi_{11} & \pi_{12} & \pi_{13} & 0 & 0 & 0 \\ \Delta\eta_2 & \pi_{12} & \pi_{11} & \pi_{13} & 0 & 0 & 0 \\ \Delta\eta_3 & \pi_{31} & \pi_{31} & \pi_{33} & 0 & 0 & 0 \\ \Delta\eta_4 & 0 & 0 & 0 & \pi_{44} & 0 & 0 \\ \Delta\eta_5 & 0 & 0 & 0 & 0 & \pi_{44} & 0 \\ \Delta\eta_6 & 0 & 0 & 0 & 0 & 0 & \pi_{66} \end{bmatrix} \quad (6)$$

and

$$[\eta_o+(\pi_{11}+\pi_{12})t]x^2+[\eta_o+(\pi_{11}+\pi_{12})t]y^2+[\eta_e+(2\pi_{31})t]z^2=1 \quad (7)$$

For optical indicatrix we then have

$$\frac{x^2+y^2}{N_0^2\left(1-N_0^2\frac{(p_{11}+p_{12})r}{2}\right)^2}+\frac{z^2}{N_e^2\left(1-N_e^2 p_{31}r\right)^2}=1 \quad (8)$$

i.e the film is again uniaxial with the same orientation of the principal axes. However, refractive indexes of ordinary and extraordinary beams are changed to

$$N_0^{new}=N_0\left(1-N_0^2\frac{(p_{11}+p_{12})r}{2}\right)$$
$$\text{and } N_e^{new}=N_e\left(1-N_e^2 p_{31}r\right) \quad (9)$$

2. ELLIPSOMETRI APPROACH FOR ZnS/GaAs AND $CuGaS_2$/GaP SYSTEMS

In anizotropic systems we have the most general relationship between p- and s- components of the complex amplitude of the reflected (r) and incident (i) waves [10]

$$E_p^r=R_{pp}E_p^i+R_{sp}E_s^i \quad (10)$$
$$E_s^r=R_{sp}E_p^i+R_{ss}E_s^i \quad (10^*)$$

or

$$\frac{E_p^r}{E_s^r}=\frac{\left(\frac{R_{pp}}{R_{ss}}\right)\frac{E_p^i}{E_s^i}+\left(\frac{R_{ps}}{R_{ss}}\right)}{\left(\frac{R_{sp}}{R_{ss}}\right)\frac{E_p^i}{E_s^i}+1} \quad (11)$$

where Rpp/Rss, Rps/Rss and Rsp/Rss are the relative coefficients of reflection , which we have to be determine by solving Wave Equation [10]

$$\Delta E\text{-grad}\,\text{div}E+(2\pi/\lambda)^2 D=0 \quad (12)$$

It follows from section 1 (see 1.1 and 1.2) that we shall consider an isotropic substrate and a uniaxial film on, with the same z axis for the film and film/substrate system. It follows from Eq. (12) that in this case the x- and y- components of the electrical vector obey the following equations:

$$\varepsilon_e\frac{\partial^2 E_x}{\partial z^2}+\varepsilon_0\left[\left(\frac{2\pi}{\lambda}\right)^2\varepsilon_e-k_x^2\right]E_x=0, \text{ and}$$
$$\frac{\partial^2 E_y}{\partial z^2}+\left[\left(\frac{2\pi}{\lambda}\right)^2\varepsilon_0-k_x^2\right]E_y=0 \quad (13)$$

where, $k_x=\text{const}=(2\pi/\lambda)\sin\varphi$, and $\varepsilon_o=(n_o-ik_o)^2$ and $\varepsilon_e=(n_e-ik_e)^2$ are the complex diagonal components of the dielectric function tensor. Now let us consider s-component of the incident wave. In this case Ey=Es; Ex=Ez=0; Hy=0. Using the Abbeles method, from solutions of the Eq.(8) the following matrix of tangential components of electric and magnetic field can be constructed:

$$M_s(0,d)=\begin{pmatrix} m_{s11}m_{s12} \\ m_{s21}m_{s22}\end{pmatrix}=\begin{pmatrix} \frac{1}{2}\left[e^{-i\delta_0}+e^{-i\delta_0}\right]\frac{1}{2g_0}\left[e^{-i\delta_0}-e^{i\delta_0}\right] \\ \frac{g_0}{2}\left[e^{-i\delta_0}-e^{-i\delta_0}\right]\frac{1}{2}\left[e^{-i\delta_0}+e^{i\delta_0}\right]\end{pmatrix} \quad (14)$$

where $\delta_0=\frac{2\pi}{\lambda}d\sqrt{\varepsilon_0-\sin^2\varphi}$

and $g_0=\sqrt{\varepsilon_0-\sin^2\varphi}$

Now tangential components in the interfaces between the film and ambient and between the film and substrate can be connected through matrix

$$Q_s(0)=\begin{pmatrix} E_s(0) \\ H_x(0)\end{pmatrix}=M_s(0,d)\begin{pmatrix} E_s(d) \\ H_x(d)\end{pmatrix} \quad (15)$$

Hereafter let us distinguish between thick and thin substrate. In the thick or absorptive substrate we have no waves reflected from the interface between substrate and ambient and this case, as it will be seen afterwards, corresponds to the situation in ZnS/GaAs system. In the thin substrate, we have waves reflected from its bottom boundary and this will modify the total reflected field. (This case will correspond to the experimental situation in $CuGaS_2$/GaP system).

2.1 Thick substrate

$$R_{ss}=\frac{-(m_{s21}+gm_{s22})+g_{sub}(m_{s11}+gm_{s12})}{(m_{s21}-gm_{s22})-g_{sub}(m_{s11}-gm_{s12})}e^{-2ik_z d} \quad (16)$$

where $g = \cos\varphi$, and $g_{sub} = \sqrt{\varepsilon_{sub} - \sin^2\varphi}$ (17)

2.2 Thin substrate

In this case R_{ss} will be given by the relation (9)

$$M_s(0, d_{sub} + d) = \begin{pmatrix} m_{s11} & m_{s12} \\ m_{s21} & m_{s22} \end{pmatrix} = M(d_{sub}, d)M(0, d_{sub}) \quad (18)$$

Here $M(d_{sub},d)$ is the same as matrix (14), matrix $(0, d_{sub})$ has the form similar to that of matrix (14) in which δ_0 and g_0 must be replaced by δ_{sub} and g_{sub}, respectively, i. e.

$$M_S(0, d_{sub}) = \begin{pmatrix} \frac{1}{2}\left[e^{-i\delta_{sub}} + e^{i\delta_{sub}}\right] & \frac{1}{2g_{sub}}\left[e^{-i\delta_{sub}} - e^{i\delta_{sub}}\right] \\ \frac{g_{sub}}{2}\left[e^{-i\delta_{sub}} - e^{i\delta_{sub}}\right] & \frac{1}{2}\left[e^{-i\delta_{sub}} + e^{i\delta_{sub}}\right] \end{pmatrix} \quad (19)$$

where $\delta_{sub} = \frac{2\pi}{\lambda} d_{sub}\sqrt{\varepsilon_{sub} - \sin^2\varphi}$ and $g_{sub} = \sqrt{\varepsilon_{sub} - \sin^2\varphi}$

Similary to R_{ss} it is easy to show that R_{pp} can be written in both cases (thin and thick substrate) so as it is shown in the next subsection.

2.3 Thick substrate

$$R_{pp} = \frac{-(m_{p21} - gm_{p22}) - \frac{g_{sub}}{\varepsilon_{sub}}(m_{p11} - gm_{p12})}{(m_{p21} + gm_{p22}) + \frac{g_{sub}}{\varepsilon_{sub}}(m_{p11} + gm_{p12})} e^{-2ik_z d} \quad (20)$$

$$M_p(0, d) = \begin{pmatrix} \frac{1}{2}\left[e^{-i\delta_e} + e^{i\delta_e}\right] & -\frac{\varepsilon_e}{2g_e}\left[e^{-i\delta_e} - e^{i\delta_e}\right] \\ -\frac{g_e}{2\varepsilon_e}\left[e^{-i\delta_e} - e^{i\delta_e}\right] & \frac{1}{2}\left[e^{-i\delta_e} + e^{i\delta_e}\right] \end{pmatrix} \quad (21)$$

where,

$$\delta_e = \frac{2\pi}{\lambda} d\sqrt{\varepsilon_0 - \left(\frac{\varepsilon_0}{\varepsilon_e}\right)\sin^2\varphi} \quad \text{and} \quad g_e = \sqrt{\varepsilon_e - \left(\frac{\varepsilon_0}{\varepsilon_e}\right)\sin^2\varphi} \quad (22)$$

2.4 Thin substrate

In this case $M_p(d_{sub},d)$ equals

$$M_p(0, d_{sub}) = \begin{pmatrix} \frac{1}{2}\left[e^{-i\delta_{sub}} + e^{i\delta_{sub}}\right] & -\frac{\varepsilon_{sub}}{2g_{sub}}\left[e^{-i\delta_{sub}} - e^{i\delta_{sub}}\right] \\ -\frac{g_{sub}}{2\varepsilon_{sub}}\left[e^{-i\delta_{sub}} - e^{i\delta_{sub}}\right] & \frac{1}{2}\left[e^{-i\delta_{sub}} + e^{i\delta_{sub}}\right] \end{pmatrix} \quad (23)$$

The ratio of $g_{sub}/\varepsilon_{sub}$ must be replaced by $g=\cos\varphi$. The coefficients m can then be obtained from

$$M_p(0, d_{sub} + d) = \begin{pmatrix} m_{p11} & m_{p12} \\ m_{p21} & m_{p22} \end{pmatrix} = M_p(d_{sub}, d)M_p(0, d_{sub}) \quad (24)$$

3. DIRECT ELLIPSOMETRY TASK FOR ZnS/GaAs, ZnSe/GaAs AND $CuGaS_2$/GaP

Direct ellipsometry task implies a computation of ellipsometric angles ψ and Δ of the system under consideration using analytic expressions obtained in Section 2. Our main target is the photoelastic effect in stressed film/substrate system. To calculate the magnitude of the effect in ψ-and Δ-units we will do the following. First, we will calculate ψ and Δ for unstressed film/substrate systems at different thicknesses of the film d. After that we

will calculate ψ and Δ for stressed film/substrate system with above values of the thicknesses and different values (p_{mn}r, r is known) of the photoelastic effect. In both cases we will construct Δ=f(ψ) dependencies and will estimate the smallest value of the photoelastic effect, which we are still be able to detect.

3.1 Unstressed ZnS/GaAs system

ZnS/GaAs system presents an isotropic film/substrate system for which the principal equation of the ellipsometry ($\tan\psi e^{i\Delta}=R_p/R_s$) is very well known and given by

$$\tan\psi\times e^{i\Delta}=\frac{r_{01p}+e^{-2\delta_2}e^{-2i\delta_1}r_{12p}}{1+e^{-2\delta_2}e^{-2i\delta_1}r_{01p}r_{12p}}\times$$

$$\times\frac{1+e^{-2\delta_2}e^{-2i\delta_1}r_{01s}r_{12s}}{r_{01s}+e^{-2\delta_2}e^{-2i\delta_1}r_{12s}} \quad (25)$$

$$r_{12p}=\frac{\sqrt{\varepsilon_{sub}-\frac{\varepsilon_{sub}\sin^2\varphi}{\varepsilon_{film}}}-\sqrt{\varepsilon_{film}-\frac{\varepsilon_{film}\sin^2\varphi}{\varepsilon_{sub}}}}{\sqrt{\varepsilon_{sub}-\frac{\varepsilon_{sub}\sin^2\varphi}{\varepsilon_{film}}}+\sqrt{\varepsilon_{film}-\frac{\varepsilon_{film}\sin^2\varphi}{\varepsilon_{sub}}}}$$

$$r_{12s}=\frac{\sqrt{\varepsilon_{film}-\sin^2\varphi}-\sqrt{\varepsilon_{sub}-\sin^2\varphi}}{\sqrt{\varepsilon_{film}-\sin^2\varphi}+\sqrt{\varepsilon_{sub}-\sin^2\varphi}}$$

$$r_{01s}=\frac{\cos\varphi-\sqrt{\varepsilon_{film}-\sin^2\varphi}}{\cos\varphi+\sqrt{\varepsilon_{film}-\sin^2\varphi}},$$

$$\delta_1=\frac{\sqrt{2}\pi}{\lambda}\times d\times\sqrt{\sqrt{a^2+b^2}+a},$$

$$\delta_2=\frac{\sqrt{2}\pi}{\lambda}\times d\times\sqrt{\sqrt{a^2+b^2}-a}$$

$$a=n_{film}^2-k_{film}^2-\sin^2\varphi\ ,$$

$$\varepsilon_{film}=n_{film}^2-k_{film}^2-i2n_{film}k_{film},$$

$$\varepsilon_{sub}=n_{sub}k_{sub}^2-i2n_{sub}k_{sub}$$

Let us select the experimental wavelength in region where sensitivity of a Jobin-Ivon spectroscopic ellipsometer is high and the substrate is absorptive enough to avoid formation of the reflected beam from the bottom boundary of the substrate.

3.2 Unstressed $CuGaS_2$/GaP system

There exists a possibility to simplify the problem by selecting the experimental wavelength at λ=6400 Å where $N_0=N_e$ (isotropic point) and uniaxial optical indicatrix turns into sphere. It is easy to show that in this case,

$$\tan\psi\times e^{i\Delta}=\frac{r_{01p}+e^{-2\delta_2^{film}}e^{-2i\delta_1^{film}}r_{12p}+e^{-2\delta_2^{sub}}e^{-2i\delta_1^{sub}}r_{01p}r_{12p}r_{23p}+e^{-2(\delta_2^{film}+\delta_2^{sub})}e^{-2i(\delta_1^{film}+\delta_1^{sub})}r_{23p}}{1+e^{-2\delta_2^{film}}e^{-2i\delta_1^{film}}r_{01p}r_{12p}+e^{-2\delta_2^{sub}}e^{-2i\delta_1^{sub}}r_{12p}r_{23p}+e^{-2(\delta_2^{film}+\delta_2^{sub})}e^{-2i(\delta_1^{film}+\delta_1^{sub})}r_{01p}r_{23p}}\times \quad (26)$$

$$\times\frac{1+e^{-2\delta_2^{film}}e^{-2i\delta_1^{film}}r_{01s}r_{12s}+e^{-2\delta_2^{sub}}e^{-2i\delta_1^{sub}}r_{12s}r_{23s}+e^{-2(\delta_2^{film}+\delta_2^{sub})}e^{-2i(\delta_1^{film}+\delta_1^{sub})}r_{01s}r_{23s}}{r_{01s}+e^{-2\delta_2^{film}}e^{-2i\delta_1^{film}}r_{12s}+e^{-2\delta_2^{sub}}e^{-2i\delta_1^{sub}}r_{01s}r_{12s}r_{23s}+e^{-2(\delta_2^{film}+\delta_2^{sub})}e^{-2i(\delta_1^{film}+\delta_1^{sub})}r_{23s}}$$

The other coefficients are given by

$$r_{23p}=\sqrt{1-\frac{\sin^2\varphi}{\varepsilon_{sub}}}-\sqrt{\varepsilon_{sub}}\cos\varphi\Big/\sqrt{1-\frac{\sin^2\varphi}{\varepsilon_{sub}}}+\sqrt{\varepsilon_{sub}}\cos\varphi,$$

$$r_{23s}=\frac{\sqrt{\varepsilon_{sub}-\sin^2\varphi}-\cos\varphi}{\sqrt{\varepsilon_{sub}-\sin^2\varphi}+\cos\varphi}$$

$$\delta_1^{film(sub)}=\frac{\sqrt{2}\pi}{\lambda}\times d_{film(sub)}\times\sqrt{\sqrt{a_{film(sub)}^2+b_{film(sub)}^2}+a}$$

$$\delta_2^{film(sub)}=\frac{\sqrt{2}\pi}{\lambda}\times d_{film(sub)}\times\sqrt{\sqrt{a_{film(sub)}^2+b_{film(sub)}^2}-a}$$

$$a_{film(sub)}=n_{film(sub)}^2-k_{film(sub)}^2-\sin^2\varphi\ \ ,\quad b_{film(sub)}=2n_{film(sub)}k_{film(sub)}$$

3.3 Selection of experimental angle of incidence

The change of polarization angles due to the change of the dielectric constant of the film is observable if the following conditions is fulfilled:

$$\delta\psi_{\min} = \left| \delta n_{film,\min}^{(\psi)} \left(\frac{\partial \psi}{\partial n_{film}} \right) - \delta\psi_{el} \right| > 0$$

and

$$\delta\Delta_{\min} = \left| \delta n_{film,\min}^{(\Delta)} \left(\frac{\partial \Delta}{\partial n_{film}} \right) - \delta\Delta_{el} \right| > 0 \qquad (27)$$

where $\delta_{film\min}^{(\psi,\Delta)}$ are the minimal value of the change of the dielectric constant of the film, $\partial\psi / \partial n_{film}$ and $\partial\Delta / \partial n_{film}$ are the first derivatives, $\delta\psi_{el}$ and $\delta\Delta_{el}$ are the threshold sensitivities of the employed ellipsometer. As seen from Fig.1, the optimum sensitivity for ψ and Δ is attained at around pseudo-Brewster angle for all considered systems. It is natural (Fig.1) that the higher the film thickness the larger response of the ellipsometric angles is.

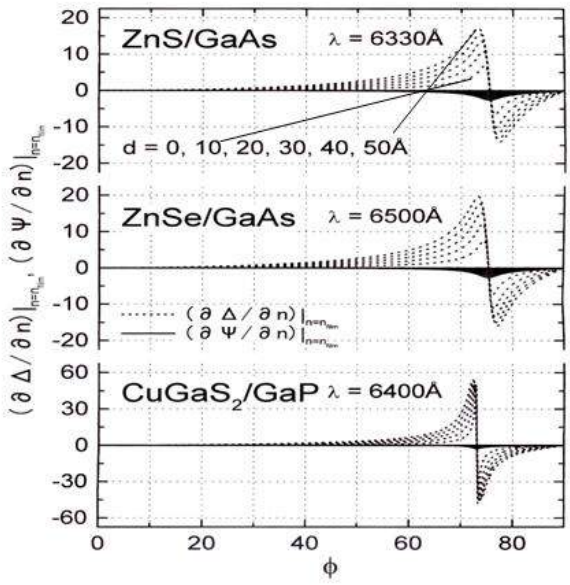

Fig 1. First derivatives of the ellipsometric parameters as function of incidence angle ϕ at various film thicknesses d.

3.4 ZnS/GaAs and ZnSe/GaAs after stress

It follows from Sections 2.3 and 2.4 that after stress the principal ellipsometry equation can be rewritten as

$$\tan\psi e^{i\Delta} = \frac{\left(\cos\varphi - \frac{g_{sub}}{\varepsilon_{sub}}\right)\cos\delta_e + i\left(\frac{g_{sub}}{\varepsilon_{sub}}\frac{\varepsilon_e}{g_e} - \frac{g_e}{\varepsilon_e}\right)\sin\delta_e}{\left(\cos\varphi + \frac{g_{sub}}{\varepsilon_{sub}}\right)\cos\delta_e + i\left(\frac{g_{sub}}{\varepsilon_{sub}}\frac{\varepsilon_e}{g_e} + \frac{g_e}{\varepsilon_e}\right)\sin\delta_e} \times \frac{(\cos\varphi + g_{sub})\cos\delta_0 + i\left(g_0 + \frac{g_{sub}}{g_0}\right)\sin\delta_0}{(\cos\varphi - g_{sub})\cos\delta_0 + i\left(g_0 - \frac{g_{sub}}{g_0}\right)\sin\delta_0} \qquad (28)$$

Here $$\delta_e = \frac{2\pi}{\lambda} d_{eff} \sqrt{\varepsilon_0 - \left(\frac{\varepsilon_0}{\varepsilon_e}\right)\sin^2\varphi} \quad , \quad \delta_0 = \frac{2\pi}{\lambda} d_{eff} \sqrt{\varepsilon_0 - \sin^2\varphi} \qquad (29)$$

and $$\varepsilon_e = n_{film}^2 (1 - n_{film}^2 p_{12} r_{eff})^2 \quad , \quad \varepsilon_0 = n_{film}^2 \left(1 - n_{film}^2 \frac{p_{11} + p_{12}}{2} r_{eff}\right)^2 \qquad (30)$$

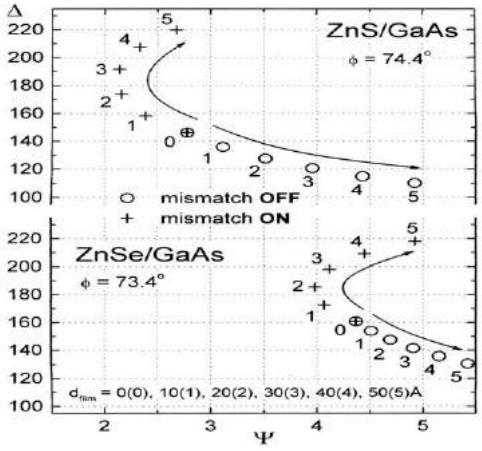

Fig 2. Δ -ψ graphs with allowance for lattice mismatch effect in ZnS/GaAs and ZnSe/GaAs at various film thicknesses.

In similar way the principal ellipsometry equation is obtained for a stressed $CuGaS_2$/GaP system.

The results of computations give the results shown in Fig.2.

4. DISCUSSION

The effect of the lattice mismatch on ellipsometric parameters ψ and Δ is shown in Fig. 2. The effect is quite large in Δ units and amounts 40˚ - 50˚ for film thickness 50Å. The films as thin as 10 Å the Δ changes by 15˚, and ψ by 6′ while ellipsometric accuracy is of 0.5′ in the worst case. Thus, lattice mismatch effect is observable using ellipsometric techniques.

[1]. *R. M. A. Azzam, N.M. J. Bashara* Opt. Soc. Amer., 63, (1973), 508

[2]. *D. Datta, V. Tripathi, P. Gogoi, S. Banerjee, S.Kumar*, Thin Solid Films, 516, 2008, 7237

[3]. *N. Mamedov, K. Wakita, Y. Shim, K. Abe, N. Ogushi*: Temperature-dependent and pump-probe ellipsometric studies of $TlInSe_2$, Thin Solid Films., 517, (2008), 1434

[4]. *Y. Shim, H. Hasegawa, K. Wakita, N. Mamedov* . $CuAl_{1-x}In_xSe_2$ solid solutions. Dielectric function and inter-band optical transitions , Thin Solid Films., 517, (2008), 1442

[5]. *Y. Shim, S. Kondo, K. Kataoka, S. Abdullayeva, N. Mamedov.*, Dispersion of Principal Refractive Indices of $CaGa_2S_4$, 47, (2008), 8174

[6]. *Y. Shim, W. Okada, K. Wakita, and N. Mamedov* "Refractive indices of layered semiconductor ferroelectrics $TlInS_2$, $TlGaS_2$ and $TlGaSe_2$ from ellipsometric measurements limited to only layer-plane surfaces"., 102, (2007), 1-4

[7]. *H. Azuma, T. Kobayasi, Y. Shim, N. Mamedov, H. Naito* "Amplifed spontaneous emission in α-phase and β-phase polyfluorene waveguids" Organic Electronics, 8, (2007), 184

[8]. *H. Fujuvara* Spectroscopic Ellipsometry : Principles and Applications (2007) John Wiley and sons

[9]. *S. Iida, H. Icinokura, Y. Toyama, A. Kato*, Journal of Physics and Chemistry of Solids, v. 64, iss. 9-10, p. 2017.

[10]. *А.В. Ржанов, К. К. Свиташев, А. И. Семененко, В. К. Соколов*. Основы эллипсометрии. Наука, 1979.

FIRST PRINCIPLE STUDIES ON GdCu

A.H. ERGUN[1], Y.O. CIFTCI[1], K. COLAKOGLU[1], H. OZISIK[2]
[1]*Department of Physics, Gazi University, 06500 Ankara, Turkey*
[2]*Physics Department, Aksaray University, 68100 Aksaray, Turkey*

Ab initio calculations have been carried out to find the structural, electronic, elastic and thermodynamic properties of GdCu, using density functional theory within generalized-gradient (GGA) apraximation. For the total-energy calculation we have used the projected augmented plane-wave (PAW) implementation of the Vienna Ab initio Simulation Package (VASP). Our results are compared to other theoretical and experimental works, and excellent agreement is obtained. We have used to examine structure parameter in different structures such as in NaCl(B1), CsCl(B2) and ZB(B3). We have performed the thermodynamics properties for GdCu by using quasi-harmonic Debye model. We have, also, predicted the temperature and pressure variation of the volume, bulk modulus, thermal expansion coefficient, heat capacities and Debye temperatures in a wide pressure (0 – 50 GPa) and temperature ranges (0- 1000 K).

I. INTRODUCTION

Binary qui-atomic intermetallic compounds of rare earth elements and group Ib and IIb metals exhibit a variety of interesting magnetic phases [1]. When Ni is substituted by a group Ib element (Cu or Ag) the structure changes to the cubic CsCI-type structure with an antiferromagnetic ordered ground state [2]

In this study, as A.V Postnikov et al.[2] and others studies, elastic and thermodynamic properties of GdCu compounds, whose magnetic and electronic properties was mainly examined in previous studies, are investigated. In that studies, where magnetic properties are concentrated on [2], elastic and thermodynamic properties are not mentioned. Therefore, in this study, these properties, which were not examined for B1, B2 and B3 phases of GdCu compound, have reported in detail.

The aim of the present paper is to reveal bulk, structural properties in NaCl(B1), CsCl(B2), ZB(B3) phase and thermodynamical and elastic properties of GdCu in B2 phase, using VASP method with plane-wave pseudopotential.

At section 3, calculations are made with this method and lastly the results of the calculations are summarized in conclusions

II. METHOD OF CALCULATION

In the present work, all the calculations have been carried out using the Vienna ab initio simulation package (VASP) [3-4] based on the density functional theory (DFT). The electron-ion interaction was considered in the form of the projector-augmented-wave (PAW) method with plane wave up to energy of 600 eV [5-6]. This cut-off was found to be adequate for the structural, elastic properties as well as for the electronic structure. We do not find any significant changes in the key parameters when the energy cut-off is increased from 600 eV to 650 eV. For the exchange and correlation terms in the electron-electron interaction, Perdew and Zunger-type functional [7-8] was used within the generalized gradient approximation (GGA) [10]. The 12x12x12 Monkhorst and Pack [9] grid of k-points have been used for integration in the irreducible Brillouin zone. Thus, this mesh ensures a convergence of total energy to less than 10^{-5} ev/atom.

We used the quasi-harmonic Debye model to obtain the thermodynamic properties of GdCu [10-11], in which the non-equilibrium Gibbs function *G*(V; P, T)* takes the form of

$$G^*(V;P,T)=E(V)+PV+A_{vib}[\theta(V);T] \tag{1}$$

In Eq.(1), *E(V)* is the total energy for per unit cell of GdCu, *PV* corresponds to the constant hydrostatic pressure condition , $\theta(V)$ the Debye temperature and A_{Vib} is the vibration term, which can be written using the Debye model of the phonon density of states as

$$A_{Vib}(\theta,T)=nkT\left[\frac{9\theta}{8T}+3\ln\left(1-e^{-\frac{\theta}{T}}\right)-D\left(\frac{\theta}{T}\right)\right] \tag{2}$$

where *n* is the number of atoms per formula unit, $D\left(\frac{\theta}{T}\right)$ the Debye integral, and for an isotropic solid, θ is expressed as [12]

$$\theta_D=\frac{\hbar}{k}\left[6\pi^{1/2}V^{1/2}n\right]^{1/3} f(\sigma)\sqrt{\frac{B_s}{M}} \tag{3}$$

where *M* is the molecular mass per unit cell and B_S the adiabatic bulk modulus, which is approximated given by the static compressibility [13]:

$$B_s \approx B(V)=V\frac{d^2E(V)}{dV^2} \tag{4}$$

$f(\sigma)$ is given by Refs. [12-14] and the Poisson ratio are used as 0.28242 for GdCu. For GdCu, *n*=4 *M*= 220.796 a.u, respectively. Therefore, the non-equilibrium Gibbs function *G*(V; P, T)* as a function of *(V; P, T)* can be minimized with respect to volume *V*.

$$\left[\frac{\partial G^*(V;P,T)}{\partial V}\right]_{P,T}=0 \tag{5}$$

By solving Eq. (5), one can obtain the thermal equation-of-equation (EOS) *V(P, T).* The heat capacity at

constant volume C_V, the heat capacity at constant pressure C_p, and the thermal expansion coefficient α are given [15] as follows:

$$C_v = 3nk\left[4D\left(\frac{\theta}{T}\right) - \frac{3\theta/T}{e^{\theta/T}-1}\right] \quad (6)$$

$$S = nk\left[4D\left(\frac{\theta}{T}\right) - 3\ln(1-e^{-\theta/T}\right] \quad (7)$$

$$\alpha = \frac{\gamma C_v}{B_T V} \quad (8)$$

$$C_p = C_v(1+\alpha\gamma T) \quad (9)$$

Here γ represent the Grüneisen parameter and it is expressed as

$$\gamma = -\frac{d\ln\theta(\mathrm{V})}{d\ln \mathrm{V}} . \quad (10)$$

III. RESULTS AND DISCUSSION

3.1. Structural and Electronic Properties

Firstly, the equilibrium lattice parameter has been computed by minimizing the crystal total energy calculated for different values of lattice constant by means of Murnaghan's equation of state (eos) [16] as in Figure.1. The bulk modulus, and its pressure derivative have also been calculated based on the same Murnaghan's equation of state, and the results are given in Table 1 along with the experimental and other theoretical values. The calculated value of lattice parameters are 5.807 A^0 in B1 (NaCl) phase, 3.509A^0in B2 (CsCl) phase, 6.265 A^0 in B3 (ZB) phase for GdCu, respectively. The present values for lattice constants are also listed in Table 1, and the obtained results are quite accord with the other experimental values [17].

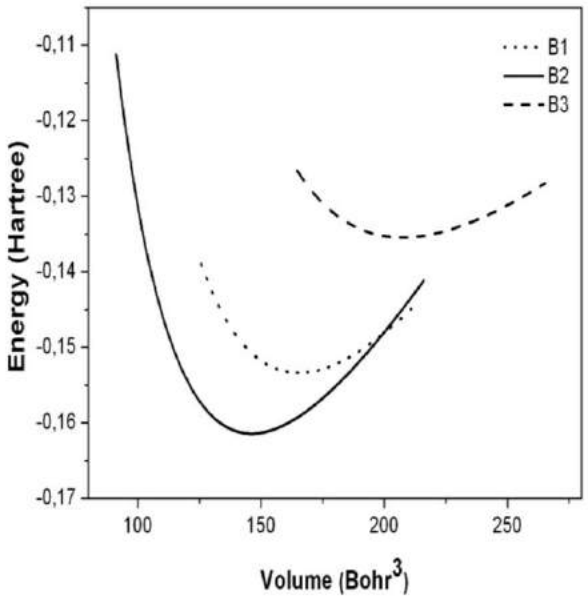

Fig.1. Total energy versus volume curve of GdCu in B1(NaCl), B2(CsCl), B3(ZB) phases.

Table1. Calculated equilibrium lattice constants (a_0), bulk modulus (B), pressure erivatives of bulk modulus (B'), formation enthalpy (ΔH) and other theoretical works for GdCu in B1, B2, B3 structures

Material	Structure	Ref.	a	B(GPa)	B'	ΔH
GdCu	B1	Present	5.807	57.233	3.728	4.54
	B2	Present	3.509	64.199	3.749	4.10
		Exp[17]	3.503			
	B3	Present	6.265	39.112	4.102	5.52

We have plotted the phase diagrams (equation of state) for B2 phase in Figure 2. We have also plotted the normalized volume pressure diagram of GdCu in B2 phase at the temperatures of 200K, 600K and 1000K in Figure 3.

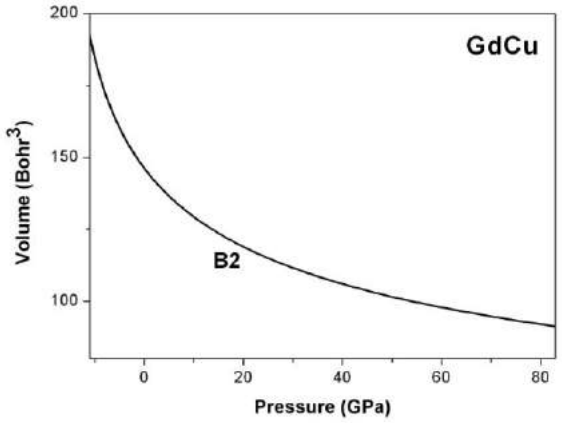

Fig. 2. Pressure versus volume curve of GdCu

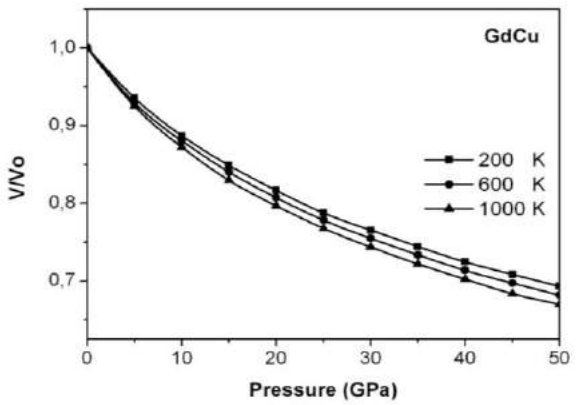

Fig. 3. The normalized volume-pressure diagram of the B2 for GdCu at different temperatures

The present first – principles code (VASP) have also been used to calculate the band structures for GdCu. The obtained results for high symmetry directions are shown in Figure 4 for B2 structures of GdCu. It can be seen from the Figure 4 that no band gap exists for studied compound, and they exhibit nearly metallic charecter. The total electronic density of states (DOS) corresponding to the present band structures are, also, depicted in Figure 4, and the disappearing of the energy gap in DOS conforms the metallic nature of GdCu. The similar stuation is observed for LaN in our recent work [18].

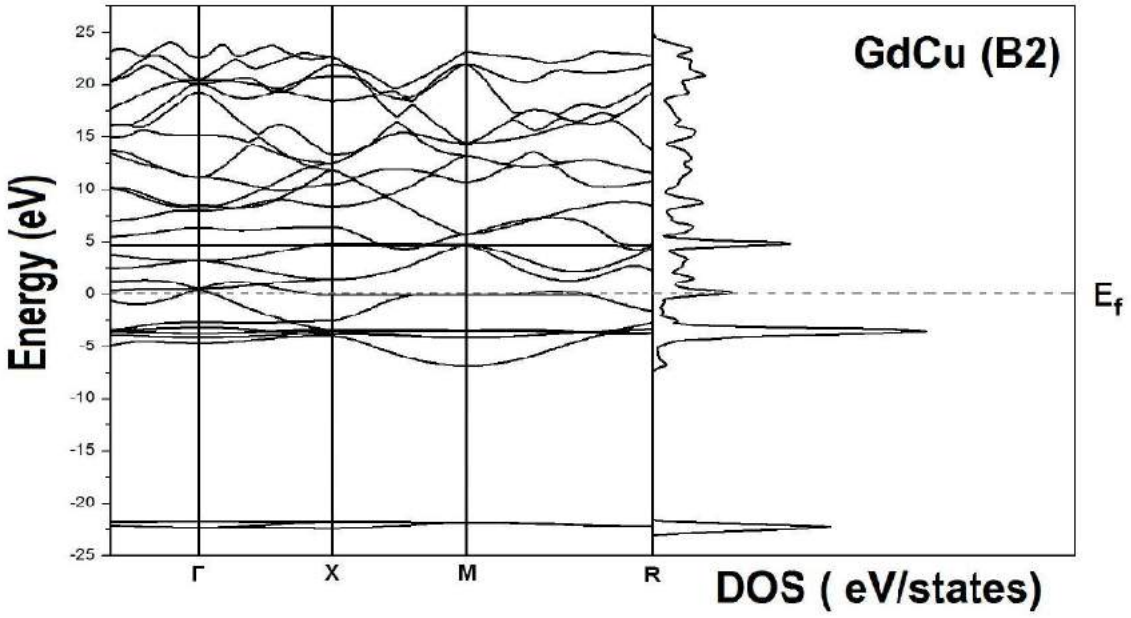

Fig. 4. Calculated band structure of GdCu in phase B2

3.2. Elastic Properties

The elastic constants of solids provide a link between the mechanical and dynamical behaviour of crystals, and give important information concerning the nature of the forces operating in solids. In particular, they provide information on the stability and stiffness of materials. Their ab-initio calculation requires precise methods, since the forces and the elastic constants are functions of the first and second-order derivatives of the potentials. Their calculation will provide a further check on the accuracy of the calculation of forces in solids. The effect of pressure on the elastic constants is essential, especially, for understanding interatomic interactions, mechanical stability, and phase transition mechanisms. It also provides valuable data for developing interatomic potentials

There are two common methods [19-20] for obtaining the elastic data through the ab-initio modelling of materials from their known crystal structures: an approach based on analysis of the total energy of properly strained states of the material (volume conserving technique) and an approach based on the analysis of changes in calculated stress values resulting from changes in the strain (stress-strain) method. Here we have used the "stress-strain" technique for obtaining the second-oreder elastic constants (C_{ij}). The listed values for C_{ij} in Table 2 are in reasonable order.

Table 2. The calculated elastic constants (in GPa unit) in different structures for GdCu

Material	Structure	C_{11}	C_{12}	C_{44}
GdCu	B1	92.784	40.321	5.627
	B2	108.699	48.170	34.392
	B3	31.684	44.128	22.188

The calculated elastic constants values of B2 structure for GdCu at 10, 20, 30, 40, 50, 60 GPa pressure values, respectively and they are also listed in Table 3.

Table 3. The elastic constants values (in GPa unit) of the B2 structure for GdCu at different pressures.

Material	Structure	Pressure (GPa)	C_{11}	C_{12}	C_{14}
GdCu	B2	10	133,27	79,16	48,65
		20	150,71	109,10	59,69
		30	167,72	135,76	69,02
		40	182,71	158,20	77,30
		50	196,79	180,26	84,45
		60	209,81	202,90	90,97

The Zener anisotropy factor *A*, Poisson ratio υ, and Young's modulus *Y*, which are the most interesting elastic properties for applications, are also calculated in terms of the computed data using the following relations [21] :

$$A=\frac{2C_{44}}{C_{11}-C_{12}}, \quad (1)$$

$$\upsilon=\frac{1}{2}\left[\frac{(B-\frac{2}{3}G)}{(B+\frac{1}{3}G)}\right], \quad (2)$$

and

$$Y=\frac{9GB}{G+3B} \quad (3)$$

where $G = (G_V + G_R)/2$ is the isotropic shear modulus, G_V is Voigt's shear modulus corresponding to the upper bound of G values, and G_R is Reuss's shear modulus corresponding to the lower bound of G values, and can be

written as $G_V = (C_{11}–C_{12} +3C_{44})/5$, and $5/G_R = 4/(C_{11}-C_{12})+ 3/ C_{44}$. The calculated Zener anisotropy factor (*A*), Poisson ratio (ν), Young's modulus (*Y*), and Shear modulus ($C'=(C_{11}-C_{12+}2C_{44})/4$) for GdCu are given in Table 4 and they are close to those obtained for the similar structural symmetry.

Table 4. The calculated Zener anisotropy factor (*A*), Poisson ratio (ν), Young's modulus (*Y*), Shear modulus (C') for GdCu in B2 structure

Material	*A*	ν	Y(GPa)	C' (GPa)
GdCu	1.136	0.282	83.811	32.328

3.3. Thermodynamics Properties

The Debye temperature (θ_D) is known as an important fundamental parameter closely related to many physical propertied such as specific heat and melting temperature. At low temperatures the vibrational excitations arise solely from acoustic vibrations. Hence, at low temperatures the Debye temperature calculated from elastic constants is the same as that determined from specific heat measurements. We have calculated the Debye temperature, θ_D , from the elastic constants data using the average sound velocity, v_m, by the following common relation given [22]

$$\theta_D = \frac{h}{k}\left[\frac{3n}{4\pi}\left(\frac{N_A\rho}{M}\right)\right]^{1/3}\upsilon_m \qquad (4)$$

where $\hbar$ is Planck's constants, k is Boltzmann's constants, N_A Avogadro's number, n is the number of atoms per formula unit, M is the molecular mass per formula unit, $\rho(=M/V)$ is the density, and v_m is obtained from

$$\upsilon_m = \left[\frac{1}{3}\left(\frac{2}{\upsilon_t^3}+\frac{1}{\upsilon_l^3}\right)\right]^{-1/3} \qquad (5)$$

where v_l and v_t, are the longitudinal and transverse elastic wave velocities, respectively, which are obtained from Navier's equations [23]:

$$\upsilon_l = \sqrt{\frac{3B+4G}{3\rho}} \qquad (6)$$

And

$$\upsilon_t = \sqrt{\frac{G}{\rho}}. \qquad (7)$$

The calculated average longitudinal and transverse elastic wave velocities, Debye temperature and melting temperature for GdCu are given in Table 5. No other theoretical or experimental data are exist for comparison with the present values.

The empirical relation [24], T_m=553 K+ (591/Mbar)C_{11} ± 300, is used to estimate the melting temperature for GdCu, and found to be 1195 ± 300K. This value is lower than those obtained for Gd (1585 K). We hope that the present results are a reliable estimation for these compounds as it contains only C_{11} which has a reasonable value.

Table 5. The longitudinal, transverse, average elastic wave velocities, and Debye temperature for GdCu in B2 structure.

Material	$\upsilon_l(m/s)$	$\upsilon_t(m/s)$	$\upsilon_m(m/s)$	$\theta_D(K)$	$T_m(K)$
GdCu	1781.53	981.00	1093.35	116.89	1195± 300

The thermal properties are determined in the temperature range from 0 to 1000 K for GdCu, where the quasi-harmonic model remains fully valid. The pressure effect is studied in the 0-50 GPa range. The relationship between normalized volume and pressure at different temperature is shown in Figure 3 for GdCu. It can be seen that when the pressure increases from 0 GPa to 50 GPa, the volume decreases. The reason of this changing can be attributed to the atoms in the interlayer become closer, and their interactions become stronger. For GdCu compound the normalized volume decreases with increasing temperature. Temperature effects on bulk modules (B) are given in Fig. 4. and can be seen that B decreases as temperature increases. Because cell volume changes rapidly as temperature increases. The relationship between bulk modulus (B) and pressure (P) at different temperatures (200, 600, and 1000K) is shown in Fig. 5. for GdCu. It can be seen that bulk modulus decreases with the temperature at a given pressure and increases with pressure at a given temperature. It shows that the effect of increasing pressure on GdCu is the same as decreasing its temperature.

The variations of the thermal expansion coefficient (α) with temperature and pressure are shown in Fig.6 and Fig.7 for GdCu, respectively. It is shown that, the thermal expansion coefficient α also increases with T at lower temperatures and gradually approaches linear increases at higher temperatures, while the thermal expansion coefficient α decreases with pressure. At different temperature, α decreases nonlinearly at lower pressure and decreases almost linearly at higher pressure. Also, It can be seen from Fig. 6 that the temperature

dependence of α is very small at high temperature and higher pressure.

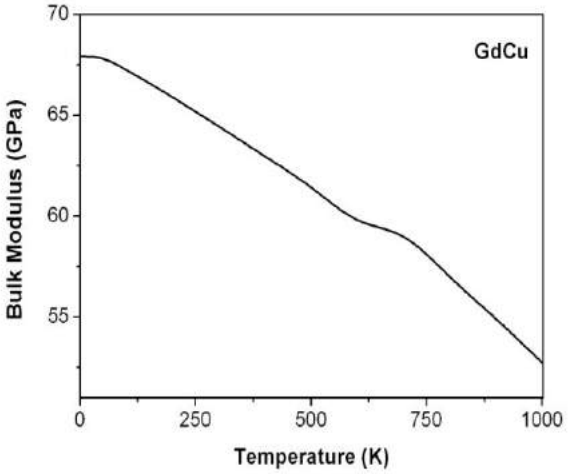

Fig.4. The bulk modulus (B) for GdCu as a function temperature T at P=0.

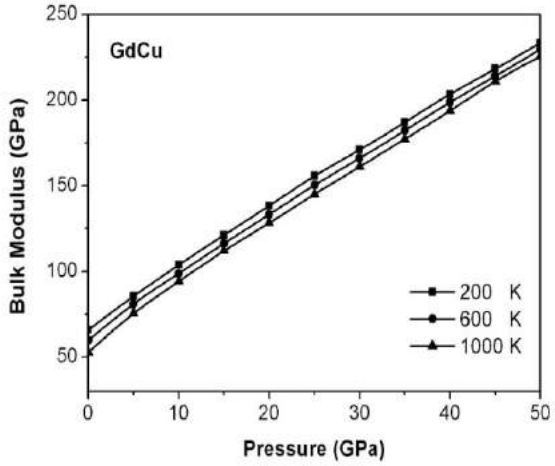

Fig.5. The reletionships of GdCu between bulk modulus (B) and pressure P at temperatures of 200 K, 600 K, 1000 K

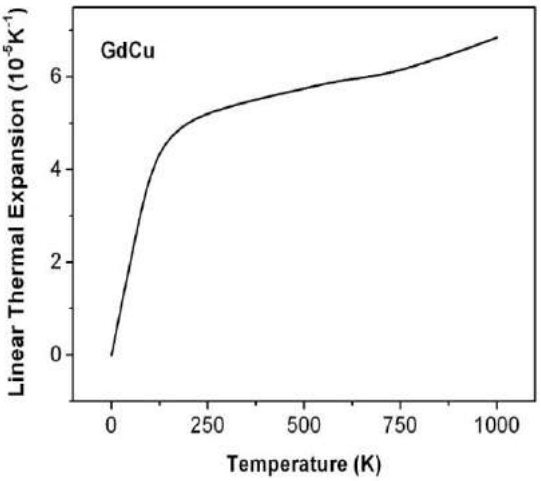

Fig. 6. The thermal expansion versues temperature for GdCu.

The relationship between heat capacity at constant pressure C_p and temperature, also the relationship between capacity at constant volume C_v and temperature at different pressures P are shown in Fig.8 for ReB. It is realized from figures that when T<500 K, C_v increases very quickly with temperature; when T>500 K, C_v increases slowly with temperature and it almost approaches a constant called as Dulong-Petit limit ($C_v(T)$~3R for mono atomic solids) at higher temperatures for GdCu.

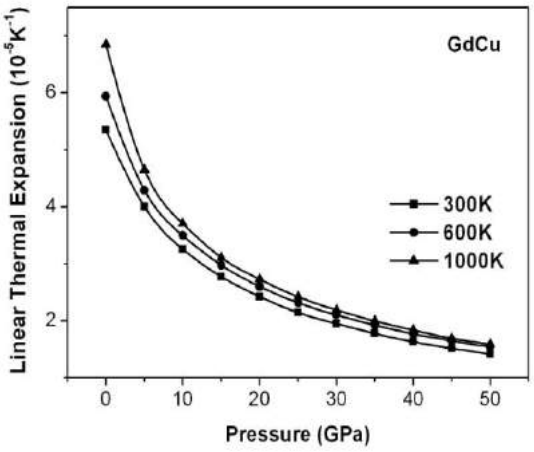

Fig. 7. The thermal expansion versues pressure for GdCu.

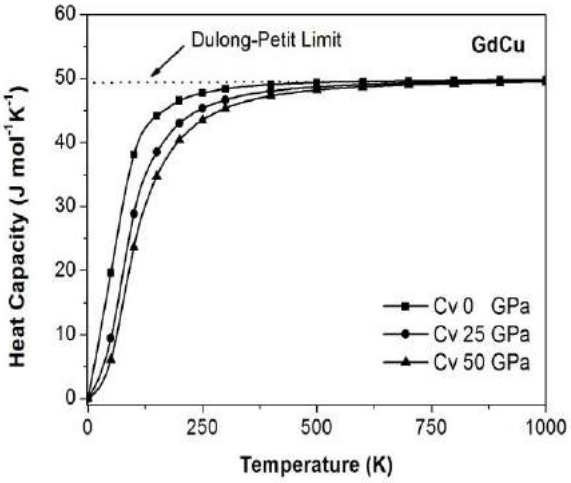

Fig. 8. The heat capacity with temperature at different pressure for GdCu

IV. CONCLUSIONS

The fist–principles pseudopotential calculations have performed on the GdCu. Our present key results are on the elastic, electronic and structural properties for GdCu. The lattice parameters are excellent agreement with the other theoretical values. The computed band structures for GdCu shows metallic character. It is hoped that some our results, such as elastic constants, Debye temperatures, and melting temperatures estimated for the first time in this work, will be tested in future experimentally and theoretically.

We hope this study will help us to have a better understanding of elastic and thermodynamic properties of GdCu, whose magnetic properties are emphasized mostly.

[1]. *K. Thkei, Y. Ishibwa, N. Watanabe and K..Tajima* Phys. Soc. Japan 47 (1979) 888

[2]. *A.V Postnikov et al*. J. Phys: Condens. Matter 4 2475-2486. (1992)

[3]. *G. Kresse and J. Hafner*, Phys. Rev. B , 47(1994)558

[4]. *G. Kresse and J. FurthmÄuller*, Phys. Rev. B, 54 (1996) 11169.

[5]. *G. Kresse and D. Joubert* , Phys. Rev. B, 59 (1999) 1758.

[6]. *P. E. Blochl*, Phys. Rev. B, 50 (1994) 17953.

[7]. *J. P. Perdew and A. Zunger*, Phys. Rev. B, (1981)23 5048.

[8]. *J. P. Perdew, J. A. Chevary, S. H. Vosko, K .A .Jackson, M. R. Pederson, D. J. Singh*
H.J. Monkhorst and J.D. Pack, Phys. Rev. B, 13(1976) 5188.

[9]. *M.A. Blanco, E. Francisco, V. Lunana.* , Comput. Phys. Commun. , 158 (2004)57

[10]. F. *Peng, H.Z. Fu, X.D. Yang* , Physica B , 403 (2008) 2851.

[11]. *M.A. Blanco, A.M. Pendàs, E. Francisco, J.M.Recio, R. Franko*, J.Mol. Struct. (Theochem)368 (1996) 245

[12]. *M. Flórez, J.M. Recio, E. Francisco, M.A.Blanco, A.M. Pendàs,* Phys. Rev. B , 66 (2002) 144112.

[13]. *E. Francisco, , J.M. Recio, M.A. Blanco, A.M.Pendàs, J. Phys. Chem.* ,102 (1998) 1595.

[14]. *R. Hill, Proc. Phys. Soc. Lond. A* , 65 (1952) 349.

[15]. *F. D. Murnaghan,* Proc. Natl., Acad. Sci. USA 30, 5390 (1994)

[16]. *A. Iandelli and A. Palenzona* J. Less-Common Metals 9 1 (1965a)

[17]. *Y.O. Ciftci, K.Colakoglu, E.Deligoz, and H. Ozısık,* Mat. Chem. And Phys., 108 (2008) 120.

[18]. *J. Mehl*, Phys. Rev. B 47 (1993) 2493.

[19]. *S.Q. Wang, H.Q. Ye*, Phys. Status Solidi B 240 (2003) 45.

[20]. *B. Mayer, H. Anton, E. Bott, M. Methfessel*, J. Sticht, and P. C. Schmidt, Intermetallics 11 (2003) 23.

[21]. *I. Johnston, G.Keeler, R. Rollins, and S.Spicklemire*, Solid State Physics Simulations, The Consortium for Upper-Level Physics Software, Jhon Wiley, New York, 1996.

[22]. *E. Schreiber, O. L. Anderson, N. Soga,* Elastic Constants and their Measurements, McGraw-Hill, New York, 1973.

[23]. *M.E. Fine, L.D. Brown, H.L. Marcus,* Scr. Metall. 18 (1984) 951.

FUNCTIONAL POLYMERS/ORGANO-CLAY HYBRID NANOCOMPOSITES THROUGH ACID/AMINE FUNCTIONALIZED MONOMER AND POLYMER NANOFILLERS

AMIR SEPEHRIANAZAR[1], NAGIHAN CAYLAK[2], ZAKIR M. O. RZAYEV[3]

[1]Department of Chemical Engineering, Islamic Azad University, Ahar Branch, 54516 Iran, amir@hacettepe.edu.tr

[2]Department of Physics, Sakarya University, 54187 Sakarya, Turkey,caylak@sakarya.edu.tr

[3]Department of Chemical Engineering, Hacettepe University, 06800 Ankara, Turkey, zmo@hacettepe.edu.tr

The functional polymers/organo-clay hybrid nanocomposites were prepared by (a) intercalation of acid/amine functionalized monomers (vinyl sulfonic, maleic and itaconic acids, allyl amine) and their homo- and copolymers, (b) *in-situ* copolymerization of pre-intercalated functional monomer with acrylic comonomers (alkyl acrylates, acrylamide, etc.) and (c) melting reactive extrusion *in situ* processing using pre-intercalated monomer(polymer)/organo-silicate systems as compotibilizer-nanofillers and isotactic polypropylene as a non-polar matrix. The 'structure–composition–properties' relationships as a function of nanostructural formation in the prepared systems were investigated by the various methods (spectroscopy, XRD, DSC-TGA, DMA and SEM). It was demonstrated that the pre-intercalation factor and strong H-bonding interactions between the monomer/polymer and the organo-silicate layers are critical to the formation of polymer-layered silicate nanocomposites with the greatly improved dispersion states.

I. INTRODUCTION

Nanotechnology is set to have a broad impact across many industrial sectors, including; packaging, wire and cable, automotive, pipes and tubing, and construction. Clear property advantages demonstrated by nanocomposites in comparison to conventional thermoplastic and thermosetting polymers and inorganic fillers. In addition to the observed improvements in performance, lower loading levels of nanofiller are required in comparison to conventional fillers to achieve the same desired effect, resulting in lighter weight materials and materials with similar structural dimensions but superior properties.

Although nanocomposites are realising many key applications in numerous industrial fields, a number of key technical and economic barriers exist to widespread commercialisation. These include impact performance, the complex formulation relationships, and routes to achieving and measuring nanofiller dispersion and exfoliation once in the polymer matrix. In the last years, nanomaterials have attracted substantial attention due to their high performance physical and mechanical properties, when compared with those of the conversional polymer composites. To synthesize polyolefin and polystyrene polymer nanocomposites, many researchers usually utilized functionalized polymers [1-3] as reactive compatibizers, which can easily intercalate the organo-modified montmorillonite (MMT) clay [4,5].

The organic-inorganic nanocomposites have attracted great interest to many researchers because they frequently exhibit unexpected hybrid properties synergistically derived from the two components [6-10]. One of most promising composite systems would be nanocomposites based on organic polymers, including anhydride functionalized polyolefins, and inorganic clay minerals consisting of silicate layers [11-13]. In clay structures of the montmorillonite (MMT) type the single silicate later have a thickness of about 1 nm and typically lateral dimensions of several hundred nanometres up to micrometers. These layers are arranged in stacks with regular interstices called interlayer galleries. Due to the small dimensions of the organo-clay particles and the resulting high surface-to-volume ratio, nanocomposites exhibit, even at low nanofiller concentrations, high performance properties [14]. Heinz et al.[15] investigated the structure and dynamics of alkyl ammonium-modified MMT clays with different cation exchange capacity (CEC), ammonium head groups, and chain length by computational molecular dynamics simulation for a large set of structures and compared to a wide array of experimental data (X-ray, IR, NMR, and DSC). They found that the relationship between computational and experimental data is very complementary in the 44 various O-MMT systems. According to the authors, the size of the computational data set surpasses prior experimental work in the area and will provide guidance in the choice of alkyl modifiers for interactions with solvents, polymers, and other nanoscale building blocks.

In the last decade, the alternating, random and graft copolymers of maleic anhydride (MA) and its isostructural analogues widenly utilized for the preparation of polymer/organo-silicate (or silica) hybrid materials through melt compounding by reactive extrusion and sol-gel methods. However, interlamellar copolymerization of MA and/or its pre-intercalated complexes with organo-clays, as well as MA copolymer/organo-clay composition–nanostructure–property relationships not have been investigated. Synthesis and characterization of some selective functional copolymer/organo-silicate or silica hybrid nanocomposites were a subject our previous publications [16-31]. This work presents the synthesis of novel type of functional polymer/MMT hybrid nanocomposites by intercalation/exfoliation of poly(allyl amine), poly(vinyl sulfonic acid), poly(acrylic acid),

maleic and itaconic acid monomers and their graft copolymers between MMT or organo-MMT clay layeres. Synthesized intercalated monomer/organo-MMT complexes and polymer/MMT systems were utilized as reactive nanofillers in the intercalative copolymerization and as compatibilizer-nanofillers for the polyolefin blends *in situ* processing via compounding in melt by reactive extrusion. The effects of the complex-formation between the functional monomer/polymer and the silicate layers of organo-clays were investigated. It was found that the pre-intercalation effect (modification of organo-silicate with functional monomers before *in situ* copolymerization) and strong H-bonding between the monomer/polymer and the silicate layers are critical to the formation of polymer-layered silicate nanocomposites. By introducing the strong H-bonding to the polymer/organo-clay hybrids through intercalation, the dispersion states of these hybrids and their thermal and dynamic mechanical properties, and morphology were significantly improved.

II. EXPERIMENTAL

Materials. *n*-Butyl methacrylate **(**BMA, allyl amine (AAm) and vinylsulfonic acid (VSA) monomers (Aldrich-Sigma, Germany) were purified before use by distillation under modernate vacuum. Maleic (MA), itaconic (IA) and acrylic (AA) acid monomers (Fluka, Switzerland) were purified by recrystallization and sublimation techniques. The α,α'-azoisobutyronitrile (AIBN) (Fluka) was recrystallized twice from methanol solution. MMT (Fluka) and DMDA-MMT orgnoclay was obtained from Bensan (Enez, Turkey). Full characteristic parameters of organo-clay were presented in our recently published works [16,17]. Poly(AAm) and poly(VSA) homopolymers were purified before use by precipitation from water solution with methanol. All other solvents and reagents were analytical grade and used without purification.

Synthesis. *Monomer/Organo-silicate Complex:* Functional monomer (M_1: MA, IA, AAm or VSA) was dispersed in methyl ethyl ketone (MEK)/DMDA-MMT mixture at monomer/organo-clay (or vigin MMT) molar ratio of 1:2 by intensive mixing at 50 ^oC for 3 h to prepare the intercalated complex of M_1 with organo-MMT. Then prepared mixture treated by lage amount of methanol at 20 ^oC by intesive mixing up to full precipitation of powder product, which is isolated by filtration, and draying under vacuum.

Intercalative complex-radical copolymerization: An appropriate amount of BMA monomer and AIBN was added to reaction mixture containing given amount of dispersed in MEK (or ionized water) M_1...Organo-MMT complex and heated with intensive mixing at 65^oC under nitrogen atmosphere for 24 h. Prepared hybrid composition was isolated by precipitation with methanol, then washed with several portions of diethyl ether and benzene, and dried under vacuum at 60^oC.

Compounding in melt by reactive extrusion: An appropriate amount of PP as a matrix polymer, pre-intercalated functional polymers (PAAm, PVSA or PAA)/MMT or copolymers (poly(M_1-co-BMA)/organo-MMT or PP-g-M_1) as compatibilizer-nanofiller were mixing by Lab.Rondon type twin screw extruder with biaxially oriented film-forming unit using the following operational conditions: the temperature profile 165, 170, 175 and 180^oC; screw speed rate 15-30.

III. CHARACTERIZATION

Structure, composition and properties of the synthesized functional monomers/organo-MMT, functional polymer/ MMT and polyolefin/functional polymer/organo-MMT hybrid nanocomposites were investigated by FTIR, (^1H and ^{13}C) NMR spectroscopy, X-ray diffraction (XRD), dynamic mechanic analysis (DMA), DSC-TGA thermal analysis and scanning electron microscopy (SEM) methods.

IV. RESULTS AND DISCUSSION

General schema of *in-situ* complex-formation and intercalative copolymerization reactions can be represented as follows (Figures 1 and 2):

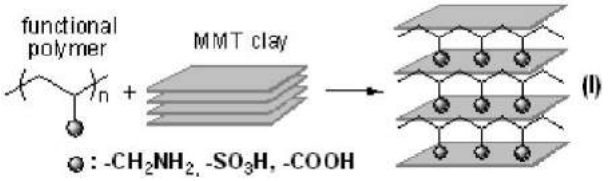

Fig. 1. Intercalation of functional polymer chains between silicate layeres. Functional polymers: poly(allyl amine), poly(sulfonic acid) and poly(acrylic acid).

Physical structure of synthesized pre-intercalated M_1…O-MMT monomer and functional polymers/ MMT complexes, as well as nanocomposites were investigated by XRD analysis method. It was showed that $d_{(001)}$ and $d_{(002)}$ values for crystallographic planes depening on the interlamellar complex formation and exfoliation of polymer chains into the silicate lamellae. Better intercalation is evidenced by the shift of 2θ values to the lower region and increasing $d_{(001)}$-spacing. Taking into the consideration that the surface area of organoclay is modified by DMDA at approximately 30 %, intercalation degree (ID) of a complexed M_1 monomer can be estimated to be approximately 95.0 % for $d_{(001)}$ and 100 % for $d_{(002)}$, respectively. The results of XRD analysis of nanocomposites show the following changes in XRD spectra: (1) disappearance of peaks at 2θ 5.20^o (d = 16.98 Å) and 8.94^o (d = 9.88 Å) and exfoliation of the silicate lamellar in XRD spectra of nanocomposites relating to 1:2 layered structure in pristine organo-MMT clay, (2) essential shift of characteristic peak at 2θ 3.62^o to lower region (2.04^o) which accompanied with increase of $d_{(001)}$ value from 24.38 Å for pristine organo-clay to around 32.81-36.05 Å for nanocomposites, increase of flexible butyl ester side-chain linkages provides relatively easily exfoliation process copolymer chains unlike decreasing M_1 complexed organo-clay in the feed copolymerizing mixtures, and (3) the formation of semi-crystalline structure in nanocomposites unlike full amorphous

structure of virgin copolymers. This observed facts allowed us to propose that the intercalative copolymerization of M_1…O-MMT with BMA comonomer was predominantly carried out through exfoliation of copolymer chains due to effects of interfacial interaction through strong H-bonding and internal plasticization of branched *n*-butyl ester linkages (Figure 2).

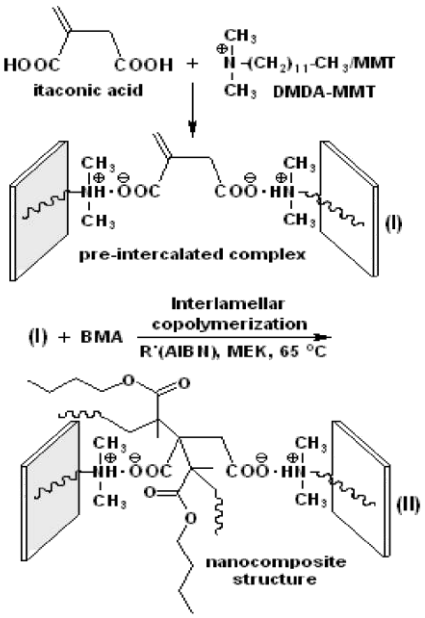

Fig.2. Intercalative complex-radical copolymerization of monomer complex of IA-COOH**...**$N(CH_3)_2$-DMDA-MMT with *n*-butyl methacrylate (BMA): (I) structure of pre-intercalated monomer complex and (II) poly(IA-*co*-BMA)/O-MMT nanocomposite.

In this work, a new approach to synthesize functional copolymer/organoclay nanocomposites by complex-radical intercalative copolymerization of pre-intercalated M_1**…**O-MMT complex and functional polymer/MMT as a 'nano-reactor' with BMA comonomer as internal plasticization agent was also described. The results of the comparative XRD and DMA analyses of copolymers and their nanocomposites indicate that the observed effects of interlayer complex formation and internal plasticization of the flexible *n*-butyl ester linkages play an important role in intercalative copolymerization and intercalation/exfoliation in situ processes. In general, an increase in the amount of flexible *n*-butyl ester linkages leads to significantly lower T_g values, and therefore, to an easier exfoliation process of copolymer chains into organo-clay galleries due to the internal plasticization effect of BMA units. On the other hand, complex-formation between M_1 units and ammonium cations of organoclay layered surface increases the force of interfacial interaction between organic (copolymer chains) and inorganic phases. This pre-intercalated monmer and polymer complexes also play an important role as a reactive compatibilizer in the formation of nano-structural architectures with given thermal and dynamic mechanical properties.

Physical structure of synthesized pre-intercalated IA**…**O-MMT monomer complex and poly(IA-*co*-BMA)s/O-MMT nanocomposites were investigated by XRD analysis method. Obtained results of XRD analysis of complex, pristine O-MMT, and nanocomposites were illustrated in Figure 3.

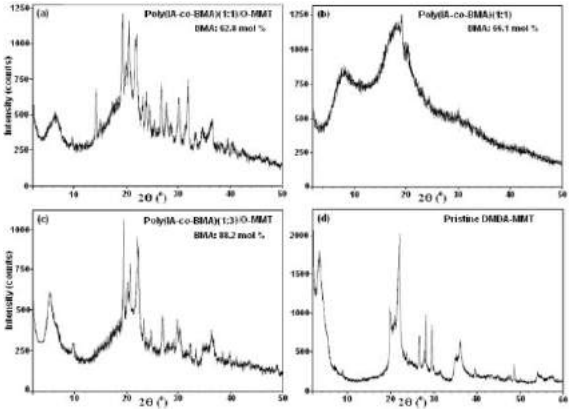

Fig.3. XRD spectra of poly(IA-*co*-BMA)s/O- MMT nanocomposites containing different amount of BMA units (mol %): (a) 62.8, (b) 82.8 and (c) 88.2, and (d) pristine DMDA-MMT clay.

As seen from these data, $d_{(001)}$ and $d_{(002)}$ values for crystallographic planes depening on the interlamellar complex formation and exfoliation of copolymer chains into the silicate lamellae. Better intercalation is evidenced by the shift of 2θ values to the lower region (from 3.62° for pristine organoclay to 2.54° for IA…DMDA monomer complex) and increasing $d_{(001)}$-spacing parameters (from 24.38 Å to 34.77 Å, respectively). Taking into the consideration that the surface area of organoclay is modified by DMDA at approximately 30 %, intercalation degree (ID) of a complexed MA monomer can be estimated to be approximately 95.0 % for $d_{(001)}$ and 100 % for $d_{(002)}$, respectively. The results of XRD analysis of nanocomposites show the following changes in XRD spectra: (1) disappearance of peaks at 2θ 5.20° (d = 16.98 Å) and 8.94° (d = 9.88 Å) and exfoliation of the silicate lamellae in XRD spectra of nanocomposites relating to 1:2 layered in pristine DMDA-MMT clay, (2) essential shift of characteristic peak at 2θ 3.62° to lower region (2.04°) which accompanied with increase of $d_{(001)}$ value from 24.38 Å for pristine organoclay to around 32.81-36.05 Å for nanocomposites, increase of flexible butyl ester side-chain linkages provides relatively easily exfoliation process copolymer chains unlike decreasing IA complexed organoclay in the feed copolymerizing mixtures, and (3) the formation of semi-crystalline structure in nanocomposites unlike full amorphous structure of virgin copolymers. This observed facts allowed us to propose that the interlamellar copolymerization of IA**…**O-MMT with BMA comonomer was predominantly carried out through exfoliation of copolymer chains due to effects of interfacial interaction through strong H-bonding and internal plasticization of branched *n*-butyl ester linkages.

Dynamic mechanical analysis (DMA) method allow to determine the loss tan δ, the storage modulus (*G*') and the loss modulus (*G*") as a function of temperature. The loss tan δ is equal to be the ratio of *G*"/*G*', which is exhibited the higher responsive to the chemical and physical structural changes and phase transitions of polymer system; the storage modulus *G*' is associated with the elastic modulus of the polymer or its composite; the loss modulus *G*" is related to the energy lost (damping factor) as a result of the friction of polymer chain movement. The results of the comparative DMA analysis of pure poly(IA-*co*-BMA)(1:2) and poly(IA-*co*-BMA) (1:2)/Organo-MMT nanocomposites, and therefore, DMA parameters as functions of temperature and content of flexible BMA unit were illustrated in Figure 4.

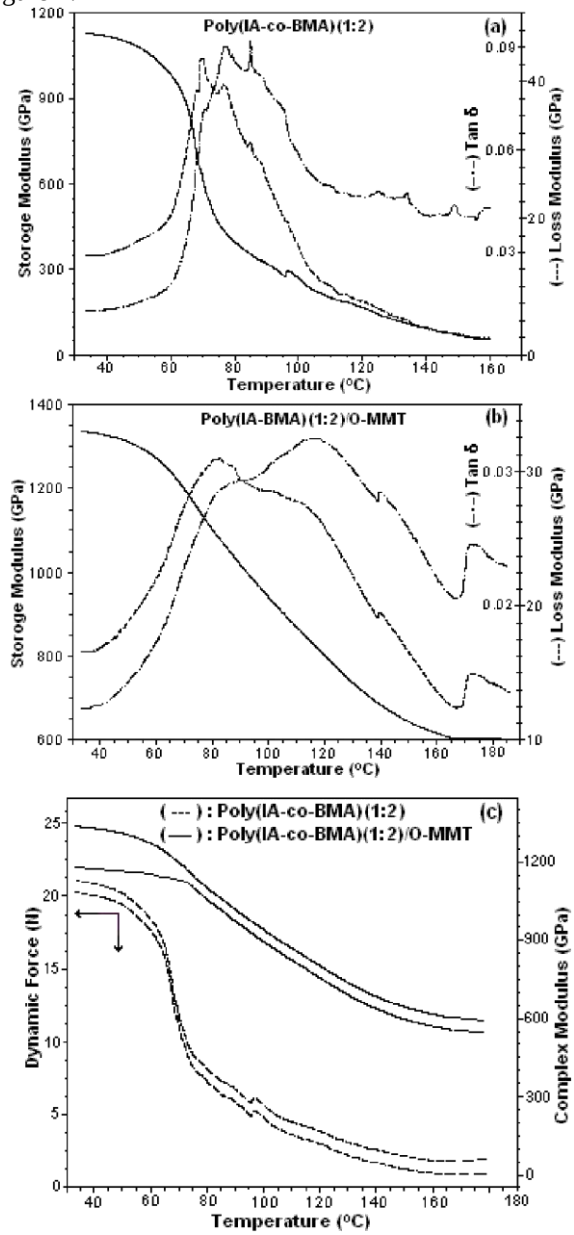

Fig.4. DMA curves of poly(IA-*co*-BMA)(1:2) and its nano-composite: (a) plots of (−) SM (*G*'), (--) LM (*G*") and (- -) Tan δ (*G*"/G') vs. temperature for the (a) copolymer and (b) copolymer/O-MMT; (c) plots of CM and DF temperature for the (---) copolymer and (–) copolymer/O-MMT.

The obtained results indicate the following changes of DMA curves when copolymer is exfoliated between organo-silicate layers by interlamellar complex-radical copolymerization of pre-intercalated H-bonding IA**…**Organo-MMT complex with BMA comonomer: (1) increase of the elastic modulus i.e., increase of the relaxation temperature from 58.3 ^{o}C up to 62.8 ^{o}C, (2) increase of the glass transition behaviour from 60.1 ^{o}C to 74.2 ^{o}C, (3) unlike pure copolymer, which has two peaks for the flexible BMA segments at 59.3 ^{o}C and rigid IA units at 80.9 ^{o}C, respectively, copolymer nanocomposites (Figure 4a) exhibits single broad peak with higher intensity at 67.9 ^{o}C; the significant increase in intensity of this peak indicates that relaxations of the flexible BMA segments decreased due to the increase of interfacial adhesion strength, i.e., the highest interaction between anhydride units and organo-MMT (Figure 4b). Dynamic force (DF) and complex modulus (CM) as functions of temperature and content of flexible BMA unit were illustrated in Figure 4c.

Observed significant difference (Δ) between these parameters [Δ = DF (nanocomposite)–DF(copolymer)] or [Δ = CM(nanocomposite)–CM(copolymer)] above T_g, relating to copolymer and its nanocomposite, can be described as a function for the formation of nano-structural architecture in poly(IA-*co*-BMA)/organo-MMT system. It can be proposed that Δ value is also characterized interfacial adhesion strength depending on the flexibility and hydrophobic/hydrophilic balance of the functional polymer chains and their ability to form interfacial complexes. The maximum values of Δ were observed around 85-95 ^{o}C corresponding to the lower values of DF and CM parameters. The obtained DMA parameters were summarized in Tables 1and 2.

As seen from the DMA analysis data, change of the amount of flexible BMA units in the copolymers and nanocomposites visible decreased the values of storage modulus and complex viscosity at temperature interval changing from 45^{o}C to 100^{o}C. These observed changes were exhibited at relatively higher values of storage modulus for the nanocomposites due to their rigid structures as comparison with virgin copolymers.

Synthesized hybrids may be utilized as nano-films and nano-coatings in the in-line coating processing for surface modification of various thermoplastic films, as reactive compatibilizer-nanofillers for the reactive thermoplastic polymer blends, especially for the acrylic polymer based systems, and also as components of the various nanomaterials prepared in melt by reactive extrusion *in situ* processing.

V. CONCLUSIONS

This report presents the synthesis of novel type of functional polymer/MMT hybrid nanocomposites by intercalation/exfoliation of poly(allyl amine), poly(vinyl sulfonic acid), poly(acrylic acid), maleic and itaconic acid monomers and their graft copolymers between MMT or organo-MMT clay layeres. Synthesized intercalated monomer/organo-MMT complexes and polymer/MMT

systems were utilized as reactive nanofillers in the nanofillers for the polyolefin blends in situ processing via compounding in melt by reactive extrusion. Structure, composition and properties of the synthesized functional monomers/organo-MMT, functional polymer/MMT and polyolefin/functional polymer/organo-MMT hybrid nanocomposites were investigated by FTIR, (^{1}H and ^{13}C) NMR spectroscopy, X-ray diffraction (XRD), dynamic mechanic analysis (DMA), DSC-TGA thermal analysis and scanning electron microscopy (SEM) methods. The effects of the complex-formation between the functional monomer/polymer and the silicate layers of organo-clays were investigated. It was found that the pre-intercalation effect (modification of organo-silicate with functional monomers before *in situ* copolymerization) and strong H-bonding between the monomer/polymer and the silicate layers are critical to the formation of polymer-layered silicate nanocomposites. By introducing the strong H-bonded linkages to the polymer/organo-clay hybrids through intercalation, the dispersion states of these hybrids and their thermal and dynamic mechanical properties, and morphology were significantly improved.

ACKNOWLEDGEMENTS

The authors thank the Türkish Scientific and Technical Research Council (TÜBİTAK), and Science and Research Unit (BAB) of Hacettepe University for the financial supports of this work through Projects TBAG-HD/249 and BAB(DPT)-K120930, respectively.

Table 1. DMA parameters of functional copolymers and their nanocomposites.

Copolymes and nanocomposites different amounts of units (mol. %)	DMA parameters* : T_α relaxation (°C)					
	T (*G*')	*T* (*G*")	Tg δ (*G"*/G')	*T* (DV)	*T* (FM)	Δ(N) (DF_c-DF_n)
Poly(IA-*co*-BMA)(66.1)	82.6	100.5 107.1	112.7	100.5	100.4	-
Poly(IA-*co*-BMA)(62.8)/O-MMT	79.1	89.3 93.6	98.8	94.0	86.9	2.27
Poly(IA-*co*-BMA)(87.2)	62.9	69.7 76.7	77.3 84.9	69.5 76.7	67.3	-
Poly(IA-*co*-BMA)(82.8)/O-MMT	59.9	81.7	91.1 115.7	81.7 101.1	75.3	10.59
Poly(IA-*co*-BMA)(92.8)	53.3	62.5 76.5	79.2 120.5	62.5 76.7	63.1	-
Poly(IA-*co*-BMA)(88.2)/O-MMT	70.4	84.0 155.8	95.9 160.2	84.9 157.3	97.2	12.23

*G'(onset) is storage modulus (MPa), $G^{"}$ (onset) is loss modulus (MPa), DV is dynamic viscosity (MPa.s), FM is flexural modulus (MPa) and $\Delta = DF_c - DF_n$ (DF_c and DF_n are dynamic forces of copolymer and nanocomposite, respectively).

Table 2. DMA results of poly(IA-*co*-BMA)s with different composition and their nanocomposites. Effect of flexible BMA unit and tempeature.

Copolymers with different contents of flexible BMA units (mol.%)*	SM (MPa) x10^5 at (^{o}C)			CV (MPa.s) x10^5 at (^{o}C)		
	45	70	100	45	70	100
Poly(IA-*co*-BMA)(66.1)	11.25	10.40	6.56	0.62	0.58	0.37
Poly(IA-*co*-BMA)(62.8)/O-MMT	10.80	10.11	4.10	0.60	0.56	0.23
Poly(IA-*co*-BMA)(87.2)	11.03	6.09	2.69	0.61	0.34	0.15
Poly(IA-*co*-BMA)(82.8)/O-MMT	13.22	11.98	9.41	0.73	0.66	0.52
Poly(IA-*co*-BMA)(92.8)	12.00	8.35	5.12	0.66	0.46	0.28
Poly(IA-*co*-BMA)(88.2)/O-MMT	14.13	13.50	11.13	0.78	0.75	0.62

*Copolymer compositions (amount of BMA units) were determined by alkali titration of itaconic acid units.

[1]. *Y. Tang, Y. Hu, L. Song, R. Zong, Z. Gui, Z. Chen, W. Fan*, *Polym. Degrad. Stab.* 82, 127 (2003).
[2]. *S. Sı, D. D. Jiang, C. A. Wilkie*, *Polym. Degrad. Stab.* 84, 279 (2004).
[3]. *W. Xu, G. Liang, H. Zhai, S. Tang, G. Hang, W. P. Pan*, *Eur. Polym. J.* 39, 1467 (2003).
[4]. C. Ding, D. Jia, H. He, B. Guo, H. Hong, *Polym. Test.* 24, 94 (2005).
[5]. *G. Gorras M. Tortora, V. Vittoria, D. Kaempfer, R. Mulhaupt*, *Polymer* 44, 3679 (2003).
[6]. *L. L. Beecroft, C. K. Ober*, *Chem. Mater.* 9, 1302 (1997).
[7]. *E. P. Giannelis*, *Adv. Mater.* 8, 29 (1996).
[8]. *G. Lagalay*, *Appl. Clay Sci.* 15, 1 (1999).
[9]. *Linnemann, A., et al.,* Phys. Lett. B 554,15(2003).
[10]. *Maser, H., et al.,* Phys. Rev. C 54, R2129 (1996).
[11]. *E. Passaglia, R. Sulcis, F. Ciardelli, M. Malvaldi, P. Narducci*, *Polym. Int.* 54, 1549 (2005).
[12]. *N. Nasegawa, H. Okamoto, M. Kawasumi, M. Kato, A. Tsukigase, A. Usuki*, *Macromol. Mater. Eng.*, 280/281, 76 (2000).
[13]. *N. Nasegawa, H. Okamoto, A. Usuki*, *J. Appl. Polym. Sci.* 93, 758 (2004).
[14]. *M. Böhning, H. Goering, A. Fritz, K.-W. Brzezinka, G. Turky, A. Schönhals*, Schartel, *Macromolecules* 38, 2764 (2005).
[15]. *H. Heins, R. A. Vaia, R. Krishnamoorti, B. L. Farmer, Chem. Mater.* 19, 59 (2007).
[16]. *Z. M. O. Rzaev, A. Yilmazbayhan, E. Alper*, *Adv. Polym. Technol.* 26, 41 (2007).
[17]. *Söylemez, Çaylak N., Rzaev Z. M. O. eXPRESS Polym. Letters* 2, 639 (2008).
[18]. *Rzayev Z. M. O.*: Nanotechnology methods in polymer engineering. Proc.4th Nanosci. nanotechnol. Conf., 11-14 June, 2007, Bilkent, Ankara-Turkey, p. 154.
[19]. *G. Kibarer, Z. M. O. Rzayev, D. Demircan*, Synthesis of poly(α-olefin-*alt*-maleic anhydride)/inorganic hybrid nanocomposites using sol-gel and interlamellar polymerization methods. Proc. 4th Nanosci. Nanotechnol. Conf., 11-14 June, 2007, Bilkent, Ankara-Turkey, p. 214.
[20]. *Z. M. O. Rzaev, H. K. Can, A. Güner*, *J. Appl. Polym. Sci.* 90, 4009 (2003).
[21]. *Z. M. O. Rzaev, A. Güner, H. K. Can*, A. Aşıcı, *Polymer* 42, 5599 (2001).

ELECTRONIC BAND STRUCTURE AND OPTICAL PROPERTIES OF Sb_2S_3 AND Sb_2Se_3: AB INITIO CALCULATION

HUSNU KOC, AMIRULLAH M. MAMEDOV
Physics Department, Cukurova University, Adana, Turkey
hkoc@student.cu.edu.tr, mamedov@cu.edu.tr

The electronic band structures, density of states (DOS) and optical properties of V_2-VI_3 -type binary compounds, Sb_2S_3 and Sb_2Se_3, are investigated using the density functional theory and pseudopotential theory under the local density approximation (LDA). The obtained electronic band structure show that Sb_2S_3 and Sb_2Se_3 crystals have the indirect forbidden gap of 0.7278 eV and 0.62 eV, respectively. The structural optimization for Sb_2S_3 and Sb_2Se_3 have been performed using the LDA. The valance band in our calculations is composed of the 3s and 3p states of the S atom and 4s and 4p states of the Se atom, 5s and 5p states of Sb, while the conduction band consists of the 5p states of the Sb, S and Se atoms. The result of Sb_2S_3 and Sb_2Se_3 have been compared with the experimental results and have been found to be in good agreement with these results. The linear photon-energy dependent dielectric functions and some optical properties such as the energy-loss function, the effective number of valance electrons and the effective optical dielectric constant are calculated.

I. INTRODUCTION

Sb_2S_3 and Sb_2Se_3, a member of compounds with the general formula V_2-VI_3 (V=Bi, Sb and VI=S, Se) are layer structured semiconductors with orthorhombic crystal structure (space group Pnma; No:62), in which each Sb-atom and each Se/S-atom is bound to three atoms of the opposite kind that are then held together in the crystal by weak secondary bond [1,2]. These crystal have 4 Sb_2B_3 (B=S, Se) molecules in a unit cell. Therefore, these compounds have a complex structure with 56 valance electrons per unit cell. In the last few years, Sb_2Se_3 has received a great deal of attention due to its switching effects [3] and its excellent photovoltaic properties and high thermoelectric power [4], which make it possess promising applications in solar selective and decorative coating, optical and thermoelectric cooling devices [5]. On the other hand, Sb_2S_3 has attracted attention for its applications as a target material for television cameras [6,7], as well as in microwave [8], switching [9], and optoelectronic devices [10-12].

Kuganathan et al [13] used density functional methods as embedded in the SIESTA code, to test the proposed model theoretically and investigate the perturbations on the molecular and electronic structure of the crystal and the SWNT (single walled carbon nanotubes) and the energy of formation of the Sb_2Se_3 @ SWNT composite. Caracas et al [14] computed the valance electron density, the electron band structure and the corresponding electronic density-of-states (DOS) of A_2B_3 (A=Bi, Sb and B=S, Se) compounds using the density functional theory. As far as we know, no ab initio general potential calculations of the optical properties of Sb_2S_3 and Sb_2Se_3 have been reported in detail.

In the present work, we have investigated the electronic band structure, the total density of states (DOS), structure optimization and photon energy-dependent optical properties of the Sb_2S_3 and Sb_2Se_3 crystals using a pseudopotential method based on the density functional theory (DFT) in the local density approximation (LDA) [15].

II. COMPUTATIONAL DETAILS

SIESTA (The Spanish Initiative for Electronic Simulations with Thousands of Atoms) code [16-18] was utilized in this study to calculate the energies and optical responses. It solves the quantum mechanical equation for the electron within DFT approach in the LDA parameterized by Ceperley and Alder [19]. The interactions between electrons and core ions are stimulated with seperable Troullier –Martins [20] norm-conserving pseudopotential. The basis set is based on the finite range pseudoatomic orbitals (PAO's) of the Sankey-Nicklewsky type [21], generalized to include multiple-zeta decays.

Table 1. Structure parameters of Sb_2S_3 and Sb_2Se_3 materials

Material		a (Å)	b (Å)	c (Å)	Space Group
Sb_2S_3	Present (LDA)	11.71	4.08	11.87	
Sb_2S_3 [23]	Experiment.	11.31	3.84	11.23	
Sb_2S_3 [24]	Experiment.	11.30	3.83	11.22	D_{2h}^{16}
Sb_2S_3 [25]	Experiment.	11.27	3.84	11.29	
Sb_2Se_3	Present (LDA)	12.22	4.14	11.98	
Sb_2Se_3 [13]	Theory (GGA)	11.91	3.98	11.70	
Sb_2Se_3 [2]	Experiment.	11.79	3.98	11.64	D_{2h}^{16}
Sb_2Se_3 [26]	Experiment.	11.78	3.99	11.63	
Sb_2Se_3 [27]	Experiment.	11.77	3.96	11.62	

We have generated atomic pseudopotentials separately for Sb, S and Se by using the $5s^25p^3$, $3s^23p^4$ and $4s^24p^4$ atomic configurations, respectively. The cut-off radii for the present atomic pseudopotentials are taken as 2.35, 1.7 and 1.85 a.u. for the s, p, d and f channels of Sb, S and Se, respectively.

SIESTA calculates the self-consistent potantial on a grid in real space. The fineness of this grid is determined in terms of an energy cut-off E_c in analogy to the energy cut-off when the basis set involves plane waves. Here by using a double-zeta plus polarization (DZP) orbitals basis and the cut-off energies between 50 and 450 Ry with various basis sets, we found an optimal value of around 350 Ry for Sb_2S_3 and Sb_2Se_3. For the final computations, 10 k-points for Sb_2S_3 and 36 k-points for Sb_2Se_3 were found to be adequate for obtaining the total energy with an accuracy of about 1meV/atoms.

III. RESULTS AND DISCUSSION

3.1. Structural optimization

All physical properties are related to the total energy. For instance, the equilibrium lattice constant of a crystal is the lattice constant that minimizes the total energy. If the total energy is calculated, any physical property related to the total energy can be determined. Firstly, the equilibrium lattice parameters were computed by minimizing the crystal's total energy calculated for the different values of lattice constant by means of Murnaghan's equation of states (EOS) [22] and the result are shown in Table 1 along with the experimental and theorical values. The lattice parameters for Sb_2S_3 and Sb_2Se_3 are found to be a= 11.71, b=4.08, c=11.87 and a= 12.22, b=4.14, c=11.987 for orthorhombic structures, respectively and it are in a good agreement with the experimental and theory. In all our calculations we have used the computed lattice parameters (Table).

3.2. Electronic band structure

For a better understanding of the electronic and optical properties of Sb_2Se_3 and Sb_2Se_3, the investigation of the electronic band structure would be useful. We first describe our calculated electronic structures along high symmetry directions in the first Brillouin zone (BZ) of the orthorhombic system. The energy band structures calculated using LDA for Sb_2Se_3 and Sb_2Se_3 are shown in Fig. 1. As can be seen in Fig.1a, the Sb_2S_3 crystal has an indirect forbidden gap with the value 0.7278 eV .

The top of the valance band positioned at the Γ point of BZ, and the bottom of the conduction band is located at the nearly midway between the X and U point of BZ.

The calculated band structure of Sb_2Se_3 are given in Fig. 1b. As can be seen from the figure, the band gaphas the same character with that of Sb_2S_3, that is, it is an indirect gap. The top of the valance band positioned at the X point of BZ, the bottom of the conduction band is located at the nearly midway between the X and U point of BZ. The indirect and direct band gap values of Sb_2Se_3 crystal are, 0.62 eV and 0.71 eV, respectively.

In the rightmost panels of Fig. 1, the density of states (DOS) are presented. The valance band in our calculations is composed of the 3s and 3p states of the S atom, 4s and 4p states of the Se atom and 5s and 5p states of Sb but on the top of valance band the weight of S 3p and Se 4p states is more than the weight of Sb 5p states, while the conduction band consists of the 5p states of the Sb, S and Se atoms.

Finally, the band gap values obtained are less than the estimated experimental results of 1.13 eV [28], 1-1.13 eV [29,30] for Sb_2Se_3 and 1.56 eV [28], 1.63-1.72 eV [31] for Sb_2S_3. For all crystal structures considered, the band gap values are underestimated than the experimental values. It is an expected case because of the use pseudopotential method.

3.3. Optical Properties of Sb_2S_3 and Sb_2Se_3

It is well known that the effect of the electric field vector, $\mathbf{E}(\omega)$, of the incoming light is to polarize the material. At the level of linear response this polarization can be calculated using the following relation [32]:

$$P^i(\omega) = \chi_{ij}^{(1)}(-\omega,\omega).E^j(\omega), \tag{1}$$

where $\chi_{ij}^{(1)}$ is the linear optical susceptibility tensor and it is given by [33]

$$\chi_{ij}^{(1)}(-\omega,\omega) = \frac{e^2}{\hbar\Omega}\sum_{nm\vec{k}} f_{nm}(\vec{k})\frac{r_{nm}^i(\vec{k})r_{mn}^i(\vec{k})}{\omega_{mn}(\vec{k})-\omega} = \frac{\varepsilon_{ij}(\omega)-\delta_{ij}}{4\pi} \tag{2}$$

Where n,m denote energy bands, $f_{mn}(\vec{k}) \equiv f_m(\vec{k}) - f_n(\vec{k})$ is the fermi occupation factor, Ω is the normalization volume. $\omega_{mn}(\vec{k}) \equiv \omega_m(\vec{k}) - \omega(\vec{k})$ are the frequency differences, $\hbar\omega_n(\vec{k})$ is the energy of band n at wavevector **k.** The $\vec{r}_{nm}$ are the matrix elements of the position operator [33].

As can be seen from equation (2), the dielectric function $\varepsilon_{ij}(\omega) = 1 + 4\pi\chi_{ij}^{(1)}(-\omega,\omega)$ and the imaginary part of $\varepsilon_{ij}(\omega)$, $\varepsilon_2^{ij}(\omega)$, is given by

$$\varepsilon_2^{ij}(w) = \frac{e^2}{\hbar\pi}\sum_{nm}\int d\vec{k} f nm(\vec{k})\frac{v_{nm}^i(\vec{k})v_{nm}^j(\vec{k})}{\omega_{mn}^2}\delta(\omega-\omega_{mn}(\vec{k})). \tag{3}$$

The real part of $\varepsilon_{ij}(\omega), \varepsilon_1^{ij}(\omega)$, can be obtained by using the Kramers-Kroning transformation [33]. Because the Kohn-Sham equations determine the ground state properties, the unoccupied conduction bands as calculated have no physical significance. If they are used as single-particle states in a calculation of optical properties for semiconductors, a band gap problem comes into included in calculations of response. In order to take into account self-energy effects, in the present work, we used the 'scissors approximation' [32].

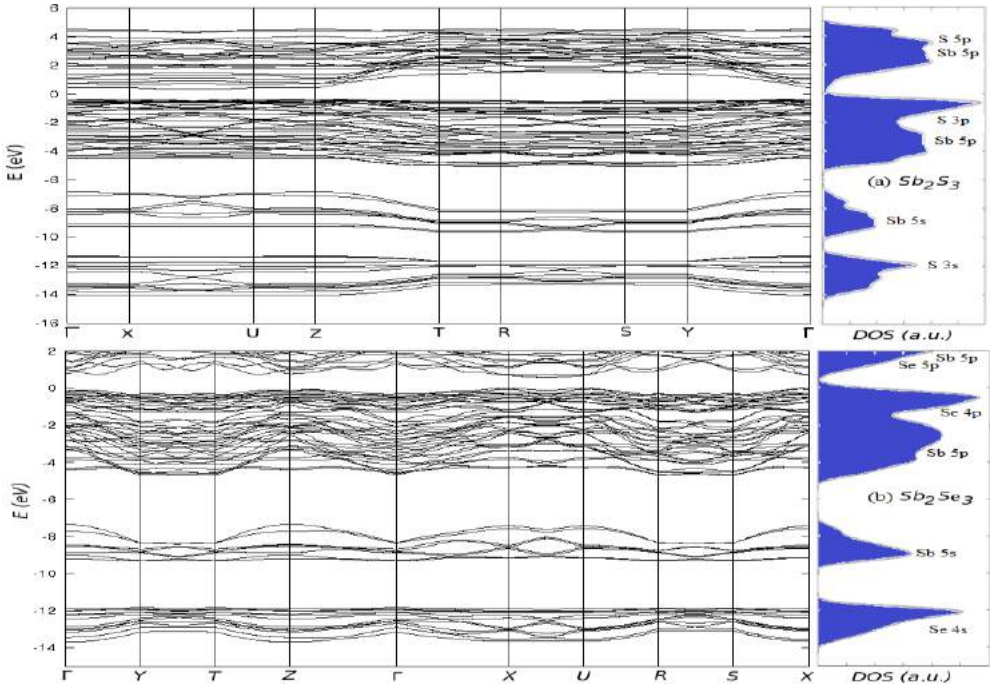

Fig. 1. Energy band structure a nd DOS (density of states) for Sb_2S_3 and Sb_2Se_3.

The known sum rules [34] can be used to determine some quantitative parameters, particularly the effective number of the valence electrons per unit cell N_{eff}, as well as the effective optical dielectric constant ε_{eff}, which make a contribution to the optical constants of a crystal at the energy E_0. One can obtain an estimate of the distribution of oscillator strengths for both intraband and interband transitions by computing the $N_{eff}(E_0)$ defined according to

$$N_{eff}(E) = \frac{2m\varepsilon_0}{\pi\hbar^2 e^2 Na}\int_0^{\infty}\varepsilon_2(E)EdE, \qquad (4)$$

where N_a is the density of atoms in a crystal, e and m are the charge and mass of the electron, respectively and $N_{eff}(E_0)$ is the effective number of electrons contributing to optical transitions below an energy of E_0.

Further information on the role of the core and semi-core bands may be obtained by computing the contribution which the various bands make to the static dielectric constant, ε_0. According to the Kramers-Kronig relations, one has

$$\varepsilon_0(E) - 1 = \frac{2}{\pi}\int_0^{\infty}\varepsilon_2(E)E^{-1}dE. \qquad (5)$$

One can therefore define an 'effective' dielectric constant, which represents a different mean of the interband transitions from that represented by the sum rule, equation (5), according to the relation

$$\varepsilon_{eff}(E) - 1 = \frac{2}{\pi}\int_0^{E_0}\varepsilon_2(E)E^{-1}dE. \qquad (6)$$

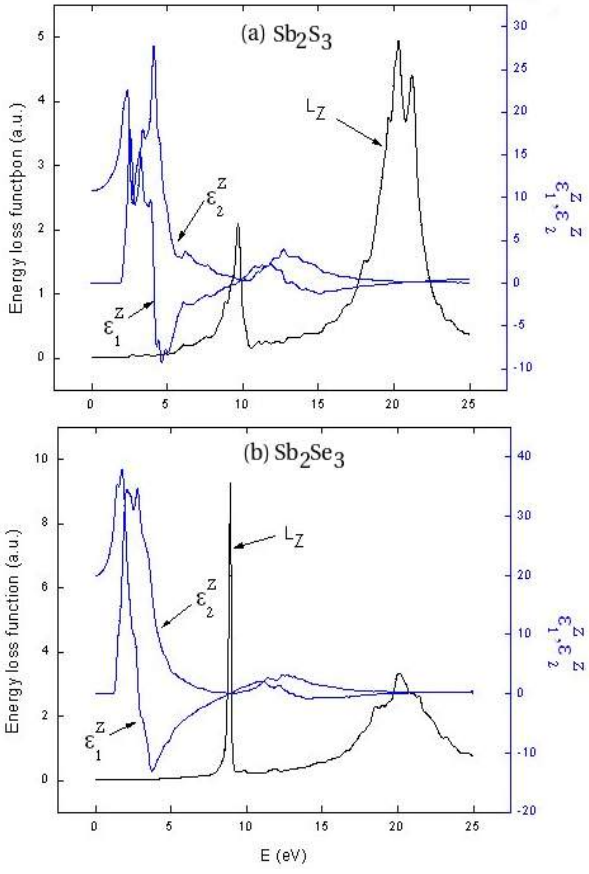

Fig. 2. Energy spectra of dielectric function $\varepsilon = \varepsilon_1 - i\varepsilon_2$ and energy-loss function (L) along the z-axes for Sb_2S_3 and Sb_2Se_3.

The physical meaning of ε_{eff} is quite clear: ε_{eff} is the effective optical dielectric constant governed by the interband transitions in the energy range from zero to E_0, i.e. by the polarizition of the electron shells.

In order to calculate the optical response by using the calculated band structure, we have chosen a photon-energy range of 0-25 eV and have seen that a 0-17 eV photon-energy range is sufficient for most optical functions.

The Sb_2S_3 and Sb_2Se_3 single crystals have an orthorhombic structure that is optically a biaxial system. For this reason, the linear dielectric tensor of the Sb_2S_3 and Sb_2Se_3 crystals have three independent components that are the diagonal elements of the linear dielectric tensor.

We first calculated the real and imaginary parts of z-components of the frequency-dependent linear dielectric function and these are shown in Fig. 2. The ε_1^z is equal to zero at about 4.12 eV, 9.61 eV, 13.37 eV and 20.1 eV in Fig. 2a for Sb_2S_3, while the ε_1^z is equal to zero at about 2.95 eV, 8.91 eV, 13.06 eV and 19.89 in Fig. 2b for Sb_2Se_3 crystal. The peaks of the ε_2^z correspond to the optical transitions from the valence band to the conduction band and are in agreement with the previous results. In general, there are various contributions to the dielectric function, but Fig. 2 shows only the contribution of the electronic polarizability to the dielectric function.

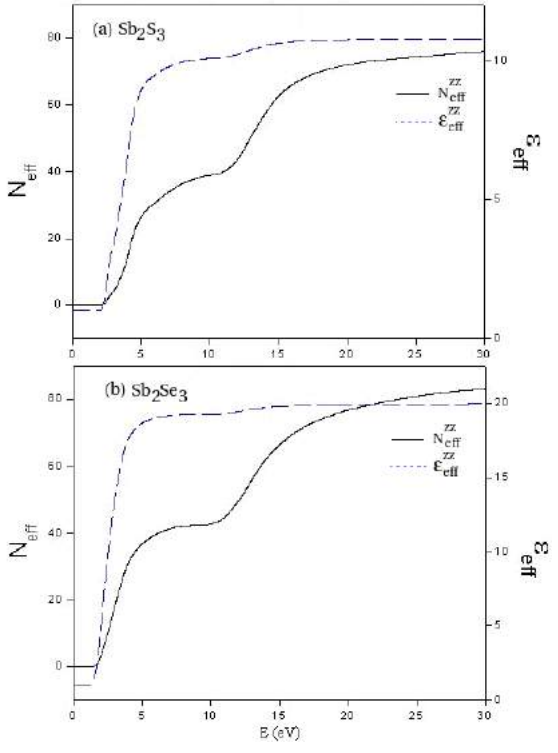

Fig. 3. Energy spectra of N_{eff} and ε_{eff} along the z- axes

Fig. 2 shows also that except for a narrow photon-energy region, between 0.5 eV and 2 eV, the ε_1^z increase with increasing photon energy, which is the normal dispersion. In the range between 2.0 eVenergy and 5.0 eV ε_1^z decrease with increasing photon-energy, which is the characteristics of an anomalous dispersion. Furthermore as can be seen from Fig.2, the photon –energy range up to 1.5 eV is characterized by high transparency, no absorbtion and a small reflectivity. The 1.9-5.0 eV photon energy range is characterized by strong absorption and appreciable reflectivity. We also calculated all optical functions along x- and y- directions. They show the different structures in the same energy region like for the z- direction, but these singularities have the similarly quantum-chemical mechanism.

The calculated energy-loss functions, $L(\omega)$, are also presented in Fig. 2a and Fig. 2b. In this figure, correspond to the energy-loss functions along the z-directions. The function $L(\omega)$ describes the energy loss of fast electrons traversing the material. The sharp maxima in the energy-loss function are associated with the existence of plasma oscillations [35]. The curves of L_z in Fig. 2 have a maximum near 20.30 eV for Sb_2S_3, and 20.83 for Sb_2Se_3.

The calculated effective number of valence electrons N_{eff} and the effective dielectric constant ε_{eff} are given in Fig. 3. The effective number of valence electron per unit cell, N_{eff}, contributing in the interband transitions, reaches saturation value at about 20 eV. This means that deep-lying valence orbitals do not paticipate in the interband transitions (see Fig. 3)

The effective optical dielectric constant, ε_{eff}, shown in Fig. 3, reaches a saturation value at about 20 eV. The photon-energy dependence of ε_{eff} can be separated into two regions. The first is characterized by a rapid rise and it extends up to 12 eV In the second region the value of ε_{eff} rises more smoothly and slowly and tends to saturation at the energy 20 eV. This means that the greatest conribution to ε_{eff} arises from interband transitions between 2 eV and 17 eV.

IV. CONCLUSIONS

In present work, we have made a detailed investigation of the electronic structure and frequency-dependent linear optical properties of the Sb_2S_3 and Sb_2Se_3 crystals using the density functional methods. The task of this work was to apply the density-functional methods to a complex crystal like the Sb_2S_3 and Sb_2Se_3. It is seen that Sb_2S_3 and Sb_2Se_3 crystals have the indirect forbidden gap. The obtained band gap values are in agreement with the previous results. The total DOS calculation shows that the valance band is composed of the 3s and 3p states of the S atom and 4s and 4p states of the Se atom, 5s and 5p states of Sb, while the conduction band consists of the 5p states of the Sb, S and Se atoms. we have photon-energy dependent dielectric functions and some optical properties such as the energy-loss function, the effective number of valance electrons and the effective optical dielectric constant along the all main axes. The results of the structural optimization implemented using the LDA are in good agreement with the experimental results. To our knowledge, this is the first detailed study of the optical properties of the Sb_2S_3 and Sb_2Se_3

[1]. *O. Madelung*, Semiconductory Other than Group IV Elements and III-V Compounds, Springer, Germany, 1992, p.50.

[2]. *E.A. El-Sayad, A.M. Moustafa, S.Y. Marzouk*, Physica B 2009, 404, 1119-1127.

[3]. *J. Black, E.M. Conwell, L. Sigle, C.W. Spencer*, J. Phys. Chem. Solids 1957, 2, 240.

[4]. *N.S. Platakis, H.C. Gatos*, Phys. Status Solidi A Appl. Res. 1972, 13, K1.

[5]. *K.Y. Rajapure, C.D. Lokhande, C.H. Bhosele*, Thin Solid Films 1997, 311, 114.

[6]. *S.V. Forgue, R.R. Goodrich, A.D. Cope*, RCA Rev. 1951, 12, 335.

[7]. *C. Ghash, B.P. Varma*, Thin Solid Films 1979, 60, 61.

[8]. *J. Grigas, J. Meshkauskov, A. Orhiukas*, Phys. Status Solidi A Appl. Res. 1976, 37, K39.

[9]. *M.S. Ablova, A.A. Andreev, T.T. Dedegkaev, B.T. Melekh, A.B. Pevtsov, N.S. Shendel, L.N. Shumilova*, Soviet Phys. Semicond.-USSR 1976, 10, 629.

[10]. *M.J. Chockalingam, N. Nagaraja Rao, K.Rangarajan, C.V. Surganarayana*, J. Phys. D. Apply. 1930,3,1641.

[11]. *E. Montrimas, A. Pazera*, Thin Solid Films 1976, 34,65

[12]. *J. George, M.K. Radhakrishnan*, Solid States Comm. 1980, 33, 987

[13]. *N. Kuganathan*, E-Journal of Chemistry 2009, 6, 5147-5152.

[14]. *R. Caracas, X. Conze*, Phys. Chem. Minerals 2005, 32, 295-300.

[15]. *W. Kohn and L. J. Sham*, Phys. Rev. 1965, 140, A1133.

[16]. <www.uam.es / siesta>

[17]. *P. Ordejon, E. Artacho, J. M. Soler*, Phys. Rev. B (Rapid Common) 1996, 53, R10441.

[18]. *J. M. Soler, E. Artaeho, J. D. Gole, A. Garsia, J. Junguera, P. Ordejon, D. Sanchez-portal*, J. Phys: Condens Matter 2002, 14, 2745.

[19]. *D. M. Ceperley, M. J. Alder*, Phys, Rev. Lett. 1980, 45, 566.

[20]. *N. Troullier, J. L. Martins*, Phys. Rev. B 1991, 43, 1993.

[21]. *O. F. Sankey, D.J Niklewski*, Phys. Rev B 1989, 40, 3979.

[22]. *F. D. Murnaghan*, Proc. Nat. Acad. Sci. USA 1944, 30, 5390.

[23]. *A. Kyono, M. Kimata, M. Matsuhisa, Y. Migashita, K. Okamoto*, Phys. Chem. Minerals 2002, 29, 254- 260.

[24]. *By D.O. Micke, J.T. Mcmullan*, Z. Kristallogr. 1975, 142, 447-449.

[25]. *A.M. Salem, M.S. Selim*, J. Phys. D: Appl. Phys. 2001, 34, 12-17.

[26]. *X. Zheng, Y. Xie, L. Zhu, X. Jiang, Y. Jia, W. Song, Y. Sun*, Inorganic Chemistry 2002, 41, 455-461.

[27]. *Z. Hurych, D. Davis, D. Buczek, C. Wood*, Phys. Rev. B 1974, 9, 4392-4404.

[28]. *G.-Y. Chen, B. Dneg, G.-B. Cai, T.-K. Zhang, W.-F. Dong, W.-X. Zhang, A.-W. Xu*, J. Phys. Chem. C 2008, 112, 672-679.

[29]. *O. Madelung*, Semiconductors Other than Group IV elements and III-V Compounds, in: R. Poerschke (ed), Data in Science and Tecnology, Springer, Berlin, 1992, p50.

[30]. *R.S. Mane, C.D. Loklande*, Mater. Chem. Phys. 2000, 65, 1.

[31]. *A.F. Skubenko, C.V. Laptii*, Soviet Phys. Solid State 1964, 4, 327.

[32]. *Z.H. Levine, D.C. Allan* . Phys Rev, Lett. 1989, 63, 1719.

[33]. *H.R. Philipp, H. Ehrenreich*, Phys. Rev. 1963, 129, 1550.

[34]. *O.V. Kovalev*, Representations of the Crystallographic Space Groups. Irreducible Representations Induced Representations and Corepresentations, Amsterdam: Gordon and Breach (1965).

[35]. *L. Marton*, Rev. Mod. Phys. 1956, 28, 172.

AN AB-INITIO STUDY of La_3Tl COMPOUND

B. KOÇAK[1], Y. Ö. ÇİFTÇİ[1], K. ÇOLAKOĞLU[1], H. B. ÖZIŞIK[1,2]

[1]Gazi University, Department of Physics, Teknikokullar, 06500, Ankara, TURKEY

[2]Aksaray University, Department Of Physics, 68100, Aksaray, TURKEY

We present a study of the structural, elastic, and thermodynamical properties of the superconductor La_3Tl compound, using density-functional theory within the generalized gradient approximation of the exchange-correlation functional. The optimized lattice parameter, elastic moduli, Zener anisotropy factor (A), Poisson's ratio (υ), Young's modulus (Y), shear modulus (C'), are systematically investigated and comparison with other experimental and theoretical calculations. Our structural results are well consistent with experimental works. Additionally, thermodynamical properties such as pressure (0-15GPa) and temperature (0-1600K) dependence of lattice parameter, bulk modulu and Debye temperature are discussed by quasi-harmonic Debye model.

I. INTRODUCTION

Since the discovery of compounds showed superconductivity properties, they have been great scientific interest due to their have unique properties. La_3Tl compound, which is crystallize Cu_3Au phase, have been exhibit strong-coupling superconductor behaviour above 0.7 ^{0}K [1-3]

Initially, the superconducting, magnetic and some thermodynamic properties of La_3Tl were performed experimentally by E. Bucher et al. [3]. F. Heiniger et al.[1] have reported superconducting and electronic properties of La_3Tl and La_3ln and some related phases. The thermodynamic properties changing with magnetic impurities were also discussed by F. Heiniger et al.[2]. P. Descouts et al. [4] have studied large temperature-dependent magnetic susceptibility, using nuclear magnetic resonance technique.

Theoretically, P. Ravindran et al. [5] have studied structural stability, superconductivity and electronic properties of La_3X and La_3XC (X=Al, Ga, In, Tl). They have reported cohesive energy, heat of formation, electronic structure and Tc calculation by using TB-LMTO and LMTO-ASA method.

In this work, we have attempted first-principles calculations of structural, elastic, and thermodynamical properties of La_3Tl compound. The paper is organized as follows: The details of the calculation method are given in Section 2. The obtained results are presented and discussed at Section 3. Finally, paper concludes with a summary in Section 4.

II. METHOD OF CALCULATION

For all our calculations have been performed using the Vienna ab-initio simulation package (VASP) [6-9] based on the density functional theory (DFT). The electron-ion interaction was considered in the form of the projector-augmented-wave (PAW) method with plane wave up to energy of 650 eV [8, 10]. For the exchange and correlation terms in the electron-electron interaction, Perdew and Zunger-type functional [11, 12] was used within the generalized gradient approximation (GGA) [10]. The 12x12x12 Monkhorst and Pack [13] grid of k-points have been used for integration in the irreducible Brillouin zone.

We used the quasi-harmonic Debye model to obtain the thermodynamic properties of La_3Tl [14-17], in which the non-equilibrium Gibbs function $G^*(V; P, T)$ takes the form of

$$G^*(V;P,T) = E(V)+PV+A_{vib}[\theta(V);T] \quad (1)$$

In Eq.(1), $E(V)$ is the total energy for per unit cell of La_3Tl, PV corresponds to the constant hydrostatic pressure condition , $\theta(V)$ the Debye temperature and A_{Vib} is the vibration term, which can be written using the Debye model of the phonon density of states as

$$A_{Vib}(\theta,T) = nkT\left[\frac{9}{8}\frac{\theta}{T}+3\ln(1-e^{-\theta/T})-D\left(\frac{\theta}{T}\right)\right] \quad (2)$$

where n is the number of atoms per formula unit, $D(\theta/T)$ the Debye integral, and for an isotropic solid, θ is expressed as [18]

$$\theta_D = \frac{\hbar}{k}(6\pi^2V^{1/2}n)^{1/3} f(\sigma)\sqrt{\frac{B_s}{M}} \quad (3)$$

where M is the molecular mass per unit cell and B_S the adiabatic bulk modulus, which is approximated given by the static compressibility [19]:

$$B_s \cong B(V) = V\left(\frac{d^2E(V)}{dV^2}\right) \quad (4)$$

$f(\sigma)$ is given by Refs. [18, 20] and the Poisson ratio are used as 0.301 for La_3Tl. For La_3Tl compounds, M= 138.9 and M= 204.38 a.u, respectively. Therefore, the non-equilibrium Gibbs function $G^*(V; P, T)$ as a function of $(V; P, T)$ can be minimized with respect to volume V.

$$\left(\frac{\partial G^*(V;P,T)}{\partial V}\right)_{P,T} = 0 \quad (5)$$

By solving Eq. (5), one can obtain the thermal equation-of-equation (EOS) $V(P, T)$. The heat capacity at constant volume C_V, the heat capacity at constant pressure C_p, and the thermal expansion coefficient α are given [21] as follows:

$$C_V = 3nk\left[4D(\theta/T) - \frac{3(\theta/T)}{e^{\theta/T}-1}\right] \quad (6)$$

$$S = nk\left[4D\left(\frac{\theta}{T}\right) - 3\ln(1-e^{\theta/T})\right] \quad (7)$$

$$\alpha = \frac{\gamma C_V}{B_T V} \quad (8)$$

$$C_p = C_v(1+\alpha\gamma T) \quad (9)$$

Here γ represent the Grüneisen parameter and it is expressed as

$$\gamma = -\frac{d\ln\theta(V)}{d\ln V} \quad (10)$$

III. RESULTS AND DISCUSSION

3.1. Structural and elastic properties

The equilibrium lattice parameter was computed by minimizing the crystal total energy calculated for the different values of lattice constant by means of Murnaghan's equation of state (eos) [22]. The bulk modulus and its pressure derivative have also been estimated, based on the same Murnaghan equation of state, and the results are presented in Table 1 along with the experimental and other theoretical values for Cu_3Au(space group Pm3m) crystal structure. From Table 1, lattice parameter (a_o) for La_3Tl is excellent agreement with the experiment values.

Table 1. Calculated equilibrium lattice constant (a_0), bulk modulus B, and the pressure derivative of bulk modulus (B') for La_3Tl

Structure Referans		a_0 (Å)	B(GPa)	B'
Cu_3Au	Present	5.077	37.574	4.129
	Theory[a]	5.13		
	Exp.[b,c,d]	5.06		

[a] Ref [5]
[b,c,d] Ref [1, 4, 23]

The elastic constants of solids provide a link between the mechanical and dynamical behaviour of crystals, and give important information concerning the nature of the forces operating in solids. In particular, they provide information on the stability and stiffness of materials. Their ab-initio calculation requires precise methods, since the forces and the elastic constants are functions of the first and second-order derivatives of the potentials. Their calculation will provide a further check on the accuracy of the calculation of forces in solids. The effect of pressure on the elastic constants is essential, especially, for understanding interatomic interactions, mechanical stability, and phase transition mechanisms. It also provides valuable data for developing interatomic potentials.

We have used the "stress-strain method" for obtaining the second-oreder elastic constants (C_{ij}). The elastic constants (C_{ij}) with the different pressure are also listed in Table 2. There are no experimental results available to us for this compound.

Table 2. The calculated elastic constants (in GPa unit) and Zener anisotropy factor, the Poisson's ratio (GPa), Young's modulus, Shear modulus for La_3Tl at 0 K with different pressure

P	C_{11}	C_{12}	C_{44}	A	υ	Y	C'
0	56.42	30.34	20.75	1.59	0.301	44.83	13.04
10	91.92	56.47	41.4	2.34	0.334	78.6	17.72
20	120.5	79	57.78	2.79	0.356	103.9	20.75
30	145.68	99.7	71.8	3.13	0.371	124.85	23
40	168.28	119.2	84.6	3.45	0.382	142.92	25.54
50	185.57	137.5	96.68	3.79	0.392	158.57	25.03

The Zener anisotropy factor A, Poisson ratio υ, and Young's modulus Y, which are the most interesting elastic properties for applications, are also calculated in terms of the computed data using the following relations [24]:

$$A = \frac{2C_{44}}{C_{11}-C_{12}} \quad (11)$$

$$\upsilon = \frac{1}{2}\left[\frac{(B-\frac{2}{3}G)}{(B+\frac{1}{3}G)}\right], \quad (12)$$

and

$$Y = \frac{9GB}{G+3B} \quad (13)$$

where $G = (G_V + G_R)/2$ is the isotropic shear modulus, G_V is Voigt's shear modulus corresponding to the upper bound of G values, and G_R is Reuss's shear modulus corresponding to the lower bound of G values, and can be written as $G_V = (C_{11}-C_{12}+3C_{44})/5$, and $5/G_R = 4/(C_{11}-C_{12})+ 3/C_{44}$. The calculated Zener anisotropy factor (A), Poisson ratio (υ), Young's modulus (Y), and Shear modulus ($C'=(C_{11}-C_{12}+2C_{44})/4$) for La_3Tl are given in Table 2, and they are close to those obtained for the similar structural symmetry .

3.2. Thermodynamic Properties

The quasi-harmonic Debye model is successfully applied to predict the thermal properties of La_3Tl in the 0-1600 K temperature and 0-15 GPa pressure range. The relationship between lattice constant and pressure at different temperature is shown in Fig. 1. One can obviously see from the Fig. 1 that the lattice constant decreases dramatically as P increases, probably, due to the stronger atomic interactions in the interlayer. At low pressure, the lattice parameter increases rapidly with the temperature, but at higher pressure, the lattice parameter varies gradually as the temperature rises.

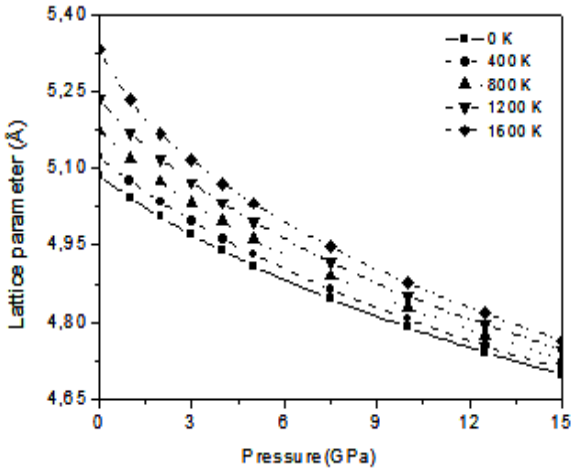

Fig. 1. Lattice parameter versus pressure at temperature of 0, 400, 800, 1200 and 1600 K for La_3Tl

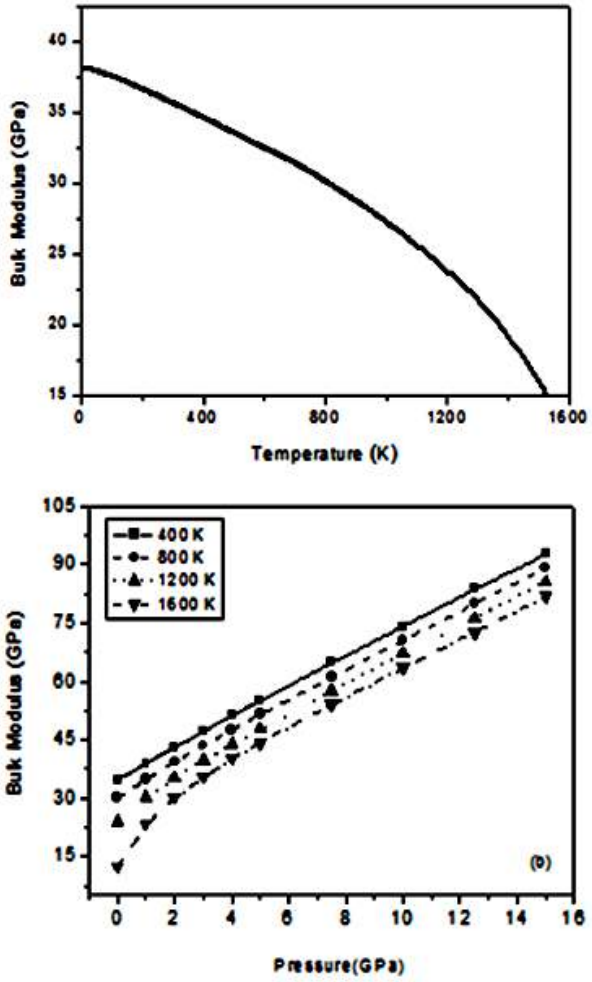

Fig. 2. (a) Bulk modulus as a function of temperature up to 1600K at zero pressure (b)Variations with pressure of the bulk modulus at different temperatures.

Temperature effects on bulk moduli (B) are given in Fig. 2(a). The Figures show that *B* decreases as temperature increases. The relationship between bulk modulus (B) and pressure (P) at different temperatures (400, 800, 1200 and 1600K) are shown in Fig. 2(b) for La_3Tl. In Fig. 2, bulk modulus *B* decreases gradually as *T* increases at a given pressure which indicates that the cell volume undergoes gradual changes and increases rapidly as the pressure *P* increases at a given temperature. We can say that, the effect of increasing pressure is the same as the decreasing temperature on La_3Tl.

Finally, the variations of the Debye temperature with temperature and pressure are shown in Fig.3 (a) and Fig.3(b) for La_3Tl, respectively. We found that Debye temperature is 179.5 K at zero pressure which is in agreement with the Debye temperatures obtained by F. Heiginer et al.(θ=163±8) and P. Ravindran et al.(θ=163). It can be seen from Fig 3. the Debye temperature behaviour similar as bulk modulus.

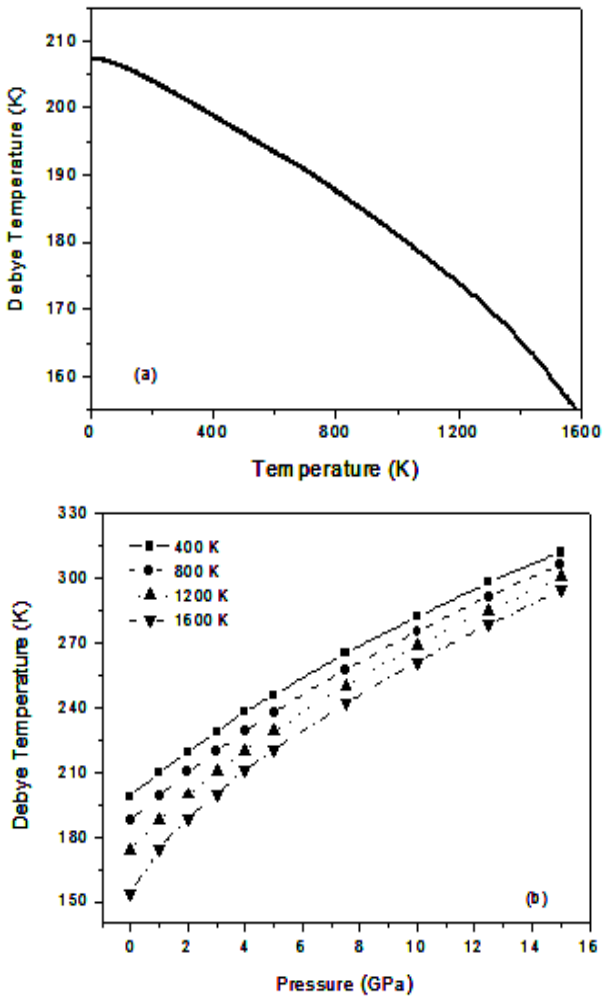

Fig. 3. (a) Debye temperature versus temperature for La_3Tl at zero pressure (b) Variations with pressure of the Debye temperature at different temperatures

IV. SUMMARY AND CONCLUSION

The plane wave pseudopotential method within the GGA and PAW approximation is used to calculate the elastic and the total energies of La_3Tl in Cu_3Au-type structures. The lattice parameters are excellent agreement with the other theoretical and experimental values. Our results for elastic constants satisfy the traditional mechanical stability conditions. The pressure and/or temperature dependence of the thermodynamical properties, including lattice parameter, bulk modulu, Debye temperature are also calculated successfully.

[1]. *F. Heiniger, E. Bucher, J. P. Maita, P. Descouts*, Phys. Rev. B, 8 (1973) 3194.

[2]. *F.Heiniger, E.Bucher, J.P.Maita, L.D.Longinotti*, Phys. Rev. B, 12 (1975) 1778.

[3]. *E. Bucher, J.P. Maita, A.S. Cooper*, Phys. Rev. B, 6(1972) 2709.

[4]. *P.Descouts, B.Perrin, A.Dupanloup, A.Treyvaud*, J. of Phys. and Chem. of Solids, 39 (1978) 161.

[5]. *P. Ravindran, R.Asokomani*, J. Phy. Condens. Matter, 7 (1995) 5567.

[6]. *G. Kresse and J. Hafner*, Phys. Rev. B , 47(1994)558.

[7]. *G. Kresse and J. FurthmÄuller*, Comp. Mat. Sci., 6 (1996)15.

[8]. *G. Kresse and D. Joubert*, Phys. Rev. B, 9 (1999) 1758.

[9]. *G. Kresse and J. FurthmÄuller*, Phys. Rev. B, 54 (1996) 11169.

[10]. *P. E. Blochl*, Phys. Rev. B, 50 (1994)17953.

[11]. *J. P. Perdew and A. Zunger*, Phys. Rev. B, (1981) 23 5048.

[12]. *J.P.Perdew,J.A.Chevary,S.H.Vosko,K.A.Jackson, M.R.Pederson, D.J. Singh and C.Fiolhais*, Phys. Rev. B ,46 (1992) 6671.

[13]. *H.J.Monkhorst and J.D.Pack*, Phys. Rev. B, 13(1976) 5188.

[14]. M.*A. Blanco, E. Francisco, V. Lunana*, Comput. Phys. Commun. , 158 (2004)57.

[15]. *F. Peng, H.Z.Fu, X.L.Cheng*, Physica B, 400 (2007) 83.

[16]. *F.Peng, H.Z. Fu, X.D. Yang*, Solid State Commun., 145 (2008) 91.

[17]. *F. Peng, H.Z. Fu, X.D. Yang*. , Physica B, 403 (2008) 2851.

[18]. *M.A.Blanco,A.M.Pendàs,E.Francisco,J.M.Recio, R.Franko*, J.Mol. Struct. (Theochem) 368 (1996) 245.

[19]. *M.Flórez, J.M. Recio, E. Francisco, M.A.Blanco, A.M. Pendàs*, Phys. Rev. B, 66 (2002) 144112.

[20]. *E.Francisco, J.M.Recio, M.A.Blanco, A.M.Pendàs*, J. Phys. Chem. ,102 (1998) 1595.

[21]. R. Hill, Proc. Phys. Soc. Lond. A, 65 (1952) 349.

[22]. *F. D. Murnaghan*, Proc. Natl., Acad. Sci. USA 30, 5390 (1994).

[23]. *K. Andres, E. Bucher, S. Darack, J. P. Maita* Phys. Rev. B, 6 (1972) 2716-24

[24]. *B. Mayer, H. Anton, E. Bott, M. Methfessel, J.Sticht, and P. C. Schmidt*, Intermetallics 11 (2003) 23.

SOME ELECTRICAL PROPERTIES OF Cd/CdS/n-GaAs/In, Zn/ZnS/n-GaAs/In AND Cu/CuS/n-GaAs/In SANDWICH STRUCTURES

B. GÜZELDİR, M. Ali YILDIRIM[*], A. ATEŞ[**], M. SAĞLAM[***]

Department of Physics, Science Faculty, Atatürk University, 25240, Erzurum/TURKEY, bguzeldir@ atauni.edu.tr

[*]*Department of Science Education, Erzincan University, 24030, Erzincan/TURKEY, mayildirim@erzincan.edu.tr*

[**]*Department of Physics, Science Faculty, Atatürk University, 25240, Erzurum/TURKEY, aytunga@atauni.edu.tr*

[***]*Department of Physics, Science Faculty, Atatürk University, 25240, Erzurum/TURKEY, msaglam@atauni.edu.tr*

In this study, the Cd/CdS/n-GaAs/In, Zn/ZnS/n-GaAs/In and Cu/CuS/n-GaAs/In structures are prepared by the Successive Ionic Layer Adsorption and Reaction (SILAR) method at room temperature. The characteristics parameters such as ideality factor (n) and barrier height (Φ_b) are obtained from current- voltage (I–V) measurement by applying a thermionic emission theory. The value of series resistance (R_s) has been calculated from high current region of the structure by using Cheung's functions. Furthermore, the energy distribution of interface state densities (N_{ss}) have been determined from the forward bias I–V characteristics by taking into account the bias dependence of the effective barrier height. It has been seen that, the N_{ss} characteristics have almost an exponential rise with bias from the mid gap toward the bottom of conduction band.

I. INTRODUCTION

GaAs is an important semiconductor used for optoelectronics, fast computers and microwave applications [1-4]. MS (metal-semiconductor) contacts have been studied both experimentally and theorically in the past decades [5-7]. Electronic properties of a MS contacts are characterized by its main electrical parameters such as barrier height, ideality factor, series resistance and interface states parameters. Surface and interface properties play an important role in the electronic properties of MS contacts.

Smaller and faster is the technological imperative of our times and so there is a need for suitable materials and processing techniques. Thin films play an important role in fullling this need. Thin film is a two dimensional structure, i.e. it has a very large ratio of surface to volume, and created by the process of condensation of atoms, molecules or ions. They do the same function with the corresponding bulk material and their material costs are smaller. Most of the electronic devices require reliable ohmic contacts for electrical signals to flow into and out of the device, and highly stable metal-semiconductor rectifying contacts as the active region.

The SILAR technique is a relative new and less investigated process reported by Nicolau [8]. As a method of thin film growth, SILAR is simple, flexible, and offers an easy way to dope film. It does not require high quality substrates, and can operate at room temperature without the need for vacuum. Besides it is also cost-effective and it can adapt to any substrate material or surface profile. Growth parameters are relatively easy to control and the stoichiometric deposit and different grain structures can be realized [8, 9-12]

In this work, the Cd/CdS/n-GaAs/In, Zn/ZnS/n-GaAs /In and Cu/CuS/n-GaAs/In sandwich structures are prepared using by SILAR method. The I-V characteristics of these structures were studied at room temperature and in the dark. In order to extract the values of the real Rs, Φ_b and n of Cd/CdS/n-GaAs/In, Zn/ZnS/n-GaAs/In and Cu/CuS/n-GaAs/In sandwich structures, Cheungs method [22] was applied at room temperature. The other purpose of this paper was to present the results of a systematic investigation of the role of N_{ss} on the I–V characteristic of these structures.

II. EXPERIMENTAL

An n-GaAs crystal of relatively carrier density $N_D = 2.5\times10^{17}$ cm^{-3}, (100) orientation was used as a substrate. After a standard cleaning process and etching in a sulfuric acid solution (5 H_2SO_4 + H_2O_2 + H_2O), an ohmic contact was formed on the back surface of the substrate by using Indium in vacuum of 10^{-5} torr, and annealing in a nitrogen atmosphere at 425 $^{\circ}$C for 3 min. After ohmic contact made, the ohmic contacat side and the edges of the n-GaAs semiconductor substrates were covered by wax so that the polished and cleaned front side of the semiconductor sample was exposed to the cationic precursor solution employed for SILAR method. The cationic precusor solutions were 0.1 M $CdCl_2$, $ZnCl_2$, $CuCl_2$ and anionic solution was 0.05 M Na_2S. The immersion times were 25 s for $CdCl_2$, $ZnCl_2$, $CuCl_2$ and 50 s for Na_2S. One SILAR cycle contained four steps: (i) the substrate was immersed into first reaction containing the aqueous cotion precusor, (ii) rinsed with water, (iii) immersed into the anion solution, and (iv) rinsed with water. Repeated these cycles, a solid solution CdS, ZnS, CuS thin films with desired thickness and composition were grown. Then to perform the electrical measurements Cd, Zn, Cu were evaporated on the CdS, ZnS, CuS thin films, respectively, at 10^{-5} Torr. In this way, Cd/CdS/n-GaAs/In, Zn/ZnS/n-GaAs /In and Cu/CuS/n-GaAs/In structures were obtained.

The I-V characteristic of these structures were measured using a HP 4140B picoampermeter at room temperature and in the dark.

III. RESULT AND DISCUSSION

The current- voltage characteristics of the *MS* contacts due to thermionic emission current with series resistance can be expressed as [13-20]

$$I = I_0 \exp\left(\frac{q(V - IR_s)}{nkT}\right)\left[1 - \exp\left(\frac{-q(V - IR_s)}{kT}\right)\right] \quad (1)$$

$$I_0 = AA^*T^2 \exp\left(-\frac{q\Phi_b}{kT}\right) \quad (2)$$

where A is the diode area, A^* is the effective Richardson constant (A^*=8.16 A/cm^{2}K^2 for *n*-type GaAs) [11], k is the Boltzmann constant, T is the absolute temperature, q is the electron charge, I_o is the saturation current and Φ_b is the barrier height.

The values of *n* were calculated from the slope of the linear regions of the forward *I-V* characteristics according to Eq. 1 The barrier height values were calculated from the y-axis intercepts of the semilog-forward bias *I-V* characteristics according to Eq. 1.The saturation current I_o, deduced from the *I-V* data by extrapolating the curves toward *V=0*, is used to obtain the zero bias barrier height

Fig.1, shows the forward and reverse bias *I-V* characteristics of the Cd/CdS/n-GaAs/In, Zn/ZnS/n-GaAs /In and Cu/CuS/n-GaAs/In sandwich structures, respectively. Fig. 1 indicating that the effect of the series resistance in linear region is not important [19]. The effective barrier height, saturation current and ideality factor values of these structures are given in Table 1. It can be seen that the forward and reverse bias semi-logarithmic in InI-V characteristics of these structures show good rectifying behaviour at room temperature. In the high current regions, there is always a deviation of the ideality which has been clearly shown to depend on parameters such as the interfacial layer thickness, the interface state density and the bulk series resistance, as one would have expected

On a semi-log scale and at low forward bias voltage, the forward bias I–V characteristics of the metal semiconductor contacts are linear but deviate considerably from linearity due to the some factors at large voltages. One of the factors is series resistance

When the applied voltage is sufficiently large, the effect of the Rs can be seen at the non-linear regions of the forward bias I–V characteristics. The lower the series resistance, the greater the range over which the I–V curve yields a straight line [21]. The values of the Rs were achieved using a method developed by Cheung and Cheung [22] in the high current range where the I–V characteristics are not linear.

In order to compute Schottky diode parameters like the barrier height, ideality factor and series resistance R_S, Cheung's functions can be obtained from Equation 1 as follows

$$\frac{dV}{d(\ln I)} = IR_s + n\left(\frac{kT}{q}\right) \quad (3)$$

$$H(I) = V - n\left(\frac{kT}{q}\right)\ln\left(\frac{I}{AA^*T^2}\right) \quad (4)$$

$$H(I) = IR_s + n\phi_b \quad (5)$$

Equation (3) should give a straight line for the data of the downward curvature region of the forward bias *I-V* characteristics. Thus, the slope and *y*-axis intercept of a plot of dV/d(lnI) vs give R_s and *nq/kT*, respectively. Using the *n* value determined from Eq. 3 and the data of downward curvature region in Eq. 4, a plot of *H*(*I*) vs *I* according to Eq. 5 will also give a straight line with the *y*-axis intercept equal to $n\Phi_b$. The slope of this plot also provides a second determination of R_s which can be used to check the consistency of Cheung's approach. These plots are drawn using the data of the downward concave curvature region in the forward bias *I-V* characteristics given in Fig. 1. The plots associated with these functions are given in Fig. 2 and Fig. 3. The three contact parameters (*n*, Φ_b and R_s) are given in Table 1.

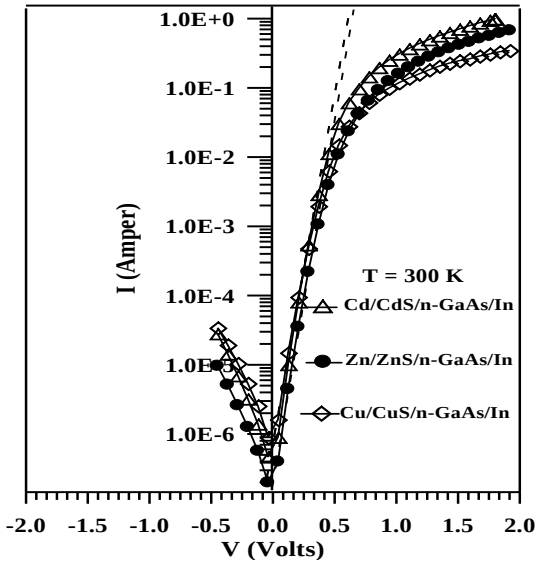

Fig.1. The semi-log forward bias current–voltage characteristics of sandwich structures at room temperature.

It is seen that there is a good agreement between the values of the series resistance obtained from two Cheung plots. However, it can clearly be seen that there is difference between the values of *n* obtained from the downward curvature regions of forward bias *I-V* plots and from the linear regions of the same characteristics. The reason for this difference can be attributed to the existence of effects such as the series resistance [2, 18, 19] and the bias dependence of the Schottky barrier height Φ_b according to the voltage drop across the interfacial layer and change of the interface states with bias in this concave region of the In*I-V* plot [2]

In n-type semiconductors, the energy of the interface states, E_{ss}, with respect to the bottom of conduction band at the surface of the semiconductor is given by [23]

$$E_c - E_{ss} = q\Phi_b - qV \quad (10)$$

where E_c is the bottom of the conduction band, Φ_b is the barrier height and *V* is the bias voltage.

Table 1. The experimentally values(n, Φ_b, R_s) obtained from different methods for these sandwich structures.

	I-V Method			*dV/dIn(I)*		*H(I)-I*	
	n	Φ_b *(eV)*	I_0 *(A)*	*n*	R_s *(kΩ)*	Φ_b *(eV)*	R_s *(kΩ)*
Cd/CdS/*n-GaAs*/In	1.567	0.603	4.252×10^{-7}	1.748.	1.048	0.716	1.174
Zn/ZnS/*n-GaAs*/In	1.604	0.623	1.979×10^{-7}	1.863	1.640	0.722	1.685
Cu/CuS/*n-GaAs*/In	1.665	0.589	7.365×10^{-7}	1.902	2.252	0.691	2.967

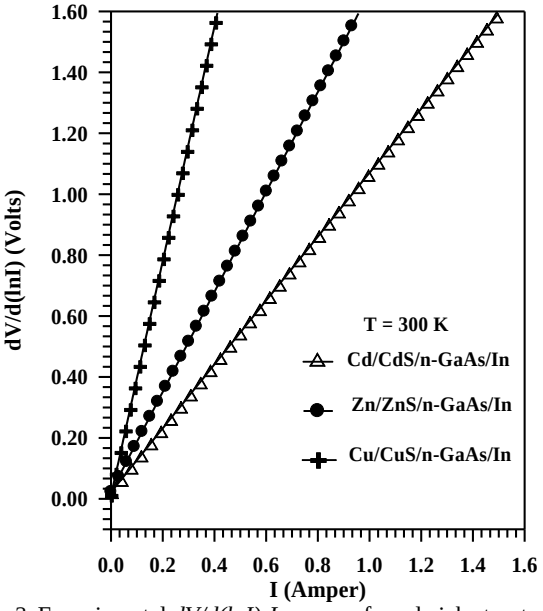

Fig. 2. Experimental *dV/d(lnI)-I* curves of sandwich structures

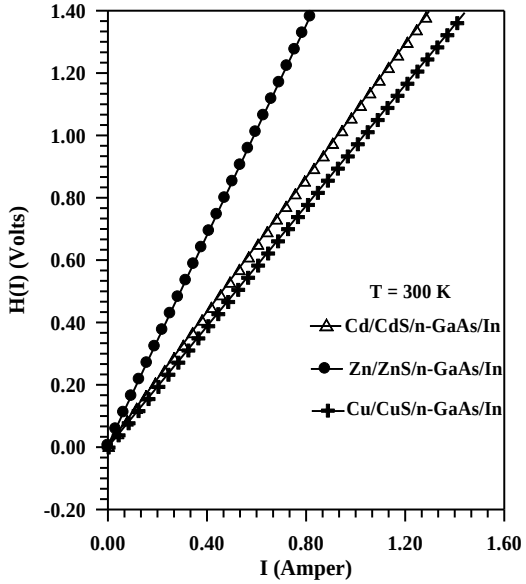

Fig 3. Experimental *H(I)-I* curves of sandwich structures

The energy distribution or density distribution curves of the interface states can be thus obtained from experimentalda of this region of the forward bias InI–V

As can be seen from Fig. 4, the the N_{ss} characteristics have an exponential rise with bias from the mid gap toward the bottom of conduction band.

The energy position of distribution lines and the absolute magnitude of the densities are in agreement with those accepted values, when the energy distribution of the interface satates and their role in the surface Fermi level pinning are considered [24].

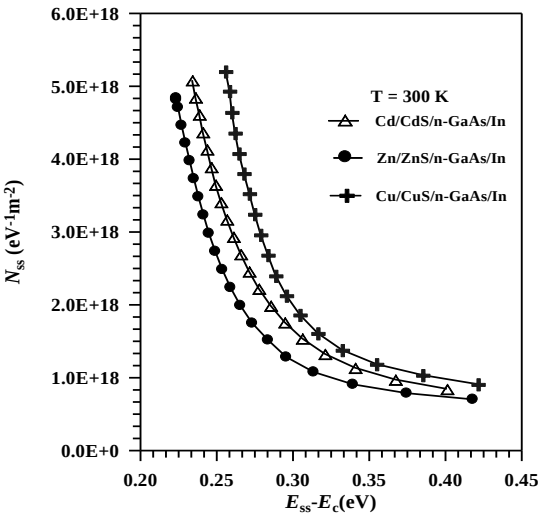

Fig 4. The energy distribution curve of the interface states obtained from the forward bias In*I-V* characteristics of sandwich structures as a function of (Ec-Ess).

I. CONCLUSION

In this study, forward and reverse bias InI-V characteristics of Cd/CdS/n-GaAs/In, Zn/ZnS/n-GaAs /In and Cu/CuS/n-GaAs/In structures were measured at room temperature. The n, Φ_b, R_s values of these structures were obtained from the different methods. The non-ideal forward bias I-V behaviour observed in these structures is attributed to change in the metal/semiconductor barrier height due to the interface states, interfacial layer and series resistance. The value of R_s has been calculated from high current region of the structure by using Cheung's functions. It is seen that there is good agreement between values of the series resistance obtained from two Cheung's plots. The energy distribution of N_{ss} have been determined taking into accounts the forward bias InI-V data. The N_{ss} have an exponential increase with bias from the midgap towards the bottom of the conduction band. In summary this study, it can be said that these structures show good diode behavior. According to the electrical characterization, in the future, it can be used rectifying contacts, integrated circuits, the other electronic devices and so on.

ACKNOWLEDGEMENTS

We would like to acknowledge the financial support given by the TUBİTAK Foundation Project No: 108T500.

[1]. *R. Van de Walle, R.L. Van Meirhaeghe, W.H.Lafkre, F. Cardon*, J. Appl. Phys., 74 (3) (1993) 1885.

[2]. *E.H. Rhoderick, R.H. Williams*, Metal-Semiconductor Contacts, vol. 48, Clarandon Press, Oxford University Press, 1988. p. 20.

[3]. *R.H. Williams, G.Y. Robinson*, Physics and chemistry of III–V compound semiconductor interfaces, in: C.W. Wilmsen (Ed.), Plenum Press, New York, 1985.

[4]. *K. Potje-Kamloth*, Chem. Rev. 108 (2008) 367

[5]. *G. N.Lu, C.Barret and T.Neffati*, Solid St. Electron, 33 (1990) 1.

[6]. *M.Sağlam, E. Ayyıldız, A. Gümüş, A. Türüt, H.Efeoğlu, S. Tüzemen*, App. Phys A 62 (1996) 269

[7]. *Ş. Altındal, S. Karadeniz, N. Tuğluoğlu, A.Tataroğlu,* Solid State Electron, 47 (2003) 1847.

[8]. *Y.F. Nicolau*, Appl. Surf. Sci. 22–23 (1985) 1061

[9]. *O. Lupan, J. Meridian* Engineering 3 (2004) 41 (ISSN-1683-853X).

[10]. *T.P. Niesen, M.R. De Guire*, J. Electroceram. 6 (2001) 169.

[11]. *S.T. Shishiyanu, T.S. Shishiyanu, O.I. Lupan*, Sens. Actuators, B 107 (2005) 379.

[12]. *O. Lupan, Ph.D. Thesis*, Technical University of Moldova, Republic of Moldova, 2005.

[13]. *J.H. Werner*: Appl. Phys. A 47(1988) 291

[14]. *E. Ayyildiz, A. Turu t, H. Efeoglu, S. Tu zemen, M. Saglam, Y.K.Yogurtcu:* Solid-State Electron. 38 (1966) 83

[15]. *P. Chattopadhyay*, :Solid-State Electron. 37 (1994) 1759

[16]. *P. Chattopadhyay, B. Ray Chaudhuri*, Solid-State Electron,. 35(1992) 1023

[17]. *P. Cova, A. Singh*: Solid-State Electron,. 33 (1990) 11

[18]. *A. Ziel*: Solid State Physical Electronics, 2nd edn. (Prentice-Hall, Englewood Clifs, NJ 1968) pp 101

[19]. *S.M. Sze*: Physics of Semiconductor Devices, 2nd edn. (Willey, New York 1981) pp 270Ð282

[20]. *U. Kunze, W. Kowalsky*: J. Appl. Phys., 63 (1988) 1597

[21]. *A. Türüt, M. Saglam, H. Efeoglu, N. Yalcın, M.Yıldırım, B. Abay*. Physica B 205, (1995);:41.

[22]. *S. K. Cheung, N.W. Cheung*. Appl Phys Lett 49 (1986) 85.

[23]. *B. Batı, Ç. Nuhoğlu, M. Sağlam, E. Ayyıldız, A.Türüt*, Phys Scr, 61 (2000) 209.

[24]. *K. Maeda, H. Ikoma, K. Sato, T. Ishida*, Appl. Phys.Lett. 62 (1993) 20

AB INITIO STUDY OF ReB

C. BÜLBÜL[1], Y. O. CIFTCI[1], K. COLAKOGLU[1], H. B. ÖZIŞIK[2]
[1]*Department of Physics, Gazi University, 06500 Ankara, Turkey*
[2]*Physics Department, Aksaray University, 68100 Aksaray, Turkey*

In this work, we have performed a first-principles study on ReB compound by using the density functional theory implemented in the projector-augmented wave (PAW) method in NaCl(B1), CsCl (B2) and ZB(B3) crystal structures. Based on the optimized structural parameter, which is in good agreement with the experimental data, the electronic structure, elastic and thermodynamics properties are calculated. We have, also, predicted the temperature and pressure variation of the volume, bulk modulus, thermal expansion coefficient, heat capacities, and Debye temperatures in a wide pressure (0 - 79 GPa) and temperature ranges (0- 2000 K).

I. INTRODUCTION

Superhard materials are known to be used in many applications, from cutting and polishing tools to wear-resistant coatings. In synthesizing and designing new superhard materials, besides the traditional B-C-N systems, transition metal carbides, borides and nitrides are also very attractive, in particular the 5d transition metal compounds because 5d transition metals have relatively high bulk modulus [1], but the shear strength is low due to the non-directional metallic bonding and therefore they have low hardness [2]. Therefore, it is expected that through the insertion of B,C, or N atom into the 5d transition metals, superhard materials might be formed by inducing the non-directional metallic bonding in pure 5d transition metals to highly directional covalent bonding in the corresponding carbides, borides or nitrides.

Other theoretical studies included ReC with NaCl [4], WC [5,6] and NiAs [5] type structures have showed that ReC with WC type structures the potential hard materials due to high bulk and shear modulus[5, 6].

Recently, ReB_2 has been investigated both experimentally [7] and theoretically [8, 9]. ReB_2 was synthesized via arc-melting under ambient pressure with hexagonal structure and the bulk modulus was 360 GPa [7]. The calculated shear modulus was around 290 GPa [8]. E. Zhao et al. have studied electronic and mechanical properties of ReB and ReC by using ab initio study [3].

We carry out density functional calculations on the structural properties in NaCl(B1), CsCl(B2), ZB(B3) structures of ReB. The aim of the present paper is to reveal bulk, structural, elastic and thermodynamical properties using VASP method with plane-wave pseudopotential. In Section 2, a brief outline of the method of calculation is presented. In Section 3, the results are presented followed by a summary discussion.

II. METHOD OF CALCULATION

In the present work, all the calculations have been carried out using the Vienna ab initio simulation package (VASP) [10-11] based on the density functional theory (DFT). The electron-ion interaction was considered in the form of the projector-augmented-wave (PAW) method with plane wave up to energy of 700 eV [12-13]. This cut-off was found to be adequate for the structural, elastic properties as well as for the electronic structure. We do not find any significant changes in the key parameters when the energy cut-off is increased from 700 eV to 750 eV. For the exchange and correlation terms in the electron-electron interaction, Perdew and Zunger-type functional [14-15] was used within the generalized gradient approximation (GGA) [13]. The 12x12x12 Monkhorst and Pack [14] grid of k-points have been used for integration in the irreducible Brillouin zone. Thus, this mesh ensures a convergence of total energy to less than 10^{-5} ev/atom.

We used the quasi-harmonic Debye model to obtain the thermodynamic properties of ReB [15-16], in which the non-equilibrium Gibbs function *G*(V; P, T)* takes the form of

$$G^*(V;P,T)=E(V)+PV+A_{vib}[\theta(V);T] \tag{1}$$

In Eq.(1), *E(V)* is the total energy for per unit cell of ReB, *PV* corresponds to the constant hydrostatic pressure condition , $\theta(V)$ the Debye temperature and A_{Vib} is the vibration term, which can be written using the Debye model of the phonon density of states as

$$\mathrm{A_{Vib}}(\theta,\mathrm{T}) = nkT\left[\frac{9\theta}{8T}+3\ln\left(1-e^{-\frac{\theta}{T}}\right)-D\left(\frac{\theta}{T}\right)\right] \tag{2}$$

where *n* is the number of atoms per formula unit, $D\left(\frac{\theta}{T}\right)$ the Debye integral, and for an isotropic solid, θ is expressed as [17]

$$\theta_D = \frac{\hbar}{k}\left[6\pi V^{1/2}n\right]^{1/3} f(\sigma)\sqrt{\frac{B_s}{M}} \tag{3}$$

where *M* is the molecular mass per unit cell and B_S the adiabatic bulk modulus, which is approximated given by the static compressibility [18]:

$$B_s \approx B(V) = V\frac{d^2E(V)}{dV^2} \tag{4}$$

$f(\sigma)$ is given by Refs. [17-19] and the Poisson ratio are used as 0.2462 for ReB. For ReB, *n*=4 *M*= 280.69 a.u, respectively. Therefore, the non-equilibrium Gibbs function *G*(V; P, T)* as a function of *(V; P, T)* can be minimized with respect to volume *V*.

$$\left[\frac{\partial G^*(V;P,T)}{\partial V}\right]_{P,T} = 0 \tag{5}$$

By solving Eq. (5), one can obtain the thermal equation-of-equation (EOS) *V(P, T)*. The heat capacity at constant volume C_V, the heat capacity at constant pressure C_p, and the thermal expansion coefficient α are given [20] as follows:

$$C_v = 3nk\left[4D\left(\frac{\theta}{T}\right) - \frac{3\theta/T}{e^{\theta/T}-1}\right] \quad (6)$$

$$S = nk\left[4D\left(\frac{\theta}{T}\right) - 3\ln(1-e^{-\theta/T})\right] \quad (7)$$

$$\alpha = \frac{\gamma C_v}{B_T V} \quad (8)$$

$$C_p = C_v(1+\alpha\gamma T) \quad (9)$$

here γ represent the Grüneisen parameter and it is expressed as

$$\gamma = -\frac{d\ln\theta(\mathrm{V})}{d\ln \mathrm{V}} \ . \quad (10)$$

III. RESULTS AND DISCUSSION

3.1. Structural and Electronic Properties

Firstly, the equilibrium lattice parameter has been computed by minimizing the crystal total energy calculated for different values of lattice constant by means of Murnaghan's equation of state (eos) [21] as in Figure.1. The bulk modulus, and its pressure derivative have also been calculated based on the same Murnaghan's equation of state, and the results are given in Table 1 along with the experimental and other theoretical values. The calculated value of lattice parameters are 4.436A^0 in B1 (NaCl) phase, 2.761A^0in B2 (CsCl) phase, 4.768A^0 in B3 (ZB) phase for ReB, respectively. The present values for lattice constants are also listed in Table 1, and the obtained results are quite accord with the other experimental values [3-22].

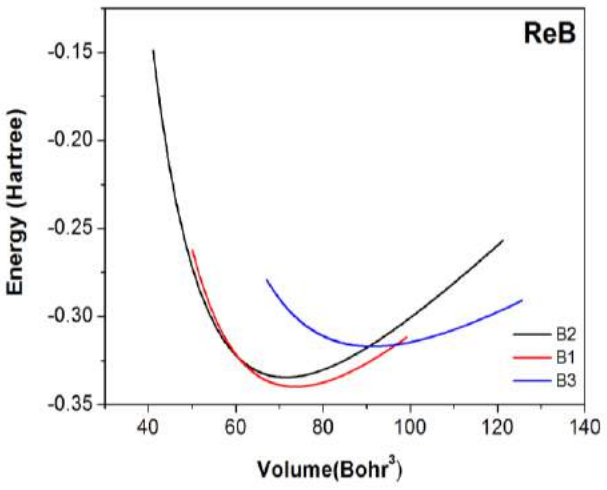

Fig. 1. Total energy versus volume curve of ReB in B1(NaCl), B2(CsCl), B3(ZB), phases.

Table1. Calculated equilibrium lattice constants (a_0), bulk modulus (*B*), pressure erivatives of bulk modulus (*B'*) and other theoretical works for ReB in B1, B2, B3 structures

Material	Structure	Referance	a	B(GPa)	B'	ΔH
ReB	B1	Present	4.436	302	4.06	333.5
		Theory[3]	4.370	335		
	B2	Present	2.761	300	4.09	333.7
		Theory[3]	2.709	386		
	B3	Present	4.768	199	4.15	334.7
		Theory[3]	4.697			

We have plotted the phase diagrams (equation of state) for both B1 and B2 phases in Figure 2. The discontinuity in volume takes place at the phase transition pressure. The phase transition pressures from B1 to B2 structure is found to be 79 GPa from the Gibbs free energy at 0 K for ReB and the related enthalpy versus pressure graphs for the both phases are shown in Figure 3 [22]. The transition pressure is a pressure at which *H(p)* curves for both phases crosses. The same result is also confirmed in terms of the "common tangent technique" in Figure.1. We have also plotted the normalized volume pressure diagram of ReB in B1 phase at the temperatures of 300K, 1200K and 2000K in Figure 4.

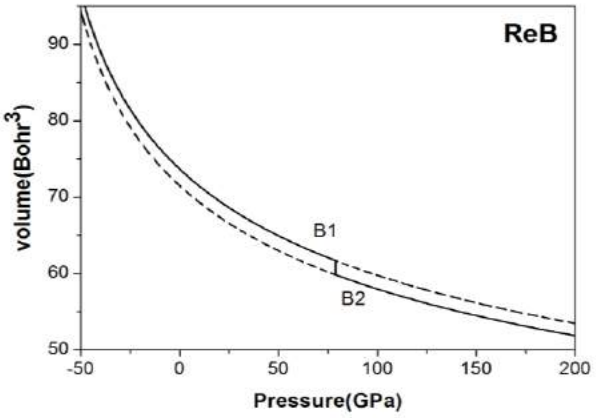

Fig. 2. Pressure versus volume curve of ReB

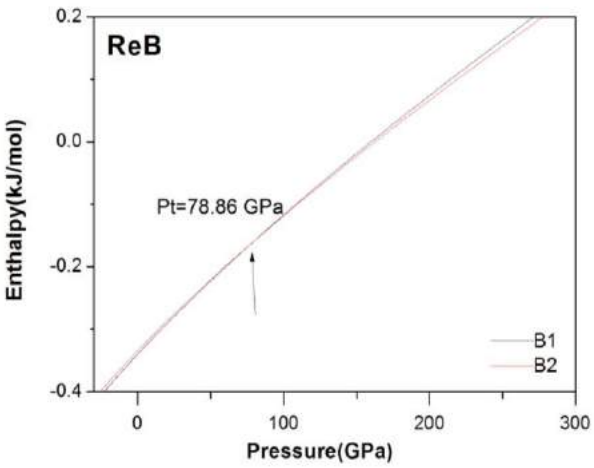

Fig. 3. Estimation of phase transition pressure from B1 to B2 of ReB

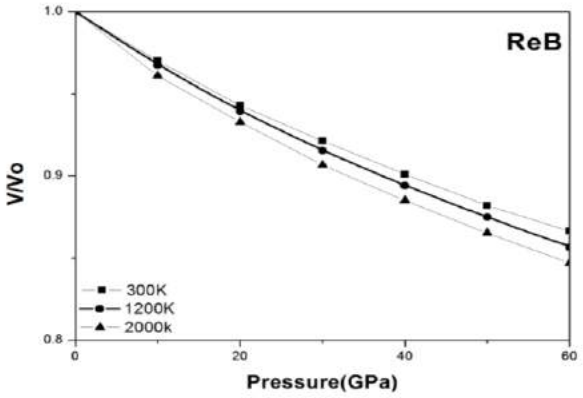

Fig. 4. The normalized volume-pressure diagram of the B1 for ReB at different temperatures

The present first – principles code (VASP) have also been used to calculate the band structures for ReB. The obtained results for high symmetry directions are shown in Figure 5 for B1 structures of ReB, respectively. It can be seen from the Figure 5 that no band gap exists for studied compounds, and they exhibit nearly metallic charecter. The total electronic density of states (DOS) corresponding to the present band structures are, also, depicted in Figure 5 and 6, and the disappearing of the energy gap in DOS conforms the metallic nature of ReB. The similar stuation is observed for LaN in our recent work [23].

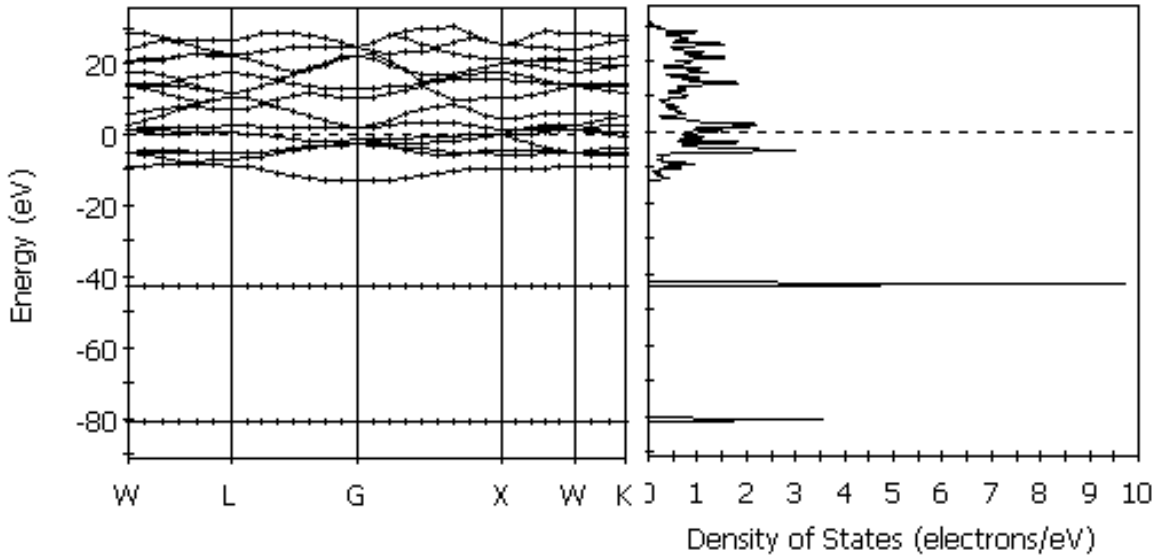

Fig. 5. Calculated band structure of ReB in phase B1

3.2. Elastic Properties

The elastic constants of solids provide a link between the mechanical and dynamical behaviour of crystals, and give important information concerning the nature of the forces operating in solids. In particular, they provide information on the stability and stiffness of materials. Their ab-initio calculation requires precise methods, since the forces and the elastic constants are functions of the first and second-order derivatives of the potentials. Their calculation will provide a further check on the accuracy of the calculation of forces in solids. The effect of pressure on the elastic constants is essential, especially, for understanding interatomic interactions, mechanical stability, and phase transition mechanisms. It also provides valuable data for developing interatomic potentials.

There are two common methods [24-25] for obtaining the elastic data through the ab-initio modelling of materials from their known crystal structures: an approach based on analysis of the total energy of properly strained states of the material (volume conserving technique) and an approach based on the analysis of changes in calculated stress values resulting from changes in the strain (stress-strain) method. Here we have used the "stress-strain" method for obtaining the second-oreder elastic constants (C_{ij}). The listed values for C_{ij} in Table 2 are in reasonable order. The experimental and theoretical values of C_{ij} for ReB are not available at present.

Table 2. The calculated elastic constants (in GPa unit) in different structures for ReB

Meterial	Structure	Referance	C_{11}	C_{12}	C_{44}
ReB	B1	Present	597	180	32
		Theory [3]	674	166	50
	B2	Present	608	214	83
		Theory [3]	702	228	119
	B3	Present	225	106	198
		Theory [3]			

The Zener anisotropy factor *A*, Poisson ratio υ, and Young's modulus *Y*, which are the most interesting elastic properties for applications, are also calculated in terms of the computed data using the following relations [26] :

$$A = \frac{2C_{44}}{C_{11} - C_{12}}, \quad (1)$$

$$\upsilon = \frac{1}{2}\left[\frac{(B - \frac{2}{3}G)}{(B + \frac{1}{3}G)}\right], \quad (2)$$

and

$$Y = \frac{9GB}{G + 3B} \quad (3)$$

where G = (G_V + G_R) /2 is the isotropic shear modulus, G_V is Voigt's shear modulus corresponding to the upper bound of G values, and G_R is Reuss's shear modulus corresponding to the lower bound of G values, and can be written as G_V = (C_{11}–C_{12} +3C_{44})/5, and 5/G_R = 4/(C_{11}-C_{12})+ 3/ C_{44}. The calculated Zener anisotropy factor (*A*), Poisson ratio (υ), Young's modulus (*Y*), and Shear modulus (C'=(C_{11}-C_{12}+2C_{44})/4) for ReB are given in Table 3 and they are close to those obtained for the similar structural symmetry.

Table 3. The calculated Zener anisotropy factor (*A*), Poisson ratio (υ), Young's modulus (*Y*), Shear modulus (C') for ReB in B1 structure

Material	*A*	υ	Y(GPa)	C' (GPa)
TbBi	0.1542	0.3845	209.5	120.25

3.3. Thermodynamics Properties

The Debye temperature (θ_D) is known as an important fundamental parameter closely related to many physical propertied such as specific heat and melting temperature. At low temperatures the vibrational excitations arise solely from acoustic vibrations. Hence, at low temperatures the Debye temperature calculated from elastic constants is the same as that determined from specific heat measurements. We have calculated the Debye temperature, θ_D , from the elastic constants data using the average sound velocity, υ_m, by the following common relation given [27]

$$\theta_D = \frac{h}{k}\left[\frac{3n}{4\pi}\left(\frac{N_A\rho}{M}\right)\right]^{1/3}\upsilon_m \quad (4)$$

where $\hbar$ is Planck's constants, *k* is Boltzmann's constants, N_A Avogadro's number, n is the number of atoms per formula unit, *M* is the molecular mass per formula unit, $\rho(=M/V)$ is the density, and υ_m is obtained from

$$\upsilon_m = \left[\frac{1}{3}\left(\frac{2}{\upsilon_t^3} + \frac{1}{\upsilon_l^3}\right)\right]^{-13} \quad (5)$$

where υ_l and υ_t, are the longitudinal and transverse elastic wave velocities, respectively, which are obtained from Navier's equations [28]:

$$\upsilon_l = \sqrt{\frac{3B + 4G}{3\rho}} \quad (6)$$

and

$$\upsilon_t = \sqrt{\frac{G}{\rho}}. \quad (7)$$

The calculated average longitudinal and transverse elastic wave velocities, Debye temperature and melting temperature for ReB are given in Table 4. No other theoretical or experimental data are exist for comparison with the present values.

The empirical relation [29], T_m=553 K+ (591/Mbar)C_{11} ± 300, is used to estimate the melting temperature for ReB, and found to be 4084 ± 300K. This value is higher than those obtained for Re (3453 K), We hope that the present results are a reliable estimation for these compounds as it contains only C_{11} which has a reasonable value.

Table 4. The longitudinal, transverse, average elastic wave velocities, and Debye temperature for ReB in B1 structure

Material	$\upsilon_l(m/s)$	$\upsilon_t(m/s)$	$\upsilon_m(m/s)$	$\theta_D(K)$	$T_m(K)$
ReB	5185.83	2246.17	2537.32	214.6	4084 ±300

The thermal properties are determined in the temperature range from 0 to 2000 K for ReB, where the quasi-harmonic model remains fully valid. The pressure effect is studied in the 0-79 GPa range. The relationship between normalized volume and pressure at different temperature is shown in Figure 4 for ReB. It can be seen that when the pressure increases from 0 GPa to 79 GPa, the volume decreases. The reason of this changing can be attributed to the atoms in the interlayer become closer, and their interactions become stronger. For ReB compound the normalized volume decreases with increasing temperature. The relationship between bulk modulus (B) and pressure (P) at different temperatures (300, 1200, and 2000K) is shown in Fig. 6. for ReB. It can be seen that bulk modulus decreases with the temperature at a given pressure and increases with pressure at a given temperature. It shows that the effect of increasing pressure on ReB is the same as decreasing its temperature.

The variations of the thermal expansion coefficient (α) with temperature and pressure are shown in Fig.7 and Fig. 8 for ReB, respectively. It is shown that, the thermal expansion coefficient α also increases with T at lower temperatures and gradually approaches linear increases at higher temperatures, while the thermal expansion coefficient α decreases with pressure. At different temperature, α decreases nonlinearly at lower pressure and decreases almost linearly at higher pressure. Also, It can be seen from Fig. 7 that the temperature dependence of α is very small at high temperature and higher pressure.

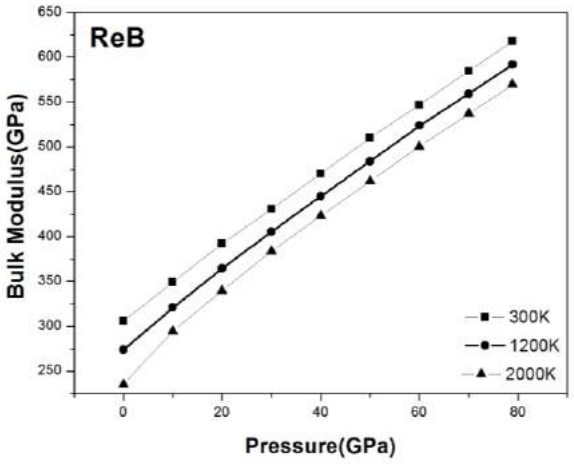

Fig. 6. The reletionships of ReB between bulk modulus (B) and pressure P at temperatures of 300 K,1200 K, 2000 K

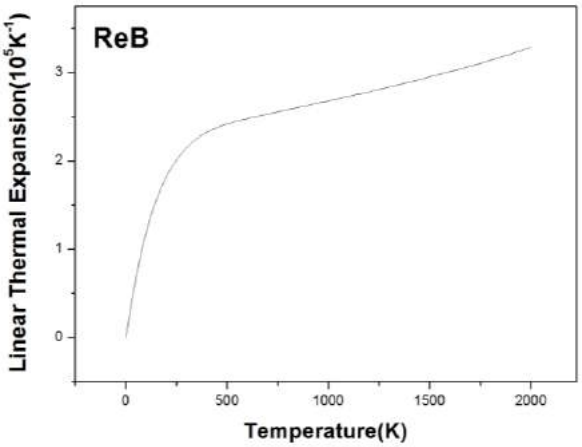

Fig.7. The thermal expansion versues temperature for ReB.

The relationship between heat capacity at constant pressure and temperature, also the relationship between capacity at constant volume C_v and temperature at different pressures P are shown in Fig.9 for ReB. It is realized from figures that when T<800 K, C_v increases very quickly with temperature; when T>800 K, C_v increases slowly with temperature and it almost approaches a constant called as Dulong-Petit limit ($C_v(T)$~3R for mono atomic solids) at higher temperatures for both compounds.

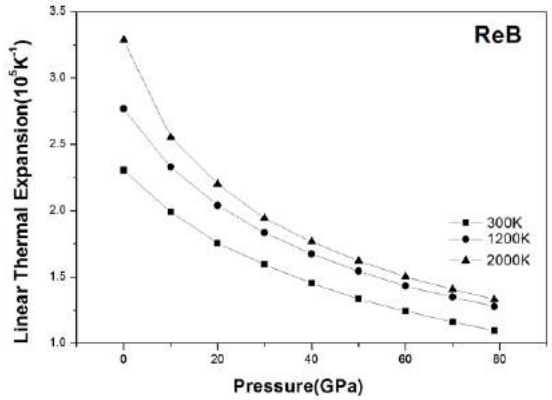

Fig. 8. The thermal expansion versues pressure for ReB.

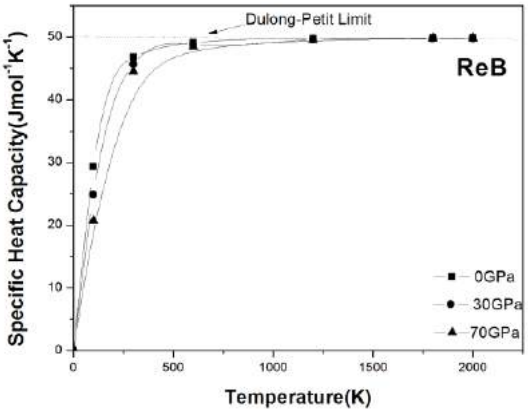

Fig.9. The variation of specific heat capacity with temperature at different pressures for ReB.

IV. CONCLUSIONS

The fist–principles pseudopotential calculations have performed on the ReB. Our present key results are on the elastic, electronic and structural properties for ReB. The lattice parameters are excellent agreement with the other theoretical values. The computed band structures for ReB shows metallic character. It is hoped that some our results, such as elastic constants, Debye temperatures and melting temperatures estimated for the first time in this work, will be tested in future experimentally and theoretically

[1]. *J.J. Gilman, R.W. Cumberland, R.B. Kaner,* Int.J.Refractory Met. Hard Mater.24 (2006) 1.
[2]. *J. Haines, J.M. Leger, G. Bocquillon*, Annu. Rev. Mater. Res. 31 (2001) 1.
[3]. *E.Zhao, J. Wang, J. Meng, Z. Wu*, Journal of Soild States Chemistry 182 (2009) 960-965
[4]. *J.C. Grossman, A. Mizel, M. Cote,M.L.Cohen, S.G. Louie*, Phys. Rev. B 60 (1999) 6343
[5]. *Z.W. Chen, M.X. Gu, C.Q. Sun, X.Y. Zhang, R.P.Liu*, Appl. Phys. Lett. 91 (2007) 061905
[6]. *Y.X. Wang*, Phys. Stat. Solidi(RRL) 2 (2008) 126.
[7]. *H.-Y. Chung, M.B. Weinberger, J.B. Levine, A.Kavner, J.-M. Yang, S.H. Tolbert, R.B. Kaner,* Science 316 (2007) 436
[8]. *X.F. Hao, Y.H. Xu, Z.J. Wu, D.F. Zhou, X.J. Liu, X.Q. Cao*,J.Meng, Phys. Rev. B 74 (2006) 224112.
[9]. *R.F. Zhang, S. Veprek, A.S. Argon*, Appl. Phys. Lett. 91 (2007) 201914.
[10]. *G. Kresse and J. Hafner,* Phys. Rev. B , 47(1994)558.
[11]. *G. Kresse and J. FurthmÄuller,* Phys. Rev. *B*, 54 (1996) 11169.

[12]. *G. Kresse and D. Joubert* , Phys. Rev. *B*, 59 (1999) 1758.
[13]. *P. E. Blochl*, Phys. Rev. *B*, 50 (1994) 17953.
[14]. *H.J. Monkhorst and J.D. Pack*, Phys. Rev. B, 13(1976) 5188.
[15]. *M.A. Blanco, E. Francisco, V. Lunana* , Comput. Phys. Commun. , 158 (2004)57.
[16]. *F. Peng, H.Z. Fu, X.D. Yang.* , Physica B , 403 (2008) 2851.
[17]. *M.A. Blanco, A.M. Pendàs, E. Francisco, J.M.Recio, R. Franko,* J.Mol. Struct. (Theochem)368 (1996) 245
[18]. *M. Flórez, J.M. Recio, E. Francisco, M.A. Blanco, A.M. Pendàs,* Phys. Rev. B , 66 (2002) 144112.
[19]. *E. Francisco, , J.M. Recio, M.A. Blanco, A.M.Pendàs,* J. Phys. Chem. ,102 (1998) 1595.
[20]. *R. Hill*, Proc. Phys. Soc. Lond. A , 65 (1952) 349.
[21]. *F. D. Murnaghan*, Proc. Natl., Acad. Sci. USA 30, 5390 (1994)
[22]. *Iandelli*, Rare Earth Research, edited by *Kleber E.V., MacMillan Co*, New York 1966, pp. 135–144. [23]. *Y.O. Ciftci, K.Colakoglu, E.Deligoz, and H. Ozısık,* Mat. Chem. And Phys., 108 (2008) 120.
[23]. *J. Mehl*, Phys. Rev. B 47 (1993) 2493.
[24]. *S.Q. Wang, H.Q. Ye*, Phys. Status Solidi B 240 (2003) 45.
[25]. *B. Mayer, H. Anton, E. Bott, M. Methfessel, J.Sticht, and P. C. Schmidt*, Intermetallics 11 (2003) 23.
[26]. *Johnston, G.Keeler, R. Rollins, and S.Spicklemire*, Solid State Physics Simulations, The Consortium for Upper-Level Physics Software, Jhon Wiley, New York, 1996.
[27]. *E. Schreiber, O. L. Anderson, N. Soga*, Elastic Constants and their Measurements, McGraw-Hill, New York, 1973.
[28]. *M.E. Fine, L.D. Brown, H.L. Marcus*, Scr. Metall. 18 (1984) 951.

ARMCHAIR DOUBLE-WALLED CARBON NANOTUBE ON RUTILE TiO_2(110)-(1×2)

CEREN TAYRAN[1], MEHMET ÇAKMAK[1], ŞİNASİ ELLİALTIOĞLU[2]
[1]*Department of Physics, Gazi University, Ankara 06500, Turkey*
[2]*Department of Physics, Middle East Technical University, Ankara 06531, Turkey*
c.tayran@gazi.edu.tr , cakmak@gazi.edu.tr, sinasi@metu.edu.tr

We have studied the atomic and electronic structures of (3,3)-in-(7,7) double-walled carbon nanotube (DWCNT) adsorbed on the reconstructed rutile TiO_2(110)-(1×2) surface by using ab initio calculations. The DWCNT is seen not to chemisorb on the reconstructed rutile surface described by the added-row model. When topmost oxygens are removed from the added-row, a significant binding for the tube was obtained through Ti–C chemical bonds. The binding energy is found to be 2.51 eV. The metallic character of (3,3)-in-(7,7) DWCNT is unchanged on this surface. We have obtained the electronic band structure, and the effect and contributions of DWCNT to the gap states is also discussed.

I. INTRODUCTION

In recent years, carbon nanotubes (CNTs) have started an immense research field, due to their unique electrical and mechanical properties [1,2]. CNTs are obtained by rolling up graphite layers [1]. Their electronic structure depends on their chirality and diameter [3]. All the armchair CNTs, equal chiral indices (*n*,*n*), show metallic character [2] are hoped to be used as wiring materials in electronic nanodevices [4,5]. CNTs attachment to technologically important substrates for nanodevices is an essential challenge. Recently, Orellana et al. [6] investigated armchair (6,6) single walled carbon nanotubes (SWCNT) adsorbed on Si (001) surface. Peng et al. [7] also studied adsorption of metallic SWCNTs on the Si (001) surface. Adsorbed SWCNTs are found to be either semiconducting or metallic depending on adsorption sites and the hydrogen content of the substrate surface. They also studied the adsorption of (2,2)-in-(6,6) DWCNT on Si (001), which was found to be similar to (6,6) SWCNTs on Si (001).

On the other hand, it is believed that future technology will make use of the metal–oxide materials that have high dielectric constants. In particular, TiO_2, $SrTiO_3$, HfO_2 have received serious interest, apart from other important fields of application. Among these, we considered TiO_2 in this work, which crystallizes mainly in three polymorphs, namely, rutile, anatase, and brookite [8]. Rutile is the most stable one and studied extensively both by experimentalists [9] as well as the theoreticians [10,11]. The most stable facet of the rutile is the (110) surface which is the lowest in energy [12–14]. Rutile TiO_2 (110) surface has essentially two models which are the stoichiometric and the nonstoichiometric (reconstructed) ones. In this work, we considered the reconstructed (Ti_2O_3, added-row) model, in agreement with Onishi's proposal based on STM patterns [15]. When the topmost oxygens are snapped out of added-row model, missing row model is obtained. The added-row model (as given by DFT) exhibits a metallic character, and may play a significant role in wiring [16].

In this paper, we have explored the electronic and structural properties of a metallic (3,3)-in-(7,7) DWCNT adsorbed on the reconstructed rutile TiO_2(110)-(1×2) added row model (ARM) surface by using ab initio calculations. In addition, we have calculated energy band structure and investigated the characteristic orbital bonding between Ti–O and Ti–C.

II. METHOD

The calculations have been performed with the Vienna ab initio simulation package (VASP) [17,18] which is a DFT code. Electronic wave functions were expanded in plane waves with a cutoff energy of 30 Ry. The electron–ion interaction was carried out in the form of projector augmented plane waves (PAW) [19,20]. The electron exchange–correlation was described by the generalized gradient approximation (GGA) using the Perdew–Burke–Ernzerhof (PBE) functional [21]. The calculated lattice constant *a*, 4.653 Å, is larger than the experimental value of 4.593 Å and *c/a*, 0.639, is good agreement with the experimental data 0.644 [22]. The band gap of bulk rutile is calculated to be 1.69 eV which is small compared to its experimentally measured value of 3.03 eV [23] for reasons due to the DFT underestimation. The Brillouin zone was determined by an 8×3×1 Monkhorst–Pack [24] grid of k-points. The slabs were separated by 21 Å of vacuum.

III. RESULTS AND DISCUSSION

Atomic structure of the rutile TiO_2(110)-(1×2) ARM surface is shown Fig. 1(a). The calculated Ti–Ti vertical bond length $d_{1\perp}$ is found to be 2.74 Å for the reconstructed clean surface. DWCNT is found not to get bonded to this reconstructed rutile TiO_2(110)-(1×2) surface of added-row model, because both this surface and the DWCNT are chemically stable. However, when the topmost bridging oxygens are removed from the added-row (ORAR) model, shown in Fig. 1(b), it now becomes possible for the armchair DWCNT to bind to the new relaxed surface which is chemically more active. For the clean ORAR surface $d_{1\perp}$ is found to be 2.72 Å, a little smaller than that for the ARM. Fig. 1(c) shows the (3,3)-in-(7,7) DWCNT adsorbed on the ORAR surface. The structure is relaxed and binding energy is calculated through the formula

$$E_{\mathrm{b}} = E_{\mathrm{TiO_2}} + E_{\mathrm{CNT}} - E_{\mathrm{CNT/TiO_2}}$$

where $E_{\mathrm{TiO_2}}$ is the energy of the clean ORAR surface, E_{CNT} is the energy of the isolated DWCNT, and $E_{\mathrm{CNT/TiO_2}}$ is the total energy of the combined system after the adsorption.

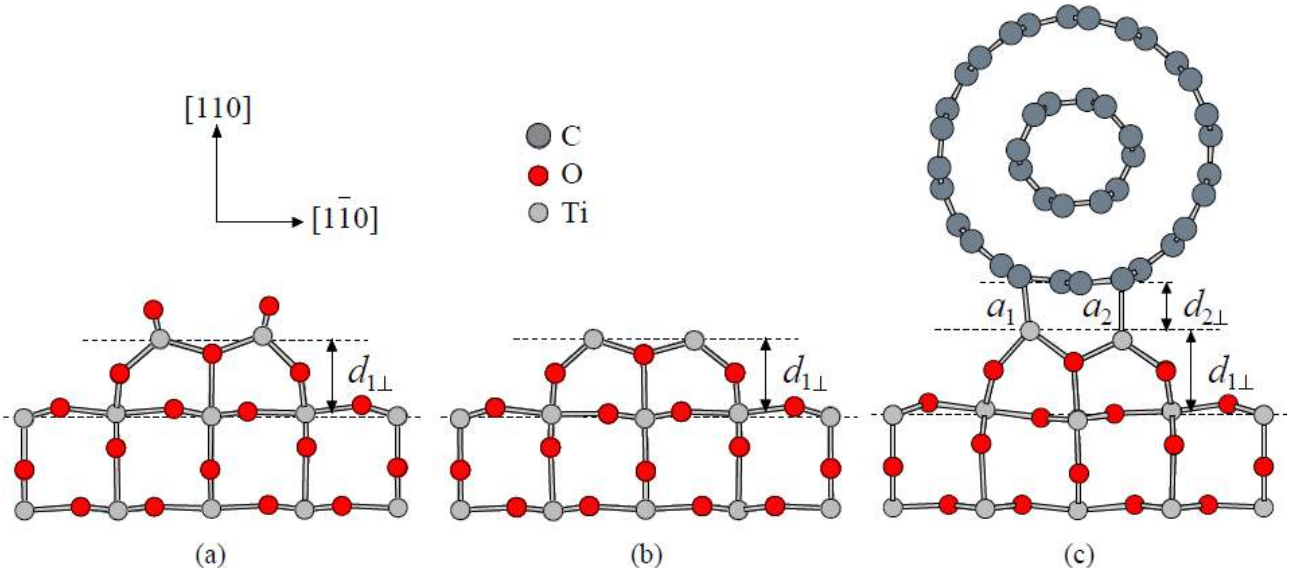

Fig. 1. Schematic side views for the atomic structures of slabs used for **(a)** rutile TiO_2(110)-(1×2) ARM surface, **(b)** oxygen-removed added-row (ORAR) surface, and (c) (3,3)-in-(7,7) DWCNT adsorbed on the ORAR rutile surface.

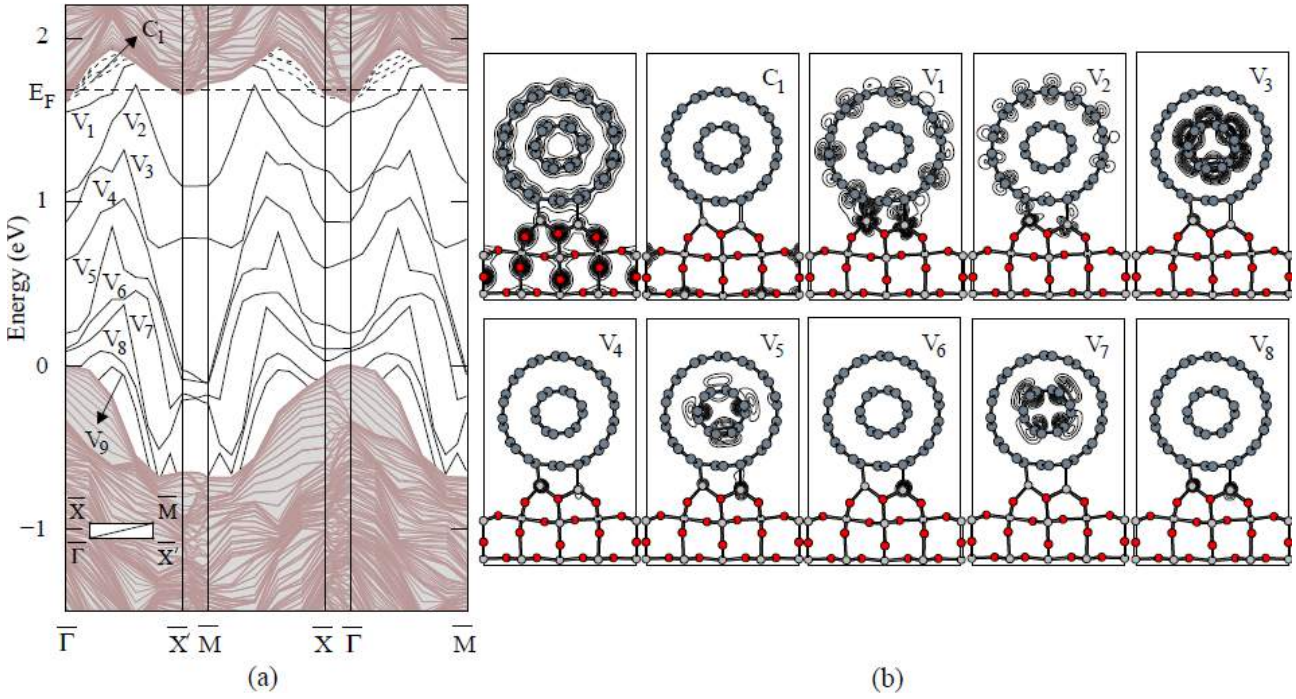

Fig. 2. (a) The surface electronic band structure for the (3,3)-in-(7,7) DWCNT adsorbed on the ORAR rutile surface. ***(b)*** The first one is the total electronic charge density, the others are electronic charge density plots fort he individual gap states.

The binding energy is found to be 2.51 eV. The reconstructed geometries of the chemisorbed DWCNT show small distortions and change in diameters because of the newly formed chemisorption bonds. The inner (3,3) CNT is enlarged in diameter from 4.0062 Å to 4.0116 Å (0.13 %), while the (7,7) CNT from 9.4655 Å to 9.6958 Å (2.43 %). The Ti–C chemisorption bonds are found to have lengths of a_1=2.40 Å and a_2=2.16 Å, as indicated in Fig. 1(c) and tabulated in Table 1. The a_1 is somewhat bigger than 2.23 Å, the sum of the covalent radii, because of the asymmetry and incommensurate positionig in longitudinal direction, whereas a_2 is somewhat shorter. The calculated Ti–Ti vertical distance $d_{1\perp}$ is found to be 2.79 Å. Also, $d_{2\perp}$, the vertical distance between Ti–C is calculated to be 1.91 Å. The results for the physical parameters of the relaxed structures are listed in Table 1.

Table 1. The relaxed geometrical parameters (in Å) for the three systems shown in Fig. 1, and the binding energy E_b (in eV) for the combined system in Fig. 1(c).

	ARM	ORAR	DWCNT/ORAR
$d_{1\perp}$	2.74	2.72	2.79
$d_{2\perp}$			1.91
a_1			2.40
a_2			2.16
E_b			2.51

We have calculated the band structure and the corresponding charge densities for the (3,3)-in-(7,7) DWCNT adsorbed on this surface which are shown in Fig. 2(a) and (b). A total of ten gap states have been observed in the surface energy band structure is shown in Fig. 2(a). The position of E_F is shown by the dashed line which is just above the conduction band edge (according to DFT). The partially unoccupied state C_1 is above the bulk conduction band edge but cut by the Fermi level. The partially occupied surface states V_1 and V_2 which show a rather complex picture are related to *s*- and *d*-orbitals of Ti atoms, with some contribution from C π-orbitals of the (7,7) CNT. The states V_3 and V_5 are due to π-bonding between C–C atoms contributed by the inner (3,3) CNT. These states are somewhat related to *s*-orbital of Ti atoms as well. The V_4, V_6, and V_8 states are resulted by *s*-orbital of Ti atoms. The state V_7 is due to π-bonding between C–C atoms. The state V_9 is entirely below the bulk valence band edge.

IV. CONCLUSIONS

In conclusion, we have presented first principles calculations for the adsorption of a metallic armchair (3,3)-in-(7,7) DWCNT on the rutile TiO_2(110)-(1×2) surface. The nanotube did not get bonded neither on the stoichiometric surface, nor on the trench of the reconstructed added-row model, not even on the added row itself. However, binding with an energy of 2.51 eV were achieved onto the modified added-row model with the outermost bridging oxygens removed. The binding is through Ti–C chemical bonds. Armchair DWCNT remained metallic upon adsorption. Hopes for the usage of CNTs as wiring materials on titania surfaces continue.

[1]. *S. Iijima*, Nature (London) 354 (1991) 56.

[2]. *M.S.Dresselhaus,G.Dresselhaus and P.C.Eklund*, "Science of Fullerenes and Carbon Nanotubes" (Academic, San Diego) (1996).

[3]. *J.W.Mintmire and C.T.White*, Carbon 33 (1995) 893.

[4]. *T.W.Odom, J.L.Huang, P.Kim, and C.M.Lieber*, J. Phys. Chem. B 104 (2000) 2794.

[5]. *Y.Homma, T.Yamashita, Y.Kobayashiand T.Ogino*, Physica 323 (2002) 122.

[6]. *W. Orellana, R.H. Miwa, and A. Fazzio*, "First-principles Calculations of Carbon Nanotubes Adsorbed on Si(001)", Phys. Rev. Lett. 91 (2003) 166802.

[7]. *G. W. Peng, A. C. H. Huan, L. Liu, Y. P. Feng*, "Structural and electronics properties of 4 Å carbon nanotubes on Si(001) surfaces", Phys. Rev. B 74 (2006) 235416.

[8]. *F. Labat, P. Baranek, C. Domain, C. Minot, and C. Adamo*, J. Chem. Phys. 126 (2007) 154703.

[9]. *V. E. Henrich*, Rep. Prog. Phys. 48 (1985) 1481.

[10]. *K. M. Glassford and J. R. Chelikowsky*, Phys. Rev. B 46 (1992) 1284.

[11]. *P. Reinhardt, B. A. Heß, and M. Causá*, Inter. J. Quantum Chem. 58 (1996) 297.

[12]. *V. Henrich and R. L. Kurtz*, Phys. Rev. B 23 (1981) 6280.

[13]. *M. Ramamoorthy, D. Vanderbilt, and R.D. King-Smith*, Phys. Rev. B 49 (1994) 16721.

[14]. *J.Goniakowski, J.M.Holender, L.N.Kantorovich, M.J.Gillan, and J.A.White*, Phys. Rev. B 53 (1996) 957.

[15]. *H. Onishi and Y. Iwasawa*, Surf. Sci. 313 (1994) L783.

[16]. *M. Blanco-Rey, J. Abad, C. Rogero, J. Méndez, M. F. López, J. A. Martín-Gago, and P. L. de Andrés*, Phys. Rev. Lett. 96 (2006) 055502.

[17]. *G. Kresse and J. Furthmüller*, Comp. Mat. Sci. 6 (1996) 15.

[18]. *G. Kresse and J. Furthmüller*, Phys. Rev. B 54 (1996) 11169.

[19]. *G. Kresse and D. Joubert*, Phys. Rev B 59 (1999) 1758.

[20]. *P. E. Blöchl*, Phys. Rev. B 50 (1994) 17953.

[21]. *J.P. Perdew, K. Burke, and M. Ernzerhof*, Phys. Rev. Lett. 77 (1996) 3865.

[22]. *J.K.Burdett, T.Hughbanks, G.J.Miller, J.W.Richardson, and J. V. Smith*, J. Am. Chem. Soc. 109 (1987) 3639.

[23]. *A. Amtout and R. Leonelli*, Phys. Rev. B 51 (1995) 6842.

[24]. *H. Monkhorst and J. Pack*, Phys. Rev. B, 13 (1976) 5188.

EFFECT OF DIFFERENT SOLUTIONS ON ELECTROCHEMICAL DEPOSITION OF ZnO

H. ASIL, K. ÇINAR, E. GÜR, C. COŞKUN, S. TÜZEMEN
Department of Physics, Faculty of Sciences,
Atatürk University, 25240, Erzurum/Turkey
ccoskun@atauni.edu.tr

ZnO thin films were grown by electrochemical deposition (ECD) onto indium tin oxide using different compounds such as $Zn(NO_3)_2$, $Zn(C_2H_3O_2)_2$, $ZnCl_2$, $Zn(ClO_4)_2$,and different solvents such as dimethylsulfoxide (DMSO) and 18 MΩ de-ionized water. Furthermore, solutions were prepared using different electrolytes and concentrations in order to determine the optimum deposition parameters of ZnO. All the grown films were characterized by X-ray diffraction, optical absorption and photoluminescence measurement techniques. It is indicated that films grown by using $Zn(ClO_4)_2$ show high crystallinity and optical quality. The X-ray diffraction analysis showed that ZnO thin films which were grown electrochemically in a non-aqueous solution (DMSO) prepared by $Zn(ClO_4)_2$ have highly c-axis (0002) preferential orientation. PL measurements showed that ZnO thin films grown in $Zn(ClO_4)_2$ indicates high quality emission characteristics compared to the thin films grown by other solutions.

I. INTRODUCTION

In recent years, electrochemical deposition of thin metal oxide films on various substrates has been a gradually active research area, because the technique provides various advantages: low temperature processing, arbitrary substrate shapes, controllable film thickness and morphology, and low capital cost due to low-temperature aqueous solution as medium [1-6]. Metal-oxide thin films, particularly wide and direct band gap semiconductors, are of great interest in optoelectronic industry, including visible and ultraviolet (UV) region optical devices, such as light-emitting diodes and laser diodes. Zinc oxide (ZnO), with a direct band gap of 3.3 eV [3-7] and a high exciton binding energy of 60 meV at room temperature [8], is an n-type semiconductor material which is candidate for these applications. ZnO thin films are usually prepared by many growth techniques, such as molecular beam epitaxy [9], chemical vapor deposition [10], radio frequency magnetron sputtering [11, 12] and electrochemical deposition [1-7,13-20]. Among these, besides ECD is the cheapest, easiest and the simplest one, it is also possible to produce high quality epitaxial layers [21]. Izaki has succeed to grow n-type ZnO electrochemically in high quality and homogeneously. Izaki and Omi [4,7] reported on the cathodic ECD of ZnO from aqueous zinc nitrate solutions. Pauporte and Lincot [13], Gao et al. [22] and Fahoume et al. [16] have grown the ZnO thin films by ECD technique using zinc chloride, zinc perchlorate and both solutions, respectively. Gal et al. [6] indicated the electrochemical deposition of ZnO in dimethylsulfoxide (DMSO), which is a widely used as non-aqueous solvent for electrodeposition due to its high dielectric constant. We have reported on the preparation of ZnO thin films by ECD growth technique and investigated the effect of different compounds and solvents on structural and optical properties of the ZnO films.

II. EXPERIMENTAL

The growth of ZnO thin films is performed in a conventional electrochemical cell with three electrodes on ITO (sheet resistance 15-25 Ω/□) substrate, the working electrode. A zinc plate is a counter electrode and an Ag/AgCl electrode has been used as a reference electrode. Prior to the ECD, substrate was subjected to trichlorethylene, acetone and methanol cleaning in an ultrasonic bath at 2 min and then rinsed in de-ionized water. An ITO cathode was thermally treated at 300 ºC for 30 min to reduce both resistance and surface roughness [1, 2, 23].

ZnO films were prepared from aqueous solutions and DMSO containing $ZnCl_2$, $Zn(ClO_4)_2$, $Zn(NO_3)_2$ and $Zn(C_2H_3O_2)_2$ (0.02 M, 0.05 M and 0.1 M, respectively) and 0.1 M $LiClO_4$ as supporting electrolyte. The temperature was kept at a temperature between 70-85 ºC for aqueous solutions and at 130 ºC for non-aqueous, DMSO. The applied volatge was -1 V with respect to the Ag/AgCl. The ECD growth of ZnO thin films was carried out by Gamry Reference 600 Potentiostat/ Galvanostat/ ZRA. The X-ray diffraction measurement is performed using Rigaku D/Max-IIIC diffractometer, with Cu Kα radiation of 1.54 Å, within the 2θ angle ranging from 20-80. Optical transmission measurements were carried out using RF 5301 PC Shimadzu spectrophotometer at room temperature in wavelength range of 310-580 nm. Absorption spectra of the films were recorded using Perkin Elmer UV/VIS spectrophotometer Lambda 2S by scanning the wavelength in the range from 200 to 1000 nm with reference to air.

III. RESULT AND DISCUSSION

Optimum growth conditions for the ZnO thin films were determined by repeating the experiments at different growth parameters such as pH, temperature of solution, growth time, growth potential, etc.. The best parameters for four different Zn sources prepared in de-ionized (DI) water are given in Table 1. Figure 1 shows XRD results of these ZnO thin films grown in different aqueous solutions. As seen in figure, no growth takes place in zinc acetate, $Zn(CH_3COO)_2$, solution. For zinc chloride ($ZnCl_2$) and zinc perchlorate ($Zn(ClO_4)_2$), very weak XRD peaks have been observed, and the films had polycrystal nature for zinc nitrade ($Zn(NO_3)_2$) source. However, the ZnO films prepared in DMSO gave very strong XRD peaks and showed a single crystal orientation preferring (0002) direction, except for zinc acetate. The optimum growth parameters and the XRD peaks for three different non-aqueous Zn solutions have been given in Table 2 and Figure 2, respectively. These results are consistent with the literature [4, 6, 13, 17-18].

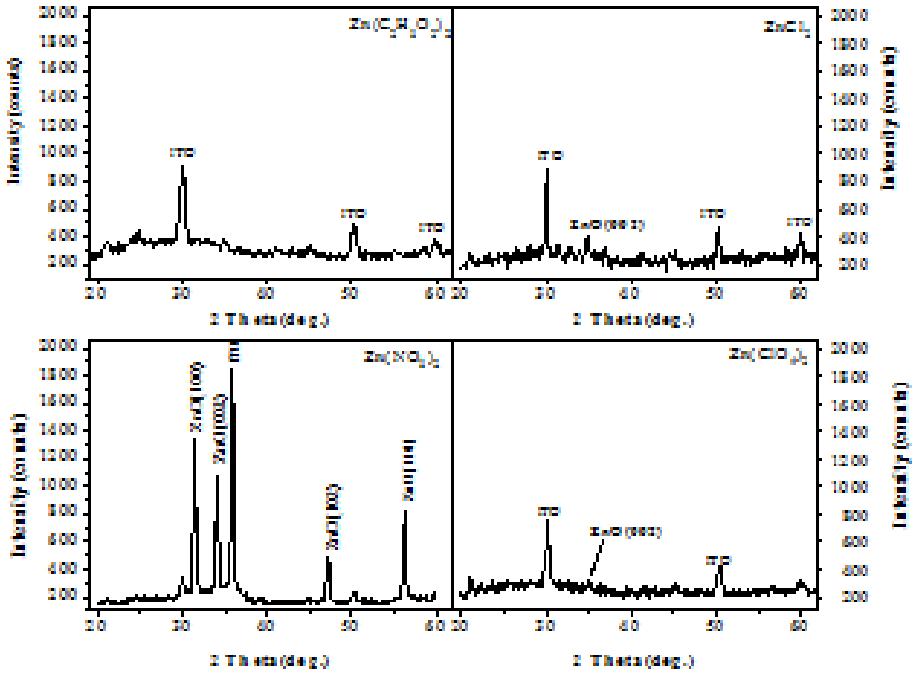

Fig. 1. XRD measurements of the ZnO thin films grown in DI water.

Table 1. Optimum growth parameters of ZnO thin films grown using different compounds in DI water.

Compound	Molarite (Zn source) (M)	Supporting Electrolyte	Potential (V)	Time (sec.)	pH	Temp. (°C)
$Zn(ClO_4)_2$	$2x10^{-2}$	0,1 M $LiClO_4$	-0,39	3600	6	65
$ZnCl_2$	$5x10^{-3}$	0,1 M $LiClO_4$	-1,16	900	5	70
$Zn(CH_3COO)_2$	$2x10^{-2}$	-	-0,89	900	6,1	50
$Zn(NO_3)_2$	$2x10^{-2}$	-	-1,25	300	6	65

Table 2.Optimum growth parameters of the ZnO thin films grown in DMSO.

Compound	Molarite (Zn source) (M)	Supporting Electrolyte	Potential (V)	Time (sec.)	pH	Temperature (°C)
$Zn(ClO_4)_2$	$5x10^{-2}$	0,1 M $LiClO_4$	-1	3600	6	130
$ZnCl_2$	$5x10^{-3}$	0,1 M $LiClO_4$	-1	3600	7	130
$Zn(NO_3)_2$	$2x10^{-2}$	0,1 M $LiClO_4$	-1	3600	6	130

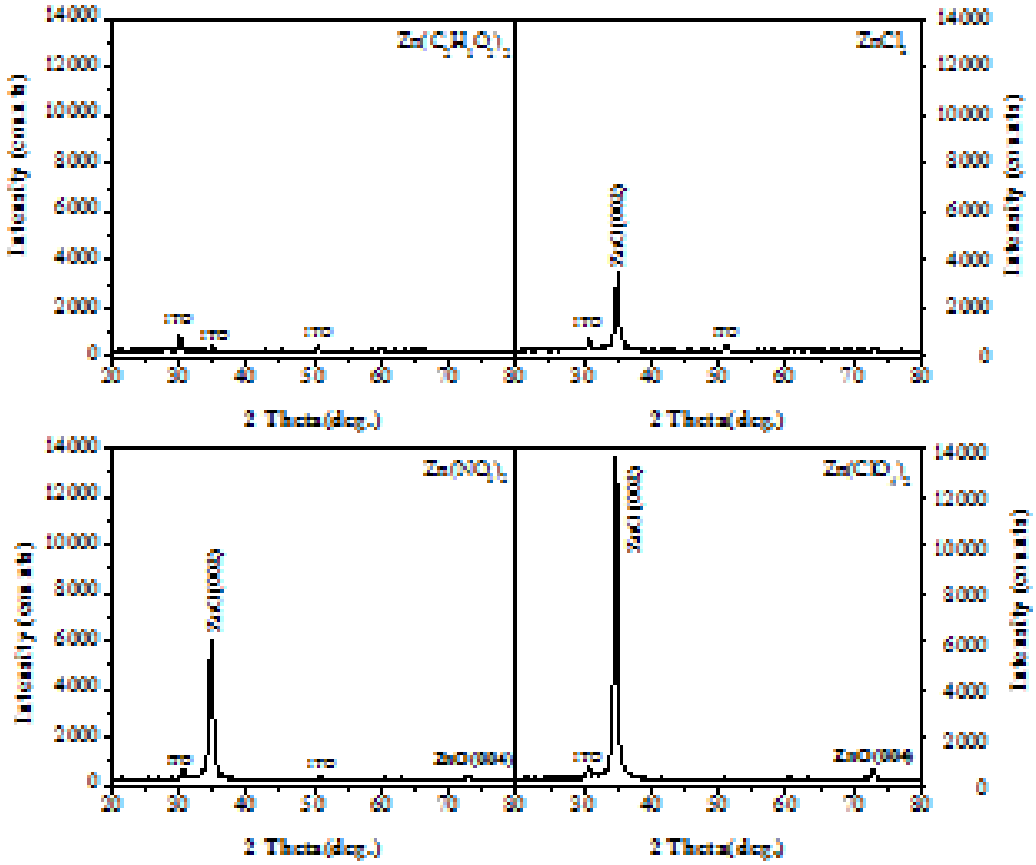

Fig. 2. XRD results of the ZnO thin films grown in DMSO

Table 3.Optimum growth parameters of the ZnO thin films grown in DMSO.

Compound	**Grain Size (nm)**	**2θ**	**d (hkl)**	**FWHM (degree)**	**Main Peak Intensity**	**Normalized Peak Intensity (ZnO/ITO)**
$Zn(ClO_4)_2$	174,25	34,76	2,579	0,478	13554	17,55
$ZnCl_2$	151,95	35	2,562	0,548	3424	4,24
$Zn(NO_3)_2$	136,04	34,7	2,583	0,612	6022	9,67

We have also calculated the grain size, peak directions, the distance between layers, full width at half maximum values (FWHM) and peak intensities from the XRD results (Table 3). The best crystal parameters have been obtained for zinc perchlorate prepared in DMSO. The crystallite sizes of ZnO thin films were calculated by means of well-known Scherrer equation. Results indicate that the higher structural quality has been reached using the $Zn(ClO_4)_2$ prepared in DMSO, as a zinc source.

Optical absorption spectra of these ZnO thin films grown in DMSO are shown in Figure 3(a). The measurements were taken with respect to air as the optical reference. As seen from the Figure 3(a), all ZnO films have a sharp absorption band edge. Optical absorption or transparency of ZnO is related to the roughness of the surface and the presence of defects. If surface of the ZnO films is smooth, they show good optical transparency or absorption [24]. The band gap energy of the grown thin films can be determined by extrapolation of the linear part of the plot of α^2 versus the incident radiation energy, *hv*, as shown in Figure 3b; which indicates that the near band edge optical absorption. The optical absorption edge has been observed at a wavelength of about 365 nm corresponding to band gap energy of about 3.4 eV for all samples. This value is quite consistent with the literature for as-deposited ZnO films [8, 23].

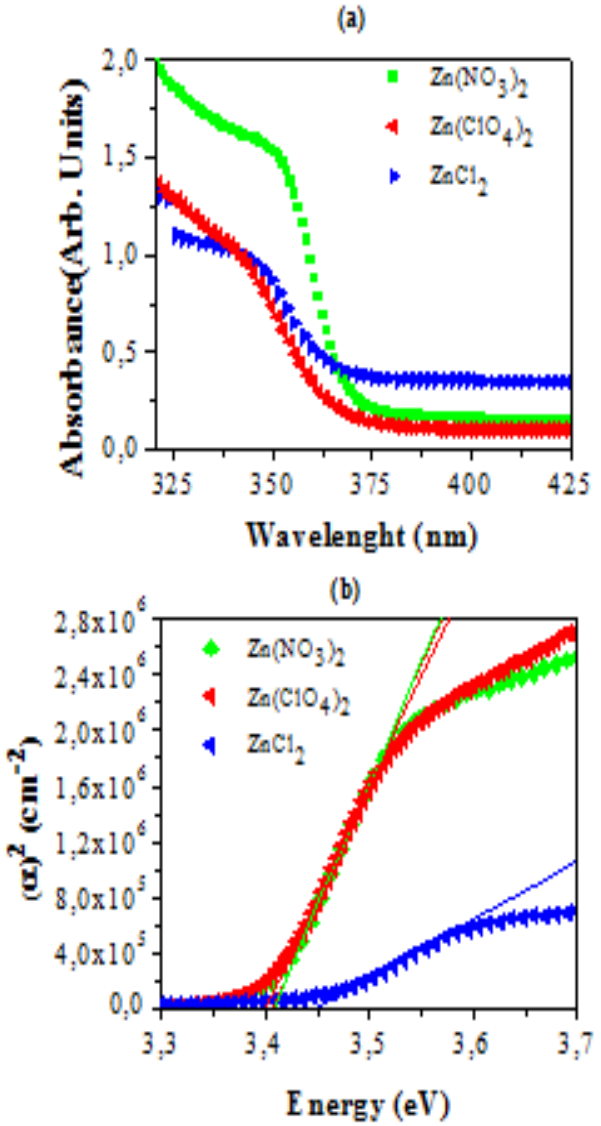

Fig. 3. a) Absorbtion spectra and b) α^2 vs. energy plot of ZnO thin films.

The actual bandgap values of the films grown by zinc chloride and zinc perchlorate solutions are 3.44 and 3,40 eV, respectively. The bandgap of ZnO film grown by chloride solution is a little bit higher than perchlorate as believed to be due to stronger adsorption of chloride [25]. The results are compatible with the results reported by Look [8] and Pauporte and Lincot. [13]. Pauporte and Lincot have reported that the bandgap of ZnO films can be remarkably changed between 3.4 eV and 3.55 eV as dependence of applied potential and the Zn sources used in this technique.

Figure 4 shows PL measurements of the ZnO thin films grown in DMSO with different Zn sources, such as $ZnCl_2$, $Zn(NO_3)_2$ and $Zn(ClO_4)_2$. Almost similar spectral shapes were observed for all thin films. The figure shows mainly three emission peaks in each ZnO thin film. Observed energies for these peaks are 3.4 eV for UV, 2.66 eV for blue emission and 2.39 eV for green emission. The UV emission is clearly due to free exciton emission in ZnO. This means that the higher emission quality is obtainable by using the $Zn(ClO_4)_2$ as a Zn source. As for blue emission around 2.66 eV (467 nm), we recently reported its origin as due to O-rich defects such as O_i, V_{Zn}, and O_{Zn} [26]. The detailed discussion on optical changes by the oxygen variation in the thin films can be found in one of our earlier reports [26].

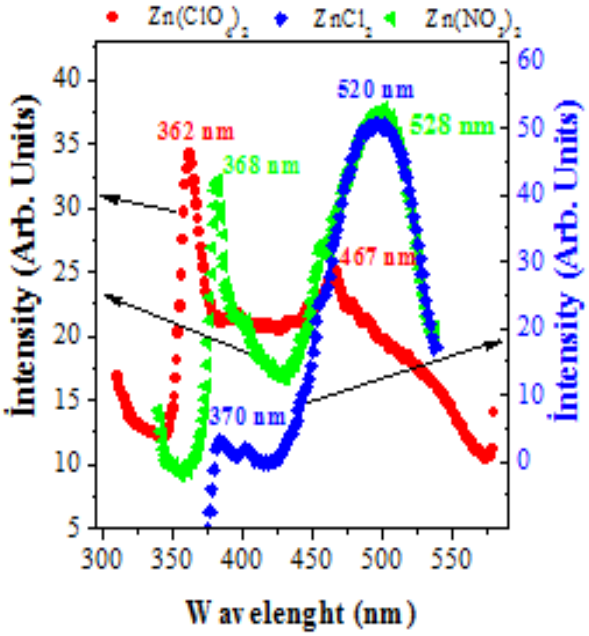

Fig. 4. PL spectra of ZnO thin films grown in DMSO.

Observed emission at 520 nm is general called as green emission in ZnO and it origin is mostly reported to be oxygen vacancy. Taking into account of both structural and optical results, one can say that $Zn(ClO_4)_2$ solution is the more efficient Zn source to grow the ZnO thin films.

IV. CONCLUSION

ZnO thin films obtained from non-aqueous solutions such as $ZnCl_2$, $Zn(NO_3)_2$ and $Zn(ClO_4)_2$ prepared in DMSO show more excellent structural and optical properties as compared to the films prepared in DI water. X-ray diffraction measurements showed that all the films are highly *c*-axis oriented indicating the quality of the grown films. Absorption measurements exhibited that the band gap energy of the films is around 3.4 eV. Photoluminescence measurements result in three emissions in all films: UV (365 nm), blue (466 nm) and, gren emissions (520 nm). The optical and structural characterization results showed that the optimum crystal parameters have been obtained using zinc perchlorate non-aqueous solution.

ACKNOWLEDGEMENTS

Support was received from The Scientific and Technological Research Council of Turkey (TUBITAK-Project No:07T004 and 107T822).

[1]. *J. Lee, Y. Tak*, Electrochem. Solid-State Lett. 4 (9) (2001) C63-C65.

[2]. *J. Lee, Y. Tak*, Electrochem. Commun. 2 (2000) 765-768.

[3]. *M. Izaki*, J. Electrochem. Soc. 146 (12) (1999) 4517-4521.

[4]. *M. Izaki, T. Omi*, J. Electrochem. Soc. 144 (1997) 1949-1952.

[5]. *J. Katayama, M. Izaki*, J. Appl. Electrochem. 30 (2000) 855-858.

[6]. *D. Gal, G. Hodes, D. Lincot, H.-W. Schock*, Thin Solid Films 361-362 (2000) 79-83.

[7]. *M. Izaki, T. Omi*, Appl. Phys. Lett. 68 (17) (1996) 2439-2440.

[8]. *D. C. Look*, Materials Science and Engineering B80 (2001) 383-387.

[9]. *Y. Chen, D. M. Bagnall, H.-J. Koh, K.-T. Park, K. Hiraga, Z. Zhu, T. Yao*, J. Appl. Phys. 84 (1998) 3912.

[10]. *H. Sato, T. Minami, T. Miyata, S. Takata, M. Ishii*, Thin Solid Films 246 (1994) 65.

[11]. *K.-H. Bang, D.-K. Hwang, J.-M. Myoung*, Appl. Surf. Sci. 207 (2003) 359-364.

[12]. *S. Tüzemen, E. Gür, T. Yıldırım, G. Xiong, R.T. Williams*, J. Appl. Phys. 100 (2006) 103513.

[13]. *T. Pauporte, D. Lincot*, Electrochimia Acta 45 (2000) 3345- 3353.

[14]. *H. Asıl, E. Gür, K. Çınar, C.Çoşkun*, Appl. Phys. Lett. 94 (2009) 253501.

[15]. *B. Cao, W. Cai, H. Zeng, G. Duan*, J. Appl. Phys. 99 073516 (2006)

[16]. *M. Fahoume, O. Maghfoul, M. Aggour, B. Hartiti, F. Chraibi, A. Ennaoui*, Sol. Energy Mater.& Sol. Cells. 90 (2006) 1437-1444.

[17]. *E. Gür, H. Asıl, C. Coşkun, S.Tüzemen, K. Meral, Y. Onganer, K. Şerifoğlu*, Nuc. Inst. Meth. B 266 (2008) 2021-2026.

[18]. *Z. H. Gu, T.Z. Fahidy*, J. Electrochem. Soc. 146 (1) (1999) 156-159.

[19]. *T. Mahalingam, V.S. John, P. J. Sebastian*, Mater. Research Bulletin 38 (2003) 269-277.

[20]. *Y. Zhang, J. Weng, Y. Zhang, L. Xu, J. Xu, X. Huang, K. Chen*, Physica E 27 (2005) 183-187.

[21]. *D. Lincot*, Thin Solid Films 487 (2005) 40-48.

[22]. *Y.-F. Gao, M. Nagai, Y. Masuda, F. Sato, K. Koumoto*, J. Crystal Growth 286 (2006) 445-450.

[23]. *C. Coşkun, H. Güney, E. Gür and S. Tüzemen,* Turk J. Phys. 33(2009) 49-56.

[24]. *S. P. Anthony, J. I. Lee, J. K. Kim*, Appl. Phys. Lett. 90 (2007) 103107.

[25]. *R. Jayakrishnan, G. Hodes*, Thin Solid Films 440 (2003) 19-25.

[26]. *E. Gür, S. Tüzemen, K. Meral, and Y. Onganer,* Appl. Phys. Mater. A *94 (2009) 549.*

DIELECTRIC PROPERTIES OF METAL-INSULATOR-SEMICONDUCTOR ($Al/SiO_2/P$-Si) STRUCTURES AT HIGH FREQUENCIES

D.E. YILDIZ*, A. TATAROĞLU

* *Physics Department, Faculty of Arts and Sciences, Hitit University, 19030, Çorum, TURKEY*

Physics Department, Faculty of Arts and Sciences, Gazi University, 06560, Ankara, TURKEY

The dielectric properties of Al/SiO_2/p-Si (MIS) structures were studied in the frequency range of 100 kHz-10 MHz at room temperature. The interfacial oxide layer thickness of 55 A^o at metal/semiconductor interface was calculated from the measurement of the oxide capacitance in the strong accumulation region. The dielectric properties of MIS structures were calculated from the admittance spectroscopy (C-V and G/w-V) method. Experimental results show that the values of the real (ε') and imaginary (ε'') part of dielectric constant and dissipation factor (tanδ) were found to decrease with increasing frequency while σ_{ac} is increased. Also, the values of ε', ε'', tanδ and σ_{ac} increase with increasing applied bias voltage. It is clear that at the inverse region (V<0 V), the values of ε', ε'', tanδ and σ_{ac} become almost voltage independent. But in the depletion and accumulation region the values increase with decreasing frequencies. The interfacial polarization may be occurred at the intermediate frequencies and/or with the number of interface state density between Si/SiO_2 interfaces, consequently, contribute to the improvement of dielectric properties of MIS structure.

I. INTRODUCTION

The metal/insulator/semiconductor (MIS) structures consist of a thin insulator layer (δ<100A^o) at metal/semiconductor interface. This insulator layer cannot only prevent inter-diffusion between metal and semiconductor substrate, but also alleviate the electric field reduction issue in MIS structures. Therefore, an insulator layer in the MIS structure gives these devices the properties of a capacitor, which stores the electric charges by virtue of the dielectric property of oxide layers. The formation of an insulator layer on Si by traditional ways of oxidation or deposition cannot completely passivity the active dangling bonds at the semiconductor surface. The oxygen ions give rise to space charge effects especially at low frequency region. Therefore it is important to study the dielectric properties and ac conductivity over wide range of frequency by impedance spectroscopy method (C-V) and (G/w-V). The performance and reliability of these devices is especially depending on the formation of interfacial insulator layer and densities distribution of interface states at the Si/SiO_2 interface.

In the recent years, due to technical important of MIS or MOS structures, there are a lot of studies in the literature[1-16], but both voltage and frequency dependent dielectric characteristics of these devices still is not clarified. The frequency dependence of the dielectric constant (ε'), dielectric loss (ε'') and dielectric tangent (tanδ) are dominated especially at low frequencies whose physical origin has long been in question. Especially, at high angular frequencies ($\omega = 2\pi f$), the carrier life time (τ) is much larger than $1/\omega$, the charges at the interface states and cannot follow an ac signal [8-18]. Therefore, in this study the voltage and frequency dependent electrical and dielectric characteristics of Al/SiO_2/p-Si (MIS) structures have been investigated at high frequency range (100 kHz - 10 MHz) at room temperature. When localized interface states and an insulator layer exist at the Si/SiO_2 interface then the device behavior is different than ideal cases. Interface states usually cause a bias shift and frequency dispersion of the C-V and G/w-V curves [19,20].

This paper presents a detailed study on the electrical and dielectric properties in the frequency range of 100 kHz-10 MHz at room temperature for Al/SiO_2/p-Si (MIS) structures. To determining the dielectric constant (ε'), dielectric loss (ε''), loss tangent (tanδ) and ac electrical conductivity (σ_{ac}) of MIS structure were used the admittance spectroscopy method [17,18]. In addition, dielectric properties of MIS structure have been investigated as function of applied bias voltage.

II. EXPERIMENTAL PROCEDURE

Al/SiO_2/p-Si (MIS) structures were fabricated on 2" (inch) diameter float zone <100> p-type (boron-doped) single crystal silicon wafer, having a thickness of 280 μm with 8 Ω-cm resistivity. For the fabrication process, Si wafer was degreased in organic solvent of $CHClCCl_2$, CH_3COCH_3 and CH_3OH, etched in a sequence of H_2SO_4 and H_2O_2, 20% HF, a solution of $6HNO_3$:1HF:$35H_2O$, 20% HF and finally quenched in de-ionized water of resistivity of 18 (MΩ.cm) for a prolonged time. High purity (99.999 %) aluminium with a thickness of ~2000 Å was thermally evaporated from the tungsten filament onto the whole backside of half wafer at a pressure of ~$2x10^{-6}$ Torr. The ohmic contacts were prepared by sintering the evaporated Al back contact at about 500 ^oC for 75 minutes under dry nitrogen flow at rate of 2 lit./min. This process served to sinter the aluminium on the upper surface of the Si wafer. After deposition of ohmic contact, the front surface of the Si wafer was exposed to air in sterile glass box for prolonged time at room temperature. The front rectifier contacts were produced by the evaporation of 2500 Å thick aluminium dots of ~1 mm in diameter onto the Si wafer. By this way, metal-semiconductor (MS) diode with a thin interfacial insulator layer (SiO_2) was fabricated on p-type Si. The interfacial layer thickness was estimated to be about 55 A^o from the oxide capacitance measurement in the strong accumulation region at high frequency (1MHz).

The C-V and G/w-V measurements were carried out by the use of HP4192A LF impedance analyzer. All measurements were carried out with the help of a microcomputer through an IEEE-488 ac/dc converter card.

III. RESULTS AND DISCUSSION

The variation of capacitance and conductance with frequency at different frequencies of the MIS structure are shown in Fig. 1(a) and (b), respectively. As can be seen in Fig.1 (a) and (b), that the capacitance and conductance is sensitive to frequency at room temperature. In addition, the values of both capacitance and conductance increase with increasing voltage. The values of capacitance increases with decrease in frequency and such behavior can be attributed to of an inhomogeneous layer at the semiconductor insulator interface acts in a series with the insulator capacitance causing frequency dispersion. This occurs because at lower frequencies the interface states can follow the ac signal and yield an excess capacitance, which depends on the frequency. In the high frequency limit (f ≥500 kHz) however, the interface states cannot follow the ac signal. This makes the contribution of interface state capacitance to the total capacitance negligibly small [21].

The frequency dependence of real and imaginary part of dielectric constant (ε'), dielectric loss (ε''), respectively, loss tangent (tanδ) and ac electrical conductivity (σ_{ac}), respectively, were evaluated from the knowledge of capacitance and conductance measurements for Al/SiO_2/p-Si structures in the frequency range of 100kHz-10MHz at room temperature. The complex permittivity can be written [22, 23] as

$$\varepsilon^* = \varepsilon' - j\varepsilon'' \tag{1}$$

where ε' and ε'' are the real and the imaginary of complex permittivity, and j is the imaginary root of -1. The complex permittivity formalism has been employed to describe the electrical and dielectric properties. In the ε* formalism, in the case of admittance Y^* measurements (C-V and G/w-V), the following relation holds

$$\varepsilon^* = \frac{Y^*}{j\omega C_o} = \frac{C}{C_o} - j\frac{G}{\omega C_{o_i}} \tag{2}$$

where, C and G are the measured capacitance and conductance of the dielectric material at M/S interface and ω the angular frequency (ω=2πf) of the applied electric field [24]. The real part of the complex permittivity, the dielectric constant (ε'), at the various frequencies are calculated using the measured capacitance values in the whole bias accumulation region from the following relation [15,25]

$$\varepsilon' = \frac{C}{C_o} = \frac{C\, d_i}{\varepsilon_o A} \tag{3}$$

where C_o is capacitance of an empty capacitor, A is the rectifier contact area of the MIS structure in cm^{-2}, d_i is the interfacial insulator layer (SiO_2) thickness and ε_o is the permittivity of free space charge ($\varepsilon_o = 8.85\text{x}10^{-14}$ F/cm). In the strong accumulation region, the maximal capacitance of the structure corresponds to the insulator capacitance (C_i) ($C_{ac} = C_i = \varepsilon' \varepsilon_o A / d_i$).

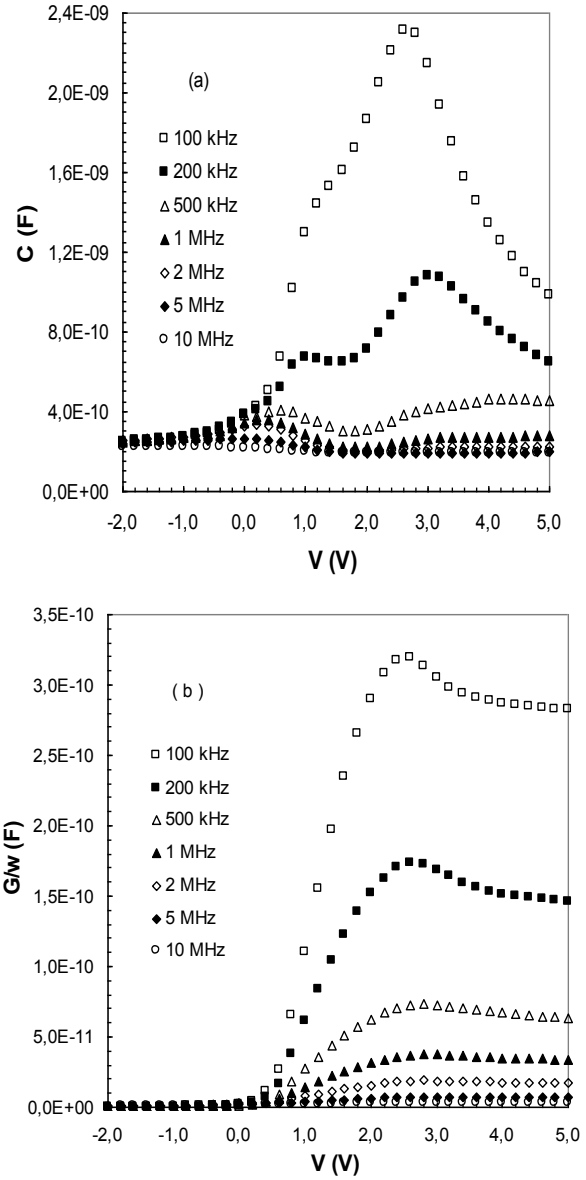

Fig. 1. Variation of the (a) capacitance (C) and (b) conductance (G/ω) with frequency at room temperature for MIS structure.

The imaginary part of the complex permittivity, the dielectric loss (ε''), at the various frequencies is calculated using the measured conductance values from the the following relation [15, 25]

$$\varepsilon'' = \frac{G}{\omega C_i} = \frac{G d_i}{\varepsilon_o \omega A} \tag{4}$$

The loss tangent (tanδ) can be given by the following equation [15,22-24],

$$\tan\delta = \frac{\varepsilon''}{\varepsilon'} \quad (5)$$

The ac electrical conductivity (σ_{ac}) of the dielectric material can be given by the following equation [22,25,26].

$$\sigma_{ac} = \omega C \tan\delta (d/A) = \varepsilon'' \omega \varepsilon_o \quad (6)$$

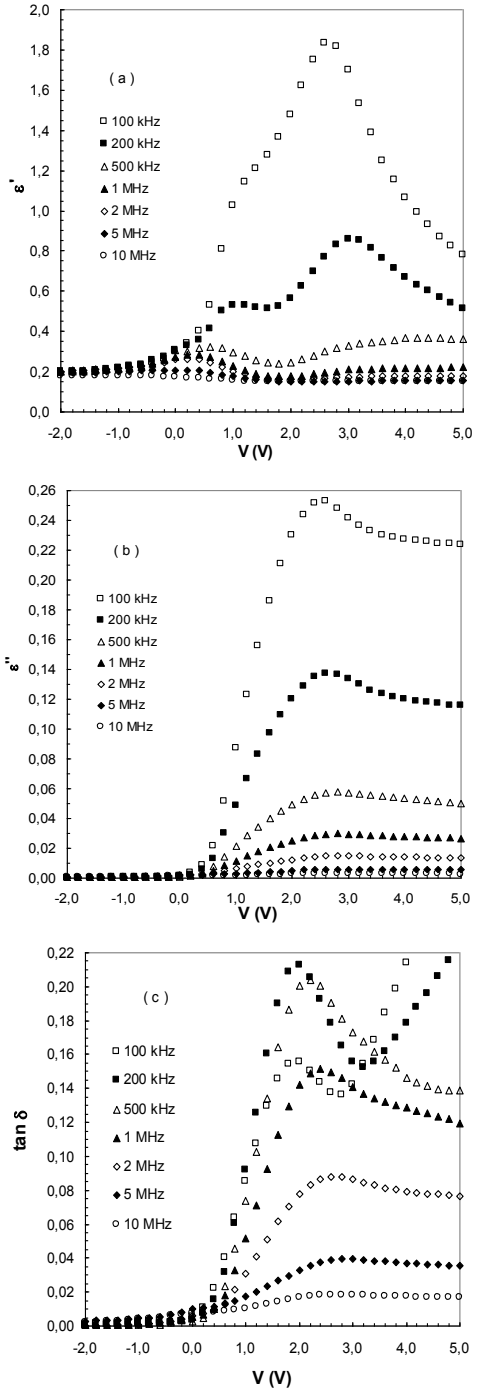

Fig. 2 The variations of (a) dielectric constant (ε'), (b) dielectric loss (ε"), (c) tangent loss (tan□) with frequency for Al/SiO_2/p-Si (MIS) structure at room temperature.

Fig 2 (a), (b) ve (c) show the the ε'-V, ε"-V and tanδ-V curves for Au/SiO_2/p-Si (MIS) structure at various frequencies (100 kHz-10 MHz) at room temperature, respectively. As can be seen in these figures, the values of ε', ε", tanδ of the Al/SiO_2/p-Si structure are strongly dependent on both frequency and applied bias voltage. The voltage dependent values of ε' also shows two peaks in the forward bias region at intermediate frequencies (f≤500 kHz) but the first peak become disappears at high frequencies and this peak positions shift towards inversion region with decreasing voltage. The ε"-V and tanδ-V have a similar behavior of ε'-V characteristics, i.e. it show a peak which have decreased with increasing frequency and the peak positions strongly shift towards inversion region with decreasing frequencies. Such behavior of dielectric constant is attributed to the existence of an insulator layer at M/S interface, interface states at Si/SiO_2 interface and series resistance of structures [27].

In generally, it is mentioned above the peak behavior of the ε', ε" and tanδ depend on a number of parameters such as doping concentration, interface state density, series resistance of diode and the thickness of the interfacial insulator layer [28]. It is well known that the capacitance and conductance values are extremely sensitive to the interface properties and series resistance [8,18]. This occurs because of the interface states that respond differently to low frequency. Similar results have been reported in the literature [18,27] and they ascribed such a peak to only interface states.

The increase of the ac electrical conductivity accompanied by an increase of the eddy current which in turn increases the energy loss tang δ. This behavior can be attributed to a gradual decrease in series resistance with increasing frequency [29]. At the same time the values of σ_{ac} decrease with increasing frequency. It is observed in the literature [30,31] that σ_{ac} are almost independent of voltage at high frequencies.

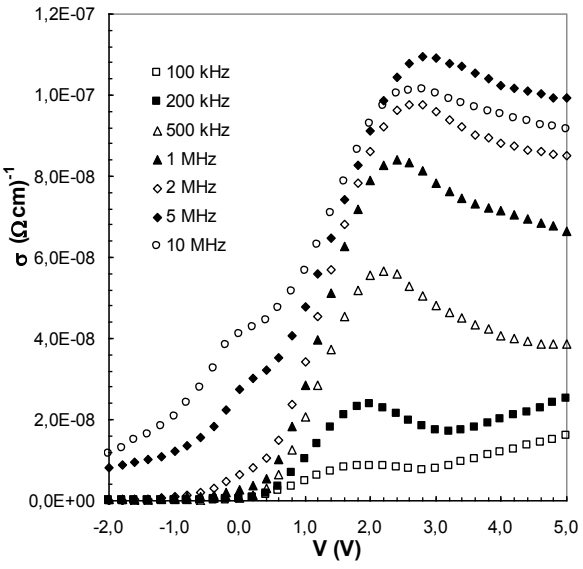

Fig. 3 The variations of ac electrical conductivity (σ_{ac}) with frequency for Al/SiO_2/p-Si (MIS) structure at room temperature.

IV. RESULTS AND DISCUSSION

The dielectric properties of the Al/SiO_2/p-Si (MIS) structure have been studied in detail in the frequency range 100 kHz-10 MHz. The values of capacitance (C) and conductance (G/w) increase with decreasing frequency. This observation may be attributed to the capacitive response of interface states to the measurement. Experimental results show that, the dielectric constant (ε'), dielectric loss (ε"), loss tangent (tanδ) and the ac electrical conductivity (σ_{ac}) of MIS structure were strongly are strongly depend on both the frequency and applied bias voltage. The values of ε' and ε" decrease with increasing frequency. The decrease in ε' and ε" with increasing frequency may be attributed to the polarization decreasing with increasing frequency and then riches a constant value due to the fact that beyond a certain frequency of external field the electron hopping cannot follow the alternative field. Also, the σ_{ac} increase with increasing frequency due to the accumulation of charge carries at the boundaries. As a result, the behavior of dielectric properties especially depends on frequency, interfacial insulator layer, the density of space charges and fixed surface charge.

[1]. *S. M. Sze*, Physics of Semiconductor Devices, 2nd Ed. Willey, New York 1981.

[2]. *K.Kano*, Semiconductor Devices, Prentice-Hall., New Jersey, 1998

[3]. *P. Cova, A. Singh, A. Medina, R.A. Masut*, Solid-State Electron. 42 (1998) 477.

[4]. *H.H. Tseng, C.Y. Wu*, Solid State Electron 30 (1987) 383.

[5]. *M.E. Aydın, K. Akkılıc, T. Kılıçoğlu,* Physica B 352 (2004) 312.

[6]. *P.L. Hanselaer, W.H. Laflere, R.L. Van Meirhaeghe, F. Cardon*, J. Appl. Phys. 56 (1984),2309

[7]. *P.S. Ho, G.W. Rubloff, J.E. Lewis, V.L. Moruzzi, A.R. Williams*, Phys. Rev. B 22 (1980), 4784

[8]. *E.H. Nicollian, J. R. Brews*, John Wiley & Sons, New York (1982).

[9]. *H. Deuling, E. Klausmann, A. Goetzberger*, Solid State Electron. 15(5) (1972) 559.

[10]. *M. Depas, R.L. Van Meirhaeghe, W.H. Lafere and F. Cardon*, Solid State Electron. 37(3) , (1994) 433.

[11]. *S. Kar, R.L. Narasimhan*, J. Appl. Phys. 61(12) (1987) 5353.

[12]. *S. Varma, K.V. Rao, S. Kar*, J Appl Phys. 56 (1984) 2812.

[13]. *M. Schulz, E. Klausmann*, App. Pys., 18, (1979) 169.

[14]. *N. Konofaos, I. P. McClean, C. B. Thomas*, Phys. Stat. Sol., (a) 161 (1997) 111.

[15]. *A. Chelkowski*, Dielectric Physics, Elsevier, Amsterdam, 1980

[16]. *K.S.K Kwa, S. Chattopadhyay, N.D. Jankovic, S.H. Olsen, L.S. Driscoll, A.G. O'Niel*, Semicond. Sci. Technol. 18 (2003) 82.

[17]. *S. Kar, W.E. Dahlke*, Solid State Electron, 15 (1972) 221.

[18]. *E.H. Nicollian and A. Goetzberger*, Appl. Phys. Let. 7 (1965) 216.

[19]. *A.Tataroğlu, Ş. Altındal, M.M. Bülbül*, Microelectron, Eng. 81 (2005) 140.

[20]. *V.Grupta, K.K. Bamzai, P.N. Kontru, B.M.Wanklyn*, Matter. Sci. and Eng. B, 130 (2006) 163.

[21]. *B. Akkal, Z. Benamara, B. Gruzza, L. Bideux*, Vacuum 57 (2000) 219.

[22]. *C.P. Symth, Dielectric Behaviour and Structure, McGraw-Hill*, New York, 1955.

[23]. *Vera V. Daniel*, Dielectric Relaxation, Academic Press, London, 1967.

[24]. *M.S. Mattsson, G.A Niklasson, K. Forsgren, and A. Harsta*, J. Appl. Phys. 85(4) (1999) 2185.

[25]. *M. Popescu, I. Bunget*, Physics of Solid Dielectrics, Elsevier, Amsterdam, 1984.

[26]. *K. Prabakar, S.K. Narayandass and D. Mangalaraj*, Phys. Stat. Sol. (a) 199(3) (2003) 507.

[27]. *İ. Yücedağ, Ş. Altındal, A. Tataroğlu*, Microelectron. Eng. 84 (2006) 180

[28]. *S.P. Szu, C.Y. Lin*, Mater. Chem. and Phys. 82 (2003) 29.

[29]. *M. Cutroni, A. Mandanici, A. Piccolo, C.Fanggao, G. A. Saunders and P. Mustarelli*, Solid State Electron., 90, (1996) 167.

[30]. *D. Maurya, J. Kumar, Shripal*, J. Phys. and Chem. Solids, 66 (2005) 1614.

[31]. *A.S. Riad, M.T. Korayem, T.G. Abdel-Malik*, Physica B 270 (1999) 140

.

LATTICE DYNAMICAL PROPERTIES OF AlB_2 COMPOUND

E. DELIGOZ[1], K. COLAKOGLU[2], H. OZISIK[1], Y. O. CİFTCİ[2]

[1]Department of Physics,
Aksaray University, 68100, Aksaray, Turkey
[2]Department of Physics,
Gazi University, 06500, Ankara, Turkey

The structural and lattice dynamical calculations are predicted on AlB_2 compound using the first-principles of total energy calculations. Generalized gradient approximations (GGA) are used to model exchange-correlation effects. Our lattice dynamical results regarding phonon dispersion curves and temperature-dependent behavior of thermodynamical properties (entropy, heat capacity, internal energy, and free energy) contribute to the existing literature on this compound. The calculated lattice parameters and phonon dispersion curves are accord with the available experimental and other theoretical results.

I. INTRODUCTION

The discovery of superconductivity in MgB_2 at Tc= 39K has revived new interest in finding superconductivity in other diborides with simple hexagonal AlB_2-type structure. However, superconductivity is observed [1-3] in only some of them, and various studies are currently directed to shed light on other properties of diborides, including their elastic, mechanical, and thermodynamical properties [3-7]. It is widely believed that diborides represent a promising group of materials for new heat-resistant, corrosion-resistant, and wear-resistant alloys and coatings [8].

A number of theoretical and experimental [9-14] studies exist in literature deal with structural, elastic, and electronic properties of AlB_2 compound. Specifically, Shein and Ivanovskii [9] have reported the structural and elastic properties using the full-potential linearized augmented plane-wave (FP-LAPW) method with the generalized gradient approximation (GGA) for AlB_2. The structural properties have been studied for this compound by Oguchi [10]. The phonon properties have been investigated by Bohmen et al [14].

In this study, we have investigated the phonon dispersion relations and thermodynamical properties of this compound in detail and interpret the salient results. To our knowledge, phonon projected density of states and thermodynamical properties, which are the important bulk properties for solids, have neither been obtained theoretically, nor experimentally for AlB_2 compound.

II. METHOD OF CALCULATION

The calculations are performed using the density functional formalism and generalized gradient approximation (GGA) through Perdew-Burke-Ernzerhof (PBE) functional [15] for the exchange-correlation energy in the SIESTA code [16,17]. This code calculates the total energies and atomic forces using a linear combination of atomic orbitals as the basis set. The basis set is based on the finite range pseudoatomic orbitals (PAOs) of the Sankey–Niklewsky type [18], generalized to include multiple-zeta decays.

The interactions between electrons and core ions are simulated with the separable Troullier–Martins [19] norm-conserving pseudopotentials. Atomic pseudopotentials are generated separately for atoms Al and B by using the $3s^2\ 3p^1$ and $2s^2\ 2p^1$ atomic configurations, respectively. The cut-off radii for the tested atomic pseudopotentials are taken as s: 1.86 au, p: 2.06 au, d: 2.22 au f: 2.22 au of Al and 1.74 au for the s, p, d and f channels of B.

Atoms are allowed to relax until atomic forces fall below 0.005 $eV\text{Å}^{-1}$. The cutoff energy is taken to be 400 Ryd. 1014 *k*-points are found to be adequate in obtaining the total energy to an accuracy of 1 meV/atom for AlB_2.

III. RESULTS AND DISCUSSION

3.1. Structural Properties

First, we optimize the lattice constants to obtain a relaxed structure. The initial lattice parameters are taken from previous theoretical and experimental values as a starting point for geometry optimization. The calculated lattice parameters are listed in Table 1, along with the available experimental and theoretical data for comparison. Findings suggest that the present lattice parameters (a,c) are in accord with the theoretical and experimental values [10-13].

Table 1. Calculated equilibrium lattice parameters (*a, c* in Å), along with the available experimental and theoretical values for AlB_2 compound.

Reference	a	c	c/a
This work	2.981	3.252	1.09
Ref [9]	2.962	3.206	1.08
Ref [10]	2.978	3.248	1.09
Ref [11]	3.007	3.260	1.09
Ref [12]	3.005	3.253	1.09
Ref [13]	3.009	3.262	1.09

3.2. Phonon Dispersion Curves

Many physical properties of solids depend on their phonon properties, including specific heat, thermal expansion, heat conduction, and electron-phonon coupling. The present phonon dispersion curves and other related quantities of AlB_2 are calculated by using the PHONON software [20] in a manner similar to our recent works [21-23]. This code is compatible with SIESTA and uses the "Direct Method" [24] and the Hellmann–Feynman forces on atoms for generating the phonon dispersion and the density of states (DOS). Its theoretical and practical details can be found in the PHONON manual and respective references.

The calculated phonon dispersion curves and corresponding one-phonon DOS for AlB_2 along the high-

symmetry directions are illustrated in Fig. 1. The calculated phonon dispersion curves not contain soft modes at any direction, which confirms the stability of P6/mmm phase for this compound. The present phonon dispersion curves are in accord with the theoretical values values [14].

The unit cell of AlB_2 contains three atoms, which give rise to a total of nine phonon branches, which contains three acoustic modes and six optical modes. Interesting features of optical phonon modes are observed at Γ point. The optical phonon branches are nearly flat at the Γ point, and this flatness of the optical modes causes a very sharp peak in the phonon density of states. Along the Γ-K directions these branches are not degenerate.

The below of the phonon dispersion curve show the corresponding total and partial density of phonon states for each compound. While the main contribution to acoustic phonons results from the Al atoms, the high-frequency phonons stem from the boron ions. This is expected because the boron atom is lighter than transition metal atoms, which leads to comparatively weaker electron-phonon interactions. The covalent character of the B-B bonding is also decisive for the high frequency of phonons involving the boron atoms.

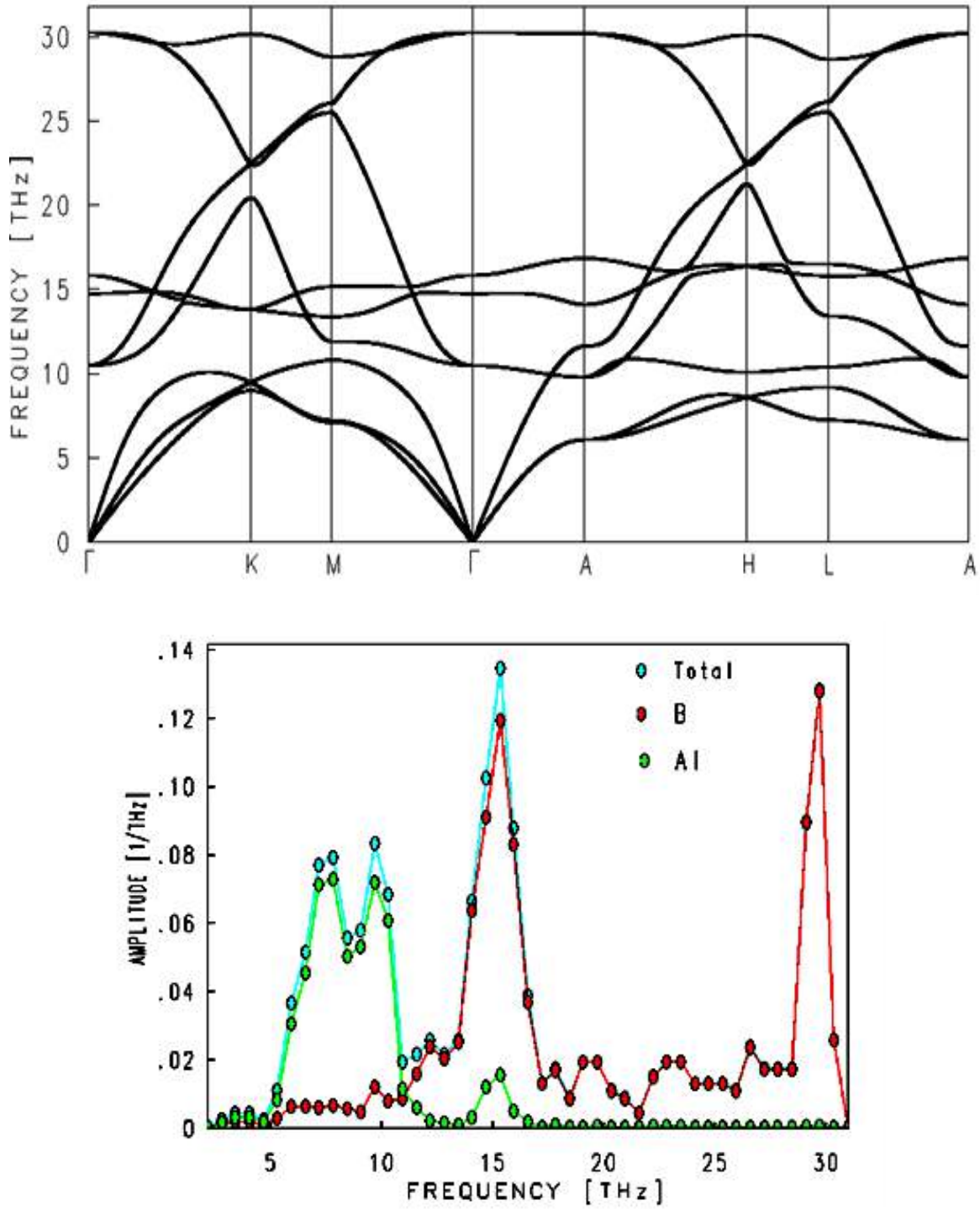

Fig. 1. The calculated phonon dispersion curve, total and partial density of states for AlB_2.

3.3. Temperature Dependence of the Thermodynamic Quantities

We use partial and total densities of states to estimate the temperature dependence of the internal energy, free energy, heat capacity, and entropy of the compound in the harmonic approximation. The temperature-dependent variations of the internal energy, free energy, entropy and heat capacity at constant volume are plotted in Figs. 2-5 for this compound and their constituent atoms, by using the data obtained from Siesta and Phonon codes. Unfortunately, there are no experimental data available for comparison with our results.

The calculated internal energies for AlB_2 as a function of temperature are displayed in Fig. 2. Results suggest that, above 300 K, the total internal energies increase almost linearly with temperature. As expected, total and partial internal energy graphs exhibit similar trend for this compound and the contribution to internal energy from boron atom (B) is more dominant than those from Al atom. At high temperatures the internal energy tends to display k_BT behavior.

Fig. 3 shows the variations of the free energy under various temperatures for the same compound. Overall profiles of all plots show similar characteristics and free energy decrease gradually with increasing temperature. The calculated values of free and internal energy at zero pressure and temperature are 302.70 meV/unitcell.

The variations of entropy under temperature for AlB_2 are given in Fig. 4 for the same temperature range. It can be seen that the entropy change increases rapidly as temperature increasing at low temperature, while the variation of entropy is small above 1000 K. The total and partial entropy graphs exhibit a similar trend and the contributions to entropy from Al atom are more dominant than those from boron atom.

The contributions to the total heat capacity from the lattice vibrations are illustrated in Fig. 5. It is suggested by the Fig. 5 that while the temperature is about T<600 K, C_v increases very rapidly with the temperature; when the temperature is about T>600 K, C_v increases slowly with the temperature and it almost approaches a constant called Dulong-Petit limit. The temperature is limited to 1000 K to minimize the potential influence of anharmonicity in all graphs.

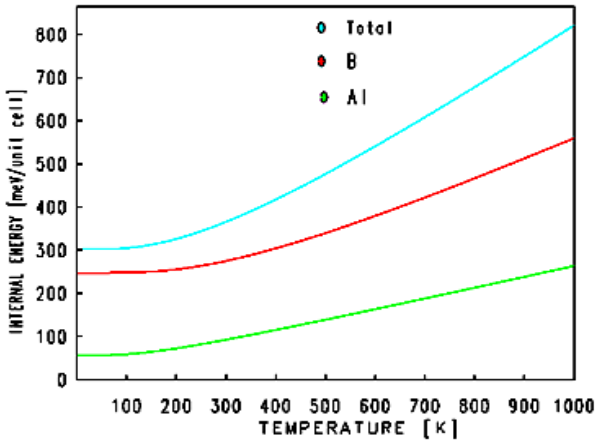

Fig. 2. Temperature dependence of internal energy for for AlB_2

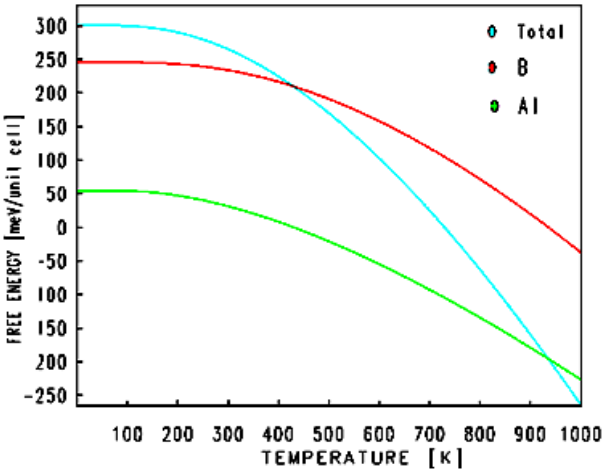

Fig. 3. Temperature dependence of free energy for for AlB_2

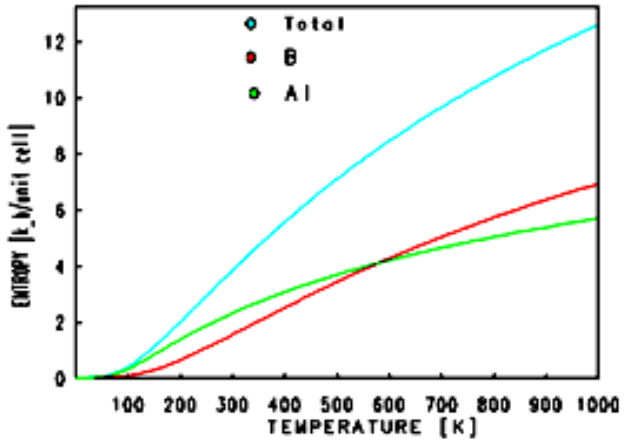

Fig. 4. Temperature dependence of entropy for for AlB_2

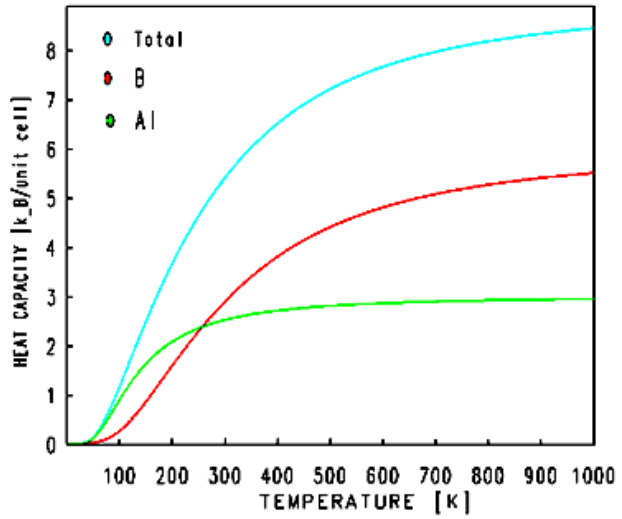

Fig. 5. Temperature dependence of heat capacity for for AlB_2

IV. CONCLUSION

The results we present on several ground states, the structural, vibrational, and thermodynamic properties for AlB_2 are obtained using the first-principles calculations implemented in Siesta within the GGA approximation. Our results are mostly in agreement with the available experimental and theoretical findings. Thermodynamical

results at various temperatures were not considered in previous experiments, and comprise the original contributions of this study. The calculated phonon dispersion curves not contain soft modes at any direction, which confirms the stability of P6/mmm phase for AlB_2.

ACKNOWLEDGMENTS

This work is supported by Gazi University Research-Project Unit under Project No: 05/2009-55.

[1]. *R. B. Kaner, J. J. Gilman, S. H. Tolbert* Mater Sci. 2005, 308, 1268.

[2]. *W. Zhou, H. Wu, and T. Yildirim*, Phys. Rev. B 2007, 76, 184113.

[3]. *H.Y. Chung, M. B. Weinberger, J. Yang, S.H.Tolbert, and R. B. Kaner App.l* Phys. Lett. 2008, 92 261904.

[4]. *K. E*. Spear, Phase Behaviour and Related Properties of Rare-Earth Borides, Phase Diagrams, Materials Science, and Technology, vol. 4: The Use of Phase Diagrams in Technical Materials, Alper, A.M., Ed., 91, (1976).

[5]. *V. V. Novikov and A. V. Matovnikov* Inorg .Mater. 2008, 44**,** 134.

[6]. *T. Mori*, in Handbook on the Physics and Chemistry of Rare Earths, edited by K. A. Gschneidner, Jr., J.-C. Bunzli, and V.Pecharsky, North-Holland, Amsterdam, 2008, 38**,** 105.

[7]. *B. T. Matthias, T. H. Geballe, K. Andres, E.Corenzwit, G. W. Hull, and J. P. Maita*, Science 1968, 159, 530.

[8]. *J. Etourneau*, J. Less Common Met. 1985, 110 267.

[9]. *I. R. Shein, A. L. Ivanovskii*, J. Phys.: Condens. Matter 2008, 20 415218.

[10]. *T. Oguchi* J. Phys. Soc. Japan, 2002, 71, 1495.

[11]. *Z. Xiao-Lin, L. Ke, C. Xiang-Rong, and Z.Jun* Chinese Phys, 2006,15,3014

[12]. *U Burkhardt, V Gurin, F Haarmann, H Borrmann, W Schnelle, A Yaresko and Y* Grin J. Solid State Chem. 2004 177 389

[13]. *I I Mazin and V P Antropov Physica* C 2003, 385, 49

[14]. *K. P. Bohmen, R. Heid, and B. Renker* Phys. Rev. Lett. 2001,86, 5771.

[15]. *J. P. Perdew, K. Burke, and M. Ernzerhof*, Phys. Rev. Lett. 1996, 77, 3865.

[16]. *P. Ordejón, E. Artacho and J. M. Soler,* Phys. Rev. B (Rapid Comm.) 1996, 53, R10441.

[17]. *J. M. Soler, E. Artacho, J. D. Gale, A. García, J.Junquera, P. Ordejón, and D. Sánchez-Portal*, J. Phys.: Condens. Matt.2002, 14**,** 2745.

[18]. *O. F. Sankey and D. J. Niklewski*, Phys. Rev. B 1989, 40, 3979.

[19]. *N. Troullier and J. L. Martins*, Phys. Rev. B 1991, 43,1993.

[20]. K. Parlinski, Software PHONON (2003), and references theirin.

[21]. *E. Deligöz, K. Çolakoğlu, Y. Ö. Çiftçi* Solid State Comm. 2009, 149**,**1843.

[22]. *E. Deligöz, K. Çolakoğlu, Y. Ö. Çiftçi* Solid State Comm. 2010, 150**,** 405.

[23]. *E. Deligöz, K. Çolakoğlu, Y. Ö. Çiftçi* Comp. Mater. Sci 2010, 47 875.

[24]. K. Parlinski, Z.Q. Li, and Y. Kawazoe, Phys. Rev. Lett. 1997, 78, 4063.

XRD AND AFM RESULTS OF IRON OXIDE THIN FILM PREPARED BY USING CHEMICAL SPRAY PYROLYSIS METHOD

F. N. TUZLUCA[1], S. M. KARADENİZ[1], A. E. EKİNCİ[1], M. ERTUĞRUL[2], Y. Ö. YEŞİLBAĞ[1]

[1] Erzincan University, Erzincan, Turkey,
ftuzluca@erzincan.edu.tr
[2]Atatürk University, Erzurum, Turkey

The preparation and characterization of iron oxide thin films by chemical spray pyrolysis technique is reported. Iron oxide films were grown on glass substrate at different deposition temperatures 500^0 C and 600^0 C. The crystalline quality and the surface morphology of the deposited Fe_2O_3 thin film were characterized using X-ray diffraction and Atomic Force Microscopy, respectively.

I. INTRODUCTION

The iron oxide material is one of the most important materials for a wide range of applications. Iron oxide thin film can be used in several fields. It can be employed as, for example:

Materials in nanometer range are found to exhibit new functional properties for a wide range of applications. Magnetic nanoparticles of iron oxide due to its biocompatibility, catalytic activity and low toxicity have dragged significant attention for their applications in various fields of medical care such as drug delivery system, cancer therapy, and magnetic resonance imaging [1–2]. Apart from the biomedical applications, these iron oxide nanoparticles are of technological importance due to their application in many fields including high density magnetic storage devices, ferro-fluids, magnetic refrigeration systems, catalysis and chemical/ biological sensors [3,4].

Properties, such as high refractive index, wide bandgap and chemical stability make them suitable for use as gas-sensors. In addition film gas-sensing materials have good sensitivity to reducing gases, but their unsatisfied selectivity, reproducibility, thermal stability, durability, etc. are common problems, which are certainly related to the composition and the microstructure of the materials [11].

A variety of techniques have been used to fabricate iron oxide thin films such as pulsed laser deposition (PLD) [5], sol–gel [6], sputtering [7,8], and molecular beam epitaxy (MBE) [9]. Compared to other vacuum deposition techniques, spray pyrolysis offers the possibility of preparing small as well as large area coating of iron oxide thin films and nanopowder at low cost for various technological applications. In spray pyrolysis technique, the deposition rate and the thickness of the films can be easily controlled over a wide range by changing the spray parameters, thus eliminating the major drawbacks of chemical methods such as sol–gel, which produces films of limited thickness [10]. This technique has been widely used to prepare iron oxide thin films using various solutions [11-12]. In the present study, we have used the simple and lowcost chemical spray pyrolysis technique to grow iron oxide thin films.

II. MATERIAL AND METHODS

Fe_2O_3 thin films were obtained by chemical spray pyrolysis in air atmosphere they were prepared from aqueous solution of $FeCl_3.6H_2O$ by dissolving it in 10 ml distilled water to concentration of 0.05M. Bare glasses were used as substrate. They were cleaned in acetone, methanol and ultrasonic cleaner before depositing prosses. Using compressed air as carrier gas. The deposition time was determined 13 min for 500 ^oC substrate temperature and determined 15 min for 600 ^oC substrate temperature. The designed setup for chemical spray pyrolysis technique is shown in Fig. 1.

The structure of as deposited Fe_2O_3 thin film caracterized by XRD and the morphologies of as-deposited Fe_2O_3 thin film characterized by two-dimensional AFM scans of the sample surface after deposition are shown in Fig. 2. and Fig. 3. a-b, respectively.

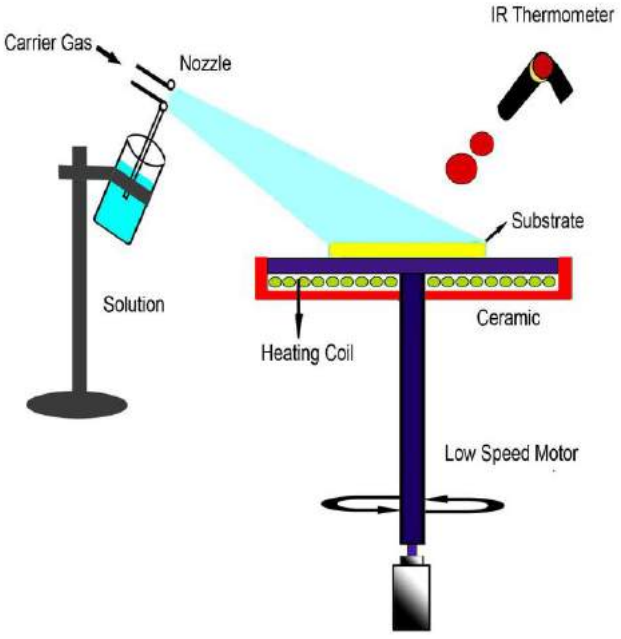

Fig. 1. Schematic diagram of chemical spray pyrolysis setup.

III. RESULTS AND DISCUSSION

The X-ray diffraction diagrams of iron oxide thin films deposited at 500^0 C and 600^0 C from purely aqueous solution of $FeCl_3.6H_2O$ with a molar concentration of 0.05M are shown in Fig. 2. The films crystallized in the rhombohedral (hexagonal hematite α- Fe_2O_3, the PDF numbers 72-0469 and 24-0072) structure with a preferred orientation along the (104) direction, while peaks

associated to other phases (e. G., magnetite, maghemite, etc.) are not observed [12].

(104) plane intensity at 600^0 C substrate temperature is sharper than (104) plane intensity at 500^0 C substrate temperature.

Fig. 3a and b are AFM micrographs of surface morphology of α- Fe_2O_3 thin films produced at substrate temperature (T_s) of 500^0 C and 600^0 C, respectively. The surface is not smooth with visible cracks or holes. At Fig. 3.a-b, grains for 600^0 C substrate temperature are smaller than grains for 500^0 C substrate temperature.

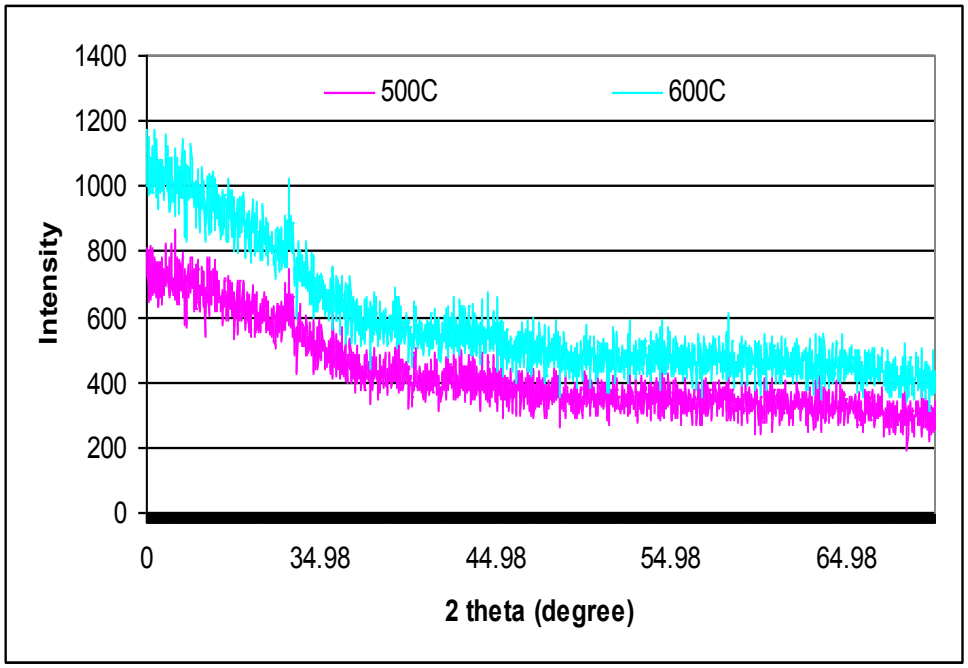

Fig. 2. The X-ray diffractograms of iron oxide thin films deposited at 500^0 C and 600^0 C substrate temperature.

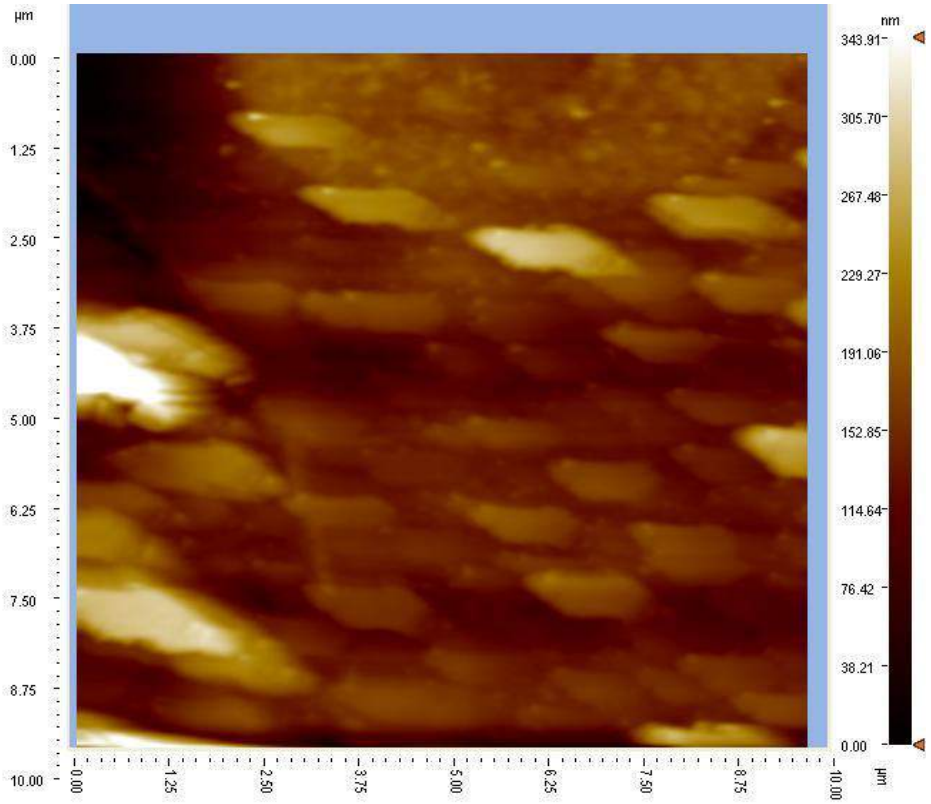

Fig. 3-a AFM image of iron oxide nano thin films at 500 ^oC.

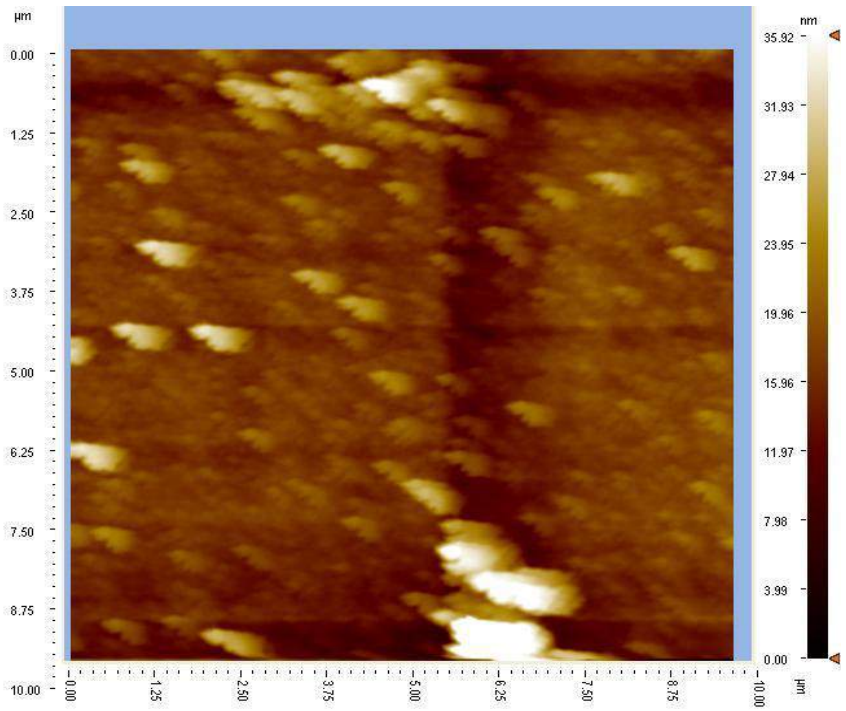

Fig. 3-b AFM image of iron oxide nano thin films at 600 ^{o}C.

IV. CONCLUSION

In the experiment, Fe_2O_3 thin films were deposited by Chemical Spray Pyrolysis technique at 500^0 C and 600^0 C. Deposited thin films were characterized by XRD and AFM. According to XRD results, the films crystallized in the rhombohedral structure with a preferred orientation along the (104) direction. Moreover according to AFM results grains show that are smaller for 600^0 C substrate temperature than for 500^0 C substrate temperature.

[1]. *Xu Jing, Y. Haibin, FuWuyou, Du Kai, Yongming Sui, Jiuju Chen, Yi Zeng, Minghui Li, Guangtian Zou*, J. Mag. Mag. Mat. 309 (2007) 307.
[2]. *A.K. Gupta, M. Gupta*, Biomaterials 26 (2005) 3995.
[3]. *V. Sreeja, P.A. Joy*, Mater. Res. Bull. 42 (2007) 1570.
[4]. *J. Du, H. Liu*, J. Magn. Magn. Mater. 302 (2006) 263.
[5]. *M.K. Krause, P. Esquinazi, M. Ziese, R. Hohne, A. Pan, A. Galkin, E. Zeldov*, J. Magn. Magn. Mater. 245 (2002) 1097.
[6]. *N.J. Tang, W. Zhong, H.Y. Jiang, X.L. Wu, W. Liu, Y.W. Du*, J. Magn. Magn. Mater. 282 (2004) 92.
[7]. *S. Ohta, A. Tterada*, Thin Solid films 143 (1986) 73.
[8]. *G. Zhang, C. Fan, L. Pan, F.Wang, P.Wu, H. Giu, Y. Gub, Y. Zhang*, J. Magn. Magn. Mater. 293 (2005) 737.
[9]. *W. Eerenstein, L. Kalev, L. Niesen, T.T.M. Palstra, T. Hibma*, J. Magn. Magn. Mater. 258–259 (2003) 73.
[10]. *Goyal, A.K. Pandey, D. Kaur, A. Kumar*, J. Nanosci. Nanotechnol. 9 (2009) 4692.
[11]. *A.A. Akl*, Appl. Surf. Sci. 233 (2004) 307.
[12]. *L. Dghoughi, B. Elidrissi, C. Bernède, M. Addou, M. Alaoui Lamrani, M. Regragui, H. Erguig*, Appl. Surf. Sci. 253 (2006) 1823.

THERMO-ELASTIC PROPERTIES OF PtBi COMPOUND

G.SURUCU[1]*, K. COLAKOGLU[1], E. DELİGOZ[2], H. B.OZISIK[1,2]

[1]*Gazi University, Department of Physics,*
Teknikokullar, 06500, Ankara, TURKEY
[2] *Aksaray University, Department of Physics,*
68100, Aksaray, TURKEY
** g_surucu@yahoo.com*

To deeply understand the structural and thermo-elastic properties of the NiAs-type (space number:194) of intermetallic compound PtBi, we have performed ab-initio density-functional theory within the local density approximation. Some basic physical parameters such as lattice constant, bulk modulus, elastic constants, shear modulus, Young's modulus, Poison's ratio, and Lamé constant are calculated. We have also obtained the temperature and pressure variations of the volume, bulk modulus, thermal expansion coefficient, heat capacity, and Debye temperature in a wide pressure (0-30 GPa) and temperature (0- 800 K) ranges. Our findings on the structural properties are in agreement with the available experimental data.

I. INTRODUCTION

Many companies are developing direct methanol fuel cells for power sources in portable electronics due to the low cost, ease of storage and distribution of methanol [1,2]. However, problems with anode electrocatalysts, typically containing Pt, challenge their entry into the electronics market [1,3] . Ordered intermetallic compounds PtBi and PtPb have proved to be superior to platinum and its alloys as catalysts for organic fuel oxidation because of their resistance to carbon monoxide poisoning as well as improved onset potential and maximum current density [4,5].

Recently, intermetallic PtBi was proposed as a powerful catalyst for formic acid oxidation [6–9]. However, neither the elastic nor the thermodinamical properties of PtBi have been studied theoretically or experimental yet. In the present paper, we aim to investigate the elastic and thermodynamical properties of PtBi compound in detail and interpret the salient results of our calculations. In addition, we have also reported some mechanical properties such as Young's modulus, Poison's ratio, Lamé constant, pressure ,and some temperature-dependent behavior of thermodynamical properties (thermal expansion coefficient, Debye temperature, and Grüneisen parameter). The method of calculation is given in Section 2; the results are discussed in Section 3. Finally, the summary and conclusion are given in Section 4.

II. METHOD OF CALCULATION

All calculations have been carried out using the Vienna ab-initio simulation package (VASP) [10-13] based on the density functional theory (DFT). The electron-ion interaction was considered in the form of the projector-augmented-wave (PAW) method with plane wave up to energy of 400 eV [12, 14]. For the exchange and correlation terms in the electron-electron interaction, Perdew and Zunger-type functional [15] was used within the local density approximation (LDA) [16]. For k-space summation the 12x12x12 Monkhorst and Pack grid of k-points have been used.

In order to obtain the thermodynamic properties of PtBi, the quasi-harmonic Debye model [17] in which the non-equilibrium Gibbs function *G*(V; P, T)* takes the form of

$$G^*(V;P,T) = E(V)+PV+A_{vib}[\theta(V);T] \quad (1)$$

is introduced. In Eq.(1), *E(V)* is the total energy for per unit cell of PtBi, *PV* corresponds to the constant hydrostatic pressure condition, $\theta(V)$ is the Debye temperature and A_{Vib} is the vibrational Helmholtz free energy and can be written as [18-22]

$$A_{Vib}(\theta,T) = nkT\left[\frac{9\theta}{8T}+3\ln\left(1-e^{-\frac{\theta}{T}}\right)-D\left(\frac{\theta}{T}\right)\right] \quad (2)$$

where *n* is the number of atoms per formula unit, $D\left(\frac{\theta}{T}\right)$ is the Debye integral. For an isotropic solid, θ is expressed as [20]

$$\theta_D = \frac{\hbar}{k}\left[6\pi^{1/2}n\right]^{1/3} f(\sigma)\sqrt{\frac{B_s}{M}} \quad (3)$$

where *M* is the molecular mass per unit cell and B_S is the adiabatic bulk modulus, which is given approximately by the static compressibility [22]:

$$B_s \approx B(V) = V\frac{d^2E(V)}{dV^2} \quad (4)$$

$f(\sigma)$ is given by Refs. [20, 21], and the Poisson's ratio is used as 0.37 for PtBi. For PtBi, *n* and *M* are taken 4 and 403.9 a.u, respectively. Therefore, the non-equilibrium Gibbs function *G*(V; P, T)* as a function of *(V; P, T)* can be minimized with respect to volume *V* as:

$$\left[\frac{\partial G^*(V;P,T)}{\partial V}\right]_{P,T} = 0 \quad (5)$$

By solving Eq. (5), one can obtain the thermal equation-of-state (eos) *V(P, T).* The heat capacity at

constant volume C_V and the thermal expansion coefficient (α) are given [21] as follows:

$$C_v = 3nk\left[4D\left(\frac{\theta}{T}\right) - \frac{3\theta/T}{e^{\theta/T}-1}\right] \quad (6)$$

$$S = nk\left[4D\left(\frac{\theta}{T}\right) - 3\ln(1-e^{-\theta/T}\right] \quad (7)$$

$$\alpha = \frac{\gamma C_v}{B_T V} \quad (8)$$

Here γ represents the Grüneisen parameter and its general expression is given as

$$\gamma = -\frac{d\ln\theta(\mathrm{V})}{d\ln \mathrm{V}} \quad (9)$$

III. RESULTS AND DISCUSSION

Structural and Elastic Properties

Firstly, the equilibrium lattice constants (a and c) for *NiAs* phase are obtained from the crystal total energy calculations, followed by the fitting of this results to Murnaghan's eos [23]. The results obtained are in reasonable agreement with the available experimental [24] value (see table 1).

The elastic constants of solids provide a link between the mechanical and dynamical behavior of crystals, and give important information concerning about the nature of

the forces operating in solids. In particular, they provide information about the stability and stiffness of materials, and their ab-initio calculation requires precise methods. Since the forces and the elastic constants are functions of the first-order and second-order derivatives of the potentials, their calculation will provide a further check on the accuracy of the calculation of forces in solids.

Here, for calculation the elastic constants (C_{ij}), we have used the *"stress-strain"* relations [25], and the results are listed in Table 1. The traditional mechanical stability conditions in hexagonal crystals on the elastic constants are known as

$$C_{11} > 0,\ C_{11} - C_{12} > 0,\ C_{44} > 0,\ (C_{11}+C_{12})C_{33} - 2C_{12}^2 > 0.$$

The present PtBi compound satisfies the above relation. To obtain some important polycrystalline properties, we have computed the Poisson's ratio (υ), shear modulus (G_{VRH}), Lamé constant (λ, μ), and Young's modulus (Y_{VRH}) based on the following relations [26-29]:

$$A = \frac{C_{33}}{C_{11}} \quad (10)$$

$$\upsilon = \frac{3B_{VRH} - 2G_{VRH}}{2\left(3B_{VRH} + G_{VRH}\right)} \quad (11)$$

$$\mu = \frac{Y_{VRH}}{2(1+\nu)},\ \lambda = \frac{\nu Y_{VRH}}{(1+\nu)(1-2\nu)} \quad (12)$$

$$\mathrm{Y}_{VRH} = \frac{9\mathrm{B}_{VRH}\mathrm{G}_{VRH}}{3\mathrm{B}_{VRH}+\mathrm{G}_{VRH}} \quad (13)$$

where $G_{VRH} = (G_V + G_R)/2$ is the isotropic shear modulus, G_V is Voigt's shear modulus corresponding to the upper bound of G_{VRH} values, and G_R is Reuss's shear modulus corresponding to the lower bound of G_{VRH} values, and can be written as

$$G_{\mathrm{V}} = \frac{1}{30}\left(C_{11}+C_{12}+2C_{33}-4C_{13}+12C_{55}+12C_{66}\right) \quad (14)$$

,and

$$G_R = \frac{5}{2}\frac{\left[(C_{11}+C_{12})C_{33}-2C_{12}^2\right]C_{55}C_{66}}{3B_V C_{55}C_{66} + \left[(C_{11}+C_{12})C_{33}-2C_{12}^2\right](C_{55}+C_{66})} \quad (15)$$

The Zener anisotropy factor *(A)* is an indicator of the degree of anisotropy in the solid structures. For a completely isotropic material, the *A* factor takes the value of 1 is taken as 1. When the value of *A* is smaller or greater than unity, it is a measure of the degree of elastic anisotropy.

The calculated Zener anisotropy factor (*A*), Poisson's ratio (υ), Young's modulus ($\mathrm{Y_{VRH}}$), Lamé constant (λ, μ), and Shear modulus ($\mathrm{G_{VRH}}$) are given in Table 1.

It is known that the isotropic shear modulus and bulk modulus can measure the hardness of a compound. The bulk modulus is a measure of resistance to volume change by applied pressure, whereas the shear modulus is a measure of resistance to reversible deformations upon shear stress [30]. Therefore, isotropic shear modulus is a better predictor of hardness than the bulk modulus. The calculated isotropic shear modulus is about 133 GPa for this compound.

The values of Poisson's ratio (υ) for covalent materials are small $(\upsilon \approx 0.1)$, whereas for metallic materials υ is typically 0.33 [31]. In the present case the υ value is 0.37 for PtBi. The Young's modulus is defined as the ratio of the tensile stress to the corresponding tensile strain, and is an important quantity for technological and engineering applications. It provides a measure of the stiffness of a solid, and the material is stiffer for the larger value of Young's modulus. The above-mentioned elastic data for the present compounds are summarized in Table 2 with available theoretical ones.

Table 1. Calculated lattice constant (a, c, in Å), elastic constant (C_{ij}, in GPa), anisotropy factors (A= C_{33}/C_{11}), and calculated values of some elastic parameters for PtBi polycrystalline ceramics as obtained in the Voigt-Reuss-Hill approximation: bulk moduli (B_{VRH}, in GPa), shear moduli (G_{VRH}, in GPa), Young's moduli (Y_{VRH}, in GPa), Poisson's ratio (ν), and Lamé constant (λ, in GPa) with the available experimental data.

PtBi	a	c	B_{VRH}	C_{11}	C_{12}	C_{13}	C_{33}	C_{44}	A	G_{VRH}	Y_{VRH}	ν	λ
This work	4.32	5.51	137	196	92	98	246	47	1.25	40	110	0.37	8
Experimental[24]	4.34	5.49	-	-	-	-	-	-	-	-	-	-	-

Finally, we have evaluated the Lamé constants, which are derived from the modulus of elasticity and Poisson's ratio (Eq.12). Physically, the first Lamé constant λ represents the compressibility of the material while the second Lamé constant μ reflects its shear stiffness.

Thermodynamic Properties

The thermal properties are determined in the temperature range from 0 to 800 K for PtBi compound, where the quasi-harmonic model remains fully valid. The pressure effect is studied in the range of 0-30 GPa. The relation between volume and temperature at different pressure is shown in Fig.1. for PtBi. It can clearly be seen from the figure that, when the pressure increases from 0 GPa to 30 GPa, the volume decreases. The reason of this decrease can be attributed to the strengthen of atomic interaction due to becoming closer of the atoms in the interlayer.

The variation of bulk modulus with pressure at different temperatures is shown in Fig. 2 for PtBi. It is obviously seen that the bulk modulus rapidly increases-almost linearly- with pressure, and the effect of the temperature T on the isothermal bulk modulus B_T is, relatively, small.

In the quasi-harmonic Debye model, the Debye temperature $\theta(T)$ and the Grüneisen parameter γ (T) are two key quantities, and they are very sensitive to the vibrational modes. Their values at various temperature (100, 300, 600, and 800 K) and pressures (0, 10, 20, and 30 GPa) are given in Table 2 and Table 3 for PtBi. It can be seen from Table 2 and Table 3 that, when the temperature increases the Debye temperature decreases and the Grüneisen parameter increases for this compound.

The heat capacity at constant volume C_v at different temperatures T and pressures P are shown in Fig.3 for PtBi. It is realized from the figures that when T<300 K, the C_v increases very rapidly with the temperature; when T>300 K, the C_v increases slowly with the temperature, and it almost approaches a constant called as Dulong-Petit.

The variations of the thermal expansion coefficient (α) with temperature and pressure are also calculated and shown in Fig.4 for PtBi. It is clearly seen that α exhibits similar trend at different temperature, and it rapidly increases with the temperature T at lower temperatures (about T < 200 K) and the above this value (about T > 200 K) its increasing rate gradually decreases. Also, the thermal expansion coefficient decreases with the increasing pressure, and it takes the highest value at all temperature ranges at lowest (P = 0 GPa) pressure.

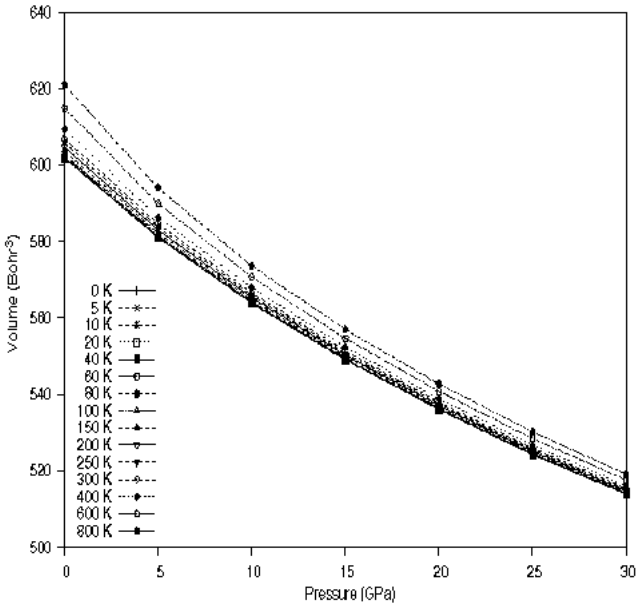

Fig. 1. The variation of volume with the pressure of PtBi for various temperatures.

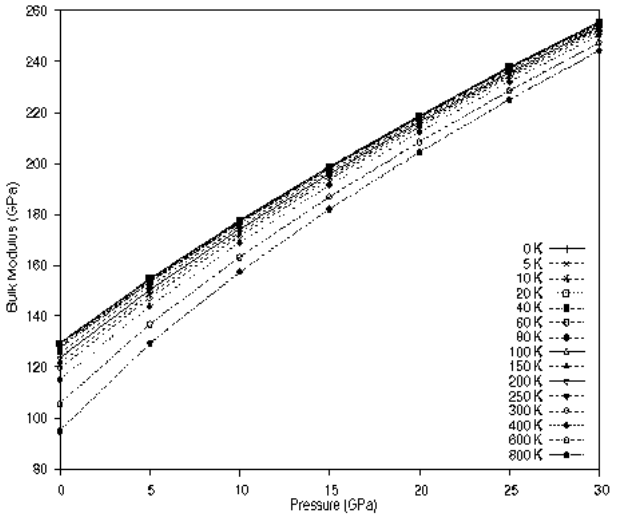

Fig.2. The variation of bulk modulus with pressure for various temperatures.

IV. SUMMARY AND CONCLUSION

In summary, we have performed the first principles total energy calculation for PtBi using the plane-wave pseudopotential approach to the density-functional theory within the local density approximation. The calculated lattice parameters and bulk modulus are, reasonably, consistent with the literature values. We hope that our other predicted results will be serving as a reliable

reference for the future experimental and theoretical studies.

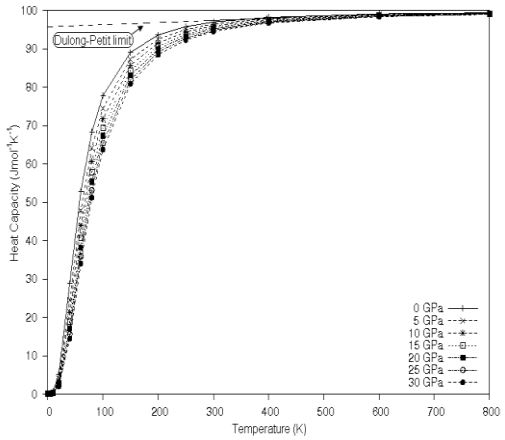

Fig.3. The variation of C_v with temperature at various pressures for PtBi.

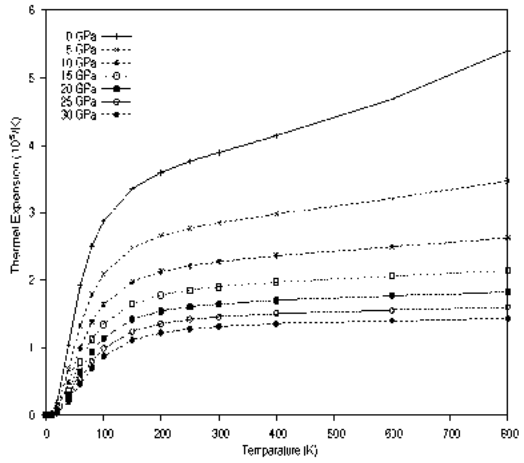

Fig.4. The variation of the thermal expansion coefficient with temperature at various pressures.

Table 2. The calculated Debye temperature Θ (K) over a wide temperature and pressure range for PtBi compound.

		PtBi			
P(GPa) →		0	10	20	30
T(K) ↓					
0	Θ	229.91	266.38	293.07	314.57
100	Θ	229.12	265.97	292.80	314.38
300	Θ	225.06	263.76	291.23	313.15
600	Θ	217.41	259.83	288.53	311.03
800	Θ	211.38	257.04	286.67	309.56

Table 3. The calculated the Grüneisen parameter over a wide temperature and pressure range for PtBi compound.

		PtBi			
P(GPa) →		0	10	20	30
T(K) ↓					
0	γ	2.515	2.025	1.765	1.597
100	γ	2.529	2.029	1.768	1.599
300	γ	2.598	2.054	1.781	1.608
600	γ	2.738	2.099	1.805	1.623
800	γ	2.858	2.133	1.822	1.634

ACKNOWLEDGMENTS

This work is supported by Gazi University Research-Project Unit under Project No: 05/2009-55.

[1] *J. Jin, M. Prochaska, D. Rochefort, D. K. Kim, L.Zhuang, F. J. DiSalvo. R.N. van Dover, H. D. Abruna* Applied Surface Science 254 (2007) 653–661.

[2] *M. Cropper*, Fuel Cells 4 (2004) 236–240.

[3] *H.A. Gasteiger, N. Markovic, P.N. Ross Jr., E.J.Cairns*, J. Phys. Chem. 97 (1993) 12020–12029.

[4] *E. Casado-Rivera, Z.Gál, A. C. D. Angelo, C.Lind, F.J. DiSalvo, H.D. Abruna*, ChemPhysChem. 4 (2003) 193-199.

[5] *E. Casado-Rivera, D.J. Volpe, L. R. Alden, C.Lind, C. Downie, T. Vazquez-Alvarez, A. C. D. Angelo, F. J. DiSalvo, H. D. Abruña.,* JACS, 126 (2004) 4043-4049.

[6] *A.V. Tripkovic, K.Dj. Popovic, R.M. Stevanovic, R.Socha, A.Kowal*, Electrochemistry Communications 8 (2006) 1492–1498.

[7] *E. Casado-Rivera, Z. Gal, A.C.D. Angelo, C. Lind, F.J. DiSalvo, H.D. Abruna*, ChemPhysChem. 4 (2003) 193.

[8] *D. Volpe, E. Casado-Rivera, L. Alden, C. Lind, K.Hagerdon, C. Downie, C. Korzniewski, F.J. DiSalvo, H.D. Abruna*, J. Electrochem. Soc. 151 (2004) A971.

[9] E. *Casado-Rivera, D.J. Volpe, L. Alden, C. Lind, C.Downie, T. Vazquez-Alvarez, A.C.D. Angelo, F.J.DiSalvo, H.D. Abruna*, J. Am., Chem. Soc. 126 (2004) 4043.

[10] *G. Kresse and J. Hafner* Phys. Rev. B 7(1994)558.

[11] *G. Kresse and J. FurthmÄuller* Comp. Mat. Sci. 6 (1996)15.

[12] *G. Kresse and D. Joubert* Phys. Rev. B 59 (1999)1758.

[13] *G.Kresse and J. FurthmÄuller* Phys. Rev. B 54 (1996)11169.

[14] *P. E. Blochl* Phys. Rev. B 50 (1994)17953.

[15] *J. P. Perdew and A. Zunger* Phys. Rev. B (1981)23 5048.

[16] *D. Ceperley and B. Alder*, Phys. Rev. Lett. 45 (1980) 566.

[17] *A.A. Maradudin, E.W. Montroll, G.H. Weiss, I.P.Ipatova*, Theory of Lattice Dynamics in the Harmonic Approximation, Academic Press, 1971.

[18] *M.A.Blanco,* PhD Thesis, Universidad de Oviedo, 1997, URL http://web.uniovi.es/qcg/mab/tesis.html

[19] *M.A. Blanco, A. Martín Pendás, E. Francisco, J.M. Recio, R. Franco*, J. Molec. Struct. Theochem 368 (1996) 245.

[20] *E. Francisco, J.M. Recio, M.A. Blanco, A. Martín Pendás*, J. Phys. Chem. 102 (1998) 1595.

[21] *E. Francisco, G. Sanjurjo, M.A. Blanco*, Phys. Rev. B 63 (2001) 094107.

[22] *M. Flórez, J.M. Recio, E. Francisco, M.A. Blanco, A. Martín Pendás*, Phys. Rev. B 66 (2002) 144112.

[23] *F. D. Murnaghan*, Proc. Natl., Acad. Sci. USA 30 (1994) 5390.

[24] *N.N. Zhuravlev, A.A. Stepanova*, Sov. Phys.-Crystallogr. 7 (1962) 241.

[25] *O. H. Nielsen and R. M. Martin*, Phys. Rev. Lett. 50 (1983) 697.

[26] *R. Hill*, Proc. Phys. Soc. Lond. A 65 (1952) 349.

[27] *W. Voigt*, Lehrbuch Der Kristallphysik. Teubner, Leipzig (1928).

[28] *A. Reuss Z. Angew*. Math. Mech. 9 (1929) 49.

[29] *R. Shein, A. L. Ivanovskii*, J. Phys.: Condens. Matter 20 (2008) 415218.

[30] *A.F.Young, C.Sanloup, E.Gregoryanz, S.Scandolo, R.E.Hemley, H.K.Mao* Phys.Rev.Lett. 96 (2001) 155501.

[31] *J.Haines, J.Leger and G.Bocquillon* Annu. Rev. Mater. Res. 31 (2001)1

RADIATION DEPENDENCE DIELECTRIC PROPERTIES OF Au/POLYVINYL ALCOHOL (Co, Zn-doped)/n-Si SCHOTTKY BARRIER DIODES (SBDs)

[1]HABİBE USLU, [2]SEÇKİN ALTINDAL

[1]Physics Department, Faculty of Arts and Sciences,
Gazi University, 06500, Teknikokullar, Ankara, TURKEY
[2]Chemical Engineering Department, Faculty of Engineering and Architecture,
Gazi University, 06500, Teknikokullar, Ankara, TURKEY
h.uslu@gazi.edu.tr, seckinaltindal@gazi.edu.tr

The ^{60}Co (γ-ray) irradiation on dielectric properties of Au/polyvinyl-alcohol (Co, Zn-doped)/n-Si SBDs have been investigated by using capacitance-voltage (*C-V*) and conductance-voltage (*G/ω-V*) measurements before and after radiation at room temperature and 1 MHz. Experimental results show that the values of the real part (□') and the imaginer part (□") of dielectric constant (□*), loss tangent (tan□), the real (*M'*) and the imaginer (*M''*) part of electric modulus (*M**) and electrical conductivity (σ_{ac}) were found a strong dependence on the radiation dose and applied bias voltage especially in depletion and weak accumulation regions. Such bias and radiation dependent of these parameters can be explained on the basis of Maxwell-Wagner interfacial polarization and restructuring and reordering of charges at interface states.

I. INTRODUCTION

In recent years, considerable attention was given the radiation effect on SBDs. There are many reports about conjugated conducting polymers on the area of electronic and optoelectronic. Among the various conducting polymers, poly (vinyl alcohol), polyaniline, poly (alkylthiophene) polypyrrole, polyophene, poly (3-hexylthiophene) became an attractive research topic owing to their potential applications and interesting properties by chemists, physicists and electrical engineers alike [1-5]. Dielectric properties of SBDs with an interfacial polymeric layer are generally related by its interface quality, interface states and the barrier formation at M/S interface. The investigation of various SBDs fabricated with different polymeric interfacial layer and those radiation resistances are important for understanding of the electrical and dielectric properties of SBDs. Especially polyvinyl alcohol (PVA) nanofabrics have attracted much attention for decades due to its unique chemical and a physical property as well as it is industrial application [5-9].

Dielectric measurements such as dielectric constant (ε'), dielectric loss (ε'') and loss tangent ($\tan\delta$) are drastically affected by the presence a dopant or dopants in the polymer and radiation effect [5,9-12]. The change of these parameters in the dark is considerably different under gamma irradiation. Under high energy particles and gamma irradiation, an excess capacitance can be occurring due to radiation induced interface states and it leads to an increase in the real capacitance of structures. Therefore, it is important to include the effect of gamma radiation and bias voltage in the investigation of both electrical and dielectric properties [10-12].

In this study, PVA film was used as an interfacial layer at M/S interface. Here, PVA doped with different ratio of Co and Zn was produced and PVA/(Co, Zn) nanofiber film on silicon semiconductor were fabricated by the use of electrospinning technique. The effect of radiation on dielectric properties such as ε', ε'', $\tan\delta$, *M'*, *M''* and σ_{ac} were investigated by using admittance spectroscopy method (C-V and G/w-V).

II. EXPERIMENTAL PROCEDURES

In this work, Au/polyvinyl-alcohol (Co, Zn-doped)/n-Si SBDs were fabricated on n-type Si wafer with (111) orientation and 0.7 Ω-cm resistivity with thickness of 3.5 μm. Before making contacts, Si wafer first was cleaned in a mix of a peroxide- ammoniac solution in 10 minute and then in H_2O+ HCl solution and then was rinsed in deionised water using an ultrasonic bath for 15 min. After surface cleaning, high purity (99.999 %) Au with a thickness of about 2000 Å were thermally evaporated on to whole back side of Si wafer at a pressure about 10^{-6} Torr in high vacuum system and then was annealed for a few minutes at 450 °C to form ohmic contact. After that 0.5 g of cobalt acetate and 0.25 g of zinc acetate was mixed with 1 g of PVA, molecular weight=72 000 and 9 ml of de-ionized water. Using a peristaltic syringe pump, the precursor solution was delivered to a metal needle syringe (10 ml) with an inner diameter of 0.9 mm at a constant flow rate of 0.02 ml/h. The needle was connected to a high voltage power supply and positioned vertically on a clamp. A piece of flat aluminum foil was placed 15 cm below the tip of the needle to collect the nanofibers. n- Si wafer was placed on the aluminum foil. Upon applying a high voltage of 20 kV on the needle, a fluid jet was ejected from the tip. The solvent evaporated and a charged fiber was deposited onto the Si wafer as a nonwoven mat. After spinning, the Schottky contacts were coated by evaporation with Au dots with a diameter of about 1.0 mm (diode area= $7{,}85\text{x}10^{-3}\text{cm}^2$). All evaporation processes were carried out in a vacuum coating unit at about 10^{-5}Torr.

The *C-V* and *G/w-V* measurements were carried out before and after ^{60}Co γ-ray gamma radiation (22 kGy) at room temperature by using an HP 4192A LF impedance analyzer (5 Hz-13 MHz) and small sinusoidal test signal of 40 $mV_{p-p.}$ from the external pulse generator is applied to the sample in order to meet the requirement [13]. All measurements were carried out with the help of a microcomputer through an IEEE-488 ac/dc converter card.

III. RESULTS AND DISCUSSION

The dielectric constant (ε'), dielectric loss (ε''), loss tangent (tanδ), ac electrical conductivity (σ_{ac}) and real and imaginary part of electric modulus (M' and M'') were evaluated from the knowledge of *C-V* and *G/w* measurements for Au/PVA (Co, Zn-doped)n-Si SBDs before and after irradiation at 1 MHz and at room temperature. The dielectric constant can be expressed as [14-16]:

$$\varepsilon^* = \varepsilon^{'} - j\varepsilon^{"} \tag{1}$$

where ε' and ε'' are the real and imaginary parts of complex permittivity, respectively, and j is the imaginary root of -1. The complex permittivity formalism has been employed to describe the electrical and dielectric properties. In the ε^* formalism, in the case of admittance Y^* measurements, the following relation holds:

$$\varepsilon^* = \frac{Y^*}{j\omega C_o} = \frac{C}{C_o} - j\frac{G}{\omega C_o} \tag{2}$$

where C and G are the measured capacitance and conductance values of the polymer material, respectively, and ω is the angular frequency ($\omega=2\pi f$) of the applied electric field.

The values of the ε' were calculated by using the measured C values for each bias voltage from the relation [11,17]:

$$\varepsilon^{'} = \frac{C}{C_o} = \frac{C\,d}{\varepsilon_o A} \tag{3}$$

where $C_o = \varepsilon_o A/d$ is capacitance of an empty capacitor, A is the rectifier contact area of the structure in cm^{-2}, d is the interfacial polymer layer thickness and ε_o is the electric permittivity of free space (ε_o = 8.85x10^{-14} F/cm). In the strong accumulation region, the maximal capacitance of the MIS capacitance corresponds to the interfacial polymer capacitance ($C_{ox} = \varepsilon' C_0 = \varepsilon^{'}\varepsilon_o A/d$). The values of the ε'' were calculated from measured C values for each bias voltage from the relation [11,17]:

$$\varepsilon^{"} = \frac{G}{\omega C_o} = \frac{Gd}{\varepsilon_o \omega A} = \varepsilon' \tan\delta \tag{4}$$

where tanδ of the polymer as dielectric material is denoted by tanδ and can be expressed as follows [14,18]:

$$\tan\delta = \frac{\varepsilon^{"}}{\varepsilon^{'}} \tag{5}$$

AC electrical conductivity (σ_{ac}) of the polymer can be expressed as [14,18]:

$$\sigma_{ac} = \omega C \tan\delta (d/A) = \varepsilon^{"}\omega\varepsilon_o \tag{6}$$

The terms complex impedance (Z^*) and complex electric modulus (M^*) formalisms with regard to the analysis of the dielectric or polymer materials have so far been discussed by several authors, most of whom have preferred electric modulus in defining the dielectric property and conduction mechanism of these materials [16,19]. The data regarding Z^* or the complex dielectric permittivity ($\varepsilon^*=1/M^*$) data can be transformed into the M^* formalism using the following relation [19,20]:

$$M^* = \frac{1}{\varepsilon^*} = M^{'} + jM^{"} = \frac{\varepsilon^{'}}{\varepsilon^{'2} + \varepsilon^{"2}} + j\frac{\varepsilon^{"}}{\varepsilon^{'2} + \varepsilon^{"2}} \tag{7}$$

The ε^* and M^* representation allows us to distinguish the local dielectric relation. Generally, extract as much information as possible, dielectric relation spectroscopy data are used in the electric modulus formalism introduced by Macedo *et al* [20]. Also, the determination of the electric modulus of these materials and their variation with applied bias voltage provide valuable information that allows study of the relaxation process for a specific electronic application [20].

Before and after irradiation of the ε'-*V*, ε"-*V* and tanδ-*V* characteristics of the SBD are given in Figs. 1 (a-c), respectively. As shown in Figs. 1, the ε'-*V*, ε"-*V* and tanδ-*V* curves show a significant difference after irradiation especially in the depletion region. However, these change in strong inversion and accumulation regions become almost independent of radiation. In addition, the *ε'-V*, *ε''-V* and *tanδ-V* characteristics have a peak in the depletion region for each condition. The magnitude of the peak values ε' and ε'' increase with increasing radiation and the peak positions shift towards the reverse bias region. Such peak behavior of *ε'-V*, *ε''-V* and *tanδ-V* curves can be attributed to particular distribution interface states (N_{ss}) at M/S interface and restructure and reordering of surface charges under radiation effect.

The voltage dependence of the real (*M'*) and imaginer (*M''*) electrical modulus are given in Fig. 2 (a) and (b) for SBD measured before and after irradiation, respectively. The values of the M' and M'' decrease with increasing radiation. The imaginary M'' reaches a peak value and then decreases down to minimum. The values and magnitudes of the peak decreases with increasing gamma-irradiation dose and the peak positions shift towards the reverse bias region under radiation.

Before and after irradiation of the σ_{ac}-*V* characteristics of the SBD were given in Fig. 3. It is clearly seen in Fig. 3 that σ_{ac} is dependent on the radiation and applied bias voltages for the measurement SBD. The values of σ_{ac} increase with increasing radiation in the depletion region due to the radiation induced N_{ss}.

IV. CONCLUSIONS

The ^{60}Co (γ-ray) irradiation on dielectric properties of Au/polyvinyl-alcohol (Co, Zn-doped)/n-Si SBDs have been investigated by using *C-V* and *G/ω-V* measurements before and after radiation at room temperature and 1 MHz. These measurements are useful in understanding the after ^{60}Co γ-ray gamma radiation effects on the

dielectric properties of these devices. Experimental results show that the ε'-V, ε''-V and M''-V characteristics have a peak in the depletion region for each condition and peak positions shift towards the reverse bias region due to radiation effect. It can be concluded that the values of ε', ε'', tanδ, σ_{ac}, M' and M'' of Au/PVA (Co, Zn-doped) n-Si SBD are strongly dependent on the applied bias voltage.

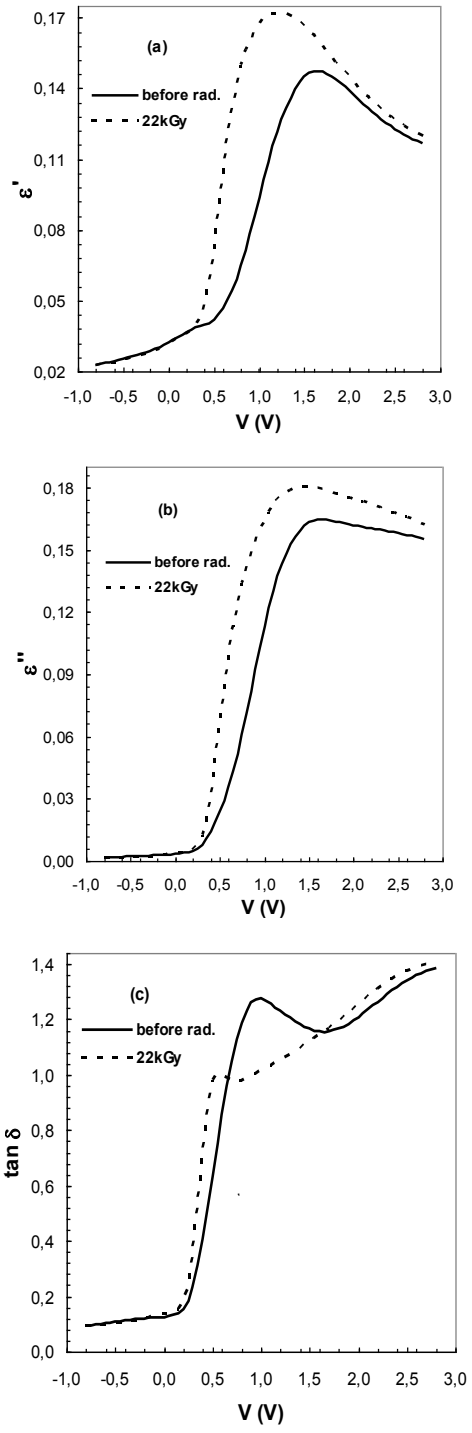

Fig. 1. The voltage dependence of **(a)** dielectric constant (ε'), **(b)** dielectric loss (ε'') and **(c)** loss tangent (tanδ) at 1 MHz and at room temperature for Au/PVA (Co, Zn-doped) n-Si SBD before and after radiation.

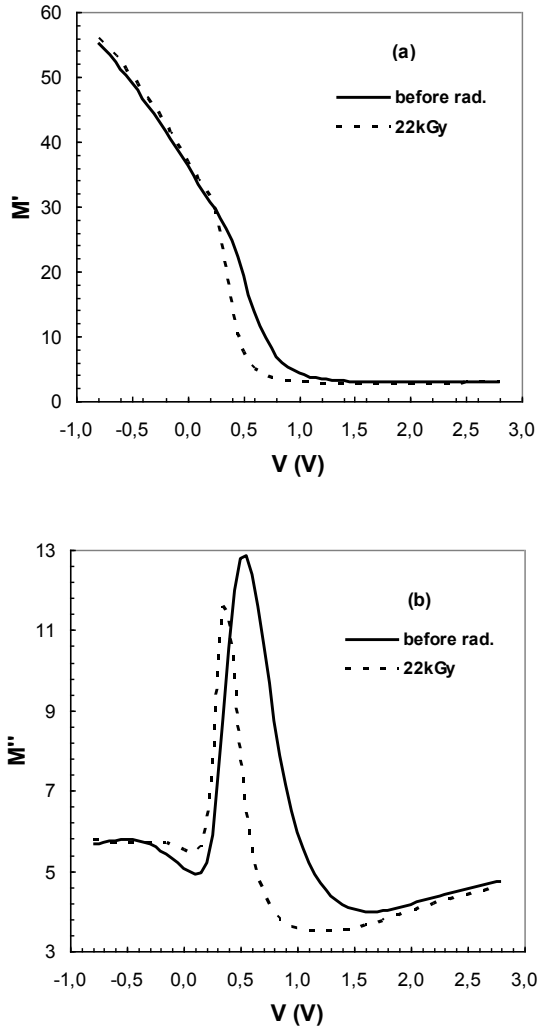

Fig. 2. The voltage dependence of **(a)** the real part M' and **(b)** the imaginary part M'' of electric modulus M^* at 1 MHz and at room temperature Au/PVA (Co, Zn-doped) n-Si SBD before and after radiation.

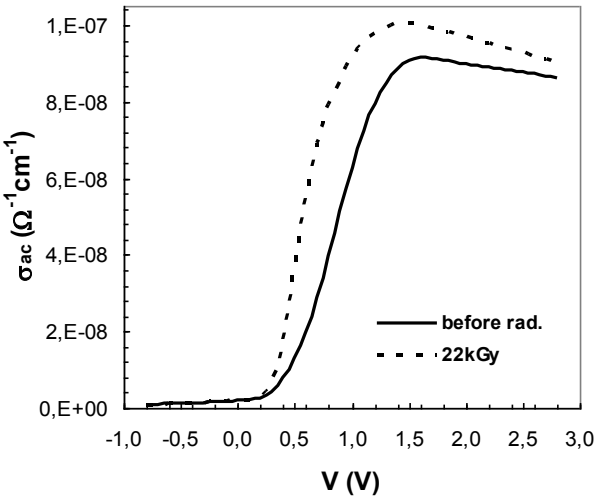

Fig. 3. The variation of the ac electrical conductivity σ_{ac} with applied bias for Au/PVA (Co, Zn-doped) n-Si SBD before and after radiation.

[1]. *P.S. Abthagir, R.Saraswathi*, Organic Electronics 5 (2004) 299.
[2]. *A.Bohler, S.Dirr, H.H.Johannes, D.Ammermann, W. Kowalsky*, Synth. Met. 91 (1997) 95.
[3]. *Y.O.Yakovlev,V.F.Zolin,* Synth.Met. 91(1997)205
[4]. *F.Garten, J.Vrijmoeth, A.R.Schlatmann, R.E.Gill,T.M. Klapwijk, G.Hadziioannou,* Synth. Met. 76 (1996) 85.
[5]. *A. Shehap, R.A. Abd Allah, A.F. Basha, F.H. Abd El-Kader*, J. App. Poly. Sci. 68 (1998) 687.
[6]. *A.Bohler, S.Dirr, H.H.Johannes, D.Ammermann, W. Kowalsky*, Synth. Met. 91 (1997) 95.
[7]. *Y.O. Yakovlev, V.F. Zolin,* Synth. Met. 91 (1997) 205.
[8]. *M.A.Ahmed, M.S.A. Ellil,* J. Mat. Sci: Met. Elec. 9 (1998) 391.
[9]. *I. Taşçıoğlu, H. Uslu, Ş. Altındal,P. Durmuş, I.Dökme,T.Tunç,* J. App. Poly. Sci. xx (2010) xx.
[10]. *H. Saito, B. Stuhn,* Polymer, 35, (1994), 475.
[11]. *M. Popescu, I. Bunget*, Physics of Solid Dielectrics, Elsevier, Amsterdam, 1984.
[12]. *B. Akkal, Z. Benamara, B. Gruzza and L. Bideux, N. Bachir Bouiadjra*, Matter. Sci. and Eng. C 21 (2002) 291.
[13]. *E.H. Nicollian, J.R. Brews*, MOS Physics and Technology, John Wiley & Sons, New York, 1982.
[14]. *C.P. Symth*, Dielectric Behaviour and Structure, McGraw-Hill, New York, 1955.
[15]. *Vera V. Daniel,* Dielectric Relaxation, Academic Press, London, 1967.
[16]. *P. Pissis, A. Kyritsis,* Solid State Ionics 97 (1997) 105.
[17]. *A. Chelkowski*, Dielectric Physics, Elsevier, Amsterdam, 1980.
[18]. *M.S. Mattsson, G.A Niklasson, K. Forsgren, and A. Harsta*, J. Appl. Phys. 85(4) (1999) 2185.
[19]. *K. Prabakar, S.K. Narayandass, D. Mangaralaj*, Phys. Status Solidi (a) 199 (2003) 507.
[20]. *P.B. Macedo, C.T. Moyniham, R. Bose*, Phys. Chem. Glass. 13 (1972) 171.

AB-INITIO FIRST PRINCIPLES CALCULATIONS ON HALF-HEUSLER NiYSn (Y=Zr, Hf) COMPOUNDS PART 1: STRUCTURAL, LATTICE DYNAMICAL, AND THERMO DYNAMICAL PROPERTIES

HACI ÖZIŞIK[1], KEMAL ÇOLAKOĞLU[2], HAVVA BOĞAZ ÖZIŞIK[1,2]

[1]Aksaray University, Department Of Physics, 68100, Aksaray, TURKEY,
hacioz@aksaray.edu.tr
[2]Gazi University, Department Of Physics, Teknikokullar, 06500, Ankara, TURKEY,
kcolak@gazi.edu.tr

The structural and lattice dynamical properties of the half-Heusler NiYSn (Y=Zr, Hf) compounds, we have been investigated using the ab-initio density-functional theory within the generalized gradient approximations. In particularly, some basic physical parameters such as lattice constant, bulk modulus and its first derivatives, elastic constants, shear modulus, Young's modulus, and Poison's ratio are calculated in the ground state configuration. The calculated elastic constants and the related sound velocities and Debye temperatures are also presented. The computed phonon dispersion curves based on the linear response method are predicted. Some thermo dynamical properties such as free energy, entropy, and heat capacity at constant volume are also estimated and interpreted for the first time.

I. INTRODUCTION

At recent years, scientists take an interest half-heusler structures for their electronic and optical properties. Like NiZrSn and NiHfSn, some half-heusler compounds with 18 valance electrons have narrow band band gap and sharp slope of density of states (DOS) around the Fermi level [1]. This properties supply large thermoelectric power to semiconductors.

Half-Heusler compounds crystallize in the $C1_b$ MgAgAs-type structure, in the space group $F\bar{4}3m$ (No:216). Atoms are positioned at X (½, ½, ½), Y (¼, ¼, ¼) and Z (0, 0, 0) [3].

Although there exist many structural and electronic studies for this compounds, mechanical and thermal properties has not been studied yet. Therefore, we have focused on these properties.

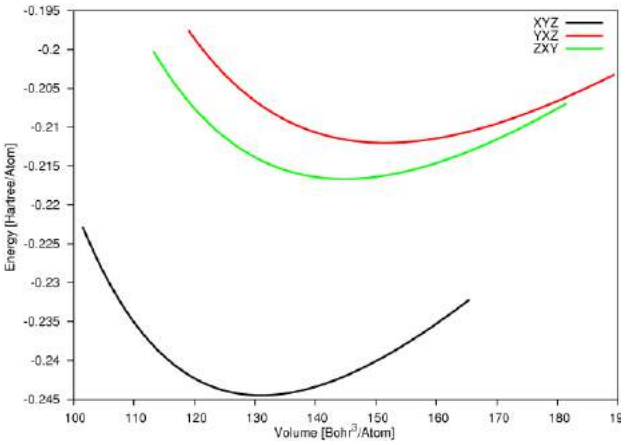

Fig. 1. Calculated cohesive Energy curves for NiZrSn. (X=Ni, Y=Zr, Z=Sn)

II. METHOD OF CALCULATION

All calculations have been carried out using the Vienna ab-initio simulation package (VASP) [4-5] based on the density functional theory (DFT) within the generalized gradient approximations (GGA). The electron-ion interaction was considered in the form of the projector-augmented-wave (PAW) method [6, 7] with plane wave up to energy of 337 eV. For the exchange and correlation terms in the electron-electron interaction, Perdew-Burke-Ernzerhof (PBE) type functional [8] was used within the GGA. We have used 11x11x11 Monkhorst and Pack mesh for k-space summation.

Table 1. Calculated elastic constants a_0 (Å), Bulk modulus B_0 (GPa) and it's pressure derivatives B_0', for NiYSn (Y=Zr, Hf) in $C1_b$ structure.

Compound	a_0	B_0	B_0'
NiZrSn	6.151	119.4	4.350
	6.11[14]	119[13], 129[13]	
	6.110[11]		
NiHfSn	6.108	125.3	4.318
	6.066[11]	110, 141[13]	

RESULTS AND DISCUSSION

Structural properties

Firstly (Determination of the electronic structure), the equilibrium lattice parameters have been computed by minimizing the crystal total energy calculated for different values of lattice constants by means of Murnaghan's eos [9] for XYZ, YXZ and ZXY compounds (X=Ni, Y=Zr and Hf, Z=Sn) to determination of ground state electronic structure (Fig. 1). From Fig. 1 we found that XYZ structure is found to be energetically favored. The bulk modulus, and its pressure derivative have also been calculated based on the same Murnaghan's eos and the results are listed in Table 1 for ground state structure. The present values of lattice parameters a_0 in $C1_b$ phase are found to be 6.151 and 6.108 Å for NiZrSn and NiHfSn, respectively. It is seen that the present lattice constants are in well agreement with experimental and other theoretical ones [See Table 1]. As a fundamental

physical property, the bulk modulus of solids provide valuable information including in average bond strengths of atoms for the given crystals [10], and its correctly calculation is one of the first-steps of the total energy calculations.

The present values of the bulk modulus for all considered compounds are given in Table 1. In the present case, the calculated bulk moduli are 119.4 and 125.3 GPa for NiZrSn and NiHfSn, respectively. So, we can say NiZrSn more compressibility than NiHfSn. The values of the bulk moduli indicate that, these compounds hard material in the ground state phase. Our calculated values are in close agreement with theoretical literature (See Table 1).

Elastic properties

The elastic constants of solids provide a link between the mechanical and dynamical behaviors of crystals, and give important information concerning the nature of the forces operating in solids. In particular, they provide information on the stability and stiffness of materials, and their ab initio calculation requires precise methods [15]. Since the forces and the elastic constants are functions of the first-order and second-order derivatives of the potentials, their calculation will provide a further check on the accuracy of the calculation of forces in solids. The elastic constants are computed by using the "stress–strain" method [16] implemented in VASP 5.2.2, and are listed in Table 2 for both compounds at the gound state $C1_b$ structure. For the stability of lattice, the Born's stability criteria's should be satisfied. Elastic moduli and mechanical stability criteria with Voigt-Reuss-Hill relations for the cubic structures are given as follows [15, 17-19]:

$$B_V = B_R = (C_{11}+2C_{12})/3,$$
$$G_V = (C_{11}-C_{12}+3C_{44})/5,$$
$$GR = 5(C_{11}-C_{12})C_{44}/(4C_{44}+3(C_{11}-C_{12})).$$

The mechanical stability criteria are given by

$$C_{11}>0,\ C_{44}>0,\ C_{11}>|C_{12}|,\ (C_{11}+2C_{12})>0.$$

From Hill average [19],

$$B=(1/2)(B_R+B_V) \text{ and } G=(1/2)(G_R+G_V)$$

Young's modulus *E* and Poisson's ratio *v* are given as

$$E=9BG/(3B+G),\ \nu=(3B-2G)/[2(3B+G)].$$

The present case elastic constants for NiZrSn and NiHfSn are given in Table 2. Our results show that NiZrSn and NiHfSn are mechanically stable at ambient conditions in $C1_b$ phase.

Young's modulus is defined as the ratio of stress and strain, and used to provide a measure of the stiffness of the solid. The material is stiffer if the value of Young's modulus is high. The calculated value of Young's modulus 185.0 and 199.4 GPa for NiZrSn and NiHfSn, respectively. The values of the Young's modulus indicate that, NiHfSn is stiffer than NiZrSn compound in C1b phase. These values are very close to value of (200 GPa) steel. Some experimental values (E, G, v_t, v_l, *vm*, and Θ_D) of the Sb doped quaternary compound $NiZrSn_{0.99}Sb_{0.01}$ in ref. [20] are in reasonable agreement with the present results, except for Young modulus (E).

Table 2. The calculated Elastic constants (C_{ij}), Bulk Modulus (B_0), Young's modulus (E), Shear modulus (G), Poisson ratio (v), the longitudinal (v_l), transverse (v_t), and their average (v_m) elastic wave velocities, Debye temperature (Θ_D), Anisotropy Factor (A), and Compressibility (K) in $C1_b$ phases for NiZrSn and NiHfSn

Par.	NiZrSn	$NiZrSn_{0.99}Sb_{0.01}$ [20]	NiHfSn	Unit
C_{11}	230.4		140.1	*GPa*
C_{12}	69.4		72.2	"
C_{44}	70.1		78.2	"
B_0	123.0		128.1	"
E	185.0	111	199.4	"
G	74.0	70.2	80.4	"
v	0.249		0.240	
v_t	3107	2461	2783	*m/s*
v_l	5377	4195	4762	"
v_m	3449	3039	3086	"
Θ_D	382	304	344	*K*°

The typical value of Poisson's ratio is about 0.1 for covalent materials and 0.25 for ionic materials [21]. In the present case the value of Poisson's ratio is 0.249 and 0.240 for NiZrSn and NiHfSn, respectively. Thus, the ionic contributions to the atomic bonding are dominant for considered compounds in $C1_b$ phase.

Finally, the typical relations between B and G are G=1.1B and G=0.6B for covalent and ionic materials, respectively [22]. G/B is found to be 0.60 and 0.63 for NiZrSn and NiHfSn, respectively and these values also supports the ionic character of NiZrSn and NiHfSn compounds.

Debye temperature

As an important fundamental parameter, the Debye temperature (Θ_D) is closely related to many physical properties of solids such as the specific heat and melting temperature. One of the standard methods for calculating the Debye temperature is to use elastic constant data since Θ_D may be estimated from the average sound velocity (v_m) using the following equation [23]:

$$\Theta_D = \frac{h}{k}\left(\frac{3n}{4\pi\Omega}\right)^{\frac{1}{3}}$$

where *h* is Plank's constant, *k* is Boltzmann's constant, Ω is the volume of unit cell and n is the number of atoms in unit cell. The average sound velocity v_m is given by

$$v_m = \left[\frac{1}{3}\left(\frac{2}{v_t^3}+\frac{1}{v_l^3}\right)\right]^{\frac{1}{3}}$$

v_l and v_t are the longitudinal and transverse elastic wave velocities, respectively, which are obtained from Navier's equations as follows [24]:

$$v_l = \sqrt{\frac{3B+4G}{3\rho}} \text{ and } v_t = \sqrt{\frac{G}{\rho}}$$

where ρ is the density, B is the bulk modulus and G is the shear modulus. The calculated Debye temperature is found to be 382 and 344 K˚ for NiZrSn and NiHfSn, respectively. We also presented the longitudinal (v_l), transverse (v_t), and their average (v_m) elastic wave velocities in Table 2.

The lattice dynamical properties

The present phonon frequencies of NiYSn (Y=Zr, Hf) compounds in C1b phase are calculated by the PHONOPY program [25] using the interatomic force constants obtained from the VASP 5.2 [4, 5] which is use linear response method within the density functional perturbation theory (DFPT) [26-28]. The Phonopy program which is based on real space supercell calculates phonon frequencies from force constants.

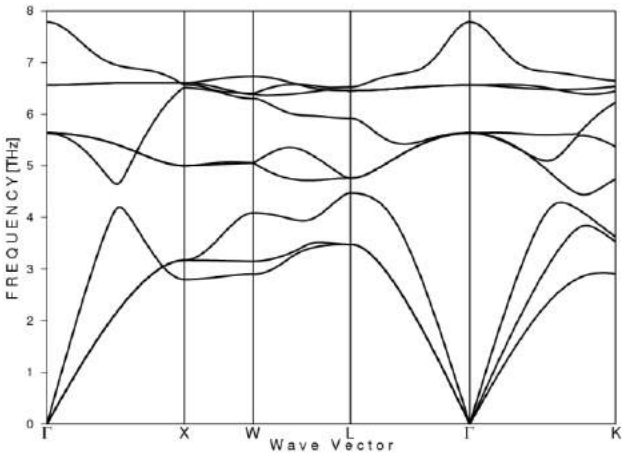

Fig. 2. Phonon dispersion curves with LO-TO along first Brillion zone for NiZrSn compound.

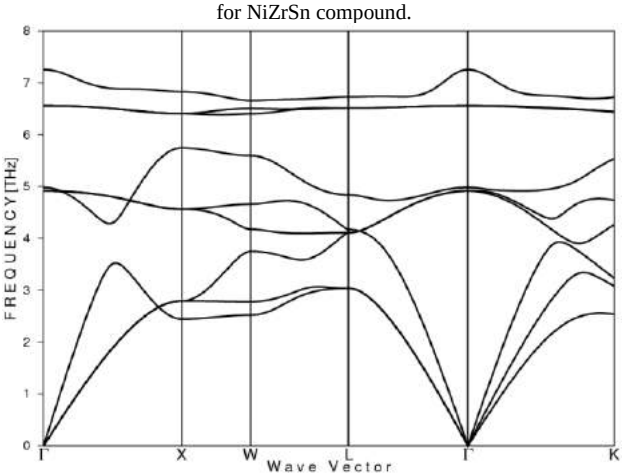

Fig. 3. Phonon dispersion curves with LO-TO along first Brillion zone for NiHfSn compound.

The present phonon dispersion curves have been calculated in high symmetry directions using a 2x2x2 supercell approach. The obtained phonon dispersion curves with the LO-TO splitting along the high symmetry directions are illustrated in Fig. 2 and Fig 3 for NiZrSn an NiHfSn, respectively. These splitting at Gamma point strongly support their ionic character. Fig. 4 and Fig. 5 shows the partial phonon density of states (DOS) for NiZrSn and NiHfSn, respectivly. In both plots, the contribution from Nickel atom is clearly dominant.

We also calculated thermo dynamical properties such as free energy, entropy, and heat capacity (See Fig. 6 and Fig. 7). For both compounds the heat capacity almost remains constant at about 250 K. The free energy and entropy curves exhibit the expected behavior at considered temperature range. Unfortunately, there is no experimental or other theoretical data on the lattice dynamical and thermo-elastic data for these compounds for the sake of comparison.

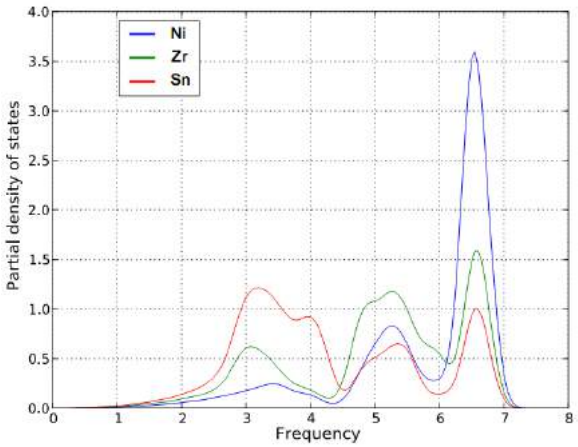

Fig. 4. Partial phonon density of states for NiZrSn compound.

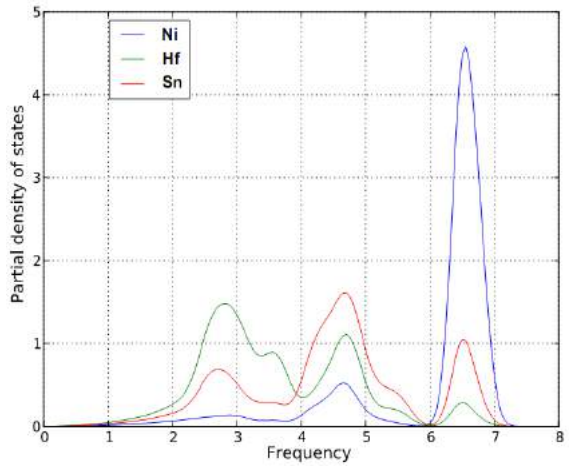

Fig. 5. Partial phonon density of states for NiHfSn compound.

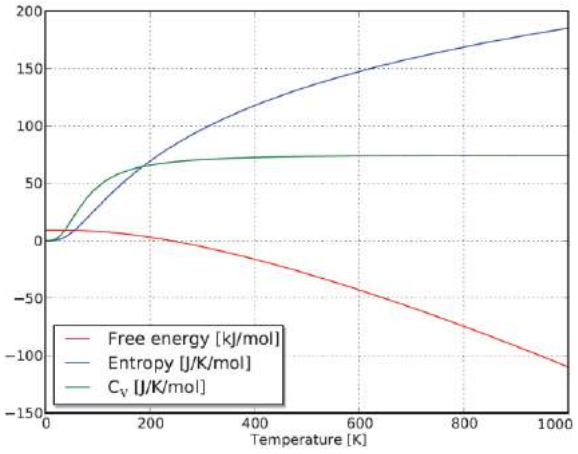

Fig. 6. Temperature dependence of free energy, entropy and heat capacity for NiZrSn in C1b phase

III. CONCLUSION

In this work, we have presented the results of ground-state structural, mechanical, vibrational, and thermo dynamical properties of NiZrSn and NiHfSn compounds in the $C1_b$ structure, using first-principles calculations based on the generalized gradient approximation (GGA) implemented in VASP. To the best of our knowledge, our calculations are the first theoretical prediction on the elastic and lattice dynamical properties of the studied compounds. The present data on the thermo dynamical properties such as free energy, entropy, and heat capacity provide valuable information about the intrinsic character of solids which are the other original aspects of the present calculations.

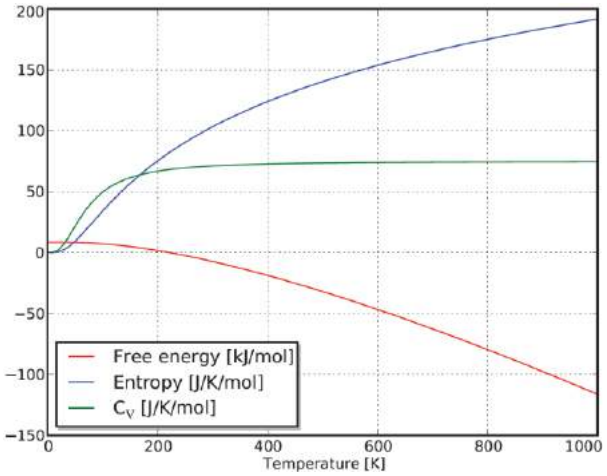

Fig. 7. Temperature dependence of free energy, entropy and heat capacity for NiHfSn in C1b phase.

ACKNOWLEDGEMENT

This work is supported by Gazi University Research-Project Unit under Project No. 05/2009/55.

[1] *T.Sekimoto, K.Kurosaki, H.Muta and S.Yamanaka* "Thermoelectric and thermophysical properties of ErPdX (X=Sb and Bi) half-Heusler compounds" *Journal of Aopplied Physics* 99 (2006) 103701.

[2] *K. Ahilan, M.C. Bennett, M.C. Aronson, N.E.Anderson, P.C. Canfield, E. Munoz-Sandoval, T. Gortenmulder, R. Hendrikx, and J.A. Mydosh* "Magnetotransport in single-crystal half-Heusler compounds" Physical Review B 69 (2004) 245116.

[3] *H.C. Kandpal, C. Felser and R. Seshadri,* Covalent bonding and the nature of band gaps in some half-Heusler compounds, J. Phys. D: Appl. Phys. 39 (2006) 776–785.

[4] *G. Kresse, J.Hafner* Ab initio molecular dynamics for liquid metals, Phys. Rev. B 47 (1994) 558-561.

[5] *G.Kresse, J.Furthmüller* Efficiency of ab-initio total energy calculations for metals and semiconductors using a plane-wave basis set, Comp. Mat. Sci. 6 (1996) 15-50.

[6] *P.E. Blöchl,* Phys. Rev. B 50 (1994) 17953.

[7] *G. Kresse, and J. Joubert,"*From ultrasoft pseudopotentials to the projector augmented wave method", Phys. Rev. B 59 (1999) 1758.

[8] *J.P. Perdew, K. Burke, and M. Ernzerhof,* Generalized Gradient Approximation Made Simple, Phys. Rev. Lett. 77 (1996) 3865–3868.

[9] *F.D. Murnaghan,* Finite Deformations of an Elastic Solid, Am. J. Math. 49 (1937) 235-260.

[10] *A.A. Maradudin, E.W. Montroll, G.H. Weiss and I.P. Ipatova,* Theory of lattice dynamics in the harmonic approximation,Second Ed., Academic Pr., New York Londen, 1971.

[11] *P. Larson, S.D. Mahanti, M.G. Kanatzidis,* Structural stability of Ni-containing half-Heusler compounds, Phys. Rev. B 62 (2000) 12754.

[12] *F.G. Aliev,* Physica B 171 (1991) 199.

[13] *S. Ogut, K.M. Rabe,* Phys. Rev. B 51 (1995) 10443-10453.

[14] *P. Villars, L.D. Calvert,* Pearson's Handbook of Crystallografic Data for Intermetallic Phases (American Society of Metals, Metals Park,OH, 1985)

[15] *E. Deligoz, K. Colakoglu, Y.O. Ciftci, H. Ozisik,* The first principles study on boron bismuth compound, Computational Materials Science, 39 (2007) 533-540 .

[16] *Y.L.Page and P.Saxe,* Phys. Rev. B63 (2001) 174103.

[17] *W. Voigt,* Lehrburch der Kristallphysik, Teubner, Leipzig, 1928.

[18] *A.Reuss, Z. Angew.* Math. Mech. 9 1929) 49.

[19] *R. Hill,* Proc. Phys. Soc. London 65 (1952) 350.

[20] *Y. Kawaharada, K. Kurosaki, H. Muta, M. Uno, S. Yamanaka,* Thermophysical properties of NiZrSn1−xSbx half-Heusler compounds, Journal of Alloys and Compounds 381 (2004) 9–11.

[21] *V.V. Bannikov, I.R. Shein, A.L. Ivanovskii,* Phys. Stat. Sol. (RRL) 1 (2008) 89-91.

[22] *P. Hermet, S. Goumri-Said, M.B. Kanoun, and L.Henrard,* First-Principles Investigations of the Physical Properties of Magnesium Nitridoboride, J. Phys. Chem. C 113 (2009) 4997-5003.

[23] *O.L. Anderson,* A simplified method for calculating the debye temperature from elastic constants, J.Phys.Chem.Solids 24(1963)909-917.

[24] *I.R. Shein, A.L. Ivanovskii,* J. Phys.: Condens. Matter 20 (2008) 415218.

[25] *A. Togo, F. Oba, and I. Tanaka,* First-principles calculations of the ferroelastic transition between rutile-type and CaCl2-type SiO2 at high pressures, Phys. Rev. B, 78, (2008) 134106-1-9.

[26] *S. Baroni, P. Giannozzi, and A. Testa*. Green's-function approach to linear response in solids. Phys. Rev. Lett., 58 (1987) 1861.

[27] *X. Gonze and J.-P. Vigneron*. Density-functional approach to nonlinear response coefficients of solids. Phys. Rev. B, 39 (1989) 13120.

[28] *X. Gonze, D. C. Allan, and M. P. Teter.* Dielectric tensor, effective charges, and phonons in alpha-quartz by variational density-functional perturbation theory. Phys. Rev. Lett., 68 (1992) 3603.

ENTHALPIES OF BINARY TRANSITION HCP METAL BASED ALLOY CALCULATED BY ANALYTICAL EMBEDDED ATOM METHOD

H. İBRAHİM DURSUN

Faculty of Science and Literature, University of Aksaray, TR-68100 Aksaray, Turkey (Tel: +90 382-2151654; e-mail: hidursun@aksaray.edu.tr

An analytical embedded atom method which can treat hcp transition metal iron has been developed. In this model, a new potential was presented and a modified term has been introduced to fit the negative Cauchy pressure $P_C = (C_{12} - C_{44})/2$ for hcp metals. The enthalpies of formation of all binary alloy systems for seven transition hcp metals are calculated with the Analytical embedded atom method. The calculated dilute-solution enthalpies and formation enthalpies of random alloys are in agreement with the experimental data available and results calculated from the Miedema Theory. One can conclude that our analytical embedded atom method is also effective to apply to the hcp metals and their alloys.

I. INTRODUCTION

Daw and Baskes [1] derived so-called Embedded Atom Method (EAM) on the basis of quasi–atom concept and density–function–theory. Since then, the semi-empirical theory attracts great interest of scientists in materials science and condensed matter physics. It has been applied successfully to metals, impurity, surface, alloys, liquids and mechanical properties [1,2], Johnson [3] proposed an analytical EAM model, Bangwei and Yifang [4], however, the model cannot treat transition metal, for its negative Cauchy pressure $P_C=(C_{12}-C_{44})/2$.

The calculations for enthalpies of solution and formation calculated with the analytical EAM by themselves only for bcc alloys were performed present author [5]. The problem is that this analytic EAM model can not be applied to the alloys containing metal Cr and other metals with a negative Cauchy pressure. And the calculated values for formation enthalpies of some alloy systems are weakly in agreement with the experimental data available. Based on the spirit of the analytic EAM model by Johnson, we proposed an analytic EAM by introducing a modified term in the total energy expression and a new potential, which can describe the metals with a negative Cauchy pressure.

The developed analytic EAM has been applied to the self-diffusion properties[6], and the enthalpies of formation [7] for all bcc transition metals and alloys, the enthalpies of formation for alkali metal alloys [8], and the enthalpies of formation for fcc transition metal alloys [9] In this paper, we present a new pair potential. In order to fit the negative Cauchy pressure, an analytic modified term *M(P)* has been introduced. The developed analytical EAM model has been applied to calculate the self-diffusion properties of the hcp transition metals [10], the results are in good agreement with the available experimental values. In the present work this model was applied to calculate the dilute-solution enthalpies and formation enthalpies of binary alloys of the hcp transition metals;

II. MODEL

The EAM is one of the distinguished potentials which gains great success in describing the interaction of particles of metals and alloys. It has been shown to give good results in simulations of reconstructions, thermal expansion, surface and liquid structure, and even for the under-cooled liquid-to-glass and liquid-to-crystalline transitions. The EAM is a procedure for designing a mathematical model of a metal which was developed by researchers at Sandia National Laboratory, from the EAM the total energy of an assembly of atoms is [1]

$$E_t = \sum_i F_i(\rho_i) + \frac{1}{2}\sum_{i\neq j}\phi\left(r_{ij}\right)$$

$$\rho_i = \sum_{j\neq i} f\left(r_{ij}\right)$$

where E_t is the total internal energy, ρ_i is the electron density at *i* due to all the other atoms, $f\left(r_{ij}\right)$ is the electron density distribution function of an atom, r_{ij} is the separation distance between atom *i* and atom *j*, $F(\rho_i)$is the embedding energy to embed atom *i* into an electron density ρ_i, and $\phi(r_{ij})$is the two-body potential between atom *i.* and atom *j*. Following the previous procedure of EAM, the negative Cauchy pressure cannot be fitted. So in the present model an analytical modified term $M(P_i)$ has been introduced. Then (1) is written in the following form:

$$E_t = \sum_i F_i(\rho_i) + \frac{1}{2}\sum_{i\neq j}\phi\left(r_{ij}\right) + \sum_i M\left(P_i\right)$$

$$P_i = \sum_{i\neq j} f^2\left(r_{ij}\right)$$

The modified term $M(P_i)$ is based on two reasons:

One is from (2), the total electron density at the position of atom *i* is the superposition of contribution from all the other atoms, this assumption is too simple and neglects the hybridization and the polarity.

The other is the spherical symmetric assumption of electron density distributions. In fact, the outer electron density distribution is not spherically symmetric except the s-electron. The modified term $M\left(P_i\right)$ represents the discrepancy between the assumptions, and the facts. According to Johnson and Oh's procedure of

development of the EAM [3], the potential function satisfies the following equations:

$$4\phi(r_1)+3\phi(r_2)=-E_{1f}$$
$$4\phi'(r_1)+3\phi'(r_2)=0$$
$$4\phi''(r_1)+3\phi''(r_2)=15\Omega G$$
$$\frac{8\left(r_1^2\phi''(r_1)-r_1\phi'(r_1)\right)}{9\left(r_2^2\phi''(r_2)-r_2\phi'(r_2)\right)}=A$$

The embedding function and the modified term satisfy the following equations:

$$F(\rho_e)=-F_0$$
$$F'(\rho_e)=0$$

$$F''(\rho_e)\frac{\left(8r_1f'(r_1)+6r_2f'(r_2)\right)^2}{\left(8f(r_1)+6f(r_2)\right)^2}+M''(P_e)\frac{4\left(8r_1f(r_1)f'(r_1)+6r_2f(r_2)f'(r_2)\right)^2}{\left(8f^2(r_1)+6f^2(r_2)\right)^2}$$
$$=9\Omega B-15\Omega G$$

$$M(P_e)=0$$
$$M'(P_e)=0$$

Where E_{1f} is the mono-vacancy formation energy, r_1 and r_2 are the nearest and next-nearest neighbor distances, respectively, the prime indicates differentiation to it is argument. The Ω is the equilibrium volume of an atom, G is the Voigt shear modulus, $G=(C_{11}-C_{12}+3C_{44})/5$, C_{11}, C_{12} and C_{44} are elastic constants, A is the anisotropic ratio, $A=2C_{44}/(C_{11}-C_{12})$, B is the bulk modules, ρ_e is the equilibrium value of the total electron density ρ, P_e is the equilibrium value of P, F_0 is the value of embedding function at the equilibrium. In order to have an applicable EAM model, the embedding function $F(\rho)$, the atomic electron density distribution $f(r)$, the two-body potential $\varnothing(r)$ and the modified term $M(P)$ must be determined. In this present model, the embedding function $F(\rho)$ is taken as the form [3], namely

$$F(\rho)=-F_0\left[1-\ln\left(\frac{\rho}{\rho_e}\right)^n\right]\left(\frac{\rho}{\rho_e}\right)^n$$

where the parameters F_0 and n are determined as follows:

$$F_0=E_c=E_{1f}$$
$$n=\sqrt{\frac{\Omega B}{A\beta^2E_{1f}}}$$

where E_c is the cohesive energy, β is the decay power of the atomic electron density distribution function. The electron density distribution function of an atom $f(r)$ is taken as [3].

$$f(r)=f_e\left(\frac{r_1}{r}\right)^\beta$$

where the parameter f_e determined in the present model is taken as [11].

$$f_e=\left(\frac{E_C-E_{1f}}{\Omega}\right)^{(3/5)}$$

and the model parameter β is empirically taken as "6"for metal and alloy.

Certainly, its exact values can be obtained by fitting (17) to the results of Clementi and Roetti [12], the two-body potential function $\phi(r)$ is taken as by Quyang et al. [11].

$$\phi(r)=K_0+K_1\left(\frac{r}{r_1}\right)^2+K_2\left(\frac{r}{r_1}\right)^4+K_3\left(\frac{r_1}{r}\right)^{12}$$

$$K_0=-\frac{1}{9}E_{1f}-15\Omega G\frac{10097924A+12332488}{96(1238475A+825650)}$$
$$K_1=15\Omega G\frac{1633023A-811174}{96(1238475A+825650)}$$
$$K_2=15\Omega G\frac{688128-137781A}{32(1238475A+825650)}$$
$$K_3=15\Omega G\frac{1024(2A-1)}{1238475A+825650}$$

as for the modified term, considering the two assumptions mentioned above, the real host electron density should be

$$\rho_{rel}=\rho+\Delta\rho$$

Where ρ_{rel} is the electron density of the host obtained by the two assumptions, $\Delta\rho$ is the deviation; results from the assumption of spherical distribution of an atomic electron density and the assumption of linear superposition of an electron density. Substituting ρ_{rel} into (14), the energy change, which results from $\Delta\rho$, is

$$\Delta E(\Delta\rho)\propto-(\Delta\rho)^2$$

Because $\Delta\rho$ is very small, then

$$\Delta E(\Delta\rho)\propto Exp\left[-(\Delta\rho)^2\right]$$

Table 1. The input physical parameters fcc metals a and E_C and E_{1f} in eV and C_{ij} in GPa [13, 14, 15]

	a	E_C	E_{1f}	C_{11}	C_{12}	C_{44}
Re	0.27600	8.03	2.30	616	273	161
Ru	0.27057	6.74	1.85	563	188	181
Zr	0.32312	6.25	1.70	144	74	33.4
Y	0.36474	4.37	1.25	77.9	28.5	24.31
Co	0.24970	4.39	1.35	295	159	71
Sc	0.33080	3.90	1.15	99.3	39.7	27.2
Ti	0.29506	4.85	1.50	160	90	46.5

Baskes et al. [16], responded that the electron density change $\Delta\rho$, results from the polarity could be expressed as

$$\Delta\rho \propto \sum_{j\neq i} f^2\left(r_{ij}\right)$$

from the above considerations (12) and (13), let P represents the $\Delta\rho$ and P_e represents the average value of P, and then the modified term $M(P)$ is empirically taken as

$$M(P)=\alpha\left[\left(\frac{P}{P_e}-1\right)^2\right]\exp\left[-\left(\frac{P}{P_e}-1\right)^2\right]$$

This has only one parameter, α which can be determined from (11) and (16). Now the model parameters K_i (i = 0,1,2,3), f_e,F_0, n and α can be determined from the input physical parameters; a, E_c,E_{1f},B,G and A with the above equations and only one adjustable parameter β is empirically taken as"6",so the present model is complete. The input physical parameters are listed in Table 1, and the corresponding model parameters are listed in Table 2. In the present model, the two-body potential and the electron density functions should have a cut-off. *A* cubic spline function is used as *a* cut-off function. The cut-off procedure is the same as that used by Bangwei and Yifang [4] with the start point (r_s= r_2) and the end point $\left(r_C=\sqrt{2r_2}\right)$. When the model is applied to study the properties of an alloy, the interaction potential between different types of atoms must be defined here, so the Johnson and Oh [4] form is taken:

$$\phi^{AB}(r)=\frac{1}{2}\left[\frac{f^A(r)}{f^B(r)}\phi^{BB}(r)+\frac{f^B(r)}{f^A(r)}\phi^{AA}(r)\right]$$

where A and B indicate the types of atoms.

III. RESULTS AND DISCUSSIONS

3.1. Alloy enthalpies of solution

The calculated alloy enthalpies of solution are shown in table 2. The experimental data available and the calculated results from the Miedema thermodynamic theory [17] are also presented in the Table for comparison. It can be seen that the present calculations are all in good agreement with the experimental data available though the calculations are much less than the experimental data for Ti in Zr. Ti in Hf and Zr in Ti. It is important to note that the agreement with the experimental data for the present calculations is much better than that for the calculations from the Johnson analytic EAM model for hcp metals [10,18], especially for the Ti in Zr, Ti in Hf and Hf in Ti alloys. The calculations from the Johsson model are all positive while the experimental are all negative. The present calculations are generally in agreement with those calculated from the Miedema's theory [17], but some of the algebraic symbols for the two kinds of values are quite the contrary for the alloys combined by two earlier or two later transition metals. As comparing to the nine experimental values available, the present ones are better than those of Miedema theory, especially for Ti in Hf and Hf in Ti because for those two alloys, the Miedema theory predicts the positive values while the experimental data are all negative.

Table 2. Calculated dilute alloy enthalpies of solution for all binary hcp alloy (the first row), the second row is the values calculated from Miedema' theory[17]. The third row the experimental data available[19,20,21]. All are (eV).

Sot.	Host					
	Re	**Zr**	**Y**	**Co**	**Sc**	**Ti**
Re		-1.8986 -1.34	-2.9753 -0.15	0.7658 0.09	-1.1132 -0.66	0.2219 -1.04
Zr	-1.7367 -1.59		-0.1935 0.35	-2.0614 -2.05	0.0771 0.17	-0.2861 -0.01 -0.03[20]
Y	-2.1235 -0.21	0.1018 0.44		-1.2725 -1.16	-0.1317 0.04	-0.3421 0.76
Co	0.1624 0.08	-2.5068 -1.42	-2.5692 -0.70		-2.2345 -1.04	-1.1264 -1.07 -1.48[21]
Sc	-0.3586 -0.75	0.0526 0.17	-0.2790 0.03	-0.5765 -1.45 -1.04[19]		0.0069 0.34
Ti	0.2256 -1.05	-0.4723 -0.01 -0.03[20]	-1.4962 0.53	-0.6198 -1.31 -1.74[21]	-0.3863 0.29	

3.2. Alloy enthalpies of formation

The calculated formation enthalpies (solid curve) of the disorder alloys with any compositions for 4 binary alloys of seven hcp transition metals are shown in Fig. 1. The following symbols stand for (□) present calculations, (♦) the results of calculations from the Johnson's EAM

model [4], (Δ) the available experimental data and (▲) the results of Miedema et al. [17].

The enthalpies of formation for all four binary disordered alloy systems with any compositions for the seven hcp transition metals are calculated using the present alloy Analytic EAM model. The comparison with experimental data available for four alloy systems is shown in Fig.1. The calculated results from the Miedema's theory [17], and the Johnson EAM model[3] are also shown in the Figure. It can be seen from Fig.1 that the agreement with experiment is good for Co −Y, Co −Z, Co −Sc and Co −Ti alloy systems. It is of interest to note that the comparison between the present calculations and the calculations from the Johnson's EAM model [3] shows that the values from the later ones are usually smaller than those for the present calculations. Especially, most of the values from the later calculations for the Co −Y alloy system are positive, which are just contrary to the experimental data. Therefore, to compare with the experimental data, the present calculations are better than the calculations from the Johnson's EAM model. The improvement results from the addition of the modified term to EAM model and proposing a new two-body potential in the Analytic EAM model. The agreement with the calculations from the Miedema theory is very good for two alloy systems (Co −Y, Co − Re), and is generally fair for the other systems except Ti −Y, Sc −Y two systems. Usually, the present calculations are less than the calculation from Miedema theory. For these two alloy systems the present values are basically negative, but the calculations from the Miedema theory are positive. The comparison shows the values calculated from the Johnson's EAM model are usually much less than the present calculated values.

IV. CONCLUSIONS

A simple analytical EAM model for the hcp metals has been developed. In the new model, a modified term of energy was introduced to fit the negative Cauchy pressure of hcp, and a new form of two-body potential was also proposed. This potential function can represent the interaction between the atoms in a wide range. The introduction of new modified term has a potential to overcome some of the problems faced with implementation of the EAM method, which excluded hcp metals in the previous studies. All parameters of the model have been determined. The calculated dilute solution enthalpies are in good, agreement with the available experimental data. The formation enthalpies are in good agreement with the available experimental data and those of the first principles calculations. As a result, the present model is generally in good agreement with Miedema's theory.

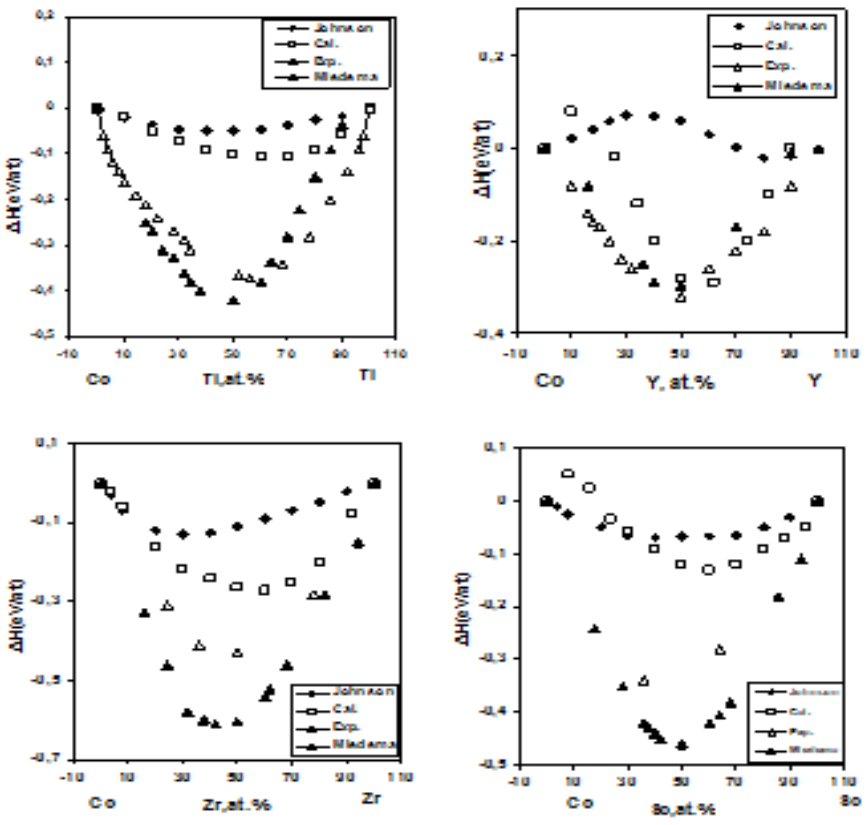

Fig.1. The calculated formation enthalpies of random alloys in whole composition range. The following symbols stand for (□) present calculations, (♦) the results of calculations from the Johnson's EAM model [4], (Δ) the available experimental data and (▲) the results of Miedema et al. [17].

[1]. *M.S.Daw, M.I.Baskes,* Phys Rev B:1984,29,6443.
[2]. *Z .Bangwei, O.Y.Yifang , L.Shuzi, J.Zhanpeng,* Physica B**:**1996, 101,161-8.
[3]. *R.A. Johnson*, Phys Rev B:1973,39,12554.
[4]. *Z.Bangwei,O.Y.Yifang*,Phys.Rev B:1993,48, 3022.
[5]. *I.H.Dursun, B.Z.Güvenç, E.Kasap,* Commun Nonlinear Sci Numer Simulat, 2010,15,1259
[6]. *R.Pasianot, D.Farkas, E.J. Savino,* Phys Rev B**:**1991,43, 6952.
[7]. *M.I. Baskes,* Phys Rev B: 1992, 46,2727.
[8]. *R.A. Johnson*, Phys Rev B: 1988, 37,3924.
[9]. *R.A. Johnson, D.J.Oh,* J. Mater Res. 1988, 3,471.
[10]. *Y.Quyang, B.Zhang, S.Liao, Z.Jin, Z.* Phys B: 1999, 262,218.
[11]. *Y.Quyang, B.Zhang, S.Liao, Z.Jin*, Z. Phys B: 1996, 101,161-8.
[12]. *E.Clementi, C.Roetti,* Data Nucl. Data Tables 1974, 14,3-4.
[13]. *C.Kittel,* Introduction to Solid State Physics (New York: Wiley) 1976, p:74.
[14]. *G.Simmon and H.Wang,* Single Crystal ElasticConstants and Calculated Aggregate Properties:a Handbook (Cambridge, MA: MIT Press) 1971.
[15]. *E.A.Brandes and G.B.Brook*, (eds) Smithells Metal Reference Book 7th edn (Oxford: Butterworths). 1992,p:15–16
[16]. *M.I.Baskes, J.S.Nelson, A.F.Wright,* Phys Rev. B: 1989;40:6085.
[17]. *F.R. de Boer, R.Boom, W.C.M.Mathens, A.R.Miedema, A.K.Nissen,* Cohesive in Metals, Amsterdam, North-Holland, 1989.
[18]. *[Y.Quyang, B.Zhang,* Z. Phys B: 1993, 92,431.
[19]. *Yu.O.Esin, S.E.Demin, V.V.Litovski,* J.Phys.Chem. 1985;59:131 Tanner I.E. Calphad.1973;3:91.
[20]. *I.Kaufman, I.E.Tanner,* Calphad.1979, 3, 91.
[21]. *I.Kaufman, I.E.Tanner,* Calphad.1978, 2, 81.

KINETICS OF CRYSTALLIZATION OF AMORPHOUS $Bi_{1.5}V_{0.5}Sr_2Ca_2Cu_3O_{x+\delta}$ GLASS

HALUK KORALAY, ŞÜKRÜ ÇAVDAR, ABDULLAH GÜNEN
Department of Physics, Gazi University,
Teknik Okullar Ankara, Turkey
E-mail: koralay@gazi.edu.tr

The kinetics of nucleation and crystal growth in a $Bi_{1.5}V_{0.5}Sr_2Ca_2Cu_3O_{x+\delta}$ amorphous alloy, prepared by glass-ceramic method were investigated using Differential Scanning Calorimeter (DSC). The crystallization kinetic parameters, including activation energy (E_a), Avrami parameter (n) were determined with non-isothermal analysis method based on the DSC data. Using the modified Kissinger equation, activation energies of crystal growth were determined as 357 kJ/mol for sample. The Avrami parameter for glass sample was calculated as 2, which indicates crystallize one-dimensionally, predicted by the Ozawa equation.

I. INTRODUCTION

In the BSCCO system three superconducting compounds are known. Their composition can be described by the general formula $Bi_2Sr_2Ca_{n-1}Cu_nO_x$ (n=1, 2, 3), where n represents the number of CuO_2 planes. They are commonly referred to as 2201 for n=1, 2212 for n=2 and 2223 for n=3, and the corresponding T_c values are 20 K, 80 K and 110 K, respectively. All three Bi superconducting compounds are reported to melt in the narrow temperature region between 1123 K and 1163 K [1- 3].

High $-T_c$ superconductors of the system BSCCO exhibit the advantage that they can be processed via a glass intermediate product. By variation of crystallization conditions, structural and microstructural properties such as phase formation, oxygen content, and grain size can easily be affected. In order to optimize the superconducting and mechanical properties of glass ceramic in the system BSCCO, it is important to investigate in detail the changes in these properties during the crystallization process. many authors have studied the crystallization mechanism since the first preparation of BSCCO glass ceramics [4-7]. main objective of the present investigation is to evaluate Avrami parameter and the activation energy for the kinetics of the crystal growth for $Bi_{1.5}V_{0.5}Sr_2Ca_2Cu_3O_{x+\delta}$ system by using DSC.

II. EXPERIMENTAL

The nominal compositions examined in this study were $Bi_{1.5}V_{0.5}Sr_2Ca_2Cu_3O_{x+\delta}$. High purity powders of Bi_2O_3 (99.99%), V_2O_5 (99.8%), $SrCO_3$ (99.99%), $CaCO_3$ (99.95%) and CuO (99.99%) all from Sigma-Aldrich Chemical Co. were mixed in an agate mortar and crushed for 45 min. The mixture of powders was loaded in an alumina crucible and melted in a resistance furnace at 1150 ^oC and quenched by pressing the poured melts between two copper plates. Thus, opaque black sheets approximately 1 mm thick glass fragments were obtained.

Approximately 12 mg of glass fragments were weighed into a aluminum crucible (5 mm x 0.1 mm x 0.4 mm). DSC (TA Instruments DSC 2010) was performed on glass fragments to identify the crystallization behavior. Samples were heated to 900 K in oxygen atmosphere at scan rates of 5, 10, 15 and 20 K min^{-1}. The temperature and energy calibrations of the instrument were performed using the well-known melting temperature and the melting enthalpy of high purity tin metal.

III. RESULT AND DISCUSSION

For determination of crystallization kinetics under non-isothermal conditions, $Bi_{1.5}V_{0.5}Sr_2Ca_2Cu_3O_{x+\delta}$ glass samples were first heated at the rates 5, 10, 15 and 20 K min^{-1} to 900 K. It is known that the start of crystallization temperature associates with the nucleation process, and the peak temperature is related to the growth process [8,9].

The thermal characteristics of the prepared glasses are given in Table 1 and Fig. 1. The prepared glasses exhibit endothermic effects due to glass transition temperature (T_g) ranging between 668 and 677 K. It is found that the T_g value increases with increasing heating rate (from 5 to 20 K min^{-1}). In the same figure, the DSC exothermic peak temperature is also shown. As a general feature of the crystallization of Bi-based glasses, the exothermic activity after the first crystalline phase appearing during thermal treatment at around 773 K is the 2201 phase.[10]. The second exothermic peak between 813 and 831 K (depending on the heating rate) can be due to the formation of low temperature impurity phases, such as Bi–Ca contained impurity phases [11].

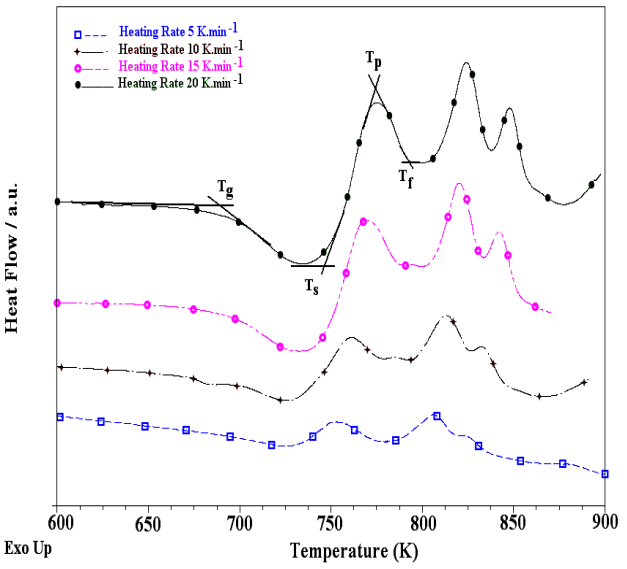

Fig. 1. Differential Scanning Calorimeter (DSC) curves of $Bi_{1.5}V_{0.5}Sr_2Ca_2Cu_3O_{x+\delta}$ glass at the scan rates of 5, 10, 15 and 20 K.min^{-1}, respectively

The values of glass-transition temperature (T_g), crystallization starting temperature (T_s), crystallization

peak temperature (T_p) and supercooled liquid (ΔT) are summarized in Table 1. The thermal stability of the glasses was calculated as the difference between the crystallization starting temperature and the glass transition temperature ($\Delta T=T_s-T_g$). The ΔT values were found to be around 60 K.

Table 1. Thermal properties of $Bi_{1.5}V_{0.5}Sr_2Ca_2Cu_3O_{x+\delta}$ glass

β (K min^{-1})	T_g (K)	T_s (K)	T_f (K)	T_p (K)	ΔT (K)	x
5	668	729	777	754	61	0.94
10	671	727	781	763	56	0.85
15	673	735	788	767	62	0.57
20	677	736	796	772	59	0.37

The DSC results were investigated by applying the following Kissinger analysis [12].

$$\ln\left(\frac{\beta}{T_p^2}\right) = -\frac{E_a}{RT_p}$$

where β is the scan rate, E_a is the activation energy for crystallization, T_p is the crystallization peak temperature, and R is the gas constant (R= 8.314 Kj.mol^{-1}). Fig. 2 shows Kissinger plots of $\ln\left(\beta/T_p^2\right)$ vs. $1000/T_p$ for the $Bi_{1.5}V_{0.5}Sr_2Ca_2Cu_3O_{x+\delta}$ glass samples. The activation energy for the crystallization of $Bi_{1.5}V_{0.5}Sr_2Ca_2Cu_3O_{x+\delta}$ glass was determined as 357 KJ/mol from the slope of the plot. This value is reported for the crystallization of Bi-2223 superconductor glass of 340 kJ/mol, reported by Fuxi *et al*. [10].

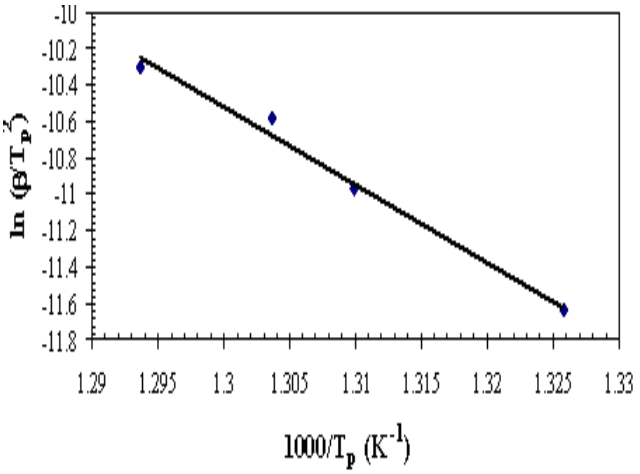

Fig. 2. Plot of $\ln\left(\beta/T_p^2\right)$ vs. $1000/T_p$ for the determination of the activation energy for the crystallization of $Bi_{1.5}V_{0.5}Sr_2Ca_2Cu_3O_{x+\delta}$ glass sample

The volume fraction (x) of the $Bi_{1.5}V_{0.5}Sr_2Ca_2Cu_3O_{x+\delta}$ glass sample transformed in crystalline phase during the crystallization event has been obtained from the DSC curves as a function of temperature. The volume fraction of crystallized can be obtained from the DSC curve by using

$$x = \frac{A_x}{A}$$

where A is the total area under the crystallization curve i.e. The area between the temperature at the start of crystallization (T_s) and the end-set temperature (T_f) is completed. A_x is the area at any temperature T between T_s and T_f at which the fractional crystallization is required to be known.

The crystallization mode of the glasses can be identified by using following Ozawa analysis [13].

$$\frac{d\ln[-\ln(1-x)]}{d\ln\beta} = -n$$

where, β is DSC scan rate (K/min), n is the Avrami parameter which indicates a crystallization mode. The variable n values indicate that the nucleation and growth takes place by more than one mechanism (Table 2.)[14].

Table 2. Values of the parameter n for various crystallization mechanisms.

Crystallization Mechanism	***n***
Surface nucleation	1
One-dimensional growth	2
Two-dimensional growth	3
Three-dimensional growth	4

Figure 3. shows the plots of $\ln[-\ln(1-x)]$ vs. $\ln\beta$. From the slopes of this relation, the value of n is found to be 1.3. The calculated value of the order of the crystallization reaction, n, indicates that ($Bi_{1.5}V_{0.5}Sr_2Ca_2Cu_3O_{x+\delta}$) glasses crystallize one-dimensionally.

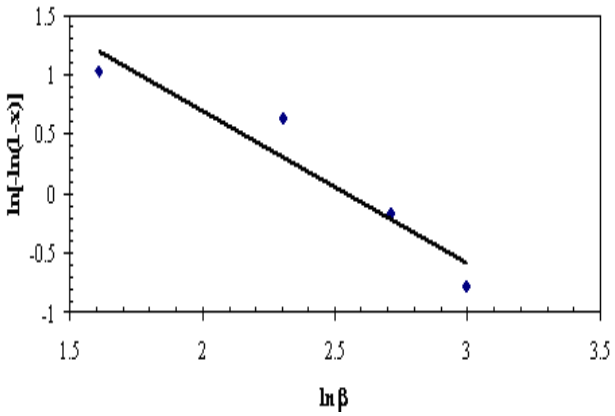

Fig. 3. The plots of $\ln[-\ln(1-x)]$ vs. $\ln\beta$.

IV. CONCLUSION

The crystallization exotherm was assigned to the crystal growth of the pre-existing nuclei, where the number of nuclei changes depending on the thermal history of $Bi_{1.5}V_{0.5}Sr_2Ca_2Cu_3O_{x+\delta}$ glass samples before the crystallization. The activation energy for crystallization found using the modified Kissinger equation is 357kJ/mol. The one-dimensional crystal growth occurs at a constant number of nuclei by interface-controlled mechanism. It is observed that the T_g and T_p values increase with increasing heating rate (from 5 to 20 $K.min^{-1}$).

[1]. *D.C. Sinclair, J.T.S. Irvine and A.R. West*. (1990) Japan. J. Appl. Phys. 29, p. L2002

[2]. *T.W. Huang, N.C. Wu, M. P. Hung, J.W Liou, W.N. Wang, S.E. Hsu, P.C. Yau, M.F. Tai, H.C.Ku and T.S. Chin* (1989) "Reproducibility of T_c in a $Bi_2Sr_2CaCu_2O_8$ superconductor" J. Mater. Sci.242319-23

[3]. *S.S. Oh and K. Osamura* (1991) "Temperature dependence of the phase relation in the Bi-Pb-Sr-Ca-Cu-O superconducting ceramics" Supercond. Sci. Technol. 4 p 239-43

[4]. *T. Komatsu, R. Sato, K. Imai, K. Matsushita and T. Yamashita*: (1988) Jpn. J. Appl. Phys. 27 p.L550

[5]. *K. Nassau, A. Miller, E. Gyorgy and T. Siegrist*. (1989) J. Mater. Res., 46 p. 1330.

[6]. *Y. Oka, N. Yamamoto, H. Kitaguchi, K. Oda and J. Takada.* (1989) Jpn. J. Appl. Phys. 28 2, p. L213.

[7]. *M.R. DeGuire, N.P. Bansal and C.J. Kim*. J. Am. Ceram. Soc. (1990) 75 5, p. 1165.

[8]. *R.M. Ribeiro, R.S. de Biasi, D.R. dos Santos, D.S.dos Santos*. J Alloy Compd (2009) 483 p 495.

[9]. *F. Liu, H.F. Wang, Z. Chen, W. Yang, G.C. Yang*. (2006) Mater Lett; 60, p 3916.

[10]. *G. Fuxi and L.I. Guangming,* "The Physics of Non-Crystalline Solids", (1992) Taylor & Francis, London, p. 406.

[11]. *M.A. Aksan, M.E. Yakinci and Y. Balci*, J. Therm. Anal. Calorim. (2005) 81, p. 417

[12]. *Kissinger, H.E.*, (1956) "Varition of Peak Temperature With Heating Rate in Differential Thermal Analysis", J. Res. Nat. Bur. Stand., 57: (4), p 217-221,.

[13]. *T. Ozawa*, (1965) Bull. Chem. Soc. Jpn., 38 1881.

[14]. *P.W. MCMillan*, (1979) "Glass-ceramics", 2nd Ed., Academic Press, London

STRUCTURAL, OPTICAL AND PHOTOLUMINESCENCE PROPERTIES OF MnS THIN FILMS GROWN ON GLASS AND GaSe SUBSTRATES BY THE CHEMICAL BATH DEPOSITION

G.M. MAMEDOV[a], M. KARABULUT[a], H. ERTAP[a], G. UĞURLU[a], M. K. ÖZTÜRK[b]

[a] *Kafkas University, Faculty of Art and Sciences, Department of Physics, Kars/TURKEY*

[b] *Gazi University, Faculty of Science, Department of Physics, Ankara/TURKEY*

[c] *Hacettepe Üniversitesi Physics Engineering Department, Ankara/TURKEY*

The MnS thin films were grown on glass and layered GaSe crystal substrates by the Chemical Bath Deposition (CBD) method and their properties were investigated. XRD measurements showed that the quasi van der Waals junctions (QvdWJ) were formed at the GaSe-MnS intersection and the structure of MnS films grown on both glass and GaSe substrates was γ-MnS which has a wurtzite like crystal structure with lattice parameters of a= 3,9792 Å, c= 6,4469 Å. AFM images showed that the sizes of MnS layers grown on GaSe increased and packed more orderly. The absorption spectra of the MnS films grown on the glass substrates were observed to be determined by the interband direct transitions. Absorption spectra had a maximum at 2,69 eV and sharply increased with hυ after 2,83 eV. This absorption peak is thought to be related with the excitation of the Frenkel excitons (E_{exc}=2,69 eV) in the transitions of the Mn^{2+} ions. The binding energy of the Frenkel excitons was determined to be approximately 140 meV from these results. The photoluminescence spectrum of MnS-GaSe QvdWJ was found to be related to the emissions characteristic of GaSe and Mn^{2+} ions in MnS.

I. INTRODUCTION

The wide band gap (E_g =2,7-3,9 eV) magnetic semiconductor MnS compound has several application potentials ranging from magneto optics to solar cells and they are generally grown on glass substrates by the Chemical Bath Deposition (CBD) method and their structural, optic and photoluminescence properties were widely investigated [1-4]. Hydrothermal, rf-sputtering and microwave radiation are some of the other methods used to grow MnS thin films [5-7]. MBE is also used to grow MnS on different substrates [8-11]. Magnetic properties such as high magnetoresistans of MnS semiconductor compound makes them proper materials in spintronics applications [1,11-15]. Photoluminescence spectra of MnS thin films show emission peaks related to Mn^{2+} ions [1,8-11]. The effect of MnS compound on the formation of high efficiency radiative cells in the UV region by the inclusion of MnS

in the ordered nanostructured mesoporous of SiO_2 is a remarkable property [16]. In a recent study on the synthesis, optical and morphological properties of MnS/polyvinylcarbozole hybrid composites, it has been reported that MnS nanoparticles were capped with PNVC [17]. The catalytic property of MnS is suitable for the formation of carbon nanotubes [18].

There are three types of MnS compound: α- MnS (rock salt type structure), β- MnS (sphalerite type structure) and γ- MnS (wurtzite type structure). It is observed that the thin films grown by CBD have metastable wurtzite type γ- MnS structure (hexagonal) at lower temperatures [1-11]. The hcp γ- MnS thin films grown on GaAs crystal substrate have been investigated [8-11].

Growth of MnS thin films on layered crystals and investigation of their properties have scientific and practical importance due to the structural compatibility. Hence, the formation of MnS-GaSe junctions on the GaSe crystals substrates that we have grown by Bridgman method and investigated the optical, photoelectric, photoluminescence and non-linear optic properties [19-21] may be more compatible. The wurtzite hexagonal structure of γ- MnS grown on hcp GaSe substrate is proper for the formation of van der Waals junctions [22-24]. Because of the van der Waals bonds between the layers, the (0001) surfaces of the GaSe layers do not have dangling bonds and MnS films grown on these substrates bind via van der Waals bonds. The MnS-GaSe junctions may be important in the spintronics application as ferromagnetic metal-nonmagnetic layered semiconductor Ni / p-GaSe [25].

Since the surface density of states of naturally mirror faced GaSe layer is very low ($\leq 10^{10}$ cm^{-2}) [25,26] the density of states of heterojunctions formed by the MnS-GaSe junctions may have low density of states and sharp transitions.

In the present study, we have formed quasi van der Waals junctions by growing MnS thin films on the layered GaSe crystal substrates by CBD for the first time and investigated the structural, morphologic, optic and photoluminescence properties of these junctions.

II. EXPERIMENTAL

The GaSe substrates were prepared by cleaving layers from the GaSe crystals grown by Bridgman method [19-21] with a razor blade. The thicknesses of the 1cm×3cm substrates were in the 100-500 μm range. No chemical process was applied to these naturally mirror faced GaSe crystals prior to growth process. MnS films were also grown on glass substrates. The glass substrates were cleaned thoroughly before the deposition process. The chemicals used for the preparation of solutions were: manganese acetate ($Mn(CH_3COO)_2$) , tri-ethanolamine, ammonia/ammonium chloride (pH=10.55), tri-sodium citrate, and thioacetamide (CH_3-CS-NH_2). The solutions were prepared in 100 mL beakers with a mixture of 12.5 ml 1M manganese acetate, 2.5 ml 3.75 M tri-ethanolamine, 12.5 ml amomonium/ammonium chloride as a tampon solution, 0.25 ml 0.7 M tri-sodium citrate and 12.5 ml 1M thioacetamide [1-4]. The rest of the beaker was filled with twice-distilled water and mixed well. Afterwards, the solutions were divided into 10 ml beakers and substrates were placed vertically. The deposition

processes on both glass and GaSe substrates were conducted at room temperatures for 24 h periods.

The surface morphology of MnS films grown on glass and GaSe substrates were studied with a Nanosurf Easycan model Atomic Force Microscopy (AFM). The structures of the films were characterized by XRD using a Rigaku D/max-2200 model diffractometer. The optical absorption spectra of MnS films were recorded with a PG Instruments T60 UV/VIS spectrophotometer. The photoluminescence measurements of MnS films grown on both substrates were conducted at different temperatures using a system consisting of a Jobin Yvon Triax 550 monochromator and a 200N type creostat.

III. RESULTS AND DISCUSSIONS

The XRD patterns of MnS thin films grown on both glass and GaSe substrates at room temperature are given in Fig. 1. The XRD pattern of GaSe substrate is also included in Figure 1 for comparison. The structure of MnS films grown on glass substrate was determined to be hcp γ-MnS belonging to P63mc space group wit lattice constants a = 3,97922 Å ve c = 6,4469 Å. This result is consistent with the literature as the crystal structure of MnS films grown on glass substrates at low temperatures by CBD usually was γ-MnS [1-4]. From the analysis of the XRD data given in Figure 2, it is found that the crystal structure of MnS films deposited on GaSe crystalline is also hcp γ-MnS belonging to P63mc space group with lattice constants a = 3,97922 Å and c = 6,4469 Å which is the same phase that crystallized on glass substrate.

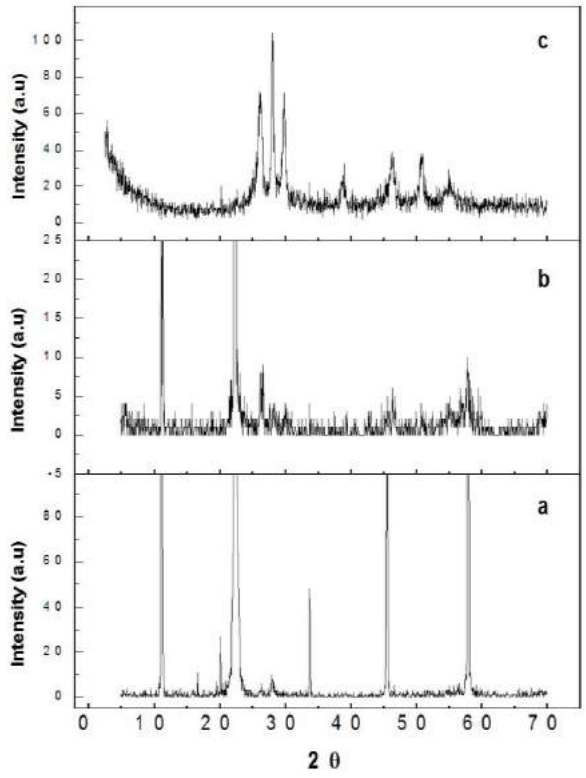

Fig.1. The XRD spectra of **a)** GaSe substrate, **b)** MnS film grown on GaSe substrate, **c)** MnS film grown on glass substrate.

The surface morphology of the MnS films grown on both glass and GaSe substrates was investigated by AFM. Fig. 2 shows the AFM image of a MnS film grown on glass substrate. It is seen that the MnS film grows as crystalline layers. The AFM image of MnS film grown on naturally mirror faced layered GaSe crystal for the first time in this study is given in Fig. 3. From this image, it is clearly observed that the sizes of layered crystalline MnS layers increased compared to that of MnS films deposited on glass substrates. It is also seen that the crystalline layers are more ordered in the MnS films grown on GaSe substrate.

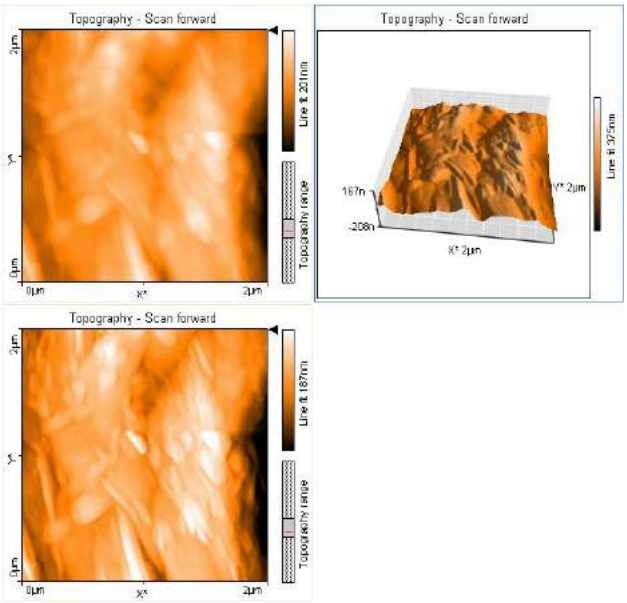

Fig.2. The AFM image of MnS films grown on glass substrate.

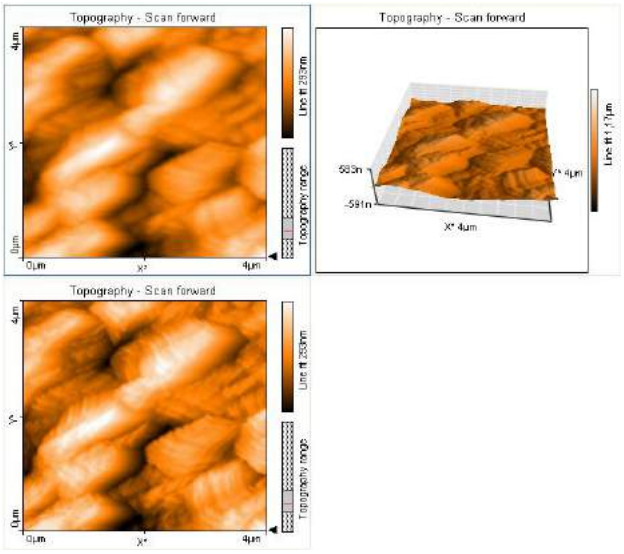

Fig.3. The AFM image of MnS thin film grown on crystalline GaSe substrate.

From the analysis of the AFM images, it is found that the widths of these crystalline MnS layers are approximately 1-3 μm.

The analysis of the XRD data showed that these crystalline layers consist of nanoparticles of different sizes. From the Debye-Sherer analysis of XRD data, the sizes of the nanoparticles of MnS films grown on glass

substrate was determined to be 34-60 nm while the nanoparticles in the layers of MnS films grown on GaSe substrate were shown to have much bigger sizes, 500-900 nm. When we evaluate the results of XRD and AFM data together, it is clearly seen that the size and order of crystalline MnS films grown on GaSe crystalline substrates increased compared to the MnS films grown on glass substrates.

At the beginning of this study, it was expected that the MnS films deposited on layered GaSe crystal would form a van der Waals heterojunction by repeating one of the polytypes of GaSe. There are four polytypes of GaSe and the lattice parameters of these polytypes are: a = 3,755 Å, c = 15,95 Å for ε-GaSe, a = 3,75Å, c = 15,94 Å for β-GaSe, a = 3,74 Å, c = 23,86 Å for γ-GaSe; a = 3,75 Å, c = 31,989Å for δ-GaSe [27]. Clearly the lattice parameters and the space group of MnS film grown on GaSe substrate are different from the lattice parameters of any of the polytpes of GaSe crystal. The crystal structures of MnS films grown at low temperature on both glass and GaSe substrates by CBD are wurtzite type γ-MnS. Even though the structures of MnS and GaSe are compatible, because of the difference between the crystal structures of MnS film and the GaSe substrate heterojunction is not formed. Hence, only the quasi van der Waals junction (QvdWJ) can form at the MnS-GaSe intersection.

The optic absorption spectrum of MnS thin films grown on glass substrate is shown in Fig. 4. As seen from the figure, absorption varies linearly with incident photon energy as $(\alpha h\upsilon)^2 \sim (h\upsilon)$.

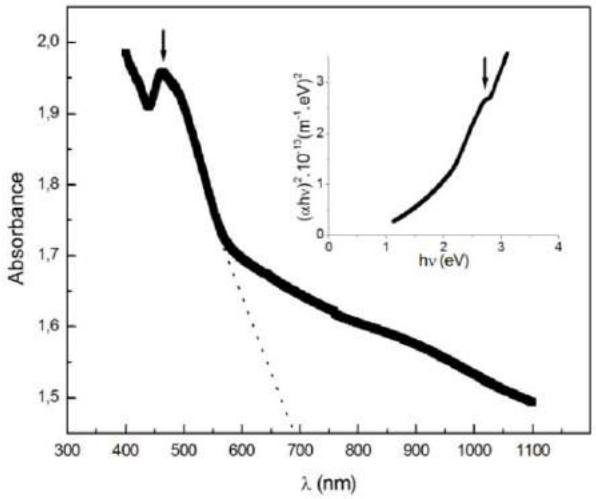

Fig.4. The optic absorption spectrum of MnS film grown on glass substrate.

Absorption tail starts at 1,1 eV. The spectrum consist of a linear region starting at 1,89 eV and after showing a maximum at 2,69 eV it continues with a sharp increase starting at 2,83 eV. From the spectrum, the band gap energy is estimated as E_g=2,83 eV. The band gap energies of MnS thin films were reported to be in the 2,7-3,3 eV range [11]. The band gap value found in the present study is consistent with these values. One of the reasons of this broad range of band gap values of MnS thin films may be the quantum confinement effect (QCE) due to the different sizes of nanoparticles constituting the MnS films [28].The absorption peak observed at hυ =2,69 eV is thought to be related with the excitation of Frenkel type excitons of Mn^{2+} ions characteristic of MnS [1,7-9,12,13]. The band observed at 1,89 eV has been attributed to Mn^{2+} ion pairs [1,8].

We have investigated the photoluminescence (PL) properties of MnS-GaSe QvdWJ. The PL spectra of MnS film grown on GaSe and bulk GaSe are given in Fig. 5.

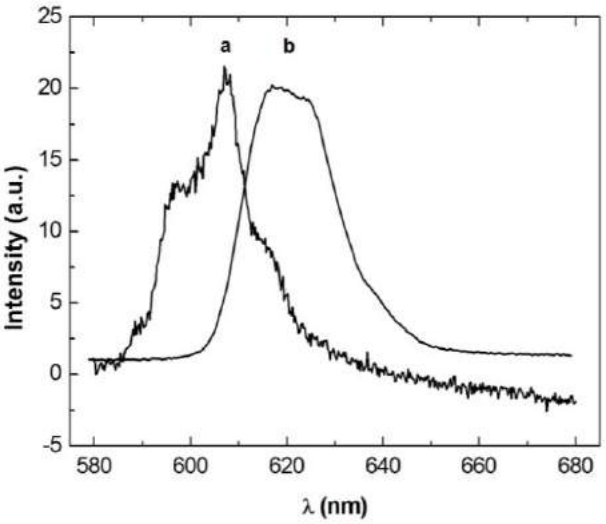

Fig.5. The PL spectra of **a)** GaSe face of MnS-GaSe junction and **b)** MnS thin film deposited face. The PL measurements were conducted at 50 K.

The bulk GaSe PL spectrum was collected from one of the faces of the sample not containing MnS while the PL spectrum of MnS-GaSe was collected from the MnS deposited face of the same sample. The PL spectrum of bulk GaSe consists of peaks at 590, 597, 607 and 617 nm. This is consistent with the PL spectra reported previously [20,29]. The PL spectrum of MnS-GaSe shifted to longer wavelengths compared to the bulk spectrum. This spectrum consists of a broad band centered at approximately 620 nm which includes two peaks at 617 and 624 nm. The peak at 617 nm is thought to be a combination of GaSe and MnS related emissions while the peak observed at longer wavelength (624 nm) is due to the Mn^{2+} ion pairs [8].

IV. CONCLUSIONS

MnS thin films were grown on GaSe crystal substrate by CBD for the first time. From the XRD and AFM results, it is found that MnS grew as crystalline γ-MnS on both glass and GaSe substrates. The quasi van der Waals MnS-GaSe junction was formed at the MnS-GaSe intersection. MnS films grew as layered crystallites and the sizes and order of these crystalline layers increased for the films grown on GaSe substrate compared to the glass substrate. The absorption peak observed at hυ =2,69 eV is thought to be related with the excitation of Frenkel type excitons of Mn^{2+} ions characteristic of MnS. The PL spectrum of MnS films grown on GaSe showed a broad peak consisting of two peaks at 617 and 624 nm which are related to GaSe and Mn^{2+} ions in MnS.

[1]. *D.B.Fan,Xiao Dong Yong,Hao Wang,Yong Cai Zhang,Hui Yan*, Physica B, 337 (2003) 165.

[2]. *D.B. Fan, Hao Wang, Yong Cai Zhang, Jie Cheng, Bo Wang,Hui Yan*, Mater. Chem. and Phys., 80 (2003) 44.

[3]. *C. Gümüş, C.Ulutaş, Y.Ufuktepe*, Opt. Mater. 29 (2007) 1183.

[4]. *C.D. Lokhande, A.Ennaoui, P.S. Patil, M.Giersing, M.Muller, K. Diesner, H. Tributsch*, Thin Solid Films 330 (1998) 70.

[5]. *Y.Zhang, H. Wang, B. Wang, H. Yan, M. Yoshimura*, J. Cryst. Growth, 243 (2002) 214.

[6]. *I. Oidor-Juarez, P. Garcia-Jimenez, G. Torres-Delgado, R. Castadeno-Perez, O. Jimenez,-Sandoval, B. Chao, S. Jimenez-Sandoval*, Mater. Res. Bull. 37 (2002) 1749.

[7]. *S. Wang, K. Li, R.Zhai, H.Wang,Y. Hou*, Mater. Chem. and Phys. 9 (2005) 298.

[8]. *M.Okajima, T.Tohda*, J. of Cryst. Growth, 117 (1992) 810.

[9]. *L. Wang, S.Sivananthan, R. Sporken, R.Caudano*, Phys.Rev. B54 (1996) 2718.

[10]. *L.David, C.Bradford, X.Tang, T.C.M.Graham, K.A.Prior, B.C.Cavenett*, J. of Cryst. Growth, 251 (2003) 591.

[11]. *Y.M.Yu, D.J.Kim, Y.D.Choi, C.S.Kim*, Appl. Surface Science, 253 (2007) 3521.

[12]. *S. S. Aplesnin, L. I. Ryabinkina, G.M Abramova, O.B Romanova, N.I Kiselev and A.F Bovina*, FTT 46 (2004) 2000.

[13]. *G.A. Petrakovski, L.İ., Ryabinkina, G.M.Abramova, N.İ. Kiselev, A.D. Balayev, D.A. Balayev, A.F. Bovina*, Lett. JETP 72 (2000) 99.

[14]. *I. Zutic, J. Fabian, S. Das Sarma*, Rev. Modern Phys. 76 (2004) 323.

[15]. *A.V. Vedyaev*, Prog. Phys. Sci. 172 (2002) 14.

[16]. *L.Barry M.Copley, J.D.Holmes, D.J.Otway, O.Kazakova, M.A.Morris*, J. Solid State Chemistry, 180 (2007) 3443.

[17]. *N. Moloto, N. J.Coville, S.S.Ray, M .J.Moloto*, Physica B, 404 (2009) 4461.

[18]. *L.Barry, J.Tobin, M.Copley, J.D.Holmes, D.J.Otway, M.A.Morris*, Appl. Catalysis, A: General, 341 (2008) 8.

[19]. *G.M. Mamedov, M. Karabulut, O. Kodolbaş, Ö. Öktü*, Phys.Stat. Sol. B, 242 (2005) 2885.

[20]. *M. Karabulut, G. Bilir, G.M. Mamedov, A.Seyhan, R.Turan*, J. Lumin. 128 (2008) 1551.

[21]. *M. Yüksek, A. Elmalı, M. Karabulut, G.M.Mamedov*, Appl. Phys. B: Lasers Opt. 98 (2010) 77.

[22]. *A. Koma*, J. of Cryst. Growth 201/202 (1999) 236-241.

[23]. *S.R.Forrest, P.E.Burrows*, Supramolecular Science 4 (1997) 127.

[24]. *S.Yang, H.Wang, W.Fu, D.F.Kelley*, J.Photochemistry and Photobiology A:Chemistry 192 (2007) 159.

[25]. *A.P. Bakhtinov, V.N. Vodopyanov, Z..D.Kovalyuk,, V.V. Netyaga, O.S. Lytvyn*, Fizika Teknika Poluprovodnikov,(FTP) 44 (2010) 180.

[26]. *T.C. Terhell, R.M.Lieth* Phys. stat, sol. (A), 10 (1982) 529.

[27]. *A. Guskov, J. Camassel, L. Guskov*, Prog. Crystal Growth and Charact., 5 (1982) 323.

[28]. *A. Cortes, H. Gomez, R.E. Marotti, G. Riveros, E.A. Dalchiele*, Sol. Energy Mat. And Solar Cells, 82, (2004) 21.

[29]. *V. Capozzi, M. Montagna*, Phys. Rev. B 40 (1989) 382.

FIRST PRINCIPLES CALCULATIONS ON THE MAl (M=Cr, Mo) COMPUNDS: ELASTIC AND DYNAMICAL PROPERTIES

H.B. OZISIK[1,2], K. COLAKOGLU[1], H. OZISIK[2]

[1]*Gazi University, Department Of Physics, Teknikokullar, 06500, Ankara, TURKEY*

[2]*Aksaray University, Department Of Physics, 68100, Aksaray, TURKEY*

The first-principles calculations based on the density-functional theory have been performed using the generalized–gradient approximation (GGA) to investigate the many physical properties of CrAl and MoAl compounds. The calculated structural parameters, elastic properties and phonon dispersion curves are presented and compared with the available other theoretical data.

I. INTRODUCTION

The most of the technologically important I-III compounds are crystallized in B32 [1] phase. The physics and chemistry of these intermetallic compounds have attracted intensive interest due to the their bound properties [2-4], low metallic conductivity [5], lattice defect [5, 6], dissolve in ammonia and amine [7], low paramagnetism and diamagnetism [8, 9].

Maiti [10] has synthesized molybdenum aluminide and studied characterization of molybdenum aluminide. Auchet [11] have studied the effect of transition metal impurities Ti, V and Cr on the electrical resistivity and the thermoelectric power of liquid Al. Cupid [12], Raghavan [13] and Gonzales-Ormen˜o [14] have investigated phase diagram. Faraoun [15] studied the elastic properties of CrAl in B2 structure. Ouyang [16] calculated the bond length, harmonic vibrational frequency, and dissociation energy of MoAl. Nguyen-Manh [17] predicted the B32 phase is the most stable one for CrAl, MoAl compounds with space group Fd-3m (227). In this phase, the Cr and Mo atoms are positioned at 8a (1/8, 1/8, 1/8), Al atoms are positioned at 8b (3/8, 3/8, 3/8).

II. METHOD OF CALCULATION

Our calculations have been performed using the augmented plane-wave pseudopotential approach to the density functional theory (DFT) implemented in Vienna Ab-initio Simulation Package (VASP) [18-21]. For the exchange and correlation terms in the electron- electron interaction, Perdew-Burke-Ernzerhof (PBE) [22] was used within generalized gradient approximation (GGA). The valence electronic wave functions expanded in the plane wave basis set up to a kinetic-energy cutoff of 450 eV. The k-points are sampled according to the Monkhorst-Pack scheme [21] which yields 13x13x13 k-points in the irreducible edge of Brillouin zone.

III. RESULTS AND DISCUSSION

Structural properties

Firstly, the equilibrium lattice parameter has been calculated by minimizing the crystal total energy by means of Murnaghan's equation of state (eos) [23], and the obtained results are displayed in Fig. 1. The bulk modulus, and its pressure derivative have also been estimated based on the same Murnaghan's equation of state, and the results are listed in Table 1 along with the other theoretical data. The present values of lattice parameters for B32 phase of CrAl and MoAl are found to be 5.887 $\mathring{A}$ and 6.216 $\mathring{A}$, respectively. The bulk modulus is a fundamental physical property of solids and can also be used as a measure of the average bond strengths of atoms of the given crystals [24]. Our values of bulk modulus in Table 1 are in reasonable agreement with the other theoretical data of Nguyen-Manh [17].

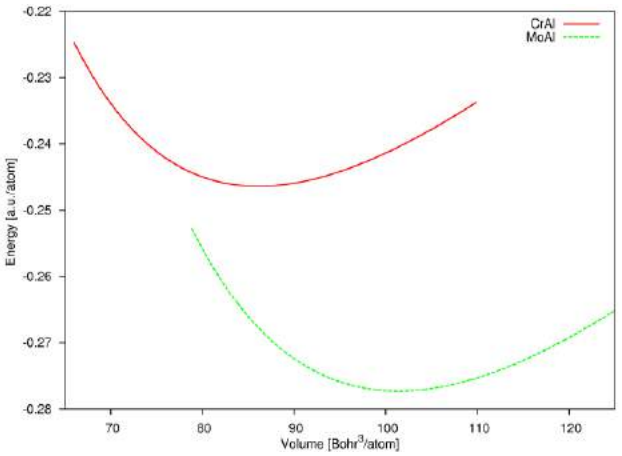

Fig. 1. The Energy-Volume curves of CrAl and MoAl in B32 structure.

Table 1. The calculated lattice constants a_0, bulk modulus B_0 and its pressure derivative B' for CrAl and MoAl in B32 structure

	a_0 (Å)	B_0 (GPa)	B'
CrAl	5.8865	173.8 189[17]	4.09
MoAl	6.21583 6.25[14]	184.3 175 [17]	4.13

Elastic properties

The elastic constants of solids provide a link between the mechanical and dynamical behaviors of crystals, and give important information concerning the nature of the forces operating in solids. Here, the elastic constants are calculated by using the stress-strain relations [25], and the results are given in Table 2. The traditional mechanical stability conditions in cubic crystals on the elastic constants are known as $C_{11}–C_{12}>0$, $C_{11}>0$, $C_{44}>0$, $C_{11}+2C_{12}>0$, and $C_{12}<B<C_{11}$. Our elastic constants in Table 2 satisfy these stability conditions, and hence we can say that CrAl and MoAl are elastically stable in B32 phase.

Table 2. Elastic constants (in GPa), isotropic shear modulus (G), Poisson ratio (υ), Zener anisotropy factor (*A*), and Young's modulus (*Y*) for CrAl and MoAl in B32 structure.

	C11	C12	C44	G	A	Y	υ
CrAl	218.7	151.4	141.3	80.0	4.2	208.0	0.30
MoAl	214.0	176.0	118.7	58.5	6.2	159.0	0.35

From the calculated elastic moduli, we derived other important mechanical properties (see Table 2), such as Zener anisotropy factor *A*, Poisson ratio υ, Young's modulus *Y*, using the following relations [26]:

$$A = \frac{2C_{44}}{C_{11} - C_{12}},$$

$$\upsilon = \frac{1}{2}\left[\frac{(B - \frac{2}{3}G)}{(B + \frac{1}{3}G)}\right],$$

and

$$Y = \frac{9GB}{G + 3B}$$

where $G = (G_V + G_R)/2$ is the isotropic shear modulus, G_V is Voigt's shear modulus corresponding to the upper bound of G values, and G_R is Reuss's shear modulus corresponding to the lower bound of G values for polycrystalline materials, and can be written as $G_V = (C_{11}–C_{12} +3C_{44})/5$, and $5/G_R = 4/(C_{11}-C_{12})+ 3/ C_{44}$.

The Zener anisotropy factor (*A*) is an indicator of the degree of anisotropy in the solid structures. The present value of *A* for CrAl and MoAl are found to be 4.2 and 6.2, respectively, and the large value of *A* implies that these materials have the strong anisotropic character. In this context, the MoAl is, relatively, more anisotropic than CrAl.

The Poisson's ratio is about υ=0.25 for ionic materials [27]. In the present case the υ values are 0.30, 0.35 for CrAl and MoAl, respectively. Therefore, one can say that the ionic contributions to the atomic bonding are rather high for these compounds. Isotropic shear modulus is a better predictor of hardness than the bulk modulus. The calculated isotropic shear modulus is 80.0, 58.5 GPa for CrAl and MoAl, respectively.

We have estimated the Debye temperature (Θ_D), which represents the effective cutoff frequency of the material, by using the calculated elastic constant data, in terms of the following common relations [28]:

$$\theta_D = \frac{h}{k}\left[\frac{3n}{4\pi}\left(\frac{N_A\rho}{M}\right)\right]^{13} \upsilon_m$$

where v_m is the average wave velocity, and is approximately given by

$$\upsilon_m = \left[\frac{1}{3}\left(\frac{2}{\upsilon_t^3} + \frac{1}{\upsilon_l^3}\right)\right]^{-13}$$

and

$$\upsilon_l = \sqrt{\frac{3B + 4G}{3\rho}}$$

where v_l and v_t, are the longitudinal and transverse elastic wave velocities, respectively, which are obtained from Navier's equations [29]:

$$\upsilon_t = \sqrt{\frac{G}{\rho}}$$

The calculated average longitudinal and transverse elastic wave velocities, Debye temperature for CrAl and MoAl are given in Table 3.

Table 3. The longitudinal, transverse, average elastic wave velocities, and Debye temperature for CrAl and MoAl in B32 structure.

	v_l	v_t	v_m	Θ_D
CrAl	7384	3943	4405	561.3
MoAl	6262	2933	3302	398.5

Phonon dispersion curves

The present phonon frequencies of CrAl and MoAl compounds in B32 phase are calculated using a 2x2x2 supercell by the PHONON code [30] uses the "Direct Method" [31]. The obtained results are illustrated in Fig. 2 and Fig. 3 for CrAl and MoAl, respectively. The maximum values of the phonon frequencies for optical branches slightly decrease on going from Mo to Cr atom, and a clear gap between the acoustic and optic branches is not observed for these compounds. The right side of the phonon curves show the related total and partial density of phonon states for each compound. One can see that the main contribution to acoustic modes of phonons comes from the Cr and Al for CrAl structure, but for MoAl, the contribution from the Al is dominant. Unfortunately, there is no experimental or other theoretical data on the lattice dynamics of these compounds for the comparison with the present data.

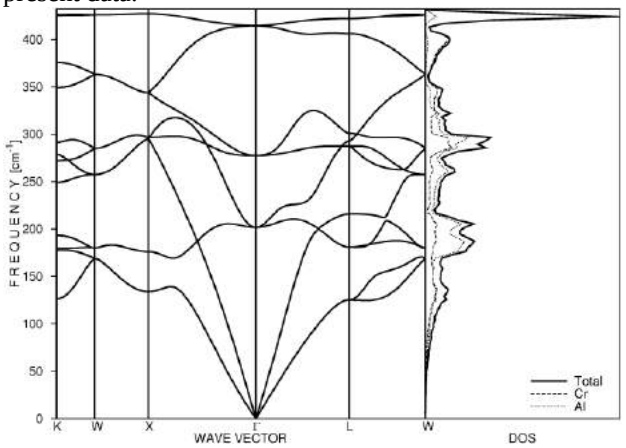

Fig. 2. The calculated phonon dispersions and total and partial density of states for CrAl in B32 structure

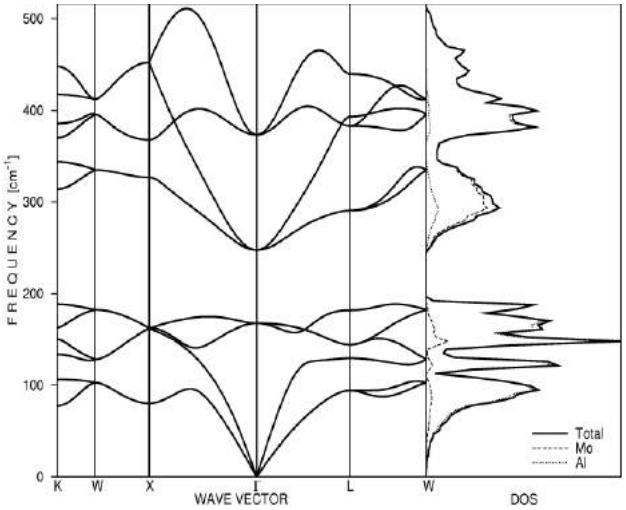

Fig. 3. The calculated phonon dispersions and total and partial density of states for MoAl in B32 structure

IV. SUMMARY AND CONCLUSION

The first–principles total energy calculations have been performed on the structural, mechanical, and vibrational properties for CrAl and MoAl. The calculated lattice constant is in excellent agreement with the experimental and other theoretical values. The elastic constants satisfy the traditional stability conditions. Beside the other contributions, the mechanical and vibrational results, which are not considered previously, are the original aspects of the present calculations. At present, our results serve as a reliable reference to the further experimental and theoretical investigations.

ACKNOWLEDGEMENT

This work is supported by Gazi University Research-Project Unit under Project No. 05/2009-55

[1]. *E. Zintl and G. Brauer,* Metals and Alloys. X. The valence electron rule and the atomic radius of non-noble metals in alloys, Z. Phys. Chem. B 20 (1933) 245.

[2]. *H. Schäfer, B. Eisenmann and W. Muller*, Zintl Phases: Transitions between Metallic and Ionic Bonding, Angew. Chem. Int. Ed. Engl. 12 (1973) 694.

[3]. *P.C. Schmidt*, The Chemical Bond in the Intermetallic B32-Type Compounds LiMe (Me=Al, Zn, Ga, Cd and In), Z. Naturforsch A 40 (1985) 335–346.

[4]. *S. Kauzlarich (Ed.)*, Chemistry, Structure, and Bonding of Zintl Phases and Ions, VCH Publishers, New York, 1996.

[5]. *K. Kishio, J.O. Brittain*, Defect structure of β-LiAl, J. Phys. Chem. Solids 40 (1979) 933.

[6]. *R. Wilhite, N. Karnezos, P. Cristea, J.O. Brittain*, Li^7 self diffusion in LiAl—An NMR study, J. Phys. Chem. Solids 37 (1976) 1073.

[7]. *A.J. Downs*, Chemistry of aluminium, gallium, indium, and thallium, Chapman&Hall, London, 1993, pp. 218.

[8]. *Y.L. Yao*, The Magnetic Susceptibility of Some Equi-Atomic Lithium Alloys, Trans. Metall. Soc. AIME 230 (1964) 1725.

[9]. *V.W. Klemm, H. Fricke*, Uber das magnetische Verhalten der intermetallischen Phasen vom NaTl-Typ, Zeitschrift Fur Anorganische Und Allgemeine Chemie 282 (1955) 162-8.

[10]. *R. Maiti, M. Chakraborty*, Synthesis and characterization of molybdenum aluminide nanoparticles reinforced aluminium matrix composites, J. .Alloys and Comp. 458 (2008) 450–456.

[11]. *J. Auchet, P. Terzieff*, The effect of Ti, V and Cr impurities on the transport properties of liquid aluminium,J. Alloys and Comp. 261 (1997) 295-298.

[12]. *D.M. Cupid, O. Fabrichnaya , F. Ebrahimi , H.J.Seifert*,Thermodynamic assessment of the Al-Mo system and of the Ti-Al-Mo System from 0 to 20 at.% Ti,Intermetallics 18 (2010) 1185-1196.

[13]. *V. Raghavan*, Al-Fe-Mo (Aluminum-Iron-Molybdenum), Journal of Phase Equilibria and Diffusion Vol. 30(4)(2009)372-374.

[14]. *P.G. Gonzales-Ormen˜o, H.M. Petrilli, C.G.Schön*, Ab initio calculation of the bcc Mo–Al (molybdenum–aluminium) phase diagram: Implicationsfor the nature of the ζ2-MoAl phase, Scripta Materialia 53 (2005) 751–756.

[15]. *H.Faraoun, H.Aourag, C.Esling, J.L. Seichepine*, C. Coddet,Elastic properties of binary NiAl, NiCr and AlCr and ternary Ni2AlCr alloys from molecular dynamic and Abinitio simulation, Computational Materials Science 33 (2005) 184–191.

[16]. *Y. Ouyang, J. Wang,Y. Hou, X. Zhong, Y. Du, Y.Feng*,First principle study of AlX (X=3d,4d,5d elements and Lu) dimer,The Journal of Chemical Physics 128(2008) 074305

[17]. *D. Nguyen-Manh, D.G. Pettifor*,Electronic structure, phase stability and elastic moduli of AB transition metal aluminides,Intermetallics 7 (1999) 1095-1106.

[18]. *G. Kresse, J. Hafner*, Ab initio molecular dynamics for liquid metals, Phys. Rev. B 47 (1993) 558.

[19]. *G. Kresse, J. Furthmüller*, Efficiency of ab-initio total energy calculations for metals and semiconductors using a plane-wave basis set, Comput. Mat. Sci. 6 (1996) 15.

[20]. *G. Kresse, J. Furthmüller*, Efficient iterative schemes for ab initio total-energy calculations using a plane-wave basis set, Phys. Rev. B 54 (1996) 11169.

[21]. *H.J. Monkhorst, J.D. Pack*, Special points for Brillouin-zone integrations, Phys. Rev. B 13 (1976) 5188-5192.

[22]. *J.P. Perdew, S. Burke, M. Ernzerhof*, Generalized Gradient Approximation Made Simple, Phys. Rev. Lett. 77 (1996) 3865.

[23]. *F.D. Murnaghan*, Finite Deformations of an Elastic Solid, Am. J. Math. 59 (1937) 235-260.

[24]. *A.A. Maradudin, E.W. Montroll, G.H. Weiss and I.P. Ipatova*, Theory of lattice dynamics in the harmonic approximation,Second Ed., Academic Pr., New York London, 1971.

[25]. *Y. L. Page and P. Saxe*, Symmetry-general least-squares extraction of elastic data for strained materials from ab initio calculations of stress, Phys. Rev. B 65 (2002) 104104.

[26]. *B. Mayer, H. Anton, E. Bott, M. Methfessel, J. Sticht, P.C. Schmidt*, Ab-initio calculation of the elastic constants and thermal expansion coefficients of Laves phases, Intermetallics 11 (2003) 23-32.

[27]. *R.A. Johnson*, Analytic nearest-neighbor model for fcc metals, Phys. Rev. B 37 (1988) 3924.

[28]. *L.Johnston, G.Keeler, R.Rollins, and S.Spicklemire*, Solid State Physics Simulations, The Consortium for Upper-Level Physics Software, Jhon Wiley, New York, 1996.

[29]. *E. Schreiber, O.L. Anderson, N. Soga*, Elastic Constants and their Measurements, McGraw-Hill, New York, 1973.

[30]. *K. Parlinski*, Software PHONON (2003), and references therein.

[31]. *K. Parlinski, Z.Q. Li, and Y. Kawazoe*, First-Principles Determination of the Soft Mode in Cubic ZrO2, Phys. Rev. Lett. 78 (1997) 4063-4066.

GROUND STATE ELECTRONIC CONFIGURATION OF HALF-HEUSLER Li-Al-Si COMPOUNDS: PHONON INSTABILITY AND ELASTIC PROPERTIES

H.B. OZISIK[1,2], K. COLAKOGLU[1], H. OZISIK[2]

[1]Gazi University, Department of Physics, Teknikokullar, 06500, Ankara, TURKEY, havva.bogaz@gazi.edu.tr

[2]Aksaray University, Department Of Physics, 68100, Aksaray, TURKEY, hacioz@aksaray.edu.tr

In this study we present the results of our calculations on the different atomic arrangement of LiAlSi compounds by performing ab initio total energy calculations within the generalized gradient approximation (GGA) in VASP package. Specifically, the structural, electronic, elastic and phonon dispersion are calculated and compared with the available experimental and other theoretical data.

I. INTRODUCTION

Heusler compounds are important for spintronic applications [1]. Many Half Heuslar compounds, which have a small band gap are important thermoelectric applications [2-6]. LiAlSi compounds takes places between Half Heuslar compounds.

Theoretically, Christensen [7, 8], Pawloska [9], Hem [10], Frederick [11] have studied the structural phase stability, bonding properties and electronic structure. Joachim [12] has investigated lattice structure, thermoelectric properties and temperature stability using X-ray powder diffraction, differential thermal analysis (DTA) and thermal gravimetry. Gröbner [13] and Kevorkow [14] have measured lattice structure, melting temperature and thermodynamic calculation using x-ray, DTA, SEM/EDX. Tillard [15] has studied energetic stabilities and electronic structure, bond populations using x-ray and DFT. To our best knowledge, no other theoretical data based on the first-principles calculations of the mechanical and vibrational properties are available to date. This paper is presented with the main aim to investigate these properties of LiAlSi compounds.

Half Heuslar LiAlSi compounds are crystallized in $C1_b$ structure type with space group 216. We have computed the many physical properties for this compound for different atomic arrangement (table 1).

Table1. Different atomic arrangement of LiAlSi compounds.

Arrangement	4a (000)	4b (1/2 1/2 1/2)	4c (1/4 1/4 1/4)	4d(3/4 3/4 3/4)
I	-	Si	Al	Li
II	-	Al	Si	Li
III	-	Li	Al	Si

II. METHOD OF CALCULATION

All calculations presented here were carried out using the Vienna Ab-initio Simulation Package (VASP) [16-19] based on the density functional theory (DFT). For the exchange and correlation terms in the electron-electron interaction, Perdew-Burke-Ernzerhof (PBE) [20] was used within generalized gradient approximation (GGA). The valence electronic wave functions expanded in the plane wave basis set up to a kinetic-energy cutoff of 306 eV. The k-points are sampled according to the Monkhorst-Pack scheme [19] which yields 11x11x11 k-points in the irreducible edge of Brillouin zone.

III. RESULTS AND DISCUSSION

Structural, Electronic Properties

Firstly, the equilibrium lattice parameter has been calculated by minimizing the crystal total energy by means of Murnaghan's equation of state (eos) [21] for different arrangement, and the obtained results are displayed in Fig. 1. The bulk modulus, and its pressure derivative have also been estimated based on the same Murnaghan's equation of state, and the results are listed in Table 2 along with the experimental and other theoretical data.

Our results for bulk moduli and lattice constant are in consistent with the other works [7, 8, 10, 12, 14, 15].

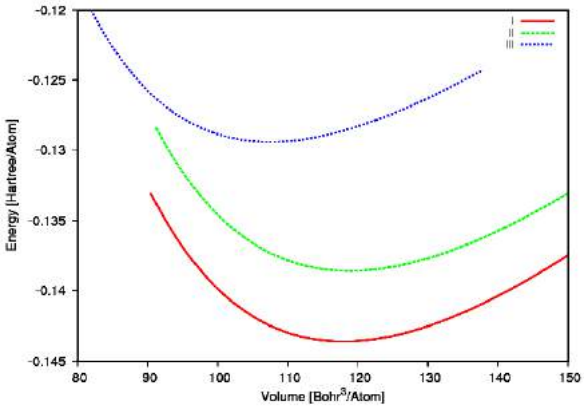

Fig. 1. The Energy-Volume curves of LiAlSi compounds.

Table 2. The calculated lattice constants a_0, bulk modulus B_0 and its pressure derivative B', and band gap for Arrangement I, II, III.

	a_0 (Å)	B_0 (GPa)	B'	Eg (eV)
I	5.93671 5.928[15] 5.932[7,8] 5.922[12] 5.937[10] 5.930[10] 5.9282[14]	60.93 63.02 62.8	4.0	0.11 0.1 0.45
II	5.95166 5.9577[15] 6.341[7,8]	58.2 60.82	4.1	0.51
III	5.75804 5.7626 [15] 5.430[7, 8]	53.96 55.98	4.4	0

The calculated band gap of Li-Al-Si compound is given Table 1. The arrangement I and II posses narrow band gap (0.11 eV and 0.51 eV, respectively) and have semiconductor nature, but for arrangement III no band gap exists and it shows metallic character.

Elastic Properties

The elastic constants are calculated by using the stress-strain relations [22], and the results are given in Table 2. The traditional mechanical stability conditions in cubic crystals on the elastic constants are known as $C_{11}–C_{12} > 0$, $C_{11}>0$, $C_{44}>0$, $C_{11}+2C_{12}>0$, and $C_{12}< B<C_{11}$. The present elastic constants, in Table 2, satisfy these stability conditions, except arrangement III, and hence one can say that the arrangement I and II are elastically stable. From the calculated elastic moduli, we derived the other important mechanical properties (see Table 2), such as Zener anisotropy factor A, Poisson ratio, Young's modulus Y, based on the following relations [23]:

$$A = \frac{2C_{44}}{C_{11} - C_{12}};\ \upsilon = \frac{1}{2}\left[\frac{(B - \frac{2}{3}G)}{(B + \frac{1}{3}G)}\right];\ Y = \frac{9GB}{G + 3B}$$

where $G = (G_V + G_R)/2$ is the isotropic shear modulus, G_V is Voigt's shear modulus corresponding to the upper bound of G values, and G_R is Reuss's shear modulus corresponding to the lower bound of G values, and can be written as $G_V = (C_{11}–C_{12} +3C_{44})/5$, and $5/G_R = 4/(C_{11}-C_{12})+ 3/ C_{44}$.

I and II compounds have elastically anisotropic character (Table 3). The present A value is found to be 1.376 and 2.687, respectively, and the arrangement II is more anisotropic than I.

The Poisson's ratio is small (0.1) for covalent materials, and it has a typical value 0.25 for ionic materials [24]. In the present case the values are 0.144, 0.178 for I and II, respectively. Therefore, we can say that the covalent contributions to the atomic bonding are rather high for I.

Table 3. Elastic constants (C_{ij}), isotropic shear modulus (G), Zener anisotropy factor (*A*), Young's modulus (*Y*), Poisson ratio ($_v$), longitudinal v_l , transverse, average elastic wave velocities, and Debye temperature and for arrangement I, II, III

	I	II	III
C_{11}	128.0	96.8	30.3
C_{12}	30.8	42.1	68.4
C_{44}	66.9	73.5	58.3
G	58.8	49.4	-
A	1.376	2.687	-
Y	134.6	116.4	-
ν	0.144	0.178	-
$\upsilon_l(m/s)$	8478	8033	-
$\upsilon_t(m/s)$	5463	5026	-
$\upsilon_m(m/s)$	5997	5536	-
$\theta_D(K)$	688.4	633.9	-

It is known that the bulk modulus is a measure of resistance to volume change by applied pressure, whereas the shear modulus is a measure of resistance to reversible deformations upon shear stress [25]. Therefore, the isotropic shear modulus is a better predictor of hardness than the bulk modulus. The calculated isotropic shear modulus is 58.8, 49.4 GPa for I and II, respectively.

We have estimated the Debye temperature (Θ_D), which represents the effective cutoff frequency of the material by using the calculated elastic constant data, in terms of the following common relations [26]:

$$\theta_D = \frac{h}{k}\left[\frac{3n}{4\pi}\left(\frac{N_A\rho}{M}\right)\right]^{13} \upsilon_m$$

where v_m is the average wave velocity, and is approximately given by

$$\upsilon_m = \left[\frac{1}{3}\left(\frac{2}{\upsilon_t^3} + \frac{1}{\upsilon_l^3}\right)\right]^{-13}$$

and

$$\upsilon_l = \sqrt{\frac{3B + 4G}{3\rho}}$$

where v_l and v_t, are the longitudinal and transverse elastic wave velocities, respectively, which are obtained from Navier's equations [27]:

$$\upsilon_t = \sqrt{\frac{G}{\rho}}$$

The calculated average longitudinal and transverse elastic wave velocities, Debye temperature for I and II are given in Table 2. Unfortunately, no other theoretically and experimentally data are exist for comparison.

Phonon Dispersion Curves

The present phonon frequencies of Li-Al-Si compounds re calculated using a 2x2x2 supercell by the PHONON code [28] uses the "Direct Method" [29] . The obtained results are illustrated in Fig. 2, 3, 4 for arrangement I, II and III, respectively. It is seen from Fig. 2, 3, 4 the arrangements I, II are dynamical stable, but arrangement III is dynamical instable. The maximum values of the phonon frequencies for optical branches of arrangement I is in the Γ-X direction, but for arrangement II is in the L direction. A clear gap between the acoustic and optic branches is not observed for these arrangements. The right side of the phonon curves show the related total and partial density of phonon states for each compound. One can see that the main contribution to phonon acoustic mode for arrangement I comes from the Al and Si, but for arrangement II the main contribution belongs to Al. Unfortunately, there is no experimental or other theoretical data on the lattice dynamics of these compounds for the comparison with the present data.

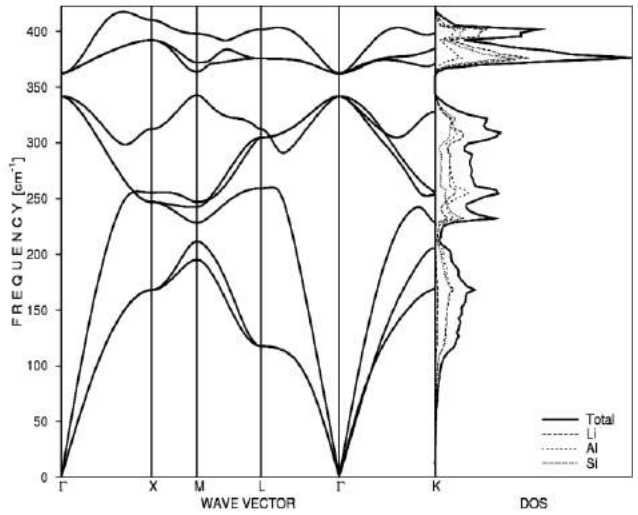

Fig. 2. The calculated phonon dispersions and total and partial density of states for arrangement I.

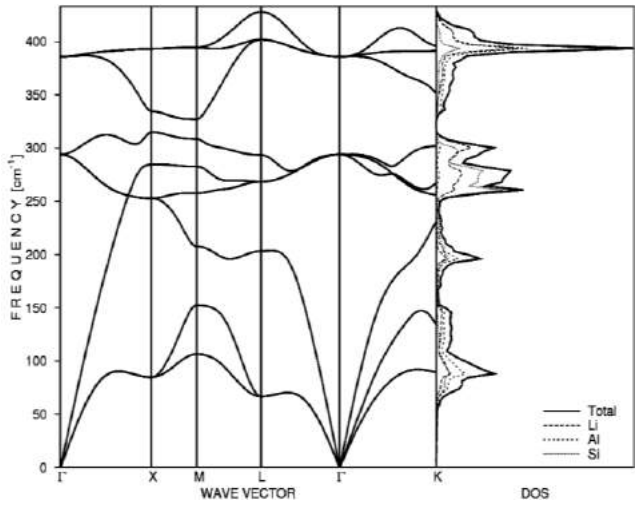

Fig. 3. The calculated phonon dispersions and total and partial density of states for arrangement II.

.

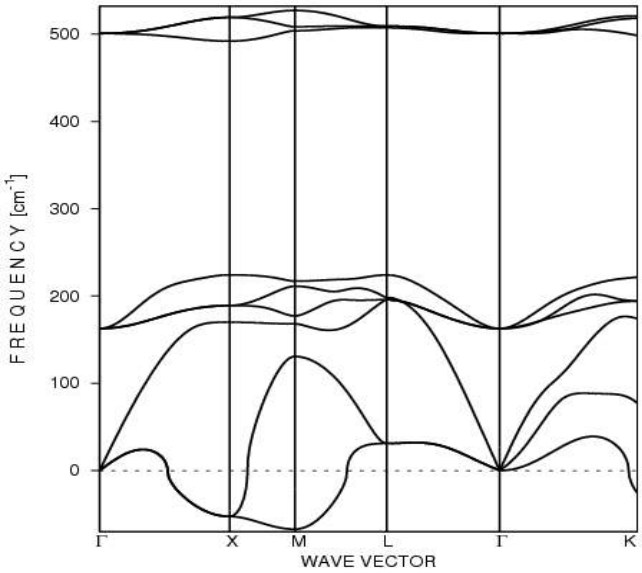

Fig. 4. The calculated phonon dispersion curves for arrangement III.

IV. SUMMARY AND CONCLUSION

The first–principles total energy calculations have been performed on the structural, mechanical, electronic, and vibrational properties for Li-Al-Si compounds. The calculated lattice constant is in excellent agreement with the experimental and other theoretical values. The elastic constants satisfy the traditional stability conditions for I, II. Moreover, these compounds have small band gap. The phonon dispersion curves and corresponding one-phonon DOS of arrangement I and II are very similar to each other with small details. The observed soft modes in the phonon dispersion curves strongly support the mechanically unstable character for arrangement III.

ACKNOWLEDGEMENT

This work is supported by Gazi University Research-Project Unit under Project No. 05/2009-55

[1]. *C. Felser, G. H. Fecher, and B. Balke*, Angew. Chem. Int. Ed. 46, 668 (2007)

[2]. *R. Asahi, T. Morikawa, H. Hazama, and M. Matsubara,* J. Phys.: Condens. Matter 20, 64227 (2008).

[3]. *S. J. Poon*, in: Recent Trends in Thermoelectric Materials Research II, Semiconductors and Semimetals, Vol. 70, edited by T. M. Tritt (Academic, New York, 2001), p. 37.

[4]. *S. Ögüt and K. M. Rabe*, Phys. Rev. B 51, 10443 (1995).

[5]. *D. Jung, H.J. Koo, and M.H. Whangbo,* J. Mol. Struct. Theochem. 527, 113 (2000).

[6]. *H. C. Kandpal, C. Felser, and R. Seshadri*, J.Phys. D, Appl. Phys. 39, 776 (2006).

[7]. *N.E. Christensen,* Phys. Rev. B 32 (10), 6490-6497 (1985).

[8]. N.E. Christensen, Physica Scripta. Vol. T19, 298-310 (1987).

[9]. *Z. Pawloska, N.E. Christensen, S. Satpathy, O.Jepsen,* Phys. Rev. B 34(10), 7080-7088 (1986)

[10]. *H.C. Kandpal, C. Felser and R. Seshadri,* J.Phys. D: Appl. Phys. 39, 776–785 (2006).

[11]. *F. Casper, R. Seshadri, and C. Felser,* Phys. Status Solidi A 206(5), 1090–1095 (2009).

[12]. *J. Barth,G.H. Fecher, M. Schwind, A. Beleanu, C. Felser, A. Shkabko, A. Weidenkaff, J. Hanss, A. Reller, M. Köhne* , Journal Of Electronic Materials,(2010),Doi: 10.1007/S11664-010-1076-9

[13]. *J. Gröbner, D. Kevorkov, and R. Schmid-Fetzer*,Journal of Solid State Chemistry 156, 506-511 (2001).

[14]. *D. Kevorkov, J. Gröbner, and R. Schmid-Fetzer*,Journal of Solid State Chemistry 156, 500-505 (2001) .

[15]. *M. Tillard , C. Belin, L. Spina, Y.Z. Jia*,Solid State Sciences 7, 1125–1134 (2005).

[16]. *G. Kresse and J. Hafner*, Phys. Rev. B 47, 558 (1993).
[17]. *G. Kresse and J. Furthmüller*, Comput. Mat. Sci. 6 15 (1996).
[18]. *G. Kresse and J. Furthmüller*, Phys. Rev. B 54 11169 (1996).
[19]. *H. J. Monkhorst, J. D. Pack*, Phys Rev B 13 5390 (1976).
[20]. J.*P. Perdew, S. Burke, M. Ernzerhof*, Phys. Rev. Lett. 77, 3865 (1996).
[21]. F. *D. Murnaghan*, Proc. Natl., Acad. Sci. USA 30, 5390 (1994).
[22]. *Y. Le Page and P. Saxe*, Phys. Rev. B 65, 104104 (2002).
[23]. B. *Mayer, H. Anton, E. Bott, M. Methfessel, J.Sticht, and P. C. Schmidt*, Intermetallics 11 (2003).
[24]. *R.A. Johnson*, Phys Rev B, 37: 3924 (1988).
[25]. *M. Florez, J.M. Recio, E. Francisco, M.A.Blanco*, A. Martı´n Penda´ s, Phys Rev B 66,144112 (2002).
[26]. *G.Johnston, R. Keeler, Rollins, and S.Spicklemire*, The Consortium for Upper-Level Physics Software, Jhon Wiley, New York, 1996.
[27]. *E. Schreiber, O. L. Anderson*, N. Soga, McGraw-Hill, New York, 1973.
[28]. *K. Parlinski*, Software PHONON (2003), and references therein.
[29]. *K. Parlinski, Z.Q. Li, and Y. Kawazoe*, Phys. Rev. Lett. 78 (1997) 4063-4066.

THE CURRENT-VOLTAGE (I-V) CHARACTERISTICS OF Au/n-Si SCHOTTKY BARRIER DIODES (SBDs) WITH $SrTiO_3$ INTERFACIAL LAYER

İ.TAŞÇIOĞLU[1], U.AYDEMİR[1], V.J.MAMEDOVA[2], Ş.ALTINDAL[1]

[1]*Department of Physics, Faculty of Science and Arts, Gazi University, 06500, Ankara, Turkey*

ilketascioglu@gazi.edu.tr

[2]*Baku State University, Z. Halilov str., 23, Baku, AZ-1148*

The metal-ferroelectric-semiconductor (MFS) type Schottky barrier diodes (SBDs) were prepared by RF magnetron sputtering method. The main electrical parameters such as ideality factor (n), zero-bias barrier height (Φ_B) and series resistance (R_s) of Au/$SrTiO_3$/n-Si (MFS) SBDs were obtained from forward bias current-voltage (*I-V*) characteristics at room temperature. I-V characteristics show that non-ideal behavior due to the presence of ferroelectric interfacial layer, interface states localized at $SrTiO_3$/n-Si interface and series resistance. In addition, the density distribution of interface states (N_{ss}) as a function of E_c-E_{ss} was obtained from the forward bias *I-V* data by taking into account the bias dependence effective barrier height (Φ_e) and R_s. The values of ideality factor and barrier height were found as 6 and 0.56 eV, respectively. The R_s of diode was calculated from Cheung's functions and it was found as 22,30 Ω from *dV/dlnI* plot and 43,68 Ω from *H(I)* plot, respectively. The N_{ss} profile shows an exponential increase from the mid-gap of Si to bottom of the conduction band with values ranging from $2.15x10^{13}$ to $3,65x10^{13}$ $eV^{-1}.cm^{-2}$. The experimental results show that the presences of an interfacial layer ($SrTiO_3$) with high-k dielectric constant, N_{ss} and R_s have a significant effect on *I-V* characteristics.

I. INTRODUCTION

The presence of an interfacial layer such as SiO_2, SnO_2, Si_3N_4, TiO_2 at metal-semiconductor (M/S) interface affects the main electrical parameters of Schottky barrier diodes (SBDs). Recently, a great attention has been focused on using alternative high k-dielectric materials such as $SrTiO_3$ (STO), $SrBi_2Ta_2O_9$ (SBT), $BaTiO_3$ (BTO) as interfacial layer at metal/semiconductor (M/S) interface in the semiconductor devices [1-10]. A poor interfacial layer constructed at M/S interface leads to high leakage current, high temperature and frequency dispersion and high defect trapped charges. Therefore, the use of material having high k-dielectrics is very suitable in order to improve performance of SBD with low leakage current, low interface state density [3-6]. Therefore, $SrTiO_3$ (STO) has attracted much attention, because it can be used an alternative material to replace the conventional interfacial layer for further development such devices. Using $SrTiO_3$ film between metal and semiconductor cannot only prevent the reaction and inter-diffusion between metal and silicon substrate, but also further improve the retention properties [1,3,8,9]. $SrTiO_3$ is a perovskite type material which provides a good buffer layer for the growth of perovskite type ferroelectric thin films and can be grown by RF magnetron sputtering method [1].

The performance and reliability of SBDs depend on various parameters such as the homogeneity of interfacial layer and barrier formation at M/S interface, R_s of devices and interface states localized at $SrTiO_3$/n-Si interface. When the interfacial layer (STO) inserted in metal/semiconductor interfaces, the current-voltage (I-V) characteristics of diode deviated from the ideal case. Also the values of N_{ss} and R_s of these devices are important parameters affecting the main electrical parameters [9-15]. Among them, R_s is effective only at high bias region but N_{ss} and interfacial layer effective in the whole measured applied bias region. Therefore, the forward bias I-V characteristics are generally linear in the semi-logarithmic scale at low bias voltages but deviate from linearity due to effect of R_s when the applied bias voltage is sufficiently large [5-11]

In this study, we reported to I-V characteristics of Au/$SrTiO_3$/n-Si SBDs at room temperature by considering the R_s and N_{ss} effects. The R_s values were calculated from Cheung's method. The energy density distribution profile of N_{ss} was obtained from the forward bias I-V data by taking into account the bias dependence Φ_e and R_s.

II. EXPERIMENTAL DETAILS

Au/$SrTiO_3$/n-Si structures were fabricated on 2 inch" diameter float zone (100) n-type (phosphorus doped) single crystal silicon wafer, having thickness of 350 μm with about 1 Ω.cm resistivity. For the fabrication a process, Si wafer was degreased in organic solvent of $CHClCCl_2$, CH_3COCH_3, and CH_3OH consecutively and then etched in a sequence of H_2SO_4 and H_2O, %20 HF, a solution of $6HNO_3$:1HF:$35H_2O$, %20 HF and finally quenched in deionized water for a prolonged time. Preceding each cleaning step, the wafer was rinsed thoroughly in deionized water of resistivity of 18 MΩ-cm.

Substrates were clamped to a stainless steel holder provided with an optical heater. Thin films of $SrTi0_3$ were deposited by UHV RF Magnetron Sputtering System hot pressed $SrTiO_3$ ceramic target, in varying $Ar+O_2$ reactive gas mixtures on n-Si. Prior to film deposition, Si substrates were sputter cleaned in pure argon ambient after raising the substrate temperature to 250 ^oC in 10^{-8} mbar high vacuum, to ensure the removal of any residual organics. The sputter cleaning process of silicon substrates were achieved in RF sputter-etching room which was separated by an electro-pneumatic actuated valve to deposition chamber. Sputtering operations were carried out with mass flow controllers. The automatic control system of gas valves were used for Ar and O_2. The

flow of Ar and O_2 were maintained at 9 sccm and 1 sccm (%90 Ar - %10 O_2), respectively. The film was deposited at a constant pressure of $4.2x10^{-3}$ mbar and a constant substrate temperature of 450 ^oC. After deposition, film was annealed for 30 min at 400 ^oC only O_2 gas. To prevent microcracks in the films cooling process was maintained a low rate 1.0 ^oC/min. Finally, ~1000 Å thick $SrTiO_3$ films were prepared under these conditions for electrical and optical measurements.

The ohmic and rectifier contacts were formed by sintering the BESTEC HV Thermal Deposition System in the pressure of 10^{-7} mbar with tungsten holder. High purity Al (%99,999) was evaporated onto the whole back surface of the substrate at 450 ^oC as a back contact, and then temperature was fixed at 400 ^oC to form good ohmic contact behavior. After that ~2000 Å thick Au (%99,999 purity) dots of 1mm diameter were evaporated onto STO film at 100 ^oC with shadow mask so rectifier contacts were formed. In this way, Au/$SrTiO_3$/n-Si structures were fabricated for the electrical measurements. The electrode connections were made by silver paste.

The forward and reverse bias I-V measurements were performed by the use of a Keithley 2400 sourcemeter at room temperature in vacuum (~10^{-3} Torr) in Janis VPF-475 cryostat. All measurements were carried out with the help of a microcomputer through an IEEE-488 ac/dc converter card.

III. RESULTS AND DISCUSSION

For a metal/semiconductor (MS) Schottky barrier diode with and without interfacial layer, when the R_s is considered, the current through a diode at a forward bias (V≥3kT/q), according to the thermionic emission (TE) theory, is given by [16-19]

$$I = AA^{*}T^{2}\exp\left(-\frac{q\Phi_{Bo}}{kT}\right)\left[\exp\left(\frac{q(V-IR_s)}{nkT}\right)\right] \quad (1)$$

where V is the applied voltage across to rectifier contact, n is the ideality factor, T is the absolute temperature in K, q is the electronic charge, k is the Boltzmann constant; and I_o is the reverse saturation current and it can be expressed as,

$$I_o = A\ A^{*}\ T^{2}\exp\left(-\frac{q\Phi_{B0}}{kT}\right) \quad (2)$$

where A is the area of rectifier contact, A^* is the effective Richardson constant and Φ_{B0} is the zero-bias barrier height and can be obtained from Eq(2) as following.

$$\Phi_{B0} = \frac{kT}{q}\ln\left(\frac{AA^{*}T^{2}}{I_o}\right) \quad (3)$$

The ideality factor is a measure of the conformity of the diode to be pure thermionic emission, and it is determined from the slope of the linear region of the forward bias ln(I)-V characteristics through the relation,

$$n = \frac{q}{kT}\frac{dV}{d(\ln I)} \quad (4a)$$

where dV/dlnI is the slope of linear region of ln(I)-V plots. Also the voltage dependent ideality factor n(V) can be written from Eq.(1) as

$$n(V) = \frac{qV}{kT\ln(I/I_o)} \quad (4b)$$

Fig. 1 shows the forward and reverse bias I-V characteristics of the Au/$SrTiO_3$/n-Si (MFS) diode at room temperature. On a semi-logarithmic scale and at low forward bias voltage, the I-V characteristics of Au/$SrTiO_3$/n-Si (MFS) SBD are linear but deviates from linearity due to series resistance and interface states effects. When the applied voltage is sufficiently large, the effect of R_s can be seen at the non-linear region of the forward bias I-V characteristics. Using Eq. (2) and (4a), the values of the barrier height and the ideality factor were found to be Φ_{B0}=0.56 eV and n=6, respectively.

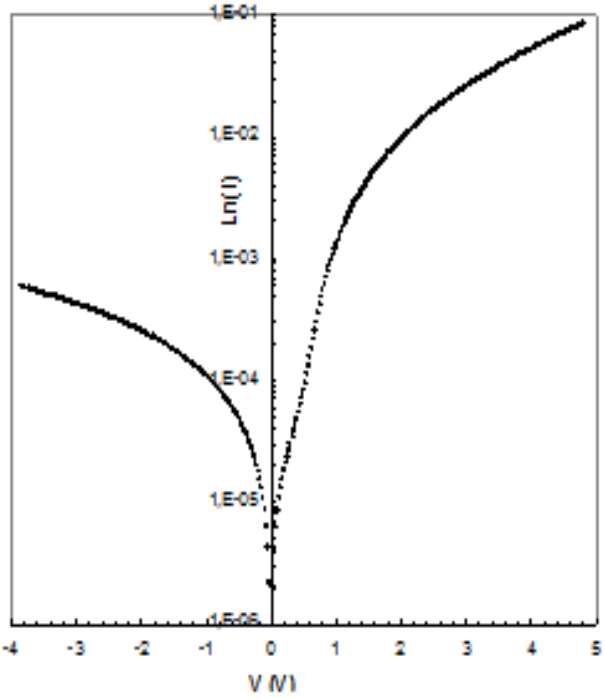

Fig 1. The I-V plot of Au/$SrTiO_3$/n-Si (MFS) SBD.

The variation of double logarithmic I-V curve for Au/$SrTiO_3$/n-Si SBD is given in Fig. 2 and the charge transport mechanisms through barrier have been determined from I-V characteristics. The charge transport properties will contribute to the I-V characteristics depending on the interfacial layer [5,6,20,21]. These properties give more information about conduction mechanisms occurring in the STO material at intermediate and high voltage regions. The charge transport can be attributed to space-charge-limited current (SCLC) mechanism for Au/$SrTiO_3$/n-Si SBD. As can be seen from the Fig 2, the graph has three distinct linear regions change in the form of $I\alpha V^m$ where m is slope of each separated linear regions. The first region

corresponds to ohmic behavior with slope of 1.09 and below voltage of about 0.3 V. The second region (varying from 0.47 to 0.95 V) can be analyzed by power law dependence with slope of about 4.08. At high forward voltages (>1 V), slope of linear region (2.50) is lower due to transition from the trap-filled to free carrier SCLC [20,23].

The voltage dependence of n and effective barrier height (Fe) is given in Fig. 3. As shown in Fig 3, the n and Φ_e increases with increasing applied voltage.

The values of series resistance have been determined from following functions developed by Cheung and Cheung [24]. From Eq. (1), the following functions can be written as;

$$\frac{dV}{d(\ln I)} = n\left(\frac{kT}{q}\right) + IR_s \qquad (5a)$$

$$H(I) = V - n\frac{kT}{q}\ln\left(\frac{I}{AA^*T^2}\right) = n\Phi_{Bo} + IR_s \qquad (5b)$$

Here, the term IRs is the voltage drop across the series resistance of the Au/$SrTiO_3$/n-Si SBD. The dV/d(lnI)-I and H(I)-I plots of the SBD are given in Fig 4. In Fig 4 dV/d(lnI)-I plot's slope gives the R_s with the value of 22,29 Ω by using Eq. (5a) and H(I)-I plot's slope also gives R_s with the value of 43,68 Ω by using Eq. (5b). The values of R_s obtained from Cheung's functions are closer with each other.

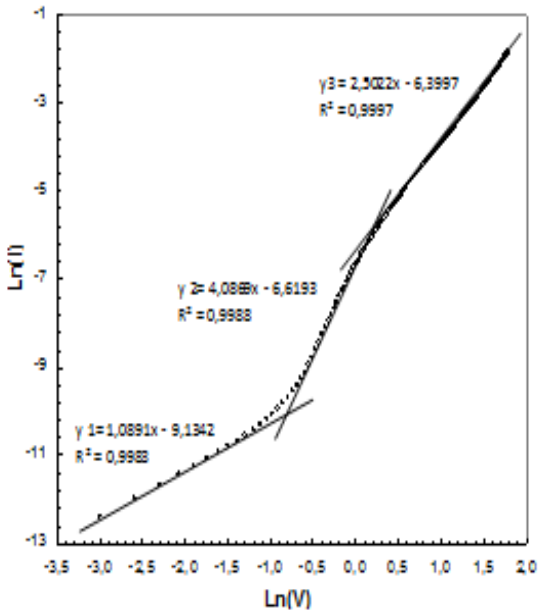

Fig.2. The forward bias double logarithmic I-V plot of Au/$SrTiO_3$/n-Si (MFS) SBD

.

For a SBD with N_{ss} which is in equilibrium with semiconductor, the expression for N_{ss} deduced by Card and Rhoderick [17] is reduced to [17, 23]

$$N_{ss}(V) = \frac{1}{q}\left[\frac{\varepsilon_i}{\delta}(n(V)-1) - \frac{\varepsilon_s}{W_D}\right] \qquad (6)$$

where ε_I (=200ε_o) and ε_s (=11,8ε_o) are the permittivities of the interfacial layer and the semiconductor, respectively, ε_o is the permittivity of free space (ε_o=8,85x10^{-14} F/cm). δ is the thickness of the interfacial layer and W_D is the width of space charge region.

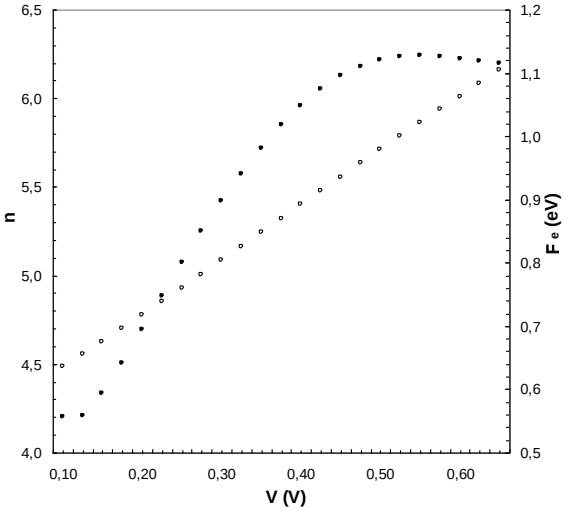

Fig 3. The voltage dependent n and Φ_e plots of Au/$SrTiO_3$/n-Si (MFS) SBD.

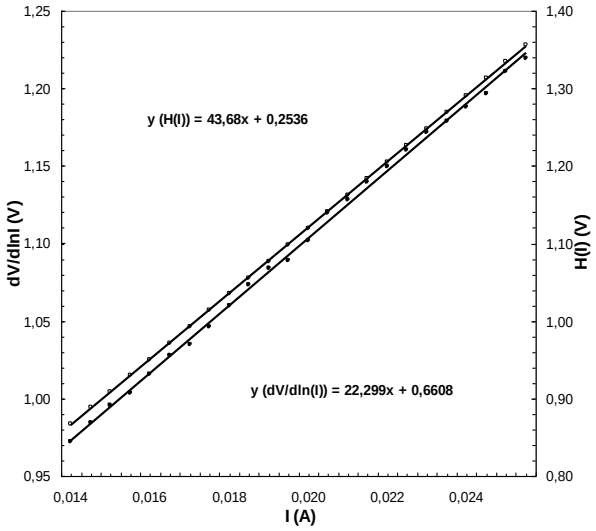

Fig 4. The dV/dlnI-I and H(I)-I plots of Au/$SrTiO_3$/n-Si (MFS) SBD.

Furthermore, in n-type semiconductors, the energy of interface states E_{ss} with respect to the bottom of the conduction band at the surface of the semiconductor is given by [23]

$$E_c - E_{ss} = q\left[\Phi_e - V\right] \qquad (7)$$

where

$$\Phi_e = \Phi_{B0} + \left(1 - \frac{1}{n(V)}\right)(V - IR_s) \qquad (8)$$

As can be seen in Fig 5, exponential growth of interface state density from mid-gap towards the top of conduction band is very apparent. There is a little peak appears in Fig 5, which can be explained by defects in interfacial layer and the particular distribution of N_{ss} in the Si band gap. The value of N_{ss} ranges from $2.15x10^{13}$ to $3,65x10^{13}$ $eV^{-1}.cm^{-2}$.

IV. CONCLUSION

In order to investigate electrical characteristics of $Au/SrTiO_3/n$-Si SBD, the I-V measurements were carried out at room temperature. The evaluation of the forward bias I-V characteristics reveals that the R_s and N_{ss} are important parameters affecting performance and reliability of SBD. The ideality factor and zero-bias barrier height values were found as 6 and 0.56 eV for fabricated Au/SrTiO3/n-Si (MFS) SBD, respectively. The energy distribution profile of N_{ss} has been determined from I-V data and it has exponential rise from mid-gap towards the top of conduction band.

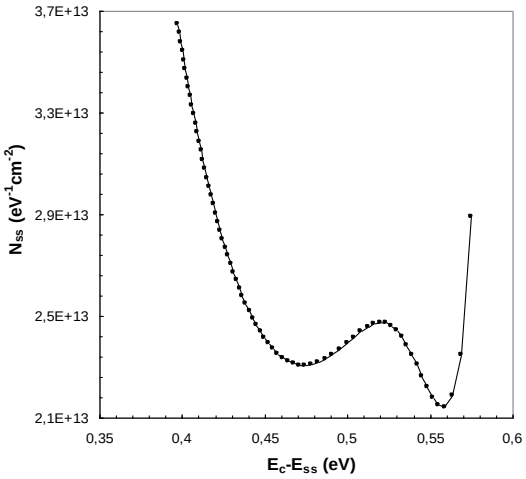

Fig 5. The N_{ss} plot of $Au/SrTiO_3/n$-Si (MFS) SBD.

[1]. *N. Konofaos, E.K. Evangelou, Zhongchun Wang, V. Kugler, U. Helmersson,* Journal of Non-Crystalline Solids, 303, (2002) 185.

[2]. *C.Y. Liu, T.Y. Tseng,* Ceramics International, 30, (2004) 1101.

[3]. *K. Eisenbeiser, J.M. Finder, Z.Yu, J. Ramdani, J.A. Hallmark, R. Droopad, et. al.* Applied Physics Letters 76, (2000) 1324.

[4]. *C. H. Huang, T. Y. Tseng, C. H. Chien, M. J. Yang, C. C. Leu, T. C. Chang, P. T. Liu, T.Y. Huang,* Thin Solid Films, 420, (2002) 377.

[5]. *F. Parlaktürk, Ş. Altındal, A. Tataroğlu, M.Parlak, A. Agasiyev,* Microelectronic Engineering, 85, (2008) 81.

[6]. *Ş. Altındal, F. Parlaktürk, A. Tataroğlu, M.Parlak, S.N. Sarmasov, A. Agasiyev,* Vacuum, 82, (2008) 1246.

[7]. *S.M. He, D.H. Li, X.W. Deng, X.Z. Liu, Y. Zhang, Y.R. Li,* Microelectronic Engineering, 66, (2003) 891.

[8]. *K.C. Chiang, C.C. Huang, G.L. Chen, W.J. Chen, H.L. Kao, Y.H. Wu,* A. C, IEEE Transactions on Electron Devices, 53, (2006) 2312.

[9]. *C.H. Park, J.H. Kim, M.C. Kim, Y.G. Son, M.S.Won,* Applied Surface Science, 249, (2005) 16.

[10]. *M.H. Tang, Y.C. Zhou, Z.J. Zheng, Z.Yan, C.P. Cheng, Z. Ye, Z.S. Hu,* Solid-State Electronics, 51, (2007) 371.

[11]. *B. H. Park, B.S. Kang, S.D. Bu, T.W. Noh, J.Lee, W. Jo,* Nature (London) 401, (1999) 682.

[12]. *K. Kim, C. Kim:* Thin Solid Films 478, (2005) 6.

[13]. *A.F. Tasch, L.H.Parker,* Proc. IEEE, 77, (1989) 374.

[14]. *P.C. Joshi, S.B. Krupanidhi,* J.Appl. Phys., 73, (1993) 7627.

[15]. *M.N. Kamalasanan, N.D. Kumar, S.Chandra,* J.Appl. Phys., 74, (1993) 679.

[16]. *S.M. Sze,* Physics Semiconductor Devices, John Wiley and Sons, New York, (1981).

[17]. *H.C. Card and E.H. Rhoderick,* J. Phys. D-Appl. Phys. 4, (1971) 1589.

[18]. *E.H. Rhoderick, R.H. Williams,* Metal Semiconductor Contacts. 2nd Ed. Oxford, Clarendon Press, (1988).

[19]. *E.H. Nicollian, J.R.Brews,* Metal Oxide Semiconductor (MOS) Physics and Technology, Wiley, Newyork, (1982).

[20]. *Y.S. Ocak, M. Kulakci, T. Kılıçoğlu, R. Turan, K.Akkılıç,* Synth. Met. 159 (2009) 1603.

[21]. *O. Vural, N. Yıldırım, Ş. Altındal, A. Türüt,* Synth. Met. 157 (2007) 679.

[22]. *S.R Forrest,* Chem. Rev., 97 (1997) 1793.

[23]. *A.Singh,* Solid State Electron 28 (1985) 223.

[24]. *S.K. Cheung, N.W. Cheung,* Appl. Phys. Lett. 49, (1986) 85.

QUANTUM BIT ON A JOSEPHSON JUNCTION WITH ANHARMONIC CURRENT-PHASE RELATION

I.N. ASKERZADE
Computer Engineering Department of Engineering Faculty, Ankara University, 06100 Tandoğan, Turkey
and Institute of Physics Azerbaijan NAS, Baku, AZ-1143, Azerbaijan
iasker@science.ankara.edu.tr

The energy spectrum of a phase quantum bit (qubit) implemented on a superconducting Josephson junction with anharmonic current-phase relation has been studied in terms of the Hamilton formalism. An analytical formula for ground level splitting in the qubit spectrum is obtained and analyzed.

I. INTRODUCTION

Study of quantum bits-basic elements of quantum computers in last years becames very actual [1]. There are different types of qubits-qubits on atomic trappings, optic and superconducting qubits [1]. In recent years, quantum bits on Josephson junctions have been extensively studied using theoretical and experimental methods [2–3]. Using of Josephson junctions in qubits is based on quantum effects manifested on the macroscopic scale in Josephson junction and in superconducting rings. Review of Josephson junction based qubits presented in [2,4-5]. In all versions of qubits current-phase relation of Josephson junctions considered as

$$I = I_c \sin\phi, \tag{1}$$

which is executed with high accuracy in low-temperature-based Josephson junctions [6]. In expression I_c is the critical current of Josephson junction. In submicron high-T_c grain boundary Josephson junctions curret-phase relation reveal anharmonic character [7,8]. In the case of presence of second harmonic current-phase relation can be written as [9]

$$I = I_c \sin\phi + I_{c2} \sin 2\phi \tag{2}$$

According to experimental data, the amplitudes the first and second harmonics should have opposite sign [8]. Microscopical expression for the I_c and I_{c2} for different superconducting structures can be found in literature. More interesting phenomena arises in structures superconductor-ferromagnetic [10]. Value of anharmonic terms is determined by the microscopical parameters of such systems. Influence of anharmonicity in current-phase relation on I-V curve of such junction was investigated in [10]. In this study we investigate quantum bit based on Josephson junction with anharmonic current-phase relation. We present the results of an investigation of the energy spectrum of a phase qubit implemented on a single Josephson junction with second term of current-phase relation (2).

II. BASIC EQUATIONS

The behavior of qubits will be analyzed in terms of the Hamiltonian formalism. The general form of a Hamiltonian for a circuit containing qubits of various types is as follows [2,11]:

$$H = \sum (K(n_j) + U(\phi_j)), \tag{3}$$

where $K(n_j)$ is the kinetic energy, which is related to the electrostatic energy, and $U(\varphi) = -E_J \cos\varphi$ is the Josephson energy with amplitude $E_J = \dfrac{\hbar I_c}{2e}$, where I_c is the critical current of the Josephson junction. Josephson phase φ are conjugated operators that are related as follows:

$$n = -i\frac{\partial}{\partial\phi} \tag{4}$$

Under consideration of Josephson qubit with current-phase relation (1), Hamiltonian of system can be written as

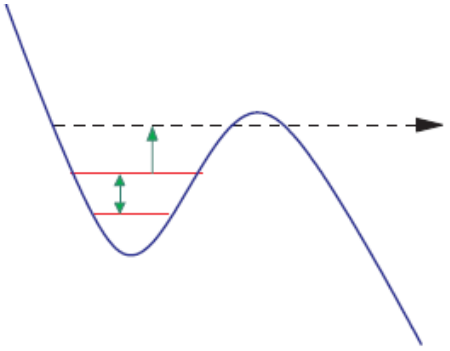

Fig.1. Quantized energy levels in the potential of a current biased Josephson junction; the two lower levels form the Josephson junction qubit, the dashed line indicates a leaky level with higher energy.

$$H = E_C n^2 - E_J \cos\varphi + \frac{\hbar I_e}{2e}\phi, \qquad (5)$$

where $E_C = \frac{(2e)^2}{2C}$ is the Coulomb energy together, I_e is the external current. Last term in expression (5) related with interaction of external current source and Josephson junction. Under small external current I_e, energy spectrum of quantum bit has a form

$$E_k = \hbar\omega_p (n + \frac{1}{2}), \qquad (6)$$

where $\omega_p = \omega_J (1 - \frac{I_e}{I_c})^{1/4}$ is the plasma frequency of phase oscillations near minimum potential energy [6]. Josephson frequency ω_J is determined by the following expression

$$\omega_J = \frac{I_c}{2e}$$

As followed from last expression, distance between 0 and 1 energetic levels is controlled by external current (Fig.1).

As shown in [10], presence of second harmonic in current-phase relation of Josephson junction is equivalent to introducing of effective inductance in series with junction circuit. Value of this inductance is proportional to amplitude of second harmonic I_{c2} [10]. It means that quantum bit with current-phase relation (2) can be considered as single junction interferometer with effective inductance $l_{eff} = 2\pi \frac{L_{eff} I_c}{\Phi_0} \prec I_{c2}$ (Fig. 2).

The corresponding Hamiltonian can be written as

$$H = E_C n^2 - E_J \cos\varphi + \frac{\hbar I_e}{2e}\phi + E_J \frac{\phi^2}{2l_{eff}} \qquad (7)$$

Estimation of results of experimental study of Josephson junctions with anharmonic current-phase shows, that $l_{eff} << 1$ [7,8].

As in the case of quantum bit with simple current-phase relation (1), we will consider that I_e is very small and we can neglected with corrresponding term in Eqs. (6,7). Such approximation leads to effective single junction approach with $\Phi_e = 0$. Small value of effective inductance leads double-well potential. Result of calculations similar to [11], gives expression for splitting of bound state of quantum bit

$$\Delta E = E_J (1 - \exp(-\frac{\hbar\omega L_{eff}\pi^2}{\Phi_0^2})) \quad . \qquad (8)$$

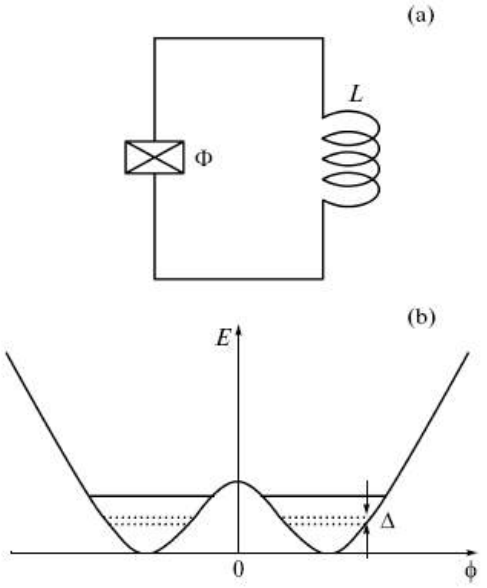

Fig. 2. Single quantum superconducting interferometer as a phase qubit: (a) equivalent circuit diagram; (b) symmetric double well potential.

For intermediate values of l_{eff}, when $\frac{L_{eff} I_e}{\Phi_0} > \frac{\pi}{2}$ we can use results of calculations in [11] and is true following expression

$$\Delta E = E_J (1 - \cos(\phi_e) \exp(-\frac{\hbar\omega L_{eff}\pi^2}{\Phi_0^2})), \qquad (9)$$

where

$$\phi_e = 2\pi \frac{L_{eff} I_e}{\Phi_0} \qquad (10)$$

III. RESULTS

Detail analysis of expressions (8) and (9) shows, that there are two different behavior in $\Delta E(L_{eff})$ dependence of energy splitting of bound state of quantum bit. In small effective inductance L_{eff} limit, the increasing amplitude of second harmonic I_{c2} leads to increasing of splitting ΔE. For intermediate value of effective inductance $\frac{L_{eff} I_e}{\Phi_0} > \frac{\pi}{2}$, due to changing sign of $\cos(\phi_e)$ ΔE has opposite character: ΔE decreases with increasing of amplitude of second harmonic I_{c2} in current-phase relation (2) (Fig. 3). In Fig. 3 was

introduced following notations: the ratio $s = \frac{E_J}{E_C}$ of the chraracteristic Josephson energy to Coulomb energy. In Fig. 3 horizontal axis denotes $\frac{I_{c2}}{2I_c}$, in vertical line we show energy splitting parameter Δ (see Fig. 2) in units of Coulomb energy $E_C = \frac{(2e)^2}{2e}$.

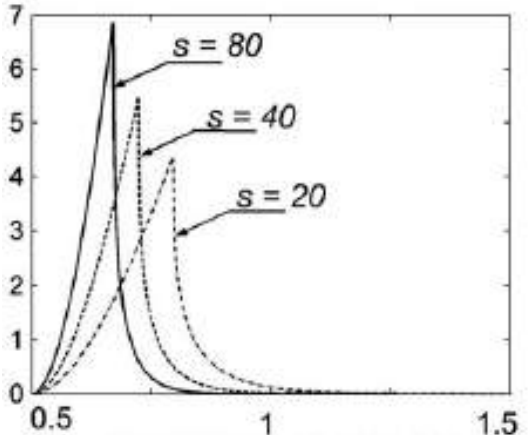

Fig. 3. Splitting gap behavior for three values of the ratio s of characteristic Josephson energy E_J to Coulomb energy E_C at the presence of the second harmonic

Obtained results in good agrimeent with conclusions of study [9]. In this paper was considered behavior of quantum bit based on two- Josephson junction interferometer. It is well known that, such double-junction interferometer is equivalent to single Josephson junction with oscillating critical current [6]. In [9] authors use energy spectrum of Mathieu equation with additional term $\cos 2\varphi$.

The possibility for macroscopic electrical circuits to exhibit a quantum behavior is rather counter intuitive. However, in fact, that is the consequence of quantum origin of the electromagnetic field. The Kirchhoff equations used to describe these circuits represent a lumped element approximation of the Maxwell equations valid for the limit of small circuit size compared to the electromagnetic wave length. Typical superconducting qubits operate at frequencies of several GHz, which correspond to the wave lengths in a centimeter range, while circuit elements are of a submillimeter size. Quantum electrodynamics being translated to the language of lumped element circuits establishes the non-commutation relations between the charges and the currents.

The superconducting qubit that have been discussed above exploit the fundamental quantum uncertainty between electric charge and magnetic flux. There are, however, other possibilities. One of them is to delocalize quantum information in a Josephson Junction network by choosing global quantum states of the network as a computational basis. Recently, some rather complicated Josephson junnction Networks have been discussed, which have the unusual property of degenerate ground state, which might be employed for efficient qubit protection against decoherence [12,13,14]. An alternative possibility is to replace macroscopic tunnel Josephson junction with a single-mode quantum point contact , and to take advantage of quantum fluctuation of microscopic bound Andreev states controlling the Josephson current [14].

IV. CONCLUSIONS

Thus, the energy spectrum of a phase quantum bit implemented on a superconducting Josephson junction with anharmonic current-phase relation has been studied in terms of the Hamilton formalism. An analytical formula for ground level splitting is obtained and analyzed. Comparision with another type Josephson junction qubits also is conducted.

ACKNOWLEDGMENT

This work partially supported by Ankara University BYÖD program.

[1]. *K. A. Valiev*, Phys. Usp.48, 1 (2005).
[2]. *G. Wendin and V. S. Shumeiko,* Low Temp. Phys. 30, 724 (2007).
[3]. *Yu. A. Pashkin, O.Astafiev, T.Yakamoto, Y.Nakamura, and J. S. Tsai,* Quant. Inform. Process. 8, 55 (2009).
[4]. *Y. Nakamura, Yu. A. Pashkin, and J. S.Tsai,* Nature 398, 786 (1999).
[5]. *J. M. Martinis,* Quant. Inform. Process. 8, 81 (2009).
[6]. *K. K. Likharev,* Introduction to the Dynamics of Josephson Junctions (Nauka, Moscow, 1985)
[7]. *T.Bauch, F. Lombardi, F.Tafuri, et al* Physical Rev. Letters, 94,087003(2005)
[8]. *M.H.S. Amin, A. Smirnov, A.Zagoskin et al*, Phys. Rev.B 73, 064516 (2005).
[9]. *N.V.Klenov, VK Kornev*, NF Pedersen, Physica C 435, 114(2006)
[10]. *I.N. Askerzade,* Tech. Phys. 48, 1496 (2003).
[11]. *N. Askerzade and Ş. Amrahov*, Tech. Phys. Lett. 34, 737 (2010).
[12]. *L.B. Ioffe, M.V. Feigel'man, A. Ioselevich, D. Ivanov, M.Troyer, and G. Blatter*, Nature 415, 503 (2002).
[13]. *M.V. Feigel'man, L.B. Ioffe, V.B. Geshkenbein, P. Dayal, and G. Blatter, Phys. Rev. Lett*. 92, 098301 (2004).
[14]. *A.Zazunov, V.S. Shumeiko, E. Bratus, J. Lantz, and G.Wendin*, Phys. Rev. Lett. 90, 0870031 (2003).

NUMERICAL STUDY OF TWO-BAND GINZBURG-LANDAU MODEL OF SUPERCONDUCTIVITY

I.N.ASKERZADE

Computer Engineering Department of Engineering Faculty,
Ankara University, 06100 Tandoğan, Turkey
and Institute of Physics Azerbaijan NAS,
Baku, AZ-1143, Azerbaijan
iasker@science.ankara.edu.tr

The discovery of superconductivity in MgB_2 having a critical temperature of 39K attract a great interest of researchers. Using a generalization of the Ginzburg-Landau model, namely the two-band time-dependent Ginzburg-Landau (2BTDGL) equations, to model the phenomena of two band superconductivity. In this study, numerical aspects of the two-dimensional, isothermal, isotropic 2B-TDGL equations in the presence of a time-dependent applied magnetic field and are investigated. The stability of finite element approximations of the solutions are presented. Numerical experiments are presented and compared to some known results which are related to MgB_2 or general two-band superconductivity.

I. INTRODUCTION

The discovery of the intermetallic compound superconductor Mg_2 stirred up intense research to investigate the novel properties of this material [1]. The compound MgB_2 differs from conventional low critical temperature (T_c) superconductors and cuprate- based high T_c superconductor compounds mainly in its possession of two distinct energy gaps; the other superconductors are known to only have one energy gap [2]. It is its two-band structure that gives MgB_2 many novel properties unseen in any other superconductors; for example, interband phase soliton textures occur in a two-band superconductor [3]. Because of the existence of multiple distinct energy gaps in a multiband superconductor, there exists multiple distinct order parameters which interact with each other through a Josephson tunneling like mechanism. The conventional isotropic or anisotropic time-dependent Ginzburg-Landau (TDGL) model [4] which has been widely accepted as a successfully phenomenological model for a single-band superconductor sample at temperatures near its critical temperature does not include any appropriate coupling terms to account for the coupling interactions that are shown to be significant factors in determining the novel properties of a multiband superconductor such as MgB_2. Therefore, the TDGL model is not a correct model for multiband superconductivity. [5] investigates the breakdown of the anisotropic GL model in modeling MgB_2. The 2B-TDGL model generalizes the TDGL model by adding coupling terms to model the interband interaction of the two distinct order parameters corresponding to the two distinct energy bands. The 2B-TDGL model has now been widely used by the physics community as a phenomenological model to investigate the properties of multiband superconductor such as MgB_2.

Up to now Ginzburg-Landau theory remains powerful method in study of some physical properties of superconductors. The vortices nucleation in the single-band isotropic superconductors was originally studied by using Ginzburg–Landau equations for single-band isotropic superconductors [6-8]. It is important to note that, the GL theory was generalized for the case superconductors with non-conventional order parameter symmetry- d-wave symmetry [9]. GL equations also are useful in study of fluctuational effects on physical properties near T_c [10] in single band isotropic superconductors. Time-dependent single-band GL theory was used for calculations of fluctuation conductivity neat T_c by Aslamazov-Larkin [11].

Previously, time independent two-band GL equations were successfully used to study the physical properties of recently discovered superconductors such as magnesium diboride *(MgB_2)* [12, 13] and nonmagnetic *$Y(Lu)Ni_2B_2C$* borocarbide compounds [14,15]. In the present study, the

vortices nucleation of vortex in external magnetic field in the framework of a two-band model two-band GL equations. Firstly we will drive time-dependent GL equations for two-band superconductors. Secondly we apply this equations for numerical modeling for vortex nucleation in the case thin superconducting film of two-band superconductor *MgB_2* with perpendicular external magnetic field. We could use the modified forward Euler method for numerical experiments. Finally, a conclusion remarks will be made.

II. TIME DEPENDENT GL EQUATIONS FOR TWO-BAND SUPERCONDUCTORS

The GL free energy functional for an isotropic two-band superconductor can be written as follows /12-15/:

$$F_{SC} = \int d^3 r (F_1 + F_{12} + F_2 + H^2/8\pi) \tag{1}$$

where

$$F_i = \frac{\hbar^2}{4m_i}\left|\left(\nabla - \frac{2\pi i\vec{A}}{\Phi_0}\right)\Psi_i\right|^2 + \alpha_i(T)\Psi_i^2 + \beta_i\Psi_i^2/2 \tag{2}$$

$$F_{12} = \varepsilon(\Psi_1^*\Psi_2 + c.c.) + \varepsilon_1\left\{\left(\nabla + \frac{2\pi i\vec{A}}{\Phi_0}\right)\Psi_1^*\left(\nabla - \frac{2\pi i\vec{A}}{\Phi_0}\right)\Psi_2 + c.c.\right\} \tag{3}$$

m_i are the masses of electrons belonging to different bands (i = 1, 2); $\alpha_i = \gamma_i(T - T_{ci})$ are the quantities linearly dependent on the temperature; β and γi are constant coefficients; ε and ε1 describe the interaction between the band order parameters and their gradients, respectively; H is the external magnetic field; and $\Phi 0$ is the magnetic flux quantum. In Eqs. (1) and (2), the order parameters are assumed to be slowly varying in space. Minimization procedure of the free-energy functional yields the time-independent GL equations describing the two-band superconductors /12-15/.

Time-dependent equations in two-band Ginzburg-Landau theory can be obtained from Eqs. (1-3) using minimization procedure in analogical way to [16]:

$$\Gamma_1(\frac{\partial}{\partial t} + i\frac{2e}{\hbar}\phi)\Psi_1 = -\frac{\delta F}{\delta \Psi_1^*}, \quad (4a)$$

$$\Gamma_2(\frac{\partial}{\partial t} + i\frac{2e}{\hbar}\phi)\Psi_2 = -\frac{\delta F}{\delta \Psi_2^*}, \quad (4b)$$

$$\sigma_n(\frac{\partial \vec{A}}{\partial t} + \nabla\phi) = -\frac{1}{2}\frac{\delta F}{\delta \vec{A}} \quad (4c)$$

Here we use notations similar to [16]. In Eqs. (4) φ means electrical scalar potential , $\Gamma_{1,2}$ -relaxation time of order parameters, σ_n-conductivity of sample in two-band case. Choosing corresponding gauge invariance we can eliminate scalar potential from system of equations (4) [16]. Under such calibration and magnetic field in form, $\vec{H} = (0,0,H)$ without any restriction of generality, time-dependent equations in two-band Ginzburg-Landau theory can be written as

$$\Gamma_1\frac{\partial \Psi_1}{\partial t} = -\frac{\hbar^2}{4m_1}(\frac{d^2}{dx^2} - \frac{x^2}{l_s^4})\Psi_1 + \alpha_1(T)\Psi_1 + \varepsilon\Psi_2 + \varepsilon_1(\frac{d^2}{dx^2} - \frac{x^2}{l_s^4})\Psi_2 + \beta_1\Psi_1^3 = 0 \quad (5a)$$

$$\Gamma_2\frac{\partial \Psi_2}{\partial t} = -\frac{\hbar^2}{4m_2}(\frac{d^2}{dx^2} - \frac{x^2}{l_s^4})\Psi_2 + \alpha_2(T)\Psi_2 + \varepsilon\Psi_1 + \varepsilon_1(\frac{d^2}{dx^2} - \frac{x^2}{l_s^4})\Psi_1 + \beta_2\Psi_2^3 = 0 \quad (5b)$$

$$\sigma_n(\frac{\partial \vec{A}}{\partial t} - \nabla\phi) = -rot\vec{A} + \frac{2\pi}{\Phi_0}\{\ \frac{\hbar^2}{4m_1}n_1(T)(\frac{d\varphi_1}{dr} - \frac{2\pi A}{\Phi_0}) + \varepsilon_1(n_1(T)n_2(T))^{0.5}\cos(\varphi_1 - \varphi_2) + \frac{\hbar^2}{4m_2}n_2(T)(\frac{d\varphi_2}{dr} - \frac{2\pi A}{\Phi_0})\ \} \quad (5c)$$

where $l_s^{-2} = \frac{\hbar c}{2eH}$ is the so-called magnetic length. In the general case, the signs of the parameters of interband interaction in Eq. (3) can be arbitrary. These signs of coefficients ε and ε_1 are determined by the microscopic nature of the interaction of electrons belonging to different bands. If ε and ε_1 is zero, the inter-band interaction vanishes, Eqs. (5a) and (5b) convert into the usual GL equations with the critical temperatures T_{c1} and T_{c2}. In Eqs. (5); $\phi_{1,2}(\vec{r})$ phase of order parameters $\Psi_{1,2}(\vec{r}) = |\Psi_{1,2}|\exp(i\phi_{1,2})$, $n_{1,2}(T) = 2|\Psi_{1,2}|^2$ -density of superconducting electrons in different bands, expressions for whichs are presented in [12–15]. Natural boundary conditions to Eqs. (5) has a form:

$$\{\frac{1}{4m_1}(\nabla - \frac{2\pi i\vec{A}}{\Phi_0})\Psi_1 + \varepsilon_1(\nabla - \frac{2\pi i\vec{A}}{\Phi_0})\Psi_2\ \}\vec{n} = 0\ , \quad (6a)$$

$$\{\frac{1}{4m_2}(\nabla - \frac{2\pi i\vec{A}}{\Phi_0})\Psi_2 + \varepsilon_1(\nabla - \frac{2\pi i\vec{A}}{\Phi_0})\Psi_1\ \}\vec{n} = 0\ , \quad (6b)$$

$$(\vec{n}\times\vec{A})\times\vec{n} = \vec{H}_0\times\vec{n} \quad (6c)$$

First two conditions correspond to absence of supercurrent through boundary of two-band superconductor, third conditions correspond to the contiunity of normal component of magnetic field to the boundary superconductor-vacuum.

As shown in [12–15], temperature dependence of some physical quantities becomes nonlinear in contrast to single-band G-L theory. It means that dynamics of order parameters in two-band superconductors differs from those of in single-band superconductors. In this study we introduce unconventional scales to non-dimensionalize the time-dependent two-band G-L system of equations. We focus mostly on experiments performed with two-band time-dependent GL system, and claim that our model yields realistic results for recently discovered compound MgB_2.

III. APPLICATION OF TD TB GL EQUATIONS TO THIN SUPERCONDUCTING FILM

In this part we present some computational results and investigate the properties and dynamics of the 2B-TDGL model in response to an applied magnetic field and/or an applied current under various Ginzburg-Landau (GL) parameter settings. In particular, we will focus our study on the following two-dimensional simulation topics: steady-state vortex lattices under the effect of a steady applied magnetic field. This includes cases involving samples consisting of Type-I/Type-II and Type-II/Type-II condensates, with two distinct critical temperatures.

We will present the results of many simulations and show that the composite and noncomposite lattice phenomena mentioned above appear only with special combinations of values of the coupling parameter ε , ε_1 and the applied field *He*; different phenomena appear in other combinations of the values of ε , ε_1 and *He.* We consider a finite homogeneous superconducting film of uniform thickness, subject to a constant magnetic field. We also consider that the superconductor is rectangular in shape. In this case our two-band GL model becomes two-dimensional [17]. The order parameters Ψ_1 and Ψ_2 varies in the plane of the film, and vector potential **A** has only two nonzero components, which lie in the plane of the film.

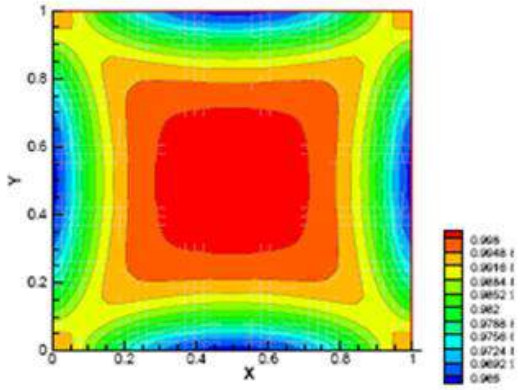

Fig.1a) $\Psi_1;\ \varepsilon=\varepsilon_1=0, H_e=1$

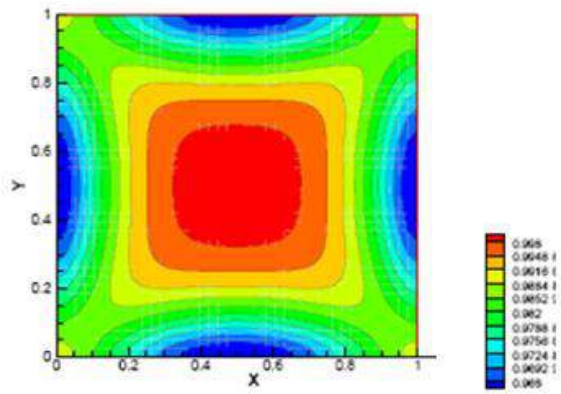

Fig.1b) $\Psi_2;\ \varepsilon=\varepsilon_1=0, H_e=1$

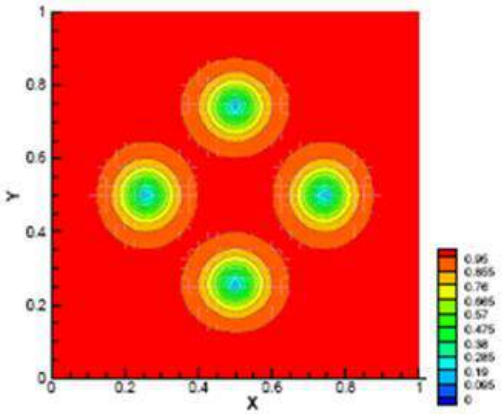

Fig. 2a) $\Psi_1;\ \varepsilon=\varepsilon_1=0, H_e=1.8$

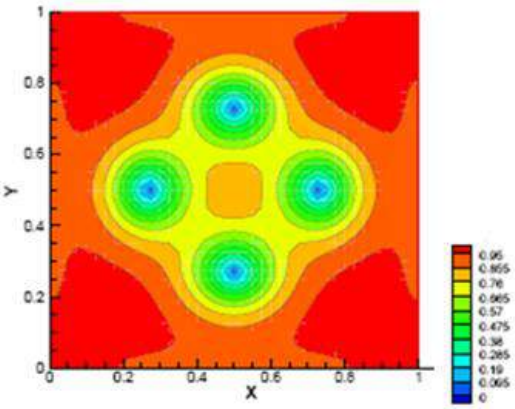

Fig. 2b) $\Psi_2;\ \varepsilon=\varepsilon_1=0, H_e=1.8$

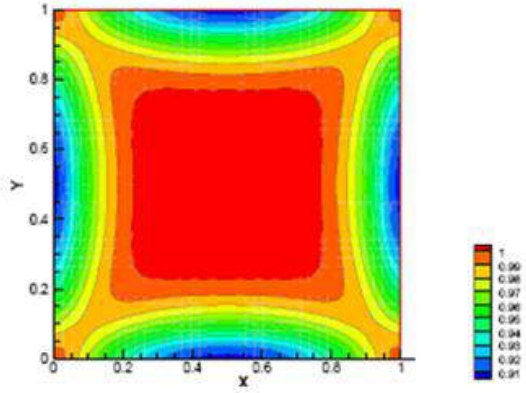

Fig.3a) $\Psi_1;\ \varepsilon^2=3/8;\eta=-0.016, H_e=1$

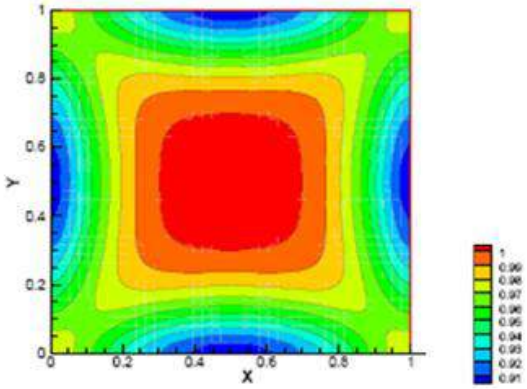

Fig. 3b) $\Psi_2;\ \varepsilon^2=3/8;\eta=-0.016, H_e=1$

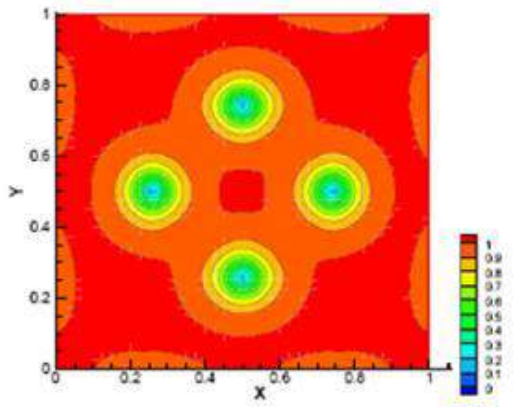

Fig.4a) $\Psi_1;\ \varepsilon^2=3/8;\eta=-0.016, H_e=1.8$

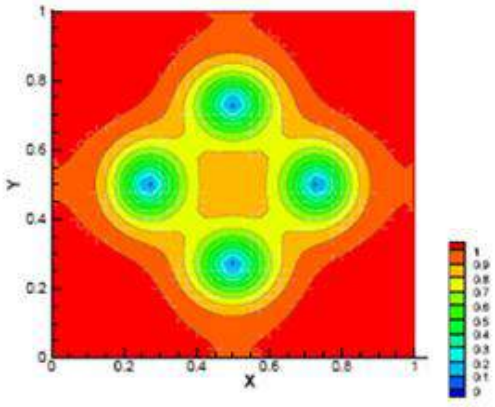

Fig. 4b) $\Psi_2;\varepsilon^2=3/8;\eta=-0.016, H_e=1.8$

Therefore, we identify the compuational domain of the superconductor with a rectangular region $\Omega \in \square^2$, denoting the Cartesian coordinates by *x* and *y*, and the *x*- and *y*- components of the vector potential by *A(x,y)* and *B(x,y)*, recpectively. Before modeling we use so-called bond variables [17] for the discretization of time-dependent two-band G-L equations

$$W(x,y) = \exp(i\kappa \int^{x} A(\zeta, y) d\zeta), \quad (7a)$$

$$V(x,y) = \exp(i\kappa \int^{y} B(x,\eta) d\eta). \quad (7b)$$

Such variables make obtained discretized equations gauge-invariant. For spatially discetization we use forward Euler method [18]. In this method we begin with partitioning the computational domain $\Omega = \left[0, N_{xp}\right] \times \left[0, N_{yp}\right]$ into two subdomains, denoted by Ω_{2n} and Ω_{2n+1} such that

$$\Omega_{2n} = \Omega \mid_{i+j=2n} \text{ and } \Omega_{2n+1} = \Omega \mid_{i+j=2n+1} \quad (8)$$

for $i = 0,.....; N_{xp}, j = 0,.....; N_{yp}$, where $N_{xp} = N_x + 1,\ N_{yp} = N_y + 1$.

For numerical calculations in two-band GL theory we assume that the size of superconducting film is $40\lambda \times 40\lambda$, where λ London penetration depth of external magnetic field on superconductor [12–15]:

$$\lambda^{-2}(T) = \frac{4\pi e^2}{c^2}\left(\frac{n_1(T)}{m_1} + 2\varepsilon_1 (n_1(T) n_2(T))^{0.5} + \frac{n_2(T)}{m_2}\right) \quad (9)$$

Under modeling we also introduce another dimensionless parameters

$$\vec{r}' = \frac{\vec{r}}{\lambda}; \Psi'_{1,2} = \frac{\Psi_{1,2}}{\Psi_{(1,2)0}}; \vec{A} = \frac{\vec{A}}{\lambda H_c \sqrt{2}};$$
$$F'(\Psi'_{1,2}, A') = \frac{F(\Psi_{1,2}, A)}{\alpha_0^2 \left|\Psi_{1,0}\right|^2 + \alpha_1^2 \left|\Psi_{2,0}\right|^2} \quad (10)$$

Expressions for $\Psi_{(1,2)0}$, and for thermodynamic magnetic field H_c are presented in [12–15]. The calculations were performed for the following values of parameters: T_c = 40 K; T_{c1} =20.0 K;T_{c2} = 10 K, $\frac{\varepsilon^2}{\gamma_1 \gamma_2 T_c^2} = 3/8$; $\eta = \frac{T_c m_2 \varepsilon_1 \gamma_2}{\hbar^2 \varepsilon} = -0.016$. This parameters was used for the calculation another physical properties of two-band superconductor MgB_2 [12–15]. External magnetic field measured in units of thermodynamic magnetic field H_c.

For solving of corresponding discretized GL equations we will use method of adaptive grid [18]. Results of numerical modelling in different cases presented in Fig. 1-4. In figures 1-2 we present profile of the order parameters Ψ_1 and Ψ_2 in the absence of interaction. Figure 1 correspond to the nucleation of magnetic field to superconductor. In Figure 2 we plot order parameter profile in more high magnetic field, at which arises nucleation of four vortex. The case of inter order parameter interaction and drag effects (intergradient interaction) presented in Figures 3-4. As followed from this calculations, due to interband interaction, order parameters in different bands becomes more strong and as result distance between vortexes increased. Also, it is clear that in initial stage of penetration of magnetic field into two-band superconductor, the symmetry of Abrikosov vortex lattices has a square character. Similar square lattice was observed experimentally in $LuNi_2B_2C$ compound in [2]. Also it is clear that, magnetic field penetrate into two-band superconductor by lateral way. İt is neccessary to note, that external magnetic field penetrate to two-band superconductor is differ from those in single-band superconductor. At high magnetic field, when distance between vortexes is small, we must take into account nonuniform distribution of magnetic field in cross-section of single vortex [19]. Detail analysis of vortex lattices at high magnetic field is the subject of future investigations.

IV. CONCLUSIONS

In this study we obtain time-dependent GL equations taking into account two-band character of the superconducting state. which was originally developed by Schmid for single band superconductors. Furthermore, we perform numerical modeling of vortex nucleation in external magnetic field in two-band superconducting films MgB_2 using two-band Ginzburg-Landau theory.

ACKNOWLEDGMENT

This work partially supported by CNRS-ANAS (2009) project (UNR 5798) .

[1]. *J. Nagamatsu, N. Nakagava, T. Muranaka, et al* Nature. 410,63(2001)
[2]. *C. Buzea , T.Yamashita* , Supercond. Sci. Techn. 14,R115(2001)
[3]. *A. Gurevich, V.M.Vinokur*, Phys. Rev. Lett. 90, 047004 (2003)
[4]. *D.R. Tilley*, Proc. Phys. Soc. of London, 86, 286 (1965)
[5]. *A.E. Koshelev, A.A. Golubov*, Phys Rev Lett 92, 107008 (2004)
[6]. *M. Doria, et al* Phys Rev B 41,6335(1990)
[7]. *Q. Du, et al* SIAM J. appl. Math, 53, 689(1993)

[8]. *M.Machida, et al*,Phys. Rev.Lett., 71, 3206 (1993)
[9]. *A.J. Berlinsky et al,* Phys. Rev.Lett. 75,2200(1995)
[10]. *A.I. Larkin, A.A. Varlamov*, Oxford Press, Theory of fluctuations in superconductors, (2007)
[11]. *L. Aslamazov, A.I.Larkin*, Sov.Phys.Solid State, 10, 1104(1968)
[12]. *I. N. Askerzade, A.Gencer et al* , Supercond. Sci. Technol. 15, L13(2002).
[13]. *I. N. Askerzade,* Physica C 390, 281 (2003).
[14]. *I. N. Askerzade,* JETP Letters 81, 583 (2005).
[15]. *I. N. Askerzade,* Physics Uspekhi 49, 1003 (2006).
[16]. *A. Shcmid*, Phys. Kondens. Matter,v.5, p.302(1966)
[17]. *M.K. Kwong, H.G. Kaper*, J.Comput. Phys. v.119. p.120(1995).
[18]. *J.F.Thompson, Z.U. A. Warsi and C.W. Martin,* Numerical Grid Generation, Elsevier. New York(1985).
[19]. *I.N.Askerzade,B.Tanatar*, Communications in Theoretical Physics, 51, 563(2009)

A NUMERICAL STUDY ON CARRIER DENSITY AND MOBILITY OF GaN AND InGaN WELLS IN AlInN/AlN/(In)GaN/GaN HEMT STRUCTURES

K. ELİBOL, P. TAŞLI, G. ATMACA, S.B. LİŞESİVDİN, M. KASAP, T.S. MAMMADOV, S. ÖZÇELİK

Gazi University Physics Department
06500 Teknikokullar,Ankara, TURKEY

This study predicts and describes the formation of two dimensional electron gas (2DEG) in III-nitride based heterostructures, as a promising candidate for future high performance high electron mobility transistor (HEMT). Indium mole fraction of the AlInN barrier layer, the Indium mole fraction and appropriate layer thickness for InGaN layer have been determined.The carrier densities in GaN well have been compared with the carrier densities in InGaN well. Electronic properties such as electron densities and energies of subband, electron probability densities are calculated by solving non-linear Schrödinger-Poisson equations, self-consistently including polarization induced carriers.

I. INTRODUCTION

The III-nitride semiconductors have extracted intense interest for electronic and optoelectronic device applications[1-3]. The large polarization charge densities present at III-nitride heterojunction interfaces profoundly influence electric field and mobile carrier distributions, necessitating their incorporation into device design and analysis and providing opportunities for device engineering [4,5]. There is a tremendous upsurge of effort for investigating AlGaN/GaN-based transistor structures [6,7]. Alternatively, the incorporation of In with the minor molar fraction (less than 0.2) into AlGaN was suggested to reduce the strain and affect two-dimensional electron gas (2DEG) characteristics at the AlInGaN/GaN heterointerface [8]. However, only a few reports are devoted to AlInN [9,10] and, to our knowledge, no experimental work is focused on AlInN/(In)GaN QWs for HEMTs. Only recently a HEMT structure based on InAlN/(In)GaN has been proposed [11]. Record power capabilities were predicted for these new types of device.

In the present study, we theoretically explore the effects of the In-mole fraction (x) of $Al_{1-x}In_xN$ layers and InGaN layer and the layer thicknesses of some layers on the carrier densities and electron probability densities in normally-on AlInN/AlN/(In)GaN/GaN-based structures. Investigations were carried out by solving Schrödinger-Poisson equations, self-consistently including polarization induced carriers was calculated using *nextnano*[3] device simulation package for wurtzite [0001] growth axis [12]. The strain relaxation limits were also calculated with simple critical thickness calculation approach [13].

II. COMPUTATIONAL METHOD

Simulation procedure begins with a strain calculation with homogeneous strain dispersion over the simulated region. For the 0001 growth axis wurtzite structure, the off-diagonal strain components are all accepted as zero. For the 0001 growth axis wurtzite structure, diagonal strain components (ε_1, ε_2, ε_3) are related with each other and can be easily calculated from the lattice parameters of the related layers as follows [14]:

$$\varepsilon_1 = \varepsilon_2 = \frac{a_{bottom} - a_{upper}}{a_{upper}}$$

$$\varepsilon_3 = -(C_{13}/C_{33})\varepsilon_1$$

Here, C_{11} and C_{33} are the elastic constants, a_{Bottom} and a_{Upper} are the lattice parameters of the bottom and related upper layers, respectively. ε_1 and ε_2 are called bi-axial strain, ε_3 is called uni-axial strain and it is perpendicular to interface. This is important because the strain in epitaxial layers of group III nitride heterostructures grown along the *c*-axis ([0001]-axis) caused by mismatch of the lattice constants *a* and/or a mismatch of the thermal expansion coefficients of layer and substrate is directed along the basal plane (parallel to the substrate). No force is applied in the growth direction and the crystal can relax freely in this direction. The resulting biaxial strain (ε_1 = ε_2) causes stresses $\sigma_1 = \sigma_2$, whereas σ_3 has to be zero.

For a top/bottom AlInN/GaN or GaN/AlInN heterojunction, the polarization induced charge density is taken as [15]:

$$\sigma = \left[P_{PE}(bottom) - (P_{PE}(top)\right] + \left[P_{SP}(bottom) - P_{SP}(top)\right]$$

The piezoelectric polarization along the c-axis is linearly dependent on the relative change of the lattice constants and the elastic constants for piezoelectric polarization depends on strain. After strain calculation, the band edges are calculated by taking full account of the van-de-Walle model and strain. The piezoelectric polarization as a function of strain can be written as [16]:

$$P_k^{pz} = \sum_l e_{kl}\varepsilon_l \qquad \text{, where } k = 1,2,3,\ l = 1,\ldots,6.$$

Here, e_{kl} is the piezoelectric constants. The non-vanishing component of the piezoelectric polarization caused by biaxial strain is [16]:

$$P^{PE} = 2\varepsilon_1\left\{e_{31} - e_{33}\frac{C_{13}}{C_{33}}\right\} \quad (\mathrm{C/m^2})$$

In analogy to the determination of piezoelectric polarization along the c-axis in dependence of biaxial strain. For the spontaneous polarization of $Al_xIn_{(1-x)}N$ layers, following formula is used [16]:

$$P^{SP}{}_{AlInN}(x) = xP^{SP}{}_{AlN} + (1-x)P^{SP}{}_{InN} + bx(1-x)$$

Here, b is bowing parameter and the bowing parameter of P^{SP}_{AlInN} as a function of *x* is 0.07. The spatial variation of total polarization, induced by internal strain of ternary alloys related to size mismatch of the two alloyed group-III-nitrides, leads to polarization induced carriers. The calculated spontaneous polarization (P^{SP}) and the piezoelectric polarization of the related layers, polarization induced charge densities are calculated.

For a AlInN/GaN heterojunction, the piezoelectric and spontoneous polarization induced is taken as [14]:

$$P^{SP}{}_{AlInN}(x) = -0.090x - 0.042(1-x) + 0.070x(1-x)\ C\ m^{-2}$$

$$P^{PZ}{}_{AlInN/GaN}(x) = \left[-0.0525x + 0.148(1-x) + 0.0938x(1-x)\right] C\ m^{-2}$$

$$P^{PZ}{}_{AlInN/AlN}(x) = \left[0.182(1-x) + 0.092x(1-x)\right]\ C\ m^{-2}$$

The material parameters i.e. lattice parameters, spontaneous polarization, piezoelectric and elastic constant values of AlN, InN and GaN are listed in Table 1 [14,18,19,20].

Table 1. Lattice parameters, elastic constants, piezoelectric constants and spontaneous polarization values of GaN, AlN and InN materials [14,17-19]

Parameter	GaN	AlN	InN
a(nm)	0.3189	0.3112	0.3545
e_{31} (C/m^2)	-0.35	-0.50	-0.57
e_{33} (C/m^2)	1.27	1.79	0.97
C_{13}(GPa)	106	108	92
C_{33}(GPa)	398	373	224
P_{SP}(C/m^2)	-0.034	-0.090	-0.042

The ground state of such a 2D system can be described simply if there are no defects apart from the donor atoms. Residual impurities are accounted as a uniform doping in the epilayers. Taking into account the polarization effects, the band edges of the HEMTs being studied as well as the sheet concentration of 2DEG can be obtained from the differential equation:

$$\left[-\frac{\hbar^2}{2}\frac{d}{dz}\frac{1}{m^*(z)}\frac{d}{dz} + V(z) - \varepsilon_\nu(k_z)\right]\phi_{\nu,k_z(z)} = 0$$

where z is the growth direction, $m^*(z)$ is the electron effective mass at the bottom of the Γ valley, ν is the subband index, k_z is the vector momentum parallel to the z-direction and V(z) represents the total potential energy. In the last step of simulation, Schrödinger's equation and Poisson's equation are both solved self-consistently in order to obtain the carrier distribution, wave functions, and related eigenenergies.

The conduction band structures, electron densities and wave functions of the electrons are calculated for different layer thicknesses and different In-mole fractions. In every case, the strain values are calculated. A simple estimation fort the critical thickness below the strain relaxation limit is given by the relation [20]:

$$t_{cr} \cong \frac{b_e}{2\varepsilon_{xx}}$$

Here, b_e is the Burger's vector with a value of b_e=0.3185 nm [8]. We assume a total homogenous strain over the GaN layers of the each pseudotriangular quantum well, which is calculated with the strain values of every layer over the related GaN layer.

In this letter, we report on a device structure D-mode HEMTs based on a 1-nm lattice-matched InAlN barrier with an additional 1-nm AlN interlayer. The structure is capped with a highly doped n^{++} GaN layer providing a low sheet resistance caused by free electrons in the cap layer and the 2DEG. Investigations were carried out by solving Schrödinger-Poisson equations, self-consistently including polarization induced carriers was calculated using *nextnano*[3] device simulation package [12].

III. RESULTS AND DISCUSSION

The carrier densities have been investigated in 17% Indium mole fraction and 5, 10, 15, 20 and 25 nm the AlInN barrier layer thickness. According to Fig 1, the carrier density is highest while AlInN barrier layer thickness 25nm. Therefore, AlInN barrier layer thickness was found to be 25nm.

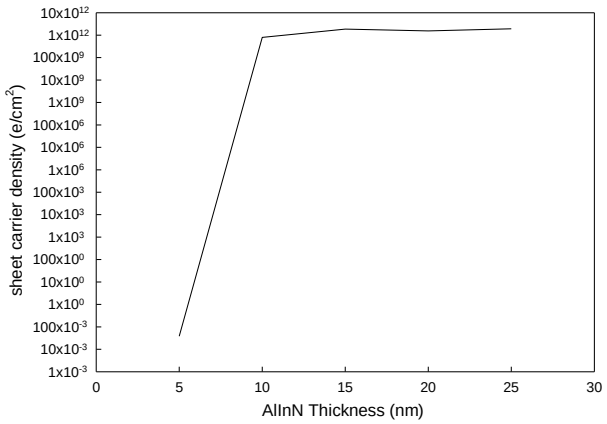

Fig 1. AlInN barrier layer thickness dependence of carrier density.

The effects to 2DEG carrier densities, electron probability densities dependent on In mole fraction in AlInN/AlN/GaN have been investigated. As seen in Fig. 2, we firstly determined appropriate In mole rate and high carrier densities in low In mole rate have been obtained. Indium (In) mole fraction of AlInN barrier must be higher then %15. Because, strain relaxation is seen in In mole fraction smaller than %15. AlInN barrier has high carrier densities in %15, %16, %17 and %18 In mole fractions.

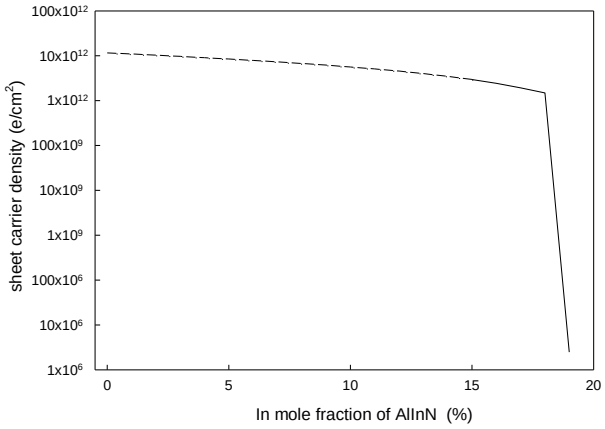

Fig.2. Determined In mole fractions for AlInN barrier with 25nm thickness in GaN quantum well. Dashed lines represent the strain relaxed situation.

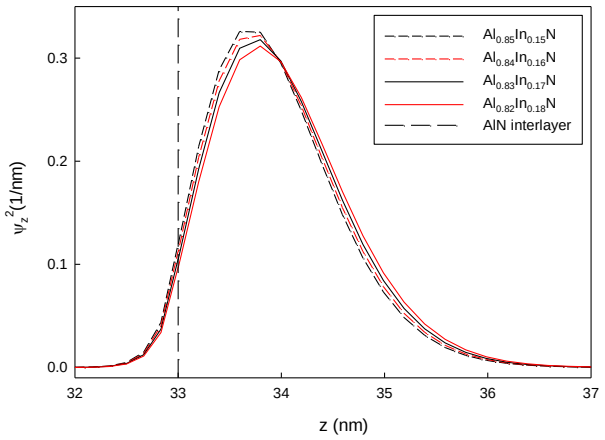

Fig.3. Probability densities of the 2DEG carriers of well for different In-mole fractions in 25nm AlInN barrier thickness.

Fig. 3. shows, probability densities of the 2DEG carriers of well for different In-mole fractions and 25 nm AlInN barrier thickness were determined. Carriers exposed to interface scattering for wave function that leak into AlN interlayer in low In mole fractions of AlInN barrier layer, Impurity scattering is dominant due to carriers is leak to GaN layer for high In mole fractions of AlInN barrier layer. Therefore, In mole fraction of AlInN barrier layer is determined to be 17%. GaN with AlInN is lattice-matched for 17% of In mol fraction in AlInN barrier layer.

While 17% of In mole fraction in AlInN barrier layer, critical thickness of InGaN layer was calculated to be 14.4 nm with Burger's vector method. Here, Burger vector is 0.324nm for InGaN [22]. This, shows can not be used more than 14.4 nm of layer thickness for InGaN layer thickness. InGaN layer thickness is determined to be 10 nm with Fig. 4, higher carrier density and not be strain relaxation in value of this layer thickness.

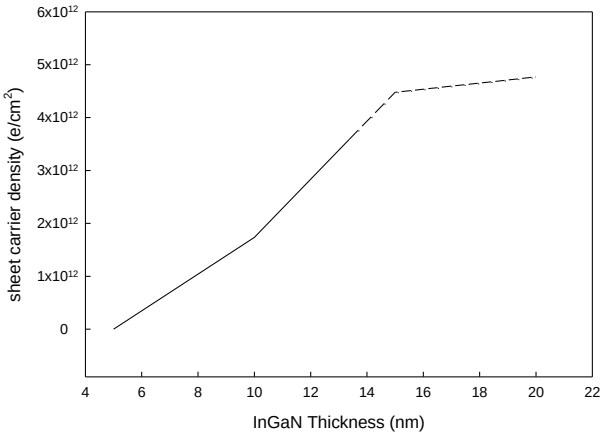

Fig.4. Sheet carrier density in different InGaN thickness for 5, 10, 15, 20 nm. Dashed lines represent the strain relaxed situation.

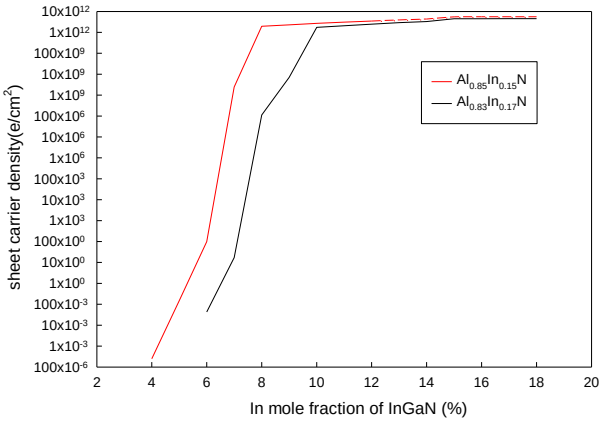

Fig.5. Sheet carrier density for different In mole fractions of InGaN layer in cases $Al_{0.85}In_{0.15}N$ and $Al_{0.83}In_{0.17}N$.

In mole fractions of AlInN barrier layer for InGaN from Fig. 2, is determined as 15% and 17% due to higher carrier density. For this two mole fractions, In containing InGaN quantum well with GaN quantum well are compared according to In mole fraction change of AlInN barrier layer. While 15% of In mole fraction in AlInN barrier layer, the strain relaxation is occurs for later than 12% of In mole fraction of InGaN layer. Carrier density is higher in case 18% In mole fraction of InGaN layer for $Al_{0.83}In_{0.17}N$ barrier layer. Obtained higher in case 12% In mole fraction of InGaN layer for $Al_{0.85}$ $In_{0.15}N$ barrier layer.

Strain relaxation limit for three wells is 15% of In mole fraction in AlInN barrier layer. 2DEG carrier density of the $In_{0.18}Ga_{0.82}N$ layer is higher than that of $In_{0.12}Ga_{0.88}N$ layer. While 18% and 12% of In mole fraction of InGaN layer in Fig (6), higher 2DEG carrier density than that of GaN quantum well. But, alloy scattering in InGaN quantum well is dominant. Therefore, mobility of the GaN quantum well is high than InGaN quantum well. From here, In mole fraction of the InGaN layer is as determined 18%.

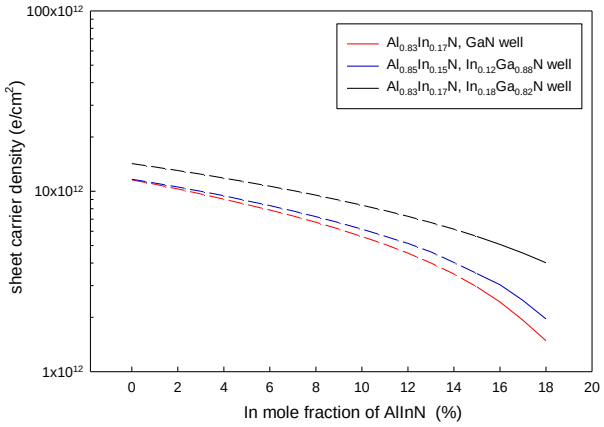

Fig.6. In different In mole fraction change In different wells of sheet carrier density for the AlInN barrier layer . Dashed lines shows the strain relaxation.

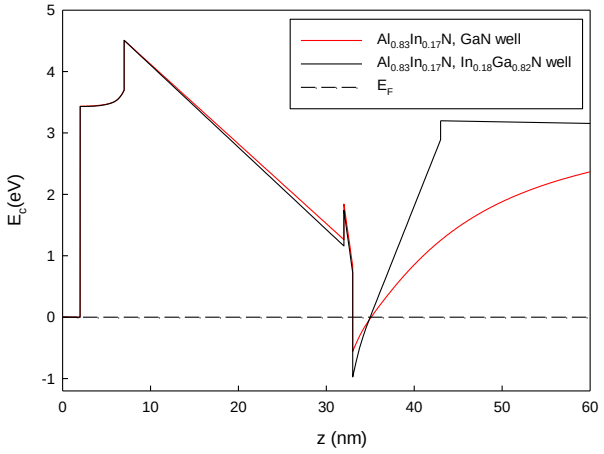

Fig.7. Optimized of the GaN and InGaN wells are band structure.

InGaN quantum wells are deeper than that of GaN quantum well. 2DEG carrier density of the InGaN quantum wells is higher. Also, carriers in InGaN quantum well are more confined than that of GaN quantum well. Therefore, carriers are accumulated more in InGaN quantum well.

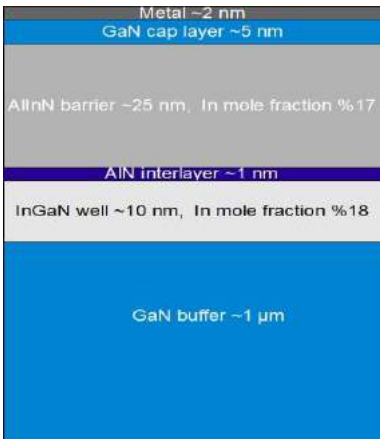

Fig.8. This structure is optimized for high 2DEG carrier density.

IV. CONCLUSIONS

In this study, the effects of Indium mole fractions in InGaN quantum well and $Al_xIn_{1-x}N$ barrier layer on carrier densities and 2DEG wave functions are examined by solving non-linear Schrödinger-Poisson equations, self-consistently including polarization induced carriers in AlInN/AlN/GaN and AlInN/AlN/InGaN/GaN HEMT structures. The carrier densities in GaN well have been compared with the carrier densities in InGaN well. The obtained simulation results in this work are in good agrrement with the previously reported ones.

ACKNOWLEDGEMENTS

This work is supported by the State of Planing Organization of Turkey under Grant No.2001K120590.

[1]. *C.Y. Lai, T.M. Hsu, W-H Chang, K.U.Tseng* Direct measurement of piezoelectric field in In0.23Ga0.77N/GaN multiple quantum wells by electrotransmission spectroscopy. J Appl Phys 2002;91:531–3.

[2]. *K.V. Smith, E.T. Yu, C.R. Elsass, B. Heying, J.S.Speck.* Localized variations in electronic structure of AlGaN/GaN heterostructures grown by molecular-beam epitaxy. Appl Phys Lett 2001;79:2749–51.

[3]. *O. Ambacher, J. Majewski, C. Miskys, A. Link, M.Hermann, M. Eickhoff, et al.* Pyroelectric properties of Al(In)GaN/GaN hetero- and quantum well structures. J Phys Condens Mat 2002;14:3399–434.

[4]. *E.T. Yu, G.J. Sullivan, P.M. Asbeck, C.D. Wang, D. Qiao, S.S. Lau.* Measurement of piezoelectrically induced charge in GaN/AlGaN heterostructure field-effect transistors. Appl Phys Lett 1997;71:2794–6.

[5]. *H. Zhang, E.J. Miller, E.T. Yu, C. Poblenz, J.S.Speck.* Measurement of polarization charge and conduction-band offset at InxGa1_xN/GaN heterojunction interfaces. Appl Phys Lett 2004;84:4644–6.

[6]. *O. Ambacher et al* 2000 J. Appl. Phys. **87** 334

[7]. *H. Morkoc, R. Cingolani and B. Gil* 1999 Solid-State Electron.**43** 1909

[8]. *A.M. Khan et al* 2000 Appl. Phys. Lett. **76** 1161

[9]. *K.S. Kim, A. Saxler, P. Kung and M.Razeghi* 1997 Appl. Phys.Lett. **71** 800

[10]. *M. Kariya, S. Nitta, S. Yamaguchi, H. Amano and I. Akasaki* 1999 Japan. J. Appl. Phys. **38** L984

[11]. *J. Kuzm´ık* 2001 IEEE Electron Device Lett. **22** 510

[12]. *S.B. Lisesivdin, A. Yildiz, S. Acar, M. Kasap, S.Ozcelik and E. Ozbay* 2007 Appl. Phys. Lett. **91** 102113

[13]. *P.M. Asbeck, E.T. Yu, S.S. Lau, G.J. Sullivan, van J. Hove and J. Redwing* 1997 Electron. Lett. **33** 1230

[14]. *O. Ambacher, J. Majewski, C. Miskys, A. Link, M.Hermann, M. Eickhoff, M. Stutzmann, F.Bernardini, V. Fiorentini, V. Tilak, B. Schaff, L.F. Eastman*, J. Phys.: Conden. Matter 14, 3399 (2002).

[15]. *O.Ambacher, B. Foutz, J. Smart, J. R. Shealy, N.G. Weimann, K. Chu, M. Murphy, A.J.Sierakowski, W. J. Schaff, L. F. Eastman, R.Dimitrov, A. Mitchell, M. Stutzmann*, J. Appl. Phys. 87, 334, (2002).

[16]. *C. Wood, D. Jena*, "Polarization Effects in Semiconductors" Springer+Business Media, New York, (2008).

[17]. *I. Vurgaftman, J.R. Meyer, L. R. Ram-Mohan*, J. Appl. Phys. 89, 5815, (2001).

[18]. *I. Vurgaftman, J.R. Meyer*, J. Appl. Phys. 96, 3675, (2003).

[19]. *H. Morkoç* "Nitride Semiconductors and Devices" Springer-Verlag, Berlin Heidelberg (1999).

[20]. *M. Gonscherek, J. –F. Carlin, E. Feltin, M. A. Py, N. Grandjean, V. Darakchieva, B. Monamer, M. Lorenz, and G. Ramm*, J.Appl.Phys. 103, 093714 (2008).

[21]. *J. Sing*, "Physics of Semiconductors and Their Heterostructures" McGraw-Hill, New York, (1992),p.734.

[22]. *M. Leyer, J.Stellmach, Ch.Meissner, M.Pristovsek, M.Kneissl* "The critical thickness of InGaN on (0 0 01) GaN" Journal of Crystal Growth 310, 4913–4915 (2008).

PHYSICOCHEMICAL AND THERMODYNAMIC PROPERTIES OF THE $GeSe_2$–A^2B^6 (A^2 = Hg; Cd; B^6 = S, Te) SYSTEMS

M.M. ASADOV, A.D. MIRZOEV

Institute of Chemical Problems, National Academy of Sciences of Azerbaijan,
H.Javid Pr. 29, AZ 1143 Baku, Azerbaijan
E-mail: mirasadov@gmail.com

The phase diagrams of $GeSe_2$–A^2B^6 (A^2 = Hg; Cd; B^6 = S, Te) systems were plotted by the methods of differential thermal and X-ray diffraction analyses, by the measurement of electromotive force (emf), microhardness and density. It is established, that phase equilibriums in the pseudo-binary $GeSe_2$ – CdTe, $GeSe_2$ – HgTe, $GeSe_2$ – HgS, $GeSe_2$ – CdS systems are characterized by formation of the limited solid solutions on basis of basic components and fourfold intermediate phases such as $A_2GeSe_2Te_2$ and $A_4GeS_4Se_2$: $Cd_2GeSe_2Te_2$ (hexagonal system; a = 5.69; c = 11.32 Å), $Cd_4GeS_4Se_2$, $Hg_2GeSe_2Te_2$ (tetragonal system; a = 7.50; c = 36.48 Å), $Hg_2GeS_2Se_2$ (hexagonal system; a = 7.20; c = 36.64 Å), $Hg_4GeS_4Se_2$ (monoclinic system; a = 12.38; b = 7.14; c = 12.40 Å). New dependences of the important physicochemical properties of solid solutions on basis of the $GeSe_2$ crosscuts of $GeSe_2$–A^2B^6 (A^2 = Hg; Cd; B^6 = S, Te) on composition are obtained. Thermodynamic characteristics of $Cd_2GeSe_2Te_2$ and $Hg_2GeSe_2Te_2$ phases were determined.

I. INTRODUCTION

Chalcogen compounds with more electropositive chemical elements are semiconductor materials. Among these materials A^2B^6 compounds possess unique physical properties [1–3]. Chalcogenids usually are receive ed by interaction of metal and chalcogen at heating in sealed and evacuated quartz ampoules. Sulfide HgS exists in two modifications α (zinnober) and β (metazinobarit). Temperature of transition $\alpha \leftrightarrow \beta$ is 345 °C. Compounds β-HgS, HgSe, and HgTe crystallize in a lattice of type blende. HgTe has practically zero forbidden zone. Degree of overlaps of a valent zone and a zone of conductivity for HgTe is 0.001 eV, for HgSe this is 0.07 eV. For α-HgS width of the forbidden zone is 2.0 eV. HgS is a material for photoresistors, a component of light composition on basis CdS. HgSe is used as a material for photoresistors, gauges of measurement of magnetic fields. Selenides are used as laser materials, as components for luminophores and thermoelectric materials. HgTe is a component of materials for receiver's of infra-red and X-ray radiation. Tellurides are used for photo cells, photosensitive layers of electron beam devices, dosimeters. $GeSe_2$ also is the semiconductor with width of the forbidden zone equal to 2.49 eV ($\rho = 10^{12}$ Ω·cm).

Stability of the pseudo-binary $GeSe_2$–CdTe, $GeSe_2$–HgTe, $GeSe_2$–HgS, $GeSe_2$–CdS systems is confirmed by methods of samples' physicochemical analysis and the measurement of electromotive force (e.m.f.) [4,5].

II. EXPERIMENTAL DETAILS

Synthesis of initial binary compounds of the $GeSe_2$–A^2B^6 crosscuts has been carried out by direct fusion of high-purity components taken in stoichiometric ratio, in evacuated up to 10^{-3} MPa quartz ampoules in electric furnace within two days. The heating of ampoules with substances has been gradually carrying out in the furnace up to the fusion temperature of corresponding binary compounds in connection with behavior of exothermic reactions of germanium, cadmium and mercury chalcogenides' formation. At temperatures of chemical reactions' behavior of binary chalcogenides' formation ampoules were being exposed during 4–6 hours [4]. Then temperature in the furnace has been smoothly increasing up to the fusion temperature of corresponding formed binary compound. During production of the $GeSe_2$, CdTe, HgTe and HgS compounds the exposure was made at 740, 1092, 670 and 820 °C correspondingly. The individuality of the obtained $GeSe_2$, CdTe, HgTe and HgS chalcogenide compounds has been controlled by methods of the physicochemical analysis by comparison of the obtained for them characteristics to the reference data.

With the purpose of definition of important parameters of intermediate phases and limited solid solutions of the threefold mutual Cd (Hg), Ge || S (Se), Te systems we investigated physicochemical and thermodynamic properties of the pseudo-binary $GeSe_2$–CdTe, $GeSe_2$–HgTe, $GeSe_2$–HgS, $GeSe_2$–CdS systems.

It is known, that using the e.m.f. measurement method [6,7,8] in establishing phase limits binary systems lies in that the potentials of the one-phase alloy electrodes at a fixed temperature, decrease with increasing content of the less noble component in the alloy whereas the potentials of the two-phase alloy electrodes, are constant and independent of composition within a two-phase region. The potentials vary, however, when passing from one-phase region to another. The temperature dependence of the e.m.f. shows a linear character if no phase transition occurs. When within the temperature range applied to the e.m.f. measurements a phase transition occurs in the alloy electrode, the temperature coefficient of the e.m.f. below and above the transition point will take different values.

An e.m.f. method with a liquid electrolyte is used to determine the partial molar thermodynamic properties of Cd in $GeSe_2$–CdTe and Ge in $GeSe_2$–HgTe quaternary solid alloys. The temperature range for the measurement at 298 and 380 K. The cell arrangement is as follows

Cd (s) / Cd^{2+} (KCl–LiCl) / $GeSe_2$–CdTe (s)
Ge (s) / Ge^{2+} (KCl–LiCl) / $GeSe_2$–HgTe (s)

Under reversible conditions the Gibbs free energy change for the reaction at temperature T is given by

$$\Delta\overline{G}_{Me} = -zFE \qquad (1)$$

were $z = 2$, *Me* = Cd, Ge, *F* the Faraday constant (96486 C mol^{-1}), *E* the measured electromotive force of the cell (V).

III. RESULTS AND DISCUSSIONS

The phase diagrams of the pseudo-binary $GeSe_2$–A^2B^6 (A^2 = Hg; Cd; B^6 = S, Te) systems were plotted by the methods of differential thermal and X-ray diffraction analyses, by the measurement of electromotive force (e.m.f.), microhardness and density. It was established, that in the $GeSe_2$–CdTe (Fig. 1), $GeSe_2$–HgTe (Fig. 2), $GeSe_2$–HgS, $GeSe_2$–CdS systems phase equilibriums are characterized by formation of limited solid solutions on basis of $GeSe_2$ and A^2B^6 components (Table 1) and quaternary intermediate phases such as $A_2GeSe_2Te_2$.

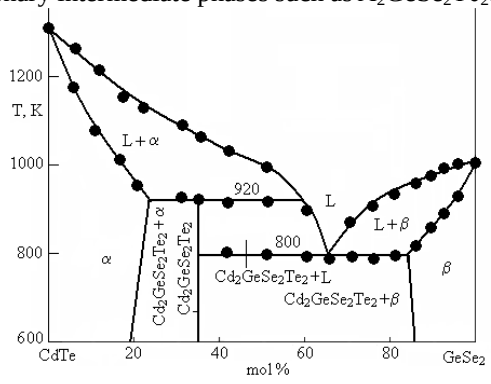

Fig. 1. Phase diagram of the CdTe–$GeSe_2$ system.

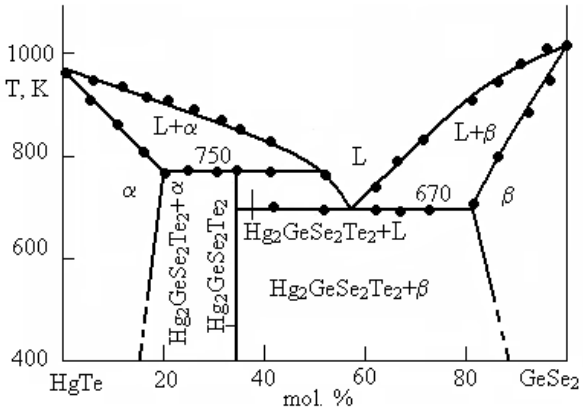

Fig. 2. Phase diagram of the HgTe–$GeSe_2$ system.

In these systems intermediate phases of $A_2GeSe_2Te_2$ composition are forming at temperatures 477°C ($Hg_2GeSe_2Te_2$; tetragonal system; $a = 7.50$; $c = 36.48$ Å), 647°C ($Cd_2GeSe_2Te_2$; hexagonal system; $a = 5.69$; $c = 11.32$ Å), 707°C ($Hg_2GeSe_2S_2$; hexagonal system; $a = 7.20$; $c = 36.64$ Å) accordingly. In $GeSe_2$–HgS system at 862°C, the $Hg_4GeSe_2S_4$ intermediate phase (monoclinic system; $a = 12.38$; $b = 7.14$; $c = 12.40$ Å) is also forming. All obtained fourfold compounds are to fuse incongruently.

Dependences of solid solutions' properties on a structure have been determined. Samples were annealed at high temperatures (on 5–10°C lower than eutectic temperature). In the Tables 2–4 concentration dependences of alloys-solid solutions on $GeSe_2$ basis with a rhombic lattice are resulted.

Table 1

Areas of solid solutions in the systems such as $GeSe_2$ – HgS and $GeSe_2$ – HgTe

Systems	Solubility, mol %	
	On $GeSe_2$ basis	On HgS (HgTe) basis
$GeSe_2$–HgS $GeSe_2$–HgTe $GeSe_2$–CdTe	18 mol% HgS (600 °C) 20 mol% HgTe (477 °C) 16 mol% CdTe (647 °C)	5 mol% $GeSe_2$ (600 °C) 20 mol% $GeSe_2$ (477 °C) 22 mol% $GeSe_2$ (647 °C)

Table 2

Physicochemical properties of the $(GeSe_2)_{1-x}$– $(CdTe)_x$ solid solutions

Composition, Mol % CdTe	Structure parameters of a lattice			Microhardness, MPa	Density, q/sm^3
	a/Å	*b*/Å	*c*/Å		
0.0	7.037	11.82	16.82	1400	4.68
2.5	7.040	11.83	16.82	1400	4.69
2.5	7.045	11.84	16.84	1420	4.70
2.5	7.050	11.84	16.84	1440	4.72
2.5	7.054	11.86	16.87	1470	4.72
2.5	7.060	11.86	16.88	1500	4.74
2.5	7.066	11.90	16.90	1510	4.76

Table 3

Physicochemical properties of the $(GeSe_2)_{1-x}$ – $(HgTe)_x$ solid solutions

Composition, Mol % HgTe	Structure parameters of a lattice			Microhardness, MPa	Density, q/sm^3
	a/Å	*b*/Å	*c*/Å		
0.0	7.037	11.82	16.82	1400	4.68
2.0	7.040	11.83	16.82	1400	4.70
3.0	7.038	11.84	16.84	1420	4.70
5.0	7.037	11.81	16.82	1450	4.72
6.0	7.035	11.81	16.80	1460	4.73
7.0	7.032	11.80	16.80	1470	4.75
8.0	7.030	11.80	16.78	1470	4.76
9.0	7.030	11.78	16.75	1480	4.79
10	7.284	11.76	16.72	1480	4.80

Table 4

Physicochemical properties of the $(GeSe_2)_{1-x}$ – $(HgS)_x$ solid solutions

Composition, Mol % HgTe	Structure parameters of a lattice			Microhardness, MPa	Density, q/sm^3
	a/Å	*b*/Å	*c*/Å		
0.0	7.037	11.82	16.82	1400	4.68
2.0	7.037	11.82	16.80	1400	4.70
3.0	7.030	11.81	16.78	1420	4.72
5.0	7.024	11.79	16.76	1450	4.83
7.5	7.020	11.77	16.74	1480	4.90
10	7.012	11.74	16.76	1500	5.06

It is established, that formation of solid solutions on A^2B^6 basis in the $GeSe_2$–A^2B^6 systems is accompanied by an appreciable negative deviation from the Raoult law. For concentration dependences of solid solutions on A^2B^6 basis the following relation don't meet the conditions: $p_{A^2B^6} = x_{A^2B^6} p^*_{A^2B^6}$, where $p^*_{A^2B^6}$ is the steam pressure of pure A^2B^6. For the $(GeSe_2)_{1-x}$–$(A^2B^6)_x$ solid solutions the appreciable deviation from the Raoult law don't appear.

The thermodynamic analysis of chemical reactions has been carrying out with use of Gibbs-Duhem equation. For conditions of $\sum_i \nu_i d\mu_i = 0$ equilibrium which binds the change of chemical potential of components of system at *T = const, p = const.* For simplicity let's consider a $A \leftrightarrow B$ reaction. Then change of Gibbs function is: $dG = \mu_A d\nu_A + \mu_B d\nu_B$. Let's assume, that the infinitesimal $d\xi$ amount of matter *A* turns into *B*; then $\Delta A = -d\xi$ and $\Delta B = d\xi$. This implies:

$$dG = -\mu_A d\xi + \mu_B d\xi = (\mu_B - \mu_A) d\xi \quad (T = const,\ p = const). \qquad (2)$$

If equation (1) is re-arranged as $(\partial G / \partial \xi)_{p,T} = \mu_B - \mu_A$ it is obvious, that at behavior of $A \leftrightarrow B$ reaction the graph slope of dependence *G* on ξ will define the $\mu_B - \mu_A$ value. It proceeds on the theory that the chemical reaction flows in direction of *G* decrease. When $\mu_A > \mu_B$, reaction flows from *A* to *B* and on the contrary when $\mu_A < \mu_B$, reaction flows from *B* to *A*. At $\mu_A = \mu_B$, the reaction is in equilibrium position. According to the above for $A \leftrightarrow B$ reaction it is possible to set values of condition's quantities for case when chemical equilibrium is occurring.

The thermodynamic potential of $A \leftrightarrow B$ reaction, according to stability condition in a system equilibrium state, is to be minimal. If take into account, that standard chemical potentials are standard mole Gibbs functions then at *T = const, p = const* in an equilibrium state the value of ΔG^0_m is to be minimal. In $\Delta G^0_m = \Delta H^0_m - T\Delta S^0_m$ relation values of ΔH^0_m and ΔS^0_m poorly depend on temperature. Subject to it for the given values of condition's quantities the probability of behavior of $A \leftrightarrow B$ reaction is estimating.

The following equilibrium conditions are generally fair: a) chemical balance; b) reaction is possible; c) reaction is not possible. In agreement with the theory for these cases

$$\left.\begin{aligned} \Delta G = 0; \Delta H = 0 \\ \Delta G < 0; \Delta H > 0 \\ \Delta G > 0; \Delta H < 0 \end{aligned}\right\} \qquad (3)$$

From (3) it follows, that at chemical reactions' calculations calculation of ΔG value is required in every case. It specifies that knowledge of chemical potentials of all reaction participants at given values of condition's quantities is necessary. For calculation of condensed

phases it is convenient to use Gibbs – Helmholtz equation subject to phases' heat capacities alloys of the $GeSe_2$–CdTe, $GeSe_2$–HgTe systems have been used as electrodes. E.m.f. measurements confirm the accuracy of plotted phase diagrams (Fig. 3 and Fig. 4).

$$\Delta G = \Delta H^0 - T\Delta S^0 + \int_{T^0}^{T} \Delta C_p dT - T\int_{T^0}^{T}\left(\frac{\Delta C_p}{T}\right)dT \quad (4)$$

On the base of plotted phase diagrams and measured partial molar thermodynamic properties of Cd in the system $GeSe_2$–CdTe and Ge in $GeSe_2$–HgTe (Table 5), the integral molar thermodynamic properties of fourfold phases have been calculated (Table 6). At this the standard molar thermodynamic properties of binary compounds $GeSe_2$, CdTe, HgTe [2,3] and potential-forming reactions in the pseudo-binary $GeSe_2$–CdTe, $GeSe_2$–HgTe cuts mutual Cd (Hg), Ge || S (Se), Te systems were also used.

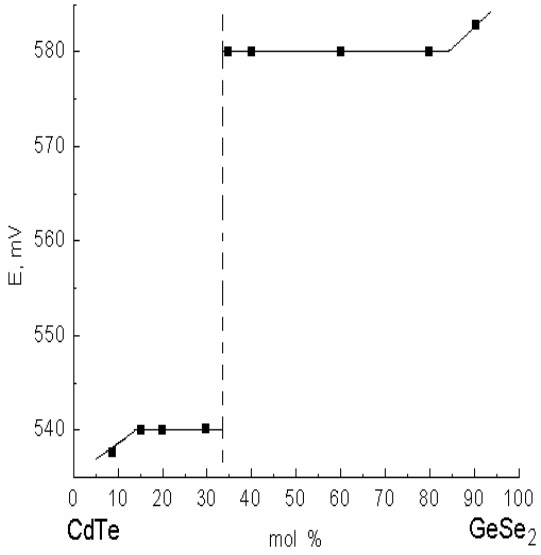

Fig. 3. Dependence of e.m.f. on composition in the CdTe–$GeSe_2$ system at 298 K.

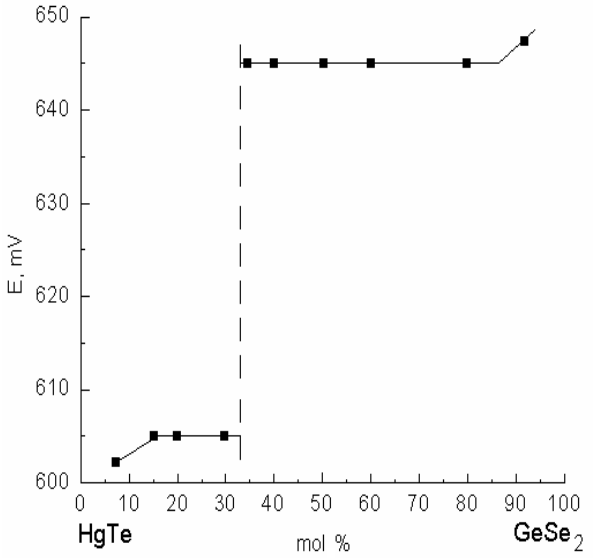

Fig. 4. Dependence of e.m.f. on composition in the HgTe–$GeSe_2$ system at 298 K.

IV. CONCLUSION

The phase diagrams of the pseudo-binary $GeSe_2$–A^2B^6 (A^2 = Hg; Cd; B^6 = S, Te) systems were plotted by the methods of differential thermal and X-ray diffraction analyses, by the measurement of electromotive force (e.m.f.), microhardness and density. New intermediate quaternary $Cd_2GeSe_2Te_2$, $Cd_4GeS_4Se_2$, $Hg_2GeSe_2Te_2$, $Hg_2GeS_2Se_2$, $Hg_4GeS_4Se_2$ phases and limited solid solutions on the base of binary components $GeSe_2$ and A^2B^6 have been found. Physicochemical and thermodynamic properties of some compositions of intermediate phases have been studied. The standard mole thermodynamic functions of quaternary $Cd_2GeSe_2Te_2$ and $Hg_2GeSe_2Te_2$ phases were determined.

The reactions flowing in a reversible galvanic cell concentrating relative to the electrodes have been studied by the method of e.m.f. measurement. The annealed

Table 5

The standard partial molar thermodynamic properties of Cd in the system $GeSe_2$–CdTe and Ge in $GeSe_2$–HgTe

Phase	$-\Delta_f \overline{G}_{Me}$ kJ mol^{-1}	$-\Delta_f \overline{H}_{Me}$ kJ mol^{-1}	$\Delta_f \overline{S}_{Me}$ J mol^{-1} K^{-1}
$Cd_2GeSe_2Te_2$	108.5 ± 11.5	82.8 ± 2.9	86.1 ± 18.9
$Hg_2GeSe_2Te_2$	402.2 ± 46.1	324.3 ± 1.6	261.3 ± 45.8

Table 6

The standard molar thermodynamic functions of quaternary phase in the systems $GeSe_2$–CdTe and $GeSe_2$–HgTe

Phase	$-\Delta_f G^0_{298}$ kJ mol^{-1}J	$-\Delta_f H^0_{298}$	$\Delta_f S^0_{298}$ J mol^{-1} K^{-1}
$Cd_2GeSe_2Te_2$	298.3 ± 1.9	276.3 ± 13.3	73.8 ± 32.7
$Hg_2GeSe_2Te_2$	605.8 ± 3.9	545.6 ± 21.2	202.0 ± 30.0

[1]. Physics and Chemistry of II-VI Compounds. Edited by *M.Aven and J.S.Prener*. GER and Development Center Schenctady, New York, USA. North-Holland Publishing company– Amsterdam. 1967.

[2]. Physico-Chemical Properties of Semiconductor Matters, Handbook, Composite authors (in Russian), Moscow, Nauka, 1978.

[3]. *O.Kubaschewski, C.B.Alcock*, Metallurgical Thermochemistry, Fifth Edition, Pergamon Press, Oxford, New York, Toronto, Sydney, Paris, Frankfurt, 1979.

[4]. *M.M.Asadov, A.C.Mirzoev, O.M.Aliev*, Azerb. Chem. J. 2 (2006) 77–81.

[5]. *A.C.Mirzoev*, Thesis of Institute of Chemical Problems, NASA (in Azerbaijani), Baku, Azerbaijan, 2008

[6]. *M.M.Asadov, Russ. J.* Inorg. Mater. 20 (1984) 38–40.

[7]. *M.M.Asadov, Russ. J.* Inorg. Mater. 20 (1984) 1621–1623.

[8]. *Z.Sztuba, K.Wiglusz, I.Mucha, A.Sroka, W.Gawel*, CALPHAD 32 (2008) 106–110.

POLARIZATION INDUCED 2DEG AT A AlGaN/GaN HETEROSTRUCTURE AND ITS TRANSPORT PROPERTIES

MEHTAP DEMİR[1], **ZEKİ YARAR**[2], **METİN ÖZDEMİR**[1]

[1] *Department of Physics, Cukurova University, 01330 Adana, Turkey*

[2]*Department of Physics, Mersin University, Ciftlikkoy 33343 Mersin, Turkey*

We consider an AlGaN/GaN hetero structure where there is no intentional doping in either material and consider only the effect of spontaneous and piezoelectric polarizations to calculate the conduction band profile through the self consistent solution of Poisson and Schrödinger equations at the junction. A high density two dimensional electron gas (2DEG) forms at the junction and therefore exchange and correlation effects are also considered. From the self consistent solutions, in addition to the potential profile, energy sub bands, their corresponding wave functions and the density of carriers at each level are obtained. Then the scattering rates for electrons due to acoustic and optical phonons and interface roughness are calculated using the sub band wave functions. An ensemble Monte Carlo method is used to find the drift velocities of the two dimensional electrons along the interface at different temperatures and applied field values.

I. INTRODUCTION

AlGaN/GaN hetero structure has a high energy band discontinuity and therefore makes it a good candidate for the production of devices operating at high power and high frequencies and therefore widely investigated [1-5]. GaN grown on sapphire crystallize in wurtzite phase and has strong piezoelectric and spontaneous polarization properties [3-4, 6-12]. Because of high band discontinuity and high polarization fields developed at the junction, electron concentrations up to 1×10^{13} cm^{-2} can be obtained in this structure even when there is no intentional doping in either of the materials at the junction[3,13].

In the present study we consider a Ga-faced AlGaN/GaN single heterojunction without any doping on either side of the junction. Spontaneous and piezoelectric polarizations just mentioned induce high electron concentrations at the junction and form a two dimensional electron gas (2DEG) which is free to move along the junction but confined along the junction planes. Because of the presence of high electron concentrations, the exchange and correlation effects in the electron gas are also considered. This leads to further band bending and in some cases alters the band profile considerably. The conduction band profile is obtained through the self consistent solutions of Poisson and Schrödinger equations at the junction. The band profile and the wave functions from self consistent solutions are used for the calculation of scattering rates for electrons and these are used for the study of transient velocity characteristics of electrons in an ensemble Monte Carlo simulation.

The organization of the paper is as follows: Section 2 provides a concise summary of piezoelectric and spontaneous polarizations used in the study. In Section 3 we present our results and their discussions and conclusions are given in Section IV.

II. POLARIZATION CHARGES AND SELF CONSISTENT SOLUTIONS

The total polarization P that exists in GaN or in AlGaN is the sum of polarizations resulting from spontaneous (P_{SP}) and piezoelectric (P_{PE}) polarizations. In the absence of any externally applied electric fields or strain in the material, piezoelectric polarization does not exist. Strain fields develop in a material at the junction region when it is grown on top of a substrate material with a different lattice constant. We consider here a structure consisting of a Ga-faced strained AlGaN grown on a relaxed GaN (see Fig. 1). Polarizations in the [0001] direction which are the epitaxial growth direction (z-direction) for AlGaN/GaN structures are considered. For the present case of AlGaN grown on a wurtzite GaN layer, the AlGaN is under a biaxial tension, whose strain components are given as

$$\varepsilon = (\varepsilon_x, \varepsilon_y, \varepsilon_z, 0, 0, 0) \tag{1}$$

While the in plane components of strain are equal and given by

$$\varepsilon_x = \varepsilon_y = \frac{a_{strained} - a_{free}}{a_{free}} \tag{2}$$

the component of strain in the growth direction becomes

$$\varepsilon_z = \frac{c_{strained} - c_{free}}{c_{free}} = -2\frac{C_{13}}{C_{33}}\varepsilon_x \tag{3}$$

where a and c are the lattice parameters of wurtzite structure, and C_{13} and C_{33} are the elastic stiffness constants. The piezoelectric polarization in the strained region therefore can be written as [3]

$$P_{PE} = e_{31}(\varepsilon_x + \varepsilon_y) + e_{33}\varepsilon_z \tag{4}$$

where e_{31} and e_{33} are the piezoelectric constants. The spontaneous polarization P_{SP} is in the growth direction (see Fig. 1). To compensate the polarization charges induced at the heterojunction, an accumulation of free electrons takes place. Polarization induced sheet charge concentration is related to the polarizations in the hetero junction for AlGAN/GaN system as

$$\begin{aligned} |\sigma(x)| &= \left| \begin{matrix} P_{PE}(Al_xGa_{1-x}N) + P_{SP}(Al_xGa_{1-x}N) \\ - P_{SP}(GaN) \end{matrix} \right| \\ &= \left| 2\frac{a(0)-a(x)}{a(x)} \left\{ e_{31}(x) - e_{33}(x)\frac{c_{13}(x)}{c_{33}(x)} \right\} \right. \\ &\quad \left. + P_{SP}(x) - P_{SP}(0) \right| \end{aligned} \tag{5}$$

The induced charge density given in (5) is used in the self consistent solution of Poisson and Schrödinger equations. An induced charge layer of about 6 A^o is assumed in the numerical calculations. The material parameters are provided in Table 1.

Table.1 Material parameters of $Al_xGa_{1-x}N$

Parametres	Symbol	Unit	Value	References
Static Dielectric Constans	ε	ε_0	8.5x+10(1-x)	[22]
Lattice Parameter	a	m	(-0.077x+3.189)1.e-10	[17]
Lattice Parameter	c	m	(-0.203x+5.185)1.e-10	[17]
Elastic Stifness Constant	C_{13}	GPa	5x+103	[17]
Elastic Stifness Constant	C_{33}	GPa	-32x+405	[17]
Piezolectric Constant	e_{31}	C/m^2	-0.11x-0.49	[17]
Piezolectric Constant	e_{33}	C/m^2	0.73x+0.73	[17]
Spontaneous Polarization	P^S	C/m^2	-0.052x -0.029	[17]
Ni Schottky Barrier	$e\phi_b$	eV	0.7	[18]
Band Offset	ΔE_c	eV	$0.7[E_g(x)- E_g(0)]$	[18]
Band Gap	E_g		$xE_g(AlN)+(1-x)E_g(GaN)-bx(1-x)$	[18]
Bowing Parameter	b	eV	1	[18]
Electron Efective Mass			0.33x+ 0.22(1-x)	[23]

The Schrödinger equation in the effective mass and Hartree approximations for a single electron is given by [15]

$$-\frac{\hbar^2}{2}\frac{d}{dz}\left(\frac{1}{m^*(z)}\frac{d}{dz}\right)\psi_i(z)+V(z)\psi_i(z) = \varepsilon_i\psi_i(z) \qquad (6)$$

where $V(z)$ is the self-consistently calculated potential energy resulting from polarization induced charges and electrons localized in the junction; $m^*(z)$ is the effective mass; $\hbar$ is Planck's constant divided by 2π; and *E* is the energy eigenvalue. The Poisson equation for the heterostructure becomes

$$\frac{d}{dz}\left(\varepsilon(z)\frac{d}{dz}\right)\phi(z)=\frac{-e\left(N_\sigma(z)-n(z)\right)}{\varepsilon_0} \qquad (7)$$

where ϕ is the electrostatic potential; *e* is the electronic charge; ε is the dielectric constant of the material; N_σ is polarization induced charge and $n(z)$ is the free electron concentration localized at the junction. The potential energy $V(z)$ is related to the electrostatic potential $\phi(z)$ as

$$V(z) = -e\phi_e(z) + \Delta E_c(z) + V_{xc}(z)$$

where ΔE_c represents conduction band discontinuities at the $Al_xGa_{1-x}N$/GaN hetero interface and $V_{xc}(z)$ is the exchange correlation potential energy of electron gas. The band discontinuity is assumed to be in the form [16, 17] $\Delta E_c = 0.7[E_g(x)-E_g(0)]$ where $E_g(x)$ is the Al fraction (*x*) dependent gap energy assumed to be interpolated between the gap energy of GaN and that of AlN as[18]

$$E_g(x) = xE_g(AlN)+(1-x)E_g(GaN)-bx(1-x)$$

where $E_g(AlN)$ and $E_g(GaN)$ are the band gaps of AlN and GaN, respectively, and *b* is the bowing parameter. The two dimensional electron concentration $n(z)$ is given by

$$n(z)=\sum_i \frac{m^*(z)k_BT}{\pi\hbar^2}\ln\left[1+\exp\left(\frac{E_F-\varepsilon_i}{k_BT}\right)\right]|\psi_i(z)|^2$$

where ψ_i are the wave functions corresponding to occupied sub bands, E_i are the energy eigenvalues, μ is the chemical potential, k_B is Boltzmann's constant and *T* is the absolute temperature. The exchange potential used in our numerical calculations is taken to be [19]

$$V_{xc}(z) = -\left[\frac{1+0.7734r_s}{21}\ln\left(1+\frac{21}{r_s}\right)\right]\frac{2E_R}{\pi\alpha r_s}$$

where $\alpha=(4/9\pi)^{1/3}$ is a parameter and $r_s=(4\pi a^{*3}n(z)/3)^{=1/3}$ and a^* is the effective Bohr radius and E_R is the corresponding effective Rydberg energy. Equations (6) and (7) are solved self consistently [20, 21]. The material parameters used in the calculations are given in Table 1. The Al concentration is x=0.2 everywhere in this study.

III. RESULTS AND DISCUSSIONS

A typical result for potential profile obtained at 300 K from the self consistent solution of Poisson /Schrödinger equations is shown in Fig. 1. The left axis corresponds to conduction band energy and right axis in the figure shows the wavefunctions corresponding to the ground state in the absence (dashed lines) and in the presence (solid lines) of exchange potential in arbitrary units. As one can see from the figure the wavefunction is more localized when exchange potential is considered because in that case the potential on the GaN side increases and leads to a deeper potential with a sharp spike shape at the bottom. The electron concentrations for the present figure are 9.46×10^{12} cm^{-2} when exchange is

considered and 9.4×10^{12} cm^{-2} when it is neglected. The number of occupied sub bands depends on temperature and whether the exchange potential is taken into account or not. At most three sub band energies are supported by the geometry considered shown in the inset of Fig. 1. But in almost all cases the upper two sub bands are very close to the conduction band edge and the localization of electrons in those bands is weak compared to the ground sub band.

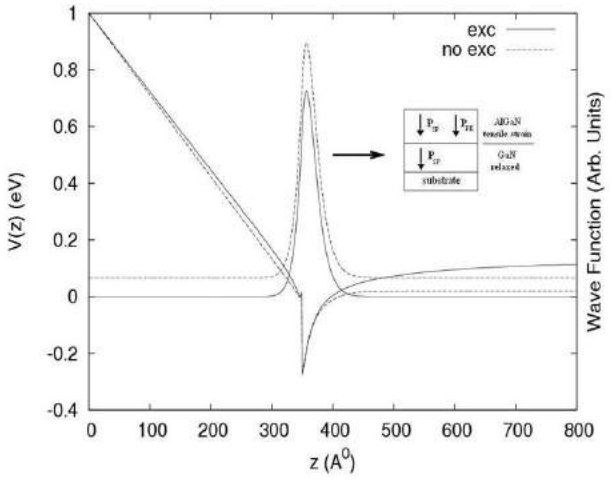

Fig.1. The conduction band profile obtained from Poisson/Schrödinger equations and the wavefunctions corresponding to ground state at 300 K. Solid lines are for the case when exchange potential is considered and dashed lines are for the case when it is neglected. The inset shows the geometry of the $Al_{0.2}Ga_{0.8}N$/GaN heterostructure considered in this study. The barrier length is 350 A°, the GaN width is 4500 A°. The chemical potential is assumed to be 1 eV below the conduction band of AlGaN.

In the following we consider the transient drift velocity characteristics and the occupation of sub band and three dimensional valleys of GaN at various applied fields and temperatures. The scattering mechanisms mentioned in Section 1 are considered in ensemble Monte Carlo simulations. The scattering rates are calculated using the self consistently determined sub band wave functions for the two dimensional electrons. Electrons that are scattered to three dimensions are also considered and their relevant scattering rates are also properly calculated. A total of 3×10^4 electrons are used in the simulations.

Fig. 2 shows the drift velocity of carriers at various applied field values at *T*=300 K. Heavy solid lines are for the case of exchange potential and light dashed lines are when there is no exchange potential. As one might expect the drift velocity of carriers increases with the increase of applied field. Note that in each case the velocity of carriers decreases when exchange effects are taken in to account. The basic reason for this is that when exchange is considered the potential at the GaN side increases and therefore the number of sub bands that are accommodated by the potential profile increases. As a result inter band scattering of particles begin to take place which reduces the drift velocity. But as mentioned above the upper sub bands are very close to the conduction band edge so that almost no electrons are held in these upper bands and they instantly are scattered to the Γ valley of GaN and become three dimensional electrons. (For energy sub band and valley occupancies see Fig. 4).

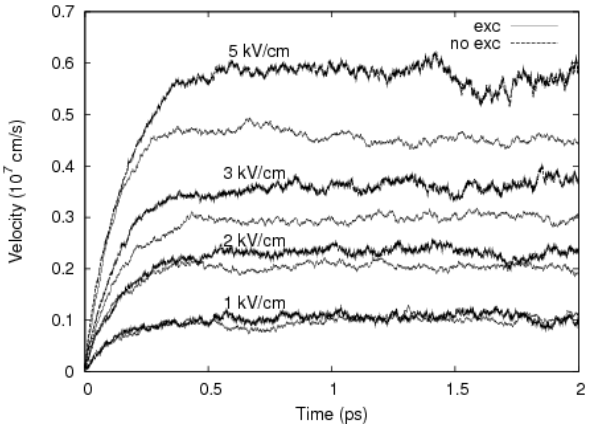

Fig..2 Drift velocity of carriers at various applied electric fields at *T*=300 K. The heavy solid lines are when exchange potential is not taken in to account and light dashed lines are when it is considered.

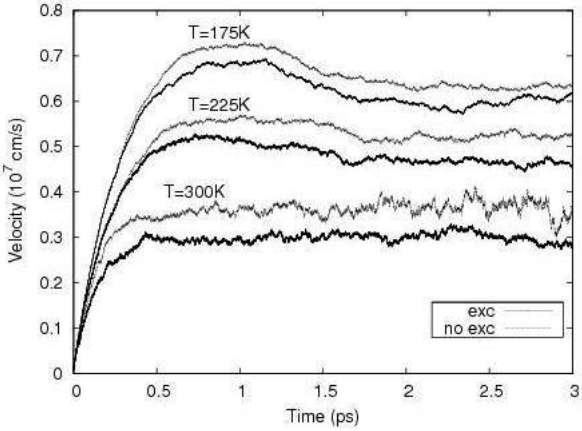

Fig.3 Drift velocity of carriers at an applied field of 3 kV/cm at various temperatures. Light dashed lines are when exchange potential is included and heavy solid lines are when it is not. A small scale velocity over shoot appears at *T*=175 K.

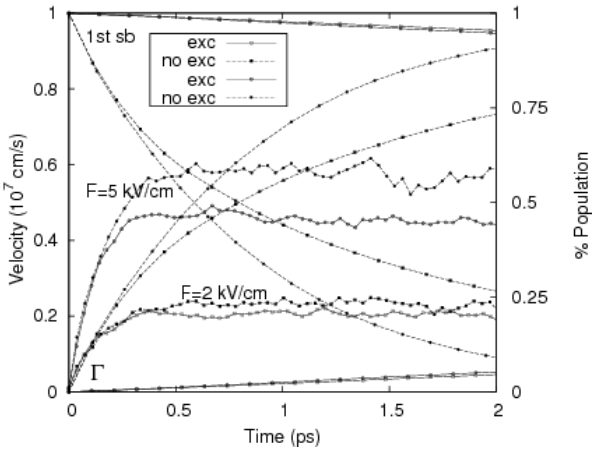

Fig.4 The occupancy of energy sub bands and three dimensional valleys at two different values of applied field. Empty squares and circles are for the case when exchange potential is included. Note that in this case the carriers are predominantly in the first sub band and a small percentage of carriers are scattered to three dimensional valleys. On the contrary, when exchange potential is not considered, a great number of particles is scattered to three dimensional valleys regardless of the applied field.

Next we consider the transient drift velocity characteristics of the 2DEG gas at the AlGaN/GaN heterostructure as a function of temperature. Fig. 3 shows the drift velocity characteristics of the electron gas at different temperatures in the presence and absence of exchange potential at an applied field value of 3kV/cm. Solid heavy lines correspond to the case when exchange effects are considered and the light (dashed) lines correspond to the case when it is neglected. For each temperature, the velocity of carriers decreases when exchange effects are taken in to account as was the case in Fig. 2 for similar reasons explained above. The velocity of carriers decreases as the temperature increases because at higher temperatures optic phonon scattering begin to become the dominant scattering mechanism for electrons. Note also that at low temperatures (T=175 K) velocity over shoot effect begin to appear in the drift velocity profile

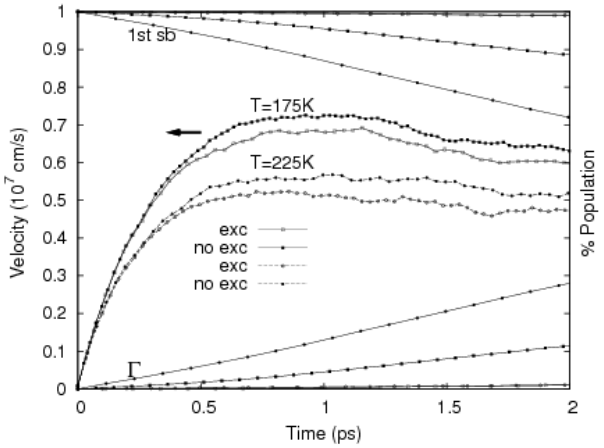

Fig.5. The occupancy of energy sub bands and three dimensional valleys with regard to temperature. Empty circles and squares are when exchange is included and filled circles and squares are when it is not. It appears that the temperature almost has no effect on the occupancy of the levels in the temperature range considered here , but rather the exchange potential is more responsible for holding the particles in two dimensions.

We now consider the occupation of energy sub bands at the heterostructure and the three dimensional valleys of GaN, the results are depicted in Fig. 4. for two applied field values at 300 K. Solid lines with filled squares and circles are when exchange is absent for 2kV/cm and 5 kV/cm applied fields, respectively. Similarly empty squares and circles correspond to the case when exchange is taken in to account for applied field values of 2 and 5 kV/cm, respectively. When there is no exchange a great deal of particles are transferred to three dimensions even at low fields. The effect of exchange is that it reduces the drift velocity of carriers but since it increases the potential energy at the GaN side, it prevents the electrons from going to three dimensional valleys. So it helps the system to preserve its two dimensional character.

Finally we consider the sub band occupancies as a function of temperature. Fig. 5 shows sub band populations at two different temperatures at an applied field of 3 kV/cm. Filled circles and diamonds correspond to the case when exchange is absent and empty circles and squares correspond to when it is considered. The situation here is similar to the one shown in Fig. 4. When there is exchange the velocity of carriers is reduced but the two dimensional character of the system is preserved. When exchange is absent the drift velocity of carriers is higher but scattering of these carriers to three dimensional valleys takes place more frequently. It also appears that the temperature almost has no effect on the occupancy of sub bands or valleys in the temperature range considered in this study.

IV. CONCLUSIONS

We studied an AlGaN/GaN heterostructure where AlGaN side is assumed to be under a tensile strain due to lattice mismatch with a relaxed GaN layer. The spontaneous polarizations on each side and the piezoelectric polarization at the junction is taken into account. To compensate the positive high sheet polarization charges a two dimensional electron gas forms at the junction. From the self consistent solution of Poisson and Schrödinger equations the energy sub bands, the number of electrons in each level and the corresponding wave functions are calculated and using these wave functions the scattering rates due to acoustic and optical phonons and interface roughness are calculated. The effect of exchange potential is also considered. Exchange interaction modifies the conduction band profile by increasing it on the GaN side. This helps to keep the two dimensional character of the system by preventing the carriers from going to three dimensional valleys when an electric field along the heterojunction is applied. But the drift velocity of carriers is reduced when exchange effect are considered. The temperature is observed to have almost no effect on the occupancy of levels in the temperature range considered in the present study.

[1]. *S. Strite and H. Morkoc,* "GaN, AlN, and InN: a Review," *J. Vac. Sci. Technol. B*, vol. 10, no. 4, 1992, p. 1237-1266.

[2]. *U.V. Bhapkar and M.S. Shur,* "Monte Carlo Calculation of Velocity-Field Characteristics of Wurtizite GaN," *J. Appl. Phys*.,vol. 82, no. 4, 1997, p. 1649-1655.

[3]. *O. Ambacher et al. and R. Dimitriv, L. Wittmer, M. Stutzmann, and W. Rieger, J. Hilsenbeck,* J.Appl. Phys., 1999, 85, No1, p. 3222-3233.

[4]. *O. Ambacher et al. and R. Dimitriv, A. Mitchell, M. Stutzmann,* J. Appl. Phys., 2000, 87, No1, p. 334-344.

[5]. *K.-S. Lee et al. ETRI J.*, 2002, 24, No4, p. 270-278.

[6]. *L. Hsu and W. Walukiewicz,* Appl. Phys. Lett., 1998, 73, p.339.

[7]. *N. Maeda, T. Nishida, N. Kobayashi, and M.Tomizawa,* Appl. Phys. Lett., 1998, 73, p. 1856.

[8]. *Y. Zhang and J. Singh, J.Appl. Phys.,* 1999, 85, p. 587.

[9]. [9]. *I. P. Smorchkova C. R. Elsass, J.P.Ibbetson, R. Vetury, B. Heying, P. Fini, E. Haus, S.P.DenBaars, J. S. Speck, and U. K. Mishra,* J. Appl. Phys., 1999, 86, p. 4520.

[10]. *N. Maeda, T. Saitoh, K. Tsubaki, T. Nishida, and N. Kobayashi,* phys. stat. sol. (b), 1999, 216,p. 727.

[11]. *Y. Zhang, I. P. Smorchkova, C. R. Elsass, S.Keller, J. P. Ibbetson, S. Denbaars, U.K.Mishra and J. Singh,* J. Appl. Phys. , 2000,87, p.7981.

[12]. *N. Maeda, T. Saitoh, K. Tsubaki, and T.Nishida,* Appl. Phys. Lett. , 2000, 76, p.3118.

[13]. *A. Khan, A. Bhattarai, J. N. Kuznia, and D.T.Olson,* Appl. Phys. Lett. , 1993, 63, p.1214.

[14]. *Changchun Shi, Peter M. Asbeck, and Edward T. Yu,* Appl. Phys. Lett**.,** 1999, vol 74**,** no. 4, p.573-575.

[15]. *G. Bastard,* Wave Mechanics Applied to Semiconductor Heterostructures, 1988, New York, Halsted Press.

[16]. *G. Martin, S. Strite, A. Botchkarev, A. Agarwal, A. Rockett, H. Morkoc, W. R. l. Lambrecht, and B. Segall,* Appl. Phys. Lett. 1994, 65, p.610.

[17]. *G. Martin, A. Botchkarev A. Botckarev, A.Rockett, and H. Morkoc,* Appl. Phys. Lett. 1996, 68, p.2541.

[18]. *D. Brunner, H. Angerer, E. Bustarre, R. Höpler, R. Dimitrov, O. Ambacher, and M. Stutzman.* J. Appl. Phys., 82, 5090.

[19]. *L. Hedin and B. L. Lundqvist,* J. Phys. C., 1971, 4, p.2064.

[20]. *H. Tan, G. L. Snider, L. D. Chang, and E.L. Hu,* J. Appl. Phys. 1990, 68, p.4071.

[21]. *Z. Yarar, B. –M. Özdemir,* Phys. Stat. Sol. (b), 2005, 242, No14, p.2872-2884.

[22]. *J. Neugebauer and C. Van de Walle, Phys. Rev. B,* vol.50, no11, 1994, p.8067-8070.

[23]. *J.A. Majewski, M. Staedele, and P. Vogl,* Mater. Res.Soc. Proc., vol. 449, Pittsburgh, PA, 1997, p.887-892.

A FIRST – PRINCIPLES STUDIES OF TbBi

M. OZAYMAN[1], Y. O. CIFTCI[1], K. COLAKOGLU[1], H. OZISIK[2]
[1]*Department of Physics, Gazi University, 06500 Ankara, Turkey*
[2]*Physics Department, Aksaray University, 68100 Aksaray, Turkey*

Ab initio calculations have been carried out to find the structural, electronic, elastic and thermodynamic properties of TbBi, using density functional theory within generalized-gradient (GGA) apraximation. For the total-energy calculation we have used the projected augmented plane-wave (PAW) implementation of the Vienna Ab initio Simulation Package (VASP). Our results are compared to other theoretical and experimental works, and excellent agreement is obtained. We have used to examine structure parameter in different structures such as in NaCl(B1), CsCl(B2), ZB(B3), WC(Bh) and tetragonal. We have performed the thermodynamics properties for TbBi by using quasi-harmonic Debye model. We have, also, predicted the temperature and pressure variation of the volume, bulk modulus, thermal expansion coefficient, heat capacities and Debye temperatures in a wide pressure (0 – 16 Gpa) and temperature ranges (0- 2000 K).

I. INTRODUCTION

The rare-earth monopnictides have attracted considerable attention due to their unusual magnetic, transport and phonon propertis [1-2-3]. It is known that the source of these anomalous arise from the presence of 4f level close to the Fermi level [4-5]. The degree of localization and itinerancy of f electrons strongly affect the electronic properties of rare-earth elements [6-5]. The Tb monopnictide TbX, has not been studied very intensively and deeply using the single crystalline sample so far because of the difficulty of the crystal growth. The lattice constant is well fitted by the rare-earth contraction as Tb³.

Although there has been existed of rare earth compounds works, none of works focus on the elastic, thermodynamics properties of TbBi. The aim of the present paper is to reveal bulk, structural properties in NaCl(B1), CsCl(B2), ZB(B3), WC(Bh) and tetragonal phases and thermodynamical, elastic and lattice dynamical properties in B1 phase of TbBi, using VASP method with plane-wave pseudopotential. In Section 2, a brief outline of the method of calculation is presented. In Section 3, the results are presented followed by a summary discussion.

II. METHOD OF CALCULATION

In the present work, all the calculations have been carried out using the Vienna ab initio simulation package (VASP) [7-8] based on the density functional theory (DFT). The electron-ion interaction was considered in the form of the projector-augmented-wave (PAW) method with plane wave up to energy of 500 eV [9-10]. This cut-off was found to be adequate for the structural, elastic properties as well as for the electronic structure. We do not find any significant changes in the key parameters when the energy cut-off is increased from 500 eV to 550 eV. For the exchange and correlation terms in the electron-electron interaction, Perdew and Zunger-type functional [11-12] was used within the generalized gradient approximation (GGA) [10]. The 12x12x12 Monkhorst and Pack [13] grid of k-points have been used for integration in the irreducible Brillouin zone. Thus, this mesh ensures a convergence of total energy to less than 10^{-5} ev/atom.

We used the quasi-harmonic Debye model to obtain the thermodynamic properties of TbBi [14-15], in which the non-equilibrium Gibbs function *G*(V; P, T)* takes the form of

$$G^*(V;P,T)=E(V)+PV+A_{vib}[\theta(V);T] \quad (1)$$

In Eq.(1), *E(V)* is the total energy for per unit cell of TbBi, *PV* corresponds to the constant hydrostatic pressure condition , $\theta(V)$ the Debye temperature and A_{Vib} is the vibration term, which can be written using the Debye model of the phonon density of states as

$$A_{Vib}(\theta,T) = nkT\left[\frac{9\theta}{8T}+3\ln\left(1-e^{-\frac{\theta}{T}}\right)-D\left(\frac{\theta}{T}\right)\right] \quad (2)$$

where *n* is the number of atoms per formula unit, $D\left(\frac{\theta}{T}\right)$ the Debye integral, and for an isotropic solid, θ is expressed as [16]

$$\theta_D = \frac{\hbar}{k}\left[6\pi V^{1/2}n\right]^{1/3} f(\sigma)\sqrt{\frac{B_s}{M}} \quad (3)$$

where *M* is the molecular mass per unit cell and B_S the adiabatic bulk modulus, which is approximated given by the static compressibility [17]:

$$B_s \approx B(V) = V\frac{d^2E(V)}{dV^2} \quad (4)$$

$f(\sigma)$ is given by Refs. [16-18] and the Poisson ratio are used as 0.2462 for TbBi. For TbBi, *n*=4 *M*= 367.91 a.u, respectively. Therefore, the non-equilibrium Gibbs function *G*(V; P, T)* as a function of *(V; P, T)* can be minimized with respect to volume *V*.

$$\left[\frac{\partial G^*(V;P,T)}{\partial V}\right]_{P,T} = 0 \quad (5)$$

By solving Eq. (5), one can obtain the thermal equation-of-equation (EOS) *V(P, T).* The heat capacity at constant volume $C_{V,}$ the heat capacity at constant pressure

C_p, and the thermal expansion coefficient α are given [19] as follows:

$$C_v = 3nk\left[4D\left(\frac{\theta}{T}\right) - \frac{3\theta/T}{e^{\theta/T}-1}\right] \quad (6)$$

$$S = nk\left[4D\left(\frac{\theta}{T}\right) - 3\ln(1-e^{-\theta/T}\right] \quad (7)$$

$$\alpha = \frac{\gamma C_v}{B_T V} \quad (8)$$

$$C_p = C_v(1+\alpha\gamma T) \quad (9)$$

Here γ represent the Grüneisen parameter and it is expressed as

$$\gamma = -\frac{d\ln\theta(\mathrm{V})}{d\ln \mathrm{V}} . \quad (10)$$

III. RESULTS AND DISCUSSION

3.1. Structural and Electronic Properties

Firstly, the equilibrium lattice parameter has been computed by minimizing the crystal total energy calculated for different values of lattice constant by means of Murnaghan's equation of state (eos) [20] as in Fig.1 The bulk modulus, and its pressure derivative have also been calculated based on the same Murnaghan's equation of state, and the results are given in Table 1 along with the experimental and other theoretical values. The calculated value of lattice parameters are 6.3530 A^0 in B1(NaCl) phase, 3.9040 A^0 in B2(CsCl) phase, 7.1047 A^0 in B3(ZB) phase, 5.1398 A^0 in tetragonal phase, 4.3618 A^0 in Bh(WC) phase for TbBi, respectively. The present values for lattice constants are also listed in Table 1, and the obtained results are quite accord with the other experimental values [21-22].

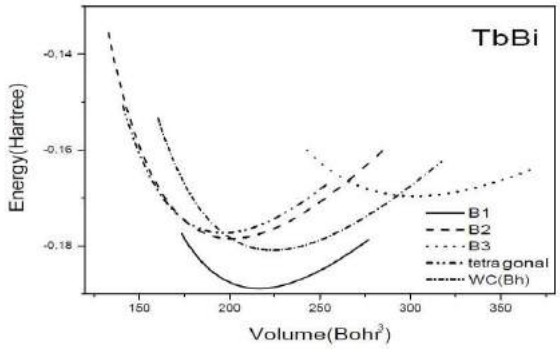

Fig. 1. Total energy versus volume curve of TbBi in B1(NaCl), B2(CsCl), B3(ZB), Bh(WC) and tetragonal phases.

Table 1. Calculated equilibrium lattice constants (a_0), bulk modulus (B), pressure erivatives of bulk modulus (B') and other theoretical works for TbBi in B1, B2, B3, Bh and tetragonal structures

Material	Structure	Reference	A	C	a/c	B(GPa)	B'
TbBi	B1	Present	6.3530			53.2426	4.2232
		Exp.[22]	6.277				
		Exp.[21]	6.280				
	B2	Present	3.9040			53.1423	3.9059
	B3	Present	7.1047			32.9155	3.9888
	WC(Bh)	Present	4.3618	4.0285	0.9236	49.0116	4.1350
	Tetragonal	Present	5.1392	4.4109	0.8583	54.4985	4.1194

We have plotted the phase diagrams (equation of state) for both B1 and B2 phases in Fig. 2 The discontinuity in volume takes place at the phase transition pressure. The phase transition pressures from B1 to B2 structure is found to be 16 GPa from the Gibbs free energy at 0 K for TbBi and the related enthalpy versus pressure graphs for the both phases are shown in Fig. 3 The transition pressure is a pressure at which *H(p)* curves for both phases crosses. The same result is also confirmed in terms of the "common tangent technique" in Fig.1 We have also plotted the normalized volume pressure diagram of TbBi in B1 phase at the temperatures of 400K, 1200K and 2000K in Fig. 4.

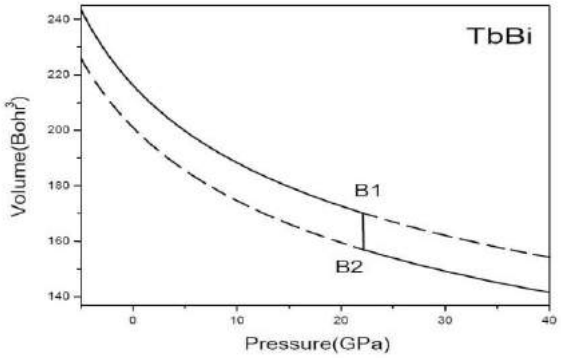

Fig. 2. Pressure versus volume curve of TbBi

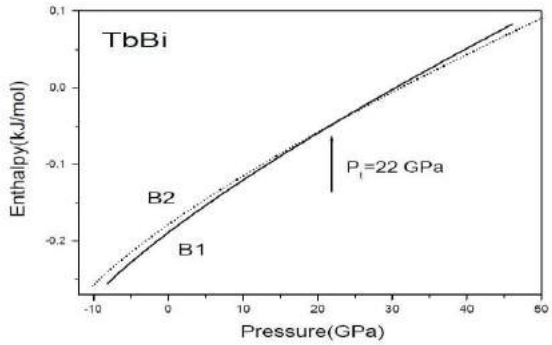

Fig. 3. Estimation of phase transition pressure from B1 to B2 of TbBi

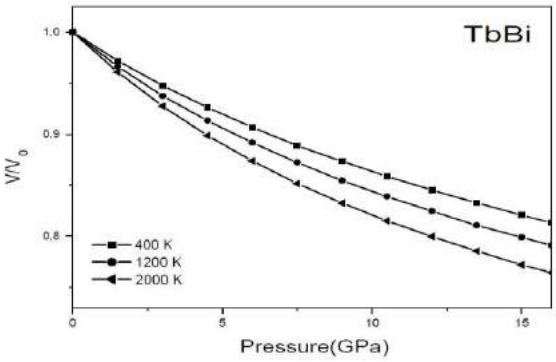

Fig. 4. The normalized volume-pressure diagram of the B1 for TbBi at different temperatures

The present first – principles code (VASP) have also been used to calculate the band structures for TbBi. The obtained results for high symmetry directions are shown in Fig. 5 and 6 for B1 and B2 structures of TbBi, respectively. It can be seen from the Fig. 5 and 6 that no band gap exists for studied compounds, and they exhibit metallic character. The total electronic density of states (DOS) corresponding to the present band structures are, also, depicted in Fig. 5 and 6, and the disappearing of the energy gap in DOS conforms the metallic nature of TbBi.

The similar situation is observed for LaN in our recent work [23].

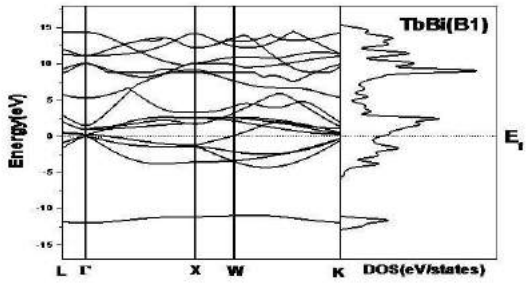

Fig. 5. Calculated band structure of TbBi in phase B1

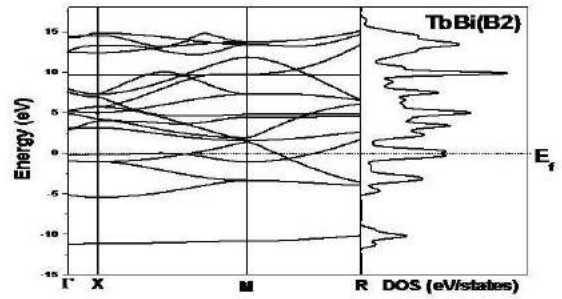

Fig. 6. Calculated band structure of TbBi in phase B2

3.2. Elastic Properties

The elastic constants of solids provide a link between the mechanical and dynamical behaviour of crystals, and give important information concerning the nature of the forces operating in solids. In particular, they provide information on the stability and stiffness of materials. Their ab-initio calculation requires precise methods, since the forces and the elastic constants are functions of the first and second-order derivatives of the potentials. Their calculation will provide a further check on the accuracy of the calculation of forces in solids. The effect of pressure on the elastic constants is essential, especially, for understanding interatomic interactions, mechanical stability, and phase transition mechanisms. It also provides valuable data for developing interatomic potentials

There are two common methods [24-25] for obtaining the elastic data through the ab-initio modelling of materials from their known crystal structures: an approach based on analysis of the total energy of properly strained states of the material (volume conserving technique) and an approach based on the analysis of changes in calculated stress values resulting from changes in the strain (stress-strain) method. Here we have used the "stress-strain" technique for obtaining the second-order elastic constants (C_{ij}). The listed values for C_{ij} in Table 2 are in reasonable order. The experimental and theoretical values of C_{ij} for TbBi are not available at present.

The calculated elastic constants values of B1 structure for TbBi at 10, 20, 30, 40, 50, 60, 70 GPa pressure values, respectively and they are also listed in Table 3.

The Zener anisotropy factor *A*, Poisson ratio υ, and Young's modulus *Y*, which are the most interesting elastic properties for applications, are also calculated in terms of the computed data using the following relations [26] :

$$A=\frac{2C_{44}}{C_{11}-C_{12}}, \quad (1)$$

$$\upsilon=\frac{1}{2}\left[\frac{(B-\frac{2}{3}G)}{(B+\frac{1}{3}G)}\right], \quad (2)$$

and

$$Y=\frac{9GB}{G+3B} \quad (3)$$

where G = (G_V + G_R) /2 is the isotropic shear modulus, G_V is Voigt's shear modulus corresponding to the upper bound of G values, and G_R is Reuss's shear modulus corresponding to the lower bound of G values, and can be written as $G_V = (C_{11}–C_{12} +3C_{44})/5$, and $5/G_R = 4/(C_{11}-C_{12})+ 3/ C_{44}$. The calculated Zener anisotropy factor (*A*), Poisson ratio (υ), Young's modulus (*Y*), and Shear modulus ($C'=(C_{11}-C_{12+}2C_{44})/4$) for TbBi are given in Table 4 and they are close to those obtained for the similar structural symmetry.

Table 2. The calculated elastic constants (in GPa unit) in different structures for TbBi

MATERİAL	STRUCTURE	REFERENCE	C_{11}	C_{12}	C_{44}	C_{13}	C_{33}	C_{66}
TbBi	B1	Present	137.596	15.296	20.718			
	B2	Present	48.627	58.072	-23.698			
	B3	Present	34.066	33.130	26.459			
	WC(Bh)	Present	80.900	24.656	34.850	109.4	28.12	18.29
	Tetra-gonal	Present	15.698	96.767	49.530	80.08	-26.6	-6.58

Table 3. The elastic constants values (in GPa unit) of the B1 structure for TbBi at different pressures.

MATERİAL	STRUCTURE	REFERENCE	PRESSURE	C_{11}	C_{12}	C_{44}
TbBi	B1	Present	10	231.558	13.014	18.1612
		Present	20	311.562	10.588	15.0343
		Present	30	381.983	8.7670	11.8304
		Present	40	445.691	7.4420	8.5963
		Present	50	505.046	6.4670	5.5647
		Present	60	561.020	5.5781	2.8612
		Present	70	614.328	4.8723	0.4499

Table 4. The calculated Zener anisotropy factor (*A*), Poisson ratio (υ), Young's modulus (*Y*), Shear modulus (C') for TbBi in B1 structure

MATERİAL	*A*	υ	Y(GPa)	C' (GPa)
TbBi	0.3388	0.2462	81.076	40.934

3.3. Thermodynamics Properties

The Debye temperature (θ_D) is known as an important fundamental parameter closely related to many physical propertied such as specific heat and melting temperature. At low temperatures the vibrational excitations arise solely from acoustic vibrations. Hence, at low temperatures the Debye temperature calculated from elastic constants is the same as that determined from specific heat measurements. We have calculated the Debye temperature, θ_D, from the elastic constants data using the average sound velocity, v_m, by the following common relation given [27]

$$\theta_D = \frac{h}{k}\left[\frac{3n}{4\pi}\left(\frac{N_A\rho}{M}\right)\right]^{1/3} \upsilon_m \quad (4)$$

where $\hbar$ is Planck's constants, k is Boltzmann's constants, N_A Avogadro's number, n is the number of atoms per formula unit, M is the molecular mass per formula unit, $\rho(=M/V)$ is the density, and v_m is obtained from

$$\upsilon_m = \left[\frac{1}{3}\left(\frac{2}{\upsilon_t^3}+\frac{1}{\upsilon_l^3}\right)\right]^{1/3} \quad (5)$$

where v_l and v_t, are the longitudinal and transverse elastic wave velocities, respectively, which are obtained from Navier's equations [28]:

$$\upsilon_l = \sqrt{\frac{3B+4G}{3\rho}} \quad (6)$$

and

$$\upsilon_t = \sqrt{\frac{G}{\rho}}. \quad (7)$$

The calculated average longitudinal and transverse elastic wave velocities, Debye temperature and melting temperature for TbBi are given in Table 5. No other theoretical or experimental data are exist for comparison with the present values.

The empirical relation [29], T_m=553 K+ (591/Mbar)C_{11} ± 300, is used to estimate the melting temperature for TbBi, and found to be 1366 ± 300K. This value is lower than those obtained for Tb (1631 K), We hope that the present results are a reliable estimation for these compounds as it contains only C_{11} which has a reasonable value.

Table 5. The longitudinal, transverse, average elastic wave velocities, and Debye temperature for TbBi in B1 structure.

MATERİAL	$\upsilon_l(m/s)$	$\upsilon_t(m/s)$	$\upsilon_m(m/s)$	$\theta_D(K)$	$T_m(K)$
TbBİ	3183.38	1847.16	2049.79	436	1366+300

The thermal properties are determined in the temperature range from 0 K to 2000 K for TbBi, where the quasi-harmonic model remains fully valid. The pressure effect is studied in the 0-16 GPa range. The relationship between normalized volume and pressure at different temperature is shown in Fig. 4 for TbBi. It can be seen that when the pressure increases from 0 GPa to 16 GPa, the volume decreases. The reason of this changing can be attributed to the atoms in the interlayer become closer, and their interactions become stronger. For TbBi compound the normalized volume decreases with increasing temperature. Temperature effects on bulk modules (B) are given in Fig. 7 and can be seen that B decreases as temperature increases. Because cell volume changes rapidly as temperature increases. The relationship between bulk modulus (B) and pressure (P) at different temperatures (400K, 1200K, and 2000K) is shown in Fig. 8 for TbBi. It can be seen that bulk modulus decreases with the temperature at a given pressure and increases with pressure at a given temperature. It shows that the effect of increasing pressure on TbBi is the same as decreasing its temperature.

The variations of the thermal expansion coefficient (α) with temperature and pressure are shown in Fig. 9 and Fig. 10 for TbBi, respectively. It is shown that, the thermal expansion coefficient α also increases with T at lower temperatures and gradually approaches linear increases at higher temperatures, while the thermal expansion coefficient α decreases with pressure.

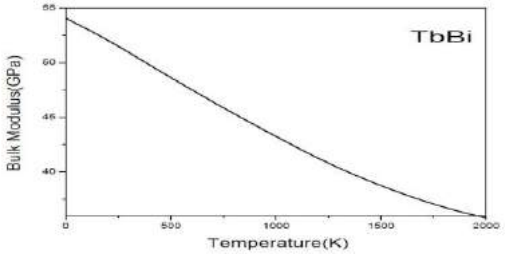

Fig. 7. The bulk modulus (B) for TbBi as a function temperature T at P=0

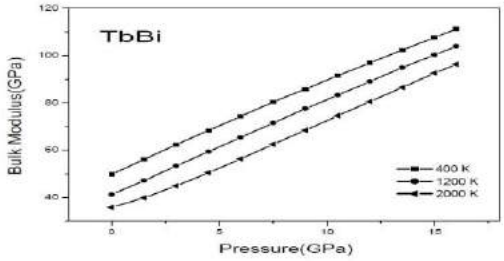

Fig. 8. The reletionships of TbBi between bulk modulus (B) and pressure P at temperatures of 400 K, 1200 K, 2000 K

At different temperature, α decreases nonlinearly at lower pressure and decreases almost linearly at higher pressure. Also, It can be seen from Fig. 9 that the temperature dependence of α is very small at high temperature and higher pressure.

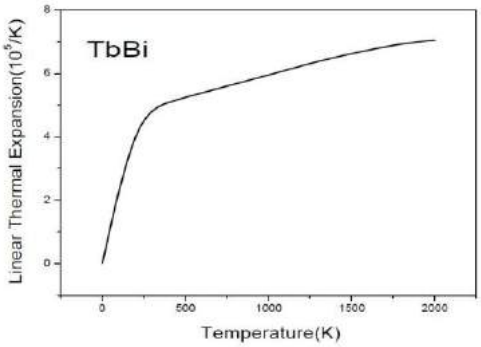

Fig. 9. The thermal expansion versues temperature for TbBi.

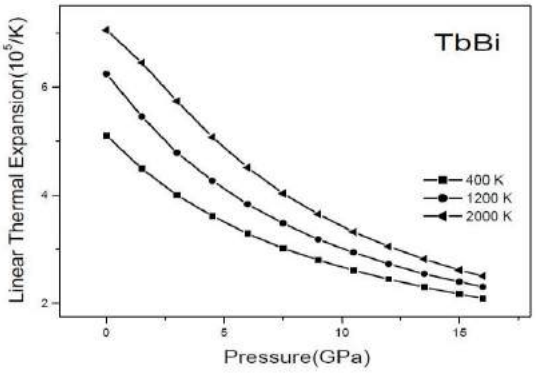

Fig. 10. The thermal expansion versues pressure for TbBi.

The heat capacity (C_v) and Debye temperature Θ as a function of pressure at the temperatures of 400K and 2000K for TbBi are shown in Fig. 11. It is shown that the

Θ increases almost linearly with pressure while, C_v decreases with applied pressures.

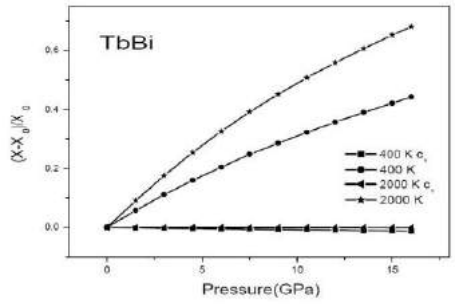

Fig.11. Variations of thermodynamic parameters X (X: Debye temperature or specific heat) with pressure *P*. They are normalized as$(X-X_0)/X_0$, where X and X_0 are the Debye temperature or specific heat under any pressure P and zero pressure at the temperatures of 400K and 2000K.

IV. CONCLUSIONS

The fist–principles pseudopotential calculations have performed on the TbBi. Our present key results are on the elastic, electronic, structural and lattice dynamical properties for TbBi. The lattice parameters are excellent agreement with the other theoretical values. The computed band structures for TbBi shows metallic character. It is hoped that some our results, such as elastic constants, Debye temperatures and melting temperatures estimated for the first time in this work, will be tested in future experimentally and theoretically.

[1]. *Chun-Gang Duan, R.F. Sabirianaw, W.N.Mei, P.A.Dowben, S.S.Jaswal and E.Y.Tsymbal*, J.Phys. Condens. Matter, 19 (2007) 315220

[2]. *P.Morin, D. Schmitt*, Physical Review B. 27 (1983) 7

[3]. *J. Kötzler*, Z. Phys. B – Condensed Matter 55, 119-129 (1984)

[4]. A.*G.Puthukov, W.R.L.Lambrecht and B.Segall*, Phys.Rev.B 53 (1996) 4324

[5]. *Q.G.Seng, B.R.Cooper and S.P.Lim*, J.Appl.Phys.73 (1993) 5409

[6]. *M.De, S.K.De*, J.Phys. And Chem. Of Sol. 60 (1999) 337

[7]. *G. Kresse and J. Hafner*, Phys. Rev. B, 47(1994)558.

[8]. *G. Kresse and J. FurthmÄuller*, Phys. Rev. B, 54 (1996) 11169.

[9]. *G. Kresse and D. Joubert*, Phys. Rev. B, 59 (1999) 1758.

[10]. *P. E. Blochl*, Phys. Rev. B, 50 (1994) 17953.

[11]. *J. P. Perdew and A. Zunger*, Phys. Rev. B, (1981)23 5048.

[12]. *J. P. Perdew, J. A. Chevary, S. H. Vosko, K.A.Jackson, M. R. Pederson, D. J. Singh, C.Fiolhais*, Phys. Rev. B ,46 (1992) 6671

[13]. *H.J. Monkhorst and J.D. Pack*, Phys. Rev. B, 13(1976) 5188.

[14]. *M.A. Blanco, E. Francisco, V. Lunana.* , Comput. Phys. Commun. , 158 (2004)57.

[15]. *F. Peng, H.Z. Fu, X.D. Yang*., Physica B, 403 (2008) 2851.

[16]. *M.A. Blanco, A.M. Pendàs, E. Francisco, J.M.Recio, R. Franko, J.Mol. Struct. (Theochem)368 (1996) 245*

[17]. *M. Flórez, J.M. Recio, E. Francisco, M.A. Blanco, A.M. Pendàs, Phys. Rev. B*, 66 (2002) 144112.

[18]. *E. Francisco, , J.M. Recio, M.A. Blanco, A.M. Pendàs, J. Phys. Chem*. ,102 (1998) 1595.

[19]. *R. Hill, Proc. Phys. Soc. Lond. A*, 65 (1952) 349.

[20]. *F. D. Murnaghan*, Proc. Natl., Acad. Sci. USA 30, 5390 (1994)

[21]. *M. N. Abdusalyamovo, O.I. Rachmatov*, Z.Naturforsch. 57ª, 101 – 102 (2002).

[22]. *A. Iandelli*, Rare Earth Research, edited by *Kleber E. V., MacMillan Co*, New York 1966, pp. 135–144.

[23]. *Y.O. Ciftci, K.Colakoglu, E.Deligoz, and H. Ozısık,* Mat. Chem. And Phys., 108 (2008) 120.

[24]. *J. Mehl*, Phys. Rev. B 47 (1993) 2493.

[25]. *S.Q. Wang, H.Q. Ye*, Phys. Status Solidi B 240 (2003) 45.

[26]. *B. Mayer, H. Anton, E. Bott, M. Methfessel, J.Sticht, and P. C. Schmidt*, Intermetallics 11 (2003) 23.

[27]. *I. Johnston, G.Keeler, R. Rollins, and S.Spicklemire*, Solid State Physics Simulations, The Consortium for Upper-Level Physics Software, Jhon Wiley, New York, 1996.

[28]. *E. Schreiber, O. L. Anderson, N. Soga*, Elastic Constants and their Measurements, McGraw-Hill, New York, 1973.

[29]. *M.E. Fine, L.D. Brown, H.L. Marcus*, Scr. Metall. 18 (1984) 951.

ELECTRON TRANSPORT CHARACTERISTICS OF WURTZITE BULK ZnO AND $Zn_{1-x}Mg_xO$

M. DERYA ÖZDEMİR[a,c], ZEKİ YARAR[b], METİN ÖZDEMİR[c]

[a]*Department of Physics, Faculty of Arts and Sciences, Aksaray University, 68100, Aksaray, Turkey*

[b]*Department of Physics, Faculty of Arts and Sciences, Mersin University, Ciftlikkoy 33343, Mersin, Turkey*

[c]*Department of Physics, Faculty of Arts and Sciences, Çukurova University, 01330, Adana, Turkey*

The electron transport characteristics of wurtzite bulk ZnO and $Zn_{1-x}Mg_xO$ are presented using an ensemble Monte Carlo method. A three valley energy band model is used for the materials under consideration. The scattering mechanisms that are taken into account in Monte Carlo simulations are acoustic and optical phonon scatterings, inter valley (equivalent and non-equivalent) scattering, ionized impurity scattering and alloy disorder scattering. The electron drift velocity and valley populations are obtained as a function of time for various applied electric fields at different temperatures. The effect of alloy concentration on transport properties is also considered.

I. INTRODUCTION

Zinc Oxide (ZnO) is a unique and promising semiconducting material among II-VI wide band gap semiconductors. It is transparent in the visible range of the spectrum and becomes conducting when doped with suitable dopants. It has a direct band gap of 3.37 eV [1] at room temperature and has potential applications in large size flat displays [2], photovoltaic cells, in transparent electronics [3,4] among others. It can also be used as an oxygen gas sensor due to its conducting mechanism resulting from oxygen vacancies [5].

The band gap of bulk ZnO can be controlled by alloying it with suitable semiconductors such as MgO to obtain $Zn_{1-x}Mg_xO$ thin films with Mg content. Matsubara *et al.* [6] proposed to use band-gap modified $Zn_{1-x}Mg_xO$ as a transparent conducting film. They reported that when a transparent conducting oxide (TCO) such as ZnO material is used as transparent electrode with a wider band gap, the efficiency of UV or blue light emitting devices is increased. On the other hand a band-gap modified TCO may be used to control band lineup in hetero structures which is expected to improve the performance of thin film solar cells [6]. Cohen et al. [7] have observed that when the Mg content of epitaxially grown $Zn_{1-x}Mg_xO$:(Al,In) thin films is increased from 0 to 20 % the band gap increases but the conductivity, mobility and electron density decreases in annealed films. The decrease in mobility is due to a combination of increasing electron effective mass and alloy disorder scattering. Ellmer and Vollweiler [8] have investigated ZnO:Al and $Zn_{1-x}Mg_xO$:(Al) films and observed the highest moblities in ZnO:Al films deposited on a (110) sapphire plane and on a (100) MgO plane.

An important parameter that characterizes the transport properties of a semiconductor is the mobility of carriers which is a measure of the ability of charge carrier to gain speed at a given applied field. Electron transport is limited by the scattering mechanisms that are efficient in the semiconductor under consideration. While ionized impurity and acoustic phonons are effective at low temperatures, optic phonon scattering becomes the dominant mechanism that limits electron transport at high temperatures. Another important scattering process that becomes efficient in alloyed semiconductors such as ZnMgO considered in this study is alloy scattering. Therefore in this study transport characteristics of bulk ZnO and $Zn_{1-x}Mg_xO$ for different Mg contents are presented in a range of temperatures where alloy scattering is also included for $Zn_{1-x}Mg_xO$. The results will provide a basis for a comprehensive understanding of transient transport characteristics of ZnO and that of ZnMgO especially with regard to alloy concentration.

The organization of the paper is as follows: Theory and material parameters are given briefly in Section 2. In section 3 the transient transport characteristics of electrons and their discussions are presented for bulk ZnO and $Zn_{1-x}Mg_xO$. The calculation of electron transport at various applied electric fields, different temperatures and the effect of alloy concentration on transport are exhibited in this section. The conclusions are presented in section 4.

II. THEORY AND MODEL DESCRIPTION

A three-valley model is employed for the conduction band of wurtzite (WZ) ZnO and $Zn_{1-x}Mg_xO$ and ref. [9] is used to obtain band structure of ZnO. The interaction of electrons with ionized impurities is taken into account by considering the Brooks–Herring [10] and Conwell-Weisskopf [11] approaches. The alloy scattering is given as [12]

$$W = \frac{3\pi^3}{8\hbar} V_0 U_{all}^2 N(E_k) x(1-x)$$

where $V_0 = a_0^3/4$ is the volume of unit cell, a_0 is the lattice constant, U_{all} is alloy potential, x is the Mg content and $N(E_k)$ is the density of states. The alloy potential U_{all} may be selected in various ways and there is no experimental data for alloy potential for $Zn_{1-x}Mg_xO$. Therefore the conduction band offset provided in ref. [13] (U_{all} =0.25) is used as the alloy potential in the present study.

The values of the band gap energy and effective masses for ZnO are well known from literature [9]. These values are also known for $Zn_{0.95}Mg_{0.05}O$, $Zn_{0.9}Mg_{0.1}O$ and $Zn_{0.8}Mg_{0.2}O$ for Γ_1 valley only [7] (see Table 2). But the effective masses are unknown for Γ_3 and U valleys of Zn_{1-}

$_xMg_xO$ systems. Therefore to have an idea of the transport characteristics of ZnMgO systems we make the following assumption without any solid justification for it: that the rate of increase of effective masses in the valleys of ZnO is exactly mimicked by the rate of increase of effective masses in the corresponding three valleys of $Zn_{1-x}Mg_xO$ systems. Since the effective masses in all three valleys of ZnO are known and since the effective masses in the Γ_1 valley of $Zn_{1-x}Mg_xO$ systems (x=0.01, 0.05 and 0.2) are also known, the effective masses in the other valleys of $Zn_{1-x}Mg_xO$ for each value of *x* can be calculated by using the assumption just mentioned. For details see Table 2. The energy differences between the bottom of Γ_1 and the other valleys and the number of equivalent valleys for ZnO are taken from ref.[9]. The number of particles (electrons) used in the Monte Carlo calculation of drift velocities and other related quantities is 8000.

Table.1

Material parameters for wurtzite ZnO and $Zn_{1-x}Mg_xO$

Parameters	**Unit**	**ZnO**	**$Zn_{1-x}Mg_xO$**
Mass density ρ	kg/m^3	5678[a]	...
Static dielectric constant ε_s	ε_0	8.12[b]	8.5[d]
Optical dielectric constant ε_∞	ε_0	3.72[b]	3.4[e]
LO-phonon energy	meV	72.[c]	…
İntervalley phonon energy	meV	72.[c]	…
Acoustic phonon velocity $(C_l/\rho)^{1/2}$	m/s	6200[a]	…
Deformation potential *D*	eV	3.8[b]	…
Inter valley Deformation Pot.			
(equivalent and non-equiv.) D_{iJ}	eV/m	$1x10^{11*}$	…
Conduction band offset	ΔE_C (eV)	…	0.25[g]
Lattice constant	Å	3.2495[a]	3.26[f]
Band gap	eV	3.4[c]	…
Band gap(x=0.05)	eV	...	3.32[d]
Band gap(x=0.1)	eV	…	3.51[d]
Band gap(x=0.2)	eV	...	3.8[d]
[a]: Ref. [17], [b]: Ref. [16], [c]: Ref. [9], [d]: Ref. [7], [e]: Ref. [18], [f]: Ref. [19], [g]: Ref. [13], [*]: Assumed to be equal to GaAs value.			

Table.2

Valley parameters for wurtzite ZnO and $Zn_{1-x}Mg_xO$

Valley ZnO		**Γ_1**	**Γ_3**	**U**
Inter valley energy sep.	ΔE_i (eV)	…	4.4[a]	4.6[a]
Number of equiv. valleys	N_{vi}	1[a]	1[a]	6[a]
Effective mass	m_i/m_0	0.318[b]	0.42[a]	0.7[a]
Valley $Zn_{1-x}Mg_xO$		**Γ_1**	**Γ_3**	**U**
Effective mass for x=0.05	m_i/m_0	0.462[c]	0.61[*]	1.02[*]
Effective mass for x=0.1	m_i/m_0	0.7338[c]	0.97[*]	1.61[*]
Effective mass for x=0.2	m_i/m_0	1.5586[c]	2.05[*]	3.4[*]
[a]: Ref. [9], [b]: Ref. [16], [c]: Ref. [7] [*]: Our assumed value (see the text for the details).				

III. RESULTS AND DISCUSSIONS

The transient electron transport characteristics for WZ ZnO and $Zn_{1-x}Mg_xO$ systems are obtained by using an ensemble Monte Carlo simulation where the scattering mechanisms mentioned in the previous sections are taken into account [14, 15]. Tables 1 and 2 show the valley and material parameters employed in simulations. A doping concentration value of $N_D = 1\times10^{17}$ cm^{-3} is used and it is supposed to be equal to the free electron concentration for all cases considered in this study.

First we consider the electron drift velocities as a function of time at different electric fields for electrons in bulk ZnO at 77 K and 300 K, the results are shown in Fig.1. The maximum attainable velocity for a given field increases as the field value increases as expected and the lower the temperature, the higher the maximum velocity. This is due to the fact that as the temperature increases the dominant scattering mechanism becomes optic phonon scattering which is higher than the other scattering processes. Velocity overshoot is observed about above 400 kV/cm applied field values as can be seen in Fig.1.

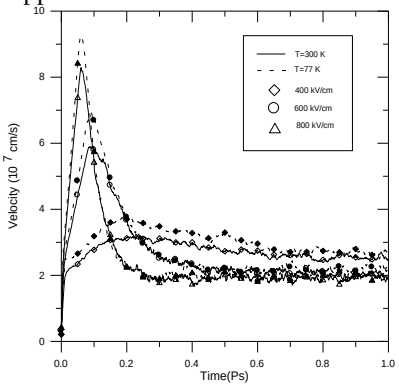

Fig.1 The electron drift velocity for bulk ZnO for various applied electric fields and the temperature of T=77 K (filled symbols with dashed lines) and T=300 K (empty symbols with lines).

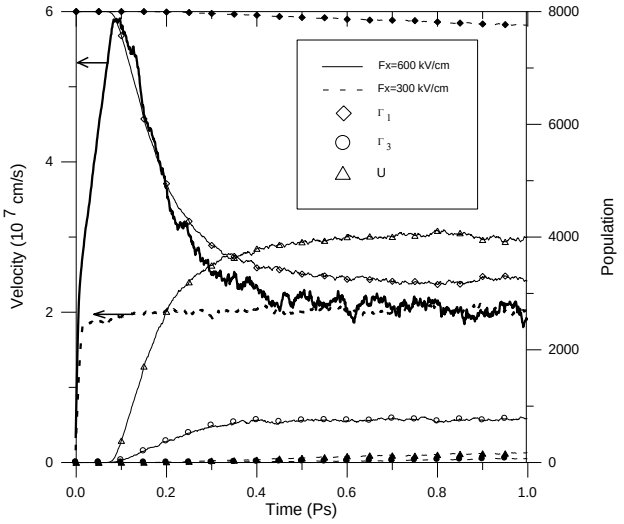

Fig.2 The drift velocity and Γ_1, Γ_3, U valley occupancies at applied two different electric fields F_x= 300 kV/cm (solid symbols) and F_x= 600 kV/cm (empty symbols) for bulk ZnO at room temperature.

Next we consider the occupancy of valleys by electrons. Fig. 2 depicts the occupancy of all three valleys of ZnO at two different values of applied electric field at room temperature. When the field is low (300 kV/cm) only the Γ_1 valley is populated primarily and the other upper two valleys are only partially occupied. When however the field value is increased to 600 kV/cm, the upper valleys also become populated. This is due to the fact that as the energy of carriers increases inter valley transfers begin to take place. But since the effective mass of electrons is higher in upper valleys (see Tables 1 and 2) the drift velocity of carriers decreases. This can clearly be seen in Fig. 2 where the maximum velocity attained by the carriers begin to decrease immediately after Γ_3 and *U* valleys begin to be populated by the carriers.

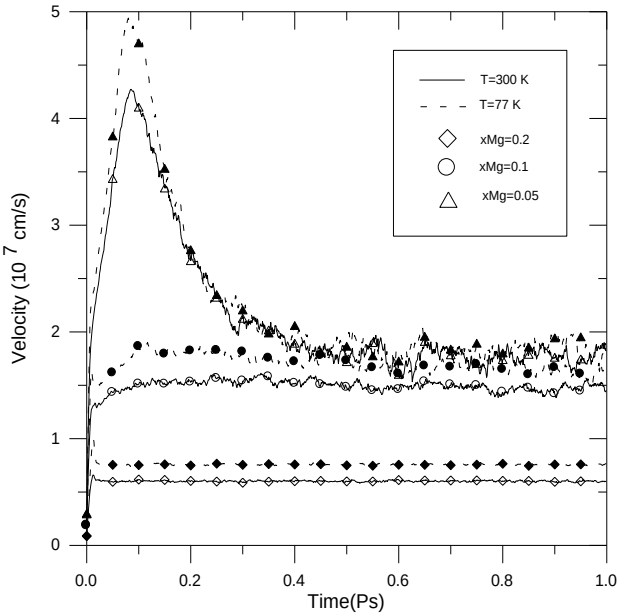

Fig.3 The electron drift velocity at different alloy concentrations in $Zn_{1-x}Mg_xO$ at an applied field of F_x= 800 kV/cm for two different temperatures. The filled symbols with dashed lines are for T=77 K and empty symbols with solid lines refer to T=300 K.

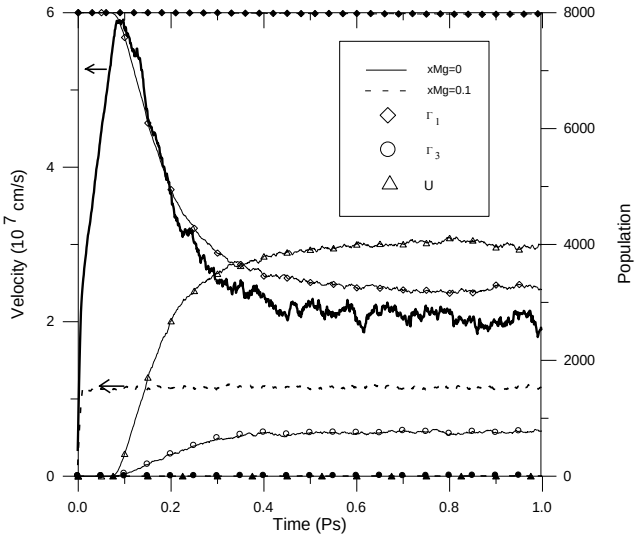

Fig.4 The drift velocity in ZnO and in $Zn_{1-x}Mg_xO$ for the case of x=0.1 and the occupancies of Γ_1, Γ_3, U valleys at an applied field of F_x= 600 kV/cm at room temperature.

The effect of alloy concentration is also considered and the results are depicted in Fig. 3. The velocity of carriers is shown at two different temperatures at an applied field of 800 kV/cm for $Zn_{1-x}Mg_xO$ for Mg concentrations x=0.05, 0.1 and 0.2. Note the tremendous effect of the presence of alloys on the velocity of carriers. Alloy scattering depends on alloy concentration nearly linearly for the concentration values considered in this study. Therefore an increase of concentration from 0.05 to 0.2 amounts to approximately a four-fold increase in scattering rate due to alloys.

Finally we consider the valley occupancies in the presence of alloys and compare the occupation of valleys for ZnO and $Zn_{1-x}Mg_xO$ for x=0.1. The results are shown in Fig. 4. Note that alloy presence suppresses inter valley transfers and only the Γ_1 valley of $Zn_{1-x}Mg_xO$ is populated at an applied field of 600 kV/cm. As can be seen in Fig. 4, alloy presence also suppresses the velocity over shoot effect which is mainly due to the difference between momentum and energy relaxation times.

IV. CONCLUSIONS

The drift velocity of electrons as a function of time is obtained at various applied electric fields and at different temperatures using an ensemble Monte Carlo technique for ZnO and $Zn_{1-x}Mg_xO$ materials. The effect of alloy concentration on the transport characteristics is also investigated. The presence of alloys even at very low concentrations reduces the peak velocity attainable at an applied field considerably. It also suppresses velocity over shoot effects. Velocity-time curves in bulk ZnO exhibit overshoot peaks after approximately 400 kV/cm and also the same overshoot effects observed nearly after 600 kV/cm for low (x=0.05) Mg content in $Zn_{1-x}Mg_xO$. The populations of valleys are also obtained in the presence and absence of alloys and it is observed that the transfer of carriers to upper valleys is reduced considerably when alloys are present.

[1]. *V. Srikant, D.R. Clarke,* J. Appl. Phys., 1998, 83, 5447.

[2]. *R. L. Hoffman, B. J. Norris, J. F. Wagera,* Appl. Phys. Lett., 2003,82, 733.

[3]. *J. F. Wager,* Science, 2003, 300, 1245.

[4]. *K. Nomura, H. Ohta, K. Ueda, T. Kamiya, M.Hirano, H. Hosono,* Science, 2003, 300, 1269.

[5]. *U. Lampe and J. Muller,* Sens. Actuators, 1989, 18 269.

[6]. *K. Matsubara, H. Tampo, H. Shibata, A.Yamada, P. Fons, K. Iwata, S. Niki,* Appl. Phys. Lett., 2004, 85, 1374.

[7]. *D. J. Cohen, K. C. Ruthe, S. A. Barnett,* J. Appl. Phys., 2004, 96, 459.

[8]. *K. Ellmer, G. Vollweiler,* Thin Solid Films, 2006, 496, 104.

[9]. *J. D. Albrecht, P. P. Ruden, S.Limpijumnong, W. R. L. Lambrecht, K. F. Brennan,* J. Appl. Phys., 1999, 86, 6864.

[10]. *H. Brooks and C. Herring,* Phys. Rev., 1951, 83, 879.

[11]. *E. M. Conwell and V. F. Weisskopf,* Phys. Rev., 1950, 77, 388.

[12]. *J. Singh, Physics of Semiconductors and Their Heterostructures,* 1993, McGraw-Hill, Singapore.

[13]. *D. J. Cohen, S. A. Barnett,* J. Appl. Phys., 2005, 98, 053705.

[14]. *K. Tomizawa, Numerical Simulation of Submicron Semiconductor Devices,* 1993, Artech House Inc, Japan.

[15]. *Z. Yarar, B. Ozdemir and M. Ozdemir,* Phys. Status Solidi (b) 2005, 242, 2872.

[16]. *D. C. Look, D. C. Reynolds, J. R. Sizelove, R.L.Jones, C. W. Litton, G. Cantwell, W.C.Harsch,* Solid State Commun., 1998, 105, 399.

[17]. *S. Adachi, Properties of Group-IV, III-V and II-VI Semiconductors,* 2005, JohnWiley and Sons, England.

[18]. *C. Bundesmann, M. Schubert, D. Spemann, T.Butz, M. Lorenz, E. M. Kaidashev, M.Grundmann, N. Ashkenov, H. Neumann, G.Wagner,* Appl. Phys. Lett., 2002, 81, 2376.

[19]. *A. Ohtomo, A. Tsukazaki,* Semicond. Sci. Technol., 2005, 20, S1.

TEMPERATURE DEPENDENT OF CHARACTERISTIC PARAMETERS OF THE Au/PVA (Co,Ni-DOPED)/N-nSi (111) SCHOTTKY DIODES

TUNCAY TUNÇ[a], İLBILGE DÖKME[b], ŞEMSETTIN ALTINDAL[c]

[a]Science Education Department, Faculty of Education, Aksaray University, Aksaray, TURKEY

[b]Science Education Department, Faculty of Gazi Education, Gazi University, Ankara, TURKEY

[c]Physics Department, Faculty of Arts and Sciences, Gazi University, Ankara, TURKEY

Current-voltage (I-V) characteristics of Au/PVA(Co,Ni-doped)/n-Si (111) SBDs have been investigated in the temperature range of 280-400 K. The zero-bias barrier height (Φ_{B0}) and ideality factor (n) determined from the forward bias *I–V* characteristics were found strongly depend on temperature. The forward bias semi-logarithmic I-V curves for the different temperatures have an almost common cross-point at a certain bias voltage. While the value of n decreases, the Φ_{B0} increases with increasing temperature. Therefore, we attempted to draw a Φ_{bo} vs q/2kT plot to obtain evidence of a Gaussian distribution of the barrier heights, and to calculate the values of mean barrier height and standard deviation at zero bias, respectively. Thus, a modified $\ln(I_o/T^2)-q^2\sigma_o^2/2(kT)^2$ vs q/kT plot gives Φ_{B0} and Richardson constant. This calculated value of the Richardson constant is very close to the theoretical value of 120 A/cm^2K^2 for n type Si. Hence, it has been concluded that the temperature dependence of the forward I-V characteristics of Au/PVA(Co,Ni-doped)/n-Si (111) SBDs can be successfully explained on the basis of thermionic emission (TE) mechanism with a Gaussian distribution (GD) of the barrier heights at Au/n-Si interface.

I. INTRODUCTION

Conducting polymers have generated a great interest owing to most attention for possible application in molecular electronic devices because of their unique properties and versatility [1-5]. Among these polymers is Poly (vinyl alcohol) (PVA) which is a water-soluble polymer produced industrially by hydrolysis of poly (vinyl acetate)[6-8]. It has been used in fiber and film products for many years. It has also a widespread use as a paper coating, adhesives and colloid stabilizer. Recently, metal/organic semiconductor Schottky junction became an attractive as an alternate to the metal/inorganic semiconductor junction. Schottky contacts play an important role in the performance of semiconductor devices. Nonetheless, the study of interface states is important for the understanding of the electrical properties of Schottky contacts. The transport properties of Schottky junctions are defined by the barrier height at the junction and by electronic states in the forbidden gap of the semiconductor [9-13]. The barrier height depends on the surface work functions of the metal and semiconductor as well on dipoles in the interface region. In this study, we have fabricated Au/ polyvinyl alcohol (Co,Ni-doped)/n-Si Schottky diodes and current–voltage (I–V) characteristics and interfacial properties of the diode have been investigated. Polyvinyl alcohol (PVA) film was used as an interfacial layer between metal and semiconductor. PVA doped with different ratio of cobalt and nickel was produced and PVA /(Co, Ni) nanofiber film on silicon semiconductor were fabricated by the use of electrospinning technique. In this work, we report on extraction of interface state density of Au/ polyvinyl alcohol (Co,Ni-doped)/n-Si Schottky diodes using the current–voltage (I–V) characteristics in the wide temperature range of 280-400 K. The other purpose of this paper is the calculation of the characteristics parameters such as ideality factor, barrier height, density of interface states and series resistance of Au/ polyvinyl alcohol (Co,Ni-doped)/n-Si Schottky diodes obtained from I–V characteristics at room temperature.

II. EXPERIMENTAL

The Au/ polyvinyl alcohol (Co, Ni-doped)/n-Si Schottky diodes were fabricated on the n-type (phosphor doped) Si single crystals, with a (111) surface orientation, 350 μm thick, 2 inch (5.08 cm) and 0.7 Ω-cm resistivity. For the fabrication process, Si wafer was degreased in a mix of a peroxide- ammoniac solution in 10 minute and then in H2O+ HCl solution and then was thoroughly rinsed in deionised water using an ultrasonic bath for 15 min. Preceding each cleaning step, the wafer was rinsed thoroughly in de-ionized water of resistivity of 18 M Ω cm for a prolonged time. After surface cleaning, high purity aluminium (Al) metal (99.999%) with a thickness of 2000A˚ was thermally evaporated on to the whole back surface of the Si wafer at a pressure about 10^{-6} Torr in high vacuum system. The ohmic contacts were formed by annealing them for 5 minutes at 450°C in N2 atmosphore. 0.5 g of cobalt acetate and 0.25 g of nickel acetate was mixed with 1g of polyvinyl Alcohol (PVA), molecular weight=72 000 and 9 ml of deionised water. After vigorous stirring for 2 h at 50°C, a viscous solution of PVA/(Co, Ni-doped) acetates was obtained. PVA(Co, Ni-doped) nanofiber film was fabricated on n-type Si by electrospinning technique[14,15]. The electrospinning system is composed (i) A high voltage power generator (ii) A syringe (iii) A collector made of a metallic material and (iv) A dosage pump (new era pump systems). The composite solution for spinning was loaded in to a 10 mL hypodermic stainless steel syringe with a needle (0.8 mm in diameter and 38 mm length) connected to a digitally controlled pump(New Era) which provides a constant flow rate of 0.02 ml/h. The metal tip of the syringe is connected to the power supply (SP-30P, Gamma High Voltage Research) and the other end is connected to the collector wrapped with Al folio. Si wafer was placed on the aluminum foil. The distance between the metal tip and the collected was kept 15 cm. Upon applying a high voltage of 20 kV on the needle, a fluid jet was ejected from the tip. The solvent evaporated and a charged fiber was deposited on to the Si wafer as a nonwoven mat.

After spining, the Schottky/rectifier contacts were coated by evaporation with Au dots with a diameter of about 1.0 mm (diode area= 7,85x10^{-3}cm^2). A simple illustration of the electrospinning system is given in Figure 1. The current–voltage (I–V) measurements were performed by the use of a Keithley 220 programmable constant current source, a Keithley 614 electrometer. All measurements were carried out with the help of a microcomputer through an IEEE-488 ac/dc converter card at room temperature.

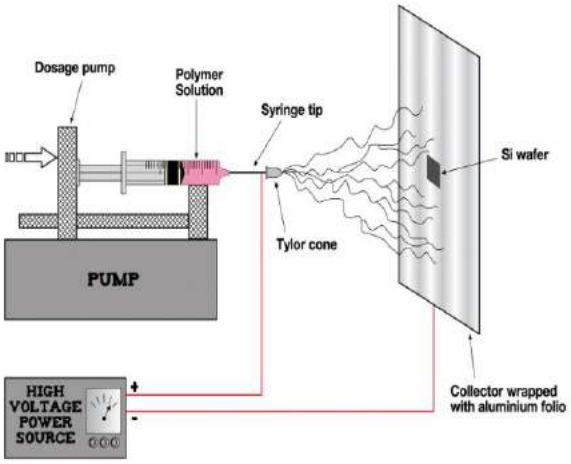

Fig. 1. Schematic representation of the electrospinning process.

III. RESULT AND DISCUSSION

The current through a Schottky barrier diode at a forward bias 'V', based on the thermionic emission theory $(V \geq 3kT/q)$, is given by the relations[2].

$$I = I_0 \exp\left(\frac{q(V - IR_s)}{nkT}\right)\left[1 - \exp\left(-\frac{q(V - IR_s)}{kT}\right)\right] \quad (1)$$

where *R*s is the series resistance, *V* the applied voltage, *n* the ideality factor, q the electronic charge, *k* the Boltzmann constant, *T* is the absolute temperature in Kelvin and Io is the reverse saturation current and can be written as

$$I_0 = AA^*T^2 \exp\left(-\frac{q\Phi_{B0}}{kT}\right) \quad (2)$$

where Φ_{B0} is the zero-bias barrier height, A is the diode area, A* is the effective Richardson constant and equals to 120 A/cm^2 K^2 for n-type Si. The ideality factor is calculated from the slope of the linear region of the forward bias ln I–V plot and can be written from Eq. (1) as

$$n = \frac{q}{kT}\left(\frac{dV}{d(\ln I)}\right) \quad (3)$$

The zero-bias barrier height F_{B0} is determined from the extrapolated I_0, and is given by

$$\Phi_{B0} = \frac{kT}{q}\ln\left[\frac{AA^*T^2}{I_0}\right] \quad (4)$$

The semi-logarithmic I–V characteristic of the Au/ PVA (Co, Ni-doped)/n-Si Schottky diode, measured at different temperatures over the range 280–400 K are shown in Fig.2. As can be seen in Fig.2, the forward and reverse bias currents of the diode increase with increase of temperature due to the increase in the numbers of carrier charges across the barrier height. This suggests that the carrier charges are effectively generated in the junction with temperature. It is seen that the temperature can improve the reverse and forward performance of the diode. The forward bias I–V characteristic is exponential at low bias voltages. But, at higher voltages, a deviation in I–V characteristic is observed due to series resistance and interfacial layer. The values of zero-bias barrier height Φ_{B0} and ideality factor (n) were calculated from Eqs. (3) and (4) for each temperature, respectively.

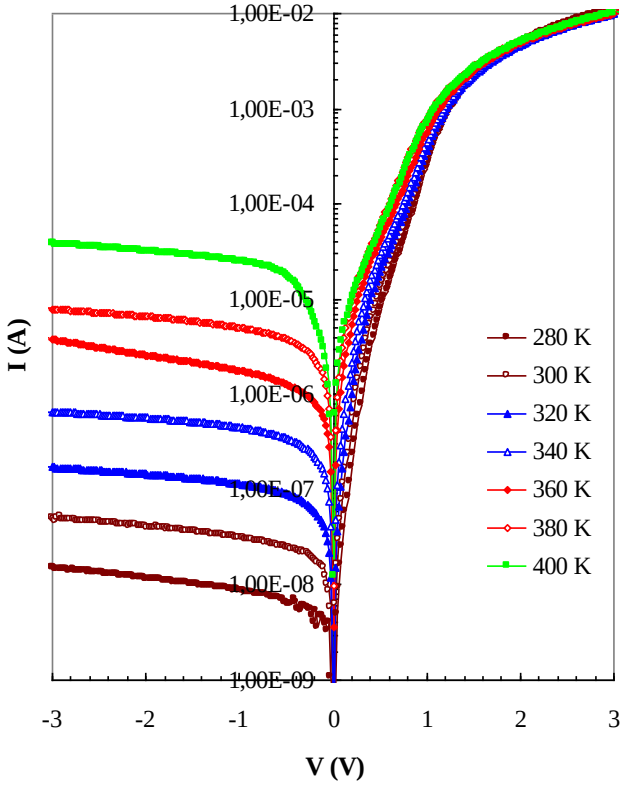

Fig. 2. The experimental forward bias I–V characteristics of the Au/ PVA (Co, Ni-doped)/n-Si Schottky diodes at various temperatures.

As shown in Table 1, the experimental values of Φ_{B0} and n for the Au/ PVA (Co, Ni-doped)/n-Si Schottky diode ranged from 0.908 eV and 1.51 (at 400 K) to 0.747 eV and 2.13 (at 280 K), respectively. As shown in Fig. 3 and 4, the values of n and Φ_{B0} determined from semi-logarithmic forward bias I–V characteristics are strong function of temperature. The obtained results from I–V characteristics show that there is a decrease in Φ_{B0} and an

increase in the ideality factor with decreasing temperature. Similar results have been reported in the literature[11].

Table 1. Temperature dependent values of various diode parameters determined from *I-V* characteristics of Au/ PVA (Co, Ni-doped)/n-Si Schottky diodes in the temperature range of 280-400 K.

T(K)	I_o(A)	*n*	F_{Bo} (eV)	F_{Bf}(eV)
280	$2{,}72\text{x}10^{-9}$	2,13	0,7470	1,362
300	$9{,}76\text{x}10^{-9}$	2,09	0,7709	1,372
320	$1{,}90\text{x}10^{-9}$	1,83	0,8074	1,283
340	$5{,}06\text{x}10^{-8}$	1,70	0,8327	1,243
360	$1{,}81\text{x}10^{-7}$	1,62	0,8458	1,208
380	$3{,}97\text{x}10^{-7}$	1,55	0,8705	1,195
400	$5{,}54\text{x}10^{-7}$	1,51	0,9084	1,225

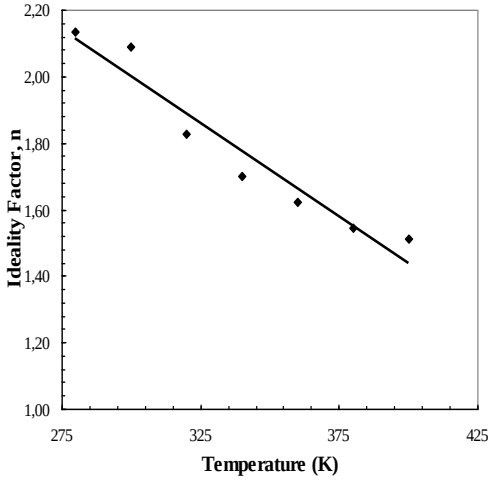

Fig. 3. The variation in the ideality factor with temperature for Au/ PVA (Co, Ni-doped)/n-Si Schottky diodes.

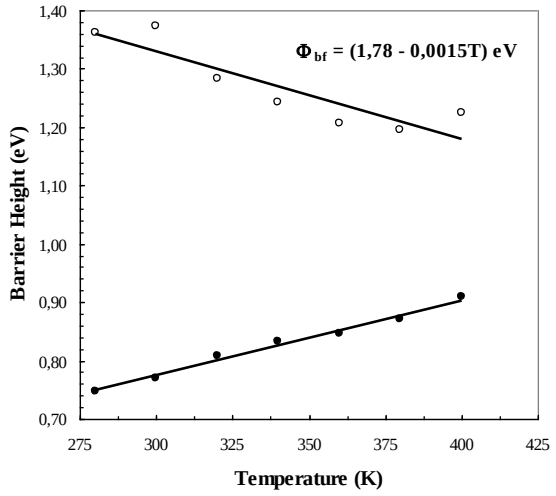

Fig. 4. Temperature dependence of zero-bias barrier height and flat-band barrier height for Au/ PVA (Co, Ni-doped)/n-Si Schottky diyotes.

Also, It is seen from Fig. 4, the flat band barrier height Φ_{bf} can be calculated from the experimental ideality factor and zero-bias BH Φ_{Bo} according to [9, 16-18].

$$\Phi_{bf} = n\phi_{BO} - (n-1)\frac{kT}{q}\ln\left(\frac{N_C}{N_D}\right) \qquad (5)$$

where N_C is the effective density of states in the conductivity band, and N_D is the carrier doping density of n-type Si with $5{,}86.10^{15}$ cm^{-3}. As shown in Fig.5, the temperature dependence of the flat band BH can be expressed as

$$\Phi_{bf}(T) = \Phi_{bf}(T=0) + \alpha T \qquad (6)$$

where Φ_{bf} is the flat band BH extrapolated to T = 0 K, and α is its temperature coefficient. The obtained experimental values, Φ_{B0} ,Φ_{bf} and n were reported in Table 1. This result is attributed to inhomogeneous interfaces and barrier heights. Also Schmitsdorf et al. [19] used Tung's theoretical approach and they found a linear correlation between the experimental zero-bias SBHs and ideality factors. Fig. 5 presents the barrier height versus the ideality factor for various temperatures. As shown in Fig.5, shows a plot of the experimental BH versus the ideality factor for various temperatures. The straight line in Fig. 5 is the least squares fit to the experimental data. It is seen from Fig. 5, there is a linear relationship between the experimental effective BHs and the ideality factors of the Schottky contact that was explained by lateral inhomogeneities of the BHs in the Schottky diode. The extrapolation of the experimental BHs versus ideality factors plot to n = 1 has given a homogeneous BH of approximately 0.993 eV. Thus, it can be said that the significant decrease of the zero-bias BH and increase of the ideality factor especially at low temperature are possibly caused by the BH inhomogeneties.

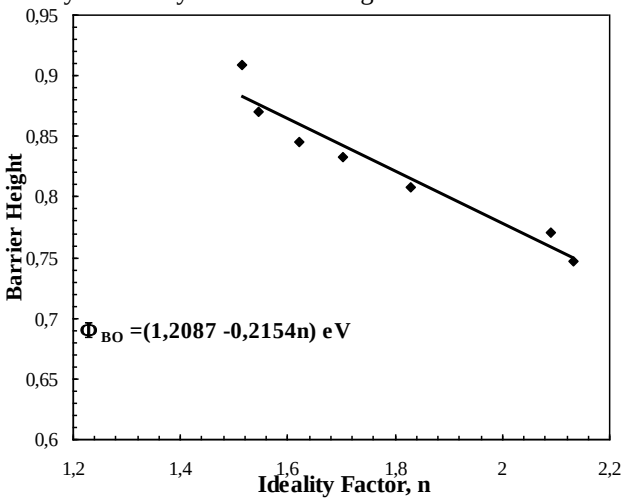

Fig. 5. Linear variation of apparent barrier height vs. ideality factors.

IV. CONCLUSION

In conclusion, the basic diode parameters such as the ideality factor and barrier height were extracted from electrical measurements of Au/ PVA (Co, Ni-doped)/n-Si Schottky diodes. The ideality factor of Au/ PVA (Co, Ni-doped)/n-Si Schottky diodes decreased with the increase in temperature but the barrier height increased. The changes are quite significant at low temperatures. Temperature dependence behavior of Φ_{B0} *(I-V)* and n is attributed to Schotky barrier inhomogenities by assuming a GD of BHs due to barrier inhomogeneties that prevailsat M/S interface.

[1]. *R.K. Gupta, R.A. Singh*, Materials Chemistry and Physics 86 (2004) 279–283.

[2]. *V.C. Nguyen, K. Potje-Kamloth*, Thin Solid Films 338 (1999) 142-148.

[3]. *Li-Ming Huang, Ten-Chin Wen, A. Gopalan*, Thin Solid Films 473 (2005) 300– 307.

[4]. *Ş. Aydoğan, M.Sağlam, A.Türüt*, Polymer, 46, (2005) 563-568.

[5]. *K.R. Rajesh, C.S. Menon*, Journal of Non-Crystalline Solids, 353, (2007) 398.

[6]. *N. Bouropoulos, G. C. Psarras, N. Moustakas, A. Chrissanthopoulos, and S. Baskoutas*, Phys. Stat. Sol.(a) 205, (2008) 2033–2037.

[7]. *S. M. Pawde, Kalim Deshmukh, Sanmesh Parab*, Journal of Applied Polymer Science, 109, (2008) 1328–1337.

[8]. *A. H. Salama, M. Dawy, and A. M. A. Nada*, Polymer–Plastics Technology And Engineering 43, (2004) 1067–1083.

[9]. *İ. Dökme, I.M. Afandiyeva, Ş.Altındal, Semıconductor Scıence and Technology*, **23** (3), Article Number: 035003 (2008).

[10]. *İ. Dökme Physica B: Condensed Matter*, 388, (2007)10-15.

[11]. *İ. Dökme and Ş. Altındal*, *Physica B: Condensed Matter*, 391**,** (2007) 59-64.

[12]. *İ. Dökme and Ş. Altındal*, *Physica B: Condensed Matter*, 393, (2007) 328-335.

[13]. *İ. Dökme and Ş. Altındal*, *Semıconductor Scıence and Technology*, 21 (8), (2006) 1053-1058.

[14]. *İ. Uslu, B. Başer, A. Yaylı, M.L. Aksu*, e-Polymers, 145, (2007).

[15]. *İ. Uslu, H. Daştan, A. Altaş, A. Yayli, O. Atakol, M . L. Aksu*, e-Polymers, 133, (2007).

[16]. *K. Akkılıç, F.Yakuphanoğlu,* Microelectronic Engineering, 85 (2008) 1826.

[17]. *L.F. Wagner, R.W. Young, A. Sugermen*, IEEE Electron. Dev. Lett. 4 (1983) 320.

[18]. *İ. Dökme, Ş. Altındal, M. Mahir. Bülbül*, Applied Surface Science 252 (2006) 7749.

[19]. *R.F. Schmitsdorf, T.U. Kampen, W. Mönch*, Surf. Sci. 324 (1995) 249.

[20]. *B. Batı, Ç. Nuhoğlu, M. Sağlam, E. Ayyıldız, A. Türüt*, Phys Scr, 61 (2000) 209.

[21]. *K. Maeda, H. Ikoma, K. Sato, T. Ishida*, Appl. Phys.Lett. 62 (1993) 20

A FIRST – PRINCIPLES STUDIES NdP

Y.O. CİFTCİ[1], K. ÇOLAKOĞLU[1], E. DELİGOZ, H. OZISIK[2]
[1]*Department of Physics, Gazi University, 06500 Ankara, Turkey*
[2]*Department of Physics, Aksaray University, 68100 Aksaray, Turkey*

We have studied the structural, elastic, electronic, thermodynamics and vibrational properties of NdP based on the the plane-wave pseudopotential approach to the density-functional theory within the GGA apraximation implemented in VASP (Viena Ab-initio Simulation Package). Specifically, lattice constant, bulk modulus, pressure derivative of bulk modulus (B'), phase transition pressure (P_t) from NaCl (B1) structure to CsCl (B2) structure, second-order elastic constants(C_{ij}) and related quantities, cohesive energy, Debye temperature (θ_D), melting temperature (T_m), band structures, and phonon dispersion curves are calculated and compared with the available experimental and other theoretical data. The most of our results presented here are obtained for the first time for NdP.

I. INTRODUCTION

The rare-earth monopnictides have attracted considerable attention due to their unusual magnetic, transport and phonon properties [1, and references given therein]. It is known that the source of these anomalous may stem from the presence of 4f level close to the Fermi level [2-5]. The degree of localization and itinerancy of f electrons strongly affect the electronic properties of rare-earth elements [3, 5]. Neodymium monopnictides, NdX, have a simple rocksalt (B1) structure at ambient conditions, and in earlier and more recent experimental works [6-16], particularly their magnetic, electrical, structural, and photoelectronic, properties were studied intensively. Theoretical calculations on the magnetic properties of the neodymium pnictides have been carried out [7] for the antiferromagnetic state. Pagare et al [4] have investigated the pressure induced phase transition of some rare earth mono-antimonides including the NdSb using the inter-ionic potential method. De et al [3] have calculated the electronic and optical properties of neodymium monopnictides using Linear Muffin-Tin Orbital method (LMTO). Sheng et al. have investigated the strength of *f* -electron localization in the rare earth mono-bismuth including the NdSb using the first principles calculations, and found it to be weakly delocalized due to the *f*- electron hybridization with pnictogen *p* and Nd *d* electrons.

The aim of the present paper is to reveal the detailed structural, elastic, thermodynamical, and lattice dynamical properties of NdP in B1 and B2 phases. In

Section 2, a brief outline of the method of calculation is presented. The section 3 is devoted to results and discussion, and in Section 4 the summary and conclusion is given.

II. METHOD OF CALCULATION

In the present work, all the calculations have been carried out using the Vienna ab initio simulation package (VASP) [17-20] based on the density functional theory (DFT). The electron-ion interaction was considered in the form of the projector-augmented-wave (PAW) method with plane wave up to an energy of 500 eV [19, 21]. This cut-off was found to be adequate for the structural, elastic properties as well as for the electronic structure. We do not find any statistically significant changes in the key parameters when the energy cut-off is increased from 500 eV to 550 eV. For the exchange and correlation terms in the electron-electron interaction, Perdew and Zunger-type functional [22-23] was used within the generalized gradient approximation (GGA) [21]. Self-consistent solutions were obtained by employing the 110 k-points for the integration over. For k-space summation the 12x12x12 Monkhorst and Pack [22] grid of k-points have been used.

III. RESULTS AND DISCUSSION

3.1. Structural and electronic properties

Firstly, the equilibrium lattice parameters have been computed by minimizing the crystal total energy calculated for different values of lattice constant by means of Murnaghan's equation of state (eos) [24] as in Figure.1. The bulk modulus, and its pressure derivative have also been calculated based on the same Murnaghan's equation of state, and the results are listed in Table 1 along with the experimental and other theoretical values. The calculated values of lattice parameters are found to be 5.897 $\mathring{A}$ in B1 structure and 3.594 $\mathring{A}$ in B2 structure for NdP. Our lattice constants are also listed in Table 1, and the obtained results are quite accord with the other theoretical and experimental findings [3, 25-26].

The cohesive energy (E_{coh}) is known as a measure of the strength of the forces, which bind atoms together in the solid state. In this connection, the cohesive energies of NdP in the B1 and B2 structures are calculated. The cohesive energy (E_{coh}) of a given phase is defined as the difference in the total energy of the constituent atoms at infinite separation and the total energy of that particular phase :

$$E^{AB}coh = [\, E^{A}_{atom} + E^{B}_{atom} - E^{AB}_{total} \,] \qquad (1)$$

where E^{AB}_{total} is the total energy of the compounds at equilibrium lattice constant and E^{A}_{atom} and E^{B}_{atom} are the atomic energies of the pure constituents. The computed cohesive energie (E_{coh}) are found to be 8.622 eV/atom in B1 structure, and 5.877 eV/atom in B2 structure for NdP, and they are also listed in Table 1.

We have plotted the phase diagrams (equation of state) for both B1 and B2 structures in Figure 2. The discontinuity in volume takes place at the phase transition pressure. The phase transition pressures from B1 to B2 structure are found to be 37 GPa from the Gibbs free energy at 0 K for NdP, and the related enthalpy versus

pressure graphs for the both structures are shown in Figure 3 .

Table1. Calculated equilibrium lattice constants(a_0), bulk modulus (B), and pressure derivatives of bulk modulus (B'), cohesive energy(E_{coh}), and other theoretical works for NdX (X= P, As, Sb and Bi) in B1 and B2 structures

NdP	Reference	a_0 (A)	B (GPa)	B'	E_{coh} (eV/atom)
B1	Present	5.897	76.851	3.88	8.622
	Exp.	5.826[a]			
	Theory	5.863[b]			
B2	Present	3.594	75.484	3.79	5.877

[a]: [25] [b]:[3]

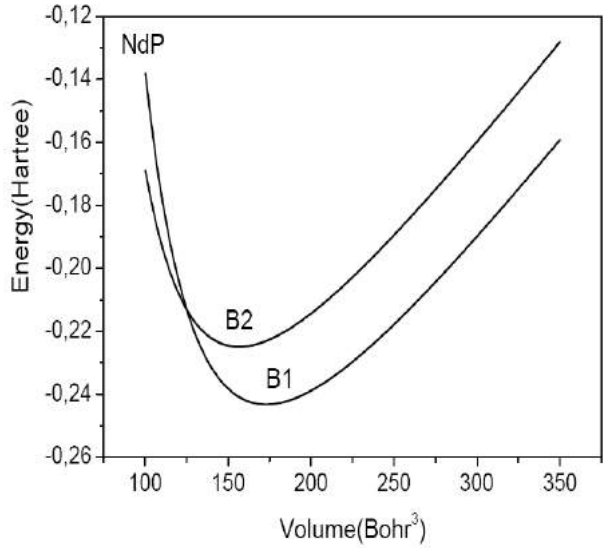

Fig. 1. Total energy versus volume curves of NdP

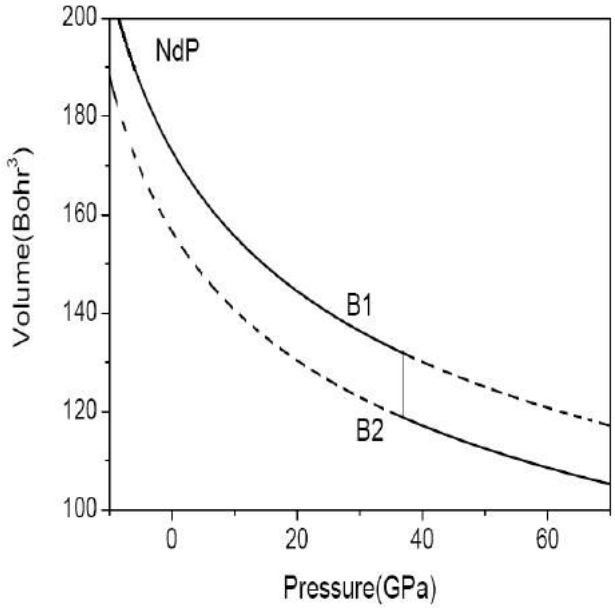

Fig. 2. Pressure versus volume curves of of NdP

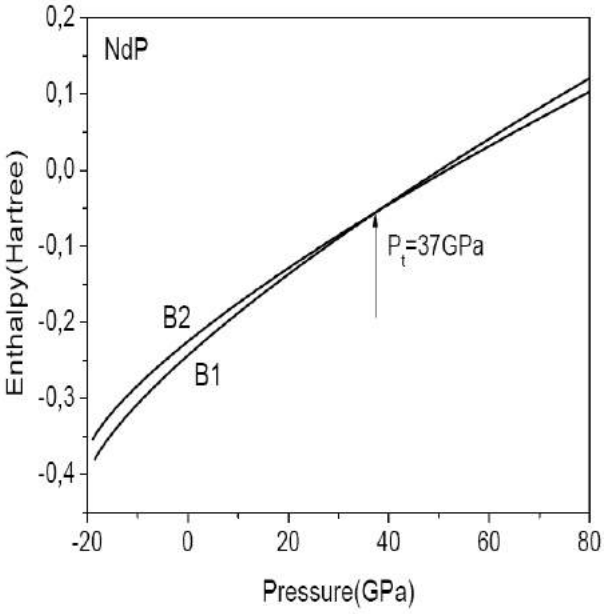

Fig. 3. Estimation of phase transition pressure from B1 to B2 of NdP

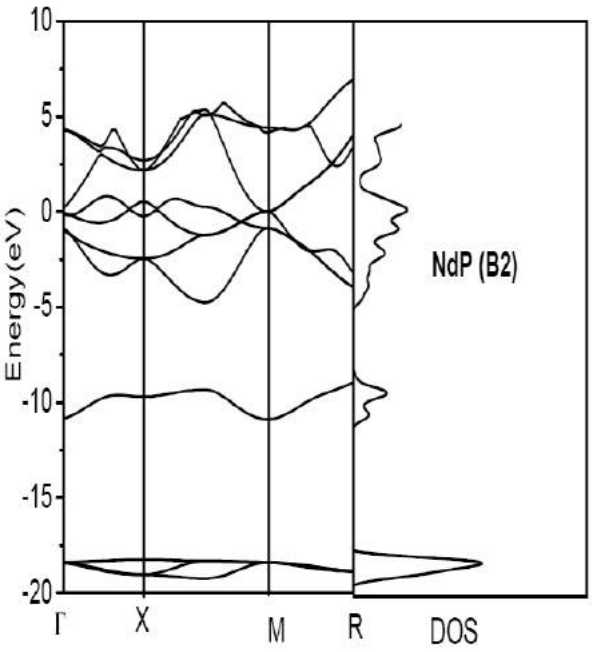

*Fig. 4.*Calculated band structure of NdP in phase B1

The calculated band structures of NdP in B1 and B2 structures are given in Figure 4 and 5 , respectively. It can be seen from the Figure 4 and 5 that no band gap exists for studied compounds, and they exhibit nearly semi- metallic character. The total electronic density of states (DOS) corresponding to the present band structures are, also, depicted in Figure.4 and 5, and the disappearing of the energy gap in DOS confirms the semi metallic nature of NdP . The similar situation is observed for LaN in our a recent work [27].

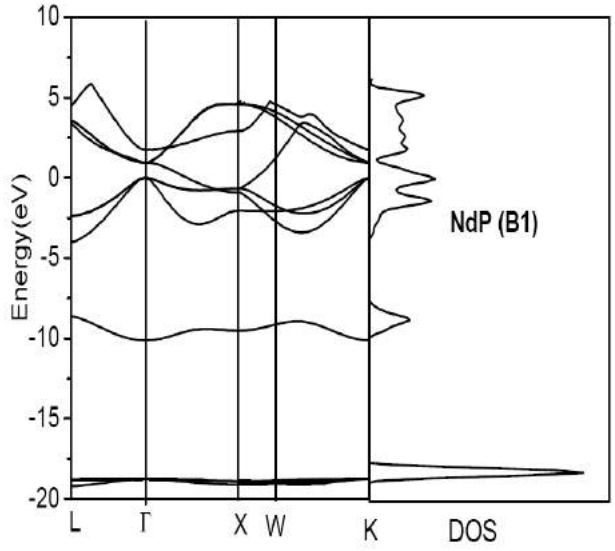

*Fig. 5.*Calculated band structure of NdP in phase B2

3.2.1 Elastic properties

The elastic constants of solids provide a link between the mechanical and dynamical behaviour of crystals, and give important information concerning the nature of the forces operating in solids. Their ab-initio calculation requires precise methods, since the forces and the elastic constants are functions of the first and second-order derivatives of the potentials.

Here we have used the "volume conserving technique" for obtaining the second-order elastic constants (C_{ij}). The listed values of C_{ij} in Table 2 are in reasonable order, and their experimental and theoretical values are not available yet.

The Zener anisotropy factor *A*, Poisson ratio υ, and Young's modulus *Y*, which are the most interesting elastic properties for technological applications, are also calculated in terms of the computed data using the following relations [28] :

$$A = \frac{2C_{44}}{C_{11} - C_{12}}, \tag{2}$$

$$\upsilon = \frac{1}{2}\left[\frac{(B - \frac{2}{3}G)}{(B + \frac{1}{3}G)}\right], \tag{3}$$

and

$$Y = \frac{9GB}{G + 3B} \tag{4}$$

where $G = (G_V + G_R)/2$ is the isotropic shear modulus, G_V is Voigt's shear modulus corresponding to the upper bound of G values, and G_R is Reuss's shear modulus corresponding to the lower bound of G values, and can be written as $G_V = (C_{11} - C_{12} + 3C_{44})/5$, and $5/G_R = 4/(C_{11} - C_{12}) + 3/C_{44}$. The calculated Zener anisotropy factor (*A*), Poisson ratio (ν), Young's modulus (*Y*), and Shear modulus ($C' = (C_{11} - C_{12} + 2C_{44})/4$) are given in Table 3.

The Debye temperature (θ_D) is known as an important fundamental parameter closely related to many physical properties such as specific heat and melting temperature. At low temperatures, the vibrational excitations arise solely from acoustic vibrations. Hence, at low temperatures the Debye temperature calculated from elastic constants is the same as that determined from specific heat measurements. We have calculated the Debye temperature, θ_D , from the elastic constants data using the average sound velocity, v_m, by the following common relation given [29]

$$\theta_D = \frac{\hbar}{k}\left[\frac{3n}{4\pi}\left(\frac{N_A \rho}{M}\right)\right]^{13} \upsilon_m \tag{5}$$

where $\hbar$ is Planck's constants, *k* is Boltzmann's constants, N_A Avogadro's number, n is the number of atoms per formula unit, *M* is the molecular mass per formula unit, $\rho(=M/V)$ is the density, and v_m is obtained from

$$\upsilon_m = \left[\frac{1}{3}\left(\frac{2}{\upsilon_t^3} + \frac{1}{\upsilon_l^3}\right)\right]^{-13} \tag{6}$$

where v_l and v_t, are the longitudinal and transverse elastic wave velocities, respectively, which are obtained from Navier's equations [30]:

$$\upsilon_l = \sqrt{\frac{3B + 4G}{3\rho}} \tag{7}$$

And

$$\upsilon_t = \sqrt{\frac{G}{\rho}}. \tag{8}$$

The calculated average longitudinal and transverse elastic wave velocities, Debye temperature and melting temperature for NdPare given in Table 4. No other theoretical or experimental data exist for comparison with the present results.

The empirical relation [31], T_m=553 K+ (591/Mbar)C_{11} ± 300, is used to estimate the melting temperature for NdP, and found to be 1407 ± 300 K. This values are higher for NdP than those obtained for Nd (1297 K), We hope that the present results are a reliable estimation for these compounds as it contains only C_{11} which has a reasonable value.

Table 2. The calculated elastic constants (in GPa unit) in B1 structure for NdP

Materials	C_{11}	C_{12}	C_{44}
NdP	144.50	93.70	10.40

Table 3. The calculated Zener anisotropy factor (*A*), Poisson ratio (ν), Young's modulus (*Y*), Shear modulus (C') for NdP in B1 structure .

Material	*A*	υ	*Y* (GPa)	C' (GPa)
NdP	0.41	0.41	42.30	25.39

Table 4. The longitudinal, transverse, average elastic wave velocities, and Debye temperature for NdPin B1 structure.

Material	$\upsilon_l(m/s)$	$\upsilon_t(m/s)$	$\upsilon_m(m/s)$	$\theta_D(K)$	$T_m(K)$
NdP	4130	1620	1843	117	1407± 300

3.3 Phonon Dispersion Curves

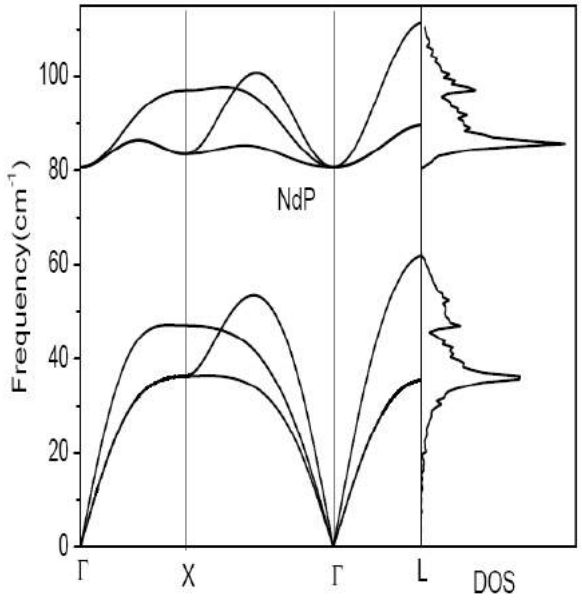

*Fig. 6.*Calculated phonon dispersions and total density of states for NdP in B1 structure

The present GGA phonon frequencies of NdP compound in B1 phase are calculated by the PHON program [32] using the forces obtained from the VASP. The PHON code calculates force constant matrices and phonon frequencies using the "Small Displacement Method" as described in References [33,34]. Specifically, the phonon dispersion curves and one-phonon density of state have been calculated in high symmetry directions using a 2x2x2 cubic supercell of 16 atoms. The obtained phonon dispersion curves and related one-phonon density of state for these compounds along the high symmetry directions are illustrated in Figure 6.

There is no experimental and other theoretical results on the lattice dynamics of these compounds in literature for the comparison with the present data. It is interesting to note that, the shape of the dispersion curves completely changes depending on the mass difference between pnictide ions. A clear gap between the acoustic and optic branches is observed for NdP.

IV. SUMMARY AND CONCLUSION

The fist–principles pseudopotential calculations have performed on the NdP. Our present key results are on the elastic, electronic, structural, thermodynamic and lattice dynamical properties for NdP. The lattice

parameters are in agreement with the other theoretical values. The computed band structures for NdP, which are not detailed, exhibite their metallic character. It is hoped that some our results, such as elastic properties, cohesive energies, Debye temperatures, and melting temperatures and vibrational properties , estimated for the first time, will be tested in the near future experimentally and theoretically

[1]. *Chun-Gang Duan , .F.Sabirianov, W.N.Mei, P.A.Dowben, S.S.Jaswal, and E.Y.Tsymbal*, J.Phys.Condens.Matter,2007, 19,315220.

[2]. *A.G. Puthukov, W.R.L.Lambrecht ,and B.Segall* ,Phys.Rev.B, 1996,53,4324.

[3]. *M. De, S.K. De*, J. Phys. And Chem. of Sol. 60,1999, 337.

[4]. *G.Pagare ,V.Srivastava, and S.P.Sanyal*, J.Phys.and Chem.Solids, 66 ,2005,1177.

[5]. *Q.G.Seng,B.R.Cooper,and S.P.Lim*, J.Appl.Phys. 73, ,1993, 5409.

[6]. *A.Furrer, J.Kjems,and O.Vogt* ,J.Phys.C :Solid State Phys. 5 ,1972,2246.

[7]. *P.Bak and P.A.Lindgard*, J.Phys.C :Solid State Phys. 6 ,1973,3774.

[8]. *A.Aeby,F.Huliger and B Natterer* ,Solid State Commun.13 ,1973,1365.

[9]. *P.S.Papomantellos,P.Fischer,O.Vogt,and E.Kaldis*, .Phys.C :Solid State Phys. 6 ,1973,725.

[10]. *S.Ono,K.Nomura and H.Hayakawa*, J.Less Common Metals,38,1974,119.
[11]. *M.Jian and R.Yufang* , Solid State Commun. 80 1991, 485.
[12]. *M.Jian and R.Yufang* ,J.Solis State Chem.95,1991, 346.
[13]. *M.Jian and R.Yufang* ,Thin Solid Films, 204,1991, 19.
[14]. *J. Hayashi, I. Shirotani, T. Adachi, K. Yamanashi, O. Shmonura, T.Kiegawa*, Solid Stat. Commun., 114, 2000, 561.
[15]. *J. Hayashi, H. Ando, Y. Sugiuchi, I. Shirotani, T.Kikegawa*, Photon Factory Activity Report, 24 Part B ,2007, 199.
[16]. *N. Wakabayashi and A. Furrer*, Phys. Rev. B. 13, 10 ,1976, 4343.
[17]. *G. Kresse and J. Hafner* , Phys. Rev. B 47, 1994, 558.
[18]. *G. Kresse and J. Furthmüller* , Comp. Mat. Sci. 6 1996,15.
[19]. *G. Kresse and D. Joubert* , Phys. Rev. B 59,1999, 1758.
[20]. *G. Kresse and J. Furthmüller*, Phys. Rev. B 54 , 1996,11169.
[21]. *P. E. Blochl*, Phys. Rev. B 50,1994,17953.
[22]. *J. P. Perdew and A. Zunger* Phys. Rev. B 23 , 1981, 5048.
[23]. *J. P. Perdew, J. A. Chevary, S. H. Vosko, K.A.Jackson, M. R. Pederson, D. J. Singh and C.Fiolhais* , Phys. Rev. B 46, 1992, 6671.
[24]. *F. D. Murnaghan*, Proc. Natl., Acad. Sci. USA 30 ,1994, 5390.
[25]. *Hulliger, K.A.Gschneidner and L. Eyring* (Eds.) Handbook on the Physics and Chemistry of Rare Earths, Vol. 4, ed. (North-Holland, Amsterdam)1979, chapter 33,p 153.
[26]. *G.L. Olcese*, J. Phys. F: Met. Phys. 9,1979, 569.
[27]. *Y.O. Ciftci, K.Colakoglu, E.Deligoz, and H.Ozısık*, Mat. Chem. And Phys.,108 , 2008, 120.
[28]. *B. Mayer, H. Anton, E. Bott, M. Methfessel, J.Sticht, and P. C. Schmidt*, Intermetallics 11 (2003) 23.
[29]. *I. Johnston, G.Keeler, R. Rollins, and S.Spicklemire*, Solid State Physics Simulations, The Consortium for Upper-Level Physics Software, Jhon Wiley, New York, 1996.
[30]. *E. Schreiber, O. L. Anderson, N. Soga*, Elastic Constants and their Measurements, McGraw-Hill, New York, 1973.
[31]. *M.E. Fine, L.D. Brown, H.L. Marcus*, Scr. Metall. 18 (1984) 951.
[32]. http://chianti.geol.ucl.ac.uk/~dario/ (1998).
[33]. *D. Alfè, G. D. Price, M. J. Gillan*, Phys. Rev. B, 64, (2001) 045123.
[34]. *G. Kresse, J. Furthmüller and J. Hafner*, Europhys. Lett. 32, 1995, 729.

THE C-V-f AND G/ω-V-f CHARACTERISTICS OF Au/ $SrTiO_3$/n-Si SCHOTTKY BARRIER DIODES (SBDs) WITH INTERFACIAL LAYER

U.AYDEMİR[1], İ.TAŞÇIOĞLU[1], T.ASAR[1], V.J.MAMEDOVA[2], T.S.MAMMADOV[1,3]

[1]Department of Physics, Faculty of Science and Arts,
Gazi University, 06500, Ankara, Turkey
uaydemir@gazi.edu.tr
[2]Baku State University, Z. Halilov str., 23, Baku, AZ-1148
[3]National Academy of Science,
Institute of Physics, Baku, Azerbaijan

In this study, the capacitance-voltage (C-V) and conductance-voltage (G/ω-V) characteristics of the Au/ $SrTiO_3$/n-Si (MFS) Schottky Barrier Diodes (SBDs) have been investigated by taking into account series resistance and interface states effects in the frequency range of 100 kHz to 2 MHz. It is shown that capacitance (C) and conductance (G/ω) values decreases with increasing frequency. The increase in capacitance especially at low frequencies is a result of the presence of interface states localized at M/S interface. The peak seen in C-V plots at low frequencies disappears with increasing frequency. Thus, the interface states (N_{ss}) can follow an ac signal more easily and contribute significantly to MFS capacitance. The voltage dependent profile of N_{ss} was obtained from Hill Coleman Method. The N_{ss} values ranges from $1.7x10^{12}$ to $3.8x10^{12}$ and decrease with increasing frequency.

I. INTRODUCTION

A large number of works were performed in the field of characterization of ferroelectric structures [1-12]. Ferroelectric thin films are highly attractive as a key material for capacitor dielectrics in future devices such as high-density dynamic random access memories [1] and on-chip electro-magnetic noise filters by their high permittivity. Recently, many kinds of ferroelectric thin films such as $SrTiO_3$ (STO), $SrBi_2Ta_2O_9$ (SBT), $BaTiO_3$ (BTO) have been extensively studied and especially STO is one of the most commonly used ferroelectric material with high-k dielectric constant. There are several methods to prepare STO thin films, including RF magnetron sputtering [6], metal-organic chemical vapor deposition (MOCVD) [7], molecular beam epitaxy (MBE) [8], sol-gel [9]. However, to perform a thin film on a substrate can not easy. Using a thin insulator layer such as SiO_2, SnO_2 and Si_3N_4 at Au/n-Si interface, MFS structure is converted to MFIS structure. This insulator layer shares the electric charge by virtue of the dielectric property of insulator layers and affects their main electrical properties.

In real MFS SBDs, the localized interface states at the semiconductor-insulator (M/S) interface and the series resistance (R_s) of the SBD lead to deviation from ideal case of MFS SBD. There are several methods [13-16] for the determination of R_s, and among them the most important one is the conductance technique developed by Nicollian and Goetzberger [14]. In this technique, the forward and reverse bias C-V-f and G/w-V-f measurement give the detail information about the distribution of interface states and series resistance of MFS SBD. In addition, the characterization of interface states in SBD has become a subject of vary intensive research in the last decade [13,17-19], and a number of workers have suggested various ways of characterization. Among them, Hill-Coleman method [18] is important in terms of being fast and reliable.

In this study, we investigate the frequency dependence of C-V and G/w-V characteristics of MFS SBD by considering R_s and N_{ss} effects. The C-V and G/w-V measurements were carried out at 100 kHz-2 MHz. The series resistance of Au/ $SrTiO_3$/n-Si (MFS) SBD was obtained from conductance method developed by Nicollian and Goetzberger [14]. In addition the frequency dependence of interface state density was obtained from the C-V and G/w-V measurements by using the Hill-Coleman method.

II. EXPERIMENTAL DETAILS

In this study, 2" diameter n-type single crystal float zone (100) silicon wafers having thickness of 350 μm with 1 Ω.cm resistivity were used as substrate materials. For fabrication a process, Si wafer was degreased in organic solvent of $CHClCCl_2$, CH_3COCH_3, and CH_3OH consecutively and then etched in a sequence of H_2SO_4 and H_2O, %20 HF, a solution of $6HNO_3$: $35H_2O$, %20 HF and finally quenched in deionized water for a prolonged time. Proceeding each cleaning step, the water was rinsed thoroughly in deionized water of resistivity of 18 MΩ-cm.

Substrates were clamped to a stainless steel holder provided with an optical heater. Thin films of $SrTi0_3$ were deposited by RF magnetron sputtering hot pressed $SrTiO_3$ ceramic target, in varying $Ar+0_2$ reactive gas mixtures on n-Si. Prior to film deposition, silicon substrates were sputter cleaned in pure argon ambient after raising the substrate temperature to 450 ^oC in 10^{-8} mbar high vacuum, to ensure the removal of any residual organics. During the sputter cleaning process of silicon substrates a shutter was used to cover the substrates. The films were deposited at a constant pressure of $4.2x10^{-3}$ mbar and a constant substrate temperature of 450 ^oC. Sputtering operations were carried out with mass flow controllers. The automatic control system of gas valves were used for Ar and O_2. The flow of Ar and O_2 were maintained at 9 sccm and 1 sccm (%90 Ar - %10 O_2), respectively. After deposition, film was annealed for 30 min at 400 ^oC only O_2 gas. To prevent microcracks in the films cooling process was maintained a low rate 1.0 ^oC/min. Finally, ~1000 Å thick STO films were prepared under these conditions for electrical and optical measurements.

The ohmic and rectifier contacts were formed by sintering the evaporation system in the pressure of 10^{-6} mbar with tungsten holder. As back contact high purity Au (%99,999) evaporated onto STO thin film at 450 ^{o}C, then temperature was decreased at 400 ^{o}C to diffuse Au into substrate. After that as rectifier contact ~1000 Å thick Al (%99,999 purity) dots of 1mm diameter were evaporated onto STO film at 100 ^{o}C with shadow mask. In this way, Al/$SrTiO_3$/n-Si structures were fabricated on the n-type Si wafer. The electrode connections were made by silver paste.

The capacitance-voltage (C-V) and conductance-voltage (G/ω-V) measurements of these structures were performed using Hewlett-Packard HP 4192A LF impedance analyzer (5 Hz–13 MHz) which was controlled by a microcomputer in the frequency range of 5 kHz - 1 MHz. Frequency dependence of C-V and G/ω-V characteristics were measured by applying a small ac signal of 40 mV amplitude and 1 MHz frequency while dc electric field was sequentially swept from (±7 V). All measurements were carried out with the help of a microcomputer through an IEEE-488 AC/DC converter card at room temperature.

III. RESULTS AND DISCUSSION

Many methods have been suggested for the study of the semiconductor/insulator interface states essentially based on differential capacitance measurement [13-15,18,20,22]. Among these methods, the conductance method maps out the energy distribution of the N_{ss} within band gap of semiconductor. Fig. 1 and Fig. 2 show the frequency dependent C_m-V and G_m/ω-V characteristics of Au/ $SrTiO_3$/n-Si MFS type SBD, respectively. As can be seen in these figures, capacitance and conductance values strongly depend on frequency and decrease with increasing frequency. The C-V plots exhibit a peak in the forward bias region about 0.9 V which disappears when the frequency is increased. Such a peak can be attributed to a distribution of deep states in the gap or the series resistance and interface states [23]. The interface states can follow easily an ac signal at low frequencies, thus, they contribute to capacitance values at low frequencies.

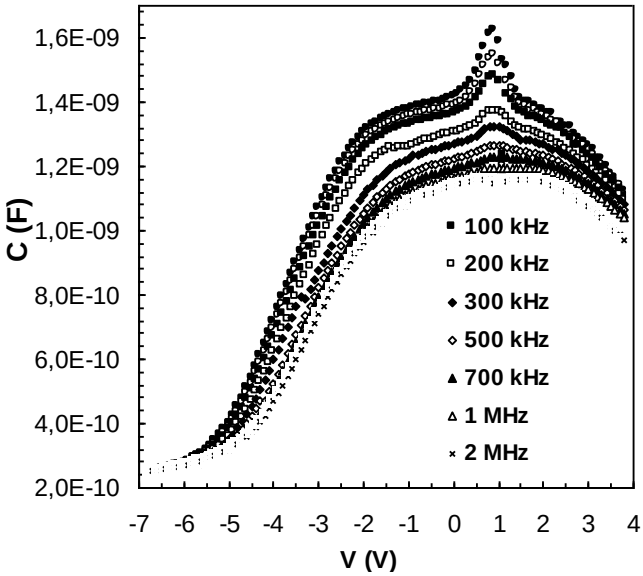

Fig.1. The frequency dependent C-V characteristics of Au/$SrTiO_3$/n-Si SBD.

The distribution profile of series resistance (R_s) was obtained as a fuction of frequency by using Nicollian and Goetzberger's method [14,15] from following Eq.

$$R_s = \frac{G_{ma}}{G_{ma}^2 + (\omega C_{ma})^2} \quad (1)$$

Here, w is the angular frequency, C_{ma} and G_{ma} represent the measured capacitance and conductance values in strong accumulation region, respectively.

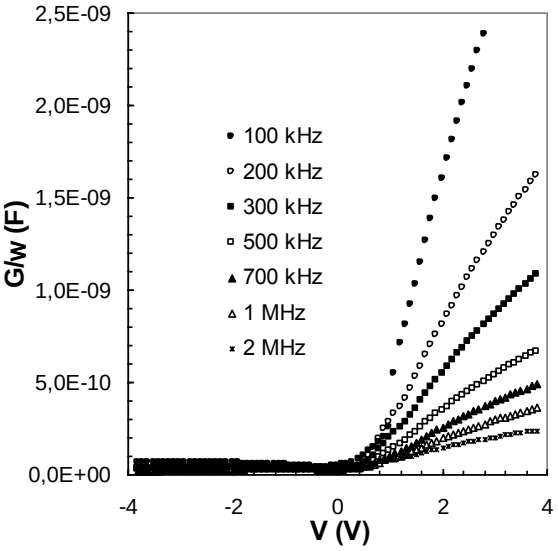

Fig 2. The frequency dependent G/ω-V characteristics of Au/$SrTiO_3$/n-Si SBD.

As seen in Fig 3. the R_s values give peak depending on frequency and amplitude of peaks decreases with increasing frequency. It is clearly said that the R_s depends on the changes in frequency. These experimental results confirm that the value of R_s is important parameters that strongly influence the electrical characteristics of Au/$SrTiO_3$/n-Si SBD [15-20].

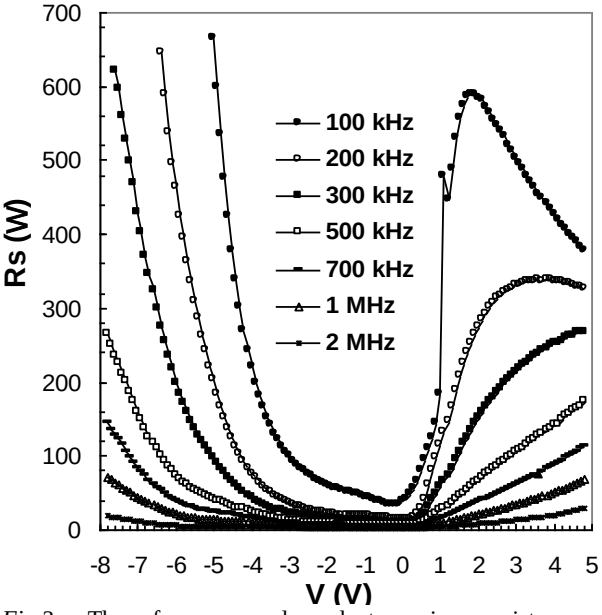

Fig.3. The frequency dependent series resistance in Au/SrTiO3/n-Si SBD.

The interface states (N_{ss}) occurring between $SrTiO_3$/Si at Si band-gap are estimated from the combination of various frequencies C-V and G/w-V characteristics by using Hill's method [19]. According to this method, density of interface states is given by

$$N_{ss} = \frac{2}{qA}\frac{(G_{ma}/\omega)_{\max}}{((G_{ma}/\omega)_{\max}C_{ox})^2 + (1 - C_{ma}/C_{ox})^2)} \quad (2)$$

where, A is the area of the diode, $(G_m/\omega)_{max}$ is the measured maximum conductance in the G/ω-V plot with its corresponding measured capacitance C_m and C_{ox} is the capacitance of interfacial layer.

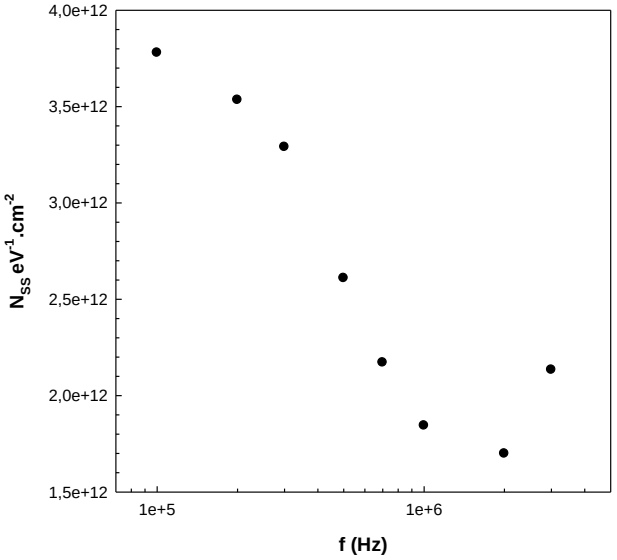

Fig.4. The variation of interface state density N_{ss} for Au/SrTiO3/n-Si SBD at room temperature.

According to Fig 4., in the low frequencies the N_{ss} in equilibrium with the semiconductor can follow the ac signal at low frequencies and yield an excess capacitance. In contrary to the low frequencies in the high frequencies, the N_{ss} cannot follow the ac signal. The N_{ss} of Au/$SrTiO_3$/n-Si SBD strongly depend on frequency and give rise to decrease in increasing frequency. As a result we can say that at enough high frequencies the N_{ss} cannot follow the ac signal and consequently cannot contribute to the device capacitance.

The C^{-2}-V plots of Au/$SrTiO_3$/n-Si SBD were given in Fig 5. In order to assess the doping concentration (N_D) and barrier height (Φ_B), C^{-2}-V plot were obtained for C-V data of Fig 5. The plots of C^{-2}-V have linear regions which indicate the formation of SBD. In rectifying contacts, the depletion layer capacitance is expressed as [14].

$$C^{-2} = \frac{2(V_R + V_0)}{q\varepsilon_s N_D A^2} \quad (3)$$

where V_R is the reverse bias voltage, V_0 is the built-in voltage at zero bias. In addition, from the slope of C^{-2}-V plot, N_D can be calculated. Also, the barrier height (Φ_B) calculated from C-V measurements is defined by

$$\Phi_B(C-V) = V_d + E_F - \Delta\Phi_B \quad (4)$$

$$V_d = V_0 + \frac{kT}{q} \quad (5)$$

where V_d is the diffusion potential, E_F is the Fermi energy measured from the conduction band edge, $\Delta\Phi_B$ is the image force barrier lowering. The calculated parameters of Au/$SrTiO_3$/n-Si SBD from C^{-2}-V data were given in Table 1.

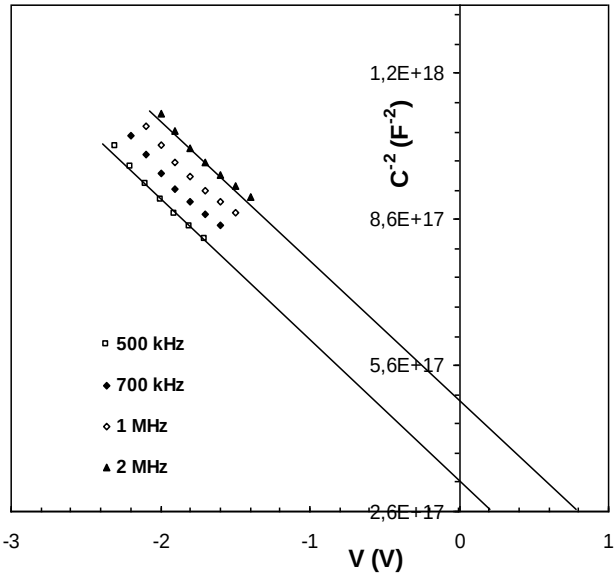

Fig 5. The C^{-2}-V plots of Au/$SrTiO_3$/n-Si SBD for various frequencies.

Table 1. The calculated electrical parameters of Au/$SrTiO_3$/n-Si SBD from C^{-2}-V plot at 1 MHz.

N_D (cm^{-3})	V_o (eV)	E_F (eV)	Φ_B (eV)	W_D (cm)
$3{,}26\times10^{17}$	0,75	0,111	0,687	$5{,}48\times10^{-06}$

IV. CONCLUSION

The frequency and voltage dependent electrical characteristics of Au/$SrTiO_3$/n-Si SBD were investigated in the frequency range of 100 kHz to 2 MHz at room temperature. The experimental results show that C and G/w are strongly influenced with applied voltage and frequency and their values decreases with increasing frequency in depletion and accumulation region due to distribution of N_{ss} between $SrTiO_3$/n-Si interface. As a result, the R_s and N_{ss} are important parameters for such devices due to affecting device performance directly

[1]. *R. Moazzami, C. Hu, W.H. Shepherd*, IEEE Electron. Device Lett., 11, 454, 1990
[2]. *A.F.Tasch, L.H.Parker*, Proc. IEEE, 77, 374 (1989).
[3]. *P.C. Joshi, S.B.Krupanidhi*, J.Appl. Phys., 73,7627 (1993).
[4]. *M.N.Kamalasanan, N.D.Kumar, S.Chandra*, J.Appl. Phys., 74, 679 (1993).
[5]. *G.D.Wilk, R.M.Wallace, J.M.Anthony*, J.Appl. Phys., 89, 5243 (2001).
[6]. *M.H.Song, Y.H.Lee, T.S.Hahn, M.H.Oh, K.H.J.Yoon*, Appl. Phys., 79, 3744 (1996).
[7]. *Y.B.Hahn, D.O.J.Kim*, Vac. Sci. Technol. A17, 1999 (1982).
[8]. *T.Tsurumi, T.Suzuki, T.Yamaze, M.Daimon*, Jpn, J.Appl. Phys., 33, 5192 (1994).
[9]. *M.Klee, U. Mackens*, Microelectron. Eng., 29, 185 (1995).
[10]. *M.K.Bera., S.Chakraborty, S.Saha, .Paramanik, S.Varma, S.Bhattacharya, C.K.Maiti*, Thin Solid Film. 504, 183 (2006).
[11]. *N. Konofaos. E.K.. Evangelou. Zhongchun Wang. V. Kugler. U. Helmersson*. Journal of Non-Crystalline Solids. 303, 185 (2002).
[12]. *N. Konofaos. E.K.. Evangelou*. Semicond. Sci. Technol. 18, 56 (2003).
[13]. *S.M. Sze*, Physics of Semiconductor Devices, second ed.. Willey, New York 1981.
[14]. Semiconductor (MOS) Physics and Technology, Wiley, Newyork, 1982.
[15]. *E.H Nicollian*, A. Goetzberger, Appl. Phys. Lett. 7, 216 (1965)
[16]. *H. Norde*, J. Appl. Phys. 50, 5052 (1979).
[17]. *S.K. Cheung, N.W. Cheung*, Apply. Phys. Lett. 49, 85 (1986).
[18]. *B. Tataroğlu, Ş. Altındal, A. Tataroğlu,* Microelectron Eng, 83, 2021 (2006).
[19]. *W.A. Hill, C.C. Coleman*, Solid State Electron., 23, 987 (1980).
[20]. *F. Parlaktürk, Ş. Altındal, A. Tataroğlu, M. Parlak, A. Agasiyev*, Microelectronic Engineering, 85, 81 (2008).
[21]. *H.C. Card, E.H. Rhoderick*, J. Phys. D 4, 1589 (1971).
[22]. *R. Castagne, A.Vapaille*, Surf.Sci. 28, 157 (1971).
[23]. *Ş.Aydoğan, K.Çınar, H. Asıl, C. Coşkun, A. Türüt*, J. Alloy. Compd., 476, 913 (2009).
[24]. *E.H. Rhoderick, R.H. Williams*, Metal Semiconductor Contacts (Clarendon, Oxford, 1988).

AB-INITIO STUDY ON THE STRUCTURAL AND ELASTIC PROPERTIES OF CUBIC STRUCTURES OF NdTe

Y.MOGULKOC[1], Y.O. CIFTCI [2], K.COLAKOGLU[2], E.DELIGOZ [3]

[1]Department of Physics Engineering, Ankara University, 06100 Tandogan, Ankara, Turkey
[2]Department of Physics, Gazi University, Teknikokullar, 06500 Ankara, Turkey
[3]Department of Physics, Aksaray University, 68100 Aksaray, Turkey

In this study, the structural, elastic and some thermodynamical properties of NdTe are investigated within the projector-augmented wave (PAW) method in cubic crystal structures of NdTe. Basic physical properties, such as lattice constant, bulk modulus, transition pressure and second-order elastic constants are calculated. We also predict shear modulus, poisson ratio, anisotropy factor, Young modulus, melting points and Debye temperatures for cubic NdTe compound.

I. INTRODUCTION

Recently, number of studies relevant to the rare-earth compounds which show crucial and interesting physical properties are performed [1-3].

Structurally, compound of NdTe has been studied experimentally. Imamalieva *et al* [4] have measured the lattice constants of NdTe compounds using differential thermal analysis (DTA) and x-ray diffraction. Lin *et al.* [5] have obtained lattice constant for NdTe using XRD technique and determined all the intermediate phases which exist in NdTe system. Schobinger *et al.* [6] have refined structural parameter values from the neutron intensities of rare earth monochalcogenides in different temperatures using neutron diffraction method.

Here, we have studied for cubic structures of NdTe. The structural, elastic and some thermodynamical properties of NdTe in NaCl(B1), CsCl(B2) and ZB(B3) phases are investigated using ab-initio method with plane-wave pseudopotential.

II. METHOD OF CALCULATION

In this study, all calculations have been made using reliable ab initio techniques by Vienna Ab initio Simulation Package (VASP) based on density functional theory. The electron-ion interaction was taken into consideration in the form of the potential projector-augmented-wave (pot PAW) method [7-10].

The cut-off energy value for resolute crystal structure has been got as 500 eV (Fig. 1). This cut-off value was found to be convenient for the structural, elastic properties as well as for the thermodynamic properties.

The 16x16x16 Monkhorst and Pack [11] grid of k-points have been used for integration in capable of being reduced part of the Brillouin zone.

III. RESULTS AND DISCUSSION

3.1. Structural properties

The equilibrium lattice constants of NdTe compound in cubic crystal structures have been found by minimizing the crystal total energy calculated for different values of lattice constant by means of Murnaghan's equation of state (eos) as in Fig. 2.

According to Figure 2 NaCl structure of NdTe has minimum energy and is more stable in studied structures.

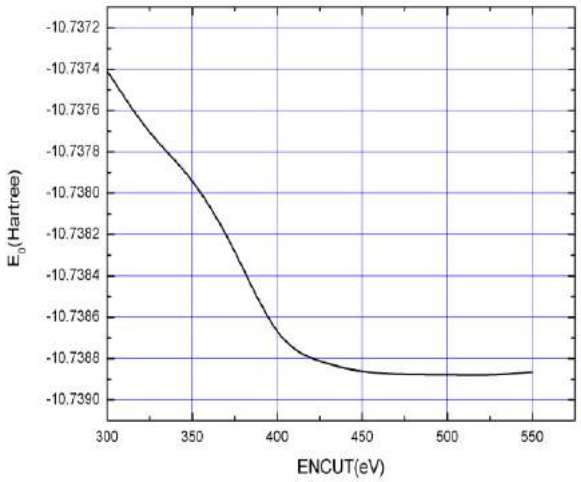

Fig. 1. Total energy versus cut-off energy of NdTe in NaCl(B1)

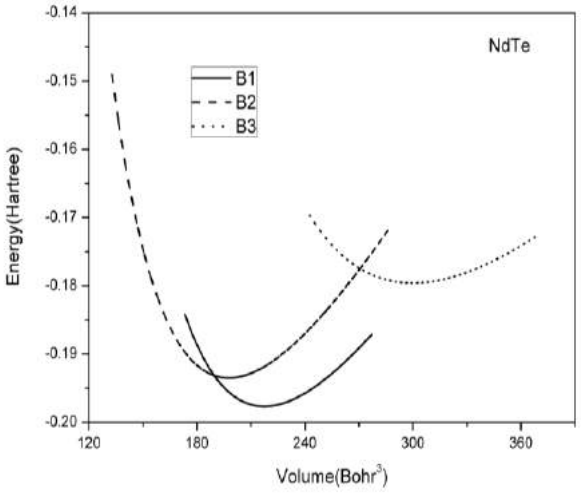

Fig.2. Total energy versus volume curves of NdTe in NaCl(B1), CsCl(B2) and ZB(B3) structure.

Murnaghan's equation is given in equation 1 [12].

$$E(V) = E_0 + \frac{B_0 V}{B_0'}\left[\frac{(V_0/V)^{B_0'}}{B_0'-1}+1\right] - \frac{B_0 V}{B_0'} \qquad (1)$$

The lattice constants of cubic of NdTe are calculated and represented in Table 1.

Table 1. Calculated lattice constants with experimental references

Material	Structure	Reference	a [Å]	B[GPa]	B'
NdTe	B1 (NaCl)	Present	6.367	57.61	4.45
		Exp. Ref: Imamalieva S.Z *et al.*	6.278		
		Exp. Ref: Lin W. *et al.*	6.262		
NdTe	B2 (CsCl)	Present	3.88	58.60	4.18
NdTe	B3 (ZnS)	Present	7.08	36.32	4.22

The calculated value of lattice constant is 6.367 $\mathring{A}$ in B1 stable phase for NdTe. The present value for lattice constant is quite accord with the other experimental values of references [4,5]. In this work the calculated lattice constant of NaCl crystal structure for NdTe is 0.014% bigger than the first reference value. It is compatible with literature. The lattice constants for other crystal structures have not been compared due to lack of references.

The formation energy is also calculated for cubic of NdTe crystal structures. The formation energy ($E_{formation}$) of a given phase is defined as the difference in the total energy of the constituent atoms at infinite separation and the total energy of that particular phase:

$$E^{AB}_{formation} = [E^{AB}_{total} - E^{A}_{atom} - E^{B}_{atom}] \qquad (2)$$

The results for NdTe compounds are given in Tabl.2

Table 2. Formation energy values for cubic structures of NdTe

Material	Reference	$E_{formation}$ [eV]
NdTe(B1)	Present	-0.0397
NdTe(B2)	Present	0.1898
NdTe(B3)	Present	0.7544

Formation energy value of NdTe in NaCl structure is negative. It is clear that B1 crystal structure is stable for cubic structure of NdTe.

We have plotted the phase diagram (equation of state) for both the NaCl and CsCl phases in Fig. 3. The discontinuity in volume takes place at the phase transition pressure. The phase transition pressures from B1 to B2 structure are found to be 6.47 GPa from the Gibbs free energy at 0 K for NdTe, and the related enthalpy versus pressure graphs for the both structures are shown in Figure 4. It can be seen that easily from the Figure 4 phase transition pressure value is 6.47 GPa from NaCl to CsCl.

3.2. Elastic properties

The elastic properties present important information about mechanical and dynamical behavior of crystals, and give the forces operating in solids. In particular, they provide information on the stability and stiffness of materials. Their ab-initio calculation requires precise methods, since the forces and the elastic constants are functions of the first and second-order derivatives of the potentials. Their calculation will provide a further check on the accuracy of the calculation of forces in solids. The effect of pressure on the elastic constants is essential, especially, for understanding interatomic interactions, mechanical stability, and phase transition mechanisms. It also provides valuable data for developing interatomic potentials.

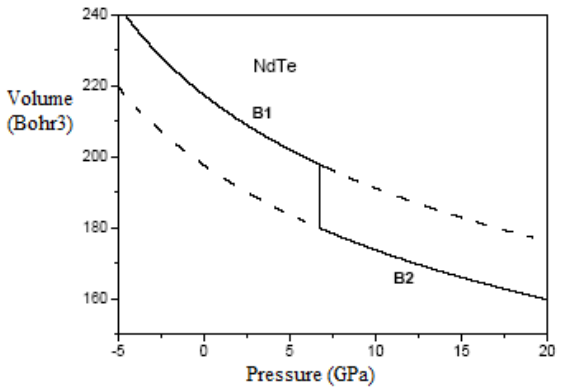

Fig.3. Pressure versus volume curves of NdTe

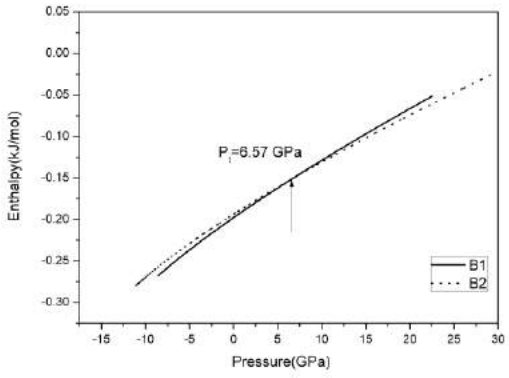

Fig.4. Enthalpy versus pressure curves of NdTe

There are two common methods [13-16] for obtaining the elastic data through the ab-initio modeling of materials from their known crystal structures: an approach based on analysis of the total energy of properly strained states of the material (volume conserving technique) and an approach based on the analysis of

changes in calculated stress values resulting from changes in the strain (stress-strain method).

Here we have used the stress/strain techniques for B1, B2 and B3 structures for obtaining the second-order elastic constants (C_{ij}). The calculated second-order elastic constant values for C_{ij} in Table 3 are in conceivable order. The experimental and theoretical values of Cij for NdTe are not available at present.

Table 3. Second-order elastic constants

Elastic constants	NdTe (B1)	NdTe (B2)	NdTe (B3)
	Stress/ Strain	Stress/ Strain	Stress/ Strain
C_{11}[GPa]	157.36	117.87	43.32
C_{12}[GPa]	12.51	34.46	34.09
C_{44}[GPa]	7.44	28.51	28.94

The Zener anisotropy factor A, Poisson ratio ν, and Young's modulus E, which are the most interesting elastic properties for applications, are also calculated in terms of the computed data using the following relations [17]:

$$A = \frac{2C_{44}}{C_{11} - C_{12}} \tag{3}$$

$$\upsilon = \frac{1}{2}\left[\frac{(B - \frac{2}{3}G)}{(B + \frac{1}{3}G)}\right] \tag{4}$$

The Young modulus is given in equation 5:

$$E = \frac{9GB}{G + 3B} \tag{5}$$

where $G = (G_V + G_R)/2$ is the isotropic shear modulus, G_V is Voigt's shear modulus corresponding to the upper bound of G values, and G_R is Reuss's shear modulus corresponding to the lower bound of G values, and can be written as $G_V = (C_{11}–C_{12} +3C_{44})/5$, and $5/G_R = 4/(C_{11}-C_{12})+ 3/ C_{44}$. The calculated Zener anisotropy factor (A), Poisson ratio (ν), Young's modulus (E), and Shear modulus ($C' = (C_{11}-C_{12}+2C_{44})/4$) for NdTe are given in Table 4, and they are close to those obtained for the similar structural symmetry.

Table 4. The calculated shear modulus, poisson ratio, anisotropy factor and Young modulus for cubic NdTe compound

	B1	B2	B3
C' [GPa]	72.425	41.703	4.615
G[GPa]	22.518	33.214	14.260
υ	0.327	0.258	0.326
A	0.103	0.684	6.270
E[GPa]	59.766	83.581	37.830

Our material exhibits compressible property in order to the fact that shear modulus has bigger value than bulk modulus. Also NdTe behavior is an anisotropic since the Zener anisotropy factor is different from 1.

The bulk modulus has also been calculated based on the same Murnaghan's equation of state and also using elastic constants. The results are given in Table 5.

Table 5. The calculated shear modulus, poisson ratio, anisotropy factor and Young modulus for cubic NdTe compound

Material	Structure	B^1 [GPa]	B^2 [GPa]
NdTe	NaCl(B1)	57.61	60.79
NdTe	CsCl(B2)	58.60	62.26
NdTe	ZB(B3)	36.32	37.17

B^1's are the optimization values of bulk modulus and B^2's are from elastic calculations. It is shown that the values of bulk modulus are reliable.

We have also calculated Debye temperature, melting point, average, transverse and longitudinal sound velocities for NdTe system using following equations. Debye temperature is given in equation 6 [18]:

$$\theta_D = \frac{\hbar}{k}\left[\frac{3n}{4\pi}\left(\frac{N_A\rho}{M}\right)\right]^{1/3} v_m \tag{6}$$

where $\hbar$ is Planck's constant, k is Boltzmann's constant, N_A is Avogadro's number, n is the number of atoms per formula unit, ρ is the density. Average sound velocity (v_m), transverse (v_t) and longitudinal (v_l) velocities are given respectively [19,20]:

$$v_m = \left[\frac{1}{3}\left(\frac{2}{v_t^3} + \frac{1}{v_l^3}\right)\right]^{1/3} \tag{7}$$

$$v_t = \sqrt{\frac{G}{\rho}} \tag{8}$$

$$v_l = \sqrt{\frac{3B + 4G}{3\rho}} \tag{9}$$

The melting temperature (T_m) has been calculated completely empirical relation [21].

$T_m = 553+(591/\text{Bar})C_{11}\pm 300\text{K}$ (10)

All these calculated values are represented in Table 6.

Table 6. The longitudinal, transverse, average elastic wave velocity, the Debye temperature and melting temperature for cubic NdTe in B1 structure.

Material	v_l [m/s]	v_t [m/s]	v_m [m/s]	θ_D [K]	T_m [K]
NdTe(B1)	3541.2	1795.1	2012.1	495.442	1483±300
NdTe(B2)	1815.2	1036.4	1151.7	375.764	1250±300
NdTe(B3)	2813.9	1428.5	1601.1	136.110	809 ±300

The melting point value is 1483±300K for NdTe in NaCl(B1). This value is bigger than that for constituent atom Nd (1294K) and for constituent atom Te (722.66K).

IV. CONCLUSIONS

In this work, the ab-initio pseudopotential calculations have been performed on the NdTe using the plane-wave pseudopotential approach to the density-functional theory (DFT) within PAW GGA approximation. Our present key results are on the structural and elastic properties for cubic structures of NdTe. The lattice constant is perfect compatible with the experimental values. The calculated elastic constants are also given in this text. It is supposed that some of our results, such as elastic constants and formation energy value for cubic NdTe is the first time in this work, will be tested in future experimentally and theoretically.

[1]. *C.G. Duan, R.F. Sabirianov, W.N. Mei, P.A.Dowben, S.S. Jaswal, E.Y. Tsymbal,* J. Phys. Condens. Matter 2007. Electronic, magnetic and transport properties of rare-earth monopnictides, 19: 315220.

[2]. *Lebegue S., Svane, S., Katsnelson, M.I.,Lichenstein and Eriksson O.* 2006. Multiple effects in the electronic structure of light rare-earth metals. Physical Review B,74: 045114.

[3]. *G. Pagare, P.S. Sanyal, P.K. Jha* 2005. High pressure behaviour of lanthanum mono pnictides. Journal of Alloys and Compounds, 398: 16-20.

[4]. *S.Z. Imamalieva, F.M. Sadygov and M.B. Babanly* 2008. New Thallium Neodymium Tellurides. Inorganic Materials. Vol.44, No.9, pp 935-938.

[5]. *W. Lin., H. Steinfink, and E.J. Weiss* 1965. The Phase Equilibria and Crystal Chemistry of the Rare Earth Group VI Systems. III. Neodymium-Tellurium. Inorganic Chemistry, Vol.4, No:6, 877-881.

[6]. Schobinger-Papamentellost P., Fischer P., Niggle A., Kaldis E. and Hildebrant V. 1974. Magnetic ordering of rare earth monochalcogenides: I. Neutron diffraction investigation of CeS, NdS, NdSe, NdTe and TbSe. J. Phys. C. Solid State Phys., Vol.7 2023.

[7]. *G. Kresse and J. Hafner* 1994. Phys. Rev. B, 47, 558.

[8]. *G. Kresse and J. FurthmÄuller* 1996. Comp. Mat. Sci. 6, 15.

[9]. *G. Kresse and D. Joubert* 1999. Phys. Rev. B, 59,758.

[10]. *G. Kresse and J. FurthmÄuller* 1996. Phys. Rev. B,54 11169.

[11]. *H.J. Monkhorst and J.D. Pack* 1976. Phys. Rev. B, 13, 5188.

[12]. *F.D. Murnaghan* 1994. Proc. Natl., Acad. Sci. USA 30, 5390

[13]. *J. Mehl* 1993. Phys. Rev. B ,47, 2493.

[14]. *O.H. Nielsen and R.M. Martin* 1993.Phys. Rev. Lett., 50, 697.

[15]. *Y. Le Page and P. Saxe* 2002. Phys. Rev.B, 65, 104.

[16]. *S.Q. Wang, H.Q. Ye* 2003. Phys. Sts. Sol.B, 240, 45.

[17]. *B. Mayer, H. Anton, E. Bott, M. Methfessel, J.Sticht, and P. C. Schmidt* 2003. Intermetallics, 11, 23.

[18]. *J.R. Christman* 1988. Fundamentals of Solid State Physics. Wiley, New York.

[19]. *O.L. Anderson* 1963. J. Phys. Chem. Solids 24 909- 917.

[20]. *E. Screiber, O.L. Anderson and N. Soga* 1973. Elastic constants and their measurements. McGraw-Hill, Newyork.

[21]. *I. Johnston, G. Keeler, R. Rollins and S. Spicklemire* 1996. Solid State Physics Simulations. The Consortium for Upper-Level Physics Software, Wiley, New York.

GROUND AND EXCITED STATE ENERGIES OF A HYDROGENIC IMPURITY OVER EXPONENTIAL TYPE ORBITALS

Y. YAKAR[1], B. ÇAKIR[2], A. ÖZMEN[2]

[1]*Physics Department, Faculty of Science and Letters, Aksaray University, 68100 Aksaray, Turkey*

[2]*Physics Department, Faculty of Science, Selçuk University, Campus 42031 Konya, Turkey*

The wavefunctions and energies of the ground and excited states of a hydrogenic impurity have been calculated by using Quantum Genetic Algorithm (QGA) and Hartree-Fock Roothaan (HFR) method. The hydrogenic impurity is considerable by assuming the confining potential to be infinitely deep and spherically symmetric. Linear combinations of Slater-Type Orbitals (STO) have been used for the description of the single electron wave functions. The results were compared with the literature results and observed to be in good agreement with literature of our results.

I. INTRODUCTION

Developments in modern technology over the past two decades have allowed the production of nanoscale semiconductor structures. Semiconductor nanostructures such as quantum wells, wires or dots have found various application areas especially as electronic devices such as single electron transistor, quantum computer, quantum dot infrared photodetector [1,2]. These nanostructures are called to be the artificial atoms that show the properties atoms such as discrete energy levels and shell structures[3,4]. Therefore, the electronic structure, optical and other physical properties of these structures have been intensively studied both theoretically and experimentally [5-13].

It is well-known that efficient and rapid computation of molecular integrals appearing in HFR approximation is of fundamental importance in study of the properties of atomic and molecular systems. The efficiency of the evaluation of these integrals strongly depends on the nature of the basis functions. The basis functions commonly used for *ab initio* calculations are the exponential type orbitals, such as the Gaussian type orbitals (GTOs) and Slater type orbitals (STOs). The great advantage for the use of GTOs is that multicenter molecular integrals can be calculated easily. However, GTOs are not able to represent the correct behaviour of the real molecular wavefunction in close neighbourhood of the nuclei and exponential decay at large distances. Due to this problem, it is desirable to use STOs, which describe the physical situation more accurately than the GTOs do.

The QGA method based on the principle of the energy minimization just like in the variational method is a version of the genetic algorithm method. The conventional linear variational method used in atomic and molecular structure calculations assumes the nonlinear parameters to be known a priori and determines only linear expansion coefficients, whereas in the QGA method both linear and nonlinear parameters can be determined from the principle of energy minimization at the same time. We combined the QGA procedure and HFR method to determine the parameters c_{ip} and ζ_p in Eq.(4) to minimizing the total energy over STOs. The details of the QGA used in this study are given in our previous works[7,8]. Since they represent the correct behaviour of the electronic wavefunctions, we have preferred STOs in the quantum mechanical analysis of the electronic structure of a QD. Therefore, we have chosen a linear combination of an *s*(or *p, d*) STOs having different screening parameters for an *s*(or *p, d*) type atomic orbital. To maintain the orthogonality of the orbitals the same set of screening parameters was used for all the one-electron spatial orbitals with the same angular momentum, and five basis sets $(k = 5)$ were taken to calculate the expectation value of the energy. On the other hand, during one iteration, to avoid repeatedly and to make minimum number of computations, in other words, to decrease computation time, we stored in an array all values of the kinetic, impurity attraction energy integrals over STOs. In the present work, we have calculated the ground and excited state energies of a hydrogenic impurity and performed the binding energy as a function of dot radius.

II. THEORY

We consider a shallow hydrogenic impurity located at the center of a spherical QD confined by an infinite spherical potential well. Within the frame work of the effective-mass approximation, the Hamiltonian of this system, in atomic units, can be written as follows

$$H = -\frac{\nabla^2}{2m^*} - \frac{Z}{\varepsilon_r\, r} + V_c(r), \qquad (1)$$

where Z is the impurity charge, r is the distance of the electron to the impurity, m* is the effective-mass of the electron and ε_r denotes the real part of the relative dielectric constant of the medium. The term $V_c(r)$ is the spherical confining potential as follows

$$V(r) = \begin{cases} 0, & r < R \\ \infty, & r \geq R. \end{cases} \qquad (2)$$

The time independent Shcrödinger equation for one-electron system is given by

$$H\psi = E\psi, \qquad (3)$$

in which E is the energy eigenvalue of the Hamiltonian operator and ψ is the eigenfunction of the operator. The wavefunction ψ is orthonormalized. The wavefunction

ψ can be expressed as linear combination of STOs, called basis functions, as follows

$$\psi_i = \sum_{p=1}^{k} c_{ip}\chi_p(\zeta_p, \vec{r}), \qquad (4)$$

where $p \to n\ell m$ are the quantum numbers of basis function, k is the size of basis sets, c_{ip} are the expansion coefficients and ζ_p is the screening constant. The unnormalized complex STO has the general form as

$$\chi_{n\ell m}(\zeta_p, r\theta\phi) = r^{n-1}e^{-\zeta r}Y_{\ell m}(\theta,\phi), \qquad (5)$$

where $Y_{\ell m}(\theta,\varphi)$ is well-known complex spherical harmonics in Condon-Shortley phase. In Eq.(3), the kinetic and the Coulomb attraction energy integrals over STOs have been extensively studied long before by many authors for the calculation of atomic system properties[14,15]. These integrals, for QDs, can be easily evaluated by modifying the expressions for atomic systems by appropriate consideration of the boundaries.

III. RESULTS AND DISCUSSION

We have calculated ground and excited state energies of a QD by using a combination of the QGA and RHF method. We have used the material parameters of GaAs, which are $m_{GaAs} = 0.067m_0$ and $\varepsilon_{GaAs} = 13.18$. The effective *Rydberg* energy $R_y^* = \hbar^2/m^*\mathrm{a}^*$ and the effective Bohr radius $\mathrm{a}^* = \hbar^2\varepsilon/m^*e^2$ have been used. The effective Rydberg energy and Bohr radius are taken $R_y^* = 5.72meV$, $a^* \cong 100\,\text{Å}$ for GaAs. Our results are given in terms of atomic units(Hartrees), and these results include only terms with a fixed magnetic quantum numbers *m*(i.e., *m*=0).

The energy results obtained for the ground E_{1s}, the first excited E_{1p} and the second excited E_{1d} states of the one-electron QD are listed in Table 1 for different values of dot radius R. This table also contains the results found in literature as well for comparison. It is clear from Table 1 that our results for the ground and excited states are in good agreement with the exact ones obtained using a simpler exact solution. As seen from Table 1, for each *n*-state, the energies of the QD with and without impurity decrease when the dot radius increases. At ranges approximatly $R < 1.85a^*$ for the *1s*-state, the kinetic energy contributes to a much grater extent than the impurity attraction energy, however, at ranges $\mathrm{R} \geq 1.15\mathrm{a}^*$, the impurity attraction contributes to much grater extent than the kinetic energy, thus the total energy of hydrogenic impurity is negative. Similarly, the impurity attraction energy contributes to a much grater extent than the kinetic energy at ranges approximately $R \geq 5.5a^*$ for the *1p*-state and $R \geq 10a^*$ for the *1d*-state, respectively. It is found that when the dot radius is large enough, the energy of the hydrogenic impurity approaches the value corresponding energies of a free space hydrogen atom $E \cong -Z^2R_y/n^2$, that is, when dot radius is large enough (R=15a*), as can be seen from Table 1, the ground state energy is -0.5au as expected, which is the ground state energy of the free space hydrogen atom. In the same way, the first excited (*1p*) and the second excited (*1d*) state energies for large dot radius (R=15a*) approaches to -0.125au and -0.055au as expected, which are the first and the second excited state energy of the free space hydrogen atom.

Fig.1 shows the energies of the ground, the first and the second excited states of one-electron QD with impurity as a function of dot radius. As seen from Fig. 1 the energies decreases with increasing dot radius, and then the energies approach a constant value corresponding to the energy of a free space hydrogen atom when dot radius is large enough.

The binding energy of an electron to impurity in a single-electron QD for the ground (*1s*), the first (*1p*) and the second (*1d*) states are given in Fig.2. The binding energy is defined as the change in energy of electron due to the existence of the impurity, that is $\Delta E = E_0 - E_{imp}$, where E_{imp} and E_0 are the electron energies with and without the impurity, respectively. As the dot radius increases the binding energy decreases.

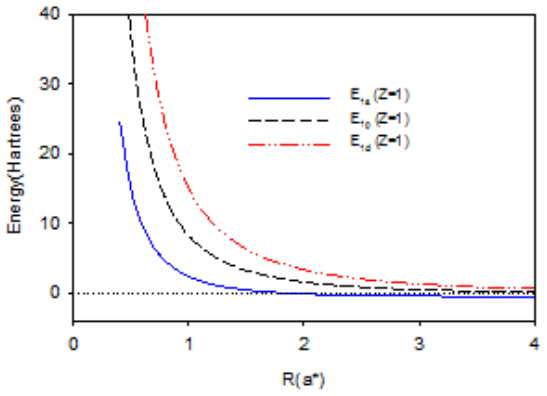

Fig. 1 Energies of the ground (1s), the first (1p) and the second (1d) excited states of a spherical QD with impurity as a function of dot radius.

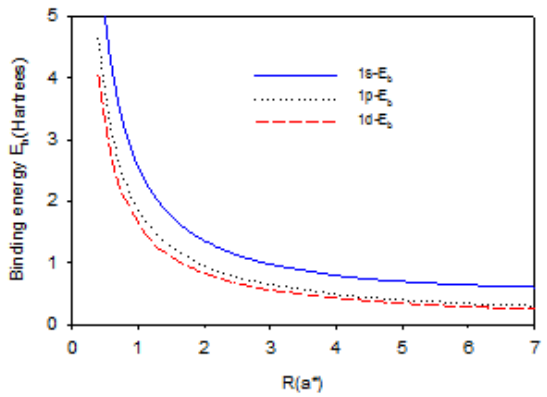

Fig. 2 Binding energy of the ground (1s), the first (1p) and the second (1d) excited states of a spherical QD as a function of dot radius.

Table 1. Energies of *1s*-, *1p*- and *1d*-states of a hydrogenic impurity and their binding energies (E_b). All energies are in Hartrees.

R	E_{1s}	E_{1s}^{a}	E_{1p}	E_{1p}^{a}	E_{1d}	E_{1d}^{a}	$1s\text{-}E_b$	$1p\text{-}E_b$	$1d\text{-}E_b$
0.4	24.63728	-	58.46742	-	99.75287	-	6.21018	4.64998	4.04376
0.5	14.75795	14.7480	36.66161	36.6590	63.16810	63.1600	4.98409	3.77608	3.31758
0.6	9.53210	9.5275	24.93788	24.9370	43.41218	-	4.18732	3.11496	2.72355
0.7	6.47350	6.4700	17.94470	-	31.58829	-	3.59990	2.66702	2.28895
0.8	4.54376	4.5434	13.44042	13.4395	23.91319	-	3.16850	2.33948	2.04555
0.9	3.26277	3.2622	10.39936	-	18.68219	-	2.83115	2.06849	1.85611
1.0	2.37498	2.3740	8.22629	8.2230	14.96912	14.9675	2.56051	1.87274	1.64979
1.3	0.91704	-	4.52931	-	8.56728	-	2.00350	1.44656	1.23000
1.5	0.43705	-	3.23213	-	6.28842	-	1.75661	1.25610	1.10028
1.8	0.03256	0.0326	2.06551	2.0654	4.21484	-	1.49085	1.05174	0.92477
2.0	-0.12500	-0.1250	1.57613	1.5762	3.32877	3.3275	1.49085	1.05174	0.92477
2.4	-0.30638	-0.3064	0.95900	0.9587	2.19797	-	1.16334	0.79442	0.68724
2.8	-0.39667	-0.3967	0.60346	0.6034	1.52713	-	1.02623	0.68516	0.59608
3	-0.42397	-0.4240	0.48128	0.4813	1.29283	1.2928	0.97239	0.64132	0.55381
4	-0.48326	-0.4833	0.14354	0.1435	0.62138	0.6213	0.79175	0.48751	0.42763
7	-0.49986	-	-0.08748	-0.0875	0.09735	0.0966	0.60061	0.29370	0.24255
10	-0.50000	-	-0.11884	-	-0.00703	-0.0071	0.54940	0.21995	0.17486
12	-0.50000	-	-0.12325	-	-0.03125	-0.0313	0.53430	0.19417	0.14692
15	-0.50000	-	-0.12474	-	-0.04663	-	0.52245	0.17014	0.12128

[a:] Exact values[6]. These values were changed into Hartrees.

IV. CONCLUSION

We have obtained an explicit analytical form over STOs of the hydrogenic impurity, and we have calculated a few physical properties of the hydrogenic impurity such as the binding energies and the ground and a few excited state energies. The results obtained by us for the ground and excited states are quite accurate within the all ragions of the dot radius and match well with the corresponding results of other accurate calculations. We have shown that STO basis sets are well suited for describing the electronic properties of a QD with and without an on-center impurity. Furthermore, we have observed that QGA can be efficiently used to determine the expansion coefficients and screening parameters of STOs, and so any observable can be evaluated using this wave function.

[1]. *B. F. Levine*, J. Appl. Phys., 1993, 74, R1.
[2]. *V. Ryzhii*, Semicond. Sci. Technol. 1996, 11, 759.
[3]. *P. A. Maksym, J. Chakraborty*, Phys. Riew.Let. 1990, 65, 108.
[4]. *M. Fujito, A. Natori, H. Yasunaga*, Pyhs. Rev. B 1996, 53, 9952.
[5]. *J. L. Marin, S. A. Cruz*, Am. J. Phys. 1991, 59, 931.
[6]. *Y. P. Varshn*i, Phys. Lett. A, 1999, 252, 248.
[7]. *B. Szafran, J. Adamowski, S. Bednarek*, Physica E 2001, 4, 1.
[8]. *B. Çakır, A. Özmen, Ü. Atav, H. Yüksel, Y. Yakar*, Int. J. Mod. Phys. C 2007, 18, 61.
[9]. *B. Çakır, A. Özmen, Ü. Atav, H. Yüksel, Y. Yakar,* Int. J. Mod. Phys. C 2008, 19, 599.
[10]. *A. Özmen, Y.Yakar, B.Çakır, Ü.Atav*, Opt. Commun. 2009, 282, 3999.
[11]. *B.Çakır, Y. Yakar, A. Özmen, M.Ö. Sezer, M.Şahin*, Supperlattices Microstruct. 2010, 47, 556.
[12]. *Y.Yakar, B. Çakır, A. Özmen*, Opt. Commun. 2010, 283, 1795.
[13]. *Y.Yakar, B. Çakır, A. Özmen*, Commun. Theor. Phys. (in Press 2010).
[14]. *Y. Yakar, A.Özmen, Ü.Atav*, Chin. J. Chem., 2006, 24, 603 (2006).
[15]. Y. Yakar, Chin. J. Chem. 2007, 25.

ENERGY STATES OF A SPHERICAL QUANTUM DOT OVER SLATER TYPE ORBITALS

B. ÇAKIR[1], Y. YAKAR[2], A. ÖZMEN[1]
[1]*Physics Department, Faculty of Science,*
Selçuk University, Campus 42031 Konya, Turkey
[2]*Physics Department, Faculty of Science and Letters,*
Aksaray University, 68100 Aksaray, Turkey

The electronic structure of GaAs/$Al_xGa_{1-x}As$ Quantum Dot (QD) confined a spherically symmetric potential of finite depth and replaced on-center impurity have been investigated by using a combination of Quantum Genetic Algorithm (QGA) and Hartree-Fock Roothaan (HFR) method. The ground and excited state energies of a QD were calculated depending on the dot radius. Expectation values of energy were determined by using the HFR method along with Slater-Type Orbitals (STOs) and we used the QGA for the wavefunctions optimization.

I. INTRODUCTION

Semiconductor structures with three-dimensional confinement of electrons, called QDs, have been fabricated by using various techniques such as molecular beam epitaxy and etching [1]. These structures display interesting behaviour and play an important role in microelectronic and optoelectronic devices so that they can affect electrical, optical and transport properties. These structures allow for confinement of electrons on scales comparable to their de Broglie wavelength. Semiconductor quantum nanostructures (quantum wells, wires or dots) have found various application areas especially as electronic devices such as single electron transistor, quantum well and quantum dot infrared photo detector (QWIP and QDIP)[2-4]. QDs are often referred to as artificial atoms that show the properties of atoms such as discrete energy levels and shell structures [5-8].

Recently, many researchers have begun to use the Genetic Algorithm (GA) method for quantum mechanical analysis of semiconductor nanostructures. The GA method, first proposed by Holland[9], is a general numerical search and optimization method. The GA method has been found many applications in the electronic structure of the quantum mechanical systems. The version of the GA method in quantum mechanical applications is named as a QGA method and the method is based on the principle of energy minimization just like in variational method. Recently, the electronic structure of a QD with a spherically symmetric potential of both finite and infinite depth has been investigated by using the QGA method [10-15].

We calculated the ground and excited state energies of one-electron QD by using the QGA method. We assumed an on-center impurity and a spherically symmetric confinement potential of finite depth, and we also calculated the ground and excited state energies as a function of dot radius.

II. THEORY

The electronic Hamiltonian, $\boldsymbol{H}$, for one-electron and an impurity located at the center of a QD with a spherically symmetric confining potential $V(r)$ can be written, under the effective mass approximation, in atomic units (a.u.), as follows

$$\boldsymbol{H} = -\frac{\nabla^2}{2m^*} - \frac{Z}{\varepsilon r_i} + V(r), \qquad (1)$$

where Z is the impurity charge, r_i is the distance of the electron to the impurity, m* is the effective mass of electron and ε denotes the dielectric constant of the medium. Here we have assumed an finitely deep spherical potential well with radius a and is given by

$$V(r) = \begin{cases} 0\ , & r < a \\ V_0\ , & r \geq a. \end{cases} \qquad (2)$$

The time independent Schrödinger equation for an *n*-electron system is given by

$$\boldsymbol{H}\psi = E\psi_n \qquad (3)$$

where the term E is the energy eigenvalue of the Hamiltonian operator, ψ is the eigenfunction of the operator. The wavefunction ψ satisfies the normalization and the boundary conditions. The wavefunction ψ can be expressed as a Slater determinant containing the spatial part of one-electron spin orbital ϕ_p for *one*-electron closed-shell system in the HFR approach. The spatial part of one-electron spin orbital ϕ_p must also satisfy the same boundary conditions. Conservation of the probability flux at the boundary gives the equation

$$\left.\frac{1}{m^*_{r<a}}\frac{d\phi_p^{r<a}}{dr}\right|_{r=a} = \left.\frac{1}{m^*_{r>a}}\frac{d\phi_p^{r>a}}{dr}\right|_{r=a} \qquad (4)$$

where $m^*_{r<a}$, $m^*_{r>a}$ are the effective masses of electron and $\phi_p^{r<a}$ and $\phi_p^{r>a}$ are the single electron spatial orbital inside and outside of the QD, respectively.

The eigenstates of the system can be determined from the variational principle by minimizing the energy of the system corresponding to the trial wave function ϕ_i

$$E_i = \langle \phi_i | H | \phi_i \rangle / \langle \phi_i | \phi_i \rangle . \quad (5)$$

In the HFR approach, the wavefunction ϕ_i are written as linear combination of Slater type orbitals (STOs), which are called basis sets. As a result our wave function is of the form

$$\begin{aligned} \phi_i &= \Theta(R-r)\phi_i^{r<R} + \{1-\Theta(R-r)\}\phi_i^{r>R} \\ &= \Theta(R-r)\sum_{k=1}^{\sigma^{r<R}} c_{ik}^{r<R}\chi_k(\zeta_{ik}^{r<R},\vec{r}) \\ &+ \{1-\Theta(R-r)\}\sum_{k=1}^{\sigma^{r>R}} c_{ik}^{r>R}\chi_k(\zeta_{ik}^{r>R},\vec{r}) , \end{aligned} \quad (6)$$

where $\Theta(x)$ is the Heviside step function, $\sigma^{r<R}$ ($\sigma^{r>R}$) are the size of the basis set used for the inner (outer) part of the wave function, $c_{ik}^{r<R}$ ($c_{ik}^{r>R}$) are the expansion coefficients and $\zeta_{ik}^{r<R}$ ($\zeta_{ik}^{r>R}$) are the screening parameters for the inner (outer) part of the wave function of *i*th eigenstate. The unnormalized complex spherical STO has the general form

$$\chi_{n_k l_k m_k}(\zeta_k, r\theta\phi) = r^{n_k-1} e^{-\zeta_k r} Y_{l_k m_k}(\theta,\phi), \quad (7)$$

where $Y_{lm}(\theta,\varphi)$ are well-known complex spherical harmonics in Condon-Shortley phase convention.

III. COMPUTATIONAL METHOD

We have assumed that the confining potential is a spherical well of finite depth. We have used the material parameters of GaAs inside the well and those of $Al_xGa_{1-x}As$ outside the well. We have used the atomic units (a.u.) throughout the study, the effective Bohr radius and the effective *Rydberg* energy are $a_0^* = \frac{\hbar^2 \varepsilon}{m^* e^2}$ and $R_y = \frac{\hbar^2}{m^* a_0^*}$ respectively, in which ε and m^* are the relative dielectric constant and the effective electron mass for GaAs.

The material parameters of $Al_xGa_{1-x}As$ are given in Ref. 16 as the functions of the stiochiometric ratio x: the difference between the band gaps of GaAs and $Al_xGa_{1-x}As$ $\Delta E_g(x) = (1.155x + 0.35x^2)$ eV, effective dielectric constant $\varepsilon(x) = 13.18 - 3.12x$ and, the effective electron mass $m^*(x) = (0.0665 + 0.0835x)m_0$. Using the above given parameters of GaAs (x=0.3) one can obtain effective Bohr radius and effective Rydberg energy as ~100 $\overset{0}{A}$ and ~5.72 *meV* respectively.

STOs are preferred in the quantum mechanical analysis of the electronic structure of atoms as STOs represent the correct behavior of the electronic wavefunctions around a point charge, i.e. they satisfy the cusp condition at the point charge and they decay exponentially in the regions far for the point charge Therefore, we have chosen a linear combination of s *(or* p, d*)* type STOs with different screening parameters for an s *(or* p, d*)* type atomic orbital. To maintain the orthogonality of orbital the same set of screening parameters was used for all the one-electron spatial orbital having the same angular momentum.

The GA method is based on three basic genetic operations: reproduction (or copying), crossover and mutation. The method starts up with an initial random population of possible solutions of the problem. A fitness value is assigned to each individual in the population. In the reproduction process the individuals of current population are copied to next generations, according to their fitness values. Therefore, in performing reproduction process, a selection procedure is necessary to choose the individuals to be copied to the next generations. In the crossover operation two individuals randomly selected from the present are combined to obtain two new individuals of the next generation population. Another operation in QGA, the mutation process plays an important role in getting out of local minima and is implemented at lower probabilities than other operations. In this process, the genetic information is changed randomly. Here we have given only the outline of the procedure. The details of the QGA used in this study are given in our previous work[10].

We have used the QGA procedure to determine the parameters to minimizing the energy E_i of the system given in Eq.(5). The parameters c_{ik} and ζ_{ik} in Eq.(6) have been considered as the genetic code of the corresponding individual, these parameters are chosen randomly for the initial population, provided that they satisfy the appropriate boundary conditions. The orbital set of each individual were orthonormalized using the Gram-Schmidt procedure, and the energy expectation value was calculated by following the approach given in Refs. [17,18] for each individual.

IV. RESULTS AND DISCUSSION

We have obtained the wavefunctions and the the ground state energy of one-electron GaAs/$Al_xGa_{1-x}As$ QD as a function of dot radius (R) by using a combination of QGA and HFR method. Also we have calculated the excited state energies and the wavefunctions of the QD. Basis sets of different sizes (σ=5) were used inside the dot whereas only one basis set was used outside of the dot. We have used atomic units(a.u.) through all calculations. All the energies and radii in tables are given in units of effective Hartree energy and effective Bohr radius, respectively.

The results obtained for the ground and excited states of a single electron QD are listed in Table 1 along with the literature results. As seen from Table 1, the energies increase when the dot radius decreases. In Table 1, the ground state energy for the large radius ($R=20a^*$) approaches to –0.5 Hartree as expected, which is the ground state energy of the hydrogen atom. Similarly, the first, the second excited and the third excited state energies for the large dot radius ($R=20a^*$) approaches to -0.125au, -0.055au and -0.0205 au as expected, which are the first, the second and the third excited state energies of the free space hydrogen atom. Negative energy values in

Table 1 indicate that the electron is bound to the impurity, that is, the impurity attraction energy contributes to a much greater extent than the kinetic energy at ranges

Table 1. The ground and excited states energies of a one-electron QD

R	E_{1s}	E_{1p}	E_{1d}	E_{1f}
0.3	13.182147	19.756336	19.853524	19.887013
0.5	6.395657	16.620843	19.853510	19.887013
0.7	3.308344	10.280816	17.730470	19.887013
0.9	1.781273	6.685109	12.123280	18.128285
1.0	1.306616	5.504465	10.155910	15.411147
1.2	0.673351	3.861714	7.353316	11.357722
1.6	0.045246	2.099627	4.261620	6.746054
1.8	-0.116038	1.602654	3.370006	5.395157
2.0	-0.225631	1.243979	2.715776	4.399112
2.2	-0.301744	0.975242	2.222935	3.643384
2.6	-0.393646	0.613660	1.545819	2.600061
3.0	-0.442432	0.390993	1.117550	1.926014
3.2	-0.457523	0.310576	0.959093	1.681400
3.8	-0.482743	0.146803	0.628035	1.153402
4.2	-0.490594	0.078151	0.484074	0.926961
4.6	-0.494929	0.028542	0.375932	0.747211
5.0	-0.497310	-0.007623	0.295054	0.614244
6.0	-0.499463	-0.063058	0.162438	0.391153
6.4	-0.497853	-0.076613	0.126310	0.329215
7.5	-0.499557	-0.100138	0.059666	0.212887
8.0	-0.499968	-0.106580	0.039141	0.176667
8.5	-0.499987	-0.110810	0.022741	0.145163
9.5	-0.499995	-0.113302	0.024587	0.193078
10.0	-0.499999	-0.119485	-0.009982	0.082852
12.0	-0.500000	-0.123442	-0.032695	0.035643
14.0	-0.500000	-0.124393	-0.043755	0.024577
16.0	-0.500000	-0.124853	-0.049465	0.009259
20.0	-0.500000	-0.124995	-0.054068	-0.020419

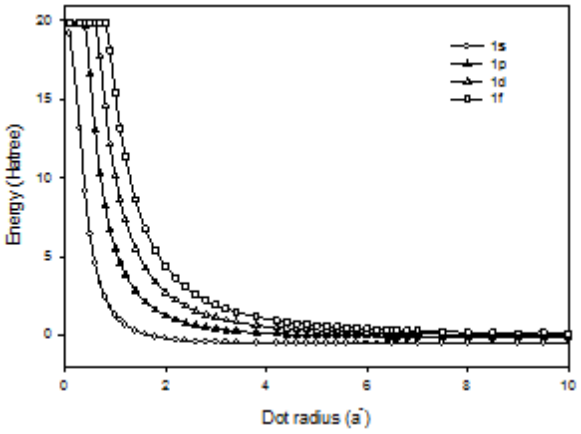

Fig. 1 Energy of the ground state *1s*, the first *1p*, the second *1d* and the third *1f* excited states versus the dot radius for a one-electron GaAs/$Al_xGa_{1-x}As$ QD for x= 0.3.

In Fig.1, we present the ground state(1s), the first (1p), the second (1d) and the third (1f) excited state energies of a one-electron QD versus the dot radius. It can be seen from Fig. 1, the electron is bound to impurity at dot radius $R = 1.8a_0^*$ for the ground state and $R = 5a_0^*$ for the first excited state, $R = 10a_0^*$ for the second excited state and $R = 18a_0^*$ for the third excited state, respectively

V. CONCLUSION

In this study, it is seen that STO basis sets are well suited for describing the electronic properties of a GaAs/ $Al_xGa_{1-x}As$ QD with an on-center impurity. Furthermore, we have observed that, QGA can be efficiently used to determine the expansion coefficients and screening parameters of STOs. We have calculated only a few physical properties of the QD. However, we obtained an explicit analytical form the wave function of the systems, and any observable can be evaluated using this wave function.

[1] *M .A.Reed, J.N.Randall, R.J.Aggarwal, R.J.Matyi, T.M. Moore, A.E. Wetsel*, Phys. Rev. Lett. 1988, 60, 535.

[2] *B. F. Levine*, J. Appl. Phys. 1993, 74, R1.

[3] *V. Ryzhii*, Semicond. Sci. Technol. 1996, 11, 759.

[4] *S. W. Lee, K. Hirakawa, and Y. Shimada*, Physica E 2000, 7, 499.

[5] *P. A. Maksym and T. Chakraborty*, Phys. Rev. Lett. 1990, 65, 108.

[6] *J. L. Marin, S. A. Cruz*, Am. J. Phys.1991,59, 931.

[7] *Y. P. Varshni*, Phys. Lett. A 1999**, 252,** 248.

[8] *B. Szafran. J. Adamowski. S. Bednarek*, Physica E, 2001, 4, 1.

[9] *J. H. Holland*, Adaptation in Natural and Artificial Systems. (University of Michigan, Ann Arbor, MI., 1975).

[10] *B. Çakır, A. Özmen, Ü. Atav, H. Yüksel, Y. Yakar*, Int. J. Mod. Phys. C 2007, 18, 61 (2007).

[11] *B. Çakır, A. Özmen, Ü. Atav, H. Yüksel, Y. Yakar*, Int. J. Mod. Phys. C 2008, 19, 599.

[12] *A. Özmen, Y.Yakar, B.Çakır, Ü.Atav,* Opt. Commun. 2009, 282, 3999.

[13] *B.Çakır, Y. Yakar, A. Özmen, M.Ö. Sezer, M. Şahin*, Supperlattices Microstruct. 2010, 47, 556 (2010).

[14] *Y. Yakar, B. Çakır, A. Özmen*, Opt. Commun. 2010, 283, 1795 (2010).

[15] *Y. Yakar, B. Çakır, A. Özmen*, Commun. Theor. Phys. (in Press 2010).

[16] *S. Adachi*, GaAs and Related Materials: Bulk Semiconducting and Superlattice Properties (World Scientific, Singapore, 1994).

[17] *Y. Yakar, A.Özmen, Ü.Atav,* Chin. J. Chem. 2006, 24, 603.

[18] *Y. Yakar*, Chin. J. Chem. 2007, 25, 25.

SERIES RESISTANCE CALCULATIONS OF Au/n-GaP SCHOTTKY DIODE

T. GÜZEL, M. ÖZER, S. ACAR AND B. SALAMOV*

Department of Physics, Faculty of Arts and Sciences, Gazi University, 06500, Ankara -Turkey metinoz@gazi.edu.tr

**National Academy of Science, Institute of Physics, AZ-1143 Baku, Azerbaijan*

The current voltage characteristics of the Au/n-GaP Schottky barrier diode have been investigated at room temperature under dark condition. Main physical parameters of the diode such as ideality factor, barrier height and series resistance were found to be 1.26, 0.77 eV and 3.1 Ω, respectively. The obtained parameters by different methods are in good agreement with each other.

I. INTRODUCTION

Metal – Semiconductor (MS) junctions have attracted considerable attention because of their many applications in the semiconductor technology. Generally, the parameters and performance of MS Schottky contacts depend on presence of interface states and series resistance at the metal-semiconductor interface. The diode behaviour is different from an ideal case due to presence of interface states and series resistance [1-5]. The full understanding MS diodes nature and their electrical characteristics have still not been achieved. Many researches have attempted to understand the electronic parameters of MS barrier diodes. The popularity of these diodes, which is important in the semiconductor industry, does not assure uniformity of the results or of interpretation [2]. The performance and stability of these structures is of vital importance to all semiconductor devices [3].

In this study, we have investigated different diode parameters such as ideality factor, barrier height and series resistance using different methods. These main parameters of diodes are determined using conventional forward bias current voltage characteristics, Cheung and Norde's methods.

II. EXPERIMENT

The semiconductor substrates used in this work were n-type S-doped GaP single crystals, with a (100) surface orientation, 300 μm thick. The wafer was chemically cleaned using the RCA cleaning procedure with the final dip in diluted HF for 30 s, and then rinsed in deionized water of resistivity of 18 MΩ cm with ultrasonic vibration and dried by high purity nitrogen. Immediately after surface cleaning, high purity gold (Au) metal (99.999%) with a thickness of 2000 Å was thermally evaporated from the tungsten filament onto the whole back surface of the wafer in the pressure of $1x10^{-6}$ Torr. Then, a low resistivity ohmic contact was followed by a temperature treatment at 400 °C for 3 min in N_2 atmosphere. The Schottky contacts were formed on the other faces by evaporating gold (Au, 99.999%) with a thickness of 1500 Å as dots with diameter of about 1.0 mm through a metal shadow mask in liquid nitrogen trapped high vacuum system in the pressure of $1x10^{-6}$ Torr. The *I–V* measurements were performed by the use of a Keithley 2400 sourcemeter in the room temperature in darkness.

III. RESULTS AND DISCUSSION

The forward and reverse bias current voltage characteristic of the Au/n-GaP Schottky barrier diode at room temperatures is shown in Fig. 1. The *I-V* characteristic of the device clearly shows diode peculiarity. Generally the forward bias *I-V* characteristics are linear on a semi-logarithmic scale at low forward bias voltage. However, at higher bias region the series resistance effect is significant in the non linear region of forward bias and results in the reducing the linear range of the forward *I-V* curves [4]. The *I-V* relation for a Schottky diode based on the thermionic emission theory is given by [5]

$$I = I_0 \exp\left(\frac{qV}{nkT}\right)\left[1-\exp\left(\frac{-qV}{kT}\right)\right] \quad (1)$$

where I_o is the saturation current derived from the straight line region of the forward bias current intercept at zero bias and is given by

$$I_o = AA^{*}T^{2}exp\left(-\frac{q\Phi_{Bo}}{kT}\right) \quad (2)$$

n is the ideality factor, *V* is the applied bias voltage, *T* is the temperature in K, Φ_{BO} is the zero bias barrier height, *A* is the rectifier contact area. Richardson constant (A*) is 120(m*/m) [6] A/cm^2K^2, *q* is the electron charge, *k* is the Boltzmann constant, However, the equation (1) is based on the neglect of the series resistance of the diode. For diode with a series resistance, the forward current is limited and departs from linearity for much of the forward region and equation (1) now becomes [7,8].

$$I = I_0 \exp\left(\frac{q(V-IR_s)}{nkT}\right) \quad (3)$$

Thus, the ideality factor is obtained from the slope of the straight line region of the forward bias ln*I-V* characteristics through the relation

$$n = \frac{q}{kT}\frac{d(V-IR_s)}{d\ln(I)} \quad (4)$$

The values of zero bias apparent Schottky barrier height (Φ_{BO}) and ideality factor (n) are obtained from equations (2) and (4), respectively, and are given in Table 1. The values of Φ_{Bo} and n for the Au/n-GaP Schottky barrier diode are 0.77 eV and 1.26, respectively.

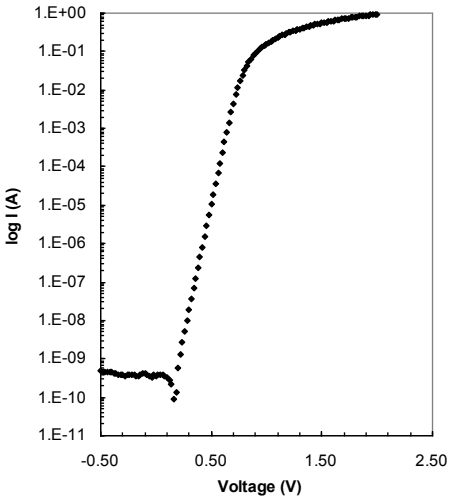

Fig. 1. Forward and reverse bias semi-logarithmic *I-V* characteristics of GaP Schottky diode at room temperature in darkness.

As can be shown in figure1, the forward bias *I-V* characteristic is linear on a semi-logarithmic scale at low forward bias voltages, but deviate considerably from linearity due to the effect of series resistance when the applied voltage is sufficiently high. The series resistance is important in the non–linear region of the forward bias *I-V* characteristics and it affects the ideality factor of diode. So, we used Cheung's [8-10] method to determine diode parameters and Cheung' functions are defined as

$$\frac{dV}{d\ln(I)} = IR_s + \left(\frac{nkT}{q}\right) \tag{5}$$

$$H(I) = V - \left(\frac{nkT}{q}\right)\ln\left(\frac{I}{AA^{*}T^{2}}\right) = IR_s + n\Phi_B \tag{6}$$

where, $R_{s,}$ is the series resistance, n is ideality factor and Φ_B is barrier height. These parameters performed using a method developed by Cheung [9] of the forward bias *I-V* plot. In Fig. 2, experimental $dV/d(\ln I)$ vs I and $H(I)$ vs I plots are presented at room temperature.

Table 1. Values of various parameters determined from forward bias *I-V* characteristics of Schottky barrier diode at room temperature

$n_{(I\text{-}V)}$	$n_{(dv/dlnI)}$	$\Phi_{Bo(I\text{-}V)}$ (eV)	$\Phi_{Bo(H\text{-}I)}$ (eV)	$R_{s(dv/dln)}(\Omega)$	$R_{s(H\text{-}I)}$ (Ω)	$R_{s(F(V)}$ (Ω)
1.26	1.20	0.77	0.74	1.22	1.21	1.65

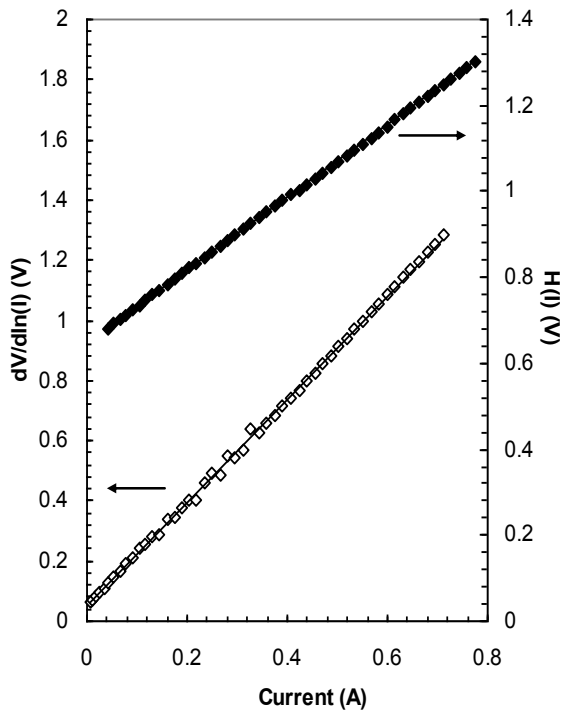

Fig.. 2. Plots of $d(V)/d(lnI)$-I and $H(I)$-I of the Au/n-GaP Schottky barrier diode in darkness.

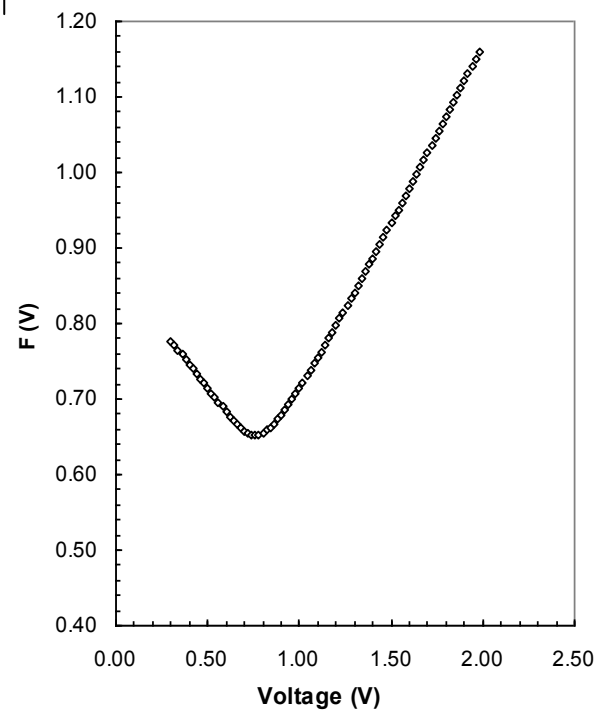

Fig. 3. F(V) vs. *V* plot of the Au/n-GaP Schottky barrier diode.

As can be seen from these figure, both Eq 5 and 6 give a straight line for the data of downward curvature region in the forward bias ln*I*-*V* characteristics. The Φ_B, n and R_s values were calculated from the slope and intercept of $dV/d(\ln I)$ vs I plot and $H(I)$ vs I plot. Calculated these parameters are given Table 1.

The another method used to determine the series resistance is Norde's method [8,11]. Norde's functions are fallow as,

$$F(V) = V/\delta - (kT/q)\ln[I(V)/AA^*T^2] \quad (7)$$

$$\phi b = F(V0) + V0/\delta - kT/q \quad (8)$$

$$R_s = \frac{\delta - n}{I}\frac{kT}{q} \quad (9)$$

where δ is a constant and greater than n, here it is taken as 2. n is the ideality factor and $I(V)$ is the current obtained from *I*-*V* measurements. The value of barrier height is calculated after getting minimum of $F(V)$ vs V plot. Fig 3. shows the $F(V)$ vs V plot of the diode.

The values of barrier height and series resistance are determined as 0.99 eV and 1.65 Ω respectively. A small difference in values of series resistance obtained for different methods is observed. These small differences may be due to Norde's model is applied to full voltage range while, Cheung's model is applicable in high voltage region of forward bias *lnI*-*V* characteristics of the junction [8].

IV. CONCLUSIONS

The diode parameters such as ideality factor, barrier height and series resistance were calculated different methods at room temperature in the dark. The diode parameters obtained by different methods are compared with each others. There is a good agreement between diode parameters obtained from the three different methods.

ACKNOWLEDGMENTS

This work is supported by Gazi University BAP research projects 05/2009-17.

[1]. *M. Ozer, D.E. Yıldız, S. Altındal*, Solid-State. Electron. 51 941 (2007)
[2]. *Ş. Karataş, Ş. Altındal, A. Türüt and M. Çakar* Physica B. 392 43 (2007)
[3]. *G Güler, Ş. Karataş and Ö.F. Bakkaloğlu*, Physica B 404 1494 (2009)
[4]. *P. Chattopadhyay and D. P. Haldar* Appl. Surf. Sci. 143 287 (1999)
[5]. *S. M. Sze* 1981 Physics of Semiconductor Devices 2nd Edn.(New York: Willey)
[6]. *R. Mientus, R. Wolf, B. Kloth, M. Protsch and A.N.Pikhtin* Surf. Coat. Technol 116-119 711 (1999)
[7]. *W. P. Kang, J. L. Davidson, Y. Gurbuz and D.V.Kerns* J. Appl. Phys. 78 1101(1995)
[8]. *R.K. Gupta. K. Ghosh. and P.K Kahol* Current Appl. Phys. 9 933 (2009)
[9]. *S. K. Cheung and N. W. Cheung* Appl. Phys. Lett. 49 85 (1986)
[10]. *F.Yakuphanoğlu and F.B. Şenkal* Synthetic Metals 158 821 (2008)
[11]. *H. J. Norde* Appl. Phys. 50 5052 (1979)

THEORETICAL ENERGY CALCULATION AND CONFORMATION ANALYSIS OF 2-PHENLY-2H-PHTHALAZIN-1-ONE MOLECULE

NEFİSE DİLEK[1], BİLAL GÜNEŞ[2]

[1]*Aksaray University, Faculty of Arts and Sciences, Department of Physics, 68100, Aksaray, Turkey,*
e-mail:nefised@gmail.com

[2]*Department of Physics, Gazi Education Faculty, Gazi University, Teknikokullar 06500, Ankara, Turkey*

In this study, geometric parameters of 2 Phenly-2H-phthalazin-1-one ($C_{14}H_{10}N_2O$) are obtained by using molecular mechanic method (MM+), semi-empirical methods (AM1, PM3, MNDO, MNDO/d) and *ab-initio* calculation method for three basis set. Also, the conformation analysis is made by using torsion angles.

I. INTRODUCTION

The crystal structure of $C_{14}H_{10}N_2O$, which formed with connection of one of the nitrogen atoms of phthalazin to phenly ring, is carried out comparison of experimental and theoretical results. The results of x-ray diffraction for the title compound are earlier published 2004 [1]. Fig. 1 represents the appearance of the molecular structure.

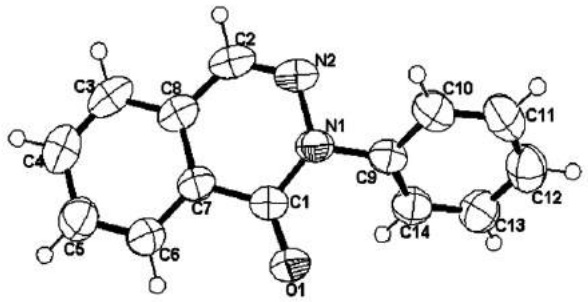

Fig.1. An ORTEP-III drawing of molecule. Thermal ellipsoids are drawn at %50 probability level.

II. CALCULATIONS

We have used the Hyperchem program package for calculations [2]. The minimum energy state of molecule was obtained by using geometry optimization and then geometric parameters were investigated at minimum energy state. Optimizations were obtained by applying the Polak-Ribiere conjugate gradient method. All the geometric parameters were fully optimized by starting from the crystallographic data.

The file containing the results of crystallographic is converted. the HyperChem data-input file.

In Table 1, the atoms at crystallographic results and the atoms at HyperChem data-input file is paired. A HyperChem drawing of molecule is given in Fig. 2.

Table 1. The atoms of HyperChem data-input file

atom 13-C1	atom 1-C7	atom 21-C13
atom 11-C2	atom 10-C8	atom 23-C14
atom 8-C3	atom 14-C9	atom 27-O1
atom 6-C4	atom 15-C10	atom 26-N1
atom 4-C5	atom 17-C11	atom 25-N2
atom 2-C6	atom 19-C12	

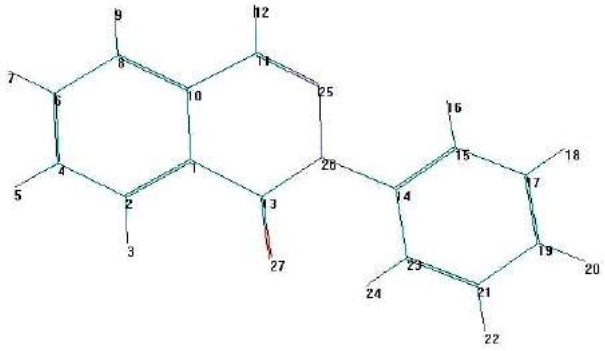

Fig. 2. A HyperChem drawing of molecule.

Firstly, optimization was performed by applying the molecular mechanics method using MM+. The RMS gradient was set to 0.1 kcal/(Å mol) in this calculation. Then, the AM1, PM3, MNDO, MNDO/d semi-empirical methods within the Restricted Hartree-Fock (RHF) formalism were performed. The SCF convergency and the RMS gradient were set to 0.01 kcal/mol and 0.1 kcal (mol/Å) in the all semi-empirical calculations, respectively. After then, the ab-initio results were obtained for three different basis set (3-21G, 631-G*, 631-G**). The results of basis sets were similar. So, we have given results for only 631-G* basis set. For ab-initio calculation, the convergency limit and the RMS gradient were set to 0.00001 kcal/mol and 0.1 kcal/(Å mol), respectively. Finally, we have calculated potential energies for four different torsion angles in molecule investigated by using semi-empirical PM3 method.

III. RESULTS AND DISCUSSION

As the results of the calculations, we have obtained the energy value by using geometric optimization. These results are given in Table 2. The dipole moment values are given in Table 3.

For four different torsion angles in molecular structure, potential energies are calculated by using semi-empirical PM3 method. The torsion angles are changed from 0° to 180° in 5° steps for calculation. Potential energies as a function of torsion angles are given in Fig..3.

Table 2. Calculated energy values by using geometric optimization.

Molecular Mechanics	**MM+**
Total Energy (kcal/mol)	26,657045
Bond Stress Energy (kcal/mol)	0,767789
Angle Bending Energy (kcal/mol)	16,4589
Torsion Energy (kcal/mol)	0,262128
Vdw (kcal/mol)	9,27824
Stress-Bending Energy (kcal/mol)	0,109982
Electrostatic Energy (kcal/mol)	0
Gradient (kcal/mol/Å)	0,000720

Semi-empirical	**AM1**	**PM3**	**MNDO**	**MNDO/d**
Total Energy (kcal/mol)	-104150,031526	-93599,2849188	-103868,664065	-103868,664065
Total Energy (a.u.)	-165,970326132	-149,156976873	-165,521947494	-165,521947494
Binding Energy (kcal/mol)	-3452,0303530	-3494,7461328	-3499,0515322	-3499,0515322
Isolated Atomic Energy	-100698,001173	-90104,5387860	-100369,612533	-100369,612533
Electronic Energy(kcal/mol)	-609964,007626	-588328,471314	-607784,092975	-607784,092975
Core-core energy (kcal/mol)	505813,9761002	494729,1863956	503915,4289096	503915,4289096
Heat of Formation(kcal/mol)	-22,4233530	-65,1391328	-69,4445322	-69,4445322
Gradient(kcal/mol/Å)	0,0080247	0,0099209	0,0097946	0,0097946

Ab-initio	**6-31G***
Total Energy (kcal/mol)	-706785,8517702
Total Energy (a.u.)	-1126,334810353
Electronic Kinetic Energy (kcal/mol)	706622,7206845
Electronic Kinetic Energy (a.u.)	1126,074844453
Nuclear Repulsion Energy (kcal/mol)	1095345,4005466
RMS Gradient (kcal/mol/Å)	0,0817757

Table 3. Dipole moment values energy values by using geometric optimization.

Method		**μ dipole moment(debye)**
Semi empirical	**AM1**	3,380
	PM3	2,487
	MNDO	3,176
	MNDO/d	3,176
Ab-initio	**6-31G***	4,7019

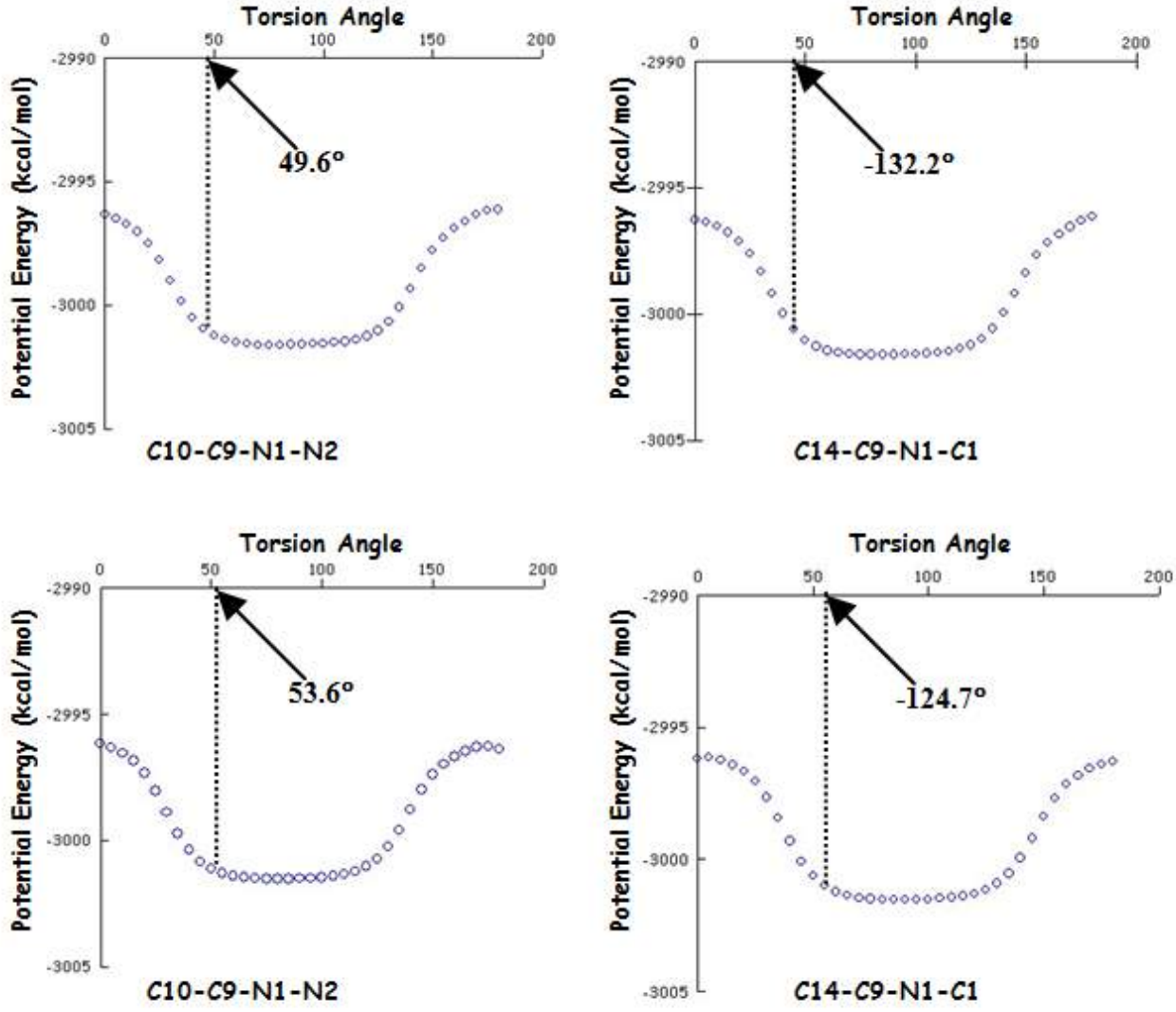

Fig.3. The potential energies as a function of torsion angles.

According to our calculation results, *ab-initio* calculation has given best fit with experimental results. Besides, all semi-empirical methods used in this work are suitable for determination of molecular structure of the title compound [3-6]. For investigated structure, minimum potential energy range is appropriate with experimental values [1].

[1]. *N. Dilek, B. Güneş, S. İde, Y. Özcan, H. Tezcan*, Anal. Sci. X-ray Struct. Anal. Online, 2004, 20, 157.
[2]. *HyperChem Demo Release 6.03 for Windows*, Hypercube, Inc., USA, 1999.
[3]. *O.V. Stroganov, G.G. Chilov, V.K. Shedas*, J. Mol. Struc.(Theochem), 2003, 631, 117.
[4]. *E. Estrada, J.C. Gonzales, L. Santana, E. Uriarte, A. Castineiras*, Struct. Chem., 2000, 11, 249.
[5]. *E. Estrada, M. Gomez, N. Castanedo, C. Perez.* J. Mol. Struct.(Theochem), 1999, 468, 193.
[6]. *C. Topaçlı, A. Topaçlı,* J. Mol. Struct., 2003, 644, 145.

AB INITIO STUDY OF TlBr INTERMETALLIC COMPOUND

N.KAHVECİ[1], Y.O. CİFTCİ[1]*, K. COLAKOGLU[1], H.B. ÖZIŞIK[2]

[1]*Gazi University, Department Of Physics, Teknikokullar, 06500, Ankara,TURKEY*

[2]*Aksaray University, Department Of Physics, 68100, Aksaray, TURKEY*

In this work, we have performed a first-principles study on TlBr compound by using the density functional theory implemented in GGA approximations in cubic crystal structure. Based on the optimized structural parameter, which is in good agreement with the experimental data, the electronic structure, elastic and thermodynamics properties are calculated. We have, also, predicted the temperature and pressure variation of the volume, bulk modulus, thermal expansion coefficient, heat capacities, and Debye temperatures in a wide pressure (0 - 30 GPa) and temperature ranges (0- 400 K).

I. INTRODUCTION

The rare-earth intermetalic compound TlBr has the cubic CsCl-type structure with a lattice constants *a*=3.838Aº at room temperature [1], 3.84 Aº[2], 3.97 Aº [3] and 3.94 Aº [4]. Recent theoretical calculations indicate that TIBr represents a class of materials with interesting properties. This class of materials is intermediate between the extensively studied ionic alkali halides and the covalent semiconductors; in particular the thallium halides are highly polarizable, partly ionic, partly covalent insulators with a band gap of about 3 eV. The delay of theoretical work on these material has been due to their more complicated nature as intermediate substances as well as due to the fact that thallium has a high atomic number (Z = 81) so that relativistic effects are important [4]. TlBr also crystallizes NaCl structure (space group Fm3m a=6.58 Aº) in cubic structures [5]

The aim of the present paper is to reveal bulk, structural, thermodynamical, elastic and lattice dynamical properties of TlBr in CsCl(B2) phases using VASP method with plane-wave pseudopotential. In Section 2, a brief outline of the method of calculation is presented. In Section 3, the results are presented followed by a summary discussion.

II. METHOD OF CALCULATION

In the present work, all calculations have been carried out using the Vienna ab initio simulation package (VASP) [6-9] based on the density functional theory (DFT). The electron-ion interaction was considered in the form of the gradient approximation (GGA) method [10] with the plane wave up to an energy of 700 eV. This cut-off was found to be adequate for the structural, elastic properties as well as for the electronic structure. We do not observe any significant change in the key parameters when the energy cut-off is increased from 700 eV to 750 eV. For the exchange and correlation terms in the electron-electron interaction, Perdew and Zunger-type functional [11,12] was used within the generalized gradient approximation (GGA) [10].

The 14x14x14 Monkhorst and Pack [13] grid of k-points have been used for integration in the irreducible part of the Brillouin zone. Thus, this mesh ensures a convergence of total energy to less than 10^{-5} ev/atom. The calculations have been performed in scalar-relativistic mode, neglecting spin-orbital coupling. Test calculations have showed that the orbital moment is very small and the inclusion of the spin-orbit term leads to negligible changes in the results. Also, the small spin-polarization effects are ignored in our calculations.

We have used the quasi-harmonic Debye model [10-13] to obtain the thermodynamic properties of TlBr, in which the non-equilibrium Gibbs function *G*(V; P, T)* takes the form of

$$G^*(V;P,T) = E(V)+PV+A_{vib}[\theta(V);T] \,. \qquad (1)$$

In Eq.(1), *E(V)* is the total energy for per unit cell of TlBr, *PV* corresponds to the constant hydrostatic pressure condition , $\theta(V)$ the Debye temperature and A_{Vib} is the vibration term, which can be written using the Debye model of the phonon density of states as

$$\mathrm{A_{Vib}}(\theta,\mathrm{T}) = nkT\left[\frac{9\theta}{8T}+3\ln\left(1-e^{-\frac{\theta}{T}}\right)-D\left(\frac{\theta}{T}\right)\right] \qquad (2)$$

where *n* is the number of atoms per formula unit, $D\left(\frac{\theta}{T}\right)$ the Debye integral, and for an isotropic solid, θ is expressed as [14]

$$\theta_D = \frac{\hbar}{k}\left[6\pi V^{1/2} n\right]^{1/3} f(\sigma)\sqrt{\frac{B_s}{M}} \qquad (3)$$

where *M* is the molecular mass per unit cell and B_S the adiabatic bulk modulus, which is approximated given by the static compressibility [15]:

$$B_s \approx B(V) = V\frac{d^2E(V)}{dV^2} \qquad (4)$$

$f(\sigma)$ is given by Refs. [14,16] and the Poisson ratio used as 0.33222 for TlBr. For TlBr, *n*=4 *M*= 284.2873 a.u, respectively. Therefore, the non-equilibrium Gibbs function *G*(V; P, T)* as a function of *(V; P, T)* can be minimized with respect to volume *V*.

$$\left[\frac{\partial G^*(V;P,T)}{\partial V}\right]_{P,T} = 0 \qquad (5)$$

By solving Eq. (5), one can obtain the thermal equation-of-equation (EOS) *V(P, T).* The heat capacity at constant volume C_V, the heat capacity at constant pressure C_p, and the thermal expansion coefficient α are given [17] as follows:

$$C_v = 3nk\left[4D\left(\frac{\theta}{T}\right) - \frac{3\theta/T}{e^{\theta/T}-1}\right] \quad (6)$$

$$S = nk\left[4D\left(\frac{\theta}{T}\right) - 3\ln(1-e^{-\theta/T}\right] \quad (7)$$

$$\alpha = \frac{\gamma C_v}{B_T V} \quad (8)$$

$$C_p = C_v(1+\alpha\gamma T) \quad (9)$$

Here γ represents the Grüneisen parameter and it is expressed as

$$\gamma = -\frac{d\ln\theta(\mathrm{V})}{d\ln \mathrm{V}} \quad (10)$$

III. RESULTS AND DISCUSSION

3.1. Structural and electronic properties

Firstly, the equilibrium lattice parameter has been computed by minimizing the crystal total energy calculated for different values of lattice constant by means of Murnaghan's equation of state (eos) [18] as in Fig.1. The bulk modulus, and its pressure derivative have also been calculated based on the same Murnaghan's equation of state, and the results are given in Table 1. The calculated value of lattice parameter for GGA is 4.045 Å in B2 phase for TlBr. The present value for lattice constant is also listed in Table 1, and the obtained result is quite accord with the other experimental values of Refs. [19-20].

The formatin enthalpy is known as a measure of the strength of the forces, which bind atoms together in the solid state. In this connection, the formation enthalpy of TlBr in the B2 structure is calculated. The formation entalphy ($E_{form.}$) of a given phase is defined as the difference in the total energy of the constituent atoms at infinite separation and the total energy of that particular phase:

$$E^{AB}_{form.} = [E^{AB}_{total} - E^{A}_{atom} - E^{B}_{atom}] \quad (11)$$

where E^{AB}_{total} is the total energy of the compounds at equilibrium lattice constant and E^{A}_{atom} and E^{B}_{atom} are the atomic energies of the pure constituents. The computed formation energy ($E_{form.}$) is found to be -2.26873 eV/atom in B2 phase for TlBr, and it is also listed in Table 2.

We have also calculated the band structures for TlBr, and the obtained results for high symmetry directions are displayed in Fig. 2. As can be seen from the Fig. 2 that band gap exists for studied compound, and it exhibits nearly semiconductor character. The total electronic density of states (DOS) corresponding to the present band structures is, also, depicted in Figure.2 and the appearing of the energy gap in DOS conforms the semiconductor nature of TlBr.

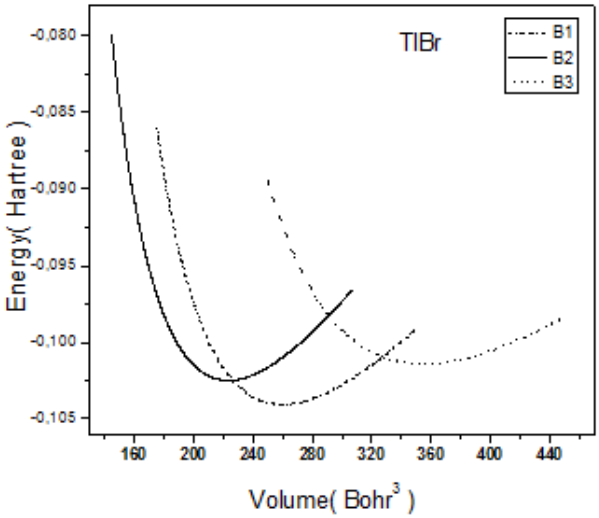

Fig. 1. Total energy versus volume curves of TlBr.

Table 1. Calculated equilibrium lattice constant (a_0), bulk modulus (B), the pressure derivative of bulk modulus (B´) together the experimental values, for TlBr.

Structure	*Reference*	Lattice Constant (Å)	B(GPa)	B'
B1	present	6.75	16.15	5.02
	Exp.[e]	6.58	-	-
B2	present	4.05	19.55	4.68
	Exp.[a]	3.84	-	-
	Exp.[b]	3.84	-	-
	Exp.[c]	3.97	-	-
	Exp.[d]	3.94	-	-
B3	present	7.49	11.03	4.76
	Exp.[e]	6.58	-	-
NbO	present	6.53	11.71	3.42
	Exp.[a]	3.84	-	-
	Exp.[b]	3.84	-	-
	Exp.[c]	3.97	-	-
	Exp.[d]	3.94	-	-

Ref [a]: [1], [b]:[2], [c]:[3], [d]: [4]

Table 2. Calculated direct gap (D), indirect gap (I) and formation enthalpy (ΔH) together the experimental values, for TlBr

Structure	Reference	ΔH(eV)	Direct Gap(eV)	Indirect Gap(eV)
B1	present	-2.34	2.35	3.02
B2	present	-2.27	1.58	1.94
	Exp.[c]	-	3.01	-
	Exp.[d]	-	3.0	-
	Exp.[d]	-	2.38	2.12
B3	present	-2.24	2.79	3.57
NbO	present	-2.38	3.87	2.52
	Exp.[c]	-	3.01	-
	Exp.[d]	-	3.0	-
	Exp.[f]	-	2.38	2.12

Ref [c] [3], [d]: [4], [e]:[22]

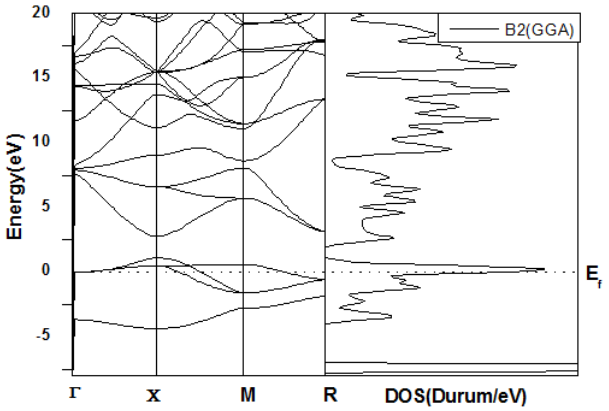

*Fig. 2.*Calculated band structure of TlBr in phase B2

3.2. Elastic properties

The elastic constants of solids provide a link between the mechanical and dynamical behavior of crystals, and give important information concerning the nature of the forces operating in solids. In particular, they provide information on the stability and stiffness of materials. Their ab-initio calculation requires precise methods, since the forces and the elastic constants are functions of the first and second-order derivatives of the potentials. Their calculation will provide a further check on the accuracy of the calculation of forces in solids. The effect of pressure on the elastic constants is essential, especially, for understanding interatomic interactions, mechanical stability, and phase transition mechanisms. It also provides valuable data for developing interatomic potentials.

There are two common methods [8,9,19, 20] for obtaining the elastic data through the ab-initio modeling of materials from their known crystal structures: an approach based on analysis of the total energy of properly strained states of the material (volume conserving technique) and an approach based on the analysis of changes in calculated stress values resulting from changes in the strain (stress-strain method). Here we have used the "stres-strain method"for obtaining the second-order elastic constants (C_{ij}). The listed values for C_{ij} in Table 3 are in reasonable order. The experimental and theoretical values of Cij for TlBr are not available at present.

Table 3. The calculated elastic constants (in GPa unit) in B1 and B2 structures for TlBr

Material	**Structure**	**C_{11} (GPa)**	**C_{12} (GPa)**	**C_{44} (GPa)**
TlBr	B1	37.85	6.81	3.55
	B2	36.69	12.82	5.30

The Zener anisotropy factor A, Poisson ratio υ, and Young's modulus Y, which are the most interesting elastic properties for applications, are also calculated in terms of the computed data using the following relations [21]:

$$A = \frac{2C_{44}}{C_{11} - C_{12}}, \tag{12}$$

$$\upsilon = \frac{1}{2}\left[\frac{(B - \frac{2}{3}G)}{(B + \frac{1}{3}G)}\right], \tag{13}$$

and

$$Y = \frac{9GB}{G + 3B} \tag{14}$$

where $G = (G_V + G_R)/2$ is the isotropic shear modulus, G_V is Voigt's shear modulus corresponding to the upper bound of G values, and G_R is Reuss's shear modulus corresponding to the lower bound of G values, and can be written as $G_V = (C_{11}–C_{12} +3C_{44})/5$, and $5/G_R = 4/(C_{11}-C_{12})+ 3/ C_{44}$. The calculated Zener anisotropy factor (A), Poisson ratio (ν), Young's modulus (Y), and Shear modulus ($C' = (C_{11}-C_{12+}2C_{44})/4$) for TlBr are close to those obtained for the similar structural symmetry.

3.3. Thermodynamic Properties

The quasi- harmonic Debye model is successfully applied to predict the thermal properties of TlBr in the 0-400 K temperature range. The pressure effect is studied in the 0-30 GPa range. The relationship between normalized volume and pressure at different temperature is shown in Fig. 3 for TlBr. It can be seen that when the pressure increases from 0 GPa to 30 GPa, the volume decreases. The reason for this changing can be attributed to the atoms in the interlayer that become closer and that their interactions become stronger. For TlBr compound the normalized volume decreases with increasing temperature.

The relationship between bulk modulus (B) and pressure (P) at different temperatures (100, 200, and 300K) is shown in Fig. 4 for TlBr. It can be seen that the

bulk modulus decreases with the increasing of the temperature at a fixed pressure and it increases with the increasing of the pressure at a fixed temperature. Namely, the effect of increasing pressure on TlBr is the same as decreasing its temperature.

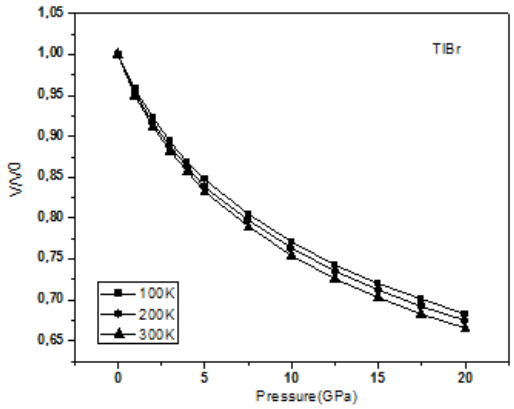

Fig. 3. The normalized volume-pressure diagram of the B2 structures for TlBr at different temperatures.

IV. SUMMARY AND CONCLUSION

The first–principles pseudopotential calculations have been performed on the TlBr using the plane-wave pseudopotential approach to the density-functional theory within GGA approximation. Our present key results are on the structural, elastic, electronic, and lattice dynamical properties for TlBr. The lattice parameter is excellent agreement with the experimental values. The elastic constants satisfy the traditional mechanical stability conditions for this structure. The computed band structures of TlBr exhibite a semiconductor character. The pressure dependence of the thermodynamical properties are also calculated and presented. It is hoped that some of our results, such as elastic constants and formation enthalpy estimated for the first time in this work, will be tested in future experimentally and theoretically.

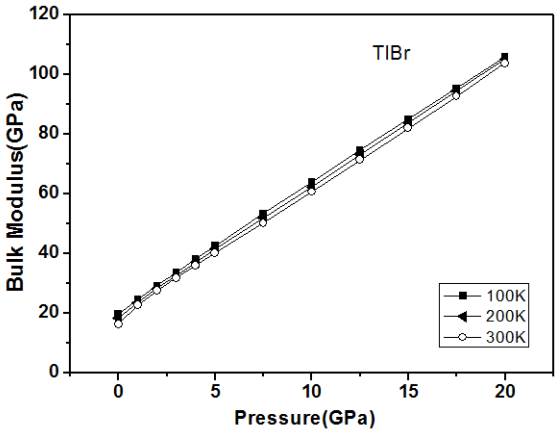

Fig. 4. The reletionships of TlBr between bulk modulus and pressure P at temperatures of100, 200 and 300 K for TlBr.

ACKNOWLEDGMENTS

This work is supported by Gazi University Research-Project Unit under Project No: 05/2009-16.

[1]. *L. Merrill*, J. Phys. Chem. Ref. Data, 6, (1977) 1205.
[2]. *I. E. Barchij, E. Yu. Peresh, N. J. Haborets, V.V.Tzigika*, Journal of Alloys and Compounds 358 (2003) 93-97.
[3]. *R. Z. Bachrach and F. C. Brown*, Physical Review B, Volume 1, No:2, (1969) 818-831.
[4]. *J. Overton and J. P. Hernandez*, Physical Review B Volume 1, No:2, (1973) 778-785.
[5]. *E. Barchij, E. Yu. Peresh, N. J. Haborets, V. V. Tzigika*, Journal of Alloys and Compounds 353 (2003) 180-183.
[6]. *K.N.R.Taylor*, Advances in Physics. 20,(1971) 551.
[7]. *T.O.Brun, G.H. Lander, D.L. Price, G.P. Felcher and J.F. Reddy*, Phy. Rev. B, 9, 1(1974) 248.
[8]. *J. Mehl*, Phys. Rev. B ,47 (1993) 2493.
[9]. *O.H. Nielsen and R.M. Martin*, Phys. Rev. Lett., 50 (1983) 697.
[10]. *Y. O. Ciftci, K. Colakoglu, E. Deligoz*, Cent. Eur. J. Phys. 6 (2008) 802
[11]. J. *P. Perdew and A. Zunger*, Phys. Rev. B, (1981)23 5048.
[12]. *J.P.Perdew,J.A.Chevary,S.H.Vosko,K.A.Jackson, M. R. Pederson, D. J. Singh*, Phys.Rev. B, 46, (1992) 6671
[13]. *H.J. Monkhorst and J.D. Pack*, Phys. Rev. B, 13(1976) 5188.
[14]. *M.A. Blanco, A.M. Pendàs, E. Francisco, J.M.Recio, R. Franko*, J.Mol. Struct. (Theochem) 368 (1996) 245.
[15]. *M. Flórez, J.M. Recio, E. Francisco, M.A. Blanco, A.M. Pendàs*, Phys. Rev. B , 66 (2002) 144112
[16]. *E.Francisco,J.M.Recio,M.A.Blanco,A.M.Pendàs*, J. Phys. Chem. ,102 (1998) 1595.
[17]. *R. Hill*, Proc. Phys. Soc. Lond. A ,65 (1952) 349.
[18]. *F. D. Murnaghan*, Proc. Natl., Acad. Sci. USA 30, 5390 (1994).
[19]. *Y. Le Page and P. Saxe*, Phys. Rev. B ,65 (2002) 104104.
[20]. *S.Q. Wang, H.Q. Ye*, Phys. Status Solidi B ,240 (2003) 45
[21]. *B. Mayer, H. Anton, E. Bott, M. Methfessel, J. Sticht, and P. C. Schmidt*, Intermetallics ,11 (2003) 23.
[22]. *J. P. Van Dyke, G. A. Samara* Phys. Rev. B, 11 (1975) 4935-4944

ZnO THIN FILMS WITH REACTIVE SPUTTER AT DIFFERENT O_2 CONCENTRATIONS AND SOME PHYSICAL PROPERTIES

S. KORKMAZ[1*], N. EKEM[1], S. PAT[1], M. Z. BALBAG[2], M. OZKAN[1], S. TEMEL[1], N. E. CETIN[1], M. OZMUMCU[1], S. ELMAS[1]

[1]*Department of Physics, Eskişehir Osmangazi University, Eskişehir, Turkey*

[2]*Education Faculty, Eskişehir Osmangazi University, Eskişehir, Turkey,*

skorkmaz@ogu.edu.tr

ZnO thin films were grown on the glass substrate using reactive sputter technique. Different concentrations of O_2 were used and the deposited ZnO thin films were investigated. Thickness and transparency of deposited films were determined using Swanepoel method. Additionally, energy gap of this films were calculated. ZnO thin films of surface morphology were determined to used AFM images.

1. INTRODUCTION

Zinc oxide (ZnO) which is one of the most important binary II–VI semiconductor compounds has a hexagonal wurtzite structure and a natural n-type electrical conductivity [1]. In addition zinc oxide thin films are very important for solar cells and optoelectronic devices. Because of zinc oxide has a low electrical resistance and high optical transmittance, it is very important and useful material for solar cells that is used to window layers.

ZnO thin films can deposit and synthesis by several deposition techniques. Some of these techniques are radio frequency sputter [2], sol gel method [3], spray-pyrolysis [2], pulsed laser deposition [4], chemical vapor deposition [5] and reactive sputter [6]. Reactive sputtering is very important technique among these techniques. Because, thin films is growth at different gas concentrations and deposited films have good properties of thin films such as high purity, homogeneities, rough surface and nanostructure features of thin film in this technique[7]. The advantages of reactive sputtering are compounds can be formed using relatively easy-to-fabricate metallic targets, insulating compounds can be deposited using RF power supplies, and films with graded compositions can be formed [8].

In this work, some physical properties were analyzed at different O_2 concentrations for ZnO films.

2. EXPERIMENTAL

Reactive sputter system consists of three parts mainly, vacuum chamber, radio frequency power supply (RF) and matching network unit, and gas mixing and filling system. Figs. 1 indicate schematic view of the reactive sputtering [1].

The primary control parameters are the deposition rate, target voltage, working gas species and pressure, and the substrate temperature and plasma bombardment conditions. The available selection range for the deposition parameters is determined largely by the apparatus. [8].

ZnO thin films were grown on the glass substrate by reactive sputter technique using from pure Zinc target. There are two parallel electrodes in vacuum chamber and target is placed over the one electrode and substrates are placed on the other one. Plasma discharge was produced between two parallel electrodes in the vacuum chamber at argon-oxygen gas mixed plasma at different partial pressures. Argon was buffer gas and O_2 was reactive gas in mixed plasma. Ar: O2 gas mixtures rates were 19:1, 9:1, 17:1, 8:2 and 7:3 which correspond to 5%, 10%, 15%, 20% and 30% of O_2 concentrations, respectively. The RF power was 400 W for all depositions. For 5%, 10% and 30% of O_2 concentrations, the vacuum chamber pressure was $2*10^{-1}$ Torr and for the other O_2 concentrations, vacuum chamber pressure was $6*10^{-2}$ Torr. The other production parameters of all ZnO thin films were the same as each other except the O_2 concentration. Thicknesses of the ZnO thin films were checked by using Cressington thin film analyzer, simultaneously. Perkin–Elmer UV/vis Spectrometer Lambda 2S was used to determine the transmittance and absorbance of the ZnO thin films. Atomic Force Microscope (AFM) was used to determine the surface morphology of produced ZnO thin films.

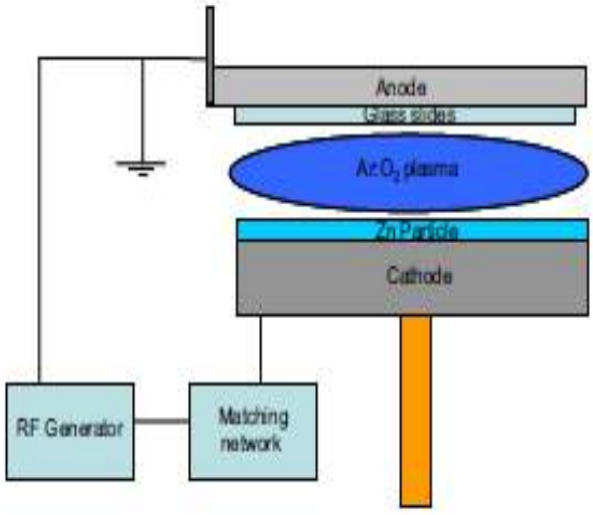

Fig. 1. Schematic of an reactive sputtering system[1].

3. EXPERIMENTAL RESULTS AND DISCUSSION

In this work, zinc oxide films are deposited by reactive sputtering on glass substrates with different O_2 concentrations. Some physical properties were analyzed for each ZnO films. Thickness and refractive index of

deposited films were determined using Swanepoel method.

The transmittance spectra were obtained via conventional spectrophotometry. The experimental data were collected in the ultraviolet-visible and near-infared ranges (λ=200-1200 nm), with a step width of 1nm. From the transmittance spectra the refractive index (n(λ)), thickness (t), absorption index (α(λ)), and extinction coefficient (κ(λ)) of the films were calculated using the Swanepoel method [9-10], and the optical band gap (E_g) was calculated from α(λ) [9-11].

The locations of the interference maximum and minimum are related to the real part n(λ) of the complex refractive index $\tilde{n}(\lambda) = n(\lambda) + j\kappa(\lambda)$ with $\kappa(\lambda)$ being the extinction coefficient, by the expression [9];

$$2tn(\lambda)=m\lambda \quad (1)$$

where m is the interference order, λ the wavelength and t is the film thickness.

The refractive index can be calculated from $T_M(\lambda)$ and $T_m(\lambda)$.

$$n(\lambda)=\left[\left(\frac{2s(T_M(\lambda)-T_m(\lambda))}{T_M(\lambda)T_m(\lambda)}+\frac{s^2+1}{2}\right)+\sqrt{\left(\frac{2s(T_M(\lambda)-T_m(\lambda))}{T_M(\lambda)T_m(\lambda)}+\frac{s^2+1}{2}\right)^2-s^2}\right]^{1/2} \quad (2)$$

$$s=\frac{1}{T_s}+\sqrt{\frac{1}{T_s^2}-1} \quad (3)$$

where s is the refractive index of the substrate and T_s is the substrate transmittance which is almost a constant in the transparent zone (λ>350 nm).

If n_1 and n_2 are the refractive indices at two adjacent maxima or minima at λ_1 and λ_2 then the thickness is given by,

$$t=\lambda_1\lambda_2 / 2[\lambda_1 n(\lambda_2)-\lambda_2 n(\lambda_1)] \quad (4)$$

absorption index (α (λ)) can be calculated from T_M (λ), T_m (λ), s and t by the following expression [9-10]

$$\alpha(\lambda)=\frac{1}{t}\ln\left[\frac{\left(\sqrt{a+\left(a^2-s^2\right)^{1/2}-1}\right)^3\left(\sqrt{a+\left(a^2-s^2\right)^{1/2}-s^2}\right)}{b-\sqrt{b^2-\left(a+\left(a^2-s^2\right)^{1/2}-1\right)^3\left(a+\left(a^2-s^2\right)^{1/2}-s^4\right)}}\right] \quad (5)$$

where a and b are the coefficients which depends on T_M (λ), T_m (λ) and s values. Then, κ (λ) is determined from α (λ) through the relation:

$$\kappa(\alpha)=\frac{\lambda\alpha(\lambda)}{4\pi} \quad (6)$$

Table 1. Physical parameters of deposited ZnO thin films at different O_2 concentrations

%Ar	$\%O_2$	n (550 nm)	K (550 nm)	Thickness (nm)
%95	%5	1,82	0,094	178 nm
%90	%10	1,78	0,067	170 nm
%85	%15	2,63	0,149	260 nm
%80	%20	2,33	0,152	155 nm
%70	%30	2,04	0,041	173 nm

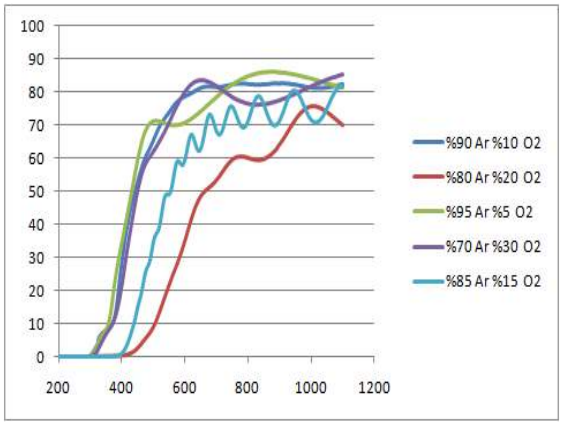

Fig. 2. Transmittance spectra of deposited ZnO thin films

ZnO thin films of surface morphology were determined to used AFM images.

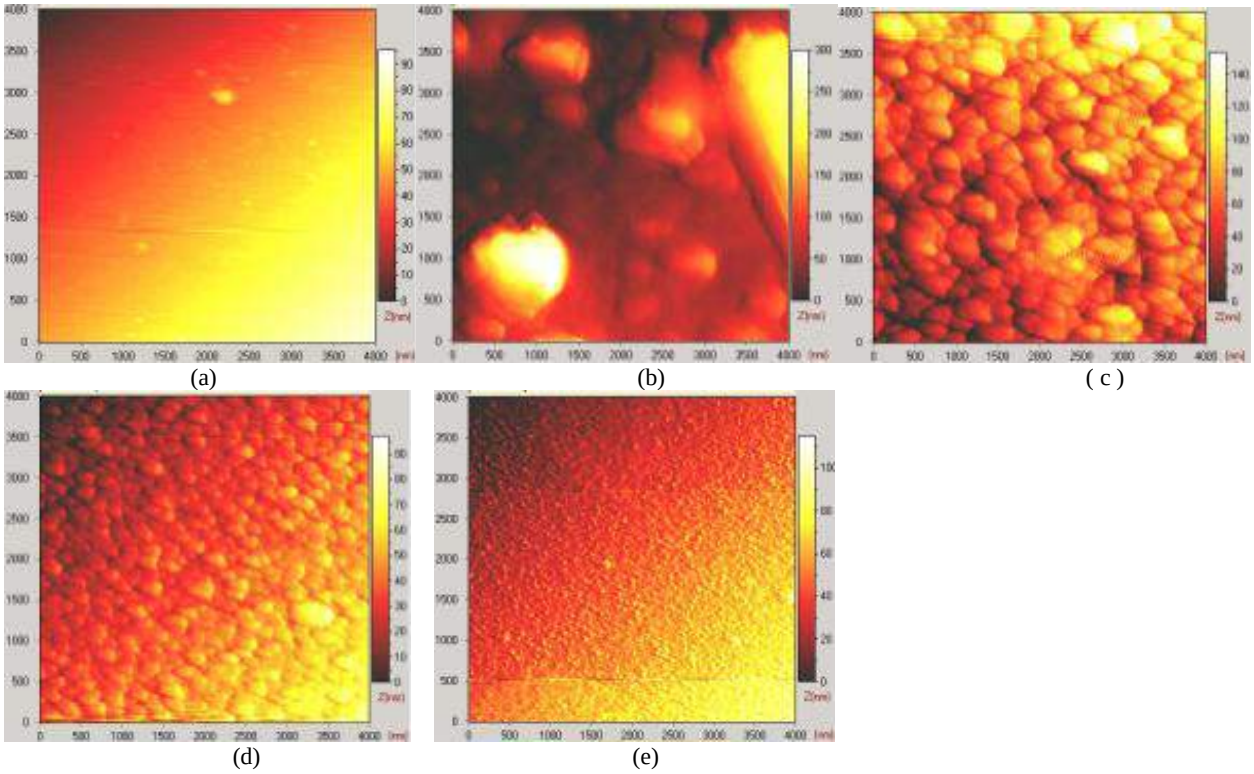

(a) (b) (c)

(d) (e)

Fig 3. AFM images(4µm×4µm) of ZnO thin films. (a) %5 O_2+ %95 Ar (b) %10 O_2+ %90 Ar (c) %15 O_2+ %85 Ar (d) %20 O_2+ %80 Ar (e) %30 O_2 +%70 Ar.

This study shows that differences between physical properties of deposited ZnO thin films in different concentration.

3. CONCLUSION

In this study, we obtained the highest transmittance of ZnO thin films at %5 O_2 concentration. The surface morphologies of the ZnO thin films are very smooth. The crystallization of ZnO thin films at %30 O_2 concentration is better than the other ZnO films.

[1]. *N. Ekem, S. Korkmaz, S. Pat, M.Z. Balbag, E.N. Cetin, M. Ozmumcu*, International Journal of Hydrogen Energy 34, 5218 (2009).

[2]. *S. Eirsermann, A. Kronenberger, M. Dietrich, S.Petznick, A. Laufer, A Polity, B. K. Meyer*, Thin Solid Films, 518(4), 1099-1102 (2009).

[3]. *D. Wong, J. Zhou, G. Z. Liu*, Journal of Alloys and Compounds, 481 (2009).

[4]. *T. Ohshima, R. K. Tharejo, T. Ikegami, K. Ebihara*, Surf. Coat. Tech., 169-170, 517-520 (2003).

[5]. *S. W. Kim, H. K. Park, M. S. Yi, N. M. Park, J. H. Park, S. H. Kim, S. L. Moeng*, App. Phys. Lett. 90, 3107-3109 (2007).

[6]. *S. Korkmaz, N. Ekem, S. Pat, M.Z. Balbag*, Balkan Physics Letters, 15 (1), 151045, (2009).

[7]. *L. Zhengwei, W. Gao*, Materials Letters, 58:1363, 70 (2004).

[8]. *R. F. Bunshah*, Handbook of Deposition Technologies for Films and Coatings, Los Angeles, California (1994).

[9]. *R. J. Swanepoel*, J. Phys. E: Sci. Instrum., 16, 1214 (1980).

[10]. *J. Sánchez-González, et al.,* Applied Surface Science 252, 6013-6017 (2006).

[11]. *V. Pandey, et al.*, Journal of Ovonic Research 3, 29-38 (2007).

[12]. *M. Selmi , F. Chaabouni, M. Abaab, B. Rezig*, Superlattices and Microstructures 44, 268–275 (2008).

[13]. *N. Ekem, Ş. Korkmaz, S. Pat, M. Z. Balbağ, N. E. Çetin, M. Özmumcu, R. Vladoio, G. Musa*, Journal of optoelectronics and advanced materials, 10(12), 2008, 3279.

[14]. *N. Ekem, S. Korkmaz, S. Pat, M.Z. Balbag, E.N. Cetin, M. Ozmumcu*, International journal of hydrogen energy 34 (2009) 5218.

[15]. *R. J. Swanepoel*, J. Phys. E: Sci. Instrum. 16 (1980) 1214.

[16]. *J. Sánchez-González, et al.,* Applied Surface Science 252 (2006) 6013-6017.

[17]. *M. Selmi , F. Chaabouni, M. Abaab, B. Rezig*, Superlattices and Microstructures 44 (2008) 268–275.

[18]. *V. Pandey, et al.*, Journal of Ovonic Research 3 (2007) 29-38.

EFFECT OF THERMAL ANNEALING ON THE STRUCTURAL PROPERTIES OF TiO_2 THIN FILM PREPARED BY RF SPUTTERING

SAİME ŞEBNEM ÇETİN[1], TARIK ASAR[1], SÜLEYMAN ÖZÇELİK[1]
[1]Gazi University, Faculty of Arts and Sciences, Department of Physics, Teknikokullar 06500, Ankara, Turkey,
e-mail:cetins@gazi.edu.tr

We have presented the structural properties of a titanium dioxide thin film which is prepared by RF magnetron sputtering system on p-type (100) Si substrate with Ar(%70) and O(%30) atmospheres. The film was conventionally thermal annealed (CTA) at 500 ^oC, 800 ^oC, 1000 ^oC during 1 h and 1000 ^oC during 2 h under air atmosphere. The structural properties of films were investigated by using high resolution X-Ray diffraction (XRD) system and Fourier transform infrared spectroscopy (FTIR) in range from 375 to 8000 cm^{-1} for as-deposited films and annealed films. **Also,** chemical bonding structures of the thin film were explained. As deposited film has anatase phase. However, in annealed films annealed, anatase and rutile phases coexist as revealed by XRD and infrared spectroscopy. Also, it is observed that during growth and the annealing of the TiO_2 film, thin SiO_2 layer was formed at the TiO_2 and Si interface

I. INTRODUCTION

Titanium dioxide (TiO_2) has three major crystalline structures: anatase, rutile and brookite which affect their optical and electrical characteristics. Therefore, TiO_2 thin films have potential applications for manufacturing electronic and optoelectronic devices such as sensor, high-speed memory devices and solar cells. The crystalline structures can be achieved by changing the film deposition conditions and post-growth processes such as thermal annealing in different gas atmospheres. TiO_2 films can be successfully grown on substrates like Si and glass, by reactive sputtering, sol-gel spin coating and laser deposition techniques [1-3]. The improvement of TiO_2 technology and the extension of implementation areas are dependent on the development of better growth conditions and methods, and the detailed research of film characteristics with all of their aspects. During the deposition process, gas pressure and substrate temperature affect the structural and crystal characteristics of TiO_2 films [4]. HRXRD is important tool to investigate of the structural properties of the thin films. Also, FTIR spectroscopy technique gives sensitive information about the existence of the crystal phases, Ti-O bond and the other chemical bonds in the films.

In the present study, a TiO_2 thin film was deposited on monocrystal p-type Si substrate by RF magnetron sputtering system with Ar and O atmospheres. The as-deposited TiO_2 film was treated by conventional thermal annealing (CTA) in air atmosphere at different temperatures. Structural properties of the as-deposited and annealed films were investigated by using HRXRD and FTIR spectroscopy.

II. EXPERIMENTAL

In this study, a TiO_2 film was grown on p-type (boron doped) mono-crystal silicon (100) wafers, having thickness of 350 μm with a resistivity of 1 Ω.cm. Before

the deposition process; Si wafer was etched and cleaning by well known procedure. Preceding each cleaning step, the wafer was rinsed thoroughly in deionized water of resistivity of 18 MΩ-cm. Thin films of TiO_2 were deposited by UHV RF Magnetron Sputtering System hot pressed and high purity (%99,999) Ti target, in $Ar+O_2$ reactive gas mixtures on p-Si. Prior to film deposition, Si substrates were sputter cleaned in pure argon ambient after raising the substrate temperature to 400 °C in 10^{-8} mbar high vacuum, to ensure the removal of any residual organics [5]. The automatic control system of gas valves were used for Ar and O_2. During the deposition, flow of Ar/O_2 of sample was maintained at 70/30. The film with 100 nm thickness was deposited at a constant pressure of $1.0x10^{-3}$ mbar at 100°C temperatures. After deposition, cutting four pieces of sample were thermally treated by conventional thermal annealing (CTA) in air atmosphere for 1 h at 500 °C, 1 h at 800 °C, 1 h at 1000 °C, and 2 h at 1000 °C. Structural analysis for as-deposited films and annealed films were carried out by using high-resolution X-ray diffractometer (Bruker, D-8) by using $CuK\alpha_1$ (1.540Å) radiation, (with a prodded mirror and a 4-bounce Ge (220) symmetric monochromator) and FTIR spectroscopy (Bruker Vertex 80 IR Spectrometer in range from 375 to 8000 cm^{-1} with 4 cm^{-1} of the resolution).

III. RESULTS AND DISCUSSION

The thin TiO_2 film was deposited on p-type Si substrate using RF reactive sputtering technique with 70/30 flow of Ar/O_2 at 100 ^oC temperature. The film was annealed at 500 °C (1 hour), 800 °C (1 hour), 1000 °C (1 hour), and 1000 °C (2 hour) temperatures under air atmosphere. Structural properties and chemical bond structure of the as-deposited and annealed films at different temperature were identified by evaluation of θ-2θ scan measured by HRXRD and absorption spectra which is obtained using the FTIR.

The HRXRD spectra of the TiO_2 film deposited on p-Si substrate as deposited and at different annealing temperatures given in Fig.1. The peaks at 2θ: 24°, 49°, 54°, 55° and 2θ: 33°, 38°, 44°, 56.° were typical anatase and rutile peaks, respectively [6-8]. It was clearly that the anatase and rutile coexisted below 1000 °C. However, at 1000 °C (2 h), it was dominantly that rutile phase peak was the strongest one.

As seen in this figure, as-deposited film has mainly amorphous structure. However, some peaks relating to anatase crystalline phase of this film was observed as seen in Fig.1.(a). After the thermal annealing of the film, anatase and rutile phase co-exist as seen in Fig.1.(b-e). The rutile phase was dominant in annealed film at 1000 ^oC during 2 hours.

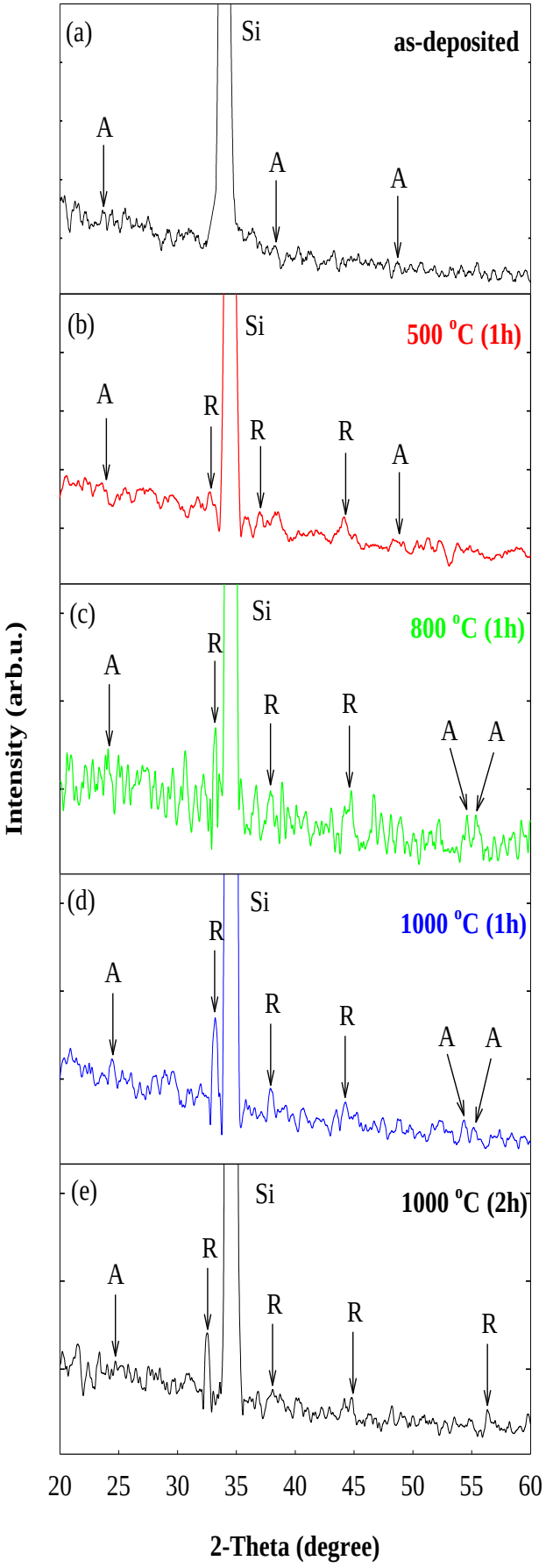

Fig.1. XRD pattern of TiO_2 thin film at different annealing temperatures.

Fig.2.(a-j) shows the FTIR spectra in range of 375-8000 cm^{-1} of the sample with as-deposited and annealed at 500 °C (1 hour), 800 °C (1 hour), 1000 °C (1 hour), and 1000 °C (2 hour) temperatures under air atmosphere. As-deposited (un-annealed) TiO_2 film contains mainly amorphous structure. However, the grown film has some anatase crystalline phase. After the thermal annealing at the high temperature, the film becomes crystalline.

The absorption peak related to anatase crystalline phase for the TiO_2 films is generally observed at around 440 cm^{-1} [9]. It is not observed any peak around this wavenumber in our measurements. However, a strong peak was observed at 407 cm^{-1} for our films as seen in Fig.2. These absorbance peaks can be corresponds to the anatase phase of the TiO_2 films. Similar peak in the absorbance spectra for TiO_2 powder samples was observed in literature [2]. After the thermally annealing, a new absorption peaks were observed as seen in Fig.2.(e,g,i). The observed peak located at around 514 cm^{-1} is associated with the rutile phase. Also, the observed peak at around 459 cm^{-1} for annealed films at 800 °C and 1000 °C may be correspond to Ti_2O_3 film formation [10] in these sample.

The shoulder peak at around 615 cm^{-1} was observed for as-deposited and annealed samples. It is well known that the intensive absorption peak at 608 cm^{-1} is characteristic of the Ti-O bond in the rutile modification [10-12]. In spite of the fact that the vibration peak of Ti-O bond is observed 608 cm^{-1}, existence of this peak may not be only the evidence of the rutile phase. On the other hand, intensities of the peaks have not changed by increasing temperatures.

The IR absorbance at around 810cm^{-1} and 1100 cm^{-1} corresponds to symmetric and asymmetric Si–O–Si stretching vibrations, respectively [13]. These peaks are may be due to the reactivity between TiO_2 film and Si substrate during annealing and during deposition at 100 °C. However, during the deposition of the TiO_2 films, thin SiO_2 film can be formed at the TiO_2 and Si interface. As seen Fig.2, the peak intensity of this absorbance for the films annealed at the 1000 °C (2 h) is bigger than the others. This indicates that the SiO_2 grain size in this sample is bigger than others. Also, full width half maximum (FWHM) of the band at located around 1100 cm^{-1} have been increased with the annealing temperature. The broadening of this vibration band can also be explained as larger Si–O–Si bond angle in the SiO_2 film [14].

The observed broad band at around 2900cm^{-1} is C-H stretching band as seen in Fig.2.(b, d, f, h, j). Also band at around 1377 cm^{-1} is C-H bending vibration. As seen Fig.2.(b, d, f, h, j), the peaks located around 1454 cm^{-1} and 2350 cm^{-1} may be corresponding to CO_2 vibrations. Their intensities of the absorption peaks were increased by increasing annealing temperature.

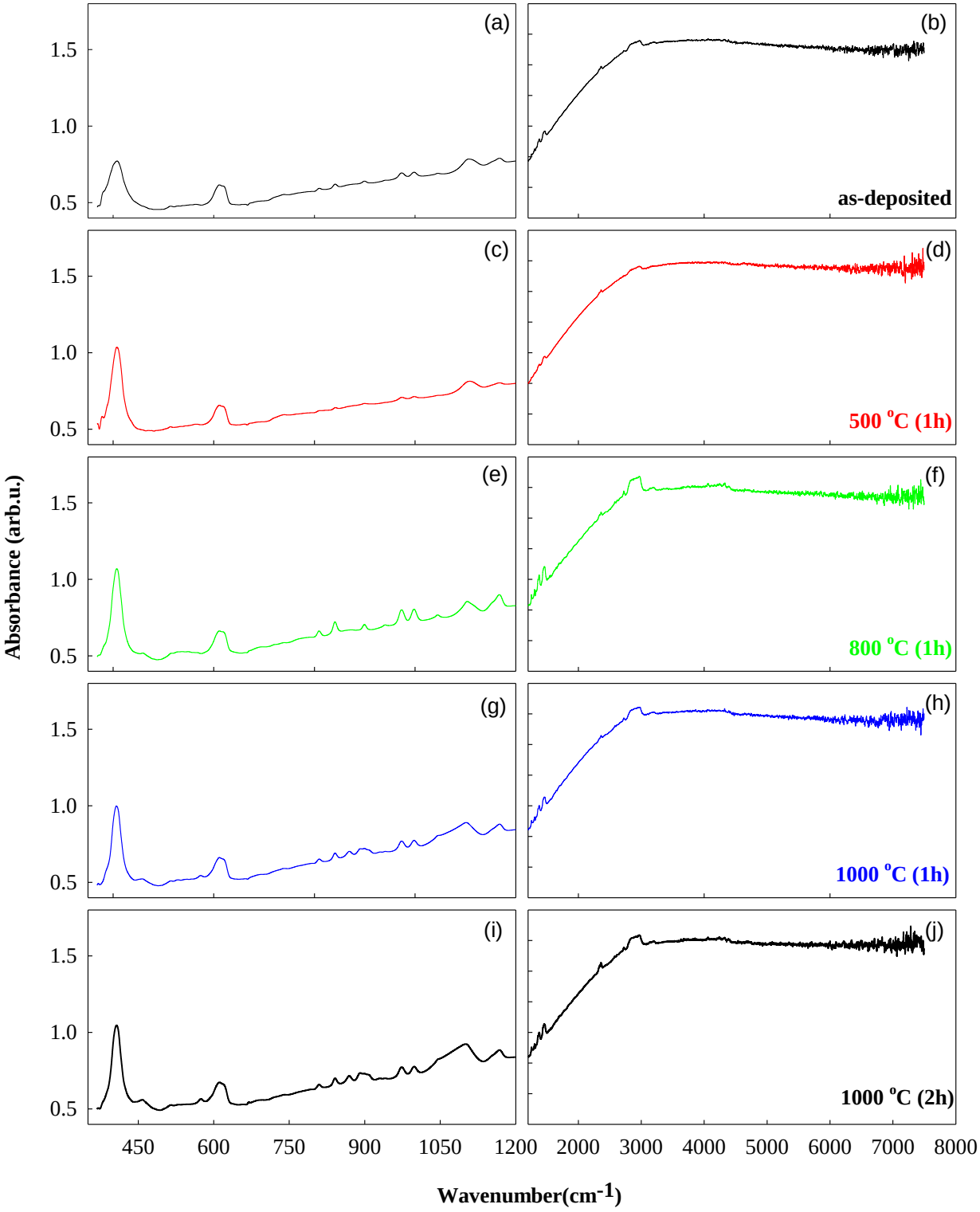

Fig.2. The FTIR spectra of the sample (a, c, e, g, i) in range of 375-1200 cm^{-1} (b, d, f, h, j) in range of 1200-8000 cm^{-1}.

III. RESULTS AND DISCUSSION

The structural properties of deposited the TiO_2 thin films by using RF reactive sputtering technique at 100 °C temperature with 70/30 of flow ratio of Ar and O_2 gas were investigated using HRXRD and FTIR spectroscopy. It was observed that the dominant crystal structures of the TiO_2 films are rutile phase when the annealing temperature up to 1000 °C (2 h). However, anatase phase structure is dominant up to 800 °C annealing temperatures. The obtaining results indicated that a thin SiO_2 layers between TiO_2 film and Si substrate in the samples are formed due to the reactivity O_2 and Si substrate.

ACKNOWLEDGMENTS

This work was supported by DPT under project No. 2001K120590.

[1]. *S.F. Wang, Y.F. Hsu, Y.S. Lee*, Ceramics International, 2006, 32, 121.
[2]. *Y. Djaoued, S. Badılescu, P.V. Ashrit*, J. .Sol-Gel Sci. and Tech., 2002, 24, 247.
[3]. *N. Inoue, H. Yuasa, M. Okoshi*, Appl. Surf. Sci., 2002, 197-198, 393.
[4]. *M.I.B. Bernardi, E.J.H. Lee, P.N. Lisboa-Filho, E.R. Leite, E. Longo, J.A. Varela*, Mat. Res., 2001, 4(3), 223.
[5]. *H. Altuntas, A. Bengi, U. Aydemir, T. Asar, S.S.Cetin, I. Kars, S. Altindal, S. Ozcelik*, Mat. Sci. Semicond. Process., 2009, doi: 10.1016/j.mssp.2009.12.001
[6]. *L. Miao, P. Jin, K. Kaneko, A. Terai, N. Nabatova-Gabain, S. Tanemura*, Appl. Surf. Sci., 2003, 212–213, 255.
[7]. *H. Long, G. Yang , A. Chen, Y. Li, P. Lu*, Thin Solid Films, 2008, 517, 745.
[8]. *P.M. Kumar, S. Badrinarayanan, M. Sastry*, Thin Solid Films, 358, 2000, 122.
[9]. *A. Hodroj, O. Chaix-Pluchery, M. Audier, U.Gottlieb, J.L. Deschanvres*, J. Mat.Res., 2008, 23(3), 755.
[10]. *D. Yoo, I. Kim, S. Kim, C.H. Hahn, C. Lee, S. Cho*, Appl. Surf. Sci., 2007, 253, 3888.
[11]. *V.G. Erkov , S.F. Devyatova, E.L. Molodstova, T.V. Malsteva, U.A. Yanovskii*, App. Surf. Sci., 2000, 166, 51.
[12]. *Z.D. Sha, Y. Yan, W.X. Qin, X.M. Wu, L.J. Zhuge*, J. Phys. D: Appl. Phys., 2006, 39, 3240.
[13]. *D.C.M. Dutoit, M. Schneider, R. Hutter, A. Baiker*, J. Catal., 1996, 161, 651.
[14]. *S.H. Jeong, J.K. Kim, B.S. Kim, S.H. Shim, B.T.Lee*, Vacuum, 2004, 76, 507.

THE CRYSTAL AND MOLECULAR STRUCTURE OF $C_{19}H_{17}N_3O_2$

S. ÖZTÜRK YILDIRIM[1*], Z. ÖNAL[2], V. MCKEE[3]

[1]Physics Department, Faculty of Sciences, University, 38039 Kayseri, Turkey

[2]Chmistry Department, Faculty of Sciences, University, 38039 Kayseri, Turkey

[3]Departmentof Chemistry, Loughborough University, Leicestershire LE11 3TU England

** ozturk@erciyes.edu.tr*

$C_{19}H_{17}N_3O_2$ was prepared and characterized by ^{1}H-NMR, ^{13}C-NMR, elemental analysis and IR spectroscopy as well as single crystal X-ray diffraction. These results indicate the centrosymmetric dimers. The molecule is composed of a pyrimidin moiety containing two methylphenyl groups, which are oriented in different directions. The pyrimidine ring is slightly distorted from planarity. The crystal structures are stabilized by intermolecular N—H …O type hydrogen bonds.

I. INTRODUCTION

As part of our X-ray crystal structure analysis of some compounds of biological interest for the structural basis for a better understanding of the effect of structural and conformational change on biological activity, the structure determination of the title compound was undertaken. Pyrimidines in general have been of much interest for biological and medical reasons, and thus their chemistry has been investigated extensively [1]. Some are frequently encountered in many drugs used for the treatment of hypothyroidism and hypertension, in cancer chemotherapy or HIV infections [2]. The title compound is a member of the family of pyrimidine derivatives which we have recently synthesized and whose crystal structures we have determined [2-7].

II. EXPERIMENTAL

Material

All starting compounds and solvents for synthesis were purchased from Across, Aldrich, Sigma and E. Merck.Solvents and all reagents were technical grade and were purified and dried by distillation from appropriate desiccant when necessary. Concentration of solutions after reactions and extractions were achieved using a rotary evaporator at reduced pressure. Analytical and preparative thin layer chromatography (TLC) was performed on silica gel HF-254 (Merck). Column chromatography was carried out by using 70–230 mesh silica gel (0.063–0.2 min, Merck).

Method

The structures of the compounds in this study were determined by the instruments mentioned below.All melting points were measured in sealed tubes using an electrothermal digital melting point apparatus (Gallenkamp) and were uncorrected. The investigation of vibrational properties of the b-enaminone was carried out on a Mattson 1000 Model FT-IR Spectrometer within the range of 4000–400 cm-1. The IR sample was prepared as KBr pellet. 1H-NMR, 13C-NMR were recorded on a resolution fourier transform Bruker WH-400 NMR spectrometer with tetramethylsilane as an internal standard.Chemical shifts were reported in ppm relative to the solvent peak. Signals were designated as follows: s, singlet; d, doublet; t, triplet; q, quartet; m, multiplet. Elemental microanalyses of the separated solid chelates for C, H, N, were performed with a Elementar Analysensysteme GmbH vario MICRO CHNS analyser.

Synthesis

20 mL of water and 5 mL of acetic acid were added to a solution of 1 g 5-(4-methylbenzoyl)-1-(methyl-4-methylphenylmethylenamino)-4-(4-methylphenyl)-1*H*-pyrimidine-2-one in 20 mL of ethanol and the mixture was the heated under reflux for 45-50 minutes. With cooling 0.43 g (57%) of 1-amino-5-(4-methylbenzoyl)-4-(4-methylphenyl)-1*H*-pyrimidine-2-one precipitated and was recrystallized from ethanol; m.p.: 198^{o}C.

Spectroscopic Studies

IR (*KBr*): υ= 3250 (-NH_2), 3036 (aromatic C-H), 2911 (aliphatic C-H), 1680 s (C=O), 1650 s (C=O), 1507-1461 cm^{-1} (C=C and C=N); ^{1}H NMR (*DMSO*): δ= 7.71-6.99 (m, 9H, ArH), 7.26 (s, 2H, N-NH_2), 2.38 ppm (s, 6H, 2xCH_3). nal. Calcd. for $C_{19}H_{17}N_3O_2$: C, 71.45; H, 5.36; N, 13.15. Found: C, 71.19; H, 5.20; N, 12.95.

Crystallographic Studies

A summary of the key crystallographic information is given in Table 1. A suitable single-crystal was selected and mounted on an Bruker APEX-II CCD diffractometer [8].

The structure was solved by direct methods with SHELXS-97 and refined by least squares on F_{obs^2} with SHELXL-97 [9]. All the hydrogen atoms were located from difference Fourier map and they were refined using riding model. Some geometrical parameters (bond lengths, bond angles and torsion angles) can be seen in Table 2).

Accurate values of the unit cell parameters were obtained using several high angle reflections in the range 2.19° < θ < 20.33° using MoK_α (λ = 0.71073 Å) radiation and with the ω and φ scans on Bruker APEX-II CCD area detector. An absorption correction of multi-scan [8] was applied. The experimental conditions used for single-crystal data collections and refinement are given in Table 1.

The structure was solved by direct methods with SHELXS-97[9]. The E-map calculated for the best phase set generated by the program revealed the positions of all

the non-H atoms. The trial structures thus obtained were refined by full matrix least-squares methods using SHELXL97 [9].

Table 1 Crystallographic and structure refinement data for $C_{19}H_{17}N_3O_2$.

Formula	$C_{19}H_{17}N_3O_2$
Formula weight	319.36
Temperature /K	150(2)
Wavelength λ /Å	0.71073
Crystal system	Monoclinic
Space Group	*C*2/*c*
Crystal size /mm^3	0.20×0.07×0.06
a /Å	24.105 (4)
b /Å	5.9547 (10)
c /Å	23.170 (4)
β /°	103.638 (3)°
Volume / Å^3	3232.0 (9)
Z	8
Density (calc.) /g cm^{-1}	1.313
θ ranges for data collection	1.74-26.35
F(000)	1344
Absorption coefficient mm^{-1}	0.087
Index ranges	$-30 \le h \le 29$
	$-7 \le k \le 7$
	$-28 \le l \le 28$
Data collected	11340
Unique data (R_{int})	1803 (0.076)
Parameters, restrains	218 , 0
Final R_1, wR_2 (Obs. data)	0.059, 0.174
Goodness of fit on F^2 (S)	0.99
Largest diff peak and hole /e Å^3	0.39, -0.40

Table 2 Selected bond distances (Å) and bond angles (°) for $C_{19}H_{17}N_3O_2$.

O1—C1	1.226(4)	N1—C4	1.336(4)
O2—C12	1.222(3)	N2—C1	1.371(4)
N1—N3	1.411(3)	N2—C2	1.321(4)
N1—C1	1.407(4)		
N3—N1—C1	118.8(2)	N1—C1—N2	116.7(2)
N3—N1—C4	118.8(2)	N2—C2—C5	115.5(2)
C1—N1—C4	122.3(2)	N2—C2—C3	122.4(3)
C1—N2—C2	121.0(2)	N1—C4—C3	120.9(3)
O1—C1—N1	119.4(3)	O2—C12—C13	121.9(3)
O1—C1—N2	123.9(3)	O2—C12—C3	119.6(3)

Initially, isotropic refinement was carried out for all the non-hydrogen atoms and this was followed by anisotropic refinement until convergence.

At this stage the positions of all the hydrogen atoms were fixed and were allowed to refine isotropically using a riding model. The refinement converged to a final R-factor of 0.059.

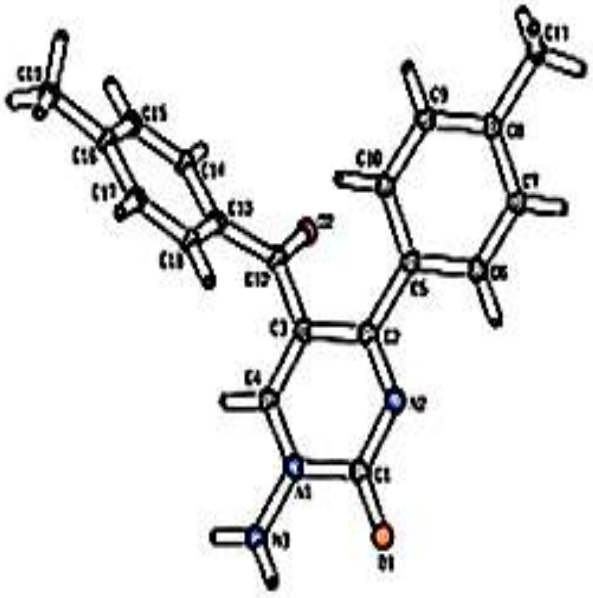

Fig.1. View of the title compound with the atom numbering scheme.

III. RESULTS AND DISCUSSION

Table 1 shows details of the data collection and refinement of the X–ray crystal structure determination. Selected bond lengths and bond angles are presented in Table 2. The PLATON view with the numbering scheme is shown in Fig. 1. The title compound has non planar conformation. All bond lengths and angles show normal values [10], and are in good agreement with those observed in similar compounds [5,6,11]. The C—N distances have values in the range 1.321(4) Å –1.407(4) Å, shorter than the single-bond length of 1.480 Å and longer than the typical C = N distance of 1.280 Å, indicating partial double-bond character and suggesting conjugation in the heterocycle. The pyrimidine ring is slightly distorted from planarity with a maximum deviation of -0.038 (3) Å for atom C1. The mean planes of the rings A (N1/N2/C1–C4), B (C5–C10) and C (C13–C18) make the following dihedral angles with each other: A/B = 34.89(14), A/C = 69.63(14) and B/C = 68.76(15)°.

In summary, the X-ray studies confirm the original structural assignments based on spectroscopic techniques and furthermore yield accurate structural parameters which are useful for future biological and pharmaceutical modeling studies.

[1]. *Z. Önal and B.Altural*, B., 2006. Asian J. Chem. 18, 1061–1064.
[2]. E. L.Burdge, 2000. Pest Manag. Sci. 56, 245–248.
[3]. *M. Akkurt, S.Öztürk, Z. Önal, B.Altural and O.Büyükgüngör*, 2004. Acta Cryst. E60, o1844–o1846.
[4]. *M. Akkurt, E.Sarıpınar, S.Öztürk , Ç.Yılmaz and H.-K. Fun*, 2003. Z. Kristallogr. 218, 488–491.
[5]. *S. Öztürk, M. Akkurt, T. Hökelek and I. Yıldırım*, (1997). Cryst. Res. Technol. 32, 585–589.
[6]. *S.Öztürk, M. Akkurt, I. A. Razak, H.-K. Fun and İ.Yıldırım*, 1999. Acta Cryst. C55, 97–99.
[7]. *S. Ö. Yıldırım, M. Akkurt, Z. Önal and O.Büyükgüngör,* 2007. Acta Cryst. E63, o1712–o1713.
[8]. Bruker (2005). APEX2, SAINT and SADABS. Bruker AXS Inc., Madison, Wisconsin, USA.
[9]. *G. M. Sheldrick*, (1997). SHELXS97 and SHELXL97. University of Göttingen, Germany.
[10]. *F. H.Allen, O. Kennard, D. G.Watson, L.Brammer, A. G. Orpen and R. Taylor,* (1987). J. Chem. Soc. Perkin Trans. 2, pp. S1–19.
[11]. *S. Ö.Yıldırım, M. Akkurt, Z. Önal and O.Büyükgüngör*, (2007). Acta Cryst. E63, o1712–o1713.

A NEW CATALYST TO SYNTHESIZE CARBON NANOSPHERES AT LOW TEMPERATURE

S. CAVDAR [*], H. KORALAY, H. DİSBUDAK [a], A. GÜNEN

Department of Physics, Gazi University,
Teknik Okullar Ankara, Turkey
[a]Saraykoy Nuclear Research and Training Center,
TAEA, Kazan/Ankara, Turkey
E-mail: cavdar@gazi.edu.tr

Carbon nanospheres were synthesized at 210 ^{o}C via Grignard reaction mechanism with a new catalyst by using magnesium powder, hexachloroethane and cobalt chloride as precursor materials and benzene as solvent. The products were characterized with X-Ray diffraction pattern (XRD) and scanning electron microscope (SEM) images. The experimental conditions are incredibly simple to operate and control.

I. INTRODUCTION

Enormous improvements on nano materials and their structures have been realized since carbon nanotubes had been discovered by Iijima in 1991 [1]. Because carbonaceous materials have so attractive unique structures these materials can be applied to a lot of industrial areas. Solid carbon nanospheres are totally new nanocarbon materials. Many applications of carbon nanospheres are summarized by various reports; for instance, in metal and plastic composites [2-7]. Carbon nanomaterials are approximately 10 times stronger and 10 times lighter than steel. Blending of solid carbon nanospheres with steel, aluminum, titanium, plastics, fiberglass, ceramics and other materials, significantly enhanced the strength and durability in addition to the reduction in weight [8-9].

Another application of carbon nanospheres is as protective armor; these materials have excellent potential for armor in composite from, such as ceramic or steel or mixed with polymers and fibers for strong and lightweight fabrics.

In addition , they may be used as airframe coatings or paints for aircraft, military and commercial vehicles for protecting against extreme aircraft environmental conditions. On the other hand, Carbon nanospheres may be applied to microcircuits, chips and super-capacitors owing to their high conductivity and high temperature operation and having functional properties. Moreover, It may be applicable to super-capacitors due to their ability to store higher voltages to be released over long periods of time. They also have unique properties of being radar / X-ray absorbing and its ability to mix in polymer solutions for uniform spray-on application to wing structures and other airframe components.

The catalytic growth of structured carbon in the form of nanofibers and nanospheres using various chloro-hydrocarbons as the carbon source, and Ni/SiO_2 as the catalyst has been examined at temperatures between 673 K and 1073 K [10]. On the other hand, large-scale syntheses of carbon nanostructures with unique morphologies were performed at 500 ^{o}C starting with magnesium powder and methanol [11]. In the mean time, another large-scale synthesis of pure carbon spheres, with diameters ranging from 50 nm to 1 μm has been achieved by direct pyrolysis of a wide range of hydrocarbons, including styrene, toluene, benzene, hexane, cyclohexane and ethane in the absence of catalyst at the pyrolysis temperatures between 900 ^{o}C and 1200 ^{o}C [12]. Carbon spheres with approximate uniform diameters of about 1-2 μm were synthesized by chemical reduction of metallic calcium by supercritical CO_2 at 550 ^{o}C [13]. The synthesis of hollow carbon nanospheres through a ZnSe nanoparticle template route at the temperature 1200 ^{o}C were also reported [14]. Another study reported was the low cost, high yield chemical vapor deposition synthesis of novel carbon nanomaterial using nickel nanocluster-catalysed dissociation of acetylene at 700 ^{o}C [15]. Meanwhile, Y. Ni et al. reported that hollow carbon nanospheres were obtained at 200 ^{o}C through a new of chemical reactions, by using magnesium powder, hexachloroethane and aliminumtrichloride as the starting materials and benzene as the solvent [16].

In this paper, we report on the synthesis of carbon nanospheres at 210 ^{o}C by using magnesium powder, hexachloroethane and cobalt chloride as a new catalyst starting material and benzene as the solvent.

II. EXPERIMENTAL PROCEDURE

All reagents were commercially available and applied without further purifications..In a typical experimental method, metallic Mg powder (0,309 g), $CoCl_2$ (0,300 g) and C_2Cl_6 (1,470 g) were mixed in a small pyrex bottle and the mixture was stirred uniformly with the addition of 15 ml C_6H_6 .

Then the small pyrex bottle was placed in an autoclave type reactor of about 150 mL capacity. The reactor was sealed and the temperature was maintained at 210 ^{o}C for 18 h and then allowed to cool down to ambient temperature. The dark blue resultant was collected from the bottle onto a filter paper and then washed with absolute ethanol for at least three times.

HCl solution of 2 mol/L was passed through the residue and then washed with distilled water. Finally the clean residue was dried in a vacuum oven at 60 ^{o}C for 4-5 h and samples were obtained.

III. RESULTS AND DISCUSSION

The phase and crystallography of the samples were analyzed by x-ray diffraction (XRD) spectrometry which was recorded by using Bruker D8 Advance.

X-ray diffractometer was equipped with CuKα radiation source (λ = 1,54178 Å) and the scanning rate of

0,05 $^{o}s^{-1}$ was applied to record the spectra in the 2θ range of 10 – 70 ^{o}.

The XRD spectra of the samples (Fig.1) indicate the presence of reflection characteristics of carbon hexagonal phase. Reflections in Figure 1 are comparable to the reported data of graphite (JCPDS card file No:41-1487), with the position of the peak angle of 2θ = 26,5 ^{o}. On the other hand, reflections in Figure 1. are consistent with reported data of periclase material, Syn-MgO-Y (JCPDS card File No:45-0946), with the position of the peak an angle of 2θ = 44 ^{o}.

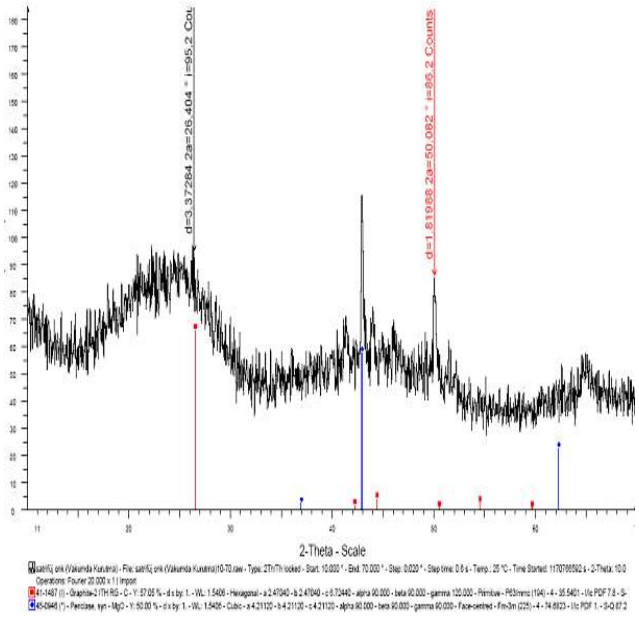

Fig. 1. XRD of the sample

The scaning electron microscopy (SEM) images were acquired with a Jeol 7000F FEG, using an accelerating voltage of 20 kV to identify the morphological properties. The typical morphology of the samples are indicated in Figure 2 via SEM observations. From Figure 2-a- -j it can be observed that most of the structures are nanospheres with diameters ranging in 15-100 nm.

The following overall reaction mechanisms with magnesium as an active metal and $CoCl_2$, easily forms Grignard reagent with the organic- chloride;

$$C_2Cl_6 + Mg \xrightarrow{CoCl_2} C + MgCl_2$$

It is thought that $CoCl_2$ in the Grignard reaction plays an important role in the formation of nano carbonaceous materials.

In addition, we also noticed that the temperature has a vital effect in the formation of nano carbonaceous structures. When the temperature was decreased to 190 ^{o}C, a large amorphous carbon was observed and no carbon nanospheres were found in the resultant products.

IV. CONCLUSIONS

To include, carbon nanospheres were obtained at 210 ^{o}C through a new Grignard reagent, $CoCl_2$. The reaction time was about 18 h.

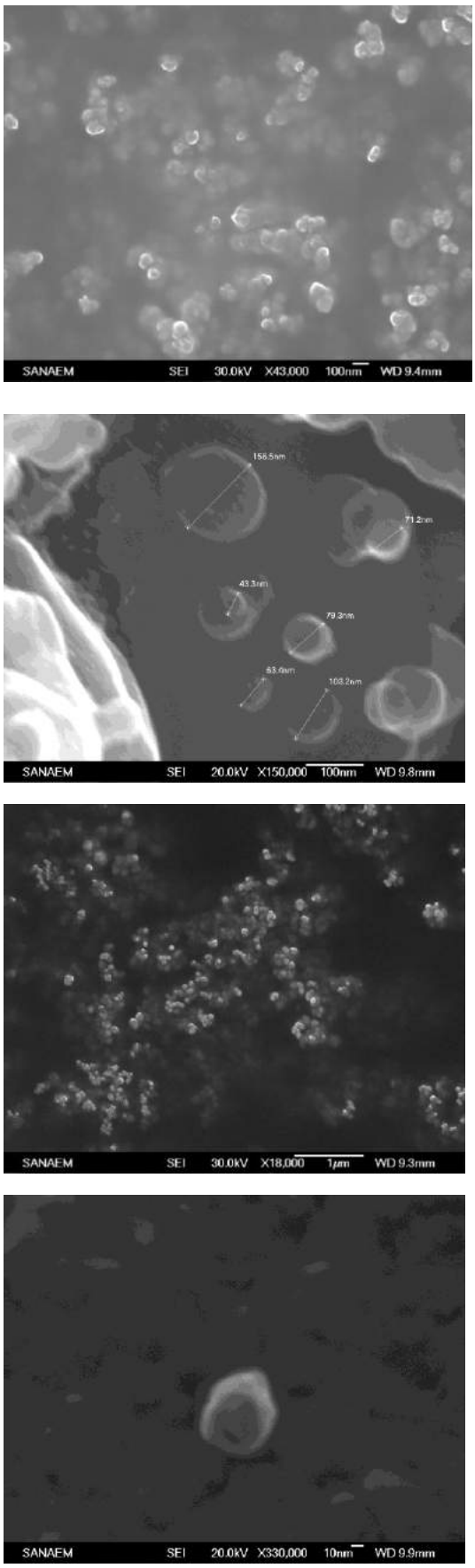

Fig. 2. a-b-c-d SEM micrographs of the sample of Carbon nanospheres

[1]. *S. Iijima* Helical Microtubules of Graphitic Carbon, Nature 1991, 354, 56.

[2]. *H. Dai, A. G. Rinzler, P. Nikolaev, A. Thess, D.T.Colbert, R. E. Smalley*: Single-wall nanotubes produced by metal-catalysed disproportionation of carbon monoxide, Chem. Phys. Lett. 1996, 260, 471

[3]. *A.Star, J. F. Stoddart, D. Steuerman, M. Diehl, A. Boukai, E.W. Wong, X. Yang, S.W. Chung, H. Choi, J. R. Heath*: Preparation and properties of polymerwrapped single-walled carbon nanotubes, Angew. Chem. Int. Ed. 2002, 41, 1721.

[4]. *W. A. de Heer, A. Châtelain, D. Ugarte*: A carbon nanotube field-emission electron source, Science 1995, 270, 1179

[5]. *K. G. Ong, K. Zeng, C. A. Grimes*: A wireless, passive carbon nanotube-based gas sensor, IEEE Sens. J. (2002) 2/2, 82

[6]. *P. M. Ajayan, O. Stephan, C. Colliex, D. Trauth*: Aligned carbon nanotube arrays formed by cutting a polymer resin-nanotube composite, Science (1994) .265, 1212

[7]. *R. W. Siegel, S. K. Chang, B. J. Ash, J. Stone, P.M.Ajayan, R.W. Doremus, L. S. Schadler* Mechanical behavior of polymer and ceramic matrix nanocomposites, Scr. Mater. 2001, 44, 2061

[8]. *M.-F. Yu, O. Lourie, M. J. Dyer, K. Moloni, T. F. Kelley, R. S. Ruoff*: Strength and breaking mechanism of multiwalled carbon nanotubes under tensile load, Science 2000, 287, 637

[9]. *D. A. Walters, L. M. Ericson, M. J. Casavant, J.Liu, D. T. Colbert, K. A. Smith, R. E. Smalley*: Elastic strain of freely suspended single-wall carbon nanotube ropes, Appl. Phys. Lett. 1999 .74, 3803

[10]. *A.Nieoto-Marquez, J.L. Valverda, M.A. Keane* Catalytic growth of structured carbon from chloro-hydrocarbons Applied Catalysis A: General 2007 332, 237 .

[11]. *J.M. Du, D.J. Kong* Synthesis of carbon nanostructures with unique morphologies via a reduction-catalysis reaction route Materials Research Bulletin 2006, 41, 1785.

[12]. *Y.Z.Jin, C.Gao, W.Kuang, Y.Zhu, A.Huczko, M. Bystrzejewski, M. Roe, C.Y. Lee, S. Acquah, H.Kroto, D. R. Walton M.* Large-scale synthesis and characterization of carbon spheres prepared by direct pyrolysis of hydrocarbons. Carbon 2005, 43, 1944

[13]. *Z. Lou, C. Chen, D. Zhao, S. Luo, Z. Li* Large-scale synthesis of carbon spheres by reduction of supercritical CO_2 with metallic calcium. Chemical physics letters 2006 ,421, 584

[14]. *B.Y. Geng, J.Z. Ma, Q.B. Du, X.W. Liu, L.D. Zhang* Synthesis of hollow carbon nanospheres through a ZnSe nanoparticle template route. Materials Science and Engineering 2007, 466, 96.

[15]. *A.Levesque, V.T. Binh, V. Semet, D. Guillot, R.Y. Fillit, M.D. Brookes, T.P. Nguyen* Monodisperse carbon nanopearls in a foam-like arrangement: a new carbon nano-compound for cold cathodes Thin solid Films 2004, 464, 308.

[16]. *Ni.Y. Shao, M.Y. Tong, G. Qian, X. Wei*, Preparation of hollow carbon nanospheres at low temperature via new reaction route. Journal of solid state chemistry; 2005, 178, 908

ATOMIC AND ELECTRONIC STRUCTURE OF THE STABLE $Ge_2Sb_2Te_5$ COMPOUND

S. ÖZKAYA[1], Ç. KADEROĞLU[2], M. ÇAKMAK[3], B. ALKAN[2]

[1] *Department of Physics, Aksaray University, 68100 Aksaray, Turkey*

[2] *Department of Engineering Physics, Faculty of Engineering, Ankara University, 06100 Ankara, Turkey*

[3] *Department of Physics, Gazi University, 06500 Ankara, Turkey*

Ab initio calculations, based on pseudopotentials and density functional theory, have been performed to investigate the atomic and electronic structure of the $Ge_2Sb_2Te_5$ compound. Two different possible models have been considered: (i) model I (atomic arrangement of Te–Sb–Te–Ge–Te–Te–Ge–Te–Sb–) and (ii) model II (atomic arrangement of Te–Ge–Te–Sb–Te–Te–Sb–Te–Ge–). From total energy calculations, it has been found that the model II is energetically favorable than the other model. The electronic band structure calculations for model II showed that the system exhibits a semiconductor character. The bonding charecter of the system is also been examined. Our results are seen to be in agreement with the other theoretical and experimental datas.

I. INTRODUCTION

Phase-change materials based on the ternary $(GeTe)_m(Sb_2Te_3)_n$ (GST) compounds play crucial roles in re-writable optical memories [re-writable compact disks (CD-RW), digital versatile disks random memory (DVD-RAM) and blue-ray disks (BDs)] [1,2]. Recording information in optical memories is achieved by using the reversible phase transition between the amorphous and crystalline phases of GST compounds. Success of technologic applications depends on the understanding of atomic and electronic properties of the GST phases. Among GST compounds $Ge_2Sb_2Te_5$ exhibits the best performance when used in DVD-RAM [3]. Therefore, recently, there has been a considerable interest in crystallization behavior of $Ge_2Sb_2Te_5$ compound. Based on x-ray diffraction (XRD) studies, Yamada *et al.* [4] and Nonaka *et al*. [5] reported that $Ge_2Sb_2Te_5$ has a metastable rocksalt structure below 300 °C. For the stable hexagonal structure (space group of $P\bar{3}m1$) observed at high temperatures, Petrov et al. [6] proposed an atomic model. In this model, the atomic stacking sequence of the atoms are Te-Sb-Te-Ge-Te-Te-Ge-Te-Sb- . On the other hand, Kooi and De Hosson [7] using XRD suggested that a stacking sequence with Sb and Ge atoms exchange their positions in model I. Matsunaga and co-workers [8] also reported that Sb and Ge atoms occupy randomly the same layer.

In spite of a large number of the experimental and theoretical studies focused on this subject, the transformation mechanism is not fully understood. Motivated by this reality, in this report, we have investigated the atomic geometry, electronic band structure, and chemical bonding of $Ge_2Sb_2Te_5$ stable compound by using the first principles pseudopotential method.

II. METHOD

All the calculations have been carried out using the Vienna *ab initio* simulation package (VASP) [9-12] based on the density functional theory (DFT). Within this method, the Kohn-Sham single particle functions were expanded in a basis of plane waves up to cut-of energy of 33 Ry. The electron-ion interactions were described by using the projector augmented-wave (PAW) method [11, 12]. For electron exchange and correlation terms, Perdew and Zunger-type functional [13, 14] was used within the generalized gradient approximation (GGA) [12] including non-linear core correction. Self-consistent solutions were obtained by employing the (6x6x6) Monkhorst-Pack [15] grid of k-points for the integration over the Brillouin Zone.

III. RESULTS AND DISCUSSION

We have performed calculations containing two possible models (model I and model II) for the atomic arrangement of the $Ge_2Sb_2Te_5$ compound.

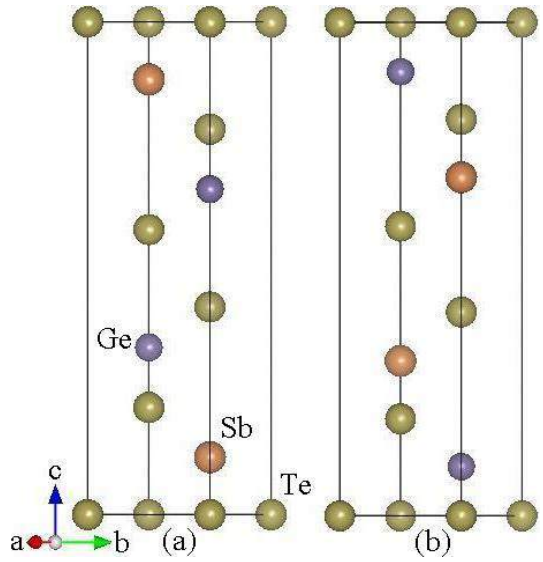

Fig.1. Schematic side views of $Ge_2Sb_2Te_5$ compound for (a) model I and (b) model II.

The optimum arrangement of the $Ge_2Sb_2Te_5$ compound has been given in Fig 1. and some of the key structural parameters have been tabulated in Table I. It is seen that the model II is energetically favorable than the other model. By examining closely the structural properties of the $Ge_2Sb_2Te_5$ for the model II we have found that the lattice parameters are a= 4.27 Å and c=17.31 Å. As it is seen from Table I, Te-Ge bond lengths are 3.01 and 2.98 Å, Te-Sb bond lengths are 3.20 and 3.00 Å, and Te-Te bond length is 3.89 Å, which are very close to the expermental and other theoretical results.

Table 1. The calculated atomic key parameters (in Å) and the relative energies for the models shown in Fig. 1.

		a_0(Å)	c_0(Å)	Te-Ge bond length (Å)	Te-Sb bond length (Å)	Te-Te bond length (Å)	ΔE (eV)
This study	Model I	4.26	17.12	3.23 2.83	3.17 3.00	3.65	0.18
	Model II	4.27	17.31	3.01 2.98	3.20 3.00	3.89	0.00
Other studies	----	4.22[a] 4.26[c] 4.25[d]	17.24[a] 17.71[c] 17.27[d]	3.15 2.83[b] 3.23 2.87[c]	3.30 2.97[c]		

[a]Experiment in Ref [7]
[b]Experiment in Ref [18]
[c]Theory in Ref [2]
[d]Theory in Ref [6]

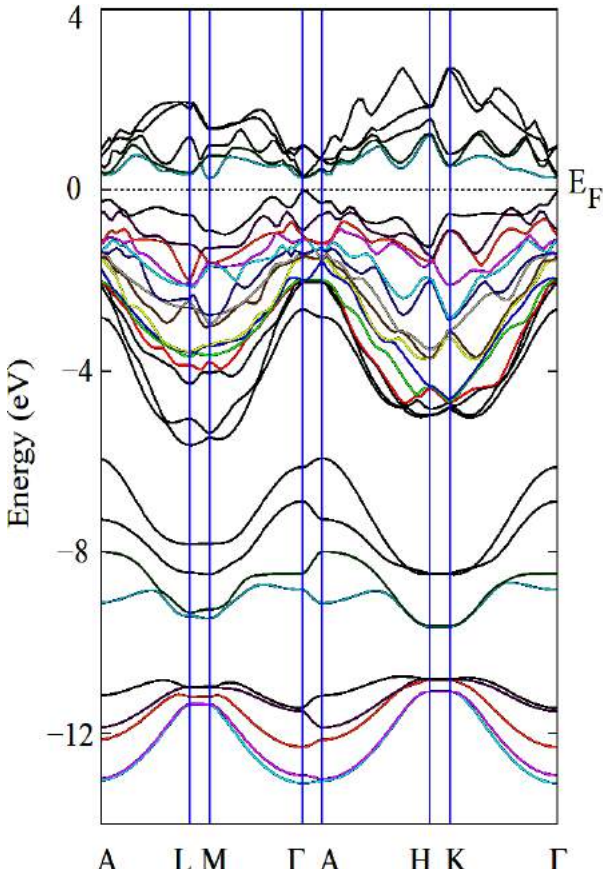

Fig2. Electronic band structure of $Ge_2Sb_2Te_5$ compound for model II.

We have calculated the band structure of $Ge_2Sb_2Te_5$ compound given in Fig 2. It can be seen from Fig 2. that this system exhibits a semiconductor character with a band gap of about 0.25 eV. The same structure has also been studied by Lee and Hoon Jhi [16] on a theoretical basis using pseudopotential method. They have calculated the band gap as 0.26 eV, while experimental band gap is 0.5 eV [17]. This discrepancy for the band gap results mainly from the DFT and also partly due to the choice of pseudopotential.

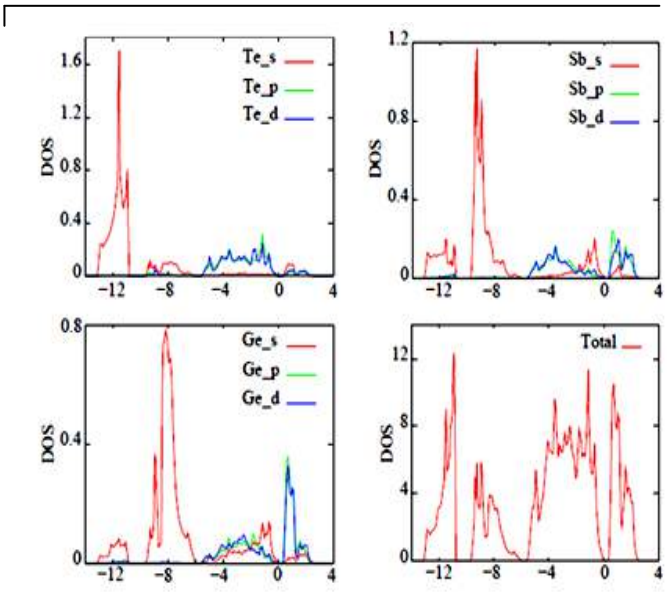

Fig 3. The calculated PDOS and total DOS of $Ge_2Sb_2Te_5$ compound for model II.

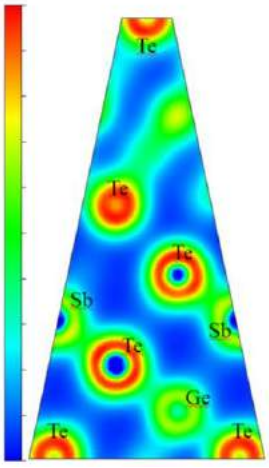

Fig. 4. Electronic charge density contour plot of $Ge_2Sb_2Te_5$ compound for model II.

We have also depicted total density of states (DOS) and projected density of states (PDOS) for Te (between the Sb and Ge layers), Ge, and Sb atoms. While the lowest

energy levels are dominantly contributed by Te 5s orbital, in the energy range between about -8 and -10 eV, 4s orbital of Ge and Sb atoms are essentially dominated. From -5 eV to Fermi level which is at 0 eV, 5p orbital of Te and 4p orbital of Ge and Sb atoms contribute to these energy levels. These results show that there is covalent bondig between the Ge–Te and Sb–Te atoms. On the other hand d core levels of Te, Ge, and Sb atoms have a similar behavior with the p levels. Conduction bands almost completely consists of the empty Ge 4p and Sb 5p states with a very little Te 5p states.

To visualize the bonding character of the model II, we have depicted the charge density distributions in (111) plane (distance from origin 2.72 Å). As seen from Fig.4, there is an increase of the electron density around the Te atoms, reveals that the Ge–Te and Sb–Te bonds are polar with some degree of polarity towards the Te atom. This is caused by a large degree of covalency plus some ionic character, giving rise to a shift in the charge-density peak towards the more electronegative Te atom.

IV. SUMMARY

We have studied the atomic geometry, electronic states, and chemical bondings on the $Ge_2Sb_2Te_5$ with various models; (i) model I (atomic arrangement of Te-Sb-Te-Ge-Te-Te-Ge-Te-Sb-), (ii) model II (atomic arrangement of Te-Ge-Te-Sb-Te-Te-Sb-Te-Ge-). We have found that the energy difference between these two models is 0.18 eV. By calculating the electronic band structure for the model II, we have identified the system exhibits semiconductor character. The Ge–Te and Sb–Te bonds have also strong covalent and some ionic charecter.

[1]. *M. Wuttig, N. Yamada,* Nature Mater. 6, (2007), 824.

[2]. *Z. Sun J. Zhou, R. Ahuja,* Phys. Rev. Lett. 96, (2006), 055507.

[3]. *N. Yamada, E. Ohno, K. Nishiuchi, N. Akahira, and M. Takao,* J. Appl. Phys. 69, (1991), 2849.

[4]. *T. Nonaka, G. Ohbayashi, Y. Toriumi, Y. Mori, and H. Hashimoto,* Thin Solid Films 370, (2000), 258.

[5]. *I. I. Petrov, R. M. Imamov, and Z. G. Pinsker*, Sov. Phys. Crystallogr. 13, (1968), 339.

[6]. *B. J. J. Kooi and T. M. De Hosson,* J. Appl. Phys. 92, (2002), 3584.

[7]. *T. Matsunaga, N. Yamada, and Y. Kabota,* Acta Crystallogr. Sect. B 60, (2004), 685.

[8]. *G. Kresse and J. Hafner*, Phys. Rev. B 47, (1993), 558, ibid. 49, (1994), 14251.

[9]. *G. Kresse and J. Furthmüller*, Comp. Mat. Sci. 6, (1996), 15.

[10]. *G. Kresse and D. Joubert*, Phys. Rev. B 59, (1999), 1758.

[11]. *G. Kresse and J. FurthmÄuller*, Phys. Rev. B 54, (1996), 11169.

[12]. *P. E. Blchl,* Phys. Rev. B 50, (1994), 17953.

[13]. *J. P. Perdew and A. Zunger,* Phys. Rev. B 23, (1981), 5048.

[14]. *J. P. Perdew, J. A. Chevary, S. H. Vosko, K.A.Jackson, M. R. Pederson, D. J. Singh, and C. Fiolhais,* Phys. Rev. B 46, (1992), 6671.

[15]. *H. Monkhorst, J. Pack*, Phys. Rev. B 13, (1976), 5188.

[16]. *G. Lee and S.-Hoon Jhi* Phys. Rev. B 77, (2008), 153201

[17]. *T. Kato, K. Tanaka,* Japan. J. Appl. Phys. 44, (2005), 7340.

[18]. *A.V.Kolobov, P.Fons, J.Tominaga, A.I.Frenkel, A.L.Ankudinov,S.N.Yannopoulos, K.S.Andrikopoulos*, and T. Uruga, Jpn. J. Appl. Phys., Part 1, 44, (2005), 3345.

ENERGY SPECTRUM OF CARRIERS IN KANE-TYPE SEMICONDUCTORS IN MAGNETIC FIELD OF CONSTANT DIRECTION WITH TRIGONOMETRIC DEPENDING VARIATION PERPENDICULAR TO THE FIELD

A.M. BABANLI[1,2], V. HÜNER[2]

1 Institute of Physics, Azerbaijan Academy of Sciences, 370143, Baku

2 Department of Physics, University of Suleyman Demirel, Isparta 32260, Turkey

arifb@fef.sdu.edu.tr and vildan-hurriyet@hotmail.com

We present compact analytical solutions for the energy spectrum and wave functions of carriers in two-dimensional Kane type semiconductors in a magnetic field *B* of constant direction with trigonometric depending variation perpendicular to the field direction.

1. INTRODUCTION

Recent experimental techniques have opened up the way to experiments in inhomogeneous magnetic fields with periods in the nanometer region [1]. This kind of field has been realized with the fabrication of magnetic dots, patterning of ferromagnetic materials, and deposition of superconducting materials on conventional heterostructures. Increased interest in studying a two-dimensional electron gas subjected to inhomogeneous magnetic fields is mainly caused by the special tunneling and kinetic properties of magnetic structures. In contrast with tunneling through electric barriers, the tunneling probability of the magnetic structures depends not only on the electron momentum perpendicular to the tunneling barrier but also on its momentum parallel to the barrier[2]

The realization of stable single-layer carbon crystals graphene triggered an explosion of interest in this material because of its unique electronic properties for reviews see, [3-5] making it a promising candidate for designing one-chip nanoelectronic devices [4] and [6–9]. However, Klein tunneling [10] hinders the application of traditional methods of current control, on-off switching, changing the current direction, etc. by tuning the voltage between various elements of a device [11]. This effect also complicates the creation of localized electron-hole states in graphene.

Exact analytical solutions for the bound states of a graphene Dirac electron in various magnetic fields with translational symmetry were obtained in [12].

In this study, using a three-band Kane model including the conduction band, light and spin-orbital hole bands, the energy spectrum of carriers are calculated in the 2D semiconductors in a magnetic field *B* of constant direction with trigonometric depending variation perpendicular to the field.

In the three-band Kane's Hamiltonian the valence and conduction bands interaction is taken into account via the only matrix element *P* (so-called Kane's parameter). We also neglect the free-electron term in the diagonal part and the Pauli spin term as they give small contributions to the effective mass and the spin *g*-value of electrons in InSb. The system of 2D Kane equations including the nondispersional heavy hole bands have the form [13]

$$-E\psi_1 - \frac{Pk_+}{\sqrt{2}}\psi_3 + \frac{Pk_-}{\sqrt{6}}\psi_5 + \frac{Pk_-}{\sqrt{3}}\psi_8 = 0 \quad (1)$$

$$-E\psi_2 - \frac{Pk_+}{\sqrt{6}}\psi_4 + \frac{Pk_-}{\sqrt{2}}\psi_6 - \frac{Pk_+}{\sqrt{3}}\psi_7 = 0 \quad (2)$$

$$-\frac{Pk_-}{\sqrt{2}}\psi_1 - (E+E_g)\psi_3 = 0 \quad (3)$$

$$-\frac{Pk_+}{\sqrt{6}}\psi_2 - (E+E_g)\psi_4 = 0 \quad (4)$$

$$\frac{Pk_+}{\sqrt{6}}\psi_1 - (E+E_g)\psi_5 = 0 \quad (5)$$

$$\frac{Pk_+}{\sqrt{2}}\psi_2 - (E+E_g)\psi_6 = 0 \quad (6)$$

$$-\frac{Pk_=}{\sqrt{3}}\psi_2 - (\Delta+E+E_g)\psi_7 = 0 \quad (7)$$

$$\frac{Pk_+}{\sqrt{3}}\psi_1 - (\Delta+E+E_g)\psi_8 = 0 \quad (8)$$

Here, *P* is the Kane parameter, *E*g - the band gap energy, Δ - the value of spin–orbital splitting and $k\pm = kx \pm iky$, $k = -i\nabla$, ψ_i are envelope functions.

In this paper, I report the completely analytical solution of the Kane equations for a single 2D electron in a magnetic field with shape

$$\vec{B} = \frac{B_0}{\sin^2 \alpha x}\vec{e_z} \quad (9)$$

If for the vector potential the gauge $A = (0, A_y, 0)$, with $A_y = -\frac{B_0}{a}\cot ax$ is chosen and $k\pm$ have the forms

$$k_-k_+ = k_+k_- + 2\frac{eB_0}{\hbar c}\frac{1}{\sin^2 \alpha x} \quad (10)$$

One can now express the envelope functions, $\psi_3, \psi_{4,,,,,}\psi_8$ by the functions ψ_1 and ψ_2, respectively, and substituting them into the first and second equations, we finally obtain the following decoupled equations for $\psi_{1,2}$:

$$[-E+\frac{P^2}{6}(\frac{1}{E+E_g}+\frac{2}{\Delta+E+E_g})k_{\mp}k_{\pm}$$

$$+P^2(\frac{1}{2(E+E_g)})k_{\pm}k_{\mp}]\psi_{1,2}=0 \quad (11)$$

If to seek the solution of equation (11) in the form

$$\psi_{1,2}=e^{i(k_y y)}f_{1,2}(x) \quad (12)$$

We obtained for the function $\psi_{1,2}$ (x) the following equation

$$\frac{\partial^2 f_{1,2}}{\partial x^2}+[-k_y{}^2+2dky\cot\alpha x-$$

$$\frac{1}{\sin^2\alpha x}\left(\mp\frac{d\alpha\Delta}{3E_g+3E+2\Delta}+d^2\right)+$$

$$d^2+\frac{E}{\frac{p^2}{3}\left(\frac{2}{E+E_g}+\frac{1}{\Delta+E+E_g}\right)}]f_{1,2}(x)=0 (13)$$

Where $d=\frac{eB_0}{\hbar c\alpha}$

The corresponding eigenvalues

$$\frac{3E(E+E_g)(\Delta+E+E_g)}{(2\Delta+3E+3E_g)\varepsilon_p}\frac{2m_0}{\hbar^2}=d^2+k^2+$$

$$\alpha^2A^2-A^{-2}d^2k^2\alpha^{-2} \quad (14)$$

where

$$A=\left(n-\frac{1}{2}+\frac{1}{2}\sqrt{1+4\left(\mp\frac{d\Delta}{\alpha(3E_g+3E+2\Delta)}+\frac{d^2}{\alpha^2}\right)}\right)$$

$\varepsilon_p=\frac{2m_0}{\hbar^2}P^2$ is the energetic Kane parameter Equation (14) is used to determine the energy spectrum of carriers in Kane type semiconductors at inhomogeneous magnetic field. Equation (14) can be useful for analyzing the influence of nonparabolicity on the energy spectrum of carriers in the 2D semiconductors in a magnetic field *B* of constant direction with trigonometric depending variation perpendicular to the field. The energy spectrum corresponding to Eq. (14) for different quantum number n is illustrated in Fig. 1

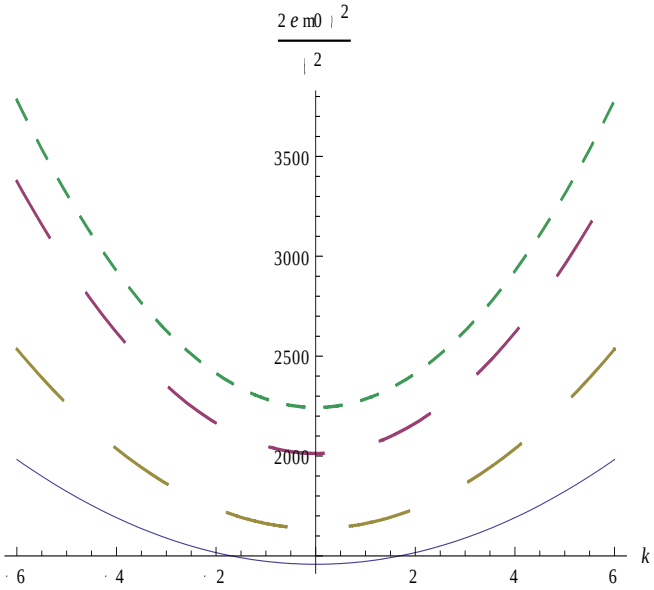

Fig1. Energy spectrum of electrons as a function of wave number k for InSb.

Effective g-factor is calculated from the Zeeman split of subbands:

$$g=\frac{E\uparrow -E\downarrow}{\mu_B B}$$

where $E\uparrow$ and $E\downarrow$ are the energy spectrum of electron for spin +z- and z-directions, respectively.

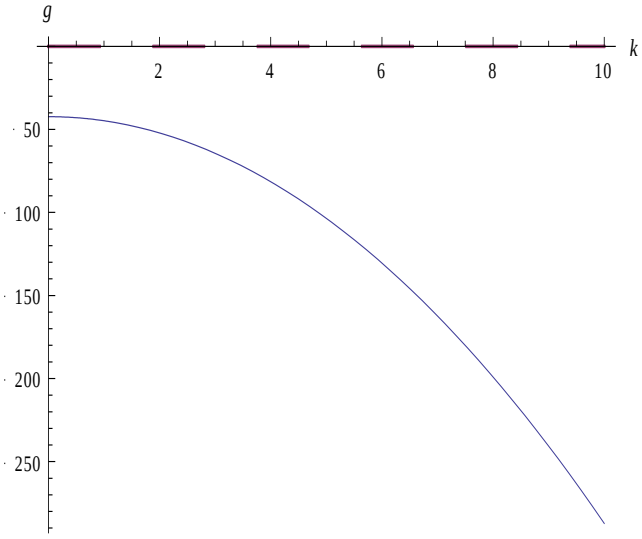

Fig. 2. Wave vector dependence of the ground state g-factor for the electron.

In Fig. 2 shows the wave vector dependence of the ground state g-factor for the electron, calculated by Eq. (14) for 2D InSb-type semiconductors for the fixed magnetic field. It has been seen that the effective g-value of the electrons are decreased with increasing wave vector.

2. CONCLUSION

In this study using the three band Kane's model the energy spectrum of carriers and local effective *g*-factor of electrons are calculated in the 2D semiconductors in a magnetic field *B* of constant direction with trigonometric depending variation perpendicular to the field.

[1]. *P.D. Ye, D. Weiss, R.R. Gerhardts, M. Seeger, K.von Klitzing, K. Eberl, and H. Nickel*, Phys. Rev. Lett. 74, 3013, 1995

[2]. *Matulis, F.M. Peeters, and P. Vasilopoulos*, Phys. Rev. Lett. 72, 1518 ,1992.

[3]. *H. Castro Neto, F. Guinea, N. M. R. Peres, K. S. Novoselov, and A. K. Geim,* Rev. Mod. Phys. 81, 109 2009

[4]. *K. Geim and K. S. Novoselov*, Nature Mater. 6, 183 ,2007

[5]. *K. Novoselov, A. K. Geim, S. V. Morozov, D. Jiang, M. I.Katsnelson, I. V. Grigorieva, S. V. Dubonos, and A. A. Firsov*, Nature _London_ 438, 197 ,2005

[6]. *M. I. Katsnelson*, Mater. Today 10, 20 ,2007

[7]. *Trauzettel, D. V. Bulaev, D. Loss, and G.Burkard*, Nat. Phys.3, 192 ,2007

[8]. *Berger, Z. Song, T. Li, Xuebin Li, Asmerom Y. Ogbazghi, Rui Feng, Zhenting Dai, Alexei N.Marchenkov, Edward H. Conrad, Phillip N. First, and Walt A. de Heer*, J. Phys. Chem. B 108, 19912 ,2004

[9]. *Y.-W. Son, M. L. Cohen, and S. G. Louie,* Nature _London_ 444, 347 ,2006

[10]. *O. Klein*, Z. Phys. 53, 157 ,1929

[11]. *M. I. Katsnelson, K. S. Novoselov, and A.K.Geim*, Nat. Phys. 2, 620 ,2006

[12]. *Ş.Kuru, J. Negro and L M Nieto*, Phys. Rev. 21, 455305, (2009).

[13]. *F. M. Hashimzade, A. M. Babayev, and B. H.Mehdiyev* Phys.Rev B 73, 245321 ,2006

XRD AND UV-VIS RESULTS OF TUNGSTEN OXIDE THIN FILMS PREPARED BY CHEMICAL BATH DEPOSITION

S.M. KARADENİZ[1], F.N. TUZLUCA[1], A.E EKİNCİ[1], M.ERTUĞRUL[2], T.KILINÇ[1]

[1]*Erzincan University, Department of Physics,*
Erzincan, TURKEY,
morkocsibel@gmail.com
[2]*Ataturk University, Department of Electrical and Electronics Engineering,*
Erzurum, TURKEY,

In the experiment, using a simple, economical, chemical bath method for depositing tungsten oxide films, Electrochromic tungsten oxide thin films were prepared from an aqueous solution of $Na_2WO_4.2H_2O$ and diethyl sulfate at boiling temperature on ITO coated glass substrate. The techniques such as X-ray and UV-VIS-spectroscopy diffraction were used for the characterization of the films. According to the results of X-ray and UV- Vis , WOx thin film is very promising material for electrochromic applications and this is simply and economically produced by chemical bath method.

1. INTRODUCTION

Over the last two decades there has been a progressive interest in fabrication of thin solid films of electrochromic materials, and electrochromic windows are the most popular area of switching technology [1]. The smart windows are fabricated with five (or less) films—coatings consisting of: two transparent conductors (TC), electrolyte or ion conductor (IC), counter electrode (CE) and electrochromic film (EF): glass/TC/ion storage/ IC/ EF/ TC/glass [1]. The most promising substance obtained from electrochromic materials is tungsten oxide [2]. The optical, electronic and structural properties of WOx materials have been widely studied in literature, being related to its practical applications and very recently technological achievements have been reported [3].

To date continuous air pollution monitoring using gas sensors is of great interest, taking into consideration the environmental problems created by exhaust gases producedby fossil fuels using factories and automobiles. Many kinds of gas sensors are used for the detection of gases including metal oxide semiconductors (MOS) [4], polymers [5], and solid electrolytes [6]. However the metal oxide semiconductorsbased sensors are preferred because of their low cost, high sensitivity, fast response, and good long-term stability. Over the time WO3 proved to be an attractive material for a MOS gas sensor, which was used to detect various gases such as NO2 [7], H2S [8], and NH3 [9]. WO3 is an n-type semiconductor which has been studiedwidely because of its possible application as ferroelectric [10], or catalyst material [11], in smart electrochromic windows [12], in optical devices [13], and in gas sensors [14–16].

Various techniques have been developed for preparation of thin electrochromic films of tungsten oxide such as thermal evaporation [17], sputtering [18] , chemical vapor deposition [19], spray deposition [20], sol–gel deposition [21] etc. The chemical bath methods have the benefit of being easily realizable from the point of view of industrialization, especially on large area devices, with the required electrochromic properties [1] and this method enables faster and easy preparation of thin films [2].

2. MATERIAL AND METHODS

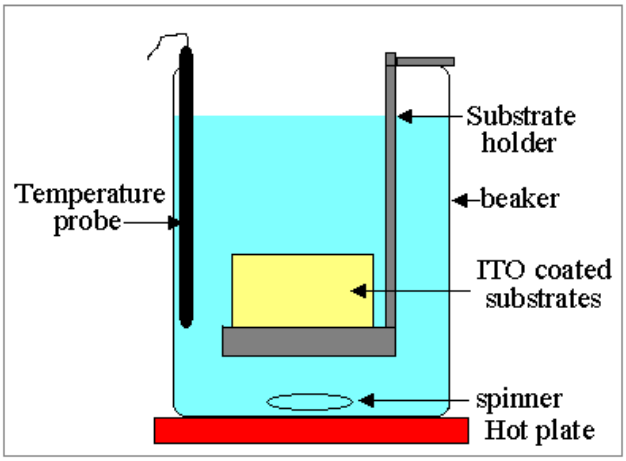

Fig. 1. Chemical Bath Deposition System

Chemical Bath deposition technique is essentially the same film processing technique as the so-called CBD technique, in which a substrate are immersed on the heated solution to be deposited as a film. The schematic representation of the CBD apparatus is shown in Fig. 1.

In the experiment, ITO coated glasses for the deposition of the tungsten oxide films were used as substrate. For the preparation of about 90mL of the bath solution 1.65 g of $Na_2WO_4{\cdot}2H_2O$ was dissolved in 90 mL of deionized water. In the prepared stock solution, 3mL of diethyl sulfate was added. After stirring solution, the bath solution was prepared for film deposition. Before immersing substrates in bath solution, ITO coated glasses were cleaned with acetone, methanol and then were placed in ultrasonic cleaner for several minutes. After cleaning substrates, one substrate was immersed in the chemical bath solution. The bath solution was then placed on a heating plate and heated to boiling temperature with continuous stirring. The deposition time was 10 min. Used substrates for the deposition of tungsten oxide films could be cleaned by immersing them into aqueous solution of sodium hydroxide for a couple of minutes [1].

The deposition thin film was analyzed by X-ray Diffraction İnstrument and UV-Vis Spectroscopy.The overall chemical reaction of the deposition process may be written as:

$$(CH_3O)_2SO_2(aq)+ Na_2WO_4(aq)+ H_2O(l) \rightarrow WOx(s)+ 2CH_3OH(aq)+ Na_2SO_4(aq)$$

The reaction rate is controlled by the pH value. The H3O+ concentration depends on the reaction rate of the following reaction:

$$(CH_3O)_2SO_2(aq)+2H_2O(l)\rightarrow \rightarrow 2CH_3OH(aq)+H_3O^+(aq)+SO_4^{-2}(aq)$$

During this reaction dimethyl sulphate undergoes hydrolysis by increase of $H_3O^+(aq)$ concentration and pH decrease. The process is highly dependent on temperature and its increased value provides favorable increase of solubility of dimethyl sulfate. Tungstic acid is slightly soluble in water and with increase of the concentration of $H_3O^+(aq)$ at elevated temperature precipitates as WOx:

$$2H_3O^+(aq)+ WO_4^{-2}(aq)\rightarrow WOx(s)+ 3H_2O(aq)$$

Most of the synthesised WOx(s) in the bath is precipitated and just a small part is a part of the thin solid film[1-2].

3. RESULTS AND DISCUSSION

The structural and optical properties were performed by XRD and UV-Vis analysis. In order to get an X-Ray Diffraction pattern, an X-Ray tube that emits only Cu Ka X-ray by absorbing Ka X-ray by an absorber was used. The wavelength of the Cu Ka X-ray is 1.54 Å. X- Ray Diffraction pattern of as–deposited CdS thin film is shown on figure 2. d values of a tungsten oxide thin film are shown in Table 1.

The *d* experimental values can be calculated using the Bragg's equation:

$$n\lambda=2d\sin\theta \quad (1)$$

The calculated d values can be compared to the ones given in the literature that are listed in Table 1. At device operation conditions, it is possible to have different polymorphs such as monoclinic (>17–330 ◦C), orthorhombic (330–740 ◦C) and tetragonal (>740 ◦C) WO_3 [22-24] Tungsten oxide is the most investigated and used material for electrochromic device in which coloration and bleaching can be reversibly obtained by an electrochemicalprocess.

Although the WO_3 coloration mechanism has been intensely studied in the last 30 years, no complete information is yet available. The comparison shows that the thin film results do not correspond to any of the given d values of tungsten oxides at table 1. So, the exact stoichiometric relation between the tungsten and the oxygen atoms is not yet known and the tungsten oxide film will be denoted as WO*x* [1-2].

Where *n* is the order of diffraction , λ is the wavelength of the incident X-rays, *d* is the distance between planes parallel to the axis of the incident beam and θ is the angle of incidence relative to the planes in question. The lattice spacing *d* was found and from (hkl) planes, lattice parameters of the unit cell *a,c* were calculated according to the relation [25],

$$1/d^2=4(h^2+hk+k^2)/3a^2+l^2/c^2 \quad (2)$$

The Grain size *D* is calculated using the equation known as Scherrer Formula [26],

$$D=0.94\lambda/\beta\chi o\sigma\theta \quad (3)$$

β is the Full Width of Half Maximum (FWHM) of the diffraction peak measuremend in radians. İts calculated value is 0.00532 in radians. 0.94 is the Scherer's constant [26], λ is a wavelength of the X-ray used and θ is the Bragg angle for (002) plane. According to Scherrer Formula, Average value of grain size is calculated 30 nm.

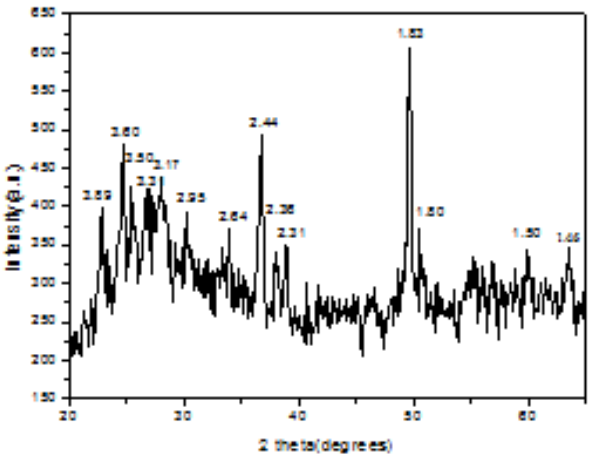

Fig. 2. XRD result of WOx film

Table 1.Literature d values in angstroms for various tungsten oxides. The values that are identical with experimental d values for the tungsten oxide film are marked with gray backgrounds.

WO_3	1.92	3.1	2.66	2.69	2.63	3.69	3.85	3.75
WO_3	2.63	2.64	2.66	2.67	1.83	3.76	3.84	3.65
WO_3	1.18	1.26	1.68	1.86	1.53	1.66	2.7	3.7
$WO_3.H_2O$	1.74	1.85	2.69	2.63	1.84	2.57	5.38	3.49
$WO_3.2H_2O$	2.07	2.51	3.37	2.58	1.94	3.21	6.8	3.67
$H_2WO_4.H_2O$	2.46	2.54	2.63	1.96	3.46	3.27	6.95	3.73
$H_2WO_4.H_2O$	2.63	2.65	3.47	3.7	3.77	6.96	3.26	3.31
WO_2	2.45	1.55	1.7	2.39	2.44	1.72	2.42	3.45
$WO_{2.9}$	2.02	3.1	1.88	2.2	1.53	1.67	2.65	3.74
$W_{18}O_{49}$	2.62	3.39	3.73	2.65	3.44	3.63	1.89	3.78
$W_{20}O_{58}$	1.7	1.88	2.62	3.64	1.55	2.21	2.73	3.77
W_{3O}	0.92	1.1	0.89	0.93	0.82	1.34	2.06	2.25

The optical spectrum of the thin film was recorded by UV-Vis Spectroscopy (Perlin-Elmer) in visible area. The optical transmittance spectrum in the range from 400 to 1200 nm for WO_x thin film is presented in figure 3. For ITO coated glass substrate, Uv-Vis result shows that transmittance increases wavelength range 400 -1200 nm. The spectrum shows that the difference in the transmittance values between 650–1200 nm is around 30%.

4. CONCLUSION

Tungsten oxide thin film prepared by the chemical bath deposition method exhibits pleasant electrochromic properties. X-ray result shows that the film is WO_x. The result of UV-Vis leads that transmittance of the film is around 30% between 650-1200 nm.

According to results, WOx thin film is very promising material for electrochromic applications and this is simply and economically produced by chemical bath method.

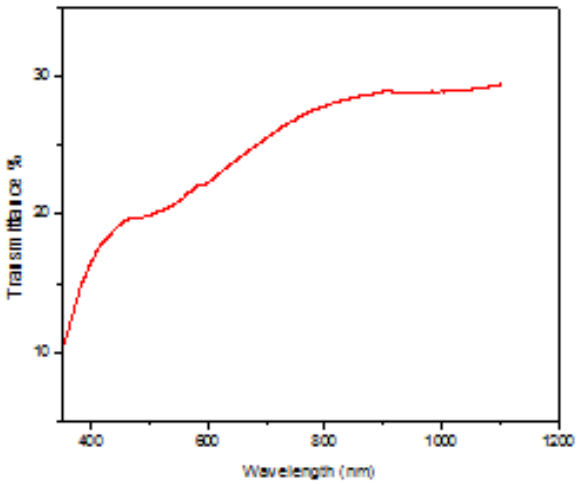

Fig. 3. UV-VIS result of WOx film

[1]. *Metodija Z. Najdoski, Toni Todorovski*, Materials Chemistry and Physics 104 (2007) 483–487

[2]. *Toni Todorovski, Metodija Najdoski*, Materials Research Bulletin 42 (2007) 2025–2031

[3]. *Jesu´ s M. Ortega, Arturo I. Martı´nez, Dwight R. Acosta, Carlos R. Magan˜*, A Solar Energy Materials & Solar Cells 90 (2006) 2471–2479

[4]. *A.M. Ruiz, G. Sakai, A. Cornet, K. Shimanoe, J.R. Morante, N. Yamazoe*, Sens. Actuators, B, Chem. 103 (2004) 312.

[5]. *H. Xie, Q. Yang, X. Sun, J. Yang, Y. Huang*, Sens. Actuators, B, Chem. 113 (2006) 887.

[6]. *I. Hasegawa, S. Tamura, N. Imanaka*, Sens. Actuators, B, Chem. 108 (2005) 314.

[7]. *L.G. Teoh, Y.M. Hon, J. Shieh, W.H. Lai, M.H.Hon*, Sens. Actuators, B, Chem. 96 (2003) 219.

[8]. *R. Ionescu, A. Hoel, C.G. Granqvist, E.Llobet, P. Heszler*, Sens. Actuators, B, Chem.] 104 (2005) 124.

[9]. *X.Wang, N. Miura, N. Yamazoe*, Sens. Actuators, B, Chem. 66 (2000) 74.

[10]. *P.M.Woodward, A.M. Sleight, T. Vogt*, J. Solid State Chem. 131 (1997) 9.

[11]. *W. Sun, L. Xu, Y. Chu, W. Shi*, J. Colloid Interface Sci. 266 (2003) 99.

[12]. *H.N. Cui, F.M. Costa, V. Teixeira, I.Porqueras, E. Bertran*, Surf. Sci. 532–535 (2003) 1127.

[13]. *M.A. Pérez, M. López Teijelo,* Thin Solid Films 449 (2004) 138.

[14]. *X. He, J. Li, X. Gao, L. Wang*, Sens. Actuators, B, Chem. 93 (2003) 463.

[15]. *A. Hoel, L.F. Reyes, S. Saukko, P. Heszler, V. Lantto, C.G. Granqvist*, Sens. Actuators, B, Chem. 105 (2005) 283.

[16]. *H. Kawasaki, T. Ueda, Y. Suda, T. Ohshima*, Sens. Actuators, B, Chem. 100 (2004) 266

[17]. *O. Bohnke, C. Bohnke, G. Robert*, Solid State Ion. 6 (1982) 121.

[18]. *T. Nanba, T. Takahashi, J. Takada, A. Osaka, Y.Miura, I. Yasui, A. Kishimoto, T. Kuda*, J. Non-Cryst. Solids 178 (1994) 233.

[19]. *D. Davazoglou, A. Donnadieu*, Sol. Energy Mater. 71 (1988) 379.

[20]. *Alexandru Enesca, Cristina Enache, Anca Duta*, Joop Schoonman, Journal of the European Ceramic Society 26 (2006) 571–576

[21]. *A. Patra, K. Auddy, D. Ganguli, J. Livage, P.K.Biswas*, Materials Letters 58 (2004) 1059– 1063.

[22]. *Jayatissa, A. H., Cheng, S. T. and Gupta, T.*, Mat. Sci. End. B, 2004, 1–7.

[23]. *Balazsi, C., Jahnke, M. F., Kotsis, I., Petras, L. and Pfeifer, J.*, Solid State Ionics, 2001, 141–142, 411–416.

[24]. *Patil, P. S., Nikam, S. B. and Kadam, L. D.*, Mater. Chem.Phys., 2001, 69, 77–83.

[25]. *B.D.Cullity*, Elements of X-Ray Diffraction, Addison-Wesley Publishing Company 1978, p.555.

[26]. *H.H. Afify, S.A. Nasser, S.E. Demian*, J.Material .Sci.: Mater. Elect. 2(1991)152-156

SYNTHESIS AND X-RAY CRYSTAL STRUCTURE ANALYSIS OF $C_6H_4(OH)_2$

S. ÖZTÜRK YILDIRIM [1], V. MCKEE [2]

[1]Physics Department, Faculty of Sciences, University,
38039 Kayseri, Turkey,
ozturk@erciyes.edu.tr
[2]Departmentof Chemistry, Loughborough University,
Leicestershire LE11 3TU England

$C_6H_4(OH)_2$ was synthesized and characterized by elemental analysis and IR spectroscopy. The crystal and molecular structure of the title compound was determined from single-crystal X-ray diffraction data. It crystalizes in the monoclinic space group P21/n (No. 14), with a = 3.790(4)Å, b = 5.988(6)Å, c = 10.835(11)Å and β = 90.544(2)°. The quinol has two hydrogen-bond donors and molecules lie on inversion centres.

1. INTRODUCTION

The creation Hydroquinone (quinol) also benzene-1,4-diol, is an aromatic organic compound which is a type of phenol, having the chemical formula C6H4(OH)2. Its chemical structure has two hydroxyl groups bonded to a benzene ring in a para position. Hydroquinone is commonly used as a biomarker for benzene exposure. The presence of hydroquinone in normal individuals stems mainly from direct dietary ingestion, catabolism of tyrosine and other substrates by gut bacteria, ingestion of arbutin containing foods, cigarette smoking, and the use of some over-the-counter medicines.

Hydroquinone is a white granular solid at room temperature and pressure. The hydroxyl groups of hydroquinone are quite weakly acidic. Hydroquinone can lose an H+ from one of the hydroxyls to form a monophenolate ion or lose an H+ from both to form a diphenolate ion. Hydroquinone has a variety of uses principally associated with its action as a reducing agent which is soluble in water. It is a major component in most photographic developers where, with the compound Metol, it reduces silver halides to elemental silver. In this study, hydroquinone was synthesized and its crystal structure was determined by single-crystal X-ray diffraction.

2. EXPERIMENTAL MATERIAL

All starting compounds and solvents for synthesis were purchased from Across, Aldrich, Sigma and E. Merck. Solvents and all reagents were technical grade and were purified and dried by distillation from appropriate desiccant when necessary. Concentration of solutions after reactions and extractions were achieved using a rotary evaporator at reduced pressure.

Analytical and preparative thin layer chromatography (TLC) was performed on silica gel HF-254 (Merck).

Column chromatography was carried out by using 70–230 mesh silica gel (0.063–0.2 min, Merck).

2.1. METHOD

The structures of the compounds in this study were determined by the instruments mentioned below.

All melting points were measured in sealed tubes using an electrothermal digital melting point apparatus (Gal-lenkamp) and were uncorrected. The investigation of vibrational properties of the b-enaminone was carried out on a Mattson 1000 Model FT-IR Spectrometer within the range of 4000–400 cm-1. The IR sample was prepared as KBr pellet. 1H-NMR, 13C-NMR were recorded on a resolution fourier transform Bruker WH-400 NMR spectrometer with tetramethylsilane as an internal standard. Chemical shifts were reported in ppm relative to the solvent peak. Signals were designated as follows: s, singlet; d, doublet; t, triplet; q, quartet; m, multiplet. Elemental microanalyses of the separated solid chelates for C, H, N, were performed with a Elementar Analysensysteme GmbH vario MICRO CHNS analyser.

2.2. INSTRUMENTATION

Fourier transformed infrared (FT-IR) spectra were recorded as KBr pellets on a Shimadzu 435 spectrophotometer, between 4000 and 400 cm-1. C, H and N analyses were carried out on a Carlo Erba MOD 1106 elemental analyzer. Melting points were determined on a digital melting point instrument (Electrothermal model 9200). Single-crystal X-ray data were collected on an Bruker APEX-II CCD diffractometer using monochromated MoKa radiation at 150(2) K [1]. Semi-empirical absorption corrections were made from equivalents.

The structure was solved by the direct and conventional Fourier methods. Full-matrix least-squares refinement was based on F2 and 37 parameters.

All non-hydrogen atoms were refined anisotropically. The program used for calculations was SHELXL97 [2]. Further details concerning data collection and refinement are given in Table 1.

3. RESULTS AND DISCUSSION

Crystal data and structure refinement details for the title compound are summarized in Table 1. The final atomic coordinates and equivalent isotropic displacement parameters of the nonhydrogen atoms are given in Table 2, bond lengths, bond and torsion angles in Table 3.

Quinol crystallizes in the monoclinic space group P21/n with two formula units per unit cell. The crystal structure consists of one independent half-molecule lie on crystallographic inversion centre. The PLATON view shown in Fig. 1.

The structures were solved by direct methods (SHELXS97) and refined by fullmatrix least squares methods (SHELXL97). Atomic coordinates and anisotropic displacement parameters were refined for all non-H atoms.

Table 1 Single crystal X-ray diffraction data collection and structure refinement details

Formula	$C_6H_4(OH)_2$
Formula weight	100.11
Temperature /K	150(2)
Wavelength λ /Å	0.71073
Crystal system	Monoclinic
Space Group	$P2_1/n$
Crystal size /mm^3	0.04×0.20×0.58
a /Å	3.790(4)
b /Å	5.988(6)
c /Å	10.835(11)
β /°	90.544(16)°
Volume / Å^3	245.9(4)
Z	2
Density (calc.) /g cm^{-1}	1.487
θ ranges for data collection	3.8-28.5
F(000)	116
Absorption coefficient mm^{-1}	0.112
Index ranges	$-5 \le h \le 5$ $-7 \le k \le 8$ $-14 \le l \le 14$
Data collected	1918
Unique data (R_{int})	528 (0.061)
Parameters, restrains	37 , 0
Final R_1, wR_2 (Obs. data)	0.059, 0.163
Goodness of fit on F^2 (S)	1.08
Largest diff peak and hole /e Å^3	0.33, -0.36

Table 2 Final atomic coordinates and equivalent isotropic thermal displacement parameters (U_{eq}) for non-hydrogen atoms $C_6H_4(OH)_2$.

Atom	*x*	*y*	*z*	U_{eq}
O1	0.0887(5)	0.1589(3)	0.41697(14)	0.0283(5)
C1	0.4006(5)	0.3326(4)	0.58544(18)	0.0190(6)
C2	0.2865(5)	0.3212(4)	0.45878(18)	0.0176(6)
C3	0.3913(6)	0.4943(4)	0.37478(18)	0.0179(6)

$U_{eq} = (1/3)\Sigma_i\Sigma_j U_{ij} a_i^* a_j^* (\boldsymbol{a}_i . \boldsymbol{a}_j)$.

Table 3 Bond lengths (Å), bond and torsion angles (°)$C_6H_4(OH)_2$.

O1 -C2	1.306(3)	C2 -C3	1.438(3)
C1 -C3a	1.370(4)	C1 -C2	1.437(3)
O1 -C2-C1	122.2(2)	C2 -C1 -C3a	120.3(2)
O1 -C2-C3	118.56(18)	C1 -C2 -C3	119.2(2)
C1a-C3-C2	120.54(18)		
C3a-C1-C2-C3	-0.4(3)	C3a-C1-C2-O1	179.8(2)
O1 -C2-C3-C1a	-179.8(2)	C2-C1-C3a-C2a	0.5(3)
C1 -C2-C3-C1a	0.4(3)		

Symmetry code : (a) 1-x,1-y,1-z

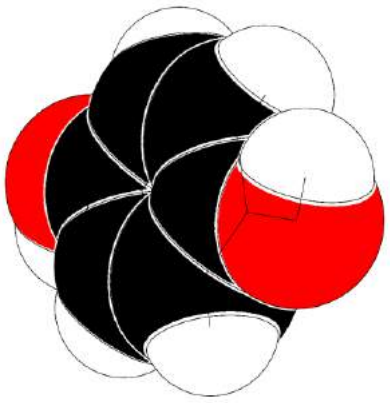

Fig. 1. View of the title compound.

Since difference Fourier syntheses did not clearly show the positions of the other H-atoms, they were placed in calculated positions at a distance of 0.930 Å from the corresponding C-atoms. A riding model was used in the refinement of the calculated H-positions. Isotropic displacement parameters of these H-atoms were taken as 1.2 times the corresponding displacement parameters of the connecting non-H atoms in quinol. The final R and wR, values are 0.059 and 0.163, respectively. The final difference Fourier maps showed max. and min. peaks of 0.33 to -0.36. The structure is shown in Figure 1 (PLATON).

In the title compound, the molecule is essentially planar with a maximum deviation from the mean plane of 0.002(1) Å for atom C2. The bond lengths and angles (I) have normal values, and are comparable with those in the related structures [5], and are in good agreement with those observed in similar compounds.

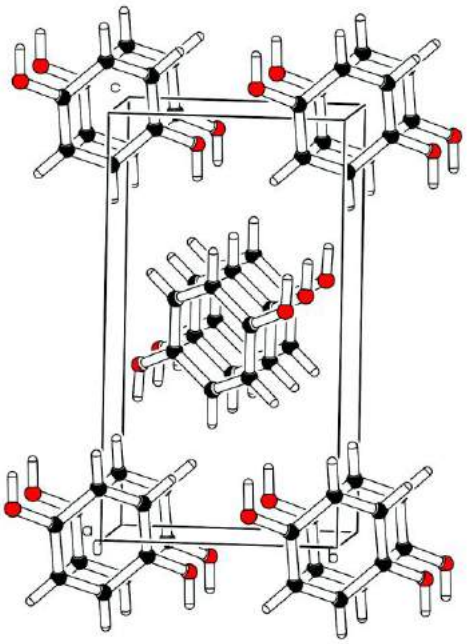

Fig. 2. The packing diagram of the title compound in the unitcell.

Quinol (I) shows a great propensity for forming co-crystals, and it is widely used to stabilize compounds that are susceptible to polymerization. A search of the

Cambridge Structural Database [CSD, Version 5.25; 3] shows that there are 92 co-crystals of quinol with a range of organic compounds. Of all these structures in the CSD, over half contain hydrogen-bond acceptors, e.g. 1,4-dioxane [4].

In the title compound one-dimensional polymeric structure. Intermolecular C — H • • • O [H • • • O = 2.52 Å] hydrogen bond interaction link the polymeric chains into an extended three-dimensional framework {base vectors: [0 1 0], [1 0 0]}. Unit cell content indicating the crystal structure of the molecule is given in Fig. 2.

In summary, the X-ray studies confirm the original structural assignments based on spectroscopic techniques and furthermore yield accurate structural parameters which are useful for future biological and pharmaceutical modeling studies.

[1]. Bruker (2005). APEX2, SAINT and SADABS. Bruker AXS Inc., Madison, Wisconsin, USA.

[2]. *G. M. Sheldrick,* (1997). SHELXS97 and SHELXL97. University of Göttingen, Germany.

[3]. *F. H. Allen and W. D. S. Motherwell,* (2002). Acta Cryst. B58, 407-422.

[4]. *J.C.Barnes, J. D. Paton, and C.S. Blyth,* (1990). Acta Cryst. C46, 1183-1184.

[5]. *F. H.Allen, O.Kennard, , D.G. Watson, L.Brammer, A. G. Orpen and R.Taylor,* (1987). J. Chem. Soc. Perkin Trans. 2, pp. S1–19.

ZrO_2 AND SiO_2 COATINGS OF MINERAL LENSES FOR ANTI-REFLECTION WITH THERMIONIC VACUUM ARC (TVA) TECHNIQUE AND INVESTIGATION OF SOME PHYSICAL PROPERTIES

N. EKEM[1*], Ş. KORKMAZ[1], S. PAT[1], M. Z. BALBAĞ[2], M. ÖZKAN[1], S. TEMEL[1], N. E. ÇETIN[1], M. ÖZMUMCU[1], S. ELMAS[1]

[1]Department of Physics, Eskişehir Osmangazi University, Eskişehir, Turkey

[2]Education Faculty, Eskişehir Osmangazi University, Eskişehir, Turkey

naciekem@yahoo.com

Thin film production method is able to change of properties of thin films. This is a most important parameter.

Lot of thin films production methods are available in literature. Thin films production methods developing for variously aims, continuously. Vacuum and plasma assisted technologies are most popular methods. In this study, a different technique is summarized whose name is Thermionic Vacuum Arc (TVA). TVA is a new type plasma source which generates pure material plasma in literatures and also, it is using for thin films production. Until today, TVA was used for research activity. At first time, TVA was developed for proper materials deposition in optical application. In applications of this research, mineral lenses were coated with anti reflective materials by TVA. Additionally, some physical properties like optical and structural properties were presented.

1. INTRODUCTION

Though procedures of dying of the sun glasses has been realized since century of 15, Primary protective coatings, which were named Anti-Reflection (AR) coatings, have been used with various type systems and methods since 1936 [1]. Nowadays, these coatings have been realized using Thermionic Vacuum Arc (TVA) technique in Plasma Physics Laboratories of Art - Science Faculty of Eskisehir Osmangazi University, Turkey.

Thermionic Vacuum Arc (TVA) is a new and different technology for thin film deposition [2-4]. TVA has been supplied many great advantages to deposited thin films like compact, low roughness, nanostructures, homogeneities, adhesive, high deposition rate, etc [2-4]. A lot of materials were used for thin films production and characterization in this technique. TVA technique gives ability to deposited pure thin films. TVA can ability to growth semiconductor thin films for photovoltaic applications and optoelectronic devices. At shortly, TVA can produce thin films of all solid materials. Additionally, all substrates like organic, mineral, etc. can deposit by TVA. Additionally, multi layer deposition processes are proper by this technique without any impurities on different substrates.

Deposition rate is bigger, and thickness control is available in this technique.

2. EXPERIMENTAL

Thermionic Vacuum Arc (TVA) is an externally heated cathode arc which can be established in high vacuum condition, in vapors of the anode material. The arc is ignited between a heated cathode provided with a wehnelt cylinder and the anode which is a crucible containing the material to be evaporated.

3. RESULTS AND DISCUSSIONS

As application of this study, SiO_2 and ZrO_2 materials are deposited on mineral spectacle lenses. Transmittance, reflectance and reflective index values are shown in figure.2-4.

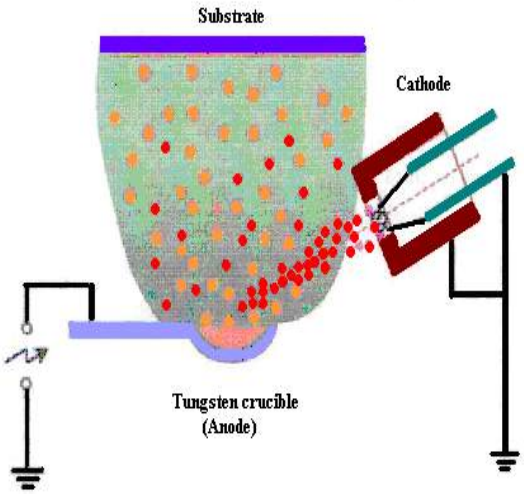

Fig. 1. Schematic representation of TVA's plasma

Transmittance of the SiO_2 and ZrO_2 is low according to undeposited materials. These results are proper with literatures because of mono layer AR coatings are not increased the transparency [5]. Reflectivities of coated samples are low. Refractive index of the coated samples is changing with slowly via wavelengths in visible region because of these coated materials are non dispersive materials. These results are shown in figure 2 and 4.

Multi layer AR caotings can produced by materials of low and high refractive index in order. Aims of this order, refrected waves of the interface surface can be disturbed each other, as a result, interferences are not shown. Finally, transperancy of the deposited materials will be increased in important levels [6,7].

Surface morphologies are very important for optical coatings. Transperancy of materials is affected by surface mophology, strongly. At the same time, adhesion of the upper layer was affected with roughness of the surface. For good adhesion, surface must be homogen rough, but this affected by transperancy. Hence, coated surface is not in lower roughness values.

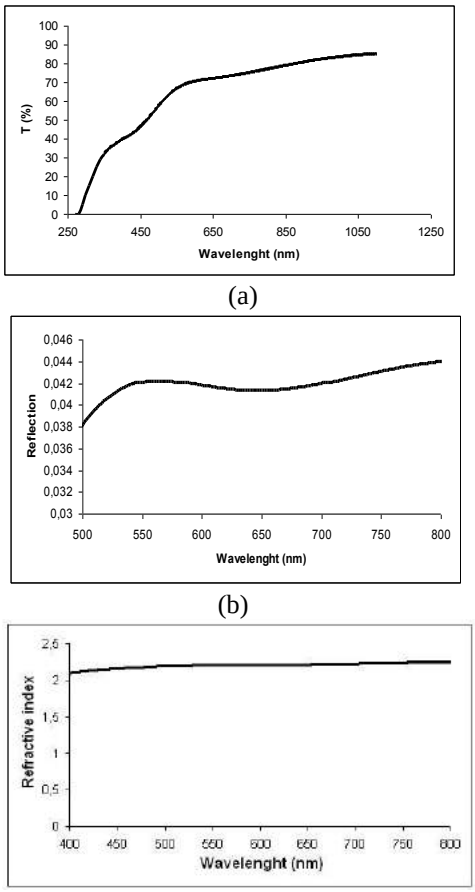

Fig.2. Transmission (a), reflection (b) and refractive index (c) values of the SiO_2 coated lenses

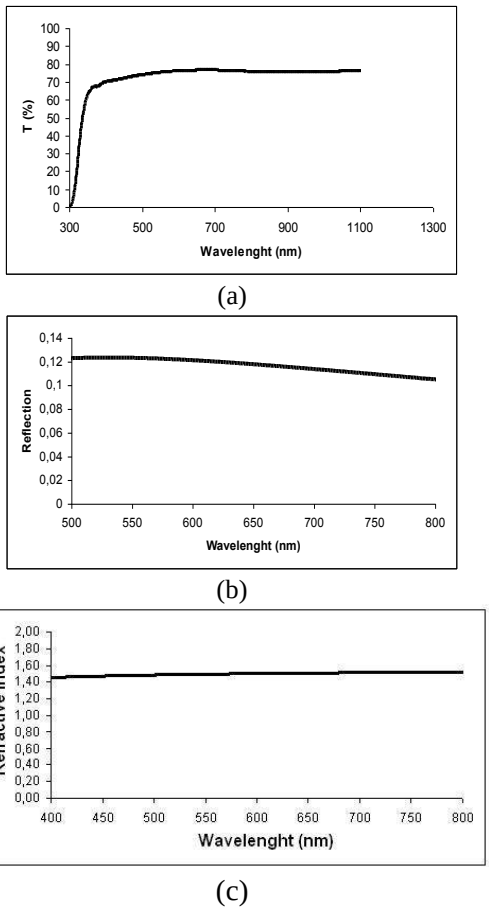

Fig.4. Transmission (a), reflection (b) and refractive index (c) values of the ZrO_2 coated lenses

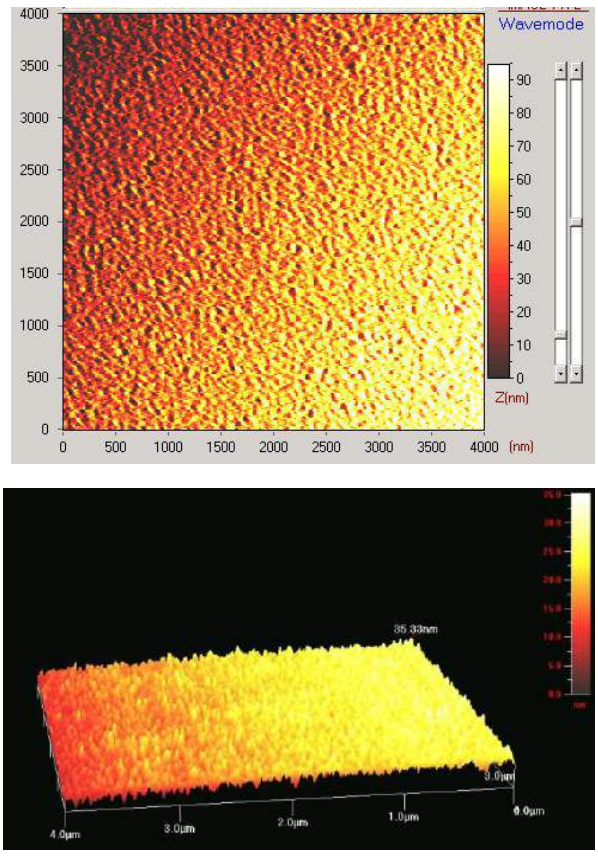

Fig. 3. AFM images (4000 nm * 4000 nm) of SiO_2 coated lenses

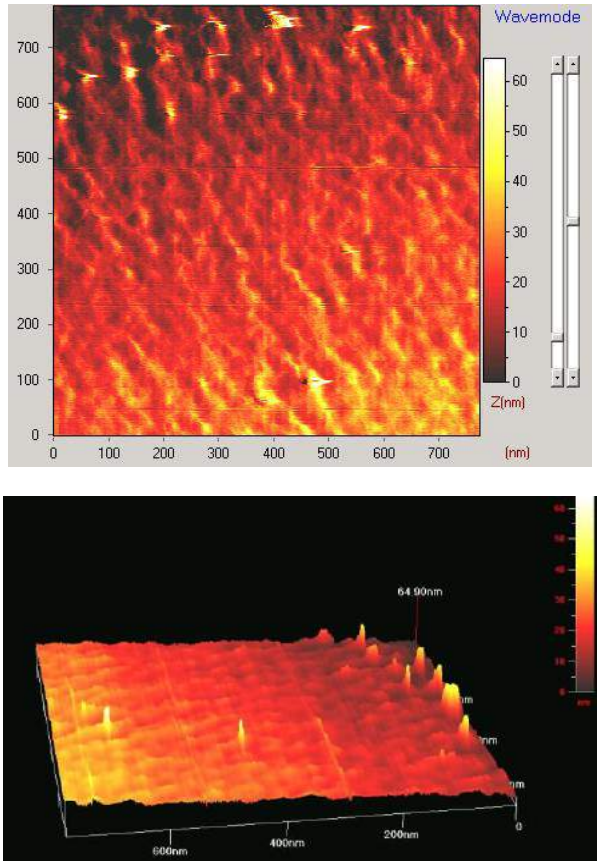

Fig. 5. AFM images (700 nm * 700 nm) of ZrO_2 coated lenses

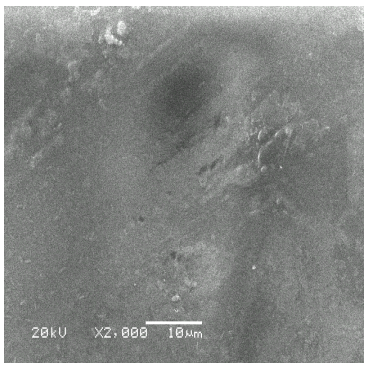

(a)

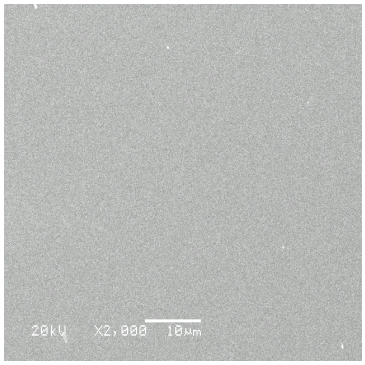

(b)

Fig. 6. SEM images of SiO_2 (a) and ZrO_2 (b) coated lenses

2D and 3D AFM images of produced SiO_2 and ZrO_2 AR coatings were shown in figure3 and 5. As can seen in figures, surface of deposited layers were in low roughness in nm scale approximately 30-40 nm.

SEM images in 2kx magnification of the deposited surface were shown in figure 6. According to SEM images, surfaces were homogenious.

4. CONCLUSION

TVA techniques have a lot of advantages according to other vacuumated techniques such as good adherence, homogeneity, low roughness, high ion energy, high deposition rate, thickness control, nano structured etc. Thus, this technique shows good results for AR coatings. Additionally, these results shown that poly atomic molecules coating were realized with TVA. This is the most important process for deposited systems. One another advantage of TVA is proper for multi layer coatings in serial productions according to high coatings speed. Surface roughness is enough for the multi layer deposition process.

Finally, we concluded that produced AR coated mineral spectacle lenses are high quality and have long life.

This research activity has been supported by TUBITAK numbered with 108M608.

[1]. *A.Thelen*, Design of the optical coatings, McGraw Hill Company

[2]. *C. Surdu-Bob, I. Mustata, C. Iacob*, J. Opt. and Adv. Mater, Vol 9, No. 9, 2007, p. 2932-2934

[3]. *I Pat S, Ekem N, Akan T, et al.,* Journal of Optoelectronics And Advanced Materials 7 (5): 2495-2499 Oct 2005

[4]. *N. Ekem, G. Musa, S. Pat, Z. Balbag, I. Cenik, R.Vladoiu*, J. Opt. and Adv. Mater, Vol. 10, No. 3, March 2008, p. 672-674

[5]. *Ö.Duyar and H.Z.Dursoy*, Turkish Journal of Physics, 28 (2004) 139

[6]. *F.L.Pedretti, L.S. Pedretti and L.M. Pedrotti,* In introduction to optics, Pearson educations, USA, 2007

[7]. *S.H.Jeong, J.K.Kim, B.S.Kim, S.H. Shin and B.T.Lee,* Vacuum, 76 (2004) 507

ESR-SPECTRUM OF $Co_{0,7}Cu_{0,3}Cr_2S_4$

E.A.EYVAZOV, U.S.PASHABEYOVA, S.SH.GURBANOV, V.I.HUSEYNOV
Azerbaijan State Pedagogical University,
AZ 1000, Baku, U.Hajibeyov str. 34 A

In the work ESR spectrum of ferritmagnetic $Co_{0,7}Cu_{0,3}Cr_2S_4$ substance was researched at 300÷450 K interval. It was defined, that the spectrum is in Lorentz form at all temperatures and when temperature increases, resonance line narrows. This was explained by the role of spin-spin interaction.

Recently, intensive development of spintronics makes actual the obtaining and research of magnetic substances of which the magnetic phase transition temperature is similar with room temperature [1]. Among such substances magnetic semi-conductors are very important. Thus, the formation of transversal magnetoelectric and electromagnetic effects in them is very possible. Certain groups of chalcospinels have magnetic transition temperature and they have semi-conductor type conductivity character [2]. That's why they are of great importance. In the present work for the first time we have researched ESR spectrum of ferromagnetic semi-conductor $Co_{0,7}Cu_{0,3}Cr_2S_4$ substance of which the Curie temperature is $T_c \approx 296K$. Obtaining technology and research of several kinetic and magnetic properties of the taken substance were given in our previously published research works [4, 8].

ESR spectrum of polycrystalline ferromagnetic $Co_{0,7}Cu_{0,3}Cr_2S_4$ substance was researched at 300÷450 K temperature range in $10 \cdot 10^3$ oersted magnetic field by "Jeoel" radiospectrometry. With the aim of abolishing possible changes of form of resonance lines at due to skin effects, the sample was powdered before investigation.

At the taken temperature range the resonance curve is practically symmetrical-Loerntz curve. For some temperatures ESR curves were given in figure 1.

As it is seen by increasing temperature the intensiveness of resonance curve is diminished. For determining character of diminishing the intensiveness of resonance curves in arbitrary units was defined by the help of the following equation:

$$İ_{ar.unit} \approx Y_{mak.} \cdot (\Delta H_{mak.})^2 \qquad (1)$$

where $2Y_{mak}$ is an amplitude between points on ESR line, but ΔH_{mak} is the width of resonance line between these points. Temperature dependence of relative intensiveness is given in figure 2.

The width of resonance curve decreases at T=300÷450 K temperature range at high temperature according to $\Delta H_{mak} = \Delta H_{mak}$ (300)- $K_1 \cdot T$ linear law, and when temperature increases the resonance lines narrow (values of ΔH_{mak} (300) and K_1 were given in the table). It can be explained by the role of spin-spin interaction. With this aim let's remember formation mechanism of heating equilibrium in ESR. It is generally known, that formation of heating equilibrium in ESR in paramagnetic system takes place by conducting excited energy to other degrees of freedom. Degrees of freedom are two by nature: degrees of freedom, related to movement of atom and molecules in substance; degrees of freedom, related to orientation of spins of non-coupled electrons. Conducting the excited energy to degrees of freedom happens first by interaction of electron with atom or molecule of a substance (spin-cell mechanism), in the other case by interaction between magnetic moment of excited electron with magnetic moments of other electrons (spin-spin mechanism)

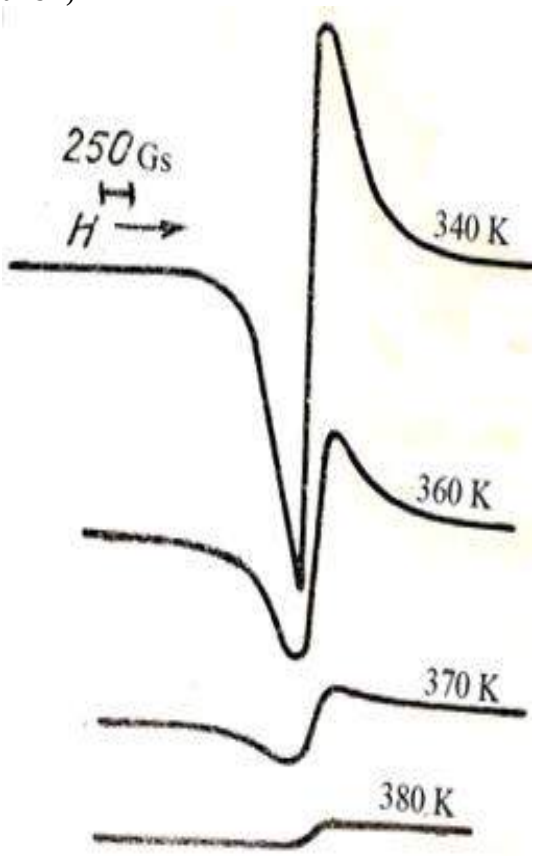

Fig. 1. ESR spectrum of $Co_{0,7}Cu_{0,3}Cr_2S_4$.

By the carried out researches it was determined, that when temperature increases, spin-cell interaction strengthens and corresponding relaxation period is reduced according to $\tau_{sq} \sim T^{-1}$ law [5]: $\Delta H \sim 1/\tau \sim T$ according to indefiniteness principle $\Delta E \cdot \Delta\tau \sim \hbar$ and according to resonance term $\Delta E \approx 2\mu \Delta H$. Due to spin-cell relaxation the width of ESR line must increase when temperature rises. That is to say, at high temperature widening of resonance line doesn't depend on spin-cell mechanism. For this purpose it is possible to consider that heating equilibrium takes place by spin-spin relaxation way. According to out estimations spin-spin relaxation period is 10^{-9} sec. and increases by $\tau_{ss} \approx \tau_{ss}$ (300)+ K_2T linear law (see table).

As it seen from the table, g-factor, calculated in the framework of spin-spin relaxation reality, is bigger than the value (g_e=2,003) of free electron and doesn't depend on the temperature. At first sight linear increase of relaxation duration can be seen incomprehensible. In many theoretical researches for example in [6] it was shown, that spin-spin interaction Hamiltonian doesn't depend on temperature. It is known, that corresponding relaxation period will not depend on temperature. But there can be two factors, which cause the dependence of spin-spin relaxation period on temperature. One of them is connected with intensive movement of paramagnetic atoms in crystal and they are effective at high temperatures. It is natural that temperature, which we have taken, is unsatisfactory for intensive diffusion in crystal and so narrowing resonance lines by temperature cannot be explained according to the mechanism. In crystal both external magnetic field and local magnetic field, formed by neighbor ions, influence on each magnet ion. That's why width of resonance line and relaxation duration will change depending on direction of spins of neighbor ions.

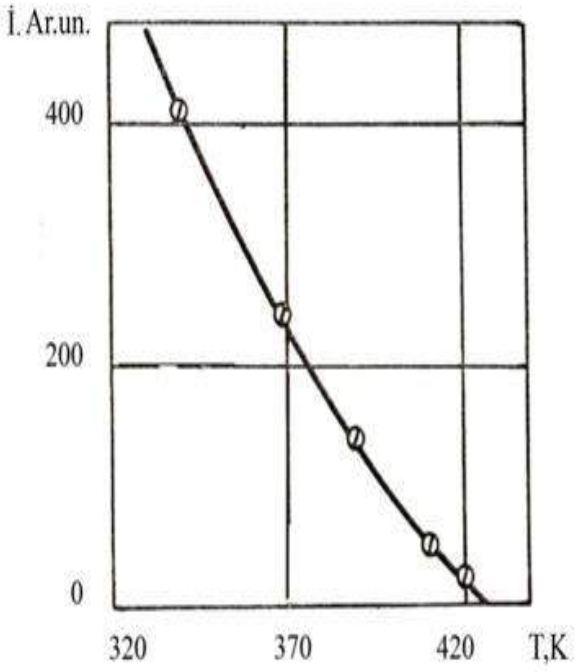

Fig.2. Temperature dependence of relative intensiveness of ESR lines of $Co_{0,7}Cu_{0,3}Cr_2S_4$.

$\Delta H_{mak(300)}$, Gs	K, Gs/k	τ_{ss} (300)· 10^9 sec.	$K_2 \cdot 10^9$ sec./K	g
328	1,90	1,08	2,60	2,26

Widening (narrowing) of resonance line depends on intensiveness ($\bar{h}$) of local magnetic field. From the other side local intensiveness is $\bar{h} \sim -r^{-3}$ (r- space between magnetic ions), will give additional ions to the width of line. It is known, that by the increase of temperature line widening can be explained by enlargement of magnetic inter-ion space (decrease of local area intensiveness).

Considering local field creates originality in heating equilibrium. In [6] it was determined, that at lower temperatures spin-spin relaxation period is defined by $\tau_{ss} \approx (2mc/\bar{h} \sim r^{-3})$ equation (m-mass of electron, c-propagation velocity of light, e-electronic charge). As it is seen when $h \sim T^{-1}$, $\tau_{ss} \sim T$, that is by increasing temperature relaxation duration increases, but resonance line narrows. We consider, that the researched Curie temperature of $Co_{0,7}Cu_{0,3}Cr_2S_4$ substance is near to temperature range and resonance line narrowing, which was observed by us, probably has connection with spin-spin relaxation mechanism.

In the present research work one of the important objects is that value of g-factor, calculated from resonance line, is higher than definite value (~2.003) of free electron (see the table). This object has been researched many times. In a special case, it was shown in [7], that the above mentioned difference is the result of spin-orbital and s-d exchange interaction and g-factor is defined by the following equation:

$$g = g_e - 8\lambda_0 K_{\pi\delta} \cdot \Delta^{-1} + 3zИ_{sd}/4E_F, \qquad (2)$$

where, Δ is decomposition quantity of energy level in intercrystal cubic field, z- number of charge bearers for one atom, E_F- Fermi energy, $İ_{sd}$-sd exchange integral, λ_0-spin-orbital bond constant of free ion and $K_{\pi\delta}$- parameter, which allows to define the addition of bond forming effects, given to spin-orbital interaction and one-electron wave function. According to NMR researches in $Co_{0,7}Cu_{0,3}Cr_2S_4$ copper ions are monovalent, chromium ions are Cr^{3+} and Cr^{4+} valency, but cobalt ions are divalent [8]. As it is seen in the researched substance magnitoactive ions are Co^{2+}, Cr^{3+} and Cr^{4+} . In [6] it was shown, that for these ions spin-orbital bond constant are 180, 87 and 164 sm^{-1} correspondingly. If we consider the above0mentioned it is possible to say, that increase of chromium ions concentration (Cr^{3+} and Cr^{4+}) must cause the decrease of g-factor (λ>0), but increase of Co^{2+} ions concentration leads to rise of g-factor (λ<0).

For the researched $Co_{0,7}Cu_{0,3}Cr_2S_4$ substance the quantities in the second and third limits on the right of (2) are unknown. That's why it is impossible to calculate the additions of spin-orbital and exchange effects of Co^{2+} ions. But we can evaluate the second limit in crystalline field ($K_{\pi\delta} \approx 1$; $\lambda_0 \approx \lambda$). For spinel sulphides $\Delta \approx 14900$ sm^{-1}[9] and for Co^{2+} ions it is $\lambda \approx 180$ sm^{-1} and if we don't consider the third limit, which is connected with s-d exchange, we will get g=2,099. As it is seen it is possible to explain the difference of experimental value ($g_{exp.}$=2,26) of g-factor from corresponding value (g=2,003) of free electron by only the additions, given by spin-orbital interaction. According to the above-mentioned and the role of positive s-d exchange interaction in the formation of $Co_{0,7}Cu_{0,3}Cr_2S_4$ ferrimagnetism we came to the conclusion, that $g_{exp.} > g_e$ has connection with joint addition of spin-orbital and s-d exchange interaction.

[1]. *I. Zutic, J.Fabian*, Dos sarma S. Rev. Mod. Phus. 76.323 (2008).
[2]. *B.P.Zakharchenya, V.L.Korenev*. UFN. 175.6. (2005).
[3]. *E.A.Eyvazov, A.F.Safarov, U.S.Pashabeyova*. Issue AS SSSR. Inorg. Mater. 14.10. (1985).
[4]. *E.A.Eyvazov, A.F.Safarov*. Issue AS SSSR. Inorg. Mater. 12.7. (1988).
[5]. *J.Verth, J.Bolton*, Theory and practical application to method of ESR, M. (1975).
[6]. *S.V.Vonsovskiy*. Magnetism. M. (1971).
[7]. *V.A.Bokov*. Physics of magnetics. S-P (2002).
[8]. *E.A.Eyvazov, A.F.Safarov*. Journal of physical chemistry. 11,7. (1994).
[9]. *H.D.Lutz, R.A. Becker* Monat. Sheftefц shemie. 5.104 (1989).

EPR AND FMR STUDIES OF Co IMPLANTED $BaTiO_3$ PEROVSKITE CRYSTAL

F.A. MİKAİLZADE[1,2], S. KAZAN[1,3], A.G. ŞALE [1], N.I. KHALİTOV[4], JU.I. GATİİATOVA[4], V.F. VALEEV[4], R.I. KHAİBULLİN[4]

[1]Department of Physics, Gebze Institute of Technology, Gebze, 41400, Kocaeli, Turkey

[2]Institute of Physics, Azerbaijan National Academy of Sciences, AZ-143, Baku, Azerbaijan

[3]Institut für Experimentalphysik/Festkörperphysik, Ruhr-Universitaet Bochum, 44780 Bochum, Germany

[4]Kazan Physical-Technical Institute of RAS, Sibirsky Trakt 10/7, 420029 Kazan, Russia e-mail: faik@gyte.edu.tr

The results of magnetic resonance measurements of Co implanted barium titanate ($BaTiO_3$) perovskite crystal are presented. It has been revealed that the implantation with Co on different fluencies of metal concentrations produces a granular composite film in the surface layer of $BaTiO_3$ substrate, which exhibits remarkable ferromagnetic behavior. Magnetic resonance measurements revealed Electron Paramagnetic Resonance (EPR) spectra originated from iron impurities of $BaTiO_3$ substrate, as well as Ferromagnetic Resonance (FMR) spectrum from Co-implanted surface layer, exhibiting an out-of-plane uniaxial magnetic anisotropy. It has been shown that the magnetization and coercivity of ferromagnetic state depends on the fluence of implantation. The observed phenomena are discussed on the base of strong magnetic dipolar interaction between Co nanoparticles inside the granular composite film formed in a result of implantation.

1. INTRODUCTION

In recent years there has been a continually increasing interest in magnetoelectric (ME) materials due to their attractive physical properties, multifunctionality, wide applications in the fields of sensors, data storage, transducers for magnetic-electric energy conversion, information technology, radioelectronics, optoelectronics, and microwave electronics [1]. In these materials the coupling interaction between ferroelectric and ferromagnetic substances could produce a magnetoelectric effect in which change in magnetization is induced by an electric field and change in electric polarization is induced by an applied magnetic field [2]. As it is known from the literature, a strong ME effect could be realized in the composite consisting of magnetostrictive and piezoelectric effects. It was recently discovered that composite materials and magnetic ferroelectrics exhibit magnetoelectric effects that exceed previously known effects by orders of magnitude [3], with the potential to trigger magnetic or electric phase transitions.

In this frame the production and research of new composite structures, especially on the base of intensive incorporation of magnetic nanoparticles into the crystal matrix of ferroelectric perovskite oxides is of great interest. Among the different techniques, ion implantation is a very attractive and prospective preparation method, such as easy control of the metal distribution and concentration, the availability of almost arbitrary metal–dielectric compositions, and the ability to surpass the solubility limits constrained by the chemical and thermodynamic equilibrium of the host matrix and metal impurities [4]. Besides, the ion implantation technique is ideally suited for fabrication of thin-film magnetic media and planar devices for magneto-sensor electronics.

In this paper the results of investigation of magnetization and magnetic resonance spectra of Co implanted $BaTiO_3$ in a wide temperature range are presented. These results show the promise of magnetic nanocomposites on the base of ferroelectric perovskites for potential magnetoelectric applications as well as the flexibility of ion implantation as a powerful method for modification of magnetic properties of materials.

2. EXPERIMENTAL TECHNIQUE

The $10\times10\times0.4$ mm^3 single-crystalline (100)- or (001)-face oriented plates of $BaTiO_3$ (supplied by Crystec GmbH, Berlin, Germany) were implanted with 40 keV Co^+ ions at ion current density of 8 $\mu A/cm^2$ using the ILU-3 ion accelerator (Kazan Physical-Technical Institute of Russian Academy of Science). The sample holder was cooled by flowing water during the implantations to prevent samples from overheating. The implantation fluence varied in the range of $0.5\text{-}1.5\times10^{17}$ ion/cm^2. After implantation, the samples were cut by a diamond cutter on smaller pieces for the subsequent structural and magnetic studies.

Elemental composition and surface morphology of the implanted samples has been studied by scanning electron microscopy (SEM) by using Philips XL30 SFEG apparatus. Magnetic resonance measurements were carried out by using Bruker EMX model X-band (9.8 GHz) spectrometer. A closed-cycle helium cryostat system and Lakeshore 340 model temperature controller were used in the measurements, which allowed to scan the temperature with a rate of about 0.2 K/min and to stabilize the temperature with accuracy better than 0.05 K. The measurements were performed in the temperature range of 10-300 K. The static magnetic field was varied in the range of 0-16000 G. A goniometer was used to rotate the sample holder which is parallel to the microwave magnetic field and perpendicular to the applied static magnetic field. The measurements were performed in two different, in-plane and out-of-plane geometries. At in-plane geometry the sample was attached horizontally at bottom edge of sample holder and the static magnetic field was scanned in the plane of the implanted surface. At out-of-plane geometry the sample was attached to the

flat platform of sample holder where the magnetic field of microwave lie in film plane during measurement and static magnetic field is rotated from the sample plane to surface normal. The field derivative of microwave power absorption (dP/dH) was recorded as a function of the DC field. To obtain intensities of EPR and FMR signals the double digital integration of the resonance curves were performed using Bruker WINEPR software package.

3. RESULTS AND DISCUSSION

As it is mentioned above, the magnetic resonance investigations of Co implanted $BaTiO_3$ revealed the presence of both EPR and FMR spectra, which can be interpreted as an evidence of paramagnetic centers inside the crystal structure, as well as the existence of ferromagnetic ordering inside the structure of the implanted samples. SEM imaging of the surface morphology of the samples implanted at different fluencies revealed the formation of granular surface layer characterized by high-density distribution of Co particles in a result of implantation. The average size of the particles is between 5 nm and 20 nm for the implantation fluency of 1.5×10^{17} ion/cm^2. So, the appearance of FMR spectra is originated from the granular composite layer, which consists of ferromagnetic cobalt particles dispersed in the surface layer of ferroelectric $BaTiO_3$ substrate.

On the other hand, the analysis of the EPR spectra of Co implanted $BaTiO_3$ revealed an unexpected behavior. It has been established that the EPR lines are originated from Fe^{3+} centers located in Ti^{4+} sites. In this way, one has to mention that the EPR signals were observed also on measuring the virgin $BaTiO_3$ plates, so the substrates was found to contain Fe^{3+} impurities. The rotational EPR patterns for "in-plane" and "out-of-plane" geometries are presented in Fig. 1.

On interpreting the EPR spectra we took into account that the paramagnetic impurity ions are located substitutionally on the titanium (Ti^{4+}) site due to their ionic radius are octahedrally coordinated with six nearest-neighbor oxygen, which can give rise to ligand crystalline field (CF) with cubic symmetry at Ti^{4+} sites. The analysis of the results of magnetic resonance measurements of both implanted and virgin $BaTiO_3$ substrate brought us to the statement, that the EPR spectrum is originated from iron impurities of virgin $BaTiO_3$ substrate. In this frame it should be mentioned that EPR spectra from paramagnetic Fe centers in $BaTiO_3$ were observed earlier in a lot of works [5-9]. In most cases, the authors considered the EPR lines to be originated from Fe^{3+} ions located at Ti^{4+} sites, pointing to the existence of uniaxial distortions of ligand fields due to Fe^{3+}-V_o vacancies formed in a result of charge compensation [10].

It is well known that the crystalline field at a positive ion site has a dominant component arising from an array of surrounding negative charged ligands atoms [11]. The degeneracy of spin multiplet of the S-state Fe^{3+} ion (S=5/2, L=0) is removed due to the crystalline field of these ligands. Using the equivalent Stevens operators, the energy level splitting of Fe^{3+} ion can be described by the following Hamiltonian:

$$H = H_Z + H_{CF} = \mu_B \vec{B}\vec{g}\vec{S} + \sum_{m=0}^{2} B_2^m O_2^m + \sum_{m=0}^{4} B_4^m O_4^m \qquad (1)$$

where $S = 5/2$ is electronic spin and μ_B is bohr magneton. The first term H_Z accounts for the Zeeman interaction, the second term H_{CF} is the crystal field Hamiltonian.

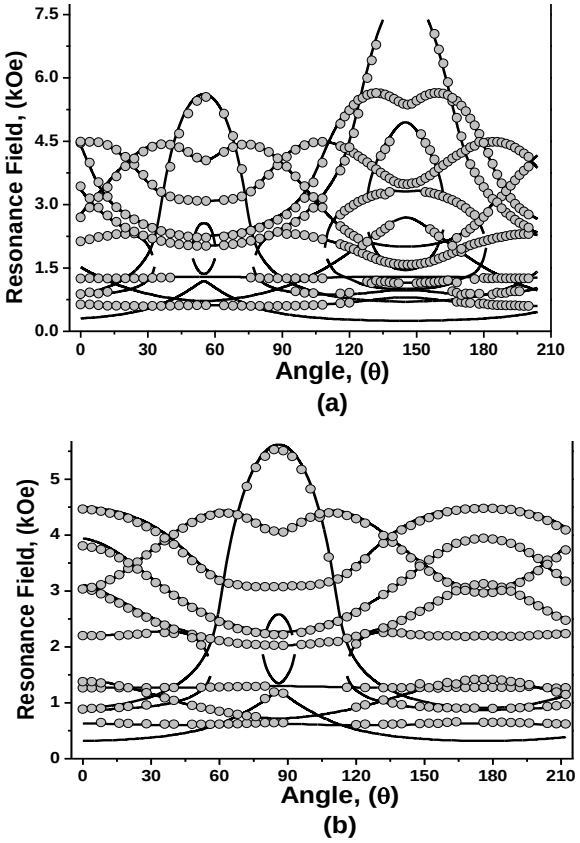

Fig.1. The observed and fitted rotation patterns of the EPR resonance field values of $BaTiO_3$ substrate possessing Fe impurities for "in-plane" (a) and "out-of-plane" (b) geometries. Full curves are calculated using the obtained spin-Hamiltonian parameters.

The Stevens operators O_4^m are defined according to Abragam and Bleaney [11]. In a cubic field with a tetragonal distortion, the equivalent operator Hamiltonian [9] is;

$$H_{tetr}^{'} = B_2^0 O_2^0 + \tilde{B}_4 (O_4^0 + 5O_4^4) + \tilde{B}_4^0 O_4^0 \qquad (2)$$

with a new parameters defined as

$$\tilde{B}_4^0 = B_4^0 - \frac{1}{5} B_4^4 \quad and \quad \tilde{B}_4 = \frac{1}{5} B_4^4 \qquad (3)$$

Using the spin Hamiltonian in the form of Eq. (2), the computer simulations of the EPR spectra of Fe^{3+} centre in $BaTiO_3$ crystal were performed and the spin Hamiltonian parameters were determined. As it is seen above, the observed and fitted EPR rotation patterns exhibit small

deviation of the ligand field at Fe^{3+} site from the cubic symmetry by the way of tetragonal distortion, which is due to the existence of the tetragonal ferroelectric phase in $BaTiO_3$ crystal in the temperature range between 5^0 C and 120 ^{0}C [7].

The results of low temperature magnetic resonance investigations of Co implanted $BaTiO_3$ substrates included Fe impurities are shown in Fig. 2. The measurements were performed also in "in-plane" and "out-of-plane" geometries in the temperature range between 10 and 300 K. As it is seen from the figure, the low temperature spectra also contain EPR and FMR lines and both of them exhibit a temperature behaviour. The temperature dependence of FMR line can be interpreted taking into account the temperature dependence of effective magnetization, which is discussed in subsequent sections. Regarding EPR spectra, it has been established that the resonance lines exhibit considerable changes at the temperatures about 276 K and 176 K. These transformations of EPR spectra are attributed to the influence of the well-known structural phase transitions in $BaTiO_3$ and were detailly discussed in [12, 13]. The angular variations of the EPR spectra, which have been obtained on rotating the sample at in plane (where the static magnetic field has been rotated in (001) plane of crystal) and out-of-plane geometries (i.e., the static magnetic field is rotated in the (100) or (010) planes) as well as the experimental and simulated rotational patterns of the resonance fields at the temperatures inside of the orthorhombic phase are presented in Fig. 3. Almost the same result has been obtained in the second out-of-plane geometry, which is perpendicular to the first one. As is seen from the figure, two groups of anisotropic EPR lines were observed in the orthorhombic phase of perovskite $BaTiO_3$. The former group consists of two lines arranged symmetrically around the field value connected to g-value about of 2, while the other group consists of more anisotropic and less intensive resonance lines.

It has been mentioned in [12], that the difficulty of the observation of EPR at lower ferroelectric phases will be due to the formation of complex domain structure. At tetragonal phase the spontaneous polarization occurs along any one of [100] crystallographic direction. Then the axis of crystallographic distortion in one plane is unique and perpendicular to each other. The EPR spectrum consists of Fe^{3+} resonance line under axial crystalline field which is interpreted above using the superposition model. When the crystal transforms from tetragonal to orthorhombic phase, c-domains (Domains which have their polarization parallel to c-axis are called c-domains) are split into domains which are polarized along any one of six equivalents [110] direction. In this case the observed EPR spectrum of the crystal will now be obscured by the overlapping of many lines originated from various ion sites of different polar axis [12].

For theoretical interpretation of the observed rotational patterns of EPR spectra, two magnetically equivalent paramagnetic centers with different polar axes aligned in two perpendicular layers were taken into account and the following spin-Hamiltonian [9] for paramagnetic Fe^{3+} ions located around oxygen ligands with octahedron environment was used [11]:

$$H_{tetr}^{'} = B_2^0 O_2^0 + \tilde{B}_4 (O_4^0 + 5O_4^4) + \tilde{B}_4^0 O_4^0 \qquad (4)$$

The results of fitting of the angular dependences of the resonance fields in both in-plane and out-of-plane orientations are shown in Fig. 3. The calculated Spin Hamiltonian parameters, by means of Eq. (3), are $|B_4^4|$=5.5 Oe (5.14 x10^{-4} cm^{-1}), $|B_4^0|$=1.1 Oe (1.028 x10^{-4} cm^{-1}), $|B_2^0|$=260 Oe (243 x10^{-4} cm^{-1}) and g=2.0036. The sign of B_2^0 was found to be opposite to that of $\tilde{B}_4$ as in the case of tetragonal phase. During the phase transformation the magnitude of $\tilde{B}_4$ parameter doesn't change more but the magnitude of axial part of CF is decreased.

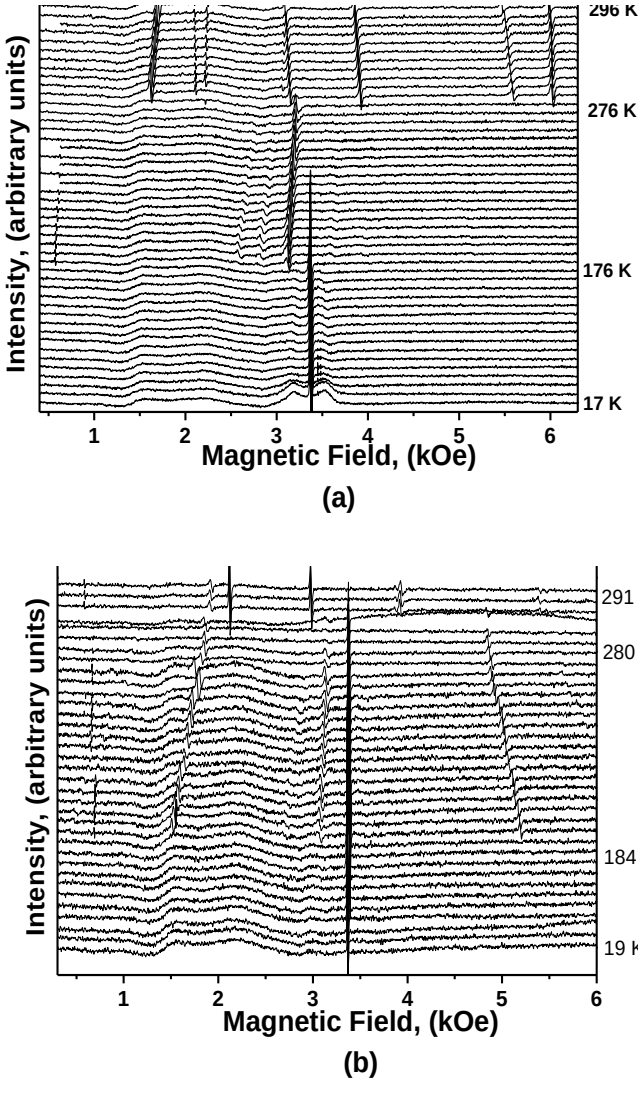

Fig.2. Temperature dependence of the EPR spectra of $BaTiO_3$ substrate possessing Fe impurities measured at "in-plane" (a) and "out-of-plane" (b) geometries.

In order to discuss the results of FMR measurements it is worth mentioning that the observed FMR line dependence on the sample orientation is similar to that observed in the FMR of granular magnetic films [14]. In this case the resonance signal from a granular magnetic

layer is considered as a result of the collective motion of particles magnetic moments, i.e. may be described in the approximation by the macroscopic magnetization of the granular layer as the whole system.

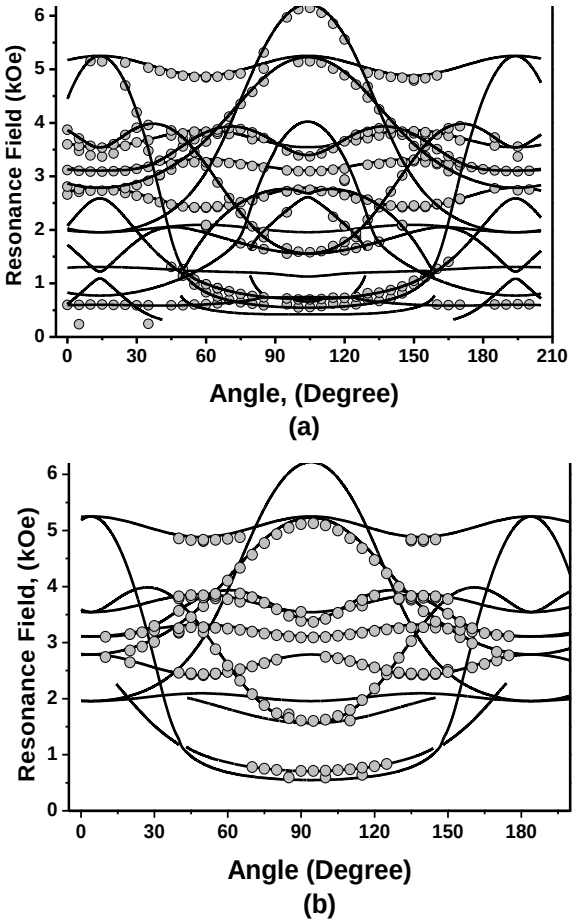

Fig.3. (a) Angular dependence of resonance field at 215 K for the rotation of magnetic field in (100) plane of single crystalline $BaTiO_3$. (b) Angular dependence of resonance field at 220 K for the rotation of magnetic field in (001) plane of single crystalline $BaTiO_3$. The solid circles show the experimental position of each resonance line in EPR spectra. The solid lines show the simulation of angular behaviors of the resonance lines.

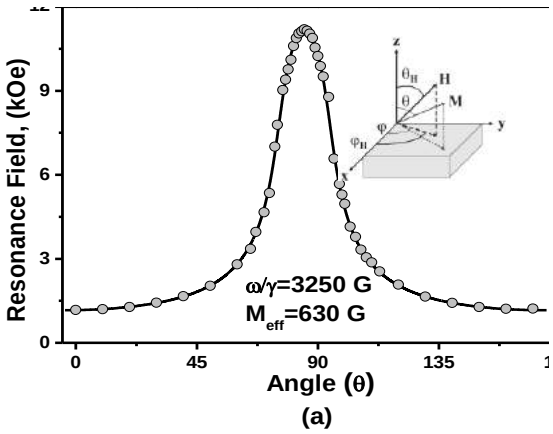

Fig.4. Angular dependence of the FMR resonance field in Co implanted surface of $BaTiO_3$ at out-of-plane geometry. The inset figure shows the coordinate system for FMR measurements.

In this framework it is possible to analyze the FMR signal as coming from a thin magnetic film with some effective values of the magnetization and g-factor. Then, the magnetic free energy density for the granular film at arbitrary orientation takes the same form as that for a continuous film;

$$\begin{aligned} E &= E_z + E_b \\ E_z &= -M_0 H(\sin\theta\sin\theta_H\cos(\phi_H-\phi)+\cos\theta\cos\theta_H) \\ E_b &= K_{eff}\cos^2\theta,\ K_{eff} = (2\pi M_0 - K_\perp) \end{aligned} \tag{5}$$

where E_z and E_b are the Zeeman and the bulk (overall) anisotropy energy terms respectively. M_o is the saturation magnetization, θ and ϕ are the spherical angles for the magnetization M, ϕ_H and θ_H the usual spherical polar angle for the applied field H as shown in Fig. 4. $K_\perp$ is the perpendicular anisotropy constant. K_{eff} is the effective bulk (shape-demagnetizing) anisotropy constant and it is related with M_{eff} as $4\pi M_{eff} = 2K_{eff}/M_0$. For the resonance condition we used classical resonance equation given in many ferromagnetic resonance studies in literature as in [15]:

$$\frac{\omega_o}{\gamma} = \frac{1}{M\sin\theta}\left(E_{\theta\theta}E_{\varphi\varphi} - E_{\theta\varphi}^2\right)^{1/2} \tag{6}$$

$E_{\theta\theta}$ and $E_{\varphi\varphi}$ are second derivative of E with respect to the θ and φ respectively. Using Eq. (5) and Eq. (6) we get following resonance equation:

$$\left(\frac{w}{\gamma}\right)^2 = \left[H\cos(\theta_H-\theta) - 4\pi M_{eff}\cos^2\theta\right] \times \left[H\cos(\theta_H-\theta) - 4\pi M_{eff}\cos 2\theta\right] \tag{12}$$

The value of the g-factor and effective magnetization was calculated from the variation of resonance field with the rotation angle of sample at out of plane geometry as 2.1 and 630 G respectively.

The observed peculiarities of the ferromagnetic behavior of Co implanted $BaTiO_3$ may be attributed to dipole-dipole interaction of magnetic cobalt nanoparticles formed in a result of high-influence implantation. The detailed phenomenon is discussed in [14, 16] and called "magnetic percolation". The fact is that when the distance between the magnetic particles becomes comparable with their sizes, the dipole–dipole interaction couples the particle magnetic moments. As a result, the granular phase behaves as a ferromagnetic continuum with respect to dipolar forces even without direct contact between the particles. The mechanism of such dipole-dipole interaction is discussed also in Ref. [17], where the authors considered a semi-quantitative model for dipolar field for regular array of closely separated spherical particles in granular magnetic layer. As a result of this model, the dipolar field exhibited an anisotropic behavior.

As a result, the angular dependence of FMR spectra in such systems is qualitatively similar to that of a magnetic thin film.

4. CONCLUSION

Thus, the results of magnetic resonance and magnetization studies of Co implanted $BaTiO_3$ perovskite crystal revealed both the presence of anisotropic EPR spectra from Fe impurities of the substrate and remarkable ferromagnetic behaviour in a result of Co implantation. It has been obtained from EPR spectra that the $BaTiO_3$ substrates used in this study contain Fe^{3+} impurities, which are located at Ti^{4+} sites of the crystal structure, so that the electric field of ligands around them possesses a local tetragonal symmetry. EPR measurements have been performed and CF parameters of low temperature phases of $BaTiO_3$ appeared at about 270 K and 190 K have been obtained.

It has been revealed that the implantation of Co into single-crystal $BaTiO_3$ on different fluences of metal concentrations produces a remarkable ferromagnetic behavior, so that ferromagnetic granular film is constructed on the surface of ferroelectric substrate. The FMR spectra measured at different crystalline orientations of substrate with respect to the applied magnetic field show an out-of-plane uniaxial magnetic anisotropy in Co-implanted $BaTiO_3$. The observed phenomena are discussed on the base of strong magnetic dipolar interaction between Co nanoparticles due to diminishing of interparticle distance with increasing of implantation dose.

.

ACKNOWLEDGMENT

The authors from Gebze Institute of Technology are indebted to Research Projects Commission of Gebze Institute of Technology for supporting this work by the Grant No. 2009-A11. The authors from Kazan Physical-Technical Institute, Russia, acknowledge support through the RFFI, Grant No. 07-02-00559, OFN RAN Programme "New materials and structures", and Russian Federal Agency on Education, contract P902

---

[1]. *G.R. Slemon,* Magnetoelectric Devices Transducers, Transformers and Machines, Wiley New York, 1966.

[2]. *M. Fiebig,* J. Phys. D: Appl. Phys. 38 (2005) R123.

[3]. *C.-W. Nan, M.I. Bichurin, S. Dong, D. Viehland, G. Srinivasan,* , J. Phys. D: Appl. Phys. 103 (2008) 031101.

[4]. *G . Dearnaley, J.H. Freeman, R.S. Nelson, J.Stephen,* Ion Implantation, North-Holland, Amsterdam, 1973.

[5]. *K. A. Müler,* J. Physique 42 (1981) 551-557.

[6]. *K. A: Müller and J. C. Fayet,* in structural Phase Transitions Studied by Electron Paramagnetic Resonance, Edited by K A müller and H Thomas (Springer, Berlin 1991), p.1.

[7]. *E. Posseenriede, P. Jacobs and O. F. Schirmer,* J.Phys.:Condens. Matter 4 (1992) 4719-4742.

[8]. *Robert N.* Schwartz and Barry A. Wechsler, Phys. Rev. B 48, (1993) 7057-7069.

[9]. C. *Rudowicz and P. Budzynski,* Phys. Rev. B 74 (2006) 054415.

[10]. *H.G.Maguire, L.V.C.Rees.* Suppl. au J, Phys., 33, 4, C2-173, 1972.

[11]. *A. Abragam, B. Bleaney,* Electron Paramagnetic Resonance of Transition Ions, Clarendon Press, Oxford, (1970).

[12]. *T. Sakudo,* J. Phys. Soc. Japan 18 (1963) 1626.

[13]. *T. Sakudo and H. Unoki,* J. Phys. Soc. Japan 19 (1964) 2109.

[14]. *G. N. Kakazei, A. F. Kravets, N. A. Lesnik, M.M.Pereira de Azevedo, Yu. G. Pogorelov, and J.B.Sousa,* J. Appl. Phys. 85 (1999) 5654.

[15]. *B. Aktaş, S, B. Heinrich, G. Woltersdorf, R.Urban , L. R. Tagirov, F. Yıldız, K. Özdoğan, M. Özdemir, O. Yalçın, and B. Z. Rameev,* J.Appl. Phys. 102 (2007) 013912.

[16]. *A. L. Stepanov, R. I. Khaibullin, B. Z. Rameev, A.Reinholdt, and U. Kreibig,* Technical Physics Letters 30 (2004) 151.

[17]. *S. Tomita, K. Akamatsu, H. Shinkai, S. Ikeda, H.Nawafune, C. Mitsumata, T. Kashiwagi, M.Nagiwara,* Phys. Rev. B. 71 (2005) 180414(R).

FMR STUDIES OF Co-IMPLANTED ZnO FILMS

B.Z. RAMEEV[1,2], N. AKDOĞAN[1], S. GÜLER[1], O. ÖZTÜRK[1], B. AKTAŞ[1], H. ZABEL[3], R. KHAIBULLIN[2], L. TAGIROV[2,4]

[1]*Department of Physics, Gebze Institute of Technology,*
41400 Kocaeli, Turkey
rameev@gyte.edu.tr
[2]*Kazan Physical-Technical Institute of RAS,*
420029 Kazan, Russian Federation
[3]*Institut für Experimentalphysik/Festkörperphysik,*
Ruhr-Universität Bochum,
D-44780 Bochum, Germany
[4]*Kazan State University,*
420008 Kazan, Tatarstan, Russian Federation

Magnetic anisotropies of Co-implanted ZnO (0001) films grown on single-crystalline Al_2O_3 (11-20) substrates have been studied by ferromagnetic resonance (FMR) technique for different cobalt implantation doses. The FMR data show a six-fold in-plane anisotropy in agreement with the hexagonal structure of the ZnO films. This kind of magnetic anisotropy is observed for the first time in ZnO-based diluted magnetic semiconductors, and attributed to the substitution of cobalt on Zn sites in the ZnO structure. Thus, our FMR studies provide a strong support for long range ferromagnetic ordering between substitutional cobalt ions in the single-crystalline ZnO films.

1. INTRODUCTION

The transition metal (TM)-doped ZnO has attracted a strong attention of researchers as a prospective material for realization of diluted magnetic semiconductor (DMS) to use in novel spintronic devices. Theoretical predictions of room temperature ferromagnetism in TM-doped ZnO [1–3] have stimulated a number of experimental works on these systems [4–17]. Some of these studies indeed claim ferromagnetic signals above room temperature. However, the main unresolved question is whether the observed ferromagnetism originates from uniformly distributed TM ions in the ZnO host matrix or it is due to the precipitation of metallic ferromagnetic clusters. In our previous studies, we have reported that the implantation of cobalt ions into the nonmagnetic ZnO film causes intrinsic ferromagnetism at room temperature and simultaneously creates *n*-type charge carriers without additional doping [16,17]. Furthermore, we have observed a magnetic dichroism at the Co $L_{2,3}$ and O *K* edges at room temperature as well as the multiplet structure in x-ray absorption spectra around the Co L_3 edge, which strongly supports the intrinsic nature of the observed ferromagnetism in Co-implanted ZnO films. Besides, we have found that the magnetic moment per substituted cobalt in ZnO is about 2.81 μ_B, which is very close to the theoretical expected value of μ_B Co for Co^{2+} in its high spin state. Very recently, we reported the six-fold in-plane magnetic anisotropy in the Co-implanted ZnO films that is observed for the first time by room-temperature FMR technique [18].

2. EXPERIMENT

The ZnO (0001) thin films were grown on sapphire (11-20) substrates by rf (13.56 MHz) sputtering of a ZnO target [19]. After postgrowth annealing, the ZnO samples were implanted with 40 keV Co^+ ions to the implantation doses in the range of $0.25–2.00\times10^{17}$ ions/cm^2. More details on growth, structural, electronic, and magnetic properties were published elsewhere [16,17]. Ferromagnetic resonance (FMR) measurements were carried out using a commercial Bruker EMX electron spin resonance spectrometer operating in *X*-band (9.8 GHz) at room temperature. Angular dependencies of FMR spectra have been recorded with the static magnetic field rotated either in the plane of the samples (in-plane geometry, θ = 90° and φ is varied) or rotated from the sample plane to the normal (out-of-plane geometry, θ is varied while φ is fixed).

3. RESULTS AND DISCUSSION

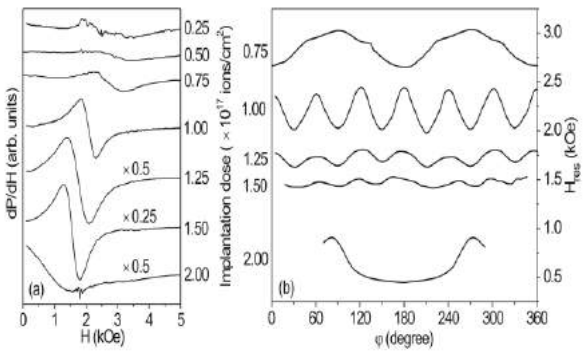

Fig. 1 FMR spectra at the in-plane geometry (a) and the angular dependence of the resonance fields (b) for different cobalt implantation doses.

In Fig. 1, we present in-plane FMR spectra of Co-implanted ZnO films and angular dependence of the in-plane resonance fields at room temperature for different implantation doses. The resonance field exhibits anisotropic behavior as a function of the azimuthal angle. It is well known that the maximum and minimum values of the resonance fields correspond to the hard and easy directions for the magnetization, respectively. The periodicity of the easy and hard axes depends on the

implantation dose. As seen in Fig. 1, at implantation doses lower than 0.75×10^{17} ions/cm^2, the FMR signal is very weak. For the dose of 0.75×10^{17} ions/cm^2, the FMR signal is more intense and a two-fold in-plane magnetic anisotropy is observed with a very small contribution from a six-fold anisotropy. The two-fold in-plane magnetic anisotropy is related to cobalt nanoparticles forming a cobalt rich layer in the sapphire substrate, close to the ZnO/Al_2O_3 interface [16]. Indeed, when the crystalline Al_2O_3 is implanted with cobalt ions, Co nanoparticles with the hexagonal structure are aligned with their c-axis parallel to the c-axis of the host sapphire [20]. Thus, the Al_2O_3 matrix provides a magnetic anisotropy to cobalt nanoclusters [21] In our case, the c-axis of the host Al_2O_3 is in the sample plane. Therefore, we infer that the two-fold in-plane magnetic anisotropy results from cobalt nanoparticles in agreement with previous studies [20,21]. However, for the dose range of $1.00–1.50\times10^{17}$ ions/cm^2, the corresponding FMR data show that the easy and hard axes have a periodicity of 60° in the film plane, in agreement with the hexagonal structure of the ZnO films. This six-fold in-plane magnetic anisotropy is attributed to the substitution of cobalt on Zn sites in the ZnO layer and it is a clear indication for long range ferromagnetic ordering between substitutional magnetic cobalt ions in the ZnO crystal structure. At the highest implantation dose of 2.00×10^{17} ions/cm^2, a two-fold in-plane magnetic anisotropy appears again. This means that for the highest dose, not only substituted cobalt ions but also metallic cobalt clusters are present in the ZnO layer, in accordance with the results published in Ref.[17]. Thus, for the highest implantation dose the resonance signal is ascribed to an overall response of the metal cobalt nanoparticles in both the ZnO layer and the sapphire substrate.In this respect, a gradual decrease of the magnitude of six-fold anisotropy for the dose of 1.5×10^{17} ions/cm^2 is noteworthy. Obviously it is related to the formation of very small cobalt clusters in ZnO layer below the dose of 2.00×10^{17} ions/cm^2. Thus, the maximum amplitude of the six-fold anisotropy, revealed at the dose of 1.00×1017 ions/cm^2, reflects the limit where the highest concentration for the substitutional cobalt phase in ZnO is reached. For higher doses, formation of the extrinsic ferromagnetic phase due to Co clusters starts. Out-of-plane FMR spectra and the FMR resonance fields as a function of polar angle (θ) are shown in Fig. 2 for different cobalt implantation doses. At low doses the resonance signal is very weak. Increase of the implantation dose results in appearance of the FMR signal, characterized by the six-fold in-plane magnetic anisotropy and attributed to the substitutional cobalt phase in the ZnO layer. In the out-of-plane geometry, this signal consists of a single line for the parallel orientation and two lines for the perpendicular orientation of the ZnO film with respect to the dc magnetic field. The splitting of this signal into two modes is related to the nonhomogeneous profile of the cobalt concentration across the film thickness. It is well known that in systems where a gradient of the magnetization as well as a difference in the surface/interface anisotropies exists, non-uniform FMR modes could be observed [22,23]. Therefore, the splitting into two modes, observed in the perpendicular orientation, is explained by excitation of the surface/interface located modes at lower/higher fields, respectively. It should be noted that in the dose range of ($1.00–1.50\times10^{17}$ ions/cm$_2$, where the six-fold anisotropy dominates, the resonance fields and intensity of the low-field mode change only slightly, while the intensity of the high-field mode gradually increases. The latter reflects increased influence of the cobalt metal nanoparticles on the overall FMR signal upon increasing the implantation dose. A strong FMR signal with high effective magnetization, observed at the highest implantation dose of 2.00_10^{17} ions/cm^{-2}, corresponds to the formation of the percolated layer of the metal Co nanoparticles in the ZnO layer.

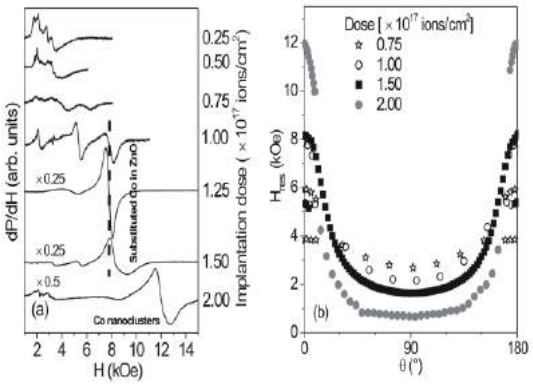

Fig.2 Out-of-plane FMR spectra (a) and the resonance field of FMR signal as a function of polar angle (b) for different cobalt implantation doses.

In order to check whether the contribution to the six-fold in-plane magnetic anisotropy originates from ZnO only, we gradually removed the ZnO layer by 500 eV Ar-beam etching and repeated the FMR measurements. When the ZnO layer is etched by about 10 nm, the six-fold symmetry of the in-plane magnetic anisotropy survives, but with a significant decrease in the magnitude of anisotropy. Besides, the signal intensity also gradually decreases with etching. For the completely etched sample the signal with six-fold symmetry completely disappears. This observation supports our conclusion that the FMR signal with the six-fold inplane magnetic anisotropy originates from the substituted cobalt in the ZnO film, rather than the cobalt nanoparticles in the Al_2O_3 substrate.

4. CONCLUSION

The magnetic anisotropies of the Co-implanted ZnO films have been investigated by FMR technique. The six-fold in-plane magnetic anisotropy of the FMR signal has been observed for the first time in ZnO (0001) thin films implanted by Co in the dose range of (1.00–1.50) $\times10^{17}$ ions/cm^2. This signal is attributed to the ferromagnetic phase formed due to long-range ordering of substitutional cobalt ions in the ZnO host matrix. We consider this finding as a strong indication for intrinsic ferromagnetism in ZnO-based DMSs.

5. ACKNOWLEDGEMENTS

We acknowledge S. Erdt-Böhm for help in the sample preparation. This work was partially supported by

DPT (State Planning Organization of Turkey) under the Grant No 2009K120730, DFG through Grant No. SFB 491, by RFBR through the Grant No. 07-02-00559-a, joint TUBITAK-RFBR Programme under Grant No. 10-02-91225-CT, and Russian Federal Agency on Education, contract P902.

---

[1]. *T. Dietl, H. Ohno, F. Matsukura, J. Cibert, and D. Ferrand*, Science 287, 1019 (2000).
[2]. *K. Sato and H. Katayama-Yoshida*, Jpn. J. Appl. Phys., Part 2 39, L555 (2000).
[3]. *K. Sato and H. Katayama-Yoshida*, Jpn. J. Appl. Phys., Part 2 40, L334 (2001).
[4]. *K. Ueda, H. Tabada, and T. Kawai*, Appl. Phys. Lett. 79, 988 (2001).
[5]. *S.J. Pearton, C.R. Abernathy, D.P. Norton, A.F.Hebart, Y.D. Park, L.A. Boatner, and J.D.Budai*, Mater. Sci. Eng., R. 40, 137 (2003).
[6]. *W. Prellier, A. Fouchet, and B. Mercey*, J. Phys.: Condens. Matter 15, R1583 (2003).
[7]. *A. C. Tuan, J. D. Bryan, A. B. Pakhomov, V.Shutthanandan, S. Thevuthasan, D.E.McCready, D. Gaspar, M.H. Engelhard, J.W.Rogers, K. Krishnan, D. R. Gamelin, and S.A. Chambers*, Phys. Rev. B 70, 054424 (2004).
[8]. *S. J. Pearton, W. H. Heo, M. Ivill, D. P. Norton, and T. Steiner*, Semicond. Sci. Technol. 19, R59 (2004).
[9]. *S. J. Pearton, D. P. Norton, K. Ip, Y. W. Heo, and T. Steiner*, J. Vac. Sci. Technol. B 22, 932 (2004).
[10]. *C. Liu, F. Yun, and H. Morkoc*, J. Mater. Sci. Mater. Electron. 16, 555 (2005).
[11]. *R. Janisch, P. Gopal, and N. A. Spaldin*, J. Phys. Condens. Matter 17, R657 (2005).
[12]. *J. J. Liu, M. H. Yu, and W. L. Zhou*, J. Appl. Phys. 99, 08M119 (2006).
[13]. *W. Pacuski, D. Ferrand, J. Cibert, C. Deparis, J.A. Gaj, P. Kossacki, and C. Morhain*, Phys. Rev. B 73, 035214 (2006).
[14]. *J. Zhang, X. Z. Li, Y. F. Lu, and D. J. Sellmyer*, J.Phys.: Condens. Matter 19, 036210 (2007).
[15]. *A. J. Behan, A. Mokhtari, H. J. Blythe, D. Score, X.-H. Xu, J. R. Neal, A. M. Fox, and G.A.Gehring*, Phys. Rev. Lett. 100, 047206 (2008).
[16]. *N. Akdogan, A. Nefedov, K. Westerholt, H. Zabel, H. W. Becker, C. Somsen, R. Khaibullin, and L. Tagirov*, J. Phys. D: Appl. Phys. 41, 165001 (2008).
[17]. *N. Akdogan, H. Zabel, A. Nefedov, K. Westerholt, H. W. Becker, S. Goek, R. Khaibullin, and L.Tagirov*, J. Appl. Phys. 105, 043907 (2009).
[18]. *N. Akdoğan, B. Rameev, S. Güler, O. Oztürk, B.Aktaş, H. Zabel, R. Khaibullin and L. Tagirov*. Appl. Phys. Lett. **95**, 102502 (2009).
[19]. *M. Ay, A. Nefedov, and H. Zabel*, Appl. Surf. Sci. 205, 329 (2003).
[20]. *A. Meldrum, L. A. Boatner, and K. Sorge*, Nucl. Instrum. Methods Phys. Res. B 207, 36 (2003).
[21]. *J. K. Lee, M. F. Hundley, J. D. Thompson, R.K.Schulze, H. S. Jung, J. A. Valdez, M. Nastasi, and X. Zhang*, Appl. Phys. Lett. 89, 182502 (2006).
[22]. *A. M. Portis*, Appl. Phys. Lett. 2, 69 (1963).
[23]. *P. E. Wigen*, Thin Solid Films 114, 135 (1984).

GIANT DIELECTRIC RELAXSATION AND CONDUCTIVITY IN ONE-DIMENSIONAL (1D) RODLIKE $TlGaTe_2$

R.M.SARDARLY, O.A.SAMEDOV, A.P.ABDULLAEV, F.T.SALMANOV
Institute of Radiation Problems, National Academy of Sciences of Azerbaijan
e_mail: sardarli@yahoo.com

Temperature-frequency dependences of dielectric permeability and conductivity of $TlGaTe_2$ crystals are investigated. Presence of a strong dielectric relaxation is revealed. It is shown, that the mechanism leading by a dielectric relaxation is connected with hoping of charges between the charged centers. It is established, that hoping character of conductivity and the mechanism of a dielectric relaxation in $TlGaTe_2$ have the identical nature.

1. INTRODUCTION

The $TlGaTe_2$ semiconductor compound crystallizes in the tetragonal space group and features a one-dimensional (1D) rodlike structure. Among the compounds of this group, the compounds TlSe and TlS (structural analogs of $TlGaTe_2$) have been most adequately studied [1–3].

The physical properties of the $TlGaTe_2$ compound were studied previously by [4-9]. The energy band structure of $TlGaTe_2$ was calculated using the pseudopotential method [4]. The calculations showed that the top of the valence band is located at the high symmetry point *T* at the surface of the Brillouin zone, while the bottom of the conduction band is located at the line *D*. The band gap obtained from performed calculations was found to be equal to 0.86 eV.

Temperature dependence of thermal capacity and the results of X-ray diffraction studies of TlGaTe2 were reported in [6,7]. Experiments were performed in the temperature range 5–300 K, the thermodynamic parameters of the crystals were calculated, and the presence of the second kind phase transition at a temperature of 98.5 K was shown. Hanias and Anagnostopoulos [8] studied the current–voltage (*I–V*) characteristics of a $TlGaTe_2$ crystal and detected the effect of negative differential resistance and voltage oscillations in the region of negative differential resistance. Photoemission spectra and the band structure of $TlGaTe_2$ were studied by Okazaki et al. [5]. Good agreement between experimental data and the results of calculations of the band structure in the flat band approximation is shown. The presence of a pseudogap in the density of states and the existence of ultimately anisotropic (1D) and rodlike structure in the crystals of this class make it possible to expect specific features in electrical conductivity; these features are related to the low dimensional type of the structure. The aim of this study was to gain insight into specific features of anisotropy of anisotropy dielectric and electric properties of $TlGaTe_2$ compound are presented at various frequencies of measuring electric field.

2. DETAILS OF THE EXPERIMENT AND DISCUSSION OF OBTAINED RESULTS

The samples of the $TlGaTe_2$ compound were synthesized by fusing the starting components (with purity no lower than 99.99%) in evacuated quartz cells; the corresponding single crystals were grown by the modified Bridgman method. Stoichiometry of the obtained compound, the single-phase characteristic, and homogeneity was controlled by the X-ray diffraction analysis and derivatographic analysis. The freshly cleaved samples to be studied with the crystallographic axis *c* oriented in the cleavage plane were of rectangular shape and had a thickness of about 0.5 mm. Indium contacts were formed on the samples; the ohmic behavior of these contacts was checked before each measurement.

For measurements of temperature dependences of dielectric permeability and conductivity of $TlGaTe_2$ crystals condensers have been made, dielectric in which plates of investigated materials served. Capacitor plates have been received by drawing of silver paste on a surface of plates. Researches of complex dielectric permeability ($\varepsilon^* = \varepsilon' + \varepsilon''$) and conductivity were measured by a digital measuring instrument E7-20 on frequencies 0.5-1000 кГц in the range of temperatures 100÷450K.

The amplitude of a measuring field did not exceed $1В \cdot см^{-1}$.

The temperature dependences of dielectric permeability and dielectric loss tangent of $TlGaTe_2$ for different frequencies (measurements are executed perpendicularly axes) are represent in Fig.1 and 2. From figures it is visible, that with temperature growth increase of value of dielectric permeability ε' is observed. And, the above frequency of a measuring field, the later begins growth ε'. Apparently, from figures, value of temperature dependence of dielectric permeability remains invariable to temperatures $\approx$ 200K and is equal $\varepsilon' \approx 40$, in all measured range of frequencies. At temperatures 275 and 340K two features $\varepsilon'(T)$ and two maxima $tg\delta(T)$ are observed. With growth of frequency of a measuring field of feature on curves $tg\delta(T)$ and $\varepsilon'(T)$ are displaced to higher values of temperature, and their size to down.

Characteristic property of crystals $TlGaTe_2$ is that they represent chains Ga - Te extended along a tetragonal axis **c**. The tetragonal axis is an optical axis. From crystal chemistry reasons it is possible to believe, that structure of $TlGaTe_2$ to the greatest degree favour to mobility of Tl^+ cations. As the favorable factor presence of the extensive cavities incorporating among themselves through the general sides-windows of conductivity, and also basic possibility of existence of surplus on Tl^+ here acts.

Such ambiguity on Tl^+ is capable to strengthen essentially frequency dependences of dielectric permeability of $TlGaTe_2$ crystal.

The received dependences $\varepsilon'(T)$ and $tg\delta(T)$ have obviously expressed features, characteristic for relaxes processes Debay type with participation of many relaxors.

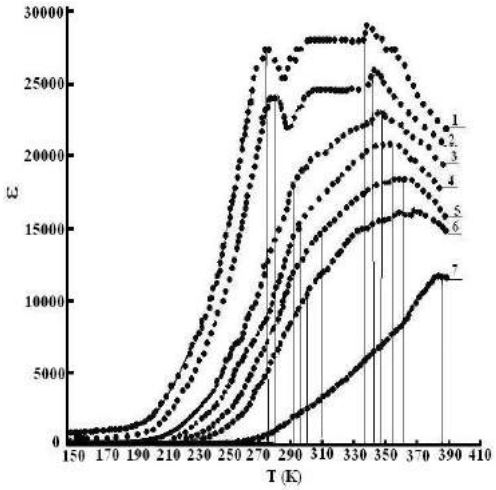

Fig.1. Temperature dependences of the permittivity of $TlGaTe_2$: 1-0, 2-1, 3-20, 4-50, 5-100, 6-500, 7-1000 kHz.

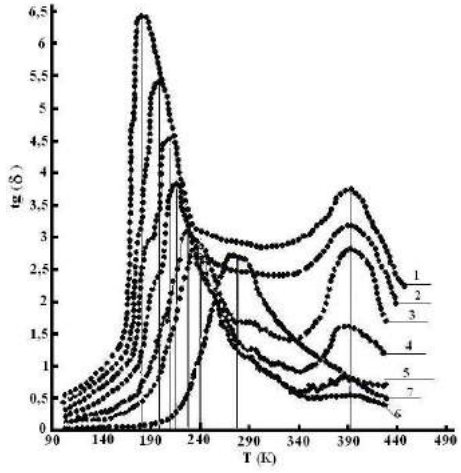

Fig.2. Temperature dependences of the dielectric loss tangent of $TlGaTe_2$: 1-0, 2-1, 3-20, 4-50, 5-100, 6-500, 7-1000 kHz.

In the field of temperatures, where anomalies ε'(T) and tgδ(T) take place, it was not possible to receive Cole's – Cole diagram's in the form of simple monotonous dependences (close to linear) an imaginary part of complex dielectric permeability from valid ε"(ε'). Most likely, it is caused by considerable distinction of parameters and a lot of relazors (Fig.3). At the given stage it is present possible to describe received related to linear dependence ε"(ε') within the framework of universal Djovanshir low for dielectrics based on the power approach [9]. In his model polarization connect with jumps of ions or electrons on long or short chains. Discrete displacement of charges is accompanied by shielding of arising polarization owing to of a lattice relaxation.

According to this model, frequency dependence of conductivity on an alternating field looks like:

$$\sigma(\omega) \sim \omega^n$$

ω - circular frequency provided that $0 < n < 1$. Similar dependences connect with hopping mechanism of the conductivity realized as result of jumps of carriers on localized power conditions near the Fermi level. The size of n depends on spatial and power distribution of these conditions. The frequency dispersion of a dielectric susceptibility is defined by vibration properties of local conditions and depends on dynamics electrons on the impurity levels.

In fig.4 results of researches of frequency dependence conductivity of $TlGaTe_2$ crystal in alternating electric field are resulted at T=287K. As can be seen from figure, in the field of frequencies of 10^2-10^6 Hz conductivity changes under the law close to $\omega^{0,8}$. It testifies about hopping mechanism of carrying over of a charge on the conditions localized in a vicinity of Fermi level [10].

Temperature dependences of conductivity $TlGaTe_2$ has been investigated by us in [11]. Conductivity essentially depends on frequency of measurements that testifies about hopping mechanism of conductivity. On dependence lg□ from 10^3/T it is observed long exponentially part with an inclination ΔE^{σ} =0,21эВ [11] in the 210□300K temperature range. At temperature pulldown below then 250K energy of activation of conductivity had no constant inclination, i.e. continuously decreased with reduction of temperature up to 200K.

Conjunction of temperature part of increase of dielectric permeability and conductivity, energy activation both of increase of capacity ΔE^{C} =0,21eV and conductivity ΔE^{σ} = 0,21eV [11] and presence of frequency dependences of capacity and conductivity can testify that all processes enumerable above are defined hopping exchange of charges between defects.

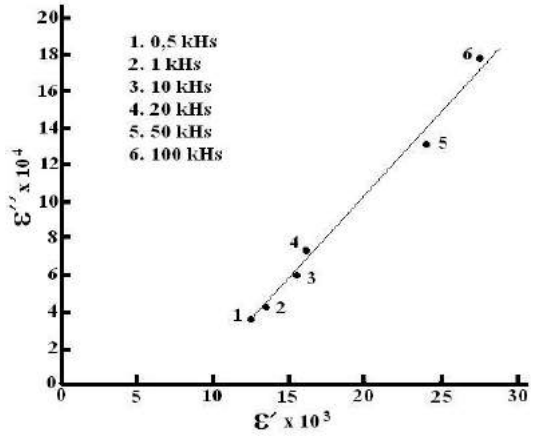

Fig.3. Cole-Cole plot of the complex dielectric constant of $TlGaTe_2$

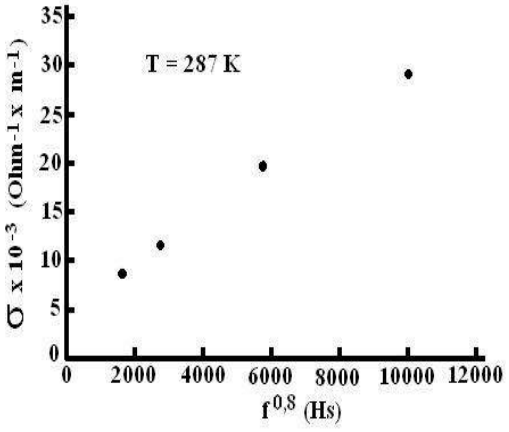

Fig.4. Frequency dependence conductivity of $TlGaTe_2$.

In order that hopping recharges there was so essential increase of dielectric permeability (more than in 1000 times fig.1), concentration of defects of an order $10^{18} \div 10^{20}$ sm^{-3} [12] are necessary.

It is necessary to notice, that such, rather high concentration of the localized conditions in the forbidden zone it is characteristic for crystals of group A^3B^6 and $A^3B^3C^6_2$ [13-16], have a layered and chained structures. The question connected with the reason of so high concentration of own defects in extremely anisotropic crystals bring up each time, both at measurements conductivity, and at research of dielectric properties. According to [15], hopping conductivity in layered crystals GaSe and GaS is connected with anion vacancies, the assumption also, that such conductivity is caused by the defects forming chains in interlayer space. According to [17,18], the reason of deficiency of structure can be presence of wide area of homogeneity of crystals of group $A^3B^3C^6_2$ reaching to 6-8 pier. %. The factor of segregation in the field of homogeneity is less than unit, therefore at cultivation of crystals there is a high probability of a deviation of structure from stoichiometry. It will be occurrence of a considerable quantity of defects of joining of layers, vacancies, dislocations.

Thus, translation invariance of a crystal lattice will be broken, and as consequence there will be localized conditions with energy, getting to an interval of the values forbidden in an ideal crystal. According to work [13] where shown, that in crystal $TlGaTe_2$ of concentration of defects exceeds $10^{18}см^{-3}$. Presence of such defects is attributed high density of conditions near to Fermi's level. The energetic level generated by various defects in crystals, play the basic role in the phenomena of carrying of a charge. Energy of activation which defines width of a band energy near to Fermi's level on which, there are jumps of carriers of a charge, represents practically all conductivity.

Thus, in the $TlGaTe_2$ crystals charge carrying accomplish by means of jumps of carriers of a charge on localized by conditions near to Fermi's level energetically more favorable though spatially more remote, that is characteristic for hopping conductivity with variable length of a jump. Hopping the exchange electrons between defects in a crystal leads to occurrence of dipoles and consequently to growth of dielectric permeability. Their hopping the recharge also can lead to growth of dielectric permeability and a dielectric loss tangent of $TlGaTe_2$. It is shown, that in the field of temperatures where anomalies $\varepsilon'(T)$ and $\varepsilon''(T)$ take place was not possible to receive Cole-Cole plot. Dependence of an imaginary part of complex dielectric permeability from valid $\varepsilon''(\varepsilon')$, submits to the linear law (close to linear) on visible, it is caused by considerable distinction of parameters of the relaxors.

[1]. *S.B. Vakhrushev, B.E. Kvyatkovskii, N.M. Okuneva, K.R. Allakhverdiev, V.I. Slisenko, and R.M. Sardarly*, Fiz. Tverd. Tela 26, 1225 (1984) [Sov. Phys. Solid State26, 746 (1984)].

[2]. *M.V. Belousov and R.M. Sardarly*, Fiz. Tverd. Tela 27,662 (1985) [Sov. Phys. Solid State 27, 410 (1985)].

[3]. *A.M. Panich and R.M. Sardarly* "Physical properties of the low dimensional A^3B^3 and $A^3B^3C^6_2$ compounds" NOVA Science Publishers, NY USA, 2010, 310p.

[4]. *E.M. Godzhaev, G.S. Orudzhev, and D.M.Kafarova*, Fiz. Tverd. Tela 46, 811 (2004) [Phys. Solid State 46,833 (2004)].

[5]. *K. Okazaki, K. Tanaka, J. Matsuno, A.Fujimori, L.F. Mattheiss, S. Iida, E. Kerimova, and N.Mamedov,* Phys.Rev. B 64, 045210 (2001).

[6]. *V.A. Aliev, M.A. Aldzhanov, and S.N. Aliev,* Pis'ma Zh.Eksp.Teor.Fiz. 45, 418 (1987) [JETP Lett. 45, 534 (1987)].

[7]. *G.D. Guseinov, A.M. Ramazanzade, E.M.Kerimova, and H.Z. Ismailov*, Phys. Stat. Solidi 22, 117 (1967).

[8]. *M.P. Hanias and A.N. Anagnostopoulos*, Phys. Rev. B47, 4261 (1993).

[9]. *A.R. Jonscher*. Scientific papers of the Institute of Electricals Engineering Fundamentals. Seria Wspolpraca 16, 1, 5(1977).Wydavnictwo Politechnik Wroclawskiej, Wroclaw.

[10]. N.*F. Mott and E.A. Davis* Electronic Processes in NonCrystalline Materials (Clarendon, Oxford, 1979; Mir,Moscow, 1974).

[11]. *R.M. Sardarly, O.A. Samedov, A.P. Abdullaev, E.K.Huseynov, F.T. Salmanov, G.R. Safarova* FTP 2010, vol. 44, No. 5, pp.610-614 [Semiconductors, 2010, Vol. 44, No. 5, pp/1-5].

[12]. *P.W.Zukowski, S.B.Kantorov, K.Kiszezak, D.Maczka, A.Rodzik, V.F. Stelmakh, E.Czarnecka Such.* Phys.St.Sol. (a),128,117 (1991).

[13]. *S.N. Mustafaeva, B.A.Aliev, M.M.Asadov,* Fiz. Tverd. Tela 40,612(1998).

LONG-TERM RELAXATION EFFECTS IN GALLIUM MONOSELENIDE DOPED BY HOLMIUM AND GADOLINIUM

A.Sh. ABDINOV, R.F. BABAYEVA*
Baku State University
Baku, AZ1148, Z. Khalilov str., 23
**Azerbaijan State Economical University*
E-mail: abdinov-axmed@yandex.ru,
abdinov_axmed@yahoo.com, Babaeva-Rena@yandex.ru.
Babaeva-Rena@yandex.ru.

The kinetics of dark current in pure and alloyed by rare-earth elements of Gd and Ho, with $10^{-5} \le N \le 10^{-1}$ at.% of the p-GaSe crystals, under different external conditions have been investigated. It has been established that at low temperatures ($T \le 150$ K) the dark current is relaxed slowly up to stationary values. The course of dependence of current on the time at that, at different temperatures shows different character (decreasing and increasing). Besides, that at long keeping the samples under the action of an external voltage higher than some boundary value the effect of electric fatigue appear. The model qualitatively explaining results received is offered.

EXPERİMENT

In this paper the results received at experimentally investigation of long-term relaxation effects in GaSe and effect of low alloying ($N \le 10^{-1}$ at %) by holmium and gadolinium on this effects are reported. Investigated samples were cut off from large *p*-GaSe <Gd> and *p*-GaSe <Ho> ingots, alloyed with REE with different content of the introduced impurity ($N = 10^{-5} \div 10^{-1}$ at. %).

RESULTS AND DISCUSSION

It is established at investigations that in studied samples at $T \le 150$ K at the moment of switching-on of the external voltage the establishing process of stationary dark current value exhibit slow ("transient") character. And rate and type of a relaxation besides various external factors (value and duration of an applied electrical voltage, light, temperature) depend also from initial dark specific resistance (ρ_{DR}) and an alloying level (N) of the crystal.

With increasing the temperature (T) process of a relaxation is accelerated, and with growth of ρ_{DR} is slowed down. The peak value change of the current also depends on ρ_{DR} ($|\Delta i| = |i_{so} - i_0|$, where i_0 and i_{so} are value of the dark current at the moment of switching-on of the external voltage and after stabilization of the current, accordingly). In not alloyed specially and in alloyed by lanthanides crystals at relatively small and higher voltages decaying relaxation (fig. 1, curves 1, 3 and 4, accordingly) is observed whereas at average values of U the rising relaxation (fig. 1, a curve 2) prevails. Character and a rate of the relaxation, as well as $|\Delta \boldsymbol{i}|$ value vary also with change of doping degree, but do not depend almost on the chemical nature of the introduced impurity. After the setting of the stationary value of the dark current, at long influence of a small external voltage, the value of $|\Delta \boldsymbol{i}_{so}|$ does not vary (fig. 1, curves 1-3).

However at long influence of an external voltage, greater some boundary (U_b) value in investigated crystals at $T \le T_k$ (where depending on the doping degree value of T_k varies in the 250 ÷ 300 K range) the decaying relaxation of the dark current is observed, i.e. the current through the sample slowly falls down from $\Delta \boldsymbol{i}_s$ to some quazi-stationary $i_s < i_{so}$ values (fig. 1, curve 4). Thus, rate of the decaying process and value $\Delta i = i_{so} - i_s$ appear dependent on the temperature, as well as on the value of applied voltage and doping level.

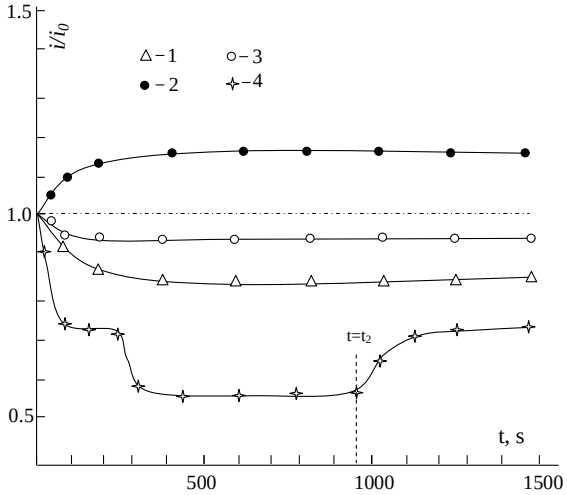

Fig. 1. Kinetics of the dark current in *p*-GaSe<Ho> crystals at different values of an external voltage. U, V: 1 - 20; 2 - 30; 3 - 40; 4 - 60. $N = 10^{-4}$at. %, T = 77 K.

It is established that process of the relaxation of the dark current from i_{so} to i_s does not depend on polarity as well as the type of the voltage applied to a sample. Both in pure and doped crystals the state with i_s has storage character – at $T \le T_k$ after switching-off the voltage $U \ge U_b$ (fig. 1, curve 4 at $t=t_2$) the initial state of the sample is restored slowly. However it can be erased by thermal or optical erasing accordingly. At thermal erasing it is enough initially to heat a sample to $T \ge 350$ K and then to cool sharply by immersing in liquid nitrogen.

With increasing of applied voltage the value of $\frac{i_s - i_0}{i_0}$ increases initially and further increases (fig. 2, curve 1). The dependence of $\frac{i_{so} - i_0}{i_0}$ on the doping level also in nonmonotonically- grows initially with N and

further, passing the maximal value (at $N_{REE} \approx 10^{-4}$ at. %) falls. The value of $\gamma = \frac{i_{so} - i_s}{i_{s0}}$ also depend on the applied voltge and doping level. The effect of the material of introduced impurity on this phenomenon under these conditions was not revealed not.

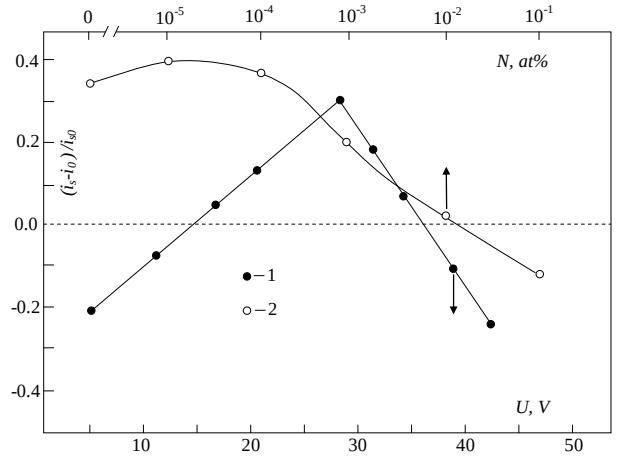

Fig. 2. Dependence of $\frac{i_{so} - i_s}{i_{s0}}$ on the applied voltage (curve 1) and doping level (curve 2) in *p*-GaSe<Ho> crystals N, at.%: 1 - 10^{-4}; U, V: 2 - 35; T = 77 K

It was shown elsewhere [1] that in the band gap of *p*-GaSe various type (shallow α- and deep β- [2]) trapping levels and (fast S-and slow r-[2]) recombination centers exist those are spatially separated by recombination barriers creating drift barriers in the volume of the sample.

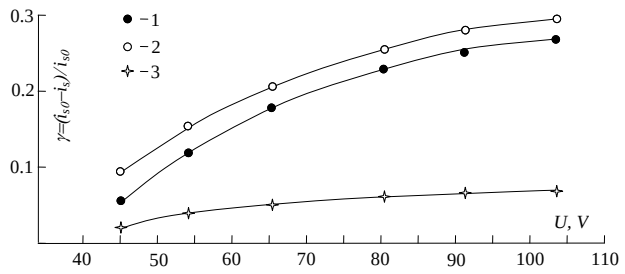

Fig. 3. Dependence of $\gamma = \frac{i_{so} - i_s}{i_{s0}}$ on voltage in *p*-GaSe<Ho> crystals with different level of doping N, at.%: 1 - 0; 2 - 10^{-4}; 3 - 10^{-1}; T = 77 K

We assume that at these semiconductors character of interaction of free charge carriers with defects depends on the external voltage. At relatively low U, because of prevalence of their capture by trapping centers it is observed stabilization of the dark current by the decaying relaxation. At average U, though interaction the carrier-the trapping center is considerably weakened, however because of gradual erasing drift barriers owing to increase of the injection level a process of relaxation of the dark current of rising character is observed. With the further increase of voltage capture of the free charge carriers by the repulsive centers starts to prevail - anew prevails decaying relaxation of the dark current but other origin.

At doping of *p*-GaSe with lanthanide atoms of Gd and Ho, initially (at small N) owing to increase of drift barriers the rising relaxation dominates. Further (at N>10^{-4} at. %) because of gradual rectification of potential fluctuations in the crystal it is replaced by decaying and/or slowly rising relaxation owing to prevalence of interaction of charges with the dot trapping centers of attracting (at relatively small voltages) and/or repulsive (at higher voltages) character.

Though at long effect on the semiconductor of the external voltage with constant value, greater some boundary value may take place decay of the dark current connected with different physical processes (polarization, phase transformations, ageing of the material). However lag, storage character, an opportunity of erasing and different futures for the found out by us dark current from i_{so} to i_s identically testify to electric fatigue of the investigated crystals. We assume, that when an external voltage $U \geq U_b$ effects on the sample for a long time owing to easing potential fluctuation in a crystal the height of the recombination barriers decreases and part of charge carriers overcoming these barriers and their hit in high-resistance region, which here they are captured by β-trapping centers. Last in turn causes growth of concentration of minority charge carriers (electrons) on the fast recombination centers and accordingly, recombination rate of the majority charge carriers. Therefore conductivity of the sample gradually decreases and a current through it decreases from i_{so} to i_s. After the termination of the effect of an external voltage or its reduction to the value $U < U_b$, the charge carriers captured at β-levels are released gradually and consequently initial (high-conductive) state of the sample is restored considerably slowly. It is established, that thus characteristic time for the process of restoration of an initial state of the sample itself appears dependent on time and increases with time. The initial value of conductivity is restored only after releasing all charge carriers captured on β-levels - after full rest of the sample. Within the framework of this model emergency returning of the sample into initial high-conductive state by heating or illumination of the sample by extrinsic light with $\varepsilon_g > h\nu_n > \varepsilon_\beta$ (where ε_g and ε_β are a width of the band gap of the investigated material and energetic depth of β-levels, accordingly), most likely occurs owing to thermal, or optical emptying of β-levels. Energetic depth of β-levels determined from optical erasing spectrum of the electric fatigue state is equal $\varepsilon_\beta = \varepsilon_v + 0.60$ eV. This value is in a good agreement with the values found from other measurements [1].

Within the framework of the offered model, the influence of doping with REE on electric fatigue effect in p-GaSe crystals can be explained by corresponding dependence of a degree of order of crystals on the doping level [3].

It is known, that in layered crystals p-GaSe along an axis "C" of crystals prevails the weak molecular, and along the "C" plane of crystal dominates strong ionic-

covalence connection. Therefore during cultivation of ingots, chipping them on separate pieces, manufacturing of samples and creation of current contacts the occurrence of appreciable mechanical infringements of ideal layered structure of crystal in separate places of the sample is unavoidable. It is natural that these infringements have chaotic on the location and microscopic from the points of view of electronic processes character. As a result of all this, investigated samples of monocrystals p-GaSe finally it is possible to consider as a whole as the ordered layered crystal system chaotic large-scale (macroscopical) infringements (defects). Such partially disorder of the sample leads to fluctuation of potential inside of it, similarly to partially-disorder crystal consisting in whole of low-resistance matrix (LR) with chaotic macroscopical high-resistance inclusions (HR). Thus on borders LR and HR arise recombination, and between next HR consequence partial overlapping of potentials of their volumetric charges - drift barriers.

We assume, that at doping by lanthanide atoms of type Gd or Ho all over again (at weak levels of doping, i.e. $N \leq 10^{-4}$at.%) ions of the entered impurity under action of an internal electric field recombination barriers, accumulate around HR and consequently, with growth of N the geometrical sizes HR increase. Accordingly increases both size, and influence of drift barriers on current passage process. This told finds the acknowledgement in the found out dependences of character of dark current on the doping level. In particular, at an establishment of stationary value of dark current after inclusion of an external voltage range of an external pressure voltage where the increasing relaxation is observed extends aside more great values of voltage. In case of electric fatigue, with increasing of N up to ~10^{-4}at. %, value of a boundary voltage (U_b) increases. However, thus dependence of U_b on the N is caused by increasing of recombination barriers with N since with increase in the sizes of HR the height of recombination barriers and accordingly for maintenance of overcoming with free carriers of these barriers grows also and their hits to HR where are grasped by deep levels of β-sticking higher external voltage is required. At the further increase of doping level (at $N>10^{-4}$ at. %) because of increase in the HR sizes, the next macroscopical defects are almost blocked also the sample behaves as quasihomogeneous semiconductor. In this case with increasing N influence of potential barriers on long-term relaxation electric effects in investigated samples gradually is weakened and at last, almost disappears. Besides with increasing of doping level the density of atoms of the entered impurity in layers of the sample increases and begins is shown effective interaction of ions of the impurity which are being the next layers and the significant image is ionic-covalence amplifies connection between the next layers of a crystal. Owing to the last the probability of occurrence of chaotic macroscopical defects in the sample decreases, also is weakened caused with presence of these defects or partial disorder of a crystal effects.

The offered model will qualitatively well be agreed with obtained by us at experimental results on long-term relaxation electric effects in layered crystals GaSe, alloyed by atoms Gd and Ho with $N=10^{-5} \div 10^{-1}$at.%.

[1]. *A.Sh.Abdinov, A.H.Kyazym-zade, A.A. Ahmedov* Negative residual conductivity in single crystals of p-GaSe//Semiconductors, 1978, v.12, N9, p.1759-1762.

[2]. *S.M. Rivkin* Photoelectrical phenomenon in semiconductors, M., Nauka, 1963,- 445 p.

[3]. *R.A.Babaeva* Abstract of a doctoral thesis, Baku, 2009, -38 p.

CURRENT OSCILLATIONS IN TWO-VALLEY SEMICONDUCTORS.

RASOUL NEZHAL HOSSEIN, E.R.HASANOV, K.B.GURBANOV

[1]*G.M. Abdullayev Institute of Physics of Azerbaijan National Academy of Sciences*
AZ-1143, G.Javid ave., 33, Baku, Azerbaijan
[2]*Baku State University,*
AZ-1148, Z.Khalilova str. 23, Baku, Azerbaijan

The frequencies of current oscillations are obtained. The theory of oscillation appearance in two-valley semiconductors of GaAs type in strong external electric and magnetic fields is constructed.

For simpleness let's consider the spatially homogeneous crystal [1-7]. In this case the current density is described by the expression:

$$j = \sigma E;\ \sigma = en\mu = \sigma(T_e) \tag{1}$$

and equation $j = j(E)$ defines the volt-ampere characteristic of considered sample the graphic picture of which is usually given in coordinates *(j,E)*. At condition at which Ohm's law is applied, the plot of function *j(E)* is the direct line passing through origin of coordinates with angular coefficient σ_0 which is equal to conduction value in weak field

As a result of heating of electron gas the volt-ampere characteristic becomes the non-linear one and for its description it is comfortable to introduce the concept of differential conductionσ_d.

When σ is scalar the σ_d value is defined by equation:

$$\sigma_d(E) = \frac{dj}{dE} = \sigma + E\frac{d\sigma}{dE} \tag{2}$$

Using the equilibrium equation:

$$\sigma E^2 = n\frac{T_e - T}{\tau_e} \tag{3}$$

and introducing the variable $R = \left(\frac{T_e - T}{\tau_e}\right)$ we obtain $\sigma E^2 = nR$. The nR value is energy given by current carriers in the lattice in unit of volume. As μ is mobility, n is concentration and τ_e is time depend on temperature T_e then:

$$\sigma_d = \sigma + E\,\frac{d\sigma}{dT_e}\frac{dT_e}{dE} \tag{4}$$

Differentiating over E the expression (3)

$$\frac{dT_e}{dE} = \frac{2\sigma E}{\frac{d(nR)}{dT_e} - E^2\frac{d\sigma}{dT_e}}, \tag{5}$$

substituting (5) into (4) and changing E^2 on $\frac{nR}{\sigma}$ we obtain:

$$\sigma_d = \sigma\,\frac{\frac{d(nR)}{dT_e} + \frac{nR}{\sigma}\frac{d\sigma}{dT_e}}{\frac{d(nR)}{dT_e} - \frac{nR}{\sigma}\frac{d\sigma}{dT_e}} \tag{6}$$

In dependence on the fact that the formula (6) increases or decreases on field strength, the plot of volt-ampere characteristic $j(E)$ will be inclined up or down from direct line $j=\sigma_0 E$. The corresponding volt-ampere characteristics of both types have the following form:

In case of *N*-type characteristic the differential conduction changes the sign passing zero (the numerator in (6) changes the sign). In case of S-type characteristic the differential conduction changes the sign passing the singular point in which the denominator in (6) takes zero value.

The formation conditions of characteristics of both types are easily found from formula (6):

for *N* – type characteristics

$$\frac{n^2\mu}{\tau_e} + (T_e - T)\frac{d}{dT_e}\left(\frac{n^2\mu}{\tau_e}\right) = 0 \tag{7}$$

for *S* – type characteristics

$$1 - \left(\frac{T_e - T}{\tau_e\mu}\right)\frac{d(\tau_e\mu)}{dT_e} = 0 \tag{8}$$

From formula (7) it follows that with increase of electron temperature the product of mobility on concentration of charge carriers should rapidly decrease, moreover T_e should enough exceed the T lattice temperature. In second case (condition (8)), the energy given by electrons in unit of time should rapidly decrease with increase of electron temperature, moreover the overheating $(T_e - T)$ shouldn't be very small one.

One can consider the following facts:

- In homogeneous *n-GaAs* the appearance of N-type characteristic is expected at room temperature. The negative differential conductivity should appear at field strength E≈2300V/cm and disappear at E≈10000V/cm.
- In *n-Ge* doped by aurum or cuprum at lattice temperature 30-35K also should appear the characteristic of N-type.

It is obvious that conception on spatial inhomogeneity in average doesn't exclude the local deviations of physical values from their average ones. The fluctuations of charge carrier concentrations and electric field strength are caused by random heat motion of charge carriers by other hand and by spontaneous homogeneities in distribution of impurity atoms and other structural defects of crystal lattice. In the case when charge carriers are in the state of thermodynamic balance or close to it the presence of these fluctuations weakly influences on transfer phenomenon. However, the situation can change if charge carriers are strongly "heated".

Then at fluctuation of electric field ΔE the fluctuation of charge carrier density should appear and according to Poisson equation it equals to following expression:

$$\Delta\rho = \frac{\varepsilon}{4D} div\, \Delta E \qquad (9)$$

and the current fluctuation has the following form:

$$\Delta j = \sigma_d \Delta E \qquad (10)$$

From this it follows that for $\sigma_d > 0$ and $\sigma_d < 0$ cases the charge inflow into fluctuation region changes and fluctuations can either damp or increase, correspondingly.

Thus, in homogeneous crystal the regions of strong and weak fields can appear, moreover, the distribution of electric fields and charge carriers will be fluctuationally instable, correspondingly. These regions so-called domains can form in any point of homogeneous crystal under influence of heat fluctuations and transfer along crystal until they disappear in one of contact electrodes. The domain path velocity essentially depends on mechanism responsible for their appearance in detail for appearance of negative differential conduction and it is possible the observance of such types of non-linear processes as drift and recombination ones.

Note that multi-valley semiconductors in the mechanism of drift nonlinearity the field dependence of mobility plays the main role. In this case the domain path velocity is drift one of majority carriers in weak field. In the mechanism of recombination nonlinearity the processes of capture and generation of charge carriers play the main role. In the dependence on field strength values the relation of concentrations of free and bound charge carrier changes. The domain movement is caused by redistribution of charge carriers between band and capture levels. This process limits the domain path velocity which as a result can be essentially less than drift one.

So in *n-Ge* doped by aurum the domain path velocity at *T=20K* varies in interval 10^{-5} - 10^{-2} cm/sec.

During domain movement along technologically homogeneous sample, the current doesn't change. Achieving to electrode the domain destroys that leads to current increase in the electric circuit. The appearance of new domain on another electrode leads to new current decrease in the electric circuit. This cyclic process of origin, motion and destroy of domains leads to periodic current oscillations in electric circuit load. The current oscillation frequency ω is easily evaluated. If v_d is domain path velocity, *L* is sample length in current direction, then domain time of flight through sample is equal to $t = \frac{L}{v_d}$. From this it follows that

$$\omega = 2\pi \frac{v_d}{L} \qquad (11)$$

In *n-GaAs* the oscillation frequency varies in interval $5\cdot10^8 \div 5\cdot10^9$ Hz.

The oscillation appearance in *n-GaAs* and in similar materials was firstly observed by Gunn and nowadays is widely used in micro-semiconductor electronics at development of microwave generators.

The current oscillations in external magnetic field in two-valley semiconductors of GaAs type had been firstly studied by Gunn. Beginning from given value of electric field, the current oscillations with microwave frequency $\omega \sim 10^9 \div 10^{11}$Hz appear. This effect is studied in many theoretical works only near threshold, i.e. when differential conductivity $\sigma_d = \frac{dj}{dE} = 0$ (*N* -type characteristics).

When conductivity becomes negative one, i.e. $\sigma_d < 0$ the distribution of electric field *E* in crystal becomes inhomogeneous one, the strongly expressed electric field regions, i.e. domains form. Moreover, the amplitude of current oscillations from some moment begins to depend on time, the task becomes nonlinear one and its theoretical solving becomes the complex one. In this part the some results of theoretical investigations of nonlinear Gunn effect in region $\sigma_d < 0$ at presence of constant electric field will be discussed [8-9].

Let's total concentration of charge carriers is as follows $N = n + n$, the mobilities of charge carriers μ and μ', diffusion coefficients *D* and *D'* satisfy the following conditions:

$$D \gg D';\ \mu \gg \mu';\ n \gg n';\ n = fN = f(E)N(E)$$
$$f(E) = (m-1)\left[m - 1 + \left(\frac{E}{E_a}\right)^m\right]^{-1} \qquad (12)$$

Parameter *m* is calculated from experimental data as the relation of ohmic current to actual one in point $E_0 = E_a$ ($\sigma_d \neq 0$).

The rate of σ dynamic conductivity to conductivity in weak field σ_0 has the form:

$$S_0 = \frac{\sigma}{\sigma_0} = \frac{1}{\sigma_0 E_a}\frac{df_0}{dx_a} = \left(f_0 + x_0 \frac{df_0}{dx_a}\right) \qquad (13)$$

Since $x_0 = \frac{E_0}{E_a}$ then in the point of zero inclination we have $x_0 = 1;\ f_0 = -\frac{df_0}{dx_a}$ and static current in it is as follows:

$$\mathcal{J}_p = \frac{m-1}{m}\sigma_0 E_a;\quad m = \frac{1}{1 - \frac{\mathcal{J}_p}{\sigma_0 E_a}} \qquad (14)$$

The dynamics of current passage through sample is described by following equations:

$$\mathcal{J} = efN\mu E + De\frac{\partial(fN)}{\partial x};\ \frac{\partial \mathcal{J}}{\partial x} = e\frac{\partial N}{\partial t}$$
$$\mathcal{J}_1 + \varepsilon\frac{\partial E_1}{\partial t} = 0;\ u_0 = -\mu E_0 \qquad (15)$$

Supposing $\mathcal{J} = \mathcal{J}_0 + \mathcal{J}_1;\ E = E_0 + E_1;\ N = N_0 + N_1$ and all inclinations from equilibrium values have the following form: $(E_1, \mathcal{J}_1, N_1) \sim e^{i\omega t}$. From equation (15) for all values $(E_1, \mathcal{J}_1, N_1) \lesseqgtr (E_0, \mathcal{J}_{10}, N_{10})$ and $y = \frac{N_1}{N_0}$ we obtain:

$$\frac{\partial^2 y}{\partial t^2} + \omega_0^2 y = \frac{\sigma_0 f_0}{\varepsilon\,\omega_0}\Phi\left(y, \frac{dy}{dt}, \frac{d^2y}{dt^2}\right) \qquad (16)$$

Here $\omega_0^2 = \frac{\sigma_0 f_0}{\varepsilon}(ku_0 + Dk^2)$. Let's introduce the designations: $r = \frac{\sigma_0 f_0}{\varepsilon\omega_0}$ and $\tau = \omega_0 t$. From this it follows that equation (16) is to equations of Van-der-Pole type

$$\frac{\partial^2 y}{\partial t^2} + \omega_0^2 y = \mathrm{rF}\left(\mathrm{y}, \frac{\mathrm{dy}}{\mathrm{dr}}, \frac{\mathrm{d}^2\mathrm{y}}{\mathrm{dr}^2}\right) \qquad (17)$$

For crystal GaAs r is small parameter ($r<<1$), $D = 130\frac{sm^2}{s}$, $u_0 \approx 10^7\frac{sm}{s}$, $\omega_c = \frac{\sigma_0}{\varepsilon} \approx 10^{12}s^{-1}$.

The solution (17) at $r=0$ has the form $y = a(0)cos(\tau + \theta) = a\cos\psi$. To solve the differential equation (17) at value $r\neq 0$ let's use Bogolubov-Mitropolsky's method:

$$\frac{da}{d\tau} = rA_1(a) + r^2A_2(a)_+;$$

$$\frac{d\psi}{dt} = \omega_0 + rB_1(a) + r^2B_2(a) + \cdots; \qquad (18)$$

$$A_1(a) = -\frac{\omega_0}{2\pi}\int_0^{2\pi} F\left(y, \frac{dy}{d\tau}, \frac{d^2y}{d\tau^2}\right)\sin\psi d\psi;$$

$$B_1(a) = -\frac{\omega_0}{2\pi a}\int_0^{2\pi} F\left(y, \frac{dy}{d\tau}, \frac{d^2y}{d\tau^2}\right)\cos\psi d\psi$$

Let's confine ourselves by second approximation and after easy calculations we obtain:

$$a_1 = a_0 exp\left(\frac{r}{2}\left[\frac{m(1-f_0)Dk\varepsilon}{u_0}\right]\omega t\right) \qquad (19)$$

$$a_2 = \frac{a_0}{\left[exp\left(-\frac{mDk\sigma_0 f_0}{2u_0}t\right) + \frac{m\omega_0 Dk\varepsilon}{4\varepsilon k u_0 u_0}a_0^2\right]} \qquad (20)$$

From (19) it follows that when external field satisfies to condition $E_0 > E_a\left(\frac{2u_0}{3Dk\varepsilon}\right)^{1/2}$ then the amplitude increases in first approximation and in second approximation $a_2 \to \left(\frac{4\varepsilon k u_0}{m\omega_0}\cdot\frac{u_0}{Dk\varepsilon}\right)^{1/2}$ tends to constant (limiting) value.

For current density propagating in crystal in external electric $\overrightarrow{E_0}$ and magnetic $\overrightarrow{H_0}$ fields let's write the following equation:

$$\vec{j} = en\mu\vec{E} + en\mu'\left[\vec{E}\vec{H}\right] + eD\nabla\vec{n} + \mathrm{eD}'\left[\nabla\vec{n}\vec{H}\right] \qquad (21)$$

One can chose the following geometry for electric and magnetic fields: $\overrightarrow{H_0} = H_{0z}\vec{h}$, $\overrightarrow{E_0} = E_{0x}\vec{i}$ where $\vec{h}$ and $\vec{i}$ are unit vectors along z and x axes. Van-der-Pole equation at presence of magnetic field has the following form:

$$\frac{\partial^2 R}{\partial t^2} + \omega_0^2 R = r\Phi\left(R, \frac{\partial R}{\partial t}\right); R = \frac{n'}{n_0}$$

$$r = \frac{\omega_0}{k_x u_0} \ll 1;\ \omega_0 = \left[\frac{\sigma_0 f_0\,(ku_0 + k_x^2 D^+)}{\varepsilon}\right]^{1/2};$$

$$\Phi = \omega\frac{\partial \mathrm{R}}{\partial \mathrm{t}}\left[\frac{\mathrm{f_0\,m(1-f_0)\sigma_0 D' k_x(1+R)}}{\mathrm{u_0\omega_0}} + \mathrm{mR(f_0-1)} - \mathrm{m} - 1\right]$$

$$+\left(\frac{\partial \mathrm{R}}{\partial \mathrm{t}}\right)^2\frac{\mathrm{m(1-f_0)+R+2}}{\mathrm{ku_0\omega_0}} \qquad (22)$$

From (23) we find the amplitude:

$$A = A_0 e^{-\frac{r\omega_{0\gamma t}}{2}}$$

$$\gamma = 2r + \frac{\sqrt{2}}{f_0^2}\cdot\frac{H_0}{H_{char.}} + \frac{k_x D}{f_0 u_0} + \frac{\sqrt{2k_x D'}}{f_0^2 u_0}\left(\frac{L_x}{L_y} - 1\right) \qquad (23)$$

The crystal is in instable state at appearance of current oscillations and at definite magnetic field strength $\overrightarrow{H_0}$ the wave the frequency of which can be defined in nonlinear approximation from the solution of following equation

$$\frac{\partial^2 R}{\partial t^2} + \omega_1\frac{\partial R}{\partial t} + \omega_2^2 R = 0 \qquad (24)$$

where ω_1 and ω_2 are character frequencies

From equation solution it follows that the external magnetic field strength varies in interval

$$H_1 < H_0 < H_2$$

where

$$H_1 = \frac{\sqrt{2m}}{m-1}H_{char.};$$

$$H_2 = H_{char.}\cdot\frac{u_0 L_x}{D}\left[\frac{mu_0}{2\pi L_x\sigma_0(m-1)}\right]^{1/2}$$

The wave frequencies

$$\omega_0 = \frac{H_{char.}}{H_0}\left[\frac{\sigma_0 k_x u_0(m-1)}{m}\right]^{1/2}$$

decrease with magnetic field increase.

[1]. *J.R.Gunn*. Solid State Communication, 1, 88, 1963.
[2]. *B.K.Ridley, T.B.Watkins*, Proc.PhysSoc.78, 293, (1961).
[3]. *C.Hilsum*. Proc IRE. 50, 185 (1962).
[4]. *A.G.Chynoweth, W.L.Feldman, D.E.McCumber*. Proc. Int. Conf. Phys. Semicond. Kyoto, 1966, p 514.
[5]. *R.W.H.Engelmann, C.F.Quate*, IEEE Trans. ED-13, 14 (1966)
[6]. *E.R.Hasanov, R.K.Gasimova, A.Z.Panahov, A.H.Demirel* Progress of Theoretical Physics, vol.121, № 3, March 2009.
[7]. *E.R.Hasanov, R.K.Qasimova, A.Z.Panahov and A.H.Demirel* Adv. Studies Theor. Phys., vol.3, 2009, №8, 293-298.
[8]. *N.N.Bogolubov, U.A.Mitropolskii* "Asymtotic methods in theory of non-linear oscillations", Gosizdat, 1963.
[9]. *E.R.Gasanov, R.K.Gasimova*. ANA of Sciences Transactions, vol.XXV, №5, 2005, 139-143.

STRUCTURAL AND MAGNETIC PHASE TRANSITIONS IN HIGH TEMPERATURE FERROMAGNETIC $Cd_{1-x}Mn_xGeAs_2$ SEMICONDUCTORS AT HIGH PRESSURE

A. Yu. MOLLAEV[1], I.K. KAMILOV[1], R.K. ARSLANOV[1], T.R. ARSLANOV[1], U.Z. ZALIBEKOV[1], V.M. NOVOTORTSEV[2], S.F. MARENKIN[2], V.M. TRUKHAN[3]

[1]Institute of Physics, Daghestan Scientific Center of the Russian Academy of Sciences, 367003, Makhachkala, Russian

[2]Kurnakov Institute of General and inorganic chemistry of the Russian Academy of Sciences, Moscow, Russian

[3]Joint Institute of Solid State Physics and Semiconductors, National Academy of Sciences of Belarus, Minsk, 220072

e-mail: a.mollaev@mail.ru

Pressure dependences of resistivity ρ(P) and Hall coefficient R_H(P) have been measured for the novel high-temperature ferromagnetic semiconductor p-$Cd_{1-x}Mn_xGeAs_2$ (x=0÷0.36) at the room temperature. Structural phase transitions with positions shifting towards low pressures, when percentage of manganese increases from 5.9 GPa for $CdGeAs_2$ to 4.8 GPa for p-$Cd_{0.64}Mn_{0.36}GeAs_2$, are found out. Some anomalies of dependence R_H(P), which we attribute to magnetic properties and the presence of impurities, are found out for the crystals with the greater percentage of manganese (x≥0.18).

I. INTRODUCTION

Structural and magnetic phase transitions have been studied in high temperature ferromagnetic $Cd_{1-x}Mn_xGeAs_2$ semiconductor (x=0 ÷ 0.36). Specific resistivity ρ, Hall coefficient Rh and relative magnetic susceptibility χ/χ_0 have been measured at high hydrostatic pressures up to 9 GPa at rise and fall of pressure in room temperatures. Parameters of studied samples are given in table 1, where x - percent content of manganese, R_H – coefficient Hall, ρ - specific resisticvity.

Table 1. Electrophysical parameters of studied samples at room temperature and atmospheric pressure

№	Samples	X	type	ρ, Om·cm	R_H, cm^3/C
1	$CdGeAs_2$	0.00	p	2.16	964.5
2	$Cd_{1-x}Mn_xGeAs_2$	0.003	p	3.0	504
3	$Cd_{1-x}Mn_xGeAs_2$	0.053	p	1.68	142
4	$Cd_{1-x}Mn_xGeAs_2$	0.06	p	10	2250
5	$Cd_{1-x}Mn_xGeAs_2$	0.18	p	0.23	10
6	$Cd_{1-x}Mn_xGeAs_2$	0.30	p	0.62	5
7	$Cd_{1-x}Mn_xGeAs_2$	0.36	p	0.12	0.5

In general, one may formulate number of conditions, and materials for application in spintronic devices must satisfy these conditions: these materials must be ferromagnetic with sufficiently high points of Curie temperature, preferably higher than room temperature, and they must have both magnetic and semiconductors properties. These requirements are met to a certain extent by diamond-like semiconductors of $A^{II}B^{IV}C_2^{V}$ type, that are characterized by high mobility of circuit carriers, small effective masses and greater relation of electron mobility to mobility of holes. A controlled introduction of atoms of transition elements of Mn, Fe, Cr ect-type into anion and cation sublattice beyond mentioned compounds in the result of change of band spectrum, is able to provide a transition of semiconductor material to a ferromagnetic state with a high point of Curie.

According to X-ray diffraction data a character of solids $Cd_{1-x}Mn_xGeAs_2$ changes with increase in Mn concentration. At low concentration the Mn occupies the vacancies of As in sub lattice, when concentration increases the Mn substituted the Cd atoms, in general and at concentrations close to the solubility limit the Mn atoms substitute the Ge atoms (fig.1.)

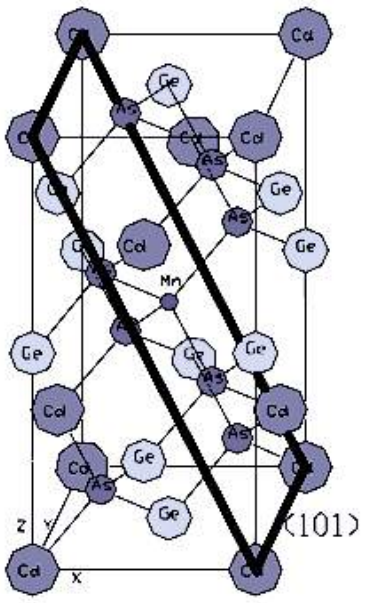

Fig.1. A scheme of $CdGeAs_2$ unit cell according to lattice parameters and atom coordinates in the unite cell (marked out a crystallographic plane (101), were obviously can be the Mn atom)

II. METHOD AND TECHNIQUE OF EXPERIMENT

Measurement have been carried out on mono- and polycrystalline p-$Cd_{1-x}Mn_xGeAs_2$ semiconductors in high pressure devices of «Toroid» type at hydrostatic pressures up to P≤9 GPa in region of room temperatures at rise and fall of pressure. The «Toroid» device was placed in solenoid of H≤5 кOe tension. As a working cell there was applied a fluoroplastic capsule of ~80 mm^3 actual capacity, which had 8 electric injections: and it allowed to measure simultaneously two kinetic effects and pressure. Pressure was controlled by manganese manometer, graduated on several reper points in all diapasons of pressures. More detailed method and technique of experiment is describe in [1, 2]. Synthesis of samples was carried out of highly pure powders of $CdAs_2$ and Ge monocrystals. The samples had a parallelepiped form of 3×1×1 mm dimensions, homogeneity of samples was controlled by values of specific resistivity and Hall coefficient by four probe method. Measuring of dynamic susceptibility was carried out by registering the measurements of frequency of magnetic system using Thomson formula $\nu = 2\pi\sqrt{LC}$ we get solenoid inductivity L, then from well-known expression $L = \mu\mu_0 n^2 S\ell$, where S – area of cross section of solenoid, l – length, ω - number of turns, n=ω/l – thickness of coil, μ - magnetic penetrability of sample, then calculate magnetic penetrability of μ sample. Knowing magnetic penetrability of sample, we calculate magnetic susceptibility χ by formula μ=1+4πχ.

III. MEASURING RESULTS AND DISCUSSIONS

A structural phase transitions are found on specific resistivity ρ(P) and Hall coefficient R_H(P) (fig 2) in all measured samples №1-7 at pressures P=5.9; 5.7; 5.5; 5.4; 5.2; 4.9; 4.8 GPa. Structural phase transitions at P=2.9; 2.8; 2.7; 2.7; 2.6; 2.5; 2.4; 2.3 GPa are observed at fall of pressure too. It is seen from fig 1 that point of phase transition at pressure rise (dark symbols) mowes to lower pressures with the increase of percent content of manganese. The same situation is observed for points of phase transition at fall of pressure (light symbols). The relation of point of phase transition at pressure rise to a point of phase transition at pressure fall is $P_{FT}=P`_{FT}=2\div2.1$, i.e. the difference is comparable with experiment error.

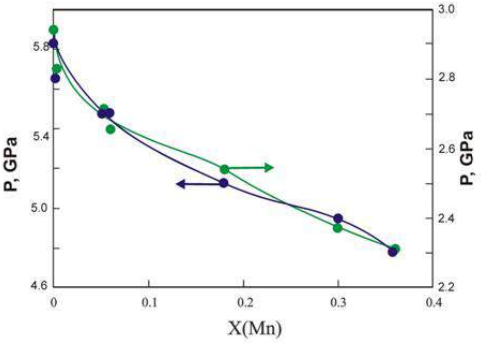

Fig.2. Dependence of position of point of phase transition from percent content of doping element (Mn) at pressure rise – left scale, dark symbols and at pressure fall – right scale, light symbols.

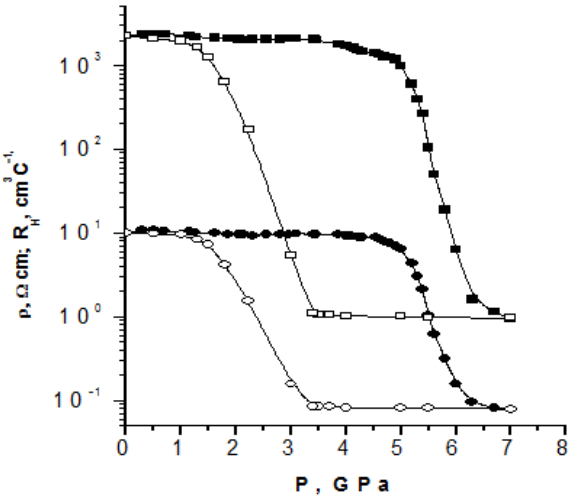

Fig.3. Baric dependence of specific resistivity (circles) and Hall coefficient (squares) at rise (dark symbols) and at fall (light symbols) of pressure for p-$Cd_{0.94}Mn_{0.06}GeAs_2$ sample.

Fig.3 shows typical curves for $Cd_{1-x}Mn_xGeAs_2$ sample. Let's consider baric dependence of specific resistivity on $Cd_{0.94}Mn_{0.06}GeAs_2$ sample at pressure rise (dark circles). Specific resistivity up to P=4.7 GPa changes very weakly, and then at P=4.7 GPa suddenly falls for 2 orders and P=6.1 GPa phase transition ends $\rho_0/\rho_H=12$, $\sigma_H=12.3$ $Om^{-1}\cdot cm^{-1}$, $\rho_0=\rho_0`$. A phase transition is observed on curve ρ(P) at fall of pressure (light points) as also as at $P_{FT}=2.7$ GPa.

Dependences of Hall coefficient from pressure is the same. Hall coefficient in region of phase transition falls for 3 orders. Concentration of carriers in saturation region $\approx 10^{18}$ cm^{-3}. $R_{H0}=R_{H0}`$. Thus, according to values of specific resistivity and Hall coefficient before and after phase transition take place in p-$Cd_{0.94}Mn_{0.06}GeAs_2$.

Relying on the approaches described in [3-6], we examined the dynamics of a phase transition in a uniform external field under the assumption that no internal-stress relaxation occurs. It follows from earlier results [3-6] that a small deviation from thermodynamic equilibrium (p_i-p_0, $p>p_i$, were pi is the pressure at which the phase transition begins) gives rise to nucleation of a new phase in the parent phase (phase 1). The phase transition reaches completion at pressure p_f: $C_1=0$ and $C_2=1$, where $C_1=V_1/(V_1+V_2)$ and $C_2=V_2/(V_1+V_2)$ are the volume fractions of the parent and forming phases, respectively, $C_1 + C_2=1$. At a constant pressure p between pi and pf the transformation rapidly reaches the ultimate extent at this pressure, following which C_2 remains unchanged. The same refers to the reverse transition, during the unloading process (2 → 1), which can be characterized by pressure p'_0, p'_i, and p'_f, having the same meaning as p_0, p_i and pf for the 1 → 2 transition. At a given disturbing force, the value of C_2 =1 - C_1 in the forward transition (1 → 2) is lower than that in the reverse transition (2 → 1), and, accordingly, all of the properties of the material that depend on C_2 exhibit hysteretic behavior at the phase transition.

The characteristic points of the forward (p'_i, p'_f) isothermal phase transition can be used to determine some parameters of the reversible structural phase transition:

the phase equilibrium points for the forward (p_0) and reverse (p'_0) transitions; the metastable equilibrium points for the forward (p_{ME}) and reverse (p'_{ME}) transitions; the thermodynamic hysteresis (p_{TH}), associated with the internal stress arising from the formation of second phase inclusions, which requires some energy; and the fluctuation hysteresis fro the forward (p_{FH}) and reverse (p'_{FH}) transitions, associated with nonuniform distribution of pressure, temperature, and defect in the sample. The characteristic points and the parameters of the phase transformation, calculated for samples 1 and 2 by the formulas presented elsewhere [7], are listed in Table 2.

Table 2. Characteristic pressures (GPa) of the phase transition in p-$Cd_{1-x}Mn_xGeAs2$

	p_i	p_f	p_0	p_{ME}	p_{TH}	p_{FH}	$p'i$	p'_f	p'_0	p'_{ME}	p'_{TH}	p'_{FH}
0.06	0.9	1.6	0.75	1.25	0.8	0.7	0.6	0.1	0.75	0.35	0.8	0.5

To analyze the hysteresis of resistivity and the high-pressure phase transformation in terms of C_1, C_2, and $X = \rho/\rho_1$ (where ρ_1 is the resistivity of phase 1 extrapolated to pressure p_X, $p_i < p_X < p_f$, in the range before the phase transition, and ρ is the effective resistivity at point p*)*, we considered a system consisting of a mixed-phase structure and an effective medium [8].

Taking into account that coefficients A_i, characterizing the configuration of second-phase inclusions, depend on the nature of the phase, pressure, and $\alpha = \rho_i/\rho_f$ in the vicinity of the phase transformation, we obtain

$$kX^2 + [3(1-C_1+\alpha C_1)-(1+\alpha)k]X - \alpha(3-k) = 0 \quad (1)$$

$$k = -[C_1(A_1 - A_2) - A_1]$$

$$\alpha = \rho_2/\ \rho_1 \qquad X = \rho/\rho_1$$

$$A_1 = 1 + 2(1-\alpha)C_1$$

and

$$A_2 = 1 + 2(1-\alpha)C_1^n$$

Using X(p) from Eq. (1), we evaluated the pressure-dependent volume fraction of phase 1, $C_1(p)$, for $n = 15$ (n is the fitting parameter taking into account the probability of the formation of high-conductivity paths in an intermediate region) (Figs. 4). It can be seen in Figs. 4 that, at a given pressure, C_1 in the forward transition is always higher than that in the reverse transition. At $C_1 = 0.17$, a high-conductivity path is formed or disrupted, depending on the transition direction. This point can be thought of as the transition point of an imperfect crystal [9].

Experimental dependencies of relative magnetic susceptibility χ/χ_0 for samples $Cd_{1-x}Mn_xGeAs_2$ (x= 0.06, 0.18, 0.3) from pressure are given in fig. 5. (χ_0- value of magnetic susceptibility at atmospheric pressure).

It is seen from figure 3 that maximum $(\chi/\chi_0)(\rho)$ with the increase of percent content of manganese (x) moves to lower pressures from P=2 for x=0.06 up to P=1.6 for x=30. Amplitude of maximum vice versa grows with the increase of percent content of manganese. A magnetic phase transition is not observed on main $CdGeAs_2$ sample. Fig. 6 shows typical curve of dependence of relative magnetic susceptibility from pressure for $Cd_{0.94}Mn_{0.06}GeAs_2$ sample a temperature dependence magnetization is on cut-in [10]. A comparative analysis of these curves shows that in $Cd_{1-x}Mn_xGeAs_2$ with (x=0.06, 0.18 and 0.3) takes place metamagnetic transition.

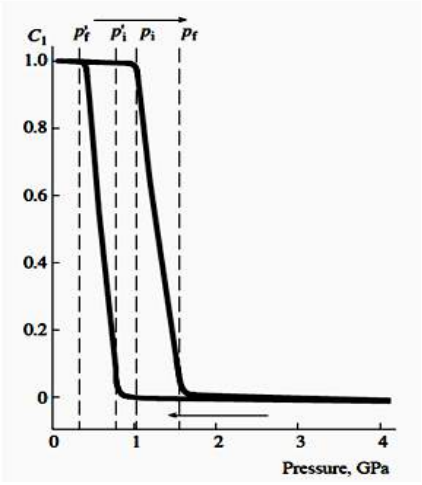

Fig. 4. Volume fraction of phase 1 as a function of pressure for p-$Cd_{1-x}Mn_xGeAs_2$ with $x = 0.06$.

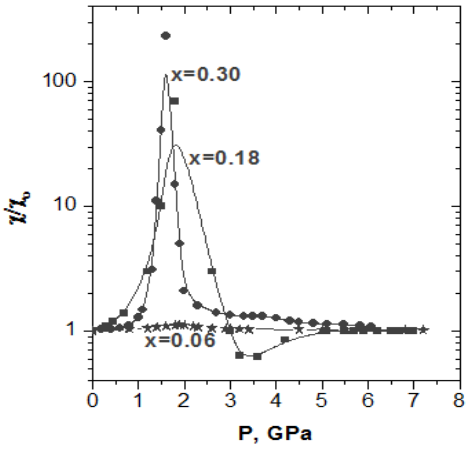

Fig.5. Baric dependence of relative magnetic susceptibility for $Cd_{1-x}Mn_xGeAs_2$ (x=0.06, 0.18, 0.30) samles.

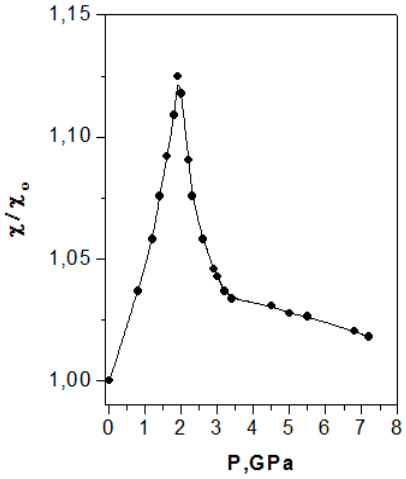

Fig.6. Baric dependence of relative magnetic susceptibility χ/χ_0 from pressure for p-$Cd_{0.94}Mn_{0.06}GeAs_2$. The cut-in shows temperature dependence of magnetization for the studied sample.

IV. CONCLUSION

There have been found structural and magnetic (FM-AFM) phase transitions in hightemperature magnetic $Cd_{1-x}Mn_xGeAs_2$ samples, positions of with move to lower pressures with the increase of percent content of manganese.

The work has been carried out under financial backing of the program of Presidium of RAS “Thermophysics and mechanics of extremal energy influences and physics of highly condensed matter” section “Physics of highly condensed matter”. The works was carried out under financial supported by programs of Presidium of the Russian Academy of Science "Heat physics and mechanics of extremal energy influences and physics of heavily condensed matter".

---

[1]. *L.G. Khvostantsev, L.P. Vereshagin, A.P. Novikov*. High Temp.-High Pressure, 1977, v.9, № 6, p.637-639.

[2]. *A.Yu.Mollaev, R.K.Arslanov, L.A. Saypulaeva, S.F. Marenkin*. Neorg. Mater, 2001, v.37, № 4, p.405-408.

[3]. *A.L. Roitburd*, Theory of Mixed-Phase Structure Formation in Solid-State Phase Transformations, Usp. Fiz. Nauk, 1974, v.113, № 1, p. 69-104.

[4]. *A.L. Roitburd*, Modified Clapeyron-Clausius Equation for the Hysteresis of Solid-State Transformations, Fiz. Tverd. Tela (Leningrad), 1983, v.25, №. 1, p. 33-40.

[5]. *A.L.Roitburd*, Equilibrium of Coherent Phases and Phase Diagrams of Solids, Fiz. Tverd. Tela (Leningrad), 1984, vol. 26, no. 7, pp. 2025-2032

[6]. *V.N.Kozlov, R.R.Umarov and A.A.Firsanov*, Pressure Effect on the Electronic Structure of Group IV and III-V Semiconductors, Fiz. Tekh. Vys. Davlenii, 1986, no. 23, pp. 9-13.

[7]. *A.Yu.Mollaev, R.K.Arslanov, R.I.Akhmedov, and L.A. Saipulaeva*, Approaches to Investigation of Reversible High-Pressure Polymorphism, Fiz. Tekh. Vys. Dav-lenii (Donetsk, Ukr.), 1994, vol. 4, no. 3/4, pp. 66-70.

[8]. *M.I.Daunov, A.B.Magomedov, A.Yu.Mollaev,* et al., On the Hysteresis of Electrical Resistance in High-Pressure Phase Transformations, Sverkhtverd. Mater., 1992, no. 3, pp. 3-6.

[9]. *B.M.Shklovskii, and A.L.Efros*, Percolation Theory and Conduction in Highly Inhomogeneous Media, Usp. Fiz. Nauk, 1975, vol. 117, no. 3, pp. 401-435.

[10]. *R.V. Demin, L.I. Koroleva, S.F. Marenkin, S.G. Mikhaylov, V.M. Novotortsev, V.T. Kalinnikov, T.G. Aminov, R. Shimchak, G. Shimchak, M.Baran*. Pisma v Jetf, 2004, v.**30**, № 21, p.81 – 86.

MAGNETIC-FORCE MICROSCOPY OF FERROMAGNETIC PARTICLES OF FD-RESISTOR SHEATH

A.A.HABIBZADEH, N.R.BABAYEVA, T.R.MEHDIYEV, A.M.HASHIMOV
H.M.Abdullayev Institute of Physics Azerbaijan National Academy of Sciences
AZ-1143 Baku, H.Javid, 33

The magnetic states of micro-particles of FD-resistor ferromagnetic sheath have been studied by methods of magnetic-force microscopy.

INTRODUCTION

The practical use of FD-resistors in devices and electric circuits of high voltages is defined by electrophysical, heat, thermal, electric and magnetic properties of their ferromagnetic sheaths and the degree of their reaction on impulsive or alternative electromagnetic fields. In [1-15, 21] the information about different constructions of resistor ferromagnetic sheath is given and the interpretation of obtained experimental results is given on the base of theoretical works [16-18].

The study of electric and magnetic properties of different FD-resistor sheaths, obtained by technology given in [13-15, 21], shows on the possibility of sheath presentation in the form of dielectric medium containing the arrays of ferromagnetic micro-dimensional particles of the one type. By other hand, it is shown that used ferromagnetic sheath formation technology leads to appearance of regions of micro-particle magnetic ordering in this sheath.

As the calculations [21, 22] show the formation of magnetic wires, the magnetic moments of which draw up in the chain form so that magnetizations of neighbor chains are directed in opposite sides and the resulting magnetic moment of structure is equal to zero consequently, is energetically profitable for the lattice of thin cylindrical and spherical granules with rectangular cell taking under consideration the magnetostatic interaction.

The magnetic interaction between ferromagnetic particles essentially depends on their sizes, space distribution and concentration. The establishment of ferromagnetic order for small granule concentrations is possible as a result of indirect exchange interaction by conduction electrons and carrying out of conditions

$$\frac{T}{T_c} < \left(\frac{\gamma_1 - \gamma_2 + J^2 I^{-1}}{\gamma_1 + \gamma_2} \right)$$

where parameters γ_1 and γ_2 don't depend on granule sizes.

At big granule concentrations γ_1 and γ_2 parameters don't depend on granule sizes.

It is shown that magnetic ordering is observed as a result of spin-dependent electron tunneling processes and at dense granule disposition in non-conducting matrixes.

In present paper the micro-particle magnetic states in FD-resistor shell prepared on the base of Ni-Zn ferromagnetic are investigated by magnetic-force microscopy method.

SAMPLE PREPARATION

The Zn-Ni-ferrite powder of composition $Zn_{0.6}Ni_{0.4}Fe_2O_4$ was created by hydrothermal procedure of the gel obtained as a result of coprecipitation by ammonia of corresponding hydrooxides. This procedure allows obtaining nanoparticles having sizes less 200Å. The use of this ferromagnetic material is connected with nonlinearity of its frequency dependence of magnetic permeability, the lesser reversal magnetization losses and by use in radio equipment for contour tuning.

Ferromagnetic sheath consist of mixture of polymer dielectric and ferromagnetic powder. The technology of making FD-resistor sheath have been improved by use, in the (rolling) process, of a weak external magnetic field, which lead to directional orientation of the ferromagnetic particles.

In the process of annealing, we observed in sheath arise of quasi-granular structure. The granules connected mechanically with a dielectric, and isolated from each other.

As follows from [15,19] for the obtaining of particle limit radius value at which uniform magnetization has been saved yet, one can use the following expression:

$$R_C \approx \frac{0.95}{J_S}(10A)^{\frac{1}{2}} \left(Q - \frac{2K}{J_s^2} - \frac{H}{J_S} \right)^{-\frac{1}{2}}$$

where J_s is saturation magnetization; A is exchange energy parameter; K is anisotropy constant; Q is demagnetizing factor; H is magnetic field strength. Note that particle with radius satisfying to above mentioned equation for all field values $H > -\frac{2K}{J_S}$, has been saved as one-domain one.

The distance between point centers *l= 1,5d; 1,75d; 2d* and *3d* in all consisting of 100 micropoints having the similar diameters *d*=0.6mcm.

The estimation of time relaxation gives the value 10^{-6}sec order for the particle with the diameter 30 nm at T=300K.

The formation conditions of different magnetic structure with ferromagnetic and anti-ferromagnetic ordering in materials consisting of ferromagnetic granules are considered in [15-20].

As calculations show the magnetic wire formation the magnetic moments of which set out in chain form as magnetization of neighbor chains direct in opposite sides and therefore resulting structure magnetic moments is equal to zero for lattice from thin cylindrical spherical

granules with rectangular cell taking under consideration the magnetic interaction is energetically profitable one.

MAGNETIC STATES OF NANO-DIMENSIONAL PARTICLES

The experimental investigations on scanning probe microscope show that the different magnetization distributions for Ni-Zn ferromagnetic particles of FD-resistor sheath having different sizes take place. The cobalt the residual magnetization of which is 0.14Tl is used as a material for the probe. In model calculation the probe field is presented as the field of singular dipole with effective magnetic moment $m_t=M_tV_t$, where M_t is probe residual magnetization and V_t is effective volume of probe magnetic covering which is equal 0.3 mcm^3 as it follows from obtained results. By other hand it is proposed that micropoint has the uniform distribution of magnetization and the direction of its magnetic moment is defined by only external magnetic field.

As it is shown in work [22] at the absence of induced currents the magnetic interaction gradient between probe and sample surface in the given point of probe disposition one can define by the following formula:

$$\frac{\partial}{\partial z}F_z(\vec{r}) = \frac{\partial}{\partial z}\iiint\limits_V \left(\overrightarrow{M_t}(\overrightarrow{r_t})\nabla\right)H_z(\vec{r}+\vec{r}_t)\,dV_t$$

To simplify calculation the influence of the needle and sample on the magnetization structure each other isn't taken under consideration. It is proposed that only dipole interaction takes place between the needle and sample surface. Then we obtain:

$$\frac{\partial}{\partial z}F_z(\vec{r}) = \sum_{\substack{t-type\\ j-sample}} \left(\left(m_t^i\nabla\right)\frac{\partial}{\partial z}H_z^{ij}\left(\vec{r}+\overrightarrow{r_t^i}-\overrightarrow{r_s^j}\right)\right)$$

where

$$H_z^{ij}\left(\vec{r}+\overrightarrow{r_t^i}-\overrightarrow{r_s^j}\right) = \frac{3\left(z+z_t^i-z_s^j\right)\left(m_s^j\left(\vec{r}+\overrightarrow{r_t^i}-\overrightarrow{r_s^j}\right)\right)}{\left|\vec{r}+\overrightarrow{r_t^i}-\overrightarrow{r_s^j}\right|^5} - \frac{m_{s_z}^j}{\left|\vec{r}+\overrightarrow{r_t^i}-\overrightarrow{r_s^j}\right|^3}$$

m_s^j is magnetic moment of *j*-element of sample discretization; $H_z^{ij}\left(\vec{r}+\overrightarrow{r_t^i}-\overrightarrow{r_s^j}\right)$ is magnetic field formed by j-element of the sample placed in $\overrightarrow{r_s^j}$ point in the disposition of *i*-dipole of the needle.

The phase shifts of cantilever oscillations under influence on magnetic field gradient are analyzed in experiments by standard technique.

The calculation results of dependences of dipole-dipole interaction energies between micropoints $E_{d\text{-}d}$ and magnetic anisotropy E_a on ratio d/l are given on fig.1. From this it follows that one can ignore their interaction for distances more than 1,5mcm between micropoints with 0.6mcm diameter. In opposite case the dipole-dipole interaction between particles will influence on reversal magnetization processes.

MCM images of magnetic structure of separate micropoint in magnetic field and the spin distribution corresponding to them, obtained by computer modeling are given on fig.2(a,b). In $H \geq H_s$ magnetic fields micropoints have the one-domain configuration with character black-white contrast of MCM. At increase of external field from negative saturation corresponding to field H=-700Oe up to positive saturation corresponding to 700Oe in micropoint array $l \geq 3d$ the graduated spin turn that leads to formation of two-domain state in the filed H=-60Oe takes place. The further increase turns the spins along the field but doesn't change the position of domain wall. At field value H > 70Oe the transformation into one-domain state is observed. Such state of micropoint array magnetization is character for isolated particles, i.e. for particle array between which the dipole-dipole interaction is absent.

The vortex core which gradually shifts to the center (fig.2b) forms in the field H = -60Oe in the interacting micropoint array ($l \leq 2d, d/l \geq 0{,}6$). In the field $H \approx 0$ the vortex core is in the center of nano-point. At further increase of field $H>0$ the vortex core shifts in opposite direction to point boundary.

Thus, the investigations of ferromagnetic matrix of micropoints show that reversal magnetization processes are essentially depend on value of dipole-dipole interaction between particles. At reversal magnetization of non-interacting micropoints the two-domain state forms and the vortex core creates in micropoint arrays connected by dipole-dipole interaction. It is established experimentally and confirmed by calculations that at $l>2d$ the dipole-dipole interaction between nanopoints in matrix becomes the negligible one. It is established that at decrease of nano-dimension particle sizes the abbreviation of number of magnetic vortexes in magnetization structure takes place. For particles the sizes of which are less than 0,6 mcm the one-domain state with quasi-uniform magnetization distribution takes place.

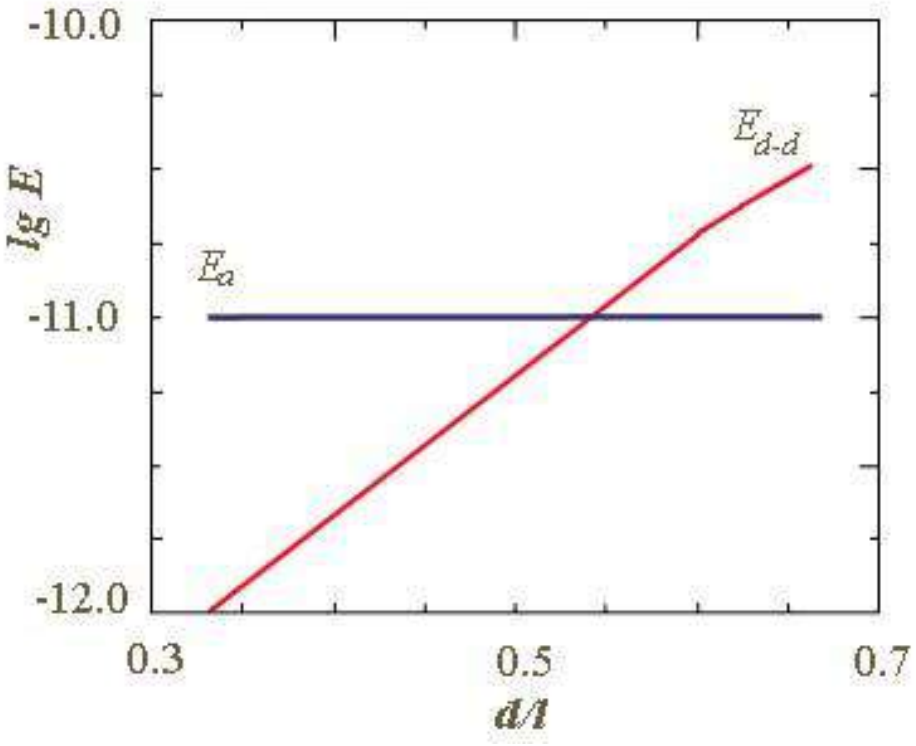

Fig.1 The dependence of energies of dipole-dipole interaction between micropoints E_{d-d} and magnetic anisotropy E_a on ratio *d/l.*

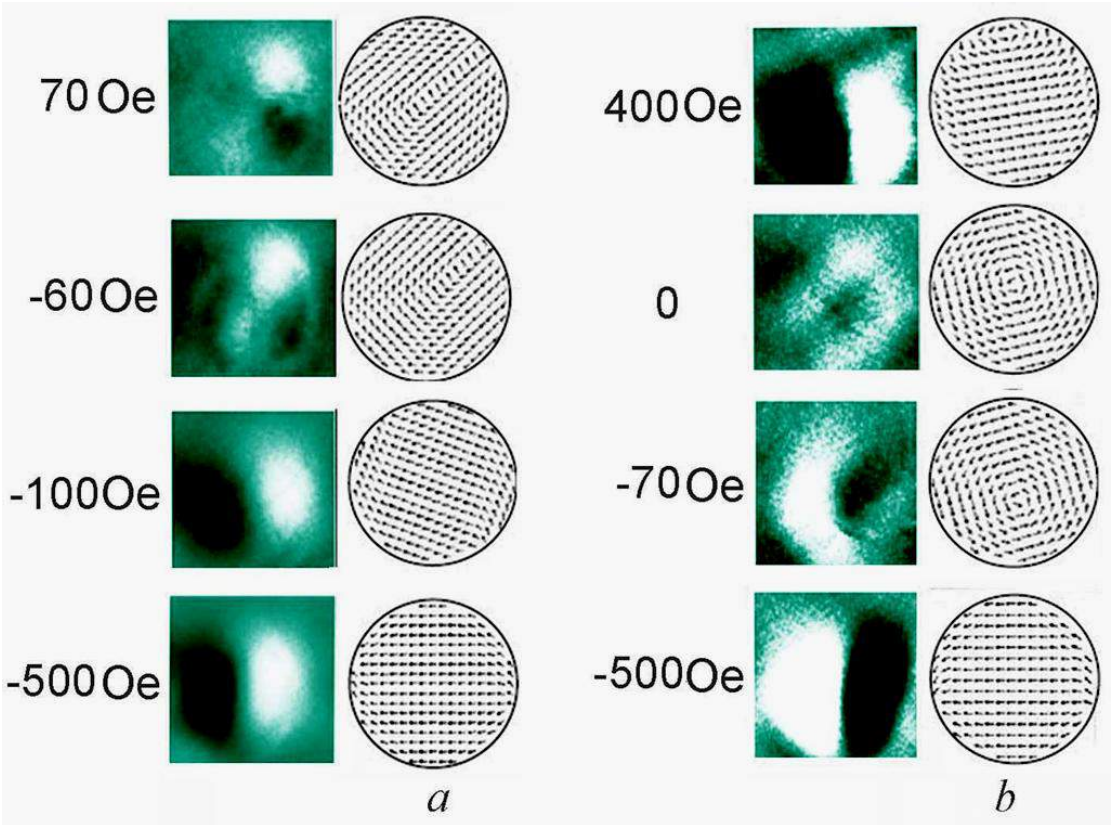

Fig.2 MCM image of micropoint magnetic structure and computer modeling of spin distribution of micriopoint array for situations a) l=3d; b) l=2d in external magnetic fields.

[1]. *N.R. Babayeva* High frequency overvoltage elimination in high voltage electric circuits and devices // Power Engineering, №4, 2005, p. 40-47. (in Russian)

[2]. *A.M.Gashimov, T.R.Mehdiyev, N.R.Babayeva* Frequency-dependent resistor. // International Conference «Physics-2005», Baku, 7-9 June 2005, p.613-617.

[3]. *A.M.Gashimov, T.R.Mehdiyev, N.R.Babayeva* Limitation possibility of high frequency overvoltages at the use of frequency-dependent resistor. / International conference energy of Moldova-2005, 21-24 september 2005, p.265-269. (in Russian)

[4]. *A.M.Gashimov, T.R.Mehdiyev, N.R.Babayeva* Effect of magnetic multi-layer to resistive properties of frequency-dependent resistor / TPE-2006, 3rd International conference on Technical and Physical Problems in Power Engineering, Ankara, Turkey 29-31 may 2006, p. 604-606.

[5]. *N.R.Babayeva* Analyze algorithm of high frequency overvoltages in commutation circuit at the use of frequency-dependent resistor. // Проблемы энергетики, №3-4, 2006, с.32-37. (in Russian)

[6]. *A.M. Hashimov, T.R.Mehdiyev, N.R. Babayeva* The electric and heat characteristics of frequency-dependent resistor //Fizika, №4,cild XII,2006,p.28-32. (in Russian)

[7]. *A.M. Gashimov, T.R.Mehdiyev, N.R. Babayeva* On appropriateness of use of frequency-dependent resistor at limitation of high-frequency overvoltages / Modern Electric Power Systems"06, Wroclaw, Poland, Sept. 6-8, 2006, p.379-382.

[8]. *Y.V.Dmitriyev, A.M.Gashimov, T.R.Mehdiyev, N.R.Babayeva* Thermal parameters and operating mode of frequency-dependent resistor. / Scientific Conference devoted by Yu.N. Vershinin "Electrophysics of materials and devices" Novosibirsk, 9-12 january 2007, c.55-60. (in Russian)

[9]. *N.R.Babayeva, A.M.Gashimov, Y.V.Dmitriyev, T.R.Mehdiyev,* Study of skin-effect and thermal conditions of frequency-dependent resistor// Fizika, № 1-2, v. XIII, 2007, p.102-107.

[10]. *N.R.Babayeva, A.M.Gashimov, T.R.Mehdiyev* On some current peculiarities through frequency-dependent resistor. // Fizika, №4, v. XIII, 2007, p.230-235.

[11]. *V.G. Kuznetsov, T.R.Mehdiyev, N.R.Babayeva* To calculation of frequency-dependent resistor characteristics. // - Технична электродинамика, Киев, 2007, с.88-91. (in Russian)

[12]. *Y.V.Dmitriyev, A.M.Gashimov, N.R.Babayeva* Computer model algorithm of high frequency processes in distribution devices containing nonlinear overvoltage limiters// - Power Engineering, Minsk, 2007, № 4, p. 29-38. (in Russian)

[13]. *T.R.Mehdiyev, A.M. Gashimov, N.R. Babayeva, Y.V.Dmitriyev, A.A.Habibzadeh* The peculiarities of current passing through frequency-dependent resistor. 4-th International Conference on Technical and Physical Problems of Power Engineering TPE-2008, 4-6 September 2008, Pitesti, Romania, II-4 – II-8

[14]. *T.R.Mehdiyev, N.R. Babayeva, A.M. Gashimov, A.A.Habibzadeh* Electromagnetic processes in frequency-dependent resistor sheath. Fizika, №2, cild XIV, 2008, p.80-87.

[15]. *T.R.Mehdiyev, A.M. Gashimov, N.R. Babayeva, A.A.Habibzadeh* Electrical and magnetic properties of frequence-dependent resistor sheath. №3, cild XIV, 2008, p.207-217. (in Russian)

[16]. *L.D. Landau, E.M. Lifshitz* Electrodynamics of continua. Наука, 1982, 629с.

[17]. *A.L.Efros, B.I.Shklovskii* Phys. Stat. Sol.(b), 1976, v.76, p.475 (in Russian)

[18]. *S.O.Qladkov* To the absorption theory of the electromagnetic radiation by strongly inhomogeneous two-component systems. JTP, 1999, v.69,7, c. 89-94 (in Russian)

[19]. *E.I. Kondorskiy* Izv. AN USSR, ser. physical, 1952, v.16, p.398 (in Russian)

[20]. *Y.I. Qorobec, Y.I.Djejera, A.F.Kravec* Magnetic ordering in a granular system. FTT, 2000, v.42, *вып*.1, 121-125 (in Russian)

[21]. *A.A.Habibzadeh, T.R.Mehdiyev, A.M. Gashimov, N.R. Babayeva* Dependence of electric and magnetic properties of the frequency-dependent resistor on concentrations and sizes of ferromagnetic granules. Fizika, №2, v. XV, 2009, p.124-128.

[22]. *D.V. Ovchinnikov, A.A. Buxarayev* Computer modeling MFM of images in framework of a static distribution model of magnetization and dipole-dipole interaction. JTF, 2001, v.71, вып. 8, с.85-91(in Russian)

COMPLEX STUDY OF HIGH TEMPERATURE FERROMAGNETIC SEMICONDUCTOR $Cd_{0.82}Mn_{0.18}GeAs_2$

A.Yu. MOLLAEV[1], I.K. KAMILOV[1], R.K. ARSLANOV[1], T.R. ARSLANOV[1], U.Z.ZALIBEKOV[1], V.M. NOVOTORSEV[2], S.F. MARENKIN[2], I.V. FEDORCHENKO[2]

[1]Institute of Physics, Daghestan Scientific Center of the Russian Academy of Sciences, 367003, Makhachkala, Russian

[2]Institute of common and inorganic chemistry of the Russian Academy of Sciences, Moscow, Russian e-mail: a.mollaev@mail.ru

There are structural and magnetic phase transitions, negative magnetoresistance induced by high pressure were found in sample $Cd_{0.82}Mn_{0.18}GeAs_2$. From the temperature dependences of the Hall coefficient calculated normal and anomalous Hall coefficients.

I. INTRODUCTION

The present work is the continuation of studies of high temperature $Cd_{1-x}Mn_xGeAs_2$ semiconductors started in [1,2]. As it follows from experimental data, given in literature [3,4]. The origin of high temperature ferromagnetism of FM state in $A^{II}B^{V}C^{V}_2$ semiconductors doped by Mn, is stipulated by two factors: increase of concentration of magnetic impurities of atoms, and growth of concentration of free carriers of circuit-holes, since Mn is acceptor. Such behavior is connected with interaction between localized magnetic Mn moments through free holes, what leads to FM order in manganese system (indirect change). Since doping character and presence of free charge carriers define magnetic properties of such materials, one may study the processes taking place in high temperature FM materials and connect with them effects of kinetic coefficients by effective influence of pressure and temperature (huge magnetic resistance, anomaly Hall effect etc.). Further studies in high direction, we believe, are perspective and promising. There have been measured baric dependences of specific resistivity ρ(P), Hall coefficient R_H(P), cross $(\Delta\rho_{xx}/\rho)$(P), and longitudinal $(\Delta\rho_{zz}/\rho)$(P), relative magnetic susceptibility χ/χ_0(P) and temperature dependence of specific resistivity ρ(T) and Hall coefficient R_H(P) in 77-450 K range.

II. METHOD AND TECHNIQUE OF EXPERIMENT

Samples for investigation were cut from polycrystalline and single-crystal $Cd_{1-x}Mn_xGeAs_2$ ingots. The crystals were grown as described previously [5]. Polycrystalline materials were synthesized from analytical-grade Mn and high-purity $CdAs_2$ and Ge powders prepared by grinding single crystals. The samples were rectangular in shape 3.0×1.0×1.0 mm in dimensions, and were single-phase as determined by x-ray diffraction (contained no manganese arsenides). The transport properties of samples 1 ($Cd_{0.82}Mn_{0.18}GeAs_2$) are summarized in Table 1. The homogeneity of the samples was checked by four-probe Hall effect measurements.

Table 1. Electrical properties of p-$Cd_{1-x}Mn_xGeAs_2$ at room temperature and atmospheric pressure.

Sample	x	R_H,cm^3/C	ρ, Ω cm	μ, $cm^2/(V\ s)$
1	0.18	10	0.23	43.4

The study of baric, magnetic field and temperature dependence of kinetic coefficient and relative magnetic susceptibility in p-$Cd_{0.82}Mn_{0.18}GeAs_2$ was carried out by use of several methods. Dependences ρ(P), R_H(P), $(\Delta\rho_{xx}/\rho)$(P), $(\Delta\rho_{zz}/\rho)$(P) and χ/χ_0(P) were measured in high pressure devices of «Toroid» type, placed in multiturn solenoid of H≤5 kOe, magnetic tension, at rise and fall of pressure in room temperatures. Detailed method is described in [6, 7].

Magnetic susceptibility was calculated out of expression $\chi=(\mu-1)/4\pi$. Measuring of dynamic magnetic penetratibility is carried out by registering of change of frequency of resonance contour, whose inductive core coil is sample. Measuring of frequency of autogenerator were carried out by use of frequencymeter. Calculation of magnetic penetratibility μ was carried out on condition of equality of inductive thoroid coil with the number of turns of N, winted on sample with inductance, obtained from own frequency of oscillatory contour of autogenerator: $\mu = \frac{T^2 \cdot 10^7}{8\pi^2 C N^2 h \ln b/a}$ where: C – condenser capacity, T – period of oscillations, a, b, h – inner radius, outer radius and altitude of toroid coil. At weak effect expression, the measuring were carried out at accumulating and averaging rate. Measuring of ρ(P) and R_H(P) dependencies were carried out by standard technique by four probe method.

III. EXPERIMENTAL RESULTS AND DISCUSSIONS

Fig.1 show ρ(P) and R_H(P) dependencies for sample p-$Cd_{0.82}Mn_{0.18}GeAs_2$. In sample p-$Cd_{0.82}Mn_{0.18}GeAs_2$ at pressure increase (dark points). ρ(P) up to pressures P≤4.5 GPa changes weakly, it is stipulated by reciprocal (mutual) compensation of change of concentration and mobility of charge carriers. ρ(P) at P=4.5±0.2 GPa suddenly decreases for almost three orders, comes phase transition and at P>6.5 GPa comes out for saturation – comes metallization (σ≈ 2850 Om^{-1} cm^{-1}). At pressure fall (light points) there is observed a considerable hysteresis and at P=3.1±0.1 GPa there takes place a phase transition on curve ρ(P). Baric dependences of Hall coefficient (fig.1) have more complex character.

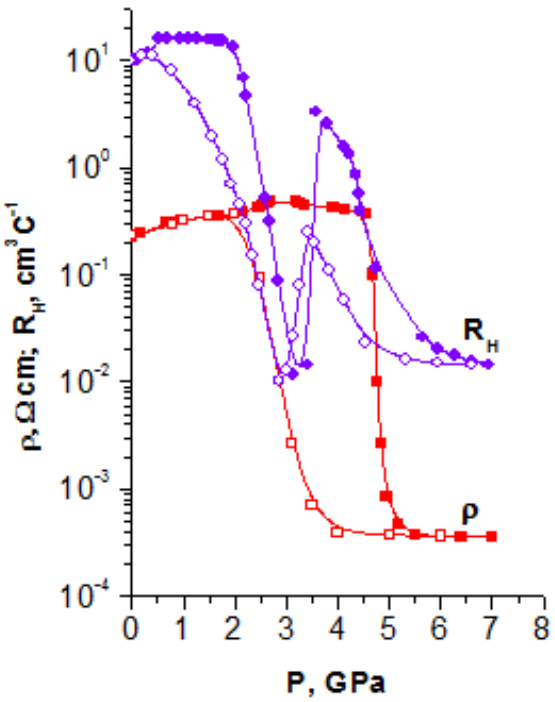

Fig.1. Dependence of specific resistivity – curve 1 and of Hall coefficient - curve 2, at rise of pressure (dark symbols) and fall (light symbols) in magnetic field H=5 kOe

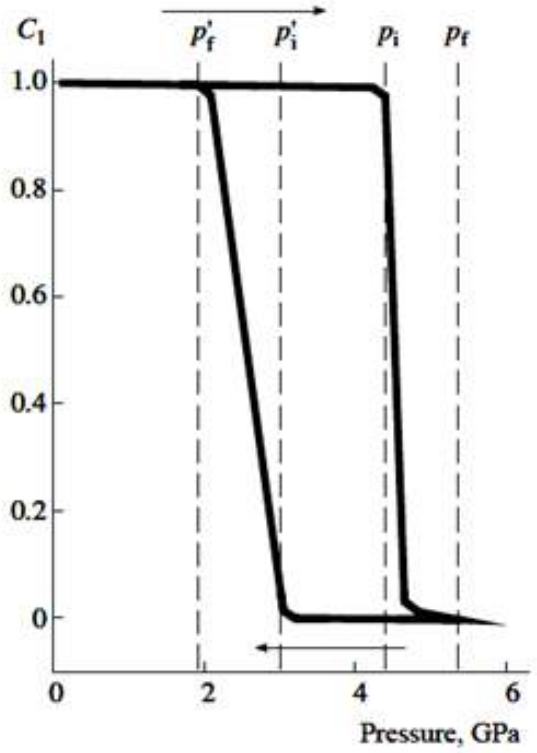

Fig.2. Volume fraction of phase 1 as a function of pressure for *p*-Cd1 – *x*Mn*x*GeAs2 with $x = 0.18$.

There may be outlined four regions on it: 1st region (P<0,6 GPa); Hall coefficient grows with pressure – region of impurity conductivity: 2-nd region (P=0,6 – 1,9 GPa): Hall coefficient comes out on plato region of exhaustion of charge carriers; 3-rd region (P=1,9 – 4.5 GPa): region of fall of Hall coefficient almost up to zero with further increase, the reason of which is under discussion; 4-th region (P=4.5-6.5 GPa): phase transition region. In the region of saturation $R_x(P)$ at P>6.5 GPa, concentration of charge carriers is ~5× 10^{20}cm^{-3}. Specific electroconductivity changes with σ=5 Om^{-1}·cm^{-1} up to σ=2850 Om^{-1}·cm^{-1}, and concentration of charge carriers p=6.25·10^{17} cm^{-3} up to p=6.25·10^{20} cm^{-3}, what proves again that there comes semiconductor-metal transition, value of specific electroconductivity and Hall coefficient before application and after fall of pressure coincide. Having analyzed the character of ρ(P) and $R_x(P)$ dependencies for $Cd_{0.82}Mn_{0.18}GeAs_2$ sample, one may come to a conclusion that there takes place a reversible structural semiconductor-metal transition in it. Relying on the approaches described in [8-11], we examined the dynamics of a phase transition in a uniform external field under the assumption that no internal-stress relaxation occurs (fig. 2).

Experimental dependencies of relative magnetic susceptibility χ/χ_0 (χ_0 – value of magnetic susceptibility at atmospheric pressure).

It is seen from fig.3 that relative magnetic susceptibility at rise of pressure grows and at P=1.8 GPa reaches maximum, then suddenly falls for two orders and at P>2 GPa comes out for saturation. To all appearance, there takes place spin reorientation transition induced by pressure. The presence of susceptibility shoulder at P>2 GPa characteristically of AFM state testifies to it. Further behavior of baric dependence is explained by structural phase transition, whose value satisfactorily agrees with data obtained in [3]. It is necessary to mark that on base sample $CdGeAs_2$ not doped by manganese. The peak of magnetic susceptibility on dependence $(\chi/\chi_0)(P)$ is absent. Fig.4. shows dependencies of relative magnetic susceptibility for various temperatures, maximum $(\chi/\chi_0)(P)$ moves to side of low pressures and value χ/χ_0 falls.

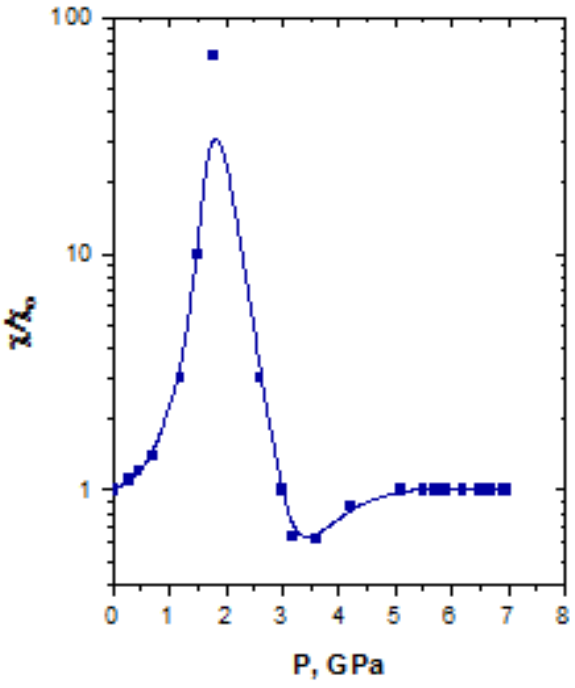

Fig.3. Dependence of relative magnetic susceptibility from pressure.

It is known that Hall effects in ferromagnetic semiconductors is described by correlation:

$$E_y = (R_0 H_2 + 4\pi R_s M_2) I_x \qquad (1)$$

where: E_y - Hall EDP; I_x - circuit along axis 0X through which is laid electric field; H_2 and M_2 - magnetic field and magnetization, or pressure along axis 0Z; R_s and R_0 - anomaly and normal Hall effects. By interactive graphic constructions of magnetic field dependences of Hall resistance for various temperatures there have been calculated temperature dependences of normal and anomaly Hall coefficients (fig.5).

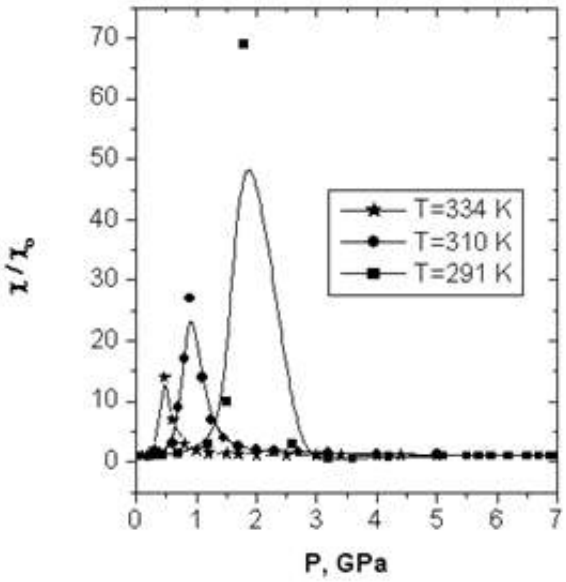

Fig.4 Dependence of relative magnetic susceptibility from pressure for pressure for various temperatures

Anomalies in the shape of breaks, which may be interpreted as magnetic phase transition were found on temperature dependences ρ(T) and $R_H(T)$ at $T_c^{\rho} \approx$ 248 K and $T_c^{RH} \approx$ 180 K (fig.6). Temperature dependence of specific electric resistivity in paramagnetic state with a good accuracy is described by activation law $\rho(T) \sim \exp(E_g/K_B T)$ with activation energy Ea=155 meV.

Fig.7 portrays dependencies $(\Delta\rho_{xx}/\rho)(P)$ circles and $(\Delta\rho_{zz}/\rho)(P)$ squares at H=5 kOe, for the sample under study it is obvious that cross and longitudinal magnetic resistance (MR) at first positively (PMR) at P≈1 GPa reaches maximum, then falls and at P>2 GPa becomes negative (NMR). NMR at P≈4 GPa reaches maximum ≈1.5% and MR at P>6 GPa again becomes positive. Curves of NMR are well described in fig.6 by expression:

$$\frac{\Delta\rho}{\rho} = -B_1^2 \ln(1 + B_2^2 H^2), \qquad (2)$$

suggested for first time in [12,13]. B_1 And B_2 in formula (4) include physical characteristics of exchange interaction.

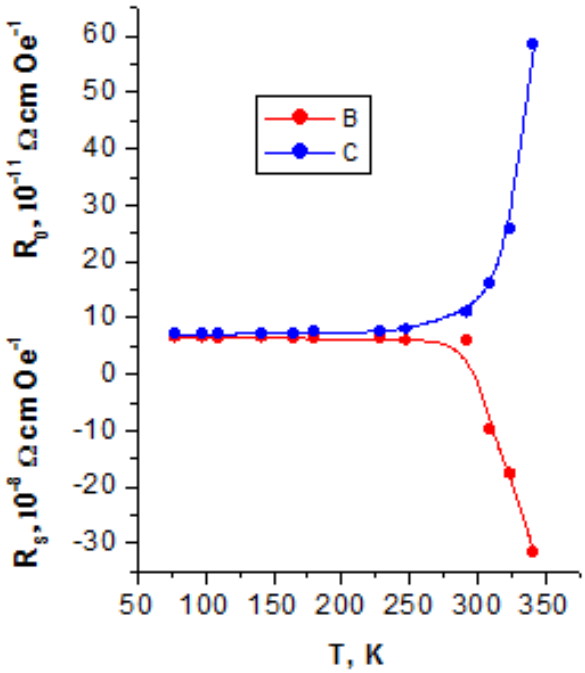

Fig.5 Temperature dependence of normal Hall coefficient $R_0(T)$ – C and anomaly Hall coefficient $R_s(T)$ – B

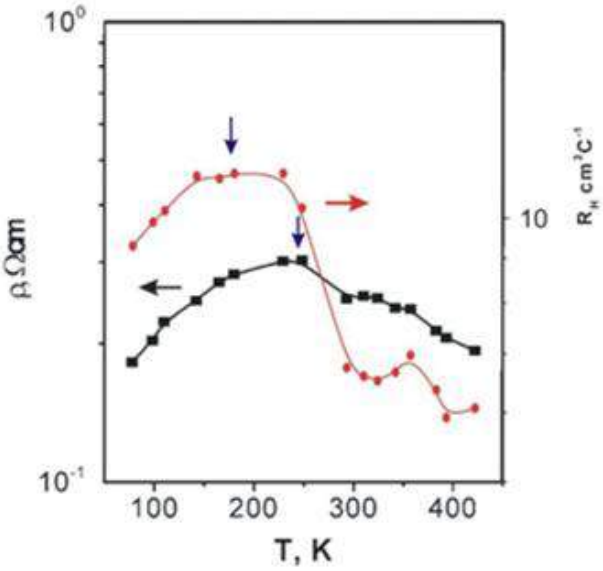

Fig.6 Temperature dependence of specific resistivity and Hall coefficient.

Particularly, coefficient B_2 is defined by expression:

$$B_2^2 = \left[1 + 4S^2\pi^2\left(\frac{2J \cdot \rho_F}{g}\right)^4\right] \frac{g^2\mu_B^2}{(\alpha \cdot kT)^2} \qquad (3)$$

Here J – energy of exchange interaction; ρ_F – density of state of Fermi level; α - some numerical factor which may be considered as equal to one.

A confrontation of expression (3) with experimental data allows calculating B_1 и B_2 coefficients. So, correlation (2) quite satisfactory describes NMR in our experiment. However since this correlation is half-empiric, and for a profound interpretation of physical processes, leading to origin of MR, there is need in

further experimental and theoretical studies. At pressure fall there was found a hysteresis of magnetic resistivity (at pressure fall) goes over straight one, since at structural phase transition goes vice versa.

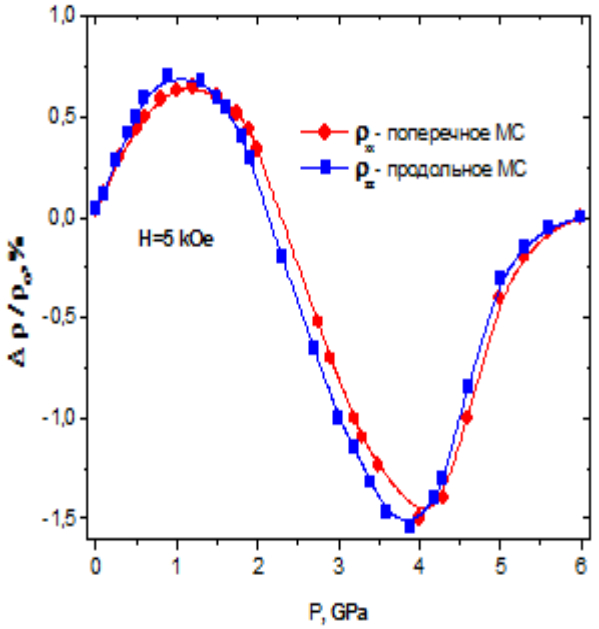

Fig.7 Dependence of cross (circles) and longitudinal (squares) magnetic resistivity from pressure

IV. CONCLUSION

Baric dependencies of specific electric resistivity, Hall coefficient and relative magnetic susceptibility at rise and fall of pressure and their temperature dependencies have been studied in hightemperature ferromagnetic semiconductor for the first time. Maxima hare been found on baric dependencies χ/χ_0 at rise and fall of pressure, and they are interpreted as transition of system induced by pressure, metamagnetic transition. Normal and anomaly Hall coefficients are market out by interactive graphic constructions from experimental magnetic field dependences of Hall resistivity. A negative magnetic resistivity induced by pressure was found in $Cd_{1-x}Mn_xGeAs_2$.

The work has been carried out under financial backing of the of the program of Presidium of RAS “Thermophysics and mechanics of extremal energy influences and physics of highly condensed matter” section “Physics of highly condensed matter”.

The works was carried out under financial supported by programs of Presidium of the Russian Academy of Science "Heat physics and mechanics of extremal energy influences and physics of heavily condensed matter".

[1]. *A.Yu Mollaev., I.K.Kamilov, R.K. Arslanov, U.Z.Zalibekov, R.R. Bashirov, V.M. Novotorsev, S.F. Marenkin, S.A. Varnavskiy* Transport peculiarities and phase transition in diluted magnetic semiconductors $CdGeAs_2$:Mn at high hydrostatic pressure, Journal of Physics: Conference Series. 2008, v.121, p.022010.

[2]. *A.Yu. Mollaev, I.K. Kamilov, R.K. Arslanov, U.Z.Zalibekov, T.R. Arslanov, R.R. Bashirov, V.M.Novotorsev, S.F. Marenkin,* Baric and temperature dependences of kinetic coefficients in p-$Cd_{0.7}Mn_{0.3}GeAs_2$ at atmospheric and high pressures, Phys. Stat. Sol B, 2009, v.246, №. 3, p.655–657.

[3]. *Medvedkin G.A., Takayuki Ishibashi, Takao Nishi, Koji Hayata, Yoichi Hasegawa and Katsuaki Sato*. Room temperature ferromagnetism in novel diluted magnetic semiconductor $Cd_{1-x}Mn_xGeP_2$, Jpn. J. Appl. Phys, 2000, v.39, p.L949–L951.

[4]. *G.A. Medvedkin, T. Ishibashi, T. Nishi, K. Sato,* A new magnetic semiconductor $Cd_{1-x}Mn_xGeP_2$, Physics technic of semicond, 2001, v.35, № 3, p.305 – 309.

[5]. *S. F. Marenkin, V.M. Novotortsev, K.K. Palkina, et al,* Preparation and Structure of $CdGeAs_2$ Crystals, Neorg. mater., 2004, v.40, № 2, p.135-137. [Inorg. mater (Engl. Transl.) v.40, № 2, p.93-95]

[6]. *L.G. Khvostanstev, L.P. Vereshchagin, A.P.Novikov,* Device of Toroid Type for High Pressure Generation, High Press. 1977, v.9, № 6, p.637–639.

[7]. *A.Yu. Mollaev, L.A. Saypulaeva, R.K. Arslanov, S.F. Marenlin*, Neorg Mater, 2001, v.37, № 4, p.405–408.

[8]. *A.L. Roitburd*, Theory of Mixed-Phase Structure Formation in Solid-State Phase Transformations, *Usp. Fiz. Nauk*, 1974, v.113, № 1, p. 69-104.

[9]. *A.L. Roitburd*, Modified Clapeyron-Clausius Equation for the Hysteresis of Solid-State Transformations, *Fiz. Tverd. Tela* (Leningrad), 1983, v.25, №. 1, p. 33-40.

[10]. *A.L. Roitburd*, Equilibrium of Coherent Phases and Phase Diagrams of Solids, *Fiz. Tverd. Tela* (Leningrad),1984, vol. 26, no. 7, pp. 2025-2032

[11]. *Kozlov, V.N., Umarov, R.R., and Firsanov, A.A.*, Pressure Effect on the Electronic Structure of Group IV and III-V Semiconductors, *Fiz. Tekh. Vys. Davlenii*, 1986, no. 23, pp. 9-13.

[12]. *P.M. Krstajic, F.M. Peeters, V.A. Ivanov, K.Kikoin,* Double-exchange mechanisms for M-doped III-V ferromagnetics semiconductors, Phys. rev. B, 2004, v.70, p.195215.

[13]. *R.P. Khosla and J.R. Fischer,* Low temperature magnetoresistance in degenerate n-type Si, Phys. rev. B. 1972, v.6. № 10, p.4073–4075.

KINETIC EFFECTS IN NEW FERROMAGNETIC MATERIAL ON THE BASIS OF $Zn_{1-x}Cd_xGeAs_2$ WITH MANGANESE.

A.Yu. MOLLAEV[A], L.A.SAYPULAEVA[A], A.G.ALIBEKOV[A], A.A.ABDULLAEV[A], S.F.MARENKIN[B]

[A]Institute of Physics, Daghestan Scientific Center of the Russian Academy of Sciences, 367003, Makhachkala, Russian

[B]Institute of common and inorganic chemistry of the Russian Academy of Sciences, Moscow, Russian e-mail: a.mollaev@mail.ru

Homogenous crystals of diluted magnetic semiconductor solid solution $Zn_{1-x}Cd_xGeAs_2$ doped with 0, 1.13 and 2.65 mass% of Mn were synthesized. Temperature dependences of electroconductivity have been studied for the novel high-temperature ferromagnetic semiconductor p-$Zn_{1-x}Cd_xGeAs_2$:Mn in the 77 – 300 K temperature range. Pressure dependences of resistivity ρ(P) and Hall coefficient R_H(P) have been measured at the room temperature. Features of ρ(P) and R_H(P) dependences indicate the structural phase transitions occurring for certain values of hydrostatic pressure. Phase transition positions shift towards low pressures, when percentage of manganese increases. Features of R_H(P) for samples with percentage of manganese greater than x=0.06, where ferromagnetic parameters are expressed more strongly, we attribute to anomalous component of Hall effect and its modulation due to presence of narrow impurity bands.

I. INTRODUCTION

Recently synthesized bulk $ZnGeAs_2$- and $CdGeAs_2$-based magnetic semiconductors with 3d element impurities are perspective for spintronics application [1, 2]. These compounds are chalcopyrites and have tetragonal singony. In metastable state these samples have a cubic singony with sfalerite type [3].

The discovery of hole-mediated ferromagnetism in compounds and progress in non-equilibrium growth of the diluted magnetic semiconductor GaAs:Mn with Curie temperature up to T_c = 173 K has encouraged research of other semiconductors structurally and chemically closely related to the III-V group. The valences in group III atoms and the double cation II-IV complexes are equal but the latter ones can contain more Mn than the III-IV compounds, without forming a second phase. Observations of room – temperature ferromagnetism in II-IV-V_2 materials. In this connection the Mn-doped room – temperature ferromagnetic chalcopyrite compounds $CdGeAs_2$ (T_c=355 K) and $ZnGeAs_2$ (T_c=333 K) have attracted attention because of their optical and structural properties, which are interesting for applications [6].

`The opportunity to change the interatomic distances and overlap of electron wave function which participates in a band structure formation and in exchange interaction stimulates our interest in research of kinetic phenomena in these compounds at high hydrostatic pressure.

Structural phase transitions finding out at certain hydrostatic pressures provide useful information for theoretical investigation of magnetism in these crystals.

II. EXPERIMENT

High purity (99.999%) Ge and Mn powders were used for synthesis of $Cd_{0.1}Zn_{0.9}GeAs_2$:Mn solid solutions from crystalline starting materials $CdAs_2$ and $ZnAs_2$ prepared by the vertical Bridgman technique. The starting materials were ground to powders with average particle size 5-10 μm and batches of 9 – 10 g weighed with an accuracy of 0.005% were loaded into quartz ampoules coated with pyrolytic graphite and evacuated to 1×10^{-2} Pa. The synthesis temperature and duration were 902 ℃ and 36 h, respectively. To maximize the solubility of Mn in the host lattice the cooling rate of the melt was adjusted to 10 – 12 K s^{-1}. The composition of the crystals was studied with atomic absorption analysis in the center and at the periphery of the ingots. For detection of possible II-As_2 and II_3-As_2 minority phases synchrotron x-ray powder diffraction analysis was carried out at diffracted wavelength λ = 1.3828(1) Å with Δ2θ = 0.01° steps of high-angle (400) reflections from an Si single crystal [6].

Pressure dependences of the resistivity ρ(P) and Hall coefficient R_H(P) have been measured at increasing and decreasing pressure at room temperature for p-$Zn_{1-x}Cd_xGeAs_2$ with different percentage of Mn in high pressure apparatus of "Toroid" type. The technique and technics of experiment is in detail described in [7].

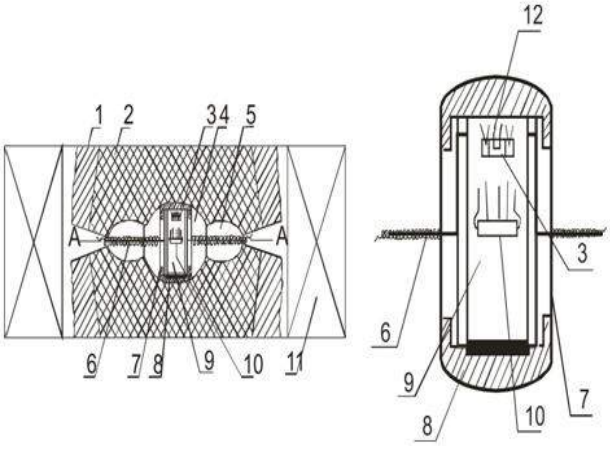

Fig. 1 A device for measuring of baric dependence parameters of solids at high hydrostatic pressure up to 10 GPa: 1 – ring of support; 2 – insert from WC-6M; 3 – manganin pressure pickup; 4 – catlinite insert; 5 – catlinite ring; 6 – electrical leads; 7 – teflon capsule; 8 – copper lid; 9 – cooper lids; 10 – sample; 11 – solenoid.

Samples had the form of a bar with dimension 2.8×1×1 mm. Parameters of studied $ZnGeAs_2$ samples with different percentage of Mn are given in table 1. Samples №№ 1 – 3 doped by Mn are ferromagnetics.

Table 1. Characteristics of measured p-$Zn_{0.9}Cd_{0.1}GeAs_2$ samples with different percentage of Mn

samples №	x	Conductivity type	ρ, Ω·cm	Concentration of majority carrier, cm^{-3} at 300 K
1	0.6	p	0.0152	$1.9\cdot10^{20}$
2	0.1	p	0.125	$1.1\cdot10^{20}$
3	0.14	p	0.114	$1.3\cdot10^{20}$

III. RESULTS AND DISCUSSIONS

Baric dependencies of the resistivity ρ(P) and Hall coefficient R_H(P) for p-$Zn_{1-x}Cd_xGeAs_2$:Mn are presented in Fig. 1 and 2. It is seen in Fig. 1 for samples, that the resistivity ρ(P) increases linearly at increasing pressure and the position of phase transition shifts towards lower pressures with an increase in percentage of manganese. For sample №2 the Hall coefficient reaches a maximum at P=1.5 GPa and tends to saturation at P>2 GPa. For sample №2 the Hall coefficient reaches a maximum at P=2 GPa and a minimum at P=5 GPa.

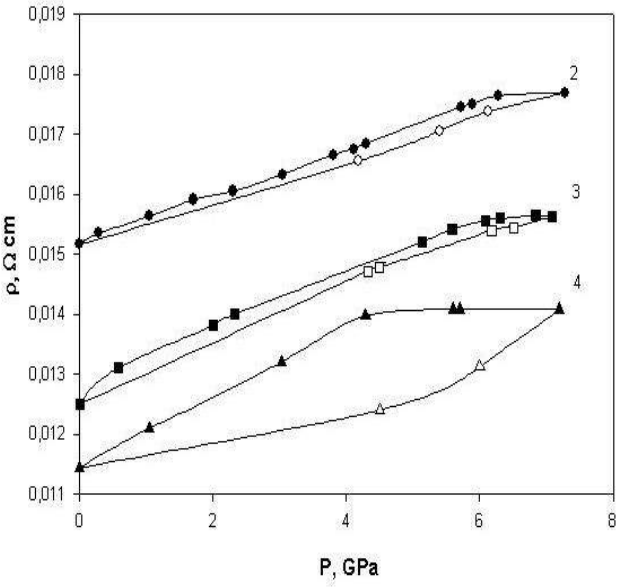

Fig.2 Pressure dependences of resistivity for the : p-$Zn_{1-x}Cd_xMn_{0.06}GeAs_2$ (№2), p-$Zn_{1-x}Cd_xMn_{0.1}GeAs_2$ (№3) and p-$Zn_{1-x}Cd_xMn_{0.14}GeAs_2$ (№4).

Features of R_H(P) for samples with percentage of manganese greater than x=0.06, where ferromagnetic parameters are expressed more strongly, we attribute to anomalous component of Hall effect and its modulation due to presence of narrow impurity bands.

Investigations of temperature dependencies of conductivity in 77-300 temperature range were carried out for samples listed in table 1 to determine the charge transport mechanism. Sample №2 demonstrates semiconductor type of temperature dependencies of conductivity (Fig. 3, curve 2). Samples with percentage of manganese x=0.1 and x=0.14 have metallic type of temperature dependences (Fig. 3, curve 3 and 4 respectively).

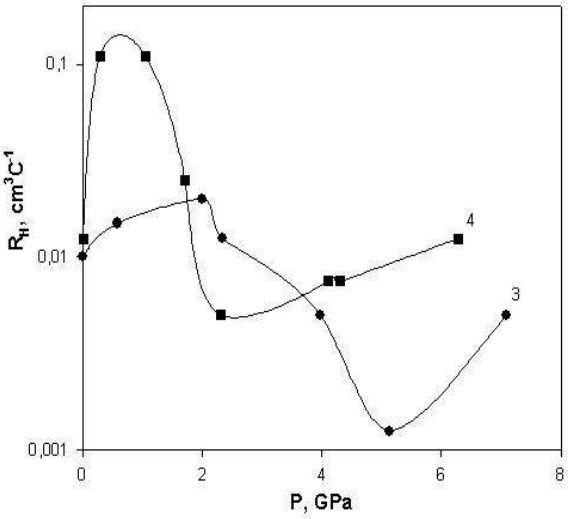

Fig. 3 Pressure dependences of Hall coefficient for the p-$Zn_{1-x}Cd_xMn_{0.06}GeAs_2$ (№2) and p-$Zn_{1-x}Cd_xMn_{0.1}GeAs_2$ (№3).

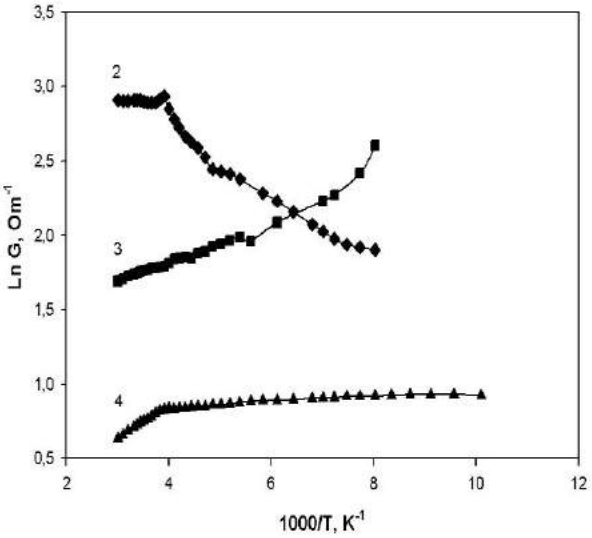

Fig. 4 Temperature dependences of resistivity for the p-$Zn_{1-x}Cd_xMn_{0.06}GeAs_2$ (№2), curve 2; p-$Zn_{1-x}Cd_xMn_{0.1}GeAs_2$ (№3), curve 3; and p-$Zn_{1-x}Cd_xMn_{0.14}GeAs_2$ (№4), curve 4.

High temperature activation energy of conductivity E_a=0.0874 eV for semiconductor type sample and low temperature activation energy of conductivity E_a=0.044 eV. For sample with percentage of manganese x=0.1 the conductivity is characterized by activation energy E_a=0.03 eV. For sample with percentage of manganese x=0.14 the activation energy E_a=0.0448 eV, which is characteristic to high temperature region, has value similar to one for sample with percentage of manganese x=0.06 in low temperature region.

The works was carried out under financial supported by programs of Presidium of the Russian Academy of Science "Heat physics and mechanics of extremal energy influences and physics of heavily condensed matter".

[1]. *L.I. Koroleva, V.Ju. Pablov, D.M. Zashchinsky, S.F.Marenkin, S.A.Varnavsky etc.* Magnetic and electric properties $ZnGeAs_2$:Mn. "Physics State Solid" 2007, v.49, №11, p.2022.

[2]. *V.M.Novotortsev, V.T.Kalinnikova, L.I.Koroleva, R.V.Demin, , S.F.Marenkin, T.G.Aminov, G.G.Shabunina, S.V.Bojchuk, V.A.Ivanov.* High-temperature ferromagnetic semiconductor $CdGeAs_2${Mn}. Magazine of inorganic chemistry, 2005, v.50, №4, p.552.

[3]. Semiconductors by edition *N.A.Gorjunovoj, J.A.Valova* «The Soviet radio», 1974.

[4]. *L.G.Khvostantsev,L.P.Vereshaghin,A.P.Novikov.* Device of Toroid type for high pressure generation. High Temp.-High Pressure, v.9**,** № 6, p.637.

[5]. *Yu. Mollaev, L.A. Saypulaeva, R.K. Arslanov, L.A.Saypulaeva, S.F. Marenkin.* Influence of hydrostatic pressure on physical properties monocrystals $CdAs_2$. Inorganic Materials, 2001, v.37, № 4, p.405.

[6]. *A.V. Kochura, R. Laiho, A. Lashkul, E.Lahderanta, M.S. Shakhov, I.S. Zakharov, S.F.Marenkin and et. al.* Synthesis and magnetic properties of Mn-doped $Cd_{0.1}Zn_{0.9}GeAs_2$ solid solutions. J. Phys.: Condens.Matter, 2008, №20, p.1.

[7]. *L.G.Khvostantsev,L.P.Vereshchagin, A.P.Novikov.* Device of Toroid type for high pressure generation. High Temp.-High Pressure, **9**(6), 637 (1977).

REACTIVE PROPERTIES OF THE COLLECTOR JUNCTION OF TRANSISTOR STRUCTURES BASED ON THE Si AND Ge

E.A.JAFAROVA, Z.A.ISKENDERZADE*,
L.A.ALIEVA, E.S.TAPDYGOV, A.A.BAYRAMOV
Institute of Physics Azerbaijan National Academy of Sciences,
AZ 1143, Baku, H. Javid av.33
**Azerbaijan Technical University,*
e-mail: celmira1@rambler.ru

Influence of the emitter current on capacity of the forward-biased collector junction of the Si and Ge transistor structures is investigated. It is shown that at emitter current leakage the non-equilibrium carriers in the collector junction cause occurrence of the additional capacity as well as facilitate the inversion of the total capacity of the collector junction to inductance (negative capacity). Thus, by means of change emitter current it is possible to manage both with size and sign of the capacity of a collector current. It is shown experimentally that at high emitter currents there is observed both increase and decrease of the barrier capacity of collector junction of the investigated transistors in dependence on the character of junctions and doping levels of base and collector ranges. The experimental results have been found to be in satisfactory agreement with calculations.

INTRODUCTION

Inversion of effective capacitance of p-n junction structures into induction observed in diodes, light-emitting diodes (LED), photo elements, emitter and collector junctions of transistors [1]. Also, negativity capacitance was observed in chalcogenide films, multilayer heterostructures, in homogeneous samples with inertial-relaxation character of reactivity, as well as in silicon p^+-n junctions irradiated by fast electrons [2,3]. Investigation negativity capacitance of semiconductor-semiconductor junctions and metal-semiconductor contacts is importance for using its induction properties in IC chips.

Using so-called "transistor effect" nonequilibrium carriers can be created due to neighbouring p-n junction in region of the volume charge layer (VCL). Number authors [2,5] have investigated an influence of emitter current through transistor on barrier capacitance of collector junction, but their results are some discrepant. Taking into account that theoretical derivation of the dependence of collector junction capacitance is very difficult, compressive study this problem is very interesting.

EXPERIMENT

Received by fused-diffusion method silicon n-p-n transistor structures (TC samples) have highly doped base region (with thickness d =10 mkm) in comparison with collector one ($\sigma_b > \sigma_к$), concentration of donors in collector region $N_D \approx 2\times10^{15}$cm^{-3}. And vice versa, received by fused method in germanium p-n-p transistor structures (TG samples) with thickness of base $d \approx 80$ mkm base region is doped less than collector one ($\sigma_b < \sigma_к$) and concentration of donors in collector region $N_D \approx 1.6\times10^{14}$ cm^{-3}. The area of collector junction S_k=0.16 cm^2 and 0.125 cm^2 for TC and TG samples, accordingly.

Measurements capacitance of collector junction for different values of emitter current (I_e=0÷150 mA) were carried out on the bridge of full conductivity MPP-300 and capacitance measuring instrument L2-7 in frequency range f=5÷465 kHz for amplitude of testing signal 25 mV.

RESULTS AND DISCUSSION

As investigations showed, diffusion capacitance of collector junction is not almost depended on emitter current for small values ($I_e \leq 10$ mA). As $I_э$ increases for low frequency ($\omega\tau << 1$), so steadily does the capacitance, for high frequency ($\omega\tau \geq 1$) the character of reactivity is inductivity and for $U_{dir} > U_{inv}$ (U_{inv}- inversion voltage) the capacitance pass by zero and is negativity.

The value of effective capacitance of collector junction and also its inversion to inductance is defined by change of concentration of free carriers and inertia of establishment of quasi-stationary state for high frequencies.

The concentration of nonequilibrium carriers entered in collector region for fixed emitter current ($I_e \leq 10$ mA) have been calculated. For small doses of emitter current ($I_e \leq 10$ mA) these values are $n_к = 5\times10^{13}$ cm^{-3} and $p_к = 8\times10^{13}$ cm^{-3}, accordingly for samples TC and TG types, these are considerably less than concentration of equilibrium carriers, so the capacitance of forward-biased collector junction almost does not change. For $I_e \geq 30$ mA dependence $C_к(I_e)$ has linear character.

Nonequilibrium carriers in collector junction are caused the appearance additional capacitance and facilitate the inversion of total capacitance of collector junction to inductance. Extrapolating the dependence U_{inv} (Ie) to large emitter currents we get value I_e^{cr}. In this case we have the inversion of reactivity of collector junction without applying external voltage to it. For TC samples this value I_e^{cr} =0.36 A, and for TG - 0.75 A, then $n_k = 1.8\times10^{15}$cm^{-3} и $p_к = 6\times10^{15}$cm^{-3}. For silicon transistor structures there is a good consent this value with donor concentration in collector region $N_D = 2\times10^{15}$cm^{-3}, and for germanium one we have increased value that may be caused weak dependence $U_{inv}(I_e.)$. So, by changing emitter current we can control both the value and sign of capacitance of collector junction.

Leaking of emitter current pass the transistor collector junction of which shifted to reverse direction, is accompanied by appearance redundant electrons (for n-p-

n transistor), concentration of which defined by value of current $I_к$ and velocity of carriers v_n.

One of advantages of this method of nonequilibrium free carriers doping into layer of volume charge (LVC) of p-n junction, for example before light injection [4] is constancy of value n_k along the whole of collector junction.

In transistor structures with high doped collector region the increase of reverse bias of collector junction is caused broadening LVC to direction base, this leads to base width decreasing. Owing to this, injected carriers more fast diffuse across narrower base, recombination of nonequilibrium free carriers in base decreases, this is cause to increase number of electrons reached collector. For transistor structures with high doped base region there is not the effect of decreasing width of base for increasing bias on collector.

For asymmetric sharp collector junction the Poisson equation:

$$W = W_0 \sqrt{\frac{N_A \cdot N_D}{(N_A + n_k)(N_D - n_k)}}\ , \qquad (1)$$

where N_A , N_D are the acceptor concentration in base region and donors in collector region during leaking emitter current, W_0 is a width of LVC of collector junction for given U and n_k=0. Therefore, barrier capacitance of sharp p-n junction changes by low:

$$C_{bar} = C_0 \sqrt{(1+\frac{n_k}{N_A})(1-\frac{n_k}{N_D})} \qquad (2)$$

In symmetric sharp p-n junctions, when N_D~N_A, barrier capacitance does not dependences on value of emitter current for its small densities. When large concentration of nonequilibrium carriers resultant barrier capacitance will decrease when n_k increases and when large emitter current, when n_k equals impurities concentration, C_b will be approach to zero.

For asymmetric sharp collector junctions changing C_b with current I_e has various characters: if base region of transistor is doped higher than region of collector N_A>>N_D, then LVC of collector junction mainly located in collector region therefore n_k/N_A<<1 and barrier capacitance decreases by low:

$$C_{bar} = C_0 \sqrt{(1-\frac{n_k}{2N_D})} \qquad (3)$$

If base region is doped weakly than collector region (N_A<<N_D), then layer of volume charge mainly located in base region and C_b, increases when emitter current increases:

$$C_{bar} = C_0 \sqrt{(1+\frac{n_k}{2N_A})} \qquad (4)$$

Both experimental and theoretical investigations influence of emitter current on barrier current of fused-diffusion collector junction are absent. For simplicity solving of Poisson equation in fused-diffusion p-n junction the distribution of impurities better present by piecewise linear function having various gradient concentration of impurities in hole (a_1) and electron (a_2) regions. Such presentation is closed to really profile of impurities distribution and allows at most simplifies difficult mathematical calculations. Calculations showed that LVC width W=x_n+ x_p, where x_n, x_p are the positions of boundaries of collector junction for various values of reverse biases for symmetric linear junctions (a_1=a_2=1.34×10^{20}cm^{-4}) doesn't dependent on value of emitter current (fig.1, curve 2). Therefore, barrier capacitance of diffusion collector junction doesn't dependent on value I_e.

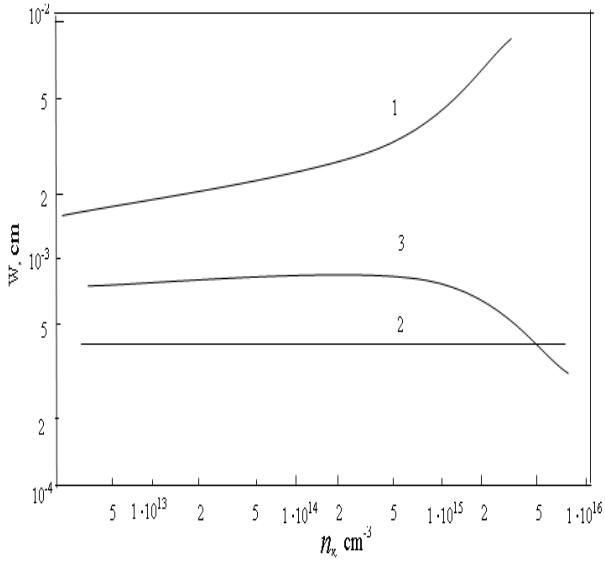

Fig.1. Calculated curves of dependences of width of the volume charge layer of collector junction on concentration of nonequilibrium carriers:1-a_1= 3.3 × 10^{18}cm^{-4}, a_2= 6.7 × 10^{17}cm^{-4} , U_{rev}= 50 V ; 2- a_1= a_2=1.3 × 10^{20}cm^{-4}, a_2= 6.7 ×10^{17}cm^{-4}, U_{rev}=10 V; 3-a_1= 3.3 × 10^{18}cm^{-4} , a_2= 4.7 × 10^{20}cm^{-4}, U_{rev} = 50 V

For cause of asymmetric linear junctions when a_2>a_1, LVC width of collector junction decreases with n_k increases (fig.1, curve 3, U_{rev}= 50 V, a_1= 3.34 × 10^{18} cm^{-4}, a_2= 4.67 × 10^{20} cm^{-4}). For a_2<a_1 (a_1= =3.34×10^{18}cm^{-4}, a_2= 6.67 × 10^{17}cm^{-4}, U_{rev}= 50 V) with increasing n_k the LVC width increases (fig.1, curve 1).

Measurements of dependence of barrier capacitance of collector junction of silicon and germanium transistor structures (TC and TG) on reverse bias for 300K and f=100 kHz are presented on fig.2. For TC samples collector region is doped weakly than base, nonequilibrium electrons compensating volume charge of donors in collector region expands LVC and the capacitance of collector junction decreases. For I_e=30 mA the concentration of nonequilibrium electrons n_k=1.5×10^{14} cm^{-3}. Decreasing the capacitance of collector junction on I_e occurs up to that the concentrations of impurities are equalized on both LVC boundaries of collector junction,

after this barrier capacitance changing with increasing I_e is slow down.

In linear asymmetric collector junctions in which the region of collector is doped weakly than base, decreasing C_b is observed only for relatively small currents. If collector current increases, when concentration of doped electrons fully neutralizes volume charge of donors there is occurs the influence of voltage drop on the successive parasitic resistance R_{par} in collector circuit, that occurs some decreasing reverse bias applied to collector junction.

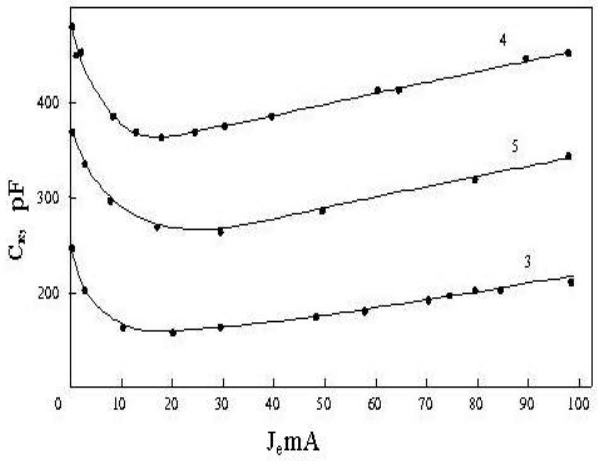

a)

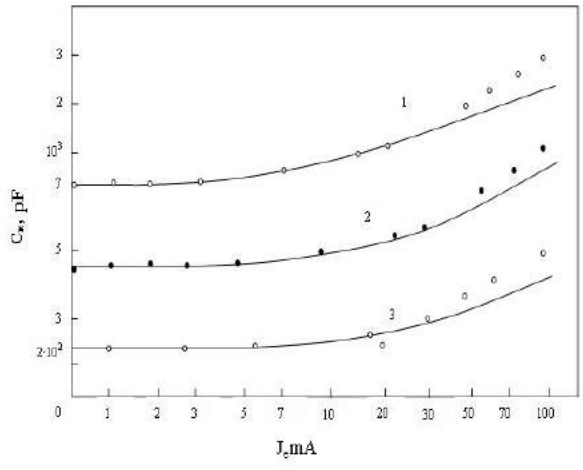

b)

Fig.2. The dependence of barrier capacitance of collector junction of TC(a) and TG(b) on emitter current for various U_{rev} (300K, f=100 kHz): 1-1V; 2-6V; 3-50V; 4-4V; 5-10V; points – experimental data, curves – calculated data.

From fig.2a it is observed, that effect begin observed for $I_к$=$I_{e.}$=30 mA. If R_{par}≈100 Ohm, then increasing C_b on $I_{e.}$ for TC sample will be noticeable and considerable exceed effect of decreasing C_b, due to LVC broadening of collector junction. This effect is large for small U_{rev}(4;10 V). For large U_{rev}(50 V) interactions both effects lead to weakening of C_b (I_e) dependence.

In germanium transistor structures (fig. 2b) for small I_e the capacitance is constant, injected holes have charge coincidental to charge of ionized donors on the base side of collector junction, and increases from I_e=5 mA. For these transistors the influence R_{par} in collector circuit only some strengthen observed effect (fig.2 – points are experimental data, curves - calculated).

Dependence of barrier capacitance of collector junction on emitter current for both types transistors do not change for frequencies f=5÷600 kHz. Really, the time flight of carriers over base $\tau \approx 10^{-7}$-10^{-8} sec, that considerable less than period of oscillation of alternate signal.

For small U_{par} on collector junction for TC samples we observe sharp increasing C_b beginning with I_e ≈30 mA, that maybe caused by influence of capacitance of mobile carriers C_{mc}: nonequilibrium electrons fully compensate volume charge of donors in LVC collector part width of which is small is small for small U_{rev}, and remains in excess.

If external voltage on collector junction is absent then barrier capacitance increases linearly with emitter current with coefficient of proportionality 1.5×10^{6} pF/A, that caused by influence of stored charge of free carriers, shifted collector junction in straight direction for leaking emitter current.

CONCLUSION

Influence of the emitter current on capacity of the forward-biased collector junction is investigated.

It is shown that by means of change emitter current it is possible to manage both with size and sign of the capacity of a collector current.

There is observed both increase and decrease of the barrier capacity of collector junction of the investigated transistors in dependence on the character of junctions and doping levels of base and collector ranges. The experimental results have been found to be in satisfactory agreement with calculations.

[1]. *E.A. Jafarova* Reactive characteristics of barrier structures on base of silicon under illumination. // Fizika, 2005, v 11, №4, p.3-10

[2]. *T.V. Kolinz* Dependence of collector capacitance on collector current of transistor made by method of double diffusion. // TIIER,1969, v.57, is.5, p.110-112

[3]. *N.A.Polonsky, S.V.Shpakovsky,N.N.Gorbachuk, S.B.Lastovsky* Negative capacitor (inductive type impendance) of silicon p^+ -n junctions irradiated by fast electrons. // FTP, 2006, v.40, is.7, p.824-828

[4]. *N.A. Shehovstev* Dependence of capacitance on current of germanium p^+-p-junctions in temperature range 290-330 K. // FTP, 2009, v.43, is.4, p. 456-459

[5]. *Ch.Prasad, M.Misra* Current dependence of collector junction capacity of alloy junction transistor under inverse operating condition. //Sol.Stat.Electr.1969,v.12,№6,p.502-505

FLUCTUATION OF THERMOMAGNETIC CURRENT IN QUANTUM FILM

R.G. AGHAYEVA
H.M. Abdullayev Institute of Physics of the NAS of Azerbaijan
Az-1143, Baku, H. Javid ave., 33
E-mail: a.rana@physics.ab.az

In the coherent-state representation the quantum mechanical calculation of thermomagnetic current fluctuations in a non-degenerate parabolic quantum film is conducted using method of effective Hamiltonian. The results obtained are applicable for study of noise in electron instruments.

INTRODUCTION

The advances in electronics, especially in the nanoscale electronics, have attracted a wide interest in the study of noise in the electron devices since a noise restricts the sensitivity of those when operating with weak signals [1].

A noise is created by the fluctuations. The fluctuations are generally small. However, they play the decisive role in the precise measurements and communication techniques [1, 2]. In addition to the equilibrium fluctuations, there is a variety of the fluctuation mechanisms detected only in the process of a current flow. The simplest measure of the fluctuations, for example, of the current, is the current dispersion.

Known currently works contain, as a rule, a general analysis of noise (see, for example, [1]). The principal object of the present paper is the calculation and the estimation of the dispersion of thermomagnetic current in concrete quantum film.

To calculate the current dispersion D equal to

$$D=\langle I^2\rangle-\langle I\rangle^2 \qquad (1)$$

it is necessary to estimate the current $\langle I\rangle$ created by the electron.

Many authors tried to solve this problem during determining the thermoelectromotive force in a quantizing magnetic field [3]. But in those papers the temperature was not included in the Hamiltonian because the temperature is related to the statistical force.

The method that includes a temperature in the Hamiltonian (MEH - the method of effective Hamiltonian) is offered in [4]. By analogy with the electric field, we assume that the temperature is the potential of a certain external field with the intensity, – grad *T*. The corresponding potential energy takes the following form $-k\vec{r}\cdot grad$. Consequently, when constructing the Hamiltonian we proceed from the formal correspondence of the electrostatic potential φ with temperature *T* and the absolute value of the electron charge *e* with Boltzmann constant *k*. MEH allows us to calculate

The results obtained may be used, for example, to increase the sensitivity of temperature sensors.

THERMOMAGNETIC CURRENT

As follows from [5] MEH works not only in case of bulk sample and the quantum wire, but in case of a quantum film. İn the paper [5]

1. we considered a non-degenerate parabolic quantum film in a quantizing magnetic field $\vec{H}$ II z,
2. we supposed that the system under consideration is weakly non-uniform, and the temperature gradient in the sample is directed along the *x* axis, i.e. *T=T(x)* . Then the temperature deviation from its equilibrium magnitude is small and in the simplest case of constant temperature gradient $T(x)=T_0\left[1+\delta\left(xL_x^{-1}+\frac{1}{2}\right)\right]$. Here L_x is the sample length along the x axis, $-\frac{1}{2}L_x<x<\frac{1}{2}L_x$, δ is the parameter of smallness, $\delta<<1$,
3. we made all the calculations in the coherent-state representation, and restricted ourselves to the first- order terms in δ,
4. we presented the Hamiltonian of the problem in the form

$$\hat{H}=\hat{H}_0-k\vec{r}\,gradT, \qquad (2)$$

where the Hamiltonian of the equilibrium system,

$$\hat{H}_0=\frac{1}{2m}\left[\hat{P}_x^2+(\hat{P}_y+m\omega_c x)^2+\hat{P}_z^2\right]+\frac{m\omega_0^2x^2}{2} \qquad (3)$$

ω_0 characterizes the parabolic potential of the quantum film, $\omega_c=eH/mc$ is the cyclotron frequency.

5. we calculated the current, based on well know expressions

$$\hat{j}_y=-e\hat{v}_y,\ j_y=-eTr(\hat{\rho}\hat{v}_y),\ \hat{v}_y=(i/\hbar)\left[\hat{H},y\right] \qquad (4)$$

where $\hat{v}_y$ is th e velocity operator, (-*e*) is the electron charge, $\hat{\rho}$ is the non-equilibriumelectron density matrix,

6. we showed that in presence of small and uniform temperature gradient the density matrix of the system is similar to that of this same system in the absence of the temperature

gradient, but exposed to an external field whose contribution to the Hamiltonian of the system is given by the operator $\hat{V}$:

$$\hat{V} = \delta\xi\left(\frac{x}{L_x}+\frac{1}{2}\right) - \frac{\delta}{\gamma}\frac{x}{L_x} - \frac{\delta}{2}\left(\hat{H}_0\frac{x}{L_x} + \frac{x}{L_x}\hat{H}_0 + \hat{H}_0\right),$$
$$\hat{\rho} = Z^{-1}\exp\left(-\hat{H}\gamma\right), \quad (5)$$

$\gamma = (kT_0)^{-1}$, Z is the statistical sum, ξ is the chemical potential, and for the non-degenerate statistics

$$\hat{\rho} = \hat{\rho}_0 + \hat{\rho}_1, \quad \hat{\rho}_0 = Z_0^{-1}\exp\left[-(\hat{H}_0 - \xi)\gamma\right],$$
$$\hat{\rho}_1 = -\hat{\rho}_0\int_0^{\gamma} d\gamma' \exp(\hat{H}_0\gamma')\hat{V}\exp(-\hat{H}_0\gamma') \quad (6).$$

Here $\hat{\rho}_0$ is the equilibrium density matrix, Z_0 is the corresponding statistical sum, and $\hat{\rho}_1$ is the non-equilibrium addition to the density matrix,

7. we derived the expression for j_y. It should be noted that this expression is proportional to δ.

CALCULATION OF THERMOMAGNETIC CURRENT DISPERSION

Let us calculate the dispersion of the thermomagnetic current in the linear approximation on the basis of equation (1). It is known [6] that

$$D = \frac{n\Omega}{L_y^2}\left(\left\langle \hat{j}_y^2\right\rangle + \left\langle \hat{j}_y\right\rangle^2\right) \quad (7)$$

Here n is the density of the conductivity electrons, $\Omega = L_xL_yL_z$, L_y, L_z - is the sample length along the y and z axis,

respectively. Considering that the current $\langle \hat{j}_y \rangle$ is proportional to δ, we omit $\langle \hat{j}_y \rangle^2$ in the linear approximation. Then based on expression (7) we write the dispersion of our system in the form

$$D = n\,\frac{\Omega}{L_y^2}e^2 Tr(\hat{\rho}\hat{v}_y^2) \quad (8)$$

It can be easily shown that in the coherent-state representation

$$\left[\hat{H}_0, y\right] = -\frac{i\hbar}{m}\left(\frac{\omega_0}{\omega}\right)^2\hat{p}_y \quad (9)$$

Using the density matrix $\hat{\rho}$ from (6), the velocity operator (4) and (9) we find

$$D = \frac{n\Omega}{L_y^2}\left(\frac{e}{m}\right)^2\left(\frac{\omega_0}{\omega}\right)^4 \cdot$$
$$\cdot Tr\left[\hat{\rho}_0\left(1-\delta-Tr\hat{\rho}_1\right)\hat{p}_y^2 - 2\frac{\delta}{L_x}\hat{\rho}_0\hat{p}_y^2 x + \hat{\rho}_1\hat{p}_y^2\right] \quad (10)$$

The member $Tr\hat{\rho}_1$ appears in the first term of the statistical sum expansion in the perturbation. The equilibrium statistical sum is widely used in equation (10).

To calculate the current we adopt the scheme from [5]. α, k_y, k_z are the quantum numbers of our problems. The second term in the expression for the dispersion D tends to zero when integrated over α.

It can easily be shown that

$$Tr\hat{\rho}_0\hat{p}_y^2 = \frac{m}{\gamma}\left(\frac{\omega}{\omega_0}\right)^2 \quad (11)$$

In this case

$$D = D_0 + D_1 \quad (12)$$

where

$$D_0 = \frac{n\Omega\, e^2}{L_y^2 m\gamma}\left(\frac{\omega_0}{\omega}\right)^2 \quad (13)$$

is the equilibrium part of the dispersion, while

$$D_1 = \frac{n\,\Omega e^2}{L_y^2 m^2}\left(\frac{\omega_0}{\omega}\right)^4 Tr\hat{\rho}_1\hat{p}_y^2 - D_0 Tr\hat{\rho}_1 - \delta D_0 \quad (14)$$

is the additional non- equilibrium part.

As may be seen from expression (8) we restrict ourselves to the dispersion due to the electron velocity fluctuation.

The expression for D_0 is obtainable from D at δ = 0, which corresponds to the equilibrium state of the system

characterized by the temperature T_0. Consequently, D_0 is related to the fluctuation due to the chaotic thermal motion of the particles forming the system (thermal noise).

If the conductor has a constant temperature gradient this gives rise to an additional contribution D_1 to the thermo-magnetic current dispersion D connected with the random character of the charge carrier diffusion.

Let us consider D_1. Subsequent to arranging the operators, using the eigenvalues and integrating over α , k_y, k_z (see [5]) we obtain

$$Tr\hat{\rho}_1 = \frac{\delta}{2}\left(1-\xi\gamma+\frac{\hbar\omega\gamma}{2}\coth\frac{\hbar\omega\gamma}{2}\right),$$
$$Tr\hat{\rho}_1\hat{p}_y^2 = \frac{\delta m}{2\gamma}\left(\frac{\omega}{\omega_0}\right)^2\left(2-\xi\gamma+\frac{\hbar\omega\gamma}{2}\coth\frac{\hbar\omega\gamma}{2}\right) \quad (15)$$

Substituting (15) into (14) and using (12) we finally get

$$D_1 = -\frac{\delta}{2}D_0 \quad (16)$$

The relation of the equilibrium part of the dispersion to the non- equilibrium part can be presented as

$$\frac{D_1}{D_0} = -\frac{\delta}{2} \quad (17)$$

Consider the longitudinal isothermal Nernst-Ettingshausen effect, i.e. the appearance of an electric field ***E*** along a temperature gradient in a solid conductor placed in a magnetic field which is perpendicular to the temperature gradient. It is known that if the temperature gradient is directed along the *x* axis and the strong magnetic field along the *z* axis, then

$$E_x = -j_y\sigma_{yx}^{-1} \quad (18)$$

$\sigma_{yx} = nceH^{-1}$ is the expression for the non-diagonal component of the conductivity tensor. The quantity ***E*** is conveniently expressed in terms of the voltage ***U***:

$$U = -j_y\sigma_{yx}^{-1}L_x \quad (19)$$

Taking into account the thermomagnetic current dispersion we obtain the mean-square noise voltage in the form:

$$\left(\left\langle\overline{U^2}\right\rangle\right)^{1/2} = -D^{1/2}\sigma_{yx}^{-1}L_x \quad (20)$$

This noise limits the sensitivity of the temperature sensor based on the longitudinal isothermal Nernst-Ettingshausen effect. The input signal is really indistinguishable from the background of random vibrations if it is less than $\sqrt{\left\langle\overline{U^2}\right\rangle}$.

It is easy to verify that the ratio of noise voltage (19) to the noise voltage (19) at δ = 0 is equal to $[1-(\delta/4)]$, and the term $(-\delta/4)$ is associated with correction D_1. It is clear that the correction D_1 decreases the noise voltage.

Therefore, it should be considered the contribution from D_1 into the temperature sensors performing the measurements in a small temperature range but with sufficiently high accuracy.

CONCLUSION

The results obtained may be used, for example, to increase the sensitivity of temperature sensors whose operation is based on the longitudinal isothermal Nernst-Ettingshausen effect.

I would like to express my deep gratitude to Acad. Hashimzadeh F.M. for support.

[1]. *M.Di.Ventra*. Electrical Transport in Nanoscale Systems. N-Y.,"Cambridge University Press", 2008

[2]. *W.H.Louisell.* Radiation and noise in quantum electronics. N-Y., "McGrow-Hill Book Company", 1964.

[3]. *B.M.Askerov*. Elektronnie yavleniya perenosa v poluprovodnikakh.M., "Nauka",1985(inRussian).

[4]. *R.G.Agayeva*. J.Phys.C:SolidState Phys. 1985, 18, p. 5841-5848

[5]. *R.G.Agayeva*. Dokl. NAN Azerb. LXVI, №1, 2010 (in Russian).

[6]. *A.M.Vasiliyev*. Introduction to statistical physics. M., "Vysshaya shkola", 1980

TEMPERATURE DEPENDENCE OF THE KINETIC PROPERTIES OF ALLOY $BI_{0.94}SB_{0.06}$

ELTAJ YUZBASHOV[1] , BAKIR TAIROV[1]

[1] *Institute of Physics of Azerbaijan National Academy of Sciences, H.Javid pr., 33, Baku, AZ 1143, Azerbaijan*

eltaj100@yahoo.com, btairov@physics.ab.az

I. INTRODUCTION

Investigation of solid solutions of $Bi_{1-x}Sb_x$ (x = 0.03 ÷ 0.2) displays that those solutions are perspective materials for solid coolers functioning on the basis of galvano- and thermomagnetic effects [1]. Moreover those materials are of broad interest from the theoretical aspect. Due to the smallness of the characteristic energetic parameters of solid solutions of Bi-Sb, those materials are very sensitive to the external impacts (temperature, pressure, presence of electroactive impurities, defects, etc.). By varying external influence in comparatively small range, it is possible to investigate topology of Fermi surface, various phase transitions, alter the statistics of charge carriers in rather broad range etc. That is why these materials are still being investigated as bulk materials, thin films and nanoscale structures [2-4].

In itself studying the transport phenomena in the system of Bi-Sb represents a powerful tool for investigating energetic zone structure and mechanisms of scattering of charged carriers in these materials. But studying galvano- and thermomagnetic effects in these materials at intermediate (77K-300K) and high (more than room temperature) temperatures become irreplaceable, because the rest powerful methods for investigating energetic zone structure and mechanisms of scattering of charged carriers, as oscillation and resonance methods, are effective only at ultra- and low temperatures.

II. METHOD

Investigation of temperature dependence of low-field galvanomagnetic coefficients of the alloy of $Bi_{0.94}Sb_{0.06}$ at the temperature range of 77÷300 K was carried out in the paper. Single crystals of $Bi_{0.94}Sb_{0.06}$ were grown by the method of Chokhralsky in the experimental equipment [5] using solid replenishment. Two types of rectangular samples were cut from the single crystal ingot by electrospark method; large edges of the first group of samples were parallel to binary axe, but the second group ones were aligned parallel to trigonal axe.

For diminution of influence of parasite thermomagnetic effects on the precision of measurement of isothermal galvanomagnetic coefficients, the measurements were carried out in special module filled with helium. Due to the precautions the temperature gradient between contact points was reduced up to 0.03 ÷ 0.05 K. For reducing of thermal leakage over measuring wires and thermocouples were used thin ones (having diameter less than 0.1 mm). All measuring wires and thermocouples were thermostateted. Calculation of the wires' length was carried out according to the work [6]. As known during the measurement of specific resistance of a thermoelectrical specimen an additional error make its appearance due to the Peltier effect. But using a fast-acting, precious digital voltmeter allows to make this error negligible. The measurement of other galvanomagnetic coefficients were conducted by the high-precious D.C. Potentiometer. In every case the fulfillment of the low-field condition ($\mu B << 1$) were tested, because this varies in the rather broad range depending on temperature and orientation of magnetic field with respect to main crystallographic axes (usually its magnitude not exceeds 200 ÷ 400 Oersted at nitrogen temperatures).

The following components of the tensor of electric resistance in low magnetic field for the alloy of $Bi_{0.94}Sb_{0.06}$ - two components of specific resistance (ρ_{11} and ρ_{33}), two components of Hall effect (R_{231} and R_{123}) and, five components of magnetoresistance ($\rho_{11,11}$, $\rho_{11,22}$, $\rho_{11,33}$, $\rho_{33,11}$, $\rho_{33,33}$) – were measured.

The dependence of components of specific resistance (ρ_{11} and ρ_{33}) on temperature at the investigated temperature range showed metallic character. The temperature dependence of the Hall and magnetoresistance coefficients is shown in the figures 1 and 2, correspondingly. From the figure 1 it is clear that both Hall components greatly decrease with temperature.

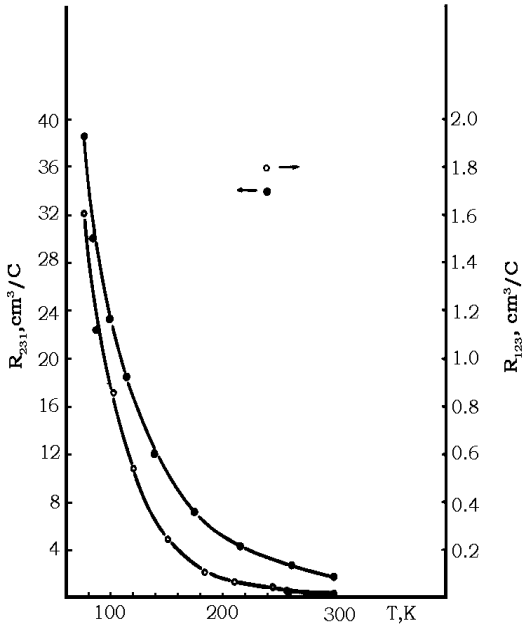

Fig.1. Temperature dependence of the Hall coefficients.

Such decreasing may be caused by increasing of the concentration of charge carriers. However, as the conductance of Bi-Sb alloys is intrinsic at the given temperature range, the changes of Hall coefficients may be related to the alteration of ratio of mobilities of electrons and holes. Therefore, the temperature

dependence of Hall coefficients cannot quantitatively characterize alteration of the concentration of current carriers and more complicated calculations considering of adopted model of energetic spectra must be conducted.

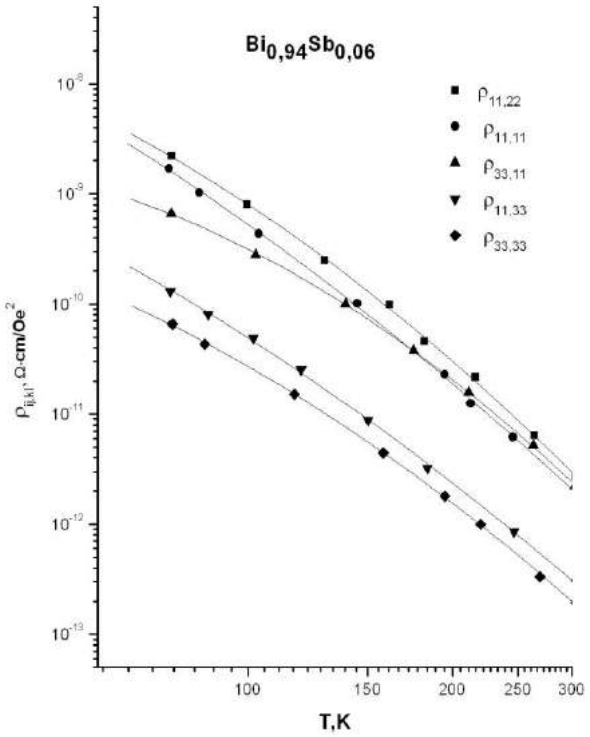

Fig.2. Temperature dependence of the magntoresistance coefficients.

From the figure 2 it is clear that common features of the temperature dependences of all measured components of magnetoresistance are identical. Each graph representing the dependence of $lg\ \rho_{ij,kl}$ on $lg\ T$ may be considered as two nearly linear sections: low-temperature section (from 77K to 120 ÷ 160K) which monotonically turn into high-temperature section (from 160 ÷ 200K to 300K). These dependences bear exponential character ($\rho_{ij,kl} \sim T^{P}$), and index of power P is greater at the high-temperature section than at low-temperature one, and its value depends on the direction of a component.

III. RESULTS AND DISCUSSION

For the quantitative interpretation of the obtained experimental data were used relations between low-field components of the galvanomagnetic tensor and kinetic parameters of electrons and holes which are determined from the selected model of energetic zone structure for the given alloy [5] . To obtain a fairer assessment of the experimental data, a computer program producing a least-mean-squares best fit to all nine coefficients were devised. Due to the calculations the following kinetic parameters were determined: currier densities of electrons N and holes P; their mobilities μ_1 , μ_2 , μ_3 and ν_1 , ν_3 , correspondingly; and the tilt angle of electronic isoenergetic ellipsoids to the bisectrix axis (φ_e). It should be noted that not all of these parameters were determined with the same accuracy. The most preciously were determined N (P), μ_1, μ_3 and ν_1. The contribution of μ_2 is small and is almost swamped by μ_1, and μ_3.

The solution shown in table 1 was obtained for the case of equality the carrier densities of electrons N to carrier densities of holes P, localized at T-point of the Brillouin zone.

Table1.

T	N=P	φ	μ_1	μ_2	μ_3	ν_1	ν_3
K	$*10^{16}$ cm^{-3}	Deg.	$*10^5 cm^2/v\cdot sec$				
77	10.97	6.41	12.52	0.65 /-1/	8.23	0.944	1.46
90	14.27	6.58	9.43	0.54 /-1/	5.5	0.76	1.29
110	20.43	7.08	6.29	0.38 /-1/	3.43	0.53	0.8
130	28.46	6.75	4.56	0.24 /-1/	2.22	0.375	0.527
150	37.41	7.29	3.23	0.16 /-1/	1.51	0.28	0.40
170	48.87	6.99	2.39	0.10 /-1/	1.02	0.21	0.31
190	62.62	6.99	1.78	0.76 /-2/	0.74	0.16	0.22
210	77.51	7.62	1.35	0.55 /-2/	0.55	0.13	0.18
250	123.2	7.67	0.76	0.36 /-2/	0.31	0.76 /-1/	0.95 /-1/
270	148.3	7.9	0.60	0.31 /-2/	0.24	0.62 /-1/	0.77 /-1/
300	199.1	7.9	0.40	0.24 /-2/	0.17	0.45 /-1/	0.46 /-1/

The result of calculations for the case of equality carrier densities of electrons N to the sum of carrier densities of holes localized at T- and L- points of the Brillouin zone (i.e. $N_L = P_L + P_T$) is shown in the table 2.

Table 2.

T	N	P_T	P_L	R	μ_1	μ_2	μ_3	ν_1
K	$*10^{16}$ cm^{-3}			%	$*10^5 cm^2/v\ sec$			
77	11.93	11.40	0.53	4.4	11.42	4.74 /-2/	8.31	0.66
90	15.59	14.72	0.87	5.6	8.29	4.62/-2/	5.86	0.58
110	22.50	21.03	1.47	6.5	5.37	3.55 /-2/	3.77	0.42
130	31.07	28.79	2.28	7.34	3.71	2.46 /-2/	2.45	0.31
150	40.67	37.46	3.21	7.9	2.73	1.76 /-2/	1.7	0.25
170	53.10	48.50	4.60	8.66	1.99	1.27 /-2/	1.17	0.19
190	67.67	61.57	6.10	9.0	1.49	0.96 /-2/	0.84	0.14
210	83.71	75.70	8.01	9.6	1.15	0.79 /-2/	0.63	0.11
250	131.2	118.5	12.7	9.7	0.67	0.52 /-2/	0.35	0.70 /-1/
270	157.9	142.75	15.15	9.6	0.54	0.47 /-2/	0.27	0.58 /-1/
300	209.4	192.26	17.14	8.2	0.39	0.35 /-2/	0.19	0.44 /-1/

In this calculation the tilt angle of electronic isoenergetic ellipsoids to the bisectrix axis (φ_e) was chosen as a constant equaled to $6^0 40''$. This assumption is valid, because in the temperature range studied the alteration of φ_e does not greatly affect to the result of the calculation. Further the calculations indicated that as the temperature increases the results of the calculation are less sensitive to the value of ν_3. The table II shows that a contribution of

light holes P_L into the total hole conductivity ($P=P_L+P_T=N$) increases as the temperature rises, but a relative contribution of light holes to the total hole conductivity R [$R=P_L/(P_L+P_T)$] has a maximum at the temperature about 250K. Such dependence may be explained, if we take into account that in the narrow-gap semimetals as Bi-Sb the energetic gap E_g, in the first approximation, is increasing in quadratic law /4/, but activation thermal energy in linear law by the increasing of temperature. Therefore, a contribution of light holes P_L decreases as the temperature rises in the range of high temperatures.

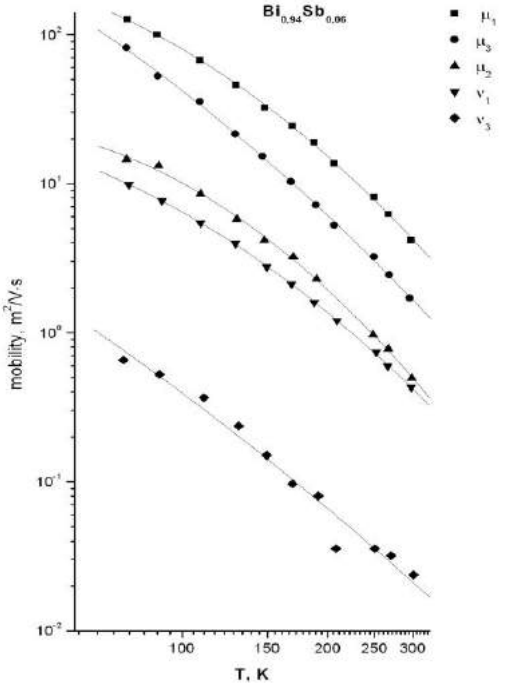

Fig.3. Temperature dependence of the charge carriers densities.

The figure 3 shows the temperature dependence of carrier densities of electrons N, light P_L and heavy P_T holes in double-logarithmic scale. From the figure it is clear that densities of the charge carriers change in accordance of power law:

$N \sim T^{1.8}$ (T=77K) 110K)
$N \sim T^{2.6}$ (T=200K) 300K) } electrons

$P_T \sim T^{1.7}$ (T=77K) 170K)
$P_T \sim T^{2.6}$ (T=210K) 300K) } heavy holes

$P_L \sim T^{2.6}$ (T=90K) 270K) light holes

In the figure 3 it is presented data taken from the table 1, which show the temperature dependence of the densities of charge carriers. For this case we have:

$N,P \sim T^{1.7}$ (T=77K) 170K)

$N,P \sim T^{2.54}$ (T=200K) 300K)

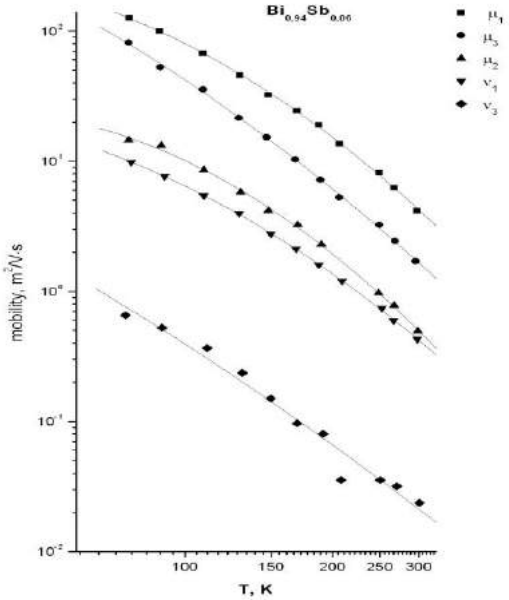

Fig.4. Temperature dependence of the charge carriers' mobilities.

The figure 4 shows the temperature dependence of the components of the mobility tensor in double-logarithmic scale. The following results may be deduced from the figure:

$\mu_1 \sim T^{-2.1}$ (T=77K) 110K)
$\mu_1 \sim T^{-3.0}$ (T=190K) 300K)
$\mu_2 \sim T^{-2.3}$ (T=110K) 300K) } electrons
$\mu_3 \sim T^{-2.0}$ (T=77K) 110K)

$\mu_3 \sim T^{-3.2}$ (T=210K) 300K)

$\nu_1 \sim T^{-1.95}$ (T=120K) 170K)

$\nu_1 \sim T^{-2.7}$ (T=190K) 300K)

The data for ν_3 is not cited, because an accurate value of it cannot be obtained.

It is known that magnetoresistivity coefficients may be approximately estimated as the ratio of carrier mobilities to their carrier densities. Therefore the temperature dependence of the latter parameters should approximately determine the temperature dependence of $\rho_{ij,kl}$. For the given alloy in the low-temperature region (77K) 110K) we have: μ_1, $\mu_3 \sim T^{-2}$; $N \sim T^{1.8}$ Ψ ($\frac{\mu}{N} \sim T^{-3.8}$) and for the components of $\rho_{ij,kl} \sim T^{(-3.2)-4.1)}$. In the high-temperature region (200K) 300K) we have μ_1, $\mu_3 \sim T^{(-3)-3.2)}$; $N,P \sim T^{(2.54)2.6)}$ Ψ ($\frac{\mu}{N} \sim T^{(-5.5)-5.8)}$), correspondingly and for the components of $\rho_{ij,kl} \sim T^{(-5.2)-6.0)}$.

Taking into the account that formulas connecting $\rho_{ij,kl}$ with kinetic coefficients in each concrete case contain different combinations of μ_i, ν_i and the temperature de-

pendencies of abovementioned parameters, strictly speaking, do not expressed as exponential functions, then there is good reason to believe that determined temperature dependencies of kinetic parameters are reasonable.

One of the factors leading to the strong temperature dependencies of the magnetoresistivity coefficients is the strong temperature dependence of mobility ($\mu \sim T^{-3}$). Such strong dependence of mobility cannot be explained only by scattering of current carriers on intravalley acoustic phonons. It is possible that intervalley scattering by optical phonons may play active role at high temperatures. It should be noted that alteration of the effective mass of current carriers might make contribution to the strong temperature dependency of the mobility.

.

[1]. *W.M.Yim, A.Amith* – Solid State Electronics, 1972, v.15, pp.1141-1165

[2]. *S. Dutta, V. Shubhaa and T.G. Ramesha*, Physica B: Condensed Matter, **v.405,** N**o 5**, (2010), p.1239.

[3]. *D.Choi. A.Balandin, and et.al.* Appl. Phys. Lett. 89, (2006), p.1415.

[4]. *S.Dutta, V. Shubha, T.G. Ramesh, Florita D'Sa*. Journal of Alloys and Compounds, **467,** (2009), p. 305.

[5]. *А.А. Мусаев.* Гальваномагнитные эффекты, дисперсия геликоновых волн и рассеяние носителей тока в сплавах Bi-Sb при 77К-300К. – Дисс.канд.физ.-мат. наук. – Баку, 1981

[6]. *Дж. Хаст* Приборы для научных исследований, 1970, № 5, с. 8-11

[7]. *M.Vecchi, E.Mendez, M.S.Dresselhaus*. "Physics of semiconductors", Proceedings of the 13-th International Conference, Rome, 1976, 459-462.

THE MAGNETO-DIELECTRIC PROPERTIES OF CONDENCED MATERIALS IN THE SYSTEMS OF $TlInS_2$-$TlCr(Fe,Co)S_2$,$TlGaSe_2$-$TlCr(Fe,Co)Se_2$

R.G.VELIYEV

Institute of Physics, Azerbaijan National Academy of Sciences,
Az-1143, Baku, Azerbaijan
E-mail: ramizveliyev@gmail.com

In the temperature region 77÷300K were investigated the dielectric properties of layered compounds $TlInS_2$ and $TlGaSe_2$, which revealed, that those compounds are ferroelectrics with the intermediate incommensurable phase. Analysis of publications was carried out by us on magnetic properties of $TlCrS_2$ and $TlCrSe_2$, $TlFeS_2$ and $TlFeSe_2$, $TlCoS_2$ and $TlCoSe_2$ compounds allows drawing a conclusion, that those compounds are quasi two-dimensional ferromagnets, quasi one-dimensional antiferromagnets, ferrimagnets accordingly. It is necessary to note, that $TlCoS_2$ is quasi two-dimensional ferrimagnet, but $TlCoSe_2$ is three-dimensional ferrimagnet. The differential-termographic analysis define areas of homogenous and heterogeneous coexistence of ferroelectric and magnetic orderings in the systems of $TlInS_2$ – $TlCr(Fe,Co)S_2$ and $TlGaSe_2$ – $TlCr(Fe,Co)Se_2$.

1. INTRODUCTION

The triple compounds with the common crystalchemical formulas $TlMeX_2$ (where Me-Ga,In,Cr,Fe,Co; X=S,Se) presents themselves the wide class of the strongly anisotropic (layered, chained) compounds with the physical properties, including almost all modern physics of inorganic condensed matter. Between them are semiconductors $TlGaS_2$, $TlInSe_2$ [1-3], ferroelectrics – semiconductors $TlInS_2$, $TlGaSe_2$ [4-7], ferromagnetics – semiconductors $TlCrS_2$, $TlCrSe_2$ [8-10], antiferromagnetics-semiconductors $TlFeS_2$, $TlFeSe_2$ [11-13], ferrimagnetics ($TlCoS_2$ – semimetal, $TlCoSe_2$ – metal) [14,15], disorder structures ($TlInS_2$, $TlGaSe_2$) [4-7,16], low-dimensional magnetic structures ($TlCrS_2$, $TlCrSe_2$, $TlFeS_2$, $TlFeSe_2$, $TlCoS_2$) [9,11,12,17-19]. Moreover, each of the note compounds can be in the different phase, states in the dependence from the temperature, hydrostatic pressure and defection degree, and transfer from one phase state to another [20-23], since theirs structure features, before low symmetry of the crystalline lattice, such transformations are supposed.

However, the most interest and important from the scientific point of view is the possibility of the purposeful variation of the factual chemical composition of above mentioned compounds with the aim of the obtaining in the one alloy the state of the coexistence of the magnetic and electrical orderings (magnetoelectric materials), for it was historically formed so that entire existing set of the mechanisms of electrical ordering (ferroelectrics, antiferroelectric materials, extrinsic ferroelectrics, intrinsic and extrinsic ferroelectrics with the intermediate, incommensurable phase, ferrielectrics) was predicted, and then realized in the concrete compounds, on the basis of the analogy of phenomena with the mechanism of magnetic ordering in the magnets. Such materials exhibit a magnetoelectric effect which is characterized by the appearance of an electric polarization on applying a magnetic field and by the appearance of a magnetization when applying an electric field [24]. The study of the co-existence of electrical and magnetic orderings in both homogeneous and heterogeneous (composites) alloys, acquired an even larger urgency in connection with the development of the technical capabilities of nanotechnology [25].

In connection with accounted above the dielectric properties of layered compounds $TlInS_2$, $TlGaSe_2$ are investigated. Analysis of publications was carried out by us on magnetic properties of $TlCrS_2$, $TlCrSe_2$, $TlFeS_2$, $TlFeSe_2$, $TlCoS_2$ and $TlCoSe_2$ compounds. The molar relations in the systems of $TlInS_2$ – $TlCr(Fe,Co)S_2$ and $TlGaSe_2$ – $TlCr(Fe,Co)Se_2$ were characterized by differential thermographic analysis (DTA).

2. EXPERIMENTAL PART

For investigating the temperature dependence of dielectric permittivity ε(T) of the layered compounds $TlInS_2$, $TlGaSe_2$ samples in the form of the plates of polar shear, cut out from the single-crystal ingot of those compounds were used. The single-crystal ingot of $TlInS_2$, $TlGaSe_2$ was grown by Bridgman-Stockbarger method; in this case the rate of the movement of crystallization front was 2mm/h. The face of sample perpendicular to the polar axis was gently polished, cleaned and covered with silver paste. The dimensions of the electrodes were about 5×5mm with an inter-electrode distance of 1mm. Measurements of the real part of the dielectric permittivity ε were performed using variable current bridge at the frequency of 5kHz.

Research was carried out in the temperature range 77÷300K in the quasi static regime; in this case the rate of the temperature change was 0.2K/min. During the measurements the samples were inside the nitric cryostat and temperature was measured by differential copper-constantan thermocouple, whose thermo joint was fixed on a crystal holder near the sample. The support thermo joint of the thermocouple was stabilized at the temperature of thawing ice.

The compounds and alloys were investigated by DTA method, which was carried out on the low frequency thermograph recorder (NTR-64), which allowed fixing temperatures of phase transformations with accuracy of ±5K. Heating rate was about 2-4K/min. Temperature was controlled by Pt-Pt/Rh thermocouple, graded according to fiducial elements in the interval of 430÷1560K.

3. RESULTS AND DISCUSSION

On Fig.1 the temperature dependence of the dielectric permittivity of $TlInS_2$ measured under the atmospheric pressure is given. As can be seen from figure, curve ε(T) is characterized by anomalies in the form of maximums at ~206.3K and ~202.4K, and also by the presence of small “bend” around 201K. It is known

that with a temperature decrease under the atmospheric pressure the layered crystal $TlInS_2$ experiences the complex sequence of structural phase transitions (PT), including PT in the incommensurate (IC) and commensurate (C) ferroelectric phases [4-7]. The initial paraelectric phase of $TlInS_2$ posses monoclinic crystalline structure is characterized by Space Group of Symmetry (SGS) C_{2h}^6 [26]. PT in IC phase is related to the condensation (under $T_i \approx 216K$) of soft mode at the point of Brillouin zone with the wave vector of $\vec{k}_i(\delta; \delta; 0.25)$, where δ - the parameter of incommensurability [16]. At $T_c \approx 201K$ value δ abruptly becomes zero and crystal of $TlInS_2$ passes into the extrinsic ferroelectric (vector of spontaneous polarization is located in the plane of layer) C-phase with the wave vector $\vec{k}_c(0; 0; 0.25)$ [16, 20-23].

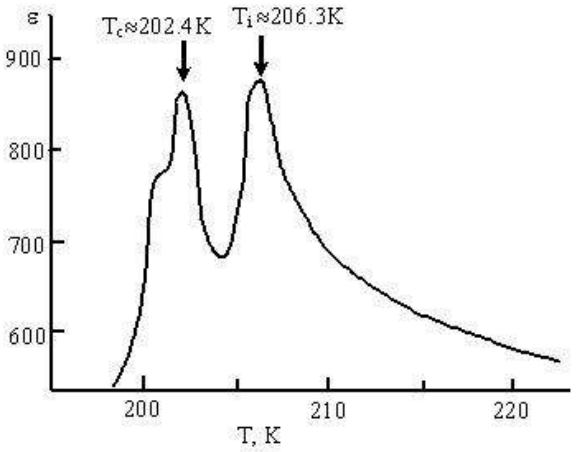

Fig.1. The temperature dependence of the dielectric permittivity of $TlInS_2$.

Comparing our results with the data, represented in [4-7, 23] it is possible to conclude that the curve ε (T) of the investigated sample sharply differs from the analogous curves, represented in the literature, both with the number of anomalies and their temperature positions. Let us note also that the color of the sample under investigation is characterized by orange nuance, whereas the crystals of $TlInS_2$, selected from the different parties and investigated in [4-7], possessed different nuances of yellow. Relying on data [21, 22], in which strong sensitivity of the physical properties (including temperatures PT) of the layered compound $TlInS_2$ is determined to a quantity of admixtures in the sample and to the degree of the defectiveness of its crystal structure, it can be supposed that observed anomaly on the curve ε (T) at 206.3K is related to PT in IC phase**,** and at 202.4K - with PT into the commensurate ferroelectric phase. Additionally, the "bend" around 201K is the temperature interval of the co-existence of the remainders of the not disintegrated solitons of IC-phase and domains of low-temperature commensurable ferroelectric phase [4].

On fig.2 the temperature dependence of dielectric permittivity of $TlGaSe_2$, measured at the atmospheric pressure, is given. As it is seen from the figure, curve ε(T) is characterized by anomalies in the form of maximums in connection to the phase transition (PT) points in the incommensurate (IC) phase at T_i=117.2K and commensurate (C) ferroelectric phase at T_c=114K. It is noted that temperature position of the anomalies on the curve ε(T) and the value of Curie constant of $TlGaSe_2$ are also well agreed with the results obtained by others authors [6, 27-29]. In the both triple compounds $TlInS_2$, $TlGaSe_2$ the temperature curves ε(T) in the paraelectric and ferroelectric phases are well approximated by Curie-Weiss law with the value of Curie constant of about 10^3K.

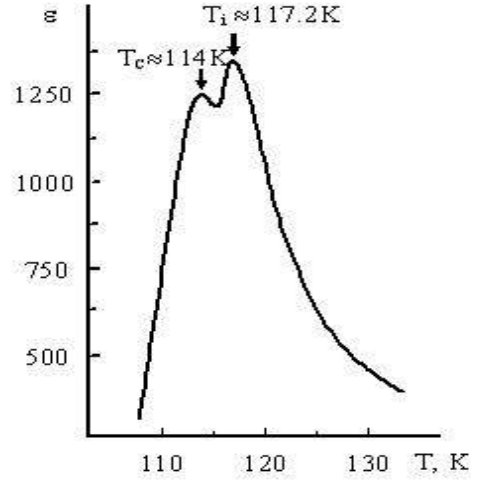

Fig.2. The temperature dependence of the dielectric permittivity of $TlGaSe_2$.

The temperature dependence of the inverse paramagnetic susceptibility $\chi^{-1}(T)$ of the $TlCrS_2$ and $TlCrSe_2$ compounds (fig.3) is characteristic of ferromagnetic materials [9]. X-ray investigations performed in [8] assume low dimensionality of the magnetic structure of layered ferromagnets $TlCrS_2$ and $TlCrSe_2$. The distinction of magnetic characteristics (T_c, T^p_c, μ_{ef}) of the ferromagnets $TlCrS_2$ and $TlCrSe_2$ determined in [9] compared with investigations [8] is apparently associated with a different duration of annealing, namely, 480h by technology [9] and 12h in [8]. The prolonged homogenizing annealing introduces rather substantial corrections to the formation of the spin system of a magnetic substance with a complex chemical composition. The behavior of magnetic characteristics of the ferromagnets $TlCrS_2$, $TlCrSe_2$ is explaining in [9] with Ising-Heisenberg model [30]. This circumstance is allowed conclude that the compounds $TlCrS_2$, $TlCrSe_2$ are quasi two-dimensional ferromagnets.

On fig.4 the temperature dependence of reverse magnetic susceptibility $\chi^{-1}(T)$ of chain antiferromagnets $TlFeS_2$, $TlFeSe_2$ is represented (figure with our comments corresponds to publication [12]). It is seen on the figure, that magnetic properties of $TlFeS_2$ and $TlFeSe_2$ are dependent of crystallographic orientation. Authors of the work [12] consider wide minimum existing on the dependence of $\chi^{-1}(T)$ at ~196K ($TlFeS_2$) and ~290K ($TlFeSe_2$) to be Neel temperature T_N, below which has three-dimensional antiferromagnetic ordering. According to authors of [12], above these temperatures quasi one-dimensional antiferromagnetic ordering in magnetic structure of $TlFeS_2$ and $TlFeSe_2$ is formed. This conclusion is wrong, because authors of [12] didn't take into account specifics of crystalline structure of $TlFeS_2$ and $TlFeSe_2$ compounds. It is known that spin system (magnetic structure) of magnet is formed by its crystalline structure.

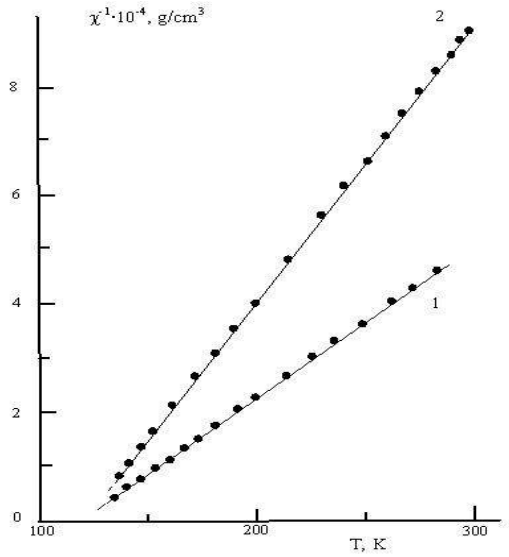

Fig.3. The temperature dependence of the inverse paramagnetic susceptibility of $TlCrS_2$(1) and $TlCrSe_2$(2). (Figure corresponds to publication [9].)

$TlFeS_2$ and $TlFeSe_2$ compounds have monoclinic structure [31-33], which has chain constructions of FeX_4 tetrahedron (X-chalcogen) with joint edges. In the center of tetrahedrons Fe^{3+} ions are located, and chalcogen ions (S^{2-} or Se^{2-}) are placed in vertexes. Tl^{1+} ions are situated in prismatic voids of crystalline structures of $TlFeS_2$ and $TlFeSe_2$. FeX_4 tetrahedrons are connected into linear chains and are parallel to crystallographic axis $\vec{c}$. Exchanging magnetic interaction between iron ions in the direction of crystallographic axis $\vec{a}$, perpendicular to FeX_4 tetrahedrons chain, is done along –Fe-X-Tl-X-Fe- atoms chain. It is known that if two magnetic ions are separated by two anions, then energy of this cation-anion-anion-cation interaction is smaller by an order of magnitude than energy of cation-anion-cation interaction [34]. It means that energy of super-exchange along the chain –Fe-X-Tl-X-Fe- should be two orders of magnitude smaller than energy of –Fe-X-Fe- interaction, occurring along the chain of tetrahedrons. It can be assumed that magnetic properties of $TlFeS_2$ and $TlFeSe_2$ compounds will be mainly defined by exchanging interaction between iron ions, situated within tetrahedrons chain, i.e. $TlFeS_2$ and $TlFeSe_2$ can be viewed as quasi one-dimensional magnetic systems.

The dependences of $\chi^{-1}(T)$ for $TlFeS_2$ and $TlFeSe_2$ (fig.4) measured both in arbitrary crystallographic orientation (filled squares) and in the direction of $\vec{c}$ axis, contains the anomalies at the temperature, ~12K and ~14K respectively, which indicate three-dimensional antiferromagnetic transition (long-range magnetic order). Neel temperatures, found in [11] from the temperature dependence of magnetic susceptibility of $TlFeS_2$ and $TlFeSe_2$, were equal to ~10K and ~12K respectively. Additionally, on the $\chi(T)$ dependence for $TlFeS_2$ [11] at ~200K, wide maximum is present, which satisfies condition $T>>T_N$, corresponding to the Ising–Heisenberg model [30].

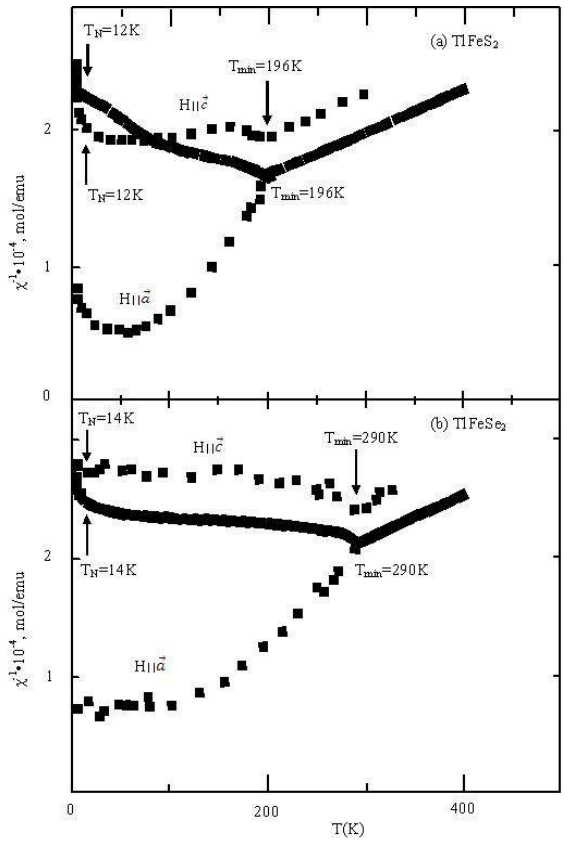

Fig.4. The temperature dependence of the inverse magnetic susceptibility of $TlFeS_2$(a) and $TlFeSe_2$(b). (Figure with our comments corresponds to publication [12].)

In publication [35] neutron diffraction research found three-dimensional antiferromagnetic ordering for $TlFeS_2$ below 16K (long-range magnetic order with T_N≈16K), which are close to results of works [11, 12]. Concerning broad minimums on $\chi^{-1}(T)$ dependence at T_{min}≈196K ($TlFeS_2$) and T_{min}≈290K ($TlFeSe_2$), which were observed in work [12], authors of [30] mention that magnetic susceptibility of strongly anisotropic antiferromagnet is characterized by the presence of wide maximum in the case of $\chi(T)$ or broad minimum - case of $\chi^{-1}(T)$, which is characterized by strongly developed short-range magnetic order with $T>>T_N$, i.e., based on this assertion, it is possible to draw a conclusion that in the paramagnetic region of $TlFeS_2$ higher than the temperature of 12K, quasi one-dimensional magnetic ordering is formed, which is retained up to ~196K, after which begins the disordering of the magnetic structure of the strong-chained antiferromagnet of $TlFeS_2$, and for $TlFeSe_2$ higher than the temperature of 14K quasi one-dimensional magnetic ordering is formed, which is retained up to ~290K, after which begins the disordering of the magnetic structure of the strong-chained antiferromagnet of $TlFeSe_2$.

Low-dimensional of magnetic structure of antiferromagnets $TlFeS_2$ and $TlFeSe_2$ is also shown by the fact that on the temperature dependence of thermal capacity, studied in adiabatic calorimeter under constant pressure $C_p(T)$ in the temperature interval 4÷300K, anomaly with evident deviation from λ-type is seen [11], corresponding to the Ising-Heisenberg model [30].

The temperature dependence of reverse paramagnetic susceptibility $\chi^{-1}(T)$ of $TlCoS_2$ and $TlCoSe_2$ compounds is

given on the fig.5. From the figure it is seen, that this dependence is character for ferrimagnetic materials, because have the hyperbolic appearance [14, 15]. The experimental researches showed that $TlCoS_2$ is quasi two-dimensional ferrimagnet [15, 19] and $TlCoSe_2$ is three-dimensional ferrimagnetic material [14, 15].

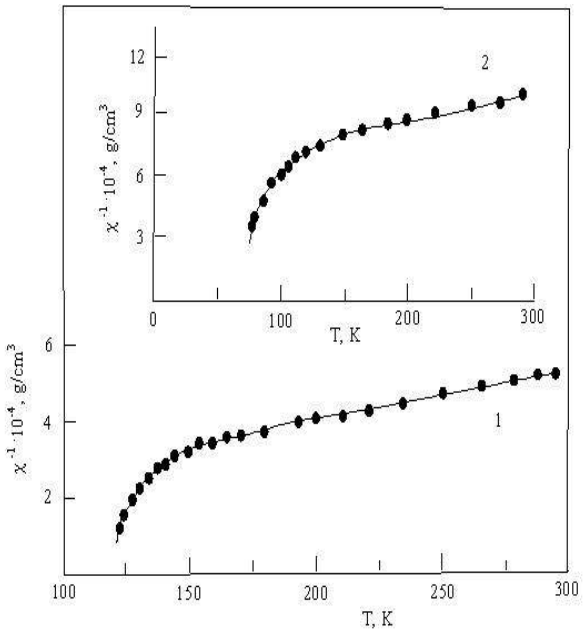

Fig.5. The temperature dependence of the inverse paramagnetic susceptibility of $TlCoS_2$(1) and $TlCoSe_2$(2). (Figure corresponds to publication [15].)

For solving of the physical problem given in the article beginning, it is necessary to define the areas of homogeneous and heterogeneous co-existence of $TlInS_2$ and $TlGaSe_2$ ferroelectrics with $TlCrS_2$ and $TlCrSe_2$ ferromagnets, $TlFeS_2$ and $TlFeSe_2$ antiferromagnets, $TlCoS_2$ and $TlCoSe_2$ ferrimagnets. The following systems $TlInS_2$-$TlCrS_2$ and $TlGaSe_2$-$TlCrSe_2$, $TlInS_2$-$TlFeS_2$ and $TlGaSe_2$-$TlFeSe_2$, $TlInS_2$-$TlCoS_2$ and $TlGaSe_2$-$TlCoSe_2$ have been investigated by DTA method.

The state diagram of $TlInS_2$-$TlCrS_2$ system constructed according to the results of DTA is presented on fig.6. This system is eutectic type quasi-binary with solid solutions on $TlInS_2$ base (homogeneous area of co-existence of ferroelectric and ferromagnetic orderings) achieving up to 10mol% $TlCrS_2$ at room temperature (~300K). The eutectic forms at components relation 1:1. Eutectic melts at 925K and has a composition $(TlInS_2)_{0.5}(TlCrS_2)_{0.5}$, i.e. in this eutectic alloy ferroelectric and ferromagnetic orderings coexist heterogeneously (compositionally).

State diagram of $TlGaSe_2$-$TlCrSe_2$ system constructed on the results of DTA is presented on fig.7. This system is eutectic type quasi-binary with solid solutions on the base of $TlGaSe_2$, reaching up to 10mol% $TlCrSe_2$, on the base of $TlCrSe_2$, reaching up to 8mol% $TlGaSe_2$ (homogenous areas of the co-existence of ferroelectric and ferromagnetic orderings) at room temperature (~300K). The eutectic forms at component relation 1:1.

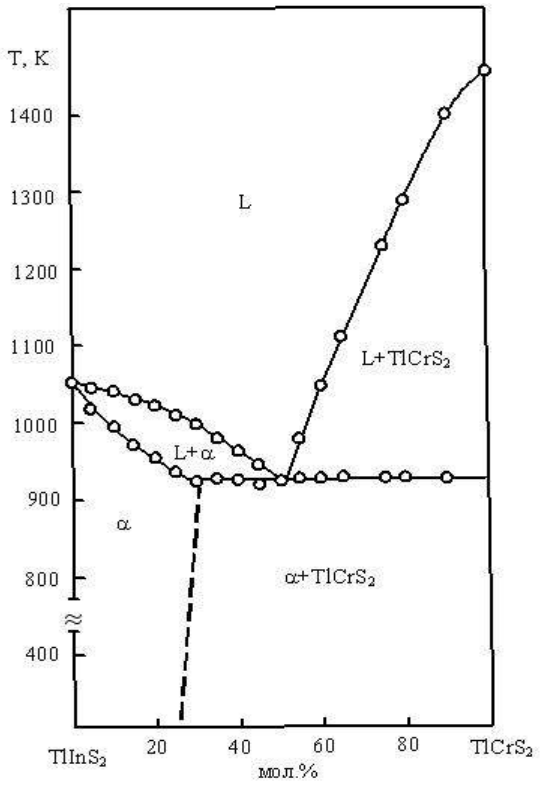

Fig.6. $TlInS_2$-$TlCrS_2$ system state diagram.

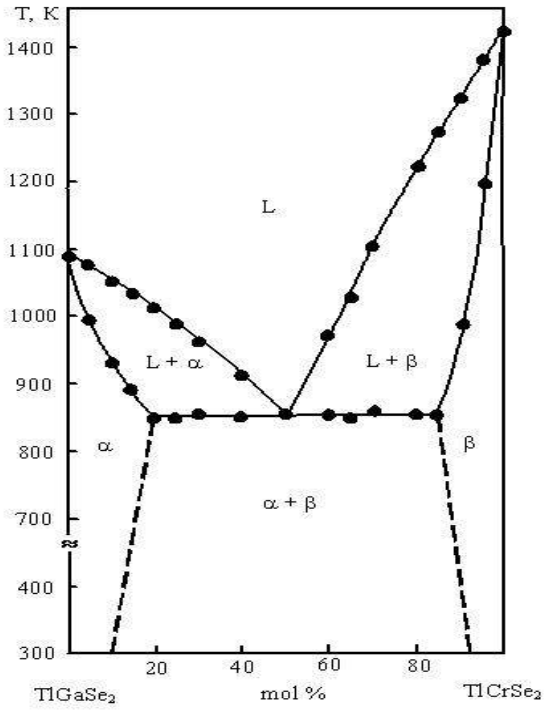

Fig.7. $TlGaSe_2$-$TlCrSe_2$ system state diagram.

The eutectic melts at a temperature 850K and has the composition $(TlGaSe_2)_{0.5}(TlCrSe_2)_{0.5}$, i.e. in this eutectic alloy ferroelectric and ferromagnetic orderings coexist heterogeneously (compositionally).

Constructed according to the results of DTA diagram of state of the system of $TlInS_2$-$TlFeS_2$ is represented in fig.8. As follows from the diagram, the system of $TlInS_2$-$TlFeS_2$ is quasi-binary section. Continuous rows of solid solutions are formed in it with

the minimum at a temperature 640K and 70mol% of $TlFeS_2$; i.e. in alloys of $TlInS_2$-$TlFeS_2$ system ferroelectric and antiferromagnetic orderings for all changes of molar relations of initial compounds homogeneously co-exist.

The diagram of state of the system of $TlGaSe_2$-$TlFeSe_2$ is given on fig.9.

This system is eutectic type quasi-binary with solid solutions on the base of $TlGaSe_2$, reaching up to 10mol% $TlFeSe_2$ (homogeneous areas of the co-existence of ferroelectric and antiferromagnetic orderings) at room temperature (~300K). Eutectic melts at a temperature 600K and has a composition $(TlGaSe_2)_{0.69}(TlFeSe_2)_{0.31}$, i.e. in this eutectic alloy the ferroelectric and antiferromagnetic orderings coexist heterogeneously (compositionally).

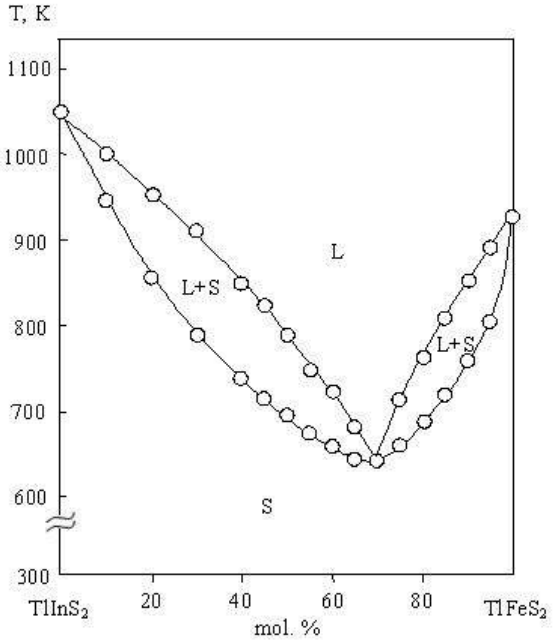

Fig.8. $TlInS_2$-$TlFeS_2$ system state diagram.

The state diagram of $TlInS_2$-$TlCoS_2$ system constructed on DTA results is presented on fig.10. This system is eutectic type quasi-binary with solid solutions on the base of $TlInS_2$ which reach up to 15mol% $TlCoS_2$, on the base of $TlCoS_2$ reaching up to 10mol% $TlInS_2$ (homogeneous areas of co-existence of ferroelectric and ferrimagnetic orderings). The eutectic forms at components relation 1:1. Eutectic melts at 525K and has a composition $(TlInS_2)_{0.5}(TlCoS_2)_{0.5}$, i.e. in this eutectic alloy ferroelectric and ferrimagnetic orderings coexist heterogeneously (compositionally).

The state diagram of $TlGaSe_2$-$TlCoSe_2$ system constructed on the results of DTA is presented on fig.11. This system is eutectic type quasi-binary with solid solutions on the base of $TlGaSe_2$ which reach up to 14mol% $TlCoSe_2$ (homogeneous area of co-existence of ferroelectric and ferrimagnetic orderings) at room temperature (~300K). Eutectic melts at a temperature 610K and has a composition $(TlGaSe_2)_{0.69}(TlCoSe_2)_{0.31}$, i.e. in this eutectic alloy heterogeneously (compositionally) coexist ferroelectric and ferrimagnetic orderings.

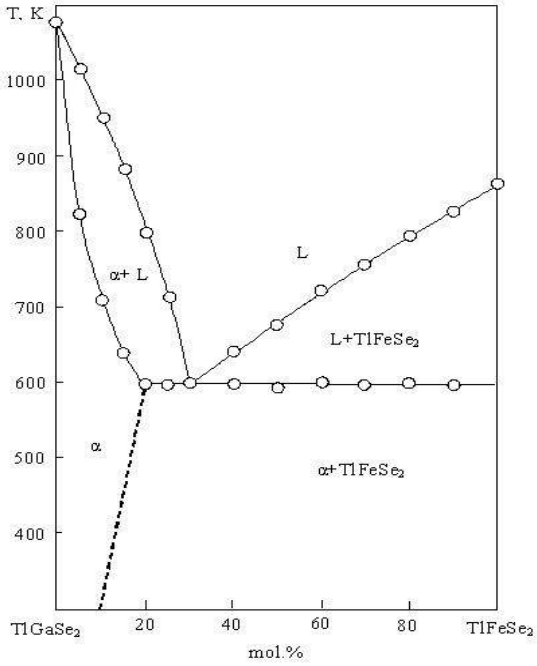

Fig.9. $TlGaSe_2$-$TlFeSe_2$ system state diagram.

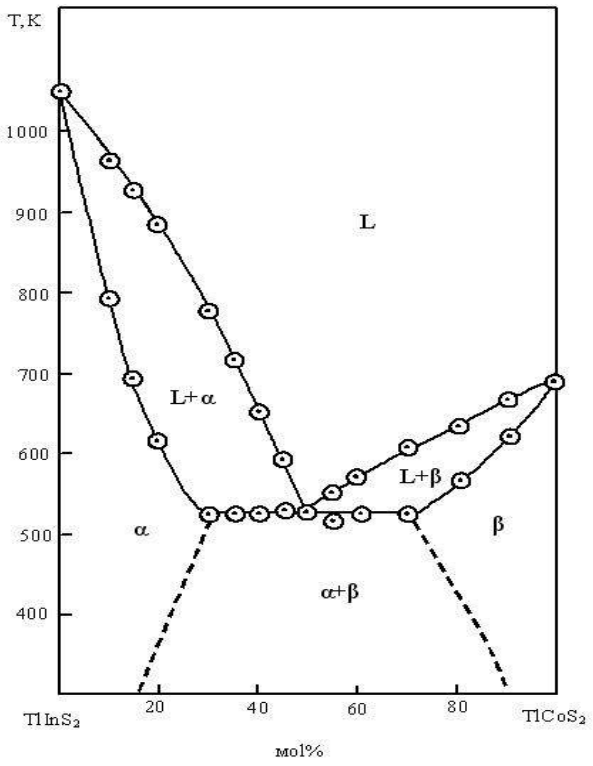

Fig.10. $TlInS_2$-$TlCoS_2$ system state diagram.

4. CONCLUSION

A study of the temperature dependence of the dielectric permittivity of $TlInS_2$ showed that this layered compound it is extrinsic ferroelectric (T_c≈202.4K) with intermediate incommensurable phase (T_i≈206.3K). The temperature dependence of dielectric permittivity of layered compound $TlGaSe_2$ has two anomalies which are associated with phase transitions to an incommensurate phase at T_i≈117.2K and to a commensurate ferroelectric

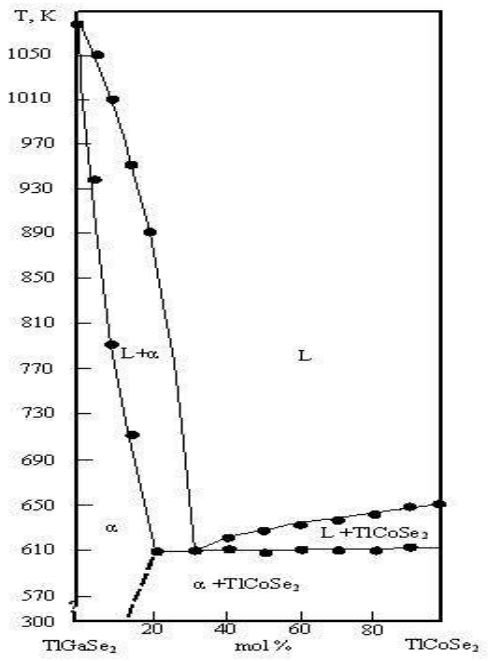

Fig.11. $TlGaSe_2$-$TlCoSe_2$ system state diagram.

phase at $T_c \approx 114K$. In both $TlInS_2$ and $TlGaSe_2$ compounds the temperature curves ε(T) in the paraelectric and ferroelectric phases are well approximated by Curie-Weiss law with the value of Curie constant of about 10^3K.

Analysis of publications was carried out by us on magnetic properties of $TlCrS_2$ and $TlCrSe_2$, $TlFeS_2$ and $TlFeSe_2$, $TlCoS_2$ and $TlCoSe_2$ compounds allows to draw a conclusion, that $TlCrS_2$ and $TlCrSe_2$ are quasi two-dimensional ferromagnets, $TlFeS_2$ and $TlFeSe_2$ are quasi one-dimensional antiferromagnets, $TlCoS_2$ and $TlCoSe_2$ are ferrimagnets. It is necessary to note, that $TlCoS_2$ is quasi two-dimensional ferrimagnet but $TlCoSe_2$ is three-dimensional ferrimagnet.

Using DTA method the areas of the homogeneous and heterogeneous co-existence of ferroelectric and magnetic orderings in the systems of $TlInS_2$ – $TlCr(Fe,Co)S_2$ and $TlGaSe_2$ – $TlCr(Fe,Co)Se_2$ are determined.

I wish to express my sincere thanks to collaborates of Optoelectronics laboratory for help in investigation of temperature dependence of dielectric permittivity of $TlInS_2$, $TlGaSe_2$ compounds and discussion of obtained results.

[1]. *G.D. Guseinov, A.M. Ramazanzade, E.M.Kerimova, M.Z. Ismailov*. J. Phys. Stat. Sol., 1967, 22, 2, K117.
[2]. *G.D. Guseinov, E. Moozer, E.M. Kerimova, R.S.Gamidov, I.V. Alekseev, M.Z. Ismailov*. J.Phys. Stat. Sol., 1969, 34, 1, 33.
[3]. *G.D. Guseinov, G.B. Abdullayev, S.M.Bidzinova, M.Z. Ismailov, A.M.Pashayev*. J. Phys. Lett. A., 1970, 33, 7, 421.
[4]. *F.M. Salayev, K.R. Allakhverdiyev, F.A.Mikailov*. J. Ferroelectrics, 1992, 131, 1-4, 163.
[5]. *R.A. Suleymanov, M.Yu. Seyidov, F.M. Salayev, F.A. Mikailov*. FTT, 1993, 35, 2, 348 (in Russian).
[6]. *K.R. Allakhverdiyev, N.D. Akhmedzade, T.G.Mamedov, T.S. Mamedov, M.Yu. Seyidov*. FNT, 2000, 26, 1, 76 (in Russian).
[7]. *F.A. Mikailov, E. Basaran, T.G. Mammadov, M.Yu. Seyidov, E. Senturk*. J. Physica B, 2003, 334, 1-2, 13.
[8]. *M. Rosenberg, A. Knulle, H. Sabrowsky, C.Platte*. J. Phys. Chem. Solids, 1982, 43, 2, 87.
[9]. *R.G. Veliyev, R.Z. Sadikhov, E.M. Kerimova, Yu.G.Asadov, A.I. Jabbarov*. FTP, 2009, 43, 9, 1175 (in Russian).
[10]. *R.G. Veliyev, R.Z. Sadikhov, E.M. Kerimova, Yu.G.Asadov, A.I. Jabbarov*. J. Inorganic Mater., 2009, 45, 5, 528 (in Russian).
[11]. *M.A. Aldzhanov, N.G. Guseinov, G.D. Sultanov, M.D. Nadzhafzade*. J. Phys. Stat. Sol.(b), 1990, 159, 2, K107.
[12]. *Z. Seidov, H.A. Krug von Nidda, J. Hemberger, A.Loidl, G. Sultanov, E. Kerimova, A. Panfilov*. J. Phys. Rev. B, 2001, 65, 1, 014433.
[13]. *S.N. Mustafayeva, E.M. Kerimova, A.I. Jabbarli*. FTT, 2000, 42, 12, 2132 (in Russian).
[14]. *R.Z. Sadikhov, E.M. Kerimova, Yu.G. Asadov, R.G.Veliyev*. FTT, 2000, 42, 8, 1449 (in Russian).
[15]. *R.G. Veliyev, E.M. Kerimova, R.Z. Sadikhov, Yu.G.Asadov, A.I. Jabbarov*. Fizika, 2009, 15, 2, 111 (in Russian).
[16]. *S.B. Vakhrushev, V.V. Zhdanova, B.E.Kviatkovsky, N.M. Okuneva, K.R.Allakhverdiyev, R.A. Aliyev, R.M. Sardarli*. Lett. in JETF, 1984, 39, 6, 245 (in Russian).
[17]. *M.A. Aljanov, A.A. Abdurragimov, S.G.Sultanova, M.D. Nadjafzade*. FTT, 2007, 49, 2, 309 (in Russian).
[18]. *M. Aljanov, M. Nadjafzade, Z. Seidov, M.Gasumov*. Tr. J. Physics, 1996, 20, 9, 1071.
[19]. *M. Aljanov, E. Kerimova, S. Mekhtieva, M.Nadjafzade, G. Sultanov, G. Akhmedova*. Fizika, 2002, 8, 1, 20.
[20]. *K.R. Allakhverdiyev, A.I. Baranov, T.G.Mamedov, V.A. Sandler, Ya.N. Sharifov*. FTT, 1988, 30, 6, 1751 (in Russian).
[21]. *S. Ozdemir, R.A. Suleymanov, E. Civan*. J. Solid State Commun., 1995, 96, 10, 757.
[22]. *S. Ozdemir, R.A. Suleymanov, E. Civan, T. Firat*. Solid State Commun., 1996, 98, 5, 385.
[23]. *R.A. Aliyev, K.R. Allakhverdiyev, A.I. Baranov, N.R. Ivanov, R.M. Sardarli*. FTT, 1984, 26, 5, 1271 (in Russian).
[24]. *L.D. Landau, E.M. Lifshiz*. Electrodynamics of continuous Media, Pergamon Press, Oxford, 1960.
[25]. *N. Mamedov, K. Wakita, S. Akita, Y. Nakayama*. Jpn. J. Appl. Phys., 2005, 44, 113, 709.
[26]. *D. Müller, F. Poltman, H. Hahn*. Naturforsch., 1974, 29, 1-2, 117.
[27]. *H. Hochheimer, E. Gmelin, W. Bauhofer*. J.Phys. B: Condens. Matter, 1988, 73, 2, 257.

[28]. *R.M. Sardarly, O.A. Samedov, I.Sh. Sadikhov*. J.Sol. State Comm., 1991, 77, 6, 453.

[29]. *A.K. Abiyev, N.A. Bakhishov, A.E. Bakhishov, M.S.Gadzhiyev*. Izv. Vuzov, Fizika, 1989, 12, 84 (in Russian).

[30]. *K.S. Aleksandrov, N.V. Fedoseyeva, I.P.Spevakova*. Magnetic phase transitions in galoid crystals, Science, Novosibirsk, 1983, 193p. (in Russian).

[31]. *K. Klepp, H. Boller*. Monatsh. Chem., 1979, 110, 5, 1045.

[32]. *M. Zabel, K. Range*. Naturforsch. B,1979,34,1, 1.

[33]. *G.I. Makovetskiy, E.I. Kasinskiy*. Inorganic Materials, 1984, 20, 10, 1752 (in Russian).

[34]. *D. Gudenaff*. Magnetism and chemical bond. Metallurgy Press, Moscow, 1968, 325p. (in Russian).

[35]. *H. Sabrowsky, M. Rosenberg, D. Welz, P. Deppe, W. Schafer*. J. Magnetizm and magnetic Mater., 1986, 54-57, 1497.

FREQUENCY-DEPENDENT DIELECTRIC CHARACTERISTICS OF $Bi_{1.7}V_{0.3}Sr_2Ca_2Cu_3O_{10+\delta}$ GLASS-CERAMIC

A. GÜNEN, H. KORALAY, Ş. ÇAVDAR
Department of Physics, Gazi University,
Teknik Okullar, Ankara, Türkiye
e-mail: agunen@gazi.edu.tr

The influence of vanadium additions on microstructure and phase formation of $Bi_{1,7}V_{0,3}Sr_2Ca_2Cu_3O_{10+\delta}$ (Bi-2223) system is investigated. Phase analysis and micro structural observations were carried out by X-ray diffraction (XRD) and scanning electron microscopy (SEM) respectively. XRD results reveal two main phases (Bi-2212 and Bi-2223). The crystal structure of the sample was found as orthorhombic with the lattice parameters of a=5,390 nm; b=5,413 nm ; c=30,813 nm for the low T_c phase and a=5,435 nm ; b=5,412 nm ; c=36,926 nm for the high T_c phase. SEM photographs show that the substitution by vanadium affects the mechanism of the grains growth. The sample was investigated by the measurement of dielectric properties at different voltage values as a function of frequency at room temperatures.

I. INTRODUCTION

Among the CuO based superconductors, Bi-based systems are only spreading over a large used in the fabrication of long length wires, tapes, glass ceramic and bulk [1-5]. These fabricating techniques are very attractive for the fabrication of dense superconductors with desired shapes. In order to fabricate high performance superconductors through glass ceramic processing, it is necessary to clarify the crystallization mechanism in precursor glasses.

In the present study we report the dielectrical properties of $Bi_{1,7}V_{0,3}Sr_2Ca_2Cu_3O_{10+\delta}$ (Bi-2223) glass ceramic system at room temperature.

II. EXPERIMENTAL DETAİLS

The starting materials, Bi_2O_3, $SrCO_3$, $CaCO_3$, CuO and V_2O_5 powders used for the production of the superconducting sample, were mixed for 1 h to obtain a homogeneous mixture and then the mixture was melted and held at 1150 ^oC for 90 min. Later, the sample obtained was rapidly quenched between two copper plates and it was produced as black glass sheet having 1mm thickness and sintered at 860 ^oC for 50 hours [5]. The surface morphology of the superconducting sample was investigated by SEM technique and crystallographic structure of this sample was also obtained by X-ray diffraction (XRD). Following these measurements, the sample surfaces were coated with Al films. $Al/Bi_{1.7}V_{0.3}Sr_2Ca_2Cu_3O_{10+\delta}/Al$ structure was investigated by the calculation of the dielectric constants (ε' and ε'') and dielectric loss (tan δ), as a function of frequency at room temperature via capacitance and conductance measurements. DC electrical resistivity was measured by at two-point probe method described previously [6]. The pellet was prepared by glass ceramic. The dielectric constant (ε') measurements were carried out in the frequency range from 10 kHz to 1MHz at room temperature using Agilent 4284 A model LCR meter.

The capacitance, dielectric constant and dielectric loss are important parameters in the selection of materials for device application. The dielectric constant *(ε')* is evaluated from the equation

$$C = \varepsilon' \varepsilon_o A/d \quad (1)$$

Where *C* is the capacitance of the pellet, *d* is the thickness of the pellet, ε_0 is the permittivity of free space *(ε_0 = 8,85 × 10^{-12} F m^{-1})* and *A* is the area of the electrode. The imaginary part of the dielectric loss *(ε'')* of the various frequencies was calculated using the measured conductance values *(G)* from the relation

$$\varepsilon'' = dG/A\varepsilon_0\omega \quad (2)$$

Where *G* is the dc conductance of the sample, and ω is the angular frequency.

The dielectric loss tan δ was calculated from the relation

$$\tan\delta = \varepsilon''/\varepsilon' \quad (3)$$

III. RESULT AND DISCUSSIONS

The sample sintered in oxygenized medium for 50 hours at 860^0C shows the existence of crystalline peaks indicating the transformation of the sample from amorphous to crystalline structure. The crystal structure and crystallization phases were identified by XRD method. Thus the crystal structure of the sample was found as orthorhombic with the lattice parameters of a=5,390 nm; b=5,413 nm; c=30,813 nm for the low T_c phase and a=5,435 nm; b=5,412 nm; c=36,926 nm for the high T_c phase.

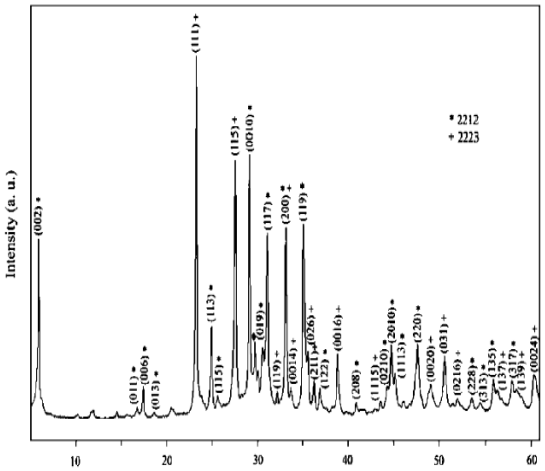

Fig.1. XRD of the samples after the calcinations.

From the micrograph of the sample given in the Figure 2. above, the crystals having different orientations can easily be seen. The sample shows weak intercrystal connectivity in some regions and better in the other regions. It is also observed that there are voids between crystals.

It has been reported dielectric properties of $Al/Bi_{1.7}V_{0,3}Sr_2Ca_2Cu_3O_x/Al$ glass ceramic sandwich prepared by glass-ceramic method for Bi_2O_3, $SrCO_3$, $CaCO_3$, CuO and V_2O_5 and then, evaporation technique for Al coating.

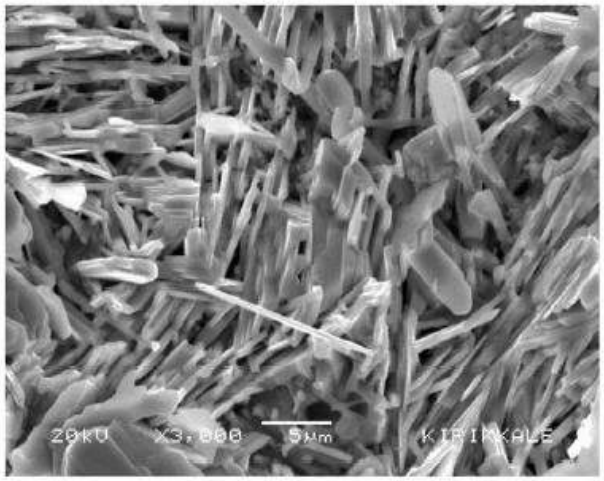

Fig. 2. SEM micrographs of the sample

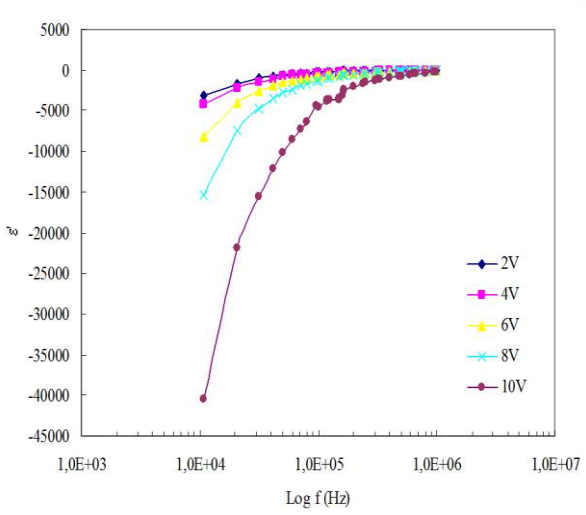

Fig. 3. Variation of dielectric constant *(ε')* with frequency at different voltages

We find that the capacitance in the $Bi_{1,7}V_{0,3}Sr_2Ca_2Cu_3O_{10+\delta}$ Bi-2223) sample becomes negative at all frequencies and all voltages in figure 3. Negative capacitance effects in relaxation material have been described explicitly only briefly in the literature [8, 9, 10, 11, 12]. A negative capacitance phenomenon has been observed in $Al/Bi_{1.7}V_{0,3}Sr_2Ca_2Cu_3O_{10+\delta}/Al$ ceramic compounds at different voltages and frequencies at room temperature. It is believed that the dielectric dispersion and the negative capacitance effects are attributable to the dipolar polarizations. The polarization corresponding to this mechanism occurs at a frequency range of 10^3–10^6 Hz at room temperature.

ε' dependents on both the voltage and the frequency, provided the frequency of the applied field is in the lower frequency range of 10 kHz–1MHz; the dielectric constant increases with increasing frequency and saturates at low frequency and high voltage values.

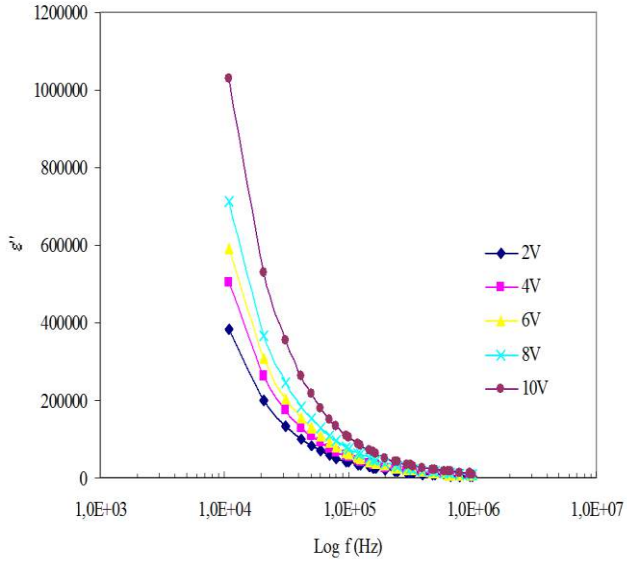

Fig. 4. Variation of imaginary dielectric constant (ε'') with frequency at different temperatures.

ε'' increases with decreasing frequency and with decreasing voltages in figure 4. At the lowest voltage, the value of *ε''* decreases from a value of about $3{,}81x10^5$ to $4{,}12x10^3$ in the frequency range 10kHz- 1MHz , becomes almost constant at highest voltage.

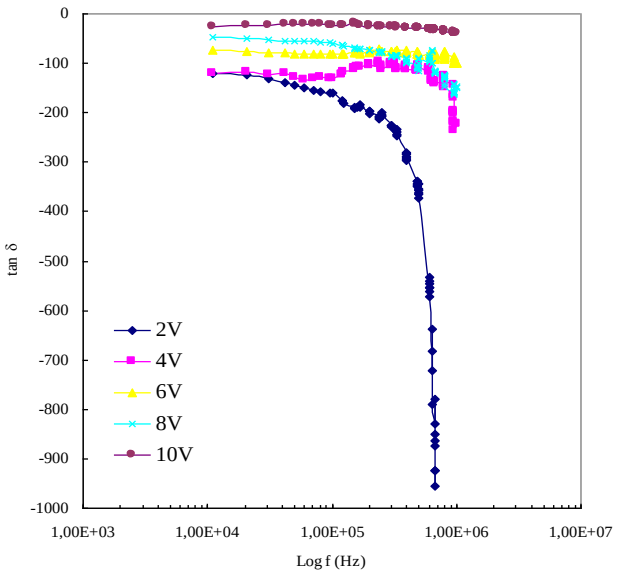

Fig. 5. Plot of dielectric loss (tanδ) versus frequency at different voltages

Dielectric loss, tan δ, of a system can be explained as the ratio of the energy dissipated per radian in the material to the energy stored at the peak of the polarization. Knowledge of dielectric loss enables us to understand the mechanism of ac conduction and dielectric relaxation. Figure 5 shows dependence of dielectric loss on frequency and voltages. The following information is available from this figure at the highest voltage 10 V, the value of tan δ becomes almost constant from 10KHz to

1MHz. However, At the lower voltages, the value of tan δ rapidly decreasing in high frequencies.

IV. CONCLUSION

We have reported dielectric properties of $Bi_{1,7}V_{0,3}Sr_2Ca_2Cu_3O_{10+\delta}$ (Bi-2223) glass ceramic compounds prepared by glass ceramic reaction method using Bi_2O_3, $SrCO_3$, $CaCO_3$, CuO and V_2O_5 . A negative capacitance phenomenon has been observed in BSCCO glass ceramic compounds at different voltages and frequencies.

The dielectric constants (ε' and ε'') and the dielectric loss (tan δ), of the $Bi_{1,7}V_{0,3}Sr_2Ca_2Cu_3O_{10+\delta}$ (Bi-2223) sample is strongly dependent on the voltage and the frequency of the applied ac field.

[1]. *E.Gencer, Ö.Aksu, Özoğul and M.E. Yakıncı*, Physica C 2006, 445-448 (1-2), pp. 772-776

[2]. *H.Sözeri, N.Ghazanfari , H.Özkan , A.Kilic* Superconductor Science and Technology 2007, 20 (6), art. no. 007, pp. 522-528

[3]. *S. Cavdar, E. Aksu, H. Koralay, H. Ozkan, N.M.Gasanly, I. Ercan*, Phys. Status Solidi A 199 (2) (2003) 272.

[4]. *H. Martínez, A. Mariño, J. E. Rodríguez* Physica C: Superconductivity, 2004, 408-410, 568-570

[5]. *H. Koralay, F. Yakuphanoglu, S. Çavdar, A.Günen and E. Aksu* 2005 Physica B Vol 355 Issues 1-4, Pages 64-71

[6]. *S.Çavdar, H. Koralay, N. Tuğluoglu and A. Gunen* 2005 Supercond. Sci. Technol. 18 *Pages* 1204-1209

[7]. *N. Tugluoglu, Ş. Altındal, A. Tataroglu and S.Karadeniz* 2004 Microelectronics Journal, Vol 35, Issue 9,, Pages 731-738

[8]. *K.S.A. Butcher, T.L.Tansley and D. Alexiev* 1996 Solid-State Electron. 39 333

[9]. *X. Wu, E.S. Yang and H.L. Evans* 1990 J. Appl. Phys. 68 2845

[10]. *C.H. Champness and W.R. Clark* 1990 Appl. Phys. Lett. 56 1104

[11]. *H.J. Queisser* 1972 Proc. ESSDERC p 145

[12]. *H.J. Queisser* 1972 IOP Conf. Proc. No 15 (London: Institute of Physics Publishing)

[13]. *W. Van Roosbroeck* Phys. Rev. Lett. 1972, 28, 1120

DIELECTRIC PROPERTIES AND AC CONDUCTIVITY OF METAL-SEMICONDUCTOR STRUCTURES

ADEM TATAROĞLU
Physics Department, Faculty of Arts and Sciences, Gazi University, 06500, Teknikokullar, Ankara, TURKEY

Dielectric properties and ac conductivity of the metal-semiconductor (MS) structures have been investigated using capacitance-voltage (C-V) and conductance-voltage (G/ω-V) characteristics in the frequency range of 1 kHz-1 MHz at room temperature. Calculation of the dielectric constant (ε'), dielectric loss (ε"), loss tangent (tanδ) and ac electrical conductivity (σ_{ac}) are given in the studied frequency ranges. Experimental results show that the values of the dielectric parameters are strongly frequency and voltage dependent. In general, ε' and ε" decreased with increasing frequency, while σ_{ac} increased with increasing frequency. The results can be concluded to imply that the interfacial polarization can more easily occur at low frequencies consequently contributing to the deviation of dielectric properties of Au/n-GaAs (MS) structures.

I. INTRODUCTION

Semiconductor devices are the basic components of integrated circuits and are responsible for the startling rapid growth of electronics industry. Because there is a continuing need for faster and more complex systems for the information age, existing semiconductor devices are being studied for improvement, and new ones are being invented [1-3]. The metal-semiconductor (MS) structures have an important role in modern electronics, and MS structures are one of the most widely used rectifying contacts in the electronics industry [1,4,5].

Gallium arsenide (GaAs) is one of the advantageous semiconductors for high-speed and low-power devices. However, the performance of GaAs-based devices, including metal-semiconductor field effect transistors (MESFETs) and heterostructure bipolar transistors (HBTs), depends on the surface and interface defect density [6,7]. In contrast to silicon (Si), GaAs does not have a surface stabilizing native oxide. The performance and reliability of these devices is dependent especially on the formation of the interfacial insulator layer, interface states (N_{ss}) localized at the semiconductor/insulator interface and the series resistance (R_s).

The interfacial insulator layer, interface state and series resistance values cause the electrical characteristics of MS structures to be non-ideal [8-10]. Also, the change in bias voltage and frequency has important effects on the electrical and dielectric parameters of these structures [11-16]. When voltage is applied across the MS structure, the combination of the interfacial insulator layer, depletion layer and the series resistance of the device will share applied voltage.

This paper presents a detailed study on the electrical and dielectric properties in the frequency range of 1 kHz-1 MHz at room temperature for Au/n-GaAs (MS) structure. To determine the dielectric constant (ε'), dielectric loss (ε"), loss tangent (tanδ) and the ac electrical conductivity (σ_{ac}) of MS structure, the admittance technique was used [5,14].

II. EXPERIMENTAL DETAIL

The metal-semiconductor (Au//n-GaAs) structures used in this study have been prepared using cleaned and polished as received from manufacturer n-type single crystals GaAs wafer with <100> surface orientation and $5x10^{17}$ cm^{-3} carrier concentrations. Before making contacts, the n-GaAs wafer were dipped in $5H_2SO_4+H_2O_2+H_2O$ solution for 1.0 min to remove surface damage layer and undesirable impurities and then in H_2O + HCl solution and then followed by a rinse in de-ionized water of 18 MΩ. The wafer dried with high-purity nitrogen and inserted into the deposition chamber immediately after the etching process. Au-Ge (88% and 12%) for ohmic contacts was evaporated on the back of the wafer in a vacuum-coating unit of 10^{-6} Torr. Then low-resistance ohmic contacts were formed by thermal annealing at 450 ^oC for 3 min in flowing N_2 in a quartz tube furnace. Then, the wafer was inserted into the evaporation chamber for forming the reference Schottky contacts. The Schottky contact was formed by evaporating Au as dots with diameter of about 1 mm onto all of n-GaAs surfaces. The interfacial insulator layer thickness was estimated to be about 27 Å from high frequency (1 MHz) measurement of the interface oxide capacitance in the strong accumulation region for Au/n-GaAs (MS) structures.

The capacitance-voltage (C-V) and conductance-voltage (G/ω-V) measurements were performed in the frequency range of 1 kHz-1 MHz at room temperature by using a HP 4192A HF/LF impedance analyzer (5 Hz-13 MHz) working in parallel circuit mode. The ac signal amplitude was kept at 50 mV. Furthermore, all measurements were carried out with the help of a microcomputer through an IEEE-488 ac/dc converter card.

III. RESULTS AND DISCUSSION

3.1. Frequency dependence of capacitance and conductance

The capacitance-voltage (C-V) and conductance-voltage (G/ω-V) characteristics of the Au/n-GaAs (MS) structure was measured in the frequency range 100 kHz-1MHz at room temperature.

Fig. 1(a) and (b) show the capacitance (C) and conductance (G/ω) as a function of frequency in the voltage range of 0-1 V, with the step of 0.25 V as a parameter. As can be seen in Fig. 1(a) and (b), the measured C and G/ω in depletion region decrease with increasing frequency in the frequency range of 1 kHz-1 MHz. This behavior is attributed to the presence of a continuous distribution of N_{ss}, which leads to a progressive decrease of the response of the N_{ss} to the applied alternating-current voltage [17-21].

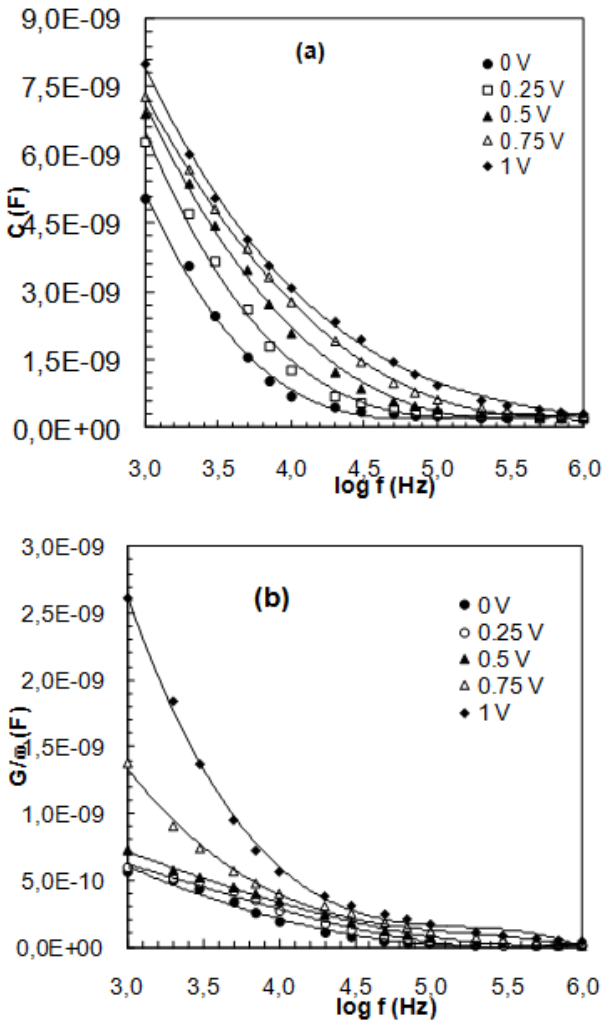

Fig. 1. The frequency dependence of (a) the $C(V_G)$-logf and (b) $G/\omega(V_G)$-logf characteristics of the Au/n-GaAs (MS) structure for various forward bias voltages at room temperature.

3.2. Frequency dependence of dielectric properties

In this section, frequency dependence of dielectric constant (ε'), dielectric loss (ε"), loss tangent (tanδ) and ac electrical conductivity (σ_{ac}), are studied for Au/n-GaAs (MS) structure. At room temperature, the values of the dielectric properties measured as a function of frequency in the 1 kHz to 1 MHz range.

The complex permittivity can be defined in the following complex form [22,23],

$$\varepsilon^*(\omega) = \varepsilon'(\omega) - j\varepsilon''(\omega) \tag{1}$$

where ε' and ε" are the real and the imaginary parts of complex permittivity, and j is the imaginary root of -1. The real part of the permittivity, ε'(ω), is a measure of the energy stored from the applied electric field in the material and identifies the strength of alignment of dipoles in the dielectric. The imaginary part, ε"(ω), or loss factor, is the energy dissipated in the dielectric associated with the frictional dampening that prevent displacements of bound charge from remaining in phase with the field changes [24].

The complex permittivity formalism has been employed to describe the electrical and dielectric properties. In the ε* formalism, in the case of admittance measurements, the following relation holds

$$\varepsilon^* = \frac{Y^*}{j\omega C_o} = \frac{C}{C_o} - j\frac{G}{\omega C_o} \tag{2}$$

where Y^*, C and G are the measured admittance, capacitance and conductance values of the dielectric material, respectively, and ω is the angular frequency ($\omega=2\pi f$) of the applied electric field [25].

The real part of the complex permittivity, the dielectric constant (ε'), at the various frequencies is calculated using the measured capacitance values at the strong accumulation region from the relation [26,27]

$$\varepsilon'(\omega) = \frac{C_m}{C_0} \tag{3}$$

where C_o is capacitance of an empty capacitor. $C_0 = \varepsilon_0(A/d)$; where A is the rectifier contact area in cm^{-2}, d is the interfacial insulator layer thickness and ε_o is the permittivity of free space charge (ε_o = $8.85\text{x}10^{-14}$ F/cm), and C_m is measurement maximal capacitance of MS structure in the strong accumulation region, correspond to the oxide capacitance.

The imaginary part of the complex permittivity, the dielectric loss (ε"), at the various frequencies is calculated using the measured conductance values from the relation

$$\varepsilon''(\omega) = \frac{G_m}{\omega C_0} \tag{4}$$

The dissipation factor or loss tangent (tanδ) can be expressed as follows [22,23,26-28],

$$\tan\delta = \frac{\varepsilon''(\omega)}{\varepsilon'(\omega)} \tag{5}$$

The ac conductivity of all samples has been calculated from the dielectric losses according to the relation

$$\sigma^* = i\varepsilon_0\omega\varepsilon^*(\omega) = \varepsilon_0\omega\varepsilon'' + i\varepsilon_0\omega\varepsilon' \tag{6}$$

The real part of $\sigma^*(\omega)$ is given by

$$\sigma_{ac} = \omega C \tan\delta(d/A) = \varepsilon_0\omega\varepsilon'' \tag{7}$$

The C-V and G/ω-V measurements have been made within the frequency range 1 kHz-1MHz of the Au/n-GaAs (MS) structure at room temperature, and thus, the frequency-dependent changes in the dielectric constant (ε'), dielectric loss (ε"), loss tangent (tanδ) and ac electrical conductivity (σ_{ac}) have been obtained.

Fig. 2(a), (b) and (c) show the frequency-dependent ε', ε" and tanδ curves of the Au/n-GaAs structure for various forward bias voltages at room temperature. As seen in Fig. 2, changes in the frequency and applied bias

voltage considerably affect ε', ε" and tanδ values. As can be seen from these figures, the values of ε' and ε" decrease with an increase in frequency for each voltage.

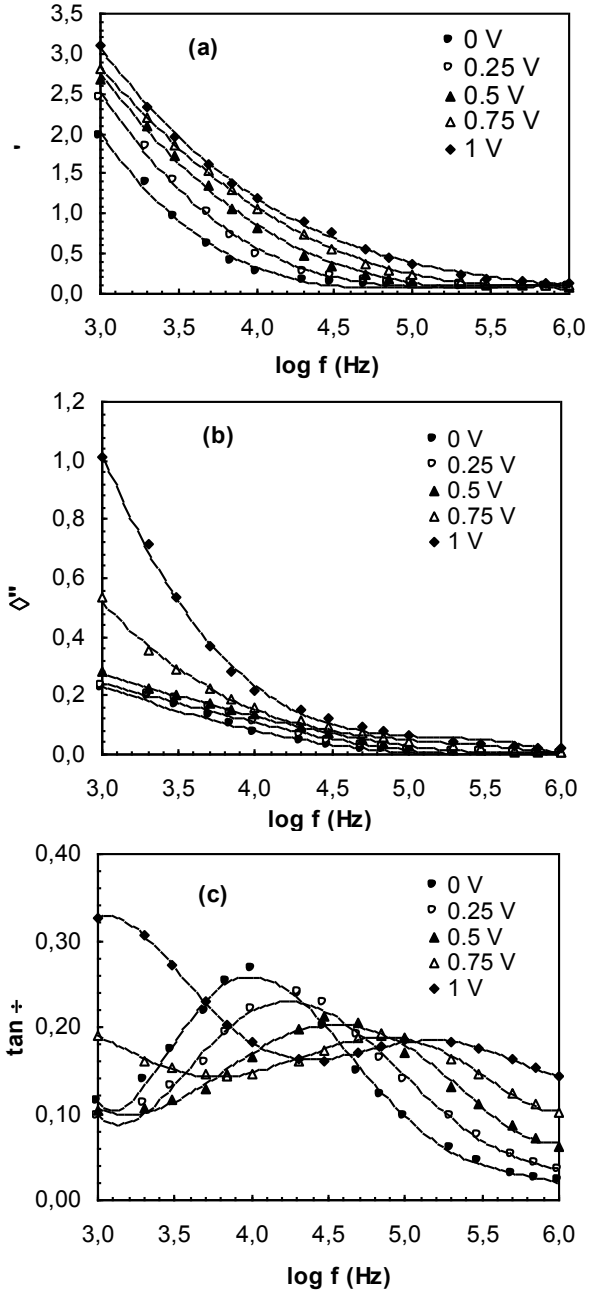

Fig. 2. Frequency dependence of the (a) ε', (b) ε" and (c) tanδ for various applied voltage of Au/n-GaAs (MS) structure.

This is the normal behavior of a dielectric material. In principle, at low frequencies, all the four types of polarization processes, i.e., the electronic, ionic, dipolar, and interfacial or surface polarization contribute to the values of ε' and ε". With increasing frequency, the contributions of the interfacial, dipolar or the ionic polarization become ineffective by leaving behind only the electronic part. Furthermore, the decrease in ε' and ε" with an increase in frequency is explained by the fact that as the frequency is raised, the interfacial dipoles have less time to orient themselves in the direction of the alternating field [29-33]. On the other hand, after 100 kHz, the change in dielectric properties (ε' and ε") continuous slightly to decrease, and also remains almost constant at higher frequencies (100 kHz-1 MHz), with increasing frequency. This behavior in dielectric properties of MS structures at the high frequencies may be due to the interface states that cannot follow the ac signal at high frequency. The carrier lifetime of interface trapped charges are much larger than 1/ω at very high frequency, that is, the charges at interface cannot follow an ac signal [12,28].

If the electric polarization in a dielectric is unable to follow the varying electric field, dielectric loss occurs. An applied field will alter this energy difference by producing a net polarization, which lags behind the applied field because the tunneling transition rates are finite. This part of the polarization, which is not in phase with the applied field, is termed as dielectric loss. Fig. 2(c) shows the variation of the loss tangent (tanδ) with frequency for each voltage. As shown in Fig. 2(c), the peak values of tanδ-logf have decreased with increasing voltage and the peak positions tend to shift towards high frequency region.

Fig. 3 shows the frequency-dependent ac electrical conductivity (σ_{ac}) changes of the MS structure at various voltages. As can be seen in Fig. 3, ac conductivity increases with increasing frequency. As observed in Fig. 2(b) and 3, dielectric loss decreases with increasing frequency and, accordingly, σ_{ac} increases. This result is also compatible with the literature, where it is suggested that the increase in ac conductivity with increasing frequency is attributed to the series resistance effect. Similar behavior was observed in the literature [28,29-31,33].

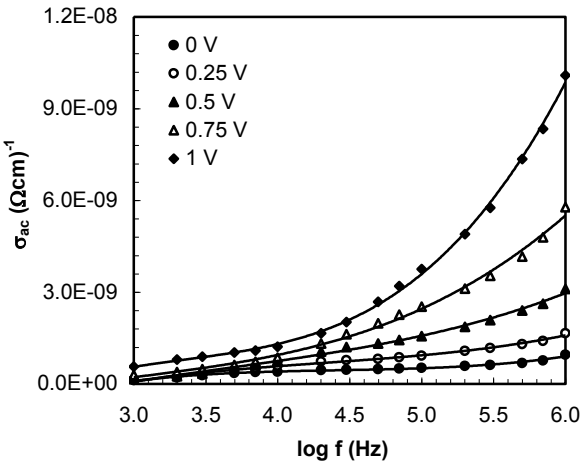

Fig. 3. Frequency dependence of ac electrical conductivity (σ_{ac}) for various applied voltage of Au/n-GaAs (MS) structure.

IV. CONCLUSIONS

Dielectric properties and ac conductivity MS structures using capacitance-voltage (C-V) and conductance-voltage (G/ω-V) characteristics have been studied in detail in the frequency range 1 kHz–1MHz at room temperature. It was shown that the electrical properties of Au/n-GaAs (MS) structure were found to be strongly dependent to frequency and voltage. Since the presence of the interfacial insulator layer, interface states, fixed surface charge and series resistance causes changes in the electrical and dielectric characteristics of MS structures, they do not obey the ideal C-V and G/ω-V

behavior. The values of dielectric constant (ε') and dielectric loss (ε") decrease with increasing frequency for each bias voltage. These behaviors are attributed to the decrease of polarization with increasing frequency in the metal-semiconductor interface. It is concluded that the values of dielectric parameters of the Au/n-GaAs (MS) structure are strongly dependent on both the frequency and applied bias voltage.

V. ACKNOWLEDGMENTS

This work is supported by Gazi University Scientific Research Project (BAP) FEF. 05/2009-34.

[1]. *S.M. Sze, S M and K. Ng. Kwog*, Physics of Semiconductor Devices, 3rd ed. Wiley, New Jersey, 2007.
[2]. *M.S. Tyagi*, Introduction to Semiconductor materials and Devices, Wiley, New York, 1991.
[3]. *K.K. Kwok.*, Complete Guide to Semiconductor Devices, McGraw-Hill, New York, 1995.
[4]. *A.Hiraki*, Surface Sci. Rep. 3 (7) (1983) 357.
[5]. *E.H. Rhoderick, R.H. Williams*, Metal-Semiconductor Contacts, 2nd ed., Clarendon, Oxford, 1988.
[6]. *M. Ambrico, M. Losurdo, P. Capezzuto, G. Bruno, T. Ligonzo, L. Schiavulli, I. Farella, V.Augelli*, Solid-State Electron. 49 (2005) 413.
[7]. *Ş. Karataş, A. Türüt, Ş. Altındal*, Nucl. Instr. and Meth. A, 555 (1-2) (2005) 260.
[8]. *H. Deuling, E. Klausmann, A. Goetzberger*, Solid State Electron. 15(5) (1972) 559
[9]. *U. Kelberlau, R. Kassing*, Solid State Electron. 22 (1) (1979) 37.
[10]. *R. Castagne, A. Vapaille*, Surf. Sci. 28 (1) (1971) 157.
[11]. *E.H. Nicollian, J.R. Brews*, MOS (Metal-Oxide-Semiconductor) Physics and Technology, John Wiley, New York, 1982.
[12]. *A.Tataroğlu*, Microelectron. Eng. 83 (2006) 2551.
[13]. *A.Tataroğlu, İ. Yücedağ, Ş. Altındal*, Microelectron. Eng. 85 (2008) 1518.
[14]. *E.H. Nicollian, A. Goetzberger*, Appl. Phys. Lett. 7 (1965) 216.
[15]. *M.Schulz, E. Klausmann*, Appl. Phys. 18 (1979) 69.
[16]. *M.Siad, A. Keffous, S. Mamma, Y. Belkacem, H.Menari*, Appl. Surf. Sci. 236 (2004) 366.
[17]. *E.H. Nicollian, A. Goetzberger*, Bell. Syst. Tech. J. 46 (1967) 1055.
[18]. *P.Cova, A. Singh, R.A. Masut*, J. Appl. Phys. 82 (1997) 5217.
[19]. *B. Akkal, Z. Benamara, B. Gruzza, L. Bideux*, Vacuum 57 (2000) 219.
[20]. *J .H. Werner*, Metallization and Metal-Semiconductor Interface, Plenum, New York, 1989.
[21]. *P. Chattopadhyay, B. Raychaudhuri*, Solid State Electron. 36 (1993) 605.
[22]. *C.P. Symth*, Dielectric Behaviour and Structure, McGraw-Hill, New York, 1955.
[23]. *Vera V. Daniel*, Dielectric Relaxation, Academic Press, London, 1967.
[24]. *D. Cheng*, Field and Wave Electromagnetics, 2nd Ed., Addison-Wesley, New York, 1989.
[25]. *N.G. McCrum, B.E. Read, G. Williams*, Anelastic and Dielectric Effects in Polymeric Solids, Wiley, New York, 1967.
[26]. *M. Popescu, I. Bunget*, Physics of Solid Dielectrics, Elsevier, Amsterdam, 1984.
[27]. *A.Chelkowski*, Dielectric Physics, Elsevier, Amsterdam, 1980.
[28]. *A.Tataroğlu, Ş. Altındal, M.M. Bülbül*, Microelect. Eng. 81 (2005) 140.
[29]. *S.P. Szu, C.Y. Lin*, Mater. Chem. and Phys. 82 (2003) 295.
[30]. *D. Maurya, J. Kumar*, Shripal, J. Phys. and Chem. Solids, 66 (2005) 1614
[31]. *A.A.Sattar, S.A. Rahman*, Phys. Stat. Sol. (a) 200(2) (2003) 415.
[32]. *M. R. Ranga Raju, R. N. P. Choudhary, and S.Ram*, Phys. Stat. Sol. (b) 239(2) (2003) 480.
[33]. *İ.M. Afandiyeva, İ. Dökme, Ş. Altındal, M.M.Bülbül, A. Tataroğlu*, Microelect. Eng. 85 (2008) 247.

TEMPERATURE DEPENDENCE ELECTRICAL CHARACTERISTICS OF n-GaAs STRUCTURE GROWN BY MBE

BARIŞ KINACI[1,*], TARIK ASAR[1], YUNUS ÖZEN[1], ŞEMSETTIN ALTINDAL[1], TOFIG MAMMADOV[1,2], SÜLEYMAN ÖZÇELİK[1]

*[1]Physics Department, Faculty of Arts and Sciences, Gazi University, 06500, Teknikokullar, Ankara, TURKEY, *b.kinaci@gazi.edu.tr*

[2] National Academy of Science, Institute of Physics, Baku, Azerbaijan

The current-voltage (*I-V*) characteristics of n-GaAs structure were measured in the temperature range of 80-295 K**.** An abnormal decrease in the zero-bias barrier height (Φ_{Bo}) and an increase in the ideality factor (*n)* with decreasing temperature have been observed. Such behaviour of Φ_{Bo} and *n* have been attributed to the barrier inhomogeneities by assuming a single Gaussian distribution (GD) of barrier heights (BH) between metal and semiconductor. The Φ_{Bo} vs q/2kT plot was drawn to obtain evidence of GD of BH, and the values of Φ_{Bo} = 0,639 eV and σ_0 = 0,0989 V for the mean BH and zero-bias standard deviation have been obtained from this plot, respectively. Furthermore, the mean values of Φ_{Bo} and the effective Richardson constant A* obtained from the modified Richardson $\ln(I_0/T^2)-q^2\sigma_0^2/2(kT)^2$ vs q/kT plot are found as 0.642 eV and 10.46 A/cm^{2}K^2 , which is close to the theoretical value 8 A/cm^{2}K^2.

I. INTRODUCTION

Metal-semiconductor (MS) contact have been studied in the six decades years [1-16]. MS structures are important research tools in the characterization of new semiconductor materials and at the same time the fabrication of these structures plays a crucial role in constructing some useful devices in technology. The temperature dependence of the current-voltage (*I-V*) characteristics in wide temperature range allows us to understand different aspects of current transport mechanisms. The current transport mechanism is dependent on various parameters such as device temperature, barrier height, the applied bias voltage, density of interface states and series resistance.

Analysis of the forward bias *I-V* characteristics based on thermionic emission (TE) theory usually reveals an abnormal decrease in the Φ_{Bo} and an increase in the ideality factor *n* with a decrease in temperature [4-10]. The barrier inhomogeneities are described mainly by Gaussian distribution function and it has been widely accepted to correlate the experimental data [5-12]. In this study, the *I-V* characteristics of n-GaAs structure was measured over the temperature range of 80-295 K. The temperature dependence of electrical parameters such as Φ_{Bo} and *n* were extracted from forward bias *I-V* measurements.

II. EXPERIMENTAL PROCEDURE

The n-GaAs structure was grown by V80-H solid source molecular beam epitaxy (MBE) system. In MBE system, firstly 500 nm InGaAs/GaAs superlattice (SL) buffer layer was grown on (100) GaAs substrate to prevent the migration of defects and the impurities from substrate. Then, n-type Si doped 500 nm GaAs epilayer was grown with 1μm/h growth rate. The structure was cleaned using acetone, methanol and deionized water, sequentially for 10 min each for the removal of organic impurities from the surface of the sample. After surface cleaning, high-purity gold (Au) metal with a thickness of 1070 Å was thermally evaporated with thermal evaporation system onto the whole back surface of the structure in the pressure of ~ 10^{-7} Torr. In order to perform the ohmic contact, structure was annealed at 400 ^{o}C for 3 min in this system. Immediately after ohmic contact, circular dots shaped Au Schottky contacts 1100 Å thickness were formed by evaporating Au in the pressure of ~ 10^{-7} Torr. The schematic diagram of the n-GaAs structure is given Fig. 1.

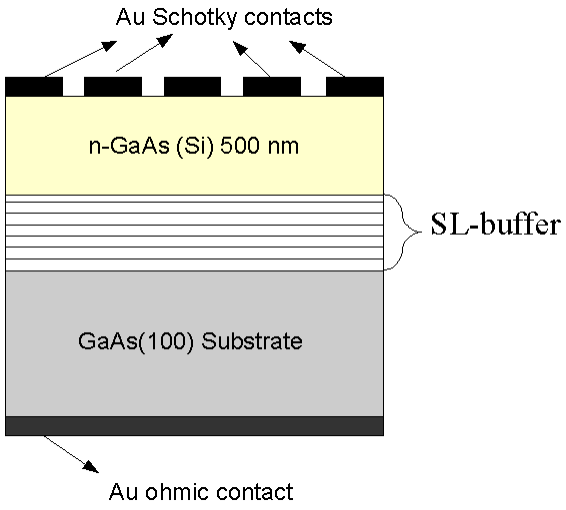

Fig. 1. The schematic diagram of the n-GaAs structure.

The forward bias *I-V* measurements were performed using a Keithley 2400 source meter in the temperature range of 80-295K. All measurements were performed in a temperature controlled Janis vpf-475 cryostat, which enables us to make measurements in the temperature range of 77-450 K. The sample temperature was always monitored using a copper-constantan thermocouple close to the sample and measured with a dmm/scanner Keithley model 199 and a Lake Shore model 321 auto-tuning temperature controllers with sensitivity better than ± 0.1K

III. RESULTS AND DISCUSSION

Fig.2 shows the semi-logarithmic *I-V* characteristics of the n-GaAs structure at various temperatures over the range of 80-295 K. The current through these structures at a forward bias ($V \geq 3kT/q$), according to TE theory, is given by [1,2]

$$I = I_o \exp\left(\frac{qV}{nkT}\right)\left[1-\exp\left(-\frac{qV}{kT}\right)\right] \quad (1)$$

where I_o is the reverse saturation current derived from the straight-line intercept of lnI at zero bias and is defined by

$$I_o = AA^*T^2\exp\left(-\frac{q\Phi_{Bo}}{kT}\right) \quad (2)$$

where q is the electronic charge, A^* is the effective Richardson constant and equals to 8 A cm^{-2} K^{-2} for n-type GaAs, Φ_{Bo} is the zero bias barrier height, n is the ideality factor, A is the effective diode area, k is the Boltzmann constant and T is the absolute temperature in unit of K. The ideality factor is calculated from the slop of the linear region of the forward bias $ln(I)$-V plot for each temperature as following equation.

$$n = \frac{q}{kT}\left(\frac{dV}{d(\ln I)}\right) \quad (3)$$

The Φ_{B0} (= $\Phi_B(I\text{-}V)$) is determined from the extrapolated I_o values for each temperature as following equation.

$$\Phi_{Bo} = \frac{kT}{q}\ln\left[\frac{AA^*T^2}{I_0}\right] \quad (4)$$

The obtained experimental values of I_o, n and Φ_{Bo}were given in Table 1. As shown in Table 1, the experimental values of Φ_{B0} and n for the n-GaAs structure ranged from 0.19 eV and 4.90 (at 80 K) to 0.52 eV and 2.00 (at 295 K), respectively.

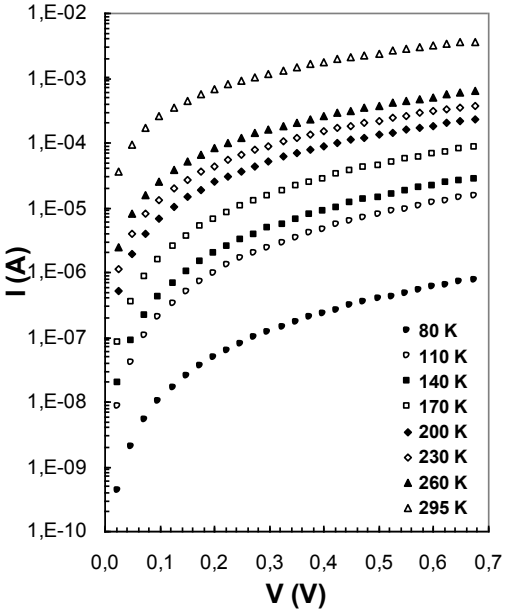

Fig. 2. The experimental forward bias *I-V* characteristics of the n- GaAs structure at various temperatures.

The values of n decrease with increasing temperature. Such behavior of n can be attributed to particular distribution of interface states [6,9,17-25]. On the other hand the values of Φ_{Bo} increase with increasing temperature. Similar results have been reported in the literature [3-14]. Such temperature dependence is an obvious disagreement with the reported negative temperature coefficient of the Schottky barrier height. This result is attributed to inhomogeneous interfaces and barrier heights. The BH, obtained from Eq. (4) called apparent or zero-bias barrier height, which increase with increasing temperature of Schottky contact depending on the electrical field across the contact and consequently on the applied bias voltage.

Table 1. Temperature dependent values of various diode parameters determined from *I-V* characteristics of n-GaAs structure at various temperatures.

T(K)	I_o(A)	n	Φ_{Bo} (eV)
80	$6.00\text{x}10^{-10}$	4.90	0.19
110	$4.00\text{x}10^{-9}$	3.75	0.25
140	$2.55\text{x}10^{-8}$	3.07	0.30
170	$1.09\text{x}10^{-7}$	2.82	0.35
200	$5.16\text{x}10^{-7}$	2.58	0.39
230	$1.46\text{x}10^{-6}$	2.40	0.43
260	$3.15\text{x}10^{-6}$	2.18	0.47
295	$8.00\text{x}10^{-6}$	2.00	0.52

Fig. 3 shows a plot of the experimental BH versus the ideality factor for various temperature. The straight line in Fig. 3 is the least squares fit to the experimental data and indicates a linear relationship between the experimental barrier heights (BHs) and the ideality factors of the Schottky contact, which was explained by lateral inhomogeneties of the BHs in the structure [26]. The extrapolation of the experimental BHs versus ideality factors plot to n=1 has given a homogeneous BH of approximately 0.65 eV. Thus, it can be said that the significant decrease of the zero-bias barrier height and increase of the ideality factor especially at low temperature are possibly caused by the BH inhomogeneties.

To evaluate the BH in another way, we use the Richardson plot of reverse saturation current I_o. By taking the natural logarithm of Eq.(2), one can obtain

$$\ln\left(\frac{I_0}{T^2}\right) = \ln\left(AA^*\right) - \frac{q\Phi_{Bo}}{kT} \quad (5)$$

The conventional energy variation of ln (I_o/T^2) vs q/kT and q/nkT plot is found to be linear in the temperature range measured as shown in Fig. 4. However, when the experimental data are shown to fit asymptotically with a straight line it yields an activation energy of 0.598 eV from $\ln(I_o/T^2)$ versus q/nkT and from $\ln(I_o/T^2)$ versus q/kT 0.086 eV. The Richardson constant (A^*) value of $3.87\text{x}10^{-7}$ $Acm^{-2}K^{-2}$ and $1.42\text{x}10^{-3}$ $Acm^{-2}K^{-2}$ are found lower than the real value 8 $Acm^{-2}K^{-2}$ for n-GaAs. In order to obtain evidence of a Gaussian distribution of the barrier heights, we have drawn a Φ_{Bo} versus q/2kT plot (Fig. 5), and the values of Φ_{Bo} = 0.639 eV and σ_0 = 0.0989 V for the mean barrier height and zero-bias, respectively, have been obtained from this plot.

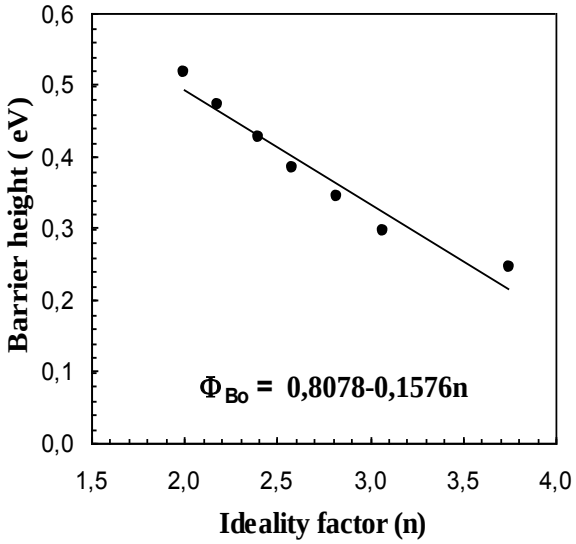

Fig. 3. Linear variation of apparent barrier height versus ideality factors at various temperatures.

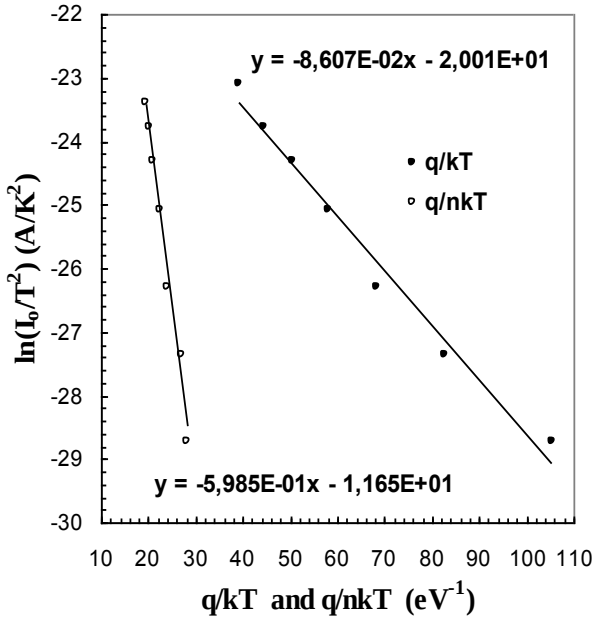

Fig. 4. The plot of ln (I_o/T^2) vs q/kT and q/nkT for n-GaAs structure.

This deviation in the A^* may be due to the spatial inhomogeneous barrier heights and potential fluctuation at the interface that consist of low and high barrier areas [22,24]. According to these results, this inhomogeneity and potential fluctuation dramatically affect low-temperature *I-V* characteristics [8, 27].

$$\ln\left(\frac{I_0}{T^2}\right)-\left(\frac{q^2\sigma_0^2}{2k^2T^2}\right)=\ln\left(AA^*\right)-\frac{q\Phi_{Bo}}{kT} \qquad (6)$$

The plot of a modified $\ln(I_0/T^2)-q^2\sigma_0^2/2(kT)^2$ versus q/kT plot according to Eq. (6) should give a straight line with the slope directly yielding the mean Φ_{Bo} as 0.639 eV and the intercept (=lnAA*) at the ordinate determining A* for a given diode area A as 10.46 $Acm^{-2}K^{-2}$ (Fig. 6), respectively, without using the temperature coefficient of the zero-bias barrier height for n-type GaAs. It can be seen that Φ_{Bo} = 0.642eV calculated from Fig.4 (according to Eq. (6)), is in agreement with the value of Φ_{Bo} = 0.639 eV the plot of q/2kT (Fig. 5).

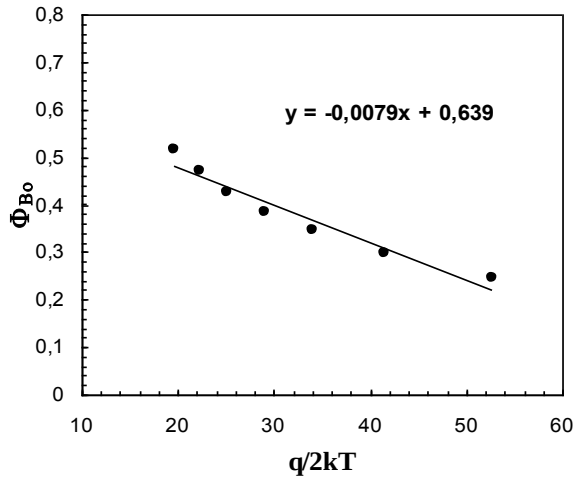

Fig. 5. The plot of Φ_{Bo} versus q/2kT for n-GaAs structure.

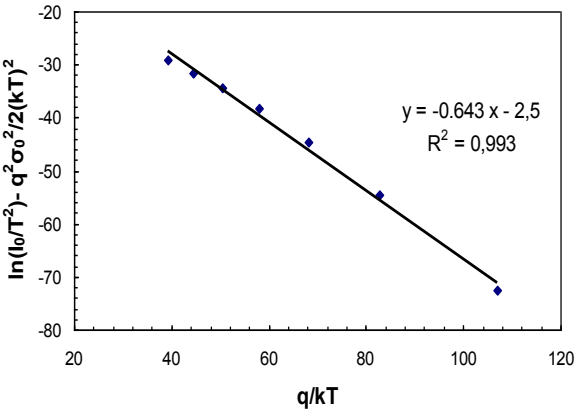

Fig. 6. The plot of $\ln(I_0/T^2)-q^2\sigma_0^2/2(kT)^2$ versus q/kT for n-GaAs structure.

IV. CONCLUSION

The forward bias *I-V* characteristics of n-GaAs structure were measured in the temperature range of 80-295 K. The experimental forward bias *I-V* analysis based on the TE theory has revealed that Φ_{Bo} decrease and *n* increase with decreasing temperature. In order to obtain evidence of a Gaussian distribution of the barrier heights, we was drawn a Φ_{Bo} versus q/2kT plot, and the values of Φ_{Bo} = 0.639 eV and σ_0 = 0.0989 V for the mean barrier height and zero-bias, respectively, have been obtained from this plot. The value of the Richardson constant obtained from modified $\ln(I_0/T^2)-q^2\sigma_0^2/2(kT)^2$ versus q/kT plot was found as 10.46 A/cm^2K^2. This value is close to the known theoretical value of 8 A/cm^2K^2.

V. ACKNOWLEDGMENT

This work is supported by the State of Planning Organization of Turkey under Grant no. 2001K120590.

[1]. *E.H. Rhoderick, R.H. Williams*, Metal-Semiconductor Contacts, second ed, Clarendon Press, Qxford, 1988.
[2]. *S.M. Sze*, Physics of Semiconductor Devices, second ed, Wiley, New York, 1981.
[3]. *W. Mönch, J. Vac*. Sci. Technol. B. 17 (1999) 1867.
[4]. *Ş. Altındal, S. Karadeniz, N. Tuğluoğlu, A.Tataroğlu*, Solid State Electron. 47(10) (2003) 1847.
[5]. *S. Chand, J. Kumar*, Semicond. Sci. Technol. 11 (1996) 1203.
[6]. *Ş. Altındal, İ. Dökme, M.M. Bülbül, N. Yalçın, T. Serin*, Microelectron. Eng. 83 (2006) 499
[7]. *S. Zeyrek, Ş. Altındal, H. Yüzer, M.M. Bülbül*, Appl. Surf. Sci. 252 (2006) 2999.
[8]. *Ş. Karataş, Ş. Altındal, A Türüt, A. Özmen*, Appl. Surf. Sci. 217 (2003) 250.
[9]. *S. Zhu, R.L. Van Meirhaeghe, C. Detavernier, F. Cardon, G.P. Ru, X.P. Qu, B.Z. Li*, Solid State Electron. 44 (2000) 663.
[10]. *M.K. Hudait, P. Venkateswarlu, S.B.Krupanidhi*, Solid State Electron. 45 (2001) 133.
[11]. *Subnash, J. Kumar*, Semicond. Sci. Technol. 10 (1995) 1680.
[12]. *S. Chand, J. Kumar*, J. Appl. Phys. 80 (1996) 288.
[13]. *R.T. Tung*, Mater. Sci. Eng. R. 35 (2001)1.
[14]. *J.P. Sullivan, R.T. Tung, M.R. Pinto, W.R.Graham*, J. Appl. Phys. 70 (1991) 7403.
[15]. *S. Kar, K.M. Panchal, S. Bhattacharya, S.Varma*, IEEE Trans, Electorn. Devices 29 (1982) 1839.
[16]. *Ş. Karataş, Ş. Altındal, M. Çakar*, Physica B 357 (2005) 386.
[17]. *H.C. Card., E.H. Rhoderick*, J. Phys. D: Appl. Phys. 4 (1971) 1589.
[18]. *P. Cova and A. Singh*, Solid-State Electron. 33 (1) (1990) 11.
[19]. *İ. Dökme, Ş. Altındal*, Semicond. Sci. Technol. 21 (8) (2006)1053-1058
[20]. *R.F. Schmitsdorf, T.U. Kampen, W. Mönch*, Sur. Sci. 324 (1995) 249.
[21]. *J. H. Werner and H. H. Gűttler*, Physica Scripta. T39 (1991) 258.
[22]. *J. H. Werner and H. H. Gűttler*, Physica Scripta. T39 (1991) 258.
[23]. *İ.Dökme, Ş. Altındal, M. M. Bülbül*, Appl. Surf. Sci. 252 (22) (2006) 7749-7754
[24]. *Y.P. Song, R.L. Van Meirhaeghe, W.H. Laflere, F.Cardon*, Solid-State Electron. 29 (1986) 663.
[25]. *A. Gümüş, A. Türüt, N. Yalçın*, J. Appl. Phys. 91 (2002) 245.
[26]. *W. F. Kosonocky, H. Elabd*, SPIE 443 (1983) 167.
[27]. *Ş. Aydoğan, M. Sağlam, A Türüt, Y. Onganer*, Synth. Met. 150 (2005) 15.

THICKNESS DEPENDENCE OF THE DIELECTRIC PROPERTIES OF $TlSbS_2$ THIN FILMS

M.PARTO, D.DEGER*, K.ULUTAS
Istanbul University, Science Faculty, Physics Department,
Vezneciler, Istanbul, TURKEY,
denizdeger@yahoo.com

Capacitance and the dielectric loss of $TlSbS_2$ thin films, obtained via thermal evaporation of $TlSbS_2$ crystals grown by Stockber-Bridgman technique, have been measured using ohmic Al electrodes in the frequency range 200-1000 Hz and within the temperature interval 293-373K. Thickness of the $TlSbS_2$ thin films are obtained 400 A^o - 4000 A^o.

In the dielectric $TlSbS_2$ thin films, correlations between the film thickness and the dielectric properties are investigated. As the film thickness increased, the dielectric constant decreased. Both capacitance and the dielectric loss factor are found to decrease with increasing frequency and increase with increasing temperature.

I. INTRODUCTION

The compound $TlSbS_2$ belongs to the group of ternary semiconductors of the $A^{III}B^{V}C_2^{IV}$ type. Ternary semiconductive compounds of type $TlB^{V}C_2^{VI}$ attached much attention owing to their interesting physical properties. Interesting thermo-electric and electro-optic properties of these compounds make them good materials for possible applications such as photo-receiver, phototransducer, detectors of pulsed laser radiation, acusto-electric and thermo-electric devices[1-4]. The high photosensitivity and the low density of surface make possible the extensive applications of these compounds [5,1].

The heat conductivity, photoelectric optical properties of bulk $TlSbS_2$ and structure, optical and photoelectric properties of $TlSbS_2$ thin films were hardly investigated. [6-10]. Furthermore, as far as we know no data concerning the ac conductivity and/or dielectric properties of films from that compound are available in literature. In this paper, the temperature, frequency and esspecially film thickness dependence of dielectric properties measured for thermal evaporated $TlSbS_2$ films are presented.

II. EXPERIMENTAL

Films were prepared on glass substrates by thermal evaporation technique of $TlSbS_2$ crystals using a quartz crucible in a vacuum of 10^{-6} Torr. The base and counter Al electrodes, each of 3000 A^o thick, were evaporated at a pressure of 10^{-5} Torr. The film thickness was measured by Tolansky interferometric method. Thickness of the $TlSbS_2$ thin films are obtained 400 A^o - 4000 A^o.

The resulting Al / $TlSbS_2$ / Al thin film sandwich stuructures have a capacitive configuration of effective area 6 mm^2. The areas of capacitors were measured with a travelling microscope.

A Gen-Rad 1615-A Scheering Bridge, A Gen-Rad 1232 Null dedector and a Good Will GFG 8016 D Generator were used for the capacitance and dissipation factor measurements. These measurements were made in approximately 10^{-5} Torr vacuum and were carried out in the temperature range 293 - 353 K.

Temperatures of the samples during the study were measured with an copper-constantan thermocouple.

III. RESULTS AND DISCUSSION

Thin layers of the chalcogenides were produced by thermal evaporation of the initial substrates from quartz crusible in a vacuum. It was found that ,the thin chalcogenide layers produced under these conditions were amorphous. It was found that amorphous films could be obtained by thermal evaporation of bulk material [11].

3.1 Temperature and frequency dependence of the capacitance

Variations of capacitance of the prepared Al/$TlSbS_2$/Al thin film sandwich structures with temperature in the 293 - 373 K range were measured for several frequencies in the 200-1000 Hz interval. The obtained capacitance - temperature curves for the chosen frequencies, that are shown in Fig.1, are in good agreement with the literature [12-14].

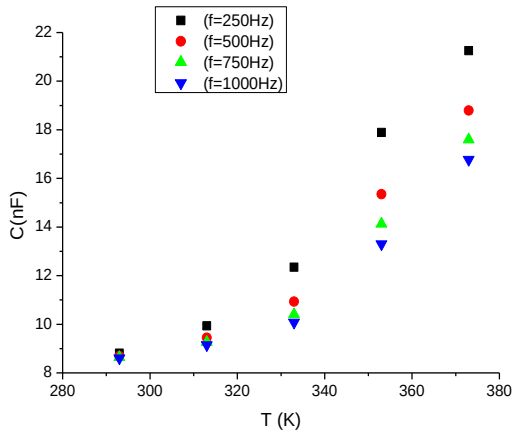

Fig.1. Variation of the capacitance with temperature of $TlSbS_2$ thin films at different frequencies. Film Thickness: 730 A^o

Fig.1 shows the variation of the capacitance as a function of frequency at different temperatures. A decrease in the capacitance with increasing frequency is observed. At room temperature, capacitance is almost independent of the frequency. The high capacitance at lower frequencies may be attributed to the significant polarization of charge carriers. The dipoles can not orient themselves at higher frequencies and hence the capacitance decreases.

The variation of capacitance with frequency is given in Eq.1 [15]

$$C = C_g + [s\tau / (\omega^2 \tau^2 + 1)] , \qquad (1)$$

where C_g is the geometrical capacitance, s is the conductance corresponding to absorption current, τ is the dipole relaxation time and the ω is the angular frequency. According to this, capacitance is maximum when $\omega = 0$ and minimum when $\omega = \infty$.

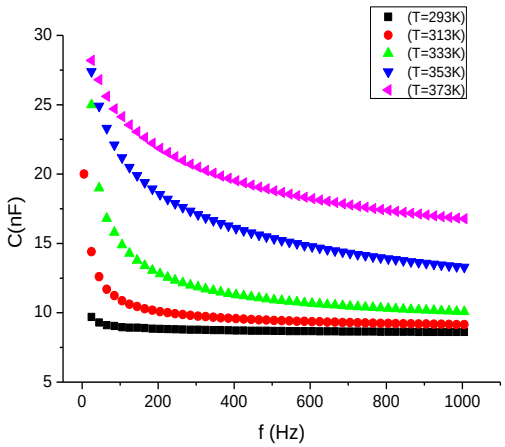

Fig.2. Variation of the capacitance with frequency of $TlSbS_2$ thin films at different temperatures. Film Thickness: 730A^o

In our case, the decrease in capacitance with increasing frequency (Fig.2) is in accordance with Eq.(1). At low frequencies and high temperatures the mechanism of long relaxation time are dominant so capacity increases and *vice versa*, according to Eq. 1.

3.2 Temperature and frequency dependence of the dielectric constant

The temperature dependence of the dielectric constant, ε_1, of $TlSbS_2$ at different frequencies is shown in Fig.3. At all frequencies the dielectric constant increases with increasing temperature.

Fig.4 shows the variation of the dielectric constant with frequency (200-1000 Hz) at different temperatures. A significant variation in ε_1 with frequency was observed at higher temperatures but this variation is insignificant at low temperatures. The dielectric constant takes larger values at higher temperatures in the overall frequency region.

$TlSbS_2$ has a dielectric constant greather than 25 at temperatures equal or higher than 300 K and in the frequency region 200 - 1000 Hz.

The increase of ε_1 with temperature can be attributed to orientational polarization connected with thermal motion of molecules. Increasing temperature facilitates orientation of molecules and this causes increase of polarization

3.3 Frequency and temperature dependence of the dielectric loss factor

Knowledge of dielectric loss factor provides us to understand the mechanism of ac conduction and dielectric relaxation. Therefore , we studied the dependence of dielectric loss factor on the frequency and temperature.

Fig.5 and Fig.6 show the variation of the dielectric loss, with the frequency at different temperatures.and thus ε_1 .

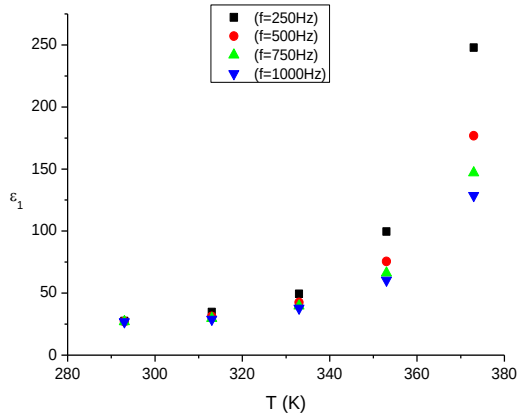

Fig.3. Temperature dependence of the dielectric constant ε_1, of $TlSbS_2$ thin films at different frequencies. Film Thickness: 4090 A^o

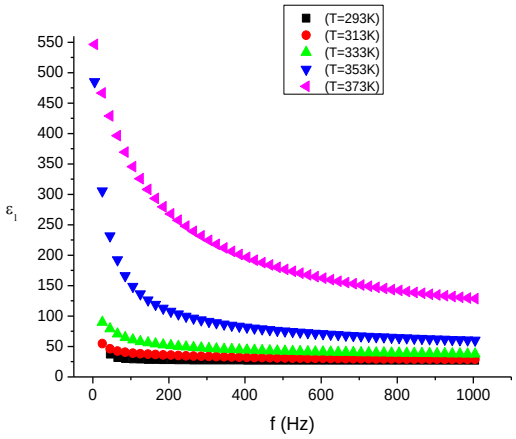

Fig.4. Frequency dependence of the dielectric constant ε_1, of $TlSbS_2$ thin films at different temperatures. Film thickness: 4090 A^o

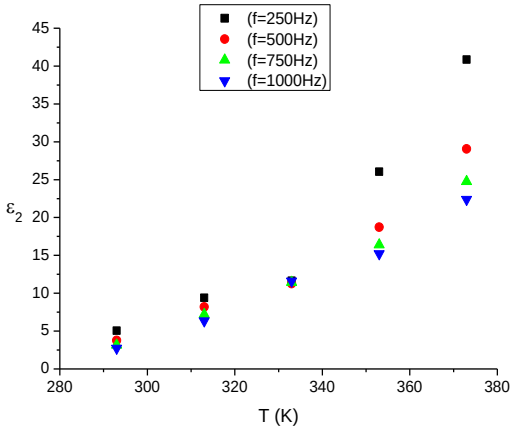

Fig.5. Temperature dependence of the dielectric loss factor ε_2, of $TlSbS_2$ thin films at different temperatures. Film thickness: 2198 A^o

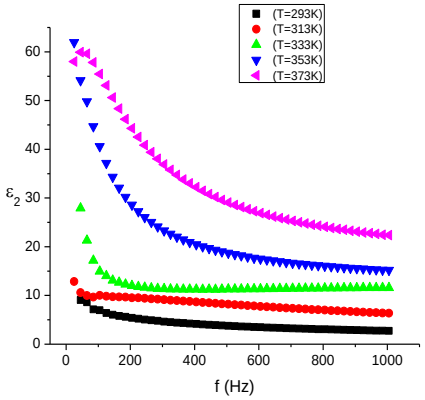

Fig.6. Frequency dependence of the dielectric loss factor ε_2, of $TlSbS_2$ thin films at different temperatures. Film Thickness: 4090 A^o

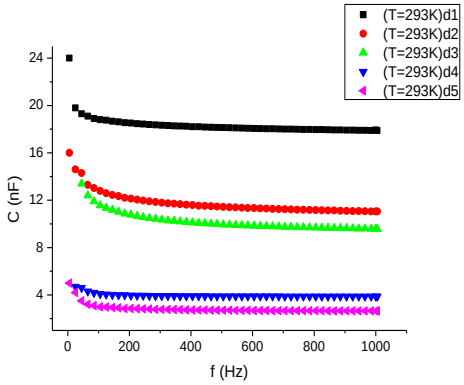

Fig.7. Variation of the capacitance with frequency of $TlSbS_2$ thin films at different thickness. $d_1 < d_2 < d_3 < d_4 < d_5$

3.4 Thickness dependence of the dielectric constant and capacitance

The $TlSbS_2$ film thickness was measured by Tolansky interferometric method ranged from 400 A^o-4000 A^o .

Fig.7 shows the variation of the dielectric constant with frequency at different thickness. Fig.8 shows the variation of the dielectric constant with film thickness at 1 KHz. We saw that the dielectric constant have similar thickness dependence characteristics in the studied temperatures range. This figure clearly shows that the dielectric constant decreases as the film thickness is increased. This results are in good agreement with the literature [16].

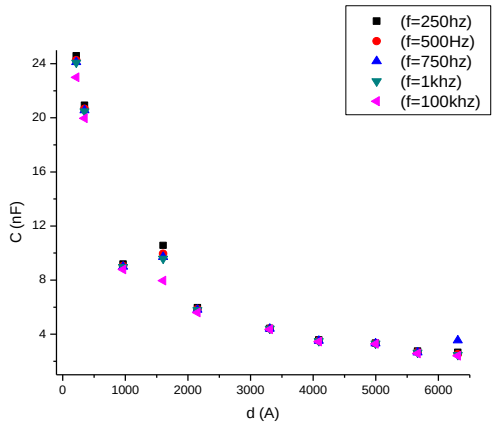

Fig.8. Variation of the capacitance with thickness of $TlSbS_2$ thin films at different temperatures.

IV. CONCLUSION

In this study, $TlSbS_2$ thin films have been successfully deposited on glass substrates by thermal evaporation. Frequency and temperature dependence of capacitance, dielectric constant and loss factor of Al/$TlSbS_2$/Al thin film sandwich structures were studied in detail. The capacitance are found to decrease with increasing frequency and increase with increasing temperature. The dielectric constant evaluated from the measured capacitance was about 25. The dielectric constant increases with temperature at all frequencies. The dielectric constant varies with frequency. The increase in the dielectric constant is small at low frequencies while a significant variation is observed at high frequencies.

[1]. *N. Grincheshen and N. S. Popovich*, Fiz.Tekh. Poluprovodn. 19, 230 (1985)

[2]. *O.Valassiades, S.K.Polychroniadis, J.Stoemenos and N. A. Economou*, Phys. Stat. Sol.(a) 65, 215 (1981)

[3]. *V. A. Bazakutsa, L. G. Voinova, L. P. Zozulya and N. N. Ivanova*, Vacuum, 24, Issue3, 141 (1974)

[4]. *V. F. Krasovskii, I. N. Grincheshe, M. M. Markus and N. S. Popovich*, Neor. Mat., 24, 2074 (1988)

[5]. *V.F.Zhitar et al*.,'' Photoconductivity of TlSbS2 crystals'' Fiz.Tekh.Polurovodn.,8, No.5,996-997(1974)

[6]. *A.Goullet, P. Rouquette and J. Camassel, J.Pascual, J.C. Jumas*, Sol.Sta.Comm., 62, 3 (1987)

[7]. *P. Bohac, E. Brönnimann and A. Gaumann*, Mat. Res. Bull., 9, Issue8, (1974)

[8]. *P. Rouquette, J. Allegre, H. Mathieu, C. Ance and J. Olivier-Fourcade* Sol.Sta.Comm.,59,12(1986)

[9]. *Palatnik et al.*, Vacuum, 24, 3(1974)

[10]. *Voinova et al*., Vacuum, 21, 8(1971)

[11]. *Z.G.Pinsker, S.A. Semiletov and E.N. Belova*, Dokl. Akad. Nauk SSSR, 106,1003(1956)

[12]. *S.Yildirim,K.Ulutas, D.Deger, E.O.Zayim, I.Turhan*, Vacuum 77(2005) 329-335

[13]. *D.Deger, K.Ulutas* Vacuum 72(2004) 307-312

[14]. *Mahalingam T, Radhakrihnan M,Balasubramanian C*, Thin Solid Films 1981; 78:229

[15]. *B.Tareev*, Physics of Dielectrics, MIR Publications, 1979; Moscow

[16]. *A.A. Ibrahim, N.Z. El-Sayed, M.A.Kaid and A.Ashour*, Vacuum, 75,3 (2004)

FERROMAGNETIC RESONANCE STUDY ON COBALT THIN FILMS

M. ERKOVAN
Gebze Institute of Technology, Physics Department,
Çayırova, Kocaeli-Turkey
merkovan@gyte.edu.tr

Different thickness cobalt thin films were growth on p-type Si (100) substrate by magnetron sputtering at UHV conditions. Magnetic properties of cobalt thin films were characterized by ferromagnetic resonance technique. We developed computer program for experimental results. The program gives all of magnetic parameters of the films.

I. INTRODUCTION

Cobalt is widely used in magnetic recording because it is the only one of three room temperature ferromagnetic materials that has unaxial symmetry and therefore can be used in digital recording. Cobalt has a relative permeability two thirds that of iron. Metallic cobalt occurs as two crystallographic structures hexagonal close package and face centered cubic.

In this study, we were growth three different thin films by magnetron sputtering at UHV conditions. To determine deposition ratio and films quality, we used X Ray Photoelectron Spectroscopy (XPS). Spin wave resonance helped to characterized the magnetic properties of the films.

II. SAMPLE PREPARATION

Co films were grown on p-type Si (100) substrate by magnetron deposition technique attached to a cluster ultrahigh vacuum chamber, containing analytical chamber besides to sputtering chamber and a sample-loading section. Prior to insertion into the sample loading section, the substrates were washed with methanol and ethanol in ultra sonic cleaner for 5 minutes. The substrates were transferred under the etching gun to clean by cycles of Ar^+ sputtering followed by annealing at ~ 600° C for 30 minutes. The power of magnetron rf-sputtering gun was 70W for the 300 second-etching process. During the etching process, Ar pressure was maintained at 2.5×10^{-3} mbar. After finishing sample preparation step, in UHV condition the silicon substrates were transferred under the rf-magnetron gun in the sample preparing chamber. Rf-magnetron gun attached Co-target is operated at 24 W. The distance between the target and the substrate is 50 mm. Although the base pressure of the sample preparing chamber is 5×10^{-9} mbar, high purity Ar (99,9999%) is leaked to the chamber with 2 sscm flow rate so that the pressure is fixed to 2.6×10^{-3} mbar during the period of sputtering deposition process. MKS flow meter 1179A was used to control gas flow with ±1% sensitivity. The deposition rate is monitored with the quartz crystal thickness monitor (QCM), calibrated by using XPS. SPECS-Phoibus 150 Electron Analyzer (with Medium Magnification, 3400eV detector voltage for 9 Channels, and 5mm slid) and SPECS-XR50 x-ray source (with 350W power) are used for XPS analyses. During the XPS data acquisition the sample current was about 2μA. Although $Si2p_{3/2}$ is the most favorable photoemission peak for thickness calibration using XPS signals, the attenuation of $Si2p_{1/2}$ peak coming from the surface of the film is observed as a function of cobalt exposure, shown in Figure 1a. Since $Si2p_{3/2}$ and Co2s photoemission peaks sit close at the spectroscopy it makes peak-fitting-process hard to calculate Co converges. In converting ratios to Co thickness, the electron mean free path is calculated by using the TPP formula [1]. The relationship between the Co film thickness, x, and the $Si2p_{1/2}$ photoemission attenuation can be written as

$$\ln\left(\frac{I_s(x)}{I_s(0)}\right) = -\frac{x}{\lambda_s}, \qquad (1)$$

where $I_s(x)$ is the substrate photoemission intensity when covered by a Cr film of thickness x, $I_s(0)$ is the clean substrate photoemission intensity, and λ_s is the inelastic mean free path of the substrate photoelectrons. Electrons with kinetic energy of ≈ 151 eV (AlK_α excitation) for Si $2p_{1/2}$ have an inelastic mean free path of approximately 14.4 Å. Figure 1b shows thickness versus deposition time. The deposition rate is found 0.15 Å from the slope of the line in Figure 1b. Base on this calibration, the various thicknesses of Co films (500 Å, 1000 Å and 1500 Å) were prepared. After every deposition, XPS with AlK_α radiation (hν=1486.6 eV) provided twin anode Specs X-ray Source XR 50 is used to confirm the sample cleanliness and composition.

III. FERROMAGNETIC RESONANCE MEASUREMENT

All spectra were obtained at microwave frequencies X-band (9.8 GHz). We note that all Ferromagnetic Resonance (FMR) Spectra are presented in first derivative format since AC modulation magnetic field of 100 kHz was applied parallel to the external DC magnetic field to get field derivative curves of microwave resonant absorption.

The external magnetic field was swept in the range 0-20 kG in the horizontal direction. Data were collected from each film for two different orientations at room temperature. The first one is in plane (in-plane geometry, $\theta_H = 90^0$) and the second one is perpendicular to the film plane (out of- plane $\theta_H = 0^0$). In order to rotate samples about vertical direction in the horizontal DC magnetic filed a goniometer was used. The spectra have been recorded as a function of angle between DC magnetic field and the film normal, shown in figure 2 [2].

Figure 3 shows room temperature FMR spectra taken at X-band for each Co film thicknesses for comparison. The three spectra with resonance peaks at lower fields represent in-plane geometry while at higher fields represent out of-plane where magnetic field is perpendicular to the film plane. Resonance lines for

parallel geometries of all the films are shifted to very low fields. The large differences between the resonance fields for parallel and perpendicular geometries are related to the demagnetizing field. The value of this separation of the resonance peaks is slightly changed with film thickness.

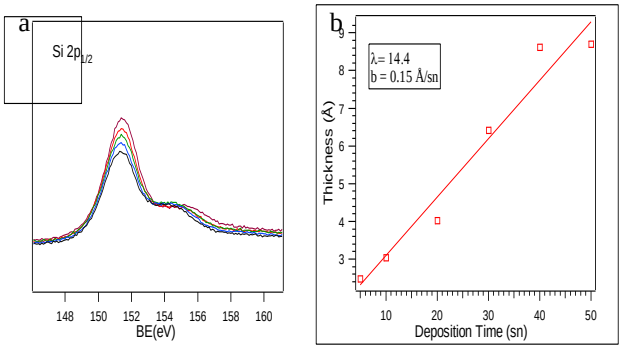

Fig. 1. Since the peaks of Co2s and $Si2p_{3/2}$ are at the same place at the photoemission spectrum the $Si2p_{1/2}$ attenuation was used to calculate Co coverage for this work. The figure (a) shows the attenuation of the $Si2p_{1/2}$ photoemission intensity as a function of Co film thickness. (b) The Co film thickness is calculated from equation 1 using a value of 14.4 Å for the $Si2p_{1/2}$ inelastic mean free path.

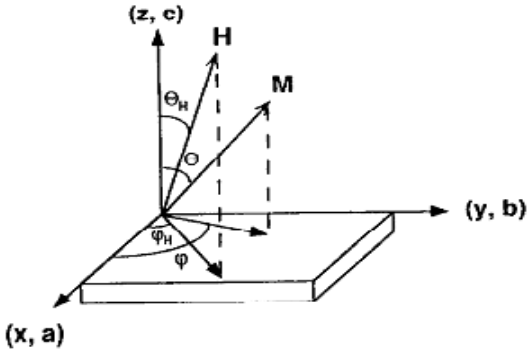

Fig. 2. The axis system used in FMR measurement. Here H is the external magnetic field and M is the magnetization vector. The microwave component of the magnetic filed is always along the x-axis while the DC magnetic filed remains in the yz plane which is also perpendicular to the rotation axis.

For thicker film the separation is slightly larger. These values are 17.5 kG, 19.5 kG and 18.5 kG respectively for 500 Å, 1000 Å and 1500 Å film thicknesses. We except that the resonance field of thickest film is the biggest but the resonance field of 1000 Å film is biggest. The differences is due to inplane anisotropy. 500 Å and 1000 Å cobalt films have in plane anisotropy, but 1500 Å films do not have in plane anisotropy (figure-7).

The other most noticeable feature in Figure 3 is the number of peaks in the spectra. The cobalt film with 500 Å thickness there is only one main peak for both parallel and perpendicular geometry. However a close looking to the spectrum reveals a very weak mode at the lower side of main peak. The cobalt film with 1000 Å thickness has two strong peaks which are well resolved at perpendicular position. Relative intensities of two modes in perpendicular geometry are comparable.

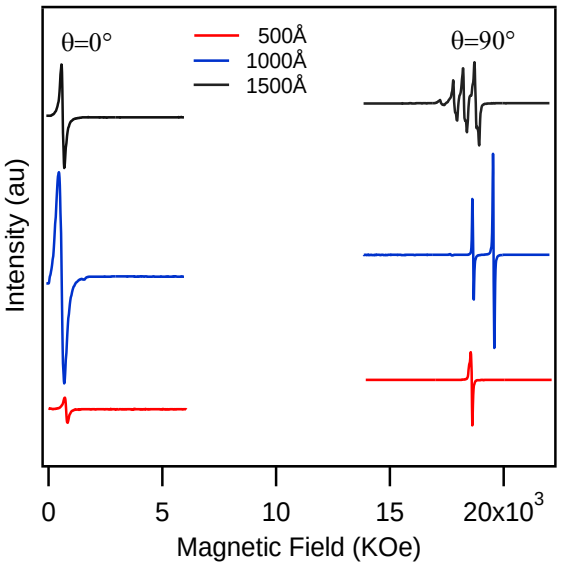

Fig .3. Room temperature experimental SWR spectra taken X-band from three different cobalt thicknesses for both parallel $\theta = 90°$ and perpendicular $\theta = 0°$ geometries.

The peak at higher magnetic filed will be named first mode and the peak is at lower field will be named second mode. A very weak peak also appeared at the lower side of the second mode. For some selected angles angular dependence of SWR spectra for this film (1000 Å) are given in Figure 4. As the magnetic field is rotated away from film normal towards the film plane such as 2.5 degree intensity of main mode improved while intensity of second mode becomes much weaker. The resonance peaks of both first and second modes shift to lower fields and separation between first and second mode slightly increased. The second mode and third mode are disappeared at 3.5^0 away from film normal and only observable peak was the main mode. The line widths for both modes are quite increased as the magnetic field is rotated away from film normal. All these features indicate that this film has easy plane and relatively weak surface anisotropy energy.On the other hand, the number of observed peaks is larger for the thickest film, 1500 Å (shown in figure 3). As we can see clearly there are many modes in the spectra taken at perpendicular geometry. As magnetic field rotated away from film normal the number of peaks decreases and finally all modes except the main mode are disappeared at 4^0 away from film normal.

The line separation between modes is smaller compare to 1000 Å thickness. This separation between bulk modes are expected to be inversely proportional to the square of the film thickness [3].

The line width of spectra taken for 1500 Å is little broader compare to 1000 Å cobalt film resulting in overlaps. However qualitative behavior of the spectra is similar to that of the 1000 Å thick film. Figure 5 shows the angular dependence of spectra for some selected angles for 1500 Å. Here also the line widths for all modes increase as the magnetic field is rotated away from film normal and takes its maximum value at the angle 5^0 and line width becomes narrow again when magnetic filed is parallel to film surface.

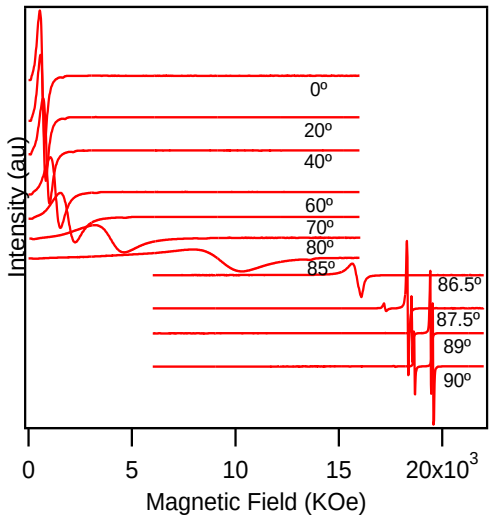

Fig. 4. Angular behavior of experimental SWR spectra taken at room temperature from 1000 Å thickness Co thin film. Magnetic filed is parallel to film surface where the spectrum corresponding 0^0 degree and it is perpendicular to the film surface where angle is 90^0.

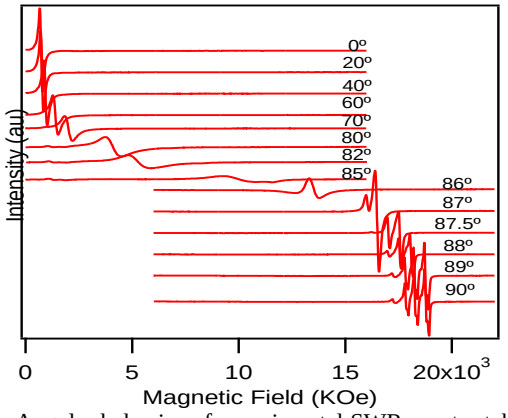

Fig. 5. Angular behavior of experimental SWR spectra taken at room temperature from 1500 Å thickness Co thin film. Direction for magnetic filed is same as in the figure 4.

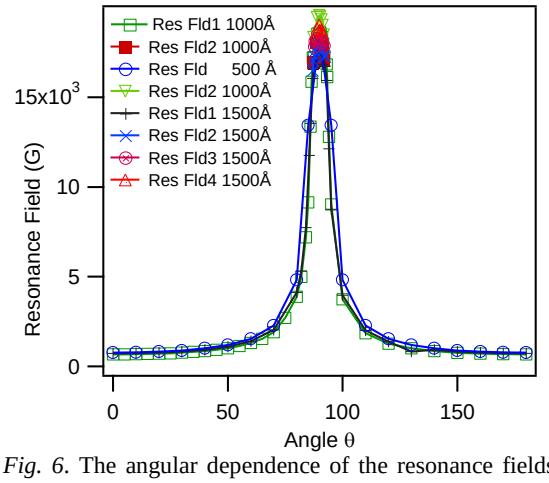

Fig. 6. The angular dependence of the resonance fields for all samples taken at room temperature for the perpendicular geometry. The value of resonance filed is maximum at 90^0 where magnetic field is perpendicular to the film surfaces.

This behavior was same for thinner films. It should be noted that in Figure 3 the single mode of the thinnest film corresponds to the second mode in the spectrum for thicker film while it corresponds to the first mode at the highest field of the spectrum for the thickest film. In figures 6 the angular dependence of the resonance fields (out of plane position) for each samples are presented. As it can seen from this angular dependence is highly anisotropic for each film. The resonance filed values for each mode are maximum at 90^0 where magnetic field is perpendicular to the film surfaces. Figure 6 also shows the angular dependence of other modes in the spectra.

DC magnetic field was also rotated in the film plane for each cobalt films. Noticeable anisotropy was observed. The angular dependence of resonance filed values is presented in the figure 7. As it can bee seen angular dependency of resonance lines for thicker film is more anisotropic than thinner film. The difference between maximum and minimum resonance value is nearly 60 G. The directions of the easy and hard axes of magnetization were obtained from in plane rotation. The easy axis corresponds to the minimal in-plane resonance filed, and the hard axis corresponds to the maximal in-plane resonance filed.

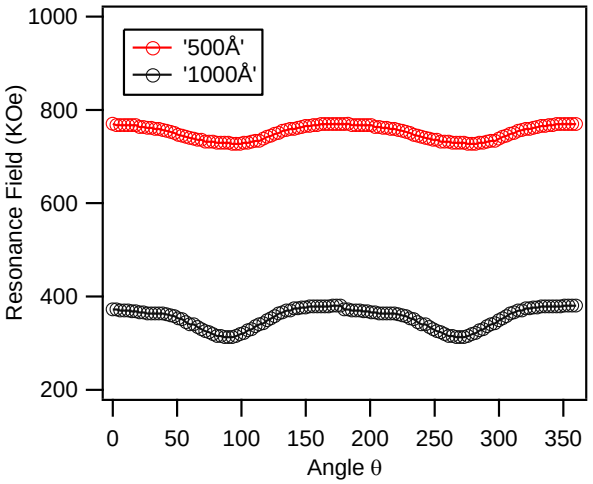

Fig. 7. The angular dependence of the resonance fields for both 500 Å and 1000 Å thickness cobalt films taken at room temperature. Here magnetic filed is rotated within the film plane

IV. THEORETICAL MODEL

$$E = \boldsymbol{M}.\boldsymbol{H} + K_{eff}Cos^2(\theta) + K_1Sin^2(\theta) + K_2Sin^4(\theta) \qquad (2)$$

where $\boldsymbol{M}$ is the magnetization, $\boldsymbol{H}$ the external DC magnetic field, $K_{eff}(2\pi M^2 - K_b)$ the effective unaxial volume (bulk) anisotropy parameter. Here K_1 and K_2 are, respectively, the unaxial and biaxial surface anisotropy energy parameters [4-8] and θ is angle of M with respect to the film normal, as shown figure 2.

For any arbitrary direction of static field H, the basic dispersion relation for spin waves is given [9] as,

$$(\frac{w}{\gamma})^2 = (\frac{1}{M_s Sin^2\theta}\frac{\partial^2 E}{\partial\varphi^2} + Dk_n^2)\times(\frac{1}{M_s}\frac{\partial^2 E}{\partial\vartheta^2} + Dk_n^2) \quad (\frac{1}{M_s Sin\theta}\frac{\partial^2 E}{\partial\varphi\partial\vartheta})^2 \qquad (3)$$

where γ is the gyro-magnetic ratio, w is the microwave frequency, θ and φ are the usual spherical polar angles for M, $D(=2A/M_s)$ is the exchange parameter and k_n is the spin wave vector for nth mode. Here θ is determined by the static equilibrium condition for the magnetization

$$\boldsymbol{M.H}\, Sin(\theta \quad \theta_H) + K_{eff}\, Sin(2\theta) = 0 \qquad (4)$$

Thus, using equation (2) and equation (4) in the general resonance condition which given by equation (3) one can obtain the following expression for resonance field for nth SWR mode;

$$[\frac{w}{\gamma}]^2 = [H\,\frac{\sin(\theta_H)}{\sin(\theta)} + Dk_n^2] \times [HCos(\theta_H - \theta) + (2K_{eff}/M_s)Cos^2\theta + Dk_n^2] \qquad (5)$$

for any direction θ_H of the measurement field. The real and imaginary parts of spin wave vector k_n are determined from the following expression [7,8]

$$tan(k_n L) = \frac{k_n(P_1 + P_2)}{k_n^2 \quad P_1P_2}$$

$$tanh(k_n L) = \frac{k_n(P_1 + P_2)}{k_n^2 + P_1P_2} \qquad (6)$$

for the bulk and the surface modes, respectively. Here L is the film thickness and P_i' s are the surface pinning parameters which are defined for either surface as [6-7].

$$P = \frac{2(K_1 + K_2)L}{A}Cos(2\theta) + \frac{2K_2L}{A}Cos(4\theta) \qquad (7)$$

The second term of equation (7) is the normal derivative of the saturation magnetization and the first one comes from the surface energy the analytical form of the absorption curve is more complicated and has been given in a previous work. [6]

V. DISCUSSION

After collecting enough spectra (film was rotated relative to magnetic field for each 2.5^0 degree) for each film at room temperature the theoretical model that explained above has been used for analyzing the data. The parameters are found from these theoretical simulations are presented in the Table 1. The calculated spectra are presented in figure 6 along with corresponding experimental ones. As seen in the figure 6 fairly good agreements are obtained between experimental and theoretical spectra as a function of the applied filed angle. The symbol in the figure represents the values which were obtained from theoretical model for the calculated resonance field to the corresponding experimental ones (solid lines). It should be emphasized that the fitting parameters were first optimized for perpendicular position for each different thickness films and then all spectra with different angles were fitted with these fixed parameters. A constant value of 3250 Gauss was used for ω/γ which corresponds to a g-value of 2.16 for cobalt. This value was same for all three films. From analysis of angular dependency of the SWR spectra for 500 Å, the strong peak at high field value for perpendicular geometry was identified as the surface mode. The weak peak at the lower side of strong mode was identified as the bulk mode. Same analyses were carried for both 1000 Å and 1500 Å cobalt films. For thinner film, the strong peak at higher field value and relatively strong peak at lower filed for perpendicular geometry were identified as the surface mode and first bulk mode respectively. Relatively weak peak appeared at the lower side of first bulk mode was also identified as second bulk mode. Sharp single surface mode indicates that the boundary conditions on both surfaces are the exactly same. The pinning parameters are governed mainly by surface anisotropy energy including uniaxial term in equation 1. The surface anisotropy has an easy-plane character. For the thickest film the two modes at the highest filed are identified as first and second surface modes. Their anisotropy parameters are quite different indicating that boundary conditions on both surfaces are different and are affected by the film-substrate interface for this thickness. Similar to 1000 Å film uniaxial surface anisotropy has an easy-plane character.

As shown in Table 1 Spin wave exchange stiffness constant, D (=2A/M_s) was same from all of the as-prepared 500, 1000 and 1500 Å cobalt films at room temperature. This value is in between the values given in literature [10-11]. The effective volume (bulk) anisotropy parameter, K_{eff}, which stands for demagnetization field ($-4\pi M_s$) is increased from 500 Å film to 1000 Å film but the value decreased significantly for 1500 Å film. On the other hand high anisotropy was observed for in plane the measurements compare to 1000 Å thick film. So the reason for decrease in K_{eff} value is connected with in-plane anisotropy. The uniaxial surface anisotropy parameters for both surfaces, K_1^{s1} (free surface) and K_1^{s2} (substrate surface) were varied with thickness and were noticeably increased for 1500 Å film especially for the free side of the film. While the symmetric magnetic boundary conditions were found for both 500, 1000 Å cobalt films, asymmetric magnetic boundary condition were found for 1500 Å since both surface modes are clearly resolved and have quite different values. A difference in pinning conditions at the two surfaces is the reason for two surface modes.

Table-1: Spin wave exchange stiffness constant, surface anisotropy and linewidth values were determined by theoretical models

Samp.	D (cm^2 G)	$2K_{eff}$ / M (G)	K_1^{s1} L / A	K_1^{s2} L / A	ΔH (G)
500 Å	0.9×10^{-9}	15250	-6.10	-6.10	100
1000Å	0.9×10^{-9}	15575	-9.41	-9.41	100
1500Å	0.9×10^{-9}	14605	-15.10	-9.50	110

VI. CONCLUSION

Different thickness of cobalt thin films were very well growth by magnetron sputtering deposition technique. The films thickness determined with Quart Crystal Monitoring. Also XPS used for deposition ratio and the films quality. Ferromagnetic resonance technique helped to characterize magnetic properties of the cobalt thin films. The ferromagnetic experimental results were shown very good compatible with theoretical modeling results

[1]. *S.Tanuma, C.S. Powell and D.R.Penn,* Surface Science 192, L 849 (1987).

[2]. *B. Aktaş.* Thin Solid Films, vol. 307, 1997, p. 250.

[3]. *C. Kittel,* Introduction to Solid State Physics, 6th Edition, John Wiley and Sons, Inc. 1986

[4]. *R.F.Soohoo,* Magnetic Thin Films, (Harper&Row, New York, 1965).

[5]. *P.E.Wigen,* Thin Solid Films 114 (1984) 135.

[6]. *L.G.Maxymowich and D.Sonderek,* J. Magn. Magn. Mater 37 (1983) 177.

[7]. *B.Aktas and M.Ozdemir* Physica B 193 (1994) 125.

[8]. *B.Aktas, Y.Oner and H.Z.Durusoy* J. Magn. Magn. Mater 119 (1993) 339.

[9]. *G.T Rado* Phys. Rev. B 18 (1978) 6160.

[10]. *P.E. Tannenwald, R. Weber,* Phys. Rev. 121(3), 715, 1961.

[11]. *Yark Yean Kim, Seong-Cho Yu and Woo Young Lim,* J.Magn. Magn. Mater. 226-230, 487, 2001

EFFECTS OF THE InAlN GROWTH TEMPERATURE AND In MOLE FRACTION ON SUBBAND TRANSPORT IN $In_xAl_{1-x}N$/(AlN)/GaN/AlN HETEROSTRUCTURES

P. TASLI[1], S. B. LISESIVDIN[1], M. KASAP[1], S. OZCELIK[1], T. S. MAMMADOV[1] , E. OZBAY[2]

[1]Department of Physics, Gazi University, 06500 Ankara, Turkey

[2] Department of Physics, Bilkent University, Bilkent, 06800 Ankara, Turkey; and Department of Electrical and Electronics Engineering, Bilkent University, Ankara, Turkey

Subband transport properties of the two-dimensional electron gas (2DEG) in $In_xAl_{1-x}N$/(AlN)/GaN/AlN heterostructures were investigated by means of variable magnetic-field Hall measurement between 30K and 290K. The experimental data was analyzed by using quantitative mobility spectrum analysis (QMSA) technique. The 2-dimensional electron gas (2DEG) with 1 or 2 subbands and the 2-dimensional hole (2DHG) were detected with i-QMSA technique. Mobility of the second subband of 2DEGs was found to be higher than that of the first subband. The sheet carrier density for hall, the first and the second subband were reduced while Indium (In) mole fraction was increasing. This behavior is a result of total bound interface sheet density (σ / e). During In mole fraction was increasing, second subband mobility was decreased. As In mole fraction was increasing from ~%9 to ~%11, the first subband and hall mobility were increased. However, while the fraction was increasing from ~%11 to ~%14, the first subband and hall mobility were decreased but the second subband mobility was increasing at a rate of every In composition. Indium (In) mole fraction was decreased once InAlN growth temperature was increased.

I. INTRODUCTION

Intensive investigations have been concentrated on III-nitride semiconductor materials (Gallium Nitride (GaN), Aluminum nitride (AlN), and Indium Nitride (InN)) due to their various potential microelectronic and optoelectronic applications in the last decade [1-6]. This holds in particular for their ternary alloys, $Al_xGa_{1-x}N$, $In_xAl_{1-x}N$, and $In_xGa_{1-x}N$ ($0 \le x \le 1$) (5,7,8). Owing to the intrinsic properties of the group III-nitride binary and ternary alloys, the material system has several promising applications in high-frequency, high power devices and sensors. The advantageous intrinsic properties of this materials system contain large band gap, high electron mobility, high satisfied electron drift velocity, high thermal conductivity, small dielectric constant, large breakdown field, strong spontaneous and piezoelectric polarization fields [9-12]. These properties express breakdown electric field forces higher than silica or GaAs based devices and facilitate higher device operating temperatures. Various barrier and channel for upgrade the performance of devices have been used in nitride based high-electron-mobility-transistors (HEMT) alternatives [13-17]. The basic structure of a HEMT is the heterojunction between the channel layer with lower energy conduction band and the barrier layer with higher energy conduction band. A two-dimensional gas (2DEG) at the interface between the channel and the barrier layer is formed by modulation-doped barrier layer. The most important feature is that the 2DEG is separated from the ionized donors in the barrier layer. For application in high frequency, high power devices, high density and high mobility 2DEG make HEMTs promising [18].

AlInN/GaN- based heterostructures were also offered as a suppression of AlGaN/GaN-based heterostructures due to their higher sheet carrier densities that are obtained by spontaneous polarization of these systems [19,20]. One of the main features of the lattice-matched (LM) InAlN/GaN heterostructures is the facility to hold a high polarization induced sheet charge density at the heterointerface even for a disappearance piezoelectric part due to the default of strain. Essentially, a net positive charge rises at the interface due to the discrepancy in spontaneous polarization between InAlN and GaN. Afterwards, electrons from surface states and remaining donors tend to atone for these polarization charges forming a 2DEG.

Recently, the AlGaN layer is replaced by an InAlN barrier has been fulfilled for enhancement the HEMT performance [21]. The advantage of using an InAlN barrier is to arrange the composition of the alloys to gain polarization matched heterostructure or a lattice. GaN is latticed matched when the indium composition is arranging to ~ 18% the alloy. Due to the fact that the structure is free of strain and the piezoelectric polarization is zero, the polarization charge is fully defined by spontaneous polarization. At the same time, the HEMTs with an InAlN barrier layer were fundamentally expected to satisfy higher carrier densities than an AlGaN barrier layer [22]. Since the growth of AlN and InN requires different growth temperatures, there is a major difficulty in growing an InAlN based structure from the epitaxial in point of. So, the formation of InAlN with the variance of the compound in a controlled way is obscure. Additionally, of these fruitful results reported in the literature there are just a few reports in the way of the particular analysis of the transport characteristics of InAlN-GaN HEMTs [21,23].

In this work, the variable field resistivity and Hall Effect data were analyzed using the quantitative mobility spectrum analysis (QMSA) technique that enhanced and defined in previous studies [24-27]. Variable field resistivity and Hall coefficient measurements obtained with the QMSA technique allow subtraction of mobilities and the individual carrier concentrations in semiconductor materials. Hall coefficient and variable field resistivity measurements in conjunction with the QMSA technique

permit extraction of the mobilities and individual carrier concentrations in semiconductor materials. The individual carriers (2DEG) and their effect on the electron transport are investigated using the QMSA technique in $In_xAl_{1-x}N$/GaN/(AlN)/GaN/AlN heterostructures grown by metal-organic chemical vapor deposition (MOCVD) in this study. The susceptibility and credibility of this technique offers that it is a convenient standard tool for routine characterization of multi-carrier semiconductor devices [26-29]. We investigated the transport properties of high-quality $In_xAl_{1-x}N$/(AlN)/GaN/AlN heterostructures that were grown by metal organic chemical vapor deposition (MOCVD) with Hall Effect measurements. The effects of indium mole fraction and growth temperature of AlInN layers are investigated.

II. EXPERIMENTAL DETAILS

The GaN epilayers were grown on c-plane (0 0 0 1) sapphire (Al_2O_3) substrates in a low-pressure metalorganic chemical vapor deposition (MOCVD) reactor. Prior to epitaxial growth, the sapphire substrates were cleaned in H_2 ambient at 100^0C for 10 min in order to remove surface contamination, and then a 10-nm thick low-temperature (LT) AlN nucleation layer (NL) was grown at 840^0C.

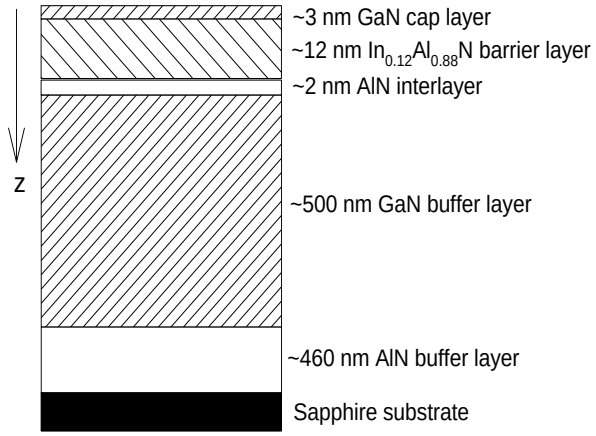

Fig. 1. Layer structure of the investigated samples.

The reactor pressure was set to 50 mbar during the substrate cleaning and nucleation growth. Then, 460-nm thick high-temperature AlN buffer layers were grown at a temperature of 1150^0C. A 500-nm-thick undoped GaN buffer layer was grown at 1070^0C and the reactor pressure was set to 200mbars. After the deposition of the GaN buffer layers, approximately a ~2-nm-thick AlN interlayer was grown at 1085^0C with a pressure of 50 mbars. Finally, InAlN layers with low In content with ~3-nm-thick GaN cap layer (1085^0C) were grown under various temperatures for different samples at 50 mbars. All of the layers are nominally undoped. In mole fractions of the barrier layers were determined by high-resolution x-ray diffraction (XRD) measurements. The details of samples are given in Fig. 1 and he growth temperatures of the barrier layers and thicknesses of the layer are shown in Table1.

For the resistivity, the magnetoresistivity and Hall effect measurements by the van der Pauw method were performed in which the square shaped ($5x5mm^2$) samples were prepared with Ti/Al/Ni/Au evaporated dot contacts in the corners. Ohmic behavior of the contacts was confirmed by the current–voltage (I/V) characteristics. The measurements were taken in a temperature range of 33–300K using a Lakeshore Hall effect measurement system (HMS). At temperature steps, the Hall coefficient and resistivity (with 0.2% accuracy) were measured for both current directions, magnetic field polarizations, and all possible contact configurations at the 15 magnetic field steps between 0 and 1.4 T. The magnetic field-dependent data has been analyzed using the QMSA [24, 25] software provided by Lakeshore. Obtained individual carrier mobilities and carrier densities for electrons and holes in bulk semiconductor materials and heterostructures can be easily extracted [26, 30].

Table.1 Growth temperatures, thicknesses, and the In composition of the InAlN layers in the investigated samples

Sample	$In_xAl_{1-x}N$ layer		
	Growth Temperature (^{0}C)	Thickness (nm)	In composition (x)
B1034	800	9.28	10.6
B1040	830	9.28	9.22
B1041	770	11.14	13.98
B1053	810	10.76	6.43

III. RESULTS AND DISCUSSION

The resistivity and Hall measurements of $In_{1-x}Al_xN$ /GaN/AlN heterostructures as a function of the magnetic field (0-1.5 T) were carried out at 14 temperatures steps in the temperature interval of 30-300 K. In order to extract effective conduction channels in the samples, QMSA analysis was performed on magnetic field dependent Hall data at each temperature step for every sample. The QMSA method is superior to other methods such as the two-carrier fit, multi carrier fit, and mobility spectrum analysis methods [25-28]. For each sample, Quantative Mobility Spectrum Analysis (QMSA) is utilized on magnetic field dependent Hall data at each temperature step. Highly relaxation in interface for B1053 sample is the reason of the degragtion of mobility and carrier density. Because of these reasons sample 1053 is not appropriate for QMSA. For the samples B1034, B1040 and B1041, a hole carrier and two electron carriers were observed in the temperature range from 30K to 300K. These two distinct electron carriers and a hole carrier show 2D behavior with respect to temperature dependent mobility and carrier density behaviors. Our investigations showed that these two 2DEG carriers can be the two subbands of a 2DEG system. Fig. 2 (a) and (b), it can be seen that one electron (denoted with triangles) and one hole carrier (denoted with circles), which are obtained from QMSA, are contributing to charge transport throughout the entire studied temperature range. At high temperatures, the mobilities of both carriers decrease with increasing temperature while they are independent of temperature at low temperatures. At high temperatures, mobilities are highly limited by the polar optical phonon scattering mechanism[32]. On the other hand, both carrier densities are also nearly independent of temperature in the studied temperature range. These behaviors of mobilities and carrier densities extracted from QMSA are typical of

2DEG and 2DHG behaviors. It is clear that these mobility and carrier density behaviors are typical for those samples that 2D conduction is dominant [31].

Fig. 3 shows the growth temperature dependent In mole fraction of the InAlN layers for the investigated samples. In mole fraction(%) decreases with increase of the temperature except B1053. It is widely known that usage of thicker AlN interlayers causes strain relaxation at the interface [32] and at high growth temperature such as 800 ^{0}C, adsorbed In atoms are easy to desorb from the growing surface,because dissociation temperature of In–N bonds is very low, and thus only small amount of In atoms can be incorporate into the crystal. Therefore, although the compositional splitting will become intense if growth temperature rises, indium incorporation coefficient becomes small above 800 ^{0}C.

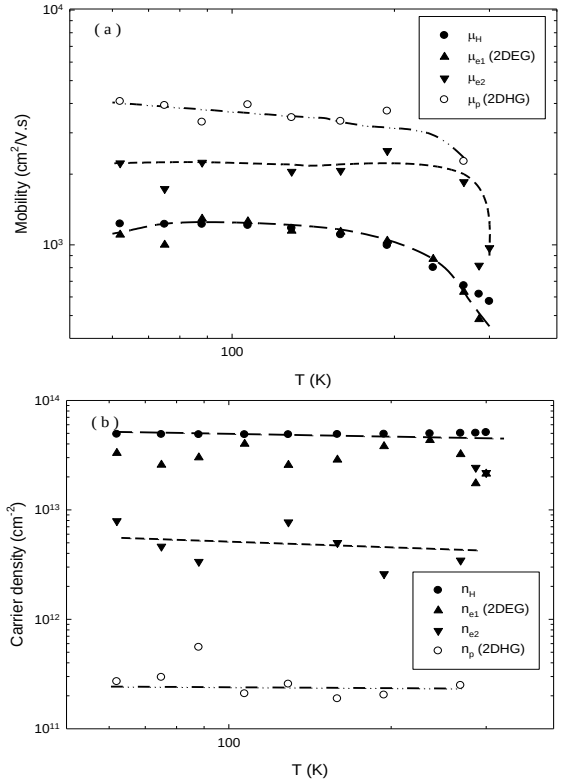

Fig. 2. (a) Mobility and (b) carrier density versus temperature. The closed circles represent the measured mobility and carrier density taken at 0.5 Tesla. The triangles represent the extracted 2DEG mobility and carrier density. The open circles represent the extracted 2DHG mobility and carrier density. The stars and squares represent the bulk carriers. The lines are guide for the eyes.

These results suggest that strong compositional inhomogeneity and/or phase separation occur in AlInN and the extent of the compositional inhomogeneity becomes large at the growth temperature of 750 ^{0}C. When the AlN interlayer thicknesses exceed a critical value of about 1 nm, the interface is destroyed due to increased the probably partial strain relaxation. Therefore, Hall mobility, sheet carrier density in the channel is decreased. This is in good agreement with investigations on AlInN/AlN/GaN HEMTs [21,33]. The strain relaxation of the samples causes a lower 2DEG mobility and sheet carrier density. For the investigated samples, we calculated the critical thickness of barrier layer with a simple homogoneous strain distribution through the all barrier layers [34]. Critical thickness is calculated by;

$$t_{cr} \sim b_e / 2\varepsilon_{xx} \quad (1)$$

Here, ε_{xx} is inplane strain and be is the Burger's vector (b_e = 0.31825nm). Figure 3 shows the critical thickness ratio versus In-mole fraction. Critical thickness is located at 1.0 and with the increasing ratio, the probability of strain relaxation increases. As can be clearly seen Fig. 3, B1053 sample has the greatest critical thickness ratio [1.64] which means it has an important strain relaxation at the interface. High strain relaxation causes a reduction in mobility due to interface roughness scattering. Also, a reduction in carrier density is expected due to reduction in piezoelectric polarization induced carriers.

We have seen hole carriers that expected in our previous article. Indium (In) mole fractions dependent mobility and carrier densities of hall and subbands electrons with QMSA are shown in Fig.4 and Fig.5. Hall measurements and measurements of the first subband with respect to the second subband is close.

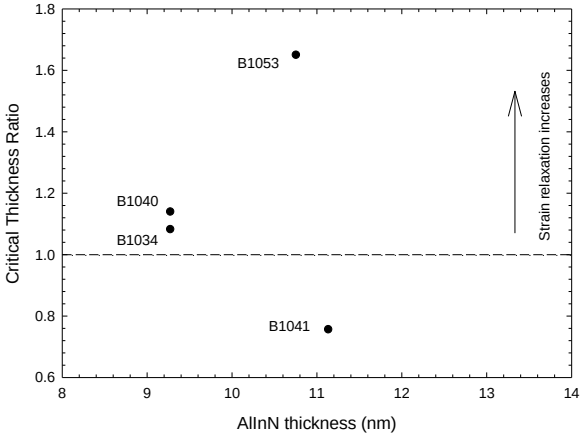

Fig. 3. The critical thickness ratio according to InAlN thickness of investigated samples.

The reason for this, the first subband measurements is more dominant than the secon subband, and the mobilitiy of the second subband is be higher than the lowest subband. Because electrons in the first subband interact with the interface related scattering mechanicsm more than the second subband's electrons for the GaN-based heterostructures.

Indium composition(x) dependent density of forming 2DEG at heterointerface can be described by following implicit equation:[35]

$$n_s(x) = \frac{\sigma(x)}{e} - \left[\frac{\varepsilon_0 \varepsilon(x)}{d_{AlInN} e^2}\right]\{e\Phi_b(x) + E_F[x, n_s(x)] - \Delta E_C(x)\} \quad (2)$$

Where sigma is the total bound sheet charge density, e is the electron charge, ε and ε_0 are the relative dielectric constant and the dielectric permittivity of the vacuum, respectively, d_{AlInN} is the thickness of the barrier, $e\Phi_b$ is the Schottky barrier height, E_F is the Fermi level with respect to the GaN conduction band, and ΔE_C is the conduction band ofset between AlInN and GaN, which depends on Indium (In) composition x.

As seen in Fig. 4 and Equation 2, density of forming 2DEG at heterointerface is reduced with the increasing rate of Indium for first, second subbands and hall measurements, and this behavior is a result of total bound interface sheet density (σ / e) which reduced with increased indium (In) composition[34].

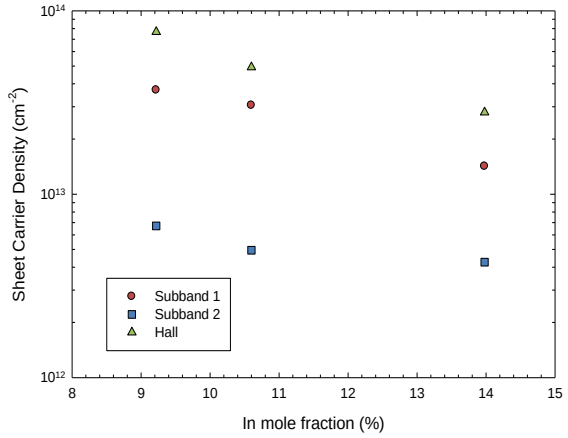

Fig. 4 In mole fraction dependent sheet carrier density for hall, first and second subband.

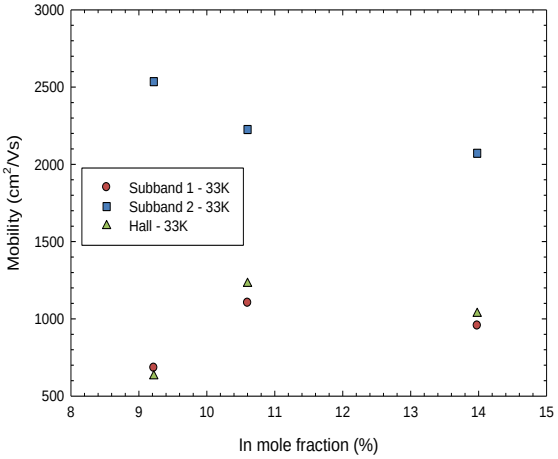

Fig. 5 In mole fraction dependent mobility for hall, first and second subband

As seen in Fig.5, while In mole fraction was increasing from ~%9 to ~%11, the first subband and hall mobility were increased. However, while the fraction was increasing from ~%11 to ~%14, the first subband and hall mobility were decreased but the second subband mobility was increasing at a rate of every In composition. Due to decreased sheet carrier density with increased In composition, interface roughness mobility increase. This conclusion was confirmed by equation 3[36].

$$\mu_{ab} = \left(\frac{2\varepsilon_0 \varepsilon_s}{n_s \Delta \Lambda} \right)^2 \frac{\hbar^3}{e^3 m^{*2}} \frac{1}{J_{ab}(k)} \qquad (3)$$

where Δ is the lateral size of disorders , Λ is relation length and $J_{ab}(k)$ is integral.

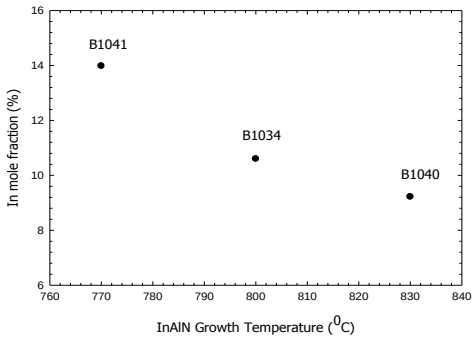

*Fig. 6.*InAlN Growth Temperature dependent In mole fraction

As shown in Fig.6, Indium (In) mole fraction was decreased once InAlN growth temperature was increased. At high growth temperature such as 800 ^{0}C, adsorbed In atoms are easy to desorb from the growing surface, because dissociation temperature of In–N bonds is very low, and thus only small amount of In atoms can be incorporate into the crystal. Therefore, although the compositional splitting will become intense if growth temperature rises, indium incorporation coefficient becomes small above 800 ^{0}C. These results suggest that strong compositional inhomogeneity and/or phase separationoccur in AlInN and the extent of the compositional inhomogeneity becomes large at the growth temperature of 750 ^{0}C .

IV. CONCLUSIONS

We studied the transport properties of subbands of AlInN heterostructures with analyzed of the QMSA method. The 2DEG with 1 or 2 subbands and the 2DHG were detected with QMSA technique. Mobility of the second subband of 2DEGs was found to be higher than that of the first subband. For the GaN-based heterostructures, electrons in the first subband interact with the interface related scattering mechanisms more than the second subband's electron. The sheet carrier density for the first and the second subband and hall were reduced while Indium (In) mole fraction was increasing. This behavior is confirmed with In mole fraction dependent total bound interface sheet density (σ / e) (34). During In mole fraction was increasing, second subband mobility was decreased. As In mole fraction was increasing from ~%9 to ~%11, the first subband and hall mobility were increased. However, while the fraction was increasing from ~%11 to ~%14, the first subband and hall mobility were decreased but the second subband mobility was increasing at a rate of every In composition. The second subband mobility is increasing with increased In mole fraction, so it is effect interface roughness (aboz.ref). Indium (In) mole fraction was decreased once InAlN growth temperature was increased. In mole fraction (%) diminished with increase of the AlInN growth temperature. Because the indium flux decreases drastically due to enhancement of indium desorption at elevated temperatures. All this information helps us to produce high mobility device and to improve device performance.

[1]. *H.Morkoç, S.Strite, G.B. Gao, M.E.Lin, B.Sverdlov, and M. Burns*, J.Appl. Phys. 76(3), 1363 (1994).

[2]. *S.N.Mohammad and H. Morkoç*, Prog.Quant.Elecr. 20, 361 (1996).

[3]. *S. J. Pearton*, "GaN And Related Materials", (Gordon and Breach science publishers, New York (1997).

[4]. *B.Gil*, "Group III Nitride Semiconductor Compounds", (Clarendon Pres, Oxford (1998).

[5]. *O. Ambacher*, J. Phys. D31, 2653 (1998).

[6]. *S. C. Jain, M.Willander, J.Narayan, and R.Van* Overstraeten, J.Appl.Phys.87, 965 (2000).

[7]. *B. Monemar*, J. Cryst. Growth 189/190, 1 (1998).

[8]. *S. J. Pearton, J. C. Zolper, R. J. Shul, and F. Ren*, J.Appl.Phys. 86,1(1999).

[9]. *R. Tülek, A. Ilgaz, S. Gokden, A. Teke, M.K.Ozturk, M. Kasap, S. Ozcelik, E. Arslan, and E. Ozbay*, J. Appl. Phys. 105, 013707 (2009).

[10]. *L. Shen, R.Coffie, D. Butteri, S. Heikman, A.Chakraborty, A. Chini, S. Keller, S.P. DenBaars, and U.K. Mishra*, IEEE Electron Device Lett. 25,7 (2004).

[11]. *K. Boutros , M. Regan, P. Rowell, D. Gotthold, R.Birkhahn, and B. Brar*, International Electron Devices Meeting, Washington D.C., p.981, (December 2003).

[12]. *K. Joshin, T. Kikkawa, H. Yayashi, T. Moniwa, S.Yokokowa, M. Yokoyama, N. Adachi, and M.Takikowa*, International Electron Devices Meeting, Washington, p.983, (D.C. December 2003).

[13]. *A. Bykhouski, B. L. Gelmant, and M.S. Shur*, J.Appl. Phys. 81,6332 (1997).

[14]. *P. M. Asbeck, E. T. Yu, S. S. Lau, G. J. Sullivan, J.Van Hove, and J. M. Redwing*, Electron Lett. 33, 1230 (1997).

[15]. *E. T. Yu, G. J. Sullivon, P. M. Asbeck, C. D. Wang, D. Qiao, and S. S. Lau*, Appl. Phys. Lett. 71, 2794 (1997).

[16]. *M. B. Nardelli, K. Rapcewicz, and J. Bernholc*, Appl. Phys. Lett. 71,3135 (1997).

[17]. *T. Takeuchi, H. Takeuchi, S. Sota, H. Sakai, H.Amono and I. Akasaki*, Jpn. J.Appl.Phys., Part2, 36, L177 (1997).

[18]. *L. Shen, R. Coffie, D. Buttari, S. Heikman, A.Chakraborty, A. Chini, S. Keller, S.P. DenBaars, and u.K. Mishra*, IEEE Electron Device Lett. 25, 7 (2004).

[19]. *A. Gold*, Phys. Rev. B 46, 2339 (1992).

[20]. *S. Das. Sarma and F. Stern*, Phys. Rev. B 32, 8442 (1985).

[21]. *M. Gonschorek, J.-F.Carlin, E. Feltin, M. A. Py, and N. Grandjean*, Appl. Phys. Lett, 89, 062106 (2006).

[22]. *J. Kuzmík*, Semicond. Sci. Technol. 17, 540 (2002).

[23]. *R. Butté, J.-F. Carlin, E. Feltin, M. Gonschorek, S.Nicolay, G. Christmann,D. Simeonov, A.Castiglia, J. Dorsaz, H. J. Buehlmann, S.Christopoulos, G. Baldassarri Höger von Högersthal, A. J. D. Grundy, M. Mosca, C.Pinquier, M. A. Py, F. Demangeot, J. Frandon, P. G. Lagoudakis, J. J. Baumberg, and N. Grandjean*, J. Phys. D 40, 6328 (2007).

[24]. *J. Antoszewski, D. J. Seymur, L. Farone, J.R.Meyer, and C. A. Hoffman*,J. Electron. Mater. 24, 1255 (1995).

[25]. *J. R. Meyer, C. A. Hoffman, J. Antosewski, and L.Farone*, J. Appl. Phys. 81, 709 (1997).

[26]. *B. C. Dodrill, J. R. Lindemuth, B. J. Kelley, G. Du, and J. R. Meyer*, Compound Semicond. 7, 58 (2001).

[27]. *J. Antoszewski, L. Faraone, I. Vurgaftman, J.R.Meyer, and C. A.Hoffman*, J. Electron. Mater. 33, 673 (2004).

[28]. *M. Kasap and S. Acar*, Phys. Status Solidi A 201, 3113 (2004).

[29]. *S. Acar, M. Kasap, B. Y. Isik, S. Ozcelik, N.Tugluoglu, and S. Karadeniz*, Chin. Phys. Lett. 22, 2363 (2005).

[30]. *S. B. Lisesivdin, A. Yildiz, S. Acar, M. Kasap, S.Ozcelik, E. Ozbay*, Appl. Phys. Lett. 91, 102113, (2007).

[31]. *S. B. Lisesivdin, S. Demirezen, M. D. Caliskan, A.Yildiz, M. Kasap, S. Ozcelik, and E. Ozbay*, Semicond. Sci. Technol. 23, 095008, (2008).

[32]. *A Teke, S Gökden, R Tülek, J H Leach, Q Fan, J.Xie,Ü Özgür, H Morkoç, S B Lisesivdin and E.Özbay*, New Journal of Physics 11, 063031, (2009).

[33]. *J. Xie, X. Ni, M. Wu, J. H. Leach, Ü. Özgür and H.Morkoç, Appl. Phys. Lett.* 91, 132116, (2007).

[34]. *M. Gonschorek, J.-F. Carlin, E. Feltin, M. A. Py, N. Grandjean, V. Darakchieva, B. Monemar, M.Lorenz, and G. Ramm*, J. Appl. Phys. 103, 093714 (2008).

[35]. *O.Ambacher, J. Majewski, C. Miskys, A. Link, M.Hermann, M. Eickhoff, M. Stutzmann, F.Bernardini, V. Fiorentini, V. Tilak, B. Scaff, and L. F. Eastman*, J. Phys.:Condens. Matter 14, 3399 (2002).

[36]. *D. Zanato ,S. Gokden, N. Balkan, B. K. Ridley, and W. J Schaff*, Semicond. Sci. Technol., 19 (3): 427-432 (2004).

STRUCTURE AND ELECTRICAL RESISTIVITY OF LIQUID K-Rb ALLOY

S. D. KORKMAZ[1], Ş. KORKMAZ[2]

[1]Eskişehir Osmangazi University, Department of Elementary Science Education, 26480, Eskişehir, TURKIYE

sduysal@ogu.edu.tr

[2]Eskişehir Osmangazi University, Department of Physics, 26480, Eskişehir, TURKIYE

skorkmaz@ogu.edu.tr

A comparative study is presented for the electrical resistivity of liquid $K_{1-x}Rb_x$ metal alloys. In the electrical resistivity calculation, Faber-Ziman formula, and $2k_F$ scattering theory developed by Morgan et al. are used. Partial structure factors have been calculated from the solution of Ornstein–Zernike equation with Rogers-Young closure and the transferable electron-ion potential of Fiolhais et al. has been used as the input pseudopotential. VWN screening functions are used in calculation of form factors which are necessary for the calculation of resistivity. The results are compared with experimental ones.

I. INTRODUCTION

Considerable interest has caused the investigation of the properties of liquid metals and their alloys for several years since liquid metals are used as defense goods, industrial coating, electronic casing etc. The study of the electronic transport properties of liquid metals and their alloys remains one of the most important areas for condensed matter physics, materials science, chemistry and metallurgy.

The theoretical investigation of the electronic transport properties of liquid metals and their alloys has been within pseudopotential formalism for several years. The most popular method for studying the electrical resistivity of liquid metals is the electrical conduction theory developed by Ziman [1] using Nearly Free Electron model and it was extended to liquid binary alloys by Faber and Ziman [2]. Two key ingredients appear in Faber-Ziman formula, namely the electron-ion pseudopotential $W_{ij}(q)$ and the partial structure factors $S_{ij}(q)$ obtained from $W_{ij}(q)$. Faber-Ziman formalism utilizes a perfectly sharp Fermi surface.

The finite mean free path corresponds to a finite uncertainty in the electron position. Thus the Fermi surface is not perfectly sharp but it is blurred. One of the attempts to take into account this blurring has been made by Ferraz and March [3]. The formula supposed by Ferraz-March takes the mean-free-path of electron into account of calculation of resistivity. Ferraz and March approach has been applied recently for a number of liquid metals and alloys [4-6].

These might signal the need to go beyond the modification of Faber-Ziman Theory by one particle properties such as density of states and two-particle properties namely the quantum –interference effects , could very well dominate the physics of short-mean-free-path systems. In 1985, the $2k_F$ scattering model was proposed by Morgan, Howson and Saub [7] (it is also called the MHS model). It was based on the quantum kinetic equation and gave formula for the resistivity that included the quantum interference effect.

The model have been applied amorphous [8,9] and liquid metal alloys [10,11] for resistivity calculations. In the present work we have calculated electrical resistivities using the Faber-Ziman formula for $K_{1-X}Rb_X$ liquid metal alloys at 373 K.

II. THEORY

The extension of well known Ziman formula for the resistivity to a liquid metal binary alloy is done by Faber-Ziman [2] as

$$\rho = \frac{3\pi\pi^{2}}{4Ze^{2}\hbar^{3}n_{el}k_{F}^{6}} \times \left[\int_{0}^{\infty} q^{3}\left[c_i w_i(q)^2 S_{ii}(q) + c_j w_j(q)^2 S_{jj}(q)\right]\theta(2k_f - q)\,dq + \int_{0}^{\infty} q^{3}\left[2(c_i c_j)^{1/2} w_i(q) w_j(q) S_{ij}(q)\right]\theta(2k_f - q)\,dq\right]$$

where $S_{ii}(q)$ is the partial structure factor, $w_{ij}(q)$ is the screened ion pseudopotential, n_{el} is the conduction electron density and it is related to Fermi wave vector k_F by $k_F = (3\pi^2 n_{el})^{1/3}$, e is the electron charge, m is the electron mass and, h is planck constant. The unit step function θ is defined as

$$\theta(2k_F - q) = 0 \quad \text{for} \quad q > 2k_F$$
$$= 1 \quad \text{for} \quad q \le 2k_F .$$

The theory of MHS takes into account the quantum-interference effects in terms of an effective medium theory for the wigner distribution function. The resistivity in the MHS ($2k_F$ scattering) model is given by the formula [7]

$$\rho = \frac{m_e}{ne^2\tau_{tr}}$$

where the transport lifetime τ_{tr} is expressed

$$\frac{1}{\tau_{tr}} = \frac{1}{\tau_{FZ}} \frac{1 + \frac{1}{2}\frac{\tau_{FZ}}{\tau} x^2 F_{MHS}^{1/2}(x)}{1 - \frac{3}{64} x^4 F_{MHS}(x)} .$$

Here τ_{FZ} is the transport relaxation time corresponding to the Faber-Ziman theory and τ is the one-electron lifetime, $x = \hbar/(\tau E_F)$, E_F Fermi energy and

$$F_{MHS}(x)=\left[\ln\left[\frac{(1+x^2)^{1/2}+1+\sqrt{2}\left[(1+x^2)^{1/2}+1\right]^{1/2}}{(1+x^2)^{1/2}+1-\sqrt{2}\left[(1+x^2)^{1/2}+1\right]^{1/2}}\right]^2\right]^2.$$

The FZ model lifetimes for binary alloy are expressed as [2]

$$\frac{1}{\tau_{FZ}}=\frac{m_e\Omega_0}{4\pi\hbar^3k_F^3}\int_0^{2k_F}q^3\lambda(q)\,dq$$

$$\frac{1}{\tau}=\frac{m_e\Omega_0}{4\pi\hbar^3k_F}\int_0^{2k_F}q\,\lambda(q)\,dq$$

where Ω_0 is the average volume per one atom in the system, and $\lambda(q)$ is

$$\lambda(q)=\sum_{i=1}^{2}\sum_{j=1}^{2}\sqrt{c_ic_j}S_{ij}(q)w_i(q)w_j(q).$$

In this equation c_i stands for the number concentration of ith component, $w_{ij}(q)$ are the screened pseudopotentials' form factors and $S_{ij}(q)$ are the Ashcroft Langreth partial structure factors[12]. In this study, we have combined the local field correction proposed by VWN [13] and the form factor developed by Fiolhais et al. for solid state [14,15]. It is noteworthy that this model provides an accurate description of the interactions in liquid alkali metals [16] and also in the liquid alkali metal alloys as we have already observed [5,17].

The partial structure factors $S_{ij}(q)$ are determined from the solution of Ornstein-Zernike equation with Rogers-Young closure [18]. To the best of our knowledge, previously no one has reported such a study to investigate electrical resistivity using structure factor from this transferable pseudopotential and this closure. We have also calculated the electrical resistivities of the system studied present work using Faber-Ziman formula. We have compared our calculations with theoretical results obtained from $2k_F$ scattering model and experimental data.

III. RESULTS AND DISCUSSION

The effective pair potentials are computed by using individual versions of Fiolhais pseudopotential with parameters for K α=3.321, R= 0.683 and for Rb α=3.197, R=0.760 [14] at 373 K.

In Fig. 1, we display screened form factors of pseudopotential (a) and partial pair potentials (b) for $K_{0.5}Rb_{0.5}$ liquid alloy at 373 K. As is seen Fig. 1 (b), a sharp repulsive part at short distances is followed by a first negative minimum at about the first neighbour's distance and decreasing friedel's oscillations at medium range which become negligible at about three times the interatomic distance.

The first minimums of partial pair potentials of K-K, K-Rb and Rb-Rb are at the same positions approximately and as we expected that the first minimum of K-Rb partial pair potential is between those of K-K and Rb-Rb.

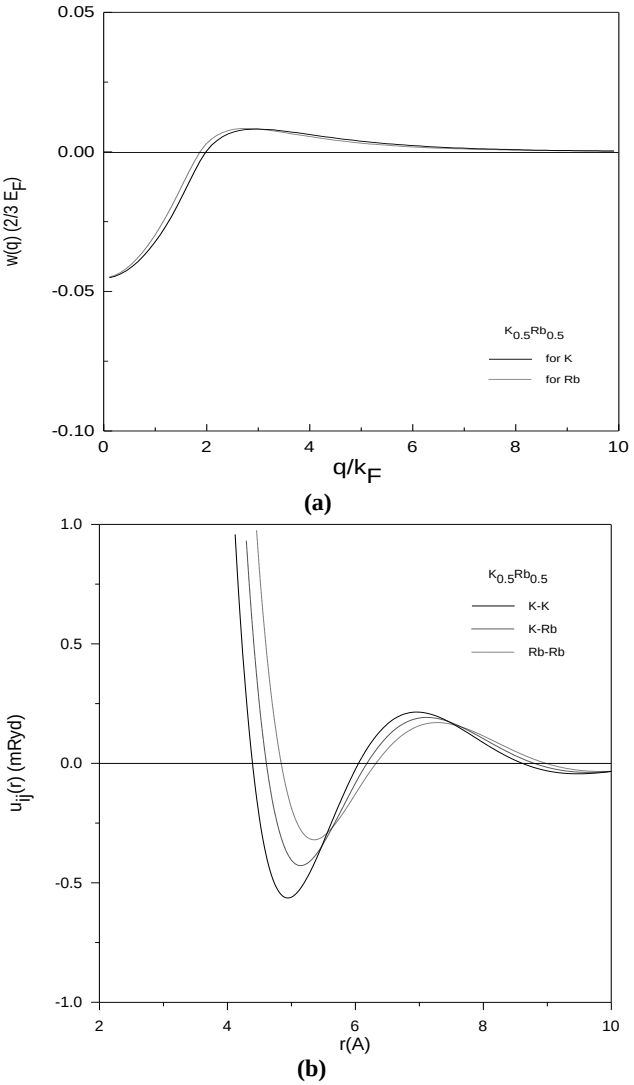

Fig. 1 Screened form factors of pseudopotential (a) and partial pair potentials (b) for $K_{0.5}Rb_{0.5}$ liquid alloy at 373K.

The partial pair distribution functions of the metals studied in this work are determined from the solution of Ornstein-Zernike equation. Labik, Malijevsky and Vonka algorithm [19] is used for the numerical solution of the Ornstein Zernike equation with RY closure [18]. After the calculation partial pair distribution functions $g_{ij}(r)$from O-Z equation, we computed the Ashcroft-Langreth's partial structure factors [12].

In Fig. 2, we present the Ashcroft-Langreth partial structure factors of three $K_{1-x}Rb_x$ alloys. Some usual features are recovered namely $S_{KK}(q)$ and $S_{RbRb}(q)$ oscillate around 1 as q tends to infinity, while $S_{KRb}(q)$ oscillates around 0 in the limit. The curves are very sensitive to the composition. When the concentration varies, $S_{KK}(q)$ and $S_{RbRb}(q)$ change symmetrically. The concentration in the corresponding element increases from 10 to 90 at %, the function goes from a rather flat curve around 1 even in the small-q range, to a curve looking like the one of a dense pure fluid, exhibiting sharp peaks corresponding to a pronounced structure and low-q values close to 0.

As is seen from figure 3, for all cases, the resistivity values calculated by using $2k_F$ scattering model are bigger than the ones calculated by using Faber-Ziman formula. On the other hand, the resistivity values calculated by

using VWN screening function are in good agreement with experimental data [20] especially while K concentration in the $K_{1-x}Rb_x$ alloy increases.

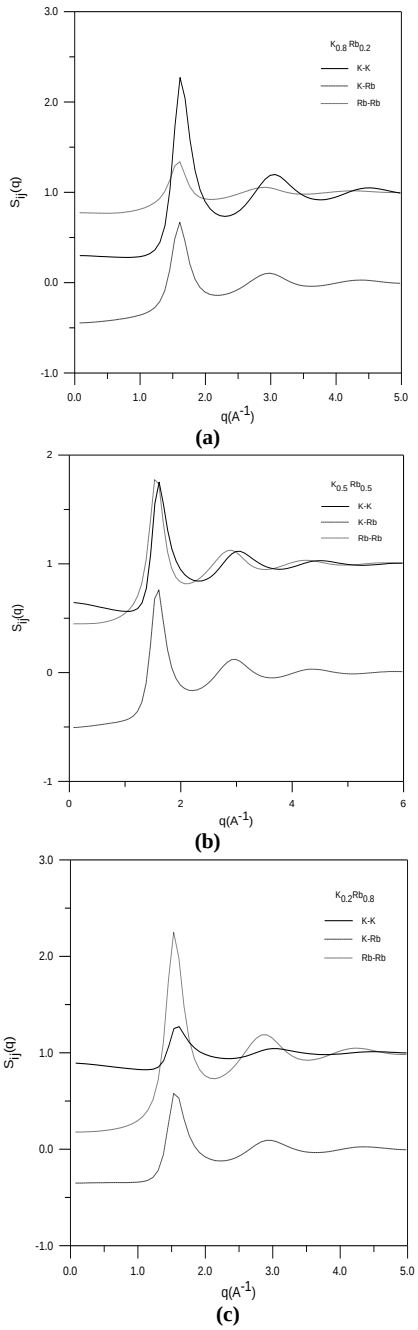

Fig. 2 Ashcroft-Langreth partial structure factors for the three alloys under consideration. Solid, dot-dashed and dotted lines represent K-K, K-Rb, Rb-Rb functions, respectively.

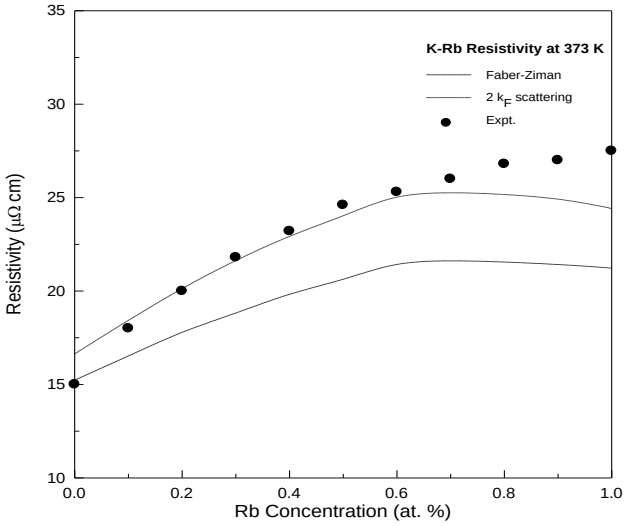

Fig. 3 Calculated electrical resistivities of K-Rb alloys together with available experimental data [18] at 373 K.

IV. CONCLUSION

We investigated the electronic transport properties of liquid $K_{1-x}Rb_x$ metal alloys using Faber-Ziman formula and $2k_F$ scattering model. To calculate the resistivity using both formulas, we computed the static structure factor using the individual version of pseudopotential proposed by Fioalhais and coworkers. In the calculation of form factors which are necessary for the calculation of resistivity the screening function namely LDA screening with the correlation energy of VWN is used. Partial structure factors have been determined from the solution of Ornstein-Zernike integral equation with RY closure.

We extended our calculations for the electronic transport properties of the systems concerned. Our calculated resistivity values obtained by using $2k_F$ scattering model are in very good agreement with experimental values while K concentration increases in the alloy.

[1]. *J.M. Ziman*, Phil. Mag. 1961, 6, 1013.
[2]. *T.E. Faber, J.M. Ziman*, Phil. Mag. 1967, 11, 153.
[3]. *A. Ferraz, N.H. March*, Phys. Chem. Liq. 1979, 8, 271.
[4]. *T.M.A. Khajil, M. Tomak*, Phys. Status Solidi B 1986, 134, 321.
[5]. *S.D. Korkmaz, S. Korkmaz, E. Terken*, Optoelectron. Adv. Mater. Rapid Commun. 2009, 3, 827.
[6]. *S.D. Korkmaz, S. Korkmaz*, Comp. Mat. Sci., 2010, 48, 466.
[7]. *G.J. Morgan, M.A. Howson, K. Saub*, J. Phys. F: Met. Phys. 1985, 15, 2157.
[8]. *G.J. Morgan, R. Gilbert, B.J. Hickey*, J. Phys. F: Met. Phys. 1985, 15, 2171.
[9]. A.*Pasturel, G.J. Morgan*, J. Phys. F: Met. Phys. 1987, 17, 1561.
[10]. *T.M.A. Khajil, M. Tomak*, Phys. Rev. A, 1988, 37, 4377.

[11]. *M. Ornat, A. Paja*, J. Phys.: Condens. Matter, 2008, 20, 375102.
[12]. *N.W. Ashcroft, D.C. Langreth*, Phys. Rev., 1967, 155 685.
[13]. *S.H. Vosko, L. Wilk, M. Nusair*, Can. J. Phys. 1980, 58, 1200.
[14]. *C. Fiolhais, J.P. Perdew, S.Q. Armster, J.M. McLaren, M. Brajczewska*, Phys. Rev. B, 1995, 51, 14001.
[15]. C. Fiolhais, J.P. Perdew, S.Q. Armster, J.M. McLaren, M. Brajczewska, Phys. Rev. B, 1996, 53, 13193.
[16]. *S.D. Korkmaz, S. Korkmaz*, Comp. Mat. Sci., 2006, 37 618.
[17]. *Ş. Korkmaz, S.D. Korkmaz*, J. Phase Equilib. Dif. , *2010*, 31 15.
[18]. *F.J. Rogers, D.A. Young*, Phys. Rev. A, 1984, 30, 999.
[19]. *S. Labik, A. Malijevsky, P. Vonka*, Mol. Phys. 1985, 56, 709.
[20]. J.F. Devlin, M.R. Leenstra, W. van der Lugt, Physica, 1973, 66, 593

.

A COMPARATIVE OF ENERGY DENSITY DISTRIBUTION OF SURFACE STATES PROFILES WITH 50 AND 826 Å INSULATOR LAYER IN Al/SiO_2/p-Si STRUCTURES

ŞEMSETTIN ALTINDAL, AHMET KAYA, ZEKAYI SÖNMEZ, YASEMIN ŞAFAK

Physics Department, Faculty of Arts and Sciences, Gazi University,
06500, Teknikokullar, Ankara, TURKEY
altundal@gazi.edu.tr, yaseminsafak@gazi.edu.tr,
ahkaya@windowslive.com, zekayis.19@hotnail.com

In the recent study, in order to achieve a better understand of the effects of different charge surface states and thickness of oxide layer (SiO_2) on the electrical characteristics, we fabricated with thin (50 Å) and thicker (826 Å) metal-insulator-semiconductor (Al/SiO_2/p-Si) structures and these structures are called sample A and sample B, respectively. The energy density distribution profile of the surface states (N_{ss}) of these structures have been investigated by use of the high-low frequency capacitance (C_{LF}-C_{HF}) method. The increase in the capacitance at low frequency (1 kHz) results from the presence of surface states at Si/SiO_2 interface. The value of N_{ss} in sample A is almost one order higher than in sample B. This indicates that the insulator layer at metal/semiconductor interface can passivate the surface states effectively.

I. INTRODUCTION

Silicon is still dominating semiconductor in the microelectronic industry because of the excellent properties and stability of its oxide and the silicon-silicon dioxide (Si/SiO_2) interface. Growth an insulator layer on the semiconductor is more important process step in the metal-insulator-semiconductor (MIS) or metal-oxide-semiconductor (MOS) devices fabrication. There are several suggested methods for determine energy density distribution profile of surface states such as high-low frequency capacitance [1-6], quasi-static capacitance [7], surface admittance [8] and conductance [9,10] methods. Among them, Nicollian's and Goetzberger's conductance method [9] is generally accepted more accurate then others. But, it takes much time. In addition, high-low frequency capacitance method is easy and fast then others and give reliable results. In general, the C-V curve in ideal case is frequency independent and increases with increasing forward bias [10-13]. The surface states can be created by crystal lattice discontinuous (dangling bonds), inter-diffusion of atoms or a large density of crystal lattice defects at semiconductor/oxide (Si/SiO_2) interface. At low frequencies (f≤ 100 Hz) the charges at interface can easily follow an ac signal and they are capable of these charges increase with decreasing frequencies. Therefore, high-low frequency capacitance method of these structures allows us to obtain the parameters characterizing the Si/SiO_2 interface phenomena [9, 10].

As far as our known, until now, a detailed investigation of the various features of surface states in these structures with interfacial layer thickness in the range of 50-826 Å has not been reported in the literature. Therefore, in this study, in order to achieve a better understand of the effects of different charge surface states and thickness of oxide layer on the electrical characteristics we fabricated with thin (50 Å) and thicker (826 Å) metal-insulator-semiconductor (Al/SiO_2/p-Si) structures and these structures are called sample A and sample B, respectively. The interfacial insulator/oxide layer (SiO_2) thicknesses were obtained from high frequency (1 MHz) measurements of the oxide capacitance (C_{ox}) in the strong accumulation region. The forward and reverse bias C-V measurements of these structures were performed by using a computerized HP 4192A LF impedance analyzer (5 Hz-13 MHz) at room temperature for two frequencies (1 kHz and 1 MHz). As small sinusoidal signal of 40 mV p-p from the external pulse generator is applied to the sample in order to meet the requirement [9,10]. The energy density distribution profile of the surface states (N_{ss}) of these structures have been investigated by using the high-low frequency capacitance (C_{LF}-C_{HF}) method.

II. EXPERIMENTAL PROCEDURES

The Al/SiO_2/p-Si structures were fabricated using p-type (boron-doped) single crystal silicon wafer with <100> surface orientation, having thickness of 350 μm, 2" diameter and 1 Ω.cm resistivity. For the fabrication process, Si wafers were degreased in organic solutions of CHCl CCl_2 , CH_3COCH_3 and CH_3OH, then etched in a sequence of H_2SO_4 and H_2O_2, 20% HF, a solution of $6HNO_3$: 1HF: $35H_2O$, 20% HF and finally quenched in de-ionized water of resistivity of 18 MΩ.cm for 10 minutes. The oxidation was carried in a resistance heated furnace in dry oxygen with a flow rate of 1.5 lt/min. The oxide layer thickness of 50 Å and 660 Å were grown at the temperatures of 750 ^oC during 1.5 hours and 900 ^oC during 4 hours, respectively. Following oxidation, circular dots of 1.2 mm diameter high purity (99.999 %) Al with a thickness of ~2000 Å contacts were deposited on to the oxidized surface of the wafer through a Cu shadow mask in a liquid nitrogen trapped vacuum system in a vacuum of ~ $2x10^{-6}$ Torr. Finally, Al with a thickness of ~2000 Å is also thermally evaporated on the whole back surface of the wafer after etching away the oxide layer (SiO_2) from the back surface in HF. The metal thickness layer and the deposition rates were monitored with the help of quartz crystal thickness monitor. In order to get C-V measurements, the electrical contacts are made on to the upper electrode on the oxide with the help of fine phosphor-bronze spring probe. The measurements were carried out at room temperature in electrically shielded metal box.

The C-V measurements have been performed by the use of a computerized HP 4192A LF impedance analyzer (5 Hz-13 MHz). The low frequency capacitance (1 kHz) and high frequency capacitance (1 MHz) have been measured at room temperature. Small sinusoidal signal of 40 mV peak to peak from the external pulse generator is applied to the sample in order to meet the requirement

[9,10]. All measurements were carried out with the help of a microcomputer through an IEEE-488 AC/DC converter card.

III. RESULTS AND DISCUSSION

Several experimental methods have been developed for the study of the semiconductor-insulator (Si-SiO_2) surface states essentially based on differential capacitance measurement [7, 10, 14]. The advantage of (C_{HF}-C_{LF}) method comes from the fact it permits determination of many properties of the interfacial insulator layer, the semiconductor substrate, and surface states (N_{ss}) as both easily and accurately. In this method [1], the energy density distribution profile of the (N_{ss}) is extracted from its capacitance contribution to the measured experimental capacitance-voltage (C-V) curve. In the equivalent circuit of MIS or MOS diodes, the interfacial insulator layer/oxide capacitance C_{ox} is in series with the parallel combination of the surface state capacitance C_{ss} and the space charge capacitance C_{sc}: C_{ss} can be determined by subtracting the space charge capacitance C_{sc} (extracted from the measured high frequency capacitance C_{HF}) from the space charge capacitance in parallel with the surface state capacitance (extracted from the measured low frequency capacitance C_{LF}) and is given as :

$$C_{SS} = \left[\frac{1}{C_{LF}} - \frac{1}{C_{ox}} \right]^{-1} - C_{sc} \tag{1}$$

At high frequencies, N_{ss} cannot respond to the ac excitation, so they do not contribute to the total capacitance directly, but stretch out of the C-V curve occurs. Therefore, the equivalent capacitance is the series connection of C_{ox} and C_{sc}, is given as:

$$\frac{1}{C_{HF}} = \frac{1}{C_{ox}} + \frac{1}{C_{sc}} \tag{2}$$

Thus combining equations (1) and (2), the surface state density N_{ss} is calculated from;

$$qAN_{ss} = \left[\frac{1}{C_{LF}} - \frac{1}{C_{ox}} \right]^{-1} - \left[\frac{1}{C_{HF}} - \frac{1}{C_{ox}} \right]^{-1} \tag{3}$$

where, A is the rectifier contact area and q is the electronic charge. This integration is performed numerically from the flat band to strong accumulation and to strong inversion as in [15]. The measured high-low frequency curves are shown in Figs. 1 (a) and (b), for samples A and B, respectively. Surface potential (φ_s) versus applied voltage for the of Al/SiO_2/p-Si Schottky diode is shown in Fig. 2 for samples A and B, respectively. The energy position in the p-Si band gap is calculated as:

$$E_{ss} - E_v = q(\varphi_s - \phi_F) \tag{4a}$$

where ϕ_F is the position of Fermi energy level and is given as

$$\phi_F = \frac{kT}{q} \ln(N_V / N_A) \tag{4b}$$

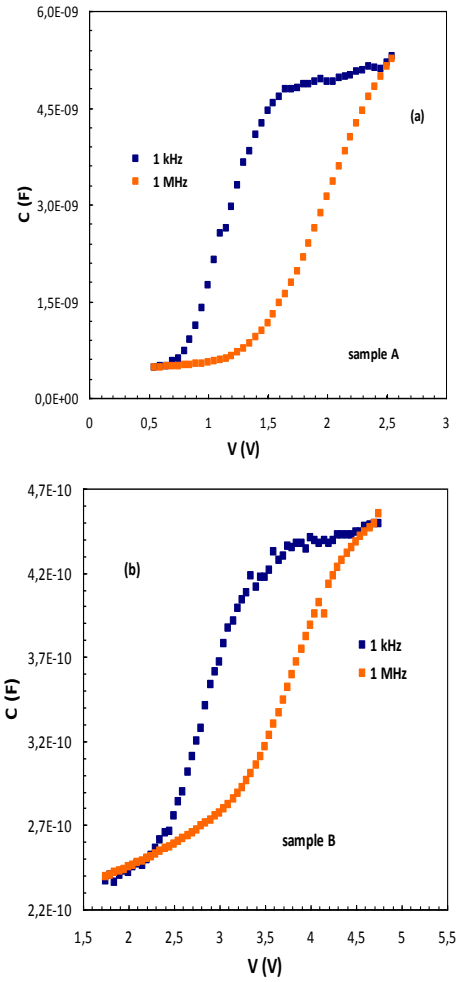

Fig. 1. The measured high-low frequency capacitance (C_{HF} - C_{LF}) plots of the Al/SiO_2/p-Si Schottky diodes for samples A and B at room temperature.

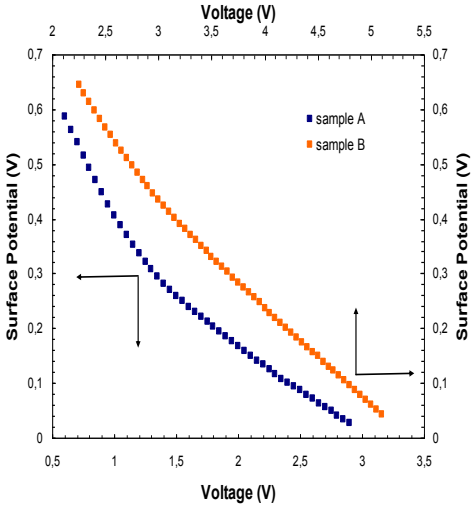

Fig. 2. The surface potential vs V plot of the Al/SiO_2/p-Si Schottky diodes for samples A and B at room temperature.

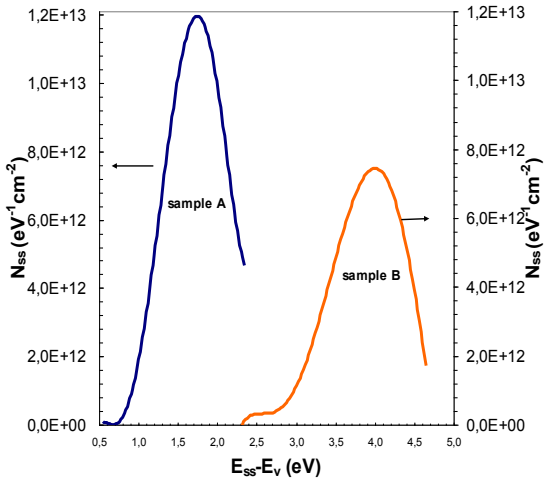

Fig. 3. The energy density distribution profile of surface states in the Al/SiO_2/p-Si Schottky diodes for samples A and B at room temperature.

The surface potential as a function of bias is found from the numerical integration of the lowest measurable frequency capacitance-voltage curve according to,

$$\bar{\varphi}_s = \int_{V_a}^{V_G} \left(1 - \frac{C_{LF}}{C_{ox}}\right) dV_G + \varphi^* \qquad (5)$$

where V_a is the bias voltage in strong accumulation region when the capacitance is equal to the oxide capacitance C_{ox} and the integration constant φ* was found by extrapolating the C_{sc}^{-2}- φ_s curve in the depletion region (0.14 eV) to $C_{sc}^{-2} = 0$ [10,15]. Thus, the density of surface states distribution profiles of the sample was obtained from the high-low capacitance measurements is shown in Fig. 3.

As can be seen in Fig. 3, the surface states distribution profiles over accessible band gap energy with peaked structure and the peak position is different for samples A and B. Such peak behavior of Nss can be attributed to particular distribution of N_{ss} in the Si band gap [9,10]. The surface states distributions with peaked structure were also observed in the past [8,12,14].

IV. CONCLUSIONS

In order to understand the effect of different charge at surface states and thickness of oxide layer (SiO_2) on the electrical characteristics, we fabricated with thin (50 Å) and thicker (826 Å) metal-insulator-semiconductor (Al/SiO_2/p-Si) structures and these structures are called sample A and sample B, respectively. The energy distribution profile of surface states (N_{ss}) have been obtained from high-low frequency capacitance (C_{LF}-C_{HF}) method for samples A and B with 50 and 826 Å at room temperature. The high value of the capacitance at low frequency (1 kHz) results from the presence of surface states at Si/SiO_2 surface. The value of N_{ss} for sample A is almost one order higher than for sample B. This result indicates that the insulator layer at metal/semiconductor interface can passivate the surface states.

[1]. *R. Castagne, A. Vapaille*, Surface Science 28(1), (1971) 157.

[2]. *U. Kelberlau, R. Kassing*, Solid-State Electron. 24, (1981) 873.

[3]. *N., Konofaos, E.K., Evangelou, Zhongchun Wang, V. Kugler, U. Helmersson*, Journal of Non-Crystalline Solids, 303 (2002) 185.

[4]. *E.J. Miller, X.Z. Dang, H. H. Wieder, P.M.Asbeck, and E. T. Yu, G.J. Sullivan, J.M.Redwing*, J. Appl. Phys.,87 (11) (2000) 2071.

[5]. *Ş. Altındal, H. Kanbur, İ.Yücedağ, A. Tataroğlu*, Microelect. Eng. 85 (2008) 1495.

[6]. *A.Tataroğlu, Ş Altındal*, Microelect. Eng. 85 (2008) 2256.

[7]. *M. Kuhn*, Solid State Electron. 13(6) (1970) 873.

[8]. *S. Kar, S. Varma*, J. Appl. Phys. 58(11) (1985) 4256.

[9]. *E. H. Nicollian, A. Goetzberger*, Bell Syst. Tech. J. 46 (1967)1055.

[10]. *E.H. Nicollian, J.R. Brews*, MOS (metal/oxide/semiconductor) Physics and Technology, John Wiley & Sons, New York (1982)

[11]. *P. Chattopadhyay, B. Ray Chaudhuri*, Solid-State Electron. 35 (7) (1992) 1023.

[12]. *H. Deuling, E. Klausmann*, Solid-State Electron. 15(5) (1972) 559.

[13]. *G. Pananakakis, G. Kamarinos*, M. El-Sayed, Solid-State Electron. 26 (1983) 415.

[14]. *K.K. Hung, Y.C. Cheng*,. Appl. Surf. Sci., 30 (1987) 114.

[15]. *C. N. Berglund*, IEEE Trans. Nucl. Sci. ED-13(10) (1966) 701.

CHARACTERISTICS OF Au/*n*-GaAs SCHOTTKY DIODES BASED ON I-V MEASUREMENTS AT HIGH TEMPERATURES

Z. KARA[a], M. YAZICI[b], Ş. KARATAŞ[a]

[a]Kahramanmaraş Sütçü İmam University,
Faculty of Science and Arts, Department of Physics,
46100 Kahramanmaraş, Turkey
[b]Kilis 7 December University,
Faculty of Science and Arts, Department of Physics ,
80100 Kilis, Turkey

The aim of this work is to experimentally investigate the effect of current-voltage (*I-V*) characteristics of metal-semiconductor (MS) Au/n-GaAs Schottky diodes at high temperatures. The MS Schottky diode showed nonideal behaviour of *I-V* characteristics. The current-voltage characteristics showed that the Schottky diodes formed at high temperature had a much improved barrier height compared to those formed at room temperature. It is shown that the occurrence of a Gaussian distribution of then barrier heights is responsible for the increase of the apparent barrier height Φ_b, decrease of the ideality factor *n* with the increasing temperature. A Φ_{bo} vs 1/*T* plot was drawn to obtain evidence of a Gaussian distribution of the BHs, and values of $\overline{\Phi}_{bo}$ = 1.076 eV and σ_o = 0.171 V for the mean BH and zero-bias standard deviation have been obtained from this plot, respectively. Thus, a modified $\ln(I_0/T^2) - q^2\sigma_o^2/2k^2T^2$ vs 1/*T* plot gives $\overline{\Phi}_{bo}$ and *A** as 1.078 eV and 8.87 A/cm^{2}K^2, respectively, of which latter is approximately the same as the value of 8.16 Acm^{-2}K^{-2} for *n*-type GaAs.

I. INTRODUCTION

The metal-semiconductor (M-S) contacts play a very important role in modern microelectronic devices. Schottky barrier diodes have been studied extensively but satisfactory understanding in all details has still not been achieved [1-4]. The performance and stability of metal semiconductor is of great importance to the electronic devices. Due to their role in the fabrication of electronic devices, semiconductors are an important part of our lives [1,3,5-6]. The speed of electronic devices (particularly integrated circuits) has grown exponentially over the same time period [7-12].

GaAs is used as a basic material for high speed electronic and optoelectronic device because they allow highly efficient absorption and emission of light [13-15]. It is well known that the barrier height of a SBD as determined from forward bias *I-V* measurements decreases whereas an ideality factor increases with decrease in temperature [3,16-19]. To understand the nature of the barrier and the conduction mechanism, the SBD parameters should be also determined at high temperatures. Because analysis of the *I–V* characteristics of the SB measured only at room temperature and low temperatures does not give detailed information about the conduction process and the barrier nature formed at metal–semiconductor interface. This implies that there is an excess current flow in the Schottky diode than the predicted by TE theory. The zero-bias barrier height Φ_b as obtained from forward bias *I-V* characteristics for the thermionic emission (TE) increases with increasing temperature. In recent studies, the origin and nature of the increase in the ideality factor and decrease in the barrier height with decreasing temperature in the Au/n-GaAs Schottky diodes have been successfully explained on the basis of the thermionic emission mechanism with Gaussian distribution of the barrier height [20–24]. In our previous works [25-27], we investigated the effects of the interface states, series resistance and electron-tunneling factor ($\alpha\chi^{1/2}\delta$) on the current transport mechanism of the Au/*n*-GaAs Schottky diodes at a wide temperature, and examined the electronic properties of main parameters obtained from current-voltage (*I-V*) and capacitance-voltage (*C-V*) measurements and interface state density distribution properties of interface states of Au/*n*-GaAs Schottky barrier diode. In this study, we have only studied the forward bias *I-V* characteristics of an Au/*n*-GaAs Schottky diode at the high temperature range of 300-400 K.

II. EXPERİMENTAL PROCEDURE

The samples have been prepared using cleaned and polished *n*-GaAs (as received from the manufactured) with (100) orientation and 2-5x10^{17} cm^{-3} carrier concentrations. Before making contacts, the *n*-GaAs wafer were dipped in $5H_2SO_4+H_2O_2+H_2O$ solution for 1.0 min to remove surface damage layer and undesirable impurities and then in H_2O+HCl solution and then followed by a rinse in de-ionized water of 18 MΩ. The wafer dried with high-purity nitrogen and inserted into the deposition chamber immediately after the etching process. Au-Ge (88 and 12 %) for ohmic contacts was evaporated on the back of the wafer in a vacuum-coating unit of 10^{-6} Torr. Then low resistance ohmic contacts were formed by thermal annealing at 450 ^{o}C for 3 min in flowing N_2 in a quartz tube furnace. Then, the wafer was inserted into the evaporation chamber for forming the reference Schottky contacts. The Schottky contact formed by evaporating Au as dots with diameter of about 1.5 mm onto all of *n*-GaAs surfaces.

The current-voltage (*I-V*) measurements carried out by the use of a Keithly 220 programmable constant current source and a Keithly 614 electrometer. The *I-V* characteristics of Au/*n*-GaAs Schottky diodes studied at the high temperature ranges (300-400 K) by using a temperature controlled janes vpf -475 cryostat, which enables us to make measurements in the temperature range of 77 -450 K.

III. RESULTS AND DISCUSSION

The current-voltage (*I-V*) characteristics of the Schottky diode are plotted as a function of temperature in Fig 1.

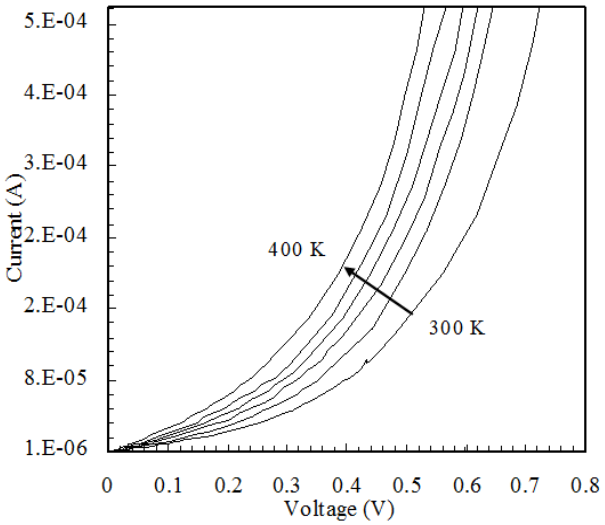

Fig.1. The *I-V* characteristics of the Au/n-GaAs Schottky diode

In a metal-semiconductor contact where the conduction process is dominated by thermionic emission, the current-voltage (*I-V*) relationship is given by [3]

$$I = I_o \exp\left(\frac{qV}{nkT}\right)\left[1-\exp\left(-\frac{qV}{kT}\right)\right] \qquad (1)$$

where the saturation current I_o is expressed as

$$I_o = AA^*T^2 \exp\left(-\frac{\Phi_{bo}}{qV_T}\right) \qquad (2)$$

where A is the effective diode area, T is the absolute temperature, q the electron charge, $V_T = kT/q$, k the Boltzmann constant, Φ_{bo} the barrier height, A^* the Richardson constant for n-type GaAs (A=8.16 $Acm^{-2}K^{-2}$), n an ideality factor and a measure of conformity of the diode to pure thermionic emission and is contained in the slope of the straight line region of the forward bias ln*I-V* characteristics through the relation

$$n = \frac{q}{kT}\left(\frac{dV}{d\ln I}\right) \qquad (3)$$

If n is equal to one, pure thermionic emission is occurring. However, n has usually a value grater than unity. The barrier height is an important parameter which controls the electrical conduction across Schottky barrier diodes. A convenient method to determine this parameter is to plot the logarithmic value of the current density as a function of voltage. In the usual analyses of the experimental data on Schottky contacts, the barrier height Φ_{bo} is determined from the extrapolated I_o and is given by:

$$\Phi_{b0} = \frac{kT}{q}\ln\left[\frac{AA^*T^2}{I_0}\right] \qquad (4)$$

The experimental SBHs and ideality factors are found to be strong function of temperature. Using Eq. (3) and Eq. (4), the values of the ideality factor n and barrier height of the diode at different temperatures were calculated and these values are plotted as a function of temperature in Fig. 2. As can be seen in Fig. 2 and Table 1 , the ideality factor, n, exhibits an increasing trend with decreasing temperature, whereas the zero-bias barrier height, Φ_{bo}, decreases with decreasing in temperature. The experimental values of n and Φ_{bo} for the device change from 4.258 and 0.515 eV (at 300 K) to 2.057 and 0.657 eV (at 400 K), respectively. The experimental values of n indicated by closed squares and Φ_{bo} indicated by open circles obtained depending on the temperature are given in Fig. 2.

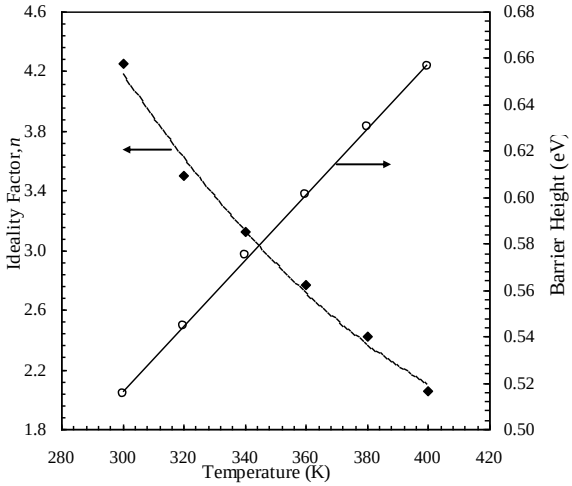

Fig. 2. The variation of the ideality factor and the barrier height.

The high values of ideality factor are attributed partly to the low barrier height and to a native interfacial oxide layer and/or a wide distribution of low Schottky barrier height (SBH) patches [3,11,28].

The variation of the experimental barrier height against the ideality factor is shown in Fig. 3. As shown in the Fig. 3, there is a linear relationship between the experimental effective barrier heights and the ideality factors of the contacts that can be explained by lateral inhomogeneities of the barrier heights in Schottky barrier diodes [12,21,29]. The straight line in Fig. 3 that is the least squares fit to the experimental data. The extrapolation of the experimental BHs versus ideality factors plot to n =1 has given a homogeneous BH of approximately 0.721 eV. Thus, it can be said that the significant decrease of the zero-bias BH and increase of the ideality factor especially at low temperature are possibly caused by the BH inhomogeneities.

For evaluation of barrier height, one may also make use of the Arrhenius plot of the saturation current. Eq. 2 can be written as

$$\ln\left(\frac{I_o}{T^2}\right)=\ln\left(AA^*\right)-\left(\frac{q\Phi_{bo}}{kT}\right) \qquad (5)$$

Thus, the $\ln(I_0/T^2)$ versus $10^3/T$ plot should yield a straight line with a slope giving the zero-bias barrier height Φ_{bo} and the intercept at the ordinate, the Richardson constant (A^*) if the diode area A is known.

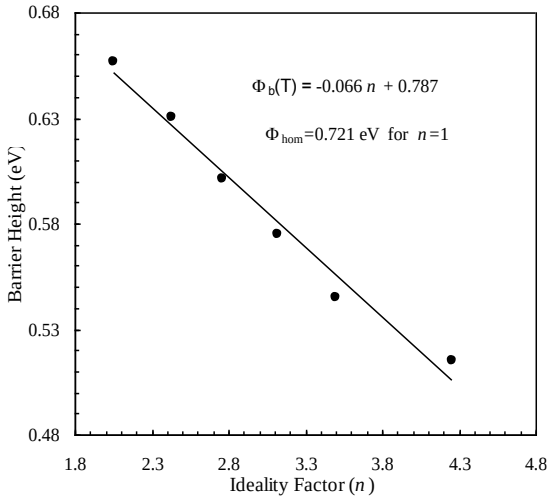

Fig.3. The barrier height vs. ideality factor with temperature

Fig.4 shows the plot obtained by the usual method. This plot yields a Richardson constant of 0.165 $AK^{-2}cm^{-2}$ and a Φ_{bo} of 0.11 eV. Both the Richardson constant A* and barrier height energy are too low; the reported values being 8.16 $AK^{-2}cm^{-2}$ and (0.7-0.9 eV) [1,3], respectively. This value of Richardson constant is 49 times lower than known value for n-type GaAs. Since, if the ideality factor is a strong function of temperature, a modified Richardson plot has been proposed which uses a plot of $\ln(I_0/T^2)$ versus 10^3/nT [27]. Fig.4 also shows such a plot of $\ln(I_0/T^2)$ versus 10^3/nT. The values of A* and the barrier height determined from this plot 0.18 $AK^{-2}cm^{-2}$ and 0.23 eV, respectively. The values determined from the usual method in the temperature range of 300-400 K and by using the modified Richardson constant plot are lower than the theoretical values for n-type GaAs.

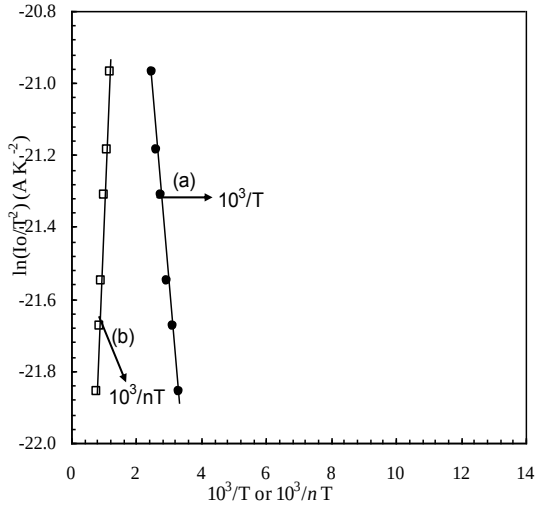

Fig.4. Richardson plots of the $\ln(I_0/T^2)$ or 1/T or 1/nT and $\ln(I_{0f}/T\ 2)$ versus $1/nT$ for Au/n-GaAs Schottky diode.

As will be discussed below, the deviation in the Richardson plots may be due to the spatially inhomogeneous barrier heights and potential fluctuations at the interface that consist of low and high barrier areas [3,5,12], that is, the current through the diode will flow preferentially through the lower barriers in potential distribution [31].

Fig. 5 shows the experimental series resistance values obtained from semi-log *I–V* characteristics as a function of temperature. The forward bias *I–V* characteristics of the MS contacts are linear on a semi-log scale at low forward bias voltage but deviate considerably from linearity due to the some factors at large voltages.

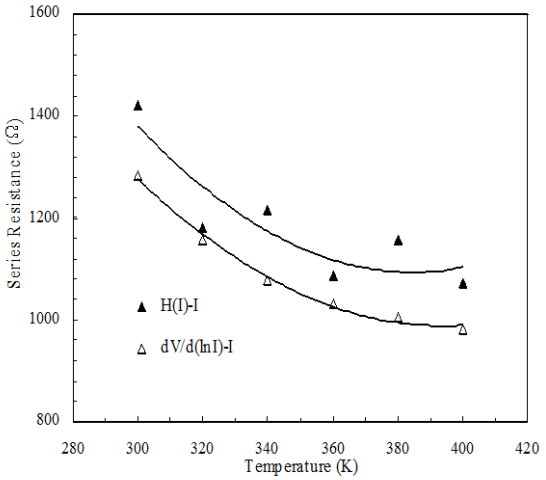

Fig. 5. Temperature dependence of series resistances

Table 1.Temperature dependence values of various parameters determined from *I-V* characteristics.

T (*K*)	*n* (*I-V*)	*n* *H*(*I*)-)	*n* dV/*d*(lnI)	Φ_b eV (*I V*)	Φ_b eV *H*(*I*)	R_S (Ω) *H*(*I*)-*I*	R_S (Ω) dV/*d*(lnI)
300	4.258	4.427	4.541	0.515	0.535	1419.79	1284.53
320	3.500	3.743	4.257	0.545	0.583	1180.97	1156.85
340	3.125	3.513	4.007	0.575	0.646	1217.33	1077.54
360	2.765	3.078	3.784	0.601	0.669	1086.49	1032.56
380	2.426	2.725	3.585	0.631	0.709	1156.86	1004.75
400	2.056	2.328	3.406	0.657	0.744	1071.18	982.25

These values were achieved using a method developed by Cheung and Cheung [31]. These values are given in Table 1. The forward bias *I–V* characteristics due to the TE of a Schottky diode with the series resistance can be expressed as [3]:

$$I = I_o \exp\left(\frac{q\left(V - IR_S\right)}{nkT}\right) \qquad (6)$$

where the IR_s term is the voltage drop across series resistance of device. The values of the series resistance can be determined from the following functions using Eq. (6):

$$\frac{\mathrm{dV}}{\mathrm{d}\left(\mathrm{lnI}\right)} = IR_s + \left(\frac{\mathrm{nkT}}{\mathrm{q}}\right) \qquad (7)$$

$$H(I) = V - n\left(\frac{kT}{q}\right)\ln\left(\frac{I}{AA^{*}T^{2}}\right) \qquad (8)$$

and $H(I)$ is given as follows:

$$H(I) = IR_s + n\Phi_b \qquad (9)$$

A plot of dV/d(ln I) versus I will be linear and give R_s as the slope and nkT/q as the y-axis intercept, and then n value can be determined from Eq. (7). Moreover, $H(I)$ versus I will be linear from Eq. (9). The slope of this plot provides a second determination of R_s. By using the values of the n determined from Eq. (7), the values of Φ_b can be obtained from the y-axis intercept. The three diode parameters, n, Φ_b, R_s, determined from Cheung functions as a function of temperature are given in Table 1 and the series resistance versus temperature is given in Fig.5. The increase of series resistance with the decrease in temperature is believed to result due to factors responsible for increase of n and/or lack of free carrier concentration at low temperature [20].

Performing this integration from -∞ to +∞, the current $I(V)$ through a Schottky barrier at a forward bias V has a similar from Eqs.(1) and (2) but with the modified barrier height as

$$I(V) = I_0 \exp\left(\frac{qV}{n_{ap}kT}\right)\left[1 - \exp\left(-\frac{qV}{kT}\right)\right] \qquad (10)$$

with

$$I_o = AA^{*}T^{2}\exp\left(-\frac{q\Phi_{ap}}{kT}\right) \qquad (11)$$

where Φ_{ap} and n_{ap} are the apparent barrier height and apparent ideality factor, respectively. An apparent BH given by [9],

$$\Phi_{ap} = \overline{\Phi}_{bo}(T=0) - \frac{q\sigma_o^2}{2kT} \qquad (12)$$

instead of Φ_b. In the ideal case (n=1), the expression is obtained as

$$\left(\frac{1}{n_{ap}} - 1\right) = \rho_2 - \frac{q\rho_3}{2kT} \qquad (13)$$

By assuming a linear voltage dependence of the mean ($\overline{\Phi}_b$) and standard deviations (σ_s) such that $\overline{\Phi}_b = \overline{\Phi}_{bo} + \rho_2 V$ and $\sigma_s = \sigma_o + \rho_3 V$ (where ρ_2 and ρ_3 are bias coefficients of the mean and the standard deviation of the distribution, and $\overline{\Phi}_b$ and σ_0 are the zero-bias mean and standard deviation, respectively).

Fitting of the experimental data in Eq.(2) or (11) and in Eq.(3) gives Φ_{ap} and n_{ap}, respectively, which should satisfy Eqs. (12) and (13). Thus, the plot of Φ_{ap} vs 1/T (Fig. 6) should be a straight line that gives $\overline{\Phi}_{bo}$ and σ_o from the intercept and slope, respectively. The values of 1.076 eV and 0.170 V for $\overline{\Phi}_{bo}$ and σ_o (the zero-bias standard deviation), respectively, were obtained from the experimental Φ_{ap} vs 1/T plot (Fig. 6). The open circles in Fig. 2 represent data estimated with these parameters using Eq.(12). The standard deviation is a measure of the barrier homogeneity. The lower value of σ_o corresponds to more homogeneous BH. It was seen that the value of σ_o = 0.170 V is not small compared to the mean value of $\overline{\Phi}_{bo}$ =1.076 eV, and it indicates the presence of the interface inhomogeneities. The temperature dependence of the ideality factor can be understood on the basis of Eq. (13), which indicates that $(1/n_{ap} - 1)$ versus 1/T plot should give a straight line with an y-axis intercept and a slope dependence on the voltage coefficients ρ_2 and ρ_3, respectively. The plots are shown in Fig. 6. Using least square linear fitting the experimental data, the coefficients are obtained as ρ_2=0.171 V and ρ_3=0.0491 V (using the previous σ_0 value) for the Au/GaAs Schottky diode. The closed squares line in Fig. 2 represents data estimated with these parameters using Eq. (13). These results reveal that a bias voltage obviously homogeneous the barrier height fluctuation, i.e., the higher the bias, the narrower the barrier height distribution, which can be explained that image forces shift the effective barrier maxima deeper into the semiconductor when the bias voltage increases, thus homogenizing the Schottky barrier height distribution.

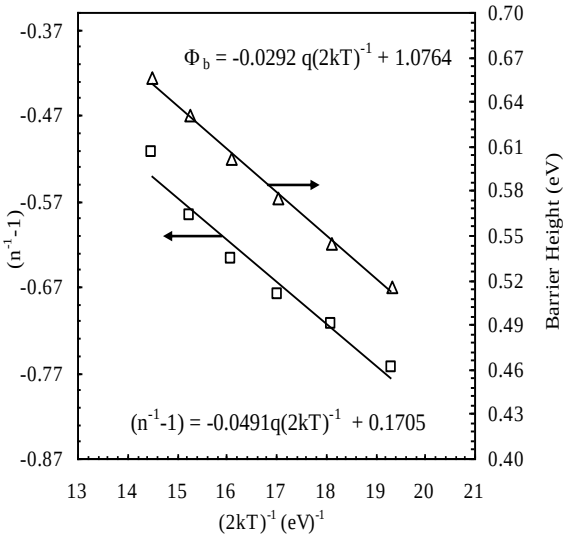

Fig. 6. The barrier height and ideality factor versus 1/T curves according to Gaussian distribution of the barrier heights

IV. CONCLUSION

The *I-V* characteristics of the Au/n-GaAs Schottky diodes were studied in the temperature range of 300-400K. The zero-bias barrier height decreases and the ideality factor increases with decreasing temperature. This behavior was successfully explained on the basis of the thermionic-emission mechanism by incorporating the concept of barrier height inhomogeneity, which is described as a Gaussian distribution over the contact area. The high values of ideality factor are attributed partly to

the low barrier height and to a native interfacial oxide layer. As known, the distribution of the barrier height is caused by inhomogeneities that are present at the interface. Furthermore, the experimental results of Φ_{ap} and n_{ap} fit very well with the theoretical equations related to the Gaussian distribution of Φ_{ap} and n_{ap}. As a result, it is clear that the quality of the Au/n-type GaAS Schottky diode is good, and hence the Au/GaAs Schottky diodes can be better used in space applications at high temperatures.

---

[1]. *S. M. Sze*, Physics of Semiconductor Devices, 2nd Ed. Willey, New York 1981.

[2]. *J.H. Warner, U.Rau, I: J.F.Luy, et al*. (Eds.), Springer Series in Electronics and Photonics, Vol. 32 (1994) (1994)

[3]. *E.H.Rhoderick, R.H. Williams*, Metal-Semiconductor Contacts, 2nd Edition, Clarendon Press, Oxford, 1988

[4]. *K. Radermacher, A. Schüppen, S. Mantl*., Solid-Satet Elecron.37 (1994) 443

[5]. *R. T. Tung*, Mat. Sci. Eng. R , 35 (2001) 1-138,

[6]. *Ş. Karataş, A.Türüt*., Vacuum, 74 (2004) 45

[7]. *F.E. Jones, C. Hafer, B. Wood, R.G. Danner, M.Lonergan*, J. Appl. Phys. 90 (2001) 1001

[8]. *Y.P. Song, R.L. Van Meirhaeghe, W.H. Lafle´re, F.Cardon*, Solid-State Electron. 29 (1986) 633

[9]. *J.H. Werner, H.H. Güttler*, J. Appl. Phys. 69 (1991) 1522.

[10]. *S. Chand, J. Kumar*, J. Appl. Phys. 82 (1997) 5005.

[11]. *J.P. Sullivan, R.T. Tung, M.R. Pinto, W.R.Graham*, J. Appl. Phys. 70 (1991) 7403

[12]. *R.T. Tung*, Phys. Rev. B 45 (1992) 13509

[13]. *J.L. Davis*., Surface Sci., (1964) 2 :33

[14]. *M.S. Carpenter, M.R.Melloch, T.E.Dungan*., Appl. Phys. Lett.,53 (1988) 66

[15]. *Y. Wang, Y.Derici, P.H. Holloway*., J. Appl. Phys., 71 (1992) 2746

[16]. *V.G.Bozkhov, D.Ju. Kuzyakov* J. Appl. Phys. 92 (2002) 4502.

[17]. *Zs.J. Horvath*, Current Applied Physics. 6 (2006) 205.

[18]. *A.N. Saxena*., Surf. Sci. 13 (1969) 151

[19]. *C.R. Crowell*, Solid State Electron. 20 (1977) 171.

[20]. *S. Zhu, R. L. Van Meirhaeghe, C. Detavernier, F.Cardon, G. P. Ru, X. P. Qu, B. Z. Li, Solid-St Electron*. 44 (2000) 663.

[21]. *J. Osvald, Zs.J. Horvath*, Applied Surface Science. 234 (2004) 349

[22]. *S. Bandyopadhyay, A. Bhattacharyya, S.K. Sen*, J. Appl.Phys. 85 (1999) 3671

[23]. *O.S. Anilt.urk, R. Turan*, Solid-State Electron. 44 (2000) 41

[24]. *F.E. Jones, B.P. Wood, J.A. Myers, C.H. Daniels, M.C. Lonergan*, J. Appl. Phys. 86 (1999) 6431.

[25]. *Ş. Karataş, A.Türüt*., Physica B 381 (2006) 199

[26]. *Ş.Karataş, Ş.Altındal*, Mat.Sci. Eng.B.122 (2005) 133

[27]. *Ş. Karataş Ş. Altın dal*., Solid State Electron. 49 (2005) 1052

[28]. *M.C.Waener, J.R. Botha, A.W.R. Leitch*., Semicond. Sci. Technol.,14 (1999) 1080

[29]. *R.F. Schmitsdorf, T. U. Kampen, W. Mönch*, Surf. Sci. 324 (1995) 249

[30]. *R.Hackam, P. Harrop*., IEEE Trans. Electron Dev., 19 (1972) 1231

[31]. *S.K. Cheung, N.W. Cheung*, Appl. Phys. Lett. 49 (1986) 85.

EFFECT OF GAMMA-RAY (^{60}Co) IRRADIATION ON THE C-V AND G/W CHARACTERISTICS OF Au/n-CdTe SCHOTTKY BARRIER DIODES (SBDs)

YASEMIN ŞAFAK[1], HATICE KANBUR[2], HABIBE USLU[1], TOFIG MAMMADOV[1,3]

[1]*Physics Department, Faculty of Arts and Sciences, Gazi University, 06500, Teknikokullar, Ankara, TURKEY*

[2]*Physics Department, Faculty of Arts and Sciences, Bozok University, 66200, Yozgat, TURKEY*

[3]*Azerbaijan Natl Sci Akad, Inst Phys, Baku, Azerbaijan*

yaseminsafak@gazi.edu.tr hatice.kanbur@bozok.edu.tr

h.uslu@gazi.edu.tr mts@gazi.edu.tr

In order to investigate the radiation effect on the main electrical parameters of the Au/n-CdTe Schottky barrier diodes (SBDs), they have been exposed to ^{60}Co γ-ray source. The SBDs were irradiated at doses up to 25 kGy at room temperature. The capacitance-voltage (C-V) and conductance-voltage (G/ω-V) measurements have been carried out at 1 MHz before and after radiation. Experimental results show that γ-irradiation induce a decrease in the barrier height (Φ_B) obtained from reverse bias C-V measurements and doping concentration (N_D), whereas series resistance (R_s) increases with increasing dose. In addition, the voltage dependent series resistance (R_s) profile for Au/n-CdTe SBD was obtained from admittance-based measurement method of (C-V and G/ω-V) before and after radiation.

I. INTRODUCTION

Cadmium telluride (CdTe) is important semiconductor for electrical contacts on the semiconductor surface in order to obtain metal/semiconductor (MS) interfaces with desired electrical characteristics. The performance of contacts depend strongly both on the electrode metal and CdTe surface preparation before metallization [1, 2]. The first reported data, by Mead and Spitzer [3] were for devices fabricated on vacuum-cleaved CdTe surfaces and they found that the barrier height (BH) on such structures were substantially independent of the Schottky barrier metal. However, Ponpon et al show that the BH depends on the work function of the Schotty barrier metal. Cadmium telluride (CdTe) is an important material among the II-VI semiconductors and it has been widely used in satellites, space stations and space vehicles as power sources, which operates in radiation environments due to it is excellent high optical absorption coefficient and their direct band gap of 1.45 eV [4]. Therefore, metal-CdTe Schottky barrier diodes (SBDs) extremely sensitive to high level radiation such as ^{60}Co (γ-ray), electrons, neutrons or ions. The influence of such high level radiation on semiconductor materials produces quasi-stable changes in the characteristics of such materials [5-10].

Especially CdTe and Si based solar cells and the other electronic devices have been used as a power sources by many satellites and they have played an important role in a wide range of communications, broadcast, meteorological, scientific research and space development applications. Since, radiation in space is severe considerable amount of lattice defects are induced in semiconductors due to irradiations and these defects caused as degrade of semiconductor devices. In generally, there are two main effects of radiation: the transient effects are due to electron-hole pair generation and permanent effect is due to the bombardment of devices with radiation which causes changes in the crystal lattice of semiconductor [6-10]. There are several studies in the literature about the effect of radiation in MS or metal-insulator-semiconductor (MIS) type SBDs [5,10,11], solar cells [9,12,13] and metal-oxide-semiconductor (MOS) structures [6-8,14].

In this work, we aimed to investigate how irradiation changes the forward and reverse bias C-V and G/ω-V characteristics of Au/n-CdTe Schottky diodes by considering R_s effect. We exposed a maximum cumulative dose of 25 kGy on diodes at room temperature. In addition, before and after irradiation we investigated the effect of series resistance of device, which causes non-ideal behavior on the electrical properties of the MS structure.

II. EXPERIMENTAL PROCEDURES

Epitaxial layers of CdTe were grown on monocrystalline CdTe (111) substrate by photostimulated vapor phase epitaxy (PSVPE). Approximately a 5 μm epitaxial layers were deposited at 650 ºC with a 350 μm/h growth rate. In the growth, Cd source temperature was kept at 350 ºC for control to stoichiometry while CdTe source temperature was 750 ºC [15-18]. By controlling stoichiometry, the growth process makes it possible to obtain n-type epitaxial layers of CdTe. The CdTe wafers were cleaned by using standard cleaning method. Immediately after surface cleaning, high purity gold (Au) metal (99.999 %) with a thickness of 1000 Å was thermally evaporated with a 2.2 Å/s grow rate onto the whole back surface of the wafer in the vacuum system. To form ohmic Au back contact, samples were temperature treatment at 400ºC for 30 minutes in the vacuum system. After ohmic contact, circular dots of 1 mm in diameter and 1100Å thick Au rectifying contacts were deposited onto CdTe surface. All evaporation processes were carried out in a turbo molecular fitted vacuum coating system (Bestek Technique) in the pressure of 10^{-8} mbar.

The capacitance-voltage (C-V) and conductance-voltage (G-V) characteristics of Au/CdTe SBDs were carried out with the help of a microcomputer through an IEE-488 ac/dc converter card by using the HP 4192A LF impedance analyzer meter (5 Hz - 13 MHz) and the test signal of 40mV_{rms} at 1 MHz before and after irradiation. All measurements were carried out in vacuum ($\leq 10^{-3}$ mbar) to avoid the noise at room temperature.

III. RESULTS AND DISCUSSION

The irradiation sources' damage occurs through two basic mechanisms: bulk damage, which is due to the displacement of atoms from their lattice sites, and surface damage, which is due to charges built up at the M/S interface [10]. Figure 1 shows the typical C-V measurements at room temperature for the Au/n-CdTe Schottky barrier diodes (SBDs) at 1 MHz before and after γ-ray irradiation. It is clear that each C-V curves have three different distinct regions of accumulation, depletion and inversion. Also, the C-V curves are dependent on both the bias voltage and radiation dose. The values of capacitance (C) decrease with increasing radiation dose especially in the depletion and inversion regions. Such changes in the C-V curves can be attributed to the restructure and reordering of interface states at M/S interface and their time dependent response. By analyzing the high frequency (1 MHz) C-V curves in Fig. 1, it is clearly seen the stretch-out of C-V curves under the influence of γ-irradiation, reflecting the generations of charges due to the electron-hole pair generation by the radiation [6-8].

Figure 2 shows the typical G/ω-V measurements at room temperature for the Au/n-CdTe SBDs at 1 MHz before and after γ-ray irradiation. As shown in Fig. 2, the values of conductance (G/ω) decrease regularly with increasing applied bias voltage. In addition, the values of G/ω decrease with increasing dose rate but, this change in low radiation (2 kGy) contrary to C becomes very low and it can be eliminated. It is well known at high frequency the R_s become significant especially at accumulation region.

It is well know, the interface states are effective for the inversion and depletion region. On the other hand, series resistance of device is effective only in accumulation region or at sufficiently forward bias region [14, 19].

There are several methods to extract the values of R_s of SBDs with and without an interfacial insulator layer in the literature [19-21]. In this study we have applied the method by Nicollian and Goetzberger [19]. According to this method, the real value of R_s can be obtained from the measured C_m and G_m in strong accumulation region at sufficiently high frequency (f≥1 MHz), using the following equation.

$$R_s = \frac{G_{ma}}{G_{ma}^2 + (\omega C_{ma})^2} \quad (1)$$

where C_{ma} and G_{ma} represent the measured capacitance and conductance in strong accumulation region. In addition, the value R_s can be obtained from any bias voltage. Both the real and voltage dependence of R_s were calculated from Eq. (1) before and after irradiation and are given in Fig. 3. As can be seen from Fig. 3 the values of R_s increase with increasing radiation dose. Such behavior of R_s can be attributed to the particular distribution of interface states at M/S interface and their reordering and restructure under radiation effect.

In order to assess some main electrical parameters of Au/n-CdTe SBDs such as donor concentration N_D, Fermi energy level E_F, and barrier height Φ_B values, we drawn the C^{-2} vs V curves (Fig. 4) which were obtained from the reverse bias C-V data before and after irradiation. As can be seen in Fig. 4, C^{-2} vs V curves give a straight line in the wide bias region.

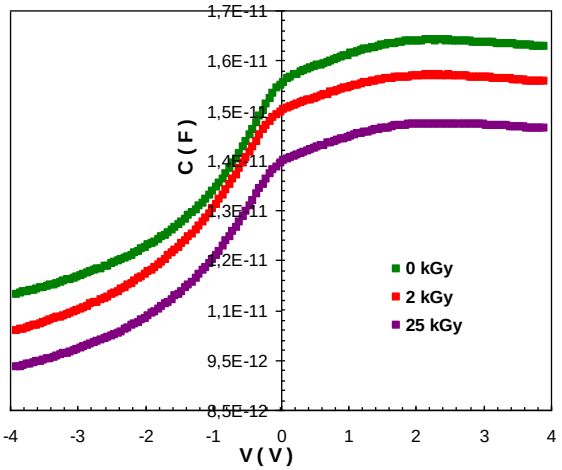

Fig.1. The irradiation dependent curves of the C-V characteristic of the Au/CdTe Schottky barrier diodes.

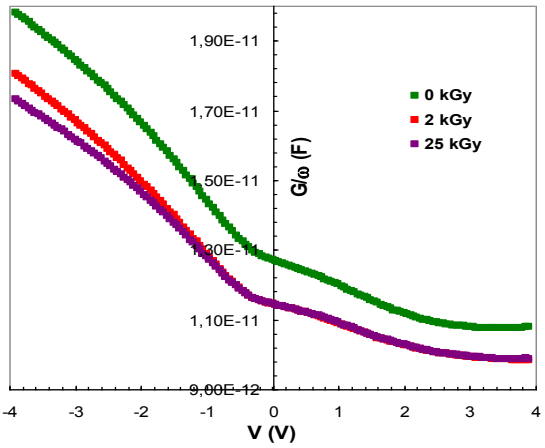

Fig.2. The irradiation dependent curves of G/ω-V characteristics of the Au/CdTe Schottky barrier diodes.

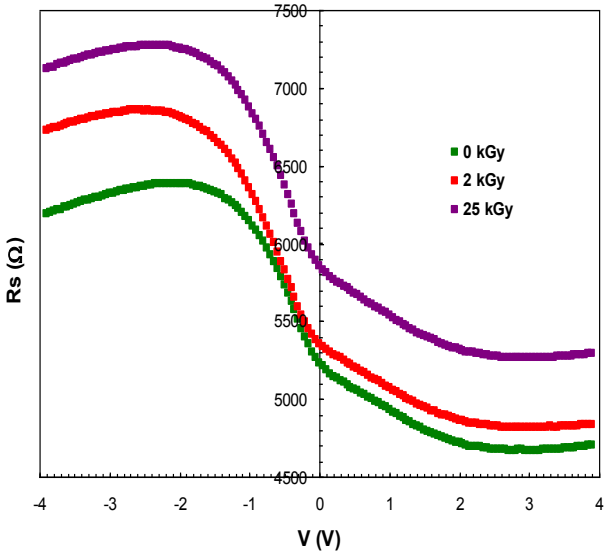

Fig.3. The irradiation dependence of series resistance as a function of bias voltage for the Au/CdTe Schottky barrier diodes.

The relation between C and V for the SBDs is given as [1,2].

$$C^{-2} = (2/qA^2\varepsilon_s N_d)(V_D - V - kT/q) \quad (2)$$

where V is the applied voltage across the diode, V_D is built-in voltage and the first term in Eq. (2) is the slope of the C^{-2} vs V curvet.

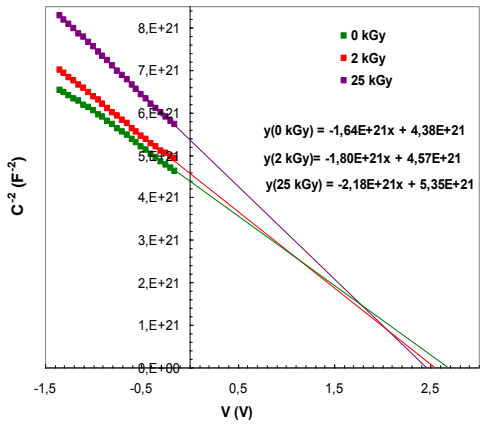

Fig.4. The C^{-2}-V curves of Au/CdTe Schottky barrier under various irradiation doses at room temperature

Table 1. The values of various parameters for Au/CdTe Schottky barrier diodes determined from C-V measurements under various doses.

	V_o (Volt)	N_D (cm^{-3})	E_F (eV)	Φ_B (eV)	R_s (kΩ)
0 kGy	2.671	$1.370x10^{14}$	0.220	0.835	4.706
2 kGy	2.539	$1.248x10^{14}$	0.222	0.755	4.845
25 kGy	2.454	$1.031x10^{14}$	0,227	0.652	5.298

The N_D value was obtained from the slope of C^{-2} vs V curve while the barrier height Φ_B (C-V) was obtained from the extrapolated intercept with the V-axis (V_D-kT/q) with aid of following equation as [1,2] and are given in Table 1.

$$\Phi_B(C-V) = V_0 + \frac{kT}{q} + E_F - \Delta\Phi_B = V_D + E_F - \Delta\Phi_B \quad (3)$$

The values of N_D and for Au/n-CdTe SBD were found as $1.370x10^{14}$ cm^{-3} and 0.835 eV before irradiation (0 kGy), and $1.031x10^{14}$ cm^{-3} and 0.652 eV after irradiation (25 kGy), respectively. It is clear that, these values were strongly dependent of radiation and decrease with increasing radiation. In conclusion, the magnitudes of radiation dose and series resistance are strongly influenced on the C-V and G/ω-V measurements and they must be taking into consideration in applications.

IV. CONCLUSIONS

The effect of ^{60}Co γ-ray irradiation and series resistance effect on the C-V and G/ω–V characteristics of Au/n-CdTe Schottky barrier diodes (SBDs) have been studied before and after irradiation. The SBDs were irradiated at doses up to 25 kGy at room temperature. In addition the main electrical parameters of the Au/n-CdTe SBD were found from the reverse bias C^{-2}-V plots. A decrease in C and G/ω due to the irradiation induced defects at the interface has been observed. The values of the barrier height (Φ_B) obtained from reverse bias C-V measurements and doping concentration (N_D) decrease with increasing radiation dose, whereas series resistance (R_s) increases. In addition, the voltage dependent series resistance (R_s) profile of Au/n-CdTe SBD was obtained from admittance-based measurement method of (C-V) and G/ω-V) before and after radiation.

[1]. *E.H. Rhoderick, R. H. Williams,* Metal Semiconductor Contacts 2nd Edn. (Clarendon Press: Oxford) (1988).

[2]. *S. M. Sze*, Physics of Semiconductor Devices 2nd Edn.(New York: Willey) (1981).

[3]. *C.A.Mead, W.G.Spitzer,* Phys. Rev.,134(1964)713.

[4]. *S. Krishan, G. Sanjeev, M. Pattabi,W. Mathew,* Solar Energy Mater. and Solar Cells ,93(2009) 2.

[5]. *G.A. Umana-Membreno, J.M. Dell, G. Parish, B.D. Nener, L. Faraone,* U.K. Mishra, IEEE Trans. Electron Dev., 50 (2003) 23.

[6]. *P.S. Winokur, J.M. McGarrity, H.E. Boesch*, IEEE Trans. Nucl. Sci. NS-23, (1976) 1580.

[7]. *P.S. Winokur, J.R. Schwank, P.J. McWhorter, P.V.Dressendorfer, D.C. Turpin*, IEEE Trans. Nucl. Sci. NS-31, (1984) 1453.

[8]. *T.P. Ma*, Semicond. Sci. Technol. 4, (1989) 1061.

[9]. *O. Tüzün, Ş. Altındal, Ş. Oktik*, Renewable Energy 33 (2008) 286.

[10]. *Ş. Karataş, A. Türüt, Ş. Altındal,* Radiation Phys. and Chem. 78 (2009) 130.

[11]. *S. Ashok, J. M. Borrego, R. J. Guttmann*, IEEE Trans. Electron. Nucl. Sci., 25 (6) (1978) 1473.

[12]. *M. Ashry, S. A. Fayek*, Renewable Energy 23 (2001) 441.

[13]. *M. Y. Feteha, M. Soliman, N. G. Gomaa, M. Ashry*, Renewable Energy 26 (2002) 113.

[14]. *A. Tataroğlu, M. H. Bölükdemir, G. Tanır, Ş.Altındal, M. M. Bülbül*, Nucl. Instr. And Meth. in Pysc. Res. B 254 (2007) 273.

[15]. *T. R. Oldham, F. B. McLean, H. E. Boesch Jr, J.M.McGarrity*, Semicond. Sci. Technol. 4 (1989)986.

[16]. *Tataroğlu A, Altındal Ş, M.M. Bülbül,* Microelectric Engineering 81, 140 (2005).

[17]. *G.A. Kaljuzhanya, T.S. Mamedov, K.H.Herrman, M. Wendt*, Kristall und Technik 14, 849 (1979).

[18]. *G.M. Guro, G.A. Kaljuzhanya, T.S. Mamedov, Shelepin* Sov. Phys. JETP 50, 1141 (1979)

[19]. *E.H. Nicollian, J.R. Brews*, MOS Physics and Technology, John Wiley & Sons, New York, 1982.

[20]. *S.K.Cheung, N.W.Cheung*, Appl. Phys. Lett., 49 (1986) 85

[21]. *H. Norde*, J. Appl. Phys., 50, 5052 (1979).

A NEW AVALANCHE PHOTODIODE WITH WIDE LINEARITY RANGE

Z.Y. SADYGOV[1,2], R.M. MUKHTAROV[3], A.A. DOVLATOV[1], N.A. SAFAROV[1]

[1] *Institute of Physics,*
AZ-1143 Baku, Azerbaijan

[2] *Joint Institute for Nuclear Research,*
141980, Dubna, Russia

[3] *National Academy of Aviation,*
AZ-1045, Baku, Azerbaijan

A new microchannel avalanche photodiode (MC APD) with gain up to 10^5 and linearity range improved an order of magnitude compared to known similar devices. A distinctive feature of the new device is a directly biased p-n junction under each pixel which plays role of an individual quenching resistor. This allows increasing pixel density up to 40000 per mm^2 and making entire device area sensitive.

In the last decade a significant success was achieved in development of micropixel avalanche photodiodes (MP APD) capable of detecting single photons at room temperature. The MP APD gain can reach values of 10^5–10^6 and photon detection efficiency 20-40 % in a wide wavelength range. It's parameters are comparable with those of vacuum photomultiplying tubes (PMT) [1, 2].

Basic design of such devices is described in papers [3, 4]. The device consists of an array of small p-n-junctions (pixels) with typical dimensions 10-100 μm created on the surface of silicon substrate. Pixels are placed with some gap between them in order to avoid charge cross-talk. Each pixel is connected with a common bias line by an individual film resistor with resistance 10^5–10^7 Ω.

Pixel area and resistance of the individual resistor are chosen so that within characteristic time of the pixel capacitance relaxation probability of dark charge carrier generation in the sensitive region was much smaller than one. This provides a possibility for MP APD pixels to operate in overvoltage mode, i.e. at potentials higher than breakdown voltage. A self-quenching avalanche with a constant charge value occurs in the pixel sensitive area then single photoelectron (or dark electron) is created in it. The avalanche is similar to the Geiger discharge. The avalanche in the pixel quenches due to potential drop on it below breakdown voltage. The individual film resistor prevents significant charge of the pixel from power supply during the avalanche process. Signals from fired pixels are added on a common load (bias line) what provides linearity of the device. Photo response of the device is linear until probability that two or more photons hit the same pixel reaches a significant value.

However the above mentioned MP APDs do not have wide enough linearity range because of low pixel density. Design of the device is such that significant part of its surface is occupied by bias line, film resistors, and guard rings at each pixel. For this reason increase of number of pixels over 1000 per mm^2 results in significant decrease of sensitive area necessary for photon detection. This in turn leads to decrease of photon detection efficiency (PDE) and as result to decrease of the device amplitude resolution [5].

This paper presents description of design and operation principle of microchannel avalanche photodiode (MC APD) with ultrahigh density of independent multiplication channels that provide for wide photo response linearity range. The distinguishing feature of the MC APD is that it does not have a common bias line and function of an individual quenching resistor is performed by directly biased p-n-junction located under each pixel. Design of the device is shown in Figure 1. The device consists of silicon substrate with n- type of conduction on the surface of which two 4 μm deep epitaxial layers with the same specific resistance of 7 Ω·cm are grown. An array of highly doped regions with n^+-type of conduction with a step from 5 to 15 μm, depending on implementation, is formed between the epitaxial layers. This provides for increase in pixel density up to 40000 channels per mm^2 and makes entire device surface sensitive. Technology of the MC APD manufacturing is described in [6].

In the operation mode negative relative to the substrate voltage is applied to the MC APD. Depletion of the device starts at the first p-n-junction located between the first epitaxial layer and the substrate. At certain voltage value the depletion reaches the array of n^+-regions and partly opens the second p-n-junction located there. After that depletion only the third p-n-junction located between the array of n^+-regions and the second epitaxial layer begins. Subsequent increase of the voltage leads to full depletion of the second epitaxial layer. As a result of this an array of potential wells in the n^+-regions is initiated in the MC APD depleted region. Above each n^+-region there is semispherical electric field that provides for charge collection from the sensitive area of the pixel. Therefore the sensitive area of the device is divided into photosensitive regions with separate multiplication microchannels independent from each other.

Avalanche multiplication of charge carriers takes place in the border region of the second epitaxial layer with n^+-regions where high electric field is created. Created in a process of multiplication electrons are accumulated in the potential wells within the n^+- regions. This leads to decrease of electric field in the second epitaxial layer below

some threshold level. As a result avalanche in given channel quenches. Recovery of the original field in the multiplication microchannel is a result of charge leakage into the substrate through the directly biased p-n-junction between the first epitaxial layer and n^+-region.

Photoelectron collection in the n^+-regions can be investigated at small bias voltages on the device when there is no amplification of the photoresponse.

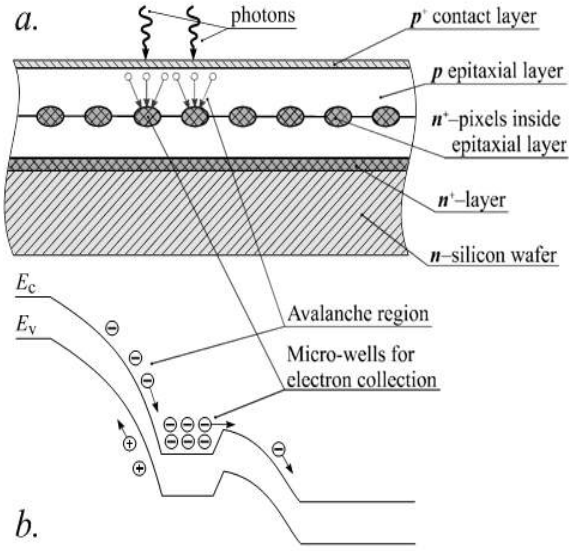

Fig.1. MC APD cross-section (a) and energy zone diagram (b) then bias voltage is applied.

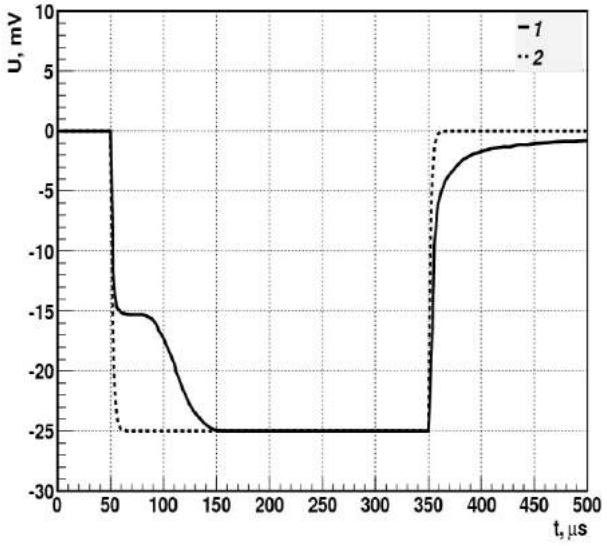

Fig.2. Oscilloscope picture of MC APD (1) and regular APD (2) photoresponse to 300 μs long light pulses. Applied voltage was equal to 20 V and gain was equal to 1.

The MC APD sample under investigation was produced by Zecotek Photonics Inc. and had = $1{,}35 \cdot 10^5$ multiplication channels on the 3×3 mm^2 sensitive area ($1{,}5 \cdot 10^4$ channels per mm^2). Figure 2 shows an oscilloscope picture of the MC APD photo response to 300 μs long light pulses (curve 1). The signal was read out from 5 kΩ load resistor. For comparison in the same picture a response from regular APD without n^+-regions is shown (curve 1). The APD was manufactured parallel to MC APD in the same technological conditions. A light emitting diode (LED) with 450 nm wavelength was used as a light source. Light was completely absorbed in the top part of the second epitaxial layer, i.e. before the depth of the n^+-regions location.

In the beginning photoelectrons created photocurrent passing through the second epitaxial layer. Then they were collected in the potential wells causing appearance of a plateau on curve 1 of Figure 2. After some time defined by the light intensity the potential wells were filled and the photoresponse amplitude grew to its maximum which was equal to amplitude of the regular APD. Total charge collected in all potential wells of the device can be determined as an area (integral) of the difference between two curves 1 and 2 in the front part of signals. After graphical integration the total charge $Q_{tot}=1{,}1 \cdot 10^{-10}$ C was obtained. This means that in each n^+-region potential well charge equal to $Q_p=Q_{tot}/N_p=8 \cdot 10^{-16}$ C was collected (about $5 \cdot 10^3$ photoelectrons). This charge provides for electric field screening in the second epitaxial layer, i.e. in the avalanche region. This leads to the avalanche quenching then device operates in avalanche mode.

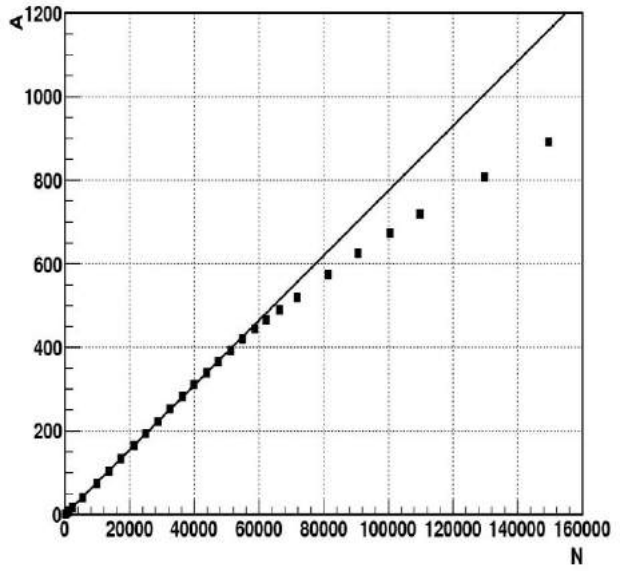

Fig.3. Dependence of MC APD photoresponse amplitude A (in relative units) on a number of incident photons N.

In order to investigate the MC APD photoresponse linearity an operating voltage 90 V was applied to the device. Gain at this voltage was equal to $5 \cdot 10^4$ and photon detection efficiency was equal to 25 %. The device was illuminated with 30 ns long light pulses with 450 nm wavelength and 1 kHz frequency. Hamamatsu S8664-55 APD with known spectral sensitivity was used at gain value equal to one to determine a number of photons in the light pulse. Result of the MC APD photoresponse linearity measurement is shown in Figure 3. One can see that amplitude of the MC APD photoresponse is linear up to $6 \cdot 10^4$ photons in the pulse.

Therefore, new supersensitive avalanche photodiode with high gain and wide photoresponse

linearity range was designed and produced. Such a device can be used as light detector in equipment which requires high amplitude resolution, especially in high energy physics and nuclear medicine. The photodiodes were used recently in electromagnetic calorimeter prototypes [7].

---

[1]. *N.Anfimov et al.,* Nucl. Instr. and Meth., A572, (2007), 413.

[2]. *D.Renker, E.Lorenz.*, Journal of Instrumentation, 4, (2009), 04004.

[3]. *Z.Ya.Sadygov*, Russian Patent № 2102820, priority from 10.10.1996.

[4]. *Z.Sadygov et al.,* Nucl. Instr. and Meth. A567, (2006), 70.

[5]. *A.Stoykov et al.,* Journal of Instrumentation, 2, (2007), 06005.

[6]. *Z.Ya. Sadygov*, Russian Patent № 2316848, priority from 01.06.2006.

[7]. *I. Chirikov-Zorin et al.*, Beam Test of Shashlyk EM Calorimeter Prototypes Readout by Novel MAPD with Super High Linearity. Frontier Detectors for Frontier Physics. XI Pisa Meeting on Advanced Detectors La Biodola, Isola d'Elba, Italy, May 26-30, 2009.

ACOUSTIC-PHOTOVOLTAIC EFFECT IN $TlIn_{1-x}Gd_xSe_2$ (x=0; 0.02) SINGLE CRYSTALS

E.M.GODZHAEV, A.M.NAZAROV*, H.S.KHALILOVA, B.SH.BARKHALOV*, L.P.ALIEV**

Azerbaijan Technical University,
AZ1073, H.Javid av. 25, Baku, Azerbaijan Republic
**Institute of Physics of the Azerbaijan National Academy of Sciences*
AZ1143, H.Javid av. 33, Baku, Azerbaijan Republic
***Baku State University,*
AZ1148, Z.Khalilov str. 23, Baku, Azerbaijan Republic
E-mail: afinnazarov@yahoo.com

In the paper it is revealed and investigated acoustic-photovoltaic effect arising at simultaneous influence of electromagnetic radiation and sound waves in $TlIn_{1-x}Gd_xSe_2$ (x=0; 0.02) single crystal.

At research of photo-electric features of $TlInSe_2$ single crystals and solid solutions on its basis the physical effects consisting in occurrence of the electromotive force on the ends of the focused homogeneous non-piezoelectric crystal under action of the uniform electromagnetic radiation (visible, IR and X-ray) owing to action on it sound waves and polarity and area of which spectral sensitivity precisely coped, in particular, frequency of a sound [1].

The similar effect has been found out on $TlIn_{1-x}Gd_xSe_2$ (x=0; 0.02) single crystals. Single crystalline plates of thickness 0.2-0.5 mm and width 1.0 ÷ 1.5 mm prepared from $TlIn_{1-x}Gd_xSe_2$ crystals with two symmetric ohmic separated electrodes through short rigid acoustic contact were established on a radiator of sound waves. At an irradiation by electromagnetic radiation in absence of the effect of the sound waves was absent also appreciable e.m.f. on electrodes the same as in darkness at influence of the sound. However at simultaneous effect of light and sound waves of 100 to 107 Hz essential e.m.f appears on electrodes or a direct current at their short circuit. Value of the originated acoustic-photovoltaic (APV) e.m.f. depends on intensity and spectral composition of light, as well as on the frequency and amplitude of the sound, and can be come to naught by absolute blackout of the crystal or removal of the acoustic waves. For various samples at amplitude of a voltage of the acoustic transmitter 10 V and light exposure 1000 lx maximal e.m.f. varied in limits from 1.0 to 12 V. Observable thus APV- e.m.f. according to the results of researches spent to the present time shows also other specific features distinguishing it from other known photo-voltaic phenomena. For example, at constant illumination by white light with change of frequency of acoustic waves in a direction of its increase periodic inversion of the sign of total APV-e.m.f. took place. Unique feature possesses spectral dependence of the given effect: as against widely known photo-voltaic effects the form and character of spectral dependence of the short circuit current are controlled by power and frequency of mutual orientation of crystallographic axes of the material and external waves effect on it, as well as the size of inter-electrode distances, by the variation of the above mentioned factors it is possible to give a spectrum of the same crystal the set selective character (Fig.1, a,b).

We note that inverse points observed by us on spectral characteristics for $TlIn_{1-x}Gd_xSe_2$ crystals are characteristic points at which the material does not react at all to light quanta of the given energy and does not perceive a sound with the given frequency, i.e. the crystal in the specified points "does not see" and "does not hear" - "is blind and deaf". In other sites of the spectrum, especially in a maximum of photosensitivity, crystals possess high sensitivity as to perception of the sound. As an obligatory condition for generating of e.m.f. is simultaneous effect of the light and the sound on the crystal, then developed on these principle "visual" and "acoustical" devices should possess unique features, namely "see" only at occurrence of the sound and on the contrary "to hear" at presence of illumination and to be "deaf device" in the absence of the light.

The mechanism of some features of the found out by us APV effect, most likely, is connected to resonant excitation integrated independent (loosely coupled) anion radicals in corresponding specific $TlIn_{1-x}Gd_xSe_2$ crystals by electrostatic induction or the non-uniform elastic deformation, leading to re-charging of the corresponding surfaces at the sound frequency. On the same frequency, probably, a modulation of surface states occurs. The lagging behind the modulation frequency minority charge carriers generated by light, collect at a corresponding surface and result in occurrence observable APV-effect. At validity of the similar mechanism, frequency dependence of the effect should highly sensitive to surface condition and recombination centers existing in the crystal.

We shall note that the effect found out by us in $TlIn_{1-x}Gd_xSe_2$ crystals can find wide technical application in a hydrolocation, underwater communication lines, optical switches, frequency discriminators of the optical range, and also as basic new types of controlled selective receivers of radiation.

Observed APV effect can be considered in part as a change of the known acoustoelectric effect under action of light. The physical essence of the given effect consists in occurrence of the e.m.f. in the semiconductor owing to increase in density of the charge carriers by an elastic wave. As follows from [2] in the range of low frequencies of the sound wave, i.e. at $q\ell = \frac{\omega_s}{\vartheta_s}\ell << 1$, where ω_s and υ_s are frequency and speed of the sound wave,

$\ell = \vartheta_T \tau = 10^{-6}$ cm - the length of free path for charge carriers, owing to entering by virtue of a quantum-mechanical parity of uncertainty, loses sense the interaction between individual electrons and approach of collisionless plasma lose significance.

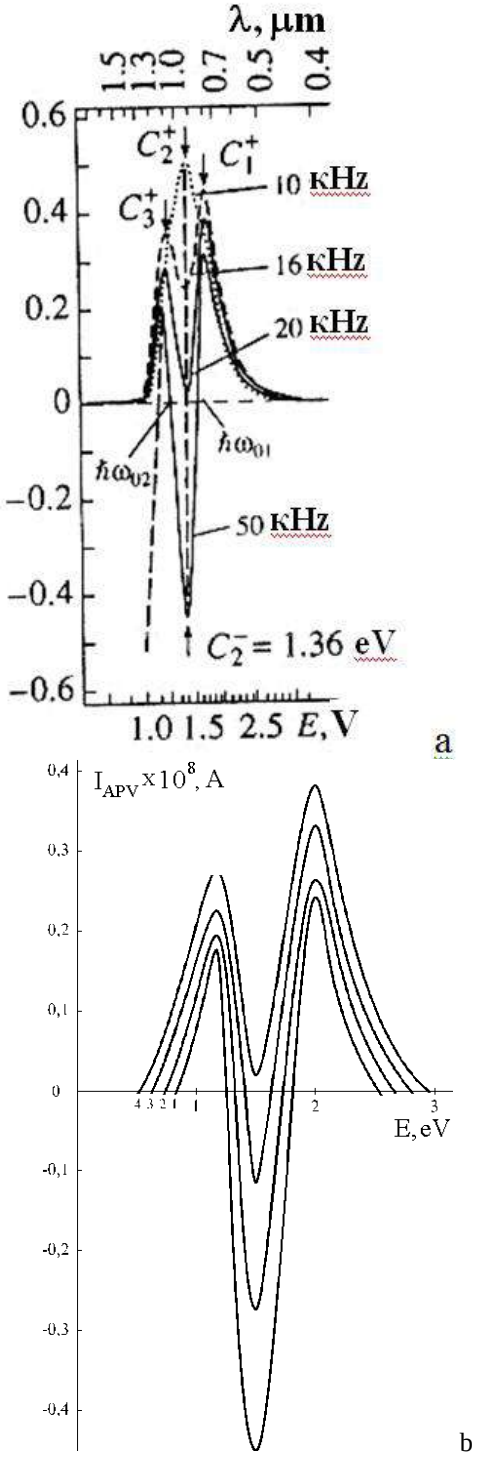

*Fig.1.*Spectral distribution of the short-circuited current of the acousto-photo-voltaic effect at different frequencies in $TlIn_{1-x}Gd_xSe_2$ single crystals: a) x=0, b) x=0.02 (1-50 кHz; 2-40 кHz; 3-30 кHz; 4-20 кHz)

Processes here get collective character and with a sound wave as an elastic wave in continuum interact clots of the space charge. Expressions for acoustoelectric e.m.f. here it is possible to receive directly from a parity between intensity of a wave, i.e. density of energy flow ω_s and mechanical pulse $\vec{P}$ transferred by it :

$$\vec{P} = \frac{\omega_s}{\vartheta_s} q_0 \tag{1}$$

where υ_s is a speed of the sound, $\vec{q}_0$ an unit vector in a direction of the sound wave. As a result of the absorption of an elastic wave its pulse is transferred to conductivity electrons (holes) that results in occurrence of some average (outside) force acting on electrons and dragging them in a direction of distribution of a wave. Absorbed energy of a crystal in a thin layer d_k with unit area perpendicular to $\vec{q}_0$ for a unit time will make $\gamma\omega_s d_s$ (γ is the absorption factor that according to (1) corresponds to receive pulse $\frac{\gamma\omega_s dx}{\vartheta}\vec{q}_0$. If to equate this pulse to the force acting on $n_0 dx$ electrons inside of the layer, we shall receive: $-e\varepsilon_n^* n_0 dx = \frac{\gamma\omega_s dx}{\upsilon}\vec{q}_0$, where intensity of the outside forces field:

$$\varepsilon_n^* = -\frac{\gamma\omega_s}{en_0\vartheta}\vec{q}_0 \tag{2}$$

Arising full e.m.f. at the end of the electronic semiconductor plate with a length d will be equal:

$$V_{a.e}^T(n_0) = -\int_\nu^d \varepsilon_n dx = -\frac{\gamma\omega_s}{en_0\vartheta} d = -\frac{\gamma\mu_n\omega_s}{\sigma_n^T\vartheta}\cdot d \tag{3}$$

For a case of purely hole conductivity similar to photosensitivity, positive holes under the same conditions being dragging also in a direction of distribution of a sound wave will create e.m.f. of the opposite sign

$$V_{a.e}^T(P_0) = -\frac{\mu_p\gamma\omega_s}{\sigma_p^T}\cdot d \tag{4}$$

And for a case of mixed conductivity total e.m.f. will be

$$V_{a.э}^T(n_0, P_0) = \frac{\gamma\omega_э}{\vartheta}\left(\frac{\mu_p}{\sigma_p^T} - \frac{\mu_n}{\sigma_n^T}\right)\cdot d \tag{5}$$

Thus, depending on prevailing type of conductivity controlled, in particular, by intensity and spectral distribution of light acting on the crystal, observable thus total e.m.f. (and corresponding short circuit current) can have both positive and a negative sign. Inversion of a sign having a place on spectral dependence of the short circuit current of the APV- effect partly can be caused also by this reason.

As researched crystals $TlIn_{0.98}Pr_{0.02}Se_2$ mainly have hole conductivity at first we shall be limited to consideration of a case with the given type of conductivity.

APV-effect caused by change of acoustoelectric effect under action of light. can be presented as:

$$V_{apv}(P) = V_{ae}^{e}(P) - V_{ae}^{T}(P_0) = -\frac{\mu_p \gamma \omega_a \cdot d}{\vartheta} \cdot \frac{\sigma_p^L - \sigma_p^D}{\sigma_p^D \cdot \sigma_p^L}$$

where indexes "L" and "D" correspond to light and darkness. Taking into account, that

$$V_{ae}^{T}(P_0) = \frac{\mu_p \omega_a}{\vartheta \sigma_p^D} \cdot d \qquad (6)$$

and

$$\Delta\sigma_{LD}(\hbar\omega_c) = \sigma_P^L - \sigma_p^D \,, \qquad (7)$$

we shall obtain

$$V_{apv}(P) = -V_{ae}^{T}(P_0) \cdot \frac{\Delta\sigma_{LD}(\Delta P)}{\sigma_p^L(P)} \qquad (8)$$

Hence, APV e.m.f. at such consideration is opposite on a sign to acoustoelectric one in darkness V_{ae}^{T} and will not exceed it on absolute value, since in practice always

$$\frac{\Delta\sigma_{e_D}}{\sigma_P^e(P)} \le 1$$

.

On a sign they coincide in extremely rare cases, at presence of negative conductivity, i.e. $\Delta\sigma_{LD}(\hbar\omega_L) < 0$.

It is necessary to emphasize that at simultaneous acting of light and a sound on the end of the crystal should occur addition of two opposite e.m.f., (5) equations (5) and (7) crystals i.e.:

$$V_{ae}^{L}(P) = \frac{\gamma\omega_s d}{\upsilon} \cdot \frac{\mu_p}{\sigma_p^L} = \frac{\gamma\omega_s d}{e\upsilon} \cdot \frac{1}{P_0 + \Delta P} = V_{ae}^{T}(P_0) \cdot \frac{P_0}{P_0 + \Delta P} \,, \qquad (9)$$

here as it is usual, $\Delta P = \Delta P(\hbar\omega_L) > 0$ in all the investigated spectral range. In a considered spectral range for crystals $TlIn_{0.9}8Gd_{0.02}Se_2$ intrinsic photoconductivity prevails. Therefore, it is necessary to take into account thus also e.m.f. with the opposite polarity, caused by presence of electrons in the crystal:

$$V_{ae}^{L}(n) = -\frac{\gamma\omega_s d}{\upsilon} \cdot \frac{\mu_n}{\sigma_n^L(p)} = \frac{\gamma\omega_s d}{e\upsilon} \cdot \frac{1}{n_0 + \Delta n} = V_{ae}^{T}(n_0) \cdot \frac{\Delta n}{n_0 + \Delta n} \qquad (10)$$

Total e.m.s. consisting of two photons energy dependent components in (5) of an opposite sign, determining character of spectral dependence of the short circuit current, it is possible to present so:

$$V_{ae}^{L}(n,P) = V_{ae}^{e}(n) + V_{ae}^{L}(P) = \frac{\gamma\omega_s \cdot d}{e\vartheta} \left(\frac{1}{P_0 + \Delta P} - \frac{1}{n_0 + \Delta n} \right)$$

or

$$V_{ae}^{L}(n,P) == \frac{\gamma\omega_s \cdot d}{e\vartheta} \cdot \frac{1}{P_0 + \Delta P} \left(1 - \frac{P_0 + \Delta P}{n_0 + \Delta n} \right) , \qquad (11)$$

where p_0 also n_0 concentration of dark holes and electrons, Δp and Δn are a share of excited by light holes and electrons have time ($\tau_{n,p} >> 1/\omega_s$) to interact with an elastic wave of a sound of the given frequency (ω_s).

The measured on experiment short circuit current created by electromotive force $V_{ae}^{L}(n,P)$ according to (11) is:

$$J_{apv} = -\frac{V_{ae}(n,p)}{d} \cdot \sigma^L(n,p) = \qquad (12)$$
$$= \frac{\gamma\omega_s}{\upsilon} \mu_n \left(1 + \frac{p_0 + \Delta p}{n_0 + \Delta n} \cdot \frac{\mu_p}{\mu_n} \right) \cdot \left(\frac{n_0 + \Delta n}{p_0 + \Delta p} - 1 \right)$$

Spectral dependence $J_{apv}(\hbar\omega_L)$ thus will be defined by change of non-equilibrium charge carriers with photons energy, with dependences $\Delta n(\hbar\omega_L)$ and $\Delta p(\hbar\omega_L)$. According to (12) total short circuit current (SCC) consists, actually, from two components with opposite polarity. Depending on spectral area falling light parities of absolute values of the specified components can change, as will involve behind itself inversion of the sign on SCC spectrum. According to (12) in sites of a spectrum, where $n_0 + \Delta n(\hbar\omega_0) > p_0 + \Delta p(\hbar\omega_0)_{SCC}$, APV- effect should have a negative sign ($J_{apv} < 0$), and in sites, where $n_0 + \Delta n < p_0 + \Delta p$ must have a positive sign ($J_{apv} > 0$). In the range of a spectrum where $n_0 + \Delta n \approx p_0 + \Delta p$ counter-polar components compensate each other and the total current tends to zero ($J_{ap\phi в} \approx 0$). Last situation is realized, as a rule, in the field of intrinsic conductivity ($\hbar\omega_L^{\max} \approx 1.31\, eV$ for $TlIn_{0.98}Gd_{0.02}Se_2$) non-equilibrium charge carriers of both types considerably exceed equilibrium values $\Delta n >> n_0$ and $\Delta p >> p_1$ and number created non-equilibrium electrons and holes thus it appears approximately identical: $\Delta n(\hbar\omega_L^{\max}) \approx \Delta p(\hbar\omega_L^{\max})$. Hence, SCC at $\hbar\omega_L^{\max}$ should trend to zero.

However, as follows from figure, the maximum of the intrinsic photoconductivity in spectral dependence $J_{apv}(\hbar\omega_0)$ most vulnerable and sensitive point for controlling its value with a change of frequency and power of the sound and inter-electrode distances. Marked high sensitivity of APV-effect in the point $\hbar\omega_L = \hbar\omega_L^{\max}$ probably is caused by that circumstance that in the given point its positive and negative components are counterbalanced among themselves only in specific case

when there is no neither time, nor dimensional restrictions for carriers of both types .

Frequency restrictions for electrons and holes, in particular, are defined by conditions $\tau_n >> \tau_s (\omega_s \tau_n >> 1)$ и $\tau_p >> \tau_s (\omega_s \tau_p >> 1)$, where $\omega_s = q_s \upsilon$.

As electrons and holes lifetimes for $TlIn_{0.98}Gd_{0.02}Se_2$ appreciably differ, then by variation of the frequency it is possible to achieve restriction of participation of electrons (occurrence $J_{apv}>0$), or holes $J_{apv}<0$ in formation SCC of the APV-effect $\hbar\omega_L = \hbar\omega_L^{\max}$ =1.31 eV. Probably, for this reason the peak at $\hbar\omega_L = \hbar\omega_L^{\max}$ for $TlIn_{0.98}Gd_{0.02}Se_2$ with other things being equal depending on change of the sound frequency is sharply displaced on a vertical both to positive and a negative scale of J_{apv}.

---

[1]. *E. M. Godzhaev, E. A. Allakhyarov, V.D.Rustamov, A.M.Nazarov, G. S. Dzhafarova* "Synthesis, growth and investigation of acousto-photo-voltaic effect in $TlIn_{1-x}Pr_xSe_2$ and $TlIn_{1-x}Pr_xTe_2$ single crystals", *Inorganic materials.*, v. 40, **9**, pp. 1054-1059, 2004 (in Russian).

[2]. *V. A. Grinberg, S. A. Saddullaeva, L. V. Urod* "Acousto-photoelectric effect under photoionization of impurity centers", *FTP*, v. 9, **12**, pp. 2329-2333, 1975 (in Russian)

LASER FREQUENCY STABILIZATION ON SUB-DOPPLER RESONANCES IN THIN GAS CELLS

A. Ch. IZMAILOV
Institute of Physics, Azerbaijan National Academy of Sciences,
H. Javid av. 33, Baku, Az-1143, AZERBAIJAN
e-mail: azad57@mail.ru

This paper is the brief review on the laser frequency stabilization methods by means of sub-Doppler absorption and fluorescence resonances (on centers of quantum transitions), which arise because of the specific optical selection of comparatively slow-speed atoms (or molecules) in a thin cell with a rarefied gas. We consider two following mechanisms of such a velocity selection of atomic particles connected with their flight durations between walls of the thin cell: (1) optical pumping of sublevels of the ground atomic (molecular) term and (2) optical excitation of long-lived (metastable) quantum levels.

1. INTRODUCTION

Optical frequency standards are widely used in the high resolution spectroscopy, precision physical experiments, metrology, location, geophysics, communication, space research, and are necessary for construction of optical clocks with the time scale [1].

For creation of the optical frequency standard (that is the laser with the high stable frequency), the reference is necessary, to which the laser frequency is tied. Comparatively narrow spectral lines of atomic or molecular gas are the most suitable for this purpose. The broadening of these lines, connected with moving of atomic particles, is the main reason, which restricts the high frequency stability. Removal of such a Doppler broadening is achieved by methods of high-resolution laser spectroscopy [2], which are based on the velocity selection of atomic particles on quantum levels of the transition resonant with the laser field.

This paper presents brief review on laser frequency stabilization methods by means of the recently elaborated sub-Doppler spectroscopy in thin gas cells. The characteristic transverse size D in such a cell is much greater than its inner thickness L. Sub-Doppler resonances are caused by the velocity selection of atomic particles in definite light-induced quantum states, which are destroyed at atomic collisions with cell walls.

2. OPTICAL PUMPING SUB-DOPPLER RESONANCES

In 1992-1993 methods of the sub-Doppler laser spectroscopy were theoretically suggested, which were based on the stationary optical pumping of the atomic ground term during transits of atoms of a rarefied gas between walls of a thin gas cell [3,4]. Later given methods were successfully realized at experiments for the precision spectral analysis of atoms [5-10] and for the laser frequency stabilization [10-13] on the basis of thin cells (with various inner thicknesses from 10 μm to 10 mm) containing *Cs* [5-9, 11-13] or *Rb* [10] vapors. The paper [14] presents the review of achievements of this direction of the high-resolution spectroscopy (up to 2006). In particular, the effective spectroscopy method was theoretically elaborated with different pumping and probe light beams which may travel even in orthogonal directions [4]. Indeed, let us assume, that atoms (or molecules) of a rarefied gas to be pumped throughout of the thin cell by the broadband radiation (fig.1). Then populations of the long-lived levels of particles will relax to their equilibrium values primarily in collisions with the cell walls. Such a process is determined by the wall-to-wall transit time $\tau = l/|v_z|$, where v_z is the particle velocity component along the cell. The optical pumping of particles will be efficient if

$$W \cdot l \geq |v_z|, \qquad (1)$$

where W is the probability (in the unit time) of a population redistribution among the long-lived particle quantum states through the light-induced excitation from these states with a subsequent radiative decay of the excited levels. Thus the transit time effects in a gas cell can be used to produce a nonequilibrium distribution of particles on the velocity component v_z for long-lived quantum states in the region of sufficiently small values $|v_z|$ defined by Eq.(1). Under certain conditions, this nonequilibrium distribution will create sub-Doppler resonances in frequency dependences of absorption (dispersion) of the probe radiation in the gas medium and of its induced fluorescence. Indeed we assume that the optically pumped gas medium under consideration to be probed along the cell by a traveling monochromatic wave with the frequency ω and the wave vector $\boldsymbol{k}$ (fig.1). We also assume that this wave induces the direct n-quantum (n≥1) transition $a \leftrightarrow c$ to an excited level c from a long-lived state a, where the pump radiation drives an dipole transition $a \leftrightarrow b$ (fig.2) so that the atomic velocity projection v on the wave vector $\boldsymbol{k}$ satisfies condition (1).

According to the Doppler effect, the probe wave is efficiently absorbed by particles whose velocity projections v_z satisfy the relationship:

$$|\delta - nkv_z| \leq \gamma, \qquad (2)$$

where $k=|\boldsymbol{k}|$, $\delta=(n\cdot\omega-\omega_0)$ is the frequency detuning with respect to the n-quantum resonance transition $a \leftrightarrow c$, which is characterized by the central frequency ω_0 and the homogeneous spectral line half-width γ (substantially smaller than the corresponding Doppler broadening). We can see from Eqs.(1) and (2), that at sufficiently low pumping intensity, when $W\, l \leq \gamma/(kn)$, the probe wave efficiently interacts with particles having a nonequilibrium velocity distribution in the state a only at small frequency detuning $|\delta| \leq \gamma$. Hence the amplitude and

polarization characteristics of the wave and also fluorescence of the excited state *c* (versus the detuning δ) may exhibit Doppler-free resonances in the region $|\delta| \le \gamma$. It is important that such narrow resonances in the absorption of the probe beam may be observed directly by the record of the difference between signals with and without pumping radiation (fig.1).

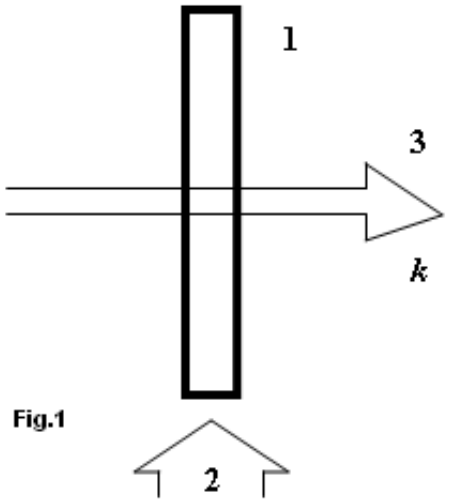

Fig.1

Fig.1. Scheme of the pump-probe method: {1} is the gas cell, {2} is the pumping radiation, {3} is the monochromatic probe wave.

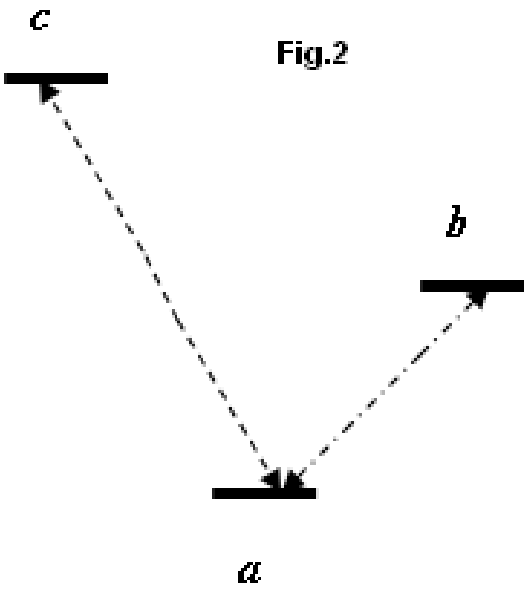

Fig.2

Fig.2. Diagram of atomic levels and transitions: $a \leftrightarrow b$ is the pumping transition, $a \leftrightarrow c$ is the n-quantum probe transition from the long-lived state *a.*

Later given method of sub-Doppler spectroscopy was realized at experiments by Japanese scientists [7-12]. At first two independent laser beams were used for optical pumping and probing traveling in orthogonal directions [7,11]. As a result, a hyperfine-resolved sub-Doppler spectrum of the D line of the cesium was observed even with a 10-mm cell (having the inner diameter 34 mm). In particular the effective frequency stabilization of a diode laser was achieved on the hyperfine component of the *Cs* D line using the elaborated spectroscopic method [11].

Then the more simple and convenient experimental configuration was realized, where a single laser beam, split into two paths, pumps and probes atoms in perpendicular directions [8]. In this case hyperfine components of the *Cs* D line also were clearly resolved in a series of glass cells with thicknesses from 0.5 mm to 5 mm. Later a novel method of stabilizing laser frequency was developed on the basis of this new experimental configuration with use of recorded sub-Doppler spectrum of *Cs* atoms [12]. Thus the extended-cavity diode laser was frequency locked to a hyperfine component of the $Cs\ D_2$ line. The line width and the signal-to noise ratio of the *Cs* spectrum were systematically investigated to find a cell inner thickness *L* that gave best long-term stability. In the Allan-variance measurements on the beat note between two lasers thus stabilized, a frequency stability of 6.2×10^{-11} was achieved at an averaging time of 5s for the cell thickness *L*=5mm. Corresponding sub-Doppler resonances were clearly observed even at quite low pumping intensity of $100\,\mu W / cm^2$.

In work [9], we continue the analysis of the potential of this spectroscopic method. In particular sub-Doppler resonances were observed not only in absorption of the probe wave but also in the fluorescence of the *Cs* vapor. Moreover, unlike paper [8], we used the frequency modulation technique for recording the first and third frequency derivatives of the absorption (transmission) spectrum. As a result, the Doppler-broadened background was essentially reduced and interesting features of narrow nonlinear absorption resonances were revealed, which may be used for an optimization of the laser frequency stabilization.

Afterwards dichroic-atomic-vapor laser lock method was successfully realized for the sub-Doppler spectroscopy and frequency stabilization in the thin (1mm-long) *Rb* vapor cell [10].

As was shown in the theoretical paper [15] on example of sufficiently simple model, the resolution of sub-Doppler spectroscopy in thin gas cells may be essentially risen by means of the definite spatial separation of pump and probe radiations. Later Japanese scientists confirmed the essential narrowing of the absorption sub-Doppler resonances by the spatial separation of unidirectional pump and probe laser beams in experiments with the 1mm-long *Rb* vapor cell [16].

Moreover these scientists suggested and realized the new method of sub-Doppler spectroscopy (with the same *Rb* cell), based on the starting optical pumping of the ground *Rb* term by the pulse of the monochromatic radiation [16]. In the definite time *t* after the action of this pulse, the vapor cell was probed by the comparatively weak light pulse with the same frequency and direction (from the same diode laser). Thus authors of the paper [16] have revealed the contribution of comparatively slow-speed atoms with the pumped ground term, which had not time to undergo collisions with walls of the thin cell during the time *t*. Therefore, by means of the controllable change of the delay time between pumping

and probe pulses, narrow sub-Doppler absorption resonances were recorded on centers of resonance atomic transitions at the scanning of the laser radiation frequency.

Unlike the saturated absorption spectroscopy [2], noted methods of sub-Doppler spectroscopy in thin gas cells avoid crossover resonances and corresponding stabilization systems are much less affected by frequency fluctuations of the pumping radiation because the velocity selection of optically pumped atoms originates from the cell geometry. Really, a collection of optically pumped atoms (molecules) in the thin cell is the compact analog of the atomic (molecular) beam. The divergence of such a beam is determined, in particular, by the small ratio $L/D<<1$ of the cell inner thickness L to its transversal dimension D [4 -16].

It is important also to note, that light shifts of quantum levels of the resonance transition essentially restrict the laser frequency stability on nonlinear resonances characteristic, in particular, for the saturated absorption spectroscopy [1,2]. However it is possible to decrease essentially such light shifts by the spatial or temporal separation of the pump radiation from the weak probe beam in thin gas cells.

3. SUB-DOPPLER RESONANCES ON FORBIDDEN OPTICAL TRANSITIONS

Mentioned (in the previous chapter 2) resonances are direct manifestations of the radiative relaxation of excited quantum levels. At the same time it is interesting to analyze sub-Doppler spectral structures caused as an effect of velocity selection of atoms (or molecules) when the radiative damping of quantum states is negligible in comparison with their relaxation due to the atomic (or molecular) collisions with the cell walls. This may take place for many atoms and molecules, if the laser radiation is resonant with a forbidden transition that connects a sublevel of the ground state to a sufficiently long-lived (metastable) level. Indeed, the radiative lifetime of such excited levels may be much longer than the free flight time ($10^{-3} - 10^{-5}$ s) of atoms (molecules) in a rarefied gas, moving at the thermal speed u in a cell with a transversal dimension D of the order of some centimeters. The collisions against the cell walls interrupt the interaction between such an atom and the resonant radiation. Thus, in the gas cell with a small inner thickness $L<<D$, only atoms with a sufficiently small longitudinal velocity component $|v_z|<(L/D)u<<u$ can interact with the laser beam for a long enough to be efficiently excited to the metastable level [17]. As a consequence, the contribution of the Doppler broadening to the width of the spectral resonance will be reduced roughly by a factor D/L which can be very large ($\sim 10^4$). This effect may be exploited both for high-resolution spectroscopy and for laser frequency stabilization. In the paper [17] we theoretically investigated this process of atomic velocity selection on long-lived excited quantum level in a thin cell when the atomic sample was irradiated (in the normal direction) by a resonance monochromatic laser beam having the ring-shaped cross-section (fig.3). It should be possible to detect sub-Doppler resonances simply monitoring the fluorescence due to the radiative decay of the metastable atoms in the central black region of the annular laser beam (fig.3). However, the fluorescence intensity will be quite low, and signal-to noise ratio will be quite poor, also for the unavoidable background due to the light scattered from the pumping beam.

More efficient schemes, valid also for transitions with very long metastable level lifetime, are possible, by using a second probe laser, which is resonant with a transition leaving from the metastable level. It is convenient to direct this additional radiation coaxially to the pumping beam inside the central dark hole (the region with a radius r_1 in fig.3). With this geometry, due to the spatial separation of the pump and the probe light fields in the cell, the probe radiation will not contribute to light–shift of the clock transition, nor will affect on the optical velocity selection of metastable atoms induced by the pumping beam. The number of collected fluorescence photons is then simply limited by the diffusion rate of metastable atoms inside the detection volume ($\approx u/r_1$). Moreover, it is possible in this scheme to use a phase sensitive detection technique by frequency modulating the pumping beam, allowing the discrimination of the fluorescence photons from the scattered ones. A large suppression of the background radiation can be obtained, if a probe transition is chosen that produces fluorescence mostly on a different spectral region from absorption. Alternatively, the use as probe of a close transition leaving from the metastable level can greatly increases the number of fluorescence photons produced by a single metastable atom, with a consequent reduction of the shot noise.

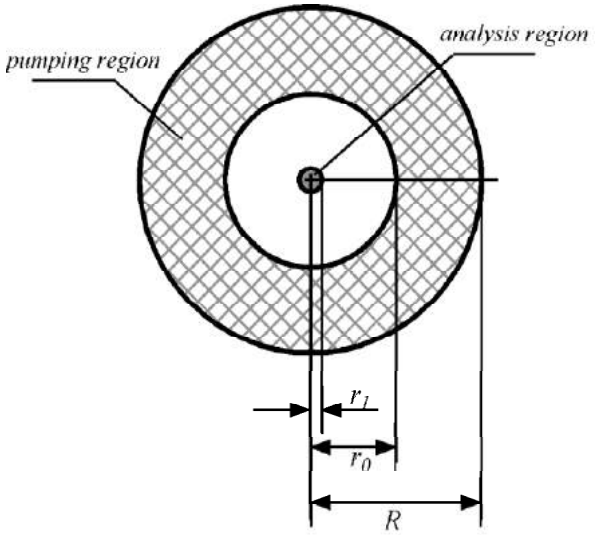

Fig.3. Irradiation of the thin gas cell (in the axial direction) by a monochromatic laser beam, having the ring-shaped cross-section with the external radius R and the inner radius r_0. The excited state population is probed by a second laser beam in the central region of radius r_1.

Thus a high-sensitive method for recording the narrow sub-Doppler resonance, caused by the optical selection of excited atoms with small velocity projections $|v_z|<(L/D)u<<u$ was theoretically suggested in paper

[17]. In particular, the case of the $^1S_0 - ^3P_1$ intercombination transition of the calcium (with the wavelength λ=657 nm) was analyzed. However the proposed sub-Doppler spectroscopy scheme may be applied also to transitions between the ground state and a long-lived metastable level for various alkali-earth atoms (*Mg ,Ca, Sr, Ba, Yb*) with the lowest energy triplet state $^3P_1$ or the lowest energy $^1D_2$ state (which are connected to the ground state respectively by a spin-forbidden intercombination line and an electric quadrupole line) .

In the following paper [18] we discussed possible applications of given results to optical atomic reference standards based on alkali-earth atom forbidden transitions. In particular, we presented possible schemes for building compact optical atomic standards, potentially with an accuracy at 10^{-12} level, operating in the thin cell, with very small sizes, mass and electrical consumption,so that they will be easily transportable and suitable also for satellite operation.

[1]. *F. Riehle*. Frequency Standards-Basics and Applications (Wiley-VCH, Berlin, 2004).

[2]. *W. Demtröder*. Laser Spectroscopy: Basic Concepts and Instrumentation (Springer, Berlin, 2003).

[3]. *A.Ch. Izmailov*. Laser Phys., 1992, 2, N5, 62; *A.Ch.Izmailov*. Opt. and Spectr., 1993, 74, N1, 25.

[4]. *A.Ch. Izmailov*. Laser Phys., 1993, 3, N2, 507; *A.Ch.Izmailov*, Opt. and Spectr., 1993, 75, N3, 395.

[5]. *S. Briaudeau, D. Bloch, and M. Ducloy*. Europhys. Lett., 1996, 35, N5, 337.

[6]. *S. Briaudeau, D. Bloch, and M. Ducloy*. Phys. Rev. A, 1999, A59, N5, 3723.

[7]. *M. Tachikawa, K. Fukuda, S. Hayashi, T.Kawamura*. Jpn. J. Appl. Phys., 1998, 37, N12B, L1556.

[8]. *M. Otake, K. Fukuda, and M. Tachikawa*. Appl. Phys., 2002, B74, 503.

[9]. *A.Ch. Izmailov, K. Fukuda, M. Kinoshita, and M.Tachikawa*. Laser Phys., 2004, 14, N1, 30.

[10]. *S. Imanishi, U. Tanaka, and S. Urabe*. Jpn. J. Appl. Phys., 2005, 44, N9A, 6767.

[11]. *K. Fukuda , M. Furukawa , S. Hayashi , and M. Tachikawa*. IEEE Trans. Ultr., Ferroel. Freq. Control., 2000, 47, N2, 502.

[12]. *K. Fukuda, M. Kinoshita, and M. Tachikawa*. Appl. Phys., 2003, B 77, 823.

[13]. *Y.T. Zhao, J.M. Zhao, T. Huang, L.T. Xiao, and S.T. Jia*. J. Phys. D.: Appl. Phys., 2004, 37, 1316.

[14]. *A.Ch. Izmailov*. Proc. of SPIE 6727, 2007, 67270B.

[15]. *A.Ch. Izmailov*. Laser Phys. Lett., 2006, 3, N3, 132.

[16]. *A. Mikata, U. Tanaka, and S. Urabe*,.Applied Optics 2008, 47, N5, 639.

[17]. *N. Beverini, A.Ch. Izmailov*. Optics Commun., 2009, 282, 2527.

[18]. *N. Beverini, A.Ch. Izmailov*. Proc. 23th European Frequency and Time Forum, EFTF 09, 2009, 1030.

EFFECT OF ELECTRICAL PHOTO QUENCHING IN POLYMER - FERROCENE

G.Z. SULEYMANOV, N.A. SAFAROV, A.F. GOCHUYEVA, M.A. KURBANOV, A.A. BAYRAMOV, I.N. ORUJOV, E.A. JAFAROVA

Institute of Physics, Azerbaijan National Academy of Sciences
Javid av. 33, AZ-1143, Baku, Azerbaijan
e-mail: mkurbanov@physics.ab.az

In paper the result of investigation of a photoelectric composite material based on polyolefines, halogenated polymers and organometallic compounds, possessing a high coefficient of conductivity photo quenching. Photoelectric composite material consists of high density polyethylene, polyvinylidenftoride and ferrocene.–organometallic compounds.

1. INTRODUCTION

Negative internal photoelectric effect is to reduce the electrical conductivity photo semiconductors under the influence of electromagnetic or corpuscular radiation. It is known that this phenomenon is rarer phenomena of the normal internal photoelectric effect in which the electrical conductivity of the substance under the influence of light increases. With the continued importance attached to photo semiconductors voltage (or electric field), there is a negative photo effect observed in the direction of the photocurrent, it is opposite to the direction of the photocurrent at normal photo effect thus the current in the illuminated crystal (the sum of the photocurrent and dark current) less current flowing through the unlit crystal. Currently, the electronic application developed photosensitive polymer composites based on organic and inorganic materials [3,4].

2. METHOD OF EXPERIMENT

Of particular interest are light-sensitive composites based on polymers, photosensitive semiconductors and organometallic compounds. *Fig.1* shows the schematic diagram of observation of the negative photoelectric effect: in the "*a*" device registers the magnitude of the current composite in the dark (dark current); in position "*b*" device registers the current increase in the coverage of the composite (normal photoelectric effect); in the "*в*" device registers reduce the current under illumination of the composite in comparison with the dark current (negative photoelectric effect).

Multi charge centers are formed at the imperfections of the composite thereby creating volume and surface polarization during illumination, called photoelectret state, regardless of the polarization caused by the applied electric field.

To establish the role of a photosensitive polymer and phase in the formation of photo quenching conductivity composites had the following components:

- As a polymer matrix used in non-polar polymer is high density polyethylene *(HDPE)*:
- As a polymer matrix used halogenated polymers *F2* and*F3;*
- As used in the photosensitive phase of *CdS, ZnS;*
- As organometallic phase ferrocene used with a variety of derivatives. Experiments have shown that in composites *HDPE + CdS, HDPE + ZnS, F2 + CdS, F3 + CdS, F2 + ZnS, F3 + ZnS* has not been detected effect photo quenching conductivity. Effect photo quenching conductivity in composites based on *HDPE*, *F2* and *F3* – containing *ferrocene*.

The volume content of ferrocene in the composite varied from *10%* to *50%*. *Fig. 1* shows the ratio R_f / R_0 of the volume content of ferrocene for the *composite HDPE - ferrocene*, where the R_f - resistance of the sample under illumination, R_0-dark resistance of the volume content of ferrocene was varied from *10%* to *50%*.

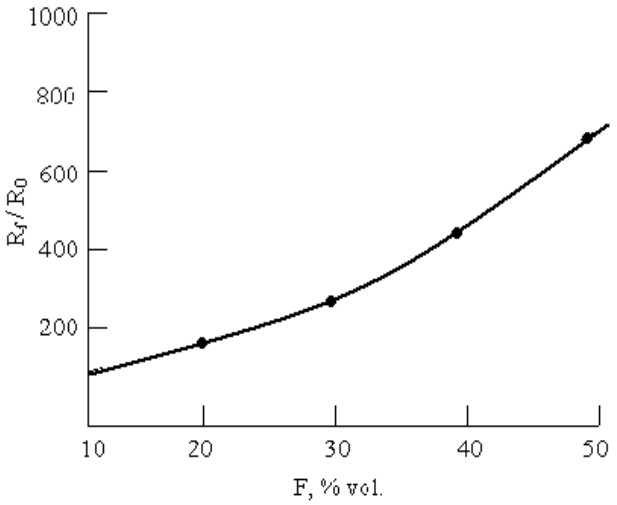

Fig.1. Dependence of the ratio R_f / R_0

It is seen that when covering the material in the visible light intensity of *4000 V/m*^{2}, the resistance of the material increases from *150* to *700 times*, i.e. at the same time decreases the conductivity of the material (the effect of negative photoconductivity). Was obtained photoelectric material with a negative photoconductivity, consisting of *PVDF* and *ferrocene*. The volume of content of ferrocene in the composite ranged from *10%* to *50%*. *Fig. 2* shows the R_f / R_0 of the volume content of ferrocene.

It is seen that when covering the material in the visible light intensity of *4000 V/m*^{2}, the resistance of the material increases from *6* to *120 times*, i.e. at the same time decreases the conductivity of the material (the effect of negative photoconductivity). We measured the dependence of the resistance of the sample *HDPE (80%) + Ferrocene (20%)* of the intensity of incident light. Fig. *3* shows the dependence of ferrocene content.

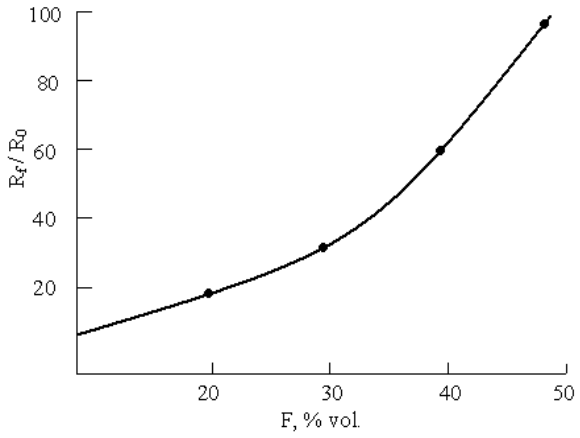

Fig.2. R_f/R_0 of the volume content of ferrocene in the visible light intensity of 4000 V/m^2

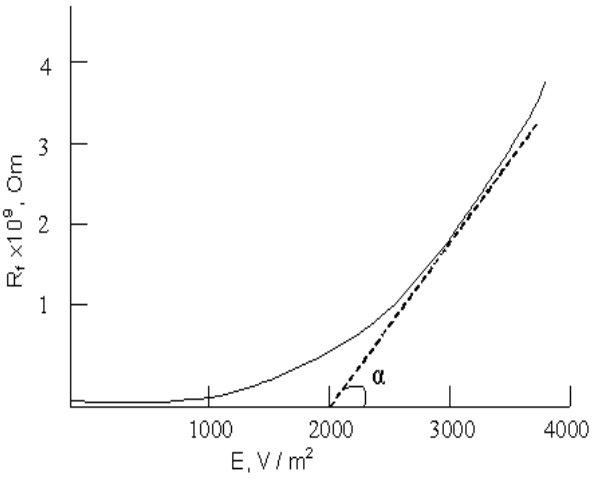

Fig. 3. The resistance value depends on E (intensity)

Here, $\alpha = \frac{\Delta R_f}{\Delta E} = 18{,}85 \times 10^5 \frac{Om \times m^2}{Vt}$ - attitude change in the resistance to changes in light intensity. From *Fig. 3* shows that the volume resistivity of the proposed photographic material depends on the intensity of incident light *(E)* and the resistance as a function of *E* grows faster than linearly. Thus, the first discovered the effect photoquenching conductivity in polymers *HDPE* and *F2-ME*, the dispersed particles of ferrocene. After turning off the light resistance of the restoration or increase the current was slow. This effect depends strongly on the choice of the components of the composite.

The main reasons for the negative photo effect can constitute:

1) fast recombination of carriers released by light from the main course of providing dark current;
2) centre step-down carrier mobility as a result of their short jam in traps, including those created under illumination;
3) the existence or occurrence under the effect of lighting a lot of charging centers, creating a local field whose strength exceeds the applied external field and are directed in the opposite direction in relation to him aside.

The analysis results suggest that in the samples effect photo quenching conductivity, mainly related to processes taking place in the ferrocene phase. Changes in photo quenching *(α)* conductivity, composites when used as a nonpolar polymer phase *(HDPE)* and polar *(F2 or F3)* polymers means that when this change altered the properties of traps for the carriers.

However, it should take into account the effect photo induction dipoles. The direction of photoinduced dipole moment can be mismatch with the direction of the lines of force of the external electric field. Based on the structural features of polymers, ferrocene can be assumed that the traps for charge carriers appear near the boundaries of the phases.

Photoinduced dipole moment may arise as a result of capture of carriers by traps in the volume of the composite. Changing the concentration of these traps (dipoles) with the variation of the intensity of incident light. Can initiate the electric field inside the composite, and consequently step-down probability of charge carrier transport.

The proposed mechanism is clearly the primary and the detail should begin with the charge transfer in a strong heterogeneous system polymer - ferrocene. It is known that charge transfer in photosensitive systems is related to the concentration of photoinduced charges, transfer and capture them in various traps. If the proceeds from this concept, we can say that the phase of photoinduced charge generation can life the polymer matrix, since the band gap of more than *10 eV*.

Photosensitive properties of ferrocene and its organic derivatives have not yet been studied. In addition to these two phases in the composites and interfaces. The physical structure of the polymer phase in these boundaries is formed under the influence of ferrocene. If the proceeds from such fact that ferrocene is an organometallic compound that can be put that he width of the forbidden zone is less than the similar parameter of the polymer phase. Therefore, when exposed polymer - ferrocene is an exchange of charges between him and formed the interphase potential barrier.

The parameters of the interfacial barrier (amplitude and width of the barrier) is determined by the electronic state, electrical parameters (permittivity and conductivity) phases. Modulation of these characteristics at a given value of external stress, exposure to light should determine the photoelectric conductivity. However, in practice there photo quenching conductivity and therefore this effect can not be linked to life photo devastation of the boundary charges.

So, photoconductivity effect in the polymer - ferrocene not significant. In a first approximation, consider that the effect of photo quenching conductivity associated with reversible photochemical reactions, which occur as a result of the induced dipoles that compensate the external applied electric field. Note that the proposed mechanism requires further research and refinement.

The analysis results suggest that in all the samples studied photo generation of charge carriers is not always the case when molecules are excited, which is part

(HDPE, LDPE), halogen-containing polymers and ferrosen front of their contacts may occur trapping centers of carriers (traps) of physical and chemical nature if we assume that the activation energy of these centers is much larger *CT*, we can assume that these traps can act in photo quenching conductivity of the composites. For our studies more attractive is the trap the chemical nature, arising from the coverage of the composite. They are additional centers and occur only under illumination and reversible neutralized with the termination of the light. Therefore, the photo generation of chemical traps is the rate of capture of charge carriers, and consequently, a strong decrease of electrical conductivity of the composite polymer-ferrosene. Confirmation of the role of chemical photoinduced molecular traps in the process photo quenching conductivity is the results obtained when used as a polymer phase polar polymers. The thickness of transition layer and the pattern of segments of different macromolecular polymers in the transition layer formed at the contact boundary of two polymers depends on the difference of the polarity of their macromolecules. The thickness of the transition layer at the contact is usually greater, the smaller the difference in the polarities of the mixed components, i.e. the smaller the difference of cohesive energy ingredients. The thickness of segmental solubility may be tens.

The formation of this layer limits the formation of the supramolecular structure in the amorphous-crystalline polymers in close proximity to the layer. The thickness of boundary layers with constant supramolecular structure and properties of polymers on the contact surface can reach many hundreds and even thousands. No systematic comparative data on the properties of non-polar polymer *(HDPE) - ferrocene* and polar *polyvinylideneftoride PVDF - ferrocene*. $\mu = 6{,}9 \cdot 10^{-28}$ kl.sm and the dipole moment of the molecule of ferrocene is zero, i.e. it is nonpolar. Therefore, the depth of the layer of segmental solubility of these two-phase systems will be different in favour of the composite *HDPE - ferrocene*. Formation of reversible chemical bond at the interface under the influence of light provides photo quenching conductivity in composites. As has been noted that in ferrosene keep composites dispersant is ferrocene, which is a metal organic compound, a molecule which the iron atom is linked directly with all the carbon atoms. Iron atom "sealed" between two highly symmetrical five-membered rings in such a way that all the distance *Fe - C*, i.e. chemical bonds *Fe - C* (and ten of them in this molecule), were the same. And besides, the rings rotate freely in the molecule relative to each other around the axis connecting the centers of rings and running through the iron atom through. This structure provides high stability, flexibility and reversibility of chemical processes. Even in the presence of air, which contains aggressive for ferrocene oxygen, ferrocene is stable when heated to *400 ^0C.* Using electro photochemical properties of ferrocene is based on the easy and reversibility of processes taking place one-electron oxidation or reduction. Very successful was the use of this property for light-sensitive composites. In the films of composites based in ferrocen on *HDPE, PVDF* and ferrocene in absorption photon with energy hν phase is possible following processes:

$$(C_5H_5)_2Fe^0 + h\nu \rightarrow (C_5H_5)_2Fe^+ + e^-$$
$$(C_5H_6)_2Fe \rightarrow Fe^0 + C_5H_5$$

bond energies *Fe-C, C-C, C-A* specified processes may lead to the formation of the composite photo resist effect. However, such a composite, *HDPE - ferrocene* and *PVDF - ferrocene* is observed.

3. CONCLUSION

Thus, we offer a photoelectric composite material has several advantages over other known similar polymeric materials with a negative electroconductivity and exactly: *1)* a higher rate photo quenching wiring, *2)* simple technology of materials and *3)* capability generation said emulsion based on various polymer matrices.

[1]. *B.U. Barshevsky*. Kvantovoopticheskie phenomenon. M. Vysschaya School, 1982, 136 pages
[2]. *E.A. Aleksandrov*. FTS, 38 (10), 1153 (2004)
[3]. *N.A. Davidenko, V.N. Kokozay, D.V.Shevchenko*. Teor. and experimental. Chemistry, 40 (1) 34 (2004)
[4]. *N.A. Davidenko, A.A. Ishchenko*. Teor. and experimental. Chemistry, 38 (2), 84 (2002)

THE OPTICAL PROPERTIES OF p-CuAgTe THIN FILMS

SH. ALEKPEROVA, KH.D. JALILOVA, G.S. GADJIEV, A.I. AKHMEDOV
Institute of Physics, National Academy of Sciences of Azerbaijan
AZ1143, Baku,H.Javid av.33
E-mail:physic@lan.ab.az
Fax: (99412) 39-59-61

The paper presents a new data on reflection and absorption and fundamental optics functions of thin films p-CuAgTe. The treatment of data by Kramers-Kronigs relations alloved to estimate the complete of fundamental optical constants: $\varepsilon_1;\varepsilon_2;-Im\varepsilon^{-1},n,k$ in the energy range $0.05 \div 0.50$ and $1.0 \div 6.2\ eV$ and make suppositions about the electrons transmissions from low-lying level to conduction zone. the effective mass of charge carriers ,of lifetime of the plasma oscillations ,the plasma energy and direct transition energy in between the zones was estimated also

There are very few papers on narrow-band triple chalkogenides of I group in the literature.The optical spectra of CuSSe, CuSeTe with anion substitution of components were investigation in energy range $0.5 \div 5.0\ eV$ [1].

By differential-thermal and electro physical methods it is shown, that similarity of structural types and the nature of band-strength in copper and silver chalcogenides allowed obtaining of the triple chalkogenides CuAgS(Se,Te) by equimolar cation substitution in $Ag_2x - Cu_2x$ systems.The formation of the triple compounds takes a peritectic reaction course at 903K(p-CuAgS), 1033K (n-CuAgSe) and 1123K(p-CuAgTe) [2]. The edge absorption and the absorption by free carries in n-CuAgSe are investigated in [3,4].In paper with the object to investigation of energy band structure of p-CuAgTe in the range of own absorption the fundamental optical functions: refractive index -n(ω), absorption index –k(ω), dielectric constants-$\varepsilon_1(\omega)$, $\varepsilon_1(\omega)$, ε_∞, the function of the characteristic volume energy losses-Imε^{-1} (ω),the effective mass of charge carriers are estimated. p-CuAgTe is undergoes polymorphism at 473÷478K.

The law-temperature α-modification crystallizes into rhombic lattice with parameters $a = 4.19\,°A; b = 20.02°A; a = 6.38°A$. The thin films of p-CuAgTe $(0.25 \div 0.35)$ mμ were obtained by vacuum deposition $(10^{-3}Pa)$ on freshly cleaved surface NaCl and optical glass heated up to $350 \div 370K$. By X-ray and electron graphic analyses determined the identity of thin films p-CuAgTe with parent compound . The transmission and reflection spectra (at perpendicular incidence of beam) in non-polarized light, in range $0.05 \div 0.50$ and $1.0 \div 6.0$ are measured on two- beam and double-wave spectrometr Hitachi (model 556-557) and two-beam spectrometer "Specord-75-IR and duplicated on IKS-29. The treatment of experimental spectra are produced on known Kramer-Kroning's relations.

In fig. I it was presented the reflection spectra in the range $(1.0 \div 6.2)eV$(a) and $(0.05 \div 0.50)eV$ (b).There are two minimum on reflection spectra in the IR range : at 0.05 and 0.141 eV. By higher steep of low-energy slope and the peak frequency of - $Im\varepsilon^{-1}(\omega)$ it is established that plasma minimum corresponds to 0.056 eV.

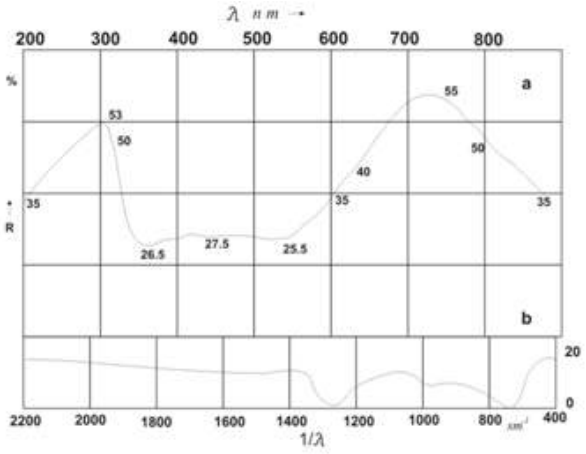

Fig.1. The reflections spectrums of p-CuAgTe a-in range $1.0 \div 6.2eV$; b- in range $0.05 \div 0.50eV$

From the relations

$\omega_{min.} = \omega_p(\varepsilon_0/\varepsilon_0 - 1)^{1/2}$ and
$\omega_p^2 = 4\pi e^2\, n/m * \varepsilon_0$

the plasma resonance frequency ω_p=$0.85 \cdot 10^{14}c^{-1}$ and the effective mass of charge carriers $m_p^x = 0.3m_e$.has been determined. From the relation$\chi = ne^2/\omega_{min}^2 \cdot \omega_p^2$ dielectric suscep-tibility of p-CuAgTe is determined . In energy range $(1.0 \div 6.2)eV$ on reflection spectra have been developed two distinc maxima without any particular peaks and steps. With rise of energy a reflection 0.26 and keep one`s in the range $(2.30 \div 3.65)eV$,and then suddenly increases up to 0.54 (4.16 eV). The ultraviolet reflection allows to locate the electrons states, distant from edges of foribdden band.These two maxima 1.7eV and 4.1 eV are taken as symtom of direct interband taransitions from lower valent bands into condiction band. In fig.2(a,b) have been presented the absorption spectra in IR $(0.05 \div 0.50)eV$,visible and close UV

$(1.0 \div 6.2)eV$ regions.In absorption spectrum occurs a number of intensive peaks at1.4; 1.9; 2.6; 2.9 eV. The property of silver and copper chalkogenides is the presence of high cation conductivity [5]. These structures arise from ionic skeleton. In energy scale they underlies well below of valent band. A few lines of oscillation type are observed in close UV region $(4.0 \div 6.2)eV$.

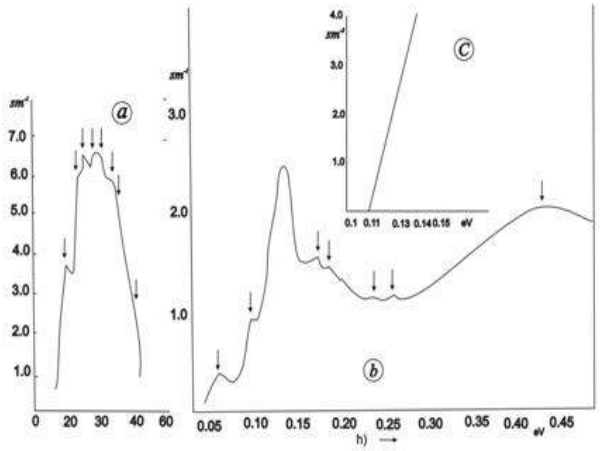

Fig.2. The absorption spectrums of p-CuAgTe a-in range $1.0 \div 6.2eV$; b-in range $0.05 \div 0.50eV$; c- $\alpha^2 \sim h\gamma$

They can to correspond to transitions from the top of 3d-band of copper into conduction band near Fermi energy.The transition`s stripts from d-band into condiction band are wide ,as they take place in different points of Brillouin zone and lifetime $-\tau$ is short, respectively.Duplex in the interval $3.0 \div 3.5eV$ is due to spin-orbit splitting of copper`s 3d level,i.e. spilitting like that is not observed on Ag_2Te spectrum[6].The frequency ranges near $\omega \geq \omega_g$ is the most important section of spectrum to yield the quantitative data about energy band structure near absolute extremum of Brillouin zone. In fig.1b the asbsorption spectrum covers just this region. By extrapolation of straight line $(\alpha^2 \sim h\vartheta)$ have been determined optical band gap $E_{opt} = 0.12eV$. Has been exceded forbidden band (0.10eV) by 0.02eV. In general ,in ionic crystals the cutoff of direct transitions can be a few higher than band gap due to polarization of crystals lattice , do not manage to change for shot time of interaction of photon with electron[7]. The difference is equal to polaron energy for p-CuAgTe -0.02eV beyond of absorption edge have been observed peaks at 0.17; 0.26; 0.37; 0.43; 0.5 eV. There are special points in zone structure p-CuAgTe ,of pointing to energy of vertical transitions between the extremum points of Brillouin zones . The structures at 0.07 and 0.10 eV are due to selective absorption by free carriers and acceptor impurity level , respectively. In fig. 3(a,b) was presented the spectral dependencies $\varepsilon_1; \varepsilon_2; -Im\varepsilon^{-1}, n, k$ in the energy range $0.05 \div 0.50\ eV$.

.

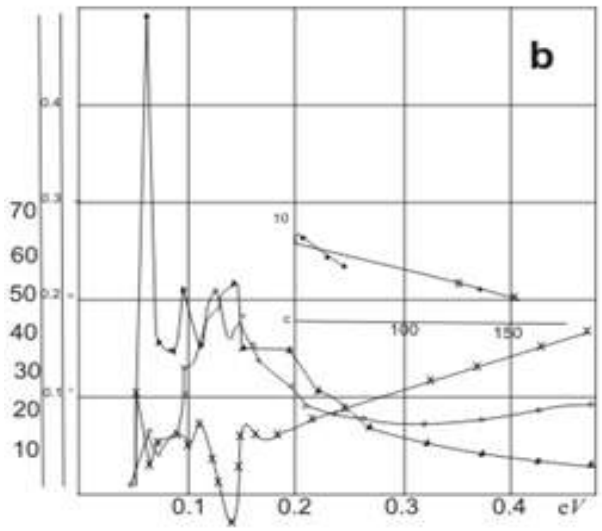

Fig.3. Spectrum of characteristic electronic losses $(-Im\varepsilon^{-1})$ and fundamental optics constants $(\varepsilon_1; \varepsilon_2; n, k)$ in range $0.05 \div 0.50eV$

On spectrum $-Im\varepsilon^{-1}(3b)$ expect main peak at 0.056eV (pointing to plasma frequency) there have been found features as extra peaks at 0.096; 0.14; 0.18; 0.28 eV Extra peak energies correlate with direct interband transitions in corresponding points CuAgTe , pointing to energy of vertical transitions between the extremum points of Brillouin zone. In fig .(3c) have been derived the dependence $\varepsilon_1 = f(\lambda^2)$. By extrapolation this straight line to $\lambda = 0$, the high-frequency dielectric constant-$\varepsilon_\infty = 7.8 \div 8.2$ is found . The real part of dielectric constant ε_1 reaches the biggest values 3.5 (0.11eV); 8.8 (0.50eV) and it is negative in the range $(0.13 \div 0.46)eV$. Consequently , in this range n<K.

Spectra $\varepsilon_2, \lambda, K$ are similar in all energy ranges . Their biggest values are equal to

ε=5.1 (0132eV); K=1.77 (0.136eV);
λ=2.46·10^{4}cm^{-1} (0.13 eV)

and closely resembles on energy.

The lifetime of plasma oscillations is calculated from peak $-Im\varepsilon^{-1}(\omega)$ on the half-width level by relation $\Delta\omega/\omega = 2/\omega_p\tau$[5] . It is equal to $\tau = 4.7 \cdot 10^{-13}c$. The plasma resonance energy $\hbar\omega_p = 0.05eV$. Maxima of main volume plasmons :0.21 (0.10eV) and 0.22 (0.144eV) indicates that in excitation of volume plasmons besides valent electrons also deeper level`s electrons are taken place. The shift of main peak $-Im\varepsilon^{-1}(\omega)$ about maximum ε_2 on 0.07eV (fig 3b) and in visible region on 0.75 determines energy of longitudinal-cross splitting of transitions .

In conclusion in Table i have been given set of fundamental optic functions of p-CuAgTe close to plasma resonance

Table 1 Set of fundamental optic functions of p-CuAgTe close to plasma resonance.

ω_p c^{-1}	ω_p c^{-1}	$\hbar\omega_p$ eV	τ_{opt} c	χ	ε_1	ε_2	ε_∞
$0.88\cdot10^{14}$	$0.85\cdot10^{14}$	0.05	$4.7\cdot10^{-13}$	0.6	1.0	3.0	$7.8\div8.2$

Table 2 Magnitudes of direct interband transitions

Energy range, eV	E_8	E_7	E_7^1	E_6	E_5	E_4	E_3	E_2
$1.0\div6.2$	6.0	5.0	4.7	4.0	3.5	3.0	2.6	1.9
$0.05\div0.50$	0.43	0.26	0.24	0.17	0.14	0.132	0.097	0.06

So by the investigation of fudamental optic functions in infrared , visible and close UV regions the peculiarities of interband transitions in p-CuAgTe has been determined and the first data about structure of energy zones near absolute extremum of Brillouin zone was obtained.

[1]. *V.V.Sobolev* "Energeticheskaya strutura uzkozonnikh polyprovodnikov ". Kishinyov,"Shtinitsa" 1983, p.227 (in Russian)

[2]. *M.J.Agayev, Sh.M.Alekperova, M.J.Zargarova*. Dokladi AN Azerb.SSR №5,1989 p.129

[3]. *Sh.Alekperova, I.P. Akhmedov , L.NAliyeva, G.S.Hadjijeva, Kh.Khalilov* Neorganicheskiye Materiali, RAN,v.28(8) ,1992,p.1803.

[4]. *Sh.M.Alekperova, N.N.Abdul-zade, I.A. Akhmedov, G.S.Hadjieva* .JCTMC-12 Taiwan Conference Procuging, March, 2001, p.310

[5]. *V.M.Berezin,G.P.Vyatkin, V.N.Konev,L.J.Karikh*, Fizikai tekhnica poluorovodnikov, v.18 (2) , 1984, p.312.

[6]. *H.Philipp, H.Ehrenreich*,"Optical properties of semiconductors " Moskva " Mir" 1970,p.130.

[7]. *J.Tauc* "Opticheskiye svoystva polyprovodnikov " Izdatelstvo "Mir" Moskva 1967,p.41. (in Russian)

CHARACTERISTICS OF INTERFACIAL PHENOMENA IN HEAT CONDUCTING COMPOSITES BASED ON POLYOLEFIN - NITRIDE - CARBIDE METALS

A.I. MAMEDOV, G.KH. KULIEVA, S.N. MUSAEVA, U.V. YUSIFOVA, A.MEHDILI, S.A. ABASOV, M.A. KURBANOV

Institute of Physics, Azerbaijan National Academy of Sciences
Javid av. 33, AZ-1143, Baku, Azerbaijan
e-mail: mkurbanov@physics.ab.az

The possibility of prediction of interfacial phenomena at the interface of polymer – carbide and nitride metals composites studied posistor effect in them.

INTRODUCTION

Interfacial phenomena that significantly alter the physical-mechanical and thermal properties of polymer matrix systems depend on the degree of interaction of polymer with filler. The structure of the polymer at the interface and its adhesion with surface of the particle dispersant (filler) will depend on from the degree of interaction.

It can be assumed that the processes, taking place in one phase will affect similar processes in another phase: the electronic state of surface dispersant and its electro physical characteristics contribute to a structural change of the polymer at the interface. Therefore, obtaining information from the boundary of phases, they will purposefully change the physical and mechanical properties of the composite, in particular, heat-conducting characteristics.

METHOD OF EXPERIMENT

Numerous studies have shown that in composites based on amorphous-crystalline polymers and inorganic particles are formed posistor effect [1 ÷ 3]. In the investigated composites based on thermoplastic polyolefin and gollogen composition polymers and particles of nitrides and carbides are formed clearly posistor effect, ie the temperature dependence of bulk resistance (ρ_v) has a positive temperature coefficient at a certain temperature range and has three characteristic plot: first, with increasing temperature slightly decreases the resistance of the composite and pass through a minimum and is growing rapidly (10^4 - 10^7) times, and then decreases. The experimental results show that the values of the temperature at which the marked increase the resistance, as well as the maximum temperature dependence $\lg\rho_v = f(T)$ essentially depend on the composition and polarity of the polymer phases. At the half-width of the peak also affects the polarity of polymer matrix and electronegativity of inorganic phase - BN, AlN, TiO2, SiO2, BaTiO3. Determine the activation energies of these areas depending $\lg\rho_v = f(T)$ we can predict the intermolecular interactions in polymer - inorganic particles.

Fig. 1 shows the temperature dependence of the resistivity of composites based on HDPE with various fillers at volume content of filler φ= 30% vol. As seen from Fig.1 a position of the minimum conductivity depends on the type of filler. The dependence of the electrical conductivity of the composites on the temperature can be explained by the tunneling mechanism of charge transfer in composites.

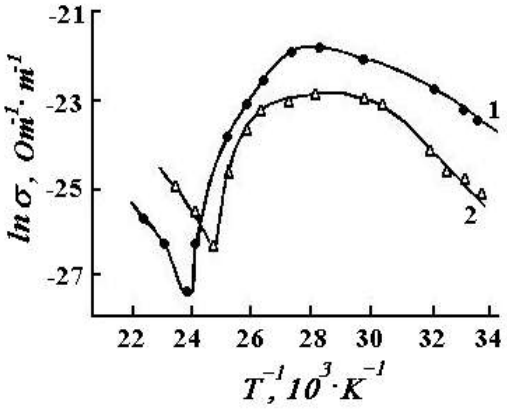

Fig. 1. Dependence lnσ from 1/T. 1-HDPE+BN;2-HDPE+AlN.

The composite system of polymer - filler consists of two phases, which differ sharply in their physical properties, which leads to the formation of barriers at the interface. The electrical conductivity of composites is carried out by tunneling of carriers through these barriers. The tunneling mechanism of electrical conductivity of the composites is confirmed by many experimental facts, in particular, the dependence of electrical conductivity of the composites of the volume content of filler and non-linear current-voltage characteristics of the composites. For example, Fig. 2 shows the dependence of the specific bulk resistance (ρ_v) number of composites on the content of filler. At low filler content the electrical conductivity of the composites is close to the conductivity of the polymer and is virtually independent of φ. When φ reaches a certain critical value of ρ_v composites decrease sharply, and from a certain value of φ reaches almost constant value close to the conductivity of the filler. In the first area the distance between the filler particles so large that the tunneling of carriers across borders are impossible. Increasing of φ particles approach and tunneling probability increases and when $\varphi>\varphi_{kr}$ the conductivity other composites is due, mainly, the tunneling mechanism. For large values of φ the filler particles are in direct contact, forming a continuous chain, and the electrical conductivity of the composites is close to the conductivity of the filler.

Thus, the temperature dependence σ_k composites can be described as combination of the following processes: of firstly, increasing the electrical conductivity of the

filler and the polymer with temperature, and secondly, the thermal expansion of the polymer and filler particles.

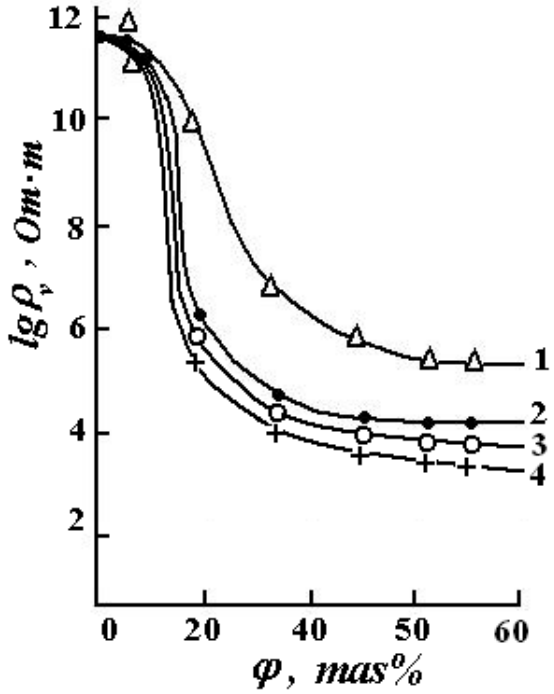

Fig. 2. Dependence lgρ from φ. 1-HDPE + TiC; 2-Treated discharge HDPE + TiC; 3-HDPE + TiCN; 4-Treated discharge HDPE + TiCN.

The first process leads to a decrease a potential barrier at the border between the filler particles and, consequently, to increase the electrical conductivity of the composite, and the second process, on the contrary, to increase the barrier and reduce σ_k. In the first part of the growth of the electrical conductivity of the filler dominates the thermal expansion of the polymer (here, the electrical conductivity of the polymer is virtually independent of temperature and thermal expansion of the filler particles can be neglected), and therefore the electrical conductivity of the composites increases. At higher temperatures the contribution of thermal expansion of polymer matrix becomes significant, and increasing the electrical conductivity of the composite is slowed down and is replaced on the decline. Finally, when the temperature reaches the melting temperature of the polymer crystalline phase, the volume of the polymer matrix increases sharply, and this leads to an increase in the average distance between particles of filler and, hence, to a sharp decrease electroconductivity composite. Further increase in temperature leads to a change the spatial distribution of particles in thick-flowing straightened polymer matrix and a decrease in the effective thickness of the sample. Furthermore, in this temperature range the electrical conductivity of the polymer matrix markedly increased. All this leads again increase the electrical conductivity of the composite.

Thus, the degree of crystallinity of the polymer phase and the interfacial interactions should affect posistor effect in composites. Consider the effect of various factors on the electrical conductivity of the composites.

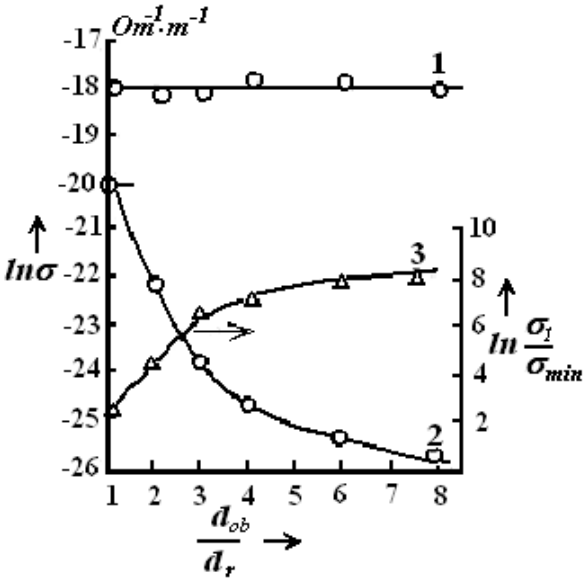

Fig. 3 Dependence $ln\sigma_0$, $ln\sigma_1$, and $ln\sigma_1/ln\sigma_{min}$ from *ds/dr*. 1- $ln\sigma_0$; 2- $ln\sigma_1$; 3- $ln\sigma_1/ln\sigma_{min}$.

Fig. 3 shows the dependence conductivity of the composite HDPE + BN at room temperature σo at the melting temperature of crystalline phase $\sigma_{k\ min}$, as well as the $ln\sigma_1/\sigma_{k\ min}$ the ratio of sample thickness d_s to the average diameter d_r of filler particles: d_s/d_r. Here σ_1 - electroconductivity sample at a temperature corresponding to the beginning of a sharp decrease in electrical conductivity. The value of $ln\sigma_1/\sigma_{min}$ characterizes the electrical shock of composition during the melting of the crystalline phase of polymer matrix and is associated, ceteris paribus, with the degree of crystallinity. The value of d_s/d_r varied by changing the thickness of the sample at a constant average diameter of particles. Fig. 3 shows that with increasing d_s/d_r conductivity σ_0 remains constant and $ln\ \sigma_1/\sigma_{0min}$ at first increases up $d_s/d_r \sim 4$ quickly and then slows down the growth of this magnitude. This can be explained by the fact that at changing the ratio $d_{об}/d_r$ the degree of crystallinity of the polymer matrix practically unvaryings and a modified in the $ln\sigma_1/\sigma_{min}$ is associated with an increase almost thickness of polymer interlayer between the filler particles with an increase in d_s/d_r. When d_s/d_r the particle is practically shunted electrodes while the thermal expansion of polymer is insignificant effects on the temperature dependence of electrical conductivity compositions. With the growth of d_s/d_r increases the number of particles of filler and polymer layers between them. Therefore, increase the value of $ln\sigma_1/\sigma_{min}$.

Fig. 4. shows the dependence σ_0, σ_{min} and $ln\ \sigma_1/\sigma_{min}$ from pressing time t_{pr} for composite HDPE + BN. It is evident that σ_0 increases to t_{pr}~10 min. and then decreases, at the same time σ_{min} changes in the opposite way and a $ln\ \sigma_1/\sigma_{min}$ varies with t_{pr} while as σ_0. This dependence of electrical conductivity from the t_{pr} can be explained by the fact that with increasing time of compression increases the degree of crystallinity of the polymer in the composite.

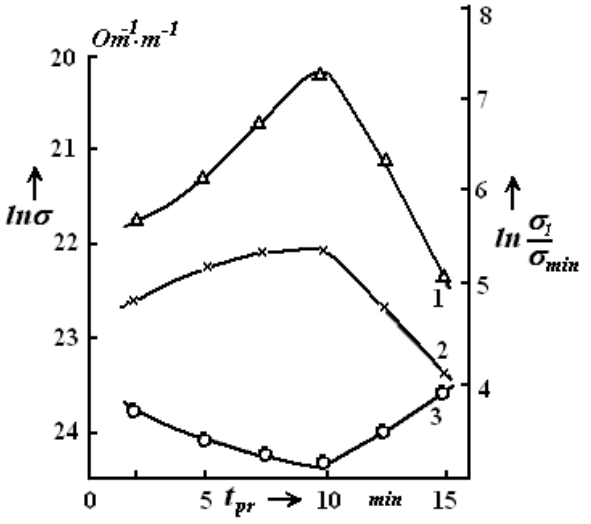

Fig. 4 Dependence $ln\sigma_0$, $ln\sigma_{min}$ and $ln\sigma_1/\sigma_{min}$ from t_{pr}. 1-$ln\sigma_0$; 2-$ln\sigma_1/\sigma_{min}$; 3-$ln\sigma_{min}$.

This leads to an increase electrical conductivity at room temperature due to the fact that the filler is concentrated mainly in the amorphous phase of polymer, and therefore with increasing degree of crystallinity increases the packing density of filler in the amorphous phase of the polymer matrix. Increasing the degree crystallinity with increasing time compression also leads to decreases of σ_{min} and an increase electrical shock in during the melting of the crystalline phase. Along with increasing degree of crystallinity of the polymer matrix during the pressing take place its oxidizes. This leads to the fact that after t_{pr} >10 min. electrical conductivity of composite at room temperature the σ_0 and the $ln\sigma_1/\sigma_{min}$ decreases.

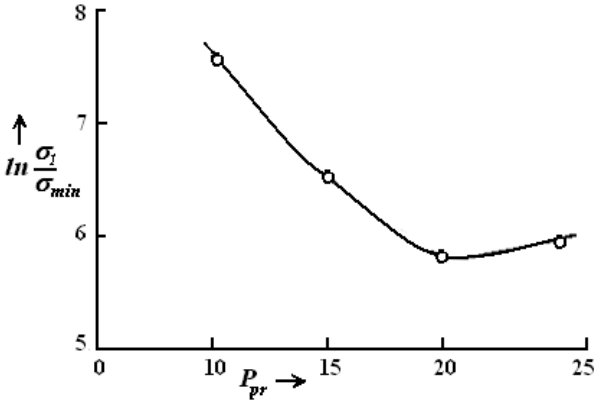

Fig. 5. Dependence $ln\sigma_1/\sigma_{min}$ from compacting pressure of composite HDPE +30% vol BN.

Fig. 5 shows the dependence a $ln\ \sigma_1 / \sigma_{min}$ from compacting pressure for composite HDPE+BN. It is evident that with increasing pressure the value $ln\sigma_1/\sigma_{min}$ decreases to a ~20 MPa, and then with further increase of pressure practically unchanged. It also reflects dependence of degree of crystallinity of the polymer matrix from P_{pr}. However, it is also possible that with increasing compacting pressure increased interfacial interaction, the density of the composite, reduced the number of defects and air inclusions. Compacting pressure and cyclic thermo-pressure of the composites have a significant influence on their temperature coefficient of expansion (Fig. 6). Such a change α mainly can attribute to the change of interfacial interactions under the influence of P_{pr} and the process of cyclic thermo- pressure.

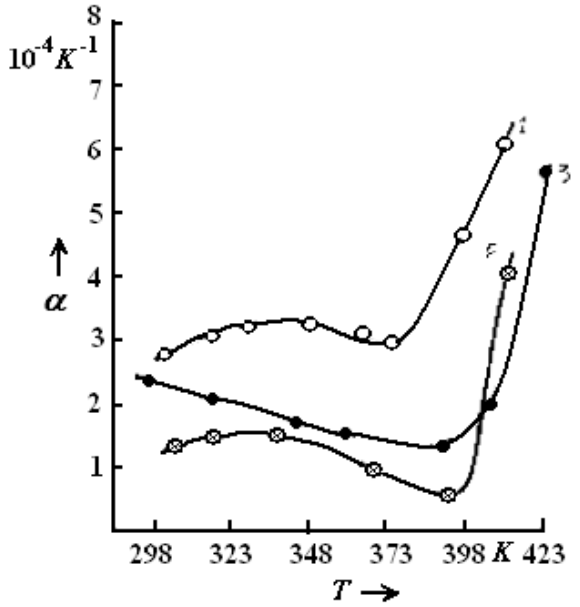

Fig. 6. The dependence α from *T* composite of HDPE +60% vol BN. 1-compacting pressure 10 MPa-1 cycle; 2-compacting pressure 10 MPa-2 cycle; 3-compacting pressure 40 MPa-1cycle.

Thus, the electrical conductivity of the composite system of polymer-filler due to tunneling of carriers through the barriers between the filler particles, whose parameters are determined by the properties of the composite components and interfacial interactions at the interface. Temperature dependence electrical conductivity of the composite be formed by increasing of the filler with increasing temperature and thermal expansion of polymer matrix. The sharp decrease in electrical conductivity of the composite polymer-filler connects with the sharp increase of volume of the polymer matrix in during the melting of its crystalline phase.

CONCLUSION

Summarizing the results of a study on posistor effect, to judge the interfacial phenomena in composites based on polyolefins, dispersed particles of BN or AlN, can highlight the following points:

1. Change in temperature rise and half-width of the posistor peak is determined by the interphase interactions.

2. Temperature corresponding to the beginning of melting of the crystalline phase depends on the type of filler.

3. Technological conditions for obtaining and the ratio the sample thickness of the composite to the average particle diameter of the filler significantly affect the amplitude of the posistor peak, and therefore, the physical - chemical processes occurring at the interface of polymer - filler.

4. Transition from the first section to the second depending $ln\gamma_v=f(1/T)$ is smooth, with the temperature range of this transition depends on technological conditions and properties of the filler.

5. Slope, temperature range, the point of transition from growth to its lower the activation energy and the steepness of the posistor peak depends on the physical and chemical processes that occur at the interface.

---

[1]. *M.A. Kurbanov, Kh.S. Aliev, A.O. Orudzhov, Z.A.Allakhverdiev, S.N. Niftiev, I.A. Faradzhzade.* Influence of the polarity of the polymer matrix on thermal, electric and mechanical properties of composites on the basis of polymer-nitrides and carbides of metals. TMMOB Elektrik Muhendisleri Odasi, Ankara Subesi, EEBM 7 Ulusal kongresi, 1997, Ankara, p. 673- 675.

[2]. *M.A. Kurbanov, I.A. Faradzhzade, S.N. Musaeva, M.G. Shakhtakhtinski.* Composite materials for high-temperature proximity switches - posistors. Problems of Energy 2001, № 2 p.76-81.

[3]. *M.M. Kuliev, S.N. Musaeva, I.A. Faradzhzade, M.G. Shakhtakhtinski.* Composite posistors with solid fillers. Problems of Energy 2000, № 3-4 c.98-103

SPRITE PHOTODETECTORS WITH IMPROVED PARAMETERS

A.A.ALIEV, E.K.HUSEYNOV, SH. M.KULIEV, A.K.MAMEDOV, R.I.MUKHTAROVA
Institute of Physics of NAS of Azerbaijan
370143, Baku, etc. H. Javid 33

The design of SPRITE-photodetectors with improved parameters on the basis of the $Cd_xHg_{1-x}Te$ bulk crystal and epifilms is offered. Advantages of the offered design are shown in comparison with existing both in technological, and in design aspects.

The SPRITE photodetectors (an abbreviation from Signal Processing In The Element) represents the photoresistor with three electrodes, two of which provide a current, and the third (potential) - is a potential probe for signal read-out (fig. 1a). The bias level, affixed to a photoresistor, is selected such, that time of the photogenerated carriers drift was equal or less of their lifetime. Image scan rate v_s, focused on the photoresistor, corresponds to drift speed of the photogenerated carriers packet, and the density of photocarriers in the place of the split image depends on coordinate *x*. At correctly chosen image scan rate, the signal reading from a potential electrode is defined by a light fluxe in a place of the split image, integrated in time, equal to the generated charge carriers lifetime *τ.* As *τ* there is more than time, of one device of decomposition in a ruler of discrete photodetectors array, that is equivalent to time over the read-out zone τ_a (one device of decomposition corresponds to the area between potential and pulling electrodes) there is an amplification of a signal in τ/τ_a time. So as the noise is not correlated, the noise amplify in $(\tau/\tau_a)^{1/2}$ times. Thus, one SPRITE-photodetector with a preamplifier replaces the discrete receivers array with series scanning, together with preamplifiers and circuits of a charge time delay and integration of [1].

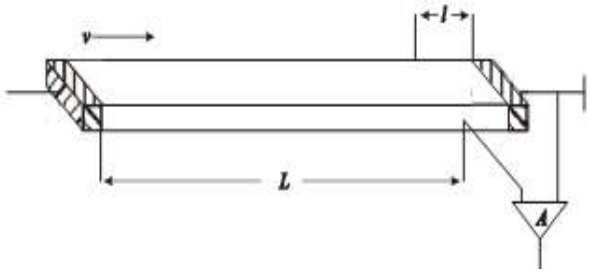

Fig. 1. The structure of the SPRITE detector. + U - plus DC bias voltage, L - band drift NCC, l - the zone read, A - signal processing circuit, v - velocity of ambipolar diffusion and scanning, v = v a = v s

The basic photoelectric parameters of SPRITE-photodetectors for small spatial frequencies are defined by the following expressions:
- Sensitivity

$$R_\lambda = \frac{\eta\tau E_b l}{h\nu W^2 tn}[1-\exp(-\frac{L}{\mu_a E_b \tau}] \qquad (1);$$

- Reduced detectivity for a lengthy strip ($L >> \mu_a E_b \tau$) and BLIP mode

$$D^* = \frac{\eta^{1/2}}{2h\nu}\left(\frac{1}{\Phi_b W}\right)^{1/2}\left[1-\frac{\tau}{\tau_a}\left\{1-\exp\left(-\frac{\tau_a}{\tau}\right)\right\}\right]^{-1/2} \qquad (2);$$

Where η – quantum yield, E_b – bias field, *l* – length of the read-out zone, W, t- width and thickness of the sensing device, n – free charge carriers density, μ_a – ambipolar mobility, L – device length, Φ_b – background flux density.

Efforts of developers basically are concentrated on the making design of the SPRITE-photodetectors, allowing to improve the temperature and spatial resolution of thermovision systems. The temperature resolution improves by increasing the array length, or manufacturing the two-dimentional matrixes. The spatial resolution expressed by modulation transfer function:

$$MTF = \frac{1}{1+K_s^2 \cdot Q_a^2} \cdot \frac{2\cdot\sin\left(\frac{K_s \cdot l}{2}\right)}{K_s \cdot l} \qquad (3),$$

where Ks - spatial screen frequency; Q_a - ambipolar diffusion length; and is defined by diffusion bleed of the non-equilibrium carriers packet and spatial averaging in the readout zone.

From this expressions follows, that manufacturing of the SPRITE-detectors needs a material possessing significant lifetime and small diffusion length of minority carriers. From this point of view the most suitable is n-CdxHg1-xTe.

It is known a number of the devices on the basis of this material, one of which has horn type geometry of read-out zone and conic geometry of the drift region, that considerably has improved a photodetectors basic photoelectric parameters [2]. The horn type geometry of read-out zone, has allowed to overcome disadvantage of the structure, connected with inhomogeneity of the electric field in bulk, that result to considerable straggling of time over of carriers drifting to read-out zone. Besides higher electric intensity at the negative electrode has reduced the delay of the minority carriers recombination near to contact. However even in this design, it was not possible completely to overcome the pointed deficiencies. The carrier drifting near back side of the device, transits the greater trajectory under action of weaker field, than carrier drifting in the front side. The small width of a negative electrode, even higher electric intensity has not allowed completely to overcome accumulation of carriers on contacts resulting in to increasing of accumulation time and, therefore, to a time blurring of the image. The arrangement of reading contact on the one side of device, results in losses of a useful signal from the carriers, drifting on the distant side of the device, which

consequently leads to deterioration of the device's resolution. The listed above deficiencies of the sensing device design by the as the meander is dispossessed. Such design also has led to improvement of pulse function. However, in this design, the small width of bar, about 15 microns, rather essential influence on parameters renders the carriers recombination on sides, reducing a lifetime of carriers. Though modern technologies have allowed partially to overcome this deficiency, presence of backlashes between strips result in losses of a part of a light fluxe.

In [3], we proposed modification of IR receivers photosensitive elements, will improve their performance by drawing on the back side of the contact area symmetrical metallization, leading to a equalizing of the electric field across the thickness of the crystal. Usage of a similar design for SPRITE-photodetectors manufacturing in addition should lead to a significant reduction of the accumulation of carriers near the negative contact, due to the doubling of the actual width of the contact, while maintaining the advantages of horn-shaped geometry of the reader, increasing the field strength near the contact, and contribute to a higher resolution.

To estimate the spatial resolution instead of the function (1), we used an expression which is obtained by phasing out the functions of the diffusion spreading of a rectangular characteristic of the pickup area:

$$F(t) = \int_{-\infty}^{\infty} \exp\left(-\frac{|vt - x|}{Q_a}\right) \cdot rect\left(\frac{x}{l}\right) dx \quad (4)$$

where t - time of observation, and v - speed of scanning images.

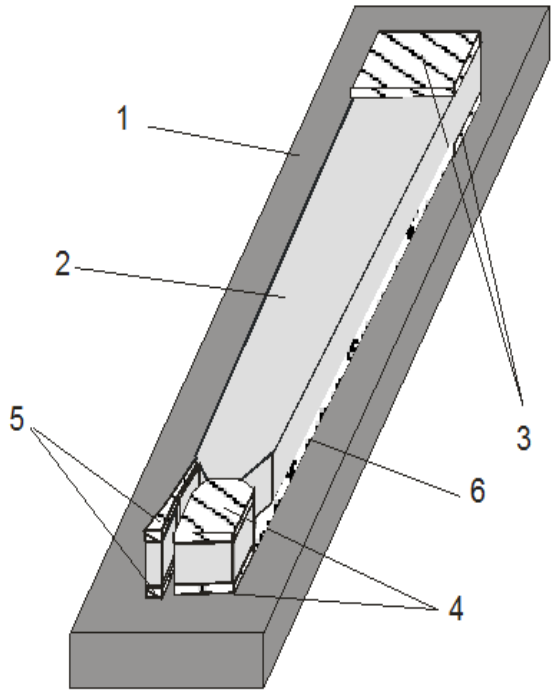

Fig. 2. General view of the photosensitive element of the proposed sensor. 1 - substrate, 2 - crystal Cd0.2Hg0.8Te; 3 and 4 - current contacts, 5 - reads the contact, 6 - glue.

Parameters of the detector made by this design [4]: length 700 μm, effective wide 62,5 μm, thickness 12 μm, read-out zone length 62 μm, generated charge carriers lifetime ~ 3,8 μs, average reduced detectivity for one element of decomposition D ~ $5x10^{10}$ и $5,5x10^{10}$ $W^{-1}Hz^{1/2}cm$, on the traditional and proposed detector respectively. Pulse width of the proposed design in terms of 1/e is 90 microns, while that of the standard configuration of more than 110 microns.

The results can be explained as follows. Increasing detectivity associated with improved sensitivity reader contact. Indeed, in the traditional design carriers drifting pass by the potential contact closer to the back side make a smaller contribution to the potential change on the front surface, where dislocated the potential contact, and the proposed design, this shortcoming is eliminated by metallizing the back side. Shortening the length of the accumulation region due to the fact that the metallization of the back side of contact results in an actual doubling of the width of the contact, which helps to reduce the delay time of recombination, and this in turn leads to improvement of impulse response. Improvement of the impulse response is also associated with a decrease in the transit time spread of nonequilibrium charge carriers due to alignment of the electric field across the thickness of the sample and the distance, flying vehicles, born near the front and back sides of the photosensitive element.

Thus the proposed design can significantly improve the MTF SPRITE-photodetector due to alignment of the electric field along the sample and to reduce the accumulation in the negative contact, and improve the detectivity by improving the quality of potential electrode.

However, bulk crystal technologies have some difficulties, it is possible also to refer necessity of the contacts manufacturing with descent, splitting of readout zone for manufacturing potential and pulling contacts, problem of the current carrying paths distributing at multielement arrays and matrixes manufacturing. Besides are made great demands and on homogeneity of initial bulk chips.

The progress of epitaxial technologies, achieved in last years has allowed to growth $Cd_xHg_{1-x}Te$ epilayers with low concentration ~ 10^{14} cm^{-3} and high minority carriers lifetime $>10^{-6}$ s. The advantage of epifilms consists in their high homogeneity. At the same time, epitaxial film have a number features, connected with gradient of the forbidden band on thickness, resulting in to originating of the variband field, pushing minority carriers to the side with smaller E_g.

Earlier we offered the design of the CIS imager [5] on the basis of the $Cd_xHg_{1-x}Te$ epilayers, grown in the furrows beforehand created in a substrate, with further usage of a substrate as a contact raster and interconnection of the matrix elements. Usage of a similar design for SPRITE-photodetectors making, allows to shun a number of technological complications and design lacks which have been mentioned above.

On the fig. 3 the design of the SPRITE-photodetector on the basis of $Cd_xHg_{1-x}Te$ epilayers is shown. Thus, in this design successfully are solving the mentioned above technological problems, connected to the block of SPRITE-photodetectors making by traditional planar technology on the basis of bulk crystals.

Sequences of technological operations of the pointed photodetector making is described in [6].

Now we shall consider the physical aspects allowing to the offered design substantially to overcome constructive lacks of traditional SPRITE-photodetectors.

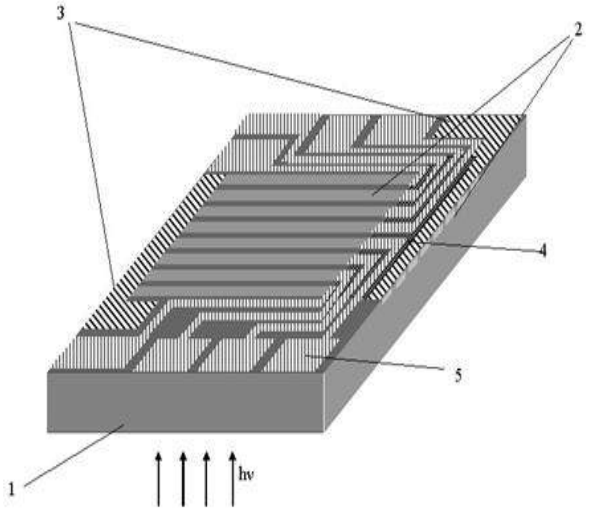

Fig. 3. SPRITE-detector on the base of epitaxial layer. 1 – substrate, 2 – epilayer, 3- current contact, 4 – dielectric layer, 5 read-out contacts.

As the epifilms, are grown in furrows in identical condition on a homogeneous substrate, physical properties, such as free carriers density, their mobility, electrical conductivity, and also lifetime and the diffusion length of nonequilibrium carriers for all strips is practically identical. In that case, the bias voltage to each device necessary for the coordination of time over of carriers with scan rate, also will be identical. Therefore, it is possible to connect current contacts of all strips in bridge to one power supply. It allows to reduce quantity of contacts up to (N+2), instead of 3N for bulk photodetectors, where N is quantity of sensing devices in the block, to make distributing only of potential electrodes. It considerably easies further switching of the photodetector. Besides flat, without backlashes the surface of the offered design allows to make without problems jointing with a multiplexer.

In optimal of known design of SPRITE-photodetectors on bulk chips having horn type geometry of readout zone, the disorder of the time over of carriers generated on edge and middle of the device reaches 110-130 mcs, that is bound to geometry of the device. In the offered design the readout zone has the square form, that result to identical to the carriers drifting on periphery and in the middle of the device, trajectories before pulling contact, that results in equal time over and their simultaneous registration. The vajor width of contact interferes with strong accumulation of carriers in the readout zone, improving resolution. The greatest time difference of registration in a known design is observed for carriers transiting far from potential contact. In our case the potential contact is superimposed on all breadth of a device, resulting to simultaneous registration of carriers drifting on all width of the device, that is inaccessible at manufacture the split contacts.

In epifilms during their growth the maintenance of cadmium from a substrate on thickness smoothly varies from telluride of cadmium up to a composition on a surface. Thus arises a varyband field, which one operates only on minority carriers and pushes them to more narrow-bandgap side. Thus, the packet of carriers generated by radiation, does not blur on a thickness of the chip, and moving to a surface, on which contacts are marked and drifts in narrow near-surface area of the film, that also reduces a blurring of the carriers packet. Furthermore, in an offered design the epifilms are grown in furrows, that is grow from three walls, therefore, and on width of the device also exists varyband field, which one pushes carriers from sides of the strip, promoting diminution influence of lateral areas being a radiant of a surface recombination. Besides such design allows to improve removal of Joule heat from devices, accordingly they can work at higher electric fields. Apparently from the expression (1), the sensitivity is inversely proportional to thickness of the device. For this reason usually the thickness of the device is makes no more than 10 microns. In our case the varyband fields presence allows to speak about an effective thickness of a device. So at usual for holes mobility 500 cm^2V/s and built-in field about 100 V/cm, the carrier overcomes distance 10 microns during the order 20 ns, and it appears in near-surface area. It is practically possible to count, that the carriers are agglomerated by a built-in field in the channel, is significant smaller, than the sectional area of the film, where happens their drift. The estimation which has been carried out for above mentioned dimensions, show, that the effective width decreases up to 50 microns, and the thickness twice. And it is true for the mechanism of drift, and at photogeneration, all width of the device works. It allows to use thicker layer loss free of sensitivity, and even on the contrary it is better to use a light flux. At a flare with large-band side, it is possible to expand the spectral region of the photodetector. In [7] it has been shown, that at nonlinear change of the forbidden band on thickness of the film, it is possible to receive a wide spectral characteristic practically overlapping all range between maximal and minimum value of the forbidden band. In [8] we have shown, that it is possible to approximate the changes of the forbidden band wide in $Cd_xHg_{1-x}Te$ epifilms, brought up by the LPE method, by three sites with different declinations. The first area with a major steepness is very small and it is large-band part. The second area begins approximately in compositions about 0.5, that there correspond to a wavelength 2 microns, and third is site is on area of compositions less than 0.25. Thus, there is an real opportunity to overlap a spectral range 2-14 microns by one photodetector.

[1]. *C.T.Elliott, D.Day and D.J.Wilson*. Infrared Physics, v.22, 1982, pp. 31-42
[2]. *C.T.Elliott*. Proc. SPIE 1038, 2-8 (1988)
[3]. *А.А.Алиев, Ш.М.Кулиев, Э.К.Гусейнов, А.К.Мамедов, Р.И.Мухтарова*. Приборы и техника эксперимента, 1996, № 2, с. 150-151.
[4]. *А.А.Алиев, Ш.М.Кулиев, А.К.Мамедов*. Приборы и техника эксперимента, 2004, № 1, с. 162-163
[5]. *A.A.Aliyev, A.K.Mamedov, E.K.Huseynov and etc*, Azerbaijan Republic patent I 2000 0216, 2000
[6]. *A.A.Aliyev, E.K.Husseynov, A.K.Mamedov*, Proc. SPIE, v. 5834, 2005, pp. 117-122
[7]. *V.A.Kudinov, G.P.Peka, A.N.Smolyar*, Ukr.Phis.Jour., v.34, pp.742-745, 1989
[8]. *A.A.Aliyev, .K.Mamedov, E.K.Huseynov and etc.*, Proc SPIE, v. 4340, pp 128-132, 2000

PERSISTENT PHOTOCONDUCTIVITY RELAXATION IN SINGLE CRYSTALLINE CADMIUM TELLURIDE

ALI A. RONASSI, ALEXANDER K. FEDOTOV
Belarusian State University,
Independence av. 4, 220030 Minsk, Belarus fedotov@bsu.by
Tel. +375-17-2095451, fax +375-17-2095445

Persistent photoconductivity (PPC) has been investigated in details in undoped and doped with Sb Cadmium Teluride single crystals. It was found that in the temperature region of 77 - 300 K the decay of PPC in time for CdTe follows the "stretched-exponential" function, whereas the PPC in CdTe:Sb was found to follow a power-like law with the exponent less than unity. The behavior of PPC observed can be attributed to the random local-potential fluctuations in the samples studied.

INTRODUCTION

CdTe is one of the known semiconductor materials which can be used for producing of noncooled X-Ray and γ-Ray detectors and other optoelectronic devices. To use it in practice we need crystals without imperfections and having resistivity higher than 10^8 Ω·cm. However, when growing of the crystals by usual Bridgement method, uncontrolled defects (impurities, intrinsic point defects, dislocations, Te precipitates, etc.) are always presented giving trap centers concentration up to 10^{16} cm^{-3} that results in sharp decrease of resisitivity of the material [1] and high leakage currents in complete devices [2]. The presence of such defects can become apparent, in particular, in conservation of photoconductance after crystal lightning that was called as persistent Photoconductance (PPC).

PPC phenomenon been observed in several groups of semiconducting materials. Much studies on this subject have been concentrated on II-VI ($Zn_xCd_{1-x}Se$, etc.) and III-V (Al_xGa_{1-x} As, etc.) semiconductors [3-7] in which the defects (DX centers, charged extended defects and impurities, etc.) are a well-known cause of strong PPC effect at temperatures T < 150 K. As to II-VI semiconductors, it suggests that the spatial separation between stored charge carriers by random local-potential fluctuations (RLPF) caused by compositional fluctuations is responsible for PPC observed in many of these materials [4-6].

PPC decay behavior observed in these materials at low temperatures T < 90 K for $A1_{0.3}Ga_{0.7}As$ [7] and 70 K < T < 220 K for $Zn_{0.3}Ga_{0.7}Se$ [5] usually followed a stretched-exponential function, $i_{PPC}(t) = i_{PPC}(0)\exp[-(t/\tau)^{\beta}]$, where τ is the relaxation time constant and β the decay exponent. Although the PPC decay in both kinds of materials can be very often described by Kolrausch functions, the decay parameters can be very different: for II-VI semiconductors, β is around 0.8 and τ is on the order of 1000 s at low temperatures, whereas for $A1_{0.3}Ga_{0.7}As$ the values of β and τ are between 0.2 and 10^{13} s, respectively.

These works on impurity doped and compensated II-VI and III-V semiconductors has indicated that microscopic inhomogeneity caused by impurity and extended defects distribution is the most likely reason for PPC phenomenon [8]. Hence, PPC is very often used as an evidence for the presence of atomic and extended defect centers in semiconductors which supposedly have unusual properties.

Full understanding of PPC is also very important from the point of view of practical applications. The PPC effect can be utilized to optically vary the carrier concentration in a single crystalline semiconductors by simply varying excitation photon fluence. Because most semiconductors exhibit the PPC effect only at low temperatures (usually below 150 K), device applications based on PPC phenomenon have not been previously established.

In this paper, we present the results comparing PPC behavior in undoped and Sb doped CdTe single crystals grown by modified Bridgment method where PPC can be attributed to RLPF caused by compositional fluctuations.

EXPERIMENTAL

Experiments were performed on the samples of undoped and Sb doped CdTe single crystals grown by the modified Bridgman method [9]. Slices of the ingots were prepared by mechanical polishing followed by the chemical etching in 2% Br_2 in methanol solution to remove the remaining damaged surface layer.

Ohmic contacts were produced by soldering silver paste onto the fresh surface of the samples. For the conductivity measurements a four point method was applied. In order to make sure that the contacts were ohmic, we measured I-V characteristics. The linear character of I-V confirmed that these contacts were fully ohmic.

In this work, the temporal kinetics of conductivity was measured at temperatures between 100 and 297 K using liquid Nitrogen to provide low temperatures. To eliminate the creation of frost at the sample surface during experiments, we put the samples in a special chamber with vacuum of about 10^{-3} mbar. A thermal conductive copper holder which had a thin insulation layer for avoiding any electric contact with the samples was used to put samples in this vacuum chamber. For applying different temperatures, a thin wire electrical heater was put on the back of the copper holder. In this way the heat transmission and the samples' temperature changes was quite fast and easy. A highly sensitive thermocouple was used to measure and control temperature. The temperature was kept constant during experiments with the maximum deviation of 0.1 K.

The monochromatic light beam coming out of the monochromator was focused with the help of a special optic onto the sample. The monochromatic light of photon energy equal to 2.11 eV was chosen for lightening of the samples studied.

We defined and applied a closed-loop procedure for testing the samples behavior under changing the temperature. After each test after switch-off the lightening at the next low temperature, the temperature of the sample studied was increased again to room temperature in the dark to retract the sample to the initial state and then decreased to the new desired temperature. The balance-out time allocated for each temperature was 20-40 minutes. It provided similar initial state for experiment at each temperature.

In all experiments, bias voltage applied to the sample was 3 volts and the time of lightening was kept at 70 seconds. The current decay was measured by a highly sensitive Keithley nanoampermeter, which was logged to a computer.

RESULTS AND DISCUSSION

Undoped CdTe: In accordance with [10], just from the moment of optical excitation switching-off (t = 0) of the sample PPC *i* relaxation in time can be described by the normalized function

$$i_{PPC} = [I(t) - I_d]/[I(0) - I_d], \quad (1)$$

where I(0) is photocurrent at t = 0 after the lightening switching-off, I(t) - photocurrent at the moment t after the lightening switching-off and I_d – dark current difining by outcoming of the relaxation curve I(t) on saturation. The time dependent PPC decay $i_{PPC}(t)$ can be very well described by a "stretched-exponential" function (Kolrausch law) which is frequently used to describe the PPC relaxation in a wide class of II–VI and III–V semiconductors [11,12]

$$i_{PPC}(t) \approx i_{PPC}(0)\cdot\exp[-(t/\tau)^{\beta}], \quad (2)$$

where τ is is the decay time constant, and β (0 < β < 1) is the decay exponent.

As follows from examples of the relaxation curves at different temperatures and applied biase voltage V = 2 V in Fig. 1, for the undoped CdTe samples $i_{PPC}(t)$ actually obey the law (2) at the whole temperature range. The values of PPC relaxation parameters τ and β for the undoped CdTe single crystal, deconvoluted from curves in Fig. 1 using equation (2) fitting, were 50 < τ < 600 s and 0.2 < β < 0.3. As follows from this fitting, the PPC relaxation time constant τ for the undoped CdTe crystals increases with temperature decrease. The presented in Fig. 2 linear dependence of τ(T) in Arhenius scale indicate that τ(T) has thermoactivated character $\tau = \tau_o\exp(E_a/kT)$, where τ_o is high-temperature limit of the relaxation time constant. In this case, PPC effect, on the analogy of [13-26] for II-VI and III-V semiconductors, can be ascribed to the formaton of RLPF (see, [4-6]) with the mean values of modulation of energy bands edges E_a of the order of 0.026 eV (see, Insert in Fig. 2).

CdTe doped with Sb: As for previous case, in the studied CdTe(Sb) samples PPC relaxation in time $i_{PPC}(t)$ can be also described by the normalized function (1). In these samples we observed four different temperature regions where $i_{PPC}(t)$ behavior were characterized by substantially diverse behavior.

In the region 1 for T < 90 K, no PPC effect was observed. In region 2 for 90 K < T < 105 K, the light irradiation of the samples induced the low-level PPC with a short relaxation time periods (less than 20 s). In range 3 for 105 K < T < 205 K, as shown in Fig. 3, the PPC decay became faster at the temperature decrease.

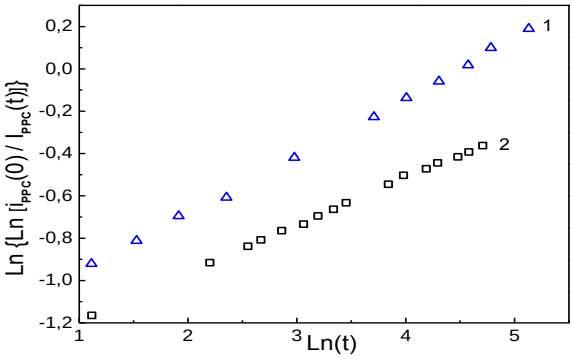

Fig. 1. PPC relaxation curves at V = 2 V for the undoped CdTe single crystal at temperatures 90 K (1) and 120 K (2) and 180 K(3) after 15 s lightening in different scales

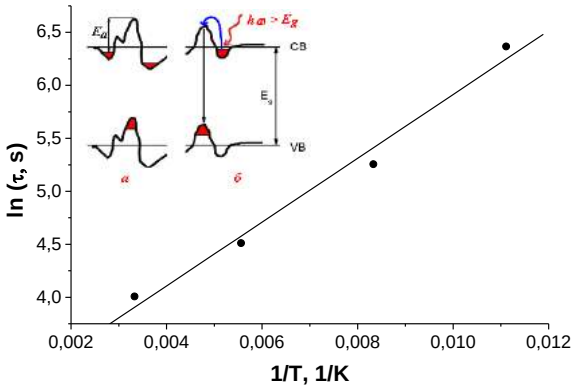

Fig. 2. Temperature dependences of PPC relaxation time constant τ in Arhenius scale for the undoped CdTe crystal. In Insert, a schematic presentation of the randomly modulated edges of energy bands with the mean values E_a of RLPF before (a) and after (b) lightening.

In addition, the dark current decreased with the temperature growth in this region. This result is quite unexpected as compared to the results for the undoped CdTe crystals in Fig. 1 and is in contradiction to the most of the above mentioned models (except RLPF model [3-6, 27,28]). Taking into account the predictions of these models, we could expect that the PPC effect would be more tangible when lowering the temperature and its relaxation would take a longer time.

At the same time, when the temperature is increased higher than 205 K (range 4), the PPC decay shows an ordinary behavior observed in the previous case: when the temperature is increased, the PPC decays faster although the dark current decreases with the temperature growth in this region too (see Fig. 3).

It is seen from Fig. 3 and 4, as opposed to the behavior of undoped CdTe samples, the $i_{PPC}(t)$ behavior in

CdTe:Sb in the temperature ranges 3 and 4 for times $t > t_0$ (where $t_0 \approx 1$ s) can be described by the power law

$$I_{ppc}(t) \sim t^{-\delta}, \quad (3)$$

where δ is a decay exponent. The condition related to PPC phase is obtained for $\delta < 1$.

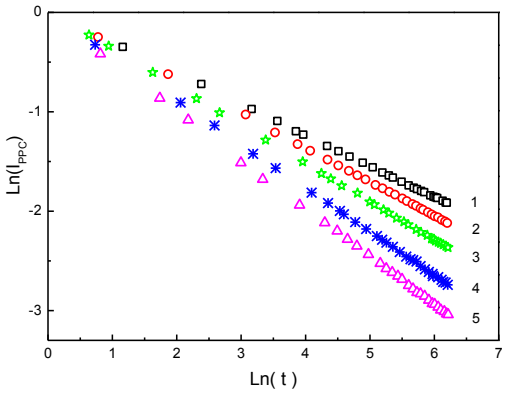

Fig. 3. The PPC decay curves in logarithmic scale for CdTe(Sb) in the temperature range 3 for temperatures T = 205 K (1), 175 K (2), 150 K (3), 125 K (4), 105 K (5)

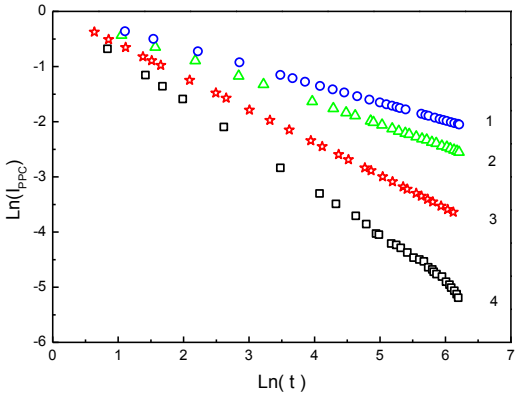

Fig. 4 The PPC decay curves in logarithmic scale for CdTe(Sb) in the temperature range 4 for temperatures T = 225 K (1), 245 K (2), 275 K (3), 295 K (4)

Collection of the curves in Fig. 3 and 4 allowed us to calculate the temperature dependence of δ values. Fig. 5 shows changes in the exponent δ *vs* temperature in the temperature range of 105 K < T < 295 K studied in our experiments for two times (20 s and 120 s) of relaxation measurements. Considering these two curves, which fully overlapped, we conclude that the minimal value of parameter δ takes place at the temperature 205 K which may be considered as a turning point on the curve. Note that this temperature just corresponds to the boundary between regions 3 and 4 where the character of the $i_{PPC}(t)$ behavior is changed.

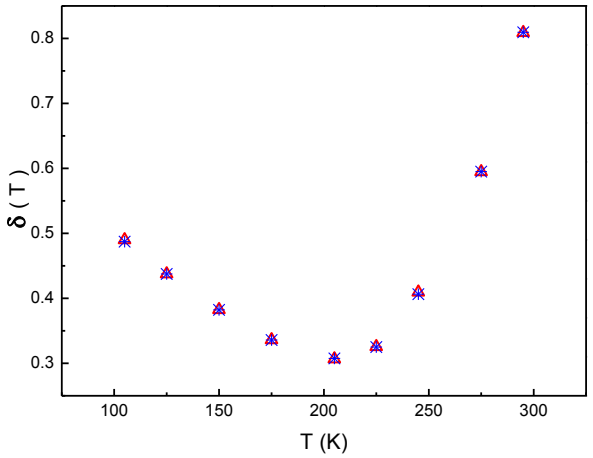

Fig, 5. The exponent δ *vs* temperature for CdTe(Sb) for two values of relaxation times (20 s and 120 s). Curves were recorded after 70 seconds lightening and with bias voltage 3 volts.

RESUME

The presented in this paper results on PPC relaxation in CdTe single crystals grown by modified Bridgment method show different behavior of the PPC dacay laws for the undoped and Sb doped samples. The physical origin of this difference in PPC relaxation kynetics in the undoped CdTe (stretched–exponential relaxation) and in Sb doped CdTe (power law relaxation), is not clear. However, it is believed that both are able to describe the relaxation kinetic of a wide range of disordered systems tending towards balance in different conditions [29, 30].

In whole, the results of this work can indicate that random local-potential fluctuations, induced by composition fluctuations or impurity potential, can be the main origin of PPC both in the undoped CdTe and CdTe(Sb) sample studied.

[1]. *A.Zumbiehl, S.Mergui, M.Ayoub, M. Hage-Ali et al.* Mater. Sci. Eng. B. 2000. Vol. 71. P.297.

[2]. *D.M.Hoffmann, W.Stadier, P.Cristman, B.K.Meyer* Nucl. J. and Meth. Phys. Res. 1996. Vol. A 380. P.117.

[3]. *D.V. Lang and R.A. Logan*, Phys. Rev. Lett. 39, 635 (1977).

[4]. *H.X. Jiang and J.Y. Lin*, Phys. Rev. Lett. 64, 2547 (1990).

[5]. *H.X. Jiang and J.Y. Lin*, Phys. Rev. B 40, 10025 (1989).

[6]. *J.Y. Lin and H. X. Jiang*, Phys. Rev. B 41, 5178 (1990).

[7]. *J.Y. Lin, A.Dissanayake, G.Brown, and H.X.Jiang*, Phys. Rev. B 42, 5855 (1990).

[8]. *M.K. Sheinkman and A.Ya. Shik*, Sov. Phys-Semicond. 10, 128 (1976).

[9]. *S.Sen, W.H.Konkel, S.J.Tighe, L.G.Bland, S.R.Sharma, R.E.Taylor*, J. Cryst. Growth. V. 111. P. 198886.

[10]. *J.Y.Lin, H.X.Jiang*, Phys. Rev. B. 1990. Vol. 41. P. 5178.

[11]. *A.Dissanayake, M.Elahi, H.X.Jiang, J.Y.Lin* Phys. Rev. B. 1992. Vol. 42.

[12]. *J.Trzmiel, E.Palaczek-Popko, K.Weron, J.Szatkowski, E.Wojtyna* Acta Physica Polonica. V. 114. P. 1417.
[13]. *H.X. Jiang, G.Brown, J.Y.Lin* J. Appl. Phys. 1991. Vol. 69. P. 6701.
[14]. *B. I.Shklovskii and A. J.Efros,* Zh. Eksp. Teor. Foz., 1971, Vol. 60, P. 867.
[15]. *M.Ryvkin and I. S.Shlimak,* Phys. Status Solidi, 1973, Vol. A16, P. 515.
[16]. *R.Fang, R.F.Brebrick* J. Phys. Chem. Sol. 1996, Vol. 57. P. 443.
[17]. *S.Sen, W.H.Konkel, S.J.Tighe, L.G.Bland, S.R.Sharma, R.E.Taylor* J. Cryst. Growth. V. 111. P. 198886.
[18]. *A.Dissanayake, M.Elahi, H.X.Jiang, J.Y. Lin* Phys. Rev. B. 1992. Vol. 42.
[19]. *J.Trzmiel, E.Palaczek-Popko, K.Weron, J.Szatkowski, E.Wojtyna* //Acta Physica Polonica. V. 114. P. 1417.
[20]. *J.Kakalios , R.A.Streef , W.B. Jackson* // Phys. Rev. Lett. 1987. Vol. 59. P. 1037.
[21]. *E.Gombia, F.Bissoli, M.Zha, A.Zappettini, T.Görög, L.Zanotti* Phys. Stat. Sol. C. 2003. Vol. 0. P. 881.
[22]. *E.Arslan, S.Butun, Bora S.Lisesivdin, M.Kasap, S.Ozcelik, E.Ozbay* J. Appl. Phys. 2008. Vol. 103. P. 103701.
[23]. *J. Trzmiel, E.Palaczek-Popko, K.Weron* J. Appl. Phys. 2008. V. 103. P. 114902.
[24]. *A.Jurlewicz, K.Weron* Cell. Mol. Biol. Lett. 1999. V. 4. P. 56.
[25]. *A.Jurlewicz, K.Weron* J. Non-Cryst. Solids 2002. V. 305. P. 112.

PECULARITIES OF ELECTROREFLECTANCE SPECTRUM OF $BI_2 TE_3$ LAYERED CRYSTAL RELATED TO LOW-SYMMETRIC POINTS IN BRILLOUIN ZONE

B.M. RUSTAMBEKOV, F.H. MAMMADOV
Azerbaijan National Academy of Sciences,
Institute G.M.Abdullayev Institute of Physics,
G.Javid ave.33, AZ-1143, Baku, Azerbaijan

There have been investigated $Bi_2 Te_3$ layered crystal electroreflectance spectrum peculiarities related to interlaminar interaction and transitions in low-symmetric critical points.

1. INTRODUCTION

$Bi_2 Te_3$ layered crystals due to the strong anisotropy of properties attract investigators' attraction. Practical aspect of investigation results of materials like these relates to the growing interest to thermoelectric devices and IR detectors.

Bismuth telluride with $D_{3\alpha}^5 (R\bar{3}m)$ symmetry are distinguished by mixed behaviour of chemical bond, which causes complexity of its zone structure. Optic measurements allow data of crystal energy bands to be refined, also modulation method of optic measurements offers scope for obtaining sharp point of peaks appropriate to critical points.

As it is noted in $Bi_2 Te_3$ crystal ER spectra there have been observed peaks not considered in papers (2,3). Field broadening of spectra at high voltages of shift and modulation impede resolution of these peaks and at low levels of modulation and shift total intensity of spectra falls. Let′s consider and investigate such peculiarities in ER bismuth telluride crystal spectra.

2. EXPERIMENTAL PART

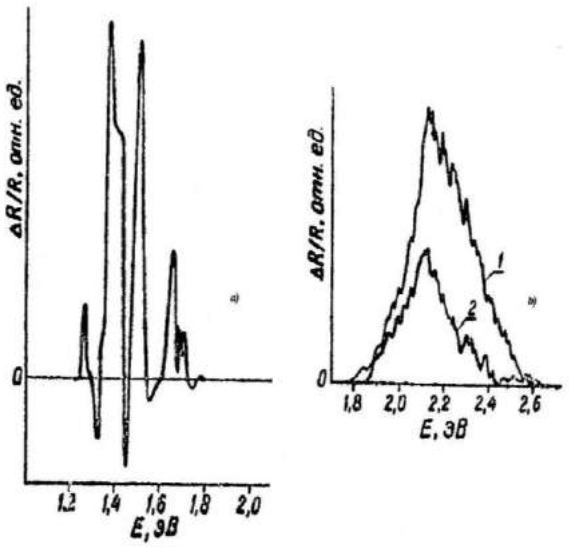

Fig.1. Bi_2 Te_3 ER spectra obtained in nonpolarized (a) and polarized (b) light where curve I is in agreement with polarization $\vec{E} \perp C$, curve 2 - $\vec{E} \| C$.

As a specimen $Bi_2 Te_3$ crystals obtained by Bridgman method with concentration $n=4{,}3 \cdot 10^{19} sm^{-3}$, conductivity $\sigma=1300\ om^{-1} \cdot sm^{-1}$ and thermal power $\alpha=170\ mkv/deg$ have been used. Reflection is observed from the planes perpendicular to optical axis in nonpolarized and linearly polarized light.

On Fig.1 there have been presented $Bi_2 Te_3$ ER spectra taken in the range *1,2-1,8 eV(a)* and *1,8-2,6 eV* at slift voltages $U_{-}=0{,}3$ *V* and modulation $U_{\sim}=0{,}75$ *V* and $U_{-}=-0{,}2$ *V*, $U_{\sim}=0$, respectively.

To consider given peculiarities of spectrum and further investigation of critical points there has been carried out Kramer – Krouig function analysis $\Delta R/R$ that allows modulation line forms of real $(\Delta\varepsilon_r)$ and imaginary $(\Delta\varepsilon_i)$ parts of dielectric constant just from the experiment to be obtained

$$\Delta\varepsilon_r = \frac{n_r}{2n_L}\left(n_r^2 - n_L^2 - 3n_i^2\right)\frac{\Delta R}{R} + \frac{n_i}{n_r}\left(3n_r^2 - n_L^2 - n_i^2\right)\Delta\Theta$$

$$\Delta\varepsilon_i = \frac{n_i}{2n_L}\left(3n_r^2 - n_L^2 - n_i^2\right)\frac{\Delta R}{R} + \frac{n_i}{n_r}\left(3n_r^2 - n_L^2 - n_i\right)\Delta\Theta$$

Here n_r and n_i are real and imaginary parts of refractive index of the material, but n_L is the refractive index of transparent electrolyte.

$$\Delta\Theta(\omega) = \frac{\omega}{\pi} P\int_0^0 \left(\frac{\Delta R(\omega^1)}{R(\omega^1)} - \frac{\Delta R(\omega)}{R(\omega)} d\omega^1 / \left(\omega^{12} - \omega^2\right)\right)$$

Is the modulation of phase angle and P$\int$ is the main part of integral in terms of Cauchy.

On Fig.2 there have been presented curves $\Delta\varepsilon_r$ and $\Delta\varepsilon_i$ corresponding to spectra $\Delta R/R$ (Fig.1). These curves have revealed a wide variety of significantly broadened peculiarities which part denoted in Fig.2 by arrowed lines can be related to the transitions in the vicinity of three – dimensional critical points.

On the one hand broadening of obtained peculiarities is due to the processes of phonon absorption and emission temperature (300 K) in the experiment, on the other hand by significant excess of Bi atoms compared to stoichiometry.

Both factors cause complications of spectrum interpretation. Obtained results show fair coincidence with the data of other authors [2,3].

Comparison of results with theoretical values given in Table 1 shows good agreement that enables their proper

interpretation to be hoped. Only peak E_1 is not explained well. It is probably connected with the fact that theoretical curve has a peculiarity within *0-1,5 eV* which can be spitted up to a number of narrow peaks at higher accuracy of calculations.

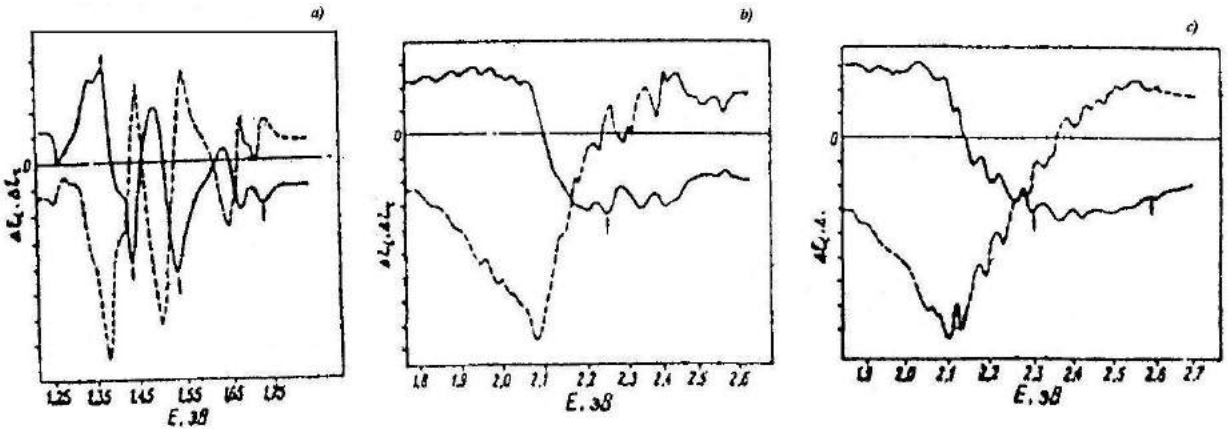

Fig.2. Curves ΔE_i (solid) and ΔE_i (dotted) for cases of nonpolarized light (a), polarization $\vec{E} \perp C$ (b) and $\vec{E} \,||\, C$ (c).

Table I Interpretation of ER spectrum

Peak, E, eV		**Peak, *E, eV***		**Transition symmetry**	$i\upsilon_{ij}C$	**Polarization**
experiment		**threory**				
E_1	1,37	k_1	1,25	$\Lambda_6 \to \Lambda_6$	14,1	$E_{\parallel}$
				$\Lambda_6^- \to \Lambda_6^+$	14,1	
				$\Pi\,\Xi, U, \Sigma$	13,1	$E_{\parallel}$, $E_\perp$
E_2	1,43	k_2	-	-	-	-
E_3	1,54	k_2	1,51	Π	13,1	$E_{\parallel}$, $E_\perp$
				Π	14,1	$E_{\parallel}$, $E_\perp$
				Π, U	12,1	$E_{\parallel}$, $E_\perp$
				U	9,1	$E_{\parallel}$, $E_\perp$
E_4	1,73	k_3	1,83	$L_6^- \to \{L_4^+ + L_5^+\}$	14,3	$E_\perp$
				Σ', F	14,3	$E_{\parallel}$, $E_\perp$
				R	14,3	$E_{\parallel}$, $E_\perp$
E_5	2,27	k_4	2,1	Π, Ξ	9,1	$E_{\parallel}$, $E_\perp$
				Π, Ξ	11,1	$E_{\parallel}$, $E_\perp$
				Π, Ξ	13,2	$E_{\parallel}$, $E_\perp$
E_6	2,56	k_5	2,5	Π, Ξ	14,3	$E_{\parallel}$, $E_\perp$
				Π, Ξ	14,3	$E_{\parallel}$, $E_\perp$
				Π, Ξ	12,1	$E_{\parallel}$, $E_\perp$
				Π, Ξ	14,2	$E_{\parallel}$, $E_\perp$

P.S. Points of Brillouin zone are denoted according to (13) Π, Ξ - planes of reflection, transitions in points Π,Ξ,U have symmetry $\{\Pi_3 + \Pi_4\} \to \{\Pi_3 + \Pi_4\}$. Representations degenerated due to time inversion.

To interpret spectrum peculiarities one can use dispersion curves $E_{jc}(\vec{k}) - E_{i\vartheta} \perp$ obtained by the results of theoretical calculation of bismuth telluride energy structure.

Here $E_{jc}(\vec{k})$, $E_{i\vartheta}(\vec{k})$ are electron energy in point *k* of Brillouin zone, indices *jc* number energy bands of conduction, i_υ is the valence band. There has been checked existence condition of critical points $\nabla E_{jc}(\vec{k}) - \nabla E_{i\upsilon}(\vec{k}) = 0$, their localization in Brillouin zone is carried out and symmetry of appropriate transitions is determined

Analysis shows that all the peaks except E_1 and E_4 relate to numerous transitions in low-symmetric points, therefore they have been observed in ER spectra obtained at both polarizations of light. Peculiarities E_1 and E_4 contribute to as high-symmetric points *L* and *A* as low-symmetric ones. They have been observed in both spectra. Obtained result is in agreement with the conclusions of low-symmetric crystal theory about the fact that their spectrum peculiarities relate with the nonindividual transitions in high-symmetric points of Brillouin zone but predominantly with big set of its low-symmetric points.

3. MAIN RESULTS

Earlier there have been found out unobservable peculiarities in bismuth telluride ER spectra. By Kramers – Krouig analysis there have been obtained data of these peculiarities which are interpreted on the base of dispersion curves of photon energy participating in crossover electron transitions. It is shown that these peculiarities of ER spectra relate to numerous transitions in low-symmetric points of Brillouin zone and are not practically susceptible to polarization of light.

[1]. *B.M.Yoltsmann, V.A.Kudinov, I.A. Smirnova* Semiconductive thermoelectric materials on the base of Bi and Te. M.Nauke. 1972, p.320

[2]. *A.Balzarotti, E.Burattini, P.Pacazzi* Phys. Rev. 1991, B.3, p.1159

[3]. *B.M.Yoltsmann, V.A.Kudinov, I.A.Smirnov.* Bi_2Te_3-based semiconductive thermoelectric materials. M.Nauke. 1972. pp.14, 110

[4]. *B.M.Yoltsmann, Z.M.Dashevski, V.I.Kaydanov, V.I.Kolomoets*. Film thermoelements: physics and use. M.Nauke, 1985, pp.170-174

[5]. *V.A.Tyagai, O.V.Skitko*. Electroreflection in semiconductors. Kiev. Naukova Dumka. p.302

[6]. *Yu.A.Baykov, V.A.Danilov*. Journal of technical physics. 2008, vol.78. ed.3. pp.63-67

[7]. *I.S.Virt, T.P.Shkumbatyuk and etc.* FTP, 2010, vol.44. ed.4

GROWTH AND PROPERTIES OF PENTANARY SOLID SOLUTIONS GaInAsPSb FOR 3-5 WAVELENGTH RANGE OPTOELECTRONIC DEVICES

G. S. GAGIS[1], V. I. VASIL'EV[1] AND N.N. MURSAKULOV[2]

[1]*Ioffe Physico-Technical Institute of the Russian Academy of Sciences,*
26 Polytekhnicheskaya st., St Petersburg 194021, Russian Federation
e-mail: giman@mail.ioffe.ru

[2]*Institute of Physics of Azerbaijan National Academy of Sciences,*
33, H.Cavid ave., Az-1143, Baku, Azerbaijan
e-mail: nmursakulov@physics.ab.az

In this work, the opportunity for utilization of novel semiconductor materials GaInAsPSb for active layers of room-temperature optoelectronic devices for 3 – 5 μm wavelength range was investigated. GaInAsPSb epitaxial layers lattice matched to GaSb and InAs were grown by LPE from antimony-rich melt solutions. It was shown that suggested pentanary solid solutions demonstrate high crystal quality and sufficient efficiency of optical radiation. High luminescent properties of GaInAsPSb solid solutions can be explained as the result of favorable band structure. Analysis has shown that addition of phosphorous changes the spin- splitting is greater than band gap value $E_g < \Delta_{SO}$

1. INTRODUCTION

An interest to optoelectronic devices of mid-infrared (MIR) wavelength range (2-5 μm) is caused by their applications for all-semiconductor gas analyzers, capable to control concentration of many toxic gases with absorption lines within MIR range (methane (2.3 μm and 3.3 μm), ethylene (3.17 μm), acetone (3.4 μm and 4.6 μm), nitrogen dioxide (3.9 μm and 4.5 μm), sulfurous anhydride (4.0 μm), carbonic gas (4.27 μm) and carbon monoxide (4.7 μm)).

2. METHODS AND APPROACHES

2.1 Materials

Semiconductor materials for MIR range are typically A^3B^5 solid solutions containing antimony. However, development of 3-5 μm radiation sources based on conventional quaternary solid solutions GaInAsSb and InAsPSb is difficult because spin-orbital splitting value Δ_{SO} in these materials is smaller than the bandgap value E_g. This is the reason for strong non-radiative Auger processes predominating over radiative recombination. In these materials CHHS process between conductivity (C) and heavy-holes band (H) with excitation of second heavy-hole (H) to the split-off band (S) is resonant, while CHCC Auger-recombination between conductivity (C) and heavy holes (H) band with electron transition within conductivity (CC) band has smaller rate [1].

The novel approach utilizing active layer material with $E_g < \Delta_{SO}$. In such materials, the energy of recombination between electron and hole is not sufficient for transition of the second hole into spin-orbital split-off band, resulting in suppression of CHHS-process. Moreover, in this case intraband absorption of radiation by holes is also suppressed, that is also favorable to laser threshold characteristics. Our investigations show that materials for 3-5 μm wavelength range with $E_g < \Delta_{SO}$ can be realized in pentanary solid solutions GaInAsPSb lattice-matched to InAs or GaSb.

Important advantage of pentanary solid solutions GaInAsPSb in comparison with their quaternary counterparts is availability of additional 'degree of freedom' allowing manipulation of any composition-depending property of material (in our case this is spin-orbital splitting value Δ_{SO}) at fixed lattice-constant and bandgap values (figure 1).

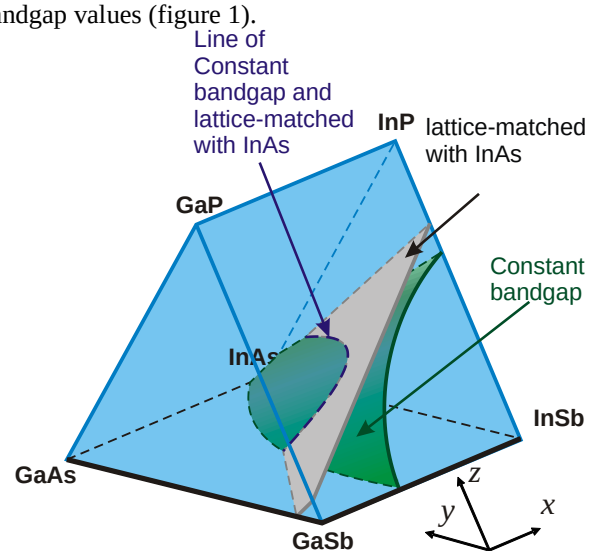

Fig.1. Lattice-matched with InAs and constant bandgap (Eg=0.37 eV) surfaces in concentration prism of Pentanary Solid Solutions $Ga_{1-x}In_xAs_yP_zSb_{1-y-z}$.

Preliminary estimation of required compositions was based on theoretical dependence of bandgap value on composition of solid solutions lattice-matched to InAs and GaSb. Calculation was carried out with parameters presented in [2]. Results of such calculations for solid solutions GaInAsPSb lattice-matched to InAs are shown at figure 2.

2.2. Growth procedure

Liquid phase epitaxy (LPE) is inexpensive and relatively simple technological process, therefore suitable for growth of sample layers. Also LPE is convenient for production of epilayers with compositions inside the miscibility gap, because growth process is sufficiently fast (10 – 60 seconds) thus preventing diffusion which gives rise to phase decomposition of solid solution. Availability of solid solutions with compositions falling into miscibility gap can extend the range of achievable physical characteristics of semiconductor materials.

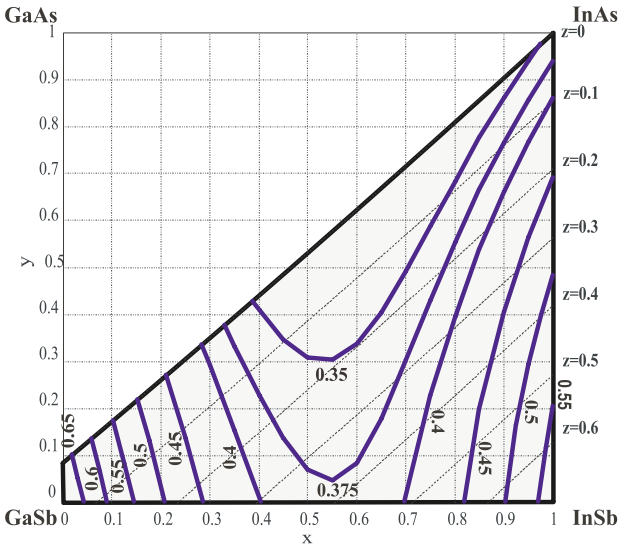

Fig.2. Projections on composition square of the intersection lines between lattice-matched with InAs and constant bandgap surfaces for pentanary solid solutions $Ga_{1-x}In_xAs_yP_zSb_{1-y-z}$. Numbers indicate E_g values.

Tendency to phase separation can be essentially decreased by introduction of elastic stresses in the layer (in this case the enthalpy component of free energy can be compensated by elastic component [3]). Elastic stresses can be provided in heterostructures by lattice mismatch between interfacing layers. According to calculations, required value of elastic deformation must be relatively large. This fact places a limitation on thickness of the stressed layers. In case of thickness greater than the critical value, defects appear that reduce elastic stresses. Our earlier experimental investigations have shown that said critical thickness does not exceed 50 nm [3, 4].

3. EXPERIMENT

GaInAsPSb epitaxial layers lattice matched to GaSb and InAs were grown by LPE from antimony-rich melt solutions. Conditions of epitaxial growth were chosen according to calculations of thermodynamic equilibrium between liquid and solid phases in A^3B^5 systems. Results of calculations were corrected using earlier defined segregation coefficients of Ga, As and P components [5] and measurements of liquidus temperature T^L and spontaneous crystallization temperature T^{Cr} for corresponding liquid phases by visual thermal analysis method *in-situ*. The temperature of epitaxial growth T^E must lie inside the interval [T^{Cr}, T^L], moreover, optimal growth condition are realized when T^E is close to T^{Cr}. Typical critical overcooling value $\Delta T = T^L - T^{Cr}$ for liquid phase of pentanary systems Ga-In-As-P-Sb is 7 - 20 ºC, depending on composition of liquid phase.

GaSb and InAs substrates were processed in chemical etchant before epitaxial process (water solution of hydrogen peroxide, tartaric acid and hydrofluoric acid). Melt solution for epitaxial growth was preliminary homogenized at temperature about 650 ºC for 30 – 45 minutes. Duration and temperature of homogenization were selected to minimize the negative effects caused by evaporation of volatile components (As and P).

4. RESULTS

In our experiments, we have obtained the layers of $Ga_{1-x}In_xAs_yP_zSb_{1-y-z}$ with compositions $0.9 < x < 0.99$, $0.7 < y < 0.85$, $0.01 < z < 0.07$. Epitaxial growth was carried out at temperatures 570 - 605 °C. Thickness of grown layers was 0.5 – 3 μm at crystallization rates 2 – 4 μm per minute.

4.1 Structural properties

Compositions of the epitaxial layers were measured using X-ray microanalyzer "Camebax". Boundaries between substrate and epilayer were sufficiently sharp, being the evidence of absence of interphase redistribution of components on substrate-melt interface during the growth.

Lattice mismatch between obtained layers and substrates was measured by X-ray diffractometry. At optimal epitaxial overcooling conditions during LPE $\Delta T = T^L - T^E$, diffraction curves with full width at half maximum (FWHM) so small as 12 – 42`` in wide range of lattice-mismatch values $|f| \leq 5.5 \cdot 10^{-3}$, were measured, indicating good crystal quality of grown layers.

For some GaInAsPSb samples it was observed that the epilayer consists of general matrix and small inclusions of solid phase with different composition (microcrystallites). Microcrystallites were sized in range from 1×1.5 to 2×4 μm. Their chemical compositions essentially differed from that of general matrix, and varied within the range: $0.43 < x < 0.99$, $0.20 < y < 0.42$, $0.02 < z < 0.04$. X-ray diffraction reflection curves of the layers with microcrystallites have several peaks. During experimental investigations it was ascertain that microcrystallites appear in case when the epitaxial layer composition falls into miscibility gap and its thickness exceeds 50 nm. We believe, that formation of microcrystallites can be associated with binodal decomposition processes.

4.2 Luminescent characteristics

Spectra of photoluminescence (PL) were investigated on the setup with closed cycle helium cryostat allowing measurements at wide temperature range from 4 to 350 K. Semiconductor 980nm wavelength laser was used for excitation. Optical signal was registered with high-aperture spectrometer SDL-1 (LOMO) and cooled Hg-Cd-Te photoresistor (Hamamatsu).

Comparisons of PL characteristics of sample series grown on GaSb and InAs substrates were reported earlier [6] and it was found out that GaInAsPSb grown on InAs has more good PL properties that ones grown on GaSb.

We believe this is caused by the following two reasons:

1) Physical parameters of solid solutions GaInAsPSb for investigated wavelength range (3 – 3.8 μm) lattice-matched to InAs substrate can appear to be more optimal for room temperature operation comparing to that of similar GaInAsPSb solid solutions lattice-matched to GaSb substrate.

2) Linear coefficient of thermal expansion of GaSb is significantly higher then that of any other A^3B^5 compound and corresponding solid solutions. This means that cooling of samples grown at high temperatures (570 –

650 ºC) and corresponding variation of lattice-mismatch between the layer and substrate is more probable to cause defects in case of GaSb substrate than for InAs.

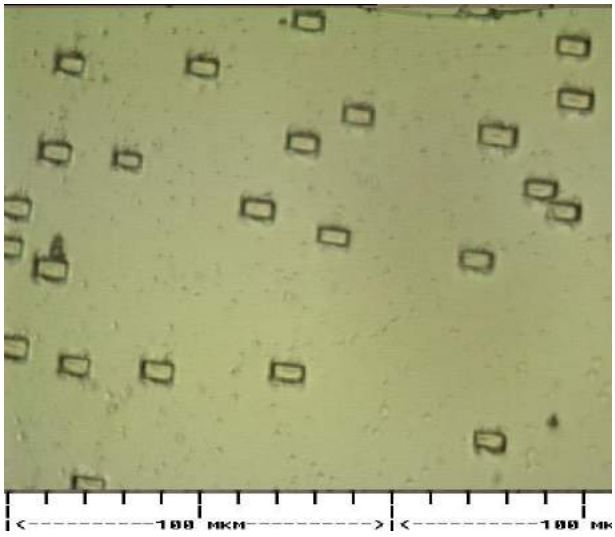

a)

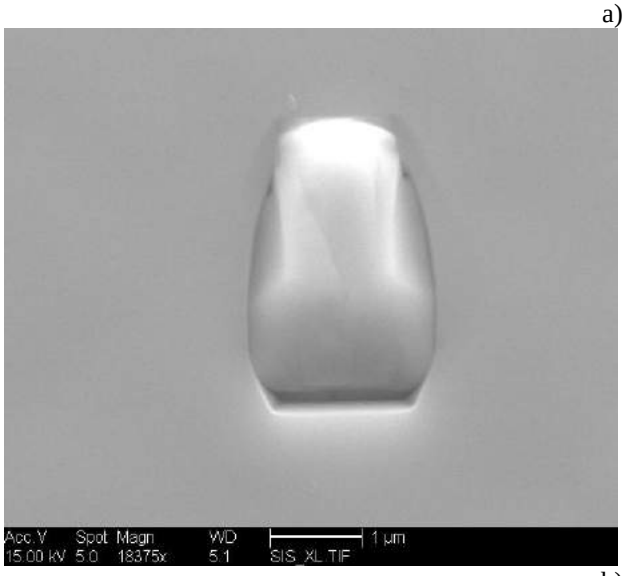

b)

Fig.3. Images of microcrystallites in GaInAsPSb epitaxial layers. Images were taken by optical microscope (a) and electron microscope "CamScan" (b).

In present work luminescent characteristics of samples grown on InAs substrates were studied (figure 4). PL properties at room temperature was sufficiently high whereas non-perfect (but satisfactory) crystal quality (figure 5).

High luminescent properties of GaInAsPSb solid solutions can be explained as the result of favorable band structure. Analysis has shown that addition of phosphorous changes the spin- splitting is greater than bandgap value $E_g < \Delta_{SO}$ [7]. In such case, suppression of non-radiative CHHS recombination takes place resulting in improvement of luminescent characteristics. Moreover, such approach is capable to enable room temperature electroluminescence as was reported earlier for p-i-n GaInAsPSb/p-GaSb homostructures at wavelength about 4 µm [8].

5. CONCLUSION

In this work, the opportunity for utilization of novel semiconductor materials GaInAsPSb for active layers of room-temperature optoelectronic devices for 3 – 5 µm wavelength range was investigated. It was shown that suggested pentanary solid solutions demonstrate high crystal quality and sufficient efficiency of optical radiation.

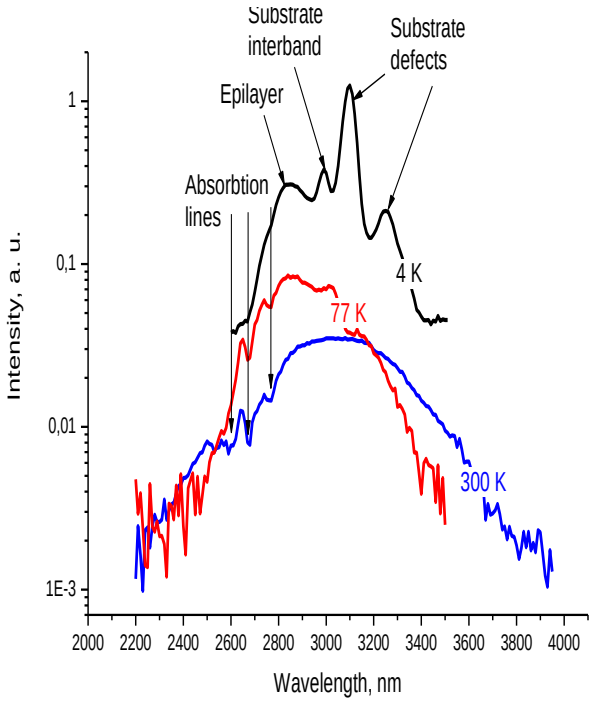

Fig.4. PL spectra of $Ga_{0.04}In_{0.96}As_{0.77}P_{0.11}Sb_{0.11}$/InAs(100)

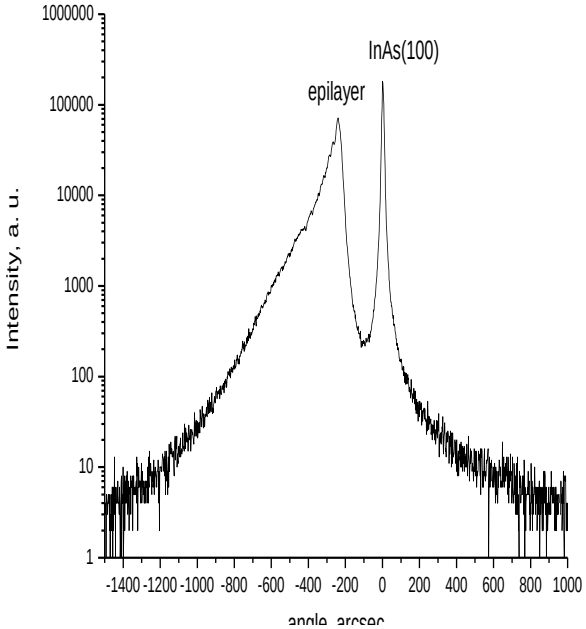

Fig.5. X-ray diffraction pattern for $Ga_{0.04}In_{0.96}As_{0.77}P_{0.11}Sb_{0.11}$/InAs(100)

[1] *M.Sh. Aidaraliev, G.G. Zegrya, N.V. Zotova, S.A.Karandashov, B.A. Matveev, N.M. Stus', G.N.Talalakin* 1992 Nature of the temperature dependence of the threshold current density of long-wavelength InAsSbP/InAs and InAsSbP/InAsSb double-heterostructure lasers. Semiconductors 26 (2) 138-43.

[2] *I. Vurgaftman, J.R. Meyer and L.R. Ram-Mohan* 2001 Band parameters for III–V compound semiconductors and their alloys. J. Appl. Phys. 89 (11) 5815-75.

[3] *V.I. Vasil'ev, I.P. Nikitina, V.M. Smirnov and D.N.Tretyakov* 1999 Isoperiodical heterostructures GaInAsSb/GaSb grown by LPE from Sb-rich melts in spinodal decomposition area Materials Science and Engineering B 66 (1-3) 67-69.

[4] *V.I. Vasil'ev, D. Akhmedov, A.G. Deryagin, V.I.Kuchinskii, I.P. Nikitina, V.M. Smirnov and D.N.Tret'yakov* 1999 GaInAsSb/GaSb heterostructures grown in the spinodal decay region by liquid-phase epitaxy from Sb-enriched solution-melts. Semiconductors 33 (9) 1034-36.

[5] *V.I.Vasil'ev,M.V.Baidakova, E.A.Kognovitskaya, V.I. Kuchinskii, I.P. Nikitina and V.M. Smirnov* Abstracts of 3-rd Int. Conf. on Mid-infrared Optoelectronics. *Materials&Devices* Growth and characterization of GaInAsPSb pentanary solid solutions, isoperiodic to GaSb substrates 5-7 September 1999, paper P-9 Aachen, Germany.

[6] *G S Gagis, V I Vasil'ev, A G Deryagin, V.V.Dudelev, A S Maslov, R V Levin, B.V.Pushnyi, V M Smirnov, G S Sokolovskii, G.G.Zegrya and V I Kuchinskii.* Novel materials GaInAsPSb/GaSb and GaInAsPSb/InAs for room-temperature optoelectronic devices for a 3–5 мм wavelength range (GaInAsPSb/GaSb and GaInAsPSb/InAs for 3–5 мм)// Semicond. Sci. Technol. 23 (2008) 125026 (6pp)

[7] *S.A. Cripps, T.J.C Hosea, A.Krier, V.M.Smirnov, P.J.Batty, Q.D.Zhuang, H.H.Lin, Liu Po-Wei and G.Tsai* 2007 Midinfrared photoreflectance study of InAs-rich InAsSb and GaInAsPSb indicating negligible bowing for the spin orbit splitting energy Appl. Phys. Lett. 90 172106-1-3.

[8] *A.Krier, V.M.Smirnov, P.J.Batty, V.I.Vasil'ev, G.S.Gagis and V.I.Kuchinskii* 2007 Room temperature midinfrared electroluminescence from GaInAsSbP light emitting diodes Appl. Phys. Lett. 90 211115-1-3

EXPERIMENTAL STUDY OF $Cu(In_{1-x}Ga_x)(S_{1-y}Se_y)_2$ THIN FILM FOR SOLAR CELL APPLICATIONS

E.P. ZARETSKAYA[1], V.F. GREMENOK[1], I.A. IVANOV[1], V.B. ZALESSKI[2], N.N. MURSAKULOV[3], N.N. ABDULZADE[3], Ch.E. SABZALIYEVA[3]

[1]State Scientific and Production Association "Scientific-Practical Materials Research Centre of the National Academy of Sciences of Belarus", National Academy of Sciences of Belarus, P. Brovka 19,220072 Minsk, Belarus, 840888; email:ezaret@ifttp.bas-net-by

[2]Institute of Electronics, National Academy of Sciences of Belarus, Logoiski trakt 22,220090, Minsk, Belarus,

[3]Institute of Physics, Azerbaijan National Academy of Sciences, H. Cavid ave., 33, Az-1143, Baky, Azerbaijan email: nmursakulov@iphysics.ab.az

Homogeneous $Cu(In,Ga)(S,Se)_2$ (CIGSS) thin films have been prepared using a two-step process consisting of annealing of Cu-In-Ga precursors in S/Se ambient. The influence of growth conditions on film composition was studied. Full characterizations have been carried out using XRD, SEM, AES, Raman spectroscopy, electrical and optical absorption measurements. AES depth profiling revealed homogeneous distribution of constituent elements throughout the depth of film grown under optimized selenization/sulfurization conditions. Depending on overall Ga and S contents CIGSS thin films exhibited a shift in band gap from 1.04 to 1.47 eV.

1. INTRODUCTION

The pentenary semiconductor $Cu(In_{1-x}Ga_x)(S_{1-y}Se_y)_2$ (CIGSS) is an excellent absorber material for hetero-junction solar cells and modules [1,2]. The band gap energy of CIGSS material varies from 1.0 up to 2.4 eV and can be perfectly adjusted to the solar spectrum [3]. Furthermore, the use of compositional variations through the depth of the absorber allows the design of a band gap engineering which leads to an improved module performance.

The objective of this work is to develop a process to form wide-gap CIGSS films with optimized Ga and S profiles. The technology is based on sequential deposition of the Cu-In-Ga precursors followed by their annealing in S/Se-containing atmosphere under N_2 flow.

The process is reproducible, at the same time accomplishes the controlled incorporation of both gallium and sulfur into the bulk of the material.

2. EXPERIMENTAL

$Cu(In,Ga)(S,Se)_2$ thin films were synthesized in two stages: (i) sequential deposition of Cu-In-Ga precursors and (ii) reactive annealing of these structures in S/Se-containing atmosphere under N_2 flow [4]. Reaction time, temperature and S/Se weight ratio in reaction system were used to control the reaction kinetics.

In the first step of the process, Cu-In-Ga metallic precursors with the total thickness of about 1.0 μm were deposited onto the Corning glass substrate by ion-beam plasma evaporation in vacuum ($6 \cdot 10^{-4}$ Pa) at substrate temperature T_s = 100 ^{0}C. The typical chemical composition of the metallic precursors were 47.6 at.% Cu, 40.1 at.%, In 35.5 at.% and 16.9 at.% Ga. In the first stage, the precursors reacted with elemental Se/S vapor under N_2 flow for a period of 20-30 min at 260 ^{0}C. Then the temperature was raised to recrystallization temperature T_2 = 400 ^{0}C or to 500 - 540 ^{0}C at 9 ^{0}C min^{-1} and thereafter held for 20 min. The S/Se-source weight ratio in the reaction system was altered from 0.1 to 0.4 in order to determine the optimum material properties. CIGSS films with a thickness ranging from 2.0 to 2.5 μm were obtained.

The bulk composition and surface morphology of the films were investigated using wavelength dispersive X-ray (WDX) analysis using a CAMECA SX-100 and JEOL 6400 SEM apparatus. Depth profiling was carried out by Auger electron spectroscopy (AES) using a Perkin Elmer Physical Electronics model 590. Crystal structure of the materials was studied by X-ray diffraction (XRD) using a Siemens D-5000 diffractometer (having CuK_α λ = 1.5418 Å radiation and a Ni filter) operated at 30 kV and 20 mA. The observed phases were determined by comparing the *d*-spacing with the Joint Committee on Powder Diffraction Standard (JCPDS) data files. The Raman scattering (RS) measurements were performed in backscattering configuration at room temperature with unpolarized light using DILOR XY 800 spectrometer and an AR laser with 514.5 nm wavelength as a light source. The optical transmission and reflectance measurements were conducted using a Cary-500 spectrometer (Varian).

3. RESULTS AND DISCUSSIONS

3.1. Structural and morphological properties

It is well known that grain size distribution through the depth of the CIGS film grown by selenization (or sulfurization) of Cu-In-Ga precursors is non-uniform with small grains near the Mo/interface due to Ga segregation. Therefore, the small-grain region associated with Ga-rich composition is expected to accommodate the highest concentration of S [5] However, this trend was not confirmed by the examination of the cross-sectional SEM images and depth profiles of the CIGSS samples grown by our method. In case of the low-temperature reaction process, all films were morphologically rough and non-uniform but did not show distinct layers and significant

difference in the grain size in the surface-near region and in the bottom-near region (Fig. 1).

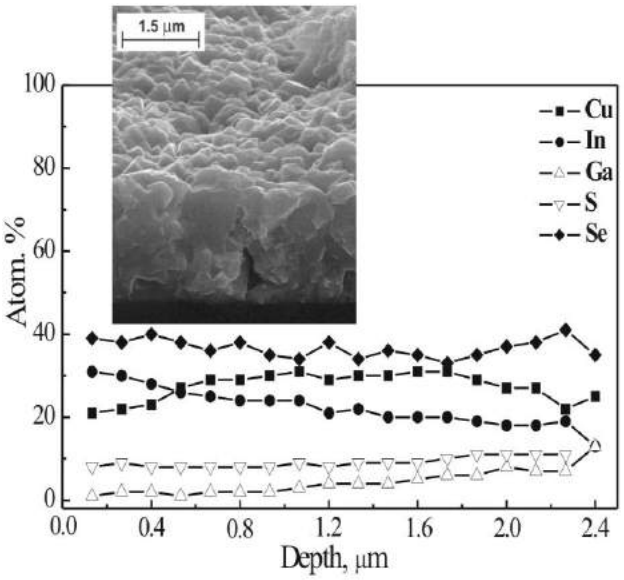

Fig. 1. SEM cross-section image and AES profiles of CIGSS layer grown under 400 ^{0}C

It should be noted, that AES profiles of these samples showed relatively uniform distribution of sulfur and selenium through the depth of the film with overall bulk concentration of (S+Se) near 50%. (Fig. 1).

A change in morphology was revealed with the increasing of the recrystallization temperature to 500 ^{0}C. These films were relatively uniform and dense and consisted of interconnected grains approximately 1-2 μm in size (Fig. 2). Grain boundaries in vertical direction and a dense arrangement of crystallites with a vertical dimension of 1.5 μm can be discerned.

Fig. 2 also shows AES depth profiles of Cu, In, Ga, Se and S in the films prepared at T_s in the range 500 – 540 ^{0}C. The distribution of Ga is homogeneous throughout the depth of the film with the overall concentration of 7 at. % and very low gradient near the bottom.

It is remarkable that the Cu/(In+Ga) ratio was fixed at the near-stoichiometric value of 0.92 and the S/Se atomic ratio remained virtually constant through the entire depth of the film obtained at the optimized conditions of high-stage.

XRD data from the samples annealed at low temperatures for 30 min showed that the recrystallization process was incomplete. XRD pattern (Fig.3) indicated the coexistence of two $CuInSe_2$ and $CuInS_2$ phases in the films prepared by process with the recrystallization temperature of 400 ^{0}C (temperature of high-stage) and S/Se –source weight ratio ranging from 0.1 to 0.2.

The peaks corresponding to the reflections of $CuInSe_2$ and $CuInS_2$ atomic planes (112), (103), (220/204) and (312/116) of the CH structure are identified by comparison to the JCPDF data cards 40-1487 and 89-6095. There is no evidence for binary phases (Cu-S, Cu-Se or In-Se) or other ternary or quaternary compounds in these samples. It should be noted that these phases are difficult to detect due to low peak intensities and partial overlapping of their reflections with the majority chalcopyrite peak positions.

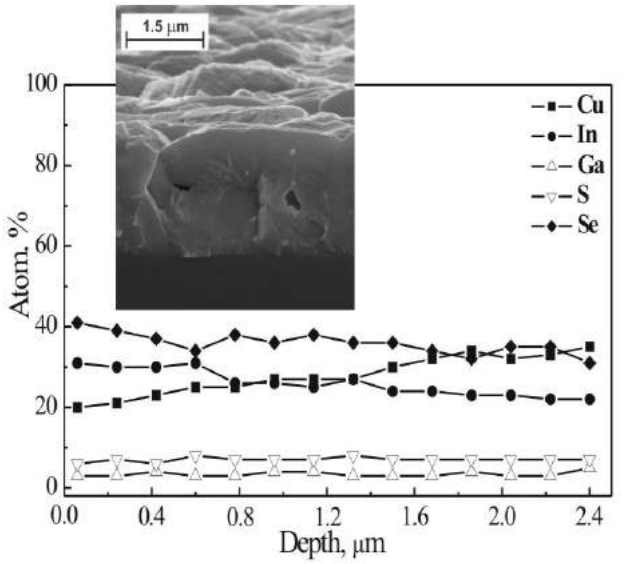

Fig. 2. SEM cross-section image and AES profiles of CIGSS layer grown under 520 ^{0}C

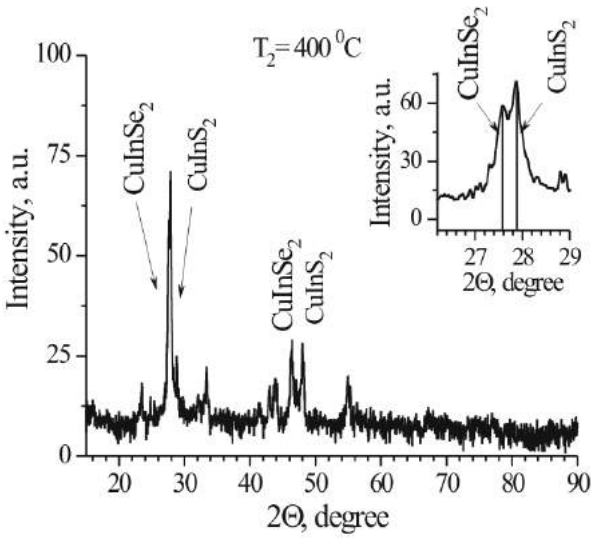

Fig. 3. XRD pattern of CIGSS film grown under 400 ^{0}C

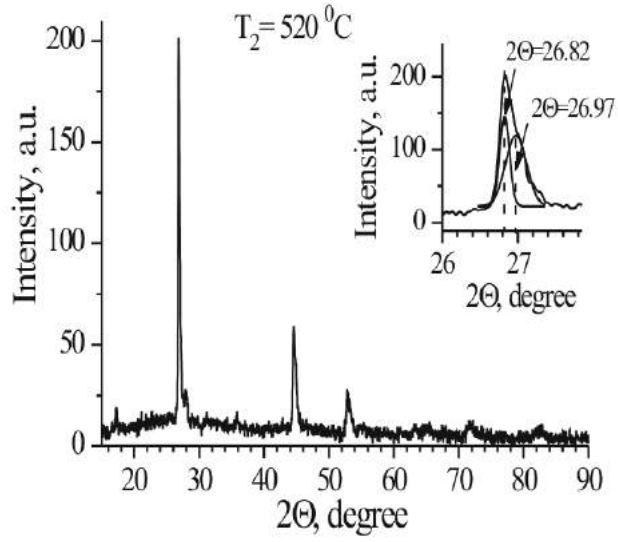

Fig. 4. XRD pattern of CIGSS film grown under 520^{0}C

XRD measurements of the samples prepared by a high - temperature process (T_s = 500 ^{0}C) revealed a high intermixing of the material (Fig. 4). However, all the peaks related to $CuInSe_2$ have a shoulder, which corresponds to a mixture of $CuInS_2$ and $CuGaSe_2$ phases.

Single-phase CIGSS thin films of the CH structure with [112] preferred orientation were formed under optimized conditions (T_2 of 520 ^{0}C).

Fig. 5 (a)-(c) shows XRD patterns from the CIGSS films with different sulphur content grown under these conditions. The shift of the (112) and (220/204) reflections to a higher 2 Θ angle is in accordance with a decrease in a lattice parameters associated with the incorporation of sulfur and gallium.

As seen from Fig. 5 the (112) reflections of the respective pentenary alloy films are almost symmetric, which confirm their compositional uniformity.

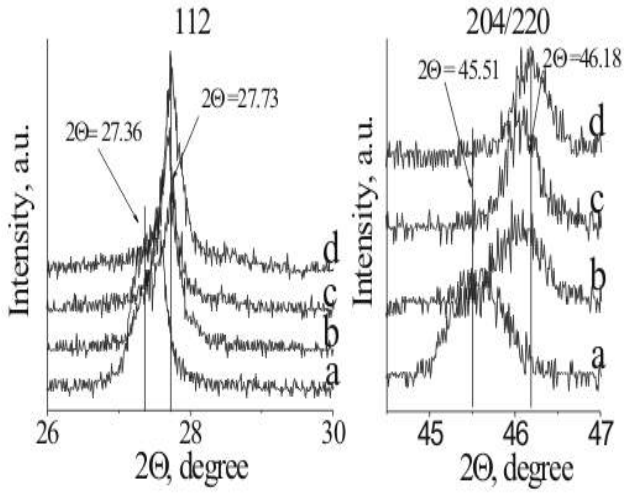

Fig. 5. Shift of (112) and (204/220) reflections CIGSS films in dependence on S/Se ratio: a - 0.77, b - 2.0, c - 3.3, d - 5.40.

3.2 Raman spectra

In our previous study, we reported the detailed characterisation of $CuInSe_2$ films grown by the selenization on the basis of the analysis of spectral characteristics of A_1 CH mode [7]. It was shown that the A_1 intensity increases and its FWHM decreases with enhancement of the structural ordering of $CuInSe_2$ thin films (when recrystallization temperature was increased up to 540^{o}C). In addition to these changes in the A_1 band, some dependency on thin film surface morphology was observed. That is why, in order to relate Raman spectra to the crystalline structure and to eliminate the effect of microstructure, CIGSS thin films of different composition with similar morphological features (densely packed grains of sizes 2 –2.5μm and approximately equal surface roughness) were chosen for investigation.

Figure 6 (plots a-c) presents the normalized Raman spectra of CIGSS films of different S/(S+Se) ratios grown at the optimized conditions. For characterizing the material, special attention was paid to the spectral position of the A_1 band, which is the most intense band in the spectra of $A^IB^{III}C^{IV}_2$ semiconductors of CH-type structure. This mode has a purely ionic nature and originates from vibrations of VI atoms in <001> planes, while the rest of the atoms in the lattice are stationary. The A_1 vibration is expected to be highly sensitive to local vibrations of the surrounding of the VI atoms. This band appears at 174 cm^{-1}and 292 cm^{-1} for $CuInSe_2$ and $CuInS_2$ respectively, and at 184 cm^{-1} and 312 cm^{-1} for $CuGaSe_2$ and $CuGaS_2$ respectively [8].

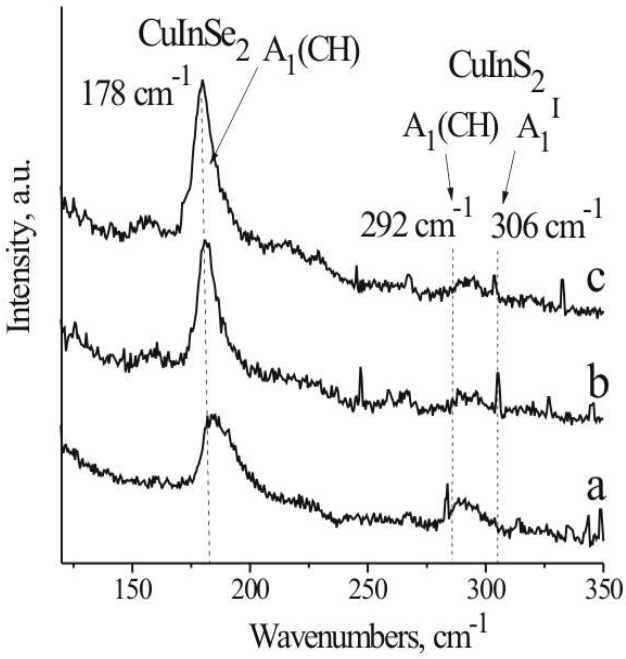

Fig. 6. Raman spectra of CIGSS layers with different S/(S+Se) ratios: a - 0.28; b - 0.19; c - 0.14.

When to compare Raman spectra of CIGSS films with different S/(S+Se) ratio it was found that that the intensity of Raman peaks strongly depends on the composition of the films. RS spectra of CIGSS films with sulfur content above 30 at. %. (Fig. 6, a, b) shows the coexisting of both group of bands from $CuInSe_2$ and $CuInS_2$ phases, i.e. a bimodal behavior. The dominant A_1 modes of $CuInSe_2$ and $CuInS_2$ at approximately 176 cm^{-1} and at 292 cm^{-1} are clearly observed in these spectra. The peaks at 116, 212, 247 and 348 cm^{-1} due to B_2 and E modes of these compounds, which correspond to the combined vibrations of all the atoms were also observed in the RS spectra. The presence of possible $CuGaSe_2$, $CuInGaSe_2$ and $CuGaS_2$ phases was not indicated in RS spectra. This is most probably be due to the similarity in frequency of vibrations of In–Se, In–S bonds with Ga–Se and Ga–S bonds. It is important that an isolated peak at 258 cm^{-1} related to the presence of a high-conductive Cu_xSe phase with symmetry of lattice vibrations different from chalcopyrite [7, 8] was not observed in RS spectra.

Some of the spectra also show an additional A_1^I "companion" mode in the range 302 - 307 cm^{-1}. The origin of this mode is not fully clear. It was established that the "companion" mode is not related to chemical effects, but to structural ones [9]. According to the detailed analysis of this mode presented in papers [9,10] this band is related to the formation of metastable domains with a different crystallographic order, which was identified as 'Cu-Au' (CA) ordering.

The presence of A_1^I mode is strongly affected by the temperature of growth, and its contribution is higher for the samples grown at low temperatures [9].

The decreasing of the sulfur content leads to the decrease of A_1 and "companion" modes of $CuInS_2$ and to the improvement of the position and FWHM of A_1 mode of $CuInSe_2$ (Fig. 6, c). This peak shifts with respect to the composition of layers from 182 to 176 cm^{-1} when sulfur content decreased. The disappearance of the 307 cm^{-1} mode in RS spectra can be explained by the formation of single phase material with enhanced crystalline ordering.

In the RS spectra of CIGSS with S/(S+Se) = 0.14 the A_1 peak is more prominent (its intensity increases and its FWHM decreases from 12 to 7.5 cm^1), indicating a higher structural ordering.

Table 1. Chemical composition and band gap values E_g of CIGSS absorber layers.

Molar fraction	E_g, eV
$Cu_{0.73}In_{1.18}Ga_{0.09}S_{0.87}Se_{1.13}$	~ 1.27
$Cu_{0.82}In_{1.22}Ga_{0.04}S_{1.29}Se_{0.63}$	~ 1.29
$Cu_{0.85}In_{1.19}Ga_{0.09}S_{1.45}Se_{0.43}$	~ 1.31
$Cu_{0.79}In_{1.22}Ga_{0.02}S_{1.66}Se_{0.31}$	~ 1.38
$Cu_{0.80}In_{1.21}Ga_{0.06}S_{1.54}Se_{0.38}$	~ 1.39
$Cu_{0.81}In_{1.21}Ga_{0.06}S_{1.68}Se_{0.24}$	~ 1.47

3.3. Electrical and optical properties

Film resistivity was measured by the Van der Pouw method at room temperature. The "Leit-C" conductive glue was used as ohmic contacts to the films. Thermoelectric properties of the films were investigated at room temperature with the temperature difference between the "hot" and "cold" probes ΔT = 25 K. Since the investigated films had some inhomogeneity of physical properties distribution on the surface, measurements were carried out in ten points and the resulting thermopower was accepted to be the arithmetic mean value.

Main attention was paid to films with Cu/(In+Ga)<1 ratio, which is one of quality criteria of CIGSS-films used for solar cells production [1]. According to the sign of thermopower all synthesized films are of p-type conductivity.

Activation energies of intrinsic defects levels arising during films synthesis were determined with the help of measurements of temperature dependence of resistivity in the range 80 – 400 K. These experiments gave a possibility to separate three ranges of activation energy values: 110 – 120 meV, 140 – 160 meV and 180 – 200 meV. We suppose that activation energy of 110 – 120 meV corresponds to the copper vacancies (V_{Cu}) [11 – 13]; activation energy of 140 – 160 meV – to the substitutional defects (In_{Cu}) [11]; activation energy of 180 – 200 meV – to the interstitial defects (In_i) [14, 15].

The types of dominant defects existing in the films do not depend on the temperature of the second stage and S/(S+Se) ratio. I.e. the decreasing of the recrystallization temperature, as well as selenium ↔ sulfur substitution, has no evident influence on the ensemble of dominant defects.

The (Cu+In+Ga)/(S+Se) ratio in the investigated films (from 1.00 to 1.15) is close enough to the required stoichiometric value and does not have any noticeable influence on their electric parameters (resistivity and thermopower). In spite of the selenium ↔ sulfur substitution influence on the resistivity value is not revealed, it allows to control the thermo-power value (Fig. 7).

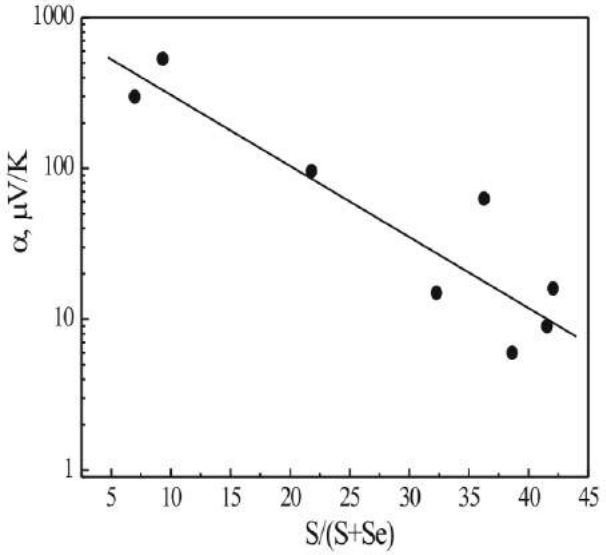

Fig.7. The thermopower dependence on the S/(S+Se) ratio for CIGSS films.

In order to determine band gap values of the films, optical transmission [$T(\lambda)$] and near-normal specular reflectance [$R(\lambda)$] measurements were carried out at 300 K in the wavelength range between 190 and 300 nm. Chemical composition some of the CIGSS films grown under optimized conditions (T_2 = 520 ^{0}C) and their respective band gap values E_g are summarized in Table 1.

The band gap of the CIGSS films increases in dependence on the gallium and sulfur content from 1.04 eV to 1.47 eV. These values are intermediate between $CuInSe_2$ and $CuGaSe_2$ band gap energies which are 1.01 and 1.68 eV, respectively.

4. CONCLUSIONS

The CIGSS thin films have been prepared by annealing of Cu-In-Ga precursors in S/Se–containing ambient. The XRD and Raman analysis showed that CIGSS films were polycrystalline and composed of $CuInS_2$ and $CuInSe_2$ phases when annealing under low temperatures (of 400 ^{0}C). Complete intermixing of these phases was observed in the case of high-temperature process. A homogeneous Ga depth distribution and a band gap 1.27-1.47 eV were obtained by modifying the process conditions.

The decreasing of the recrystallization temperature, as well as selenium ↔ sulfur substitution, has no evident influence on the ensemble of dominant defects. It allows to alter depth layer components distribution by the

recrystallization temperature and S/Se weight ratio choice, not causing a change of defect composition in the films.

5. ACKNOWLEDGEMENT

This work has been supported by the Belarus Republic Fund of Fundamental Investigations and Azerbaijan National Academy of Sciences (NASA).

---

[1]. *U. Rau, H.W. Schock*, Appl. Phys. A: Materials Science & Processing A 69 (1999) 131.

[2]. *K. Ramanathan, M.A. Contreras, C.L. Perkins, S. Asher, F.S. Hasoon, J. Keane, D. Young, M.Romero, W. Metzger, R. Noufi, J. Ward, A.Duda*, Prog. Photovolt. Res. Appl. 11 (2003) 225.

[3]. *M. Gossla, W.N. Shafarman*. Thin Solid Films 480-481 (2005) 33.

[4]. *E.P. Zaretskaya, V.F. Gremenok, V.B. Zalesski* // Method for preparation of the $Cu(In,Ga)(S,Se)_2$ thin films. Russian Patent № 20071243. Priority 28/06/2007.

[5]. *B.M. Basol, A. Halani, C. Leidholm, G. Norsworthy, V.K. Kapur, A. Swartzlander, R.Matson*, Prog. Photovolt. Res. 8 (2000) 227.

[6]. *H. Tanino*, Physical Review B. 45, 23 (1992-I) 13323.

[7]. *E.P. Zaretskaya, V.F. Gremenok, V. Riede, W. Schmitz, K. Bente, V.B. Zalesski, O.V. Ermakov*, J.Phys. and Chemistry of Solids, 64 (2003) 1989.

[8]. *J. Alvarez-Garcia, J. Marcos-Ruzafa, A. Perez-Rodriguez, A. Romano-Rodriguez, J.R.Morante, R. Scheer*, Thin Solid Films 361-362 (2000) 208.

[9]. *J.H. Park, I..S. Yang, H.Y. Cho*, Appl. Physics A, 58 (1994) 125.

[10]. *K. Kondo, S. Nakamura, K. Sato*, Jpn. J. Appl. Phys. 37 (1998) 5728.

[11]. *E.I. Rogacheva*, Inst. Phys. Conf. 152 (1998) 1.

[12]. *J.M. Binsma, L.J. Giling and J. Bloem*, Journal of Luminescence, 27 (1982) 35.

[13]. *H.Y. Ueng and H.L. Hwang*, J. Phys. Chem. Solids 50, 12 (1989) 1297.

[14]. *R.R. Philip, B. Pradeep, G.S Okram and V.Ganesan*. Semicond. Sci. Technol., 19 (2004) 798.

[15]. *H.J. Lewerenz and N. Dietz*, Applied Physics Letters 59, 12 (1991) 1470.

GROWTH AND OPTICAL PROPERTIES OF Cu(In,Ga)Se_2 THIN FILMS ON FLEXIBLE METALLIC FOILS

A.V. MUDRYI, A.V. KOROTKI,V.F. GREMENOK, E.P.ZARETSKAYA,
State Scientific and Production Association "Scientific-Practical Materials Research Centre of the National Academy of Sciences of Belarus , P. Brovka str. 19, 220072 Minsk, Belarus, email: gremenok@ifttp.bas-net.by
V.B. ZALESSKI
Institute of Electronics, National Academy of Sciences of Belarus, 220090, Logoiski trakt 22, 220090 Minsk, Belarus, email: zalesski@inel.bas-net.by
N.N. MURSAKULOV, N.N.ABDULZADE, Ch.E.SABZALIYEVA
Institute of Physics, National Academy of Azerbaijan, H. Cavid ave., 33, Baky, Az-1143, email: nmursakulov@physics.ab.az

Polycrystalline Cu(In,Ga)Se_2 (CIGS) thin films on flexible metallic foils were prepared by two-stage selenization of sputter-deposited Cu- Ga- In precursors. The phases, surface morphologies, microstructures and elemental depth profiles of the CIGS films prepared on different metallic flexible foils (titanium, molybdenum, aluminum and stainless steel) were analyzed. To characterize the structure quality and intrinsic defect nature low-temperature (4.2 – 300 K) photoluminescence (PL), photoluminescence excitation (PLE) and optical transmission measurements were performed. Experiments show that the structural and optical properties of CIGS absorber layers strongly depend on the growth condition, chemical composition and type of the substrate.The band gap energy (E_g) of CIGS chalcopyrite compounds, grown on nontransparent flexible metallic substrates was estimated from PLE data. Excitation power and temperature dependent PL measurements shows that the broad bands in the near-band edge spectral region are caused by the band-tail recombination.

1. INTRODUCTION

The chalcopyrite semiconductor Cu(In,Ga)Se_2 (CIGS) thin-film cells have demonstrated the highest efficiency on the laboratory and industrial scale. The conversion efficiency approaching the theoretical value of over 20 % are already reached for CIGS thin-film solar cells on glass substrates [1,2]. In the last years an increasing number of the studies have been performed on the CIGS thin films fabricated on ultralightweight flexible metallic foils and polymer substrates [3-5]. The use of flexible substrates instead of the commonly used rigid soda lime glasses offers new possibilities for the application of solar cells in space and terrestrial photovoltaic power system. Conversion efficiencies up to 16 – 17.5 % have achieved for the CIGS solar cells on flexible metallic substrates [6].

In this paper we report new results on a study of physical properties (structural, morphological and optical) of CIGS thin films grown on different flexible metallic foils (titanium, molybdenum, aluminum, stainless steal). To study the intrinsic defect nature detailed low-temperature (4.2 – 300 K) PL and PLE measurements of CIGS thin films were performed.

2. EXPERIMENTAL

The CIGS films with thickness about of 1 – 2.5 μm were grown on thin metallic foils by DC magnetron sputtering of the Cu-In-Ga metallic alloys with subsequent two-stage selenization. In the first stage the precursor layers were heated for 10 min to temperature of 260 ^oC, and the initial reaction period for all selenization processes was maintained at 20 min. The selenization was completed by second recrystallization step (T_s) under temperatures 400 – 520 °C for ~ 20 – 60 min. The CIGS films with the same chemical composition were also prepared on soda lime glasses at the time for comparison.

The films surface morphology and microstructure were analyzed by scanning electron microscopy (SEM) using JEOL 6400 SEM apparatus. The chemical composition and the depth profiling were determined by energy dispersive X-ray (EDX) analysis using a CAMEC SX-100 and Auger electron spectroscopy (AES) with simultaneous sputter etching using a Perkin Elmer Physics Electronic 590 model apparatus. The crystalline structure of the layers was studied by the X-ray diffraction (XRD) using a Siemens D5000 diffractometer with CuK_α (λ = 1.5418 Å) radiation. The optical parameters of the reference CIGS thin films deposited onto Corning glass substrates were determined from transmittance (T) and reflection (R) measurements in the spectral range of 200 – 3000 nm at room temperature using a Carry 500 Scan UV-Vis-NIR spectrophotometer (Varian, USA). The PL spectra were analyzed using a 0.6 m diffraction monochromator. A liquid nitrogen cooled InGaAs p-i-n detector (Hamamatsu, Japan) was used for the PL signal detection. Signal amplification was based on lock in technique. For excitation, the 488 line of the Ar ion laser was used in the PL experiments. The samples were immersed into liquid nitrogen or helium during the measurements of the PL at 78 are 4.2 K, respectively. Temperature dependent measurements from 4.2 to 300 K were carried out in an evaporation cryostat equipped with suitable heaters and temperature sensors. The PLE spectra were measured using a 400 W halogen tungsten lamp combined with a grating monochromator (1200 groves mm^{-1}, focal length of 0.3 m) as an excitation source.

3. RESULTS AND DISCUSSION

The aim of these investigations was to develop a reproducible process of CIGS thin films deposition on different metallic foils for solar cells applications. Table 1 presents the average values of Cu, In, Ga and Se amounts determined by AES method for the all investigated films on metallic foils. The same elemental composition (Cu:In:Ga:Se in atomic %) in near-surface

region of CIGS films has been confirmed by EDX method. The chemical composition was determined by averaging the values from 5 different points on the surface of the same film.

Table 1. Chemical composition of CIGS thin films deposited on different metallic substrates (selenization temperature was maintained at 520 °C for 20 min)

Sample notation	Type substrate	Cu, at %	In, at %	Ga, at %	Se, at %
2X118	glass	26.2	24.8	1.9	46.7
1MX	Mo	29.1	22.2	3.3	45.4
2TX	Ti	24.1	26.1	2.2	47.6
1TMX	Ti with Mo layer	25.0	23.4	2.0	49.6
1HCMX	stainless steel with Mo layer	26.7	21.9	2.5	48.9
1AlDX	Al	21.7	26.0	2.2	50.1
1AlMX	Al with Mo layer	35.4	22.8	2.1	39.7

The AES spectra of CIGS thin films were analyzed over a range of kinetic energies from 100 to 1400 eV, using the primary electron beam of energy 5 keV. An example of these spectra, taken with a magnification of 1000 x, equivalent to an area of 100x100 μm^2 is shown in Fig. 1. This spectrum showed the presence of the following chemical elements: indium at 298, 345 and 408 eV; copper at 775, 848 and 921 eV; gallium at 1010 eV; selenium at 1193, 1205, 1237, 1312

and 1352 eV. The elemental composition at the surface was calculated from the relative intensity of the peak in the AES spectra and to be as follows; copper 30 at %, indium 21 at %, gallium 3 at % and selenium 46 at %. The chemical composition analyzed by EDX gives the same average atomic concentration (5 point on the surface of films).

The AES depth profile measurements were used to study the element distribution in the bulk of CIGS films. The chemical composition was obtained by sputtering on area with dimension approximate by of 100x100 μm^2 with energetic argon ions at a rate 500 Å/min or 1000 Å/min. The typical depth profile for 1MX sample obtained at optimal selenization conditions (T_s ~ 520 °C, t = 20 min) is shown in Fig. 2. The depth profile presented in Fig. 2 is from the surface up to molybdenum foil. As observed, Cu, In, Ga and Se atomic concentrations remained fairly uniform through the depth of the CIGS films during 8 min of the sputtering process.

Further copper and indium concentration decreased rapidly. Ga concentration remained constant during the 6 min of the sputtering process, and then slightly increased. It is clear seen from Fig. 1 that Mo atomic concentration is sharply increased after initial stage of sputtering (8 min). The irregular distribution of elements Cu, In and Mo in the bordering to Mo-substrate region indicates formation of two-phase material $MoSe_2$ and CIGS in the bottom of the layer and agrees with XRD data and SEM image.

The AES measurement for other CIGS thin films (see Table 1) showed the uniform distribution of elements Cu, In, Ga and Se through the depth of the layers withought the formation additional phases in material that agrees with the XRD data. The inhomogeneous elemental distribution was found only near interface between CIGS layers and corresponding metallic foils.

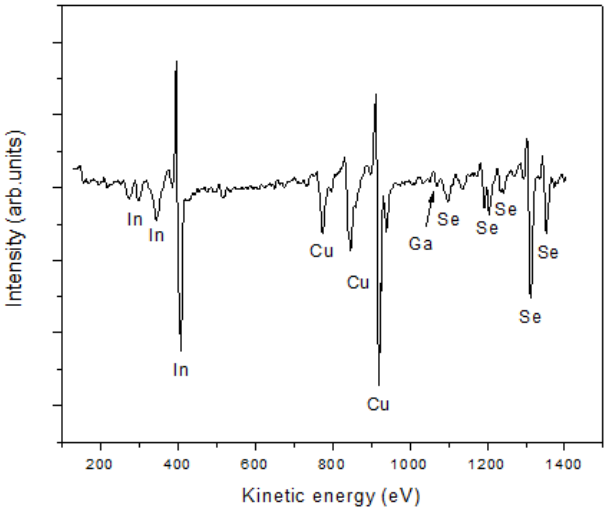

Fig. 1 A typical AES spectrum of the CIGS film (sample 2X118)

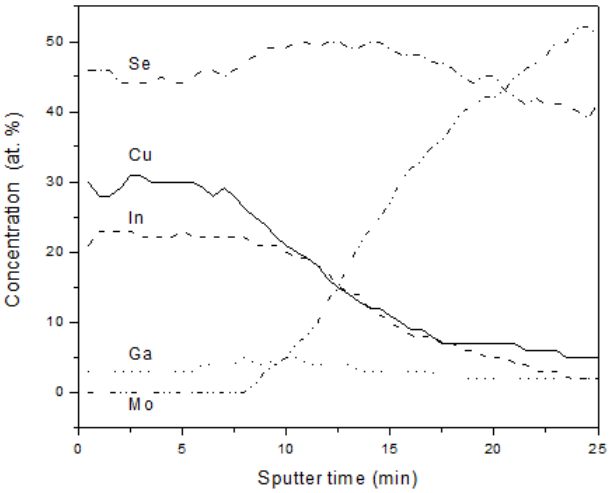

Fig. 2 A AES depth profile of CIGS films on Mo foil (sample 2X118)

The phase formation and structure of CIGS thin films were characterized by X-ray diffraction. Fig. 3 show XRD pattern of structure – molybdenum foil/chalcopyrite semiconductor absorbing layer (sample 1MX). The observed phases in XRD pattern were identified by comparing the d-spacing with Joint Committee on Power Diffraction Standard (JCPDS) data files. The intense peak at $2\Theta \approx 58.63°$ and weak peak at $2\Theta = 73.6°$ were from Mo foil, reflection (200) and (211), respectively, (JCPDS card 42-1120), that agrees with XRD data for similar structures [7]. The XRD pattern indicate the formation of two-phase material – $MoSe_2$ and CIGS. It was found that both of the materials $MoSe_2$ and CIGS are polycrystalline in nature. In the Fig. 3, the peaks at $2\Theta \approx 55.9°$ belong to the $MoSe_2$ phase (JCPDS card 72 – 1420). The XRD pattern also contains main reflections of CIGS phase such as (101), (112), (103), (211), (204)/(220), (116)/(312), (008)/(400), (316)/(332), (228)/(424). The strongest peak for chalcopyrite semiconductor compound CIGS was from the (112)

plane, indicating that the layer have preferred orientation towards to [112] direction.

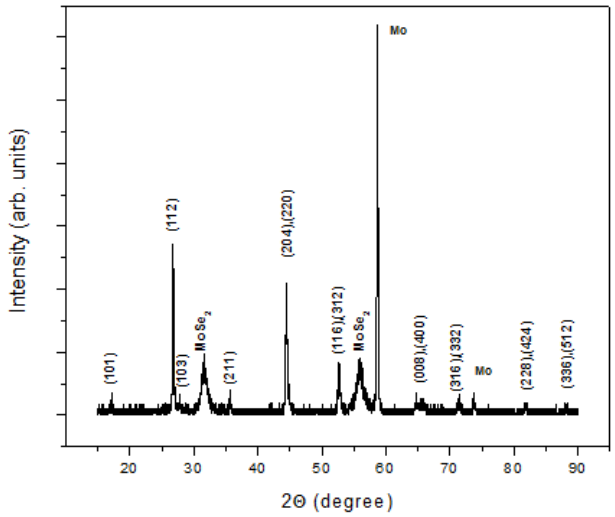

Fig.3 X-ray diffraction spectra for a CIGS thin films on Mo foil (sample 2X118)

It was found that the degree of preferred orientation, evaluated from the intensity ratio $I_{112}/I_{204/220}$ to be ~ 1.4. It is shown that in the case of random orientation this ratio should be ~ 5 [8]. Lower value of $I_{112}/I_{204/220}$ for 1 MX film shows a poor degree of (112) preferred orientation. However, the degree of preferred orientation for 1MX film is increased from 1.1 to 1.4 with increasing of selenization temperature from 400 to 520 °C, respectively. XRD patterns of other samples (see Table 1) show characteristic diffraction peaks that can be also index on the basis of the tetragonal chalcopyrite structure CIS. All patterns showed a dominant (112) reflection and two weaker double reflections 204/220 and 116/132. The degree of preferential orientation of these films varies from 1.5 to 4. The diffraction peak (112) is strong in all patterns and becomes more dominant with increasing selenization temperature from 400 to 520 °C. No other phases were found for all CIGS thin films indicated in Table 1, excluded 1MX sample.

The surface morphology of CIGS thin films grown on metallic foils was found to be strongly dependent on the deposition condition and selenization temperature. The surface SEM micrograph of 1MX sample is shown in Fig.4. SEM image showed large, well-faceted dense grain structure and grain size to be about ~ 1-2.5 μm, i.e. comparable to the film thickness. It was also found from the SEM micrographs that the uniformity and adhesions of the films on different metallic foils improved with increasing of selenization temperature from 400 to 520 ºC. The presence of the $MoSe_2$ sublayer (additional phase) the interface region it is clear seen from Fig. 4. SEM surface micrographs for other samples (Table 1) revealed structure that changed in density and grain sizes ~ 0.3 – 2.5 μm in dependence of selenization temperature and type of metallic substrate. Our investigations show that CIGS thin films with remarkable structural quality can be prepared by two-stage selenization method with different morphology ranging from polycrystalline to continuous single-crystalline depending on the selenization temperature and time of annealing. However, we observe that CIGS films are not always as dense as shown in Fig. 4. In some cases the layer can become porous.

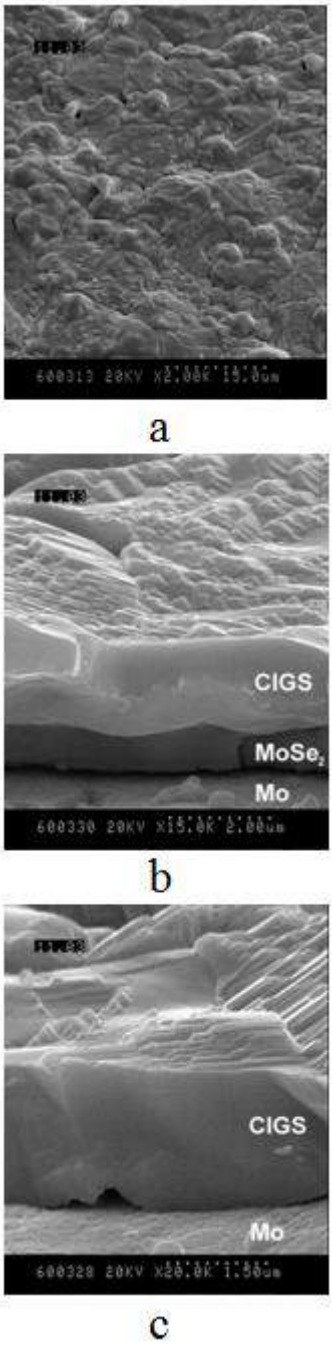

Fig.4 SEM micrographs of CIGS of CIGS films on Mo foil (sample 2X118): (a) – plane view; (b), (c) – cross-section image of a different parts of film with and without $MoSe_2$ sublayer, respectively

The optical properties of reference CIGS thin films on glass substrate were studied by measuring both transmittance (T) and reflection (R) spectra. Fig. 5a shows the T spectrum taken at room temperature. Sample 2X118 exhibit transparency ~ 35 - 45% in near-infrared region and has relatively sharp edge of an intrinsic absorption. The absorption coefficient of the film has been calculated using both optical transmission and reflection data and following relation [9]:

$$\alpha = -\frac{1}{d}\ln\frac{\sqrt{(1-R)^4+4T^2R^2}+(1-R)^2}{2T}, \quad (1)$$

where α is the absorption coefficient, d is the thickness of the film, T and R are the transmission and reflection, respectively. The reflectivity R was measured in the photon energy region of 1 - 2.5 eV and to be ~ 0.21 for 2X118 sample. In the case of allowed direct transitions the absorption coefficient is written as a function of the incident photon energy $h\nu$ using the following equation [10]:

$$\alpha = A(h\nu - E_g)^{1/2} \quad (2)$$

were E_g and A are the optical band gap and a constant, respectively. The optical bang gap of the CIGS film was determined by extrapolating of the linear part of the spectral dependence $\alpha^2 \sim f(h\nu)$ to the photon energy axis, Fig. 5b. The E_g value determined from transmittance measurements to be ~ 1.06 eV for 2X118 sample.

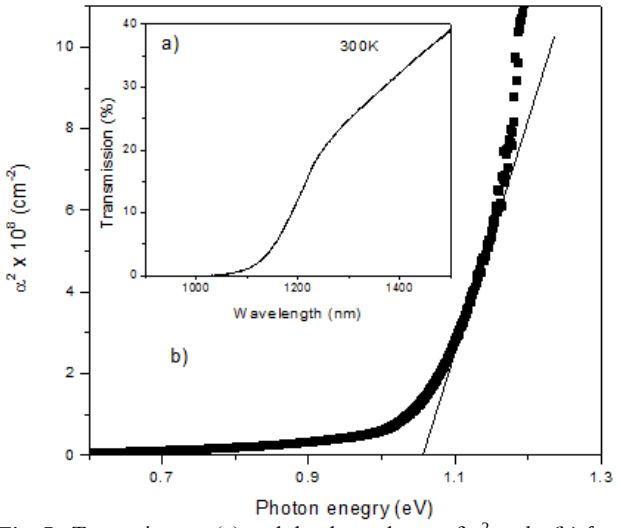

Fig. 5. Transmittance (a) and the dependence of α^2 vs $h\nu$ (b) for CIGS film on glass substrate (sample 2X118).

A typical PL spectra of CIGS films at 4.2, 78 and 300 K are shown in Fig. 6. The single brood band at 1.03 with full-width at half-maximum intensity (FWHM) ~ 80 meV dominates the spectrum from 1MX sample at 4.2 K. It can be seen that broad band has an asymmetric spectral shape with a longer tail towards lower energies. This band shifts to a higher energy with increasing temperature as seen in the normalized PL spectra in Fig. 6b. This significant temperature shift can not be attributed to the band gap variation since the experimentally observed increase up to around 80 – 100 K is only about of 1.5 – 2 meV [11,12]. The FWHM and shape of a broad band change also upon increasing the temperature. The PL band become more symmetrical and it's FWHM slightly increase from 4.2 to 300 K. The single bands with similar temperature effects were also found in the PL spectra of other CIGS samples which composition a given in Table 1, see as an example Fig. 6. In order to identify the origin of the broad bands the excitation power dependence of the PL bands have been carried out. The excitation density dependence of the PL bands is known to usually give an indication of the type of a recombination process involved. As an example Fig.7 shows the dependence of the broad bands energy position on excitation power at 4.2 K for three different levels of excitation density – 1 W·cm^{-2}, 5 W·cm^{-2} and 100 W·cm^{-2}. It is clear seen that increasing excitation intensity generate a significant high-energy shift of the bands (blue j-shift). The experiments show that j-shift has a different value and strongly depend on chemical composition and structural quality of CIGS films, Table 1. The shift increases for our samples from 2 to 18 meV per decade of change in excitation density.

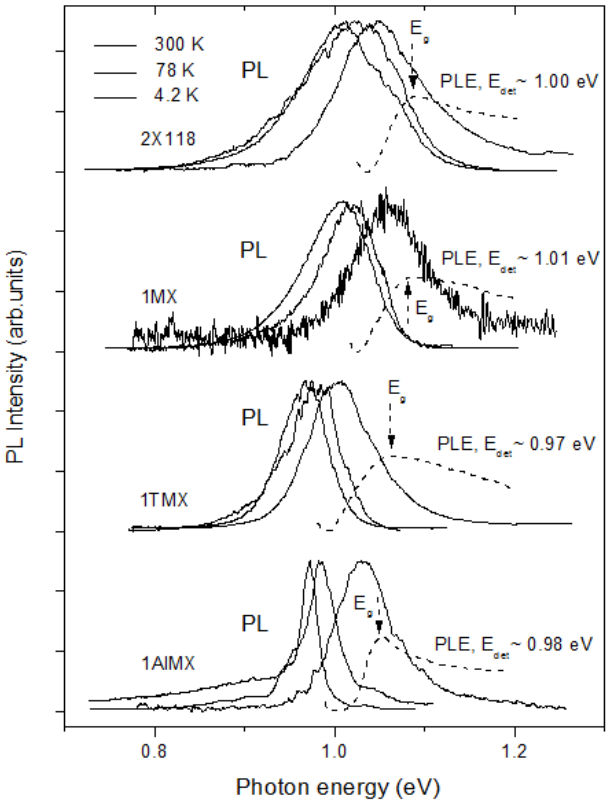

Fig.6 PL spectra of CIGS films taken at different temperatures 4.2, 78 and 300 K and PLE spectra taken at 78K.

Such large blue shift is in contradiction with donor-acceptor pair (DAP) recombination process. Usually the moderate shift-rate of 2 meV /decade of excitation density are characterized for donor-acceptor pair recombination in semiconductors [13,14]. Our experimental results may be consistently explained in the framework of the model of fluctuating potentials in highly doped and compensated semiconductors introduced by Shklovskii and Efros [15]. The statistically distributed potential fluctuations are due to high concentration of charged donors, acceptor and other defects. The spatial fluctuations in CIGS films cause fluctuations of the band gap energy and widening of the impurities levels within the forbidden gap of material and so-called band tails are formed [16,17]. The strong blue shift of the PL bands with increasing excitation density and temperature are due to changes of the carrier distribution in the energy levels of band tails. The amplitude of potential fluctuations strongly depends of the level defect concentration and degree of

compensation which are governed by the excess of (In+Ga) over Cu. This ratio determines the energy position of the band in PL spectra and j-shift magnitude [16,17]. More higher amplitude of potential fluctuation are induced the greater j-shift. As follows from Table 2 and Fig. 7 sample 1AlMX has more smaller j-shift for the main PL band at 0.97 eV.

Table 2. Chemical composition ratio and optical parameters of CIGS thin films (E_g values were determined from PLE measurements at 78 K)

Sample hotation	Composition ratio		E_g, eV	j-shift, meV/decade
	$\frac{Cu}{In+Ga}$	$\frac{Ga}{In+Ga}$		
2X118	0.99	0.07	1.08	15
1MX	1.14	0.13	1.08	18
2TX	0.85	0.08	1.05	13
1TMX	0.98	0.08	1.06	10
1HCMX	1.09	0.05	1.07	12
1AlDX	0.77	0.08	1.04	6
1AlMX	1.42	0.08	1.05	2

The dominant relatively narrow PL band at 0.97 eV has several low-energy phonon replica with an energy distance of $hw_{LO} \approx 29$ meV [18]. The narrow emission peak at 1.034 eV can also be found in a PL spectra of 1AlMX films. This peak caused by a bound exciton recombination [11,18]. Our earlier tentative identification indicate the relation of intense narrow band at 0.97 eV with the free-to-bound optical transitions, i.e. electron transitions to the acceptor levels (e-A-transitions) of Cu_{In} [18]. This analyzes leads us to conclude that 1AlMX is more structural and electronic perfect CIGS film among others, which were investigated. As an example Fig. 7 also compares PLE spectra of the broad bands for different samples. The PLE spectra were detected near the maxima of the corresponding broad bands, i.e. at E_{det}. as indicated in Fig. 7. As seen from PLE spectra the emission slightly grows reaching a maximum near gap energy E_g and than it slowly dropped forming structure less tails. In the most case the PL and PLE spectra are overlapped. This can be explained in the framework a model of fluctuating potentials. The bending of energy bands of semiconductor and the considerable increase in the density and depth of impurity band tails are occurs. The PL and PLE spectra are overlapped due to the absorption which extends to energies that are lower that the apparent band gap E_g (impurities tails). This experimental fact indicates that PLE spectra in the case of highly doped and compensated semiconductors, i.e. with fluctuating band edges, can be used only for an approximation determination of the corresponding bang gap E_g of semiconductor material. The PLE spectrum of 1AlMX sample exhibit a sharp edge and in this case the PL band the PLE tails do not overlap indicating more perfect quality of CIGS films. The value of the band gap E_g determined for such type of the PLE spectra in this case is more reliable and exact. More detailed consideration of these effects may be found in recent paper [19].

So, our investigations show that under optimized conditions of high-temperature stage selenization (T_s ~ 500 – 520 °C, t ~ 20 min) single phase CIGS material with (112) preferred orientation can be grown. The chemical composition of films to be independent on the type of metallic foils but, as expected, strongly dependent on the composition and uniformity of the precursors as well as on the deposition conditions. It is also found that CIGS films have a strong adhesion to Mo, Al and stainless steel with the exception to Ti foil.

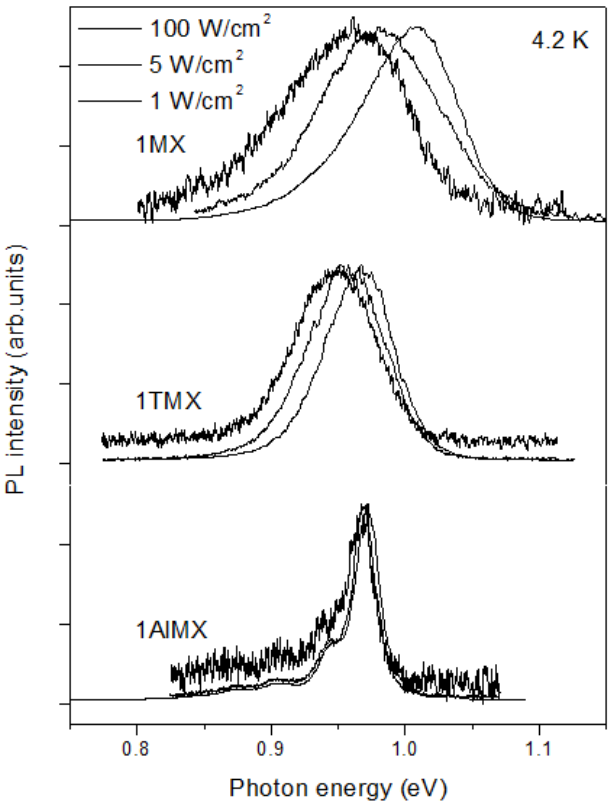

Fig.7 Excitation power dependence of PL spectra for different excitation densities.

4. CONCLUSIONS

Thin films of CIGS were grown by two-stage selenization of sequentially deposited Cu, Ga and In precursors. The precursors were deposited on flexible metallic foils by DC magnetron sputtering.. XRD, EDX and AES measurements revealed a near stoichiometric composition of the films for T_s not exceeding 520 °C. X-ray patterns showed preferred [112] orientation for all investigated CIGS film on different metallic foils (titanium, molybdenum, aluminum, stainless steel). Optical absorption measurements of the reference CIGS films on the glass substrate revealed value of E_g about of 1.06 eV. For the first time PLE measurements were employed to determine the band gap energy of CIGS film on nontransparent metallic substrates. It is found that the structural and optical properties of CIGS absorber layers are strongly depend on the growth condition, type of substrate and chemical composition. CIGS films of high structure and electronic quality were obtained with selenization at 520 °C for 20 min on Al foils.

ACKNOWLEDGEMENT

This work has been supported by the Belarus Republic Fund of Fundamental Investigations and Azerbaijan National Academy of Sciences (NASA).

[1]. *K. Ramanathan, M.A. Contreras, C.L. Perkins, S. Asher, F.S. Hasoon, J. Keane, D.L. Young, M. Romero, W. Metzger, R. Noafi, J. Ward, A. Dauda,* Prog. Photovolt. Res. Appl. 11 (2003) 225.

[2]. *M.A. Contreras, K. Ramanathan, J. AbuShama, F.S. Hasoon, D. L. Young, B. Egaas, , R. Noafi,* Prog. Photovolt. Res. Appl. 13 (2005) 209.

[3]. *N.G. Dhere, V.S. Gade, A.A. Kadam, A.H. Jahagirdar, S.S. Kulkarni, S.M. Bet* Mater. Sci. Engin. B 116 (2005) 303.

[4]. *F. Kessler, D. Herrmann, M. Powalla,* Thin Solid Films 480-481 (2005) 491.

[5]. *T. Satoh, Y. Hashimoto, S. Shimakawa, S. Hayashi, T. Negami,* Sol. Energy Mater. Sol. Cells 75 (2003) 65.

[6]. *F. Kessler, D. Rudmann,* Solar Energy 77 (2004) 685.

[7]. *J. Cowen, L. Lucas, F. Ernst, P. Pirouza, A. Heppb, S. Bailey,* Mater. Sci. Engin. B 116 (2005) 311.

[8]. *J. Muller, J. Nowoczin, H. Schmitt,* Thin Solid Films 496 (2006) 364.

[9]. *D.K.Schroder,* Semiconductor Material and Device Characterisation, Wiley, New York, 1990.

[10]. *J.I.Pankove,* Optical Processes in Semiconductors, Prentice Hall, Englewood, New York, 1971.

[11]. *A.V.Mudryi, M.V.Yakushev, R.D.Tomlinson, A.E.Hill, R.D.Pilkington, V.Bodnar, I.A.Victorov, V.F.Gremenok,* Appl. Phys. Lett. 77 (2000) 2542

[12]. *P.W.Yu,* J.Appl. Phys. 47 (1976) 677.

[13]. *S.Zott, K.Leo, M.Ruckh, H.W.Schock,* J. Appl. Phys. 82 (1997) 356.

[14]. *E.Zacks, A.Halperin,* Phys. Rev. B6 (1972) 3072.

[15]. *B.I.Shklovskii, A.L.Efros,* Electronic Properties of Doped Semiconductors. Springer Verlag, Berlin, 1984.

[16]. *I.Dirnstorfer, M.Wagner, D.M.Hofmann, M.D.Lampert, F.Karg, B.K.Meyer,* Phys. Status Solidi (a) 168 (1998) 163.

[17]. *J. Krustok, H.Collan, M.Yakushev, K.Hjelt,* Physica Scripta T79 (1999) 179.

[18]. *M.V.Yakushev, A.V.Mudryi, V.F.Gremenok, V.B.Zalesski, P.I.Romanov, Y.V.Feofanov, R.W.Martin, R.D.Tomlinson,* J. Phys. Chem. 64 (2003) 2005.

[19]. *S.Siebentritt, N.Papathanasiou, M.Lux-Steiner,* Phys. Status Solidi (b) 242 (2005) 2627.

OPTICAL POLARONS IN SEMI-MAGNETIC SEMICONDUCTORS

S.M.SEYID-RZAYEVA
Institute of Physics of NAS of Azerbaijan
AZ 1143, Baku, G.Javid ave, 33 S-Nisa@rambler

The solution of problem about anisotropic bulk optical polaron is generalized for the case of weak coupling in one valley cubic crystal structure. Then , on basis of obtained results expressions for the ground state energy and polaron mass of the electron are given in the SMSC with an anisotropic energy spectrum. Based on obtained calculations it is found that the transverse and longitudinal polaron mass, renormalized due to electron-phonon interaction, increases compared with corresponding band values. However, polaron mass of electrons decreases owing to exchange interaction with increasing magnetic field.

I. INTRODUCTION

Physical properties of various condensed media, including semi-magnetic semiconductors (SMSC), are mainly determined by phenomena of electron transfer excitations. Polaron effects are among these phenomena. SMSC on the basis of A^2B^6 compounds that have wide technical significance, are polar materials and charge carriers in them can be in the polaron state. These polaron states can essentially influence the electron energy spectrum in SMSC.

In most of SMSC on the basis A^2B^6 compounds there realizes polarons of large radius and they are more clearly show their properties in a magnetic field. The study of polaron effects provide unique resources to determine the band parameters as well to study the electronic spectrum of relevant materials in a magnetic field [1,2].

In the literature polaron effects in an external magnetic field in the SMSC [3,4,5] are studied considerably less compared with the corresponding works for polar semiconductors in the absence of a magnetic field. The theory of the optical polaron i.e., interaction of the electron with longitudinal optical -LO phonons, is developed in [6,7] in the presence of an external magnetic field in three-dimensional gapless SMSC $Hg_{1-x}Mn_xTe$.

The band structure of SMSC compared with ordinary semiconductors are more sensitive to external magnetic field due to the presence of the exchange interaction between conduction electrons and localized electrons of magnetic ions [8,9]. In particular, the exchange interaction effect on the parameters of energy band and the energy spectrum of charge carriers in the SMSC becomes anisotropic [10,11], which leads to the appearance of new physical effects in these materials.

Main aim of this work is an investigation of features of behavior of the optical polaron in a magnetic field in narrow-gap bulk SMSC.

The principal objective of this work is theoretical study of the effect of the exchange interaction due to the presence of magnetic impurities on the basic characteristics of the polaron (such as the polaron mass of the electron, ground state energy of polaron) in the narrow gap SMSC.

For this, we first give in brief the general form of solution of problem for the anisotropic bulk optical polaron in the case of weak coupling in cubic crystals. Further, on the basis of this solution, we obtain expressions for the ground-state energy and polaron masses of the electron in the SMSC with an anisotropic energy spectrum, which takes into account the influence of non-quantizing magnetic field through the exchange interaction between spins of conduction electrons and paramagnetic ions.

II. ANISOTROPIC POLARON OF LARGE RADIUS IN CUBIC CRYSTALS

The spectrum for the band electrons in many semiconductors with an one-valley cubic crystal structure is an ellipsoid of rotation of the form:

$$\varepsilon_{\vec{k}} = \frac{\hbar^2}{2}\left(\frac{k_\perp^2}{m_\perp} + \frac{k_z^2}{m_z}\right), \qquad (1)$$

where $m_\perp$, m_z - transverse and longitudinal effective mass of band electrons in the xy plane and the direction of the z axis, respectively. The conduction electrons are considered in the one-electron approximation. In this case, using well-known adiabatic approximation we assume that the weakly bound conduction electrons move quite slowly.

The anisotropy of the phonon spectrum was not considered, assuming that phonons with any wave vector $\vec{q}$ is divided into longitudinal and transverse. Introducing a positive parameter anisotropy $\gamma = \frac{m_\perp}{m_z}$ this problem is also solved for negative values m_z (but here anisotropy parameter is considered positive).

In the work of Pekar [12], the theory of anisotropic optical polaron of large radius with a weak coupling is generalized for the case of multi-valley cubic crystals for the spectrum of the form (1) with m_z>0 in the absence of a magnetic field.

Here the solution of this problem is derived for one-valley cubic crystal structure with an anisotropic spectrum of the form (1) in the general form both in the case m_z>0 and m_z<0. In the framework of the standard perturbation theory correction to the energy of a conduction electron, in the second order due to the weak interaction with phonons at low temperatures has the form [13]:

$$\Delta\varepsilon_{\vec{k}} = -\frac{4\pi\alpha_\perp}{V}\frac{(\hbar\omega_L)^2}{u_\perp}\sum_{\vec{q}}\left\{q^2\left[\varepsilon_{\vec{k}-\vec{q}} - \varepsilon_{\vec{k}} + \hbar\omega_L\right]\right\}^{-1}, \qquad (2)$$

where:: $\alpha_\perp = \frac{1}{2}\frac{e^2 u_\perp}{\hbar\omega_L}\left(\sigma_\infty^{-1} - \sigma_0^{-1}\right)$ is the electron-phonon coupling constant, $u_\perp = \left(\frac{2m_\perp\omega_L}{\hbar}\right)^{1/2}$, ω_L is the frequency of the longitudinal optical phonon, σ_0 and σ_∞ are static and high-frequency dielectric constants, $\vec{k}$ and $\vec{q}$ are wave vectors of the electron and phonon correspondingly. Computation (2) is carried out under assumption that for small $\vec{k}' = \vec{k} - \vec{q}$ the constant-energy surface is also an ellipsoid of rotation and the direction of its axis of rotation coincides with the corresponding direction of the ellipsoid (1). Further introducing the cylindrical coordinates $q_\perp$, q_z and the polar angle φ, for the expression $\varepsilon_{\vec{k}-\vec{q}} - \varepsilon_{\vec{k}} + \hbar\omega_L$ we obtain the following relation:

$$\varepsilon_{\vec{k}-\vec{q}} - \varepsilon_{\vec{k}} + \hbar\omega_L = \hbar\omega_L\left\{\left(1 + x \pm z^2 \mp 2z\xi\right) - 2x^{1/2}\chi\cos\varphi\right\}, \quad (3)$$

where: $x = \left(\frac{q_\perp}{u_\perp}\right)^2$, $z = \frac{q_z}{u_z}$, $\chi = \frac{k_\perp}{u_\perp}$, $\xi = \frac{k_z}{u_z}$ and $u_z = \left(\frac{2m_z\omega_L}{\hbar}\right)^{1/2}$. In relation (3) the upper sign refers to the case $m_z > 0$, the lower sign does to $m_z < 0$.

Next, we use the standard way transfer from summation $\vec{q}$ to integration in cylindrical coordinates $q_\perp$, q_z and φ. Substituting (2) into expression (3) after integration over polar angle φ we get:

$$\Delta\varepsilon(\chi,\xi,\gamma) = -\frac{\alpha_\perp\hbar\omega_L}{2\pi}\gamma^{1/2}\int_0^\infty\int_{-\infty}^{\infty}\frac{dx\ \ dz}{\left(x\gamma + z^2\right)\left[\left(1 + x \pm z^2 \mp 2z\xi\right)^2 - 4\chi^2 x\right]^{1/2}}. \quad (4)$$

Then we expand in a series under the integral expression in (4) for small values of the parameters χ and ξ, while retaining second order terms. After these transformations carrying out integration in (4) for the spectrum $\mathrm{E}(k_\perp, k_z, \gamma)$ of the polaron we obtain

$$\mathrm{E}(k_\perp, k_z, \gamma) = \Delta\mathrm{E}(0,\gamma) + \mathrm{E}(k_\perp^2, \gamma) + \mathrm{E}(k_z^2, \gamma). \quad (5)$$

The energy of the ground state polaron $\Delta\mathrm{E}(0,\gamma)$ takes the form:

$$\Delta\mathrm{E}(0,\gamma) = -\alpha_\perp\hbar\omega_L\mathrm{I}(\gamma). \quad (6)$$

If $m_z > 0$:

$$\begin{cases}\mathrm{E}(k_\perp^2,\gamma) = \dfrac{\hbar^2 k_\perp^2}{2m_\perp}\left[1 - \alpha_\perp\left(\dfrac{1}{4\sqrt{\gamma}} + \dfrac{1}{2}\dfrac{d\mathrm{I}(\gamma)}{d\gamma}\right)\right], \\ \mathrm{E}(k_z^2,\gamma) = \dfrac{\hbar^2 k_z^2}{2m_z}\left[1 + \alpha_\perp\gamma\dfrac{d\mathrm{I}(\gamma)}{d\gamma}\right],\end{cases} \quad (7)$$

where: $\mathrm{I}(\gamma) = \frac{1}{\sqrt{\gamma - 1}}\,Arsh\sqrt{\gamma - 1} \quad \rightarrow$

$$\begin{cases}\mathrm{I}(\gamma) = \dfrac{1}{\sqrt{1-\gamma}}\arccos\sqrt{\gamma}, & |\gamma| \le 1 \\ \mathrm{I}(\gamma) = \dfrac{1}{\sqrt{\gamma - 1}}\ln(\sqrt{\gamma} + \sqrt{\gamma - 1}), & |\gamma| \ge 1.\end{cases} \quad (8)$$

If m_z <0:

$$\begin{cases}\mathrm{E}(k_\perp^2,\gamma) = \dfrac{\hbar^2 k_\perp^2}{2m_\perp}\left(1 + \dfrac{\alpha_\perp}{2}\dfrac{d\mathrm{I}(\gamma)}{d\gamma}\right) \\ \mathrm{E}(k_z^2,\gamma) = \dfrac{\hbar^2 k_z^2}{2m_z}\left(1 + \alpha_\perp\gamma\dfrac{d\mathrm{I}(\gamma)}{d\gamma}\right),\end{cases}$$

where: $\mathrm{I}(\gamma) = \frac{\pi}{2}\frac{1}{\sqrt{1+\gamma}}$. (9)

Effective mass of the polaron are determined by expressions for the following two cases: 1) in the case of $m_z > 0$:

$$\begin{cases}\dfrac{1}{m_\perp^*} = \dfrac{1}{m_\perp}\left[1 - \dfrac{\alpha_\perp}{4(1-\gamma)}\left(\mathrm{I}(\gamma) - \sqrt{\gamma}\right)\right] \\ \cdot \\ \dfrac{1}{m_z^*} = \dfrac{1}{m_z}\left[1 + \dfrac{\alpha_\perp\gamma}{2(1-\gamma)}\left(\mathrm{I}(\gamma) - \dfrac{1}{\sqrt{\gamma}}\right)\right].\end{cases} \quad (10)$$

2) in the case of m_z < 0:

$$\begin{cases} \dfrac{1}{m_{\perp}^{*}} = \dfrac{1}{m_{\perp}}\left(1 - \dfrac{\alpha_{\perp}\pi}{8(1+\gamma)^{3/2}}\right), \\ \dfrac{1}{m_{z}^{*}} = \dfrac{1}{m_{z}}\left(1 - \dfrac{\alpha_{\perp}\gamma\pi}{4(1+\gamma)^{3/2}}\right). \end{cases} \qquad (11)$$

It should be noted that neglecting inter-valley transitions of expression obtained in [12] for the energy shift of the polaron and polaron masses coincide with (6) and (10). If limiting case of the two-dimensional case when $\gamma = 0$, from general expressions (6) and (10) we obtained well-known results for $\Delta E(0,0)/\alpha_{\perp}\hbar\omega_L$ = - $\pi/2$ and $\Delta m_{\perp}^{*}/\alpha_{\perp} m = \pi/8$ [14], where $\Delta m_{\perp}^{*} = m_{\perp}^{*} - m_{\perp}$. Also with $\gamma = 1$ the results obtained from (6) and (10) coincide with the expressions $\Delta E(0,1)/\alpha_{\perp}\hbar\omega_L = -1$ и $\Delta m^{*}/m = \alpha/6$ for the bulk case [15]. In these calculations do not provide for the limit to one-dimensional case.

Now obtained results apply to SMSC. In the presence of an external magnetic field for SMSC we use the energy spectrum of electrons given in [11], which is obtained by the $\vec{\kappa}\ \vec{p}$ - method in the framework of the Kane model. The influence of non-quantizing magnetic field on the spectrum of conduction electrons is taken into account through the exchange interaction between the spins of conduction electrons and paramagnetic ions.

In the parabolic approximation the energy of electrons of lowest conduction band with spin $\downarrow$ is as follows:

$$\lambda = \varepsilon_g - 3A + \frac{\hbar^2}{2M_{\perp}}(\kappa_{\perp}^2 + \gamma^{*}\kappa_z^2). \qquad (12)$$

In (12) $\gamma^{*} = \dfrac{M_{\perp}}{M_z}$ is an anisotropy parameter of the spectrum in SMSC. Because of the exchange interaction band electron effective masses $M_{\perp}$ and M_z are depended on the magnitude of the exchange interaction constants and they are determined by the expressions:

$$\frac{1}{M_{\perp}} = \frac{\varepsilon_g}{4m_e}\left[\frac{3}{\varepsilon_g - 3A + 3B} + \frac{1}{\varepsilon_g - 3A - B}\right], \qquad (13)$$

$$\frac{1}{M_z} = \frac{1}{m_e}\frac{\varepsilon_g}{\varepsilon_g - 3A + B}$$

where $m_e = \dfrac{3\hbar^2\varepsilon_g}{P^2}$ is the effective mass of electrons, ε_g is the gap width in the absence of a magnetic field, P is the Kane parameter, $A = \dfrac{a}{b}B$ and $B = \dfrac{1}{6}N_0 bx\langle S_z\rangle$, $N_0 x$ - is the concentration of magnetic ions. The exchange constants $a = \langle S|J|S\rangle$ and $b = \langle x|J|x\rangle$ characterize the contribution of the exchange interaction to the energy of band electrons. The average value of the spin of the magnetic ion $\langle S_z\rangle$ along the direction of the applied field is determined by the Brillouin function $B_S(Y)$: $\langle S_z\rangle$ = -S $B_S(Y)$, where $Y = \dfrac{\bar{g}\mu_B SH}{\kappa_0 T}$ [8].

The calculations carried out according to formulas (13) show that with increasing *H*, while their own effective mass of conduction electrons $M_{\perp}, M_z$ decrease, the degree of anisotropy of the electron spectrum increases.

Further, restricted ourselves to weak magnetic fields *H*, we consider so-called non-resonant polarons [7]. This approximation is justified for weak magnetic fields when the condition $\omega_c << \omega_{LO}$ holds true; where $\omega_c = eH/m_e c$ is the cyclotron frequency. This assumption means that at low temperatures virtual transitions of an electron interacting with phonons within the lower conduction sub band [14,15] are taken into account. However, such an approach to solving the problem of non-quantizing magnetic field requires:

$$\hbar\omega_c < \kappa_0 T < 6A, \qquad (14)$$

where 6A is the distance between the lowest conduction bands of spin $\downarrow$ and spin $\uparrow$. The value of *H* satisfying this condition depends on the specific values of parameters: ε_g, P, A, B and $N_0 x$ for the considered sample.

Estimates carried out for most investigated narrow-gap $Hg_{1-x}Mn_xSe$ SMSC with x = 0.066 for the values P = 5.09 10-8 eV cm [10] $N_o a$ =- 0.32 eV, $N_o b$ = 0.92 eV, ε_g = 24 meV, $\bar{g} = 2$, S= $5/2$ [16,17] give the following results: condition (14) at T = 1K is satisfied for the values of H in the range $H \approx 10{,}5 \div 39$ Oe and at T = 2K for the range $H \approx 42 \div 78$ Oe. The discovered threshold mechanism for the optical polaron in SMSC occurs in the range of magnetic fields, where the subbands splitting by spin at the conduction band do not overlap with the temperature. The such overlap for the sample $Hg_{1-x}Mn_xSe$ with x = 0.066 takes place at temperature higher than 3.5 K.

In accordance with relations (6), (8), (10) for the shift of the polaron band bottom and for the polaron effective masses, we have the following expressions:

$$\Delta E\left(0,\gamma^*\right) = -\alpha_\perp^* \hbar\omega_L I\left(\gamma^*\right), \qquad (15)$$

$$\begin{cases} \dfrac{1}{N_\perp^*} = \dfrac{1}{M_\perp}\left[1 - \dfrac{\alpha_\perp^*}{4\left(1-\gamma^*\right)}\left(I\left(\gamma^*\right) - \sqrt{\gamma^*}\right)\right], \\ \dfrac{1}{N_z^*} = \dfrac{1}{M_z}\left[1 + \dfrac{\alpha_\perp^*}{2\left(1-\gamma^*\right)}\left(I\left(\gamma^*\right) - \dfrac{1}{\sqrt{\gamma^*}}\right)\right]. \end{cases} \qquad (16)$$

where:

$$\alpha_\perp^* = \frac{1}{2}\frac{e^2 u_\perp^*}{\hbar\omega_L}\left(\sigma_\infty^{-1} - \sigma_0^{-1}\right), u_\perp^* = \left(\frac{2M_\perp\omega_L}{\hbar}\right)^{1/2}.$$

Since for the narrow-gap $Hg_{1-x}Mn_xSe$ SMSC with $x = 0.066$ $\gamma^* < 1$, in the calculations we use:

$$I\left(\gamma^*\right) = \frac{1}{\sqrt{1-\gamma^*}} \arccos\sqrt{\gamma^*}. \qquad (17)$$

In expressions (15), (16), (17) $\alpha_\perp^*$, $I\left(\gamma_\perp^*\right)$ and γ^* depend on the magnetic field. Numerical calculations for the polaron effective mass carried out at the values $\hbar\omega_L = 16.8$ meV, $\sigma_0 = 28.5$, $\sigma_\infty = 13$, T = 2 K for the $Hg_{1-x}Mn_xSe$ SMSC with x = 0.066, which has the structure of zinc blend (sphalerite) up to $x = 0.37$. The calculated dependencies of H are shown in the figure for $M_\perp/m_e$, $N_\perp/m_e$ and M_z/m_e, N_z/m_e. From the figure it is shown that the transverse and longitudinal polaron mass, renormalized due to electron phonon interaction, increases compared to the corresponding band values. However, polaron mass of electrons decreases owing to exchange interaction with increasing magnetic field.

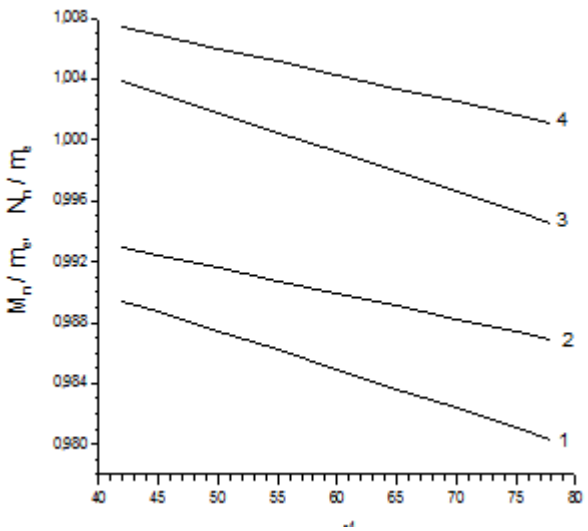

Fig. Dependences $M_\perp/m_e$, $N_\perp/m_e$ and M_z/m_e, N_z/m_e on the of the magnetic field *H;* the lines with the number $n = 1,3$ correspond $M_\perp/m_e$ and M_z/m_e; $n = 2, 4$ - $N_\perp/m_e$ and N_z/m_e.

ACKNOLEDGEMENT

The author is grateful to prof. F.M.Gashimzade for an useful discussion the topic of the present investigation.

[1]. *Kotelnikov, V.A. Kokin, Yu Feder, AV Guk, D.T.Talbaev*, JETP Lett, vol 71,N 9, p.564, (2000).
[2]. *G.Bauer, J.Kossut, R.Faymonville, R.Dornhaus*, Phys.Rev.B 31, No 4,2040(1985).
[3]. *C.E.T.Goncalves da Silva*, Phys.Rev.B 32, N10,6962(1985).
[4]. *Gilmar E.Marques, Valmir A.Chitta, Marcos H.Degani*, Oscar Hipolito Phys.Rev.B 36, N9,5066 (1987).
[5]. *L.Jacak, J.Krasnyj, D.Jacak, P.Machnikowski*, Phys.Rev.B 67,035303 (2003).
[6]. *P.Pfeffer and W.Zawadzki*,Phys.Rev.Lett.,61,762 (1988).
[7]. *P.Pfeffer*.Semicond.Sci.Technol.,5, 295 (1990).
[8]. *I.I. Lyapilin, I.M. Tsidilkovskiy*. UFN, 146, 35-72 (1985).
[9]. *J.K.Furduna*, J.Appl. Phys.,64, R 29-63 (1988). Edited by J.Furduna and J.Kosuta. Semimagnetic semiconductors. Moscow "Mir" 495 pp., (1992).
[10]. *F.M.Gashimzade, S.T.Pavlov, R.S.Nadirzade, N.G.Ismailov, B.I.Belitski*. Phys.Stat.Sol.(b), 155, K161 (1989).
[11]. *Pekar*. JETF, vol.55, issue 5 (11), 1997 (1968).
[12]. *Ju. A. Firsov*, Polarons, Nauka, 423 pp., (1975).
[13]. *N.M Guseinov, S.M.Seid-Rzayeva*. Fizika Tverdogo Tela (Solid State Physics) t.31, № 9, p.32 (1989);*N.M.Guseinov, K.A.Rustamov and S.M.Seid-Rzayeva*, Mod.Phys.Lett.B, 5, 139 (1991).
[14]. S.*Das Sarma*, Phys.Rev.B, 27,2590-2593 (1983).
[15]. *N.B.Brandt and V.V.Moshchalkov*,Advances in Physics, 33, 193 (1984).
[16]. *S.Takeyama, R.R.Galazka*. Phys. St. Sol.(b), 96, N1, 413 (1979).

GaSe AND InSe CRYSTALS IN QUANTUM ELECTRONICS

V.M. SALMANOV[1], A.A. SALMANOVA[2],
E.M. KERIMOVA[3], D.A. HUSEINOVA[3]
[1]Baku State University, [2]Azerbaijan State Oil Academy,
[3]Institute of Physics, National Academy of Sciences
vagif_salmanov @ yahoo.com

The nonlinear light absorption and its time evolution in the exciton resonance region at high optical excitation levels in GaSe and InSe layered crystals have been investigated experimentally. The observed time dependences of the absorption coefficient GaSe and InSe crystals and its excitation intensity dependences are determined by exciton - exciton interaction and exciton screening by the plasma of nonequilibrium carriers. It is shown, that filling of zones in GaSe the nonequilibrium carriers generated by laser light allows to create semi-conductor lasers on their basis. On the basis of crystals GaSe and InSe high-speed not cooled detectors of optical radiation and optical filters of laser radiation are developed.

1. INTRODUCTION

Among the basic directions of fundamental development in the field of laser physics the basic place occupies research of interaction of intensive radiation with substance. Interaction of light waves high power and high monochromaticity with substance has resulted a pain in creation of new area of physics - nonlinear optics. The nonlinear optics studying nonlinear optical effects, which character depends on intensity of light, allows to receive the rich information on properties of material environments. In a problem of interaction of laser radiation with a firm body, special interest represents a question on studying of the phenomena proceeding in semi-conductor crystals, raised by ultrahigh light streams. In the semiconductors having in rather big size of polarizability, nonlinear effects are expressed especially strongly, that allows to use effectively them for detection and research of essentially new nonlinear optical phenomena. Now in quantum electronics a number of semi-conductor crystals is applied. However, the further development of quantum electronics demands search of the new semi-conductor materials, satisfying growing to requirement of this actual area of physics. As have shown the researches lead by us, layered semi-conductor crystals GaSe and InSe are perspective materials for quantum electronics. It is known, that layered crystals GaSe and InSe have the big nonlinear susceptibilities, strong anisotropy of physical properties, the big exciton binding energy (~20 meV), in small factor of absorption at edge of fundamental absorption ($\alpha \sim 10^3$ sm^{-1}), without mechanical and chemical processing are possible to make samples with thickness down to one micron and have width of the forbidden gaps which are taking place in the field of generation of modern lasers.

In on worth work the basic experimental and theoretical results of research of the nonlinear optical and nonequilibrium phenomena in layered crystals GaSe and InSe are resulted at laser excitation and opportunities of application of this class of semiconductors are specified as materials and elements of quantum electronics.

2. A TECHNIQUE OF EXPERIMENT

Researches were carried out on specially not alloyed crystals p-GaSe and n-InSe, grown up by method Bridgman. Samples with thickness 10÷30 a micron and the areas~1sm^2 have been made by way splitting of large ingots in a direction parallel optical axis – "c". On the surface of a sample in vacuum has been put by a method of thermal evaporation ohmic contact In. It agrees Holl to measurements, mobility and concentration of carriers of a current made $\mu_n = 1.2 \times 10^3 sm^2/(V \cdot s)$, $n = 7 \times 10^{14} sm^{-3}$ and $\mu_p = 20 sm^2/(V \cdot s)$, $p = 1 \times 10^{14} sm^{-3}$ for InSe and GaSe, accordingly. As sources of radiation have been used YAG:Nd^{+3} the laser (length of a wave 1.06 microns, duration of a pulse ~ $2.5 \cdot 10^{-11}$s, the maximal power ~ 10^9 Vt/sm^2) and Rhodamine 6G dye laser (the output wavelength could be tuned in the range 473÷540 nm, duration of a pulse ~ $3 \cdot 10^{-9}$s, the maximal power ~ $1.2 \cdot 10^7$ Vt/sm^2). Intensity of radiation changed by means of the calibrated neutral filters. In work modern methods of laser spectroscopy, such as a two-beam method, a method of measurement of time of a delay, a non-stationary method of research of photoconductivity, a method of " light impact », with application of non-stationary digital system which included a remembering oscillograph and Board Master 800 ABI 8 computer system were applied.

3. EXCITON ABSORPTION IN GaSe AND InSe CRYSTALS AT PICOSECOND EXCITATION

Fig. 1,a illustrates dependence of the magnitude of transmission coefficient on the emission intensity for an InSe single crystal excited by laser light having an energy hν=1.327eV (resonant excitation of exciton) at 77 K. As it is seen from the figure, a nonlinear absorption in the exciton resonance region and occurrence of sample bleaching in the indicated light frequency at high excitation levels are observed. Diminishing of the magnitude exciton absorption may be explained by the process of screening (Mott transition) for a high density exciton system. The density of electron-hole pairs in our experiment reached ~10^{20} sm^{-3}, which exceed the density necessary for Mott transition in InSe [1]. The detailed investigation of the bleaching and dynamics of nonlinear absorption in the exciton resonance region have been realized by using double beam method at 4.2 K. similar to single beam excitation, in this case also a bleaching is observed in the exciton absorption region at 4.2 K. Fig. 1,b illustrates clearly dependence of optical density on the excitation intensity in a frequency where the exciton absorption is maximum (the time delay between the probe and pump pulses is zero). The observed bleaching saturates at higher excitation levels with respect to the case of resonant excitation of exciton (Fig.1,в).

Disappearance of the exciton peak in this case may be explained by screening of the Coulomb interactions by free charge carriers. The screening length can be defined by the following equation [2]

$$L = \hbar / 2(\pi/3)^{1/6} N^{-1/6} \varepsilon^{1/2} / em^{*1/2} \quad (1)$$

where ε is dielectric constant of the crystal, m^* is the effective mass, N is concentration of the generated carriers.

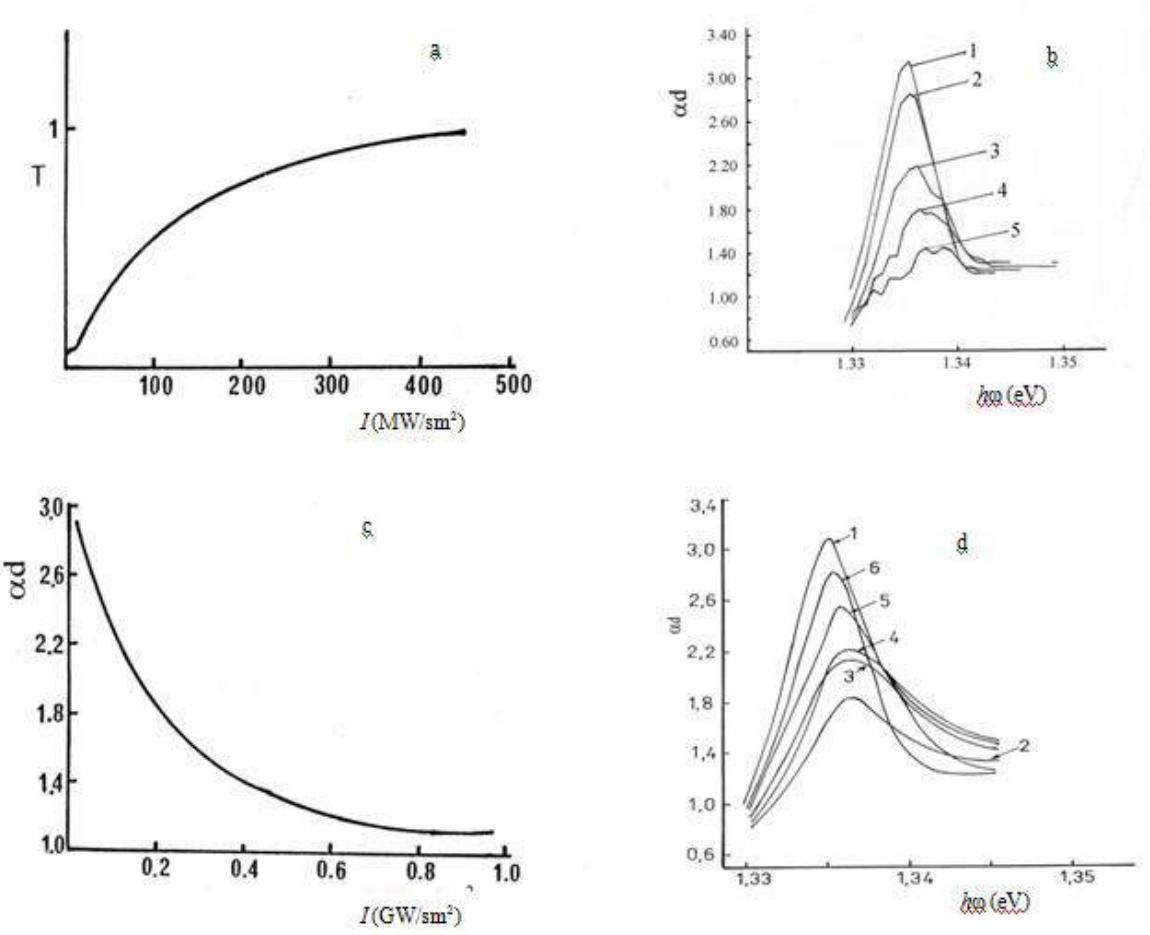

Fig.1. (a) Dependence of the transmission coefficient on the excitation intensity in InSe (in the case of resonant excitation of exciton, hν=1,327eV) at 77 K; (b) Absorption spectra of InSe for different excitation intensity $I_{pump.}$(MW/sm^2): 1 - 0, 2-12, 3-60, 4-250, 5-600 (time delay between the probe and pump pulses Δt=0) at T= 4,2 K; (c) Dependence of the optical density on the excitation intensity ($h\nu_{pump.}$ = 2,34eV, $h\nu_{probe}$ =1,336eV, Δt = 0) at T= 4,2 K; (d) Absorption spectra of InSe for different time delays between the probe and pump pulses: 1 - $I_{pump.}$= 0, 2 - Δt = 24ps, 3 - Δt = 98ps, 4 - Δt = 297ps, 5-Δt = 660ps, 6-Δt = 910ps, $I_{pump.}$ =600 MW/sm^2, $h\nu_{pump.}$ = 2,34eV, T= 4,2 K.

Substituting values of corresponding parameters of crystals InSe, we shall receive, that the screening length L ~10A^0 which is less than exciton radius (~37 A^0). In Fig.1,r the absorption spectra of InSe crystals for different time delays between the probe and pump pulses are shown. It is clear from the figure that, the exciton absorption peak broadens and shift towards higher energies with respect to the nonexcitation case. In the energy region between the exciton level and edge the conduction band, an induced absorption is appeared. Nonlinear absorption in GaSe, in the exciton resonance region can be explained as well as, and in case of crystals InSe, process of screening (transition of the Mott) for system excitons to high density. The density of the pairs generated by laser light in GaSe, is equal 3x10^{19} sm^{-3}, that considerably exceeds the density necessary for Mott transition in GaSe (n_{Mott} =10^{17} sm^{-3} [3]).

4. EFFECT FILLING OF ZONES IN CRYSTALS AT HIGH LEVELS OF OPTICAL EXCITATION

It is known, that in semiconductors at high levels of optical excitation a plenty of electron-hole pairs is generated. As electrons and holes are Fermions according to Pauli principle on each quantum condition can be no more than two electrons with different backs (±1/2). The conditions occupied with carriers are, as though final conditions during optical absorption. According to a principle of minimization of energy, carriers in quasi-equilibrium fill in zones, starting from a bottom, therefore, in the beginning is filled the lowest power conditions. As a result of it vicinities of a zone of conductivity are filled electrons, and a ceiling of a valent zone holes. Filling of zones, finally results in nonlinear absorption in the region of absorption edge, with its simultaneous shift in high-energy area of a spectrum.

The absorption spectra of GaSe at low (curve 1) and high (curve 2) excitation intensities are given in Fig. 2,a. As it is seen from the figure, at high excitation levels, the absorption coefficient is decreased and along with the onset of absorption is also shifted towards higher energies. The change in the absorption coefficient (Δα) can be obtained by direct subtraction of curves 1and 2 in Fig. 2,a. The result is plotted in Fig. 2,b. It is seen that the maximum absorption change takes place in the vicinity of the band gap. The observed nonlinear absorption near the band gap at high excitation intensities can be attributed to optical filling effects in GaSe, i.e. electrons and holes generated by absorption of light which relax rapidly to a thermal distribution, blocking absorption states near the band edge. Effectively, this is like a shift of the band edge to higher energies with increasing laser intensity, which causes the absorption at the vicinity of the band edge to decrease. In this case optical absorption becomes negative and it results in amplification of light past through a sample that is the precondition for creation of the semi-conductor laser on the basis of crystals GaSe. Experimentally found values (Δα) have been compared with theoretical [4] according to which relative change $\frac{\Delta\alpha \cdot 100\%}{\alpha_0}$ for GaSe makes ~12 %. This is in good agreement with the corresponding observed value of 15 %. The small difference between these values can be due to the fact that, the exciton interactions were neglected in [4], while in wide-band-gap materials (such as GaSe), Coulomb electron-hole correlation effects should be taken into account which can eventually lead to the enhancement of the nonlinear absorption. Such filling of zones leads both to nonlinear absorption and to a strong intensity dependence of the refractive index.

From the Kramers-Kronig relation we may write the change in refractive index at photon energy $\hbar\omega$ as [5]

$$\Delta n(\hbar\omega) = \frac{hc}{\pi}\int_0^{\infty} \frac{\Delta\alpha(\hbar\omega')}{(\hbar\omega')^2 - (\hbar\omega)^2} d(\hbar\omega') \qquad (2)$$

Using Eq. (2) to compute the index change related to the absorption change of Fig. 3, we obtain the result plotted in Fig, 2, c. As can be noted from Fig. 2 the change in the refractive index leading to nonlinear effects, Δn(ω) is negative at frequencies below the absorption edge and positive on the high-energy side[12].

5. PHOTOCONDUCTIVITY AND LUMINESCENCE IN GASE CRYSTALS AT HIGH LEVELS OF OPTICAL EXCITATION

Research of photoconductivity of crystals GaSe under action of laser radiation shows, that anisotropy of crystals influences not only their electric properties, and also on photo-electric and optical properties. It is shown, that spectra of photoconductivity GaSe in the absorption edge at various configurations contacts are defined by two factors: localization of electronic states at band edges, caused by presence of defects of packing and nonlinear absorption of light in region exciton absorption. Really, apparently from Fig.3,a and at E⊥c in spectra are observed impurity and excitonic photoconductivity.

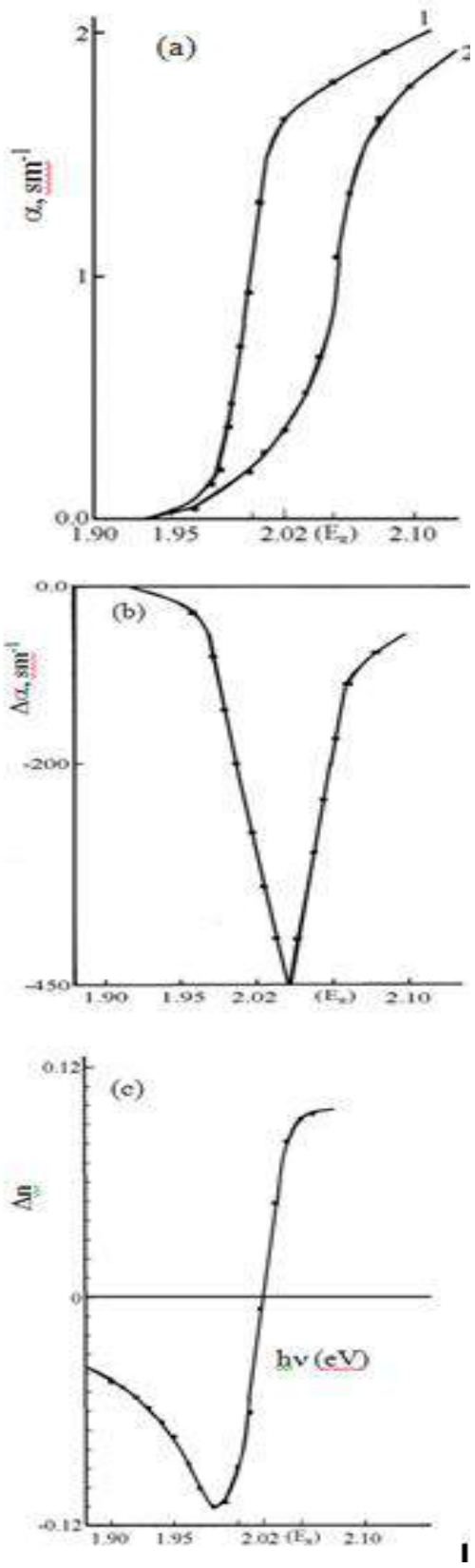

Fig. 2. (a) Absorption spectra of GaSe at low (~3,5 MW/sm^2, curve 1) and high (~12 MW/sm^2, curve 2) intensity excitation; (b) The change in the absorption coefficient Δα; (c) The change in the refractive index Δn(ω).

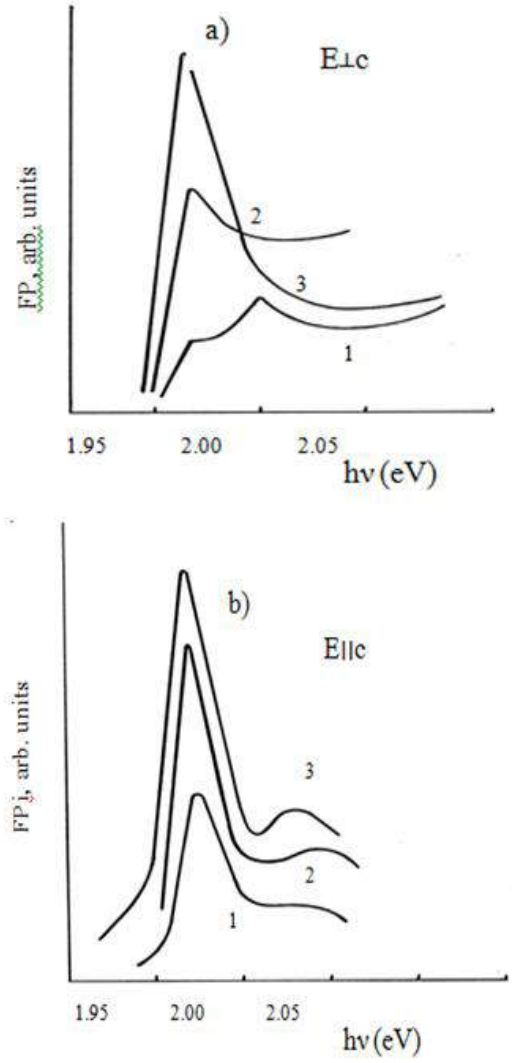

Fig.3. Photoconductivity (FP) spectra of GaSe crystals for two contact configurations: (a) E⊥c, excitation intensities of (1) 0.05, (2) 0.16 and (3) 0.40 MW/sm^2; (b) E||c, excitation intensities of (1) 0.55, (2) 1.15 and (3) 6.40 MW/sm^2.

With increasing incident intensity, both peaks grow, but at very excitation densities, only the longer wavelength peak persists, while the exciton peak disappears. In the case E||c configuration, we observe only the longer wavelength photoconductivity (Fig.3,б). Fotoluminescence spectra of GaSe are shown in Fig.4 for different excitation intensities. As is evident from Fig.4, in addition to the excitonic line corresponding to free excitons (the FE line observed at the wavelength 591 nm at 80 K), the spectra involve a low-energy band (the L band). At low excitation levels, the fotoluminescence spectrum exhibits only the FE emission line of free excitons (curve 1). However, as the pump intensity is increased, an emission line appears in the long-wavelength region of the spectrum at 20 meV below the FE emission line of free excitons. At very high excitation levels, the L band prevails in the emission spectrum. The experimentally observed specific features of the photoconductivity and fotoluminescence spectra are attributed to nonlinear optical absorption controlled by exciton - exciton interaction.

6. OPTICAL FILTERS AND HIGH-SPEED DETECTORS OF LASER RADIATION ON THE BASIS OF CRYSTALS GaSe AND InSe

On the basis of crystals GaSe and InSe we had been created optical filters and high-speed detectors of laser radiation. The mechanism of action of attenuators of the laser radiation working in seen and near infra-red region of a spectrum, is connected to effect of displacement of absorption edge of crystals GaSe and InSe under action of an electric field. The absorption edge of GaSe moves towards longer wavelength by increasing the applied voltage. A large shift of about 16 nm in the absorption edge corresponding to 50 meV is observed for the applied voltage of 16 V. In samples InSe under applied voltage the absorption edge is a red shift achieving a mark 1.074 μm at about 7.3V. Value of shift is about 75.8 nm (88meV). The shift of the absorption edge $\Delta\lambda$ with the applied voltage E varies as $\Delta\lambda=E^n$ (n=2.1÷2.5), which is independent of compositions samples. Fig.5 represents the experimental results of attenuating the radiation of a dye laser at different wavelengths (curves 1, 2, 4), He-Ne laser (curve 3) and YAG: Nd^{+3} laser (curve 5). As it is seen from the figure at the appropriate applied voltage 100% modulation of intensities of laser radiation occurs. In conclusion we should note that device offered on the base of GaSe and InSe, can also be used as an efficient cutting-off filter. For example, when investigated the luminescence on photostimulated processes, when it is necessary to separate a useful signal from the signal generated by high-power radiation.

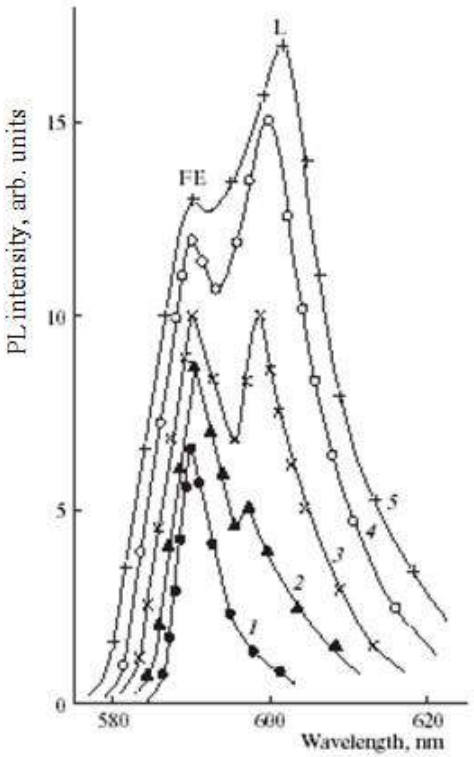

Fig. 4. Photoluminescence (PL) spectra of GaSe crystals at different excitation intensities I_0 (MW·sm^{-2}): 1- 0.12, 2- 1.01, 3- 4.02, 4- 6.03 and 5- 12. T=80 K.

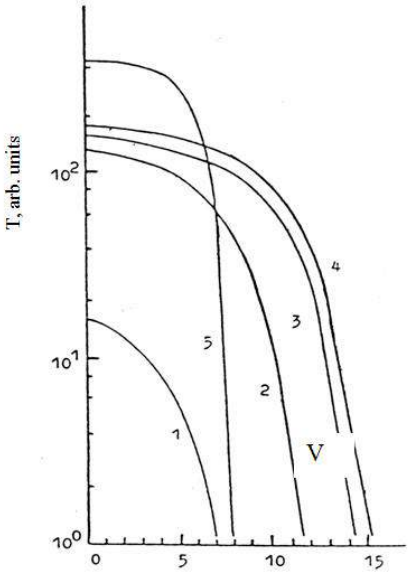

Fig. 5. Intensity of laser radiation with wavelengths of (1) - 625 nm, (2) – 629nm, (3) - 632,8nm, (4) – 634nm and (5) - 1060нм transmitted through the attenuator (GaSe crystal – 1-4; InSe crystal – 5) as a function of constant voltage applied to the device.

Registration of laser pulses at room temperature is one of pressing questions of laser technics. Among the new materials tested for laser pulse detection, GaSe and InSe crystals seem to be the most promising candidates. Fig. 6 shows a typical oscillogram for the p-GaSe samples. It is seen that the rise and fall times of the photosignal do not exceed 10 ns, and the dark current equals $6x10^{-6}$ A at an applied voltage of ~ 1V. The sensitivity of the detectors was 0.25 μA/μV for incident radiation wavelength λ=600nm. In the power density range 1.42÷12.00 MW/cm^2, the photocurrent linearly depends on the applied voltage up to 30V.

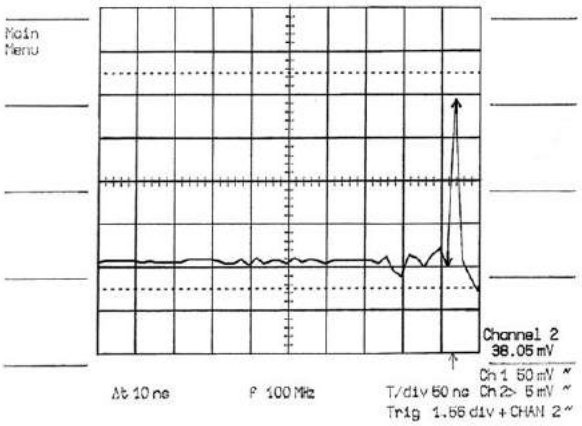

Fig.6. Oscillogram taken of the GaSe structure.

7. THE CONCLUSION

On the basis of above-stated it is possible to assert, that layered crystals GaSe and InSe are perspective materials for quantum electronics, having the big value of a nonlinear susceptibility and the big variety of mechanisms of nonlinearity of a parameter of refraction and factor of absorption. These crystals can successfully be applied as optical modulators, semi-conductor lasers, optical filters and ultrashort (10^{-9}÷10^{-12} s) detectors.

[1]. *A.Cingolani, R.Cingolani, A.Ferrara, M.Lugara*, Sol. Stat. Com. 1985, v. 55, №11, p. 1011.
[2]. *P. Gross* Free electrons in sol. stat., M. 1982, p. 35.
[3]. *A.Frova, Ph.Schmid, A.Grisel, F.Levy*, Sol. Stat. Com. 1977, v. 23, №1, p. 45.
[4]. *R.K.Kalia*, Phys. Rev. (B) 1982, v.25, p.6492.
[5]. *N.O.Yamamura, O.Yamamura, T.Matsuo*, Phys. Chem. Sol. 1992.v.53, №2, p. 277.
[6]. *N. Peyghambarian, S.W.Koch, A.Mysyrovicz*, Phys. Rev. 1993, v.153, p.567.

PHOSPHOR CONVERTED LIGHT EMITTING DIODES FOR SOLID STATE ILLUMINATION

R.B.JABBAROV, N.N.MUSAYEVA, S.H. ABDULLAYEVA
H.M.Abdullayev Institute of Physics,
Azerbaijan National Academy of Sciences,
AZ-1143 Baku, Azerbaijan,
e-mail: rjabbarov@physics.ab.az

InGaN light emitting diode structures was grown by low pressure metalorganic vapor phase epitaxy on a c-plane sapphire substrate. $(Ca_{1+x-y}Eu_y)Ga_2S_{4+x}$, phosphors have been synthesized one step by solid state reaction. Combined phosphors with 415 nm-emitting GaN chips, white Light Emitting Diodes have been fabricated. Their chromaticity coordinates and color temperature indicate that $(Ca_{1+x-y}Eu_y)Ga_2S_{4+x}$, phosphors are promising phosphors for GaN-based white LED.

INTRODUCTION

Rapid research and development from 90th years of effective light-emitting diodes (LEDs) based on nanostructures with GaN quantum wells have lead to a possibility to establish the illumination of the future – Solid-State Lighting (SSL) [1]. Saving of electrical energy after introducing solid-state lighting would be equivalent to building of 100 atomic energy power stations (USA evaluation). It has been widely accepted that solid state lighting, in terms of white LEDs, will be the fourth illumination source to substitute the incandescent lamp, fluorescent lamp and high pressure sodium lamp. Major developments in wide-band-gap III-V nitride compound semiconductors and color converted phosphors have led to the commercial production of white phosphors-converted pcLEDs. Research and technological development during last years have increased commercial white LED's luminous efficacy from 20 to 80-100 lm/W. Laboratory records of leading companies LEDs are of 160 lm/W. Correlated color temperature of the LED's radiation may be changed by various phosphors in the range from 6000 K ("cool" white light) to 2500 K ("warm" white light). These facts determine possibilities of a wide commercial use of white LEDs and bright perspectives of SSL. However, in the conventional pcLED structure, it is important to improve the low conversion efficiency of the phosphor layer in order to meet the goal of SSL, as defined by the Department of Energy (DOE) and Optoelectronics Industry Development Association (OIDA) [2]. The U.S. Department of Energy anticipates 137 lm/W white power LED performance by 2015. Currently the efficiency achieved is 100 lm/W. This means if all conventional lights worldwide were replaced with LEDs, savings would approach 1000 TW*h/year. In addition to reducing carbon emissions by 200 Mtons/year and saving $100 billion/year in energy production in developed countries, it can improve the quality of life of third world countries that do not have a power distribution infrastructure. Therefore, realizing advanced LED-based SSL with controllable color emission would be the ultimate goal of lighting technology.

EXPERIMENT

Some of the InGaN light emitting diode structures used to excite the phosphors for these studies was grown by low pressure metalorganic vapor phase epitaxy on a c-plane sapphire substrate. A 2 μm thick undoped GaN buffer layer including a thin in-situ deposited SiN defect reduction layer [3] was grown after AlN nucleation layer. The active region consisted of a single InGaN quantum well grown at about 800 °C with an In content of about 10% covered by a 10 nm thick AlGaN electron barrier layer. The structure was finished by a 200 nm thick Mg-doped GaN layer. The bare LED structure shows strong electroluminescence at 415 nm with a FWHM of 110 meV at room temperature. Other LEDs used to excite phosphors were commercial structures emitting at wavelengths of 405 (chip C405XB290, Cree Inc.) and 450 nm (Svetlana – Optoelectronika), respectively.

To make white LEDs the phosphor was put in a two component optical gel in liquid phase. Then the chip was covered with this mixture and the gel–phosphor composition was polymerized. The gel–phosphor compositions have been prepared in identical polycarbonate lenses having special cavities to put it. The samples have been prepared with identical phosphor concentration in gel to receive qualitative the same performance of different phosphors used in our experiments. Their optical characteristics have been investigated by exciting them with the different wavelengths provided by the three LED types as described above.

RESULTS AND DISCUSSION

Figure 1a) and b) illustrate the InGaN light emitting diode structure and its electroluminescence spectrum.

The spectrum has a maximum at 415 nm with FWHM of 110 meV at room temperature. Phosphor is considered the most important material, and its emission spectrum determines the luminous flux according to visual sensitivity function. Color indices such as CCT and CRI also depend on the characteristics of phosphor. The unique characteristic of white pcLEDs is that the color of light can be controllable by varying the configurations of phosphor. Novel phosphor $(Ca_{1+x-y}Eu_y)Ga_2S_{4+x}$, which has many advantages, for example, one-step synthesis, double emission bands and excited by different wavelength LED chip efficiently was grown and characterized in view of elaborating white LED phosphors. Judged from excitation spectrum [3], it is very clear that the obtained phosphors can be well excited by 400-460 nm LEDs and emits yellow and red lights. So the

excitation spectrum matches well with the emission of GaN chip (Fig.2).

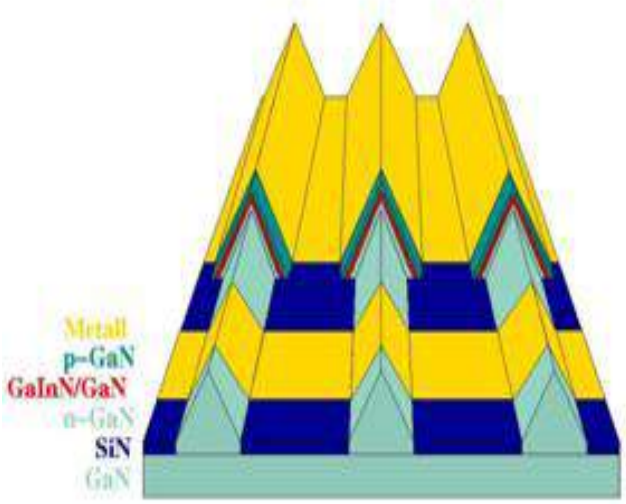

Fig.1(a).InGaN diode structure

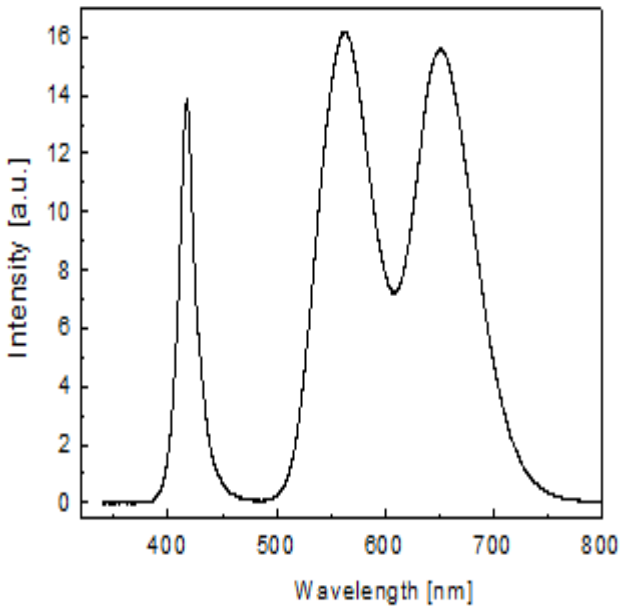

Fig.2. Emission spectrum of InGaN chip with phosphor

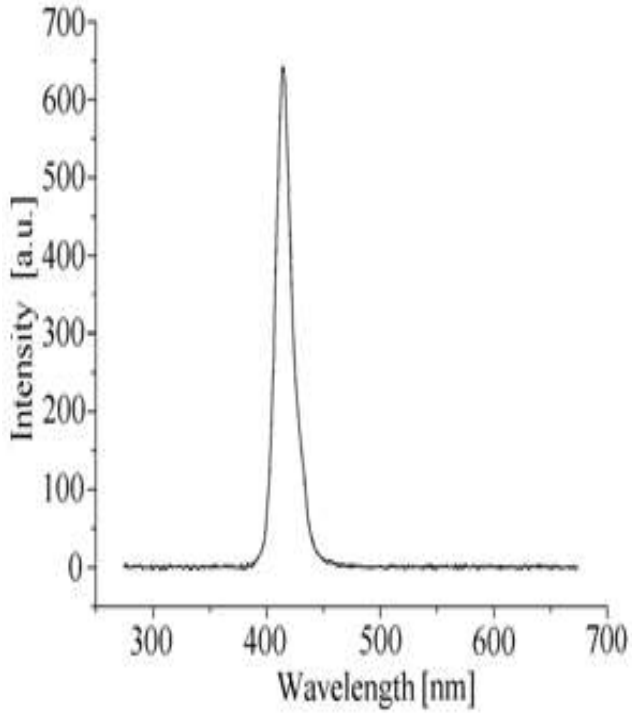

Fig.1 (b). Electroluminescence spectra of InGaN structure

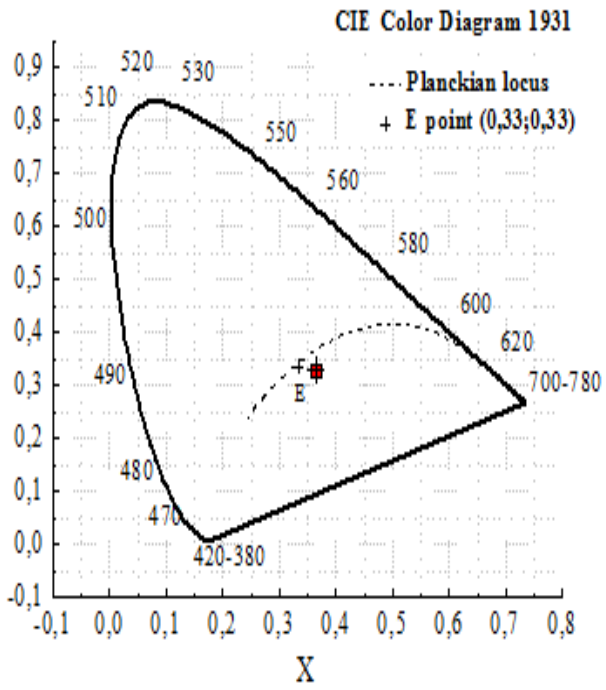

Fig.3. Color coordinates of the spectra shown in Fig. 2.

The emission bands attribute to the down-conversion emission of phosphor excited by GaN chip. This kind of down-conversion light mix with the remainder light of GaN chip emitted, and white light produce. The calculated color coordinate have been depicted in the 1931 CIE Chromaticity Diagram, and shown in Fig.3. The color coordinate (x;y)= (0.367; 0.325) of fabricated LEDs situate at the zone of white light with CCT is 3982K.

CONCLUSIONS

1. An inGaN LED structure used to excite the phosphors for these studies was grown by low pressure metalorganic vapor phase epitaxy on a c-plane sapphire substrate.
2. Phosphor can be synthesized one-step and has double emission bands.
3. The coating technology using $(Ca_{1+x-y}Eu_y)Ga_2S_{4+x}$ phosphor becomes simple.
4. It is very promising phosphor for GaN based white LEDs.

[1]. *F.Schubert*. Light-emitting diodes, 2nd ed.; Cambridge Univ. Press, 2006, 422 pp.

[2]. OIDA, 2002, Light emitting diodes (LEDs) for general illumination: An OIDA technology roadmap updates 2002.

[3]. http://lighting.sandia.gov/lightngdocs/OIDA_SSL_LED_Roadmap_Full. pdf.

[4]. *R. Jabbarov, N. Musayeva, F. Scholz, T.Wunderer, A. N. Turkin, S. S. Shirokov, and A. E. Yunovich*. Phys. Status Solidi A 206, No. 2, 287–292 (2009)

HYDRODYNAMICS OF LASER PLASMA EXPANSION FOR GOLD TARGETS: COMPARISON OF EXPERIMENTS WITH SIMULATIONS

A.ALIVERDIEV[1,2], D. BATANI[2], R. DEZULIAN[2], T.VINCI[2,3], A.BENUZZI-MOUNAIX[3], M.KOENIG[3], V. MALKA[4]

[1] *Institute of Physics DSC RAS, Makhachkala, Russia*

[2] *Dipartimento di Fisica "G. Occhialini", Università di Milano-Bicocca, Milan, Italy*

[3] *Laboratore pour l'Utilisation des Lasers Intenses, Ecole Polytechnique, Palaiseau, France*

[4] *Laboratoire d'Optique Appliquee, Ecole Polytechnique, Palaiseau, France*

E-mail: aliverdi@mail.ru

Here we consider the results of an experimental investigation of the temporal evolution of plasmas produced by high power laser irradiation of Au targets. We obtain "high-quality" interferometric data on the evolution of the plasma electronic profile, which can directly be compared to existing 1D analytical model and numerical simulations. Results of our experiments have confirmed the necessity of an account of radiate transport and probable absence of LTE for the plasmas generated by laser pulse with intensities the intensities about 10^{13}-10^{14} W/cm^2. Finally we have obtained appropriable accordance with the theory and numerical simulations and have found a quite simple approximation of experimental dependences.

1. INTRODUCTION

The investigation of hydrodynamics of laser-produced plasmas is fundamental for several areas of physics: material science, astrophysics, and first of all inertial confinement fusion (ICF). A clear modelling of plasma expansion and a revelation of the role of radiation transport during expansion are key problems in the physics of ICF driven by lasers. Although several theoretical models of plasma expansion were developed already in the 70's and in the 80's [1-3] and many experiments have studied this aspect, still there are not many clean experimental results. Indeed, most previous experiments were strongly influenced by 2D effects in the hydro expansion of the plasma, either because the focal spot was quite small compared to the expansion size, or because the irradiation profile was not uniform, but characterized by hot spot. Recently several optical smoothing techniques have been introduced to eliminate the problem of large-scale hot spots. 2D effects in plasma expansion may be strongly reduced, both because of the use of Phase Zone Plates (PZP) [4] and of large focal spots, producing a situation which is much closer to that described by 1D theoretical models. The use of time-resolved laser-plasma interferometry [5] has been also a very important step to resolve plasma evolution in the rapidly evolving, denser regions of a laser produced plasma. Streak cameras in combination with optical interferometers [6] give the way to more systematic studies, competitive with emerging soft X-ray techniques [7-9].

2. EXPERIMENT, PRINCIPLES AND PRELIMINARY ANALYSIS

Our experiment was realized at the LULI laboratory using 2 beams from the Nd:glass high power laser system converted to 2ω and together delivering a typical intensity of 10^{14} W/cm^2 on target. The temporal profile was approximately trapezoidal with rise and fall time of 150 ps and a flat top duration of 600 ps, the spot diameter produced by the lens coupled to the PZP had a FWHM of 400 μm with central flat top region of 200 μm diameter. A probe beam (Nd:YAG laser converted to 2ω) was coupled to Mach-Zehnder interferometer and to a streak-camera with ps resolution. The diagnostic system allowed the evolution of the plasma density profile to be measured as a function of time.

Recently we published results of our experimental investigation of plasma hydrodynamical expansion [10,11]. Now we continue this work, concentrating in singularities of results, obtained for Au targets. Fig. 2 shows streak camera interferograms obtained with very close initial data (total initial laser energy 54.4 J and 51.5 J, that gives in our case the intensity ~ $5.5\cdot10^{13}$ W/cm^2). How we can see, the images demonstrate quite good repeatability of our experiment. The total image dimensions are 375 μm (horizontal scale) and 1.065 ns (vertical scale) in both cases. Here x_1 represents the shadow of the target in the image plane. Initially the fringes are stationary because there is no plasma expansion. At the time t_1 they begin to move, first close to the target surface and then more and more distant.

Fig. 1a shows streak camera interferograms obtained with very close initial data (total initial laser energy 54.4 J and 51.5 J, that gives in our case the intensity ~ $5.5\cdot10^{13}$ W/cm^2). How we can see, the images demonstrate good repeatability of our experiment. Here x_1 represents the shadow of the target in the image plane. Initially the fringes are stationary because there is no plasma expansion. At the time t_1 they begin to move, first close to the target surface and then more and more distant. Our data are streaked and only 1D in space, in direction perpendicular to the target surface. Let's notice that the size of spot (FWHM of 400 μm) is comparable to the distance from the target, which we can see in our streak-camera image, therefore plasma expansion can be considered approximately 1D at least at the first order. To validate our approach we have realized some 2D simulations [12].

Figure 2 shows the result of these simulations of the plasma expansion (mass density) for the parameters of considered experiments. We can see that within FWHM spot size (D=400μm) the density variations in the radial direction are small, while the density decrease is very fast outside.

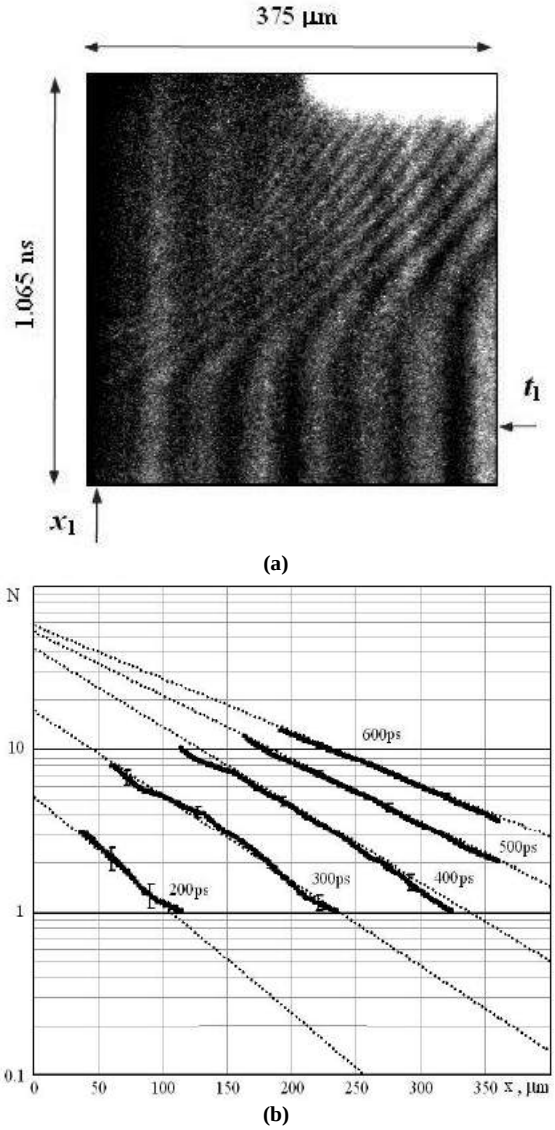

Fig. 1: **(a)** Typical interferograms recorded with the streak camera for Au target (Au, shot #7): The total image dimensions are 375 μm (horizontal scale) and 1.065 ns (vertical scale) for both images. **(b)** Experimental profiles of π-phase shifts obtained from the corresponded interferograms. Typical error bars are also shown in the figures (at late times the size of the error bars is comparable with the marker size so it cannot be seen in the graph). Time is measured starting from the time t_1 at which the fringes in the image begin to move

Turn back to the fig. 1. The plasma-induced phase shift in a point x of the interferometric picture is

$$\Delta\phi_{plasma}(x,t) = \frac{2\pi}{\lambda}\left(L - \int_{-L/2}^{L/2} n(x,y,t)dy\right) \qquad (1)$$

where λ the wavelength of the laser beam, L the effective plasma length, n the plasma refraction index. In the approximation of 1D plasma expansion (i.e. no dependence on radial distance, or on coordinate y) and assuming the usual expression for the plasma refraction index, we get

$$\Delta\phi_{plasma}(x,t) = \frac{2\pi L}{\lambda}\left(1 - \sqrt{1 - \frac{n_e(x,t)}{n_c}}\right) \qquad (2)$$

where $n_c = \frac{4\pi^2 c^2 \varepsilon_0 m_e}{\lambda^2 e^2}$ is the critical density, and n_e is the free electrons density.

If $n_e << n_c$, then $\frac{\lambda\Delta\phi_{plasma}}{2\pi L} \approx \left(1 - \left(1 - \frac{1}{2}\frac{n_e}{n_c}\right)\right)$, i.e. $\frac{\lambda\Delta\phi_{plasma}}{\pi L} = \frac{n_e}{n_c}$. Hence $N = \frac{L}{n_c\lambda} n_e$ and

$$n_e = \frac{n_c\lambda}{L} N\,. \qquad (3)$$

where $N=\Delta\phi/\pi$ is the number of π-phase shifts in the interferometric streak-camera images (the dependences N vs. x for a set of times) are presented in fig. 1b).

For a precise evaluation of N we have applied a technique of averaging with time shifts [13]. Indeed, how we can see from fig. 3, the time behaviour of intensity from a streak-camera image for a fixed x is affected by a strong noise, which can result both in neglecting or shifting of a real extremes (maxima and minima of interferogrammes) and in the appearance of false extremes. False extremes can usually be removed by traditional means (e.g., by applying Gauss-filter), but the shift of real extremes remains a problem (fig. 3b). Averaging over a small range of values of x also doesn't give good results because it smoothes the picture. In alternative, averaging with time shifts, with a characteristic velocity on the order of the real velocity, gives both a good resolution and a good contrast in the obtained densitometry. Fig. 3c shows the stability of this procedure for a small variance of spatial co-ordinate, and fig. 3d demonstrates the stability for a quite large variance of characteristic velocity. Finally the precision of π-phase shifts points in time-spatial square had an order of 1-2 pixels.

Let's notice that experimental data directly provide only the value of N (not n_e). To calculate n_e we need to know the plasma size L.

This value we have assigned 315 μm, the same like for Al and CH_2 targets, which was found from the comparison of experimental data with 1D self-similar models of isothermal plasma expansion in the same series of experiments [10,11]. From other hand logically the same value can be obtained like $\pi D/4$, where D is FWHM of a spot size.

3. RESULTS AND DISCUSSION

Turn back to the fig. 1b. We can see that dependences $N(x)$ are well interpolated by straight (dotted) lines, i.e. by exponential profiles, and can be described by:

$$\ln\big(N(x,t)\big) = b_0(t - t_0) - b_1(t - t_0)\cdot(x - x_0)\,, \qquad (4)$$

where t_0 marks the beginning of the laser-target interaction (when the laser pulse reaches the target front side), and x_0 is the initial position of the solid surface.

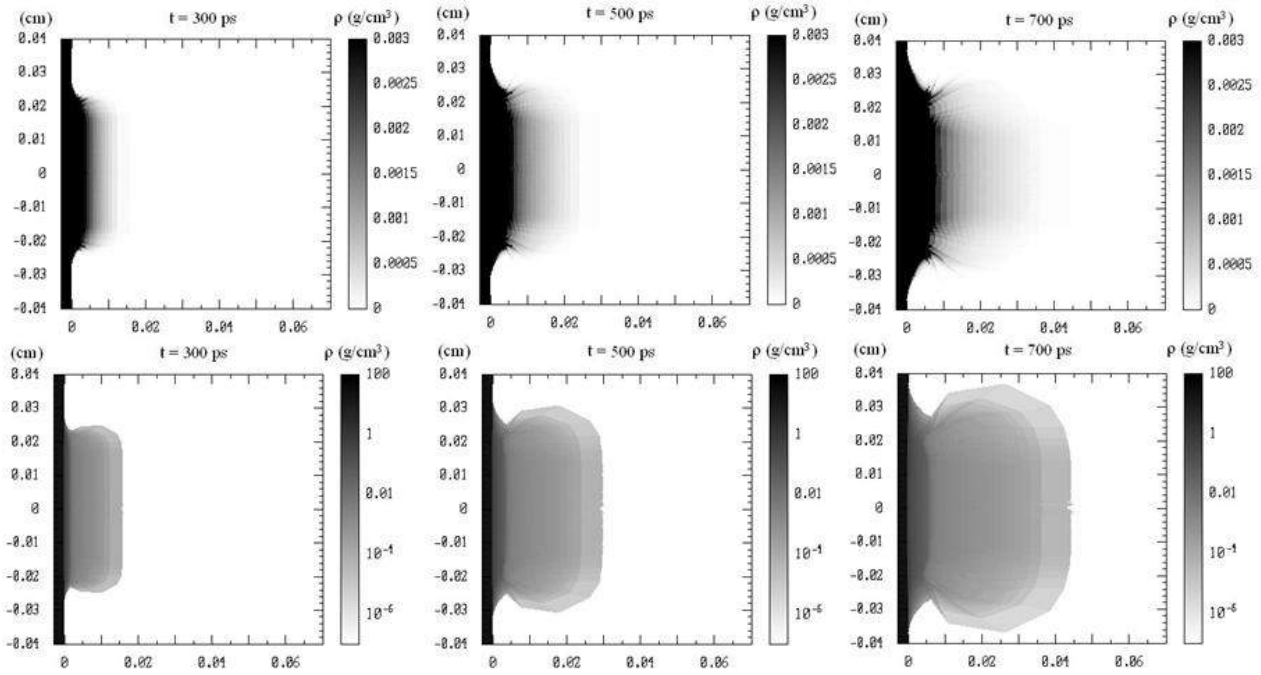

Fig. 2. The result of 2D MULTI hydro code simulation of plasma expansion for a gold target with laser beam parameters corresponded to considered shots: in linear (up) and in logarithmic (down) scales.

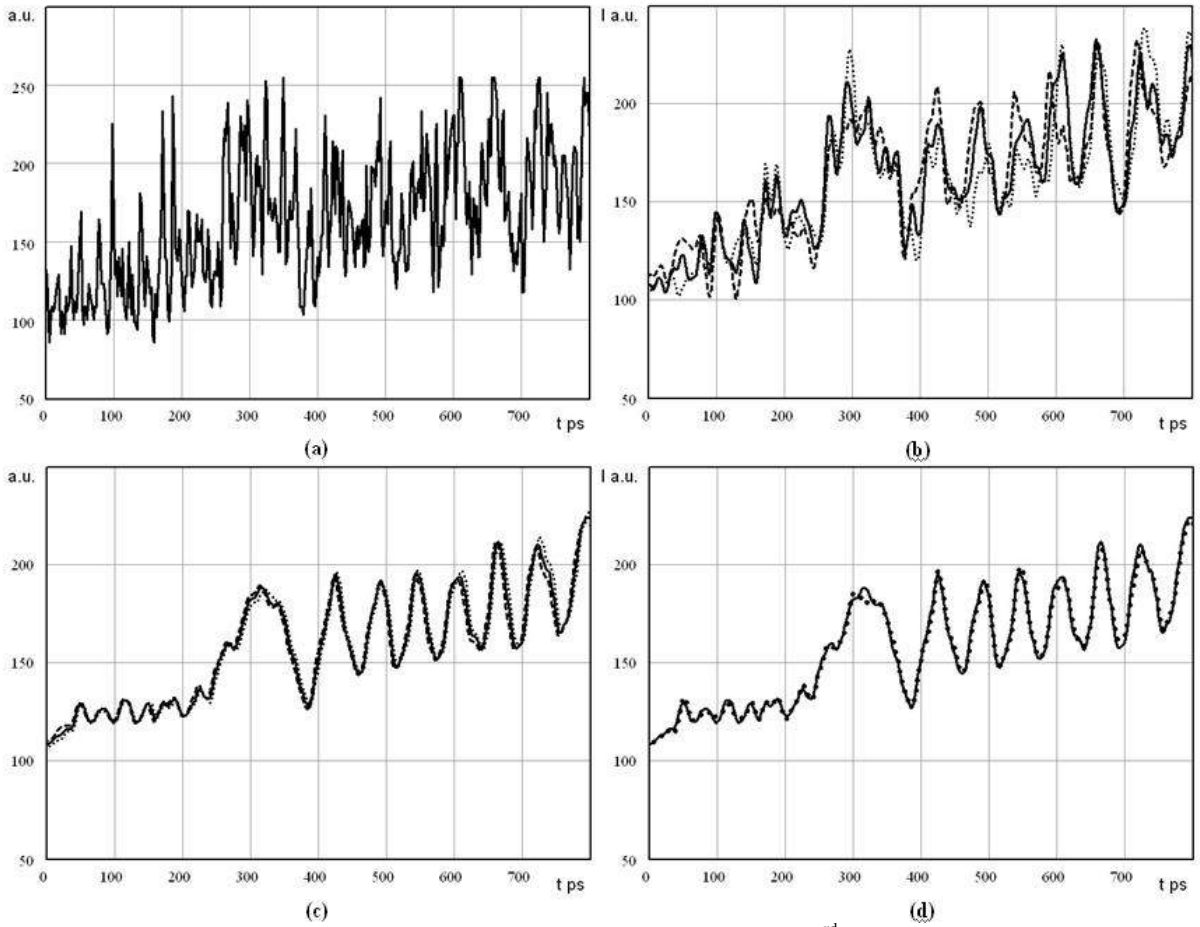

Fig. 3. (a) Time-dependence of intensity of a streak-camera image (Au, shot #7, for the 3rd minimum from the right, that is 320 pixel from the left). (b) The Gauss-filter application for the line on fig.a (solid line) and for the neighbour intensity lines, corresponded to 319 pixel (dotted line) and 321 pixel (dashed line). (c) The same but with the prior time-shift averaging in the spatial interval ±10 pixels (7.3 μm) with characteristic velocity 3.5 10^7 cm/sec. (d) Time-shift averaging in the spatial interval ±7.3 μm (10 pixels). The dotted line corresponds to characteristic velocity 4.6 10^7 cm/sec, the solid line to 3.5 10^7 cm/sec, finally a time Gauss-filter has been applied.

Moreover the extrapolation of straight lines (found from experimental ones by the list square method) for large times have a quite clear intersections in one point for each shot. How we already shown in [10,11] value of x_0 can be reasonably estimated from this point, and than the time t_0 can be found by extrapolating the line at which the fringes begin to move back to x_0.

Let's notice that in all interferometric streak-camera images we see the shadow of the target (position x_1). However, due to a small tilt of the target (~2 mm large) the position of the focal spot does not correspond to x_1 but to $x_1 \approx x_0 - L \tan(\theta)$, where θ is the angle between the target plane and a probe beam, so for $L \approx 1$ mm and $\theta \sim 6^o$ we find $x_1 - x_0$ can have an order 100 μm.. Let's notice also that exactly x_0 should correspond to the actual position of the critical surface, which moves inward the target due to the ablation of the material. However because the ablation velocity is much smaller (more than one order of magnitude) than the sound velocity we can neglect the time dependence of x_0. By shifting the origin of the co-ordinates to (x_0,t_0), we can then write Eq. 4 as

$$\ln\big(N(x,t)\big) = b_0 - b_1 \cdot x \qquad (5)$$

Starting from our experiment results for *N(x,t)* and using the least square method, we find the time dependences of b_0 and b_1.

The exponential character of the profile is in a good agreement with theoretical 1D self-similar models of isothermal plasma expansion [1-3] according to which

$$n_e(x,t) = n_c \exp\left(-\frac{x}{c_s \cdot t}\right) \qquad (6)$$

where

$$c_s = 9.79 \cdot 10^5 \sqrt{\frac{\gamma Z^* T_e}{\mu}} \qquad (7)$$

in cm/s is the adiabatic sound velocity, γ the adiabatic constant (γ=1 if electrons are isothermal), μ the atomic number, and Z^* is the ionisation degree, which can for instance be calculated with the formula by (Tonon & Colombant, 1973), which is valid in collisional-radiative equilibrium conditions. T_e is the electron temperature in eV, which in classical models (where energy is absorbed at the critical surface in the plasma and transported inward by electronic conduction) is typically given by

$$T_e\,(\text{eV}) = 10^{-6}\,(I_L\,\lambda^2)^{2/3} \qquad (8)$$

where I_L in W/cm^2 is the laser beam intensity, and λ is in μm.

Fig. 4 presents the experimental dependences n_e (grey rings for the shot # 7 and black squares for the shot # 10) with the calculation, made by formulae (6)-(8) (black straight lines) and extrapolation of experimental results (dotted straight lines). We can see the correspondence between experiment and theory by the order of values, but this correspondence is not brilliant, like it was found for the target from aluminium or plastic. [10, 11] The reason of this difference (as noted below) first of all seems to be in the large influences of radiation transport, which could be negligible for aluminium.

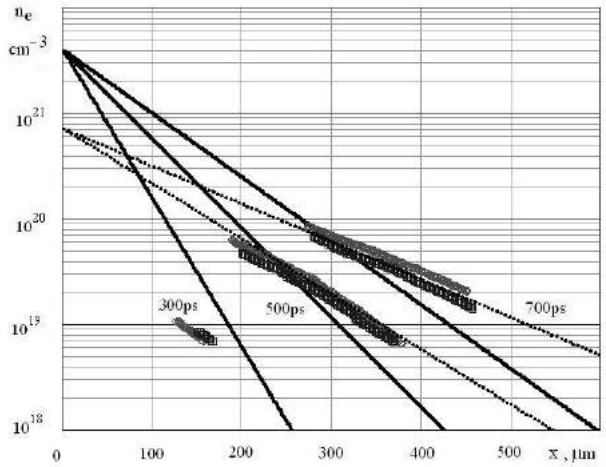

Fig. 4: Comparison of experimental profiles of electron density with the predictions of the analytic 1D model: experimental data for shot # 7 (rings) and shot # 10 (squares), prediction of 1D self-similar model (solid straight lines), and the linear extrapolation of experimental results (middle between shock # 7 shot # 10, dotted straight lines).

In order to refine our analysis, we compared our experimental results to numerical simulations performed using the 1D hydro code MULTI (multigroup radiation transport in multilayer foils) [14]. Both LTE (local temperature equilibrium) and non-LTE opacities have been obtained from an average hydrogenic model implemented in the code SNOP [15-17].

The results are presented in the figure 5. We can see that (i) the account of radiation transport is really important, especially in the non-LTE case, (ii) the account of radiation transport in the LTE case is not enough for the description of experimental data (even qualitative), and (iii) all experimental lines principally are located in frameworks of the area, limited by the curves of simulations without (black dashed line) and with (grey dashed line) LTE with account of radiation transport (small jut can be neglected by the small change of initial laser energy; real losses in experiment could be a little higher than it was considered, so this-like correction could be well-founded).

Thus we can conclude that our experimental data are not in close agreement, but in the same time don't conflict with the existing theoretical and numerical predictions. The perfect explanation of experimental curves (obtained with a high repeatability) probably could be done by a better description of LTE and non-LTE plasma opacities, which is the task for future work. Nevertheless now from the experimental coefficients b_0 and b_1 we can find a good phenomenological description of the plasma behaviour for the gold target (for t>450 ps) by:

$$n_e(x,t) = n_c * \exp\left(-\frac{x}{c_s * \cdot t}\right) \qquad (9)$$

where for laser intensity ~ 10^{13}-10^{14} W/cm^2 n_c^*=0.18 n_c, and c_s^*=0.54 c_s (where the sound velocity c_s is calculated by (9)-(10)). The clearness of physical mean of n_c^* and c_s^* demands other experiments.

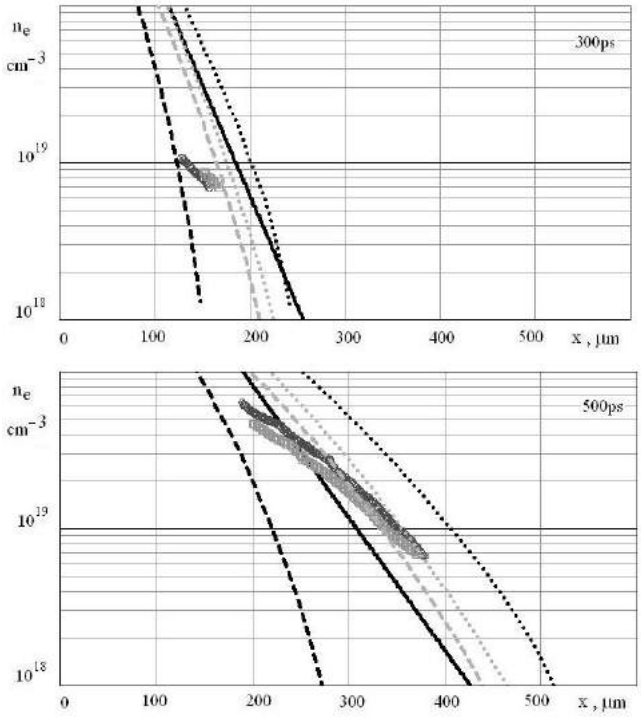

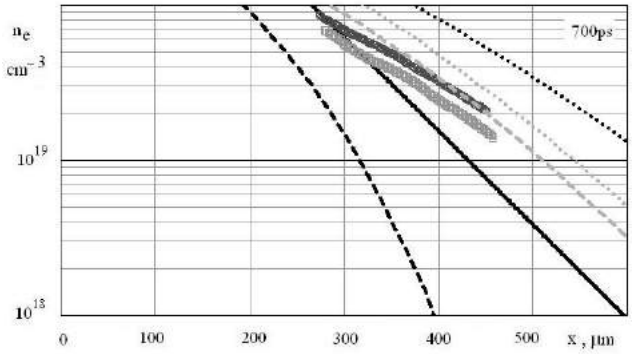

Fig.5. The dependences of electron density (rings for shot #7 and squares for shot # 10), calculation from the 1D self-similar model (solid straight lines), results of 1D MULTI simulation: with LTE (grey), without LTE (black), with account of radiation transport (dashed), without account of radiation transport (dotted).

4. CONCLUSION

We can conclude that results of our experiments have confirmed the necessity of an account of radiate transport and the probable absence of LTE for the plasmas generated from gold targets by laser pulses with intensities about 10^{13}-10^{14} W/cm^2. We also have found a quite simple approximation of experimental dependences.

ACKNOWLEDGMENTS

The authors warmly acknowledge the help of the LULI technical staff for the realization of this experiment. A.A. is also grateful to Landau Network - Centro Volta - Cariplo Foundation, INTAS (06-1000014-5638), ESF (SILMI, 2783) and RFBR (09-01-96508).

[1]. *C.E. Max, et al., Phys. Fluids*, 23, 1620 (1980).
[2]. *W.M. Manheimer, et al., Phys.Fluids*,25,1644 (1982)
[3]. *P. Mora, Phys. Fluids* 25 (6) (1982)
[4]. *M. Koenig, et al., Phys. Rev. E* 50, R3314 (1994)
[5]. *M. Borghesi et al.*, Phys. Rev.E 54 , 6769 (1996)
[6]. *Y.B.S.R. Prasad et al., Rev. Sci. Instruments* 77, 093106 (2006)
[7]. *M. M. Murnane, et al., Science* 251, 531 (1991)
[8]. *D. Ress, et al., Science* 265, 514 (1994)
[9]. *J. Workman, et al., Appl. Phys. Lett.*, 70, 312 (1997)
[10]. *A.AAliverdiev, et al., Phys. Rev. E*, 78, 046404 (2008)
[11]. *A.AAliverdiev, et al., Plasma Phys. Control Fusion*, 50, 105013 (2008).
[12]. *R..Ramis, and J. Meyer-ter-Vehn*, MPQ Report 174. Garching, Germany: Max-Planck-Institut für Quantenoptik (1992)
[13]. *A.A. Aliverdiev*, Optical Memory & Neural Networks (Information Optics), 15, 97 (2006).
[14]. *R. Ramis, et al.* Comput. Phys. Commun. 49, 475 (1988).
[15]. *K. Eidmann*, Laser and Particle Beams, 12, 223 (1994)
[16]. *K. Eidmann, et al.*, J. of Quantitative Spectroscopy and Radiative Transfer, 51, 77 (1994)
[17]. *G.D.Tsakiris & K.Eidmann*, J. of Quantitative Spectroscopy and Radiative Transfer, 38, 353 (1987)

AN ULTRAVIOLET LIGHT-INDUCED PHOTOPHYSICAL AND PHOTOCHEMICAL STUDY OF LASER-DYE RODAMIN-610 AND ITS PHOTOPRODUCT IN SOLUTION

ALİ YAMAN
Department of Physics, Faculty of Sciences,
Ankara University, Ankara, 06100, Turkey

In this work an ultraviolet light-induced photophysical and Photochemical changes of rodamin-610 in ethanol have been studied by photolysis technique at room temperature, due to its potential applications in Photonics, Photochemistry, and Electronic Spectroscopy. During the optical pumping, rodamin-610 showed photochemical changes, therefore as the concentration of rodamin-610 decreased, a photoproduct concentration increased rapidly. An absorption band of the product was observed at around 300 nm. Photoproduct emission spectra characteristics show that photoproduct molecules can also be used as a laser-dye at different emission frequency.

I. INTRODUCTION

Understanding the photophysics of dye molecules in solution has been an area of intense research in recent years . Most of the rodamins are intensly fluorescent and have been found useful as optical brightners, fluorescence indicators. Due to their industrial uses the photophysical and photochemical study of rodamin derivatives has assumed a great importance. Optical-gain for these rodamins are still interest for the spectroscopists. The processes like excited state absorption, intersystem crossing, internal conversion, ground state complex formation play dominant role in the study of optical gain. Recently there have been a large number of studies focusing on the vibrational energy redistribution and relaxation in solution phase. By optical excitation, vibrational excess energy is produced locally inside a molecule. Dissipation of the excess energy strongly influences the pathway and rate of the chemical reaction. The detailed understanding of dynamics in the excited state just after the photoexcitation is necessary to compare experimental results and theoretical prediction of chemical reaction in liquids. In general, a transient absorption spectrum consists of three contributions: Absorption of the transient states, bleach of the ground state, and stimulated emission from the excited states. These different contributions often overlap with each other in the spectrum, which makes interpretation very complicated. Therefore, it is rather difficult to discuss separately the intramolecular energy redistribution from the internal conversion to the first electronic excited state in the transient absorption spectrum. In contrast, a spontaneous emission measurement has advantage in studying the excited state dynamics, since only the excited state can be probed [1-5].

II. RESULTS AND DISCUSSION

Spectroscopically pure laser-dye rodamin-610 was from Exciton Co. Inc., and used as received, without further purifications. The steady-state absorption and fluorescence spectra were recorded with an absorption spectrophotometer (Unicam UV2-100), and a fluorescence spectrophotometer (Shimadzu RF-5301PC), respectively. All measurements were performed at an ambient temperature (293 K), at a concentration 1.5 x 10^{-5} M. Photolysis cells were spectrosilica grade, pure fused silica material. Rodamin-610 was irradiated by CW-low-pressure mercury arc lamp.

Rhodamine 610 can be pumped by incoherent or laser sources. Figure 1 and 2 show absorption and emission spectrum of rodamin-610. Absorption intensity has a maximum at 530 nm and fluorescence intensity has a maximum at 556 nm.

After optical pumping, (CW or pulse) into the ground state of the molecule some excited states and photoproducts are created, then stimulated emissions from the excited states can be observed. Transient absorption spectrum consists of three contributions: Absorption of discrete UV-lights by the transient states, bleach of the ground state, of the original molecule, therefore a new molecule which is photoproduct produced according to the concentration of the original molecule and the photon-flux intensity of the optical pumping device.

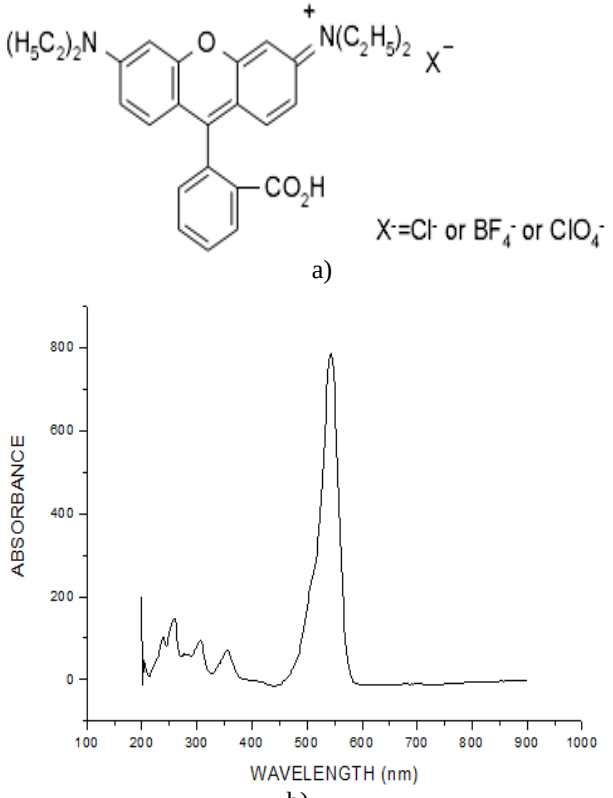

Fig. 1 a) chemical structure and b) absorption spectrum of rhodamine 610 in ethanol at room temperature.

Rodamin-610 is a spectroscopically pure chemical, which is the laser-dye therefore the transitions from S_1 to S_0 were the coherent emissions. Different contributions of the excited states often causes overlap with each other in

the emission spectrum, for large molecules like rodamin and its derivatives, electronic absorption and emission spectra is very complicated due to the overlaps of vibrational and rotational bands with the electronic bands. Figure 3, shows the FTIR spectrum of rodamin-610.

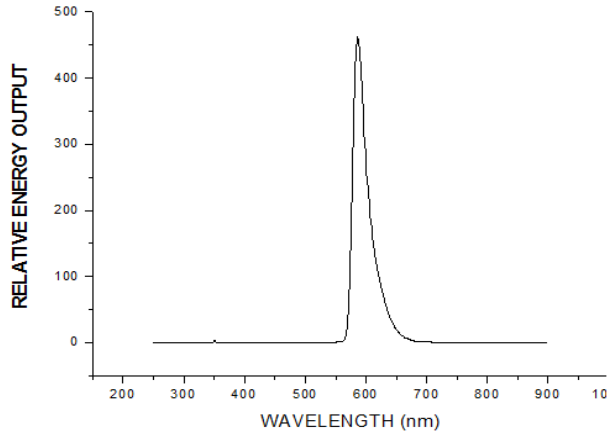

Fig. 2. Emission spectrum of rhodamine 610.

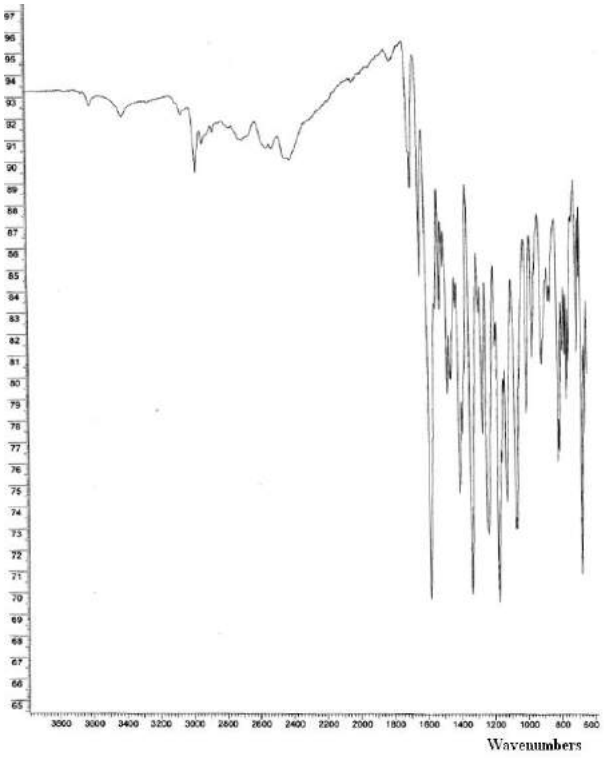

Fig. 3. FTIR spectrum of rodamin-610.

Therefore, it is rather difficult to discuss separately the intramolecular energy redistribution from the internal conversion to the first electronic excited state S_1, in the transient absorption spectrum. In contrast, a spontaneous emission measurement has advantage in studying the excited state dynamics, since only the excited state can be probed. By comparing the experimental results with a simple spectral calculation, Bayrakçeken and his co-workers suggested that the vibrational excitation relaxes very quickly, therefore in the nanosecond scale measurements either vibrational excitations and emissions can not be seen, because vibrational and rotational systems too-fast (ps or fs) [6]. These time scales are extraordinary short, and it is worthwhile investigating them further to clarify underlying physics of the ultra-fast relaxation. In this work we excite rodamin-610 laser-dye molecule by a low-pressure mercury CW-light source, to several excited states, "S_n". The fluorescence emissions of rodamin-610, and its photoproduct were observed with the transitions of $S_1 \rightarrow S_0$. Rodamin-610 in ethanol photolysed from 0 to10 hours at room temperature and after each optical pumping, absorption spectra were recorded, as it is seen in figure 4. The concentration of rodamin-610 was decreasing as the concentration of photoproduct increased.

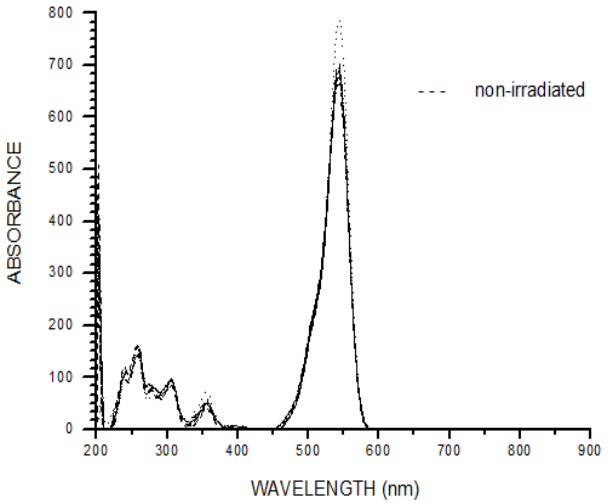

Fig.4. Photochemical change in rodamin-610 from 0 to10 hours at room temperature

Therefore after 10 hours photolysis, laser-dye rodamin-610 emitted two-different coherent fluorescence light due to the parent molecular emission and photoproduct emission. Figure 3, shows the absorption spectrum of rodamin-610, and its photoproducts. The optical excitation in the ultraviolet always produces an excess vibrational energy from the "0-0" band of the S_1 state, this effect causes the broadening in the emission lines or bands. The observed fluorescence signals are considered to originate from "S_1" state. The fluorescence band of the "$S_n \rightarrow S_0$" transition is expected to appear at shorter wavelengths then the region were we observed, since the oscillator strength of the absorption bands of the "$S_n \rightarrow S_0$" transition is estimated to be smaller than of the "$S_1 \rightarrow S_0$" transition. For a large molecule such as rodamin-610, the density of the vibronic state is too high to excite a particular vibrational state, because many vibronic levels are located within the bandwidth of the femtosecond pulse, the decrease amount of rodamin-610 concentration was not proportional with the increase of photoproduct concentration, therefore probably more than one photoproduct were created. There is also a blue-shift in the photoproduct absorption spectra. This phenomenon shows that there is more than one photoproduct. By optical pumping, (photolysis), we create a vibrational excess energy within the molecule therefore blue-shift could be observed in the absorption spectra of photoproducts produced. In solution the thermochromism has rarely been observed, probably because the NH form is too unstable to be populated in solution.

[1]. *S. M. Johnson, and L.G. Johnson*, J. Appl. Phys. 1986, 60, 2008-2015
[2]. *J.Wolfrum*, 1988. Appl. Phys. 1988, B46, 221-236
[3]. *Y. Yang, M. Wang, G. Qian, Z. Wang and X. Fan*, *Opt. Mater.2004*, 24, 621
[4]. *Bindhu C V, Harilal S S, Issac R C, V.P. Nampoori N and Vallabhan C P* G *Pramana J. Phys.1995*, 44, 225
[5]. *J H Brannon and D. Magde J. Phys. Chem.1978*, 82 705
[6]. *F. Bayrakceken*, Spectrochim. Acta Part A, 2004, 60, 923.

FEATURES OF CHARGE TRANSPORT IN SEMICONDUCTOR GAS DISCHARGE ELECTRONIC DEVICES

S. KARAKÖSE [1], M. SHİRİNOV [2], B.G. SALAMOV [1,2*]

[1] *Physics Department, Faculty of Arts and Sciences, Gazi University, Beşevler 06500 Ankara, Turkey*

[2] *National Academy of Science, Institute of Physics, AZ-1143 Baku, Azerbaijan*

** bala@gazi.edu.tr*

Experimental results with nonlinear features and hysteresis characteristics in the prebreakdown Townsend discharge regime is studied experimentally for a microstructure with a *GaAs* photocathode, an interelectrode gap thickness of 445 μm and gas pressure in the range 28-66 Torr. A linearly increasing voltage (i.e. 3 V s^{-1} and 5 V s^{-1} voltage rate) was applied to the system to study current instability. The nonlinear transport mechanism of carriers through the cross-section of the discharge gap i.e. the appearance of the spatio-temporal self organization of a nonlinear dissipative system, non-equilibrium electron motion and autocatalytic effect of carrier accumulation in the gas layer attributed to decrease of current with the increase of applied voltage. On the other hand, the oscillatory current and hysteresis peculiarities in postbreadown region are known to be related to a nonlinear mechanism of carrier transport in the semiconductor material caused by *EL2* defect centers.

I. INTRODUCTION

In this paper we have experimentally investigated the non-linear transport mechanism of carriers in semiconductor gas discharges (*SGD*) electronic devices. This is a sandwich-like microstructure that consists of a thin plane gas dischar-ge gap and a thin semiconductor cathode serving simultane-ously as a ballast resistance. This microstructure is the ba-sic element of an *IR*-to-visible image converter that has an ultrafast response in the *IR* range of light [1]. Recently, ne-gative differential resistance (*NDR*) phenomena have re-ceived a considerable attention due to undesirable electrical instabilities that affect adversely the operation of the devi-ces. Investigation of *NDR* peculiarities in the Townsend re-gime and/or semiconductor material are particularly impor-tant in relation to the application of system used, for i.e. *IR* converter. Interest in using a microdischarge in the Town-send regime in many industrial fields is partly due to fact that active gas discharge media are homogenous and expe-rimental conditions are optimizable and controllable. Ho-wever, among other interesting features of the Townsend discharge is its nonlinear dynamics and formation of spatio-temporal structures [2]. In particular, it has been found that the planar *SGD* microstructure represents an experimentally flexible electronic device in this article mainly the electrical peculiarity is studied. Application of high voltage to the electrodes across the gas layer induces conducing gas me-dia, which in return initiate an avalanche due to charge multiplication and eventually establishes a self-sustained discharge. Carrier transport in gas discharge is characteri-zed by nonlinear transport mechanism. The negative slope of Townsend discharge is related numerous factors, namely (1) to a decrease in the probability for the electrons to return to the cathode due to backscattering when increasing the discharge current [3], (2) to an autocatalytic effect of carrier accumulation in the interelectrode distance on the avalanche multiplication process. The loss of stability of the homogenous state may result in spatially homogenous or periodically spatial structure [4] and (3) non-equilibrium electron motion in a discharge gap [3]. In the gas discharge, most of the *NDR* has been report in molecular gas [5] and it is related to Ramsauer-Townsend minimum in the electron momentum-transfer cross section. Atomic and molecular gases are characterized to have one or more inelastic energy loss in the region of that minimum [6].

The falling characteristic of current–voltage in Townsend discharge onset instable discharge behavior. When the discharge current reaches certain threshold value I_{th} the spatially inhomogeneous self-sustained current oscillations are excited [7]. At higher current values lateral uniform discharges may appear which manifest themselves as the lateral constriction and the transition to the normal glow discharge [8]. Application of *SGD* in electronic devices is used for rapid visualization of electrical and structural defects in semiconductors [9] and fast sources of *UV* radiation with a large area of emitting surface and high spatial uniformity of *UV* radiation, which are controlled by *IR* light. Instability of the Townsend discharge, resulting in oscillations and the formation of the current filaments [10], hampers the operation of the device.

On the other side, the nonlinear *NDR* characteristic of the semi-insulated (*SI) GaAs* cathode is also investigated. The presence of the *NDR* in *SI GaAs* cathode is associated with instabilities of a homogeneous steady state produced by spatial fluctuations in the electric field or in the carrier density. The transport properties of a semiconductor device present instabilities such as current runaway, current oscillations, discontinuities in the current and/or voltage, switching and hysteretic current–voltage phenomena. Such instabilities are found in a wide variety of materials, temp-erature ranges and excitation conditions [11]. Therefore, the presence of *NDR* phenomena can be seen as the signature for intrinsic instability in semiconductor devices. In *SI GaAs*, the defect *EL2* [12] is the most important candidate for the role as the electron trap. There is considerable inte-rest in the properties of the *EL2* defect because *SI GaAs* has an increasing relevance, e.g. as a particle detector and for optical data storage [13]. It is vital to have *SI GaAs* of the best quality in order to improve the performance of the circuits where it is used. This requirement directly involves a thorough understanding of the defects (especially *EL2*) that cause *SI GaAs* to be insulating. Since the high electric-field domains in *SI GaAs* are caused by electron capture by *EL2* centers, the study of these domains is a natural way to investigate the properties of *EL2* [14]. In our previous study [15], we

found preliminary experimental results with *NDR* in the post-breakdown Townsend discharge regime for a planar microstructure with a *GaAs* photocathode. At the same time, we suppose the influence of the microstructure on the charge transport in *SGD* are attributed to the formation of non-equilibrium unstable current structures in the gas depending on the *d*, effective *D* parameters and emission properties of the semiconductor electrode surface. Therefore, in this work, we have systematically studied the effect of the voltage amplitude on the dynamics of transient processes and electrical instability in various region of Townsend discharge regime such as (i) pre-breakdown, (ii) breakdown and (iii) post-breakdown through dynamic of current and hysteresis behaviors.

II. EXPERIMENTAL

The experiments have been carried out on the system set-up shown schematically in Fig.1. The discharge light emission (*DLE*) intensity from the cell was detected by photomul-tiplier head (*ELSEC* 9010). The photomultiplier tube of the unit (*Thorn-EMI* 9235 QA) has a high sensitivity in the *UV*-blue region of the spectrum which coincides with the *DLE* from the cell. Electrical peripherals consist of a Digital Multimeter (Keithley 199) and a *DC* Power Supply (*Stanford PS* 323. 2500V). The electrical circuit is interfaced to PC by data acquisition card.

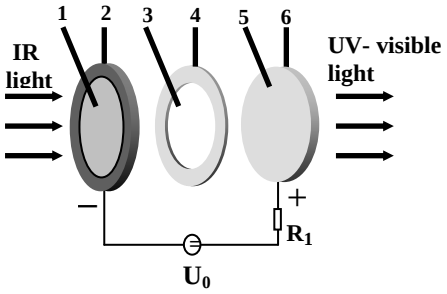

Fig.1. Scheme of the gas discharge cell; 1 – semi-transparent Au - contact; 2 - GaAs cathode; 3 - gas discharge gap; 4 – mica foil; 5 - transparent conductive SnO_2 contact; 6 - flat glass disk.

Fig.1 represents cathode plate (2) made of a *SI n*-type *GaAs* [16]. The *GaAs* crystal plates with a [100] surface was cut from single-crystal ingot grown by the liquid-encapsulated Czochralski method. The diameter and the thickness of the photocathode were 36 mm and 1.0 mm, respectively [17]. To realize the systems the external sur-face of each the photocathode (2) was covered with *Au* layer (1) of high conductivity, thickness of each contact is ≈ 40 nm thick. Therefore, it is transparent to *IR* light. Oppo-site the semiconductor layer, the anode is a glass plate (6) (with 30 mm diameter and 2 mm thickness) is covered with a transparent and conductive SnO_2 layer (5). The surface of the semiconductor cathode was separated from a flat anode by an insulating mica sheet (3) with a circular aperture at its centre (4), the internal diameter of which determined the active electrode diameter *D*. The SnO_2 and the *Au* electrode are connected to the external electric circuit, which consists of a dc high voltage supply and a series load resistor R_1 that is included to measure the current in the circuit. Data are given within the experimental control parameters, the mag-nitude of the feeding voltage U_0 and conductivity σ of the *GaAs* electrode. The initial low value of $\sigma_{sem} \approx 10^{-8}$ $(\Omega cm)^{-1}$ at room temperature of experiments (T~300 K) is determi-ned by doping *GaAs* with *Cr* impurity. The stability of the discharge is provided there by using a setup with a thin discharge gap [18]. As dependent on the feeding voltage, the device may be either in dielectric or conductive state. Conductive state is observed when feeding voltage is higher than breakdown point ($U_0 > U_B$).

The light of an incandescent halogen lamp with a Si-filter in front illuminates the cathode uniformly. The illumination intensity *L* is varied in the range 10^{-6}–10^{-2} Wcm^{-2} by the use of neutral density filters. The internal photoeffect mechanism in semiconductors is responsible for the broad range of the system sensitivity in the *IR* spectral range [16]. The discharge gap of the cell is filled with atmospheric room air. Air was studied due to its widespread application and availability. The breakdown voltage U_B is measured accurately to ± 3 and 5 V. When determining the breakdown voltage U_B, the growth rate of the discharge voltage does not exceed 1 V/s. The maximum sensitivity for the current axis was 10^{-9} A and for the voltage axis is around 0.5 V. Due to the internal photoeffect, the specific conductivity of the *GaAs* electrode can be manipulated by irradiating with the light. When the light is absorbed by the material of the semiconductor electrode, electrons from the valence band are excited into the conduction band. Hence, the specific conductivity is raised. Besides, the feeding voltage U_0 or the rate of feeding voltage can be changed easily in the experiments. Therefore, these two quantities are used as the main control parameters. Other parameters like gas pressure *p* and discharge gap thickness *d* remain fixed or changed discontinuously in a wide range. In a running experiment, the pressure *p* and the conductivity of the semiconductor cathode are fixed and the U_0 is slowly increased from 0 V thereby increasing the voltage drop at the gas layer. As soon as U_0 reaches the critical voltage for breakdown in the gas, homogeneous ignition of the discharge takes place. The value of the critical voltage is determined by the so-called Paschen curve [16].

III. RESULTS AND DISCUSSION

Experimental study of instable *CVC* in Townsend dis-charge regime is of practical importance due to undesirable electrical phenomena that hampers stable operation of the device. Theoretical analysis [3] and experimental findings exhibit that homogenous Townsend discharge mode can turn into non-homogenous oscillatory mode. Systematic investigation of current instability and falling behavior of *CVC* conducted for a wide range of gas pressure and applied voltage at different ramping voltage *k* per unit time. In the experiment, the feeding voltage U_0 applied to the system was gradually increased with time in two sets of increments 3 Vs^{-1} and 5 Vs^{-1}. The conductivity of semicon-ductor was rather low and the rate of charge separation in the semiconductor was substantially greater than the rate of the voltage growth. Therefore, until breakdown, the entire voltage U_0 was applied to the discharge gap. When U_0 became equal to

U_B, the discharge was ignited and a weak glow was observed with a current of a few μAcm^{-2}.

Figure 2a,b present detailed information about *CVC* of parallel-plane geometry with respect to pressure when a dc voltage of a high enough magnitude is applied to the system. The range of unstable operation depends on the gas pressure p (28–66 Torr) for active electrode diameter D = 22 m. It is clear that: (i) the negative slope of *CVC* exist for a wide pressure range. (ii) The amplitude of oscillation changes erratically with gas pressure. (iii) Maximum range of steady state current value is $1.75\text{x}10^{-8}$ A upon the application of voltage U_0= 0 which is nearly constant for all gas pressures, whereas the (iv) minimum current values at breakdown points U_B for 66 Torr are $2\text{x}10^{-10}$ A and $2.5\text{x}10^{-10}$ A respectively for ramping voltage k (3 Vs^{-1} and 5 Vs^{-1}) and (v) the negative slope of *CVC* behavior for k = 5 Vsec^{-1} is higher compared to k=3 Vs^{-1}.

Instability of the Townsend discharge which result in oscillations and the formation of the current filaments [19] that hinders the operation of the device. Therefore, analysis of such instability is of practical importance. Detailed ana-lytical study of spatial instability in Townsend discharge is given in [20]. In which the experimental result from micro-discharge systems showed instability of the normal glow discharge with several current filaments occur instead of a normal cathode spot [21]. The formation of the arranged current filaments in a dielectric barrier discharge was stu-died in [22] by direct numerical modeling and the deve-lopment of spatial–temporal instability for semiconductor–gas discharge system.

The negative slope of Townsend discharge attributed to the decrease in the probability of an electron to return to the cathode due to backscattering when increasing the dischar-ge current [3], and to autocatalytic effect of carrier accu-mulated in the interelectrode distance on the avalanche multiplication process.

The loss of stability of the homogenous state may result in spatially homogenous or periodically spatial structure [4] and non-equilibrium electron motion in a discharge gap [3]. In the gas discharge, most of the *NDR* has been report in molecular gas [5] and it is related to Ramsauer-Townsend minimum in the electron momentum-transfer cross section σ_m. Atomic and molecular gases own one or more inelastic energy loss in the region of that minimum [6]. The underly-ing theoretical works is that the *NDR* is connected with the growing dependence of the secondary electron emission (*SEE*) coefficient γ on the cathode electric field E_C and con-sequently on the discharge current density [23]. The mecha-nism of *SEE* is described by the Townsend condition [8];

$$\gamma(e^{\alpha d}-1)=1 \qquad (1)$$

Here γ, is the *SEE* coefficient describing the number of electrons (avalanches) that start from the cathode per in-cident ion, α is the first Townsend coefficient, d is the gap length, and the factor $(e^{\alpha d}-1)$ describes the number of ions produced in the avalanche initiated by one secondary electron.

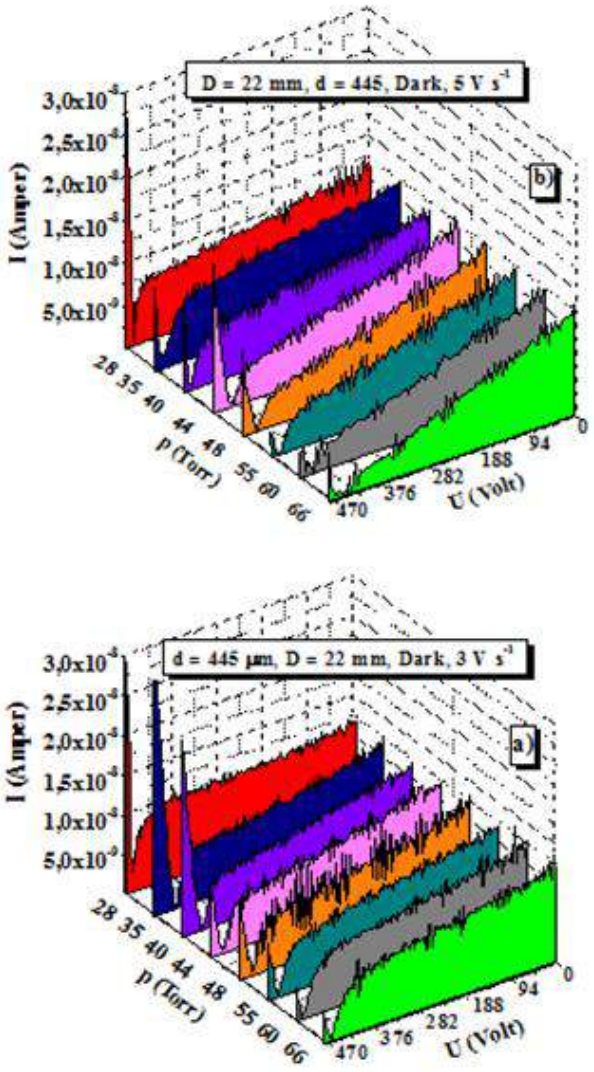

Fig.2. CVC of a planar discharge cell with respect to pressure **(a)** 3 Vs^{-1} rate of ramping applied voltage per unit time, (**b**) 5 Vs^{-1} rate of ramping applied voltage per unit time. System parameters; D = 22 mm, d = 445 µm and in darkness.

Thus $\gamma(e^{\alpha d}-1)$, the production shows the number of ions produced in the gap per one ion lost at the cathode. We consider Townsend discharges in the gaps with clean cathode surfaces, for pd ≈0.7–2.5 Torr cm and E_B/N ≈ 400–1000 Td ($E_B = U_B/d$ is the breakdown field and N is the density of the gas). Under these conditions, electrons are produced in the gas due to avalanche-like electron impact ionization and the *SEE* at the cathode is induced mainly by slow ions. The ion–electron emission is pronounced much more than that by photons [24]. Under the conditions consi-dered, the probability of ion-induced electron emission γ is approximately constant that corresponds to the potential ejection of electrons (ion energies are ε ~ 1 eV for E_B/N ~1000 Td). Note that at low E/N photons give a large cont-ribution to *SEE*, whereas at very high E/N bulk ionization and ejection of electrons from the cathode by fast positive ions are essential[24].Our suppositions concerning the emi-ssion process are not appropriate for the cases of discharges with a dirty cathode surface (for any pd and E_B/N) [24].

The considered conditions i.e. $pd \approx 0.7–2.5$ Torr cm, correspond to a region where the Paschen breakdown curve has the minimum. However, we do not think that there is any profound physical correlation between charge emission mechanism and the existence of the breakdown voltage minimum. Therefore, the contributions of various emission mechanisms depend on the values of E_B/N and pd but not on U_B. Thus, E_B/N and pd are related by the monotonic dependence. As the U_0 grows, the ion density grows too which in turn strengthens discharge process. The polarized opposite charge deposited on the electrodes as a result of discharge is relatively large enough to creates electric field across the gap which oppose the electric field driven by dc power source. Hence, the discharge process due to two opposite vector electric field disturb the current stability until the feeding voltage across the gap rises again, then the next discharge starts, and so on such fluctuation reflects in current oscillation. Fig.3 shows U_B and corresponding current value at breakdown point (I_B) measured from Fig.2a,b curves with *NDR*. The dependence of U_B on the rate k ramping of applied voltage is proportional $U_B = f(k)$. The U_B is characterized as the minimum point of *NDR* in Townsend regime with current value in order of 10^{-10} A. The high k value gives higher U_B. Due to statistical nature of generation and recombination of charge carrier in gas medium, the breakdown may not occur even if the applied voltage exceeds a certain threshold point $U_0 > U_B$.

Also, the appearance of initial electron does not necessarily initiate breakdown event. The probability of breakdown depend on several factors of discharge cell such as, gas purity, gas pressure, cathode material, volume of cell, electric field, and Townsend coefficients [25]. Due to linear ramp, k is in fact the ratio between the voltage step and the time interval between successive steps. The voltage step was 1 V, 3 V and 5 V, while the time interval was varied from 0.01 to 1 s. Our experimental result is in agreement with the theoretical and experimental result obtained by independent author [25]. However, the statistical and formative time lag is not studied due to large time interval between applications of successive voltage.

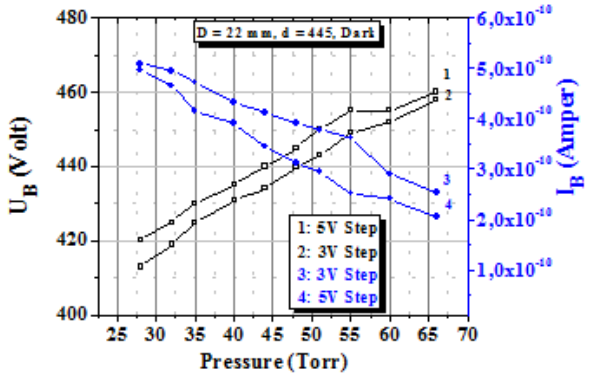

Fig.3. Dependence of U_B and minimum current I_B on ramping voltage k (3 V s^{-1} and 5 V s^{-1}) for different gas pressures. System parameters: D = 22 mm, d = 445 μm and in darkness.

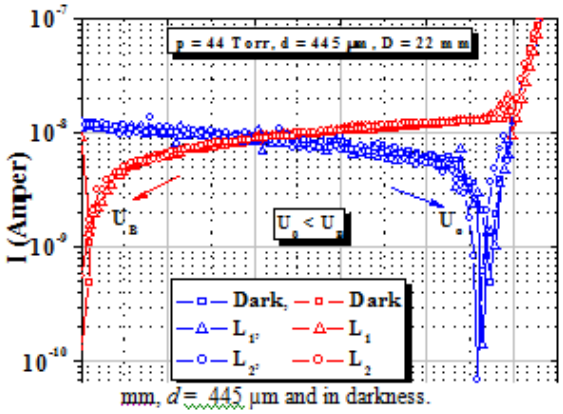

Fig.4. CVC with hysteresis behavior for discharge cell with GaAs cathode; blue (black) and red (grey) colour curves refer to forward increment and reverse decrement of U_0 on the *SGD* whilst the *GaAs* cathode is exposed to strong and weak illumination intensity and in darkness, respectively. System parameters d = 445 μm, D = 22 mm, p = 44 Torr.

Hysteresis peculiarities of *CVC* in Townsend discharge regime is presented in Fig.4 for pre-breakdown region ($U_0 < U_B$). The curves indicate non-equilibrium processes (i.e carrier loss and produce) that occur during forward incre-ment and reverse decrement of dc applied voltage across gap. During forward power increment across the discharge gap *NDR* behaviour is observed while in power decrement mode *NDR* phenomena do not take place. One possible reason can be attributed to the pre-formed active charged particles in the cell which inhibits *NDR* effect to occur. Moreover, Fig.3 show the U_B is lower when the cell is illu-minated by *IR* light. The latter is in accordance with an earlier result that had shown that additional ionization in interelectrode space decreases the U_B [26]. As a rule, a de-crease of the resistivity of the semiconductor cathode due to illumination is found to decrease the voltage range characterizing the U_B. In contrary, whilst decreasing of applied *dc* voltage across gap *NDR* behavior not observed. From Fig.3 the breakdown voltages for forward voltage increment at different illumination intensities L_2, L_1 and darkness are 460, 465 and 475 V, respectively.

IV. CONCLUSION

Nonlinear electrical phenomena in a planar dc-driven *SGD* microstructure with *SI GaAs* photodetectors is studied ex-perimentally. The results demonstrate that the nonlinearity of the electrical conduction process is accompanied in *SI GaAs* photodetectors by the formation of high-contrast, spatially non-uniform distributions of the current through gas discharge medium at $U_0 < U_B$. Experimental conditions led to the existence of the *NDR* in prebreakdown region with oscillatory non-monotonic steady state current in Townsend discharge regime. Based on numerous theoretic-cal and experimental studies [3-6] the *CVC* exhibits nega-tive slope by linearly increasing applied voltage. Our expe-rimental study for ramping voltage of k=3 V s^{-1} and 5 V s^{-1} show same effect but less pronounced effect for k = 3 V s^{-1} versus k = 5 V s^{-1}. It is shown, negative slope and steady state current at U_B point for smaller k is greater compared with higher k. In

contrary breakdown voltage U_B of lower k is smaller compared to higher k [25]. For all experimental conditions the current density increases over the entire range of voltages $U > U_B$ as the D increases. It is shown that when the system is driven with a stationary voltage, it generates current instabilities with different amplitudes of oscillation. We suppose that the peculiarities of the current passage are attributed to the formation of non-equilibrium unstable current structures in the gas depending on the d, effective D parameters and emission properties of the semi-conductor electrode surface. On the other side, the hystere-sis peculiarity in the post-breakdown region is based on the mechanism of electron trap and release from *EL2* deep cen-tre defects in bulk semiconductor material [27]. The micro-scopic structure of *EL2* is still a controversial subject; it is accepted that its core is an arsenic antisite (*AsGa*) [28] acting as a double donor, it has three charge states $EL2^0$, $EL2^+$ and $EL2^{++}$ which introduce two ionization levels in the band gap (Ev +0.75 eV for 0/+ and Ev + 0.54 eV for +/++). Its neutral charge state has an excited state, $EL2^0$, which is metastable and optically and electrically inactive at low temperatures [29].

V. ACKNOWLEDGMENT

This work is supported by the Gazi University BAP research projects 5/2009-44.

[1]. *B.G. Salamov, C.Y. Oztekin, K. Colakoglu* 2004 IEEE Trans. Plasma Sci. (Part 2*)* 32 2093

[2]. *H. Kurt, B.G. Salamov* 2008 Acta Phys. Polonica 114 4

[3]. *M.S. Mokrov, Y.P. Raizer*, 2008 Plasma Sources Sci & Technol .17 035031.

[4]. *Y.A. Astrov*, 2003 IEEE Computer Society 3 883-894.

[5]. *W.H. Long, Jr, W.F. Bailey, A. Garscadden* 1976 Phys. Rev. A 13 471.

[6]. *Z.L.Petrovic, R.W.Crompton, G.N.Haddad*, 1984 Aust. J. Phys. 37 23-34.

[7]. *C.Strumpel, Y.A.Astrov, H.G. Purwins* 2000 Phys.Rev. E 62 4889.

[8]. *Y.P.Raizer* 1991 Gas Discharge Physics (Berlin: Springer) p 449.

[9]. *A.K.Zeinally, N.N.Lebedeva, L.G.Paritskii, B.G.Sala- mov* 1991 J. Photogr. Sci. 39 114.

[10]. *E. Ammelt, Y.A. Astrov, H-G. Purwins* 1998 Phys. Rev. E 58 7109.

[11]. *M.P.Shaw, V.V.Mitin, E.Scholl, H.L.Grubin*, 1992 The Physics of Instabilities in Solid State Electron Devices (New York: Plenum)

[12]. *A. Neumann* 2001 J. Appl. Phys. 90 1.

[13]. *V.Alex, J.Weber* 1998 Appl. Phys. Lett. 72 1820. [14].H.Y.Kurt, Y.Sadiq and B.G.Salamov 2008 Phys.Status Solidi A 205 321.

[14]. *B.G Salamov and H Y Kurt* 2005 J.Phys.D:Appl.Phys. 38 1–6

[15]. *B.G. Salamov, A.A. Agasiev, N.N. Lebedeva, V.I. Or-bukh, H. Kurt, K. Colakoglu* 2002 J.Phys.D:Appl. Phys. 35 716.

[16]. *N.N. Lebedeva, V.I. Orbukh, B.G. Salamov* 1996 J. Phys. III France 6 797.

[17]. *B.G. Salamov, S. Altındal, M. Özer, K. Colakoglu, E. Bulur* 1998 Eur. Phys. J. AP 2 267.

[18]. *E. Ammelt, Y.A. Astrov and H.G. Purwins* 1998 Phys. Rev. E 58 7109.

[19]. *A.A. Kudryavtsev, L.D. Tsendin* 2002 Tech. Phys. Lett. 28 1036.

[20]. *K.H. Schoenbach, M. Moselhy*, ShiW 2004 Plasma Sources Sci. & Technol. 13 177.

[21]. *L. Stollenwerk, S. Amiranashvili, J.P. Boeuf, H.G. Purwins* 2006 Phys. Rev. Lett. 96 255001.

[22]. *A.A. Kudryavtsev, L.D. Tsendin* 2002 Tech. Phys. Lett. 28 1036.

[23]. *A.V. Phelps, Z. L. Petrovic* 1999 Plasma SourcesSci. & Technol. 8 R21.

[24]. *M.M. Pejovic, C. Milosavljevic and Pejovic Momcilo* M 2003 Rev. Sci. Instruments 74 6.

[25]. *R. Filipovic* 1987 MSc Thesis Faculty of Electronic Engineering, University of Nis, Yugoslavia

[26]. *B.G. Salamov, N.N. Lebedeva, H.Y. Kurt, V.I.Orbukh, E.Y. Bobrova* 2006 J. Phys. D:Appl. Phys. 39 2732.

[27]. *J.M. Spaeth, K. Krambrock* 1993 Festkorper probleme 33 111.

[28]. *M.Pinheiro,K.Krambrock* 1999 Brazilian J.Phys. 29 4

TEMPERATURE DEPENDENT DIELECTRIC PROPERTIES OF SCHOTTKY DIODES WITH ORGANIC INTERFACIAL LAYER

İLBİLGE DÖKME[a], TUNCAY TUNÇ[b], ŞEMSETTİN ALTINDAL[c]

[a]*Science Education Department, Faculty of Gazi Education, Gazi University, Ankara, TURKEY*

[b]*Science Education Department, Faculty of Education, Aksaray University, Aksaray, TURKEY*

[c]*Physics Department, Faculty of Arts and Sciences, Gazi University, Ankara, TURKEY*

The dielectric properties of Au/PVA(Co,Ni-doped)/n-Si Schottky diodes (SDs) have been studied in the temperature range of 80-400 K. Investigating various SDs fabricated with different type interfacial layer is important for understanding of the dielectric properties of SDs. Therefore, in this study polyvinyl alcohol (PVA) film was used as an interfacial layer between metal and semiconductor. The interfacial polymeric layer thickness between metal and semiconductor was calculated from the measurement of the oxide capacitance in the strong accumulation region. The dielectric properties of Au/PVA(Co,Ni-Doped)/n-Si SDs were calculated from capacitance-voltage (*C–V*) and conductance-voltage (*G–V*) measurements. The dielectric constant (ε'), dielectric loss (ε''), dielectric loss tangent (tan δ) and the ac electrical conductivity (σ_{ac}) obtained from the measured capacitance and conductance are studied for Au/PVA(Co,Ni-Doped)/n-Si SDs. Experimental results show that the values of ε', ε'' and tanδ were found a function of temperature. The ac electrical conductivity (σ_{ac}) of Au/ PVA(Co,Ni-Doped)/n-Si SDs is found to increase with temperature.

I. INTRODUCTION

In recent years, considerable attention was given the fabrication and electrical characterization of organic semiconductor devices due to their unusual electrical and optical properties and their ease of fabrication and processing. Particularly conducting polymers have generated a great interest owing to most attention for possible application in molecular electronic devices because of their unique properties and versatility [1-4]. Among the various conducting polymers, poly (vinyl alcohol) which is a water-soluble polymer produced industrially by hydrolysis of poly (vinyl acetate) became an attractive research topic due to their potential applications and interesting properties by chemists, physicists and electrical engineers alike)[5-7]. PVA has been used in fiber and film products for many years. It has also a widespread use as a paper coating, adhesives and colloid stabilizer. Recently, metal/organic semiconductor Schottky diodes became interesting as an alternate to the metal/inorganic semiconductor junction because investigating various Schottky diodes fabricated with different type interfacial layer is important for understanding of the electrical and dielectric properties of Schottky contacts [8-10].

In this study polyvinyl alcohol (PVA) film was used as an interfacial layer between metal and semiconductor. PVA doped different ratio of Cobalt and Nickel was produced and PVA /(Co, Ni) nanofiber film on n-type silicon semiconductor were fabricated by the use of electrospinning technique.

Electrospinning process utilizes electrical force to produce polymer fibers. However, the main aim of this study is to try to determine the temperature dependent electric and dielectric properties of Au/PVA(Co, Ni-Doped)/n-Si structures and the variation of dielectric constant (ε'), dielectric loss (ε''), loss tangent (tanδ) and ac electrical conductivity (σ_{ac}) have been investigated as a function of temperature and voltage.

II. EXPERIMENTAL PROCEDURE

The Au/PVA (Co,Ni-doped)n-Si SDs were fabricated on the 2 inch (5.08 cm) diameter flot zone (111) n-type (phosphor doped) single crystal Si wafer having thickness of 350 μm with ≅ 0.7 Ωcm. Si wafer first was cleaned in a mix of a peroxide- ammoniac solution and then in H_2O+ HCl solution in 10 minute. After it was thoroughly rinsed in deionised water resistivity of 18 MΩcm using an ultrasonic bath for 15 min, immediately high purity Au metal (999.999 %) with a thickness of about 2000 Å was thermally evaporated onto the whole back side of Si wafer in the a pressure about 10^{-6} Torr in high vacuum system. In order to perform a low resistivity ohmic back contact, Si wafer was sintered at 450 °C for 5 min in N_2 atmosphere. The PVA film was fabricated on n-type Si by electrospinning technique. A simple illustration of the electrospinning system is given in Fig. 1. 0.5 g of cobalt acetate and 0.25 g of nicel acetate was mixed with 1g of polyvinyl Alcohol (PVA), molecular weight=72 000 and 9 ml of deionised water. After vigorous stirring for 2 h at 50 °C, a viscous solution of PVA/(Co, Ni) acetates was obtained. Using a peristaltic syringe pump, the precursor solution was delivered to a metal needle syringe (10 ml) with an inner diameter of 0.9 mm at a constant flow rate of 0.02 ml/h. The needle was connected to a high voltage power supply and positioned vertically on a clamp. A piece of flat aluminum foil was placed 15 cm below the tip of the needle to collect the nanofibers. Si wafer was placed on the aluminum foil. Upon applying a high voltage of 20 kV on the needle, a fluid jet was ejected from the tip. The solvent evaporated and a charged fiber was deposited onto the Si wafer as a nonwoven mat. After spinning process, circular dots of 1 mm in diameter and 1500 Å thick high purity Au rectifying contacts were deposited on the PVA surface of the wafer through a metal shadow mask in liquid nitrogen traped oil-free ultra high vacuum system in the pressure of about 10^{-7} Torr.

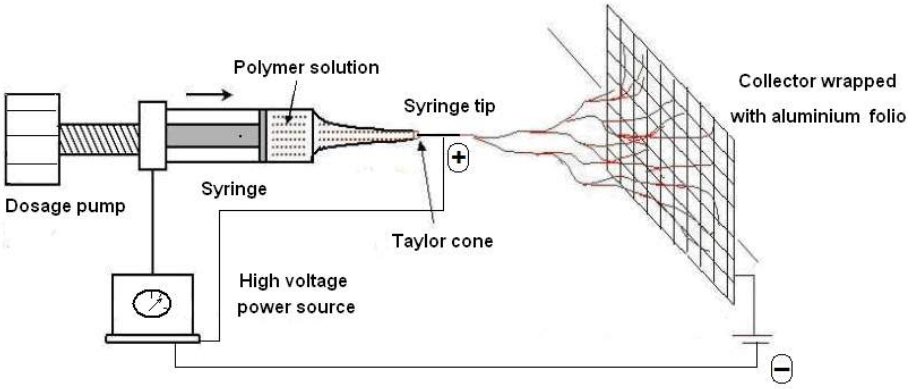

Fig. 1. Schematic representation of the electrospinning process.

The *C-V* and *G/ω-V* measurements were performed in the temperature range of 80-400K at 1 MHz by using a HP 4192A LF impedance analyzer and small sinusoidal test signal of 20 $mV_{p-p.}$ from the external pulse generator is applied to the sample in order to meet the requirement. The sample temperature was always monitored by using temperature-controlled Janes vpf-475 cryostat, which enables us to make measurements in the temperature range of 77-450 K. All measurements were carried out with the help of a microcomputer through an IEEE-488 ac/dc converter card.

III. RESULT AND DISCUSSION

The dielectric constant (ε'), dielectric loss (ε''), loss tangent (tanδ), ac electrical conductivity (σ_{ac}) and electric modulus were evaluated from the knowledge of capacitance and conductance measurements for Au/PVA (Co,Ni-doped)n-Si SD in the temperature range of 80-400 K. The complex permittivity can be written [11] as

$$\varepsilon^* = \varepsilon' - i\varepsilon'' \tag{1}$$

where ε' and ε'' are the real and imaginary of complex permittivity of the dielectric constant, and i is the imaginary root of $\sqrt{-1}$. The complex permittivity formalism has been employed to describe the electrical and dielectric properties. In the ε^* formalism, in the case of admittance Y^* measurements, the following relation holds

$$\varepsilon^* = \frac{Y^*}{j\omega C_o} = \frac{C}{C_o} - i\frac{G}{\omega C_{o_i}} \tag{2}$$

where, C and G are the measured capacitance and conductance of the device, ω is the angular frequency ($\omega=2\pi f$) of the applied electric field [11]. The real part of the complex permittivity, the dielectric constant (ε'), at the various temperatures is calculated using the measured capacitance values at the strong accumulation region from the relation [12],

$$\varepsilon' = \frac{C}{C_o} = \frac{C\, d_i}{\varepsilon_o A} \tag{3}$$

where $C_o = \varepsilon_o A/d_i$ is capacitance of an empty capacitor, A is the rectifier contact area of the structure in cm^{-2}, d_i is the interfacial layer thickness and ε_o is the electric permittivity of free space (ε_o = 8.85x10^{-14} F/cm). In the strong accumulation region, the maximal capacitance of the structure corresponds to the insulator capacitance ($C_{ac} = C_i = \varepsilon'\varepsilon_o A/d_i$). The imaginary part of the complex permittivity, the dielectric loss (ε''), at the various frequencies is calculated using the measured conductance values from the relation,

$$\varepsilon'' = \frac{G}{\omega C_o} = \frac{G d_i}{\varepsilon_o \omega A} \tag{4}$$

The loss tangent (tanδ) can be expressed as follows [11,12],

$$\tan\delta = \frac{\varepsilon''}{\varepsilon'} \tag{5}$$

The ac electrical conductivity (σ_{ac})) of the dielectric material can be given by the following equation [12],

$$\sigma_{ac} = \omega C \tan\delta (d/A) = \varepsilon'' \omega \varepsilon_o \tag{6}$$

The complex impedance (Z^*) and complex electric modulus (M^*) formalisms were discussed by various authors with regard to the analysis of dielectric materials [13]. Analysis of the complex permittivity (ε^*) data in the Z^* formalism ($Z^*=1/Y^*=1/i\omega C_o\varepsilon^*$) is commonly used to separate the bulk and the surface phenomena and to determine the bulk dc conductivity of the material [14]. Many authors prefer to describe the dielectric properties of these devices by using the electric modulus formalize [15]. The complex impedance or the complex permittivity ($\varepsilon^*=1/M^*$) data are transformed into the M^* formalism using the following relation [13,14]

$$M^* = i\omega C_o Z^* \tag{7}$$

Or

$$M^* = \frac{1}{\varepsilon^*} = M' + jM'' = \frac{\varepsilon'}{\varepsilon'^2 + \varepsilon''^2} + j\frac{\varepsilon''}{\varepsilon'^2 + \varepsilon''^2} \tag{8}$$

The real component $M^{'}$ and the imaginary component $M^{''}$ are calculated from ε' and ε".

As can be seen from Fig. 2, ε' and ε'' increase as the temperature is increased. As the temperature rises, imperfections/disorders are occurred in the lattice and the mobility of the majority charge carriers (ions and electrons) increases. The combined effect gives rise to a rise in the values of ε' and ε'' with rising temperature. This may be possible due to both the ion jump and the orientation and space charge effect resulting from the increased concentrations of the charge carriers[16,17]. Furthermore, the increase in temperature induced an expansion of molecules which causes some increase in the electronic polarization and hence an increase in the ε' and ε'' of the dielectric material [16-19].

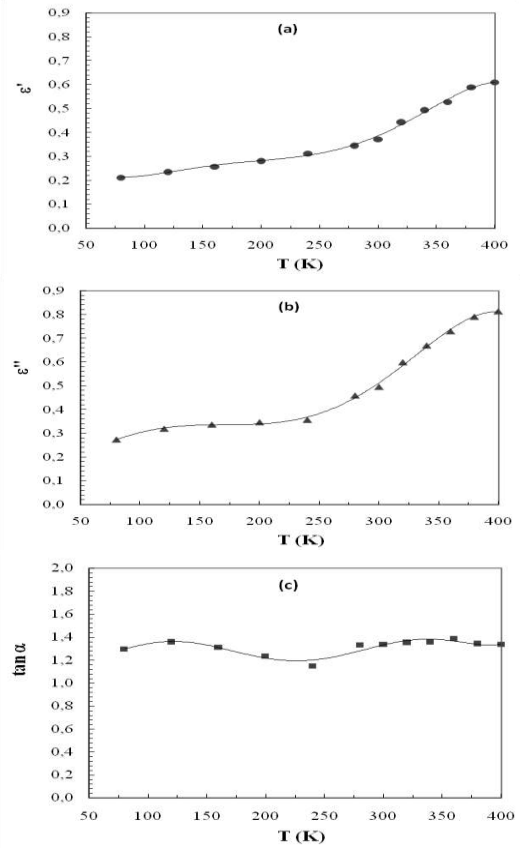

Fig. 2. Temperature dependence of the (a) ε', (b) ε'' and (c) tanδ of Au/ PVA(Co, Ni-doped)/n-Si structure

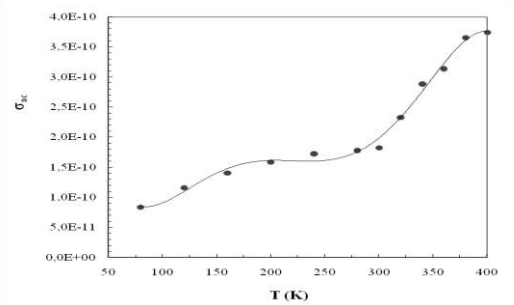

Fig. 3. Temperature dependence of ac electrical conductivity (σ_{ac}) of Au/ PVA(Co, Ni-doped)/n-Si structure.

The variation of the ε', ε'' and tan δ with temperature is a general trend in ionic solids. It may be due to space charge polarization caused by impurities or interstitials in semiconductor and polymeric interfacial layer. Furthermore in narrow band semiconductors, the charge carriers are not free to move but are trapped causing a polarization. By increasing temperature, the number of charge carriers increases exponentially and thus produces further space charge polarization and hence leads to a rapid increase in the dielectric constant ε' [18]. Fig. 3 shows the temperature dependence of the ac electrical conductivity measured at a constant frequency of 1 MHz. It is clear that the conductivity increases with temperature. Similar results have been reported in the literature [16,18,21, it is suggested that the process of dielectric polarization in Au/PVA (Co,Ni-doped)n-Si SDs structure takes place through a mechanism similar to the conduction process. The increase in the electrical conductivity at low temperature is attributed to the impurities, which reside at the grain boundaries [12, 17, 22]. These impurities lie below the bottom of the conduction band and thus it has small activation energy. This means that the contribution to the conduction mechanism comes from the grain boundaries while it mainly results from the grains for higher temperature. The real component $M^{'}$ and the imaginary component $M^{''}$ are calculated from ε' and ε''. Fig 4(a) and (b) depict the real part of M' and the imaginary part of M'' of electric modulus M^{*} versus temperature. As can be seen in Fig 4 (a) and (b) $M^{'}$ and $M^{''}$ decrease with increasing temperature.

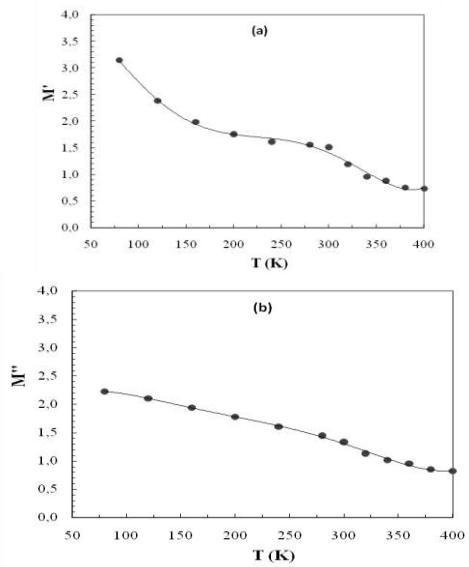

Fig. 4. (a) The real part $M^{'}$ and (b) the imaginary part $M^{''}$of electric modulus M^{*} vs temperature for Au/ PVA(Co, Ni-doped)/n-Si structure.

IV. CONCLUSION

In this study, we were used PVA material in replacing SiO_2 as interfacial layer at metal semiconductor interface due to its easy processing, cost and high dielectric constant. Dielectric properties of Au/PVA(Co, Ni-Doped)/n-Si SD have been reported in detail from *C-V* and *G/w-V* measurements in the temperature range of 80-400 K at 1 MHz. The analysis of experimental dielectric characteristics of Au/ PVA(Co,Ni-Doped)/n-Si SD have shown that the values of real part of dielectric constant (ε'), dielectric loss (ε''), loss tangent (tan δ) and the ac conductivity (σ_{ac}) of Au/PVA(Co,Ni-Doped)/n-Si SD depends on the temperature. The behavior of dielectric properties especially depends on polymeric interfacial

layer, the density of space charges, and temperature. Therefore, it can be concluded that the accuracy and reliability of semiconductor devices with Schottky contact depend on the type and thickness of interfacial layer, fixed surface charge.

[1]. *R.K. Gupta, R.A. Singh*, Materials Chemistry and Physics, 86, 279–283 (2004).

[2]. *V.C. Nguyen, K. Potje-Kamloth*, Thin Solid Films, 338, 142-148 (1999).

[3]. *Li-Ming Huang, Ten-Chin Wen, A. Gopalan*, Thin Solid Films, 473, 300– 307 (2005).

[4]. *Ş. Aydoğan, M.Sağlam, A.Türüt*, Polymer, 46, 563-568 (2005).

[5]. *N. Bouropoulos, G. C. Psarras, N. Moustakas, A. Chrissanthopoulos, and S. Baskoutas*, Phys. Stat. Sol. (a), 205, 2033–2037 (2008).

[6]. *S. M. Pawde, Kalim Deshmukh, Sanmesh Parab*, Journal of Applied Polymer Science, 109, 1328–1337 (2008).

[7]. *A. H. Salama, M. Dawy, and A. M. A. Nada*, Polymer–Plastics Technology And Engineering, 43, 1067–1083 (2004).

[8]. *İ. Dökme, I.M. Afandiyeva, Ş.Altındal*," Semıconductor Scıence and Technology, 23 (3), Article Number: 035003 (2008).

[9]. İ. *Dökme* Physica B: Condensed Matter, 388, 10-15 (2007).

[10]. *İ. Dökme and Ş. Altındal*, Semıconductor Scıence and Technology, 21 (8), 1053-1058 (2006).

[11]. *M.S. Mattsson, G.A Niklasson, K. Forsgren, and A. Harsta*, J. Appl. Phys. 85(4) 2185-2291 (1999).

[12]. *I.M. Afandiyeva, İ. Dökme, Ş.Altındal, M.M. Bülbül, A. Tataroğlu* , "Microelectronic Engineering, 85 (2) 247-252 (2008) .

[13]. *P. Pissis and A. Kyritsis*, Solid State Ionics, 97, 105-110 (1997).

[14]. *K. Prabakar, S.K. Narayandass and D. Mangalaraj*, Phys. Stat. Sol. A, 199 (3), 507-511 (2003).

[15]. *M.D. Migahed, M. Ishra, T. Famy, A. Barakat*, Jour. of Phys. And Chems. of Solid., 65, 1121-11-29 (2004).

[16]. *D. Maurya, J. Kumar and Shripal*, J. Phys. Chem. Solids, 66, 1614-620 (2005).

[17]. *İ. Dökme and Ş. Altındal*, Physica B: Condensed Matter, 391, 59-64 (2007).

[18]. *M.R. Ranga Raju, R.N.P. Choudhary and S. Ram*, Phys. Stat. Sol. B, 239, (2) 480- 490 (2003).

[19]. *İ. Dökme and Ş. Altındal*, " Physica B: Condensed Matter, 393 (1-2), 328-335 (2007).

[20]. *M.S. Mattsson, G.A. Niklasson, K. Forsgren and A. Harsta*, J. Appl. Phys,. 85 (4), 2185-2191 (1999)

[21]. *K. Prabakar, S.K. Narayandass and D. Mangalaraj*, Phys. Status Solidi A, 199, (3), 507-512 (2003).

[22]. *A.A. Sattar and S.A. Rahman*, Phys. Status Solidi A, 200 (2), 415-420 (2003).

TUNING OPTICAL ABSORPTION EDGE BY COMPOSITION AND TEMPERATURE IN $TlGa_xIn_{1-x}S_2$ LAYERED MIXED CRYSTALS ($0 \le x \le 1$)

K. GOKSEN[1], N. HASANLI[2], H. OZKAN[2]
[1]*Department of Physics, Yuzuncu Yil University, 65080 Van, Turkey*
[2]*Physics Department, Middle East Technical University, 06531 Ankara, Turkey*

The transmission and reflection measurements were carried out on $TlGa_xIn_{1-x}S_2$ mixed crystals ($0 \le x \le 1$) in the wavelength range of 400–1100 nm. The optical indirect band gap energies were determined through the analysis of the absorption data. It was found that the energy band gaps increase with increasing of gallium atoms content in the $TlGa_xIn_{1-x}S_2$ mixed crystals. The transmission measurements, accomplished in the temperature range of 10–300 K, revealed the rate of change of the indirect band gap with temperature for the different compositions of mixed crystals studied.

I. INTRODUCTION

$TlInS_2$ and $TlGaS_2$ compounds belong to the group of semiconductors with layered structure [1,2]. The lattice structure of these crystals is composed of rigorously periodic two dimensional layers arranged parallel to the (001) plane and each such consecutive layer is rotated by a right angle with respect to the previous one. Tl and S atoms are bonded to form interlayer bonds whereas In(Ga) and S atoms are bonded to form intralayer bonds. The Tl atoms are located in trigonal prismatic voids resulting from the combination of the $In_4(Ga_4)S_6$ polyhedra into a layer.

Optical and photoelectrical properties of $TlInS_2$ and $TlGaS_2$ crystals were studied in Refs. [3–11]. A high photosensitivity in the visible range of spectra, high birefringence in conjunction with a wide transparency range of 0.5–14 μm make this crystal useful for optoelectronic applications [12].

The compounds $TlInS_2$ and $TlGaS_2$ form a series of $TlGa_xIn_{1-x}S_2$ ($0 \le x \le 1$) mixed crystals. Previously, the structural and optical properties of the $TlGa_xIn_{1-x}S_2$ mixed crystals were investigated by X-ray diffraction [13], infrared reflection [14,15], Raman [15–17] and Brillouin [18] spectroscopy.

Recently, we studied the effect of isomorphic atom substitution on the optical absorption edge of the $TlGa_{1-x}In_xSe_2$ mixed crystals [19]. A structural phase transition (monoclinic to tetragonal) due to substitution of cation (indium for gallium) was revealed in the composition range of $0.50 \le x \le 0.75$. From the transmission and reflection measurements, the compositional dependence of the indirect band gap energy was established. The band gap energy was shown to drastically decrease from 1.89 eV ($x = 0.50$) to 0.94 eV ($x = 0.75$) in the region of the structural phase transition.

The aim of the present paper was to study the effect of the isomorphic cation substitution (indium by gallium) and the temperature on the absorption edge of $TlGa_xIn_{1-x}S_2$ mixed crystals through the transmission and reflection measurements in the wavelength range of 400–1100 nm and in the temperature range of 10–300 K.

II. EXPERIMENTAL DETAILS

Single crystals of the $TlGa_xIn_{1-x}S_2$ ($0 \le x \le 1$) mixed crystals were grown by the Bridgman method. The chemical composition of the $TlGa_xIn_{1-x}S_2$ mixed crystals were determined by the energy dispersive spectroscopic analysis using JSM-6400 electron microscope. The atomic composition ratio of the studied samples were estimated as 25.6 : 25.2 : 49.2 ($x = 0$), 25.8 : 6.6 : 19.2 : 48.4 ($x = 0.25$), 25.9 : 13.0 : 13.1 : 48.0 ($x = 0.50$), 26.1 : 19.0 : 6.1 : 48.8 ($x = 0.75$), 25.4 : 25.6 : 49.0 ($x = 1$). The freshly cleaved platelets (along the layer plane (001)) were mirror-like. That is why no further polishing and cleaning treatments were required.

The transmission and reflection measurements were carried out in the 400–1100 nm wavelength regions with a "Shimadzu" UV-1201 model spectrophotometer. The transmission measurements were done under the normal incidence of light with the polarization in the (001) plane, which is perpendicular to the ***c***-axis of the crystal. For the room temperature reflection experiments, the specular reflectance measurement attachment with 5° incident angle was used. An "Advanced Research Systems, Model CSW-202" closed-cycle helium cryostat was utilized to cool the sample from room temperature down to 10 K.

III. RESULTS AND DISCUSSION

The transmittance (T) and the reflectivity (R) spectra of the $TlGa_xIn_{1-x}S_2$ mixed crystals were registered in the wavelength range from 400 to 1100 nm in the temperature range 10–300 K. The absorption coefficient α was calculated using the following relation [20]

$$\alpha = \frac{1}{d}\ln\left[\frac{(1-R)^2 + \sqrt{(1-R)^4 + 4R^2T^2}}{2T}\right], \quad (1)$$

where d is the sample thickness.

The reflection measurements were carried out using the specimens with natural cleavage planes and the thickness such that $\alpha d >> 1$. The sample thickness was then reduced (by repeated cleaving using the transparent adhesive tape) until it was convenient for measuring the transmission spectra in the temperature range of 10–300 K. The thick samples with $d \approx 300$ μm were used in the experiments since the thin layered samples broke into the pieces at low temperatures due to their high

fragility. Therefore, we were only able to analyze the temperature dependence of the indirect band gap energy (E_{gi}). Technical reasons did not allow us a direct measurement of the reflectivity spectra at low temperatures. The point is that we utilized the specular reflectance attachment for "Shimadzu" UV−1201 model spectrophotometer, which is not adapted for the low-temperature reflection measurements by using closed-cycle helium cryostat. Therefore, for the calculation of absorption coefficient α at low temperatures, the spectral dependence of the room temperature reflectivity was uniformly shifted in the energy according to the blue shift of the absorption edge.

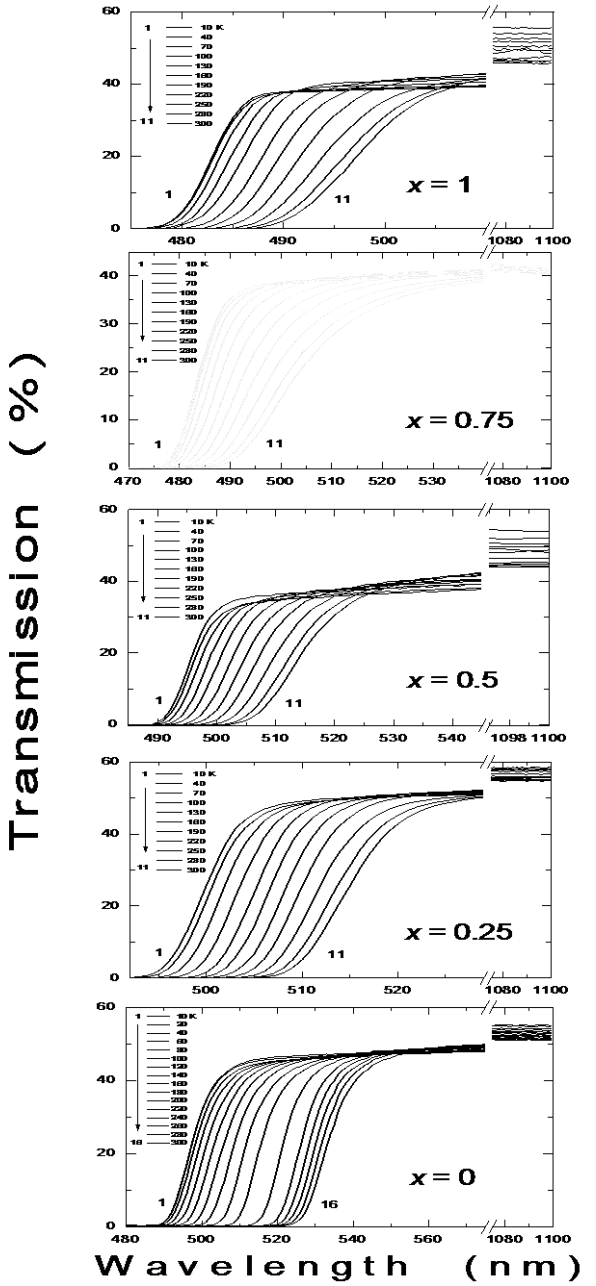

Fig.1. The spectral dependencies of transmission for $TlGa_xIn_{1-x}S_2$ mixed crystals in the temperature range of 10-300 K.

Figure 1 shows the transmission spectra of the $TlGa_xIn_{1-x}S_2$ mixed crystals that were registered in the temperature range of 10–300 K. Figure 2 presents the dependencies of absorption coefficient on photon energy at different temperatures (10–300 K) for one of the representatives of mixed crystals ($TlIn_{0.5}Ga_{0.5}S_2$). We observed the blue shift of these dependencies with decreasing temperature for all the compositions of mixed crystals studied. In order to obtain the detailed information about the energy band gaps, E_g , the dependence of absorption coefficient on photon energy is studied in the high absorption regions.

The relation between absorption coefficient α and photon energy $h\nu$ is given by

$$(\alpha h\nu) = A\,(h\nu - E_g)^p \qquad (2)$$

where A is a constant, which depends on the transition probability and p is an index, which is theoretically equal to 2 or 1/2 for indirect and direct allowed transitions, respectively. Equation (2) can be also written as [21]:

$$\frac{d\,[\ln(\alpha h\nu)]}{d(h\nu)} = \frac{p}{h\nu - E_g}. \qquad (3)$$

The type of optical transition can be determined by finding the value of p. In order to obtain the preliminary value of E_g, $d\{\ln(\alpha h\nu)\}/d(h\nu)$ versus $h\nu$ was plotted.

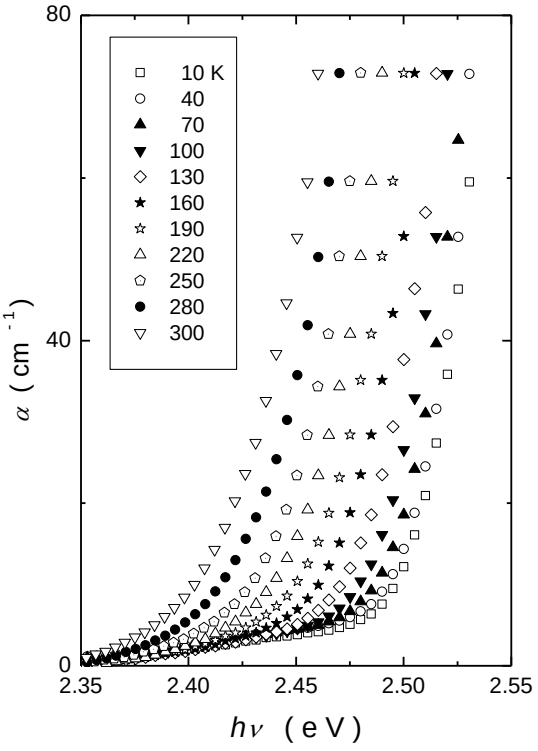

Fig.2. Absorption coefficient versus photon energy for $TlIn_{0.5}Ga_{0.5}S_2$ crystal in the temperature range of 10–300 K.

This dependence comprises a peak and the position of peak maximum gives approximately the optical band gap. Then, the curve of $\ln((\alpha h\nu)$ versus $\ln(h\nu - E_g)$ was plotted to determine p value, which was found to be about 2 from the slope of plotted curve. Thus, in order to

calculate the more precise value of the optical band gap, we plotted $(\alpha h\nu)^{1/2}$ as a function of photon energy, and this plot gives the straight line. The linear dependence of $(\alpha h\nu)^{1/2}$ on photon energy $h\nu$ suggest that the fundamental absorption edge in studied crystal is formed by the indirect allowed transitions. Using the extrapolations of the straight line down to $(\alpha h\nu)^{1/2} = 0$, the value of the indirect band gap energy was determined for the $TlGa_xIn_{1-x}S_2$ mixed crystals. The compositional dependencies of determined energy band gaps are demonstrated in Fig. 3 for the temperatures of 10 and 300 K. As seen from this figure, the energy band gaps increase with the increase of gallium atoms content in the $TlGa_xIn_{1-x}S_2$ mixed crystals.

The obtained values of the indirect energy gaps decrease with increasing temperature from 10 to 300 K, as displayed in Fig. 4. The temperature dependence of the energy band gap can be represented by the relation [20]

$$E_{gi}(T) = E_{gi}(0) + \frac{\gamma T^2}{T + \beta} \quad , \qquad (4)$$

where $E_{gi}(0)$ is the absolute zero value of the band gap, $\gamma = dE_{gi} / dT$ is the rate of change of the band gap with temperature, and β is approximately the Debye temperature.

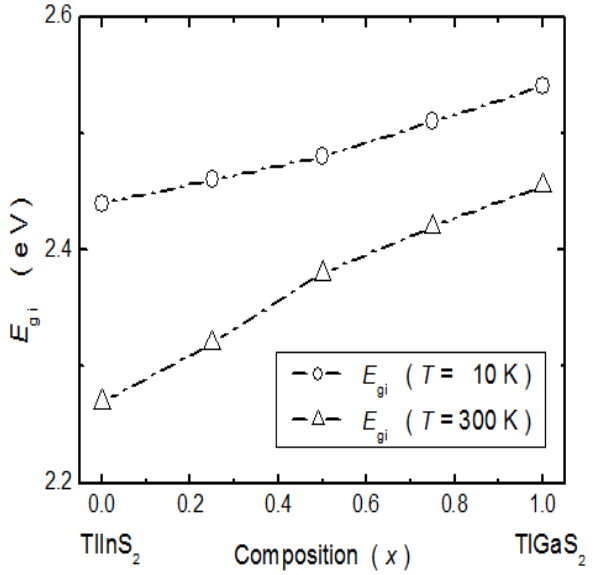

Fig. 3. Compositional dependencies of the indirect band gaps of $TlGa_xIn_{1-x}S_2$ mixed crystals at T = 10 and 300 K. The dashed-dotted lines are only the guides for the eyes.

The experimental data for the dependencies of E_{gi} on the temperature (10–300 K) in $TlGa_xIn_{1-x}S_2$ mixed crystals were fitted using equation (4) as shown in Fig. 4 (the solid lines correspond to the theoretical fits).

The fitting parameters were found to be $E_{gi}(0)$ = 2.44, 2.46, 2.48, 2.51 and 2.54 eV, $\gamma = -9.2 \times 10^{-4}$, -6.0×10^{-4}, -4.7×10^{-4}, -6.0×10^{-4} and -5.4×10^{-4} eV/K, and β = 160, 180, 169 190 and 203 K for the values of x = 0, 0.25, 0.50, 0.75 and 1, respectively. It should be noted, that the Debye temperatures, evaluated by Lindemann's melting rule [22] by using the X-ray results [23-25] and the melting temperatures, were found to be β = 155, 173, 173, 183 and 195 K, respectively.

It is well known that the temperature dependence of the band gap energy for a semiconductor can be expressed in two main parts as [20],

$$\frac{dE_g}{dT} = \left(\frac{dE_g}{dT}\right)_{l.\exp.} + \left(\frac{dE_g}{dT}\right)_{e-ph} . \qquad (5)$$

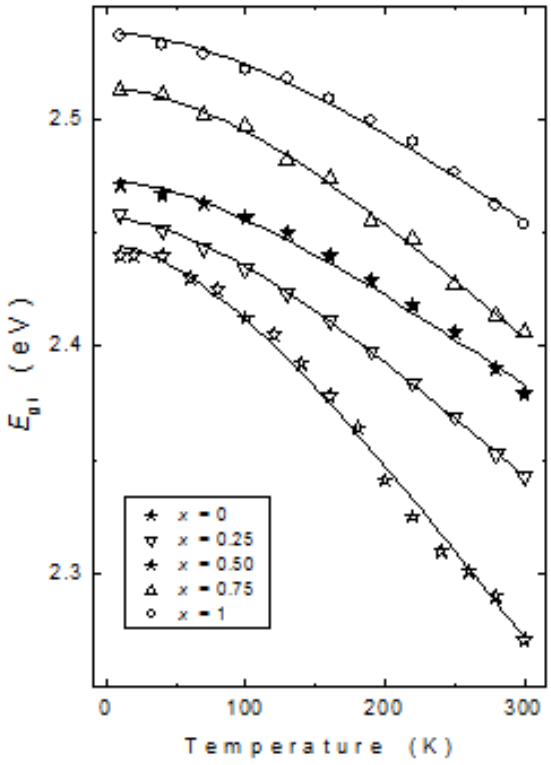

Fig. 4. The indirect band gap energies as a function of temperature for $TlGa_xIn_{1-x}S_2$ mixed crystals. The solid lines represent the fits using equation (4).

The first term results from the variation of the band gap due to the thermal expansion of the crystal. It may be either positive or negative in sign depending on the specific properties of the electron states of the band extrema and the relative ordering of levels [3]. The second term represents the change in the energy band gap arising from electron-phonon interaction and is always negative in sign for all semiconductors. Therefore, overall dependence of the band gap of the material on temperature may be either negative or positive depending on the term that contributes more. The temperature coefficients of indirect band gaps of $TlGa_xIn_{1-x}S_2$ mixed crystals were found to have negative signs which suggest that the electron-phonon interaction term is larger than the lattice expansion contribution.

IV. CONCLUSIONS

From the transmission and reflection measurements in the wavelength range of 400–1100 nm, the compositional dependencies of the indirect band gaps of $TlGa_xIn_{1-x}S_2$ mixed crystals were established. It was revealed that the energy band gaps increase with the increase of gallium atoms content in these mixed crystals. Moreover, the transmission measurements in $TlGa_xIn_{1-x}S_2$

mixed crystals were carried out in the temperature range of 10-300 K. The absorption edge was observed to shift toward lower energy values as temperature increases from 10 to 300 K. The data were used to calculate the indirect energy band gaps of the crystals as a function of temperature. As a result, the rates of the change of the indirect band gap with temperature were determined for different compositions of mixed crystals studied.

[1]. *K.A. Yee, A. Albright*, J. Am. Chem. Soc. 1991, 113, 6474.

[2]. *A.M. Panich*, J. Phys.: Condens. Matter 2008, 20, 293202.

[3]. *M. Hanias, A. Anagnostopoulos, K. Kambas, J.Spyridelis*, Physica B 1989, 160, 154; Mat. Res Bull. 1992, 27, 25.

[4]. *S.R. Samedov, O. Baykan, A. Gulubayov*, Int. J. Inf. Millimet. Waves 2004, 25, 735. *T.D. Ibrahimov, I.I. Aslanov*, Solid State Commun. 2002, 123, 339.

[5]. *N. Kalkan, J.A. Kalomiros, M.P. Hanias, A.N.Anagnostopoulos*, Solid State Commun. 1996, 99, 375.

[6]. *B. Abay, H.S. Guder, H. Efeoglu, H.K. Yogurtcu*, Phys. Stat. Sol. (b) 2001, 227, 469.

[7]. *A.Kato, M. Nishigaki, N. Mamedov, M. Yamazaki S. Abdullaeva, E. Kerimova, H. Uchiki, S. Iida*, J. Phys. Chem. Sol. 2003, 64, 1713.

[8]. *I.M. Ashraf*, J. Phys. Chem. B 2004, 108, 10765.

[9]. *G.A. Gamal*, Semicond. Sci. Technol. 1998, 13, 185.

[10]. *M.M. El-Nahass, M.M. Sallam, A.H.S. Abd Al-Wahab*, Current Appl. Phys. 2009, 9, 311.

[11]. *K.R. Allakhverdiev*, Solid State Commun. 1999, 111, 253.

[12]. *N.M. Gasanly, A. Culfaz , H. Ozkan, S. llialtioglu*, Cryst. Res. Technol. 1995, 30, 109.

[13]. *Sh. Nurov, V.M. Burlakov, E.A. Vinogradov, N.M.Gasanly, B.M. Dzhavadov*, Phys. Stat. Sol. (b) 1986, 137, 21.

[14]. *N.M. Gasanly, A.F. Goncharov, N.N. Melnik, A.S.Ragimov, V.I. Tagirov*, Phys. Stat. Sol. (b) 1983, 116, 427.

[15]. *K.R. Allakhverdiev, N.M. Gasanly, A. Aydinli*, Solid State Commun. 1995, 94, 777.

[16]. *N.M. Gasanly, R.E. Guseinov. A.S. Ragimov, V.I.Tagirov*, Phys. Stat. Sol. (b) 1980, 101, K121.

[17]. *N.M. Gasanly, B.G. Akinoglu, S. Ellialtioglu, R.Laiho, A.E. Bakhyshov*, Phys. B 1993, 192,371.

[18]. *N.M. Gasanly*, J. Korean Phys. Soc. 2006, 48, 914.

[19]. *J.I. Pankove*, Optical Processes in Semiconductors, Prentice-Hall , New Jersey, 1971.

[20]. *F. Yakuphanoglu*, J. Phys. Chem. Sol. 2008, 69, 949.

[21]. *J.R. Drabble, H.J. Goldsmid*, Thermal Conduction in Semiconductors, Pergamon, Oxford, 1961.

[22]. *M. Isik, K. Goksen, N.M. Gasanly, H. Ozkan*, J. Korean Phys. Soc. 2008, 52, 367.

[23]. *K. Goksen, N.M. Gasanly, H. Ozkan*, J. Phys.: Condens. Matter 2007, 19, 256210.

[24]. *K. Goksen, N.M. Gasanly*, J. Phys.: Condens. Matter 2007, 19, 456221.

THE SERIES RESISTANCE AND INTERFACE STATES IN Au/N-SI(111) SCHOTTKY BARRIER DIODES (SBDS) WITH NATIVE INSULATOR LAYER USING *I-V-T* MEASUREMENT METHODS

PERIHAN DURMUŞ, MERT YILDIRIM
Physics Department, Faculty of Arts and Sciences,
Gazi University, 06500, Teknikokullar, Ankara, TURKEY

The effect of interface state (N_{ss}) and series resistance (R_s) on the current-voltage (I-V) and capacitance-voltage (C-V) characteristics of Au/n-Si (111) (MIS) Schottky barrier diodes (SBDs) were carried out at 110, 200, 320 and 400 K. The energy distribution profile of N_{ss} was extracted from the forward bias I-V measurements by taking into account the bias dependence of the effective barrier height(Φ_e) for each temperature. Experimental results show that the value of barrier height (Φ_{Bo}) decreases and ideality factor (n) increases with a decrease in temperature. The high value of n was attributed to the presence of a native insulator layer at metal/semiconductor (M/S) interface and the high value of N_{ss} localized at Si/SiO_2 interface, changing from the ~$1x10^{14}cm^{-2}eV^{-1}$ (at 110 K) to ~$5x10^{13}$ $cm^{-2}eV^{-1}$(at 400 K).

I. INTRODUCTION

It is well known, the presence of an interfacial insulator layer such as SiO_2, SnO_2, TiO_2 and Si_3N_4, native or deposited, transforms the metal-semiconductor (MS) SBDs into a metal-insulator-semiconductor (MIS) type SBD and its I-V characteristics are considerably deviate from those expected for an ideal SBDs. Also, the particular distribution of interface states (N_{ss}) [1-6], series resistance of device [5,7-11], device temperature [3,6-10] and barrier formation at M/S interface [10-15] are important parameters and they cause deviation from the ideal SBDs. In general, the forward bias I-V plots are linear in the semilogarithmic scale at low voltages

($3kT/q \leq V \leq 0,7V$) but deviate considerably from linearity due to the effect of R_s when the applied bias voltage is sufficiently large ($V \geq 0.7V$) [1,5,12,11-17].

On the other hand, the N_{ss} is effective in both the linear and non-linear regions of these characteristics [1,18]. Therefore, to determine the main electrical parameters such as the reverse saturation current (I_o), n and Φ_{Bo} of these devices, difficulties will arise due to the existence of interfacial insulator layer, N_{ss} and R_s. For instance, when the values of R_s is enough large, the linear part of Ln(I)-V plots will be too small to get a reliable value of BH and ideality factor. There are several suggested methods [23-29] to the determination of the R_s, but they suffer from a limitation of their applicability, in this field, to practical devices with an interfacial insulator layer [30-32]. For example, although the procedure proposed by Cheung et al. [29] requires only one forward bias I-V curve and eliminates the task of determining the minimum of the Norde' s [24] function, it does not give the expected value of R_s of the neutral region as was also indicated by them [29,30].

In addition, the presence of interfacial insulator layer and its thickness, R_s and N_{ss} can affect the *C-V* characteristics of MIS type SBDs, causing a bending of the $1/C^2$-*V* as well as increasing the ideality factor. In general, a *C-V* plot shows an increase in capacitance with an increase in forward bias. However, in recent years, an anomalous peak in forward *C-V* characteristics attributed interface states and series resistance has been reported [19-21]. Ashok [18] derived an expression for the dependence of the *n* on the interface parameter and applied voltage. $1/C^2$ vs *V* plots into linear ones were given by Vasudev et al.[22], where a quantity called "excess capacitance" C_o, which causes a non linearity in the reverse bias region, was introduced.

In this study, we investigate the effects of the R_s and N_{ss}, causing non-ideal behavior I-V characteristics of Au/n-Si (111) SBD with native insulator layer at 110, 200, 320 and 400 K. Temperature dependence of Φ_{Bo}, R_s and N_{ss} values were obtained by using the standard [1,2], Bohlin [26] and Cheung's [29] methods from the forward bias I-V measurements. The non-ideal I-V behavior observed in Au/n-Si (111) SBD were attributed to the presence of R_s of device, a native insulator layer (SiO_2) at M/S interface and a particular distribution of N_{ss} at Si/SiO_2 interface.

II. EXPERIMENTAL DETAILS

The Au-/n-Si(111) SBDs were fabricated on 2 inch (5.08 cm) diameter n-type (P doped) epilayer silicon wafer with (111) surface orientation, 0.7 Ω-cm resistivity and 350μm thickness. For the fabrication a process, Si wafer was decreased in organic solvent of $CHClCCl_2$, CH_3COCH, and CH_3OH consecutively and then etched in a sequence of H_2SO_4 and H_2O, %20 HF, a solution of $6HNO_3$:1HF:$35H_2O$, %20 HF and finally quenched in deionized water for a prolonged time. Preceding each cleaning step, the wafer was rinsed thoroughly in deionized water of resistivity of 18 MΩ-cm. After this cleaning process, high purity (99.999 %) Au with a thickness of about 1500 Å were thermally evaporated onto whole back side of Si wafer at a pressure about 10^{-6} Torr in high vacuum system. In order to perform a low resistivity ohmic backcontact, Si wafer was sintered at 500 ^oC for 3 min in N_2 atmosphere. After that ~1500 Å thick high purity Au (%99,999) dots of 1 mm diameter were evaporated onto front of Si wafer at in high vacuum system and at same pressure. In this way, the fabrication process of Au-/n-Si (111) SBDs was completed. The native interfacial insulator layer thickness was estimated to be about 30 Å from high frequency (1 MHz) measurement of the oxide capacitance in the strong accumulation region. The *I-V* and *C-V* measurements were performed by the use of a Keithley 2400 sourcemeter. Small sinusoidal signal of 40 mV peak to

peak from the external pulse generator is applied to the sample in order to meet the requirement [23]. All measurements were carried out with the help of a microcomputer through an IEEE-488 AC/DC converter card. The temperature control were carried out using a temperature-controlled Janes vpf-475 cryostat with a Lake Shore model 321 auto-tuning temperature controllers in a vacuum of $5x10^{-4}$ Torr which enables us to make measurements in the temperature range of 77-450 K.

III. RESULTS AND DISCUSSION

3.1. The forward bias current-voltage-temperature (I-V-T) characteristics

When a MS Schottky barrier diode with a R_s is considered, based on the TE mechanism, it is assumed that the relation between the applied forward bias voltage ($V \geq 3kT/q$) and the current, I, can be expressed as [1]

$$I = I_o \exp\left(\frac{q(V - IR_s)}{nkT}\right)\left[1 - \exp\left(\frac{-q(V - IR_s)}{nkT}\right)\right] \quad (1)$$

where the term of IR_s is voltage drop across the R_s of the diode and I_o is the reverse saturation current and it can be derived from the straight-line intercept of the current axis (lnI) at zero bias and is given by

$$I_o = AA^*T^2 \exp(-q\Phi_{Bo}/kT) \quad (2)$$

where, the quantities A, A^*, q, k, T and Φ_{Bo} are the rectifier contact area, the effective Richardson constant and equals to 120 A/cm^2K^2 for *n*-type Si [1], the electronic charge, the Boltzmann constant, temperature in K and the zero-bias barrier height, respectively. Fig.1. shows the experimental semi-logarithmic forward and reverse-bias Ln(I)-V characteristics of Au/n-Si (111) SBD at 80, 200, 320 and 400 K. It is clear that the forward bias semi-logarithmic ln(I)-V characteristics of the Au/n-Si (111) SBD show a good rectifying behavior. Moreover, the "soft" or slightly non-saturating behavior was observed as a function of bias in the reverse bias branch especially at low temperatures, which may be explained in terms of the image force lowering of SBH [33-35] and the presence of the interfacial layer between the metal and n-Si (111) wafer [17]. Using the values of Io, the values of Φ_{Bo} were calculated from Eq. (2) for each temperature. The values of ideality factor were obtained from the slope of the linear region of the forward bias lnI-V plots for each temperature using the Eq. (1)

$$n = \frac{q}{kT}\frac{dV}{d(Ln\, I)} \quad (3a)$$

To obtain the interface states (N_{ss}) energy distribution from the forward bias I-V data, the bias dependence of ideality factor n(V) and barrier height are necessary. Furthermore, the bias dependent n(V) can be written from Eq. (1) as

$$n(V) = \frac{qV}{kTLn\left(\frac{I}{I_o}\right)} \quad (3b)$$

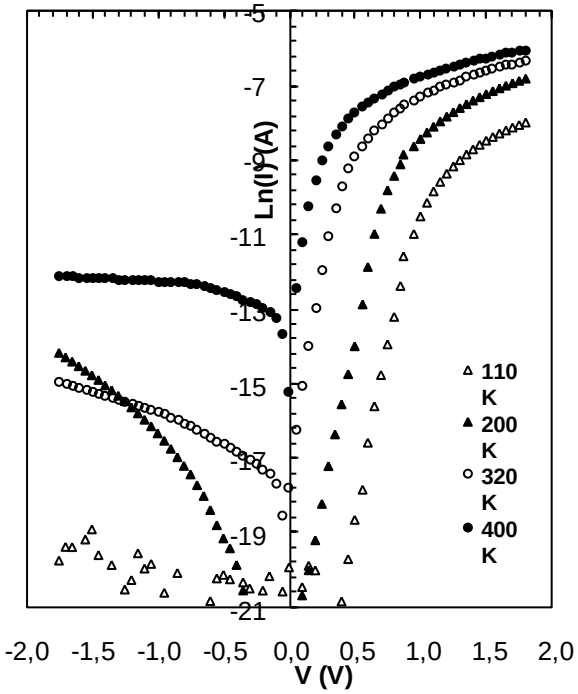

Fig. 1. The forward and reverse bias Ln(*I*)-*V* characteristic of the Au-/n-Si(111) SBDs with native insulator layer at four different temperatures.

Table 1. Direct determination of R_s, R_{sh}, n, and Φ_B by using the standard and modified Norde method developed by Bolin at four different temperatures for the Au/n-Si (111) SBD.

T (K)	I_o (A)	n	Φ_{Bo} (eV)	V_o (V)	I (A)	F(Vo) (V)	Φ_B (eV)	R_s (Ω)	R_{sh} (Ω)
110	$2.54x10^{-13}$	5.09	0.40	1.148	$6.78x10^{-5}$	0.231	0.260	1805	$3.7x10^9$
200	$1.55x10^{-10}$	3.28	0.60	1.148	$3.59x10^{-4}$	0.390	0.421	787	$2.4x10^8$
320	$5.76x10^{-13}$	1.89	0.81	0,869	$5.59x10^{-4}$	0.616	0.643	621	$5.5x10^5$
400	$4.12x10^{-6}$	1.60	0.89	0,399	$7.30x10^{-4}$	0.787	0.802	265	$1.3x10^4$

The some main electrical parameters obtained from the forward bias Ln(*I*)-*V* characteristic of the Au-/n-Si(111) SBDs at various temperatures are given in Table 1. As shown in Table 1, the value of Φ_{Bo} and n obtained from the Ln(I) vs V plots were found to be a strong function of temperature. The value of n was found to increase while the value of Φ_{Bo} decrease with decreasing temperature (n=5.83 and Φ_{Bo}=0.40 eV at 110 K, n=1.60 and Φ_{Bo}=0.89 eV at 400 K). The high values of n especially at low temperatures are probably due to the potential drop on the interfacial insulator layer, the presence of excess current at low temperature region,

barrier inhomogeneity and a particular distribution of N_{ss} at M/S interface [13-17].

As can be seen from Fig. 1, the Ln(I) vs V plots clearly depict the linear behavior (at the intermediate bias voltages) over a several orders of current and shift towards the high bias side with decreasing in temperature, but deviate considerably from linearity due to the effect of series resistance of the device at efficiently high bias voltages. Thus, the value of R_s and Φ_{Bo} were obtained from the modified Norde method developed by Bohlin [26]. However, Bohlin only used two different values of arbitrary parameters of γ and thus two experimental data points. Here, we used the Bohlin method for each temperature as

$$F(V, \gamma) = V/\gamma - kT/q \, Ln\,(I/(AA^*T^2)) \qquad (4)$$

where γ is the dimensionless and greater than ideality factor. According this method, once the minimum of the $F(V, \gamma)$ vs. V plot is determined, the value of BH and R_s can be obtained from Eq.(5) and (6), respectively, as

$$\Phi_B = F(V_0) + V_0/\gamma - kT/q \qquad (5)$$

$$R_s = (kT/qI)(\gamma - n) \qquad (6)$$

where $F(V_0)$ is the minimum point of $F(V, \gamma)$ vs V plot, V_o and I are the corresponding bias voltage and current, respectively. Fig. 2 (a) shows the F(V) vs V plots for the Au-/n-Si(111) SBDs with native insulator layer at four different temperatures. The values of Φ_B and R_s obtained from equations (5) and (6), respectively, at four different temperatures are given in Table 1 together with standard method. As shown in Table 1, the value of Φ_B and Rs obtained from the $F(V, \gamma)$ vs V plots were found to be a strong function of temperature. The value of Φ_B was found to increase, while the value of R_s increase with decreasing temperature (Φ_B =0.213 eV and R_s=2501 Ω at 80 K, and Φ_B =0.802 eV and R_s=265 at 400 K). It is clear that the value of R_s is quite high for all temperatures. Therefore, before any analysis could be done, all the measurements (I-V, C-V and G/w-V) must be corrected for R_s [23-29].

In addition, the bias voltage dependent series resistance profile of the Au-/n-Si(111) SBDs with native insulator layer was obtained from the I-V data as $\delta V/\delta I$ and are given in Fig. 2 (b). As can be shown in Fig. 2 (b), at sufficiently high forward bias region (V≥4 V) the value of series resistance is almost independent of bias voltage. At zero-bias, the value of resistance which is equal to the diode shunt resistance (R_{sh}) decreases rapidly with increasing temperature. It is clear that both the value of R_s and R_{sh} were found strongly temperature dependent and decrease with increasing temperature. Such behavior of R_s and R_{sh} can be explained by the enhanced conductivity of the Si and this is expected behavior. On the other hand, the values of R_{sh} were remains relatively high even at sufficiently high temperatures (320 and 400 K), thus, its effect on the I-V characteristics can be neglected.

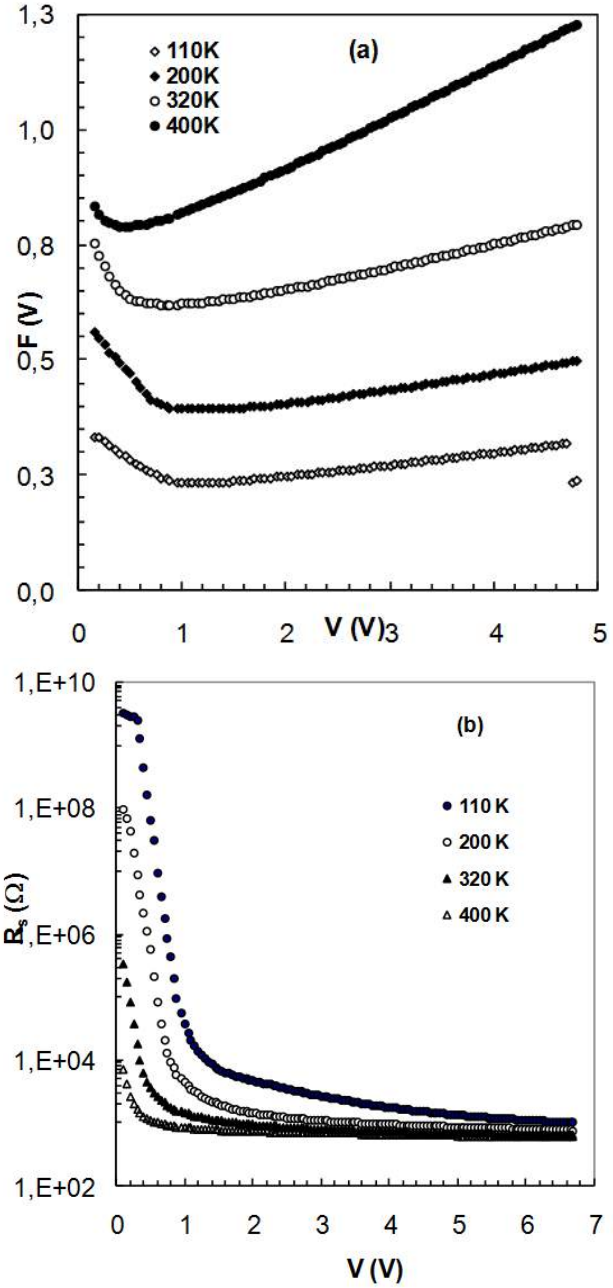

Fig.2. The F(V) vs V and R_s vs V plots of the Au-/n-Si(111) SBDs with native insulator layer at four temperatures, respectively.

3.2. The density distribution of the interface states profile obtained from the forward bias I-V-T characteristics

The non-linearity of the forward bias Ln*I-V* characteristic especially at high bias values indicated a continuum of N_{ss}, which equilibrates with semiconductor [36]. For SBDs with native or deposited interfacial insulator layer, the relation between the density of the interface states (N_{ss}) in equilibrium with the semiconductor and the value of the ideality factor greater than unity can be expressed as [3].

$$n(V) = 1 + \frac{\delta}{\varepsilon_i}\left[\frac{\varepsilon_s}{W_D} + qN_{ss}(V)\right] \qquad (7)$$

where δ is the thickness of interfacial insulator layer, W_D is the width of the depletion layer calculated from C^{-2} vs

V characteristics at 1 MHz. The energy density distribution of N_{ss} for the Au/n-Si (111) SBD with native insulator layer can be obtained from the forward bias I-V data by taking into account the bias dependence of the n(V) and effective BH (Φ_e). The effective barrier height Φ_e is given as

$$\Phi_e = \Phi_{bo} + \beta(V) = \Phi_{bo} + (1 - \frac{1}{n(V)})\, V \qquad (8)$$

by considering the applied voltage dependence of the BH, where β is the voltage coefficient of the effective barrier height Φ_e used in place of the barrier height Φ_B and it is a parameter that combines the effects of both interface states in equilibrium with the semiconductor [6,10,37]. Thus, the energy profile of N_{ss} in equilibrium with semiconductor was obtained by substituting the voltage dependent *n(V)* values and ε_s=11.8ε_o, ε_i=3.8ε_o, δ=30Å in Eq. 9 for each temperature and is given in Fig. 3.

$$N_{ss}(V) = \frac{1}{q}\left[\frac{\delta}{\varepsilon_i}\left(n(V) - 1\right) - \frac{\varepsilon_s}{W_D}\right] \qquad (9)$$

where ε_i and ε_s are the permittivity of the insulator layer and the semiconductor, respectively. The interfacial insulator layer (S_iO_2) thickness δ was obtained from high frequency (1 MHz) C-V measurements. Furthermore, in *n*-type semiconductors, the energy of the N_{ss} with respect to the bottom of the conductance band (E_c-E_{ss}) at the surface of semiconductor is given by

$$E_c - E_{ss} = q(\Phi_e - V) \qquad (10)$$

Fig. 3 shows the energy distribution profile of N_{ss} as function of E_c-E_{ss} using Eq.10 at 110, 200, 320 and 400 K. As can be seen in Fig. 3, it is very apparent that there is an exponential increase of the N_{ss} towards to bottom of the conductance band for each temperature, and it shifts towards the conductance band (E_c) in the N_{ss} plots due to the effect of temperature and interfacial insulator layer at different temperatures. The value of N_{ss} decreases with increasing temperature due to molecular restructuring and reordering of the M/S interface under the temperature effect. The mean value of the N_{ss} changes from the order of ~1x10^{14}cm^{-2}eV^{-1} (at low temperatures) to ~5x10^{13} cm^{-2}eV^{-1}(at high temperatures). Similar results have been reported in the literature [38-42].

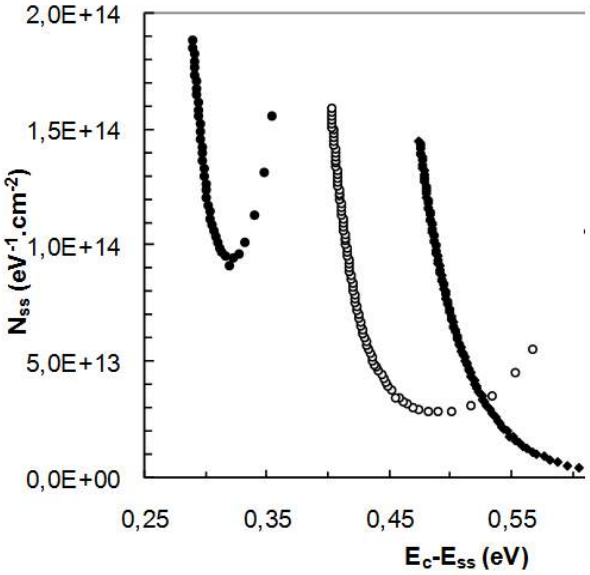

Fig.3. The energy distribution profile of N_{ss} obtained from the forward bias I-V characteristics of the Au/n-Si SBD with the native SiO_2 layer at different temperatures.

IV. CONCLUSIONS

In order to analysis the interface states (N_{ss}) and series resistance (R_s) effect on the conduction mechanism of Au/n-Si (111) (MIS) SBDs, I-V, C-V and G/ω-V characteristics were investigated at 110, 200, 320 and 400 K. The energy density distribution profile of the N_{ss} was extracted from the forward bias I-V measurements by taking into account the bias dependence of the n(V) and Φ_e for each temperature. The values of Φ_{Bo} (I-V), n and R_s were estimated from both standard and Norde function modified by Bohlin. They were found strongly temperature dependent. It was observed that the values of Φ_{Bo} decreases and the n increases with a decrease in temperature. The values of N_D, barrier height (Φ_{Bo} (C-V)) and N_{ss} are also obtained from the current-voltage and C^{-2}-V characteristics and compared. The high values of n were attributed to the presence of an interfacial native insulator layer at M/S interface and the high density of N_{ss} localized at Si/SiO_2 interface. It is clear that the temperature dependent I-V characteristics of SBDs are affected by not only N_{ss} and interfacial insulator layer but also in R_s, and these three parameters have a significant influence on electrical characteristics of SBDs.

[1]. *S.M. Sze*, Physics Semiconductor Devices 2nd Ed. New York, (1981).

[2]. *E.H.Rhoderick, R.H.Williams*, Metal-Semiconductor Contacts, second ed, Clarendon, Oxford,1988

[3]. *H.C.Card, E.H.Rhoderick*, J. Physi. D: Appl. Phys. 4 (1971) 1589.

[4]. *R. T. Tung*, Phys. Rev. B, 45 13509.

[5]. *H.Kanbur, Ş.Altındal, A.Tataroğlu*, Appl. Surf. Sci. 252 (2005) 1372.

[6]. *W.Mönch*, J. Vac. Sci. Technol. B 17 (1999) 1867.

[7]. *J.H.Werner, H. H.Guttler*, J. Appl. Phys. 69 (1991) 1522.

[8]. *P. Chattopadhyay, A.N. Daw*, Solid-State Electron. 37 (1994) 1759.

[9]. *P.Cova, A.Singh*, Solid-State Electron. 33 (1990) 11.

[10]. *S.Chand, S.Bala*, Apply. Surf. Sci. 252 (2005) 358.
[11]. *Ş.Altındal, A.Tataroğlu, İ.Dökme* Solar Energy Mater. Solar Cells 85 (2005) 345.
[12]. *S. Chand, J. Kumar*, Semicond. Sci. Technol. 11 (1996) 1203.
[13]. *J. P. Sulvian, R. T. Tung, M. R. Pinto, W.R.Graham*, J. Appl. Phys. 70 (1991) 7403.
[14]. *Ş.Karataş, Ş.Altındal, A.Türüt, A.Özmen*, Appl. Surf. Sci. 217 (2003) 250.
[15]. *R. T.Tung*, Mater. Sci. and Eng. R. 35 (2001)1.
[16]. *O. Pakma, N.Serin, T.Serin, Ş.Altındal*, Semicon. Sci. and Technol, 23 (2008) 105014.
[17]. *S.Ashok, J. M.Borrego, R. J.Gutmann*, Solid-State Electron. 22 (1979) 621.
[18]. *Z.Quennoughı*, Phys. Stat. Sol.(a) 160 (1997) 127.
[19]. *J.Osvald, E. Burıan*, Solid State Electron. 42(2) (1998) 191.
[20]. *M.Depas, R.L.Van Meirhaeghe, W.H. Laflere, F.Cardon*, Semi. Sci. Tech. (1992) 1476.
[21]. *P.K. Vasudev, B.L.Matters, R.H. Bube*, Solid State Electronics 19 (1976) 557.
[22]. *E.H.Nicollian, J.R.Brews*, MOS Physics and Techonology, Wiley, New York, (1982).
[23]. *H.Norde*, J. Appl Phys 50 (1979) 5052.
[24]. *K.Sato, Y. J.Yasamura*, Appl Phys 58 (1985) 3656.
[25]. *K.E.Bohlin*, J. Appl Phys 60 (1986) 1223.
[26]. *C.D.Lien, F.C.T. So, M.A.Nicolet*, IEEE Trans. Electron. Devices, ED-31 (1984) 1502.
[27]. *R. M.Cibils, R. H.Buitrago*, , J. Appl Phys 58 (1985) 1075.
[28]. *S. K.Cheung, N. W.Cheung*, Appl. Phys Lett 49 (1986) 85.
[29]. *M.Sağlam, E.Ayyıldız, A.Gümüş, A.Türüt, H.Efeoğlu, S.Tüzemen*, Appl. Phys, 62 (1996) 269.
[30]. *V.Aubry and F.Meyer*, J. Appl Phys 76 (1994) 7973.
[31]. *F.Parlaktürk, Ş.Altındal, A.Tataroğlu, M.Parlak, A.Agasiev*, Microelect, Eng, 85 (2008) 81.
[32]. *R.T.Tung*, Phys. Rev. B. 45 (1992) 13509.
[33]. *J.P.Sullivan, R.T.Tung, M.R.Pinto, W.R.Graham*, J. Appl. Phys. 70 (1991) 7403.
[34]. *H.Doğan, H.Korkut, N.Yıldırım, A.Türüt*, Appl. Surf. Sci. 253 (2007) 7467.
[35]. *W.Mönch*, J. Vac. Sci. Technol. B 17 (1999) 1867.
[36]. *A.Gümüş, A.Türüt and N.Yalçın*, J. Appl. Phys., 91(2002) 245.
[37]. *Tataroğlu, Ş. Altındal*, Microelectronic Eng. 83 (2006) 582.
[38]. *B.Akkal, Z.Benamara, B.Gruzza, L.Bideux, N.Bachir Bouiadjra*, Mater. Sci. Eng. C 21 (2002) 291.
[39]. *H.A.Çetinkara, A.Türüt, D.M.Zengin, Ş.Erel*, Appl. Surf. Sci. 207 (2003) 190.
[40]. *A.Türüt and M.Sağlam*, Physica B 179 (1992) 285.
[41]. *B.Akkal, Z.Benemara, L.Bideux, B.Gruzza*, Microelectronics J. 30 (1999) 673.

APPLICATION OF INDUCTIVELY COUPLED PLASMA MASS SPECTROMETRY (ICP/MS) TO DETECTION OF TRACE ELEMENTS, HEAVY METALS AND RADIOISOTOPES IN SCALP HAIR

S. ÖZTÜRK YILDIRIM[1*], Y. BENDERLİ CİHAN[2]

[1]*Physics Department, Faculty of Sciences, University, 38039 Kayseri, Turkey*

[2] *Kayseri Training & Res Hosp, Dept Radiat Oncol, 38010 Kayseri, Turkey*

* ozturk@erciyes.edu.tr

Trace element analysis of human hair has the potential to reveal retrospective information about an individual's nutritional status and exposure. As trace elements are incorporated into the hair during the growth process, longitudinal segments of the hair may reflect the body burden during the growth period. We have evaluated the potential of human hair to indicate exposure or nutritional status over time by analysing trace element profiles in single strands of human hair. By using inductively coupled plasma mass spectrometry (ICP-MS), we achieved profiles of 43 elements in single strands of human hair, namely, Li, Be, B, Na, Mg, Al, K, Ca, Sc, Ti, V, Cr, Mn, Fe, Co, Ni, Cu, Zn, Ga, As, Se, Rb, Sr, Rh, Pd, Ag, Cd, Sn, Sb, Cs, Ba, Ce, Pt(194), Pt(195), Pt(196), Au, Pt(198), Hg, Pb, Bi, U(234), U(235) and U(238). We have shown that trace element analysis along single strands of human hair can yield information about essential and toxic elements, and for some elements, can be correlated with seasonal changes in diet and exposure. The information obtained from the trace element profiles of human hair in this study substantiates the potential of hair as a biomarker.

I. INTRODUCTION

Multi-element determinations in biological samples have been described in the literature with focus on the analytical method development [1–22]. These papers are dealing with the analyses of blood [1–4], serum [4–12], urine [1,4,6,13– 18], hair [19,20] nails [19] bones [21] or saliva [22]. Only a few papers describe both, the method development for the determination of a large number of elements and the analysis of a statistically relevant number of real samples [2,23–26]. Rodushkin et al. [3] developed a method for the determination of 60 elements in whole blood by sector field ICP-MS. In another paper [2] of this author 50 elements were determined in blood samples of 31 non-exposed human subjects. Minoia et al. [24] determined 46 elements in urine, blood and serum by graphite furnace atomic absorption spectrometry (GF-AAS) and inductively coupled plasma optical emission spectrometry (ICP-OES). For many elements the power of detection of these two methods is not sufficient to determine elemental background concentrations. In general, lower limits of detection (LODs) are possible by inductively coupled plasma mass spectrometry (ICP-MS). To avoid spectral interferences, which are often described as the major disadvantage in ICP-MS, high-resolution sector field ICP-MS was suggested for the analysis of biological materials [2–6,11,12,16,17].

In our approach the application of a new ICP-MS instrument with the collision/reaction cell technology was used to remove spectral interferences but keeping all other unique capabilities of ICP-MS, such as low detection limits, multi-element capability and a wide linear calibration range. Compared with sector field ICP-MS it is also lower in investment costs. For the rapid and reliable routine analysis with high sample throughput collision/reaction cell ICP-MS was established for urine analysis [26].

Biomonitoring of trace elements in urine samples of healthy humans has been published for many elements at different geographical locations. Many of these papers deal with elements described as toxic or carcinogenic, such as As [24,26–28,33], Cr [24,26,29–33], Ni [24,26,30–33], Hg [24,32,33] or Pb [13,24,26,32,33]. Other publications deal with biomonitoring of essential trace elements, for example, for Se [24,26,32–34], Cu [24,26,33], Mo [24,26,33,35] or Zn [24,26,33]. For some elements (e.g., Se or Mn) other biological fluids (serum or blood) are preferred for analyses to investigate the essential trace element concentrations, however, in the case of intoxications urine is often used. For As, Cd, Cr, Cu and Hg in urine a representative population study was performed in the German Environmental Survey in 1992 [36] and this was repeated 6 years later with Pb, Cd, Hg, Au, Ir and Pt in urine [37,38]. Reference values for Cd, Hg, As in urine were derived from this survey [39]. For the US population urinary concentrations of the elements Pb, Cd, Hg, Co, U, Sb, Ba, Be, Cs, Mo, Pt, Tl, W were published in the Second National Report on Human Exposure to Environmental Chemicals [40]. Both surveys, in Germany and in the US, provide results for children. Other Reference values for youngsters in the urban area of Rome were described for Ni, Cr and V [41].

In this paper the analysis results of some hair samples from non-exposed humans are presented. The major goal of the analyses was to determine background concentrations of those elements for which only little data are available in the literature.

II. MATERIALS AND METHODS

2.1. Technique

As the name implies, ICP-MS is a combination of an inductively coupled plasma (ICP) with a mass spectrometer (MS). Typically, the sample is introduced into the ICP by a sample introduction system consisting of a peristaltic pump and a nebuliser, which generates a fine aerosol in a spray chamber. The spray chamber separates the small droplets from the large droplets. Large droplets fall out by gravity and exit through the drain tube at the end of the spray chamber, while the small droplets pass between the outer wall and the central tube and are eventually transported into the sample injector of the

plasma torch using a flow of argon gas. The aerosol is then transported to the ICP, which is a plasma ion source. This plasma is formed by the application of a high voltage spark to a tangential flow of argon gas, which causes electrons to be stripped from their argon atoms. These electrons are caught up and accelerated into a magnetic field, formed by a radio frequency (RF) energy which is applied on a RF coil surrounding the plasma torch. This process causes a chain reaction of collision-induced ionization leading to an ICP discharge. The ICP reaches temperatures of 6,000– 8,000 K. As the aerosol transits the plasma, the droplets undergo numerous processes which include desolvation, dissociation, atomization, and ionization [42]. Ions produced by the argon ICP are principally atomic and singly charged, making it an ideal source for atomic MS. Since the ICP works at atmospheric pressure and the MS requires a vacuum, an interface typically consisting of a coaxial assembly of two cones (sampler and skimmer cone) and a series of pressured differentials to allow efficient sampling of the atmospheric pressure plasma gases while minimally perturbing the composition of the sample gases.

After passing through the sampler and skimmer cones, several electrostatic lenses or ion optics focus the ions into the MS, where the ions are separated based on their mass-to-charge (m/z) ratios. Three main mass separation principles are used in ICP-MS systems: quadrupole, magnetic sector, and time offlight (TOF). The quadrupole is the most commonly used type in ICP-MS. It comprises of two pairs of parallel cylindrical rods. The voltages applied to these rods give a dynamic hyperbolic electric field, in which any ion above or below the set mass enters an unstable trajectory and is lost from the ion beam. By varying the voltages applied to these rods, a full mass spectrum can be obtained [42]. While the quadrupole MS is used in the majority of ICP-MS instruments, some systems utilize a magnetic sector or high resolution (HR) analyzer, typically employed when higher mass resolution is required [43]. This analyzer uses a magnetic field, which is dispersive with respect to ion energy and mass and deflects different masses through different angles. The ions subsequently enter an electrostatic analyzer, which is dispersive with respecttoion energy and focuses the ions to the detector. In a TOF MS [44], a uniform electrostatic pulse is applied to all ions at the same time, causing them to be accelerated down a flight tube. Because lighter ions achieve higher velocities and arrive at the detector earlier than heavier elements, the arrival times of the ions are determined by their m/z ratios.

After passing the mass separator, the ions strike the active surface of the detector, typically an electron multiplier. Each ion which hits the channel electron multiplier generates a cascade of electrons leading to a discrete pulse. The pulses are counted and the output signal is given in counts per second.

2.2. Interferences

One of the main limitations of ICP-MS is the appearance of interferences, which can be classified into two major groups. The first group comprises the spectral interferences, which arise from other elements (isobaric interferences), polyatomic ions (e.g., oxides) with the same m/z ratio as the analyte isotope, or doubly charged ions when half of their masses are similar to the mass of the analyte isotope. Elemental isobaric interferences can usually be avoided by choosing an interference free analyte isotope when the analyte of interest is not monoisotopic. Alternatively, because of the constant nature of isotope ratios for most of the naturally occurring elements, elemental isobaric interferences can be easiliy corrected mathematically by monitoring the intensity of an isotope of the interfering element which is free from spectral interferences [42]. For the three most abundant Pt isotopes (^{194}Pt: abundance 33.0%, ^{195}Pt: 33.8%, ^{196}Pt: 25.2%), only ^{196}Pt is subject to an isobaric interference (^{196}Hg). However, this interference can be corrected online by monitoring ^{202}Hg signals. For the most abundant isotopes of Ru (^{99}Ru: 12.7%, ^{101}Ru: 17.0%, ^{102}Ru: 31.6%, ^{104}Ru, 18.7%), ^{99}Ru, ^{102}Ru, and, ^{104}Ru are subject to isobaric interferences of respectively ^{99}Tc, ^{102}Pd, and ^{104}Pd, which can also be corrected online.

Polyatomic or molecular interferences can be produced by the combination of two or more atoms and/or ions leading to a molecule ion and are usually associated with either the argon plasma, atmospheric gases, or matrix components of the solvent or the sample. These interferences can be overcome by choosing an interference free isotope, removing the matrix [45], using alternative sample introduction systems, using mathematical corrections equations [46], employing cool plasma conditions [46], using a collision or reaction cell [47], or by using a high resolution mass analyzer [48]. Elements with high masses, such as Pt, are less susceptible to molecular interferences than lower masses, such as Ru [49-50]. However, metal oxide interferences, which can occur as a result of incomplete dissociation of the sample matrix or from recombination within the plasma or the interface, can interfere with the analysis of Pt and Ru. Pt isotopes may be subject to interferences from hafnium oxides [51-52] and tungsten oxides. Ru isotopes can be subject to oxide interferences from krypton, bromine, selenium, strontium, and rubidium. Oxide formation, though, can be minimized by optimizing the gas flow rate, pump rate, and ionization conditions of the plasma. Since metal oxide formation is typically controlled, via the plasma conditions, to be less than 2% and because hafnium background concentrations in biological samples are typically lower than Pt backgrounds [53], hafniumoxides will not interfere significantly with Pt signals [54]. Prior to the development of an ICP-MS assay for Pt or Ru, however, background concentrations of the elements of potentially interfering metal oxides in the biological matrix should be investigated.

The last type of spectral interferences are the doubly charged ions, which are analyzed at half the mass of the element, since the mass spectrometer measures m/z ratios. Pt isotopes are not susceptible to interference of doubly charged ions as no element with a mass two times the mass of Pt exists.Ru isotopes, however, might be interfered by some doubly charged ions ($[Pt]^{2þ}$, $[Hg]^{2þ}$, and $[Pb]^{2þ}$). The formation of doubly charged ions can, however, be minimized by optimizing ICP-MS parameters such as lens voltages and plasma conditions. However, because background levels of heavy metals

such as Pt might vary it is advisable to monitor the signals of these elements routinely during analysis.

The second group of interferences are the nonspectral interferences which can be broadly divided into two categories: first the physical signal suppression resulting from (un)dissolved solids or organics present in the matrix. Matrix components may have an impact on the droplet formation in the nebuliser or droplet size selection in the spray chamber, which can affect the transport efficiency and thus the signal intensity (Thomas, 2002). In the case of organic matrices, the viscosity of the sample that is aspirated is modified. In addition, the solids present in the matrix might lead toa deposition of solids on the cones and subsequently result in an altered ion transmission. Furthermore, undissolved solids can clog the nebuliser and torch. A decrease in these physical effects is possible by an adapted sample pretreatment (e.g., dilution), the use of proper calibration techniques (Jarvis, Gray, & Houk, 1992) preferably combined with the use of an internal standard (IS), or by adjustment of the sample introduction system.

The second category of nonspectral interferences are the matrix interferences (Thomas, 2002) which are caused by changes in the loading of the plasma or space-charge effects and result in signal alteration. An extensive loading of the plasma may effect the ionization efficiency of the analyte ions. High concentrations of easily ionisable matrix elements, such as sodium, might result in a decreased ionization efficiency of elements with higher ionization energies and thus a decreased signal of these elements. In general, the lower the degree of ionization of the analyte in the plasma, the greater the effect of a matrix component on the ion count rate of the element will be.

Space-charge effects are frequently seen in the analysis of light elements. The magnitude of signal suppression generally increases with decreasing atomic mass of the analyte ion. This is the result ofapoor transmission ofions through the ion optics due to matrix induced space-charge effects. The high-mass matrix element will dominate the ion beam and pushes lighter elements out of the way resulting in a suppression of the signal.

It is difficult to measure and quantify nonspectral matrix interferences. Again, separation of the analytes from the matrix or dilution of samples may reduce this type of nonspectral interferences. Furthermore, internal standardization may be successful in reducing the interferences. The IS, however, must be closely matched in both mass and ionization energy because they are to behave equal to the analyte. Also, the use of matrix matched calibration standards or standard addition might correct the matrix interferences. Although the signal suppression of the analyte will be corrected by proper calibration methods, the actual space-charge effects will not be solved. The most common approachtoreduce space-charge effects is to apply voltages to the individual ion lens components. This will steer the analyte ions through the mass analyzer while rejecting a maximum number of matrix ions [55].

2.3. Combination of Icp-Ms Detection with Speciation Techniques

ICP-MS can be used as a Pt or Ru specific detector for several speciation technologies. ICP-MS has several advantages over other methods of detection including a wide linear dynamic range, low detection limits, potential for isotope determinations, and multi-element capability. Moreover, the signal intensities are independent of the chemical structure of the analyte incorporating Pt or Ru and hence the method does not require standards of each analyte/metabolite/adduct. ICP-MS can provide quantitative information for structurally noncorrelated metal compounds.

2.4. Method Validation

Following development of an ICP-MS assay and before implementation into routine use, the assay needs to be validated to demonstrate that it is suitable for its intended use. Validation is required to ensure the performance of the method. As chromatography is widely used in bioanalysis, validation guidelines have already been extensively described for speciation methods (U.S. Food and Drug Administration et al., 2001). In contrast, no such guidelines are available for ICP-MS. This has led to some discrepancies concerning the definition of validation parameters in literature describing ICP-MS based bioanalytical assays. No stringent procedure is followed for the assessment of limit of detections (LODs), lower limit of quantifications (LLOQs), precision, accuracy, and linearity in the field of ICP-MS. The LOD and LLOQ for instance can be obtained by several approaches such as; signal-to-noise ratios, the standard deviation of the noise, or the standard deviation of the noise and slope of the calibration curve [56]. For reported ICP-MS assays it is not always defined which approach has been used. Furthermore, the LOD, LLOQ, and calibration range are reported either in the processed sample matrix (the final matrix entering the ICP-MS) or in the unprocessed sample matrix. The difficulty is, that the matrix in question is not always clearly defined. Another intricacy is that concentrations of compounds are commonly reported in weight per volume (w/v) instead of molar concentrations (moles/v). In case of an elemental detection technique like ICP-MS, it therefore is pivotal to report whether the metal or the metal-containing compound is used for calculation of the concentrations. Unfortunately, this is not always clear from the reported data. Because of these issues it is difficult to compare assays based on their detection limits and other validation parameters.

In our opinion, procedures followed in, for example, the FDA guidelines could, as far as applicable for ICP-MS, serve as an example for the development of a guideline for the validation of ICP-MS assays in biological matrices (U.S.Food and Drug Administration et al., 2001). Validation parameters could include assessment of the LLOQ, carry-over, linearity, specificity, accuracy, precision, cross analyte /IS interference, and stability.

2.2.5. Assay Development

For ICP-MS analysis, biological samples cannot be analyzed directly, but require a pretreatment to reduce the

matrix effects of endogenous compounds, such as cell constituents, proteins, salts, and lipids. The development of ICP-MS methods for metals in biological matrices is generally focused on the selection of an appropriate sample pretreatment and the selection of calibration proceduresto avoid and compensate matrix effects. Additionally, instrumental modifications can be used to further optimize the assay. For the analysis of low concentrations of metal it is important to consider that, whatever sample pretreatment procedure is used, special care has to be taken to avoid contamination of samples. A careful selection of pretreatment devices and reagents should be performed. Glassware should be avoided as it may contain considerable amounts of Pt. Moreover, sample pretreatment needs to be performed in a dedicated area to prevent environmental Pt or Ru originating from, for example, pollution by car exhaust catalysts (Barefoot, 1997), from interfering with the analysis. Besides the prevention of contamination it is relevant that blanks do not contain detectable levels of analyte. Screening of background levels is, therefore, necessary.

An Agilent model 7500a inductively coupled plasma mass spectrometer was used for the determination of uranium and thorium. The instrument was optimized daily before measurement and operated as recommended by the manufacturers. The conditions are given in Table 1.

Table 1. Operating conditions of ICP-MS

Inductively coupled plasma	Agilent 7500 a
Nebulizer	Babington
Spray chamber	Quartz, double pass
RF power	1260 W
Frequency	27.12 MHz
Sampling depth	7.0 mm
Plasma gas flow rate	15 L min^{-1}
Auxiliary gas flow rate	1.0 L min^{-1}
Carrier gas flow rate	1.15 L min^{-1}
Sample uptake rate	0.3 mL min^{-1}
Detector mode	Auto
Integration time	0.10 s
Number of replicates	3
Analytical masses	^{238}U, ^{232}Th
Internal standard	^{209}Bi, Be, Rh, Sc

Table 2. Basic statistical paremeters for selected trace elements distribution (µg/g,) in the scalp hair.

Trace element	Range	Median	Mean	Std. Error	Std. Deviation	Skewness
Li	1,38-0,03	0,452	0,5625	0,16964	0,56264	0,315
Be	0,09-0,00	0,0092	0,0151	0,00782	0,02594	3,247
B	23,95-0,20	0,1959	5,8229	2,48439	8,23979	1,252
Na	42,96-0,01	0,40	4,1696	3,87945	12,86667	3,316
Mg	0,91-0,50	0,88	0,8483	0,03462	0,11482	-3,283
Al	56,22-0,17	12,90	15,9907	5,63981	18,70512	1,488
K	9,12-0,07	3,12	3,1328	0,95721	3,17469	1,127
Ca	295,00-0,00	0,00	42,9936	29,90152	99,17213	2,224
Sc	0,03-0,03	0,0272	0,0272	0,00000	0,00000	0,00000
Ti	1,00-0,16	0,54	0,5707	0,08457	0,28048	0,210
V	9,48-0,03	0,511	1,8717	0,87358	2,89733	2,104
Cr	6,99-0,19	1,19	2,4178	0,79579	2,63933	0,769
Mn	8,30-,08	1,12	1,8420	0,68033	2,25640	2,751
Fe	4,02-4,02	4,01	4,0190	0,00000	0,00000	0,00000
Co	0,15-0,01	0,171	0,0387	0,01390	0,04609	1,857
Ni	0,13-0,13	0,128	0,1287	0,00000	0,00000	0,00000
Cu	52,06-4,53	34,627	36,5976	4,41572	14,64530	-0,913
Zn	362,5-34,8	261,78	227,6433	30,09715	99,82097	-0,665
Ga	7,20-0,01	0,0054	0,6591	0,65373	2,16817	3,317
As	0,25-0,07	0,253	0,2346	0,01663	0,05514	-3,258
Se	14114,58-0,6	1066,6	2340,1155	1231,00718	4082,78893	2,834
Rb	1,76-0,00	0,0037	0,3071	0,17554	0,58221	1,960
Sr	5,40-0,00	0,1504	1,4961	0,65927	2,18656	1,268
Rh	0,00-0,00	0,0042	0,0038	0,00037	0,00124	-3,317
Pd	0,08-,01	0,0144	0,0205	0,00608	0,02017	3,317
Ag	7,78-,01	0,0549	1,8075	0,83581	2,77206	1,570
Cd	0,70-,01	0,069	0,1740	0,06293	0,20872	1,869
Sn	54,40-0,14	5,392	9,3290	4,72255	15,66292	2,805
Sb	0,02-0,02	0,015	0,0156	0,00000	0,00000	0,00000
Cs	0,15-0,00	0,0088	0,0351	0,01563	0,05183	1,588
Ba	5,17-0,08	0,079	1,2012	0,51727	1,71559	1,586
Ce	0,40-0,03	0,135	0,1806	0,03999	0,13262	0,694
Au	50,63-0,54	0,543	5,5480	4,53009	15,02460	3,260
Hg	5,93-0,21	1,315	1,7150	0,53660	1,77968	1,645
Pb	22,38-0,37	5,02	7,6008	2,10282	6,97427	1,301
Bi	0,42-0,00	0,071	0,1376	0,04624	0,15336	0,896
Pt(194)	0,02-0,2	0,021	0,0217	0,00000	0,00000	0,00000
Pt(195)	4,00-0,35	1,500	1,7015	0,33179	1,10042	0,836
Pt(196)	0,02-0,01	0,016	0,0157	0,00027	0,00090	-3,317
Pt(198)	0,28-0,01	0,029	0,0675	0,02447	0,08116	2,008
U(234)	14,97-0,00	2,940	3,9435	1,43643	4,76410	1,333
U(235)	1,14-0,14	0,655	0,6447	0,07344	0,24357	0,001
U(238)	1,37-0,1	0,022	0,3375	0,15778	0,52330	1,477

High purity reagents were used for all preparations of the standard and sample solutions. The standard solutions used for the calibration procedures were prepared before use by dilution of the stock solution with 1 mol L^{-1} HNO_3. Stock solutions of diverse elements were prepared from the high purity compounds (99.9%, E. Merck, Darmstadt). A solution of 5 ml HNO_3 (99.9%, E. Merck) was used for accelerated samples.

A pH meter, WTW Inolab Level 3 Model glass-electrode was employed for measuring pH values in the aqueous phase. The water was purified in Millipore Synergy 185.

About ~3 g of hair were cut from the nape of the neck close to scalp, as strands ~1–3 cm long, with a pair of plastic scissors. The samples were directly stored in zip-mouthed polythene bags, duly labelled with relevant codes related to the donor's name, age, eating and drinking habits, social and general health status, all recorded and compiled on regular proforma at the time of sampling. The individual hair samples were washed with 5% (w/v) detergent solution and rinsed with plentiful distilled water to remove exogenous matter (Dombo-vari and Papp 1998). The samples were dried overnight at 50°C in an electric oven and cooled to room temperature in a desiccator containing silica gel as the desiccant. An accurately weighed portion (~1 g) of the hair sample was treated with 10.0 ml of concentrated (65%) nitric acid and heated at 80°C for 10 min. It was cooled to room temperature, followed by addition of 5.0 ml of perchloric acid with subsequent heating to a soft boil until white dense fumes evolved. Sample was cooled to room temperature and diluted to 50 ml with distilled water. The blank was prepared the same way but without the hair sample. All reagents used were of ultrahigh purity (certified >99.99%) procured from E-Merck. All statistical analyses were performed using computer program Excel X State (Microsoft Corp., Redmond, WA) and SPSS 13.0 software was used for all statistics. Data are expresssed as means ± standart deviations for our group.

III. RESULTS AND DISCUSSION

Concentrations of Cd, Cr, Cu, Mn, Mo, Ni, Pb, Se, Tl, Zn, …. were analyzed by ICP-MS in the scalp hair of male subjects from an urban area, three different quarters of Kayseri, Turkey. A questionnaire on personal data, nutritional habits, socio-economic, occupation and health status was completed by the subjects.

The main descriptive statistics of metal concentrations in scalp hair are summarized in Tables 2. Our results are in general agreement with values reported by other authors [57-68].

Our results were obtained for a relatively small group of subjects, and this fact precludes the assessment of normal ranges and firm general conclusions. Further studies need to be carried out in order to identify the greater number of analytical data in this area.

IV. ACKNOWLEDGMENT

The authors are grateful for the financial support of the Unit of the Scientific Research Project of Erciyes University (Project no.: **EÜBAP- FBA-09-959**).

---

[1]. *D.E.Nixon, T.P. Moyer* Routine clinical determination of lead, arsenic, cadmium and thallium in urine and whole blood by inductively coupled plasma mass spectrometry. Spectrochim Acta Part B Atom Spectrosc 1996;51:13–25.

[2]. *I.Rodushkin, F. O¨dman, S.Branth* Multielement analysis of whole blood by high resolution inductively coupled plasma mass spectro-metry. Fresenius' J Anal Chem 1999;364:338–46.

[3]. *I.Rodushkin, F. O¨ dman, R. Olofsson, M.D.Axelsson* Determination of 60 elements in whole blood by sector field inductively coupled plasma mass spectrometry. J Anal At Spectrom 2000;15:937–44.

[4]. *J.M.Marchante-Gayo´n, C.S.Muniz, J.Garcia, I.Alonso, A.Sanz-Medel* Multielemental trace analysis of biological materials using double focusing inductively coupled plasma mass spectrometry detection. Anal Chim Acta 1999;400:307–20.

[5]. *E. Barany, I.A.Bergdahl, A.Schu¨tz, S.Skerfving, A.Oskarsson* Inductively coupled plasma mass spectrometry for direct multi-element analysis of diluted human blood and serum. J Anal At Spectrom 1997;12:1005–9.

[6]. *B.Bocca, A.Alimonti, F.Petrucci, et al.* Quantification of trace elements by sector field inductively coupled plasma mass spectro-metry in urine, serum, blood and cerebrospinal fluid of patients with Parkinson's disease. Spectrochim Acta Part A Mol Spectrosc 2004;59: 559–66.

[7]. *A.Alimonti, F.Petrucci, F.Laurenti, P.Papoff, S.Caroli* Reference values for selected trace elements in serum of term newborns from the urban area of Rome. Clin Chim Acta 2000;292:163–73.

[8]. *C.S.Hsiung, J.D.Andrade, R.Costa, K.O. Ash* Minimizing spectral interferences in the quantitative multielement analysis of trace elements in biological fluids by inductively coupled plasma mass spectrometry. Clin Chem 1997;43:2303–11.

[9]. *L.Yu. S.R.Koirtyohann, M.L.Rueppel, A.K.Skipor, J.J.Jacobs* Simultaneous determination of aluminium, titanium and vanadium in serum by electrothermal vaporization-inductively coupled plasma mass spectrometry. J Anal At Spectrom 1997;12:69–74.

[10]. *C.Huang, D.Beauchemin* Direct multielement analysis of human serum by ICP-MS with on-line standard addition using flow injection. J Anal At Spectrom 2003;18:951–2.

[11]. *C.S.Muniz, J.M.Marchante-Gayo´n, J.I.Garcia Alonso, Sanz-Medel.* Accurate determination of

iron, copper and zinc in human serum by isotope dilution analysis using double focusing ICP-MS. J Anal At Spectrom 1999;14:1505–10.

[12]. *J.Begerow, M.Turfeld, L.Dunemann* New horizons in human biomonitoring of environmentally and occupationally relevant metals — sector field ICP-MS versus electrothermal AAS. J Anal At Spectrom 2000;15:347–52.

[13]. *P.Schramel, I.Wendler, J. Angerer* The determination of metals (antimony, bismuth, lead cadmium, mercury, palladium, platinum, tellurium, thallium, tin and tungsten) in urine samples by inductively coupled plasma mass spectrometry. Int Arch Occup Environ Health 1997;69:219–23.

[14]. *A.T.Townsend, K.A.Miller, S.McLean, S.Aldous* The determination of copper, zinc, cadmium and lead in urine by high resolution ICP-MS. J Anal At Spectrom 1998;13:1213–9.

[15]. *P.Schramel, I. Wendler* Antimony, lead, cadmium, platinum, mercury, tellurium, thallium, bismuth, tungsten, tin. In: Angerer J, Schaller KH, editors. Analyses of hazardous substances in biological materials, vol. 6. Weinheim' Wiley-VCH; 1999. p. 79–109.

[16]. *P.Schramel, L.Dunemann* Aluminum, chromium, cobalt copper, manganese, molybdenum, nickel, vanadium. In: Angerer J, Schaller KH, editors. Analyses of hazardous substances in biological materials, vol. 7. Weinheim' Wiley-VCH; 2001. p. 73–96.

[17]. *A.T. Towsend* The accurate determination of the first row transition metals in water, urine, plant, tissue and rock samples by sector field ICP-MS. J Anal At Spectrom 2000;15:307–14.

[18]. *G.Centineo, M.Montes Bayo´n, A. Sanz-Medel* Flow injection analysis with inductively coupled plasma time-of-flight mass spectrometry for the simultaneous determination of elements forming hydrides and its application to urine. J Anal At Spectrom 2000;15:1357–62.

[19]. *I. Rodushkin, D. Axelsson* Application of double focusing sector field ICP-MS for multielement characterization of human hair and nails: Part 1. Analytical methodology. Sci Total Environ 2000;250: 83–100.

[20]. *J.Yoshinaga, J.Shibata, M.Morita* Trace elements determined along single strands of hair by inductively coupled plasma mass spectro-metry. Clin Chem 1993;39:1650–5.

[21]. *P.D´Haese, M.M.Couttenye, L.V. Lamberts, et al.* Aluminum, iron, lead, cadmium, copper zinc, chromium, magnesium, strontium and calcium content in bone of end-stage renal failure patients. Clin Chem 1999; 45:1548–56.

[22]. *M.A.Vaughan, A.D.Baines, D.M. Templeton* Multielement analysis of biological samples by inductively coupled plasma mass spectrometry: II. Rapid survey method for profiling trace elements in body fluids. Clin Chem 1991;37:210–5.

[23]. *E.Sabbioni, C.Minoia, R.Pietra, S.Fortaner, M.Gallorini, A. Saltelli* Trace element reference values in tissues from inhabitants of the European Community: II. Examples of strategy adopted and trace element analysis of blood, lymph nodes and cerebrospinal fluid of Italian subjects. Sci Total Environ 1992;120:39-62.

[24]. *C.Minoia, E.Sabbioni, P.Apostoli, et al.* Trace element reference values in tissues from inhabitants of the European Community: I. A study of 46 elements in urine blood and serum of italian subjects. Sci Total Environ 1990;95:89-105.

[25]. *M.Rukgauer, J.Klein, J.D. Kruse-Jarres* Reference values for the trace elements copper, manganese, selenium and zinc in serum/plasma of children, adolescents and adults. J Trace Elem Med Biol 1997;11: 92-98.

[26]. *P.Heitland, H.D. Koster* Fast, simple and reliable routine determination of 23 elements in urine by ICP-MS. J Anal At Spectrom 2004;19: 1552-8.

[27]. *V.Spevackova, M.Cejchanova, M.Cerna, V.Spevacek, J.Sm´ıd, B. Benes* Population based biomonitoring in the Czech Republic: urinary arsenic. J Environ Monit 2002;4:796-8.

[28]. *A.H.Milton, Z.Hasan, A.Rahman, M.Rahman* Chronic arsenic poisoning and respiratory effects in Bangladesh. J Occup Health 2001;43:136-40.

[29]. *J.L.Chen, Y.L.Guo, P.J.Tsai, L.F. Su* Use of inhalable Cr(VI) exposures to characterize urinary chromium concentrations in plating industry workers. J Occup Health 2002;44:46-52.

[30]. *T.Eikmann, V.Makropoulus, S.Eikmann, T.Krieger* Cross-sectional epidemiological study on chromium, manganese mercury nickel, selenium excretion in urine of populations in areas with with different air pollution. Fresenius Environ Bull 1992;1:706-11.

[31]. *M.Kiilunen, J.Jarvisalo, O.Makitie, A.Aitio* Analysis, storage stability and reference values for urinary chromium and nickel. Int Arch Occup Environ Health 1987;59:43-50. [32] Herber RFM. Review of trace element concentrations in biological specimens according to the TRACY protocol. Int Arch Occup Environ Health 1999;72:279-83.

[32]. *V.Iyengar, J. Woittiez* Trace elements in human clinical specimen: evaluation of literatire data to identify reference values. Clin Chem 1988;34:474-81.

[33]. *B.Gammelgaard, O.Jons* Determination of selenite and selenate in human urine by ion chromatography and inductively coupled plasma mass spectrometry. J Anal At Spectrom 2000;15:945-9.

[34]. *B.S.Iversen, C.Menne´, M.A.White, J.Kristiansen, J.Molin Christensen, E. Sabbioni* Inductively coupled plasma mass spectrometric determination of molybdenum in urine from a Danish population. Analyst 1998;123:81– 5.

[35]. *C.Krause, W.Babisch, K., Becker et al.* Umwelt-Survey 1990/92 Band 1a: Studienbeschreibung und Human-Biomonitoring. Umweltbundesamt, ed., 1996.

[36]. *K.Becker, S.Kaus, C.Krause, et al*. Umwelt-Survey 1998 Band III: human-biomonitoring. Umweltbundesamt, ed., Berlin, 2002.

[37]. *K.Becker, C.Schulz, S.Kaus, M.Seiwert, B.Seifert* German Environmental Survey 1998 (GerES III): environmental pollutants in the urine of the German population. Int J Hyg Environ Health 2003; 206:15–24.

[38]. *M.Wilhelm, U.Ewers, C.Schulz* Revised and new reference values for some trace elements in blood and urine for human biomonitoring in environmental medicine. Int J Hyg Environ Health 2004;207:69– 73.

[39]. Second national report on human exposure to environmental chemicals. NCEH Pub, vol. 02-0716. Atlanta, Georgia' Department of Health and Human Services; 2003.

[40]. *A.Alimonti, F.Petrucci, M.Krachler, B.Bocca, S.Caroli* Reference values for chromium, nickel and vanadium in urine of youngsters from the urban area of Rome. J Environ Monit 2000;2:351 – 4.

[41]. *K.E.Jarvis, A.L.Gray, R.S.Houk* 1992. Handbook of inductively coupled plasma mass spectrometry. London: Blackie Academic&Professional.

[42]. *U.Giessmann, U.Greb* 1994. High resolution ICP-MS—A new concept for elemental mass spectrometry. Fresenius J Anal Chem 350:186–193.

[43]. *N.H.Bings* 2005. Plasma time-of-flight mass spectrometry as a detector for short transient signals in elemental analysis. Anal Bioanal Chem 382: 887–890.

[44]. *H.E .Evans, J.J.Giglio* 1993. Interferences in inductively coupled plasma mass spectrometry—A review. J Anal Atom Spectrom 8:18.

[45]. *R.F.J Dams, J.Goossens, L.Moens* 1995. Spectral and non-spectral interferences in inductively coupled plasma mass-spectrometry. Mikrochim Acta 119:286.

[46]. *F.Vanhaecke, S.Saverwyns, G.de Wannemacker L.Moens, R.Dams* 2000. Comparison of the application of higher mass resolution and cool plasma conditions to avoid spectral interferences in Cr(III)/Cr(VI) speciation by means of high-performance liquid chromatographyinductively coupled plasma mass spectrometry. Anal Chim Acta 419: 55–64.

[47]. *I.Feldmann, N.Jakubowski, C.Thomas, D.Struewer* 1999. Application of a hexapole collision and reaction cell in ICP-MS. Part II: Analytical figures of merit and first applications. Fresenius J Anal Chem 365:422–428.

[48]. *N.Nonose, M.Kubota* 2001. Non-spectral and spectral interferences in inductively coupled plasma high-resolution mass spectrometry. Part I. Optical characteristics of micro-plasmas observed just behind the sampler and the skimmer in inductively coupled plasma high resolution mass spectrometry. J Anal Atom Spectrom 16:551–559.

[49]. *C.S.Hsiung, J.D.Andrade, R.Costa, O.K.Ash*. 1997. Minimizing interferences in the quantitative multielement analysis of trace elements in biological fluids by inductively coupled plasma mass spectrometry. Clin Chem 43:2303–2311.

[50]. *E.E.M.Brouwers, M.M.Tibben, H.Rosing, J.H.M.Schellens, J.H.Beijnen*. 2007c. Determination of ruthenium originating from the investigational anticancer drug NAMI-A in human plasma ultrafiltrate, plasma, and urine by inductively coupled plasma mass spectrometry. Rapid Commun Mass Spectrom 21:1521–1530.

[51]. *L.Lustig, S.Zang, B.Michalke, P.Schramel, W.Beck* 1997. Platinum determination in nutrient plants by inductively coupled plasma mass spectrometry with special respect to the hafnium oxide interference. Fresenius J Anal Chem 357:1157–1163.

[52]. *E.Rudolph, S.Hann, G.Stingeder, C.Reiter* 2005. Ultra-trace analysis of platinum in human tissue samples. Anal Bioanal Chem 382:1500–1506.

[53]. I.Rodushkin, E.Engstrom, A.Stenberg, D.C.Baxter. 2004. Determination of low-abundance elements at ultra-trace levels in urine and serum by inductively coupled plasma-sector field mass spectrometry. Anal Bioanal Chem 380:247–257.

[54]. *S.Hann, G.Koellensperger, K.Kanitsar, G.Stingeder, M.Brunner, B.Erovic, M.Muller, C.Reiter* 2003a. Platinum determination by inductively coupled plasma-sector field mass spectrometry (ICP-SFMS) in different matrices relevant to human biomonitoring. Anal Bioanal Chem 376: 198–204.

[55]. *R.Thomas* 2002. A beginner's guide to ICP-MS: Part XII—A review of interferences. Spectroscopy 17:24–31.

[56]. *H.Rosing, W.Y.Man, E.Doyle, A.Bult, J.H.Beijnen* 2000. Bioanalytical liquid chromatography method validation: A review of current practices and procedures. J Liq Chrom Rel Technol 23:329–354.

[57]. *S.Caroli, O.Senofonte, N.Violante, L.For-Narelli, A.Powar* 1992. Assessment of reference values for elements in hair of urban normal subjects. Microchem J. 46, 174.

[58]. *D.E.Ryan, J.Holybecner* 1978. Stuart D.E. Trace elements in scalp hair of persons with multiple sclerosis and of normal individuals. Clin Chem. 24, 1996,

[59]. *A.A.E.Wibowo, R.F.M. Herber, H.A.Das, N.Ro-Eleveld, R.L.Zielhuis*, 1986. Levels of metals in hair of young children as an indicator of environmental pollution. Environ Res. 40, 346.

[60]. *H.H.Skypeck, B.J.Joseph*, 1983. Chemical Toxicology and Clinical Chemistry of Metals, edited by Brown SS, Savory J, London Academic Press, London, pp. 159-163.

[61]. *H.Merzenich, A.Hartwig, W.Ahrens, D.Bey-Ersmann, R.Schlepegrell, M.Scholze, J.Timm, K.H.Jockel*, 2001. Biomonitoring on carcinogenic metals and oxidative DNA damage in a cross-sectional study. Cancer Epidemiol Biomarkers Prev. 10, 515.

[62]. *C.P.Case, L.Ellis, J.C.Turner*, 2001. Fairman B. Development of a routine method for the determination of trace metals in whole blood by magnetic sector inductively coupled plasma mass spectrometry with particular relevance to patients

with total hip and knee arthroplasty. Clin Chem. 47, 275.

[63]. *J.F.Maurice, G.Wibetoe, K.E.Sjastad*, 2002. Longitudinal distribution of thallium in human scalp hair determined by isotope dilution electrothermal vaporization inductively coupled plasma mass spectrometry. J Anal At Spectrom 17, 485.

[64]. A.Taylor, 1986. Usefulness of measurements of trace elements in hair. Ann Clin Biochem 23, 364.

[65]. *B.Seifert, K.Becker, D.Helm, C.Krause, C.Schulz, M.Seiwert*, 2000. The German Environmental Survey 1990/1992: reference dust, drinking water and indoor air. J Expo Anal Environ Epidemiol 10, 552.

[66]. *N.Miekeley, L.M.D.Forteas, C.L.P.Da Silveira, M.B.Lima*, 2001. Elemental anomalies in hair as indicators of endocrinologic pathologies and deficiencies in calcium and bone metabolism. J Trace Elem Med Biol. 15, 46. Report WIOŚ Cracow. Poland, unpublished data, 2001.

[67]. *I.Rodushkin, M.D.Axelsson*, 2000. Application of double focusing sector field ICP-MS for multielemental characterization of human hair and nails. Part II. A study of the inhabitants of northern Sweden. Sci Total Environ. 262, 21.

CHARACTERIZATION OF MBE GROWN InGaAs/GaAs QUANTUM WELL SOLAR CELLS (QWSCs)

TARIK ASAR[1,*], BARIŞ KINACI[1], UMUT AYDEMİR[1], TOFIG MAMMADOV[1,2], SÜLEYMAN ÖZÇELİK[1]

[1]Physics Department, Faculty of Arts and Sciences, Gazi University, 06500, Teknikokullar, Ankara, TURKEY

** trkasar@gazi.edu.tr*

[2]National Academy of Science, Institute of Physics, Baku, Azerbaijan

In this study, we have reported structural and electrical characterization of InGaAs/GaAs quantum well solar cells (QWSCs) grown by Molecular Beam Epitaxy (MBE) technique. Structural and electrical properties of QWSCs' were carried out with High Resolution X-Ray Diffraction (HRXRD) and Current-Voltage (I-V) measurements, respectively. The design of the cells was presented together with determining values of the forward bias dark current density, efficiency (η), filling factor (FF), open-circuit voltage (V), short circuit current (I) and light response. Calculating cell efficiencies under AM 0 illumination and standard air mass (AM) 1.5 of the cells were discussed. Growth conditions of the structures and interface effect on the efficiency of the solar cells were also discussed.

I. INTRODUCTION

The improvement of single-junction solar cell performance and also the purpose of different regions of solar spectrum's absorption require new solar cell device designs. One of these ideas is that of multiple quantum wells (MQW) solar cells, in which a number of quantum wells are combined in the cell [1]. In such an arrangement, the intrinsic (i)-region of the positive-intrinsic-negative (p-i-n) solar cell structure consists of a number of wells from semiconductor of a lower energy gap than the barrier, p and n regions material.

Thus, longer wavelength light can be absorbed in the wells, which contributes to the photogenerated current [2]. Specially, the usage of the GaAs p-i-n structures in photovoltaic applications has received a lot of interest during the last decade due to the high efficiency of the cells [3-6]. Using electrical characterization techniques such as admittance spectroscopy and current voltage measurements, allow the identification of the diode performance in the particular i-region width [7].

In this work we have demonstrated that the efficiencies of the quantum well solar cells (QWSCs) were improved by thermal annealing. The InGaAs/GaAs QWSC structure was grown using solid source V80H-MBE system. The sample was cut into two pieces and one of them was annealed in rapid thermal annealing (RTA) system. The solar cells (as-deposited and annealed) were fabricated on these samples. The structural properties of the samples were performed with evaluations HRXRD measurements. Some electrical parameters such as efficiency and filling factor of the cells were also discussed using current-voltage (I-V) measurements.

II. EXPERIMENTAL PROCEDURES

Firstly, InGaAs quantum well solar cell (QWSC) was grown on Zn-doped (111) p-GaAs substrate by solid-source molecular beam epitaxy (MBE) system. To produce In and Ga beams was used conventional effusion cells with their elemental source. A cracker cell was used to obtain As_2 beam. Before the growth the GaAs substrate cleaning was done. After the thermally oxide desorption under As_2 flux at 670 C^o in deposition chamber, a 0.3 μm thick Be doped n-GaAs buffer layer was grown to trap impurities that may diffuse from the substrate with 1μm/h growth rate at 660 ^oC. After the buffer layer 7 nm thick i-InGaAs QW and 70 nm thick i-GaAs barrier layers were grown. This step was repeated 8 times to complete the growth of active region. After then 7 nm thick i-InGaAs QW and 50 nm thick n-GaAs layers were grown. During the growth, the grown surface was observed from reflection high energy electron diffraction (RHEED) system.

The schematic diagram of the grown sample is given in Figure 1. After the growth the sample was cut into two 1cm x 1cm square pieces. One of these pieces was annealed at 610 ^oC in N_2 atmosphere. After this process the high resolution x-ray diffraction (HRXRD) measurement of the samples were carried out on a D-8 Bruker high-resolution diffractometer by using $CuK\alpha_1$ (1.5406 Å) radiation, a prodded mirror, and a 4-bounce Ge (220) symmetric monochromator, with the Si calibration sample; its best resolution was 16 arcsec. After than to perform electrical characterization the ohmic contacts were formed. (Before the ohmic contacts the samples was cleaned in ultrasonic bath using acetone, methanol, and de-ionized (DI) water.) To form back side metallization the whole side was coated by Au with 1500 Å thickness in thermal evaporation system at 400 $^\circ C$. To form upper metallization firstly 1500 Å thickness, 1 mm wide Au grids, after than the 1500 Å thickness, 2 mm wide Au collecting grid was evaporated at 370 $^\circ C$. After these metallization procedures to form ohmic contacts the samples was annealed at 350 $^\circ C$ for 25 s.

The room temperature current voltage (I-V) measurements were performed using Keithley 2400 programmable constant current source and Keithley 614 electrometer under illumination from a NewPort 250-W solar simulator with AM1.5G filters. A Newport 818T-10 thermopile detector is used to calibrate the light intensity.

All measurements were carried out with the help of a microcomputer through an IEEE-488 ac/dc converter card.The thicknesses of the films were measured using a Dektak profilometer.

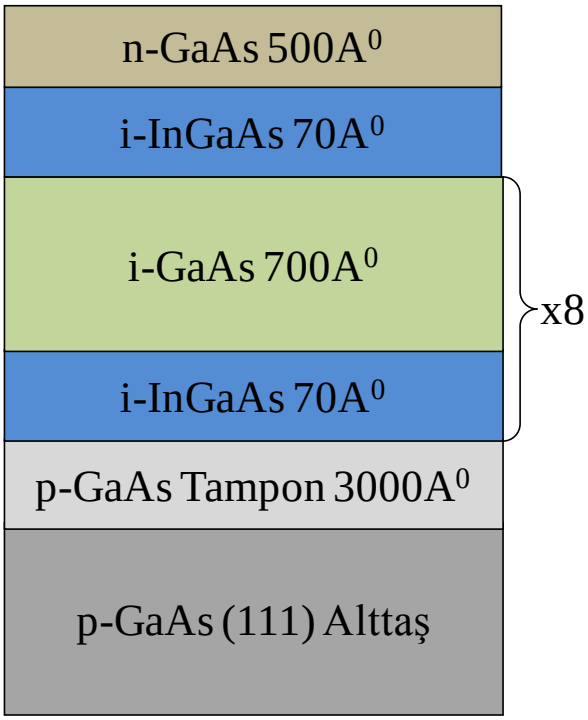

Fig.1. The schematic diagram of the MBE grown InGaAs/GaAs QWSC

III. RESULTS AND DISCUSSION

The quantum well solar cell's (QWSC's) structural properties were carried out with HRXRD measurements for observing crystal quality. The measurements were performed by Bruker D8-Discover diffractometer. Rocking curves of the as deposited (20 ^{o}C) and annealed (610 ^{o}C) samples were obtained from $\varpi/2\theta$ scan (where ϖ and 2θ are the angles of the sample and detector relative to the incident X-ray beam, respectively) and given in Figure 2. In previous paper, the $\varpi/2\theta$ scans were analyzed to obtain structural properties and the results were compared each other [8].

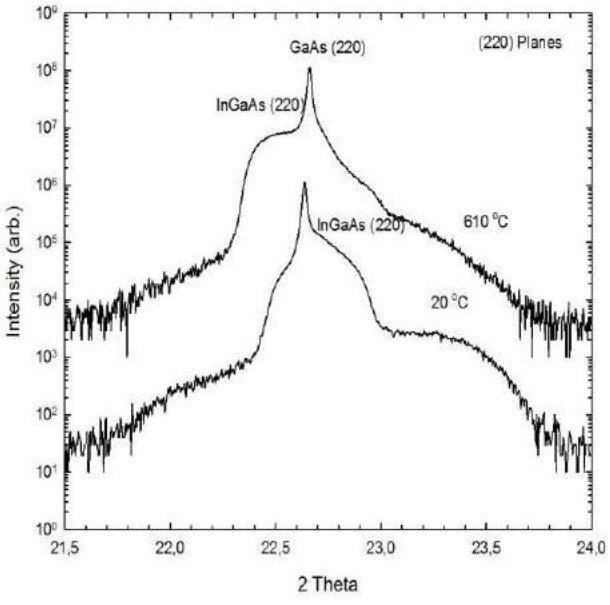

Fig. 2. The $\varpi/2\theta$ scans of InGaAs/GaAs QWSCs.

The information on crystal imperfections like point defects and dislocations and the interactions can also deduce from the sizes and positions of the ω/2θ peaks, as well as the changes of lattice parameters of the unit cell in a film, caused by misfit strain relaxation [8].

The photovoltaic forward bias dark and under AM1.5G illumination current-voltage (I-V) characteristics of the InGaAs/GaAs solar cells with Au contact are shown in Figure 3.

It can be clearly seen from the figure that the open-circuit voltage (V_{oc}) and short-circuit current (I_{sc}) increase with annealing procedure. The device parameters for this cell are given in Table 1 where FF and η are filling factor and energy conversion efficiency, respectively.

Two important parameters which were strongly affected with annealing process are FF and I_{sc} [9,10] and obtained using:

$$FF = \frac{I_{\max}.V_{\max}}{I_{sc}.V_{oc}} \quad (1)$$

and

$$\eta = \frac{P_{out}}{P_{in}} = \frac{I_{\max}.V_{\max}}{P_{in}} x100 \quad (2)$$

where I_{max}, V_{max}, P_{out} and P_{in} are the maximum current, maximum voltage, output power and input power, respectively.

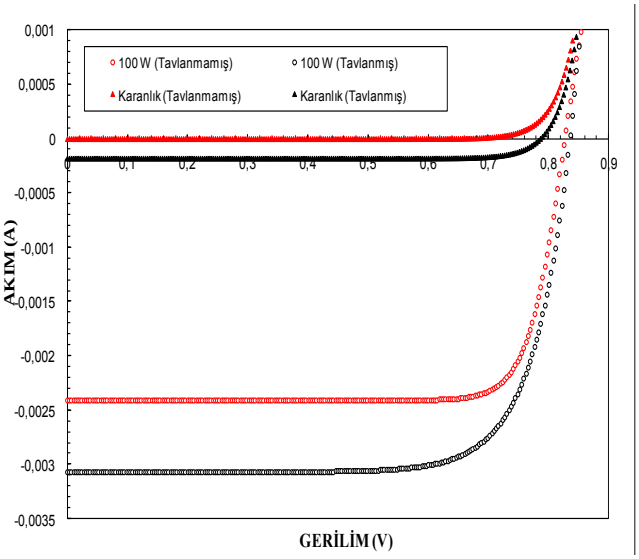

Fig.3. The photovoltaic forward bias dark and under AM1.5G illumination current-voltage characteristics of the as deposited and annealed InGaAs/GaAs solar cells.

The obtained electrical characterization parameters for as-deposited and annealed samples are given in Table 1 [11].

Table 1. The obtained electrical characterization parameters.

Cell	I_{sc} (mA)	V_{oc} (V)	I_{max} (mA)	V_{max} (V)	FF	η
As deposited	2,41	0,82	2,31	0,71	0,83	0,14
Annealed	3,07	0,83	2,82	0,68	0,75	0,16

For the cell made from annealed sample, it was observed that while the short-circuit current and energy conversion efficiency increase, the filling factor decrease. The low fill factor may be attributed to series resistance in the contacts, which can be lowered by contact redesign. The interfacial resistance of the InGaAs/GaAs sample used as the solar cell was only around 10% of the total series resistance that was estimated from the photovoltaic I-V characteristics. The V_{oc} of the as-deposited cell and annealed cell were 0.83 and 0.82V, respectively. Annealing procedure made no change on the V_{oc} of InGaAs/GaAs cells, therefore, the V_{oc} values for as-deposited and annealed samples were found approximately equal [11]. While the metallization does not degrade the V_{oc}, the generated defects that act as recombination centers reduce it [12,13]. Also, the metal-semiconductor interface has no significant carrier recombination rate to reduce the V_{oc}.

IV. CONCLUSIONS

The InGaAs/GaAs quantum well solar cell (QWSC) structure was grown by solid source V80H-MBE system. The sample was cut into two pieces and one of the pieces was annealed to compare the annealing effect on the structural and electrical parameters of solar cells.

The high resolution XRD results show that the annealed samples have improved crystal structure to make better solar cell then as-deposited sample. Also, we can say that attributed in (Ref. 8), if new solar cell structures are growth in symmetric planes, we can produce a quality device which is not depend on the change in temperature.

The ohmic contacts were formed to make electrical characterization. The photovoltaic forward bias dark and under AM1.5G illumination current-voltage (I-V) characteristics of the InGaAs/GaAs QWSCs show that the open-circuit voltage (V_{oc}), short-circuit current (I_{sc}) and energy conversion efficiency (η) increase while the filling factor decrease with annealing procedure. The lowering of the filling factor may be attributed to series resistance in the contacts, which can be lowered by contact redesign. In spite of this result, energy conversion efficiency (η) increased from 14% to 16% [11].

So, we can clearly say that QWSCs' conversion efficiencies (η) increased as 2% with annealed.

V. ACKNOWLEDGEMENTS:

This work is supported by the State of Planning Organization of Turkey under Grant no. 2001K120590.

[1]. *K.W.J. Barnham and G. Duggan*, J. Appl. Phys, 67 (1990) 3490.

[2]. *E. Aperathitis, C. G. Scott, D. Sands, V.Foukaraki, Z. Hatzopoulos, P. Panayotatos*, Materials Science and Engineering B, 51 (1998) 85.

[3]. *E. Aperathitis, A. C. Varonides, C. G. Scott, D.Sand, V. Foukaraki, M. Androulidaki, Z.Hatzopoulos, P. Panayotatos*, Solar Energy Materials and Solar Cells, 70 (1) (2001) 49.

[4]. *B. Reinicke, H. Eschrich, H.G. Wagemann*, 11th E.C. Photovoltaic Solar Energy Conference Proceedings, Switzerland, 1992.

[5]. *J.J. Liou*, Solar Energy Mater. Solar Cells, 29 (1993) 261.

[6]. *D.P. Rancour, M.R. Melloch, R.F. Pierret, M.S.Lundstrom, M.E. Klausmeier-Brown, C.S. Kyono*, J. Appl. Phys., 62 (4) (1987) 1539.

[7]. *N. Konofaos, E. K. Evangelou, F. Scholz, K.Zieger, E. Aperathitis*, Materials Science and Engineering B, 80 (1-3) (2001) 152.

[8]. *T. Asar, B. Sarıkavak, M. Kemal Öztürk, T.Mammadov, S.Özçelik*, Journal of Optoelectronıcs And Advanced Materials, 11 (11) (2009) 1627.

[9]. *A. U. Ebong, S. H. Lee, W. Warta, C. B. Honsberg, S. R. Wenham*, Solar Energy Materials&Solar Cells, 45 (1997) 283.

[10]. *G. Aberle, S. C. Robinson, A. Wang, J. Zhao, S. R. Wenham, M. A. Green*, Proc. Photovoltaics, 1 (1993) 133.

[11]. *T. Asar*, "The Fabrication of GaInP and InGaAs Quantum Well Solar Cells (QWSC)", M. Sc. Thesis, Gazi University Institute Of Science And Technology, (2009).

[12]. *O. Tuzun, S. Oktik, S. Altindal, T.S. Mammadov*, Thin Solid Films, 511 (2006) 258.

[13]. *T. Sasaki, K. Arafune, H.S. Lee, N.J. Ekins-Daukes, S. Tanaka,Y. Ohshita, M. Yamaguchi*, Physica B , 37 (2006) 626

CONTROL AND MEASUREMENT OF SPATIAL COHERENCE OF A LASER BEAM

S.AHMADI KANDJANI, R.ABAZARI
Photonics Group, Research Institute for Applied Physics and Astronomy,
Tabriz University, Tabriz, Iran
s_ahmadi@tabrizu.ac.ir
r.abazari87@ms.tabrizu.ac.ir

In this experimental work a method for variation of complex degree of spatial coherence of a monochromatic light field is introduced. The monochromatic light field which is partially coherent is produced by passing a focused laser beam through a rotating ground glass plate. By increasing the distance between rotating ground glass and focal point of the laser beam, i.e. increasing the illuminated area on the rotating ground glass, we could decrease the complex degree of spatial coherence.

I. INTRODUCTION

The fluctuations of electromagnetic fields in nature are so fast that cannot be observed directly. The most evident consequence of correlation between light fields is the interference. The complex degree of spatial coherence is the normalized form of correlation function of the light field at two points [1], which is determined by interferogram of different regions of light field [2]. Having equal intensities in both apertures of a Young interferometer, according to Van Cittert-Zernike theorem, degree of coherence is obtained through the visibility of the interference fringes [1]. In order to measure the degree of coherence of laser beam, different methods have been used, e.g. Tompson-Wolf scheme of Young experiment, Zernike scheme of Young experiment, Michelson stellar interferometer, Henbry-Brown-Twiss method, Wollaston prism, Savart polariscope [3,4], performing Young experiment with two optical fibers [5], and using a mask with multiple apertures [6].

The most widely used method for controlling of spatial degree of coherence of laser beam is to pass it through rotating ground glass [7]. It should be mentioned that by applying a voltage to specific nematic liquid crystal, the same result can be obtained [8].

II. THEORY

Usually, in order to measure the complex degree of spatial coherence, one may analyze several interferogram of a pair of aperture with different separations. However, recent researches show that just by using one interferogram obtained from a mask with multiple apertures, the same result can be obtained [6].

In order to study a partially coherent quasi-monochromatic beam with a complex degree of spatial coherence with a wavelength of λ, we use a mask of N identically circular apertures to sample the light field. We consider that the area of apertures is much smaller than the coherence area. Far field interferogram generated by the mask of Eq.(1), can be obtained by placing a convergent lens of focal distance f just behind the mask. The geometry of the apertures is given by the circle function $h(\rho) = circ(\rho / a)$, where a is the radius. Under this condition we can say that the light field within each aperture does not change. Let us write the sampled light field as:

$$U(\rho) = h(\rho) \otimes \sum_{n=1}^{N} V(\rho_n)\, \delta(\rho - \rho_n). \qquad (1)$$

where $V(\rho_n)$ is the complex amplitude of the light field within the nth-aperture, $\delta(\rho - \rho_n)$ is the Dirac's delta function that places the center of the nth aperture at ρ_n in the mask plane (with coordinates $\rho = (\xi, \eta)$). The symbol $\otimes$ represents the convolution operation. The far field interferogram yielded by the multiple aperture array placed in front of a lens of focal distance f is registered at the focal plane of the lens (with coordinates $r = (x, y)$). The intensity distribution of the far field interferogram is given by

$$I(\upsilon\lambda f) = \frac{|H(\upsilon)|^2}{\lambda^2 f^2}\left[\sum_{n=1}^{N} I_n + \sum_{n=m+1}^{N}\sum_{n=1}^{N-1}\sqrt{I_n I_m}\left\{\mu_{nm}\, exp(-i2\pi\upsilon.(\rho_n - \rho_m)) + \mu_{nm}^{*} exp(i2\pi\upsilon.(\rho_n - \rho_m))\right\}\right] \qquad (2)$$

where λ is wavelength and $\upsilon = r/\lambda f$ is the spatial frequency coordinates. $H(\upsilon) = \pi a^2\, jinc(2\pi a\upsilon)$ is the Fourier transform of $h(\rho)$, and $jinc(2\pi a\upsilon) = 2J_1(2\pi a\upsilon)/2\pi a\upsilon$ with J_1 the Bessel function of the first kind and order 1. Eq. (2) shows that the intensity distribution in the interferogram depends on two factors: the intensity I_n from each aperture and the complex degree of spatial coherence μ_{nm} that corresponds to the aperture pair(n, m). The Fourier transform of Eq. (2) becomes:

$$\tilde{I}(\rho) = \Lambda(\rho) \otimes \left[\sum_{n=1}^{N} I_n \delta(\rho) + \sum_{n=m+1}^{N}\sum_{n=1}^{N-1}\sqrt{I_n I_m}\left\{\mu_{nm}\, \delta(\rho - (\rho_n - \rho_m)) + \mu_{nm}^{*}\delta(\rho + (\rho_n - \rho_m))\right\}\right]. \qquad (3)$$

Eq. (3) describes a symmetrical distribution of peaks whose shapes are determined by $\Lambda(\rho)$ which is the autocorrelation function of $h(\rho)$. The separation vector $(\rho_n - \rho_m)$ of the aperture pair (n, m) locates the peaks in the Fourier spectrum. Therefore, for the most general situation, we need a mask with a non-redundant array of apertures [6]. Each peak in the Fourier spectrum is associated to just one aperture pair. A class of aperture pairs is defined as the set of aperture pairs with the same separation vector. The Fourier spectrum of the

interferogram described by Eq. (3) is a symmetrical and conjugate distribution of peaks with respect to the origin. Therefore, for measuring the complex degree of spatial coherence we omit the peaks of the spectrum given by $\mu^*_{nm}\,\delta(\rho+(\rho_n-\rho_m))$. If we number the peaks of the right side as $j = 1,2,3,\ldots$, let $\mu_j = |\mu_j| exp\{i\alpha_j\}$ be the complex degree of spatial coherence corresponding to jth peak and let $c_j = |c_j| exp\{i\phi_j\}$ be the maximum value of the jth peak. Let us define $S_0 = \sum_{n=1}^{N} I_n$ and $S_j = \sum_{n=m+1}^{N}\sum_{m=1}^{N}\sqrt{I_n I_m}$. Then from Eq. (3) we have:

$$|\mu_j| = \frac{|c_j|}{|c_0|}\frac{S_0}{S_j}, \quad (4)$$

$$\alpha_j = \phi_j \quad (5)$$

where $|c_0|$ the modulus of the central peak and $|c_j|$ the modulus of the jth peak.

Following Eq. (4) to find the magnitude of the complex degree of spatial coherence from a class of apertures it is necessary to know the intensity of the field inside the apertures that compound the class. Having 27 apertures with a radius of $b = 0.5\,mm$ and separation between their centers 2mm, one measures the intensity from each of them, one by one, for all the apertures in sequence. Considering the conservation of energy between the screen plane and the interferogram plane we take $I_n = \frac{1}{\pi b^2}\int_{Airy} I(x,y)\,dx\,dy$.

III. EXPERIMENT

In this experimental work, we used He-Ne laser beam ($\lambda = 632.8\,nm$) in the fundamental mode TM_{00} and after passing it through neutral density filters (NDF), we focused it on a rotating ground glass (RGG) by means of a convergent lens L_1 of the focal distance $f_1 = 50\,mm$. The L_1 lens is placed on a mobile stage in order to be able to vary the area of illuminated region on the RGG through varying of the distance between RGG and the focal point of L_1 lens. The light field that diverges from the RGG, arrives to a mask with multiple apertures (MMA) is now partially coherent with a Gaussian intensity profile. The MMA is placed at the distance $850 \pm 1\,mm$ from the RGG and behind the MMA a couple of convergent lenses L_2 with the focal distance of $300 \pm 1mm$ (spaced $30 \pm 1\,mm$) are placed at $36 \pm 1\,mm$. The far field interferogram is observed at a plane at the distance $182 \pm 1\,mm$ from L_2. In order to avoid the moiré effect that can be formed between the interference fringes and the pixel array of the CCD camera we insert an imaging lens L_3 of focal distance $30\,mm$. So the intrferogram magnified and imaged by L_3 onto the input plane of a CCD camera ($^1/_4$ *in.* format, pixels 640×480 ($H \times V$), monochrome). The complex degree of spatial coherence of the light field at the mask plane according to the theorem on Van Cittert-Zernike [1], is given by

$$\mu_{nm} = \exp\left(-i\frac{\pi}{\lambda z}(\rho_n^2-\rho_m^2)\right)\exp\left(-\frac{(\rho_n-\rho_m)^2}{w^2}\right), \quad (6)$$

where $w = \frac{\lambda z}{\pi w_0}$ is the size of the coherence area and w_0 is the spot size at the beam waist onto the RGG; z is the distance from RGG to MMA. Since the light field at the mask plane has axial symmetry, it is enough to measure the complex degree of spatial coherence along one direction. The mask is an opaque circular screen with four circular holes along the horizontal direction (Fig.2),each one has a radius of $a = 0.4\,mm$. The apertures are labeled as {1,2,3,4} and their positions with respect to the intersection of the optical axis with the plane mask are $\xi = \{-7.5, -6.0, +3.0, +7.5\}mm$, respectively. This distribution of the apertures yields 6 classes of aperture pairs all composed by only one aperture pair. The aperture pairs generated by this screen are shown in Table1.

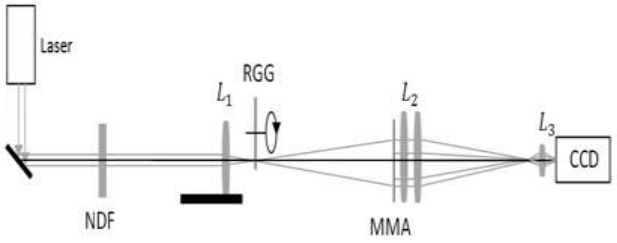

Fig.1. Experimental set-up to measure the complex degree of spatial coherence.

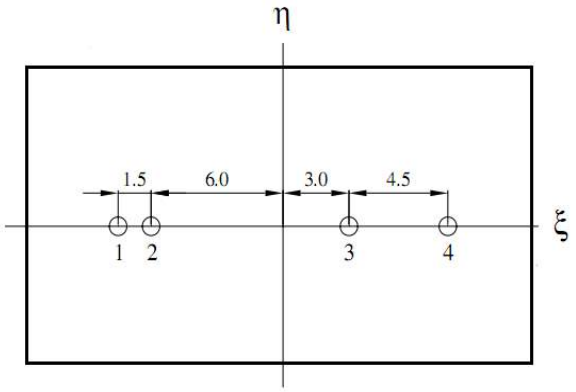

Fig.2. Mask with multiple apertures.

Table.1 Classes of aperture pair yielded by the mask of Fig.2

j −th class	Pair $\{n, m\}$	Separation d_j(mm)
1	{1,2}	1.5
2	{3,4}	4.5
3	{2,3}	9.0
4	{1,3}	10.5
5	{2,4}	13.5
6	{1,4}	15.0

We obtain the far field interfreogram which is generated by this mask and it's profile along the horizontal direction (x) crosses the optical axis. Then we analyze the fourier spectrum of the interferogram along the horizontal direction. For instance, for $l = 0\,mm$ (is the distance between focal length of the lens and RGG)the interferogram generated by the multiple mask, it's profile along the horizontal direction and the Fourier transform of that are shown in Figs.3,4,5 , respectively.

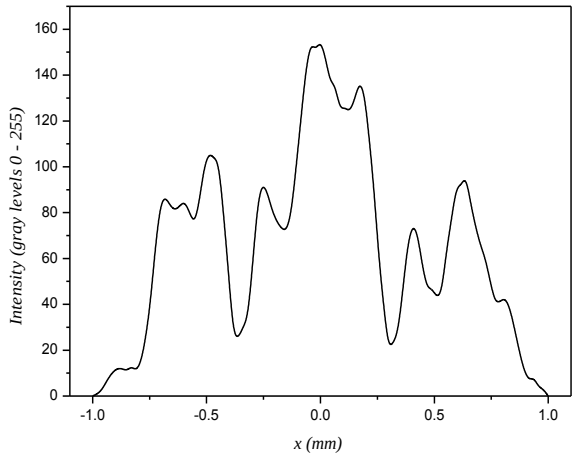

Fig.3. Profile of the interferogram for $l = 0$ along the horizontal direction.

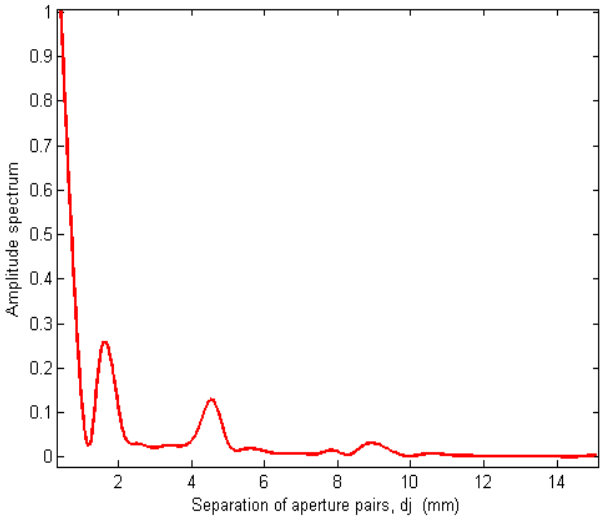

Fig.4. Right side of the amplitude of the Fourier spectrum normalized to the height of the central peak. From the 6 classes of aperture pairs generated by the mask of Fig.2.

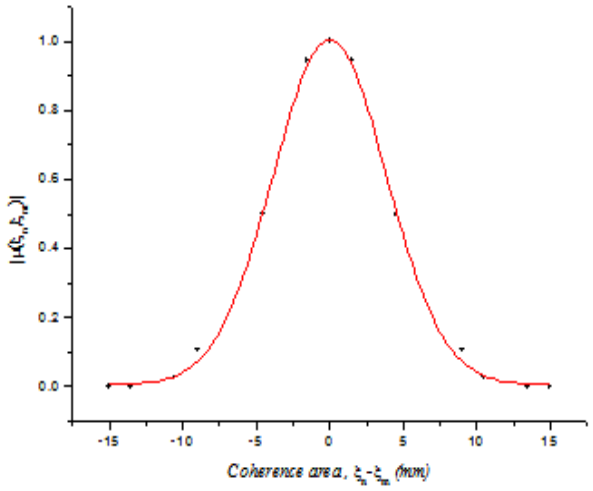

Fig.5. Modulus of the complex degree of spatial coherence vs. coherence area.

The intensity distribution on the mask plane can be obtained by a $27-$aperture mask with a aperture radius of $b = 0.5mm$ and separation of $2.0mm$ between them.

$$I(\rho) = I_0 \exp(-\frac{\rho^2}{h^2}) \quad (7)$$

where I_0 is in the scale 0–255.

From the above equation, it is possible to calculate the intensities in the place of apertures and S_0, S_j for them are obtainable.

Using Eq.4 the modulus of the complex degree of spatial coherence for each of the classes is obtained. Then experimental data is fitted and the values of complex degree of spatial coherence for the under consideration light field is calculated.

$$|\mu(\xi_n, \xi_m)| = \exp(-\frac{(\xi_n, \xi_m)^2}{k^2}) \quad (8)$$

where ξ_n, ξ_m are now the coordinates of any point pairs at the mask plane. Fig.6 shows the fitting curve of modulus of the complex degree of spatial coherence, in terms of coherence area (ξ_n, ξ_m), for $l = 0mm$. It follows from Eq.8 that the width of Gaussian curve, which corresponds to the diameter of coherence area, equals to $2k$.

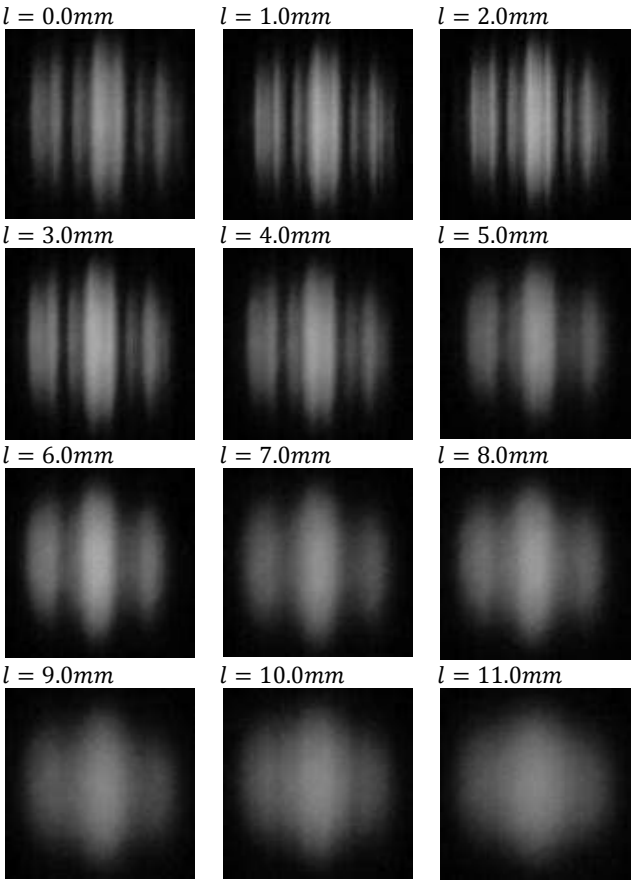

Fig.6. Interferogram generated by the mask, for increasing distances between focal point of the lens L_1 and RGG, starting from $l = 0.0\ mm$ to $l = 11.0\ mm$.

The same approach can be used to calculate the diameter of the coherence area for different values of l, which is explained in table.2.

It should be mentioned here that the width of the Gaussian curve which relates the modulus of the complex degree of spatial coherence to the coherence area, is the diameter of coherence area.

Table.2 The calculated diameter of coherence area for different ls.

$l(mm)$	Diameter of coherence area (mm)
0.0	11.5
1.0	8.84
2.0	8.12
3.0	6.76
4.0	5.4
5.0	4.78
6.0	4.42
7.0	3.56
8.0	3.02
9.0	2.68
10.0	2.56
11.0	2.2
12.0	2.14

IV. CONCLUSION

Our aim is to present a method to control the complex degree of spatial coherence of light field. We could vary the diameter of the coherence area of the partially coherent light field via varying of the distance between focal point of L_1 lens and RGG, as is evident from Fig.7. We observed that by increasing the area of the illuminated region on RGG, the modulus of the complex degree of spatial coherence is decreased and so the diameter of the coherence area

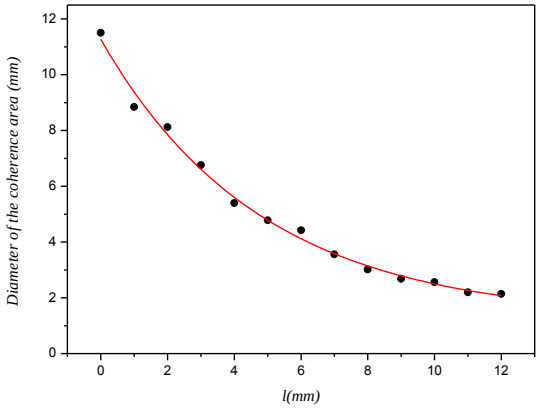

Fig.7 Diameter of the coherence area with respect to $l(mm)$

[1]. *M. Born, E. Wolf,* 'Principles of Optics', 7th edition, *Cambridge University Press*, (2001).

[2]. *J. W. Goodman*, 'Statistical Optics', *Wiley*, (2000).

[3]. *P. Hariharan*, 'Optical Interferometry', Academic Press, (2003).

[4]. *P. Hariharan*, 'Optical Interferometry', Second Edition, Elsevier Science, Academic Press, (2003)

[5]. *M. Zohrabi*, 'Measuring spatial coherence by using two optical fibers', MSc thesis, IASBS, Zanjan, Iran (2006).

[6]. *Y. Mejia and A. I. Gonzalez*, Opt Commun 273,428-434, (2007).

[7]. *F. Gori*, "Coherence of Light", in Second Winter College on Optics, International Centre for Theoretical Physics, 20 Feb-10 Mar. 1995. Available http://cdsagenda5.ictp.trieste.it/askArchive.php?base=agenda&categ=a02251&id=a02251slt24

[8]. *H. Mizuno, S. Tanaka*, Application of nematic liquid crystals to control the coherence of laser beams, *Opt. Commun*, 971, V3. N5, 320-321

INCOHERENT SWITCHING OF CAVITY SOLITONS IN SEMICONDUCTOR MICRORESONATORS ABOVE LASER THRESHOLD

R.KHERADM AND M.ESLAMI
Photonics Group, Research Institute for Applied Physics and Astronomy,
Tabriz University, Tabriz, Iran
r_kheradmand@tabrizu.ac.ir
m.eslami87@ms.tabrizu.ac.ir

In this paper, switching of cavity solitons and its mechanism is investigated in semiconductor microresonators. There are several methods to carry this operation, e.g. coherent and incoherent switching. But what is of great interest here is Incoherent switching of cavity solitons. We have made use of local carrier injection as the so-called Incoherent switching, and this is done through simulations as the result of local creation of population inversion which locally enhances the rate of light emission. Simulations show that the cavity soliton can be created and continues to exist even after removing the carrier injection process.

I. INTRODUCTION

Cavity solitons are localized peaks of intensity which can be created on a homogeneous background of radiation [1]. Their potential application in information technology, optical information processing, and recently, in performing logical operations via logic gates [2-4], is the goal of intensive work in the area of transverse optical pattern formation and cavity solitons in nonlinear optical systems. Among the several applications which have been mentioned, the potential of cavity solitons for optical storage, where a bit of information is represented by a cavity soliton, has attracted a great deal of interest.

Cavity solitons can appear either spontaneously or through introducing a laser pulse in the nonlinear cavity, together with the holding beam. The ability of switching them, i.e. turning On and Off, and controlling their position and mobility, either by laser pulse or by local injection of carriers, makes them an appropriate alternative to make use in reconfigurable arrays or in all-optical processing units. Arrays of cavity soliton are nonlinear optical structures within which independent manipulation of the intensity peaks is possible.

Cavity solitons belong to the class of localized structures, which also exist in other fields (see, for example [5]), and arise under conditions of coexisting of a homogeneous stationary state and a patterned stationary state for the same value of the parameters. Localized structures coincide with the pattern state in a certain restricted region of the plane, and homogeneous state outside.

In experiments, as mentioned above, cavity solitons can appear either spontaneously, by sweeping a parameter (holding beam power or pump power) or by local addressing with an external beam. If the addressing beam is coherent with the holding beam, it is sufficient to control the phase mismatch between local addressing beam and the holding beam to switch on or switch off a cavity soliton. This process has been studied in [6] and is now well understood. However, cavity solitons are composite objects since they have an electric field component and a carrier-density component, and what is going to be realized in this paper is to take into account the latter component to perform switching.

This way of switching, that is using localized injection of carriers, has interesting consequences, in that it is possible to create or erase cavity soliton with almost any energy able to generate carriers inside the semiconductor material filing the cavity. There is no need for a precise control of the phase of the addressing beam.

II. THEORY

We considered a semiconductor laser of the type VCSEL (vertical cavity surface emitting laser) with a homogeneous holding beam. The rate equation model adopted to describe the formation of patterns and cavity solitons in the driven VCSEL below threshold is no longer adequate for the VCSEL above threshold. In fact, as already evidenced for two-level lasers [7], the standard adiabatic elimination of the polarization variable, which leads from the Maxwell–Bloch equations to the rate equations, introduces un-physical effects in presence of diffraction. In the case of a laser with injected signal, the rate equation model predicts that below the threshold of injection locking all transverse wave numbers are unstable, as a consequence of the fact that the standard adiabatic elimination of the polarization implicitly assumes that the gain width is infinite. However, in the case of a two-level laser such a wrong result disappears as soon as one considers the full set of effective Maxwell–Bloch equations [8].

In this work, we introduce the quadratic fitting of the gain curve in the equations, which makes the model more realistic. So, the full set of effective Maxwell-Bloch equations describing our system will be:

$$\begin{cases} {}^{\partial E}/_{\partial t} = \sigma[P + Ei - (1 + i\theta)E + i\nabla^2 E] \\ {}^{\partial D}/_{\partial t} = -b\left[{}^{1}/_{2}\,(E^{*}P + P^{*}E) + D - J - d\nabla^2 D\right] \\ {}^{\partial P}/_{\partial t} = \Gamma(1 + i\Delta)[(1 - i\alpha)D(1 - \beta D)E - P] \end{cases} \quad (1)$$

where E and P are the slowly varying envelopes of the electric field and of the effective macroscopic polarization, and D is a population variable proportional to the excess of carriers with respect to transparency. Time is scaled to the dephasing rate τ_d of the microscopic dipoles and the decay rates σ and b are defined as $\sigma = \tau_d/\tau_p$ and $= \tau_d/\tau_c$, where τ_p and τ_c are, respectively, the photon life time and the carrier recombination time. An important parameter is , which represents the difference between the cavity longitudinal mode frequency and the frequency of the injected field,

multiplied by τ_p. The amplitude of the injected field (holding beam) is denoted by E_I, while J is a parameter related to the pump current normalized in such a way that the threshold is $J_{th} = 1.171$. Finally, d is the diffusion coefficient for carriers and β is the parameter which takes into account the quadratic fitting of the gain curve.

We have also two real parameters Γ and Δ which determines the shape of the effective susceptibility. The two parameters are assumed to depend on the population variable D and can be phenomenologically derived by a quadratic fitting of the gain curve.

We set $\Gamma(D) = \frac{2.308D+1.206}{\sqrt{1+\alpha^2}}$, $\Delta = -\alpha + \frac{2\delta}{\Gamma}$,

$\delta(D) = 0.155D - 0.146$. $\Gamma(D)$ is associated with gain line width, while $\delta(D)$ is the detuning between the reference frequency and the frequency where the gain is maximum.

The values of the physical parameters we kept fixed throughout this paper is as follows:

Table 1. The fixed values for physical parameters

d	α	b	σ	τ_d	τ_p
0.052	4	10^{-4}	4×10^{-2}	$100\ fs$	$2.5\ ps$

So the free parameters of the system are the intensity of the HB, the pump parameter J and the detuning θ.

III. HOMOGENOUS SOLUTION AND LINEAR STABILITY ANALYSIS

By putting $\partial/\partial t = 0$, $\nabla^2 = 0$, we arrive at the homogenous stationary solution:

$$|Ei|^2 = |Es|^2\{(1 - Ds + \beta Ds^2)^2 + (\theta + \alpha Ds - \alpha\beta Ds^2)^2\}, \quad (2)$$

$$Ds = \frac{J}{1+|Es|^2}. \quad (3)$$

As can be seen in the Fig.1, the homogeneous stationary solution exhibits bistability in some parameter region, and this allows the system to perform switching operations. Using an ansatz of the form:

$$\begin{cases} E = Es + \delta Es\ e^{\lambda t - i(k_x x + k_y y)} \\ P = Ps + \delta Ps\ e^{\lambda t - i(k_x x + k_y y)}, \\ D = Ds + \delta Ds\ e^{\lambda t - i(k_x x + k_y y)} \end{cases} \quad (4)$$

we can determine the domains of Turing and Hopf instabilities, as shown in Figs.2, 3.

The cavity soliton characteristics below and close to the VCSEL threshold may induce to think that, to exist and be stable, the cavity soliton need a stable background. Hence, they cannot exist when the lower branch is unstable. Yet, this is not the case, as will be evident in this paper.

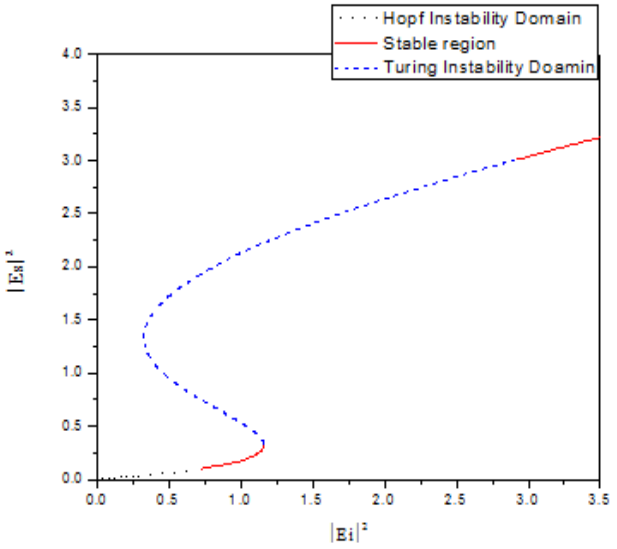

Fig.1. Stationary intensity $|E_s|^2$ versus the injected intensity $|E_I|^2$, J = 1.288, θ = −2, α = 4.

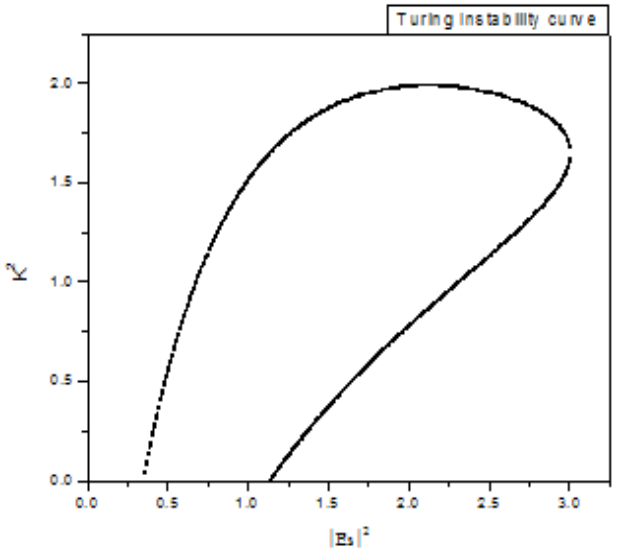

Fig.2. Instability domain for the Turing instability, J = 1.288, θ = −2, α = 4.

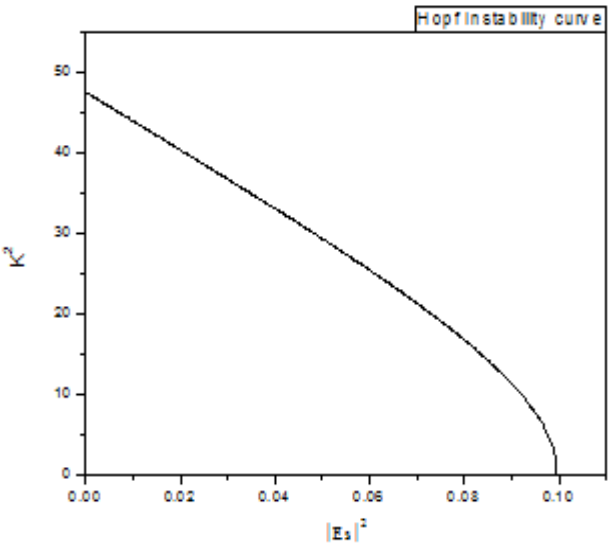

Fig.3. Instability domain for the Hopf instability, J = 1.288, θ = 2, α = 4.

IV. SIMULATION RESULTS

The dynamical equations were integrated numerically using a split-step method with periodic boundary conditions. This method consists in separating the algebraic and the Laplacian terms on the right-hand part of the equations; the algebraic term is integrated using a Runge-Kutta algorithm, while for the Laplacian operator a fast Fourier transform is adopted. This implies that the number of points for each side of the grid must be a power of 2 and we mostly assumed a 64 × 64 grid.

The technique used to switch on a cavity soliton consists in local injection of carries in presence of holding beam of the intensity equal to $|\mathbf{E_I}|^2$=0.6. The process of injection started at time 4(t.u.) and continued until time 4.92(t.u.). As can be seen in Fig.4, simulations show that the cavity soliton is created and is stable even in absence of injection process. What is evident as to the formation of cavity soliton is due to the population inversion which is created because of local carrier injection in the specific region of transverse plane, the rate of carrier recombination is enhanced and consequently we have increased intensity of the emitted light. This is the property of the nonlinear medium filling the cavity that balances diffraction effects and cavity losses and makes the formation of cavity soliton possible.

Finally, it is worth mentioning that, as stated earlier, existing of a stable background for creation of cavity solitons is not necessary and this fact is shown in Fig.5.

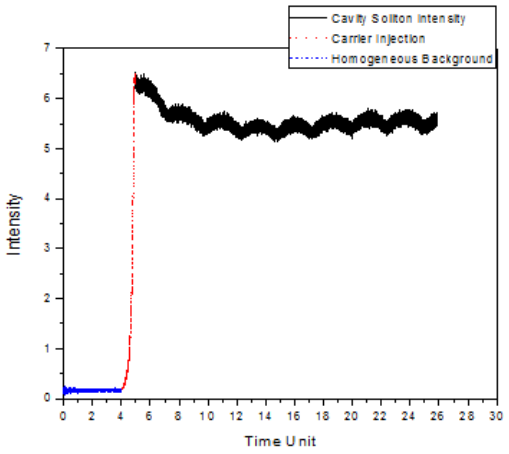

Fig.4. Switching on a cavity soliton in presence of $|\mathbf{E_I}|^2$=0.6.

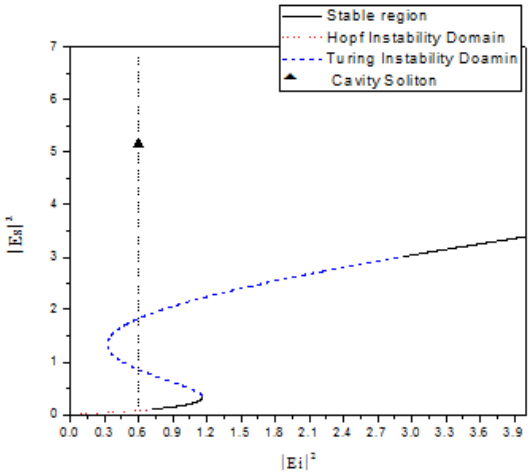

Fig.5. Formation of a cavity soliton on an unstable background

.

[1]. *S. Barland, J. R. Tredicce , M. Brambilla, L.A.Lugiato, S. Balle, M. Giudici, T. Maggipinto, L. Spinelli, G. Tissoni, T. Knodl, M. Miller, and R.Jager*, "Cavity solitons as pixels in semiconductor microcavities," Nature, vol. 419, pp. 699–702 , London, (2002).

[2]. *D. Gomila, M. A. Matias, and P. Colet* Phys. Rev. Lett. 94, p. 063905, (2005).

[3]. *D. Gomila, A. Jacobo, M. A. Matias, and P. Colet* Phys. Rev. E 75, p.026217, (2007).

[4]. *A. Jacobo, D. Gomila, M. A. Matias, and P. Colet*, Phys. Rev. A 78, 053821, (2008).

[5]. *O.Thual, & S.Fauve*, Localized structures generated by subcritical instabilities. J. Phys. 49, 1829–1923, (1988).

[6]. *X. Hachair, L. Furfaro, J. Javaloyes, M. Giudici, S. Balle, and J. Tredicce*, "Cavity-solitons switching in semiconductor microcavities," Phys. Rev. A 72,013815, (2005).

[7]. *G. L. Oppo, G. D'Alessandro, and W. J. Firth*, "Spatiotemporal instabilities of lasers in models reduced via center manifold techniques," Phys. Rev. A, vol. 44, pp. 4712–4720, (1991).

[8]. *X. Hachair, F. Pedaci, E. Caboche, S. Barland, M.Giudici, R. Tredicce, F. Prati, G. Tissoni, R.Kheradmand, L. A. Lugiato , I. Protsenko and M. Brambilla*, IEEE J, vol 12, No 3 (2006).

[9]. *Robert W. Boyd*, 'Nonlinear Optics', Elsevier, third Edition, (2008).

[10]. *S. Barland, M. Brambilla, L. Columbo, L. Furfaro, M. Giudici, X. Hachair, R. Kheradmand, L.A.Lugiato, T. Maggipinto, G. Tissoni, and J. Tredicce*, "Cavity solitons in a VCSEL: Reconfigurable micro pixel arrays," Euro-phys. News, vol. 34, pp. 136–139, (2003).

[11]. *Giovanna Tissoni, Lorenzo Spirielli, Luigi A.Lugiato, Massimo Brambilla*, 'Thermal and electronic nonlinearities in semiconductor cavities,' Proceedings of SPIE, Vol. 4283, (2001).

[12]. *S. Barbay, Y. Ménesguen, X. Hachair, L. Leroy, I.Sagnes, and R. Kuszelewicz*, 'Incoherent and coherent writing and erasure of cavity solitons in an optically pumped semiconductor amplifier OPTICSLETTERS, Vol.31, No.10, May15, (2006).

[13]. *S. Barbay and R. Kuszelewicz*, 'Physical model for the incoherent writing/erasure of cavity solitons in semiconductor optical amplifiers' OPTICS EXPRESS, Vol. 15, No. 19, (2007).

SOME PROPERTIES OF THE CENTRAL HEAVY ION COLLISIONS

Z. WAZIR[1], M. K. SULEYMANOV[1, 2,3], O.B. ABDINOV[3], E. U. KHAN[1], MAHNAZ Q. HASEEB[1], M. AJAZ[1], K. H. KHAN[1], Sh. GANBAROVA[3]

[1]CIIT, Islamabad (Pakistan),
[2]JINR, Dubna (Russia)
[3]Institute of Physics ANAS (Azerbaijan Republic)

Some experimental results are discussed in connection with the properties of the central heavy ion collisions. These experiments indicate the regime changes and saturation at some values of the centrality. This phenomenon is considered to be a signal of the percolation cluster formation in heavy ion collisions at high energies.

1. INTRODUCTION

Study of the centrality dependence of the characteristics of hadron-nuclear and nuclear-nuclear interactions is an important experimental way for obtaining information on phases of strongly interacting matter formed during the collision evolution. L. Wan Hove was first in attempting to use the centrality to get information on the new phases of matter [1] using the data coming from the ISR CERN experiments on pp-interactions. To fix the centrality the particle density (Δn) in given region of rapidity was considered (Δy) -- $\Delta n/\Delta y$. The ISR data shows that by increasing the values of the $\Delta n/\Delta y$ starting from some values of the $\Delta n/\Delta y$ the p_t distribution becomes wider (see Fig.1). Wan Hove aimed to explain the fact as a signal on deconfinement [2] in hot medium and formation of the Quark Gluon Plasma (QGP) [3]. In this paper we discuss some properties of central collisions. These are necessary to get the signal on the deconfinement and to identify QGP.

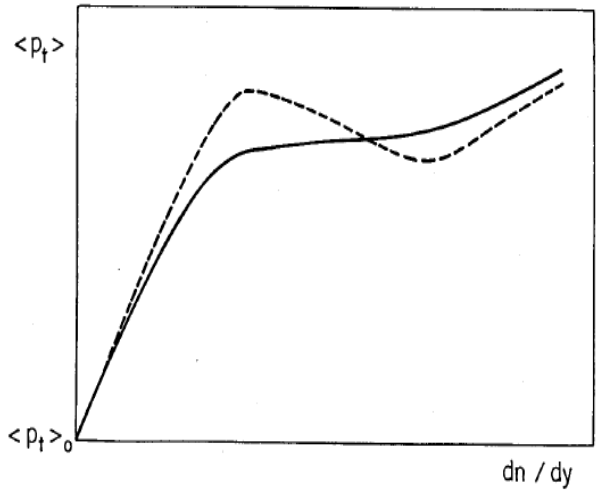

Fig. 1. P_t vs. n Correlation could provide a signal for the deconfinement transition of hadronic matter.

2. SOME PROPERTIES OF CENTRAL COLLISIONS

2.1 HADRON-NUCLEUS COLLISIONS

Fig.2 demonstrates a number of $\pi^{-12}C$-interactions (N_{star}) as a function of the number of identified protons N_p [4]. In this experiment N_p was used to fix the centrality. One can see the regime change in the behavior of the values of N_{star} as a function of N_p near the value of N_p=4. The value was used to select the $\pi^{-12}C$-reactions with total disintegration of nuclei (central collisions).

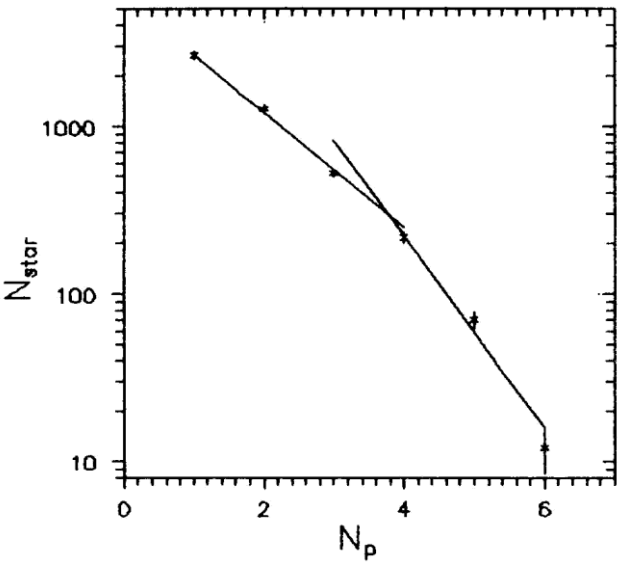

Fig.2 A number of $\pi^{-12}C$-interactions (at P_{π^-}=40 GeV/c) as a function of the number of identified protons.

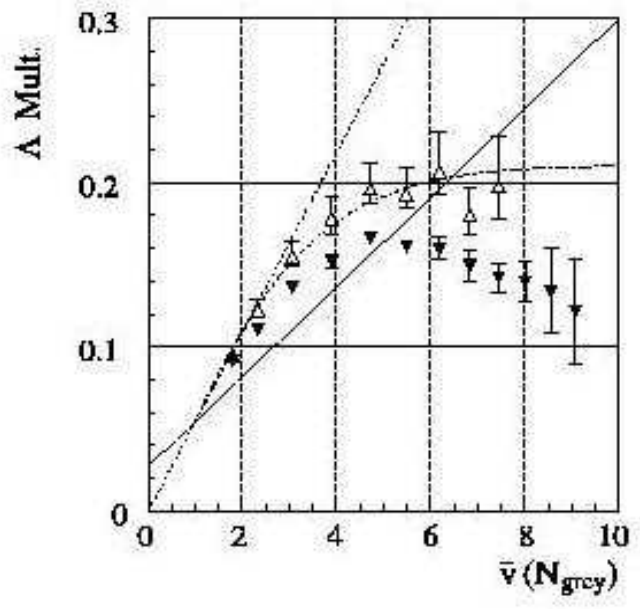

Fig.3 The Λ yield versus ν.

As an example of existence of the regime change in proton-nucleus collisions we can show Λ production (see Fig.3) as a function of collision centrality for 17.5 GeV/c

p–Au collisions has been measured by BNL E910 [5]. The centrality of the collisions is characterized using a derived quantity ν, the number of inelastic nucleon-nucleon scatterings suffered by the projectile during the collision. The open symbols are the integrated gamma function yields, and the errors shown represent 90% confidence limits including systematic effects from the extrapolations. The full symbols are the fiducial yields. The various curves represent different functional scaling. The same results have been obtained by BNL E910 Collaboration for π^--, K^0_s- and K^+- mesons emitted in *p+Au* reaction.

2.2 NUCLEUS-NUCLEUS COLLISIONS

From Fig.4 one can see the behaviors of the event number as a function of centrality for light nuclei interactions: *dC*-, *HeC*- and *CC*-interaction at 4.2 A GeV/c [6]. There are regime changes again for these interactions. These points of regime change could be used to select the central collisions**.**

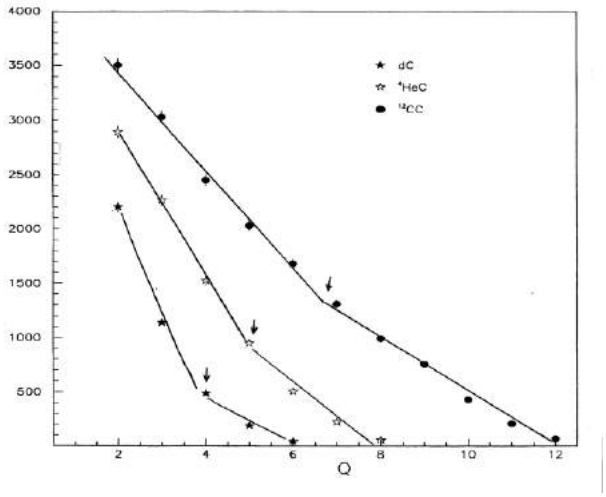

Fig.4 The number of *dC*-, *HeC*- and *CC*- reactions as a function of centrality at 4.2 A GeV/c.

2.3 HEAVY ION COLLISIONS

Experimental ratios of $<K^+>$, $<K^->$, φ, and Λ to $<\pi^\pm>$ plotted as a function of system size (Fig.5). Statistical errors are shown as error bars, systematic errors if available as rectangular boxes. The curves are shown to guide the eye and represent a functional form

$$a - b\ exp(-<N_{part}>/40).$$

At $<N_{part}>=60$ they rise to about 80% of the difference of the ratios between N_{part} =2 and 400 [7].

The ratio of the J/ψ to Drell-Yan cross-sections has been measured by NA38 and NA50 SPS CERN (see Fig.6) as a function of centrality of the reaction estimated, for each event, from the measured neutral transverse energy E_t [8]. Whereas peripheral events exhibit the normal behavior already measured for lighter projectiles or targets, the J/ψ shows a significant anomalous drop of about 20 % in the E_t range between 40 and 50 GeV. A detailed pattern of the anomaly can be seen in Fig. 6 which shows the ratio of the J/ψ to the Drell-Yan cross-sections divided by the exponentially decreasing function accounting for normal nuclear absorption. Other significant effect which is seen from this picture is a regime change in the E_t range between 40 and 50 GeV both for light and heavy ion collisions and saturation.

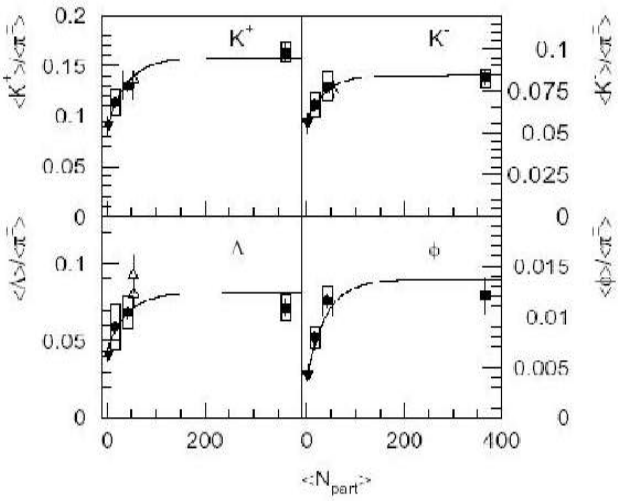

Fig.5 The experimental ratios of $<K^+>$,$<K^->$,φ, and Λ to $<\pi^\pm>$ plotted as a function of system size (▼ *p+p*, *C+C* and *Si+Si*, ● *S+S*, ■ *Pb+Pb*).

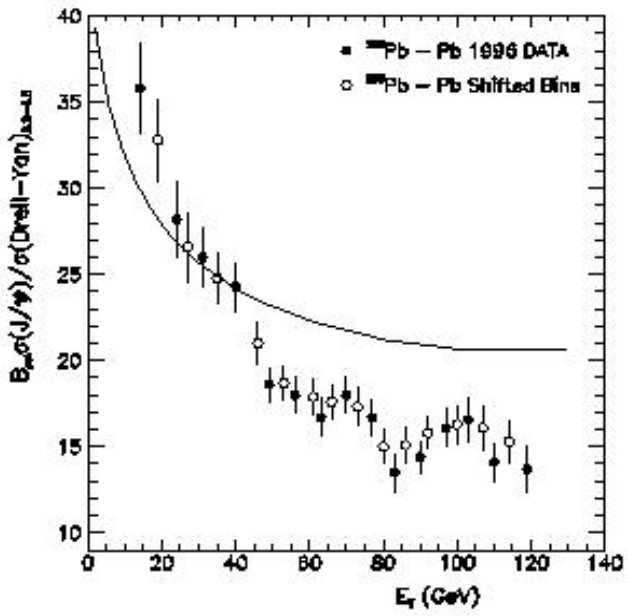

Fig.6. The ratio of the J/ψ to Drell-Yan cross-sections as a function of centrality.

Recent data obtained by STAR RHIC BNL[9] on the behavior of the nuclear modification factors of the strange particles as a function of the centrality in *Au+Au*- and *p+p*-collisions at $\sqrt{s_{NN}}$ = 200 GeV is shown in Fig.7. One can see regime change and saturation for the behavior of the distributions. To fix the centrality the values of participants (N_{part}) was used.

Recent results from RHIC on heavy flavor production [10] show nuclear modification function (R_{AA}) distributions for *Au+Au* and *Cu+Cu* collisions (see Fig.8) as a function of centrality. A number of participants (N_{part}) were used to fix the centrality. We can see again the regime change and saturation in the behavior of the distributions.

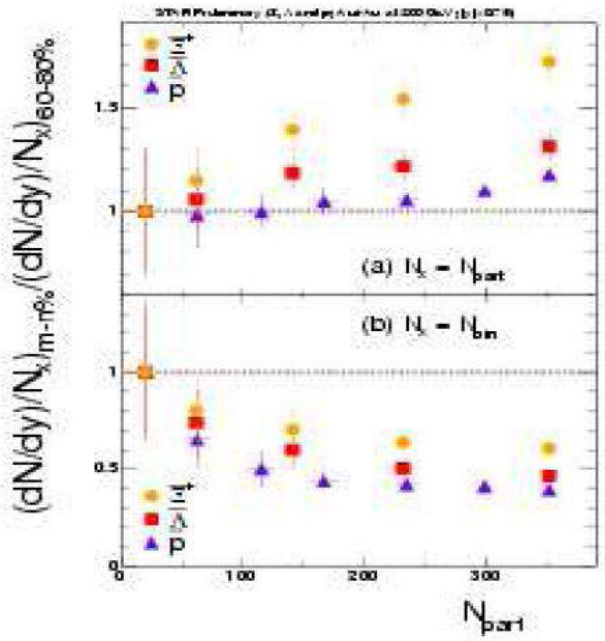

Fig.7. The nuclear modification factors of the strange particles as a function of centrality.

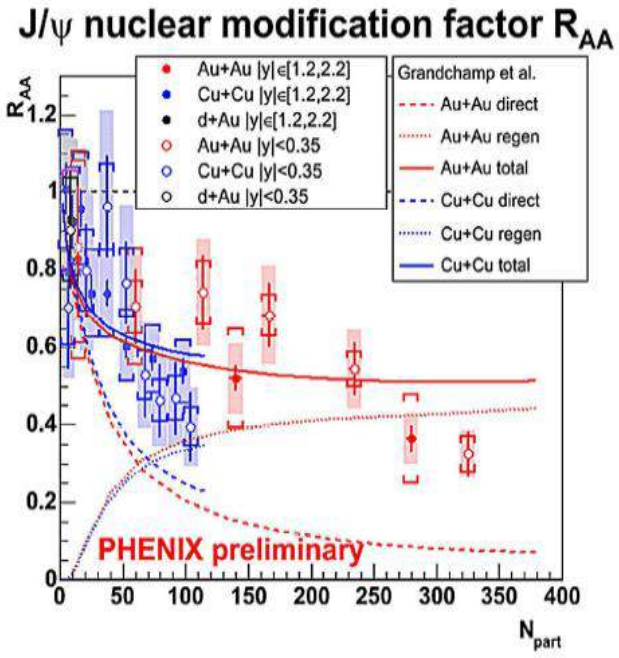

Fig.8 The values R_{AA} as a function of N_{part} for heavy flavor coming from RHIC.

3. DISCUSSION

The points of regime change appear for the behavior of some characteristics of events as a function of centrality as some critical phenomena for hadron-nuclear, nuclear-nuclear interactions and for ultrarelativistic ion collisions. The phenomenon observed in the wide range of energy and almost for all particles (mesons, baryons, strange particles and heavy flavor particles). After point of regime change the saturation is observed. The simple models (such as wounded-nucleon model and the cascade model) which are usually used to describe the high energy hadron-nuclear and nuclear-nuclear interactions could not explain the results. To explain this result it is necessary to suggest that the dynamics of the phenomena is same for hadron-nuclear, nuclear-nuclear and heavy ion interactions and is independent of the energy and mass of the colliding nuclei. The responsible mechanism to describe the above mentioned phenomena could be statistical or percolation ones because phenomena have a critical character. In Ref. [11] complete information was presented about using statistical and percolation models to explain the experimental results coming from heavy ion physics. However, it is known that the statistical models give more strong A-dependences than percolation mechanisms. That is why we believe that the responsible mechanism to explain the phenomena could be percolation cluster formation [12]. Big percolation cluster may be formed in the hadron-nuclear, nuclear-nuclear and heavy ion interactions independent of the colliding energy. But the structure and the maximum values of the reached density and temperature of hadronic matter could be different for different interactions depending on the colliding energy and masses within the cluster. Ref. [13] shows that deconfinement is expected when the density of quarks and gluons become so high that it no longer makes sense to partition them into color-neutral hadrons, since these would strongly overlap. Instead we have clusters much larger than hadrons, within which color is not confined; deconfinement is thus related to cluster formation. This is the central topic of percolation theory, and hence a connection between percolation and deconfinement [13] seems very likely. So we can see that the deconfinement could occur in the percolation cluster. Ref. [13] explains the charmonium suppression as a result of deconfinment in cluster.

Experimental observation of the effects connected with formation and decay of the percolation clusters in heavy ion collisions at ultrarelativistic energies and the study of correlation between these effects could provide the information about deconfinement of strongly interacting matter in clusters. We suggest two effects to identify the percolation cluster formation. One is the nuclear transparency effect and other light nuclear production.

In Ref. [14] percolation cluster is a multibaryon system. Increasing the centrality of collisions, its size and masses could increase as well as its absorption capability and we may see saturation. So after point of regime change the conductivity of the matter increases and it becomes a superconductor [13] due to the formation of percolation clusters. In such systems the quarks must be bound as a result of percolation.

The critical change of transparency could influence the characteristics of secondary particles and may lead to their change. As collision energy increases, baryons retain more and more of the longitudinal momentum of the initial colliding nuclei, characterized by a flattening of the invariant particle yields over a symmetric range of rapidities, about the center of mass - an indicator of the onset of nuclear transparency. To confirm the deconfinement in cluster it is necessary to study the centrality dependence in the behavior of secondary particles yields and simultaneously, critical increase in transparency of the strongly interacting matter.

Appearance of the critical transparency could change the absorption capability of the medium and we may observe a change in the heavy flavor suppression depending on their kinematical characteristics. It means that we have to observe the anomalous distribution of some kinematical parameters because those particles which are from area with superconductive properties (from cluster) will be suppressed less than the ones from noncluster area. So the study of centrality dependence of heavy flavor particle production with fixed kinematical characteristics could provide the information on changing of absorption properties of medium depending on the kinematical characteristics of heavy flavor particles.

In. Ref.[15] it was suggested that the investigation of the light nuclei production as a function of the centrality could give the clue on freeze-out state of QGP formation, which may be used as an additional information to confirm the percolation cluster formation near the critical point. There are two types of light nuclei emitted in heavy ion collisions: first type are the light nuclei which get produced as a result of nucleus disintegration of the colliding nuclei; while the second ones are light nuclei which are get comprised of protons and neutrons (for example, as a result of coalescence mechanism) which were produced in heavy ion interactions. In an experiment we can separate these two types of nuclei from each other using the following ideas: the yields for first type of nuclei have to decrease, by some regularity, with centrality of collisions. On the other hand, formation of the clusters could be a reason of the regime change in the behaviour of light nuclei yields as a function of centrality in the second type.

[1]. *L.Wan Hove*, preprint TH.3391-CERN, 1982, CERN.

[2]. *M.K. Suleymanov et al*. Nuclear Physics B (Proc. Suppl.) , vol. 177–178 , pp. 341–342, 2008; E-rint:nucl-ex/0706.0956 (2007).

[3]. *M.Gazdzicki and S.Mrowezynski*. Z.Phy., C54, 127(1992).

[4]. *O.B. Abdinov et al*. JINR RC, 1996, No 1[75]-96 pp. 51.

[5]. *Ron Soltz* for the E910 Collaboration, J. Phys. G: Nucl. Part. Phys., 27, pp. 319–326 (2001).

[6]. [Preprint JINR 1-12114,1979; 1-12424, 1989, P1-98-292,; *M. K.Suleimanov et al.*, Phys.Rev.C, 1998, 58, pp. 351.]

[7]. *C. Alt, et al*. Phys.Rev.Lett. 94 (2005) 052301.

[8]. *M. C. Abreu et al.*, Phys. Lett. B 1999, 450, p. 456; *M.C. Abreu et al.*, Phys. Lett. B, 1997, 410, p. 337*; M.C. Abreu et al*. Phys. Lett. B, 1997, 410, p. 327; *M. C. Abreu et al*, NA50 Collaboration, Phys. Lett. B, 2001, 499, pp. 85-96.

[9]. *Christelle Roy* for STAR Collaboration POS (HEP2005) 141.

[10]. *A.A. P. Suaide*, Brazilian Journal of Physics, vol. 37, no. 2C, June 2007, 731-735.

[11]. *Claudia Höhne, GSI Darmstadt*, Probing QCD with High Energy Nuclear Collisions, Hirschegg (2005).

[12]. *Helmut Satz* arXiv: hep-ph/0212046 (2002); Janusz Brzychczyk, arXiv:nucl-th/0407008 (2004); C. Pajares, arXiv:hep-ph/0501125 (2005).

[13]. *H. Satz*, arXiv:hep-ph/0007069 (2000).

[14]. *M.K. Suleymanov et al.*, Acta Phys. Polon. Supp.1, 405-406, (2008).

[15]. *M.K.Suleymanov et al.*, nucl-ex/0804.3133 (2008).

LIGHT NUCLEI PRODUCTION IN HEAVY ION COLLISION

K.H. KHAN[1], M.K. SULEYMANOV[1, 2,3], O.B. ABDINOV[3], Z. WAZIR[1], E.U. KHAN[1], MAHNAZ Q. HASEEB[1], M. AJAZ[1], Sh. GANBAROVA[3]

[1]COMSATS Institute of Information Technology, Islamabad

[2]Joint Institute for Nuclear Research, Dubna,

[3]Institute of Physics NAS Azerbaijan, Baku

Light nuclei production as a result of nuclear coalescence effect can give some signals on final state of Quark Gluon Plasma formation. We have studied the behavior of nuclear modification factor as a function of: Thermal Freeze out, Chemical freeze out temperatures and baryon potential using the simulated data coming from the Fast MC generator. The results demonstrated that the model could not describe the light nuclear production which should occur in freeze out state as a result of nuclear coalescence effect. We think: that this effect have to be include the model to improve the description: comparison the experimental data coming from the centrality heavy ion collisions with ones coming from Fast MC Model can give necessary information on nuclear coalescence effect.

1. INTRODUCTION

The creation of new phases of strongly interacting matter is the most interesting area of research for physicist for last many years. Physicists are interested in studying characteristics of newly formatting matter under extreme conditions. The one way to create these new phase is the heavy ion collision at relativistic and ultra relativistic energies. We are interested in centrally dependence of hadron – nucleus and nucleus -nucleus collisions. These experiments indicate the regime change at some values of the centrality as some critical phenomena. If the regime change observed in the different experiments takes place unambiguously twice, this would be the most direct experimental evidence to a phase transition from hadronic matter to a phase of deconfined quarks and gluons. After point of regime change the saturation is observed. The simple models cannot explain the effect. For this it is necessary to suggest that the dynamics is same for all such interactions independent of energy and mass of the colliding nuclei and their types. The mechanism to describe the phenomena may be statistical or percolative due to their critical character [1].The effect depend weakly on the mass of the colliding nuclei so the belief that the mechanism to explain the phenomena may be the percolation cluster formation [2-4]. There is a very great chance that the effect of the light nuclei emission [5-8] in heavy ion collisions may of the accompanying effects of percolation cluster formation and decay. So this effect may be use as some signal on percolation cluster formation.

2. LIGHT NUCLEI PRODUCTION

There are two types of light nuclei emitted in heavy ion collisions: first type is light nuclei which were produced as a result of nucleus disintegration of the colliding nuclei; second one is light nuclei which were made of protons and neutrons (for example as a result of coalescence mechanism) which were produced in heavy ion interaction at freezeout state. Here we describe the two type of collision to understand the coalescence mechanism.

Peripheral Collision. In peripheral collision (Fig.1) nuclei collide in such a way that their some nucleon interact each other known as participants, the nuclei which do not interact are known as spectators and make separate fragments. These fragments may be light or intermediate nuclei. This process is also called fragmentation.

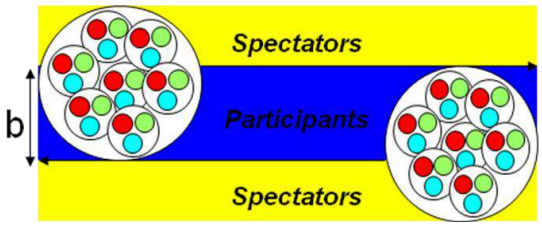

Fig. 1

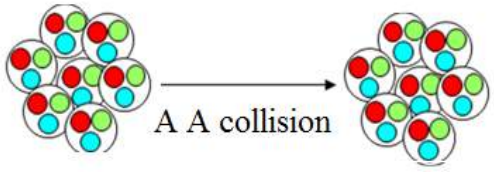

Fig. 2

Central Collision. In second type nuclei collide centrally (see Fig.2) in such a way that their maximum nucleons interact with each other and colliding nuclei waste their individuality. So the fragmentation has to suppress in these collisions. It is expected that mainly in these collisions nuclear mater could change into Quark Gluon Plasma (QGP) as a result of increasing temperature and density of nuclear matter.

We can see from above figures that as increasing the centrality fragmentation decreases .To understand the different stages of nuclear collision and phase transition mechanism we use the following figure of central collisions. We are working at last stages (e) in this stage we get both type of light nuclei may be formed as a result of coalescence effect due to high pressure as cluster formation and percolation effect and as a result of fragmentation.

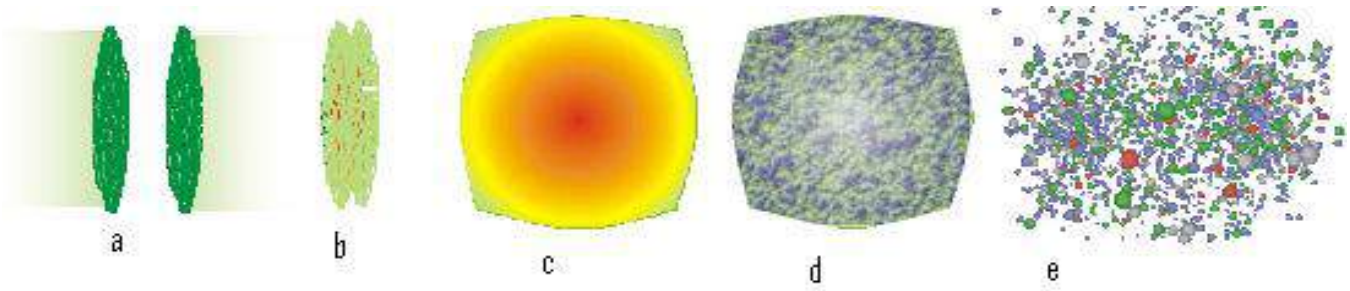

Fig.3

We can distinguish the two types of light nuclei by time of detection because fragments are detected earlier than nuclei formed as a result of coalescence. We can confirm Coalescence mechanism by measuring transparency effect for light nuclei at stages (d), if transparency at stage (d) for light nuclei is minimum and we measure light nuclei at stage (e) which is direct confirmation of coalescence effect. Some models are used to measure the light nuclei as a result of coalescence is described below.

3. MODELS

3.1. SIMPLE COALESCENCE MODEL

In 1963, Butler and Pearson developed a model for deutron formation in proton-nucleus collisions according to them [9]. The key result is that, on account of simple momentum phase space considerations, the deutron density in momentum space, d^3N_d/dP^3_d, is proportional to the proton density in momentum space, d^3N_p/dp^3_ptimes the neutron density in momentum space, d^3N_n/dp^3_n, at equal momentum per nucleon (P=2p) and can be expressed as:

$$\gamma d^3N_d/dP^3_d=B_2(\gamma d^3N_p/dp^3_p)(\gamma d^3N_n/dp^3_n)$$

Since many experiments measure protons but not neutrons, it is useful to rewrite this equation assuming the neutron and proton densities to be identical:

$$\gamma d^3N_d/dP^3_d=B_2(\gamma d^3N_p/dp^3_p)^2$$

where

$$B_2=\left|V_0\right|^2p(1+m^2/p^2)j(pR)$$

However, the underlying phase space relationship survives, and is expressed in a form generalized for nuclear species as:

$$\gamma d^3N_A/dp^3_d=B_A(\gamma d^3N_p/dp^3_p)^A$$

where

$$B_A=(2S_A+1/2^A)1/N!1/Z!(R_{np})^N(4\pi p_0{}^3/3)^{A-1}$$

S_A is the spin of the cluster of mass A, and N and Z is the neutron and proton numbers of the composite particle.

The factor R_{np} is the ratio of neutrons to protons participating in the collision.

3.2. DENSITY MATRIX MODEL

The previous models were improved by accounting for some of quantum mechanical aspects of coalescence [10] the particles distributions are represented by density matrices and the wave function of the particles are assumed to be Gaussian in shape. By considering the internal coalescence in momentum space, the coalescence parameter for fragment of a mass A is

$$B_A = \frac{2s_A+1}{2^A}(R_{np})^N A^{3/2}(4\pi\frac{\nu_A\nu}{\nu_A+\nu})^{3/2(A-1)}$$

3.3. THERMODYNAMIC MODEL

A thermodynamic model of heavy ion collisions was developed to describe the production of light nuclei in a rapidly expanding system of nucleons [11, 12].In this model the resulting invariant multiplicity of the composite particles can be expressed as:

$$d^3N_A/dp^3_d=(2S_A+1)/2^A[(2\pi)^3/V]^{A-1}e^{-E_0/T}(R_{np})^N(d^3N_p/dp^3_p)^A.$$

There are many other models but we shall not discuss here.

4. EXPERIMENTAL RESULTS

Here we discuss experimental results in comparison with model Fast MC results. The results presented in [13] on the measured yield of proton and light nuclei. The formation of light nuclei near central rapidity in a nucleus-nucleus collision requires the constituent nucleons to be close together in phase space in order to be able to coalesce.

The relative probability for the formation of a nuclear cluster is quantified in the B_A parameter, which is defined as the proportionality constant between the yield of a nucleus of mass number A and the A^{th} power of the proton yield:

$$E_A\frac{d^3N_A}{d\vec{p}^3_A} = B_A(E_p\frac{d^3N_p}{d\vec{p}^3_p})^A$$

Figure below shows the quantity B_A for various targets and event geometries in Au+Au reactions. The data points correspond to events in different centrality

bins, which are plotted against the mean number of participating nucleons for that bin as determined by Monte Carlo simulation. In data set, B_2 decreases by a factor of 2 from the most peripheral to the most-central bin, while B_3 decreases by a factor of 10 and B_4 by a factor of 100

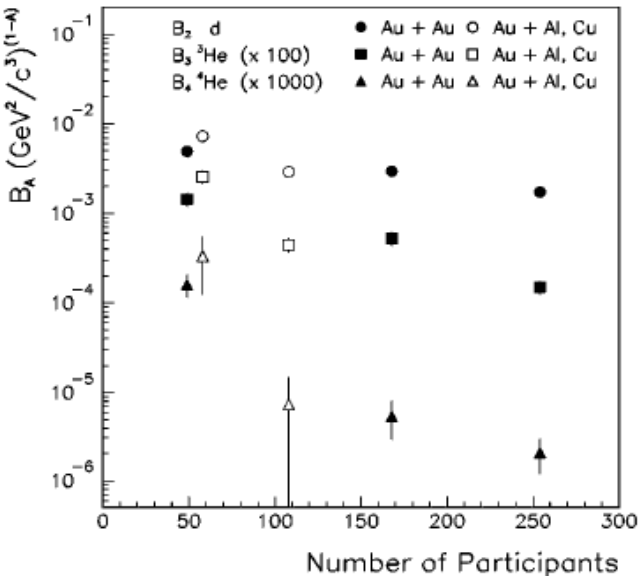

Fig.4 Dependence of the B_A parameter on the number of participants in Au+Al, Au+Cu, and Au+Au reactions

5. FAST MONTECARLO RESULTS

We studied the behavior of nuclear modification factor R as function of three variables : Thermal Freeze out, Chemical freeze out temperatures and baryon potential using the simulated data coming from Fast MonteCarlo Model (FastMC) [14]. The values of nuclear modification factor were defined as the ratio of baryons multiplicity at central to peripheral collision. We considered AuAu Collisions at 200 AGeV.

The results are shown in fig.5. It is seen that the values of R has not dependence on the mentioned variables. It means that light nuclear could not produced in freeze out state. But in other hand the data coming from Phenix RHIC BNL [15] demonstrate the light nuclear production. So we think that FastMC model does not in agree with experimental data on light nuclear production at ultrarelativistic energies. We think that it could be connected with that the Model could not include nuclear coalescence effect and to improve the situation this effect must be take into account.

6. CONCLUSION

We have studied behavior of the Nuclear Modification factor as a function on different parameters of FastMC Model, which could describe the freeze out state of Quark Gluon Plasma formation.

The results demonstrated that the model could not describe the light nuclei production which should occur in freeze out state as a result of nuclear coalescence effect. We think: that this effect have to be include the model to improve the description: comparison the experimental data coming from the central heavy ion collisions with ones coming from Fast MC Model can give necessary information on nuclear coalescence effect.

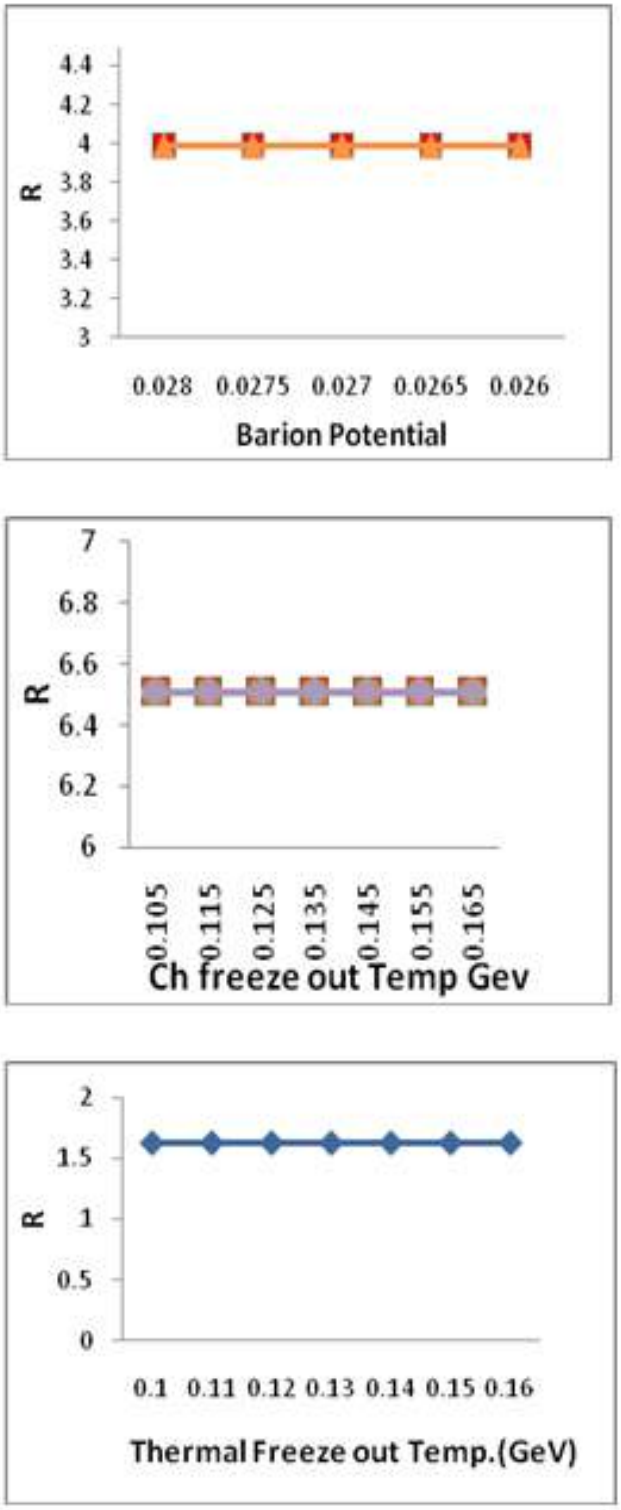

Fig.5 Dependences of nuclear modification factor on different variables

[1]. *Claudia Höhne, GSI Darmstadt*, Probing QCD with High Energy Nuclear Collisions, Hirschegg 2005.
[2]. *H. Satz* arXiv: hep-ph/0212046;
[3]. *Janusz Brzychczyk*, arXiv: nucl-th/0407008;
[4]. *C. Pajares*. arXiv:hep-ph/0501125.
[5]. *S.S. Adler et al*. arXiv: nucl-ex/0406004 .
[6]. *Zhangbu Xu* for the E864 Collaboration. arXiv: nucl-ex/9909012.
[7]. *S. Albergo et al*. Phys. Rev. C, v. 65, 034907.
[8]. *I.G. Bearden et al*. European Physical Journal C ; EPJC011124.
[9]. *S.T. Butler and C.A. Pearson*, Phys. Rev. Lett. 7, 69 (1961), Phys. Rev 129, 836 (1963).
[10]. *H. Sato and K Yasaki*, Phys.Letter.B 98.153(1981).
[11]. *A.Z. Mekjian*, Phys. Rev. Lett. 38, 604 (1977); Phys. Rev. C 17, 1051 (1978).
[12]. *S. Das Gupta and A.Z. Mekjian*, Phys. Rep. 72, 131 (1981).
[13]. *J Bennet et al.* Phys. Rev.C 61 064908(2000)
[14]. *N.S. Amelin* arXiv:nucl-th/0608057v4 13 Oct 2006.
[15]. *S. S. Adler et al.* Physical Review Letters. 94 122302 (2005)

THE POLARISATION EFFECTS OF THE $n\,^{12}C$ NEUTRON ELASTIC SCATTERING IN HIGH ENERGY

S.G.ABDULVAHABOVA, N.Sh.BARHALOVA, T.O.BAYRAMOVA
Baku State University,
Z.Khalilov, 23 Baku, Azerbaijan (AZ 1148),
sajida.gafar@gmail.com

The differential cross-section of $n^{12}C$ scattering at high energies polarization effects are calculated in the framework of the Glauber-Sitenko multiple scattering theory. By taking explicitly into account the composite quark structure of nucleons exchange effects we eliminate some discrepancies between the theory and the data that were recently pointed out. The received results also are applied to calculation angle of the deviation of neutron by nucleons of the ^{12}C .

1. INTRODUCTION

At present the theoretical and experimental research leads to the conclusion about the essential role of the spin of particles in the high energy scattering. The specific feature of this kind of reaction is that the transition amplitude is in general a sum of several nucleon contributions, each with its own phase and amplitude. This makes a basis for the hypothesis about the existence of a non-zero polarization research on the future accelerators will provide information about the structure of the nucleon interaction at large distances.

In this paper we regard the model results for the polarization effects of neutron-nuclei scattering at high energies.

2. THE MODEL FORMALISM

Early, it was shown [1] that in the framework of the hypothesis concerning the existence of quark bag in nuclei we managed to describes the behavior of the formfactors of nuclei at large q and structure functions of nuclei.

A nucleus in the quark cluster model is described as a system of many clusters- completely anti symmetrized with respect to the quark variables. Each cluster consists of three quarks and he» the nucleon quantum number, namely it has symmetry for spin-isospin symmetry for color and symmetry for the radial part. The parameters of quark distribution in the bag extracted from the data on formfactors and on deep inelastic scattering of nucleons on nuclei proved to be very close. In agreement with the Glauber theory [2], which is a rather accurate one at high energy the amplitude of the direct reaction of neutron on a nucleus may be written as

$$F(\mathbf{q}) = \frac{ik}{2\pi}\int \exp(i\mathbf{qb})\left\langle \Psi\left|\Gamma(\mathbf{b})\right|\Psi\right\rangle d\mathbf{b}\,, \qquad (1)$$

$$\Gamma(\mathbf{b}) = 1 - \prod_{j=1}^{A}\left[1-\gamma_j(\mathbf{b}-\mathbf{s_j})\right]. \qquad (2)$$

Here **q** is the momentum transfer, k is the value of the wave vector of the scattering proton, **b** is the impact-parameter vector, $\Psi(\mathbf{r}_1,\mathbf{r_2},...,\mathbf{r}_A)$ is the ground state wave function of the nuclei, $\Gamma(\mathbf{b})$ is the total neutron – nuclei interaction profile function, $\gamma_j(\mathbf{b})$ is the profile function for the elementary proton-nucleon interaction, brackets $\langle\|\rangle$ mean interactions over the nucleon coordinates.

The wave function of the neutron may be written as

$$\varphi(k_{n,r}) = (2\pi)^{-3/2}\exp(ik_n,r)x \\ [1-\Gamma(b-b_i)\theta(z-z_i)\chi_{1/2}] \qquad (3)$$

where

$$\theta(z) = \begin{cases} 1, & z>0 \\ 0, & z<0 \end{cases}, \qquad (4)$$

the function of the Heviside and $\chi_{1/2}$- spin function of the neutron.

The wave function for the ^{12}C in the cluster model can be written as [3]

$$\Psi_{^{12}C} = \phi_{N_1}(r_1,r_2,r_3)\cdots\phi_{N_9}(r_{34},r_{35},r_{36})\mathbf{x} \\ \chi(R_1,R_2,...,R_{12}) \qquad (5)$$

where the nucleus is pictured as a bag with radius R_A, located at R_{12} enclosing *A* nucleons with radius located at R_i . Using the relations

$$R = \frac{r_{3i-2}+r_{3i-1}+r_{3i}}{3}, \quad \text{i=1,2,…12} \qquad (6)$$

and $\phi(r)$ give as Gaussian function

$$\phi(r) = (\sqrt{\pi}R_h^2)\exp(-r^2/R_h^2), \qquad (7)$$

we can write (5) in a factorised for

$$\Psi_{^{12}C} = \prod_{j=1}^{12}\exp[\frac{r_{3j-2}^2+r_{3j-1}^2+r_{3j}^2}{R_h} - 2i\left(\frac{1}{R_A^2}-\frac{1}{R_h^2}\right)\mathbf{x} \\ (\mathbf{s}_{3j-2}+\mathbf{s}_{3j-1}+\mathbf{s}_{3j}) \qquad (8)$$

Then scattering amplitude (1) may be written in the form

$$F = (ik/2\pi)\int d\mathrm{b}\chi_{l+1/2}\exp(i\mathrm{qb})(\delta_{mn}\delta_{MN}) - \\ -Det\left|\delta_{mn}\delta_{MN} - \left\langle M \left| \prod_{i=1}^{3}\prod_{j=1}^{3}(1-\gamma(\mathrm{b}-\mathrm{s}_i+\mathrm{r}_j)) \right| N \right\rangle\right| \quad (9)$$

The matrix element of the profile function between the single particle states described by the quantum numbers *M* and *N* .

Use of the spin-non-flip amplitude of the $n^{12}C$ reaction, obtained from the formulae (9) permits us to calculate the correct picture of polarisation. We consider the case where spin-flip is neglected. It is important to emphasise that the case of the nucleon-nuclei scattering the leading asymptotic terms of the spiral amplitudes is also determined by the contribution of the quark cluster with the evident replacement of $F(q)$ by the pion-nucleon scattering amplitudes.

3. DEFINATION OF THE REZULTING ANGLE

At the analysis of angular distribution of coherent neutron scattering, there is a problem to finding the resulting angle ϑ of the deviation after *n* consecutive collisions of a neutron by nucleons. Many authors considered this problem approximately. On the basis of the theory of multiple scattering of Watson and of the basis of the abovementioned theory, we deduced a basic formula for distribution of intensity and defined angle of the deviation after passage of the neutron wave through the nuclei ^{12}C .

The probability of that in one act of collision a deviation of a particle will lay in a solid, angle $d\Omega = \sin\vartheta d\vartheta d\varphi$ is equal

$$W_1(\vartheta,\varphi)\,d\Omega = \frac{\sigma(\vartheta)}{\sigma}d\Omega, \quad (10)$$

where $\sigma(\vartheta)d\Omega$ and σ are differential and full cross-section, accordingly. We expand (10) over Legendre's polynom:

$$W_1(\vartheta,\varphi)\,d\Omega = \frac{1}{4\pi}\sum_l (2l+1)\,g_l P_l(\cos\vartheta)d\Omega \quad (11)$$

where:

$$g_l = \frac{1}{\sigma}\int P_l(\cos\vartheta)\sigma(\vartheta)d\Omega \quad (12)$$

After the second act of scattering (on other nucleon) the particle moves in a direction, are defined by polar angles (ϑ_2,φ_2) concerning a direction of (ϑ_1,φ_1) occurring once scattering bunch or angles (ϑ,φ) concerning falling bunch ,i.e:

$$\cos\vartheta_2 = \cos\vartheta_1\cos\vartheta + \sin\vartheta_1\sin\vartheta\cos(\varphi_1-\varphi)$$

To find probability of that after two consecutive, independent impacts the deviation of a particle will lay in a solid angle $d\Omega = \sin\vartheta d\vartheta d\varphi$, it is necessary to integrate product on $W_1(\vartheta_1,\varphi_1)W_1(\vartheta_2,\varphi_2)$ all ϑ_1,φ_1 at the fixed values ϑ and φ. Decomposing on $P_l(\cos\vartheta_2)$ attached Legendre's polynom:

$$P_l^m(\cos\vartheta_1)\exp(im\varphi_1) \text{ and } P_l^m(\cos\vartheta)\exp(im\varphi),$$

For probability it is found:

$$W_2(\vartheta,\varphi)\,d\Omega = \frac{1}{4\pi}\sum_l (2l+1)(g_l)^2 P_l(\cos\vartheta)d\Omega$$

Similarly, for probability of a deviation in a solid angle $d\Omega = \sin\vartheta d\vartheta d\varphi$ after *n* collisions it is had:

$$W_n(\vartheta,\varphi)\,d\Omega = \frac{1}{4\pi}\sum_l (2l+1)(g_l)^n x \\ P_l(\cos\vartheta)d\Omega \quad (13)$$

Let's designate through *W (n)* probability of that passing through substance the neutron will test on the average *n* collisions. Then the probability of that a neutron will deviate on a corner lying between ϑ and $\vartheta + d\vartheta$, is equal:

$$I(\vartheta)\sin\vartheta d\vartheta = \frac{1}{2}\sum_l (2l+1)\left[\sum_n W(n)(g_l)^n\right]x \\ P_l(\cos\vartheta)\sin\vartheta d\vartheta \quad (14)$$

The average of collisions ν at passage through a ^{12}C containing 12 nucleons will be written down as:

$$\nu = 12t\int\sigma(\vartheta)d\Omega$$

For $\nu > 1$ for $W(n)$ it is possible to apply Poisson's distribution:

$$W(n) = \frac{e^{-\nu}\nu^n}{n!} \quad (15)$$

Thus, we get:

$$\sum_{n=0}^{\infty} W(n)(g_l)^n \approx exp\left[-\nu(1-g_l)\right] \quad (16)$$

Considering last expressions, for distribution of intensity at multiple scattering we receive:

$$I(\vartheta) = \frac{1}{2}\sum_l (2l+1)\exp\{-24\pi tx(2l+1)x \\ \int\sigma(\theta)[1-P_l(\cos\theta)]\sin\theta d\theta \quad (17)$$

Let, further the $q(\theta)$ attitude of cross-section $\sigma(\theta)$ scattering of a neutron on nucleus of a crystal to section on a free nucleus σ_0, i.e:

$$q(\theta)=\frac{\sigma(\theta)}{\sigma_0}$$

Designating $y=\sin\frac{\theta}{2}$ expression (17) will become:

$$I(\vartheta)=\frac{1}{2}\sum_l l(l+1)\int q(\theta)\frac{dy}{y}-$$
$$-\sum_l\sum_{k=0}^{l}(-1)^k\frac{(l+k)!}{(l-1)!(k!)^2}\int_0^1 q(\theta)y^{2k-3}dy \qquad (18)$$

Function $q(y)$ possesses following properties:

$$q(0)=0,\quad q(y)=1 \quad \text{for} \quad y>y_0$$

Whence at scattering on angle θ, greater of some angle θ_0, influence of other nucleons a little. If in integral $\int_0^1 q(y)y^{2k-3}dy \quad k\geq 2$ to approximate $q(y)$ expression:

$$q(y)=1-exp\left(-\frac{y}{y_0}\right) \qquad (19)$$

and to put:

$$P_l(\cos\vartheta)\approx J_0\left[(l+1/2)\vartheta\right]=J\left(\frac{\vartheta}{\theta_0}\right)$$

It is possible to replace summation on *l* in (18) integration. With this purpose we use Euler-Maclaurin's formula:

$$\sum_l f(n+1/2)=\int_0^\infty f(x)dx+\frac{1}{24}f'(0)+\ldots \qquad (20)$$

After enough bulky calculations, in the first Boron's approach we receive:

$$J(\vartheta)\approx\exp\left(-\frac{\vartheta^2}{\overline{\vartheta}^2}\right) \qquad (21)$$

where:

$$\overline{\vartheta}^2=\theta_0^2\left(1+\frac{2\theta_0}{\beta}\right)ln\frac{\theta_0^2}{4} \qquad (22)$$

At greater angles $\vartheta/\theta_0\sqrt{ln\frac{\theta_0^2}{4}}\geq 4$ function $J(\vartheta)$ decreases with reduction ϑ much more slowly, than on Gaussian` law, and following members in (21), arising in the second and higher Born's approximation, become essential. Expression (22) allows defining an impulse of a neutron from data about an average square a scattering of angle $\overline{\vartheta}^2$.

4. CONCLUTION (13)

Use of the spin-non-flip amplitude of the $n\ ^{12}C$ scattering, obtained from the formulae (9) permits us to calculate the correct picture of polarisation scattering nucleon.

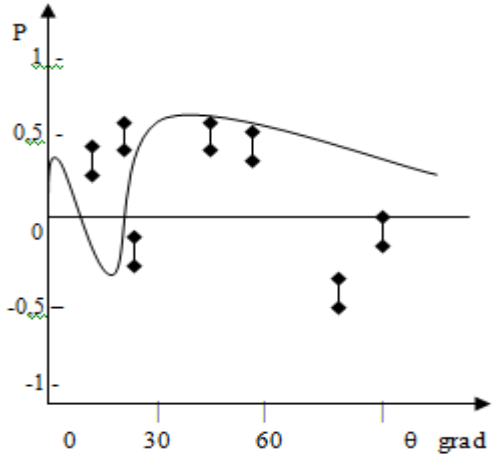

Fig.1 The polarisation of the neutron in $n^{12}C$ scattering.

We consider the case where spin-flip is neglected. It is important to emphasise that the case of the nucleon-nuclei scattering the leading asymptotic terms of the spiral amplitudes is also determined by the contribution of the quark cluster with the evident replacement of $f(q)$ by the pion-nucleon scattering amplitudes. The model prediction for the polarisation of elastic $n^{12}C$ scattering, corresponding to the experimental data is shown in fig.1.

[1]. *S.G. Abdulvahabova* //Conferece Proceeding: First International Conference on Technical and Physical Problems in Power Engineering, Baku, 2002, p.452

[2]. *A.G. Sitenko* //Particles&Nuclear, 1973,V 4, Part2, p.546.

[3]. *L. Raider*. Quantum Field Theory, Moscow, "Mir" 1987, p.512Квантовая теория поля. Москва: Изд. Мир, 1987, с. 512.

PYGMY DIPOLE RESONANCE IN ^{232}Th, ^{236}U AND ^{238}U ($K^{\pi=}1^-$)

E. GULIYEV[1] , A.A. KULIEV[1,2]
[1]*Institute of Physics, Academy of Sciences,*
H. Cavid Avenue 33, Baku, Azerbaijan
[2] *Physics Department, Faculty of Arts and Sciences,*
Sakarya University, Adapazari, Turkey

The E1 response of ^{232}Th ^{236}U and ^{238}U actinide nuclei below the particle threshold were studied using transitional and Galilean invariant quasi particle random-phase approximation (QRPA). Especially strength properties of the pygmy dipole resonance (PDR) with spin and parity ($K^{\pi=}1^+$) are investigated and studied their contribution to 6-10MeV region. Discussed the question whether the pygmy dipole resonances are like the GDR collective states in the microscopic definition. The calculated total Γ_0(M1) width for the spin-flip M1 resonances states are about a factor of 10^{-2} weaker than the summed width of the 1^- states forming PDR at this energy region and can not concurrences with PDR. The results that have been obtained for E1 dipole excitations indicate the importance of the separation of the spurious centre-of-mass motion of the nucleus for a correct description of the PDR

I. INTRODUCTION

The first evidence for strong low-lying electric dipole excitations was found three decades ago [1-3] which, often macroscopically depicted as the oscillation of a deeply bound core against a neutron skin giving rise to a so-called pygmy resonance. Recent systematic studies have shown that the PDR is a common excitation mode in most spherical and transitional nuclei (See, e.g., the review [4] and references therein). The origin of this electric dipole excitations has been discussed within with various microscopic and macroscopic approaches. For an overview over the various approaches we refer to [5] and Refs listed therein. In present there are still some discussions on the issue whether the PDR corresponds to collective or non-collective excitation [6]. Besides recently observed the fundamental discrepancy between the (γ,γ') and ($\alpha,\alpha'\gamma'$) data, i.e, a splitting of the PDR into two parts with different underlying structure for ^{140}Ce and ^{138}Ba provide a new challenge for model calculations [7,8].

While the global properties of the PDR mode are more or less reasonably understood in spherical and transitional nuclei the nature of the pygmy dipole resonance is an open question in well deformed nuclei. There are some theoretical and experimental studies on the light deformed nuclei [9,10]. No systematic study of the PDR in well deformed nuclei in the energy range up to the particle threshold has been performed so far. Its nature and systematic futures remains a subject of discussion. It would be important to extend the (γ,γ') studies to the well deformed and γ-soft nuclei with improved sensitivity in order to firmly establish pygmy resonance properties in nuclei near mid-shell. In case deformed nuclei there is a general problem that the level density is extremely high and even with (□□□') one can no longer resolve the transitions in at energies of about 5 - 8 MeV. Limited experimental information on PDR mode does not allow establish the dominant structure of this state below 10MeV in well deformed nuclei. Therefore, it might be interesting to take a theoretical look to the medium and heavy deformed neutron reach nuclei and see e.g. where the strength lays. In view of this the neodymium, samarium, hafnium and uranium isotopic chains of different deformation regions with their stable even-even isotopes and with a considerable ground state deformation, offers the rare possibility to study the pygmy resonance properties in deformed nuclei. Recently we investigated the low lying magnetic and electric dipole responses up to 4 MeV within QRPA for ^{232}Th, ^{236}U and ^{238}U nuclei. The calculation well established experimental observation [11]. Continuations of this we increase our calculation up to 10MeV for ^{232}Th, ^{236}U and ^{238}U nuclei.

Here for the first time, the strength pattern of the PDR in ^{232}Th, ^{236}U and ^{238}U actinide nuclei is obtained and investigated the question whether the PDR is like the GDR collective states in the microscopic definition. Another scope of this work is investigating if the E1 excitations strength overlaps with the spin-flip M1 strength.

The results shown here have been obtained with the QRPA model of Refs. [12,13]. There, by the selection of suitable separable effective forces, the translational and Galilean invariance is restored for the calculation of E1 excitations and as well as rotational invariance for the calculation of M1 excitations without introducing additional parameters. The applied method and the theoretical calculations have a1ready been described in refs.[12-16]. Therefore, we awoid here to present long theoretical description of the method.

II.CALCULATION

For calculation of the E1 and M1dipole transitions in the even–even ^{232}Th, ^{236}U and ^{238}U the mean field deformation parameters δ_2 are calculated according to [17] using deformation parameters β_2 defined from experimental quadrupole moments [18]. The single-particle energies were obtained from the Warsaw deformed Woods–Saxon potential [19]. The basis contained all discrete and quasi-discrete levels in the energy region up to 6 MeV. This results in about one thousand two-quasiparticle dipole states for the each parity. The pairing-interaction constants taken from Soloviev [20] are based on single-particle levels corresponding to the nucleus studied. Values of the pairing parameters Δ and λ are shown in Table 1.

Besides, the model contains a single parameter only for the calculation of either E1 or M1 transitions. The calculation for the E1 excitation was performed using a strength parameter $\chi_1 = 300/A^{5/3} MeVfm^{-2}$, which is suggested for the isovector dipole–dipole interaction in order to

describe the energy centroid of the giant dipole resonance in actinide nuclei [11]. Its magnitude is related to the isovector symmetry potential and the above value is in close agreement with the analysis of Bohr and Mottelson [17]. For M1 excitations, the isovector spin–spin interaction strength was chosen to $\chi_{\sigma\tau} = 25/A$. This value allows a satisfactory description of the scissors mode fragmentation in well-deformed rare earth nuclei [14].

Table 1. The pairing correlation parameters (in MeV) and δ_2 values

Nuclei	Δ_n	λ_n	Δ_p	λ_p	δ_2
^{232}Th	0.67	-6.136	0.74	-6.716	0.231
^{236}U	0.66	-6.329	0.86	-6.300	0.250
^{238}U	0.56	-6.117	0.86	-6.698	0.254

In models with broken symmetry each excitation has an admixture of the zero-energy spurious state [14]. In the case of the electric dipole it is the translation of the full nucleus and in the case of the magnetic dipole the spurious mode corresponds to the rotation of the full nucleus. There, by the selection of suitable effective forces, broken translational and Galilean invariance are restored for the calculation of E1 excitations and rotational invariance are restored for the calculation of M1 without introducing additional parameters. Up to now, the important influence of spurious states on the PDR has not been examined. So it might be interesting to study the effect of separation of the spurious translational states to the properties of the electric dipole states. In order to determine whether the energy region where the admixtures of the c.m. spurious 1^- state are of importance, we calculated the overlapping integrals between one-phonon states (with broken translational invariance) and the spurious $K^\pi=1^-$ state. It is found that the larger admixtures (more than 60%) of the spurious state being situated in the interval between 6 MeV and 8 MeV below neutron threshold energy region where PDR lay and in 12-16 MeV energy region where GDR lay. Analyses have shown the attractive restoring forces decrease transition strength and make them more collective than the case where only effective forces are taking into account. So for correct analyses of 1^- states it is important to use theories which take into account transitional and Galilean invariant Hamiltonian [11,14].

The calculation predicts strongly fragmented $K^\pi=1^-$ electric dipole states in the excitation energy range 6.0–9.0 MeV. The distribution of the electric dipole strength calculated in the translational invariant QRPA shows a resonance like structure at energies between 8 MeV and 9 MeV exhausting about 5% of the isovector electric dipole energy weighted sum rule for ^{232}Th, ^{236}U and ^{238}U. The obtained strengths can be interpreted as PDR. Fig.1 gives the calculated B(E1) strength distribution for the three investigated actinide nuclei.

In 6.0-9.0 MeV energy interval about 105 electric dipole $K^\pi=1^-$ excited states were calculated with the summed transition probabilities of $\Sigma B(E1)=2.16 e^2\cdot fm^2$ in ^{232}Th , $3.12 e^2\cdot fm^2$ in ^{236}U and $3.17 e^2\cdot fm^2$ in ^{238}U.

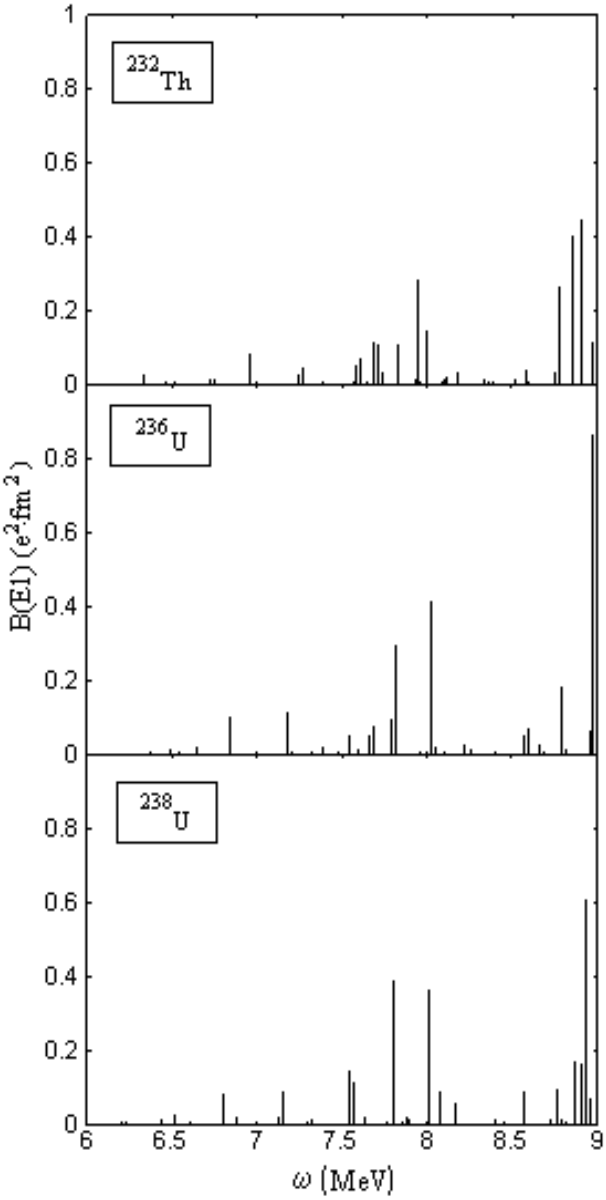

Fig. 1. The energy diagram of the B(E1) values of the ΔK=1 transitions for ^{232}Th, ^{236}U and ^{238}U. Only states with B(E1)> 0.1 ·$e^2fm^2$are displayed.

A very similar pattern is predicted in these nuclei: The group of E1 excitations at about 7.5 -8.0MeV, followed by a rich structure of E1 strength between 8.5 and 9.0 MeV. It is sign to the multi bump structure of PDR resonance. Similar structure was observed for ^{116}Sn nucleus [21]. As can be seen ^{232}Th and ^{238}U are somewhat more fragmented than ^{236}U. Another important questions if PDR mode is collective phenomena or not. In order to answer this question we performed a series of calculations within the QRPA in which we investigate single two-quasiparticle structure of the one phonon states. As showed in our previous work in actinide nuclei E1 excitations of the spectroscopic region are dominated by single two-quasiparticle transitions [11]. Present calculation shows this finding true also up to 6.0 MeV. The structure analyses have shown that for nuclei considered in 6.0-9.0 MeV energy interval together with several dipole states characterized by single two-

quasiparticle transitions relevant one phonon wave functions of the electric dipole K=1 excitations are mainly shared by a considerable number of the two-quasiparticle configurations. Among these states one can find several 1^- states in forming of which neutron-neutron (n-n) and proton-proton (p-p) two-quasiparticle configurations participate. As a rule the contribution of which to the summed B(E1) of the nuclei considered varies between 15-25 %.

A many collective dipole states has been found below particle threshold, and their wave functions represent mainly a superposition of only neutron-neutron or only proton-proton two-quasi particle configurations. Moreover as each phonon mainly formed from one kind of nucleons (protons or neutrons) so in PDR forming process together neutrons also protons play additional role for actinide nuclei where broken the shell structure and the neutron core losing its meaning. In table 2 we present the energy, the transition strength (B(E1) and the summed contributions of the neutron and proton two-quasiparticle states. In brackets of the norms a number of two-quasiparticles with contribution to the norm of the phonon wave function larger than 1% are listed. As seen from table for the pygmy dipole states the contributions of the proton response is almost same with contribution of the neutron response and even for some states bigger than neutron contribution. Analysis show that contribution of the states with B(E1)> $0.1\cdot e^2\cdot fm^2$ to the total $K^{\pi}=1^-$ dipole summed strength (6.0-9.0MeV) are more than 63% for nuclei considered. In the following paragraphs, we shall discuss separately the nuclei under investigation, ^{232}Th, ^{238}U, and ^{236}U which are shown in the Figures 1-3 and Table 2. In the presented results all sums and comparisons have been carried out for 6.0-9.0 MeV energy region.

^{232}Th: The theory predicts nine $K^{\pi}=1^-$ dipole excitation in the 6-9 MeV energy interval with a summed strength of B(E1)=$2.04\cdot e^2fm^2$. As can be seen from Table 2, the calculation indicates the presence of three collective $K^{\pi}=1^-$ electric dipole states at energy ω=7.72MeV with B(E1)=$0.11\cdot e^2fm$, ω=8.77MeV with B(E1)=$0.27\cdot e^2fm^2$ and ω=8.90MeV with B(E1)=$0.45\cdot e^2fm^2$, which composed of mainly (≈99%) neutron two-quasiparticles. The contribution of these states to the total $K^{\pi}=1^-$ dipole decay width (6.0-9.0 MeV) is about 38%. Besides there are three p-p type dipole states with B(E1)=$0.12\cdot e^2fm^2$ at at the energy ω=7.69 MeV, B(E1)=$0.12\cdot e^2fm^2$ at the energy ω=7.83 MeV and B(E1)=$0.41\cdot e^2fm^2$ at the energy ω=8.85MeV in formation of which participate mainly proton-proton two-quasiparticle configurations (≈98%). The contribution of these states to the summed $K^{\pi}=1^-$ dipole decay width is about 30%. There are three collective states forming from the configuration of neutron and proton two–quasiparticles B(E1)=$0.29\cdot e^2fm^2$ at the energy ω=7.94MeV, B(E1)=$0.15\cdot e^2fm^2$ at the energy ω=7.99MeV and B(E1)=$0.12\cdot e^2fm^2$ at the energy ω=8.99MeV. The contribution of these $K^{\pi}=1^-$ dipole states to the summed dipole decay width is about 26%.

^{236}U: The calculation predicts six electric dipole $K^{\pi}=1^-$ excitations with summed B(E1)=$1.99\cdot e^2fm^2$ at 6.0-9.0MeV energy range. In this nucleus one isolated electric dipole excitation with the strongest B(E1)=$0.87\cdot e^2fm^2$ at 9.02 MeV has been obtained. In formation of this state participate mainly n-n two-quasiparticle configurations (≈90%). The contribution of these $K^{\pi}=1^-$ dipole states to the summed dipole width is about 28%. As can be seen from the Table 2, there are three p-p type excited states. The states with B(E1)=$0.13\cdot e^2fm^2$ at the energy ω=7.18 MeV, B(E1)=$0.4\cdot e^2fm^2$ at the energy ω=8.02 MeV and B(E1)=$0.19\cdot e^2fm^2$ at the energy ω=8.78MeV. The contribution of these $K^{\pi}=1^-$ dipole states to the summed dipole width is about 23%. There are two states formed from n-n + p-p two-quasiparticle configurations of as B(E1) =$0.1\cdot e^2fm^2$ at the energy 7.818 MeV and B(E1)= $0.3\cdot e^2fm^2$ at the energy 7.82MeV. The contribution of these states to the summed $K^{\pi}=1^-$ dipole decay width is about 13%.

Table 2. Structure of the several $K^{\pi}=1^-$ dipole states with the largest B(E1) values (B(E1)>$0.1\cdot e^2fm^2$) for ^{232}Th, ^{236}U and ^{238}u nuclei.

ω [MeV]	B(E1) [e^2fm^2]	Norm Neutron [%]	Norm Proton [%]
	^{232}Th		
7.69	0.12	2 {1}	0.98 {7}
7.72	0.11	100 {11}	0.0 {0}
7.83	0.12	0.03 {5}	0.97{1}
7.94	0.29	0.36 {4}	0.64 {7}
7.99	0.15	0.75 {4}	0.25 {4}
8.77	0.27	0.98 {14}	0.02 {1}
8.85	0.41	0.02 {1}	0.98 {11}
8.90	0.45	0.99 {18}	0.01{0}
8.99	0.12	0.55 {6}	0.45 {8}
	^{236}U		
7.18	0.13	0.00 {0}	1{3}
7.82	0.10	0.47 {2}	0.53{7}
7.82	0.30	0.53 {2}	0.47{6}
8.02	0.40	0.02 {0}	0.98{8}
8.78	0.19	0.10 {2}	0.90{10}
9.02	0.87	0.90 {24}	0.10{3}
	^{238}U		
7.54	0.15	0.84 {15}	0.16{2}
7.55	0.12	0.17 {9}	0.83 {3}
7.80	0.39	0.09 {2}	0.91{9}
8.00	0.37	0.03 {2}	0.97 {8}
8.76	0.10	0.98 {4}	0.02{1}
8.87	0.18	0.01{0}	0.99 {7}
8.91	0.17	0.98 {8}	0.02{0}
8.93	0.61	0.98 {18}	0.02{1}

^{238}U: Theory predicts eight 1^- levels in the 6.0-9.0 MeV energy interval with a summed strength of B(E1)=$2.09\cdot e^2fm^2$. The calculation predicts three electric dipole K=1 excitations with the strengths B(E1)= $0.1\cdot e^2fm^2$ at the energy ω=8.76MeV B(E1) = $0.17\cdot e^2fm^2$ at energy ω=8.91MeV and B(E1)= $0.61\cdot e^2fm^2$ at the energy ω=8.93MeV which are form from mainly (98%) n-n type two-quasiparticles. The contribution of these $K^{\pi}=1^-$ dipole states to the summed dipole decay width is about 28%. Besides there are three p-p type (>90%) collective excitations with B(E1)=$0.39\cdot e^2fm^2$ at ω=7.8MeV, B(E1) = $0.37\cdot e^2fm^2$ at the energy ω=8.0MeV

and B(E1)= $0.18 \cdot e^2fm^2$ at the energy ω=8.87MeV. The contribution of these $K^\pi=1^-$ dipole states to the summed dipole decay width is about 30% There are two states forming from configuration of n-n and p-p two – quasiparticles with B(E1) = $0.15 \cdot e^2fm^2$ at energy ω= 7.54 MeV and B(E1) = $0.12 \cdot e^2fm^2$ at energy ω= 7.55 MeV. The contribution of these states to the summed $K^\pi=1^-$ dipole decay width is about 9%. As can be seen from Table 2 contribution of collective excitations formed from neutrons and protons to summed E1 dipole width less than $0.2 \cdot e^2 \cdot fm^2$ for all nuclei considered. Generally, contributions to summed E1 strength of the PDR coming from 1^- states which are formed mainly from one sort n-n or p-p configurations are around 70%.

Thus, theory predicts three n-n, p-p and n-n + p-p type collective dipole states. Our calculations showed that usually more than 90% of the wave function norm is divided among a large number of two-quasiparticle states for n-n and p-p type PDR excitations. Analysis shows that, in formation of the n-n or p-p type phonon states the contribution to the wave function norm coming from one sort nucleons are more than 90%. This indicates rather collective nature of the PDR mode.

We note that for the medium-heavy neutron-rich nuclei with $50 < N < 82$ for the pygmy states the neutron response is a factor 10 larger than the proton response see ref [6]. Besides, our work on N=82 isotones using deformed base (for proton systems) also was showed the neutron structure play dominant role with small contributions of proton system [22]. In these nuclei PDR mode can be identified as oscillation of neutron skin against static core. Since, as in well deformed nuclei neutron and proton orbits intermix energetically around Fermi surface, so for the deformed nuclei static shell structure losing it is meaning and it makes possible appearing independently proton and neutron oscillations in heavy nuclei. Therefore, macroscopically depict PDR mode is forming from oscillation of neutron skin against deeply bound static core can not be generalized for all nuclei. These analyses have shown PDR mode in well deformed nuclei has more complicate structure than the nuclei near shell closure. At present, there exists no satisfactory explanation for the surprising structure differences between the PDR in different nuclei. The data should be a challenge to modern microscopic and macroscopic models, and improved approaches for the description of deformed nuclei are important. For approval this statement needs further investigation of well deformed nuclei. So the PDR nature and systematic features remains a subject of discussion.

It is well known that in the deformed nuclei the electric dipole excitations are split into two parts: $K^\pi=1^-$ and $K^\pi=0^-$. The $K^\pi=1^-$ modes which correspond to vibrations perpendicular to the symmetry axis are shifted as compared to the $K^\pi=0^-$ modes which correspond to vibrations along the symmetry axis. This shifting to cause laying PDR resonance same place with $K^\pi=0^-$ branches of E1 excitations. Therefore it is very important to investigate energy distribution of the E1 strength of $K^\pi=1^-$ and $K^\pi=0^-$ dipole excitations. As an example in figure 3, was showed electric dipole strength distribution for both $K^\pi=1^-$ and $K^\pi=0^-$ parts of ^{236}U nucleus calculated within the QRPA method.

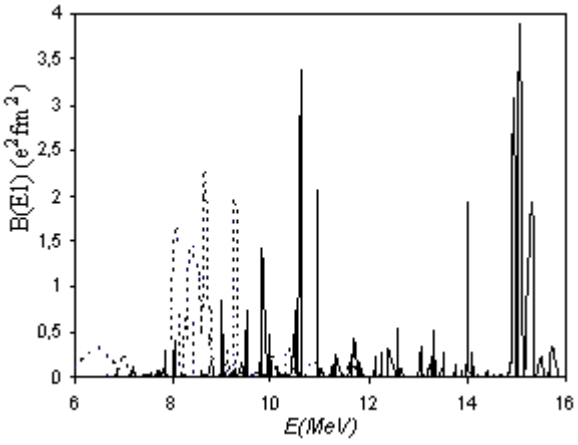

Fig. 3. K=0 and K=1 electric dipole distributions in ^{236}U nuclei

It is clearly seen that $K=1^-$ strength is rather fragmented over a wide region. In spite of shifting of $K=1^-$ states to the higher energies part of $K=1^-$ states lay in the area covered by $K=0^-$ states. As seen main contribution to the PDR mode come from K=0 branch of the 1^- states. Such picture is valid for the other isotopes considered.

In heavy spherical and deformed nuclei there are exists a very broad M1 spin-flip resonance at the energies between 7 and 11 MeV and centered an energies on the ordered of about $44 \cdot A^{-1/3}$ MeV [23]. Therefore, we have also calculated the B(M1) strength distribution below 10MeV. The summed magnetic dipole strength B(M1) (in units e^2fm^2) is $0.222 \cdot e^2fm^2$, $0.223 \cdot e^2fm^2$ and $0.224 \cdot e^2fm^2$ in ^{232}Th, ^{236}U and ^{238}U, respectively. Corresponding E1 strength is B(E1)=$2.04 \cdot e^2fm^{2\nu}$ for^{232}Th, B(E1)=$1.99 \cdot e^2fm^2$ for ^{236}U and B(E1)=$2.09 \cdot e^2fm^2$ for ^{238}U. Thus, the calculation predicts spin-flip M1 resonances with summed strength one order weaker than PDR mode in investigated energy region of 6.0–9.0 MeV.

The comparison the ground-state redused transition widths for PDR and spin-flip resonance presented in Fig.3 in ^{238}U example. The plotted values are the reduced ground state transition widths- $\Gamma_0^{red} = \Gamma_0 / \omega_i^3$ as a function of the excitation energy, separately for E1 and M1excitations with $\Delta K=1$ which are given as vertical lines and solid line of the figure, respectively.
Here

$$\Gamma_0^{red.}(E1) = 0.349 \cdot B(E1)[10^{-3} e^2\, fm^2], \text{meV}$$

and

$$\Gamma_0^{red.}(M1) = 3.86 \cdot B(M1)[\mu_N^2], \text{meV}$$

Comparative characteristics of the $I^\pi K=1^+1$ and $I^\pi K=1^-1$ excitations of ^{232}Th, ^{236}U and ^{238}U nuclei shows huge E1 strength in the considered energy region which precludes observation M1 mode. As can be seen from Figure 3 on the whole, the magnetic dipole contribution (curved line) to the summed dipole width is considerably smaller than the electric dipole part. Therefore contribution of spin-flip resonance shown smoothly background and cannot

concurrences with PDR. This gives an estimate for possible erroneously assigned B(E1) strength.

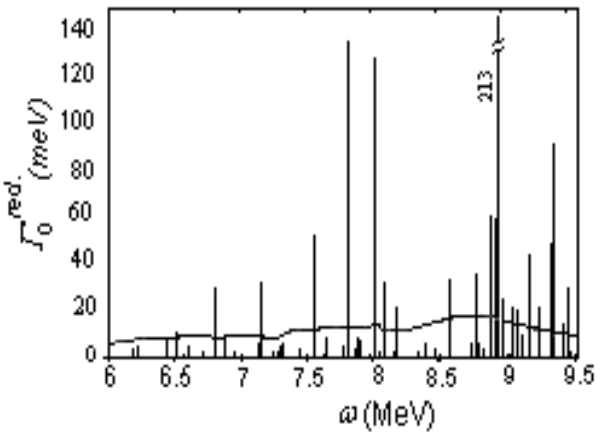

Fig.3. The reduced dipole ground-state transition widths for PDR (impulses) and for spin-flip resonance (the curved line) for ^{238}U.

III. CONCULUSION

In summary, ^{232}Th, ^{236}U and ^{238}U nuclei were studied in a transitional, Galilean and rotational invariant quasi particle random-phase approximation.

The calculations predict resonance like structure between 7.5-9.0MeV quasiparticle configurations. The analyses showed that usually more than 90% of the wave function norm is divided among a large number of two-quasiparticle states for n-n and p-p type PDR excitations. Therefore, for deformed nuclei macroscopically statement that PDR is simple oscillation of the excess neutrons with respect to an N = Z core is open question.

Besides, observation of the n-n type 1^{-} excitations in the (γ,γ') scattering experiments will be very difficult than p-p types. But these excitations can be easily observed in the nuclear scattering experiments. Therefore the results of the α-scattering experiments for PDR will be difference than the results obtained in NRF experiments

[1]. *G.A. Bartholomew et al*., Adv. Nucl.Phys. 7, 229 (1973)
[2]. *F.R.Metzger*, Phys.Rev. C 18, (1978) 1603
[3]. *F.R.Metzger*, Phys.Rev. C 18, (1978) 2138
[4]. *J.Enders et al.*, Acta Phys.Polonica B36 (2005)
[5]. *J. Enders et al*., Nucl. Phys. A724, (2003) 243
[6]. *D. Vretenar et al.,* Nuclear Physics A 692 (2001) 496
[7]. *D. Savran, et al*., Phys. Rev. Lett. 97, (2006) 172502
[8]. *J. Endres et al.,* Phys. Rev C 80, (2009) 034302
[9]. *J.Gibelin et al*. Nucl. Phys. A788 (2007)153c
[10]. *P.Ring et al*. Nucl. Phys. A788 (2007)194c
[11]. *A.A.Kuliev et al.*, Eur. Phys. J. A43 (2010)323
[12]. *E.Guliyev et al*. Phys.Lett. B 532, (2002) 173
[13]. *E. Guliyev et al*., Eur. Phys. J. A 39, (2009) 323
[14]. *A.A. Kuliev et al*., Int. J. of Mod. Phys. E9 (2000)249
[15]. *E. Guliyev et al*., Eur. Phys. J. A 27 (2006) 313
[16]. *E. Guliyev et al*., Cent. Eur. J. Phys. 7 (2009) 731
[17]. *O. Bohr, B. Mottelson, Nuclear Structure*, Vol. 2 (Benjamin, NewYork Amsterdam, 1975).
[18]. *S. Raman et al*., Atomic Data Nucl. Data Tables 78 (2001)1
[19]. *J. Dudek, T.Werner*, Jour. Phys. G4 (1978)1543
[20]. *G. Soloviev, Theory of Complex Nuclei* (Pergamon Press, New York, 1976).
[21]. *A. M. Oros, et al*. Phys.Rev. C 57(1998)990
[22]. *Guliyev et al.*, Cent. Eur. J. Phys. 2010 (in press)
[23]. *A.Richter*, Prog. Part. Nucl. Phys. 34 (1995)261

CONCEPTS OF INERTIAL, GRAVITATIONAL AND ELEMENTARY PARTICLE MASSES

OKTAY H. GUSEINOV[1] AND SEVINC O. TAGIEVA[2]

[1] Akdeniz University, Department of Physics, Antalya, Turkey

[2]H.M.Abdullayev Physics Institute, Azerbaijan National Academy of Science, Baku 370143, H.Javid ave., 33, Azerbaijan Republic

The concept of mass is analyzed based on Special and General Relativity theories and particle (quantum) physics. The mass of a particle (m = E_Q/c^2) is determined by the minimum (rest) energy to create that particle and it is invariant under Lorentz transformations. In any field, the mass of a bound particle is m < E_Q/c^2 and if it is not relativistic then the relation m = E/c^2 is valid. This relation is not correct in general and it is wrong to apply it to radiation. In atoms or nuclei (i.e. if the energies are quantized) the mass of the particles are discrete. In non-relativistic cases mass can be considered as a measure of gravitation and inertia. However, in general mass is a property of inertia and attraction energy.

1. INTRODUCTION

Lev Okun published an article on the concept of mass in special relativity in the 1989 issue of "Physics Today" [1] to show that the formula $E_0 = mc^2$ is correct and $E = mc^2$, $E_0 = m_0c^2$, $E = m_0c^2$ and $m = \dfrac{m_0}{\sqrt{1-\mathrm{v}^2/c^2}}$ are wrong. In fact they are *historical artifacts* but still they are seen in many textbooks. Mass is invariant value relative to Lorentz transform. The questionnaire among the professional physicists also supported Okun's observation that rest mass, namely m_0 and relative mass concepts are misunderstood. In fact there are a lot of physicists who take a position against Okun and other particle physicists. For example, among physicists working on General Relativity Khrapko thinks differently than Okun and other particle physicists [2].

The purpose of this article is to discuss the issue of mass basing our ideas on fundamental principles of theoretical physics and also considering general theory of relativity to show that the formula $E = mc^2$ is correct in some situations and to show that the mass concepts like the inertial and gravitational mass are often understood incorrectly.

The oldest concept of mass is the one that is developed when people started trading and later that is used as *matter content* in science. With Newton's mechanics, the concepts of inertia and attractive mass are developed. Any physical quantity must be measureable in someway directly or indirectly. This perspective was concretized by Einstein when he constructed the General Theory of Relativity. We can measure mass by using the laws of dynamics or with the scale. Matter content is measured in ordinary life and in chemistry with the scale. Therefore, matter content is nothing but the gravitational mass. In reality for the objects (not particles) a concept like matter content is not an exact thing and its measurement method is not different than that of gravitational mass, we would not deal with it in this article.

2. NEW CONCEPTS INTRODUCED BY SPECIAL RELATIVITY: ENERGY, MOMENTUM AND THE PROBLEMATIC MASS

The least action principle is one of the most fundamental principles in physics. Therefore, to obtain the most general results we take the condition that action stays constant under Lorentz transformations. By multiplying any invariant quantity by a dimensional constant we can always change its dimension to the dimensions of action. We already have a quantity that is invariant under Lorentz transformations and a scalar, namely, the interval between events, ds. For the coordinate systems moving with relativistic speeds the interval is given

$$ds = c\left(\sqrt{1-\frac{\mathrm{v}^2}{c^2}}\right)dt \tag{1}$$

Multiplying this by a dimensional constant (say b) and integrating we obtain the action as

$$S = -\int_{t_1}^{t_2} bc\left(\sqrt{1-\frac{\mathrm{v}^2}{c^2}}\right)dt \tag{2}$$

Here, the minus sign is there to guarantee that the extreme point of the integral is a minimum, instead of a maximum. The Lagrangian is obtained by taking the time derivative of the action. In the Lagrangian functional, $L = -bc\sqrt{1-\dfrac{\mathrm{v}^2}{c^2}}$, the fact that all the terms except the term b are taken from the special relativity, makes the Lagrangian valid for speeds close to the speed of light (and evidently for small velocities.) Here, we are considering a particle that is not under any influence. Moreover, except its mass, such a particle hasn't got a physical property that is important for the problem under consideration. Therefore, b should be related to mass (one can realize that since b is constant, we have taken mass as a constant automatically). For a particle moving with small velocity, expanding the Lagrangian in the ratio v/c and discarding the small terms, we obtain

$$L = -bc\sqrt{1-\frac{\mathrm{v}^2}{c^2}} \approx -bc + \frac{b\mathrm{v}^2}{2\mathrm{c}} \tag{3}$$

The constant terms of the Lagrangian does not characterize the kinetics of the particle and can be

omitted. Thus, to find the relation of the quantity b with the mass of the particle we should look at the second term in the above expansion. The Lagrangian for the free particle with small velocity is equal to its kinetic energy. Therefore,

$$\frac{b\mathrm{v}^2}{2\mathrm{c}} = \frac{m\mathrm{v}^2}{2} \tag{4}$$

This leads to $b=mc$. Then the relativistic Lagrangian is

$$L = -mc^2\sqrt{1-\frac{\mathrm{v}^2}{c^2}} \tag{5}$$

Most generally, momentum is the partial derivative of the Lagrangian with respect to its velocity

$$p = \frac{\partial L}{\partial v} \tag{6}$$

and to find the components of the momentum vector the partial derivative of Lagrangian with respect to each component of the velocity vector must be taken.

Now using equations 5 and 6, we can find the momentum of the free particle:

$$\mathbf{p} = \frac{m\,\mathbf{v}}{\sqrt{1-\frac{\mathrm{v}^2}{c^2}}} \tag{7}$$

Naturally, for small velocities (v<<c), this equation becomes the well known Newtonian formula

$$p = mv \tag{8}$$

In the above description and the description that is based on special relativity the particle that is motionless or moving with small velocities has mass m as seen from equation 8. There is no need to call mass m_o in the no relativistic case because we treated mass as constant. With this approach the coefficient $1/(1- v^2/c^2)^{1/2}$ has no physical relation with mass. The equation that is seen in many textbooks

$$m = \frac{m_0}{\sqrt{1-\frac{\mathrm{v}^2}{c^2}}} \tag{9}$$

should be accepted as wrong if it is understood in terms of rest energy (that is related to matter content). Is wrong and this mistake comes from some historical facts which are outside the scope of Einstein's theory of special relativity.

The quantity mass in the equations 5 and 7 are invariant under Lorentz transformations. Equation 7 is derived using the most important and trustworthy quantities and concepts of mechanics. This formula is valid for all speeds (naturally less than the speed of light) and approaches infinity as the speed gets closer and closer to the speed of light. Why for 100 years (since the work of Lorentz in 1899) rest and relative mass concepts are often used? Is the mass of a particle, like electric charge, baryon and lepton numbers, an *invariant* quantity?

We can go back to the force concept that is known since Newton. Force is the derivative of the momentum with respect to time. The direction of the velocity of a particle, and the direction of the force on it can be quiet different. We can look at two different cases for demonstration: the case when the force and momentum are parallel and when they are perpendicular. If the force and momentum are parallel, because of the force, the magnitude of the velocity changes, however the direction does not change. Then the derivative of the equation 7 with respect to time gives

$$\frac{d\mathbf{p}}{dt} = \frac{m}{\left(1-\frac{\mathrm{v}^2}{c^2}\right)^{3/2}}\frac{d\mathbf{v}}{dt} \tag{10}$$

If the force and momentum are perpendicular, the magnitude of the velocity does not change but the direction of the particle changes continuously. Then the derivative of the momentum becomes

$$\frac{d\mathbf{p}}{dt} = \frac{\mathrm{m}}{\left(1-\frac{\mathrm{v}^2}{\mathrm{c}^2}\right)^{1/2}}\frac{d\mathbf{v}}{dt} \tag{11}$$

Left hand side of the formulae which describes the change of momentum with respect to time (eq. 10 and 11) are the forces and the right hand side includes accelerations. In the frame of Newtonian dynamics, the ratios of the forces to the accelerations are not the same. In Newtonian physics these ratios are masses. But are these ratios

$$\frac{m}{\left(1-\frac{\mathrm{v}^2}{c^2}\right)^{3/2}} \text{ and } \frac{m}{\left(1-\frac{\mathrm{v}^2}{c^2}\right)^{1/2}} \tag{12}$$

define the mass? No, $m/(1 - v^2/c^2)^{3/2}$ and $m/(1 - v^2/c^2)^{1/2}$ are coefficients due to the relativistic motion that are not representing mass correctly. It is normal that for different situations it is natural that mass and inertia are different. However, it is not very natural that the mass of the particle depends on the direction of the force acting on the particle. These two definitions of mass are first introduced by Lorentz as longitudinal and transverse masses. Unlike Newtonian physics, here, mass is not the ratio of momentum and speed because in relativistic and especially ultra-relativistic cases, inertia depends not only on the mass, but also on energy. Without considering general relativity, we should not generalize the concept of mass in Newtonian physics.

Many authors use both the words "point particle" and "extended object" when dealing with similar problems in the frame of Special Relativity. In this section we only investigate the kinematic properties of free

particles. Extended particles are composed of other particles that are not free.

Recall that equation 5 describes the Lagrangian of a relativistic free particle. From this equation it is seen that as the velocity of the particle approaches the speed of light, the magnitude of L approaches zero and notice that L is always negative. Since the energy of a free particle is always larger than zero, in equation 5, the term which describes the quantities related with the kinematics of the particle and which is positive should be increased by the addition of a new term. This new term in the Lagrangian must also be valid in the Newtonian domain. The energy can be written as

$$E = pv - L \tag{13}$$

If we insert the Lagrangian which is valid in Newtonian physics to equation 13, we obtain

$$E = pv - \frac{mv^2}{2} = \frac{mv^2}{2} \tag{14}$$

This is the kinetic energy for the non-relativistic particle. The corresponding relativistic energy can be found by using the formulae 5 and 7

$$E = \frac{\mathrm{mv}^2}{\left(1-\frac{\mathrm{v}^2}{\mathrm{c}^2}\right)^{1/2}} + \mathrm{mc}^2\left(1-\frac{\mathrm{v}^2}{\mathrm{c}^2}\right)^{1/2} = \frac{\mathrm{mc}^2}{\left(1-\frac{\mathrm{v}^2}{\mathrm{c}^2}\right)^{1/2}} \tag{15}$$

From this formula we can see that as the velocity of the free particle approaches the speed of light in vacuum, the energy becomes infinite. When the velocity of the free particle is zero, its energy is mc^2, not zero.

Now, to determine the relation between the energy and momentum of a particle in the frame of special relativity, we subtract the square of the equation 7 from the square of equation 15

$$E^2 - \mathrm{p}^2\mathrm{c}^2 = \frac{\mathrm{m}^2\mathrm{c}^4 - \mathrm{m}^2\mathrm{v}^2\mathrm{c}^2}{\left(1-\frac{\mathrm{v}^2}{\mathrm{c}^2}\right)} = \mathrm{m}^2\mathrm{c}^4 \tag{16}$$

or

$$E^2 = p^2c^2 + m^2c^4, m^2c^4 = E^2 - p^2c^2$$

From these formulae it is seen again that the energy of a motionless particle (i.e. rest energy) is $E_0 = mc^2$.

Using the same formulae (eq 7 and 15) we find

$$p = \frac{Ev}{c^2} \tag{17}$$

The particles having zero mass (photon, graviton), their speed in vacuum is c, so

$$p = \frac{E}{c} \tag{18}$$

Therefore, these object even though they do not have mass, they have momentum and thus have pressure when the number of particles is high enough. Momentum, pressure and the inertial mass related to these (not only related to the second law of Newton) are not only related to the particles (matter) with mass.

If we take E/c as the fourth component of the 4-momentum, in the Lorentz transformations all the necessary conditions for the invariant 4-momentum would be satisfied. The components of the 4-momentum in two different coordinates can be written as

$$p_x = \frac{p'_x + \frac{\mathrm{v}}{c^2}E'}{\sqrt{1-\frac{\mathrm{v}^2}{c^2}}} \tag{19}$$

$$p_y = p'_y, \quad p_z = p'_z,$$

$$E = \frac{E' + \mathrm{v}\,p'_x}{\sqrt{1-\frac{\mathrm{v}^2}{c^2}}}$$

The last equation above is the simplified version of the four component of the 4-momentum

$$\frac{E}{c} = \frac{\frac{E'}{c} + \frac{\mathrm{v}}{\mathrm{c}}p'_x}{\sqrt{1-\frac{\mathrm{v}^2}{c^2}}} \tag{20}$$

The invariant quantity in nature is the 4-dimensional momentum (or the energy-momentum tensor). Energy and momentum are not conserved separately. The conservation of momentum and conservation of energy separately is just an approximation and valid only for some of the cases within errors. We can compare equation 15 with the square of the interval between two events

$$ds^2 = c^2dt^2 - dx^2 - dy^2 - dz^2 = c^2dt^2 - dr^2 \tag{21}$$

Here, we see that also ds^2 is the square of a magnitude of a 4-vector, just like the m^2c^4 term in equation 16. As ds^2 is invariant under Lorentz transformations, m^2c^4 is also an invariant. That means, transforming from an inertial frame to any other one, the mass of the particle does not change. We see from this and the above that the mass of a particle is Lorentz invariant.

We can explain the problems in understanding of the concept of mass up to this point as historical artifacts. In the past, even some of the brilliant and famous physicists, were unable to understand which of the two different versions of the energy that introduced in 1900 by Poincare as $E = mc^2$ and in 1905 by Einstein as $E_0 = mc^2$ is relevant. Moreover, the longitudinal and transverse masses that depend on the velocity of the particle (object) that Lorentz introduced in 1899 have been around. At those times longitudinal and transverse

mass concepts were there. (Even Einstein could only cope with these difficulties 10 years after 1905. We should not forget that at those times there were no precise experiments on these subjects. General theory of relativity showed that attraction (gravitation) and inertia are properties of energy. Later, quantum physics (particle and nuclear physics) showed that the physical mass is a different and deeper concept. However, in some of the scientific journals and books the mass that depends on speed remained. This is mostly because this confusion about mass does not affect the results of the calculations.

3 THE MASS OF PARTICLES AND OBJEKTS DEFINED LIKE INERTIA AND GRAVITATION

For the free particles that are considered as elementary until 1960's (we do not go down to the quark level here), the most important properties were their mass and rest energies ($E_0 = mc^2$). The speed of the mass less particles (photon and graviton) in vacuum is c. As the mass of elementary particles increase the number of properties that characterize them like electric charge, lepton number, baryon number, isospin, strangeness, etc. and the number of type of interactions they can have increase. (A simple example for this is that neutrinos have only lepton numbers but electrons that are much heavier than neutrinos, have lepton numbers and also electric charges. Moreover, some of the neutral particles much heavier than the electrons have no lepton or baryon numbers nor electric charges, however, they are involved in more types of interactions than electrons do.) Now the question is this: Is the mass of these particles (or rest energies) conserved in any type of process?

As known, the special theory of relativity describes the physical relation between space and time and determines the invariant physical quantities for the processes involving any type of motion. This theory is one of the fundamental theories of physics that is valid where the gravitational field is constant and its gradient is zero, where the space can be considered as flat. Therefore, to understand the concept of mass, we should consider general relativity that has a more general scope.

3.1 THE EFFECT OF INTERACTION FIELD ON NON- RELATIVISTIC PARTICLES

Recall that in any interaction field (electrical, baryonic or gravitational) in which the particle is bound to the field (E < 0), the mass of sub-atomic particles differs from their free states. Nuclear physics shows us that the free proton has a mass of 938.2 MeV/c^2 and four of them make 3752.8 MeV/c^2. The mass of the free neutron is 939.6 MeV/c^2. When four nucleons come together to form the nucleus of the Helium atom consisting of two protons and two neutrons, about 28 MeV of energy is released. Therefore, the mass of the nucleons in the nucleus becomes less than the free ones. In general, in nuclear interactions, the mass of each nucleus can not decrease more than 0.008mc^2. Rainville et al. [3] conducted a very precise and direct test of atomic mass conversion into photon energy and determined that the relation $E = mc^2$ is valid at least to a level of 0.00004%.

The binding energy of each baryon in a neutron star in its gravitational field is much higher than the binding energies in nuclear interactions. In some of the high mass and dense neutron stars the binding energies can be about 0.1mc^2. In the gravitational field of black holes, the binding energy can exceed $0.2mc^2$. Evidently, for each subatomic particle the binding energy in Earth's, Sun's or normal star's gravitational fields is much less than the energy needed to form a nucleus.

Above discussion shows that the elementary particles loose some part of their mass in the attractive fields of the nucleus or stars. This shows that, in fact, mass is not a conserved quantity in general (unlike the charges of elementary particles) and this fact is already known from special relativity. Contrary to the attractive forces, the repulsive forces between the baryons and the spin interactions of fermions increase the mass of the particles in the system. (Another example is when a photon tries to traverse a superconductor, it gains mass. Moreover, standard model of particle physics predicts that the fundamental particles obtain their mass through the interaction with the Higgs field).

Above, we have seen that the elementary particles loose more mass (rest energy) when becoming part of neutron stars and black holes. On the other hand, they gain considerable kinetic energy in rapidly rotating neutron stars (pulsars) or black holes. The newly born pulsar has a temperature about 10^{11} K and it can spin about hundreds of times per second. Because of these, for such a pulsar, the sum of thermal and rotational energy losses can be $(0.05-0.1)\,Mc^2$ (i.e. 5-10% of sum of all the rest energies of all the particles constituting the pulsar). Pulsars loose energy in general by emitting neutrino pairs, magneto dipole radiation, ultra relativistic and relativistic particles.

Naturally, electron-positron pair annihilation which occurs due to electromagnetic (and sometimes due to weak) interaction has high probability of occurrence in the reverse direction as well (pair creation). These types of interactions show that in the interaction of elementary particles, even all the mass of a particle can transform into radiation and radiation can transform completely into mass.

Therefore, the experiments on Earth and observations of the processes in the Universe prove that the formula $E = mc^2$ (for the bound particle) by Poincare in 1900 and the formula $E_0 = mc^2$ (for the free particle) by Einstein in 1905 are both correct. This means that these formulae explain the partial mass-loss (by electroweak and gravitational interactions) or complete mass-loss (by electroweak interactions) to radiation. Here, if we go beyond the concept of the mass that is related to the rest-energy of the particle, by the changing of mass with interaction, we can see that we have returned to the Poincare formula. Because, always in nuclear reactions the emitted energy is calculated using the formula $\Delta E = \Delta mc^2$.

The experimental and observational proofs of a formula does not necessarily show that all types of description of that formula or the ideas behind the formula are always correct and true. In the nuclear and electromagnetic interactions part of the mass of the particles transforms into radiation (until now we did not

observe the gravitational binding energy transforming directly into radiation) and if the mass-loss is denoted as Δm, the emitted energy is $\Delta E = \Delta m c^2$. However, if the energy of the particle increases by ΔE its mass in general does not increase. For the un-free particle $\Delta m = \Delta E / c^2$ formula is always correct and for radiation $m = h\nu / c^2$ formula is never correct. Poincare formula ($E = mc^2$) might be partially correct since the particle having high Fermi energy or thermal energy in compact stars can not exceed its rest mass. This formula is valid only when the particle is bound since the kinetic energy of the bound particle does not increase the mass of the particle.

3.2 DEFINITION OF INERTIAL AND GRAVITATIONAL MASS

In nuclear physics, high energy physics and astrophysics, the type of matter and mass as used in chemistry always change. Sometimes matter changes into light or the opposite, it is created by light. In all these processes the conserved quantity is neither the molecules or atoms themselves nor the elementary particles nor their masses. The conserved quantities are the different types of charge (electric charge, lepton number, baryon number).

In Einstein's theory of general relativity, the equivalence of inertial and gravitational masses is a postulate. Thus, there is only one mass in general relativity theory. Inertial and gravitational masses are different manifestations of the same mass. At a point, or in a very small local region of space-time, General Relativity gives the same results as Special Relativity. In such a case since there is the possibility to have no gravitational field, the need for the gravitational mass disappears for the particle (body) in the theory of special relativity. Therefore, in Special Relativity only one mass term, the inertial mass term can be used. In accelerators, magnetospheres of pulsars, shock waves of Supernova remnants and in other cosmic objects, the things that are accelerated to the speeds close to the speed of light are the elementary particles not even the atoms (except some ions of atoms). These particles have masses specific to themselves and these are the same masses that particle physicists use $\left(m = E_0 / c^2\right)$ and this is the inertial mass of the particle. But since the mass does not change there is no need for an inertial mass term. As the energy of the particle (body) increases its inertia increases. Inertia is a measure of energy. Since a particle (body) has a rest-energy it has rest inertia too. This inertia, in Newtonian physics, is defined as if it is a property of the mass.

Cosmology shows that radiation and any type of field gravitates. The gravitation is not only a property of mass, but it is mainly a property of energy. Therefore, if we take special and general theories of relativity and particle physics as fundamental, we can say that mass is not the only source of gravitational field, or the only source of inertia. Mass, having specific properties, is the quantity that corresponds to the minimum energy for the creation of free elementary particles (for example $\gamma + \gamma \rightarrow$ rest energy of any particle pair) or the quantity that corresponds to the rest-energy $\left(m = E_0 / c^2\right)$. The energy of free particles can be changed continuously but their masses are discrete, well-defined and specific to the particle. Only in this sense mass gains a different importance. When the energy of the particle (body) is close to its rest-energy we are in the domain of Newtonian physics and we can consider the properties of energy as if they are properties of mass and this makes the calculations easier.

4 CONCLUSIONS

Only free elementary particles have constant rest-energies and corresponding rest masses $\left(E_0 / c^2 = m\right)$. The mass defined in this way has a special meaning in quantum (particle and nuclear) and in all physics. This mass is the ratio of the energy needed for the creation of the particle to c^2. The energy needed for the creation of a particle in a field is $E < E_0$ and its mass changes as it happens in quantum states discretely. The particle in an atom that is isolated from external fields has a determined and constant mass. It is more correct to consider the mass of the particle (body) as Lorentz invariant. In that case, the coefficient $\left(1 - v^2 / c^2\right)^{1/2}$ for the particles moving with relativistic speeds is not physically related to the mass of the particles as defined above. Then, in this case, the same coefficient (with different exponents) that enters the equation for the relation between the forces and accelerations has no relation to mass.

When the energy of the particle is close to its rest energy, Newtonian physics become applicable and therefore we can consider the properties of the energy as if they are properties of mass and this makes the calculations easier by getting rid of c^2. For all objects in nature, whatever states they are in gas, liquid or solid, when their heats, rotational or translational velocities change, their energies, inertia and attraction changes. However, these changes are much less than the energy related to the total mass of all the particles of the system and therefore for the objects the Newtonian mass can be used. The energy and gravitation properties of particles with the speeds of light depend on their energies. All types of energy (rotation, heat and the energy of fields) gravitate and in the most general sense have inertial properties.

[1]. *L.Okun*, Physics Today, **42-6,** 31 (1989)
[2]. http://arXiv:physics/0103051 (2001)
[3]. *S.Rainville, J.K.Thompson, E.G.Myers,* , et al. Nature **438,** 1096 (2005)

THE EXCITATION OF GIANT RESONANCES IN NUCLEI BY INELASTIC SCATTERING OF PROTONS

MIRTEYMUR MIRABUTALYBOV
Azerbaijan State Oil Academy, Azadlig av.20,
Az1010, Baku, Azerbaijan

Form-factor of the scattering intermediate energy losses obtained on the base of nonrelativistic theory of proton scattering on nuclei in distorted-wave approximation and in three-dimensional form has been expressed as the functional plain wave approximation.

Calculating the double differentional cross-section of scattering, the losses of the energy of the scattered protons with falling energy of 800 MeV have been determined. The giant dipole and quadruple resonances with vibrations of ^{208}Pb nucleus surface have been investigated.

The increasing interest to the investigation of nuclei structure by the elastic and inelastic scattering of nucleons is connected with publications of plenty experimental results at different energies and high momentum transfer. To get important information from these experimental data it's necessary to get simple and exact analytical expressions for the scattering amplitudes of corresponding processes.

The purpose of the research is to spread for the inelastic scattering the general exact expression for the scattering amplitude of nucleons of intermediate energies, received by the author in [1], on the base of three-dimensional quaziclassics within the distorted wave approximation.

Let's write the double differential cross-section for the nucleon inelastic scattering, which assumes resonant parts expressed as a sum of Breit-Wigner shapes.

$$\frac{d^2\sigma}{d\Omega dE_f}=\frac{1}{E_i^{1/2}E_f^{1/2}}\frac{1}{2}\frac{2J_f+1}{2J_i+1}\sum_{L=0}^{\infty}\sum_{M=-L}^{L}\frac{|F_{LM}(q)|^2}{2L+1}\frac{\Gamma_L^2/4}{(E_x-E_L)^2+\Gamma_L^2/4} \tag{1}$$

where E_i and E_f are kinetic energies of fallen and scattered particles.

Nucleus form-factor $F_{LM}(\mathbf{q})$ received in [1] is

$$F_{LM}(\mathbf{q})=\frac{ik\sigma_{NN}(1-i\varepsilon_0)\ell^{\frac{-\beta_0^2q^2}{2}}}{4\pi}\int \ell^{i\mathbf{qx}}\Re(\mathbf{r})\rho_L(r)Y_{LM}^*(\hat{r})d\mathbf{r}, \tag{2}$$

where

$$\Re(\mathbf{r})=1+i\phi(\mathbf{r})-\beta_0^2\mathbf{q}\nabla\phi(\mathbf{r}) \tag{3}$$

To calculate integral (2) we choose the coordinate system in which $Oz\uparrow\uparrow\mathbf{q}$ and denoted $\cos\hat{qr}=\mu$. This allowed us to write transmission impulse of falling proton to the nucleus by the target, accounting the loss of energy

$$|\mathbf{q}|=|\mathbf{k}_i-\mathbf{k}_f|=\sqrt{k_i^2+k_f^2-2k_ik_f\cos\vartheta}= \\ =(\frac{2m}{\hbar^2})^{1/2}\sqrt{E_i+E_f-2E_i^{1/2}E_f^{1/2}\cos\vartheta} \tag{4}$$

The scattering angle $\vartheta=\vartheta_1+\vartheta_2$ and the angles of deviation of the falling (ϑ_1) and scattered particles (ϑ_2) relatively OX axis in three dimensional Decart system (Fig.1) are connected in the following form

$$\cos(\hat{\mathbf{r}},\hat{\mathbf{k}}_i)=\sqrt{1-\mu^2}\cos\vartheta_1\cos\varphi+\mu\sin\vartheta_1, \\ \cos(\hat{\mathbf{r}},\hat{\mathbf{k}}_f)=\sqrt{1-\mu^2}\cos\vartheta_2\cos\varphi-\mu\sin\vartheta_2 \tag{5}$$

$$tg\,\vartheta_2=\frac{E_f^{1/2}}{E_i^{1/2}}\frac{1}{\sin\vartheta}-ctg\,\vartheta \tag{6}$$

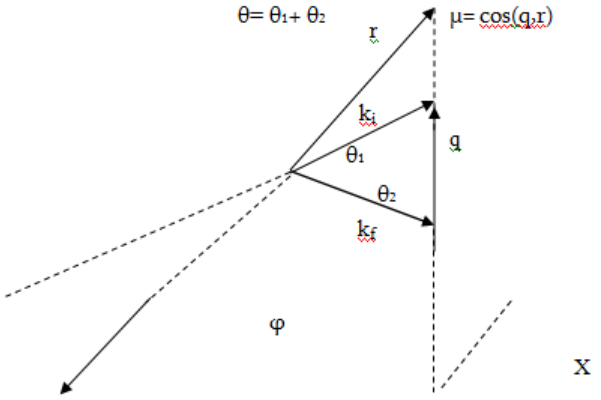

Fig.1. Incident and scattered coordinate systems.

Let's mark at once that getting the final energy (E_f) of scattered particles from the experiment we define these angles.

Now integrating (2) by azimuthally angles and then by the polar ones assuming (5), we are limited by the member $M=0$ for the value $L\neq 0$, as namely this

member contributes primarily into the modeling amplitude. After that the formfactor is

$$\tilde{F}_L(q) = \frac{2\pi i}{k_i} F_L(q) \ , \qquad (7)$$

Here

$$F_L(q) = \sum_{\varepsilon=\pm 1} \varepsilon \int_0^\infty \Re(r,q) G_L(r) \ell^{i\varepsilon qr} \rho_L(r) r dr \, , \qquad (8)$$

where

$$\Re(r,q) = \Re_0(q) + i\varepsilon \Re_1(q)\cdot r - \\ - \Re_2(q)\cdot r^2 + i\varepsilon \Re_3(q)\cdot r^3 \qquad (9)$$

The amplitude functions take the following form:

$$\Re_0(q) = 1 + \frac{U(0)}{E_i}\beta_0^2 q^2 \, , \qquad (10)$$

$$\Re_1(q) = \frac{U(0)}{2E_i} q - 4i\beta_0^2 q b_0 (k_i^2 \cos^2 \vartheta_1 + k_f^2 \cos^2 \vartheta_2) \qquad (11)$$

$$\Re_2(q) = i b_0 (k_i^2 \cos^2 \vartheta_1 + k_f^2 \cos^2 \vartheta_2) - \\ - \frac{a}{2}\beta_0^2 q (k_i^2 q + 2k_i^3 \sin^3 \vartheta_1 + 2k_f^3 \sin^3 \vartheta_2) \, , \qquad (12)$$

$$\Re_3(q) = \frac{a}{12}(3k_i^2 q + 2k_i^3 \sin^3 \vartheta_1 + 2k_f^3 \sin^3 \vartheta_2) \, , \qquad (13)$$

and

$$G_L(r) = \sum_{\nu=0}^{L} \frac{i^\nu}{(qr)^\nu} \left[\frac{\partial^\nu Y_{L0}(\mu)}{\partial \mu^\nu}\right]_{\mu=\varepsilon} \qquad (14)$$

At last we write the final expression for the double differential cross-section of the inelastic scattering of protons on the spherical nuclei in the following form:

$$\frac{d^2\sigma}{d\Omega dE_f} = \left(\frac{d\sigma}{d\Omega}\right)_{NA} \frac{1}{E_i^{1/2} E_f^{1/2}} \sum_{L=0}^{\infty} \frac{\left|\tilde{F}_L(q)\right|^2}{2L+1} \frac{\Gamma_L^2/4}{(E_x - E_L)^2 + \Gamma_L^2/4} \, , \qquad (15)$$

here

$$\left(\frac{d\sigma}{d\Omega}\right)_{NA} = \frac{\sigma_{NN}^2 k_i^4 (1+\varepsilon_0^2)}{32\pi^2 q^2} \ell^{-\beta_0^2 q^2} \qquad (16)$$

-is the cross-section of nucleon-nucleon scattering for all nucleons of the nucleus.

To learn the properties of the highly excited nuclei in the region of excitation energy where the strong resonance is located we use Goldhaber and Teller collective model which was created on the base of hydrodynamic nucleus model. According to this model a nucleus consists of proton and neutron liquids which densities are equal $\rho_p(\mathbf{r},t)$ and $\rho_n(\mathbf{r},t)$ correspondingly and we consider that the total density of the nuclear

$$\rho_N(\mathbf{r}) = \rho_p(\mathbf{r},t) + \rho_n(\mathbf{r},t) \, , \qquad (17)$$

does not depend on time.

To account the connection of the giant resonance with the vibration of the nuclear surface we'll join the low and high energetic collective freedom degrees in the collective nuclei theory. Interaction between these motions is very strong so it considerably influences on the structure of the giant resonances.

Considering the relation of the vibration density with the motion of the nuclear surface which mostly defines the structure of the giant resonances we'll write the total density of the protons $\rho_p(\mathbf{r},t)$ in the excited nucleus in the form of sum of proton density $\rho_p(\mathbf{r})$ and densities of fluctuations responsible for giant resonances $\rho_p(\mathbf{r})\eta^{Gr}(\mathbf{r},t)$, spreading from the center to the surface and the vibrations of nuclei surfaces $\rho_p(\mathbf{r})\eta^{vib}(\mathbf{r},t)$ i.e.

$$\rho_p(\mathbf{r},t) = \rho_\rho(\mathbf{r})[1 + \eta^{Gr}(\mathbf{r},t) + \eta^{vib}(\mathbf{r},t)] \qquad (18)$$

It is necessary to note that according to the hydrodynamic model, as it is shown in [2], $\eta^{Gr}(\mathbf{r},t)$ is possible to write as following

$$\eta^{Gr}(\mathbf{r},t) = \sum_{l=0}^{\infty} \sum_{m=-l}^{l} q_{lm}(t) A_l j_l(k_l r) Y_{lm}^* \qquad (19)$$

The fluctuation of density on the nucleus surface will be written as the expansion into the collective coordinate $\alpha_{\lambda\mu}(t)$ i.e.

$$\eta^{vib}(\mathbf{r},t) = \sum_{\lambda=0}^{\infty} \sum_{\mu=-\lambda}^{\lambda} \alpha_{\lambda\mu}(t) A_\lambda j_\lambda(k_\lambda r) Y_{\lambda\mu}^* \qquad (20)$$

Here the values A_l are the normalization factors which are determined from normalizing condition.

Now in order to get the kinetic energy of the vibrations of the nuclear surface it is necessary to know the solutions of the equations for speed potentials. Expanding the variables into the functions of speed

potentials $\phi(\mathbf{r},t)$ i.e. $\phi(\mathbf{r},t)=\phi(\mathbf{r})\exp(-i\varpi t)$ let's write the following equation

$$\nabla^2\phi(\mathbf{r})+k^2\phi(\mathbf{r})=0 \qquad (21)$$

The solution of this equation may be represented in form of expansion

$$\phi(\mathbf{r},t)=\sum_{\lambda=0}^{\infty}\phi_\lambda(\mathbf{r},t)=\sum_{\lambda\mu} S_{\lambda\mu}(t)\,j_\lambda(k_\lambda r)Y^*_{\lambda\mu} \qquad (22)$$

The collective vibrations of proton densities relatively to neutrons result in harmonically changing deformation of the proton substance just near the initial spherical equilibrium form, $r'=R_0$

$$r(\theta,\varphi,t)=r'\{1+\sum_{\mu=-\lambda}^{\lambda}\alpha_{\lambda\mu}(t)(\frac{r'}{R_0})^\lambda Y^*_{\lambda\mu}(\theta,\varphi)\} \qquad (23)$$

To determine the relation between coefficients $S_{\lambda\mu}(t)$, of the expansion of speed potential and coefficients $\alpha_{\lambda\mu}(t)$, defining the form of distribution of nucleon density on the nucleus surface, let's use the following condition

$$\frac{dr(\theta,\varphi,t)}{dt}\Big|_{r'=R_0}=\frac{\partial\phi(\theta,\varphi,t)}{\partial r}\Big|_{r'=R_0}, \qquad (24)$$

where r,θ,φ - are the spherical coordinates of any point of the nuclear substance.

From this it follows

$$S_{\lambda\mu}(t)=\frac{\dot\alpha_{\lambda\mu}(t)R_0}{\nabla_r j_\lambda(k_\lambda r)\big|_{r=R_0}} \qquad (25)$$

The distribution of nucleons density $\rho(r)$ in the basic state of the nucleus is chosen in the form of Fermi-function:

$$\rho_N(r)=\rho_0(1+\ell^{\frac{r-R_0}{b}})^{-1} \qquad (26)$$

Let's note at once that to ascertain the surface effect we'll write the equilibrium density in form of two components [3]:

$$\rho_p(r)=\rho_{0p}S(r-R_0)-\rho_{0p}\frac{\pi^2b^2}{6}\delta'(r-R_0) \qquad (27)$$

where S - stepped function, $S=1$ at $r<R_0$ and $S=0$ at $r>R_0$. Here δ' - is the derivative of δ - function.

In order to define the contribution of quadruple vibrations of nuclear surface to the scattering cross-section, the transitional density we'll receive

$$\rho_2=A_2\sqrt{\frac{\hbar}{2B_2^{vib}\varpi_2}}\,j_2(k_2r)\rho_p(r) \qquad (28)$$

Here the mass parameters B_λ are defined by folloing:

$$B_\lambda=\frac{m\rho_0k_\lambda^2\pi^2R_0^2}{6[\nabla j_\lambda(k_\lambda r)\big|_{r=R_0}]^2}\frac{\partial}{\partial r}[r^2j_\lambda^2(k_\lambda r)]_{r=R_0} \qquad (29)$$

This result let us write the form-factor (8) after integration in a form

$$F_{\lambda=2}(q)=\sqrt{\frac{\hbar}{2B_2^{vib}\varpi_2}}\,\frac{\pi^2b^2\rho_{0p}A_2}{6}F'(q) \qquad (30)$$

where

$$F'(q)=\sum_{\varepsilon=\pm1}\varepsilon\frac{\partial}{\partial r}[r\Re(r)\,j_2(k_2r)G_2(r\varepsilon)\ell^{i\varepsilon qr}]_{r=R_0} \qquad (31)$$

This theory was applied to inelastic scattering of protons on the nucleus ^{208}Pb with falling energy 800 MeV. In Fig.2 the experimental data of doubled cross-section and the theoretical ones at the scattering angle 13^0 are presented. At this scattering angle (where $\theta_2=1.5^0$) the loss of energy is ~ 45 MeV. This means that the contribution to the nucleus excitation is made by the giant dipole and quadruple resonances with the quadruple vibration of the nuclear surface.

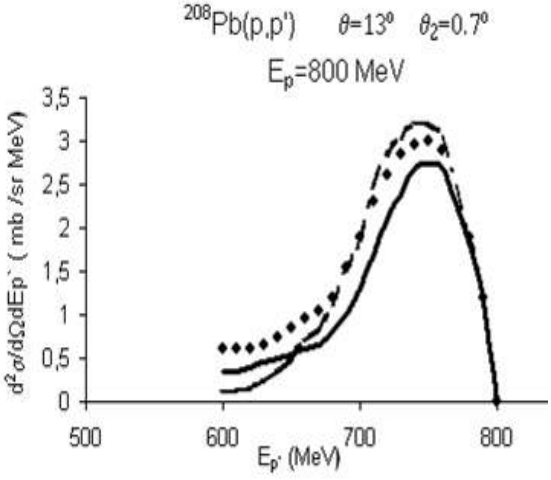

Fig.2. Energy spectra for 800 MeV (p,p') reactions on ^{208}Pb at scattering angle 13°. The dots curve is the measured spectra, the dashed curve is the calculated results in the surface response model [4], solid curve - of the calculated results.

The values of energies and the excitation width of these multiple excitations are : $\hbar\Omega_1 = 14.20$ MeV and $\Gamma_1 = 1.8$ MeV; $\hbar\Omega_2 = 22.24$ MeV and $\Gamma_2 = 1.7$ MeV, for the nuclear surface vibrations $\hbar\omega_2 = 4.2$ MeV and $\Gamma_2 = 0.9$ MeV. For the parameter characterizing by the mean-square deformation of excited nucleus value $\beta = 0.32$ was obtained.

From the analysis of the received results we can infer that the above developed distorted –a wave theory describes properly the experimental data and allow studying the essential properties of the excited nuclei.

[1]. *M.M.Mirabutalybov* Rus.AN Yad. Phys. 67, 12, 2178 (2004).

[2]. *J.Eisenberg, W.Greiner*, Nuclear Models v.I, Atom-Izdat. M. 275 (1975).

[3]. *A.Bohr, B.Mottelson*, Nuclear Structure v.I, Izdat-MIR,M.161(1971).

[4]. *H.Esbensen, G.F.Bertsch*, Phys. Rev.C 34, 1419 (1986).

$SU(3)_C \times SU(2)_L \times U(1) \times U'(1)$ MODEL OF ELECTROWEAK INTERACTION AND ELECTRIC CHARGE QUANTIZATION

O.B. ABDINOV, F. T. KHALIL – ZADE, S. S. RZAEVA
Institute of Physics of Azerbaijan National Academy of Sciences,
AZ143, Baku, G. Javid av.33

Basing on the general photon eigenstate and anomaly cancellation in the framework of the $SU(3)_C \times SU(2)_L \times U(1) \times U'(1)$ model of electroweak interaction the particles electric charges quantization is carried out. In the case of arbitrary values of hypercharges of Higgs and fermions fields, the expressions for the gauge bosons masses, eigenstates of neutral fields, and expressions for the interactions of gauges bosons with the leptons and quarks fields are calculated. Expressions for the fermions charges and the conditions leading to the electric charge quantization are found. It is shown that the Higgs fields have influence on "formation" of the particles electric charges and on the electric charge quantization.

I. INTRODUCTION

The nature of electric charge quantization remains unclear till now. There are two elegant proposals to understand this problem: magnetic monopole suggested by Dirac [1] and a hypothesis of grand unification [2]. Electric charge quantization in the framework of the different gauge models are investigated in a number of works [3-17]. Basing on the general photon eigenstate and anomaly cancellation, it has been shown [11-15] that photon eigenstate depends from the hypercharges of Higgs fields (see, also [10]) and fixation of hypercharges of fermions fields by the Higgs fields and the dependence of the electric charges quantization conditions from the hypercharges of Higgs fields can be interpreted as a influence of Higgs fields on the electric charge quantization.

This paper is continuation of works [11-15] and is devoted to research of the question of influence of Higgs fields on an electric charge quantization in model $SU(3)_C \times SU(2)_L \times U(1) \times U'(1)$. Taken into account the parity invariance of electromagnetic interaction [18], the expressions for the charges of leptons and the quarks, testifying to the natural solving of the electric charge quantization problems in the considering model are obtained. Influence of Higgs fields to the particles charges "formation" and to the electric charge quantization are investigated.

II. MODEL STRUCTURE

The electric charge is defined in general as a linear combination of the diagonal generators of $SU(3)_C \times SU(2)_L \times U(1) \times U'(1)$ group

$$\hat{Q} = \hat{T}_3 + \frac{1}{2}\hat{Y}. \tag{1}$$

The hypercharges of fermions as well as the Higgs fields are defined as

$$\hat{Y} = X\hat{I} + X\hat{I}. \tag{2}$$

Some part this hypercharge (X) causes interaction with Maxwell field B_μ, and other part (X') - with the another Maxwell field C_μ. Lagrangian describing interacting Young – Mills fields W_μ^3, Maxwell fields B_μ, C_μ and Higgs fields look likes

$$L = L_{YM} + V, \tag{3}$$

where V - the part of lagrangian , responsible for the Higgs fields.

Let's consider the case when symmetry is broken by two Higgs fields

$$\chi = \begin{pmatrix} \varphi^+ \\ \varphi^0 \end{pmatrix} \sim (1,2,X_\varphi, X'_\varphi), \qquad \phi \sim (1,1,X_\phi, X'_\phi). \tag{4}$$

In this case

$$V(\varphi, \phi) = V_0 + V_{kin},$$

where

$$V_{kin} = (D_\mu \varphi)^+ (D_\mu \varphi) + (D_\mu \phi)^+ (D_\mu \phi). \tag{5}$$

The covariant derivative is given by

$$D_\mu = \partial_\mu - ig\vec{T}\vec{A} - ig' \frac{Y}{2} B_\mu - ig'' \frac{Y'}{2} C_\mu, \tag{6}$$

where g, g' and g'' – coupling constants.

In this work, we choose the scalars to break the symmetry following the pattern,

$$\begin{array}{c} SU(3)_C \times SU(2)_L \times U(1) \times U'(1) \\ \downarrow \\ SU(3)_C \times U(1) \times U'(1), \end{array} \tag{7}$$

and give, at the same time, masses to the fermions fields in the model. Then the minimally required scalars are:

$$<\varphi>=\frac{1}{\sqrt{2}}\begin{pmatrix}0\\ \upsilon\end{pmatrix},\ <\phi>=\frac{1}{\sqrt{2}}\omega, \qquad (8)$$

here the VEV υ is responsible for the first breakdown while ω is responsible for the second breakdown.

For the lepton and quark fields we choose the following representations (we will consider one family of leptons and quarks without mixing):

$$\psi_{lL}=\begin{pmatrix}\nu\\ e\end{pmatrix}_L \sim (1,2,X,X'),$$
$$\psi_{eR}=e_R \sim (1,1,X,X'),$$
$$\psi_{QL}=\begin{pmatrix}u\\ d\end{pmatrix}_L \sim (3,2,X,X'),$$
$$\psi_{uR}=u_R \sim (3,1,X,X'),$$
$$\psi_{dR}=d_R \sim (3,1,X,X'). \qquad (9)$$

III. MASSES OF GAUGE BOSONS

The gauge boson mass matrix arises from the Higgs boson kinetic term (5). The covariant derivatives for Higgs fields write down as

$$D_\mu\psi_i=\partial_\mu\psi_i-iP_\mu\psi_i, \qquad (10)$$

Multiplet structure and hypercharges of fermions and Higgs fields of considered model are listed in Table 1.

Table1.

Fermions and Higgs fields	Hypercharge X	Hypercharge X′
$\psi_{lL}=\begin{pmatrix}\nu\\ e\end{pmatrix}_L$	y_{eL}	y'_{eL}
$\psi_{eR}=e_R$	y_{eR}	y'_{eR}
$\psi_{QL}=\begin{pmatrix}u\\ d\end{pmatrix}_L$	y_{QL}	y'_{QL}
$\psi_{uR}=u_R$	y_{uR}	y'_{uR}
$\psi_{dR}=d_R$	y_{dR}	y'_{dR}
$\varphi=\begin{pmatrix}\varphi^+\\ \varphi^0\end{pmatrix}$	X_φ	X'_φ
ϕ	X_ϕ	X'_ϕ

where ψ_i - Higgs fields (4), and the matrix P_μ looks like

$$P_\mu=\frac{g}{2}\begin{pmatrix}W^3_\mu+tXB_\mu+t'X'C_\mu & \sqrt{2}W^-_\mu\\ \sqrt{2}W^+_\mu & W^3_\mu+tXB_\mu+t'X'C_\mu\end{pmatrix}, \qquad (11)$$

here $t=g'/g$, $t'=g''/g$ and

$$W^\pm_\mu=\frac{W_{1\mu}\mp iW_{2\mu}}{\sqrt{2}}, \qquad (12)$$

In this case taking into account (4), (11) and (12) in (10) for the masses of gauge bosons we have

$$L_{mass}=M^2_W W^+_\mu W^-_\mu+\frac{g^2\upsilon^2}{8}(W^3_\mu+tX_\varphi B_\mu+t'X'_\phi C_\mu)^2+\frac{g^2\omega^2}{8}(tX_\phi B_\mu+t'X'_\phi C_\mu)^2, \qquad (13)$$

where

$$M^2_W=\frac{g^2\upsilon^2}{4}. \qquad (14)$$

For a mass matrix of neutral fields in the W^3_μ, B_μ, C_μ basis from (13), we have

$$M^2=\frac{g^2}{4}\begin{pmatrix}m_{11} & m_{12} & m_{13}\\ m_{21} & m_{22} & m_{23}\\ m_{31} & m_{32} & m_{33}\end{pmatrix} \qquad (15)$$

Where

$$m_{11}=\upsilon^2,\ m_{12}=-t\upsilon^2X_\varphi,$$
$$m_{12}=-t'\upsilon^2X'_\varphi,$$
$$m_{22}=t(\upsilon^2X^2_\varphi+\omega^2X^2_\phi),$$
$$m_{23}=tt'(\upsilon^2X^2_\varphi+\omega^2X^2_\phi),$$
$$m_{33}=\frac{2}{3}t'^2(\upsilon^2X^2_\varphi+\omega^2X^2_\phi).$$

The interactions Lagrangian, containing the mass of the neutral gauge bosons in this case, looks like:

$$L_{mass}^{NG} = \frac{1}{2} V^T M^2 V, \qquad V = \left(W_\mu^3, B_\mu, C_\mu\right) \tag{16}$$

For the mass Lagrangian of the neutral gauge bosons we have (the field A_μ remains massless)

$$L_{mass}^{NG} = \frac{1}{2}\left(M_{Z_1}^2 Z_{1\mu} Z_{1\mu} + M_{Z_2}^2 Z_{2\mu} Z_{2\mu} \right). \tag{17}$$

Neutral gauge bosons masses are

$$M_{Z_1}^2 = \frac{g^2}{8}\left[J_1 + (J_1^2 - 4J_2)^{1/2}\right], \qquad M_{Z_1}^2 = \frac{g^2}{8}\left[J_1 - (J_1^2 - 4J_2)^{1/2}\right], \tag{18}$$

where

$$\begin{aligned} J_1 &= \upsilon^2 + t^2(\vartheta^2 X_\phi^2 + \omega^2 X_\varphi^2) + \\ &+ t'^2(\upsilon^2 X_\varphi'^2 + \omega^2 X_\varphi'^2), \\ J_2 &= \upsilon^2\omega^2[(t'^2 X_\varphi'^2 + t^2 X_\varphi^2) + \\ &+ t^2 t'^2 (X_\phi X_\varphi' + X_\varphi X_\phi')^2] \end{aligned} \tag{19}$$

IV. ELECTRIC CHARGE QUANTIZATION

Transformation of neutral fields W_μ^3, B_μ, C_μ to the physical photon field, write down in the form

$$A_\mu = a_1 W_\mu^3 + a_2 B_\mu + a_3 C_\mu. \tag{20}$$

The eigenstate with zero eigenvalue follow from the equation:

$$M^2 \begin{pmatrix} a_1 \\ a_2 \\ a_3 \end{pmatrix} = 0. \tag{21}$$

It can be checked that the matrix M^2 has a non-degenerate zero eigenvalue for the arbitrary values of considered model parameters. Therefore, the zero eigenvalue is identified with the photon mass, $M_\gamma^2 = 0$ and eigenstate with zero eigenvalue with photon field.

In the considered $SU(3)_C \times SU(2)_L \times U(1) \times U'(1)$ model the equation (21) leads to the following values for quantities:

$$a_1 = \frac{tt'(X_\phi' X_\varphi - X_\phi X_\varphi')}{\bar{g}}; \qquad a_2 = \frac{t' X_\phi'}{\bar{g}}; \quad a_3 = -\frac{t' X_\phi'}{\bar{g}} \tag{22}$$

where

$$\bar{g} = \sqrt{t^2 t'^2 (X_\phi' X_\varphi - X_\phi X_\varphi') + t'^2 X_\phi'^2 + t^2 X_\phi^2}. \tag{23}$$

In this case the photon eigenstate is independent on the VEVs structure. This is a natural consequence of the $U(1)$ (and $U'(1)$) invariance – the conservation of the electric charge. However photon eigenstate depend from the Higgs fields hypercharges. Moreover, to be consistent with the QED based on the unbroken $U(1)$ gauge group (in the considering case also on the unbroken $U'(1)$ gauge group), the photon field has to keep the general properties of the electromagnetic interaction in the framework of the considering model, such as the parity invariant nature [18]. These would help us to obtain some consequences related to quantities which are independent on VEVs structure.

Let's consider interaction of fermions with gauge bosons. In the considered case the this interaction looks like

$$\begin{aligned} L = &i\bar{\psi}_{lL} \hat{D} \psi_{lL} + i\bar{\psi}_{eR} \hat{D} \psi_{eR} + \\ &+ i\bar{\psi}_{QL} \hat{D} \psi_{QL} + i\bar{\psi}_{uR} \hat{D} \psi_{uR} + i\bar{\psi}_{dR} \hat{D} \psi_{dR}. \end{aligned} \tag{24}$$

At first let us consider interaction of leptons with the electromagnetic field. In the considered model it looks like

$$L_{l\gamma} = Q_\nu \bar{\nu}\gamma_\mu(1+\gamma_5)\nu A_\mu + \bar{e}\gamma_\mu(Q_{0e} + Q_{0e}'\gamma_5)eA_\mu, \tag{25}$$

Where

$$\begin{aligned} Q_\nu &= \frac{g}{4}(a_1 + ta_2 y_{lL} + t' a_3 y_{lL}'), \\ Q_{0e} &= \frac{g}{4}[-a_1 + ta_2(y_{lL} + y_{eR}) + t' a_3(y_{lL}' + y_{eR}')], \\ Q_{0e}' &= \frac{g}{4}[-a_1 + ta_2(y_{lL} - y_{eR}) + t' a_3(y_{lL}' - y_{eR}')] \end{aligned} \tag{26}$$

Taken into account the parity invariance of the electromagnetic interaction from (25), we have

$$Q_\nu = 0, \quad Q'_{0e} = 0, \tag{27}$$

In the considered case when neutrino has not the right component the requirement parity invariance of electromagnetic interaction and the condition of neutrino charge equality to zero are equivalent. Besides, from the condition of parity invariance of electromagnetic interaction we have the relations between hypercharges of Higgs and lepton fields

$$\begin{aligned} y_{lL}X'_\phi - y'_{eL}X_\phi &= X'_\phi X_\varphi - X_\phi X'_\varphi \\ y_{eR}X'_\phi - y'_{eR}X_\phi &= 2(X'_\phi X_\varphi - X_\phi X'_\varphi). \end{aligned}, \tag{28}$$

Consequently for the electric charges of leptons we have

$$Q_\nu = 0, \qquad Q_{0e} = -Q_e, \tag{29}$$

Where

$$Q_e = tt'(X'_\phi X_\varphi - X_\phi X'_\varphi)/\bar{g}. \tag{30}$$

Let's consider the interaction of quarks with the electromagnetic field. In the considered model it looks like

$$L_{q\gamma} = \bar{u}\gamma_\mu(Q_u + Q'_u\gamma_5)uA_\mu + \bar{d}\gamma_\mu(Q_d + Q'_d\gamma_5)dA_\mu, \tag{31}$$

where

$$\begin{aligned} Q_u &= \frac{g}{4}[a_1 + ta_2(y_{QL} + y_{uR}) + t'a_3(y'_{QL} + y'_{uR})], \\ Q'_u &= \frac{g}{4}[a_1 + ta_2(y_{QL} - y_{uR}) + t'a_3(y'_{QL} - y'_{uR})], \\ Q_d &= \frac{g}{4}[-a_1 + ta_2(y_{QL} + y_{dR}) + t'a_3(y'_{QL} + y'_{dR})], \\ Q'_d &= \frac{g}{4}[-a_1 + ta_2(y_{QL} - y_{dR}) + t'a_3(y'_{QL} - y'_{dR})], \end{aligned} \tag{32}$$

Similarly to the leptons case taking into account P-invariance of electromagnetic interaction from (31) and (32) we have

$$Q'_u = 0, \quad Q'_d = 0. \tag{33}$$

These conditions lead to the following relations between hypercharges of Higgs and quarks fields

$$\begin{aligned} (X'_\phi y_{QL} - X_\phi y'_{QL}) &= (X'_\phi y_{uR} - X_\phi y'_{uR}) - (X'_\phi X_\varphi - X_\phi X'_\varphi), \\ (X'_\phi y_{QL} - X_\phi y'_{QL}) &= (X'_\phi y_{dR} - X_\phi y'_{dR}) + (X'_\phi X_\varphi - X_\phi X'_\varphi), \\ X_\phi(y'_{UR} - y'_{dR}) &= X'_\phi(y'_{UR} - y'_{dR}) - 2(X'_\phi X_\varphi - X_\phi X'_\varphi). \end{aligned} \tag{34}$$

The expressions (34) fix the left and right hypercharges difference of quarks fields. Taking into account (34), and (22) in (32) for the quarks electric charges we have

$$\begin{aligned} Q'_u &= 0, \quad Q'_d = 0, \\ Q_u &= \frac{(X'_\phi X_\varphi - X_\phi X'_\varphi) + (X'_\phi X_\varphi - X_\phi X'_\varphi)}{2(X'_\phi X_\varphi - X_\phi X')} Q_e, \\ Q_d &= -\frac{(X'_\phi X_\varphi - X_\phi X'_\varphi) - (X'_\phi y_{QL} - X_\phi y'_{QL})}{2(X'_\phi X_\varphi - X_\phi X'_\varphi)} Q_e. \end{aligned} \tag{35}$$

The obtained expressions (31) and (35) can be considered as the evidence of electric charge quantization of leptons and quarks. However these expressions do not define numerical values of electric charges of leptons and quarks (in terms of electron charge). For obtaining of the numerical values for the leptons and quarks electric charges, it is necessary to have the additional relations between fermions field hypercharges. These relations can be obtained from the conditions of cancellations of gauge [19] and mixed gauge-gravitational anomalies [20]. In the considered model we have

$$\begin{aligned}
&y_{lL} + 3y_{QL} = 0,\\
&y'_{lL} + 3y'_{QL} = 0,\\
&2y_{QL} - y_{uR} - y_{dR} = 0,\\
&2y'_{QL} - y'_{uR} - y'_{dR} = 0,\\
&2y_{lL} + 9y_{QL} - 3(y_{uR} + y_{dR}) - y_{eR} = 0,\\
&2y_{lL} + 9y_{QL} - 3(y_{uR} + y_{dR}) - y_{eR} = 0,\\
&3y^3_{lL} + 6y^3_{QL} - 3(y^3_{uR} + y^3_{dR}) - y^3_{eR} = 0,\\
&3y^3_{lL} + 6y^3_{QL} - 3(y^3_{uR} + y^3_{dR}) - y^3_{eR} = 0.
\end{aligned} \tag{36}$$

In the considered model the Yukawa interactions which induce masses for the leptons can be written as

$$L^l_Y = f_e \overline{\psi}_{lL} \varphi \psi_{eR} + h.c. \tag{37}$$

Taking into account the conservation of hypercharge, from (10) it follows that,

$$y_{eR} = y_{lL} - X_\varphi \qquad y'_{eR} = y'_{lL} - X'_\varphi \tag{38}$$

From the Yukawa interaction for quarks

$$L^q_Y = f_d \overline{\psi}_{QL} \psi_{dR} \varphi + f_u \overline{\psi}_{QL} \psi_{uR} \varphi^c + h.c, \tag{39}$$

we have,

$$\begin{aligned}
&y_{QL} = y_{uR} - X_\varphi, y_{QL} = y_{dR} + X_\varphi,\\
&y'_{QL} = y'_{uR} - X'_\varphi, y'_{QL} = y'_{dR} + X'_\varphi.
\end{aligned} \tag{40}$$

Consequently from the equations (36) for the hypercharges of fermions fields we have:

$$\begin{aligned}
&y_{lL} = -X_\varphi, y_{eR} = -2X_\varphi.\\
&y'_{lL} = -X'_\varphi, y'_{eR} = -2X'_\varphi.\\
&y_{QL} = \frac{1}{3}X_\varphi, y_{uR} = \frac{4}{3}X_\varphi, y_{dR} = -\frac{2}{3}X_\varphi\\
&y'_{QL} = \frac{1}{3}X'_\varphi, y'_{uR} = \frac{4}{3}X'_\varphi, y'_{dR} = -\frac{2}{3}X'_\varphi..
\end{aligned} \tag{41}$$

This leads to the electric charge quantization

$$\begin{aligned}
&Q_\nu = 0, Q_e = \frac{tt'(X'_\phi X_\varphi - X_\phi X'_\varphi)}{\bar{g}},\\
&Q_u = \frac{2}{3}Q_e, \qquad Q_d = -\frac{1}{3}Q_e,
\end{aligned}$$

42)

Similar expressions can be found for other fermions. Conditions (28), (34), (38) and (40) fix the hypercharges of fermions fields and depend from the Higgs fields hypercharges. The conditions following from the anomalies cancellations (taking into account (28) and (34)), fix hypercharges of all remained fields. Thus, if there are no conditions (28), (34), (38) and (40) it is obvious that to solve the equations following from the anomalies cancellations is impossible and consequently there are not electric charge quantization, hence, these conditions are electric charge quantization ones. Dependence of these conditions from the hypercharges of Higgs fields can be interpreted as the influence of Higgs fields on the electric charge quantization.

V. THE CHARGED AND NEUTRAL CURRENTS

Diagonalization the mass matrix of neutral fields gives the mass eigenstates $Z_{1\mu}$ and $Z_{2\mu}$

$$\begin{aligned}
&Z_{1\mu} = b_1 W^3_\mu + b_2 B_\mu + b_3 C_\mu,\\
&Z_{2\mu} = c_1 W^3_\mu + c_2 B_\mu + c_3 C_\mu.
\end{aligned} \tag{43}$$

where

$$b_1 = \frac{t' y_2}{\bar{g} Z_1}; \quad b_2 = \frac{t' y_1}{\bar{g} Z_1}; \quad b_3 = \frac{t y_3}{\bar{g} Z_1}. \tag{44}$$

In expressions of quantities y_i $(i = 1 \div 3)$ are

$$y_1 = \upsilon^2 m^2_{Z_1} X_\varphi X'_\varphi + \omega^2 \left(m^2_{Z_1} - \upsilon^2 \right) X_\phi X'_\phi$$

$$y_2 = \upsilon^2 \omega^2 X_\varphi \left(X'_\varphi X'_\phi - X_\varphi X'_\phi \right) - \frac{1}{t^2} m^2_{Z_1} \upsilon^2 X'_\varphi,$$

$$y_3 = m^2_{Z_1} \upsilon^2 X'_\varphi + \left(m^2_{Z_1} - \upsilon^2 \right) \left(\omega^2 X^2_\phi - \frac{1}{t^2} m^2_{Z_1} \right),$$

where $\bar{g}_{Z_1} = \sqrt{t'^2(y_1^2 + y_2^2) + t^2 y_3^2}$, and $m_{Z_1}^2 = 4M_{Z_1}^2 \Big/ g^2$.

Note that the expressions of $c_i \ (i = 1 \div 3)$ can be obtained from corresponding expression b_i by replacement $Z_1 \to Z_2$.

In the most general form the interaction lagrangian of fermions with gauge bosons has the following form:

$$L_{int} = i\sum_f \bar{\psi}_{fL}\gamma_\mu D_\mu \psi_{fL} + i\sum_f \bar{\psi}_{fR}\gamma_\mu D_\mu \psi_{fR}, \quad (45)$$

where ψ_L, ψ_R – left and right fermions fields.

Interactions of the charged vector fields with leptons and quarks are

$$L_f^{CC} = \frac{g}{2}(\bar{\nu}W_\mu e_L + \bar{d}_L W_\mu u_L + h.c.). \quad (46)$$

The neutral current interactions can be written in the form

$$L_f^{NC} = \frac{g}{4}\sum_f \bar{f}\gamma_\mu(g_{V_1}^f + g_{A_1}^f\gamma_5)fZ_{1\mu} + \frac{g}{4}\sum_f \bar{f}\gamma_\mu(g_{V_2}^f + g_{A_2}^f\gamma_5)fZ_{2\mu}, \quad (47)$$

where f takes values ν_e, e, d, u. For the coupling constants we have:

$$\begin{aligned} g_{V_1,A_1}^l &= p_1^l b_1 + tb_2(y_{lL} \pm y_{lR}) + t'b_3(y'_{lL} \pm y'_{lR}), \\ g_{V_1,A_1}^q &= p_1^q b_1 + tb_2(y_{QL} \pm y_{qR}) + t'b_3(y'_{QL} \pm y'_{qR}) \end{aligned} \quad (48)$$

where upper signs relate to vector coupling constants and lower signs relates to axial ones. Besides:

for $l = \nu$ $p_1^\nu = 1$; $y_{\nu R} = 0$; for $l = e$ $p_1^e = -1$; for $q = u$ $p_1^u = 1$; for $q = d$ $p_1^d = -1$;

Note that the expression of quantities $g_{V_2}^f$ и $g_{A_2}^f$ – can be obtained from appropriate expressions (48) by the substitution $b_i \to c_i$.

IV. CONCLUSION

Taking into account the arbitrary values of fermions and Higgs fields hypercharges the possibility of construction of electroweak interactions model, based on spontaneously broken $SU(3)_C \times SU(2)_L \times U(1) \times U'(1)$ symmetry group by two Higgs fields have been investigated. Masses of gauge bosons, arising in the considered model are calculated. Diagonalization of mass matrix of neutral fields has been performed and expressions for the neutral field's eigenstates are obtained. Expressions for the fermions charges, testifying the electric charge quantization are obtained. Conditions leading to the electric charge quantization are found. Dependence of the particles charges and electric charges quantization conditions from the hypercharges of Higgs fields can be interpreted as new property of Higgs fields. Higgs fields has influence on "formation" of the particles electric charges and consequently on particles electric charge quantization. Expressions for the interactions of gauge bosons with fermions are calculated.

It is necessary to note, that in the considered case the conditions of the electric charge quantization following from P – invariance of electromagnetic interaction does not coincide with conditions following from the mass terms. This is result of the fact that in the considering case Higgs field ϕ does not take part in acquisition of fermions masses.

[1]. *P. A. M. Dirac*. Proc. Roy. Soc. London A133, p.60, 1931.

[2]. *J. C. Pati, A. Salam.* Phys. Rev., D10, p. 275, 1974; *H. Georgi, S. L. Glashow*. Phys. Rev. Lett., 32, p. 438, 1974.

[3]. *X.-G. He, G. C. Joshi, H. Lew, B. H. McKellar, R.R. Volkas*. Phys. Rev., D40, p.3140, 1989.

[4]. *K. S. Babu, R. N. Mohapatra*. Phys. Rev. Lett., 63, p. 938, 1989.

[5]. *K. S. Babu, R. N. Mohapatra*. Phys. Rev., D42, p.3866, 1990.

[6]. *R. Foot, H. Lew, G. Joshi, R. R. Volkas*. Mod. Phys. Lett.,A5, p. 95, 1990.

[7]. *C. Geng.* Phys. Rev., D41, p. 1292, 1990.

[8]. *S. Rudaz.* Phys. Rev., D41, p. 2619, 1990.

[9]. *E. Golwich, P. B. Pal.* Phys. Rev., D41, p. 3537, 1990.

[10]. *P. V. Dong, H. N. Long*. hep – ph/0507155v1, 2005.

[11]. *O. B. Abdinov, F. T. Khalil-zade, S. S. Rzaeva*. hep – ph/0807.4359v1, 2008.
[12]. *O. B. Abdinov, F. T. Khalil-zade, S. S. Rzaeva*. Fizika, v.XV, №1, p.24, 2009.
[13]. *O. B. Abdinov, F. T. Khalil-zade, S. S. Rzaeva*. Reports of NAS of Azerbaijan Republic. XXVII, № 5, p.20,2007.
[14]. *O. B. Abdinov, F. T. Khalil-zade, S. S. Rzaeva*. Reports of NAS of Azerbaijan Republic. XXVII, № 2, p. 22,2008.
[15]. *O. B. Abdinov, F. T. Khalil-zade, S. S. Rzaeva*. hep – ph/1001.2679, 2010.
[16]. *A. Abbas. J. Phys.,G: Nucl. Part. Phys.,* 16, p.L163, 1990.
[17]. *A. Abbas.* Phys. Lett., B238, p.344, 1990.
[18]. *T. D. Lee, C. N. Yang*. Phys.Rev.,104, p. 254, 1956; *A. Salam.* Nuovo Cimento, 3, p.837, 1966; *V. Kobzarev, L. Okun, I. Pomeranchuk*. Sov. J. Nucl. Phys., 3, p.837, 1966.
[19]. *C. Bouchiat, J. Iliopoulos and Ph. Meyer*. Phys. Lett., B 38, p.519, 1972; *H.Georgi and S.L.Glashow.* Phys. Rev., D 9, p.416, 1974; *D. Gross and R. Jackiv*. Phys. Rev., D6, p.477, 1972 .
[20]. *S. L. Adler.* Phys.Rev, 177, p2426, 1968; *J. S. Bell and R. Jackiw*. Nuovo Cimento 60A, p.69, 1969; *S.L. Adler and W. Bardeen.* Rhys. Rev. 182, p.1517, 1969.

INVESTIGATIONS OF THE g_K FACTORS OF ^{161,163,165}Dy ISOTOPES

A. A. KULIEV[1,2], H. YAKUT[1], E. GULIYEV[1,2], Z. YILDIRIM[1]

[1] *Department of physics, Sakarya University, Sakarya,Türkiye, kuliev@sakarya.edu.tr*

[2]*Institute of Physics, National Academy of Sciences, Baku, Azerbaijan, guliyev@physics.ab.az*

In this paper the g_K factors of the intrinsic magnetic moments and effective spin gyromagnetic factors (g_s^{eff}) of the odd-mass $^{161-165}$Dy isotopes have been investigated within the Quasiparticle-Phonon model (QPM) by using the realistic Saxon-Woods potential. The effects on magnetic moments of the spin-spin and spin-isospin interactions were investigated. The theoretically calculated g_K and g_s^{eff} values are compared with the experimental data. The comparison of the measured and the calculated values of the effective g_s factor shows that the spin polarization explains quite well the observed reduction of g_s from its free-nucleon value. Sufficiently agreement between the calculated and the experimental values of the magnetic moment and g_K is obtained for κ=20/A MeV and q= -1.

I. INTRODUCTION

Studies of the magnetic dipole moments are important in nuclear theory due to the well-understood nature of the electromagnetic interaction. Most of the ground-state magnetic moments of odd mass rare earth nuclei have been measured by the different experimental and theoretical groups [1-26]. Today, the advancement of the technology and the development of new experimental measurement techniques have allowed for making more sensitive magnetic moment measurements.

The magnetic moments of deformed nuclei may be expressed in terms of two quantities: the intrinsic g factor g_K, describing the magnetic properties of nucleons in their motion with respect to the reference frame fixed in the nucleus, and the rotational g factor g_R describing the magnetization induced by collective rotation [21]. Since three decades the values of both g_K and g_R for a number of odd-mass nuclei in the region 150<A<190 have been determined experimentally with good accuracy, giving new possibilities of testing some more specific models of the intrinsic structure of these nuclei.

By comparing the experimentally determined nuclear moments with theoretical values, information about the spin polarization effects is obtained. De Boer and Rogers [15] have studied the magnetic moments of odd-mass nuclei and have concluded that the difference between the experimental and theoretical magnetic moments can be explained by placing $g_s^{eff} \approx 0.6 g_s^{free}$ instead of the free-nucleon value for g_s^{free}.

The deviations of the Nilsson estimates from the measured values of the intrinsic magnetic moments of odd-mass deformed nuclei may be understood as a result of the spin polarization of the even core by the odd nucleon [21]. The influence of the polarization effects on the magnetic moments was investigated in detail in a number of papers [21-24]

One of the studies on the effect of the spin-spin interactions on the magnetic moment in deformed nuclei was first made by Bochnacki and Ogaza [21] within the framework of the perturbation theory and with the assumption that the spin-spin interactions are responsible for the renormalization of g_s factors and by using first order perturbation theory they were able to show that the three quasiparticle states contribute to the wave function of the ground and low-lying excited states of the odd-mass nuclei. The spin-spin interactions between quasiparticles are not weak and cannot be treated by the perturbation method. The perturbation theory cannot properly describe the quasiparticle interaction and the magnetic moments. Later on, the spin polarization effects were studied by Kuliev and Pyatov [3] by using the Nilsson potential within the framework of the TDA approach which starts from the assumption of the oscillations of the magnetic dipole moment. These oscillations generate the 1^+ excitations above the energy gap in the even-even nuclei. On this assumption the spin polarization effects in the odd-mass nuclei are interpreted as resulting from the "scattering" of the odd nucleon on the 1^+ excitations of the even core.

There is only one microscopic TDA calculation for the magnetic moment properties of Dysprosium isotopes, namely $^{161-165}$Dy isotopes, which was made by Kuliev-Pyatov [3] on the basis Nilsson model. Therefore, to improve understanding on the mass dependence and to get more detailed information about polarization effects and magnetic g-factors it is instructive to investigate magnetic properties odd-mass $^{161-165}$Dy isotopes. Firstly, in this paper we have presented QPM calculations to available odd-mass Dysprosium isotopes using single-particle wave functions of the deformed Woods-Saxon potential.

The gyromagnetic factors g_K and g_s^{eff} of the odd-neutron $^{161-165}$Dy isotopes were calculated theoretically and compared with experimental results [1,2]. It has been observed that the theoretical results reproduce the experimental data very well.

II. THEORY

In the states of the odd-mass nucleus there is one quasi-particle, in addition to the quasi-particles and phonons of the even-even nucleus. The problem is to take into account the interaction of quasi-particles with phonons describing the collective states of even-even nuclei. Hamiltonian of the system [26] is written as follows

$$H \approx H_{sqp} + H_{coll} + H_{int.} \qquad (1)$$

where

$$H_{sqp} = \sum_{s,\tau} \varepsilon_s(\tau) B_{ss}(\tau), \quad (2)$$

$$H_{coll} = \frac{1}{2}\sum_{\tau,\tau'} \kappa_{\tau\tau'} \sum_{ss'} \sigma_{ss'}^{(\mu)}\ L_{ss'} g_{ss'} \left[Q_i^+(\tau) + Q_i(\tau)\right] \quad (3)$$
$$\sum_{mm'} \sigma_{mm'}^{(\mu)}\ L_{mm'} g_{mm'} \left[Q_i^+(\tau') + Q_i(\tau')\right]; \; g_{ss'} = \psi_{ss'} + \varphi_{ss'}$$

$$H_{int} = \sum_{\tau,\tau'} \kappa_{\tau\tau'} \sum_{mm'} \sum_{ss'} \left\{\sigma_{ss'}^{(\mu)} M_{ss'} \sigma_{mm'}^{(\mu)} L_{mm'} D_{ss'}(\tau) g_{mm'} \left[Q_i^+(\tau') + Q_i(\tau')\right] + \right. \quad (4)$$
$$\left. + \sigma_{ss'}^{(\mu)} L_{ss'} \sigma_{mm'}^{(\mu)} M_{mm'} g_{ss'} \left[Q_i^+(\tau) + Q_i(\tau)\right] D_{mm'}(\tau')\right\}$$

H_{sqp} describes the single quasi-particle motion in the nucleus, H_{coll} describes the collective excitations connected with the magnetic dipole interactions, and $H_{int.}$ the connection between the single-particle and collective motions. Here $Q_i^+(Q_i)$ are the phonon creation (annihilation) operators, $\tau(\tau')$ represent neutron (proton). $L_{ss'} = u_s v_{s'} - u_{s'} v_s$ and $M_{ss'} = u_s u_{s'} + v_s v_{s'}$ are expressed through the Bogoliubov canonical transformation parameters, u_s and v_s. $\sigma_{ss'} = \langle s|\sigma_\mu|s'\rangle$ are single-particle matrix elements of the Pauli spin operator, and $B_{ss'} = \sum_{\rho=\pm} \alpha_{s\rho}^+ \alpha_{s'\rho}$, $D_{ss'} = \sum_{\rho} \rho \alpha_{s-\rho}^+ \alpha_{s'-\rho}$ where $\alpha_{s\rho}^+$ ($\alpha_{s\rho}$) is quasi-particle creation (annihilation) operators $g_{ss'}$ is the sum of the two-quasiparticle amplitudes; $\psi_{ss'}$ and $\varphi_{ss'}$. The summation over $ss'(mm')$ means that the sum is taken over the average field single particle levels of the neutron(proton) system.

The wave function of the considered K^π state is assumed in the form

$$\Phi_K(\tau) = \left\{N_K(\tau)\alpha_K^+(\tau) + \sum_{i,\nu} G_i^{KK_\nu} \alpha_{K_\nu}^+(\tau) Q_i^+\right\}|\Psi_0\rangle \quad (5)$$

for an odd-mass nucleus. Here K is the projection of the total angular momentum on the nucleus symmetry axis and π denotes the parity of state. The function Ψ_0 represents the phonon vacuum which corresponds to the even–even core of the nucleus. The quantities $N_K(\tau)$ and $G_i^{KK_\nu}$ determine the contribution of the one quasiparticle and the quasiparticle-phonon component in the wave function, respectively. The wave function (5) is properly normalized if

$$\Phi_K^+ \Phi_K = N_K^2(\tau) + \sum_{i,\nu} \left[G_i^{KK_\nu}\right]^2 = 1. \quad (6)$$

Let us we find the average value of H over $\Phi_K(\tau)$ and determine the functions $N_K(\tau)$ and $G_i^{KK_\nu}$ using the variational principle, i.e., from the minimum energy condition,

$$\delta\left\{\langle\varphi_K(\tau)|H|\varphi_K(\tau)\rangle - \eta_K\left[N_K^2(\tau) + \sum_{i,\nu}\left[G_i^{KK_\nu}\right]^2 - 1\right]\right\} = 0 \quad (7)$$

where $\eta_K(\tau)$ is the Lagrange multiplier and assures the validity of the normalization condition (6). It is equal to the energy of the resulting state in the odd-A nucleus. After some calculation we obtain the secular equation of the form

$$-P(\eta) \equiv \varepsilon_K(\tau) - \eta_K(\tau) - \sum_{i,\nu} \frac{\kappa^2 \sigma_{KK_\nu}^2(\tau) M_{KK_\nu}^2 R_q^{i\,2}(\tau,\tau')}{(\omega_i + \varepsilon_{K_\nu}(\tau) - \eta_K(\tau))} = 0 \quad (8)$$

Here, ω_i is the energy of collective 1^+ states in the even-even nucleus. The solutions η_K determine the energy of the state (5). Equation (8) has poles at $\varepsilon_{K_\upsilon} + \omega_i$, i.e., at the sum of quasiparticle and phonon energies. Another important point is the $\eta_K = \varepsilon_K$, where the first term of the sum changes the sign. The pairing factor $M_{KK_\upsilon}^2$ in eq.(8) suggests that the interaction has a predominantly particle-particle character. The R_q^i term is given with expressions

$$R_q^n = R_n + qR_p = \frac{1}{\kappa\sqrt{Z(\omega)}}\left(1 - \frac{q^2\chi F_p}{(1+\kappa F_p)}\right) = \frac{1}{\kappa\sqrt{Z(\omega)}}(1 + qL_i)$$

$$R_q^p = R_p + qR_n = \frac{q}{\kappa\sqrt{Z(\omega)}}\left(1 - \frac{\kappa F_p}{(1+\chi F_p)}\right) = \frac{1}{\kappa\sqrt{Z(\omega)}}(q + L_i)$$

The resulting energies are shifted with respect to the values ε_K and $\varepsilon_{K_\upsilon} + \omega_i$; such shifts are caused by quasiparticle-phonon interaction. By using secular equation (8) and the normalization condition (6), the functions $N_K(\tau)$ and $G_i^{KK_\nu}$ are derived in form

$$N_K^{-2} = 1 + \sum_{i,\nu} \frac{\kappa^2 \sigma_{KK_\nu}^2(\tau) M_{KK_\nu}^2(\tau) R_q^i(\tau,\tau')}{(\varepsilon_{K_\nu}(\tau) + \omega_i - \eta_K(\tau))^2} \quad (9)$$

$$G_i^{K\nu} = \left(\frac{\kappa\ \sigma_{KK_\nu}(\tau) M_{KK_\nu}(\tau) R_q^i(\tau,\tau')}{(\varepsilon_{K_\nu}(\tau) + \omega_i - \eta_K(\tau))}\right) N_K(\tau) \quad (10)$$

The magnetic dipole moments for an odd deformed nucleus may be calculated from the relation [26]:

$$\mu = \langle\mu_z\rangle = g_R I + (g_K - g_R)\frac{K^2}{I+1} \quad (11)$$

where g_R presents g-factor for the rotational motion. In the final expression, g_K-factor for the intrinsic motion is given by the formula (K>1/2) [27]

$$g_K = K^{-1}\left[\frac{1}{2}\left(g_s^\tau - g_\ell^\tau\right)\sigma_{KK} + g_\ell^\tau K\right] \quad (12)$$

where σ_{KK} is the diagonal matrix element of the spin operator σ_z. g_s and g_l are the spin and orbital gyromagnetic factors. The g_s-factor for free neutrons is $g_s = g_s^{free} = -3.826$. In a nucleus this value is changed because of polarization effects. By comparing the experimentally determined nuclear moments for deformed nuclei, de Boer et al. [15] have estimated the effective g,-factor to be approximately $g_s = 0.6\ g_s^{free}$.

By using eqs. (5) and (12), the derived analytical expression for the effective spin g_s factor is given in the form

$$g_s^{eff} - g_\ell^\tau = (g_s^\tau - g_\ell^\tau)\left\{1 - 2N_K^2(\tau)\sum_i \frac{\kappa R_q^i(\tau,\tau')R_\tau^i}{(\varepsilon_K(\tau)+\omega_i(\tau)-\eta_K(\tau))}\right\} - \quad (13)$$
$$-(g_s^{\tau'} - g_\ell^{\tau'})2N_K^2(\tau)\sum_i \frac{\kappa R_q^i(\tau,\tau')R_{\tau'}^i}{(\varepsilon_K(\tau)+\omega_i(\tau)-\eta_K(\tau))}$$

The detailed information about the above represented equations of the Random-Phase Approximation is in ref. [25,26].

III. NUMERICAL CALCULATIONS AND CONCLUSIONS

The numerical calculations have been carried out for odd-mass $^{161\text{-}165}$Dy isotopes. The single-particle energies are obtained from the deformed Woods-Saxon potential [28]. The mean-field deformation parameters δ_2 are calculated according to [29] using deformation parameters β_2 defined from experimental quadrupole moments [30]. The pairing-interaction constants chosen according to Ref.[31] are based on the single-particle levels corresponding to the nucleus in question. The calculated values of the pairing parameters Δ, λ, the mean-field deformation parameters δ_2 and the calculated g_R-factors of the even-even core of the nuclei are shown in table 1. The ground-state configurations of ^{161}Dy, ^{163}Dy and ^{165}Dy are taken as the [642↑], [523↓] and [643↑] from ref. [1], respectively.

The theoretical calculations of g_K and g_s^{eff} factors were made using eq.(12) and (13). For the calculations of ground state magnetic moments were used eq.(11). The dependence of magnetic moment and g_s^{eff}/g_s^{free} ratio on the parameters κ and q is demonstrated in figure 1 for the ^{161}Dy isotope as an example. The parameter of the neutron-proton spin-spin interactions $q = \chi_{np}/\chi$ can take values between -1 and 1 and $\chi = \kappa/A$ MeV. The strongest influence of the neutron-proton interaction occurs at q=-1. When q=+1, the effects of spin polarization in the neutron and proton systems can cancel each other.

In table 1, collective $g_R^{th.}$ values are obtained from our theoretical calculations in basis of the Cranking Model for the even core of nuclei. In the rare-earth region, the collective gyromagnetic ratio for an even-Z odd-N isotope is generally taken to be g_R=0.25 [33]. The value of g_R in a highly deformed nucleus has also been estimated from experimental data by Prior et al. [32]. Their results substantiate this but indicate that a much lower value ($g_R \approx 0.1$) is possible.

As can be seen from the figure at q=-1 and κ=20/A MeV the predicted values of the g_s^{eff} are close to the measured values for ^{161}Dy nucleus. This picture is peculiar to other dysprosium isotopes. Further these values q and κ are used in the following calculations. The calculated results of the g_s^{eff} and g_K factors of the $^{161\text{-}165}$Dy compared with the K-P results from ref. [3], with experimental data and single-particle(s-p) model calculations are given in table 2. The empirical data of the g_s^{eff} and g_K were estimated by using measured values of the magnetic moments μ_{exp} and g_R factors.

Table 1. Pairing correlation parameters (in MeV), δ_2 values and calculated g_R-factors for the Dy isotopes.

Nuclei	Δ_n	Δ_p	λ_n	λ_p	δ_2	g_R[11]	$g_R^{exp.}$ [32]	μ_{exp} [20]
^{161}Dy	0,954	1,036	-7,751	-6,810	0,295	0,41	0,083-0,225	-0,48 (4)
^{163}Dy	0,93	1,036	-7,383	-7,398	0,295	0,378	0,269-0,289	+0,67 (6)
^{165}Dy	0,906	1,037	-6,959	-7,974	0,304	0,345	-	-0,52 (4)

As can be seen from table 2, the predicted values of the g_s^{eff} and g_K are in agreement with the measured values for $^{161\text{-}165}$Dy. However, g_K values calculated with the same q=-1 and κ=20/A MeV parameters in the basis of the Nilsson model underestimate the experimental data. It is very important that the magnetic dipole interactions lead to exceedingly small quasiparticle-phonon admixtures to the ground and low-lying excited states. Because of the coherent contribution these small components in wave function affect strongly the nuclear magnetic moments. One should note that the magnetic moments are sensitive to such admixtures was first pointed in [32-34]. The results of the calculations show that the spin polarization of the even core by the odd-particle explains quite well the experimentally observed values of g_s^{eff} with calculated data for κ=20/A MeV and q= -1.

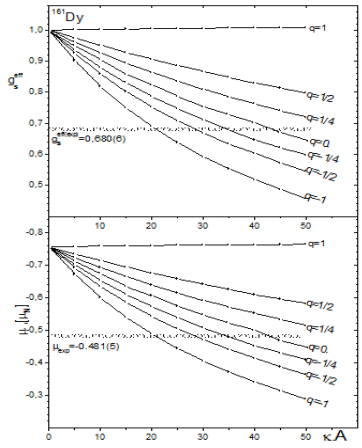

Fig. 1. The calculated magnetic moments and g_s^{eff} factors as a function of the parameters κ and q for the ground state of the odd-mass ^{161}Dy isotope as an example. The shaded region represents the experimental values [16-19] from Table 2

.

Table 2. Comparison of the g_K and g_s^{eff} values calculated in QPM using TDA and QRPA phonons with the experimental data [16-19], K-P method [1] and single-particle (s.p.) model calculations for the odd-neutron $^{161-165}$Dy isotopes. The estimated values for g_R: a) g_R=0.15 and b) g_R=0.25

Nucleus	g_s^{eff}/g_s^{free}				g_K				
	[3]	TDA	QRPA	Exp.	s.p.	[3]	TDA	QRPA	Exp.
^{161}Dy	0.637	0.638	0.690	0,680(6)[a)]	-0.484	-0.308	-0.309	-0.334	-0,329(3)[a)]
^{163}Dy	0.631	0.631	0.685	0,709(6)[b)]	0.390	0.246	0.246	0.267	0,277(2)[b)]
^{165}Dy	0.629	0.630	0.684	0,622(4)[b)]	-0.422	-0.265	-0.266	-0.289	-0.262 (2)[b)]

[1]. *N.J.Stone*, Table of nuclear magnetic dipole and electric quadrupole moments, Atomic Data and Nuclear Data Tables, 90, 1, pp. 75-176, 2005

[2]. *P.Raghavan*, Table of Nuclear Moments, Atomic Data and Nuclear Data Tables, 42, pp. 189-291, 1989

[3]. *A.A Kuliev., N .I.Pyatov*, Magnetic dipole interactions in deformed nuclei, Soviet Journal of nuclear physics, 9, 2, 185-189, 1969

[4]. *D.Verney et al.*, Deformation change in light iridium nuclei from laser spectroscopy, Eur. Phys. J. A 30, 489-518, 2006

[5]. *H Iımura,. et al.,* Nuclear moments and isotope shifts of ^{135}La, ^{137}La, and ^{138}La by collinear laser spectroscopy, Physical Revieew C 68, 054328, 2003

[6]. *M R Pearson*, Nuclear moments and charge radii of bismuth isotopes, J. Phys. G: Nucl. Part. Phys. 26, 1829-1848, 2000

[7]. *U.Georg, et al.*, Laser Spectroskopy Investigation of the Nuclear Moments and Radii of Lutetium Isotopes, European Phys. J. A, 3, pp. 225-235, 1998

[8]. *A. E. Barzakh et al.*, Isotope shift and hyperfine structure measurements for ^{155}Yb by laser ion source technique, Eur. Phys. J. A 1, 3-5, 1998

[9]. *C.König,* et al., Measurements of nuclear magnetic moments and electric quadrupole moments of Lu isotopes, Physical Rev. C 54; pp. 1027-1037, 1996

[10]. *Yu. A.Kudryavtsev* Detection of very rare isotopes by laser collinear resonant ionization of fast atoms, Hyperfine Interactions 74, 171-180, 1992

[11]. *G. D. Alkhazov et al.*, Nuclear Physics A477, 37 (1988)

[12]. *C.Ekström,* Hyperfine Structure of ^{175}Lu and Nuclear Electromagnetic Moments of the Lutetium Isotopes $^{161-181}$Lu, Physica Scripta, 13, pp. 217-224, 1976

[13]. *K.S. Krane, et al.*, Gamma-ray angular distributions in the decays of polarized ^{171,172}Lu, Phys. Rev. C, 13, pp. 1295-1311, 1976

[14]. *F.Boehm et al.*, A determination of the gyromagnetic ratios of some odd-A deformed nuclei from branching ratio measurements, Phys. Lett., 22, 5, 627-629, 1966

[15]. *J.De Boer, J.D.Rogers*, Concerning the magnetic properties of deformed nuclei in region 153≤A≤187, Physics Letters, 3, 6, pp. 304-306, 1963

[16]. *S. Muto, T. Ohtsubo, S. Ohya and K. Nıshımura,* Nuclear Magnetic Resonance on Oriented Nuclei in 175HfFe, Hyperfine Interactions, 158, 195–198, 2004

[17]. *G. Yeandle, et al.*, Nuclear moments and charge radii of the ^{171}Hf ground state and isomer, J. Phys. G: Nucl. Part. Phys., 26, pp. 839-847, 2000

[18]. *W. Jın, et al.,* Nuclear moments and charge radius of ^{175}Hf from optical measurement of hyperfine structure, Physical Review C, 55, pp. 1545-1547, 1997

[19]. *S. Buttgenbach, et al.*, Ground-state hypefine structure and nuclear magnetic dipole moments of ^{175}Hf and ^{177}Hf, Zeitschrift für Physik A, 260, 2, pp. 157-164, 1973

[20]. *A.Rosen, H.Nyqvıst,* Hyperfine Structure Investigation of ^{153}Dy, ^{155}Dy and ^{157}Dy, Physica Scripta. 6, 24-36, 1972.

[21]. *Z.Bochnackı, S. Ogaza*, Spin polarization effect on the fast allowed beta transitions between deformed odd-mass nuclei", Nuclear Physics A, 102, 3, pp. 529-533, 1967; *Z.Bochnackı, S. Ogaza*, Nuclear Physics 69, 186 (1965)

[22]. *A.B.Mıgdal,* Nuclear magnetic moments, Nuclear Physics, 75, 2, pp. 441-469, 1966

[23]. *L.P.Rapoport, A.S.Chernyshev*, Yad. Fiz., 7, 309, 1968

[24]. *E.Bodenstadt, J. D.Rogers*, In Perturbed Angular Correlations, vol. 1, NorthHolland, Amsterdam, 1964

[25]. *H.Yakut, A.A.Kuliyev, E.Guliyev,* Investigations of the g_K-factors in the ^{175,177,179}Hf isotopes, AIP Conf. Proc., 1072, pp. 258, 2008

[26]. *H.Yakut, A.A.Kuliyev, E.Guliyev, Z.Yıldırım,* Intrinsic g_K-factors of the $^{167-179}$Lu isotopes, Pramana Journal of Physics, Vol. 73, No. 5, pp. 829-837, 2009

[27]. *S. G. Nılsson,* Mat. Fys. Medd. Dan. Vid. Selsk. 29, No.16 (1955).

[28]. *J.Dudek, W. Nazarewıcz, A.Faessler*, Theoretical analysis of the single-particle states in the secondary minima of fissioning nuclei, Nucl. Phys.A, 412, pp. 61-91, 1984

[29]. *A.Bohr, B.Mottelson*, Nuclear Structure, W.A. Benjamin, v.2, NewYork, 1975.

[30]. *S.Raman, , C.W.Nestorand P.Tıkkanen*, Transition Probability From the Ground to the First-Excited 2^+ state of even-even Nuclides, Atomic Data and Nuclear Data Tables, 78, pp. 1-128, 2001

[31]. *V.G.Solovıev,* Theory of Complex Nuclei, Pergamon Press, New York 1976.

[32]. *O.Prıor,F.Boehm,* S.G.Nilss, Collective gyromagnetic ratios of deformed nuclei, Nuclear Physics A, 110, pp. 257-272, 1968

[33]. *E.M. Bernstein and de J.Boer,* Nucl. Phys. 18, 40 (1965).

[34]. *R.J.Blın-Stoyle, M.A.Perks*, The Deviations of Nuclear Magnetic Moments from the Schmidt Lines, Proceedings of the Physical Society Section A, 67, pp. 885-894, 1954

[35]. *A.Arıma, H.Horıe,* Configuration Mixing and Magnetic Moments of Nuclei, Progress of Theoretical Physics, 11, 4, pp. 509-511, 1954

[36]. *A.Arıma, H.Horıe,* Configuration Mixing and Magnetic Moments of Odd Nuclei, Progress of Theoretical Physics, 12, 5, pp. 623-641, 1954

LOW-LYING MAGNETIC DIPOLE EXCITATIONS IN THE EVEN-EVEN $^{124-132}$Ba ISOTOPES

A. A. KULIEV[1], E. GULIYEV[2], Z.YILDIRIM[1], G.SOLUK[1], H.YAKUT[1]

[1] Department of physics, Sakarya University, Sakarya,Türkiye, kuliev@sakarya.edu.tr

[2]Institute of Physics, National Academy of Sciences, Baku, Azerbaijan, guliyev@physics.ab.az

In this study, the scissors mode 1^+ states are investigated within the rotational invariant Quasiparticle Random Phase Approximation (QRPA) for $^{124-132}$Ba isotopes in energy interval 2.0-4.0 MeV. It is shown that in the $^{124-132}$Ba isotopes, the dependence of the total B(M1) transition on δ^2 is linear as in the case of well deformed nuclei, with the energy centroid of about $17.A^{-1/3}$MeV.

I. INTRODUCTION

Great experimental and theoretical efforts to study the orbital magnetic dipole response have been seen over a wide mass region in the last two decades (for a review see [1,2] and references therein). After theoretical predictions [3–5], this so-called "scissors mode" has been experimentally found in the deformed ^{156}Gd nuclei by the Darmstadt group [6]. Then obtaining this mode for the broad region showed that this is a general property of the deformed nuclei. Nowadays this mode has been found for the isotopes with permanent deformation in wide region beginning from the light nuclei (such as ^{46}Ti) up to the actinides also including the transitional and γ-soft nuclei (see Ref. [1,7] and references therein). The dipole excitation strength distribution has been investigated experimentally in less-deformed transitional nuclei, e.g., in γ-soft nuclei ^{194,196}Pt [8,9], ^{134,136}Ba [10,11], in transitional osmium nuclei [12], and in several vibrational nuclei of the tellurium isotopic chains [13,14] and ^{94}Mo [15]. In all of these cases the scissors mode was observed, however, with decay properties differing considerably from the findings in well-deformed rotors because of the loss of axial symmetry and the establishment of the d-parity quantum number [16]. Unfortunately the poverty of the data of transition nuclei does not allow the systematical analysis of the properties of the mode as a function of deformation parameters or the mass number A. Available experimental data of two platinum and barium isotopes are as yet not sufficient to reach a decisive conclusion regarding the scissors mode properties of transitional nuclei. Consequently, it would be important to extend the (γ,γ') studies to γ-soft nuclei with improved sensitivity in order to firmly establish deviations from the δ dependence in nuclei near shell closure (N,Z)=82. In view of this, the Ba isotopic chain with its broad stable even-even isotopes, with a considerable ground state deformation [17-19], offers the rare possibility to study the scissors mode properties in the nuclei of the A = 130 mass region.

By now, there have been several calculations [20-24] dealing with 1^+ excitations in a number of Ba isotopes, which were reported two decade ago. Predictive power of these calculations, however, is limited in general.

Recently the fragmentation of the scissors mode and the dependence of the B(M1) transition strength on the deformation parameter have been investigated in the [24] for $^{130-136}$Ba isotopes.

The aim of the present work is sysystematically to investigate the deformaton dependence of the scissor mode for the even-even $^{124-132}$Ba isotopes. There, by the selection of suitable separable effective isoscalar and isovector forces, within the QRPA without introducing additional parameters, rotational invariance is restored for the description of the M1 modes [26].

The use of the method [26] for this study is motivated by the satisfactory description of the experimental fragmentation and δ^2 dependence of the summed B(M1) value of the scissors mode in Sm, Nd, Ce and Te isotopic chains on the basis of the rotational invariant QRPA [25-27].

II. THEORY

Assuming that the restoring isoscalar h_0 and isovector h_1 interactions determined in Ref. [26] and the spin-spin forces generate the 1^+ states in deformed nuclei, the model Hamiltonian representing these states can be considered as

$$H = H_{sqp} + h_0 + h_1 + V_{\sigma\tau} \qquad (1)$$

where h_0 and h_1 describe the isoscalar and isovector restoring interactions, respectively. Here, H_{sqp} represents the Hamiltonian of the single-quasiparticle motion. The term $V_{\sigma\tau}$ takes into account the spin-isospin interaction, which produces the 1^+ states in deformed nuclei and has the form

$$V_{\sigma\tau} = \frac{1}{2}\chi_{\sigma\tau}\sum_{i\neq j}(\vec{\sigma}_i\cdot\vec{\sigma}_j)(\vec{\tau}_i\cdot\vec{\tau}_j), \qquad (2)$$

where $\chi_{\sigma\tau}$ is the spin-isospin interaction strength and $\vec{\sigma}_i$ and $\vec{\tau}_i$ are the Pauli matrices that represent the spin and the isospin, respectively. According to [26], the rotational invariance of the single-quasiparticle Hamiltonian can be restored with the aid of a separable isoscalar and isovector effective interactions of the form

$$h_0 = -\frac{1}{2\gamma_0}\sum_{\nu}[H_{sqp}-V_1, J_\nu]^+[H_{sqp}-V_1, J_\nu] \qquad (3)$$

and

$$h_1 = -\frac{1}{2\gamma_1}\sum_{\nu}[V_1(r), J_\nu]^+[V_1(r), J_\nu] \qquad (4)$$

where γ_0 and γ_1 are the isoscalar and isovector coupling parameters, respectively, and J_ν is the spherical components of the angular momentum ($\nu = \pm 1$). V_1 here is the isovector part of the nuclear mean field.

In the QRPA method, the collective 1^+-states are considered as one-phonon excitations described by

$$|\Psi_i\rangle = Q_i^+|\Psi_0\rangle = \frac{1}{\sqrt{2}}\sum_{ss',\tau}[\psi^i_{ss'}(\tau)C^+_{ss'}(\tau) - \varphi^i_{ss'}(\tau)C_{ss'}(\tau)]|\Psi_0\rangle \qquad (5)$$

where Q_i^+ is the phonon creation operator, $|\Psi_0\rangle$ is the phonon vacuum which corresponds to the ground state of the even-even nucleus and $C^+_{ss'}(C_{ss'})$ is two-quasiparticle creation (annihilation) operator(s). The two quasiparticle amplitudes $\psi^i_{ss'}$ and $\varphi^i_{ss'}$, are normalized by

$$\sum_{ss'\tau}[\psi^{i\ 2}_{ss'}(\tau) - \varphi^{i\ 2}_{ss'}(\tau)] = 1 \qquad (6)$$

Following the well-known procedure of the RPA method, one could find the eigenfunctions and eigenvalues of the Hamiltonian. To obtain the excitation energies, one has to solve the equation of motion

$$[H_{sqp} + h_0 + h_1 + V_{\sigma\tau}, Q_i^+] = \omega_i Q_i^+ \qquad (7)$$

Omitting details of the solution of (7), we give only the most necessary equations. In particular, the secular equation for the excitation energy of 1^+-states can be written as

$$\omega_i^2 J_{eff}(\omega_i) = \omega_i^2\left[J - 8\chi_{\sigma\tau}\frac{X^2}{D_\sigma} + \frac{\omega_i^2}{\gamma_1 - F_1}\left(J_1^2 - 8\chi_{\sigma\tau}\frac{JX_1^2 - 2J_1XX_1}{D_\sigma}\right)\right] = 0 \qquad (8)$$

and

$$D_\sigma = 1 + \chi_{\sigma\tau}F_\sigma,\ X = X_n - X_p,\ \gamma_1 = \gamma_1^n - \gamma_1^p,\ J_1 = J_1^n - J_1^p \qquad (9)$$

All the formulae are given clearly in [26] One of the solutions of Eq. (8), with $\omega_0 = 0$, belongs to the rotational excitation state because, as shown [28], it is characterized by definite values of the static electrical and magnetic moments, which coincide with 2_g^+-state in the generalized model. The static limit of the function $J_{eff}(\omega_0 = 0) = J_\sigma$ determines the moment of inertia of the nucleus and coincides in the form with well known expression in the cranking model including the spin-spin forces [29]. The remaining solutions of (8) with $\omega_i > 0$ describe the harmonic vibrations of the system, lying above the threshold of the first two-quasiparticle energy. In RPA [28], that use of the deformed mean field derived in Hartree approximation from a quadrupole-quadrupole interaction classically they correspond to the oscillations of Q_{21} component of the quadrupole moment operator in the absence of the spin-spin interactions.

Magnetic Dipole Properties of the 1^+ States

Owing to the symmetries of the spin-spin and restoring interactions, and the magnetic dipole operator, the most characteristic value of the 1^+-states is the M1 transition probability of the excitation from the ground state, which can be written in the form [26]

$$B(M1, 0^+ \to 1_i^+) = \frac{3}{4\pi}\left|R_p(\omega_i) + \sum_\tau (g_s^\tau - g_l^\tau)R_\tau(\omega_i)\right|^2 \mu_N^2 \qquad (10)$$

where

$$R_p(\omega_i) = \sum_\mu {}^{(p)}\varepsilon_\mu j_\mu L_\mu(\psi^i_\mu + \varphi^i_\mu),$$
$$R_\tau(\omega_i) = \sum_\mu {}^{(\tau)}\varepsilon_\mu s_\mu L_\mu(\psi^i_\mu + \varphi^i_\mu)$$

Here g_s and g_l are the spin and orbital gyromagnetic ratios of (the) free nucleons, respectively.

The detailed information about the above represented equations of the QRPA is given in ref. [30-31].

III. NUMERICAL CALCULATIONS AND CONCLUSIONS

The numerical calculations have been carried out for a wide range of deformation parameters in the even-even $^{124-132}$Ba isotopes. The single particle energies are obtained from the Warsaw deformed Woods-Saxon potential [32]. The basis contains all discrete and quasi-discrete levels in the energy region up to 3 MeV. The mean field deformation parameters δ_2 are calculated according to [33] using deformation parameters β_2 defined from experimental quadrupole moments [34]. The pairing-interaction constants chosen according to Soloviev [35] are based on the single-particle levels corresponding to the nucleus studied. The calculated values of the pairing parameters Δ and λ are shown in Table 1.

The model contains a single parameter of isovector spin-spin interactions. The spin interaction strength is chosen to be $\chi_{\sigma\tau} = 40/A$ MeV [36]. This value allows a satisfactory description of the scissors mode fragmentation in well-deformed rare-earth nuclei [26].

Table 1. Pairing correlation parameters (in MeV) and δ_2 values.

N	Δ_n	λ_n	Δ_p	λ_p	δ_2
68	1.37	-10.266	1.09	-3.979	0.294
70	1.37	-9.757	1.09	-4.611	0.244
72	1.3	-9.433	1.2	-5.149	0.204
74	1.3	-9.091	1.2	-5.703	0.171
76	1.3	-8.741	1.2	-6.283	0.146

Theoretical investigations of the scissors mode are rather poor and insufficient for the available transitional nuclei as $^{124-132}$Ba isotopes. Dependence of the lower 1^+ excitation states with $B(M1) > 0.3\,\mu_N^2$ on A for the investigated nuclei is given in figure 1. As seen from

figure for all barium isotopes the B(M1) value changes steeply with increasing mass number A.

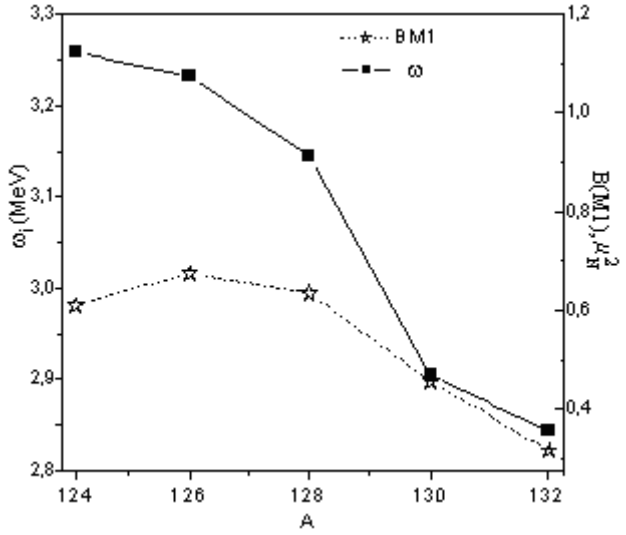

Fig.1. Variation of the lower 1^+ states with B(M1)>0,3 μ_N^2 versus mass number A.

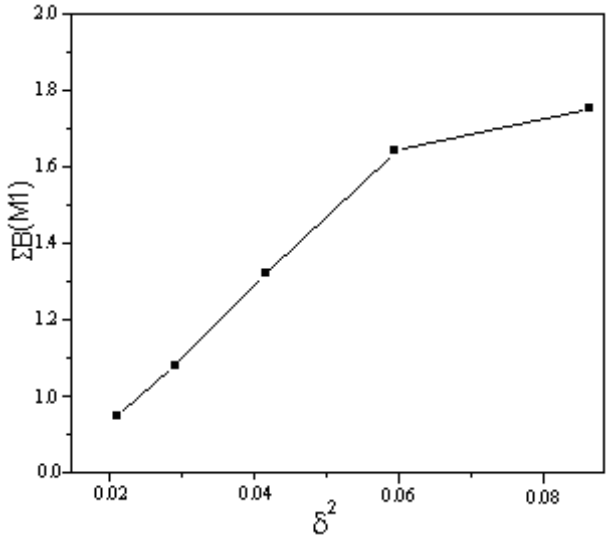

Fig. 2. Summed scissors mode strength in $^{124-132}$Ba as a function of the square of the deformation parameter δ_2.

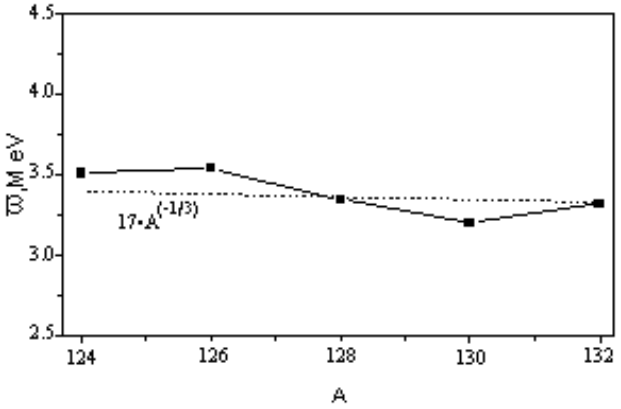

*Fig. 3.*Variation of the resonance energy centroid of the scissors mode versus A.

To study the role of the deformation on scissor mode excitation of the $^{124-132}$Ba isotopes we investigated dependence of the summed B(M1) values for 1^+ states on δ^2 (see figure 2). Consideration of the restoring forces reveals that B(M1) depends on δ^2 linearly for almost all the isotopes under study. The same situation was observed in rare-earth nuclei as Ce, Nd and Sm [25].

The other important quantity of the 1^+ state as well as B(M1) strength is the average value of the scissors mode excitation energy. In order to establish the energy centroid of the low lying excitations, we use the energy weighted and not energy weighted sum rules of dipole transition matrix elements below 4 MeV:

$$\overline{\omega} = \sum_i \omega_i B(M1,\omega_i) / \sum_i B(M1,\omega_i)$$

The theoretical values of ϖ as a function of *A* are plotted in figure 3. As seen, in contrast to summed B(M1), a weak dependence ϖ on the mass of the nucleus as $17\cdot A^{-1/3}$ is visible (dash line). This might be due to the mass dependence of $\omega \sim A^{-1/3}$ [37].

Comparative characteristics of the low-lying 1^+ excitations of $^{124-132}$Ba calculated with the rotational invariant Hamiltonian are cited in Table 2. Here the excitation energies-ω_i, *B(M1)* probabilities and orbit-to-spin ratio-M_l/M_s are also given. As seen from the table, the theory predicts several orbital collective 1^+ excitation states in the energy interval ω = 2.5–4.0 MeV with a rather large transition probability of B(M1) = 0.17–0.74 μ_N^2. Our orbit-to-spin ratio analysis shows the low lying 1^+ states (ω<3.5 MeV) with large B(M1) as a rule have $M_l/Ms > 0$, i.e. have a constructive character. The contribution of these strong 1^+ states to the summed B(M1) strength is more 50%. There are only a few levels with $M_l/Ms < 0$, the relative contribution of these orbital states to the summed B(M1) is almost 10% for all investigated nuclei. Thus most of the constructive interference between the orbital and the spin parts of the M1 strength has been found below 3.5 MeV. Such results are consistent with the microscopic analyses within QRPA for the rare-earth nuclei [38] and for the transitional barium isotopes with neutron numbers above the mid-shell [24].

In the lightest ^{124}Ba the calculation offers four M1 transitions between 3.5 MeV and 4.0 MeV with the summed B(M1) = 0.97 μ_N^2. One of them with largest B(M1) = 0.74 μ_N^2 at energy 3.896 MeV has a high orbit-to-spin ratio M_l/Ms= -16.5 and belong to the scissors mode states. In the energy range of 3.5–4.0 MeV the destructive interference between the orbit and the spin parts of the M1 strength is largely peculiar to almost all the investigated nuclei for the states.

To summarize, the QRPA approach suggested in [26] has been carried out to describe $K^* = 1^+$ states in the even-even $^{124-132}$Ba nuclei. The present calculation predicts strongly fragmented scissors mode resonance up to energy of 4.0 MeV with energy centroid $17\cdot A^{-1/3}$MeV and the quadratic dependence of the summed B(M1) values on the ground-state deformation parameter δ_2. For all the nuclei under investigation, the low-lying M1 transitions mainly have ΔK = 1 character as in well deformed rare-earth nuclei.

Table 2. Comparison of ω_i ,B(M1) and M_t/M_s ratio of $^{124-132}$Ba isotopes calculated with the rotational invariant Hamiltonian including the isoscalar plus isovector restoring forces

	^{124}Ba			^{126}Ba			^{128}Ba			^{130}Ba			^{132}Ba	
ω_i	B(M1)	M_t/M_s	ω_i	B(M1)	M_t/M_s	ω_i	B(M1)	M_t/M_s	ω_i	B(M1)	M_t/M_s	ω_i	B(M1)	M_t/M_s
2.529	0.17	2.0	2.694	0.08	2.0	3.082	0.03	2.9	2.904	0.46	13.8	2.844	0.32	2.2
3.259	0.61	10.6	3.233	0.68	6.2	3.144	0.64	6.1	3.183	0.1	-6.7	2.870	0.08	-2.7
3.534	0.06	0.7	3.611	0.15	-3.9	3.236	0.07	-2.3	3.260	0.67	0.4	3.074	0.14	-16.8
3.669	0.10	0.2	3.785	0.29	10.5	3.241	0.10	-2.0	3.472	0.05	42.1	3.149	0.05	-22.4
3.824	0.07	2.7	3.851	0.47	54.8	3.545	0.24	-22.3	3.540	0.22	-25.0	3.825	0.07	-11.3
3.896	0.74	-16.5				3.643	0.06	0.3	3.593	0.03	0.8	3.881	0.03	6.2

[1]. *A.Richter,* Prog. Part. Nucl. Phys. 34, 261 (1995).
[2]. *N. Lo Iudice*, Riv. Nuovo Cimento 23, 1 (2000).
[3]. *N.Lo Iudice, F. Palumbo,* Phys. Rev. Lett. 41, 1532 (1978).
[4]. *F.Iachello,* Nucl. Phys. A 358, 89c (1981).
[5]. *F.Iachello,* Phys. Rev. Lett. 53, 1427 (1984).
[6]. *D.Bohle,et al.*, Phys. Lett. B 137, 27 (1984).
[7]. *U.Kneissl, et al.,* Prog. Part. Nucl. Phys**.** 37, 349 (1996).
[8]. *P.Von Brentano, et al.,* Phys. Rev. Lett. 76, 2029 (1996).
[9]. *A.Linnemann, et al.,* Phys. Lett. B 554,15 (2003).
[10]. *H.Maser, et al.*, Phys. Rev. C54, R2129(1996).
[11]. *N.Pietralla, et al.,* Phys. Rev. C 58, 796 (1998).
[12]. *C.Fransen, et al.,* Phys. Rev. C 59, 2264 (1999).
[13]. *R.Georgii, et al.,* Phys. Lett. B 351, 82 (1995).
[14]. *R.Schwengner, et al.*, Nucl.Phys. A620,277(1997).
[15]. *N.Pietralla, et al*., Phys. Rev. Lett. 83,1303(1999).
[16]. *N.Pietralla, et al*., Phys. Rev. C 58, 191 (1998).
[17]. *S.Raman, et al.,* Atomic Data Nucl. Data Tables 36, 1 (1987); 78, 1 (2001).
[18]. *P.Petkov, et al.,* Phys.Rev. C 51, 2511 (1995).
[19]. *M.Scheck, et al.,* Phys. Rev. C70, 044319 (2004).
[20]. *E.Hammaren, et al.*, Phys.Lett. B 171, 347 (1986).
[21]. *A.Nowoselsky, and I.Talmi*, Phys.Lett. B 172, 139 (1986).
[22]. *G.Puddi, O.Scholten and T.Otsuka*, Nucl.Phys. A 348, 109 (1988).
[23]. *E. Guliyev, et al.*, Eur. Phys. J. A 27, 313 (2006).
[24]. *A.A.Kuliev, et al.*, J. Phys. G: Nucl. Part. Phys. 28, 407 (2002).
[25]. *A.A. Kuliev, et al.*, Int. Journ. of Mod. Phys. E 9, 249 (2000).
[26]. *E Guliyev, et al.*, Phys. Lett. B 532, 173 (2002).
[27]. *N.Lo Iudice*, Nuclear Physics A 605, 61 (1996).
[28]. *Prior O., et al.*, Nucl. Phys. A 110, 257 (1968).
[29]. *E. Guliyev, et al.*, Eur. Phys. J. A 39, 323 (2009).
[30]. *E. Guliyev, et al.*, Eur. Phys. J. A 43, 313 (2010).
[31]. *J.Dudek and T.Werner, J.* Phys. G: Nucl. Part. Phys. 4, 1543 (1978).
[32]. *O.Bohr, and B.Mottelson*, Nuclear Structure Vol 2 ed. (Benjamin, New York Amsterdam, 1975).
[33]. *S. Raman et al.,* At. Data Nucl. Data Tables 36, 1 (1987); 78, 1 (2001).
[34]. *V. G. Soloviev*, Theory of Complex Nuclei ed. (Pergamon Press, New York (1976).
[35]. *S. Gabrakov, et al*., Nucl.Phys. A 182, 625 (1972).
[36]. *J. Enders et al.*, Phys.Rev. C59 (199) R1851.
[37]. *R Nojarov, A.Faessler.* Nucl.Phys. A484,1 (1988).

EVALUATION OF RADIOACTIVITY LEVELS OF COAL, SLAG AND FLY ASH SAMPLES USED IN GİRESUN PROVINCE OF TURKEY

A. KARA[1]*, U. CEVIK[2], N. DAMLA[3], Y.Ö.YEŞILBAĞ[4]

[1]Osmaniye Korkut Ata University, Department of Physics, Osmaniye, Turkey, ayhankara@osmaniye.edu.tr

[2]Karadeniz Technical University, Department of Physics, Trabzon, TURKEY, ugurc@ktu.edu.tr

[3] Batman University, Department of Physics, Batman , TURKEY, nevzat.damla@batman.edu.tr

[4]Erzincan University, Department of Physics, Erzincan, TURKEY, oyesilbag@erzincan.edu.tr

In present work, natural radionuclides activities (^{226}Ra, ^{232}Th and ^{40}K) of the different types of coal, slag and fly ash samples used in Giresun province (Eastern Black Sea Region of Turkey) were measured by using gamma-ray spectrometry. These samples were collected as homogenously and separately around Giresun province. The mean activity concentrations of ^{226}Ra, ^{232}Th and ^{40}K radionuclides in coal, slag and fly ash samples were found as 107, 67 and 440 Bq.kg^{-1} for coal; 59, 25 and 268 Bq.kg^{-1} for slag and 136, 60 and 417 Bq.kg^{-1} for fly ash samples, respectively. To estimate health effect due to the aforementioned radionuclides, absorbed dose rates and annual effective doses have been calculated. These values were evaluated and compared with the internationally recommended values.

I. INTRODUCTION

Coal is the world's most abundant, most accessible and most versatile source of fossil energy [1]. Furthermore, ^{238}U, ^{232}Th and ^{40}K radionuclides can be found in great amount in nature, especially in the fossil fuels such as coals. In the process of combustion, these radionuclides are distributed in solid and gaseous combustion products and are discharged to and accumulate in man's environment. Most of the radionuclides accumulated in the ash. The overwhelming majority of the ash is so called bottom ash or slag that can be kept under control [2].

Giresun is a province of Turkey on the Black Sea coast. The Giresun province (Fig.1) is located in northeastern part of Turkey between the longitudes of 37° 50' - 39° 12' E and the latitudes of 40° 07' - 41° 08' N with a total population of 524,000. Giresun is an agricultural region of great natural beauty, especially in the highlands. The surrounding region has a rich agriculture, growing most of Turkey's hazelnuts as well as walnuts. Hazelnut, cultivated in this province, has been exported to many countries. The higher mountain areas are forest and pasture and in places there is mining of copper, zinc, iron and other metals [3].

The coal used in houses for heating in Giresun is generally brought from Russia and Siberia. Therefore, the aim of this study is to determine natural radioactivity (^{226}Ra, ^{232}Th, ^{40}K) levels, and to evaluate the radiological aspect from coal, slag and fly-ash samples in Giresun province of Turkey. The results obtained in this study were also compared with the internationally recommended values.

2. MATERIALS AND METHODS

A total 10 different samples (coal, slag and fly-ash) were collected from houses where the coal used as heating means in Giresun province. The samples were dried in an oven at a temperature of 105 °C during 24 h to ensure that moisture is completely removed, sieved to remove the stones and crushed in the laboratory to homogenize them. Then they were sealed in gas tight, radon impermeable, cylindrical polyethylene plastic containers (5.5 cm diameter and 5 cm height). These samples were then left for 30 days to allow ^{226}Ra and its short lived progeny to reach radioactive equilibrium.

The gamma radiation measurement was performed by using an HPGe detector of 55% relative efficiency and resolution 1.9 keV at the 1332 keV gamma of ^{60}Co (Ortec, GEM55P4 model). Maestro 32 computer software was used for spectrum analysis. The detector was shielded with a 10 cm thick lead layer to reduce the background due to the cosmic rays and the radiation nearby the system. Full energy peak efficiency was determined using Standard Reference Material (IAEA-375) prepared by International Atomic Energy Agency. Decay corrections were performed to the sampling date [4].

Gamma ray transitions of energies 351.9 keV (^{214}Pb) and 609.3 keV (^{214}Bi) were used to determine the activity concentration of the ^{226}Ra series. The gamma ray lines at 911.1 keV (^{228}Ac) and 583.1 keV (^{208}Tl) were used to determine the activity concentration of the ^{232}Th series. The activity concentrations of ^{40}K were measured directly through its gamma ray line emission at 1460.8 keV.

The activity concentrations for the natural radionuclides in the measured samples were computed using the following relation;

$$C = \frac{N}{\varepsilon P M t} \ (\text{Bq.kg}^{-1}) \qquad (1)$$

where C is the activity concentration of a radionuclide, N is the total net count of a specific gamma emission, ε is the detector efficiency for the specific gamma emission, P is the absolute transition probability for that gamma emission, M is the mass of the sample (kg) and t is the counting time (second).

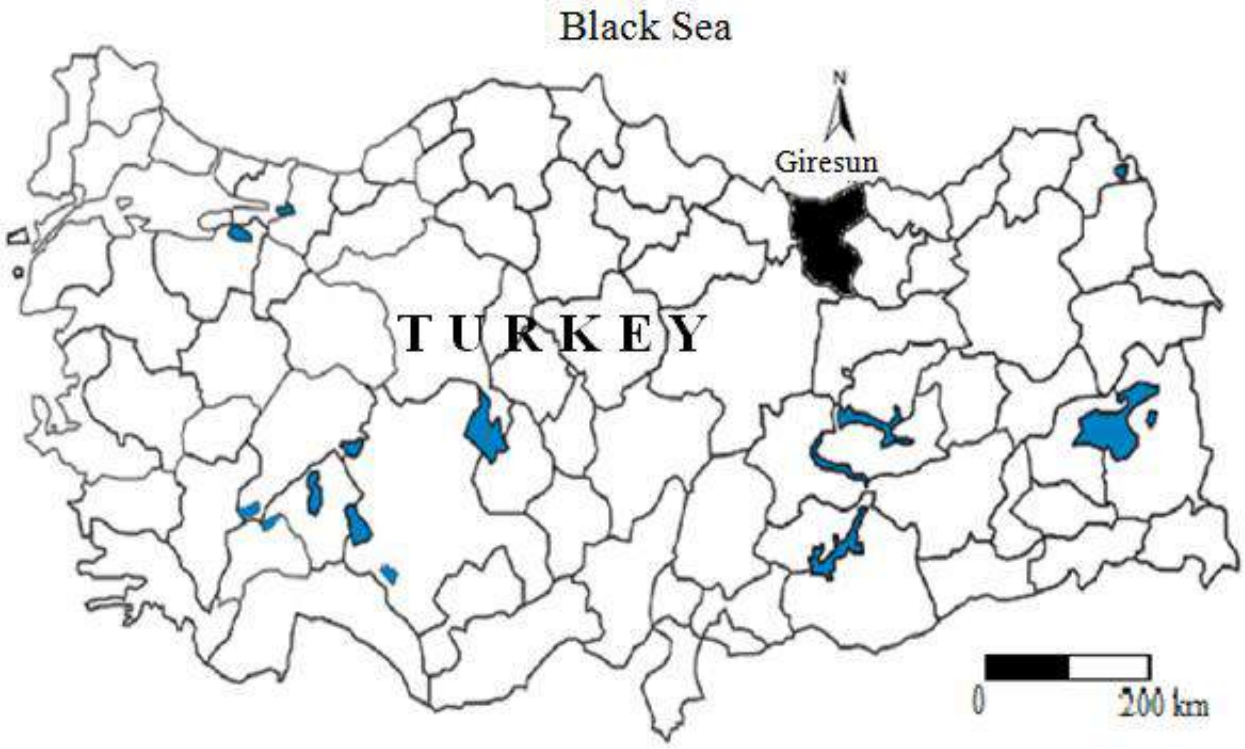

Fig1. Map of the Giresun province.

III. RESULTS AND DISCUSSION

The natural radioactivity levels due to the presence of ^{226}Ra, ^{232}Th and ^{40}K in coal, slag and fly ash samples in Giresun Province (Turkey) have been measured using gamma-ray spectroscopy with an HPGe detector. The results of activity concentrations in coal, slag and fly ash samples are given in Table 1. As seen from Table, the specific activities of ^{226}Ra, ^{232}Th and ^{40}K ranged within interval from 53 to 148 Bq.kg^{-1}, 24 to 117 Bq.kg^{-1} and 157 to 728 Bq. kg^{-1} for coal, from 41 to 88 Bq.kg^{-1}, 10 to 51 Bq.kg^{-1} and 62 to 480 Bq.kg^{-1} for slag and from 41 to 230 Bq.kg^{-1}, 26 to 111 Bq.kg^{-1} and 208 to 724 Bq.kg^{-1} for fly ash, respectively. While ^{226}Ra radionuclides have the biggest activity concentrations in fly ash samples, ^{232}Th and ^{40}K have the biggest activity concentrations in coal samples in average. According to UNSCEAR [5], the mean natural radionuclide concentration in coal is 35 Bq.kg^{-1} (range: 17-60 Bq.kg^{-1}) for ^{238}U, 30 Bq.kg^{-1} (range: 1-64 Bq.kg^{-1}) for ^{232}Th and 400 Bq.kg^{-1} (range: 140-850 Bq.kg^{-1}) for ^{40}K. Obtained values in this study are higher than the UNSCEAR [5] values in coal.

There is a concern that the coal, slag and fly ash samples will cause excessive radiation doses to the total body due to gamma rays emitted by ^{214}Pb and ^{214}Bi progeny of ^{226}Ra, ^{232}Th decay chain and ^{40}K also contributes to the total body radiation dose. The total air-absorbed rates due to the mean specific activity concentrations of ^{226}Ra, ^{232}Th and ^{40}K were calculated by the following formula [5]:

$$D\ (nGy.h^{-1}) = 0.462C_{Ra} + 0.604C_{Th} + 0.0417C_{K} \quad (2)$$

This equation is used for calculating the absorbed dose rate in air at a height of 1.0 m above the ground surface for uniform distribution of radionuclides (^{226}Ra, ^{232}Th and ^{40}K) concentration in environmental materials. The absorbed rates were computed from the measured activities in the samples (Table 1). The mean absorbed gamma doses in air for coal, slag and fly ash samples were calculated as 109, 53 and 117 nGy.h^{-1}, respectively. As the global average value of absorbed dose rate is 55 nGy.h^{-1} [5], the mean values of coal and fly ash samples are higher than this average value.

To estimate annual effective dose, it must be taken into account: (a) the conversion coefficient (0.7 Sv.Gy^{-1}) from absorbed dose in air to effective dose and (b) the outdoor occupancy factor (0.2) [5]. Therefore, the effective dose rate in unit of mSv.y^{-1} was estimated by the following formula:

$$AED\ (mSv.y^{-1}) = D\ (nGy.h^{-1}) \times 8760\ h.y^{-1} \times 0.7 \times 0.2 \times 10^{-6} \quad (3)$$

In Table 1, the results obtained for annual effective dose in the samples are presented. The computed values of annual effective dose in the coal, slag and fly ash samples are found to vary from 0.077 to 0.184 mSv.y^{-1} with a mean of 0.133 mSv.y^{-1} for coal; and from 0.036 to 0.106 mSv.y^{-1} with a mean of 0.065 mSv.y^{-1} for slag; and from 0.063 to 0.217 mSv.y^{-1} with a mean of 0.143 mSv.y^{-1} for fly ash, respectively.

Table 1. Activity concentrations, the absorbed dose rates and annual effective doses of the samples.

Sample Codes	Species	^{226}Ra (Bq.kg^{-1})	^{232}Th (Bq.kg^{-1})	^{40}K (Bq.kg^{-1})	D (nGy.h^{-1})	AED (mSv.y^{-1})
1	Coal	139± 5	117±8	380±9	151	0.185
	Slag	88±2	51± 7	366± 2	87	0.106
	Fly ash	41±5	38±4	531±12	64	0.079
2	Coal	53±6	53±5	728±16	87	0.107
	Slag	33±4	11±1	174±4	29	0.036
	Fly ash	230±17	52±7	208±5	146	0.179
3	Coal	98±9	98±9	594±13	129	0.158
	Slag	35±5	3±1	363±2	49	0.061
	Fly ash	139±13	51±7	259±6	106	0.130
4	Coal	145±13	54±7	271±6	111	0.136
	Slag	72±6	46±5	410±8	78	0.096
	Fly ash	164±10	108±9	337±8	155	0.190
5	Coal	148±10	88±8	494±11	142	0.174
	Slag	59±7	25±3	140±3	48	0.059
	Fly ash	161±15	38±5	522± 5	119	0.146
6	Coal	110±9	52±6	407±10	99	0.122
	Slag	65±6	20±2	480±11	62	0.076
	Fly ash	93±9	63±7	331±8	95	0.116
7	Coal	124±9	47±5	710±16	115	0.141
	Slag	57±6	21±3	315±7	52	0.064
	Fly ash	45±6	32±4	269±6	51	0.063
8	Coal	95±9	56±7	190±2	86	0.105
	Slag	68±7	10±2	227±5	47	0.058
	Fly ash	172±15	111±11	724±17	177	0.217
9	Coal	101±8	82±7	157±4	103	0.126
	Slag	41±5	20±3	140±1	37	0.045
	Fly ash	176±3	85±11	60±2	158	0.193
10	Coal	61±7	24±13	475±9	62	0.077
	Slag	67±6	14±2	62±2	42	0.052
	Fly ash	138±15	26±5	390±12	96	0.117

V. CONCLUSION

The study shows that the samples include natural radionuclides such as ^{226}Ra, ^{232}Th and ^{40}K. The mean activity concentrations of ^{226}Ra, ^{232}Th and ^{40}K radionuclides in coal, slag and fly ash samples were found as 107, 67 and 440 Bq.kg^{-1} for coal; 59, 25 and 268 Bq.kg^{-1} for slag and 136, 60 and 417 Bq.kg^{-1} for fly ash samples, respectively. In process of coal combustion, ^{226}Ra, ^{232}Th and ^{40}K radionuclides are distributed in solid and gaseous combustion products and they are discharged and accumulated in human's environment. Thus, measurements of coal, slag and fly ash samples should be conducted periodically. Results obtained from these data will provide a useful baseline data for adopting safety measures and dealing effectively with radiation emergencies.

[1]. *J.F.K.Akinbami, M.O.Ilori, T.O.Oyebisi, I.O.Akinwumi, O.Adeoti* Biogas energy use in Nigeria: current status, future prospects and policy implications. Renewable and sustainable Energies Reviews 5 (2001) 97.

[2]. IAEA, Technical Report Series, Vol. 295, 1989.

[3]. http://en.wikipedia.org/wiki/Giresun_Province

[4]. *U.Cevik, N.Damla, B.Koz, S.Kaya,* Radiological characterization around Afsin-Elbistan coal-fired power plant in Turkey, Energ Fuel, 22 (2008) 428-432.

[5]. UNSCEAR, 2000. Sources and effects of ionizing radiation. Report of the United Nations Scientific Committee on the Effects of Atomic Radiation to the General Assembly. United Nations Publications, New York, US

CHARGE PARTICLE EMISSION SPECTRA of ^{58,60}Ni AND ^{65}Cu NUCLEI

EYYUP TEL[1], AYNUR TATAR[1*], HÜSEYİN AYTEKİN[2]

[1]*Gazi University, Faculty of Arts and Science, Department of Physics, Ankara, Türkiye*

[2] *Karaelmas University, Faculty of Arts and Science, Department of Physics, Zonguldak- Türkiye*

**aynur@gazi.edu.tr*

Charge particle-emission spectra produced by (n,xp) and (n,xα) reactions for ^{58,60}*Ni* and ^{65}*Cu* target nuclei have been investigated by a neutron beam up to 14-15 MeV. In these calculations, the pre-equilibrium effects have been investigated. The calculated results are compared with the experimental data taken from literature.

Precise cross section data of neutron having around 14-15 MeV energy are very important for several applications, such as the structural materials of the fusion reactors and neutron dosimeter. The needs of the fast-neutron induced nuclear reaction cross-section data have been increasing in several applied fields; e.g, biomedical applications such as production of radioisotopes and cancer therapy, accelerator-driven incineration/transmutation of the long-lived radio active nuclear wastes (in particular transuranium nuclides) to short-lived or stable isotopes by secondary spallation neutrons produced by high-intensity, intermediate-energy, charged-particle beams, prolonged planstary space missions, shielding for particle accelerators, material irradiation experiments concerning research and development for fusion reactor technology. So the reaction mechanism and the systematic of (n,p), (n,α), (n,2n) cross section in reactions induced by fast neutrons have been subject of the continuous interest in neutron physics. A systematic experimental study of 14-15 MeV neutron-induced charged particle reaction cross sections such as σ(n,p), σ (n, *d*), σ (n,t), σ (n,^{3}He)and σ (n,α) has been carried out over the years for a large number of nuclei. A large number of empirical and semi-empirical cross sections formulas with different parameters have been proposed by several authors in the literature [1–9]. The experimental cross-sections are available in EXFOR for neutron induced reactions [10]. And also, these obtained cross section data are necessary to develop more nuclear theoretical calculation models in order to explain nuclear reaction mechanisms [11–13].

It has been established that pre-equilibrium processes play an important role in nuclear reactions induced by light projectiles with incident energies above about 10 MeV. Starting with the introduction of exciton model [14] by Griffin in 1966, a series of semi classical models [15] of varying complexities have been developed for calculating and evaluating particle emissions in the continuum. It was also shown that with some freedom in the choice of parameters, these models could give reasonable fit to the observed energy and angular distributions of the emitted particles. More recently, researchers have formulated several quantum–mechanical reaction theories [16,17] that are based on multi-step concepts and in which statistical evaporation at lower energies is connected to direct reactions at higher energies. The exciton model uses a unified model based on the solution of the master equation in the form proposed by Cline [18] and Ribansky et al. [19]. Integrating the master equation over time,

$$-q(n,\mathrm{t}=0) = \lambda^{+}(\mathrm{E},n+2)\,\tau(n+2)+\lambda^{-}(\mathrm{E},n-2)\,\tau(n-2) - \left[\lambda^{+}(E,n)+\lambda^{-}(E,n)W_{\mathrm{l}}(E,n)\right]\tau(n)$$

where q (n, t=0) is the initial condition on the process. In order to solve the system of algebraic equation, Capote et al. [11] were used the algorithm proposed by Akkermans et al.[20], which gives an accurate result for any initial condition of the problem. The use of master equation, which includes both the probabilities of transition to equilibrium λ^{+}(E,n) and probabilities of return to less complex stage λ^{-}(E,n), enables us to calculate, in a unified manner, the pre-equilibrium and equilibrium emission spectrum in accordance with [11],

$$\frac{d\sigma_{ab}}{d\varepsilon_b}(\varepsilon_b) = \sigma^{r}_{ab}(E_{inc})\,D_{ab}(E_{inc})\sum_{n} W_b(E,n,\varepsilon_b)\,\tau(n)$$

where $\sigma^{\mathrm{r}}_{\mathrm{ab}}(\mathrm{E}_{\mathrm{inc}})$ is the cross-section of the reaction (*a*, *b*), $\mathrm{W_b(E,n,\varepsilon_b)}$ is the probability of the emission a particle type *b* with energy ε_b from a state with *n* excitons and excitation energy E of the compound nucleus, $\tau(n)$ is the solution of the master equation which represents the time during which the system remains in a state of *n* excitons. $\mathrm{D_{ab}(E_{inc})}$ is a coefficient which takes into account the decrease in the available cross-section due to the particle emission by direct interactions with low excitation energy levels of the target nucleus and given by $D_{ab}(E_{inc})=1-\sigma^{dir}_{ab}/\sigma^{r}_{ab}$, where σ^{dir}_{ab} is the cross-section of direct interaction of the incident particle with target nucleus.

In the present work, the theoretical calculations have been made in the framework of the full exciton model using PCROSS computer code [11]. The equilibrium calculations have been made by Weisskopf-Ewing model [21] and this model doesn't include angular momentum effects. PCROSS program code, in calculations of the exciton model, use the initial exciton number as n_o =1. Thus taking into account the direct gamma emission.

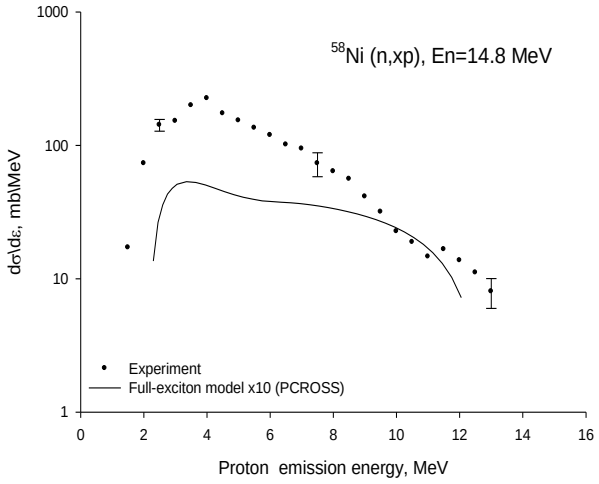

Fig. 1. The comparison of calculated alpha emission spectra of (n,x*p*) reactions with the values reported in literature for ^{58}Ni at 15 MeV. The experimental values were taken from [10].

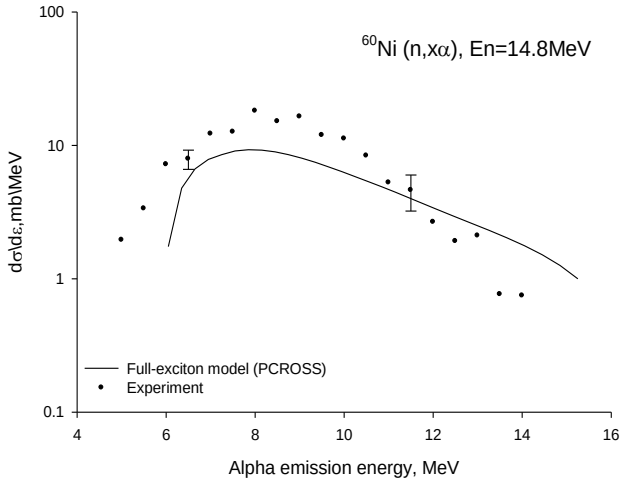

Fig. 4. The comparison of calculated proton emission spectra of (n,xα) reactions with the values reported in literature for ^{60}Ni at 14.8 MeV. The experimental values were taken from [10].

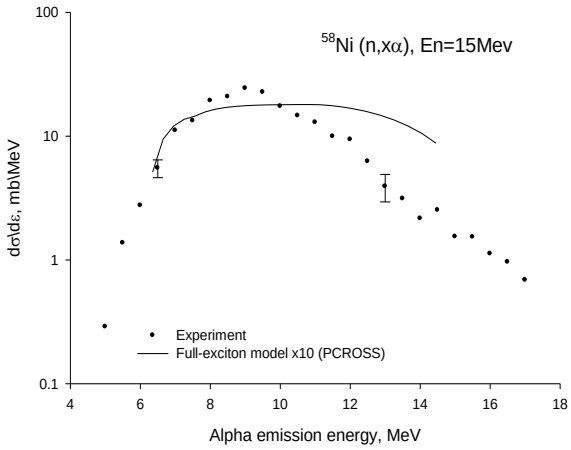

Fig. 2. The comparison of calculated proton emission spectra of (n,xα) reactions with the values reported in literature for ^{58}Ni at 14.8 MeV. The experimental values were taken from [10].

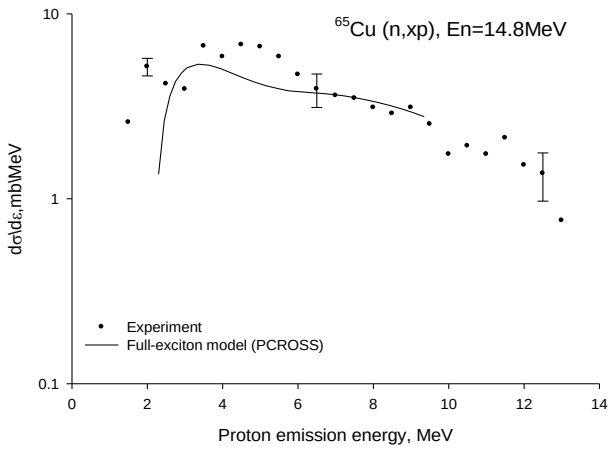

Fig. 5. The comparison of calculated alpha emission spectra of (n,x*p*) reactions with the values reported in literature for ^{65}Cu at 14.8 MeV. The experimental values were taken from [10].

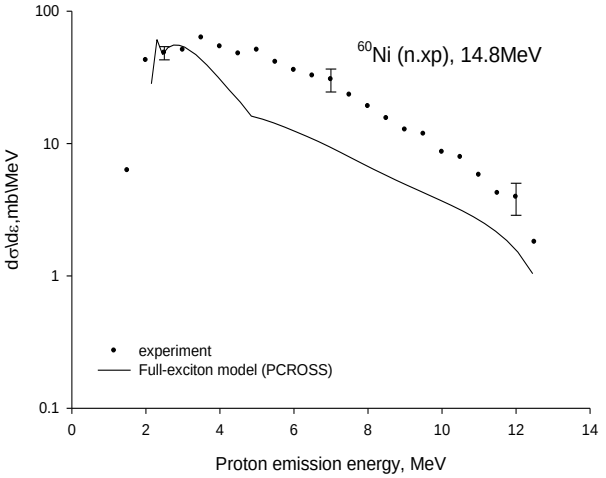

Fig. 3. The comparison of calculated alpha emission spectra of (n,x*p*) reactions with the values reported in literature for ^{60}Ni at 14.8 MeV. The experimental values were taken from [10].

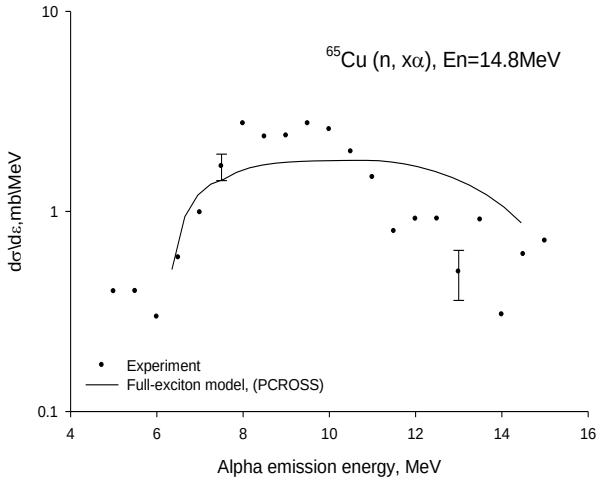

Fig. 6. The comparison of calculated proton emission spectra of (n,xα) reactions with the values reported in literature for ^{65}Cu at 14.8 MeV. The experimental values were taken from [10].

Equilibrium exciton number is taken equal to $\sqrt{1.4}$ gE , as was suggested in [22], after Pauli correction is modified. Single particle level density parameter g was equal to $A/13$ in the exciton model calculation, where A is the mass number. Level density expression given by Dilg [23] was used in the evaporation model calculation. Particle-hole state density expression reported by Williams [24] was used in the pre-equilibrium model calculation. The reaction cross-sections and the inverse cross-sections were obtained using the optical potential parameters by Wilmore and Hodgson [25], Bechetti and Greenless [26], Huizenga and Igo [27] for neutrons, protons and alpha particles, respectively. Generally, the calculated pre-equilibrium (n,xp) and (n,xα) reaction cross sections show the agreement with experimental data for the for $^{58,60}Ni$ and ^{65}Cu target nuclei. The calculations of the full exciton model with PCROSS code are lower than experimental data for ^{58}Ni(n,xp) and (n,xα) reactions. When it has been taken into consideration that the theoretical calculations have been multiplied by a constant (=10), the experimental values are in better agreement with the theoretical results for ^{58}N nuclei.

When more experimental data for the charge particle scattering and emission differential cross sections become available by using new technology, more reliable results can be obtained and more nuclear reaction mechanisms can be developed. These experimental cross–section data can be used for better understanding the basic nucleon–nucleus interaction, the binding energy systematics, nuclear structure, and for development of refined nuclear models. Improved predictions can guide the design of the target/blanket configurations and can reduce engineering over design costs.

It can be said that, at least this study contributes to the new studies on cross section and help to show the way to the future experimental studies.

ACKNOWLEDGMENT

This work has been supported by the project of Gazi University project (BAP), Code No: 05 /2009-50

[1]. *V.N. Levkovskii* 1974 Sov. J. Phys. 18 361
[2]. *E. Tel, et al.,* J. Phys. G: Nucl. Part. Phys., 29, 2169 (2003)
[3]. *E. Tel, et al.,* Phys. Rev. C, 75, 034614 (2007)
[4]. *I. Kumabe and K. J. Fukuda* 1987 Nucl. Sci. and Tech. 24 83
[5]. *E. Tel et al.,* J. Fusion Energ., 27(3), 188 (2008)
[6]. A. Aydin, et al., J. Fusion Energy., 27 (4), 308 (2008)
[7]. *A. Aydin, et al.,* J. Fusion Energy., 27(4), 314 (2008)
[8]. *M. H. Bölükdemir, et al.,* J. Fusion Energy., 29, 13(2010)
[9]. *E. Tel, et al.,* J. Fusion Energy., 28, 377 (2009)
[10]. Brookhaven National Laboratory, National Nuclear Data Center, EXFOR/CSISRS (Experimental Nuclear Reaction Data File). Database version of October 12,2009, (http://www.nndc.bnl.gov/exfor/) (2009)
[11]. R. *Capote, V. Osorio, R. Lopez, et al.,* Final Report on Research Contract 5472/RB, INDC(CUB)-004 (Higher Institute of Nuclear Science and Technology, Cuba), Translated by the IAEA on March 1991 (PCROSS program code)
[12]. *K. K. Gudima et al.,* Nucl. Phys. A, 401, 329 (1983)
[13]. *S. G. Mashnik,* User Manual for the Code CEM95, Joint Institute for Nuclear Research, Dubna, Moskow Region, (1995)
[14]. *J. J. Griffin,* Phys. Rev.Lett. 17 (1966) 478
[15]. *H. Gruppelaar, P. Nagel, P. E. Hodgson, LaRivasta Del*, Nuovo Cimento 9 (1986);
[16]. *H. Feshbach, A. Kerman, S. Koonin,* Ann.Phys. (NY), 125 (1980) 429
[17]. *T. Tamura, T. Udagawa, H. Lenske*, Phys. Rev. C 26 (1982) 379
[18]. *C. K Cline,* Nucl. Phys. A 193 (1972) 417
[19]. *I. Ribansky, P. Oblozhinsky, E. Betak,* Nucl. Phys. A 205 (1973) 545
[20]. *J. M. Akkermans, H. Gruppelaar, G. Reffo,* Phys.Rev. C22 (1980) 73
[21]. *V. F. Weisskopf and D. H. Ewing*, Phys. Rev., 57, 472 (1940)
[22]. *S. J. Zhang, X. J. Yang,* Z.Phys. A329 (1988) 69
[23]. *W. Dilg, W. Schantl, H. Vonach, M. Uhl,* Nucl. Phys. A 217 (1973) 269
[24]. *F. C. Williams,* Nucl. Phys. A 166 (1971) 231
[25]. *D. Wilmore and P. E. Hodgson,* Nucl. Phys. 55 (1964) 673
[26]. *F. D. Bechetti and G. W. Grenlees,* Phys.Rev. 182 (1969) 1190
[27]. *J.R. Huizenga and G. Igo,* Nucl. Phys. 29(1962), 462

DOSIMETRY STUDIES FOR AN INDUSTRIAL ACCIDENT

F. AYSUN UGUR, HALIDE SAHAN
Osmaniye Korkut Ata University, Faculty of Sciences and Letters, Department of Physics, 80000,Osmaniye/Turkey
aysunaf@yahoo.com, halidesahan@osmaniye.edu.tr

The paper presents the results of the dosimetric calculations made to determine the dose taken by a worker who unknowingly carried ^{192}Ir (9.15 Ci) radioactive source in his hip area. In this study, calorimetric method is used to derive the depth doses calculation. As a result, doses delivered to the skin, liver-spleen, femur, spinal cord, gonads, sternum and whole body at depth levels ranging from 0 cm to 20 cm were estimated for exposure time between 20 and 30 minutes. As expected, the more the depth of the phantom was the less the dose values obtained. It is observed that the dependence was exponential.

I. INTRODUCTION

Industrial radiography is a frequently used method of nondestructive testing for many industrial products. Industrial radiography is a routine operation requiring high radiation levels and relying primarily on human diligence in observing safety procedures to prevent accidents. Consequently, there are a number of serious over exposures each year as have been reported previously [1,2,3]**.** An accident has occurred at an industrial company in Istanbul on 1 May 1987, which has been described in Turkish Atomic Energy Authority (hereafter referred to as TAEK) website [4]. A worker who unknowingly carried an ^{192}Ir (9.15 Ci) radioactive source in his hip area was exposed to this source. This paper reports the dosimetry studies that were done to determine the dose the worker was exposed. The source was probably in contact at 3 cm from the skin of the worker's hip area during the exposure. The exposure time was estimated to be 20-30 minutes.

In this study, experiments were carried out in TAEK Çekmece Nuclear Research Center Health Physics Department SSDL (Secondary Standard Dosimetry Laboratory). Here, details of the experimental work are given together with the details of the calculations. In view of these results, this study will provide important archival information for similar events in the future.

II. MATERIAL AND METHODS

In the field of ionizing radiations the absorbed dose is one of the basic quantities commonly used in dosimetry. The main reason is that it is closely related to the biological effects of radiation. Water is of special interest as an absorbing material because it is very similar to human tissue. One of the duties of the national standards laboratories is to establish accurate standards for absorbed dose in water. To this end, much effort has been put into the development of various experimental approaches. One of the most frequently used is the calorimetric method because its basic principle is simple [5]. Therefore, the measurements made here were obtained in detail by this method. In these measurements, the values of pressure and temperature were recorded regularly and added to the calculations as correction parameters.

2.1. Depth dose calculations

The aim of the present work was to measure the depth dose rates by using a water phantom and ^{192}Ir source to obtain experimental and theoretical results. The absorbed dose (D_d) at depths from 0 cm to 20 cm in tissue with the source in surface contact was calculated by

$$D_d = \frac{0.96A\Gamma}{(d+0.24)^2} f(d) \quad (1)$$

where, A equals the source activity in unit of curie (A is the exposure rate at 1 cm), Γ is the exposure rate constant, 0.96 is the conversion factor to *rads/Roentgen*, d is the tissue depth in unit of cm, 0.24 is the estimated encapsulation thickness in unit of cm, $f(d)$ is the scatter and attenuation polynomial of Shalek and Stovall [**6**] for $d \leq 15$ cm or $\exp(-0.035d)$ for $d \geq 15$ cm.

Since there is a likelihood that the source may have been at a distance of up to 3 cm from the surface, depth doses were also calculated for these circumstances using standard depth-dose improvement factors with greater distances from the surface. These values are given in Table 2 and compared in Figure 2 and Figure 3 with the experimental measurements.

2.2. Experimental arrangement

A schematic view of the experimental arrangement is given in Figure 1. The ^{192}Ir source is 2 cm diameter and 0.56 cm in length. The manufacturer quoted the source activity as 116.21 curie (4.29 TBq) on 17 September 1986. Using half life of 74.2 days, the expected activity on the date of the experiment would have been 9.15 curie (0.33 TBq). ^{192}Ir is a meta-stable isotope of Iridium emitting gamma radiation with a low level of Lineer Energy Transfer (LET) and high penetration in human body. This isotope frequently has been used for industrial radiography [7,8]. The presence of impurities, especially those with long half-lives and high radiation energies, can significantly alter the absorbed doses. Its energy spectrum is extremely complex, because it has got 30 gammas and 40 X-rays [3]. However, for an unshielded source, Table 1 shows the most important energies and frequencies of the emitted gamma and beta particles which have been taken from data compiled by Delacroix et al. (2002) [9]. The average energies have been calculated and then added to Table 1.

The distance of the source from the reference plane of measurement is 1 m. In this plane the beam size is 10 cm×10 cm; the photon fluence at the cross-section border is 50% of that on the beam axis.

The water phantom consists of a cubic perspex tank, of side 30 cm, with walls 14 mm thick. The wall facing the beam has a thickness of 4.0 mm (0.476 g.cm^{-2}) over a section of 15 cm×15 cm to reduce the correction due to the non-equivalence of the perspex front face with water. The phantom, filled with demineralized water, is positioned in such a way that the reference plane is at a depth equivalent to 5g.cm^{-2} in water [5].

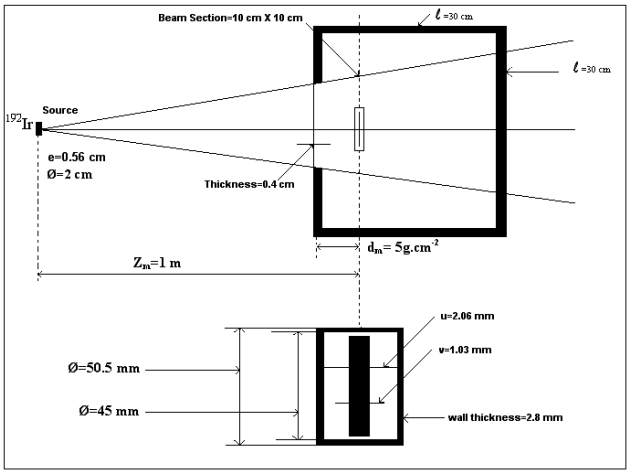

Fig. 1. Experimental arrangement used at the SSDL for measuring the adsorbed dose in the water phantom, and schematic view of the cavity ionization chamber [3].

The ionization chamber, inserted into a perspex support (1.85 mm thick), can be moved inside the water along the beam axis by means of a translation table fixed on the phantom walls. This allows an accurate adjustment of the chamber position.

Table 1. Gamma and beta energy distributions for an unshielded ^{192}Ir source [9].

^{192}Ir	Gamma E(keV)	Frequency (%)	Beta E(keV)	Frequency (%)
E1	317	83	256	6
E2	468	48	536	41
E3	604	8	672	48
Average	372		583	

To avoid long-term variation of the ionization current due to the possible influence of humidity on the ionization chamber, the phantom is filled up and drained everyday**.** The temperature of the chamber is measured with a calibrated thermistor. To match the air conditions of the chamber cavity, the thermistor is placed in air inside a Perspex tube dipped into water. The temperature difference between the positions of the thermistor and of the chamber has been checked and found to be small (less than 0.01°C), so the error introduced is negligible [5].

A Baldwin- Farmer 0.6 cc ionization chamber with a ± %3 calibration accuracy (traceable to the National Bureau of standards) was exposed, in air, at a distance of 14 cm from the source. The positioning error was estimated to be less than ± 0.5 cm. This measurement indicated an average exposure rate on 15 June 1987, of 224.06 R/h at distances of 14 cm. The standard deviation of eight such measurements was less than %3. This corresponds to a source activity of 9.15 ± 0.65 curie (0.33 TBq ± 0.02 TBq), with the uncertainty reflecting possible positioning errors. This activity determination was based on an exposure rate constant of 4.8 R-cm^2/milicurie-h as reported in NCRP (National Council on Radiation Protection and Measurements) Pamplet 40 [3,10]. Although estimates of the exposure-rate constant for ^{192}Ir range from 4.3 to 5.0 R-cm^2/milicurie-h, the value of 4.8 was selected to be consistent with the exposure and dose calculations of this paper which are based on the actual exposure measurements and are independent of the exact source activity [3].

2.3. Experiment and its calculations

Firstly, perspex tank has been filled with demineralised water. ^{192} Ir source has been placed at a distance of 3 cm from the tank. Ionization chamber has been placed at a distance of 2.5 cm. Then, radiation count per minute has been carried out at this position. The exposure unit is generally expressed in unit of Rönt/h. However, this expression can be transformed into rad/h by multiplying with a factor of 0,96 rad/Rönt as given below:

$$Exposure\,unit = \frac{Rönt}{h} \times 0.96 \frac{rad}{Rönt} = \frac{rad}{h} \qquad (2)$$

Using the proper conversion factors an expression for absorbed dose in the unit of rad/h is found as:

$$D = Count(\frac{Rönt}{h}) \times CP \times TP \times 0.96 \times 60 \qquad (3)$$

In this equation; calibration factor of ionization chamber (CP) and temperature-pressure factor (TP as also calculated from equation **(4)** below) were 1.004 and 1.0165, respectively.

$$TP = \frac{273.16^{\circ}K + 23.5^{\circ}C}{293.16} \times \frac{1013}{1008.4} = 1.01655 \qquad (4)$$

Here, the laboratory temperature on the day of the experiment was taken as 23.5 ^{o}C and pressure as 1008.4 mb. Furthermore, normal temperature and air pressure on sea level were 20 ^{o}C and 1013 mb, respectively.

Later, absorbed dose values during the period of estimated exposure time (20-30 minutes) at varying depths in water (d= 0, 7, 12, 15, 17, 20 cm) for SSD=3 has been calculated separately.

Same calculations under the same conditions have been repeated and the results are given in detail in Table 2. In this table, the estimated doses for the depths of 0, 5, 7, 12, 15, 17, 20 cm correspond to the skin, liver-spleen, femur, spinal cord, gonads, sternum and whole body (1Gy = 100 rad, 1sv = Gy.RBE = 1 (X and Gamma Rays), 1sv = 100 rad).

III. RESULTS AND DISCUSSION

According to the International Atomic Energy Agency (IAEA), industrial radiography accounts for approximately half of all reported accidents for the

nuclear related industry. Detailed information about these accidents have been published by the IAEA in its Safety Report Series [11]. In radiological accidents, health position of victims depends very much on a reliable assessment of the organ and tissue absorbed doses. Therefore, depth dose calculations are very important in this field. This paper presents the details of the calculations of the organ doses versus depth under certain conditions as mentioned above.

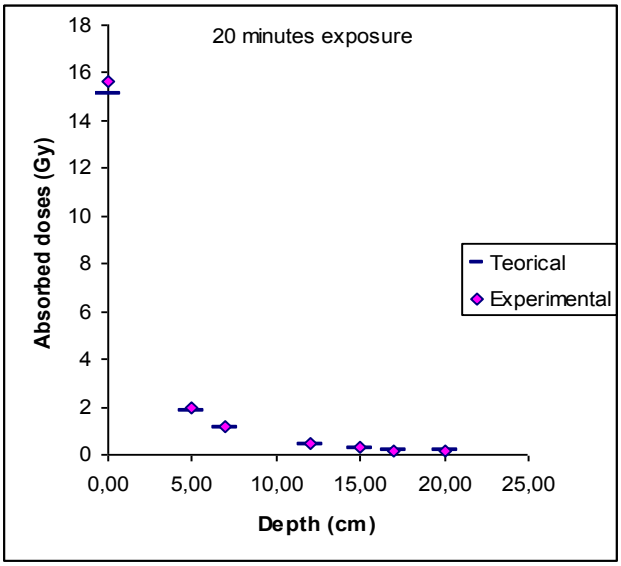

Fig. 2. Absorbed organ doses versus depth ranging from 0 to 20 for estimated exposure time (20 minutes)

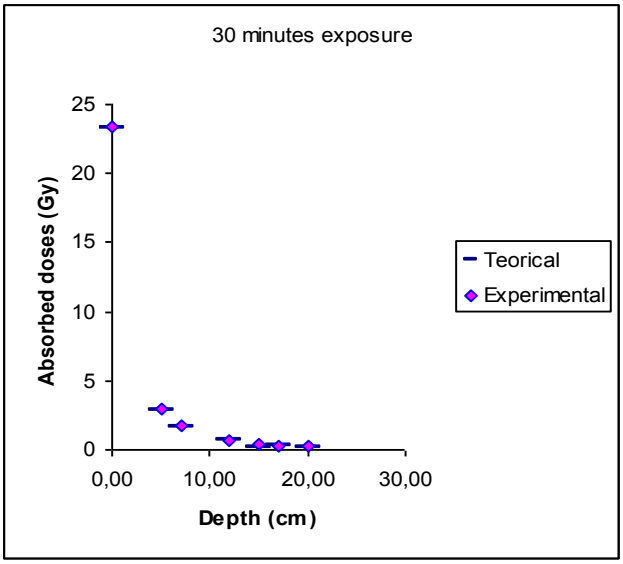

Fig. 3. Absorbed organ doses versus depth ranging from 0 to 20 for estimated exposure time (30 minutes)

In this study, measurements have been performed at varying depths in water (d = 0, 5, 7, 12, 15, 17, 20 cm), during a period of estimated exposure time (20-30 minutes) separately for SSD = 3. The absorbed dose rates at reference position were given in Table 2 and the curve of absorbed doses versus the water depth is given in Figure 2 and Figure 3.

In Table 2, organ doses corresponding to the skin, liver-spleen, femur, spinal cord, gonads, sternum and whole body were estimated to be 15.61, 1.99, 1.20, 0.47, 0.29, 0.19, 0.14 Gy for estimated exposure time of 20 minutes, and 23.42, 2.99, 1.80, 0.70, 0.43, 0.29, 0.21 Gy for estimated exposure time of 30 minutes respectively in depths ranging from 0 cm to 20 cm for SSD = 3.

As expected, the more the depth of phantom the less was the dose values obtained. The dependence is exponential. At the same time, Figure 2 and Figure 3 depict absorbed doses versus depths ranging from 0 cm to 20 cm for both exposure times (20-30 minutes) for SSD=3, including experimental and theoretical results together. In these Figures, experimental and theoretical results were in good agreement with each other. These findings are also consistent with those of the earlier studies [3].

IV. CONCLUSIONS

This paper presents the dosimetry calculations that were done to determine the dose taken by a worker who unknowingly carried such a source in his hip area. This accident has occurred at an industrial company in Istanbul on 1 May 1987, and has been given in TAEK website [4].

This study is of prime importance for comparison with archival information for similar accidents, and gives the details of the calculations of the depth doses. The experimental study carried out has been briefly described and the results reached has been presented in Table 2 and plotted in Figure 2 and Figure 3. In addition, experimental and theoretical results have been compared with each other as shown in the Figure 2 and 3. It can be seen that as in most other depth dose calculation studies done previously, the absorbed dose in tissue is greater for d = 0 cm depth than those of d = 20 cm. In this research, the maximum absorbed dose has been derived at 0 cm depth, which is in agreement with the results reported earlier. Similar results have been reported in the literature [3].

As a result, the absorbed doses were found to decrease with the increase in depth. In conclusion, this study will provide an important archival knowledge for similar accidents.

Table 2. Absorbed organ doses versus depth ranging from 0 to 20 for estimated exposure time (20 -30 minutes) for SSD=3.

SSD=3 cm		Absorbed doses (Gy) for 20 minutes		Absorbed doses (Gy) for 30 minutes	
Depth(cm)	Organ	E	T	E	T
0	skin	15.61	15.1	23.42	23.28
5	liver-spleen	1.99	1.84	2.99	2.76
7	femur	1.20	1.10	1.80	1.65
12	spinal cord	0.47	0.40	0.70	0.61
15	gonods	0.29	0.25	0.43	0.88
17	sternum	0.19	0.19	0.29	0.29
20	whole body	0.14	0.13	0.21	0.20

[1]. *M.Annamalai, P.S.Iyer, T.M.R.Panicker*, Health Physics 35:887-389, (1978).

[2]. *M.B.Biles*, in Proceedings of the Symposium on the Handling of Radiation Accidents. Vienna, p.3, (1969).

[3]. *H. F.Eugene and L. B.William*, The Medical Basis for Radiation Accident Preparedness, 265-277, (1980).

[4]. Turkish Atomic Energy Authority website (www.taek.gov.tr).

[5]. *M.Boutillon and A.M.Perroche*, Phys. Med. Biol., 38 439-454, (1993).

[6]. *R. J.Shalek, M.Stovall*, New York, Academic Press, (1969).

[7]. *A.Jalil, M.A.Molla*, Health Phys. 62(1):74-76, (1992).

[8]. *S.Milacic, J.Simic, J.Kobe* Med. Sci., 54, 2, E108-E113, (2008).

[9]. *D.Delacroix,J.P.Guerre, P.Leblanc, C. Hivkman*, Radionuclide and Radiation Protection Data Handbook 2002 Radiat. Prot. Dosim. 98 1-168, (2002).

[10]. Protection Against Radiation From Brachytherapy Sources. NCRP Pamphlet No.40, National Council on Radiation Protection and Measurements, March I, (1972).

[11]. *R.Kramer, A.M.Santoas, C.A.O.Brayner, H.J.Khoury, J.W.Vieira, F.R.A. Lim*, Phys. Med. Biol. 50 3681-3695, (2005).

CALCULATION OF FISSION BARRIER OF $^{230\text{-}234}$ Pa ISOTOPES

A.H. YILMAZ, B. ENGİN, T. BAYRAM, M. DEMİRCİ
Karadeniz Technical University, Department of Physics,
61080, Trabzon / TURKEY
E-mail: hakany@ktu.edu.tr, burcinengin@ktu.edu.tr

The fission barriers of $^{230\text{-}234}$Pa have been carried out by using the BARRIER code developed by Garcia. The nuclear shape has been parameterized in terms of Cassini ovaloids proposed by Pashkevich. The single- particle energies have been calculated as function of the deformation parameters of an axially deformed Woods-Saxon potential, as input to the shell correction calculations. To obtain the total nuclear energy, it is also necessary to add a pairing energy in order to take into consideration the short range nuclear interactions.

I. INTRODUCTION

This work is a theoretical support for the fission barriers of ground states and excited states in $^{230\text{-}234}$Pa. The isotopes nuclei of $^{230\text{-}234}$Pa have distinct fission properties. Differences have been found in the equilibrium deformation, first and second minimum, and saddle points of these Pa isotopes. Asymmetric mass division was also found of ones.

In our work, the first steps to start the optimization of the potential parameters are to fix the appropriate value of the equilibrium deformation of the nucleus. In the shell model approach, this is achieved in most of the practical applications using the Strutinsky method [1]. In this work, the extremal points were calculated with the BARRIER code [2], which includes the Strutinsky method with the Pashkevich parametrization for the nuclear shape. In our calculations, the pairing energy was evaluated accordingly to the commonly used prescriptions of the BCS approach which is including blocking effect [3, 4].

II. METHOD OF CALCULATION

Fission Barrier

Nuclear Deformation

As a function of deformation, average values of various nuclear properties are only calculated by macroscopic-microscopic method in the Strutinskys formalism [1, 5]. Within this method, the total energy surface of nuclear system is given by [3]

$$V(N,Z,\beta) = E_{LD} + E_{Shell} + E_{Pair} \tag{1}$$

The liquid drop model gives the macroscopic terms. The microscopic portion is given by E_{Shell} and E_{Pair}. In order to obtain the best results for the single-particle spectrum in the equilibrium deformation the total energy is minimized with respect to the deformation parameters. In this work we used the Cassini ovaloid shape parametrization. The equilibrium deformation parameters are the quadrupole moment term (ε) and the hexadecapole moment term (α_4).

Shell Correction Method

The fission barrier is concerned with surface energy and Coulomb energy terms. The sum of their contributions to the liquid drop energy relative to the energy of a spherical liquid drop can be written as

$$\begin{aligned} &E_{LD}(shape) - E_{LD}(0) = \\ &\{[f(shape)-1] + 2\chi[g(shape)-1]\}E_s(0) \end{aligned} \tag{2}$$

where $E_S(0)$ and χ are the surface energy of the spherical liquid drop and fissility parameter, respectively.

$$\chi = \frac{3}{5}\frac{e^2}{r_0}\frac{Z^2/A}{2a_2\{1-\kappa[(N-Z)/A]^2\}} \tag{3}$$

The fissility parameter, and the values of the coefficients a_2 and κ are crucial a determining the shape dependence of the liquid drop energy of fission barriers [2].

In order to account for the average properties of a single- particle spectrum, ones introduces a smooth function $\tilde{g}(\in,\beta)$ [2]. The auxiliary function,

$$\tilde{G}(\varepsilon,\beta) = (\pi^{1/2}\tilde{\gamma})\sum_{\nu}\exp\left(-\left\{\frac{\varepsilon-\varepsilon_{\nu}(\beta)}{\tilde{\gamma}}\right\}^2\right) \tag{4}$$

The averaging interval $\tilde{\gamma}$,

$$\tilde{\gamma} \approx \hbar w_0 \approx 7-10MeV \tag{5}$$

The function $\tilde{G}(\varepsilon,\beta)$ is obtained by smearing out the single particle energies ε_{ν}, over an energy range of the order of $\hbar w_0$ [2].

The uniform level density can be written as

$$\tilde{g}(\varepsilon,\beta) = \tilde{G} - \frac{1}{4}\tilde{\gamma}^2\left(\frac{\partial^2\tilde{G}}{\partial\varepsilon^2}\right) + ... + a_{2m}\tilde{\gamma}^{2m}\left(\frac{\partial^{2m}\tilde{G}}{\partial\varepsilon^{2m}}\right) \tag{6}$$

where the smoothing function,

$$\xi(x) = (\pi)^{-1/2} \exp(-x^2) \sum_{k=0,2}^{2m} a_k H_k(x) \qquad (7)$$

$H_k(x)$ is the Hermite polynomials, and the coefficients a_k are given by the recurrence relation.

It is convenient to introduce another density function, $g_{sh}(\varepsilon,\beta)$ in order to describe the local level density of the single-particle spectrum. The variations in the single-particle level density caused by the shells can be described by the function [2]

$$\delta g(\varepsilon,\beta) = g_{sh}(\varepsilon,\beta) - \tilde{g}(\varepsilon,\beta) \qquad (8)$$

The sum of single-particle energies are given by

$$U = 2 \int_{-\infty}^{\lambda_{sh}(\beta)} \varepsilon g_{sh}(\varepsilon,\beta) d\varepsilon \qquad (9)$$

The energy shell corrections can be written as

$$E_{shell} = 2\left[\int_{-\infty}^{\lambda_{sh}(\beta)} \varepsilon g_{sh}(\varepsilon,\beta) d\varepsilon - \int_{-\infty}^{\bar{\lambda}(\beta)} \varepsilon \tilde{g}_{sh}(\varepsilon,\beta) d\varepsilon \right] \qquad (10)$$

Renormalization in BCS theory

In this work, the pairing correlation energy was evaluated as in the commonly used prescriptions of the BCS approach. We were also calculated of the pairing energies [6]. In this way, we valued only the essential energy variation gap Δ and the pairing energy due to the shell structure [2].

We start with the following BCS equation:

$$\frac{2}{G} = \int_{\tilde{\lambda}-\Omega}^{\tilde{\lambda}+\Omega} \frac{\tilde{g}(E)dE}{\left[(E-\tilde{\lambda}) + \tilde{\Delta}^2 \right]^{-1/2}} \approx 2\tilde{g}(\tilde{\lambda}) \ln\left(\frac{2\Omega}{\tilde{\Delta}} \right) \qquad (11)$$

where, Ω is the cutoff energy and $\tilde{g}(\tilde{\lambda})$ is the average level density at the Fermi energy.

We define the energy P of the pairing correlations as the difference between the sums of single-particle energies evaluated with and without the pairing correlations [2].

$$P = \sum (\varepsilon_\nu - \lambda) \operatorname{sign}\left[\varepsilon_\nu - \lambda_0 \right] - \frac{(\varepsilon_\nu - \lambda)^2 + \frac{1}{2}\Delta^2}{\left[(\varepsilon_\nu - \lambda)^2 + \Delta^2 \right]^{1/2}} \qquad (12)$$

The shell correction in the pairing energy is defined as

$$E_{pair} = P - \tilde{P} \qquad (13)$$

Where $\tilde{P}$ is the pairing correlation energy fort he uniform distribution

$$\tilde{P} = -\frac{1}{2} \tilde{g}(\tilde{\lambda}) \tilde{\Delta}^2 \qquad (14)$$

$$E_{Barrier} = E_{LDM} + E_{Shell} \qquad (15)$$

III. RESULTS

Using the Strutinsky method with the Pashkevich parametrizations of nuclear shape, as introduced in the BARRIER code [2], we have carried out fission barrier and deformation. The parameter ε is associated with elongation and defines a concrete Cssini ovaloid, whereas α_4 is connected to the deformation parameter of hexadecapolar momentum, and are coefficients of Legendre polynomials series expansion. In Fig. 1-5 we showed our calculated fission barriers as functions of ε and α_4.

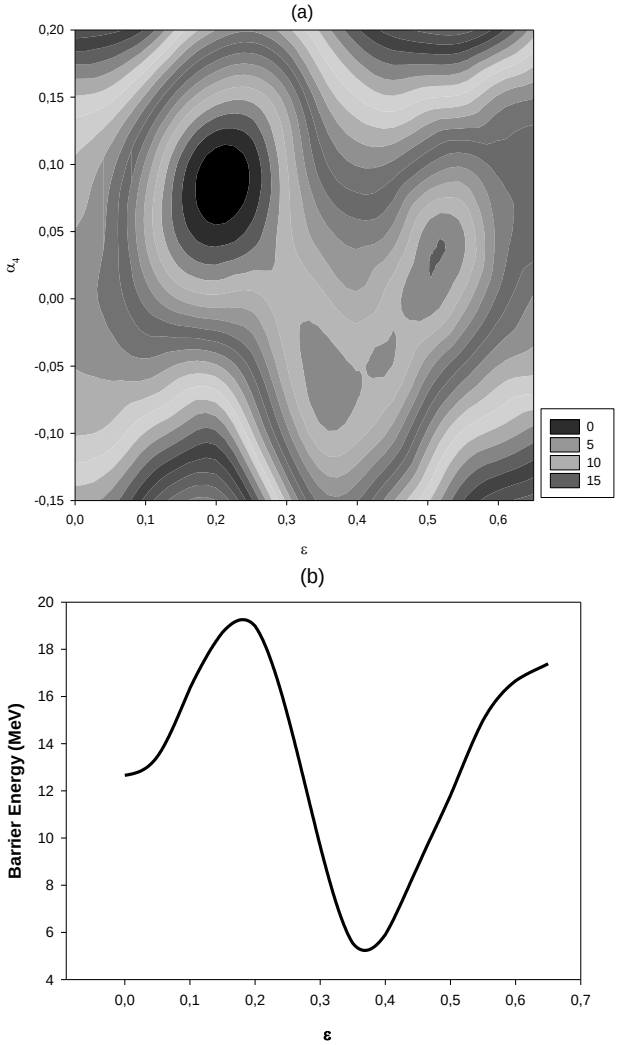

Fig.1: (a) Calculated fission barrier in the (ε, α_4) plane for ^{230}Pa. The contour line separation is 0,05 MeV. (b) Fission path through the barrier.

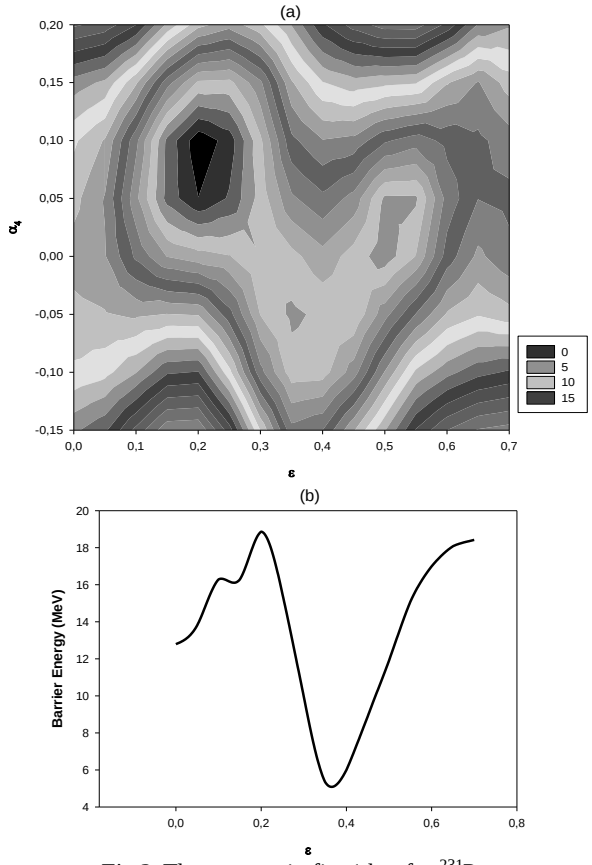

Fig.2 The same as in fig. 1 but for ^{231}Pa.

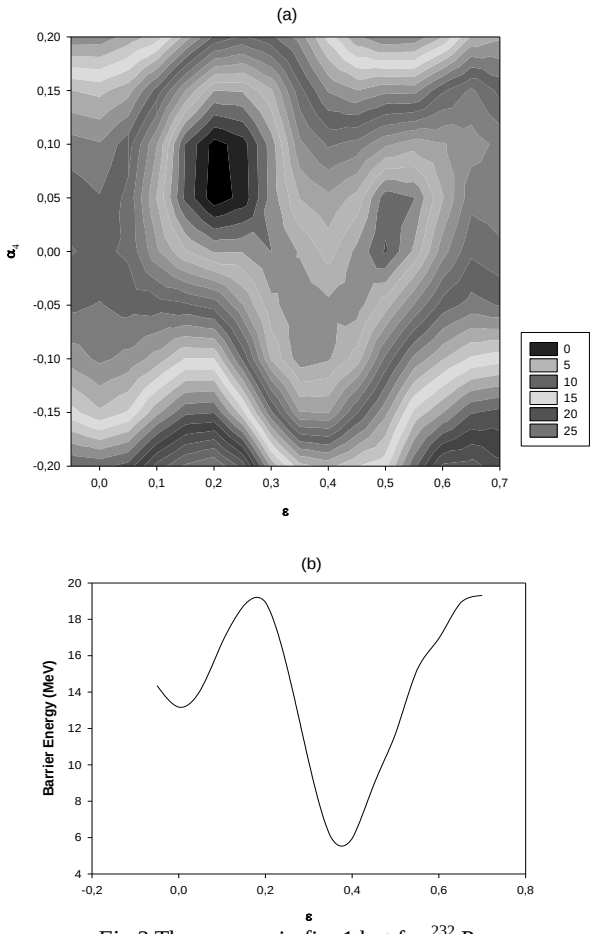

Fig.3 The same as in fig. 1 but for ^{232} Pa.

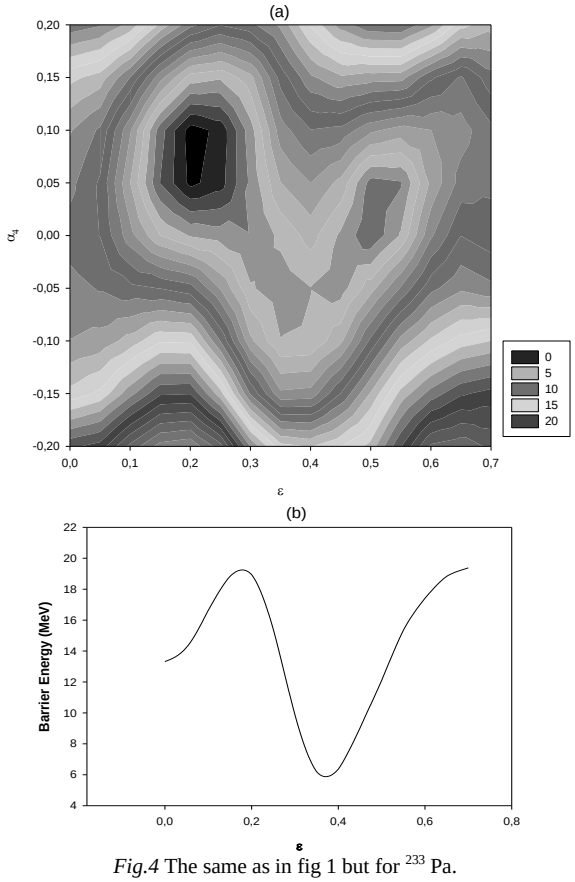

Fig.4 The same as in fig 1 but for ^{233} Pa.

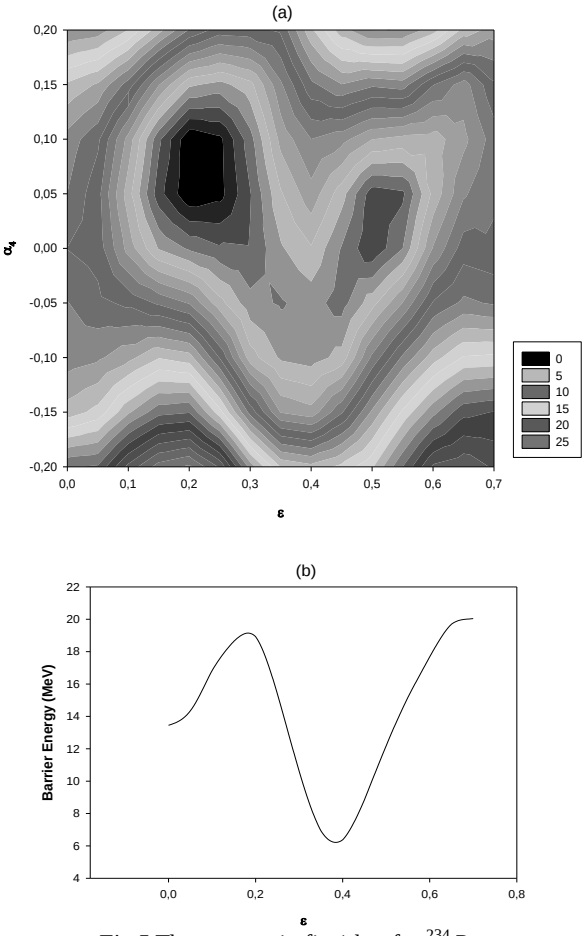

Fig.5 The same as in fig 1 but for ^{234} Pa

As shown, the deformation coordinates are sensitive to the adopted in $^{230\text{-}234}$ Pa, which only changes the relative height of the fission barrier. The fission barrier is composed of the liquid drop energy and the shell correction energy.

Table1. Results of Fission barrier

	Fission Barrier		
	This work	*Experimental*	*ETFSI*
^{230}Pa	5,90	5,80	6,00
^{231}Pa	5,61	5,50	5,80
^{232}Pa	6,06	6,40	5,90
^{233}Pa	5,92	5,80	6,00
^{234}Pa	6,18	6,15	5,30

Table 2. Deformation Parameters

	First Minimum		*Second Minimum*	
	ε	α_4	ε	α_4
^{230}Pa	0,215	0,100	0,488	0,0
^{231}Pa	0,209	0,100	0,495	0,0
^{232}Pa	0,210	0,100	0,496	0,0
^{233}Pa	0,212	0,100	0,497	0,0
^{234}Pa	0,211	0,100	0,493	0,0

The fission barriers for Pa isotopes were calculated by using the BARRIER code [2]. In Table 1, The values obtained were compared to the experimental results [7] and ETFSI results [8]. As we can see, the BARRIER code fission barriers are in good agreement with the experimental values.

By using the above mentioned method, deformations corresponding to the second minimum could be obtained. In Table 2 we showed the deformation parameters for the ground state and the second minimum of $^{230\text{-}234}$Pa. The parameters used as starting values were taken from Chepurnov[9]. Both the ε and α_4 deformation parameters in Pa isotopes are very similar around the first and second minimum.

IV. CONCLUSIONS

We have calculated the details the fission barriers of $^{230\text{-}234}$Pa. Shell effects should be present in these nuclei, come into existence structures connected to the barrier energy, saddle point, first and second minima. Shell effects are most probably characteristics responsible for fission decay strange

[1]. *V. M. Strutinsky*, Nucl. Phys. A, 1967, 95, p.420

[2]. *F. Garcia, O. Rodriguez, J. Mesa, J.D.T. Arruda-Neto, V.P. Likhachev, E. Garrote, R. Capote and F. Guzman*, Comp. Phys. Comm. 1999,120, p.57

[3]. *M. Brack, J. Damgaard, A.S. Jensen, H.C. Pauli, V. M. Strutinsky and C.Y. Wong*, Rev. Mod. Phys. 1972, 44, p.320

[4]. *F.Garcia, E.Garrote, M.L.Yoneama, J.D.T.Arruda-Neto, J.Mesa, F.Bringas, J.F.Dias, V.P.Likhachev, O.Rodriguez, F.Guzman*. Eur. Phys. J.A 1999, 6, p. 49-58

[5]. *W.D. Myers, W.J. Swiatecki*, Nucl. Phys. 1966, 81 p.258

[6]. *V.M. Strutinsky*, Nucl. Phys. A 1968, 122, p.1

[7]. http://www-nds.iaea.org/RIPL-2/fission/fis-barrier-exp.dat

[8]. http://www-nds.iaea.org/RIPL-2/fission/fis-barrier-etfsi.dat

[9]. *V.A. Chepurnov*, Sov. J. Nucl. Phys. 1968, 6, p.696

INVESTIGATION OF THE ISOSPIN IMPURITY OF THE GROUND STATE FOR $^{122\text{-}134}$Xe ISOTOPES

CEVAD SELAM[1], HASAN ALİ AYGÖR[2], NECLA ÇAKMAK[3]

[1]*Department of Physics, Anadolu University,*
26470 Eskişehir, TURKEY
[2]*Department of Physics, Alparslan University,*
49000 Muş, TURKEY
[3]*Department of Physics, Karabük University,*
78050 Karabük, TURKEY
cselamov@anadolu.edu.tr

The isospin impurity of the ground state of the parent nucleus within the framework of the quasi particle neutron-proton random phase approximation has been calculated. For the self-consistent determination of the isovector effective interaction strength parameter Pyatov-Salamov method is used. The isospin impurities were calculated with the inclusion of the pairing correlations between nucleons for $^{122\text{-}136}$Xe isotopes. Calculation results compared with spherical calculations and the other theoretical results.

I. INTRODUCTION

The investigation the isospin dependence of the nuclear matter is of importance for astrophysical and nuclear-structure studies. In the studies of astrophysics this investigation is important for the physics of supernova explosions [1] and of neutron stars [2], e.g. the chemical composition and cooling mechanism of proto-neutron stars [3,4], mass-radius correlations [5,6], and some other topics. In the studies of nuclear structure the investigation of isospin dependence is of interest in study of neutron-rich and proton-rich nuclei [7,8].

With the development of the heavy mass ion accelerator technology, many neutron-rich and proton-rich isotopes have been established. The investigations on these isotopes are very useful in understanding many nuclear aspects such as the isospin mixing effects of the nuclear states which are very important in estimating the effective vector coupling constants based on Fermi transitions, and in the description of the energies and the widths of the analog states and the isospin multiples [9–12].

The isospin mixing is basically caused by the Coulomb potential. Since the very small symmetry energy tries to minimize the difference in the proton and the neutron systems, Coulomb forces are more dominant in nuclei for which the proton and the neutron numbers are close to each other. Therefore, the isospin mixing values will be large in the ground state of the proton-rich nuclei.

The isospin admixtures in the nuclear ground states have been investigated in different theoretical and experimental studies [13–31], but we do not want to go into the details of these studies in this article since they are given in our previous studies [32,33]. One of the most conspicuous features in the theoretical studies is that the pairing correlations between nucleons are not taken into consideration. This deficiency has given us the physical motivation to our previous study in which we analyzed the effect of the pairing interaction on the energies of the isobar analog resonances in $^{112-124}$Sb and the isospin admixtures in the ground states of $^{100-124}$Sn isotopes.

In this study, Pyatov–Salamov method [31] for the self-consistent determination of the isovector effective interaction strength parameter, restoring a broken isotopic symmetry for the nuclear part of the Hamiltonian is applied to deformed nuclei. Since the same method has been applied to spherical nuclei [32–33], the formulation is identical for each model.

In this study, the isospin admixtures in the ground state of the parent nucleus were calculated for $^{122\text{-}136}$Xe isotopes in both deformed and spherical cases. Calculation results compared with the hydrodynamic model results.

II. ISOSPIN STRUCTURE OF THE GROUND STATE FOR THE PARENT NUCLEI

Expending the ground state wave function in terms of pure isospin components $|T,T_z\rangle$ we obtain:

$$|0\rangle = a\,|T_0,T_0\rangle + b\,|T_0+1,T_0\rangle, \quad a^2+b^2=1 \tag{1}$$

where T_0 is the ground state isospin of the parent nuclei. The expection value of the square of the isospin in the ground state of the parent nucleus can be expressed as [17]

$$\langle 0|\hat{T}^2|0\rangle = T_0(T_0+1) + \sum_i \left|M^i_{\beta^+}\right|^2 \tag{2}$$

where $M^i_{\beta^+}$ is the matrix element of beta transition from the ground state of the parent (N, Z) nucleus to the i^{th} 0^+ excited states of the daughter (N+1, Z-1) nucleus generated by residual Fermi interaction. On the other hand, the following expression fore the same quantity can be obtained from Eq.(1):

$$\langle 0|\hat{T}^2|0\rangle = T_0(T_0+1) + 2b^2(T_0+1) \tag{3}$$

From Eq.(2) and (3), it follows that the T_0 + 1 isospin admixture probability in the ground state of the parent nucleus is determined by the sum of the squares of the beta decay matrix elements from the isobaric states of the nucleus (N+1, Z-1):

$$b^2 = \left(\sum_i \left|M^i_{\beta^+}\right|^2\right) / \sqrt{2(T_0+1)} \tag{4}$$

III. RESULTS AND DISCUSSION

Numerical calculations have been performed for the $^{122\text{-}136}$Xe isotopes. The calculations have been done for both-spherical and deformed cases. For deformed case the Nilsson single particle energies and wave functions have been calculated with deformed Woods-Saxon potentials [34]. All energy levels from the bottom of the potential well to 8 MeV have been considered for neutrons and protons. Deformation parameters were found from minimum value of ground states energy of investigated nuclei. Values of pair correlation functions were chosen as $C_n=C_p= 12/\sqrt{A}$ [13]**.** The Ikeda sum rule is fulfilled with ≈1% accuracy. Firstly, the dependence on deformation parameter of the isospin admixture has been investigated for ^{122}Xe isotope. The calculation result for ^{122}Xe isotope is given in Figure 1. The calculations have been performed for the deformation parameters in the range of -0.3 and +0.3 with a step magnitude of 0.05. As seen from Fig.1, the dependence on deformation parameter of the ground state of the isospin admixture is a parabola. The minimum value of this parabola corresponds to the spherical state. This result is natural because the isospin admixture results from the variation of the Coulomb potential through nuclei radius.

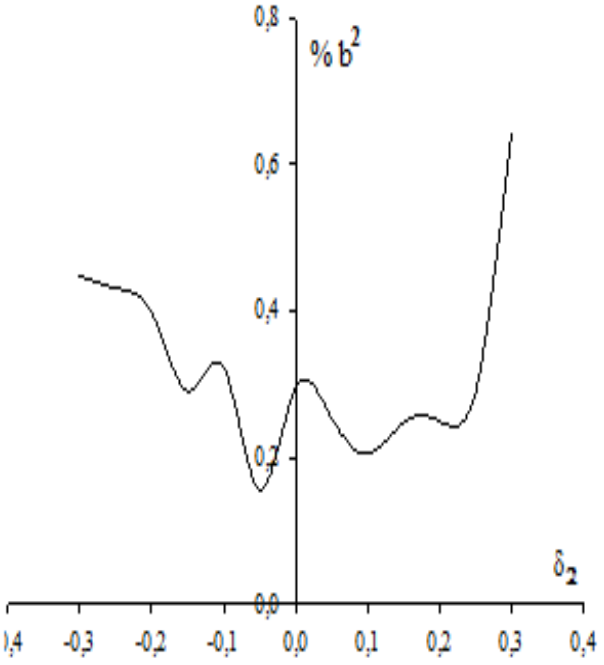

Fig. 1. Dependence on deformation parameter of isospin admixture for ^{122}Xe isotope.

In the case of deformation, the isospin admixture increase as this change increase. The fluctuations in the curve are related to the unavailability of the some solutions of the QRPA secular equation.

The calculation results for the T_0+1 isospin admixture b^2 (%) in the ground state of the parent nucleus for different Xe isotopes have been represented in Fig. 2.

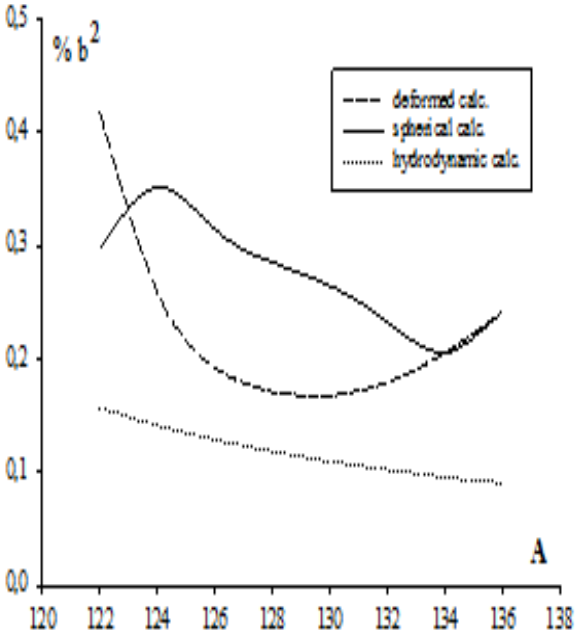

Fig. 2. Isospin admixture in the ground state for investigated isotopes.

In this figure, the solid, dashed and dotted lines correspond to the spherical, deformed, and hydrodynamic calculation { $P = b^2 = 3.5\times10^{-7} Z^2 A^{2/3}/(T_0+1)$ }[13], cases respectively. Through these calculations, it has been observed that the isospin admixture values generally decrease as the mass number increases. This decline may stem from both the T_0 isospin and the total β^+ transition strength [see Eq.(4)]. It can be seen obviously from this formula that the T_0 isospin in the denominator will certainly decrease the T_0+1 isospin admixture because the increase in mass number implies the increase in the T_0 isospin value. However, the analysis of the total β^+ transition strength values will be very beneficial in both clarifying the relationship between the $S^{(+)}$ β values and the T_0+1 isospin admixture. As seen from Fig.2, the isospin admixture values generally decrease as the mass number increases. Although calculation result of deformed case for investigating isotopes is greater than spherical cases, calculation result of deformed cases is getting smaller as the mass number increases.

IV. CONCLUSION

- Although T_0+1 isospin admixtures in the ground state of deformed nuclei for investigated isotopes are greater than ones of spherical case, they are on rapidly decreases compared with spherical case.

- This result is natural because the isospin admixture results from the variation of the Coulomb potential through nuclei radius. In the case of deformation, the isospin admixture increase as this change increase. The fluctuations in the curve are related to the unavailability of the some solutions of the QRPA secular equation.

[1]. *H.A. Bethe*, Rev.Mod. Phys. 1990, 62, 801.
[2]. *C.J. Pethick, D.G. Ravenhall, C.P. Lorentz*, Nucl. Phys. A 1995, 584, 675.
[3]. *J.M. Lattimer, C.J. Pethick, M. Prakash, P. Haensel*, Phys.Rev. Lett. 1991, 66 2701; *E.N.E. van Dalen, A.E.L.Dieperink*, J.A. Tjon, Phys. Rev. C 2003, 67, 065807.
[4]. *T. Klahn, et al.*, Phys. Rev. C 2006, 74, 035802.
[5]. *M. Prakash, T.L. Ainsworth, J.M. Lattimer*, Phys. Rev.Lett. 1988, 61, 2518; *L. Engvik, M. Hjorth-Jensen, E.Osnes, G. Bao, E. Oestgaard*, Phys. Rev. Lett. 1994, 73, 2650.
[6]. *X.R. Zhou, G.F. Burgio, U. Lombardo, H.-J. Schulze, W.Zuo*, Phys. Rev. C 2004, 69, 018801.
[7]. *I. Tanihata*, Prog. Part. Nucl. Phys. 1995, 35, 505; *P.G.Hansen, A.S. Jensen, B. Jonson*, Annu. Rev. Nucl. Part.Sci. 1995, 45, 591.
[8]. *E.N.E. van Dalena, C. Fuchs, and A.Faessler*, Eur. Phys. J. A 2007, 31, 29–42.
[9]. *R.J. Blin-Stoyle*, Fundamental interactions and the nucleus (North-Holland, Amsterdam, 1973).
[10]. *S.Raman et al*., At Data Nucl. Data Tables 1975, 16, 451.
[11]. *N.Auerbach, et al.*, Rev. Mod. Phys. 1972, 44, 48.
[12]. *A.M. Lane and A.Z. Mekjian*, Adv. Nucl. Phys. 1973, 7, 97.
[13]. *A.Bohr, J Damgaard and B.R. Mottelson*, Nuclear structure (North-Holland, Amsterdam, 1967).
[14]. *L.A. Sliv and Yu I. Kharitonov*, Phys. Lett. 1965, 16, 176.
[15]. *S.B. Khadkikar and C.S. Warke*, Nucl. Phys. A 1969, 130, 577.
[16]. *I.S. Towner and J.C. Hardy*, Nucl.Phys.A 1973, 205, 33.
[17]. *N.I.Pyatov, et al*, Sov. J. Nucl. Phys. 1979, 29, 10.
[18]. *I. Hamamoto and H. Sagawa*, Phys.Rev.C 1993, 48, 960.
[19]. *E. Hagberg, et al*, Phys.Rev.Lett. 1995, 74, 1041.
[20]. *H.Sagawa*, Nucl.Phys.A 1995, 588, 209c.
[21]. *G.Colo, et al*, Phys.Rev.C 1995, 52, 1175.
[22]. *H. Sagawa, et al*, Phys.Rev.C 1996, 53, R2163.
[23]. *I. Tanihata*, Nucl.Phys.A 1991, 522, 275.
[24]. *S. Kubono*, Nucl.Phys.A 1992, 538, 505.
[25]. *J.D. Garret*, Proceedings of International Symposium (Tokyo, 1992)
[26]. *R.Schneider, et al*, Z.Phys.A 1994, 348, 241.
[27]. *M. Lewitowicz, et al*, Phys. Lett. B 1994, 332, 20.
[28]. *J.Dobaczewski and I.Hamamoto*, Phys. Lett. B 1995, 345, 181.
[29]. *S.I. Gabrakov, N.I. Pyatov and D.I. Salamov*, Bulg. J. Phys. 1980, 7, 2.
[30]. *V.A. Rodin, M.H. Urin*, nucl-th/0201065,2003, v2.
[31]. *N.I. Pyatov, D.I. Salamov*, Nucleonica 1977, 22, 127.
[32]. *A. Kucukbursa, et al., Pramana* J. Phys. 2004, 63, 947.
[33]. *T.Babacan, et al*, J.Phys.G: Nucl.Part. Phys. 2004, 30, 759.
[34]. *M. Cerkaski, et al.*, Phys. Lett. B 1977, 70,9.
[35]. *R. Alvarez-Rodriguez et al*., Phy.Rev.C 2005, 71, 044-308.

INDOOR RADON (^{222}Rn) CONCENTRATION MEASUREMENTS IN DWELLINGS OF THE ERZINCAN PROVINCE, TURKEY

E.OZTURK[a], B. KUCUKOMEROGLU[a], Y.O. YESILBAG[b], A. KURNAZ[a], N. ALBAYRAK[c], H. TAŞKIN[c]

[a]*Department of Physics at Karadeniz Technical University, Trabzon, Turkey*

[b]*Department of Physics at Erzincan University, Trabzon, Turkey*

[c]*Cekmece Nuclear Resaarch and Training Center, Istanbul, Turkey*

Indoor radon concentration values were determined in randomly selected 80 dwellings of the Erzincan province in Turkey using Cr-39 dosimeters during the period of 2009-2010 for three months. 74 dosimeters were recovered while 6 of them were lost. The dwellings were carefully selected so as to be representative for the study area. All the dosimeters were placed in living rooms of the selected dwellings. The analysis of the dosimeters was conducted at the Istanbul Cekmece Nuclear Research and Training Center. It was observed that the indoor radon concentration values ranged from 9 to 641 Bq/m^3 with the median value of about 53 Bq/m^3.

I. INTRODUCTION

All people are exposed to natural radiation. The natural sources of radiation are cosmic rays and naturally occurring radioactive substances existing in the Earth itself and inside our bodies. A significant contribution to the natural exposure of people is due to radon gas, which emanates from the soil and may concentrate in dwellings. The level of natural exposure varies around the world, usually by a factor of about two. The radiation that emanates from cosmic rays and radioactive elements that exist in the earth, building materials and in the air is called external ionization. On the other hand, the radiation that comes into the human body through respiration system from the air cause internal exposure [1].

Concentration of the radiation around the world varies depending on many different factors. The leading factor is the different radioactive elements in different locations.

Annual average dose of radiation that people are exposed by natural sources is 2.4 mSv. Most of this dose (approximately 1.3 mSv) is radon gas and its daughters [1].

Radon emanates from the sources include uranium and the earth and as it is gas it spreads in the atmosphere by moving up in the gaps in soil. Radon goes into the lungs through respiration and causes lung cancer [4-6]. Studies show that in the individuals who exposed to high radon level has high chance of getting for lung cancer [2].

According to ICRP 10 % of the total lung cancer is caused by inhalation of radon and its decay products. As people spend around 80 % of their time in indoor environment, elevated levels of radon could cause serious damages to the respiratory system.

The concentration of radon in the dwellings varies in different countries [7]. This variation depends on the geological structure of the soil, climatic parameters and the characteristics of buildings. In recent years both in Turkey and around the world many studies have been conducted to determine the indoor radon concentration levels.

It has also been found that the levels of radon indoors are associated with factors such as cracks on the walls, the building materials used for floor and walls and the type of ventilation and heating.

The study area is chosen as it is located on a fault line for which the emanation could be high. Besides indoor radon levels for this province has not been determined before. Therefore this study has been planned and conducted in the province of Erzincan in order to determine indoor radon concentration level in the dwellings. This study is a part of project which aims to determine the background radiation level of the province including four season measurement results of indoor radon concentration values and radioactivity measurements in soil samples. The first results are presented here.

II. MATERIALS AND METHODS

The dwellings sampled were selected among houses located in the city center and in the sub-provinces. Each dwelling was visited and if the occupants agreed to participate in the survey, questionnaire information was obtained regarding the age and the type of the dwelling, ventilation practices, floor material of the flats, insulation, materials used for walls and the ceilings, the heating system, the smoking habits of the residents and any history of lung cancer in the family. The measurements were conducted during the spring season.

80 houses were designated to participate and detectors were delivered to these houses. During the period of measurement 74 of the delivered detectors were recovered while 6 of tme were lost.

CR-39 passive etched track detectors were used for the measurements. This detectors are 35x55 mm cylindrical plastic boxes with a 10x10 mm chip of 1 mm thick and in the base as the detector material. The detector was covered with a polypropylene material. This polypropylene material is responsive to alpha particles and impedes ^{220}Rn (Thoron) and dust particles. Only radon goes into the detector. The alpha particles leave tracks on the chip of the detector.

One detector was used for each house and it was left with the occupants of the dwellings: to be kept in the living groom in regular use. The location of the detector was noted on the questionnaire form with the other information about the dwelling (detectors were placed in

an open area which was not close to the heating system, electronic system or windows.) In order to obtain definite valves, we also collected samples from the earth around the houses. The detectors were collected during a return visit to the houses after an interval of approximately 12 weeks (the mean duration for measurement was 90 days). The analysis of detectors performed at the Istanbul Cekmece Nuclear Research and Training Centre (ÇNAEM) by using automatic track counting system (RadoSys) which is made up of an optical microscope connected to a computer, bath unit and radon detector. The foils were chemically etched in 30 % NaOH solution at 60 C for 17 hours. Tracks on the foils were there counted in a computer based counting device. Also on the questionnaire used for each house information was gathered about the inhabitants (their education, smoking habits and whether there was any history of cancer). Detectors were delivered considering in the population in general.

III. RESULTS AND DISCUSSIONS

74 detectors were recovered for the results. The obtained mean indoor radon activity concentration results ranged from 8.6 to 640.84 Bq/m^3 with the mean values of 52. 45 Bq/m^3. While the lowest concentration was obtained from the city center, the highest value was observed in the Kemah sub-province.

As shown in Table 1, except one value, all the others are below 400 Bq/m3 which is the action value in Turkey.

Most of the buildings were constructed after 1990. 2 (2,7 %) before 1945, 27 (36,5 %) between 1950 and 1989, 45 (60,8 %) after 1990. Twenty (27,02 %) of the flats were on the ground floor and 54 (72,97 %) were above the ground floor. It was learned from the questioners that most of the houses have the natural ventilation system. Also is was learned that 58 % of the house have central heating system, while 35 % of them have coal stove and 7 % of them have other heating systems.

Table 1. Distribution of radon concentrations (Bq/m^3) in 74 houses in Erzincan

	Arithmetic mean	Max. level	Min. level	SD
CITY CENTRE	39,77	80,37	12,9	33,22
CAYIRLI	85,54	255,86	14,13	114,34
ILIC	30,74	64,23	8,6	19,58
KEMAH	102,32	640,84	14,13	157,46
TERCAN	41,41	101,97	14,43	35,34
UZUMLU	17,51	23,34	8,6	5,57
ERZINCAN	52,45	640,84	8,6	82,07

The high levels were found in two districts of Erzincan, which are Kemah and Cayırlı. Five of the houses found to have high radon concentrations were on the ground floor. Material used for the floor of the houses was not a hard surface concrete for 5 houses.

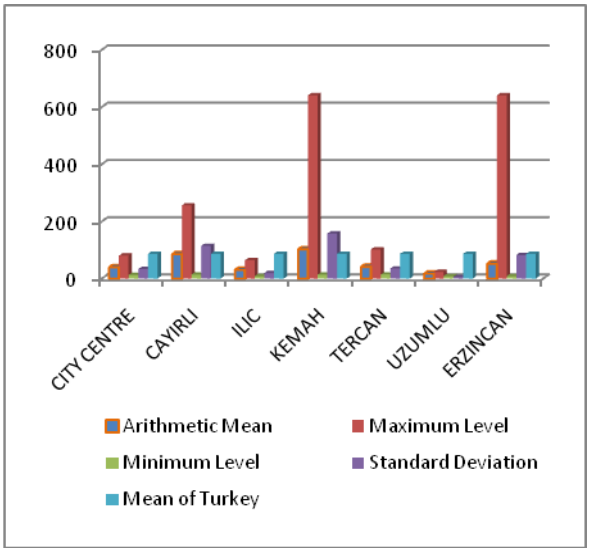

Fig 1. Indoor radon concentration results.

Figure 1 shows the obtained indoor radon activity concentrations in the dwellings of the Erzincan province. As seen from the figure two values are far higher than the other values. This could be because of the poor ventilation of the respective houses and the type of the rocks on which the houses are located. Further measurements are being done for all the houses in order to obtain for the other three seasons. Once the final data are available the relevant discussions will be made on these houses. There are quite a number of factors influencing indoor radon concentration levels. Some of them are the geology of the regions, the ventilation of the houses, the construction and the usage of the buildings [9].

Table 2. Mean indoor radon values obtained from the literature.

Cities	RC (Bq/m3)	Reference
Istanbul	50	[7], [13]
Erzurum	85	[10]
Sanlıurfa	68	[10]
Canakkale	160	[10]
Elazıg	47	[11]
Isparta	164	[12]
Antalya	29	[7]
Tekirdag	87	[14]
Manisa	97	[15]
Kastamonu	98	[16],[17]
Edirne	49	[17]
Kars	114	[5]
Giresun	130	[6]
Batman	84	[18]
Ardahan	173	[8]
Artvin	132	[8]
Erzincan	52,5	This study
Mean of Turkey	86,50	TAEK (2008)
Mean of Earth	46	UNSCEAR (2000)

Table 2 summarizes the indoor radon concentration measurement performed by the other researchers in Turkey. The data obtained in the current study is in an agreement with the other data. In Table 2, it is seen that Canakkale, Isparta, Giresun, Ardahan and Artvin have relatively higher indoor radon activity concentration values than those of the other provinces. The data in the current study is among the lower values. However as only one seasonal data is presented in this study, further discussions will be possible after having the other three seasonal values.

Table 3. Radon measurements of dwellings from cities in different countries

Countries	Radon concentration (Bq/m3)	Reference
Spain (Barcelona)	68,5	[19]
Spain (Madrid)	40,5	[19]
Greece (Patras)	38	[20]
India (Himachal Pradesh)	123	[21]
Mexico (Zacatecas)	67	[22]
Pakistan	72	[23]
Turkey	86,50	TAEK (2008)
Mean of Earth	46	UNSCEAR (2000)

In Table 3, average indoor radon concentration values of the other countries in different parts of the world are given. Considering the average world indoor radon activity concentration value, the mean value for Turkey is higher than that of the reported. The average value for the province of Erzincan is lower than that of the mean value for Turkey. Different values reported in Table 3 can be explained by the possible factors influencing the indoor radon level which are the geology of the region, ventilation, contraction and the usage of the buildings.

IV. CONCLUSION

We report the first indoor radon concentration levels in the Erzincan province. The results obtained in this study indicate that most buildings are not of high radon background considering the action level for Turkey. Most of the values are between 8 and 105 Bq/m^3. The overall arithmetic average of radon concentrations was found to be around 53. This value is below the lower limit of the reference levels. The minimum measured level of radon in the houses surveyed in the present study is about 9 Bq/m^3, and the maximum measured value of radon gas concentration is about 641 Bq/m^3.

The high radon concentration levels were recorded in rooms either having poor ventilation, unpainted walls or both, giving the fact that a typical house in this region is constructed mainly from concrete, and walls are built by using concrete bricks; therefore, radon emanation is expected. Thus, indoor radon concentration was found to be associated with presence of cracks on the walls, building materials used for floor and walls and the type of ventilation and heating system present in the houses.

Further discussions will be made once the other seasonal indoor radon concentration values are available as they are being done.

[1]. (UNSCEAR) United Nations Scientific Committee on the Effects of Atomic Radiation. Sources and effects of ionizing radiation. Report to General Assembly, with Scientific Annexes (New York: United Nations) (2000).

[2]. (ICRP) International Commission on Radiological Protection, ICRP Publication 60. Recommendations of the International Commission on the Radiological Protection, Pergamon Press Inc., ICRP, USA (1990)

[3]. (IAEA) International Atomic Energy Agency, 'Radiation Safety' IAEA Division of Public Information, 96-00725 IAEA/PI/A47E, (1996)

[4]. (IARC) International Agency for Research on Cancer. In : Man-made mineral fibres and radon. In: IARC Mono-graphs on the Evaluation of Carcinogenic Risks to Humans, 43, (Lyon, France: IARC). (1988)

[5]. *N.Çelik, A.Proffijn, U.Çevik and L.,Schepens* 2008. Indoor Radon Survey in Dwellings of the Kars Province, Turkey Radiation Protection Dosimetry, 128,432-436.

[6]. *N.Çelik, U.Çevik, A. Çevik and B.Küçükömeroğlu,* 2008. Determination of indoor radon and soil radioactivity levels in Giresun, Turkey. Journal of Environmental Radioactivity,99, 1349-1354

[7]. *E.M.Koksal, N.Çelebi, B.Ataksor, A.Uluğ, M.Taşdelen, G.Kopuz, B.Akar and M.T.Karabulut,* 2004. A survey of ^{222}Rn concentrations in dwellings of Turkey, Journal of Radioanalytical and Nuclear Chemistry, 259,213-216

[8]. *Y.Ö.Yeşilbağ,* 'Indoor Radon Concentrations in Dwellings and Radioactivity Levels in Surrounding Soils of the Artvin and Ardahan Provinces'. Master's Degree Thesis, 2008.

[9]. *S.A.Vaizoğlu, Ç.Güler,*1999. Indoor Radon Concentrations in Ankara Dwellings. Indoor Built Environ 1999,8:327-331

[10]. *N.Celebi, H.Alkan* 1997. Radition Protection Dosimetry, 69, 227-230

[11]. *A.B.Selcuk, H.Yavuz, E.M. Koksal and B.Ozcinar,* 1998. Radon concentration in Elazig houses and factories. Radiation Protection Dosimetry, 77, 211-212

[12]. *A.Ulug, M.Karabulut, and N.Celebi,* 2004. Radon Measurement with CR-39 Track Dedectors at specific Locations in Turkey, Nuclear Technology and Radiation Protection, 19,46,49.

[13]. *E.M.Koksal, N.Celebi and B.Ozcinar,* 1993. Indoor ^{222}Rn Concentrations in İstanbul Houses, Health Physics,65, 87-88

[14]. *Y.Yarar, T.Gunaydi and E. Kam,* 2005. A radon survey in some regions of Turkey. International Congress Series 1276, 385.

[15]. *F.S.Erees, S.Akozcan, Y.Parlak and S.Cam*, 2005. Assessment of dose rates around Manisa (Turkey). Radiation Measurements, 41, 598-601

[16]. *A.Bozkurt, N.Yorulmaz, E.Kam, G.Karahan and A.E.Osmanlıoglu,* 2007. Assessment of environmental radioactivity for Sanliurfa region of Southeastern Turkey. Radiation Measurement, 42,1387-1391.

[17]. *A.Bozkurt and E.Kam,* 2007. Indoor Radon Measurement in the City of Edirne, Turkey. Sixth International Conference of the Balkan Physical Union.

[18]. *N.Damla, U.Cevik, A.I.Kobya, B.Ataksor, B.Kucukomeroglu and N.Celebi,* Indoor radon measurement in the province of Batman, Turkey. 25.

[19]. *J.Gutierrez, C.Baixeras, B.Robles, C.J. Saez and L.Font,* 1992. Indoor Radon Levels and Dose Estimation in Two Major Spanish Cities. Radiation Protection Dosimetry, 45, 495-498.

[20]. H.Papaethymiou, A.Mavroudis and P.Kritidis, 2003. Indoor Radon Levels and Influencing Factors in Houses of Patras Journal of Environmental Radioactivity, 66, 247-260.

[21]. *S.Singh, A.Kumar and B.Singh,* 2002. Radon level in dwellings and its correlation with uranium and radium content in some areas of Himachal Pradesh, India Environmental International, 28, 97-101

[22]. *L.L.Quirino, J.M.Soriano, F.Mireles, J.I.Davila, H.Lopez, J.L Pinedo. and C.Rios,* 2006. Indoor ^{222}Rn survey in Zacatecas State, Mexico. Applied Radiation and Isotopes, 65, 371-374

[23]. *S.Rahman, N.Mati, Matiullah and B.M.Ghauri,* 2007. Seasonal indoor radon concentration in the Nort West Frontier Province and federally administered tribal areas-Pakistan. Radiation Measurements, 42, 1715-1722.

(n,2n) REACTIONS OF ^{59}Co, ^{60}Ni AND ^{63,65}Cu NUCLEI

EYYUP TEL[1], MUSTAFA H. BÖLÜKDEMİR[1], and ALİ ARASOĞLU[2]
[1]*Gazi University, Faculty of Arts and Science, Department of Physics, Ankara, Turkiye*
[2]*Yüzüncü Yıl University, Faculty of Arts and Science, Department of Physics, Van, Turkiye*
eyuptel@gazi.edu.tr

The (*n,2n*) reaction cross-sections of *^{59}Co*, *^{60}Ni* and *^{63,65}Cu* target nuclei have been carried out up to 40 MeV incident neutron energy. The reaction cross-sections have calculated by using evaluated empirical formulas developed by Tel et al. at 14-15 MeV energy. In these calculations, the pre-equilibrium and equilibrium effects have been investigated. The calculated results are compared with the experimental data taken from EXFOR database.

Neutron scattering cross sections have a critical importance on fusion reactors. The experimental cross-sections are available in EXFOR for neutron induced reactions [1]. These data can be extensively used for the investigation of the structural materials of the fusion reactors, radiation damage of metals and alloys, tritium breeding ratio, neutron multiplication and nuclear heating in the components, neutron spectrum, and reaction rate in the blanket and neutron dosimetry [2, 3]. And also these obtained cross section data are necessary to develop more nuclear theoretical calculation models in order to explain nuclear reaction mechanisms [4–6]. A large number of empirical and semi-empirical cross sections formulas with different parameters have been proposed by several authors in the literature [7–9]. Tel et al. suggested using these new experimental data to reproduce a new empirical formula of the cross sections of the (*n, p*), (*n, 2n*), (*n,α*), (*n, d*), (*n, t*) and *(n, ^{3}He)* reactions [6, 10–16]. Tel et al. also have investigated the s=(N-Z) /A asymmetry parameter effect for the (p, nα) reaction cross sections and they have obtained new coefficients for the (p, nα) reactions at 24.8 and 28.5 MeV energies [17]. Hadizadeh and Grimes examine straightforward extensions of the Tel et al. model to see if the fit can be improved [18]. And also, Betak et al. and J. Luo et al. have investigated the experimental cross sections by using Tel et al. formulas [19, 20]. The (*n,2n*) formulas of the Tel et al. for $14 \le A \le 241$ target nuclei have been given as follows (in mb) at 14–15 MeV [21],

$$\sigma_{(n,2n)} = \begin{cases} \ln(\sigma)=7.15\left[1-2.45\exp(-31.62s)\right] \text{ for Even-A} \\ \ln(\sigma)=7.65\left[1-1.59\exp(-23.06s)\right] \text{ for Odd-A} \end{cases}$$

Pre-equilibrium processes are important mechanisms in nuclear reactions induced by light projectiles with incident energies above about 10 MeV. In the exciton model, the pre-equilibrium and equilibrium emission spectrum in accordance with [7],

$$\frac{d\sigma_{ab}}{d\varepsilon_b}(\varepsilon_b) = \sigma^{r}_{ab}(E_{inc})\, D_{ab}(E_{inc}) \sum_{n} W_b(E, n, \varepsilon_b)\, \tau(n)$$

where $\sigma^{r}_{ab}(E_{inc})$ is the cross-section of the reaction (*a, b*), $W_b(E, n, \varepsilon_b)$ is the probability of the emission of a particle type *b* with energy ε_b from a state with *n* excitons and excitation energy E of the compound nucleus, $\tau(n)$ is the solution of the master equation which represents the time during which the system remains in a state of *n* excitons. $D_{ab}(E_{inc})$ is a coefficient which takes into account the decrease in the available cross-section due to the particle emission by direct interactions with low excitation energy levels of the target nucleus. The Cascade-Exciton Model (CEM) assumes that the nuclear reactions proceed through three stages: INC, pre-equilibrium and equilibrium [8, 9].

$$\sigma(p)\,dp = \sigma_{in}\left[N^{cas}(p)+N^{prq}(p)+N^{eq}(p)\right]dp$$

where *p* is a linear momentum. The inelastic cross section σ_{in} is not taken from the experimental data or independent optical model calculations, but it is calculated within the cascade model itself. The hybrid model and geometry dependent hybrid model (GDH) has been developed considered as density distribution of nuclei by Blann and Vonach [22]. In the density dependent version, the GDH takes into account the density distribution of the nucleus [22]. The differential emission spectrum is given in the GDH as

$$\frac{d\sigma_{\upsilon}(\varepsilon)}{d\varepsilon} = \pi \lambda\!\!\!^{-2} \sum_{\ell=0}^{\infty} (2\ell+1) T_{\ell}\, P_{\upsilon}(\ell, \varepsilon)$$

where $\lambda\!\!\!^{-}$ is the reduced de Broglie wavelength of the projectile and T_l represents the transmission coefficient for the *l*th partial wave. $P_{\upsilon}(\ell, \varepsilon)$ is number of particles of the type ν (neutrons and protons) emitted into the unbound continuum with channel energy between ε and $\varepsilon+d\varepsilon$ for the *l*th partial wave.

In the present work, (*n,2n*) reaction cross sections for some structural fusion materials as , *^{59}Co*, *^{60}Ni* and *^{63,65}Cu* target nuclei have been calculated with the equilibrium and pre-equilibrium reaction models in Figs. 1–4. Cascade Exciton Model (CEM) calculations have been made by using CEM95 [8,9]) computer code with the level density parameter by using the systematic of Iljinov et al. [23]. In details, the other CEM95 code parameters can be found in [9]. In the calculations of the hybrid and GDH model, the code as ALICE/ASH was

used. The generalized superfluid [24] has been applied for nuclear level density calculations in the ALICE/ASH code. The ALICE/ASH code use the initial exciton number as n_o =3. In details, the other code model parameters can be found in [25].

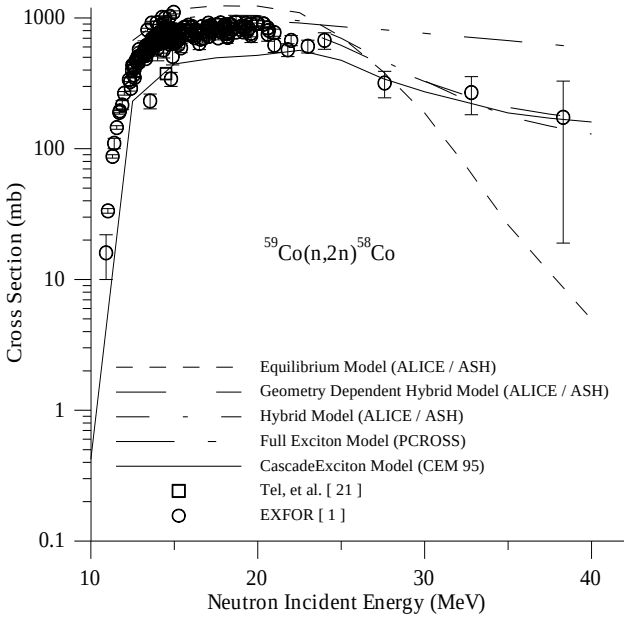

Fig.1. The comparison of calculated excitation function of $^{59}Co(n,2n)^{58}Co$ reaction with the values reported in [1].

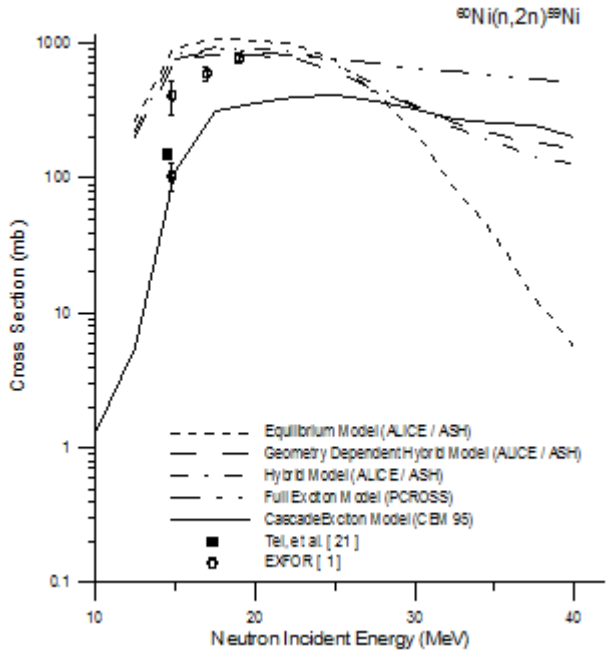

Fig.2. The comparison of calculated excitation function of $^{60}Ni(n,2n)^{59}Ni$ reaction with the values reported in [1].

The calculations of the full exciton model with PCROSS code [7] taking into account the direct gamma emission use the initial exciton number as n_o =1. The equilibrium calculations have been made by Weisskopf-Ewing model [26] with ALICE/ASH and this model doesn't include angular momentum effects. In the present study additionally, the (*n, 2n*) reaction cross-sections have been calculated by using evaluated empirical formulas of the Tel et al. at 14–15 MeV neutron incident energy.

In this study, theoretical calculations in the energy region between 10 and 40 MeV, cross-sections values appear to give maximum value about incident neutron energy 15-25 MeV and also they are nearly constant in this energy region for these nuclei in Figs. 1-4. Generally, the calculated pre-equilibrium (*n,2n*) reaction cross sections show the agreement with experimental data for the considered nuclei. The equilibrium calculations with Weisskopf-Ewing model give the highest results and also the cascade exciton model calculations (CEM95) give the lowest results.

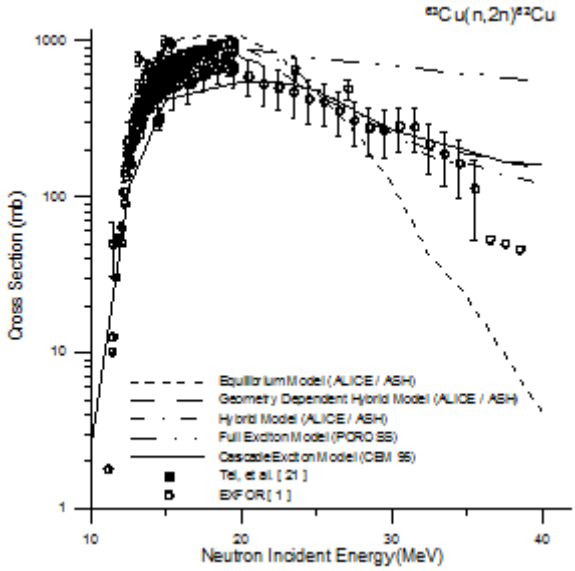

Fig.3. The comparison of calculated excitation function of $^{63}Cu(n,2n)^{62}Cu$ reaction with the values reported in [1].

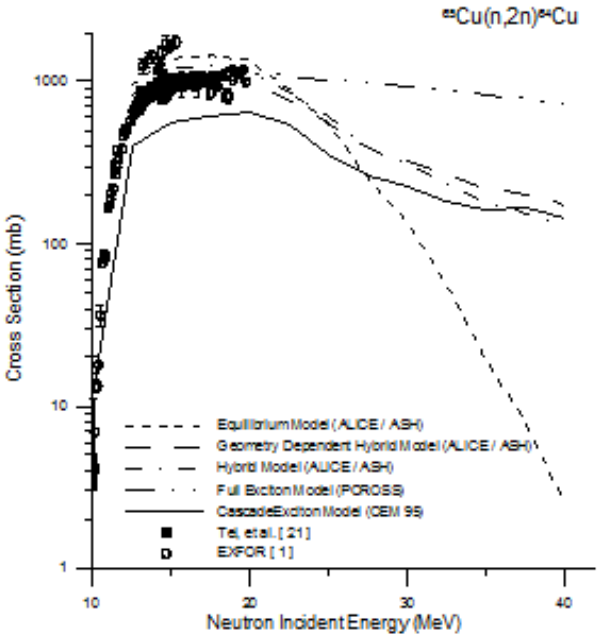

Fig.4. The comparison of calculated excitation function of $^{65}Cu(n,2n)^{64}Cu$ reaction with the values reported in [1].

Generally, the calculated (*n,2n*) reaction cross sections by using the new empirical cross-sections formula [21] show the agreement with experimental data at 14–15 MeV energy for these nuclei. The empirical formulas use the equilibrium (evaporation) model and ignore an important role of the pre–equilibrium mechanism of particle emission for medium and heavy nuclei. The empirical formulas given in [21], for the *(n,2n)* reaction can be considered to provide a very useful tool for estimating quickly. It can be said that, at least this study contributes to the new studies on cross section and help to show the way to the future experimental studies.

ACKNOWLEDGMENT

This work has been supported by the project of Gazi University project (BAP), Code No: 05 /2009-50

[1] Brookhaven National Laboratory, National Nuclear Data Center, EXFOR/CSISRS (Experimental Nuclear Reaction Data File). Database version of October 12,2009, (http://www.nndc.bnl.gov/exfor/) (2009)
[2] *M.Walt*, in Fast Neutron Physics, Part I: Techniques, edited by *J. B. Marion and J. L.Fowler*, (Interscience, New York, 1960), p. 509.
[3] *M.Übeyli and E.Tel,* J. Fusion Energ., **22**, 173 (2003)
[4] *S.L.Goyal and P.Gur*, Pramana, **72**(2), 355 (2009)
[5] *E.Tel, et al.*, Acta Phys. Slov., **54**(2), 191 (2004)
[6] *E.Tel, et al.*, J. Phys. G: Nucl. Part. Phys., **29**, 2169 (2003)
[7] *R.Capote, V.Osorio, R.Lopez, et al.*, Final Report on Research Contract 5472/RB, INDC(CUB)-004 (Higher Institute of Nuclear Science and Technology, Cuba), Translated by the IAEA on March 1991 (PCROSS program code)
[8] *K.K.Gudima, et al.*, Nucl. Phys. A, **401**, 329 (1983)
[9] *S.G.Mashnik*, User Manual for the Code CEM95, Joint Institute for Nuclear Research, Dubna, Moskow Region, (1995)
[10] *E.Tel, et al.*, Indian J. Phys. **78,** (11) 1229 (2004)
[11] *E.Tel, et al.*, Phys. Rev. C, **75**, 034614 (2007)
[12] *E.Tel, et al.*, J. Fusion Energ., **27**(3), 188 (2008)
[13] *A.Aydin, et al.*, J. Fusion Energ., **27**(4), 308 (2008)
[14] *A.Aydin, et al.*, J. Fusion Energ., **27**(4), 314 (2008)
[15] *M.H.Bölükdemir et al.,* J. Fusion Energ., **29**, 13 (2010)
[16] *E.Tel, et al.*, J. Fusion Energ., **28**, 377 (2009)
[17] *E.Tel, et al.*, Appl. Radiat. Isot., **67**(2), 272 (2009)
[18] M.H.Hadizadeh and S.M.Grimes, Nucl. Sci. Eng., **160**(2), 207 (2008)
[19] E.*Betak, T.Kempisty and S.Raman* Nucl. Sci. Eng. **132** 295 (1999)
[20] *J.Luo, et al.*, J. Radioanalytical and Nuclear Chemistry., **279(**2), 443 (2009)
[21] *E.Tel, et al.*, Int. J. Mod. Phys. E, **17**(3)**,** 567 (2008)
[22] *M.Blann and H.K.Vonach*, Phys. Rev. C, **28**, 1475 (1983)
[23] *A.S.Iljinov et al.*, Nucl. Phys. A, **543**, 517 (1992)
[24] *A.V.Ignatyuk, at al.*, Yad. Fiz., **29,** 875 (1979) [Sov. J. Nucl. Phys. **29**, 450 (1979)]
[25] *C.H.M. Broeders, A.Yu.Konobeyev, Yu.A.Korovin, V.P.Lunev, and M.Blann*, ALICE/ASH–pre-compound and evaporation model code system for calculation of excitation functions, energy and angular distributions of emitted particles in nuclear reactions at intermediate energies, FZK 7183, May 2006, http://bibliothek.fzk.de/zb/berichte/FZKA7183.pdf
[26] *V.F.Weisskopf and D.H.Ewing*, Phys. Rev., **57**, 472 (1940)

SOME CRITERIAS AT DTL DESIGN FOR TURKISH ACCELERATOR CENTER (TAC) LINAC

H.F. KISOGLU[1], A. CALISKAN[2], M. YILMAZ[2]
[1]Physics Department, Aksaray University, 68100 Aksaray, Turkey
[2]Department of Physics, Gazi University, 06600 Besevler, Ankara, Turkey

Linear acceleretors (linacs) are mostly used as first step of acceleration process in the present. Turkish Accelerator Center (TAC) linac of which technical design report will have been completed in 2011 has been designed for this purpose. Moreover it will provide working areas for some users on the acceleration line. Hence, design of drift tube linac (DTL) that is one of the basis components in linacs have importance. This study includes some criterias at DTL design for 350 MHz radio-frequency (RF) TAC linac as a preliminary work.

I. INTRODUCTION

Linear acceleretors (linacs) are mostly used as first step of acceleration process in the present. Turkish Accelerator Center (TAC) linac of which technical design report will have been completed in 2011 has been designed for this purpose. Moreover it will provide working areas for some users on the acceleration line. Hence, design of drift tube linac (DTL) that is one of the basis components in linacs have importance.

DTL designers take account of some parameters to make design. One of these primarily parameters is quality factor that is effectiveness of producing an accelerating potential per unit power wasted on cavity walls at given RF frequency;

$$Q = \frac{wU}{P} \tag{1.1}$$

Shunt impedance per unit length of cavity is defined as

$$Z_S = \frac{E_0^{\,2}}{P/L} \tag{1.2}$$

and effective shunt impedance that measures the effectiveness per unit power loss for delivering energy to a particle [1] is given;

$$Z = Z_S T^2 = \frac{\left(E_0 T\right)^2}{P/L} \tag{1.3}$$

where T is transit time factor that accounts for the RF fields are changing in time as the particle traverses between DTLs [2].

Another useful parameter is ratio of r/Q that measures the effectiveness of acceleration per unit energy stored on the walls at given RF frequency.

$$\frac{r}{Q} = \frac{\left(V_0 T\right)^2}{wU} \tag{1.4}$$

where V_0 is the acceleration potential (or axial potential) of cavity.

According to parameters above, generally, the main aim is maximizing the effective shunt impedance and optimizing DTL. Maximizing the ratio of r/Q is also one of the objectives of optimizing DTL. So, accelerating the particles as fast as possible is main aim consequently, or enhancing the RF electric field as well. But some criteria, like Kilpatrick limit, prevent us from acting freely. With reference to W.D. Kilpatrick (1957) there is a relation between RF breakdown, due to RF electric field, and RF frequency.

$$f = 1.64 E_k^{\,2} e^{-8.5/E_k} \tag{1.5}$$

where E_k is the expected breakdown threshold in MV/m [3]. So, the maximum surface electric field (E_{peak}) that is electrical field between DTL surfaces is limited as

$$1.0E_k < E_{peak} < 2.0E_k \tag{1.6}$$

for modern linacs and there could be some deformations on DTL surfaces when E_{peak} exceed this limitation

II. MATERIALS AND METHODS

In this study we analyzed effective shunt impedance for 350 MHz radio-frequency and E_0= 4.4 MV/m DTLs by tuning face angle and gap length of DTLs using SUPERFISH code to see how these two parameters effect the effective shunt impedance. Figure 1 shows face angle and gap length of a DTL.

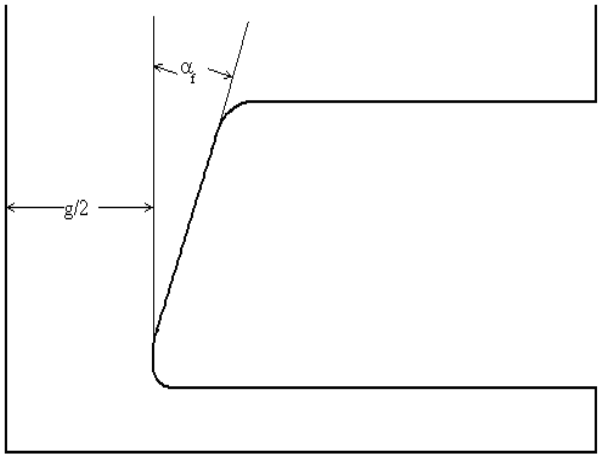

Fig 1. Face angle (α_f) and gap length (g) of a DTL. The canonical structure on the right is 1/2 of DTL.

We assume that face angle (α_f) and gap length (g) effect the E_{peak} threshold. If g is increased E_{peak} surface field will be reduced for constant acceleration potential.

Face angle helps reduce the E_{peak} surface electric field by eliminating multipactor effect that occurs when emission from DTL surfaces is in resonance with the RF electric field.

Our datas are given below. Figure 2 and figure 3 show that how effective shunt impedance (*ZTT*) and maximum surface electric field (E_{max}) change as gap length (g) and face angle (α_f) is increased respectively.

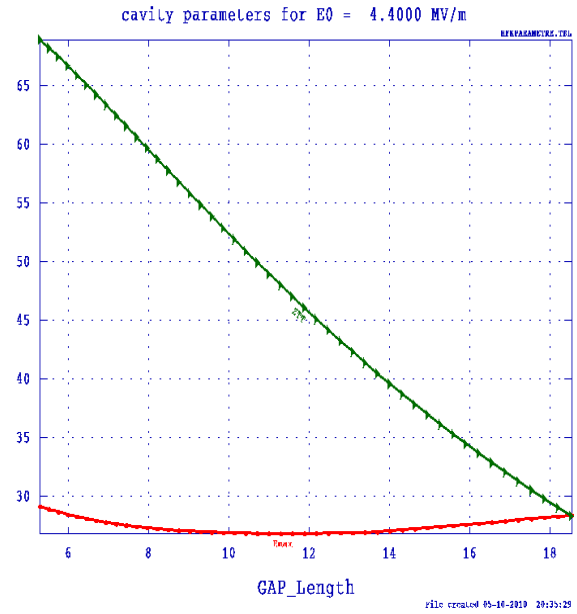

Fig 2. Relation between gap length and *ZTT* (green) and E_{max} (red).*ZTT* reduces and E_{max} is going up as g is increased. But E_{max} is still low(<.~30 MV/m).

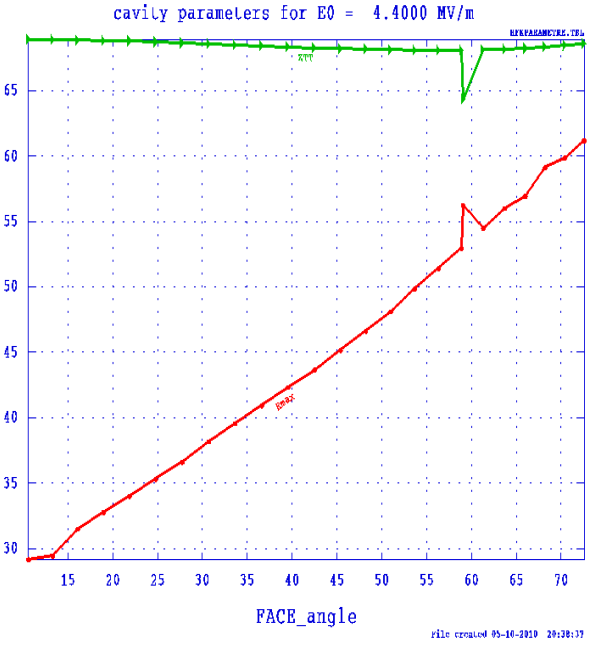

Fig 3. Relation between face angle and *ZTT* (green) and E_{max} (red). *ZTT* reduces and E_{max} is going up as α_f is increased.

Figure 4 and figure 5 show sample DTL and maximum surface electric field shape for a random g and α_f values respectively.

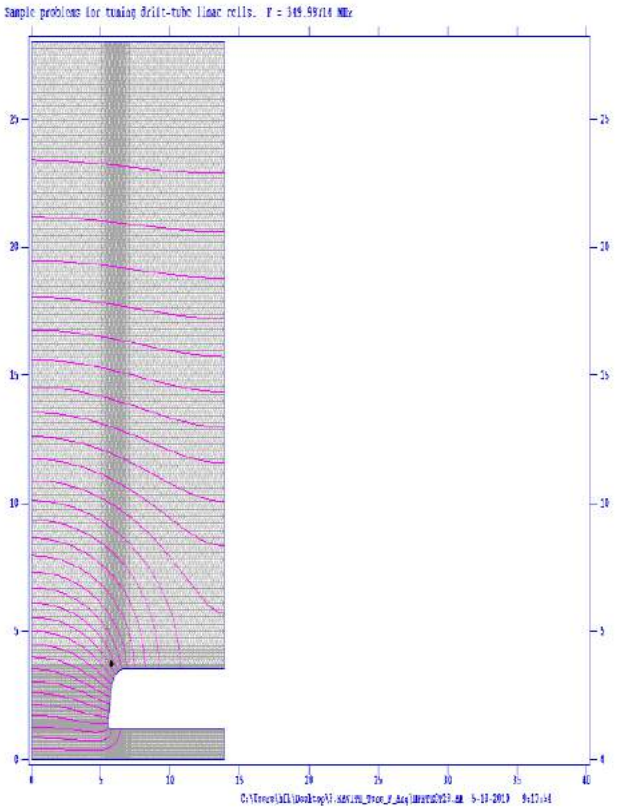

Fig 4. Sample DTL and maximum surface electric field shape for g=11.0 cm

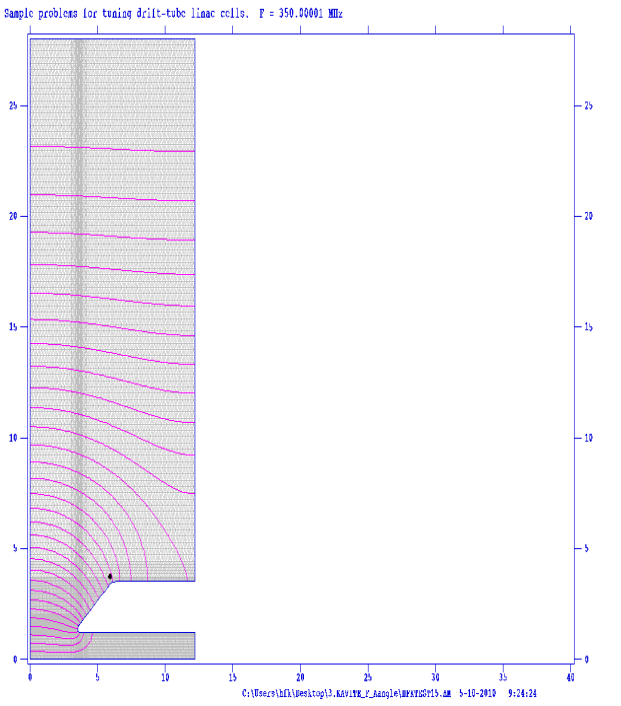

Fig 5. Sample DTL and maximum surface electric field shape for α_f=50.99 degree.

III. CONCLUSION

According to our datas face angle (α_f) and gap length (g) of DTLs effect the maximum surface electric field (E_{peak}) and effective shunt impedance (ZTT).

There is one disadvantage of this results. As we reduce the E_{peak}, the efficiency of linac is reduced. This also means that there is low acceleration although power loss is high.

We can analyze in case of presence of permanent magnet quadrupole (PMQ) that helps existence of higher frequency structure. We also have to analyze what disadvantages are in this case.

[1]. *T. Wangler,* Principles of RF Linear Accelerators, Wiley-Interscience Publication, 1998.

[2]. *H. Takeda, Parmila,* Los Alamos National Laboratory Document, LA-UR-98-4478, Rev. July 26, 2005

[3]. *J. Stovall, et al.,* RF Breakdown in Drift Tube Linacs, sLHC Project Note 007, 2009

INVESTIGATION OF THE RELATION BETWEEN ENVIRONMENTAL RADIOACTIVITY AND RADIOACTIVITY IN HUMAN TEETH WHO LIVES IN THIS ENVIRONMENT

F. AYSUN UGUR[1], HALIDE SAHAN[1], ZEHRA YEGINGIL[2], SAZIMET GORUR[2], MUHITTIN SAHAN[1]

[1]Osmaniye Korkut Ata University, Faculty of Sciences and Letters, Department of Physics, 80000,Osmaniye/Turkey

[2]University of Cukurova, Department of Physics, 01330, Adana/Turkey

aysunaf@yahoo.com, halidesahan@osmaniye.edu.tr, saziment@hotmail.com, zehra@cu.edu.tr, muhittinsahan@osmaniye.edu.tr

This work presents total alpha-beta radioactive concentrations in human teeth collected in Black Sea and Cukurova (near Mediterranean Sea) which are two different regions in Turkey. These tooth samples were measured by using 10 Channel Low-Level Counter. Thirty five human teeth samples taken from people living in these two regions were classified according to the age of dones and compared with each others. From the results, it was found that beta activity results obtained from Black sea region were higher than that of Cukurova region and it was also concluded that total alpha and beta radioactivity measurements in adult and child were variable.

I. INTRODUCTION

Radiation is an energy traveling in the form of particles or waves in bundles of energy called photons. Radioactivity is a natural and spontaneous process by which the unstable atoms of an element emit or radiate excess energy in the form of particles or waves [1].

Alpha (α) decay only occurs in very heavy elements such as uranium (^{238}U), thorium (^{232}Th) or radium (^{226}Ra). The study of α-decay is one of the oldest subjects in nuclear physics [2]. Beta (β) decay is a radioactive process in which an electron is emitted from the nucleus of a radioactive atom along with an unusual particle called an antineutrino. The neutrino is an almost massless particle that carries away some of the energy from the decay process.

In fact, an ionizing radiation is harmful for any living tissue and damages it. If the damage is slight then the tissue can often repair itself without any permanent effect. It is easy to underestimate radiation hazards because there is usually a delay, sometimes of many years, between an exposure and some of its possible consequences, including cancer, leukemia, and genetic varieties that may lead to children handicapped in various ways. In many cases, the radiation is an unwanted but inescapable and in the disposal of their wastes [1].

In general, radioactive material is found throughout nature and occurs naturally in the soil, water and vegetation. Natural radio nuclides in soil generate a significant component of the background radiation exposure of the population. The terrestrial component of the natural background depends on the compositions of the soil and rocks in which the natural radio nuclides are contained [3]. Moreover, a significant contribution from natural sources to total dose comes from terrestrial radio nuclides such as ^{238}U, ^{232}Th and ^{40}K. At the same time, human body is continuously bombarded with radiation emitted from 15000 natural radioactive sources from the environment and any body per second. Radiation emitted from any body also effects other people living around [4]. In addition, ^{40}K, ^{226}Ra, and ^{238}U are natural radio nuclides in human body. Also, ^{14}C and ^{3}H are low in human body [5].

The ways of taking these radio nuclides to human body are inhalation and ingestion [5]. In addition, radioisotopes are also transferred from other various ways such as inhalation, direct contact, and injection. There are many possible transitions by transferring injection such as water – human, water – plant – human, water – plant – animal – human, plant – animal – human, water – animal – human [6].

We must consider biological effects of the radiation in terms of their effect on living cells. In order to obtain any information about the behavior of the radioactive source, total alpha and total beta radioactivity measurements of human teeth are of prime importance. Because tooth enamel is known as a detector for in vivo dosimeter for more than three decades. The usefulness of enamel for dosimeter results from its high content of mineral hydroxyapatite. Enamel is the most stable fraction of teeth; it does not undergo remodeling in adults [6, 7, 8]. Therefore, investigation of teeth in terms of radiologic or measurement of its natural radioactivity make it an interesting subject for monitoring natural radioactivity level.

In this study, we aimed to determine the radioactivity in the tooth samples collected from Cukurova and Black Sea regions, two different regions in Turkey. In other words, the purpose of this present work was to measure alpha and beta particles in human teeth in order to obtain a database and to compare the results of both regions. Therefore, total alpha and beta radioactivity of these regions was obtained using thirty five tooth samples.

II. EXPERIMENTAL

2.1. Instrumentation

A LB-PC 10- Channel Low-Level Planchet Counter controlled by a computer gas flow proportional detector was used to determine of total alpha and beta radioactivity. For similar studies, various improved methods are used to determine radioactivity by different

authors. But, ultra thin window gas flow proportional detector is commonly used in natural radioactivity measurements. Comparing with other detectors, it has many advantages such as time consuming, accurate, safe, and low price [9]. In this study, using LB 770 model, total alpha and beta radioactivity measurements in the teeth were carried out by counting of the tooth samples obtained from both different regions.

2.2. Sample Collection And Preparation

Thirty five tooth samples (all of which required extraction for orthodontic reasons) were collected from the Dental Faculty of Cukurova University, Adana city in Cukurova region and from dentists of Karabuk, Gumushane, Hopa, Trabzon cities in Black Sea region. The age range of adult and child humans concerned was from 9 to 65, and they were from 5 different cities in Turkey, including eight tooth samples from Adana, ten tooth samples from Karabuk, four tooth samples from Hopa, seven tooth samples from Gumushane and six tooth samples from Trabzon. When the samples were collected, it was considered that what the age of human was, where they lived in, how long they lived in there, what their occupation was, whether they smoke or not, whether they took radiation therapy or not etc.

These samples firstly were placed into little serum University and then were placed into nylon by writing physiological bottles and were secondly pulverized in Mining Engineering's Laboratories of Cukurova human's ages and their living cities.This process was repeated for each sample in the same way. Each pulverized sample was placed into the pulverizer, which is a mechanical device for the grinding of many different types of materials, and then these samples pulverized in the pulverizer were sieved through 90 μm and 125 μm meshes to obtain different two meshes. Thus, the samples were obtained greater than 90 μm and smaller than 125 μm. After the samples were moistened by adding pure water and little bottles were dried at 125^{o}C in drying oven, the samples obtained in this study were placed these bottles by writing their ages and cities. Thus, the tooth samples were prepared to determine total alpha and beta radioactivity.

III. RESULTS AND DISCUSSION

In this study, we purpose to determine total alpha and total beta radioactivity in the tooth samples collected from Cukurova and Black Sea regions in Turkey and then we compare their results with each other. After these samples were prepared for suitable condition given in previous section total alpha and beta radioactivity were measured for the adult and child tooth samples originating from four different cities in Black Sea region and one city in Cukurova region by using 10 Channel Low-Level Counter as given Table 1. Table 1 includes some parameters. The first column gives the list of the sample number, the second one gives the ages of tooth taken from adult and child. The third column gives the names of cities of taken tooth samples. The fourth and the fifth columns are total alpha and total beta radioactivity in units of Bq/g, respectively. In the first column, A, T, K, G and H letters represent initial letter of Adana, Trabzon, Karabuk, Gumushane, and Hopa cities, respectively. In the second column, the age range of the adult and child humans concerned in Karabuk, Hopa, Gumushane, Trabzon, Adana was 9-59, 18-65, 9-57, 13-58, 13-59 respectively. In the fourth column, since the detector could not read values of the below 0.003 due to the detector's detection limits, total alpha radioactivity in some samples could not measured and some of total alpha radioactivity measurements were taken to be 0.000. In the final column, total beta radioactivity concentrations were given completely.

As seen in Table 1, different cities named A, T, K, G, and H letters can be compared in detail more easily about differences between two regions. If the results obtained from Table 1 is summarized, it can be seen that 18 beta radioactivity values from Black Sea region is generally higher than that of Cukurova region.

Moreover, it was concluded that total alpha and beta radioactivity measurements in human teeth in each city were varied with their ages.

As a result of these measurements, the value of tooth samples from Black Sea is generally higher than that of Cukurova region.

Generally, radioactivity measurement results on human's teeth depend on many various factors such as biological half lives of radioactive sources, dietary levels of people, the regions and where people live in, etc. Moreover, the geographic origin of plants, food and the type of water consumed by people may be also considered factors in determining the alpha and beta radioactivity in teeth [10]. Thus, it is thought that people living in these two regions must be investigated due to human dietary intake, and the living conditions. However, it is impossible to certain interpretative on subject scientifically.

IV. CONCLUSION

In this study, the measurements of total alpha and total beta radioactivity in human teeth were investigated by using a 10 Channel Low-Level Counter. The results of total alpha and total beta radioactivity in Black Sea were compared with the results of Cukurova regions mentioned above. As seen from Table 1, it was concluded that total alpha and total beta radioactivity measurements in adult and child were variable. We determined that total beta activity results of Black Sea region were higher than that of Cukurova region. Therefore, it is thought that people taken tooth sample must be investigated due to human dietary intake, and living condition. However, it is clear that many more thousands of teeth must be analyzed to obtain full account of many factors, such as dietary and ethnic differences. Regional fallout radiation measurements should also be performed.

In this work, we supposed that Black Sea region was affected more than Cukurova region by fallout from the Chernobyl accident in April 1986. Yet, since radioactivity measurement results on human depend on many various factors such as biological half- lives of radioactive sources, dietary levels of people, the regions and the environment where people live, etc., it is impossible to certain interpretative on subject scientifically.

Consequently, although the concentration of naturally occurring radioactive materials in most natural substances

is low, high concentrations may arise as the result of human activities. However, the body has defense mechanisms against many types of damage induced by radiation. Although exposure to ionizing radiation carries a risk, it is impossible to avoid exposure completely. Radiation always presents in the environment and in our bodies in past and present. Therefore, in future, such studies will continue to assess the long term behavior and consequences of total alpha and beta radioactivity into the teeth.

As a result, the aim of the present work was to measure total alpha and total beta radioactivity in human teeth to obtain a database in Turkey and to document total alpha, beta radioactivity. Therefore, total alpha and total beta radioactivity in tooth samples were determined.

Table 1. Total alpha and beta radioactivity of tooth samples from selected regions

Sample No.	Age	Region	Total Alpha Radioactivity (Bq/g)	Total Beta Radioactivity (Bq/g)
K1	9	Karabük	0,0018 (±0.0009)	0,0197 (±0,0054)
K2	11	Karabük	0,0036 (±0,0216)	0,1509 (±0,0655)
K3	13	Karabük	0,0019 (±0,0009)	0,0063 (±0,0031)
K4	28	Karabük	0,0050 (±0,0120)	0,0169 (±0,0101)
K5	30	Karabük	0,0382 (±0,0376)	0,0599 (±0,0554)
K6	35	Karabük	0,0054 (±0,0027)	0,0092 (±0,0046)
K7	38	Karabük	0	0,0563 (±0,0111)
K8	48	Karabük	0	0,0274 (±0,0064)
K9	51	Karabük	0,0023 (±0,0011)	0,0018 (±0,0049)
K10	59	Karabük	0,0014 (±0,0007)	0,0150 (±0,0075)
H1	18	Hopa	0,8539 (±0,5193)	1,0346 (±0,4261)
H2	35	Hopa	0,0087 (±0,0117)	0,0103 (±0,0142)
H3	36	Hopa	0,0065 (±0,0111)	0,0408 (±0,0110)
H4	65	Hopa	0	0,0245 (±0,0169)
G1	9	Gümüşhane	0	0,5722 (±0,1825)
G2	11	Gümüşhane	0,0022 (±0,0097)	0,0182 (±0,0101)
G3	17	Gümüşhane	0	0,0372 (±0,0294)
G4	28	Gümüşhane	0,0041 (±0,0095)	0,0293 (±0,0090)
G5	29	Gümüşhane	0	0,0252 (±0,0116)
G6	39	Gümüşhane	0	0,0103 (±0,0480)
G7	57	Gümüşhane	0	0,0172 (±0,0208)
T1	13	Trabzon	0,0008 (±0,0004)	0,0439 (±0,0213)
T2	17	Trabzon	0,0217 (±0,0178)	0,0185 (±0,0270)
T3	30	Trabzon	0,0333 (±0,0215)	0,0769 (±0,0188)
T4	35	Trabzon	0,0110 (±0,0106)	0,0249 (±0,0107)
T5	51	Trabzon	0,0076 (±0,0055)	0,0054 (±0,0048)
T6	58	Trabzon	0,0005 (±0,0054)	0,0102 (±0,0061)
A1	13	Adana	0,0183 (±0,0099)	0,0110 (±0,00110)
A2	16	Adana	0,0023 (±0,0062)	0,0244 (±0,0062)
A3	17	Adana	0,0002 (±0,0065)	0,0107 (±0,0068)
A4	29	Adana	0	0,1215 (±0,0430)
A5	30	Adana	0,0018 (±0,0009)	0,0113 (0,0056)
A6	34	Adana	0,0050 (±0,0025)	0,0060 (±0,0087)
A7	51	Adana	0,0071 (±0,0060)	0,0202 (±0,0074)
A8	59	Adana	0,0030 (±0,0015)	0,0035 (±0,0017)

[1]. A.*Beiser*, ,1987. Concepts of Modern Physics, McGraw-Hill Book Company.
[2]. *A.Insolia, R. J.Liotta,and E. Maglione.*, 1988, *Europhys. Lett*, 7 (3), pp. 209-212.
[3]. *G.Karahan, A.Bayulken,* , 2000. Journal of Environmental Radioactivity, 47, 213-221.
[4]. *Y.Atakan*, 1990. Çernobil Radyasyon Çevre ve İnsanlar Üzerindeki Etkileri,
[5]. *G.Karahan*, 1997. Phd. Thesis. Technical University of Istanbul, Science Institute. Page 118.
[6]. *R.Acar*, 1987. Phd. Thesis. University of Gazi. Science Institute. Page. 141.
[7]. *J.M.Brady, N.O.Aarestad, H.M.Swartz,* , 1968. Med. Phys. 15, 43-47.
[8]. *F.C.M.Driessens,* , 1980. Bull. Soc. Chim. Belg. 89, 663-689.
[9]. *NCRP*, 1976. Envorimental Radiation Measurements, NCRP Report No.50
[10]. *R.Acar,O.Acar*, 2003. Turkish Atomic Energy Autority. Ankara Nuclear Enerji and Research Center.
[11]. *M.A.Çetiner,*1990. Phd. Thesis. University of Gazi. Science Institute. Page. 141.

NEW CALCULATION METHOD FOR INITIAL EXCITON NUMBERS ON PRE-EQUILIBRIUM ^{50,52,54}Cr(*p, xn*) REACTIONS

HÜSEYİN AYTEKİN[1], EYYUP TEL[2], RIDVAN BALDIK[1], AYNUR TATAR[2]

[1] *Karaelmas University, Faculty of Arts and Science, Department of Physics, Zonguldak- Türkiye*

[2] *Gazi University, Faculty of Arts and Science, Department of Physics, Ankara, Türkiye*

Tel et al. have suggested a new method by which the initial exciton numbers can be calculated from the neutron and proton densities. In this work, the initial exciton numbers have been calculated on target nuclei ^{50,52,54}Cr by using a new calculation method of Tel et al. and we have investigated (*p, xn*) reaction at 30,35,40 MeV incident proton energy. The publication is continuation of ref. [3].

The initial exciton numbers are very important in PEQ nuclear reactions. Tel et al. have suggested a new method by which the initial exciton numbers can be calculated from the neutron and proton densities by using an effective nucleon–nucleon interaction with Skyrme force for nucleon induced PEQ reactions [1, 2]. This new method calculated by taking into single-particle wave functions allows an increase or decrease in pre-compound emission spectra, with simulation of effect, which are considered in the calculations, such as basic nucleon–nucleon potential interaction (such as Woods–Saxon, harmonic oscillator, etc.) for nucleon induced pre-compound reactions. It can be researched with nuclear surface properties depending on the PEQ reactions and it can give more information for new nuclear reaction mechanisms researchers. In the density-dependent version, the GDH model takes into account the density distribution of the nucleus and it takes the initial exciton number as n_o = 3 [4]. For proton induced reactions, the initial proton exciton number X_p and the initial neutron exciton number X_n are given by Blann and Vonach [4] as

$$\mathrm{X_p} = \frac{2(3\mathrm{N}+2\mathrm{Z})}{(3\mathrm{N}+2\mathrm{Z}+3\mathrm{N})}, \qquad \mathrm{X}_n = 2 - \mathrm{X}_p,$$

where *N* and *Z* are the neutron and proton numbers of the target nuclei, respectively. The ALICE/ASH code is an advanced and modified version of the ALICE codes for PEQ calculations [5]. The initial exciton numbers in the ALICE/ASH code calculations for proton induced reactions are given as

$$X_p = 2\frac{\left(\sigma_{pn}/\sigma_{pp}\right)N + 2Z}{2(\sigma_{pn}/\sigma_{pp})N + 2Z},$$

$$X_n = 2 - X_p,$$

where σ_{xy} is the nucleon–nucleon interaction cross-section in the nucleus. In details, the other code model parameters can be found in [5].

Castaneda et al. [6] have suggested that the initial neutron and proton-exciton numbers, for each partial wave, are calculated for a proton-induced reaction on a target; the initial neutron- and proton-exciton numbers for each partial wave,

$$X_p \equiv \frac{2\left[3\rho_n(R_l) + 2\rho_p(R_l)\right]}{3\rho_n(R_l) + 2\rho_p(R_l) + 3\rho_n(R_l)},$$

$$X_n = 2 - X_p$$

where *l* is orbital angular momentum. The radius for the *l* th entrance channel partial was defined by

$$R_l = \lambda\bar{}\,(l + 1/2).$$

Tel et al. have suggested that the impact parameters $\rho_n(R_l)$ and $\rho_p(R_l)$ in Eq. (4) can be replaced with the neutron density $\rho_n(R)$ and the proton density $\rho_p(R)$ calculated by taking into account single-particle wave functions [2]. For nucleon induced precompound reactions, therefore, the initial neutron and proton exciton numbers can be calculated from the neutron $\rho_n(R)$ and proton $\rho_p(R)$ densities by using an effective nucleon–nucleon interaction with Skyrme force [1,2]. In the interaction with Skyrme force, the neutron or proton densities are given by

$$\rho_q(\mathrm{r}) = \sum_{\beta\in q} w_\beta \psi_\beta(r)^+ \psi_\beta(r),$$

(q : *n*, neutron, or *p*, proton),

where ψ_β is the single-particle wave function of the state β, the occupation probability of the state β is denoted by w_β. The Hartree–Fock method with the Skyrme force interaction is widely used for studying the properties of nuclei [7–10]. This force consists of some two-body terms together with a three-body term

$$V_{\mathrm{CS}} = \sum_{i<j} V_{ij}^{(2)} + \sum_{i<j<k} V_{ijk}^{(3)}.$$

The Skyrme forces with the three-body term replaced by a density-dependent two-body term have been generalized and modified, which are unified in a single form by Ge et al. [11] as an extended Skyrme force:

$$V_{\text{Skyrme}} = t_0(1+x_0P_\sigma)\delta(r)+\frac{1}{2}t_1(1+x_1P_\sigma)\left(\delta(r)k^2+k'^2\delta(r)\right)+$$
$$t_2(1+x_2P_\sigma)k'\times\delta(r)k+\frac{1}{6}t_3(1+x_3P_\sigma)\rho^\alpha(R)\delta(r)+$$
$$it_4k'\times\delta(r)(\sigma_i+\sigma_j)\times k,$$

where k is the relative momentum, $\delta(r)$ is the delta function, P_σ is the space exchange operator, σ is the vector of Pauli spin matrices and t_0, t_1, t_2, t_3, t_4, x_0, x_1, x_2, x_3, α are Skyrme force parameters. The new Skyrme-like effective interactions (called SLy4) have been proposed by Chabanat et al. for neutron stars, supernovae and the neutron-rich nuclei [12, 13].

The theoretical initial exciton numbers for proton induced reaction have been calculated by using the new calculation method of Tel et al. suggestion [1] for ^{50,52,54}Cr and we have drawn the calculated radii versus the initial exciton numbers graph obtained from SKM* and SLy4 for proton induced reaction on target nuclei ^{50,52,54}Cr in Fig. 1.

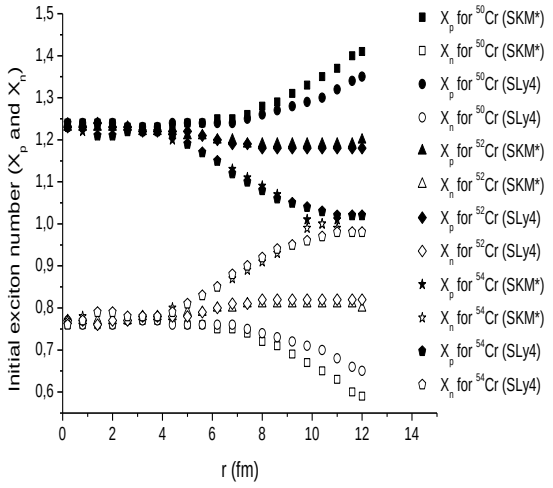

Fig. 1. Calculated density dependent initial neutron and proton exciton numbers for proton induced reaction on ^{50,52,54}Cr.

The Skyrme force parameters of the SKM* and SLy4 are given in Table 1. The theoretical values obtained by using SKM* parameters with the single-particle wave functions of the harmonic oscillator potential have been done with HAFOMN code [14], and using SLy4 with the single-particle wave functions of the Woods–Saxon potential have been done with program HARTREE–FOCK (modified for spin–orbit to accept SKI4) [15]. We have calculated the initial neutron and proton exciton numbers by using $\rho_n(R)$ and $\rho_p(R)$ density by using the new calculation method of Tel et al. suggestion [1].

The Chromium (Cr), the basic element in most alloy steels, is essential in the majority of the components of a fusion reactor. In this study, the neutron-emission spectra produced by (p,x*n*) reactions for target nuclei as ^{50,52,54}Cr have been investigated at 30, 35 and 40 MeV incident proton energy in Fig. 2-4. The pre-equilibrium calculations have been made using the new evaluated hybrid model and the GDH model [5]. In the all equilibrium and pre-equilibrium calculations, the code as ALICE/ASH was used. The ALICE/ASH code is an advanced and modified version of the ALICE codes [5]. In the calculations of the hybrid and GDH model, we have used the initial exciton number as n_o =3.

Table 1. Numerical values of the parameters t_0 (MeV fm^3), t_1 (MeV fm^5), t_2 (MeV fm^5), t_3 (MeV fm$^{3\alpha}$), t_4 (MeV fm^8), w_0 (MeV fm^5), and x_0, x_1, x_2, x_3, α corresponding to interactions SKM* and SLy4

Force	SKM*	SLy4
t_0	-2645.0	-2488.9
t_1	410.0	486.8
t_2	-135.0	-546.4
t_3	15595.0	13777.0
t_4	0	0
x_0	0.09	0.83
x_1	0	-0.34
x_2	0	-1
x_3	0	1.35
α	1/6	1/6
w_0	130.0	123.0

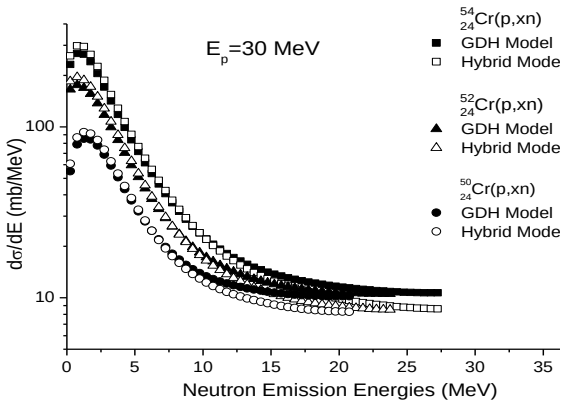

Fig. 2. Calculated neutron spectra from ^{50,52,54}Cr(p,xn) at 30 MeV.

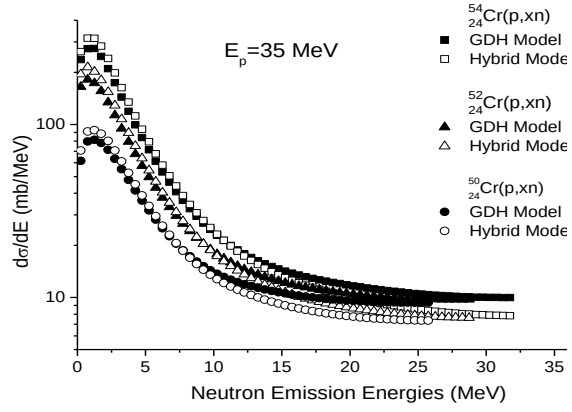

Fig.3. Calculated neutron spectra from ^{50,52,54}Cr(p,xn) at 35 MeV.

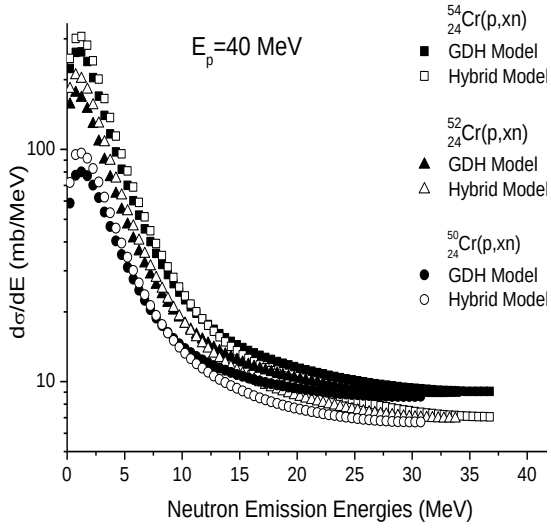

Fig. 4. Calculated neutron spectra from ^{50,52,54}Cr(p,xn) at 40 MeV.

The proton-induced nuclear reaction cross–section data can be used in technical applications such as the isotope production alternatives (for produced medical radioisotopes by using cyclotrons), spallation reactions for production of neutrons in spallation neutron source and for the other applications. The developed reaction systematic for Chromium (and for other nuclei) can be used in the estimation of unknown data and in the adoption of cross-sections among discrepant experimental values. Such predictions can guide the design of the target/blanket configurations and can reduce engineering over design costs. This study contributes to the new studies on cross section and help to show the way to the future experimental studies.

[1]. *E. Tel*, Ph. D. Thesis, Gazi University (Ankara, Turkey, 2000).
[2]. *E. Tel, A. Aydın, A. Kaplan, and B. Şarer*, Phys. Rev. C 2008, 77, 054605.
[3]. *E. Tel, R. Baldık, H.aytekin and A. Aydın,* Ann. Nucl. Energy, 2009, 36, 1333.
[4]. *M. Blann and H. K. Vonach*, Phys. Rev. C 1983, 28, 1475.
[5]. *C H M Broeders, A Yu Konobeyev, Yu A Korovin, V P Lunev and M Blann*, FZK7183, May 2006,http://bibliothek.fzk.de/zb/berichte/FZKA7183.pdf.
[6]. *C. M. Castaneda, J. L. Ullmann, F. P. Brady, et al.*, Phys. Rev. C 1983, 28, 1493.
[7]. *T. H. R. Skyrme*, *Phil*. Mag, 1956. 1, 1043; Nucl. Phys. 1959, 9, 615.
[8]. *P. G. Reinhard and R. Y. Cusson*, Nucl. Phys. A 1982, 378, 418.
[9]. *E. Tel, Ş. Okuducu, G. Tanır, N. N. Aktı, and M. H. Bölükdemir*, Commun. Theor. Phys. 2008, 49, 696.
[10]. *E. Tel, H. M. Şahin, A. Kaplan, A. Aydın, and T. Altınok,* Ann. Nucl. Energy 2008, 35 2, 220.
[11]. *L. X. Ge, Y. Z. Zhuo, and W. Norenberg*, Nucl. Phys. A 1986, 459, 77.
[12]. *E. Chabanat, P. Bonche, P. Haensel, J. Meyer, and R.* Schaeffer, Phys. Script. T, 1995, 56, 231.
[13]. *E. Chabanat, P. Bonche, P. Haensel, J. Meyer, and R. Schaeffer*, Nucl. Phys. A 1998, 635, 231.
[14]. http://www.le.infn.it/~gpco/neutrino/sk_nk.f
[15]. *P. G. Reinhard and H. Flocard*, Nucl. Phys. A 1995, 584, 467.

GROUND-STATE NUCLEAR PROPERTIES OF SOME RARE EARTH NUCLEI IN RELATIVISTIC MEAN FIELD THEORY

A.H. YILMAZ[1], T. BAYRAM[1,2], M. DEMİRCİ[1], B. ENGİN[1]

[1]*Karadeniz Technical University, Physics Department, 61080, Trabzon ,TURKEY*

[2]*Sinop University, Physics Department, Sinop, TURKEY*

hakany@ktu.edu.tr, mehmetdemirci@ktu.edu.tr

In this study, rare earth nuclei, ^{160}Gd, ^{168}Er, ^{170}Er and isotopic chain of Dy were investigated using relativistic mean field theory with non-linear NL3 and NLSH parameters sets. Binding energies per nucleon, neutron radii, proton radii, charge radii, neutron and proton quadrupole moments of these nuclei were calculated. Also, these ground state properties were calculated using non-relativistic Hartree-Fock-Bogoliubov method with parameters set SKP. Predictions of this work were compared with available experimental data and some predictions calculated with different parameters set in relativistic mean field theory.

Relativistic models of the nucleus have attracted much attention in recent 30 years. One of them is relativistic mean field theory (RMF) [1, 2]. Several attempts have been made to describe the nuclear properties using RMF theory due to its advantages over the non-relativistic density-dependent Skyrme approaches [3]. The RMF theory has been successful in describing the ground-state properties of nuclei about both the line of stability [1, 4] and far away from the line of stability [5]. On the other hand, studies of rare earth nuclei which are heavy deformed are attracted [6- 8].

The aim of this study was investigated ground-state nuclear properties of some rare earth nuclei within the framework of RMF theory using NL3 and NLSH parameters sets and was compared these results with Hartree-Fock-Bogoliubov method results.

The ansatz of the interaction in the RMF theory is based upon Lagrangian density of the form [2]:

$$\mathcal{L} = \bar{\psi}\left(i\partial\!\!\!/ - M\right)\psi + \tfrac{1}{2}\partial_\mu\sigma\partial^\mu\sigma - U(\sigma) - \tfrac{1}{2}\Omega_{\mu\nu}\Omega^{\mu\nu}$$

$$+\tfrac{1}{2}m_\omega^2\omega_\mu\omega^\mu - \tfrac{1}{4}\vec{R}_{\mu\nu}\vec{R}^{\mu\nu} + \tfrac{1}{2}m_\rho^2\vec{\rho}_\mu\vec{\rho}^\mu \qquad (1)$$

$$-\tfrac{1}{4}F_{\mu\nu}F^{\mu\nu} - g_\sigma\bar{\psi}\sigma\psi - g_\omega\bar{\psi}\omega\psi - g_\rho\bar{\psi}\vec{\rho}\vec{\tau}\psi - e\bar{\psi}A\psi$$

where the Dirac nucleon interacts with the σ and the ω meson fields. The ρ meson generates the isovector component of the force. The Lagrangian contains a nonlinear scalar self-interaction of the σ meson.

$$U(\sigma) = \tfrac{1}{2}m_\sigma^2\sigma^2 + \tfrac{1}{3}g_2\sigma^3 + \tfrac{1}{4}g_3\sigma^4 \qquad (2)$$

This term is necessary for appropriate description of surface properties. M, m_σ, m_ω and m_ρ are the nucleon, $\sigma-$, $\omega-$ and $\rho-$meson masses, respectively, while g_σ, g_ω, g_ρ and $e^2/4\pi = 1/137$ are the corresponding coupling constants for the mesons and the photon. The field tensors of the vector mesons and of the electromagnetic fields take the following form:

$$\Omega^{\mu\nu} = \partial^\mu\omega^\nu - \partial^\nu\omega^\mu \qquad (3)$$

$$\vec{R}^{\mu\nu} = \partial^\mu\vec{\rho}^\nu - \partial^\nu\vec{\rho}^\mu \qquad (4)$$

$$F^{\mu\nu} = \partial^\mu A^\nu - \partial^\nu A^\mu \qquad (5)$$

The Dirac spinors ψ_i of the nucleon and the fields of $\sigma-$, $\omega-$, $\rho-$mesons are solutions of the coupled Dirac and Klein-Gordon equations via the classical variational principle and are then solved by the self-consistent method for axially symmetric systems of nucleons with additional pairing interaction. These equations are solved by iterative procedure; starting from an estimate of the meson and electromagnetic fields, one can solve the Dirac equation and obtain the spinors. These are used to obtain the densities and currents. They are used for solution of the Klein-Gordon equations and provide the new estimates of the meson and electromagnetic fields for the next iteration. This iteration is continued till the convergence up to the desired accuracy is achieved. When densities are calculated, negative-energy states are neglected (no-sea approximation), i.e. the vacuum is not polarized. Details are given in [7]. Some input parameters corresponding values of nucleon masses, mesons masses_and coupling constants are necessary such a calculation. In this study it was used NLSH [5] and NL3 [9] non-linear parameters sets. These sets are shown in Table1.

The rare earth nuclei considered here are even-mass nuclei and these nuclei are open-shell nuclei both in protons and neutrons, thus requiring the inclusion of pairing. The parameters sets NLSH and NL3 has been employed for these nuclei. The number of shells taken into account are 12 and 20 for the fermionic and bosonic expansions, respectively. The basis parameters $\hbar\omega$ and β_0 used for the calculations have been taken to be $41A^{-\frac{1}{3}}$ and 0.3, respectively. In order to investigate these rare earth nuclei we have performed the calculations with Saxoon-Woods initial wavefunctions.

In this study, also these rare earth nuclei investigated in framework of Hartree-Fock-Bogoliubov method using SKP [10] parameters set for comparison. Ergo, HFBTHO computer code which is presented by Stoitsov et al. [11] was used. This code provides axially deformed solution of the Hartree-Fock-Bogoliubov [HFB] equations. For HFB calculations, β_0 basis parameters have been taken to be

0.3 as it is mentined above in relativistic mean field calculations.

Table1.The parameters sets NLSH [5] and NL3[9] used in the relativistic mean field Lagrangian.

Parameter	*NLSH*	*NL3*
M (MeV)	939.00	939.00
m_σ (MeV)	526.059	508.194
m_ω (MeV)	783.00	782.501
m_ρ (MeV)	763.00	763.000
g_σ	10.4444	10.217
g_ω	12.945	12.868
g_ρ	4.383	4.474
g_2	-6.9099	-10.431
g_3	-15.8337	-28.885

Our predictions of binding energy per nucleon and quadrupole deformation parameter β_2 of protons for isotopic chain of Dy in not only relativistic mean field theory with NLSH and NL3 parameters sets but also HFB method with SKP parameters set are shown in Fig.1 and Fig.2 respectively. Experimental curves are also shown for comparisons.

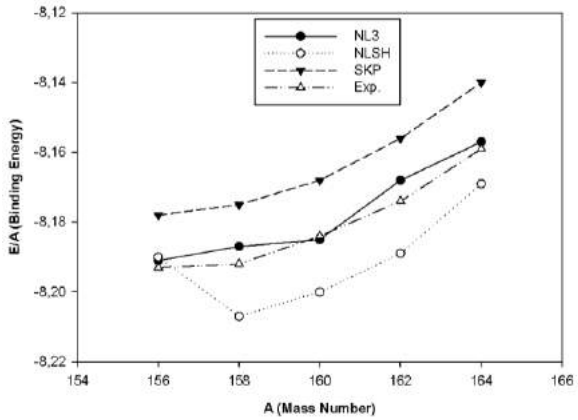

Fig.1 Binding energy per nucleon for Dy isotopes. Experimental values were obtained from [13].

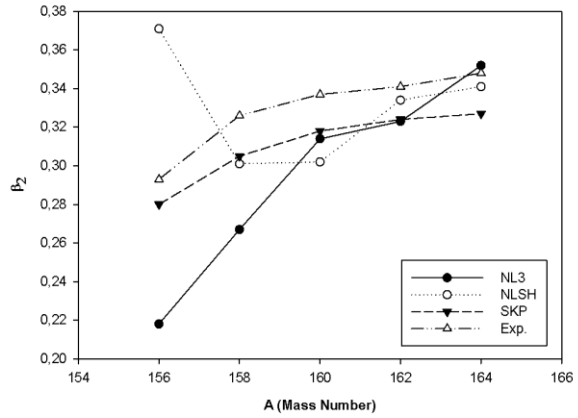

Fig.2 Quadrupole deformation parameter β_2 for Dy isotopes are shown as a function of mass number. Experimental values were obtained from [12].

As seen from the Fig.1, predictions of RMF theory with NL3 to the binding energy per nucleon for Dy isotopes are good agreement with experimental curve [13]. Maximal deviations between these values are approximately 0.01 MeV. Also predictions of the other sets are agreement with experimental value. The maximal deviations between the experimental values and the other sets are about 0.2 MeV. On the other hand, as seen from the Fig.2, predictions of HFB method using the parameters set SKP to quadrupole deformations are better agreement with experimental values than the other sets.

In Fig.3 and Fig.4, proton radii and charge radii for Dy isotopes are shown. In this figures, predictions of relativistic mean field theory with TMA parameters set [14] are also shown.

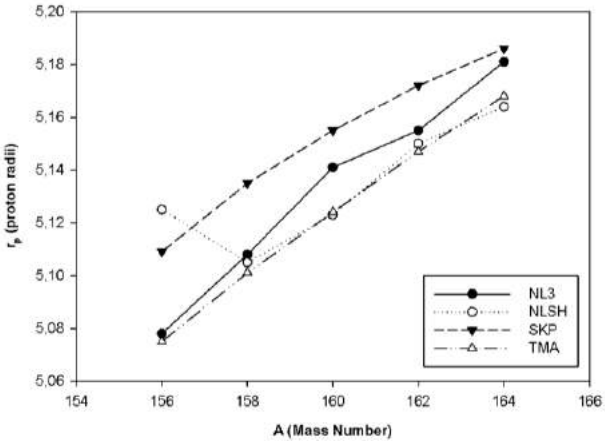

Fig.3 r_p, proton radii for Dy isotopes are shown as a function of mass number. Predictions of relativistic mean fielt theory with TMA parameters set were obtained from [14].

In Table 1, the binding energies per nucleon (E/A); proton, nötron and charge radii; quadrupole moments for neutron, proton and quadrupole deformation parameters β_2 are shown for ^{160}Gd, ^{168}Er and ^{170}Er nuclei. For comparison, predictions of NL2 parameters set [4] and available experimental values [12, 13] are shown. As seen from the Table 1, the binding energies per nucleon for ^{160}Gd, ^{168}Er and ^{170}Er nuclei are well described in both relativistic mean field theory with non-linear NL2 [4], NL3 and NLSH parameters sets and Skyrme Hartree-Fock-Bogoliubov method with SKP parameters set.

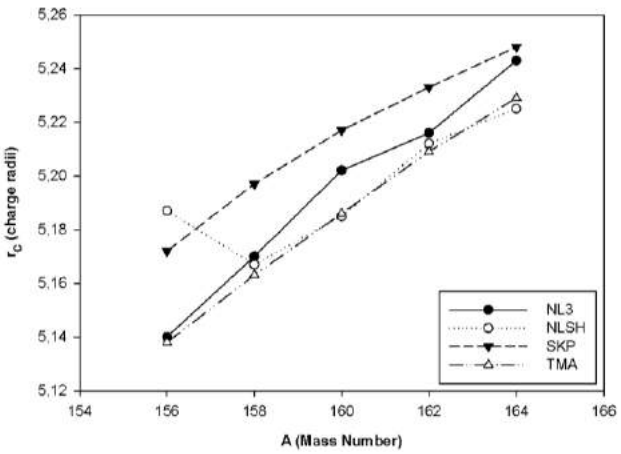

Fig.4 r_c, charge radii for Dy isotopes are shown as a function of mass number. Predictions of relativistic mean field theory with TMA parameters set are also shown [14].

The deviations between the experimental values and the predictions described above are approximately 0.2 MeV. However, for description of quadrupole deformation parameter β_2, predictions of relativistic mean field theory using NLSH set and predictions of Hartree-Fock-Bogoliubov method using SKP set are good agreement with experimental values

.

Table 2. Calculations of ground-state properties to some rare earth nuclei in both relativistic mean field theory with NL3 and NLSH parameters sets and HFB method with SKP parameters set. Also, NL2 [4] and experimental values [12, 13] are shown .

Nucleus		E/A	r_n	r_p	r_c	Q_n	Q_p	β
^{160}Gd	NL3	-8.178	5.365	5.126	6.515	10.119	6.883	0.330
	NLSH	-8.197	5.336	5.120	6.515	10.386	7.111	0.340
	SKP	-8.167	5.279	5.143	5.205	10.795	7.408	0.330
	NL2	-8.18	5.37	5.11	5.17	9.59	6.41	0.31
	Exp.	-8.173					7.265	0.353
^{168}Er	NL3	-8.126	5.446	5.225	6.621	11.652	7.940	0.351
	NLSH	-8.136	5.410	5.210	6.621	11.309	7.756	0.342
	SKP	-8.112	5.351	5.228	5.289	11.333	7.826	0.322
	NL2	-8.15	5.44	5.20	5.26	10.44	7.05	0.31
	Exp.	-8.130					7.630	0.334
^{170}Er	NL3	-8.110	5.479	5.244	6.648	12.279	8.186	0.360
	NLSH	-8.121	5.449	5.228	6.648	11.962	7.956	0.356
	SKP	-8.095	5.377	5.242	5.302	11.645	7.871	0.321
	NL2	-8.11	5.47	5.21	5.27	10.90	7.19	0.32
	Exp.	-8.112					7.650	0.336

[1]. *P. G. Reinhard,* Rep. Prog. Phys.,1989, 52, p.439-514

[2]. *B. D. Serot,* Rep. Prog. Phys., 1992, 55, p. 1855-1946

[3]. [3]. *D. Vautherin, D. M. Brink,* Phys. Rev., 1972, 5, p.626-647

[4]. *Y. K. Gambhir, P. Ring, A. Thimet,* Ann. Phys., 1990, 198, p. 132-179

[5]. *M. M. Sharma, M. A. Nagarajan, P. Ring,* Phys. Lett. B, 1993, 312, p. 377-381

[6]. *Y. K. Gambhir, P. Ring,* Phys. Lett. B, , 1988, 202, p. 5-9

[7]. *P. Ring, Y. K. Gambhir, G. A. Lalazissis,* Comp. Phys. Commun., 1997, 105, p. 77-97

[8]. *L. S. Geng, H. Toki, J. Meng,* Prog. Theor. Phys., 2005, 113, p. 785-800

[9]. *G. A. Lalazissis, J. König, P. Ring*, Phys. Rev. C, 1997, 55, p. 540-543

[10]. *E. Chabanat, P. Bonche, P. Haensel, J. Mayer, R. Schaeffer,* Nucl. Phys. A, 1997, 627, p. 710-746

[11]. *M. V. Stoitsov, J. Dobaczewski, W. Nazarewicz, P. Ring*, Comput. Phys. Comm., 2005, 167, p. 43-63

[12]. *S. Raman, C. H. Malarkey, W. T. Milner, C. W. Nestor, J. R. Stelson, P. H. Stelson,* 1987, At. Data Nucl. Data Tables, 36, p. 1-96

[13]. *G. Audi, A. H. Wapstra*, Nucl. Phys. A, 1993, 565, p. 1-65

[14]. *L. Geng*, Ground State Properties of Finite Nuclei in the Relativistic Mean Filed Theory, 2005, Doctoral thesis, Osaka University, Japan

ON THE ENERGY WEIGHTED SUM RULE

M. GÜNER[1], A.A.KULİEV[2,3], E. GULİYEV[3]

[1] *Sakarya Univ.,Fac. of Science and Art, Dept. of Mathematics, 54100Adapazarı, Turkey*

[2] *Sakarya Univ.,Fac. of Science and Art, Dept. of Physics, 54100 Adapazarı, Turkey*

[3] *Institute of Physics, Azerbaijan National Academy of Science, Baku, Azerbaijan*

In the Random Phase Approximation (RPA), using the analytic properties of the nucleus transition matrix elements and by means of contour integrals and residue theorem, we obtained an analytic formula for the energy-weighted sum rule (EWSR) of the M1 transitions as a function of the deformation parameters of the excited states of the nucleus. It is shown that an essential decrease of the experimental M1 transitions rates may be due to the change of nuclear shape caused by the transitions between different energy levels. The latter may be also responsible for the observed quenching of the M1 sum rules. The numerical calculations are carried out, and the deformed dependence of the sum rules for the ^{140}Ce and ^{196}Pt is analyzed.

In quantum mechanics, the transition probability of the system from one state to the other is restricted to the sum rules which are independent from the model and subject to transitions matrix elements. The sum rules in nuclear physics are very important to finding parameters and understanding the reliability of used models [1]. Microscopic nuclear models are used to investigate the properties of nuclear collective excitations [2]. Approximate calculation methods are used to investigate the structure of nucleus within the framework of assumed models. In these models the random phase approximation (RPA) has been extensively exploited to calculate intensities of the various nuclear processes, probabilities of electromagnetic, beta and double beta decay transitions and corresponding sum rules by taking into account ground state correlations. Numerical calculations of the sum rules within framework of the modern microscopic models of nucleus are simple with a small number of the phonon states in spherical nuclei. However, in deformed nuclei the spectrum of such states is characterized by high density. This gives rise to considerable difficulties in exact calculations of all the eigenvalues ω_n and eigenfunctions (ψ_n) of the model Hamiltonian and in the correct evaluation nuclear matrix elements of the different processes. The analytical solutions of this problem for calculation beta decay sum rules are given in [3]. Later, the developed method developed in [3] successfully applied to calculate the NEWSR and EWSR of the electric and magnetic dipole transitions and beta decay matrix elements on the ground state basis [4]. This approach based on the analytical properties of nuclear matrix elements makes it possible to describe the integral quantities as sum rules without a preliminary determination of the wide spectrum of 1^+-states and wave functions.

The experimental spin-magnetic strength was found to be quenched more than 1.5 times in heavy nuclei as compared with prediction of the QRPA (see, e.g., [5] and references therein). Up to now the reason for this disagreement between the QRPA calculation and the experiments is not exactly explained. So investigation of this disagreement is very important. The main reason of these disagreements may be due to the change of nuclear shape caused by the transitions between different energy levels. The phenomena associated with shape coexistence and intruder states in heavy and medium nuclei are discussed in [6,7]. It is experimentally known that in some nuclei, the rate transitions between levels having different shape and structure decreases [8,9]. So, one of the reason of these disagreements should be the differences of the shape of the excitations and ground state participating in transitions. For this reason, calculating the sum rules for the transition matrix elements of levels, which have deformation parameters different from the ground state is very important.

In this study, the method developed in [3] has been applied successfully for investigating magnetic dipole transitions between states having different shape. We obtained an analytical formula for the energy weight sum rule of the magnetic dipole transition matrix elements containing the excited and ground state deformation parameters of nucleus. It is shown that an essential decrease of the rate M1 excitations of the 1^+ states may be due to the change of nuclear shape caused by the M1 transitions. The numerical calculations are carried out, and the shape dependence of the EWSR for the ^{140}Ce, ^{196}Pt and ^{154}Sm and ^{156}Gd is analyzed.

The key problem in the program for investigating deformation dependence of the sum rules is the calculation of the EWSR of the M1 transitions to the states which have shapes different from the ground state ones. The sum rules for the transition matrix elements from one state to the other one are obtained by using commutation relations of the transition operators and their hermitic conjugates with each other, and with the system model Hamiltonian by making explicit use of the closure relation of exact eigenstates of the system. There are two widely used types of sum rules: none energy-weighted sum (NEWSR) rule and linear energy-weighted sum rule (EWSR).

For any one-body operator M, the transition matrix elements from the ground state to the excited states of the system is given by the NEWSR

$$\sum_{k>0} |< k \mid M \mid 0 >|^2 = < 0 \left| [M, M^+] \right| 0 > \qquad (1)$$

The energy-weighted sum rule is widely used in the nuclear physics can be written

$$\sum_{k>0}(E_k - E_0)\left|< k|M|0>\right|^2 = \frac{1}{2} < 0|[M^+,[H,M]]|0> \quad (2)$$

Here in (1) and (2) energy E_k and wave function $|k\rangle$ are eigenvalues and eigenfunctions of Hamiltonian operator of nucleus, respectively. For the transition operator M in quasi-boson approximation of the RPA the double commutator in (2) is a c-number. E_0 and $|0\rangle$ also denote the energy and wave function of the ground state, respectively. Thouless [10] showed that left-hand side of (2) calculated with RPA is equal to the right-hand side of (2) calculated using the Hartree-Fock ground state wave function. Since the right-hand side of the sum rule (2) does not contain any parameters of the effective interactions of the model used for description nuclear excitations. On the other hand, the left-hand side of the (1) contains wave functions and energy levels of nucleus, its values depend on accuracy of the methods and models used. Thus, the calculation of the EWSR allows one to make some conclusions about the accuracy of methods and approximations.

The applied QRPA method and the theoretical calculations have a1ready been described in refs.[11]. Therefore, we avoid here to present long theoretical description of the method.

Let us consider the system of nucleons in the axially symmetric average field interacting via pairing and spin-spin residual forces. We neglect for simplicity the restoring rotational invariance forces which only slightly affect the properties of high-lying 1^+ states in spin-flip M1-resonance energy region.

Then the model Hamiltonian of the intrinsic motion (for a fixed orientation of the nucleus) can be written in the quasiparticle representation [11]:

$$H = H_{sqp} + V_{\sigma\tau} \quad (3)$$

Here, H_{sqp} represents the Hamiltonian of the single-quasiparticle motion. The term $V_{\sigma\tau}$ takes into account the spin–isospin interaction, which produces the 1^+ state in deformed nuclei and has the form

$$V_{\sigma\tau} = \frac{1}{2}\chi_{\sigma\tau}\sum_{i\neq j}\vec{\sigma}_i\vec{\sigma}_j\tau_i^z\tau_j^z . \quad (4)$$

where, $\chi_{\sigma\tau}$ is the spin–isospin interaction strength; and $\vec{\sigma}_i$ and $\vec{\tau}_i$ are the Pauli matrices that represent the spin and the isospin, respectively. All relations, that are used and not explained in this paper are similar to those in Ref.[11].

In the QRPA method, the collective 1^+-states are considered as one-phonon excitations described by

$$|t\rangle = Q_t^+|\Psi_0\rangle = \frac{1}{\sqrt{2}}\sum_{ss',\tau}[\psi_{ss'}^t(\tau)C_{ss'}^+(\tau) - \varphi_{ss'}^t(\tau)C_{ss'}(\tau)]|0\rangle , \quad (5)$$

where Q_t^+ is the phonon creation operator, $|0\rangle$ is the phonon vacuum which corresponds to the ground state of the even-even nucleus and $C_{ss'}^+(C_{ss'})$ is a two-quasiparticle creation (annihilation) operator. Further s(s′) denotes the single-quasiparticle states of the nucleons and the isospin index τ takes the values n(p) for neutrons(protons). Our system has a discrete spectrum and the wave functions $|t\rangle$ form complete set satisfying $\sum_t |t\rangle\langle t| = 1$. The two quasiparticle amplitudes $\psi_{ss'}^t(\tau)$ and $\varphi_{ss'}^t(\tau)$, corresponding to the operator $C_{ss'}$ and $C_{ss'}^+$ are normalized as follows:

$$\sum_{ss'\tau}[\psi_{ss'}^i(\tau)\psi_{ss'}^k(\tau) - \varphi_{ss'}^i(\tau)\varphi_{ss'}^k(\tau)] = \delta_{i,k} . \quad (6)$$

Following the well-known procedure of the RPA method, one can find the eigenfunctions and the eigenvalues of the Hamiltonian. Employing the conventional procedure of the QRPA with the equation of motion:

$$\left[H_{sqp} + V_{\sigma\tau}, Q_t^+\right] = \omega_t Q_t^+ \quad (7)$$

and omitting the details of the solution of (7), we obtain [11] the secular equation for the excitation energy ω_t of the 1^+-states

$$D(\omega_t) = 1 + \chi_{\sigma\tau}\left(F_n(\omega_t) + F_p(\omega_t)\right) = 0 \quad (8)$$

where

$$F_\tau(\omega_t) = 2\sum_\mu{}^{(\tau)} \frac{\varepsilon_\mu \sigma_\mu^2 L_\mu^2}{\varepsilon_\mu^2 - \omega_t^2}, \quad \tau = n,p. \quad (9)$$

Here, $\varepsilon_{ss'} = \varepsilon_s + \varepsilon_{s'}$ and ε_s are the energies of the deformed single-quasiparticle states $|s>$. The single-particle matrix elements for spin operator σ_{+1} are denoted by $\sigma_{ss'}$. The expression $L_{ss'} = u_s v_{s'} - u_{s'} v_s$ is defined in the usual Bogolyubov notation.

Hereafter in order to simplify the notation we use a single index μ instead of the pair index (ss'). The sum $\sum^{(\tau)}$ denotes the summation over the neutron or the proton states. Finally, the neutron-neutron and proton-proton two-quasiparticle amplitudes are given by:

$$\psi_\mu^t = \frac{1}{\sqrt{Y(\omega_t)}} \cdot \frac{\sigma_\mu L_\mu}{\varepsilon_\mu - \omega_t} \quad (10)$$

$$\varphi_\mu^t = \frac{1}{\sqrt{Y(\omega_t)}} \cdot \frac{\sigma_\mu L_\mu}{\varepsilon_\mu + \omega_t} \quad (11)$$

where

$$Y(\omega_t) = 4\omega_k \sum_t \frac{\varepsilon_\mu \sigma_\mu^2 L_\mu^2}{(\varepsilon_\mu^2 - \omega_t^2)^2}. \quad (12)$$

The sum $\sum$ runs over all neutron and proton states. On the other hand, since energies of the magnetic dipole 1^+ states are the solutions of the function $D(\omega_t)$, after simple manipulation for $Y(\omega_t)$ the following formula is obtained

$$Y(\omega_t) = \frac{1}{\chi} D'(\omega_t) \quad (13)$$

where

$$D' = \frac{dD(z)}{dz}.$$

Due to the symmetry between the used spin-spin forces and magnetic dipole operator, the most characteristic quantity of the 1^+ states is transition matrix elements M1 from ground state to all excited states in nucleus:

$$\vec{M}_t = \langle t|\vec{M}|0\rangle \quad (14)$$

where the magnetic-dipole operator is

$$\vec{M} = \sqrt{\frac{3}{4\pi}} \sum_{m,\tau} [(g_s^\tau - g_l^\tau)\frac{1}{2}\vec{\sigma}_m^\tau - g_e^\tau \vec{j}_m^\tau]. \quad (15)$$

Here g_s^τ and g_l^τ are the spin and the orbital gyromagnetic ratios of nucleons, respectively. By using the wave function (5) and by means of (10) and (11), transition matrix elements of 1^+ states from ground state to excited states $|t\rangle$ can be expressed as

$$M_t = \sqrt{\frac{3}{4\pi}} \frac{\sum_\tau [\frac{1}{2}(g_s^\tau - g_l^\tau)F_\tau(\omega_t) - g_\ell^\tau J_\tau(\omega_t)]}{\sqrt{Y(\omega_t)}} \quad (16)$$

where

$$J_\tau(\omega_t) = 2\sum_\mu {}^{(\tau)} \frac{\varepsilon_\mu j_\mu^2 L_\mu^2}{\varepsilon_\mu^2 - \omega_t^2} \quad (17)$$

Here, j_μ denotes the single-particle matrix elements of the angular momentum operator.

The energy-weighted sum rule (2) for the M1 transitions (15) calculated using Hartree-Fock-Bogolyubov (HFB) ground state is given as follows [13]

$$\sum_{t>0} \omega_t B_t(M1) = \frac{3}{4\pi} \sum_{\mu,\tau} \varepsilon_\mu^\tau [(g_s^\tau - g_l^\tau) s_\mu^\tau - g_e^\tau j_\mu^\tau]^2 \quad (18)$$

Here, $B_t(M1) = <t|M|0>^2$ is the M1 transition probability of the excitation from the ground state. As seen the right-hand side of eq. (18) does not depend on the spin-spin interaction strength parameter $\chi_{\sigma\tau}$ and represents the quasiparticle estimate of the sum rule.

Let us now generalize the sum rule in Eq. (2) for transitions between the ground and excited states which have different form. Let us suppose that shape of the excited states $|k\rangle$ have different deformation parameter from the ground state one. After this, the quantities corresponding to excited states $|k\rangle$ which have different form from the ground state are denoted by ~ (*tilda*) over themselves. Also, using completeness $|i\rangle$ in QRPA we obtain the generalized expression for the left-hand side of the sum rule (1) for the transition matrix elements between different shapes as follows:

$$S(\delta_0, \delta_{ex.}) = \sum_{k>0} \tilde{\omega}_k \left|\sum_{i>0} M_i \langle k|i\rangle\right|^2 = \frac{1}{4}\sum_k \tilde{\omega}_k \left|\sum_i M_i \langle k|i\rangle\right|^2 \quad (19)$$

The overlap of the wave functions $|k\rangle$ and $|i\rangle$ has the following form:

$$\langle k|i\rangle = \frac{1}{2}\sum_{\mu\tau} [g_\mu^i(\tau) w_\mu^k(\tau) + w_\mu^i(\tau) g_\mu^k(\tau)] \quad (20)$$

where

$$g_q^t(\tau) = \psi_q^t + \varphi_q^t, \; w_q^t(\tau) = \psi_q^t - \varphi_q^t \quad (21)$$

Here $\vec{M}_i = \langle i|\vec{M}|0\rangle$, $\delta_{0.}$ and $\delta_{ex.}$ are quadrupole deformation parameters of the ground (core) and excited states, respectively. Further, k and i runs over all the negative and positive solutions of the $D(\omega_t)=0$. If we use (20), we find that general expression for $S(\delta_0,\delta_{ex.})$ given by (19), assumes the form

$$S(\delta_{0.}, \delta_{ex.}) = \frac{1}{4}\sum_{\mu\nu} \tilde{\Omega}_{\mu\nu} d_\mu d_\nu \quad (22)$$

where

$$\tilde{\Omega}_{\mu\nu} = \sum_k \tilde{\omega}_k g_\mu^k g_\nu^k,$$
$$d_q = \sum_i M_i w_q^i, \quad q=\mu,\nu \quad (23)$$

As a matter of convenience, let as calculate sum rule for spin part of the $S(\delta_0,\delta_{ex.})$. In this case by putting $M = \sigma$ in (22), and by exploiting the equations (8)-(13), we obtain:

$$S_\sigma(\delta_0,\delta_{ex.})=\frac{1}{4}\sum_{\mu\nu}\tilde{\Omega}_{\mu\nu}d_\mu d_\nu \qquad (24)$$

where

$$d_q=2\chi_{\sigma\tau}\sum_i\frac{\omega_i F(\omega_i)}{D'(\omega_i)}\frac{\sigma_q L_q}{(\varepsilon_q^2-\omega_i^2)}, \qquad (25)$$

$$\tilde{\Omega}_{\mu\nu}=4\chi_{\sigma\tau}\sum_k\frac{\tilde{\omega}_k}{D'(\tilde{\omega}_k)}\frac{\tilde{\varepsilon}_\mu\tilde{\sigma}_\mu\tilde{L}_\mu\tilde{\varepsilon}_\nu\tilde{\sigma}_\nu\tilde{L}_\nu}{(\tilde{\varepsilon}_\mu^2-\tilde{\omega}_k^2)(\tilde{\varepsilon}_\nu^2-\tilde{\omega}_k^2)} \qquad (26)$$

Let us calculate right-hand side of (24) using analytical properties expressions (25) and (26) for d_q and $\tilde{\Omega}_{\mu\nu}$, respectively. The mathematical formalism of the model and method of calculation sum rules are discussed in details in [3,4]. Since ω_i and ω_κ are the zeros of the function $D(\omega_t)$ of (8), the basic theorem of the theory of residues [14] now allow us to write the expression for d_q and $\tilde{\Omega}_q$ in the form of the contour integral:

$$d_q=\chi_{\sigma\tau}\frac{1}{\pi i}\sum_i\sigma_q L_q\oint_{L_i}\frac{z_i F(z_i)}{(\varepsilon_q^2-z_i^2)D(z_i)}dz_i \qquad (27)$$

$$\tilde{\Omega}_{\mu\nu}=\frac{2\chi_{\sigma\tau}}{\pi i}\oint_{L_i}\sum_k\frac{z_k}{D(z_k)}\frac{\tilde{\varepsilon}_\mu\tilde{\sigma}_\mu\tilde{L}_\mu\tilde{\varepsilon}_\nu\tilde{\sigma}_\nu\tilde{L}_\nu}{(\tilde{\varepsilon}_\mu^2-\tilde{\omega}_k^2)(\tilde{\varepsilon}_\nu^2-\tilde{\omega}_k^2)}dz_k \qquad (28)$$

The contour of the integration is given in Fig.1. Analysis shows that integral (27) contains first-order singularities of the integrand at $z_i=\pm\varepsilon_\mu$ (see Fig.1). The same integral extended over the contour L_∞ is proportional to $1/z^3$ vanishes for large z, and, therefore

$$d_q=-\oint_{L_q}-\oint_{L_{-q}}=2\sigma_q L_q \qquad (29)$$

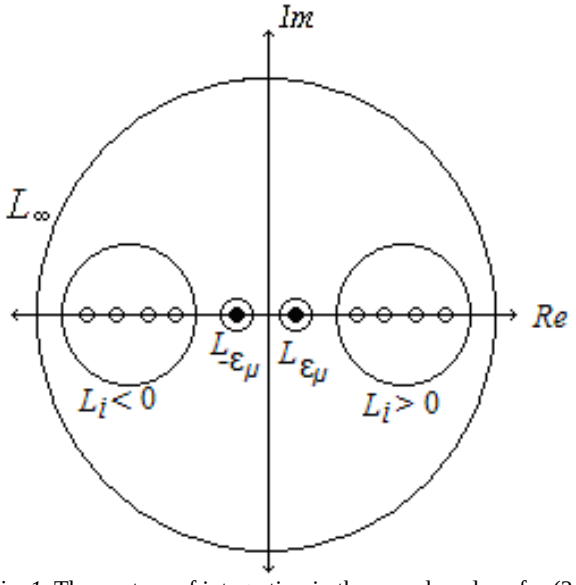

Fig. 1. The contour of integration in the complex plane for (24)

The integral $\Omega_{\mu\nu}$ over the contour L_∞ is equal to zero because as $z\to\infty$, the integrand tends to zero also as $1/z^3$. We note that in the case $\mu\neq\nu$ $z_k=\pm\varepsilon_\mu$ and $z_k=\pm\varepsilon_\nu$ are removable singularities of the integrand (28), after certain manipulations we obtain $\Omega_{\mu\neq\nu}=0$. On other hand diagonal part of $\Omega_{\mu\nu}\,\delta_{\mu\nu}$ contains first-order singularities of the integrand at $z_i=\pm\varepsilon_\mu$ (see Fig.1). Omitting the intermediate computations after laborious calculations, one can obtain the expression for the $\Omega_{\mu\nu}$ in the form:

$$\Omega_{\mu\nu}=2\tilde{\varepsilon}_\mu\delta_{\mu\nu}. \qquad (30)$$

Substituting (29) and (30) into the (24) we obtain

$$S_\sigma(\delta_0,\delta_{ex.})=\sum_\mu\tilde{\varepsilon}_\mu\sigma_\mu^2L_\mu^2 \qquad (31)$$

Applying analogous procedure of calculations for orbital part of the (15) we obtain

$$S_j(\delta_0,\delta_{ex.})=\sum_\mu\tilde{\varepsilon}_\mu j_\mu^2L_\mu^2 \qquad (32)$$

Finally, in general case for left-hand side of EWSR (2) in QRPA by exploiting (31) and (32) for M1 transitions accompanied by change of nuclear form we derived very simple formula

$$S(\delta_0,\delta_{ex.})=\frac{3}{4\pi}\sum_{\mu,\tau}\tilde{\varepsilon}_\mu^\tau L_\mu^2[(g_s^\tau-g_l^\tau)s_\mu^\tau-g_e^\tau j_\mu^\tau]^2 \qquad (33)$$

This is quite interesting result in our model. As can bee seen from (33) the deformation dependence of the EWSR is caused by the interplay of the ground and excited states structure. Thus, for M1 transitions followed by shape changing the two-quasiparticle energies calculate for the shape changed base of the excited states, meanwhile two-quasiparticle matrix elements calculate on the ground state base.. As a natural consequence, when $\delta_{ex.}=\delta_0$ the formula (33) is transformed into the known sum rule expression (18) for magnetic dipole transitions. Thus in the QRPA the EWSR (2) for M1 transitions is satisfied exactly, i.e, the value $S(\delta_0)$ of left hand side of the EWSR (2) calculated with the QRPA is equal the value of the (18) of right hand side of (2) calculated using the HFB ground state wave function). Thus, by using analytical properties of the nuclear matrix elements with help the theory of residue and contour integrals, the known energy weighted sum rule for the magnetic dipole transitions is generalized for transitions to levels which have different forms from the ground state. As can bee seen for transitions followed by shape changing the single-quasiparticle matrix elements calculated for ground states with δ_0 deformation where two-quasiparticle matrix elements calculated for the shape changed excited states.

Numerical calculations are performed in a wide interval of the deformation parameter $\delta_{ex.}$ for ^{140}Ceand ^{196}Pt in the deformed Woods-Saxon potential [15]. The

calculations are performed by using the sum rule (33) for the M1 excitations. The calculated values of the pairing quantities Δ and λ corresponding to the G_N and G_Z and the mean-field deformation parameters δ_0 are shown in Table 1. The isovector spin–spin interaction strength was chosen as $\chi_{\sigma\tau}$= 40/A MeV [11]. In calculating the B(M1) value, we have used bear spin and orbital gyromagnetic factors for nucleons.

The importance of deformation dependence of sum rule can be demonstrated by the comparison of the QRPA results with the experimental data. Dependence of the calculated S in transitional ^{140}Ce and ^{194}Pt and isotopes with respect to deformation parameter $\delta_{ex.}$ are represented in Fig.2. The results were compared with the experimentally observed M1 dipole excitations data from refs. [17] Here we want to study the effect of shape transformation of excited states to the EWSR of the M1 excitation matrix elements for $K^{\pi}=1^{+}$ states.

Table 1. Pairing correlation parameters (in MeV) and δ_0 values

Nuclei	Δ_n	λ_n	$G_N \cdot A$	Δ_p	λ_p	$G_Z \cdot A$	δ_0
^{140}Ce	1.190	-7.581	23.0	1.542	-7.118	24.1	0.090
^{196}Pt	0.815	-6.961	19.2	1.073	-7.087	25.4	0.115

The Ce and Pt isotopes are an important link in the transition region from spherical to deformed shape and from deformed to spherical nuclei, respectively. In Fig. 2, we compare the $\delta_{ex.}$-dependence of the calculated in the QRPA (solid line) $S(\delta_0,\delta_{ex.})$ value for the 1^{+} states with the single-quasiparticle model values (dashed line) and the experimental data for ^{140}Ce [17] and ^{196}Pt in the experimentally investigated energy region of 6.0–9.0 MeV.

As seen from figures the single quasiparticle model exceeds the experimental values almost **two** times in ^{140}Ce. One can observe strong deformation dependence of the calculated sum rule $S(\delta_0,\delta_{ex.})$. The calculation results of the $S(\delta_0,\delta_{ex.})$ show that deviations from the QRPA results below the δ_0 are small. In contrast in the case $\delta_{ex.}>\delta_0$ the sum rules $S(\delta_0,\delta_{ex.})$ for both nuclei change steeply with increasing $\delta_{ex.}$ which leads to the conclusion that in heavy deformed and transition nuclei a quenching M1 strength does occur mainly for $\delta_{ex.}>\delta_0$. Analysis shows that the strong deformation dependence is caused by the interplay of the two-quasiparticle energy $\tilde{\varepsilon}_{ss'}$ and $\delta_{ex.}$. Thus, the results confirm the importance of the shape transformation in the quenching. The theory predicts a giant spin-flip Ml resonance at an energy of 8.0- 9.0 MeV while M1 strength exhibit strong fragmentation in a wide region energy between 2.0 MeV and 12 MeV. Naturally the calculation predicts substantially more dipole strength than is indicated by experiment [17]. This discrepancy indicates some additional strength out of the experimental energy interval of 6.0-9.0 MeV.

To summarize, we have reported on results of the investigation of the deformation dependence of the energy-weight sum rule for M1 dipole excitation strength in the γ-soft ^{140}Ce and ^{196}Pt The calculated sum rules for M1 transitions demonstrate strong deformation dependence. It is shown, that an essential decrease of the M1transitions rates may be due to the change of nuclear shape by the excitations of the nuclear excited states.

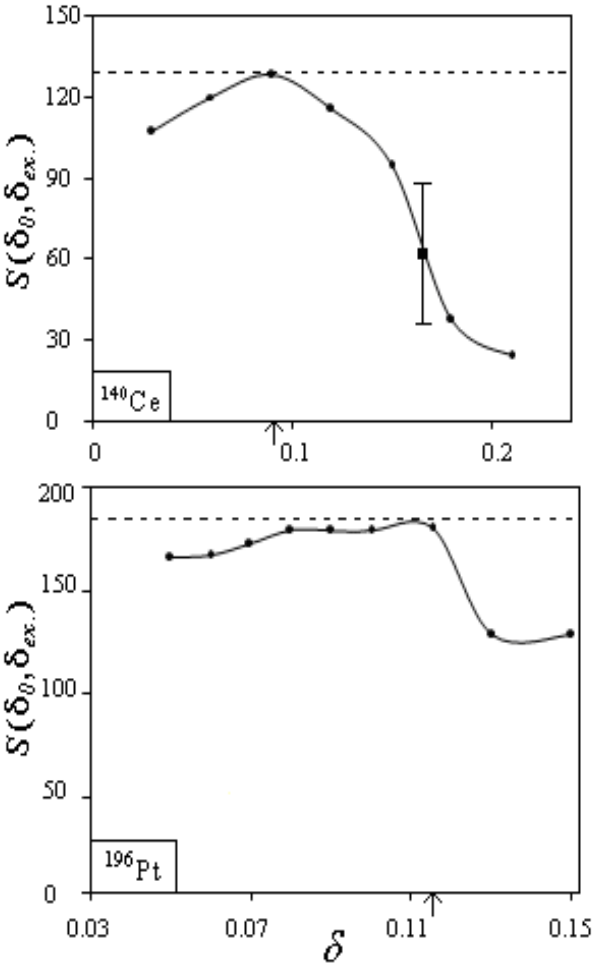

Fig. 2. Deformation dependence of the $S(\delta_0,\delta_{ex.})$ values (in units of MeV$\cdot \mu_N^2$) for the M1 transitions with $K^{\pi} = 1^{+}$ in transitional ^{140}Ce and ^{196}Pt isotopes. The right-hand side of the sum rule (33) is shown by dashed line. The solid line corresponds to the function S calculated by (33). Symbol ↧ denotes the experimental data for EWSR [17]. The value of the ground state deformation parameter δ_0 is marked with the arrows.

[1]. *D.J.Rowe,* Nuclear Collective Motion, Methuen, London(1970)
[2]. *V.G.Solovyov,* Theory of Complex Nuclei (Pergamon Press,New York,1976)
[3]. *A.A.Kulie,v et al, Bullet.* of Acad. of Sci. USSR, Ser.Phys. 53(1989) 2140
[4]. *H.Erbil et al*, Math. & Comp. Applications, 2(1997)1
[5]. *A.Richter,* Prog. Part.Nucl.Phys, 34(1995)261
[6]. *J.L. Wood ,et al,* Phys. Rep. 215 (1992) 101
[7]. *P. Sarriguren, et al,* Nucl. Phys. A 716 (2003) 230
[8]. *A.Petrovichi, et al*.Nucl.Phys.A605 (1996)290
[9]. *E.Ye.Berlovich,et al.*,Phys.Letts. 19(1965)668
[10]. *D. J. Thouless,* Nucl. Phys. 22, (1961) 78
[11]. *S.I.Gabrakov, et al,* Nucl. Phys. A182 (1972) 625
[12]. *S.I. Gabrakov et al*, Sov. Journal of Nuclear Physics 12 (1970)82
[13]. *A. G. Sveshnikov and A. N. Tikhonov*. The theory of functions of a complex variable, Nauka Moscow, 1971
[14]. *J. Dudek, T.Werner,* J. Phys. G 4 (1978) 1543
[15]. *S.Raman, et al,*At.Data Nucl.Data Tables 78, (2001)1
[16]. *R.M. Laszewski, et al,* Phys. Rev. C34 (1986) 2013n

STUDY ON ($n,^3He$) FUSION REACTIONS CROSS SECTIONS USING OPTICAL MODEL

MUSTAFA H. BÖLÜKDEMİR, EYYUP TEL
Gazi University, Faculty of Arts and Science, Department of Physics, Ankara-TURKEY
hicabi@gazi.edu.tr

Non-elastic cross-sections have been calculated by using optical model for ($n,^3He$) reactions at 22.5 MeV energy. The empirical formula including optical model non-elastic effects by fitting two parameters for the ($n,^3He$) reaction cross-sections have been suggested. Reaction Q-values depending on the asymmetry term effect for the ($n,^3He$) reaction have been investigated. The obtained cross-section formula with new coefficients has been compared with the experimental data and discussed. It has seen that the fit of formula in this paper is in good agreement with the experimental data.

The neutron scattering cross section data have a critical importance on fusion reactor (and in the fusion-fission hybrid reactors) for the calculation of nuclear transmutation rates, nuclear heating and radiation damage due to gas formation. New nuclear cross-section data are needed to improve theoretical predictions of neutron production, shielding requirements, activation, radiation heating, and materials damage. So, many experimental techniques have recently been developed to obtain and detect neutrons of different energies and measure the cross–sections of the different neutron–induced reactions, such as (n,p), (n,t), ($n,^3He$) and (n,α). These data are necessary to develop more nuclear theoretical calculation models in order to explain nuclear reaction mechanisms and the properties of the excited states in different energy ranges. Furthermore, the experimental cross–section data of neutron is very important for understanding the binding energy systematics, the basic nucleon–nucleus interaction, nuclear structure and refined nuclear models [1-9].

Through (p,xn) and (n,xn) nuclear reactions, neutrons are produced and are moderated by heavy water in the target region and light water in the blanket region. These neutrons are subsequently captured on ^{3}He, which flows throughout the blanket system, to produce tritium via the (n,p) reaction In the fusion-fission hybrid reactor, tritium self-sufficiency must be maintained for a commercial power plant. For self-sustaining (D-T) fusion driver tritium breeding ratio should be greater than 1.05 [10,11].

Empirical and semi–empirical formulas are applied for the creation of systematic studies. Empirical expressions contain the exponential dependence of cross–sections upon the number of neutrons and protons in nuclei. The empirical formulae use the evaporation model and ignore an important role of the pre–equilibrium mechanism of particle emission for medium and heavy nuclei. But the semi–empirical systematic are based on the use of analytical expressions for calculation of particle emission within the frame of pre–equilibrium exciton and evaporation models [5-7, 12–14].

In this study, we have investigated reaction Q-values depending on the asymmetry term effect for the ($n,^3He$) reaction cross sections at 22.5 MeV neutron incident energy by using 13 experimental ($n,^3He$) reaction cross–section data points for ^{27}Al, ^{31}P, ^{41}K, ^{51}V, ^{55}Mn, ^{59}Co, ^{67}Zn, ^{68}Zn, ^{75}As, ^{93}Nb (3 dot) and ^{115}In taken from EXFOR [15]. The neutron non-elastic cross-sections were obtained by using the optical potential parameters of Wilmore-Hodgson [16] for ($n,^3He$) reactions. We have suggested new parameters of semi-empirical formula including optical model non-elastic effects by fitting two parameters for the ($n,^3He$) reaction cross-sections at 22.5 MeV. The coefficients were determined from by least-squares fitting method. The obtained cross-section formulae with new coefficients have been compared with the experimental data [15] and discussed.

Optical Model and Neutron Reaction Systematic Cross Sections Calculations: The reaction cross sections applications of statistical and thermodynamical methods to the calculation of nuclear process for heavy nuclei go back to the fundamental work of Weisskopf and Ewing [17]. The statistical evaporation theory is a widely-used description for reactions at low energies. At energies in the range of several tens of MeV the pre-equilibrium models have been successful. Reaction cross-sections are also used in intra-nuclear-cascade calculations [18] and in the calculation of the nuclear reaction efficiency correction for detectors [19].

The optical reaction cross-sections at all the required energies and particle-target combinations are usually obtained bay a numerical solution of the Schrödinger equation for several partial waves. This involves a large amount of computation time. Also, where more than one global optical potential appears in the literature for the same projectile it is quite laborious to repeat the calculations for each of the sets to see the effect on the final results. The form of the optical potential is [20],

$$U(r,E)=-U_N(r,E)+V_c(r)+U_{so}(r) \qquad (1)$$

where V_c is the Coulomb potential due to a uniformly-charged sphere with radius r_c, U_{so} is the spin-orbit potential and U_N is the complex central potential taken as,

$$U_N(r,E)=V_R(E)f(x_R)+i\left[W_V(E)f(x_V)+W_S(E)g(x_S)\right] \qquad (2)$$

where $f(x_R)=\left[1+\exp(x_R)\right]^{-1}$ and $x_R=\left(r-r_R A^{1/3}\right)/a_R$, $g(x_S)=-4df(x_S)/dx_S$ (Woods-Saxon derivative) or $\exp\left(-x_S^2\right)$ (Gaussian). Here x_V and x_S are defined in the same manner with appropriate radius parameters r_S, r_V

and diffuseness parameters a_S, a_V. The spin-orbit potential U_{so} is, given by,

$$U_{SO}(r)=\lambda_\pi^2(l.\sigma)\frac{1}{r}\frac{d}{dr}f(x_{SO})V_{SO} \quad (3)$$

Using this form of the potential several extensive analyses of differential elastic, polarization and reaction cross-section data have been carried out by various workers resulting in global parameter sets [21–25].

Empirical and semi–empirical formulae for (*n,³He*) reaction cross–sections : Nuclear models are frequently needed to provide estimate of the neutron–induced reaction cross–sections, especially if the experimental data are not obtained or on which they are hopeless to measure the cross–sections; due to the experimental difficulty. In the literature, some systematic studies have been done for the (*n,³He*) reaction cross–sections around 14 MeV [21–25]. The empirical cross–sections of reactions induced by fast neutrons can be approximately given as Levkovskii's formula [26]

$$\sigma(n,x)=C\sigma_{ne}\exp[a\,s] \quad (4)$$

where σ_{ne} is the cross–section of non–elastic interaction of the incident neutron with a target nucleus, the coefficients C and a are the fitting parameters for different reactions, which they are determined by a least squares method and $s=(N-Z)/A$ is asymmetry parameter. The neutron non–elastic cross–section is written as

$$\sigma_{ne}=\pi r_0^2(A^{1/3}+1)^2 \quad (5)$$

with r_0 = 1.2 fm. Eq.(4) represents the product of the two factors, each of which might be assigned to a stage of nuclear reaction within the framework of the statistical model of nuclear reactions. The exponential term represents the escape of the reactions products from a compound nucleus. In addition, this term in Eq.(4) has a strong $(N-Z)/A$ dependence. This case has already been shown by several authors for neutron–induced reaction cross–sections [8,9]. Eqs.(4) and (5) represent the Levkovskii formulae which are the most widely used and these formulae cover a broad range of mass number with expressions giving the (*n,p*) and (*n,α*) cross–sections. Levkovskii's formula have been provided theoretical support by Pai et al. [27,28], who compared with statistical–model calculations the experimental 14 MeV (*n,p*) cross–sections of nuclei for $32\le A\le 98$. They obtained good agreement between theory and experiment, by introducing an effective Q value into the statistical–model calculation. The (*n,p*) and (*n,α*) cross–sections are strongly depend on their Q values. If the Q value decreases smoothly with increasing mass number for a given element, the cross–sections also decrease smoothly. The experimental (*n, p*) and (*n,α*) cross–sections decrease smoothly with increasing mass number depending Q value for a given element [29]. The same effects are expected for the (*n,³He*) and (*n,charged particle*) cross–sections.

The systematic study of (*n,³He*) reaction cross–section has been performed by Qaim [30]. Qaim suggested an empirical formula of the cross–sections of the (*n,³He*) reactions with dependent on asymmetry parameter as given below

$$\sigma(n,\,^3He) = 0.0846(A^{1/3}+1)^2\exp(-1.6467s) \quad (6)$$

Eq.(5) describes the contribution of the equilibrium emission in the (*n,³He*) reaction. This formula can be obtained using only the simple evaporation model without taking into account the angular momentum [31].

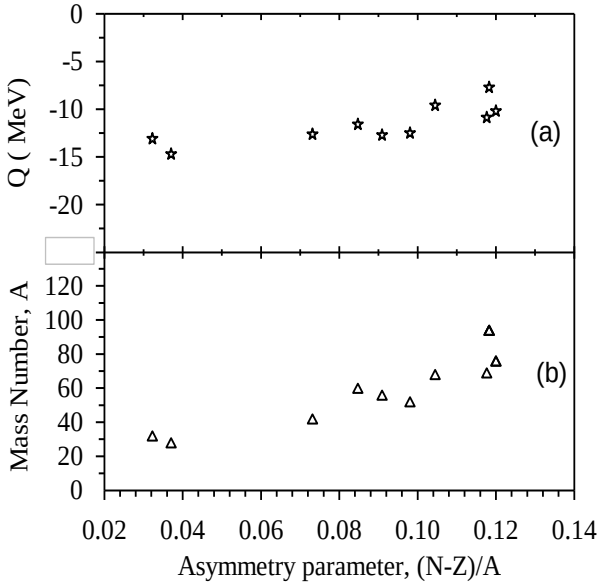

Fig.1.a. (*n,³He*) reaction Q-values by depending up on asymmetry parameter; b. Asymmetry parameter values for the target nuclei mass number-A used in this work.

We have used the number of 13 experimental (*n,³He*) reaction cross sections data taken from EXFOR file for fitting procedure [15]. We have used the nuclei which their mass numbers change from A = 27 to 93, the atomic numbers change from Z = 13 to 41. The asymmetry parameter values used in this work have changed from s= 0.037 to 0.118.

We have calculated non-elastic cross-sections by using the optical potential parameters of Wilmore-Hodgson [16] for (*n,³He*) reactions at 22.5 MeV energy. The neutron non-elastic cross-section calculations have been performed in the framework of the optical model using SCAT 2 computer code [32].

In Fig. 1a, we have shown the asymmetry parameter values depending up on the (*n,³He*) reaction Q-values at 22.5 MeV. As can be obviously seen from Figs. 1a, the reaction Q-values exhibit an almost linear increase from s= 0.037 to 0.118. The asymmetry parameter values depending up on the target nuclei mass number-*A* have been shown in Fig. 1b. The asymmetry parameter values have been associated as a linear with the target nuclei mass number-*A*.

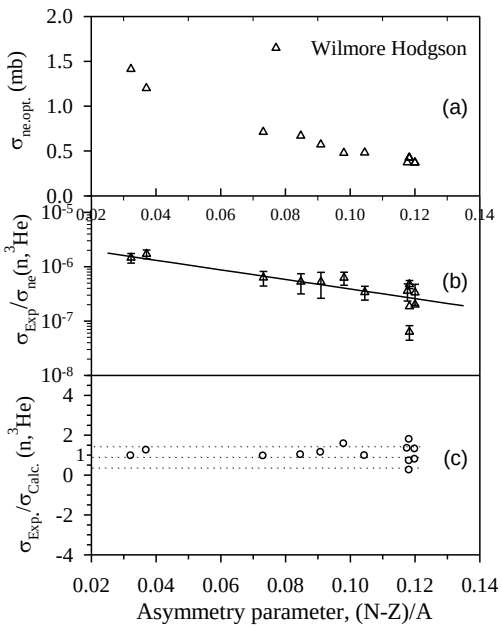

Fig.2. a) Optical model neutron non-elastic cross-section from Wilmore-Hodgson built-in parameters by depending upon asymmetry parameter, b) The experimental points were fitted with $\sigma(n,^3He)=C^{'}\sigma_{ne-opt}\exp[bs]$ and correlation coefficient for Wilmore-Hodgson (*solid line*) built-in parameters was determined as $R=0.96$, c) Ratios of the ($n,^3He$) experimental cross sections to the cross–sections calculated with empirical and semi-empirical formulae.

As it seen in Fig. 2a, non-elastic cross-sections values exhibit a gradient and they are also increasing with increasing asymmetry parameter.

In the present study, we have calculated non-elastic cross-sections by using optical model for ($n,^3He$) reactions at 22.5 MeV energy and also we have suggested new coefficients that the semi-empirical cross-sections of reactions induced by neutron can be approximately expressed as follows,

$$\sigma(n,\,^3He) = C^{'}\,\sigma_{ne-opt}\,\exp\left[bs\right] \qquad (7)$$

where the coefficients $C^{'}=2.96\times10^{-6}$ and b=-20.31 are the fitting parameters determined from the least-squares method. The $\sigma_{ne-opt.}$ represents the optical model neutron non-elastic cross-section.

The fitting parameters of the empirical formula taken into consideration the non-elastic cross-sections have been determined for all target nuclei having mass number for the ($n,^3He$) reactions cross-sections at 22.5 MeV (in *Fig*.2b). The ratios of the ($n,^3He$) experimental cross sections to the cross-sections calculated with semi-empirical formulae, in the present work, have been given in Fig.2c. The fitting formula proposed in our study give very good description of experimental data.

[1] *C.Rubbia,* CERN/LHC/96-11 (EET) (1996)
[2] *E.Betak et al.*, Nucl. Sci. Eng., 132, 295 (1999)
[3] *S.M. Qaim,* Handbook of Spectroscopy vol. 3**,** (CRC Press, Inc., Florida-USA 1981)
[4] *R.A.Forrest*, AERE R 12419, Harwell, UK, (1986)
[5] *A.Yu. Konobeyev and Yu. A. Korovin*, Nucl. Instr. and Meth. B 103, 15 (1995)
[6] *C.H. M. Broeders and A. Yu. Konobeyev*, Nucl. Phys. A 780, 130 (2006)
[7] *C.H.M. Broeders and A. Yu. Konobeyev*, Appl. Radiat. and Isot. 65, 454 (2007)
[8] *M.Belgaid and M. Asghar,* Nucl. Instr. and Meth. B 142, 463 (1998)
[9] *M.Belgaid, T. Segueni, F. Kadem and M. Asghar*, Nucl. Instr. and Meth. B 201, 545 (2003)
[10] *S. Şahin, et al.,* Fusion Techn., 10, 84 (1986)
[11] *M.Übeyli and E.Tel,* J.Fusion Energy, 22, 2 (2003)
[12] *V.M. Bychkov, A.B. Pashchenko, and V.I.Plyaskin,* Voprosi Atomnoy Nauki I Techniki. Jadernye Konstanty (Nucl. Constants) 4(31), 48 (1978)
[13] *V.M. Bychkov, V. N. Manokhin, A. B. Pashchenko and V. I. Plyaskin*, Voprosi Atomnoy Nauki I Techniki. Jadernye Konstanty (Nucl.Constants) 1(32), 27 (1979)
[14] *A.Yu. Konobeyev and Yu. A. Korovin*, Atom. Energy 85, 556 (1998)
[15] *V.Mclane*, CSISRS experimental nuclear data file, Nat.Nuclear Data Center Brookhaven National Laboratory, http://www.nndc.bnl.gov/(1997), EXFOR is accessed on line at http://www.nndc.bnl.gov/exfor
[16] *D.Wilmore and P. E. Hodgson*, Nucl. Phys., 55, 673 (1964)
[17] *F.Weisskopf, D.E.Ewing*, Phys.Rev.,57,472 (1940)
[18] *K.Kikuchi, M. Kawai*, Nucl.Matter and Nuclear Reactions(Amsterdam,North Holland,1968),p. 262
[19] *M.Q. Makino, C.N. Waddel, R.M. Eisberg*, Nucl. Inst. Meth., 60, 109 (1968)
[20] *C.M. Perey, F.G. Perey*, Atomic Nucl. Data Tables 13, 293 (1974)
[21] *I.Boztosun*, Phy. Rev. C, 66(2) 024610 (2002)
[22] *A.Chatterjee, K.H.N. Murthy, S.K. Gupta*, Pramana, 16(5) 391 (1981)
[23] *S.Ait-Tahar*, Nucl. Phys., 13, 121 (1987)
[24] *S.M. Qaim*, IAEA-TEC-DOC-457, 89 (1998)
[25] *Z.Zhixiang ,Z. Delin*, Nucl.Sci.Eng. 99, 367 (1988)
[26] *V.N. Levkovski*, Sov. J. Phys. 18, 361 (1974)
[27] *H.L. Pai, et al.*, Nucl. Phys. A 164, 526 (1971)
[28] *H.L.Pai,D.G.Andrews*,Can.J. Phys. 56, 944 (1978)
[29] *I.Kumabe*, J. Nucl. Sci. Tech. 18(8), 563 (1981)
[30] *S.M. Qaim*, J. Inorg. Nucl. Chem. 32, 1799 (1970)
[31] *S.M. Qaim, H. V. Klapdor, and H. Reiss*, Phys. Rev. C 22, 1371 (1980)
[32] *O. Bersillon*, SCAT-2 code, OCDE-NEA-Data Bank-Computer Program Service, Package ID. NEA0829/03 (1991)

MODELS FOR DEAD TIME CORRECTIONS AT X AND GAMMA RAY DETECTORS

SALİH M. KARABIDAK[1], UĞUR ÇEVİK[1], NECATİ ÇELİK[1], AHMET ÇELİK[2]

[1]Karadeniz Technical University, Sciences and Arts Faculty, Department of Physics, Trabzon, TURKEY salihm@ktu.edu.tr

[2]Giresun University, Sciences and Arts Faculty, Department of Physics, Giresun, TURKEY

Electronic devices are used to detection of radiation due to x or gamma rays. The dead time of the counting system is based on time limitations of these electronic devices that used at the counting system. In this study, an analytic equation for the dead time of the counting system was formulated. Counting losses were determined by this dead time formula. In according to counting losses, integral and differential corrections based on the live time of the counting system were proposed. Each this models was applied to different spectrum samples. Calculations from corrected spectrums were found to be closer to theoretical calculation.

I. INRODUCTION

The ionization which is generated by incident radiation within the active volume of the semiconductor detector results in charged particles which are transport by an electric field to the detector electrodes. The production and collection of the ionization is subject to random statistical variations which depend on the incident energy and detector media. An intrinsic resolution limitation exists in the process of converting incident radiation into an electrical signal [1]. The output signal undergoes various processing steps in order to correctly acquired and analyzed in semiconductor X-ray detectors. The time required to collect the charged particles produced by the incident radiation is important in many applications. If the collection time is not considerably short compared to the peaking time of the amplifier, a loss in the recovered signal amplitude occurs [2].

An optimized spectrometer system provides the best energy resolution obtainable within a given set of experimental constrains. System optimization requires the proper selection of equipment and knowledge of the compromise of resolution and count rate performance in any system. The detector/preamplifier combination is the most critical component of the system electronics. The world's best amplifier cannot compensate for poor signal-to-noise or count rate limitations caused by improper selection of the system front end. Selection of the proper amplifier will enhance the performance of the good detector/preamplifier combination. The system resolution is determined primarily by the source/detector interaction, detector/preamplifier combination, pulse processor shaping and the system count rate [1].

The major constraint on the throughput of modern gamma-ray spectrometers is the time required to collect the charge produced by ionizing radiation in the active detector volume and subsequently the pulse processing by the electronics [3]. In all detector systems, there will be a minimum amount of time called dead time of the counting system, which must separate two events in order that they are recorded as two separate pulses. During this dead time, the system cannot respond to other incoming photons and these events cannot be counted and thus can be lost. One of the major problems confronting the user of multichannel pulse analyzers is to correct the results for counts lost due to the analyzer dead time. This problem can be solved automatically by carrying out all counting runs for a known or measured total instrument live time rather than for real time [4].

Two models of the dead time behavior of counting systems have come into common usage: paralyzable and non-paralyzable response. These two models predict the same first-order losses and differ only when true event rates are high [5]. In high count rate events, both of the two modes are not applicable. The correction for the dead time losses becomes an important task of the data evaluation [6].

The troubling aspect of non-paralyzable model is the singularity at $m\tau = 1$and the fact that a maximum observed counting rate of $1/\tau$ is approached in the limit as n approaches infinity. In paralyzable model, the observed counting rate becomes zero at high count rate. Also, it should be noted that this model cannot be explicitly solved for n_0. But this model solves a transcendental equation to obtain the true counting rate. In addition, the observed counting rate is either doubled valued or does not exist above a maximum value given by $\exp(-1)/\tau$ [7].

Galushka [8] suggested a correction technique for dead time effects by inserting additional pulses into the actual series of registered events, and Muller [8] analyzed the validity of this method. Loss-free counting was introduced before the advent of digital spectrometer by Westphal [9], improving on Harms' differential dead time correction method [10]. The count losses arise from the dead time due to the pile-up rejector and ADC conversion time. A few methods are suggested to compensate for the count losses. One of these methods is zero dead time using a DSPECPLUS TM digital spectrometer. Statistical analysis related to these correction methods were made by a few researchers and a number of deficiencies of these correction methods were identified [1,3,12-14].

II. EXPERIMENTAL ARRANGEMENT

For integral correction model formed the first part of this study, the K x-ray intensities were measured for the pure Se and Zn elements by using 59.54 keV photons emitted by a 50 mCi ^{241}Am annular radioactive source. A Canberra Ultra Low Energy Ge detector (GUL 0035 model) with a resolution of 150 eV at 5.9 keV, Genie 2000 spectroscopy software, preamplifier (Model 2008) of Canberra instruments, Tennelec TC 244 spectroscopy amplifier and multiport II ADC and MCA of Canberra

instruments were used to count K_α photons emitted from samples (see *Fig. 1*).

For differential correction model formed the second part of this study, ^{22}Na and ^{60}Co standard point radioactive sources with energies ranging from 1173 to 1332 keV have been used. A Canberra HpGe detector (GC 1519 model) with a resolution of 1.9 keV at 1332.5 keV was used to measurements (see *Fig.1*).

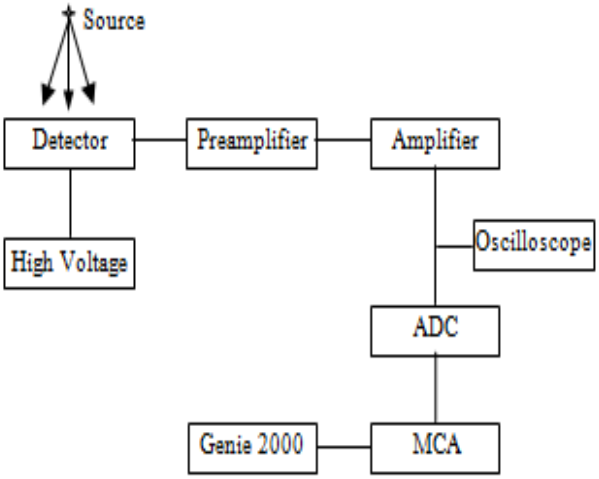

Fig. 1 Scheme of spectrometry system was used in the measurements

III. DETERMINATION OF THE SYSTEM DEAD TIME

There is a minimum resolving time which is the response to the peaking time of systems, T_P. The minimum resolving time, T_R, with respect to the peaking time of system is a discriminating time between two pulses. Minimum resolving times in response to peaking time of amplifier were calculated by Karabıdak et al. [15, 16] and the following equation given the relation between them was obtained.

$$T_R = B_2 T_P^2 + B_1 T_P + A \tag{1}$$

where A, B_1 and B_2 coefficients are 3.73746, -0.03894 and 0.00507, respectively. It is important whether the minimum resolving time is more than conversion time of ADC. Then the effective system dead time is simply determined by in the following equations [15,16]

$$T_D = T_P + T_R \tag{2}$$

Or

$$T_D = T_P + 1.5\ \mu s + T_C \tag{3}$$

A Wilkinson ADC with a 100 MHz clock is used for the measurement. Therefore, the ADC conversion time for the relevant energy lines can be calculated [17]

$$T_C = \frac{E}{\Delta E} T_{C\ lock} \tag{4}$$

where E is energy line, ΔE is energy per channel [18] and T_{Clock} is amplifier operation frequency.

IV. MODELS FOR COUNTING LOSSES CORRECTIONS

4. 1- Integral (Analytic) Correction Model

This method is based on a measuring principle on the total live time. Also, count rate corrections based on live time can be ideal in the count rates which are not predominate the system dead time. In additional, on a mathematical essence the principle of the live time is an integral mathematics. The integral mathematics is correct to be applied only to stationary Poisson processes. It should be note that time-invariant Poisson processes are valid in experimental studies with long half-life radionuclide. It is possible to estimate the probability of losing a specific number k of counts in a dead time of length T_D. Since we deal with a Poisson process, this probability is given by [10,19-20]

$$P_k = \frac{(nT_D)^k}{k!} e^{-nT_D} \tag{5}$$

where n is the count rate in each channel. Total dead time of counting system can be taken into consideration in integral dead time correction. Then total dead time (TDT) in each channel is given by [15]

$$TDT = Count * T_D \tag{6}$$

where Count is count in each channel. Therefore total dead time of counting system (STDT) overall channel is calculated by Karabıdak et al. [15]

$$STDT = \sum_{i=channel\ number} (TDT)_i \tag{7}$$

The correction counting (CC) is given by [15]

$$CC = Count + L \tag{8}$$

where L is counting losses due to the system dead time.

4. 2- Differential Correction (Decaying Source) Model

This part of the study includes count rate corrections based on differential mathematic and the proposed model in this study is ideal in the count rates which are predominant the system dead time. Differential mathematics also can be correctly applicable to processes with any changes intensity Poisson process in time. The corrections which are done by paralyzable and non-paralyzable models are problematic because of limited expressed above. Then, decaying source model was proposed by Karabıdak [21]. Count rate in this model is given by

$$n = \frac{1}{T_D}(1 - e^{-n_0\ T_D}) \tag{9}$$

where n_0 is true count rate. In decaying source approach, the dead time of both amplifier and ADC depends on the relationship between the minimum resolving time and

conversion time of ADC. In this situation, the average dead time of a compound system, $\bar{T}_{CS}$, can be given by

$$\bar{T}_{CS} = \frac{\sum_{i}^{m}\left(B_2T_P^2 + (B_1+1)T_P + A\right)Count_i + \sum_{m+1}^{\text{Channel Number}}\left(T_P + 1.5 + \frac{E_{m+1}}{\Delta E}\right)Count_{m+1}}{\sum_{i}^{\text{Channel Number}} Count_i} \quad (10)$$

In this case, corrected count, CC, in each channel at counting period is given by

$$CC = n_0 T_{\text{Real}} \quad (11)$$

where T_{Real} is the real time of the counting system.

In this part of the study, the amplifier and ADC of counting system also were simulated. Randomly generated photons were assumed to come directly to the amplifier input terminal. Interval between generated two consecutive photons was set to a fixed value depending on input counting rate. The counting rate simulation program (SAYOR) was coded in Fortran 77 programming language. The SAYOR simulation program was running for possible three peaking time likes, 3, 8 and 12 µs of the amplifier. Decaying source model and simulation results were compared.

V. RESULTS AND DISCUSSIONS

Corrected count rate graphic obtained from dead time correction in the counting system with integral correction (analytic) model suggested in this study is shown in *Fig. 2*. Also peak shape is same at each state. Hence both measurement count and correction count is obey the same statistic.

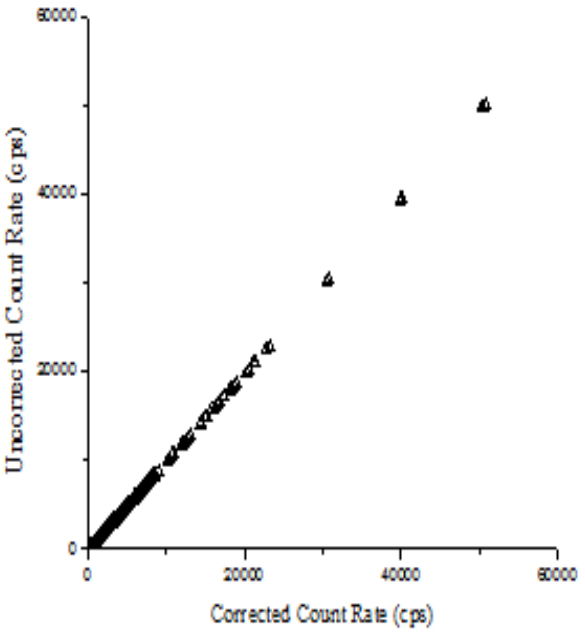

Fig.2 Variation of the uncorrected rate *n* as a function of the corrected rate n_0 for analytic model of dead time losses

An application of proposed analytic method in this work is given in *Table 1*. Application was performed as calculate to cross sections of pure Se element according to three peaking time of amplifier. These cross sections were also compared to the theoretical ones.

Table 1 An application example: K_α and K_β cross sections of pure Se element [15]

	Peaking Time (8 µs)		
Cross section	Uncorrected	Corrected	Theoretical*
Se $\sigma_{K\alpha}$ (b/atom)	124.0± 9.9	127.3± 6.4	129.0
Se $\sigma_{K\beta}$(b/atom)	18.3± 1.5	18.8± 1.0	20.9

*J.H. Scofield [22]

In decaying source model, for 8 µs the peaking time of the amplifier, the simulation result of the output counting rates of both the amplifier and ADC and the directly ADC in response to input counting rates can be seen in *Fig. 3*. For both, while up to a specific value of the input counting rate is increased as a linear, after that value this linearity is corrupted. The same behavior can be observed for 3 and 12 µs peaking times of the amplifier.

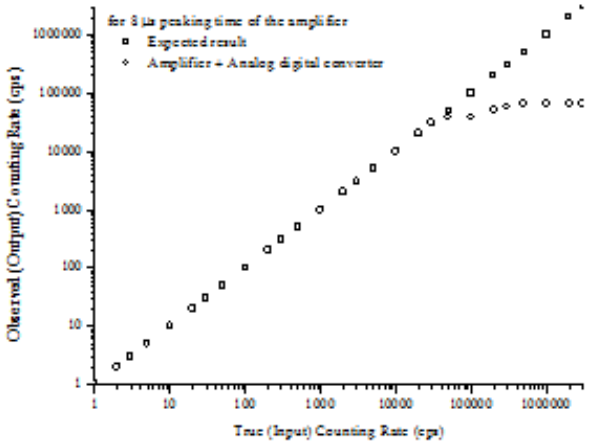

Fig.3 Changing output counting rates with input counting rates for 8 µs peaking time of the amplifier

Also, the relationship between the output counting rates and input counting rates were determined by the proposed model in this study. The results obtained by simulation program were compared with the results of the proposed model. A pretty good agreement was obtained between the theoretical model and the simulation program. A comparative example between the model results and the simulation program can be seen in *Fig. 4*.

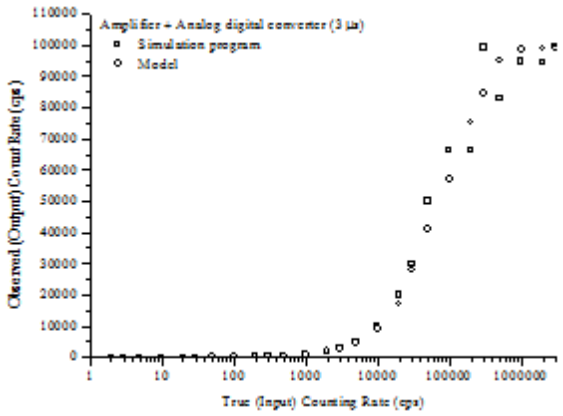

Fig. 4 For 3 µs peaking time of the amplifier, comparing proposed model in this study with simulation program in both the amplifier and the ADC case

Corrected count rate graphic obtained from dead time correction in the counting system with differential correction (decaying source) model suggested in this study is shown in *Fig. 5*.

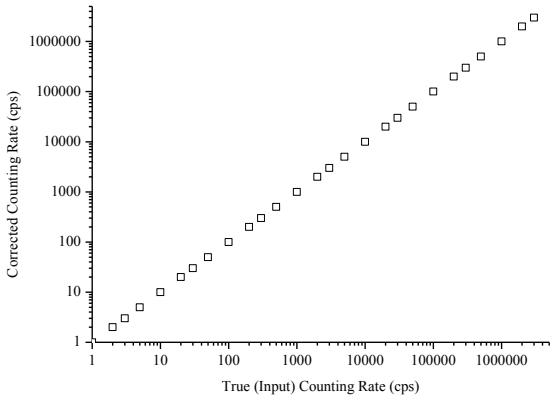

Fig. 5 Variation of the corrected rate *n* as a function of the true rate n_0 for decaying source model of dead time losses

An application related with decaying source model was performed to calculate the mass attenuation coefficients of marble sample. Results were given in *Table 2*. These mass attenuation coefficients were also compared to the theoretical ones. As seen in Table 2, these values calculated with correction made by model proposed in this study are better than ones calculated without correction.

Table 2 An application example: Mass attenuation coefficients of marble sample.

Source	Energy (keV)	Mass Attenuation Coefficients (cm^2/gr)		
		Uncorrected	Corrected	Theoretical [a]
^{22}Na	1274	0.052±0.005	0.054±0.005	0.056
^{60}Co	1173	0.049±0.006	0.051±0.006	0.058
	1332	0.052±0.006	0.053±0.006	0.054

[a]XCOM [23]

[1]. Tennelec Instruction Manual TC 244 Amplifier, 1986.

[2]. *Gerardi, L. Abbene and et. al.,* Nucl. Instr. Meth. A 2006, 571, 380.

[3]. *S. Pommé* Nucl. Instr. Meth. A 2001, 474, 245.

[4]. *M.O. Deighton* Nucl. Instr. Meth. 1961, 14, 48.

[5]. *G.F. Knoll* "Radiation Detection and Measurement" Third Edition, 2000, Jhon Wiley and Sons Inc.

[6]. *L. Szentmiklosi, T. Belgya and et al.,* Journ. Radioanal. Nucl. Chem. 2007, 271, 439.

[7]. *R.P. Gardner, L. Liu* Appl. Radiat. Isot. 1997, 48, 1605.

[8]. *A.N. Galushka* "The method of Poisson's fluxes of accidental events registration" Communication through J.W. Müller, 1993.

[9]. *G.P. Westphal* Nucl. Instr. Meth. 1979, 163, 189.

[10]. *J. Harms* Nucl. Instr. Meth. 1967, 53, 192.

[11]. *S. Pommé* Appl. Radiat. Isot. 1998, 49, 1213.

[12]. *S. Pommé, J. P. Alzetta and et. al.,* Nucl. Instr. Meth. A 1999, 422, 388.

[13]. *S. Pommé* Nucl. Instr. Meth. A 1999, 437, 481.

[14]. *S. Pommé* Appl. Radiat. Isot. 2008, 66, 941.

[15]. *S. M. Karabıdak, U. Çevik, S. Kaya* Nucl. Instr. Meth. A 2009, 603, 361.

[16]. *S. M. Karabıdak, U. Çevik, S. Kaya* in: Turkish Physical Society 25th International Physical Congress, Bodrum, 2008.

[17]. *H. Spieler* Introduction to Radiation Detectors and Electronics, 1999.

[18]. Canberra Germanium Detectors User's Manual, 1998.

[19]. *Y. Kawada, S. Kobayashi and et. Al.,* Appl. Radiat. Isot., 1998, 49, 1123.

[20]. *J. W. Müller* Some remarks on the Galushka method, Rapport BIPM 93/2, 1993.

[21]. *S. M. Karabıdak* Doctorate Thesis, unpublised, KTU, Turkey, 2010.

[22]. *J. H. Scofield* Lawrence Livermore Laboratory, Livermore, Report UCRL-51326, 1973.

[23]. *M.J. Berger, J.H. Hubbell,* 1987 XCOM: Photon cross-sections on a personnel computer (version 1.2), NBSIR85-3597, National Bureau of Standarts, Gaithersburg, MD, USA, for version 3.1, 1999, http://physics.nist.gov/.

THE STUDY OF GAMOW-TELLER TRANSITION STRENGTH FOR SOME ODD MASS ISOTOPES

NECLA ÇAKMAK
Department of Physics, Karabük University,
78050 Karabük, TURKEY, necla@karabuk.edu.tr

The violated commutation condition between the total shell model Hamiltonian and Gamow Teller operator (GT) has been restored by Pyatov method (PM). An additional effective interaction term h_0 coming from this restoration contributes to the total Hamiltonian. The eigenvalues and eigenfunctions of the restored Hamiltonian with the separable residual Gamow-Teller effective interactions in the particle-hole (ph) and particle-particle (pp) channels have been solved within the framework of proton-neutron Quasi Random Phase Approximation (pnQRPA).

I. INTRODUCTION

Nuclear β decay and electron capture processes are very important mechanisms to understand the nuclear structure. These process are also essential ingredients in calculations of supernova formation [1,2]. The investigation of GT 1^+ excited states provides useful information about the validity of theories related to the r-process [3] and the double beta decay [4].

The study of GT strength distribution is essential to get information about the GT transition properties. Nucleon charge exchange reactions are one of the most efficient ways in the experimental study of GT transitions. The different calculations are needed to reproduce the experimental data. One type is the pnQRPA method using separable GT residual interactions. The pnQRPA method with a separable GT interaction was first applied using a spherical harmonic oscillator basis [5], and was extended to deformed nuclei [6] using a deformed phenomenological single –particle basis. The pnQRPA formalism have been introduced over the years [7,8], including the effective interaction in the pp channel [9-11]. As known, the sensitivity of the $GT^{(+)}$ transition amplitude to the strength parameter of the pp interaction leads to an important difficulty in the 2νββ decay calculations. The higher versions of the pnQRPA method were developed and applied for decreasing the sensitivity of the β^+ transition amplitude to the pp interaction constant.

The aim of this study is only to present a different approximation for the solution of the problem concerning the total $GT^{(+)}$ strength. The idea of the definition of pnQRPA Hamiltonian in a different form instead of using the extended versions of the pnQRPA provides a physical motivation to solve the mentioned problem. According to the approximation, the Hamiltonian of a nucleus can be defined such a way that its commutation relation with GT operator is conserved. Hence, the broken commutation relation between Hamiltonian and GT operators due to shell model approximation should be restored. Pyatov method is a good option for this restoration. This method was originally introduced to restore Galilean invariance of the pairing interaction [12] and then extended to the restoration of some symmetry properties of total Hamiltonian and its nuclear part. Here, the same method has been applied for the restoration of the broken commutation condition between total Hamiltonian operator and GT operator.

In this study, the beta decay process odd mass nuclei have been searched by considering the GT effective interactions in the ph and pp channels.

II. THEORETICAL FORMALISM

Let us consider a system of nucleons in a spherical symmetric average field with pairing forces. In this case, Hamiltonian of the system in quasi-particle representation is given as:

$$\hat{H}_0 = \hat{H}_{SQP} + \hat{h}_{GT}^{ph} + \hat{h}_{GT}^{PP} \tag{1}$$

$\hat{H}_{SQP}$ is the single quasi-particle (SQP) Hamiltonian and described by:

$$H_{SQP} = \sum_{\tau,jm} \varepsilon_{j_\tau} \alpha^+_{j_\tau m_\tau} \alpha_{j_\tau m_\tau} \qquad (\tau = n, p) \tag{2}$$

where ε_{j_τ} is the single quasi particle energy of the nucleons with angular momentum j_τ, and the $\alpha^+_{j_\tau m_\tau}(\alpha_{j_\tau m_\tau})$ is the quasi particle creation (annihilation) operator. $\hat{h}_{GT}^{ph}$ and $\hat{h}_{GT}^{pp}$ are the residual charge-exchange spin-spin interactions in particle-hole and particle-particle channels, respectively, and given by the formula:

$$\hat{h}_{GT}^{ph} = 2\chi_{GT}^{ph} \sum_\mu T_\mu^+ T_\mu^-,$$
$$\hat{h}_{GT}^{pp} = -2\chi_{GT}^{pp} \sum_\mu P_\mu^+ P_\mu^-, \qquad \mu = 0, \pm 1 \tag{3}$$

with

$$T_\mu^+ = \sum_{\substack{n,p \\ \rho,\rho'}} \left\langle n\rho \left| \sigma_\mu + (-1)^\mu \sigma_{-\mu} \right| p\rho' \right\rangle a^+_{n\rho} a_{p\rho'},$$

$$P_\mu^+ = \sum_{\substack{n,p \\ \rho,\rho'}} \left\langle n\rho \left| \sigma_\mu + (-1)^\mu \sigma_{-\mu} \right| p\rho' \right\rangle a^+_{n\rho} a^+_{p\rho'},$$

$$T_\mu^- = (T_\mu^+)^+, \qquad P_\mu^- = (P_\mu^+)^+ \tag{4}$$

where $a^{+}_{\tau\rho}(a_{\tau\rho})$ is the nucleon creation (annihilation) operator, σ_μ is the spherical component of the Pauli operator. In the quasi-particle representation, the $T^{\pm}_{\mu}$ and $P^{\pm}_{\mu}$ operators are introduced as:

$$T^{+}_{\mu}=\sum_{n,p}[\frac{1}{\sqrt{2}}(\bar{d}_{np}D^{+}_{np}+d_{np}D_{np})+(\bar{b}_{np}C^{+}_{np}-b_{np}C_{np})],$$

$$P^{+}_{\mu}=\sum_{n,p}[\frac{1}{\sqrt{2}}(b_{np}D^{+}_{np}-\bar{b}_{np}D_{np})+(d_{np}C^{+}_{np}+\bar{d}_{np}C_{np})]$$

by using the definitions from [13] for the following quantities:

$$D_{np}\equiv\sum_{\rho=\pm1}\rho\alpha^{+}_{n,-\rho}\alpha_{p,-\rho}\,,\quad D^{+}_{np}\equiv\sum_{\rho=\pm1}\rho\alpha^{+}_{p,-\rho}\alpha_{n,-\rho}$$

$$C_{np}\equiv\frac{1}{\sqrt{2}}\sum_{\rho=\pm1}\alpha_{p\rho}\alpha_{n,-\rho}\,,C^{+}_{np}\equiv\frac{1}{\sqrt{2}}\sum_{\rho=\pm1}\alpha^{+}{}_{n,-\rho}\alpha_{p\rho}$$

$$b_{np}\equiv\sqrt{2}\langle n|\sigma_\mu|p\rangle u_p\vartheta_n,\ \bar{b}_{np}\equiv\sqrt{2}\langle n|\sigma_\mu|p\rangle u_n\vartheta_p$$

$$d_{np}\equiv\sqrt{2}\langle n|\sigma_\mu|p\rangle u_p u_n\,,\quad \bar{d}_{np}\equiv\sqrt{2}\langle n|\sigma_\mu|p\rangle\vartheta_n\vartheta_p$$

where $\vartheta_\tau(u_\tau)$ is the occupation (inoccupation) amplitude which is obtained in the BCS calculations; $|n\rangle$ and $|p\rangle$ are Nilsson single particle states; D_{np} corresponds to quasi-particle scattering operator; $C^{+}_{np}(C_{np})$ is a two quasi-particle creation (annihilation) operator for neutron-proton pair and it satisfies the following bosonic commutation rules in the quasi-boson approximation:

$$[C_{np},C^{+}_{n'p'}]\approx\delta_{nn'}\delta_{pp'},\qquad [C_{np},C_{n'p'}]=0$$

$$[D_{np},D^{+}_{n'p'}]\approx\delta_{nn'}\delta_{pp'},\qquad [D_{np},D_{n'p'}]=0$$

In QRPA method, the wave function of the odd mass (with odd neutron) nuclei is given by

$$|\Psi^{j}{}_{I_nK_n}\rangle=\Omega^{j+}_{I_nK_n}|0\rangle= \tag{5}$$

$$[N^{j}_{I_n}\alpha^{+}_{I_nK_n}+\sum_{i,I_p,K_p}R^{I_nI_p}_{ij}Q^{+}_{i}\alpha^{+}_{I_pK_p}]|0\rangle$$

It is that wave function (5) is formed by superposition of one and three quasi-particle (one quasiparticle + one phonon) states. The amplitudes corresponding to the states, $N^{j}_{I_n}$ and $R^{I_nI_p}_{ij}$, are fulfilled by the normalization condition

$$\left(N^{j}_{I_n}\right)^2+\sum_{i,I_p}\left(R^{I_nI_p}_{ij}\right)^2=1$$

Solving the equation of motion

$$[H,\Omega^{j+}_{I_nK_n}]|0\rangle=\omega^{j}_{I_nK_n}\Omega^{j+}_{I_nK_n}|0\rangle \tag{6}$$

The dispersion equation for excitation energies $\omega^{j}_{I_nK_n}$, corresponding to states given in eq.(5).

III. RESULTS AND DISCUSSION

Numerical calculations have been performed for some odd mass nuclei. Nilsson single particle energies and wave functions have been calculated with Woods-Saxon potential. Calculations have been performed within the framework of a pn-QRPA, including the schematic residual spin-isospin interaction between nucleons in the particle-hole and particle-particle channels. The effective Gamow-Teller interaction is considered and the appropriate value for the interaction constants χ_{ph} and χ_{pp} are chosen, it is possible to make the transition rate values closer to the experimental ones. In the calculations, the following values for these constants have been used: $\chi_{ph}=5.2/A^{0.7}$MeV and $\chi_{pp}=0.52/A^{0.7}$MeV units.

The calculated log(ft) values for β^+ and β^- transitions are given in the Table 1 and Table 2, respectively. As seen from Table 1 and Table 2, the values of beta transition log(ft) increase and thus become closer to the experimental value when the pp channel term is taking into account for the charge-exchange spin-spin forces. The fixed χ_{ph} and χ_{pp} values for the transitions in Table 1 and Table 2 are presented in Table 3.

Table 1. The log(ft) values for the ground state $1^+\rightarrow0^+$ GT β^+ transition calculated by different models.

Transition	Exp.[14]	SQP	PM	SM
$^{51}Cr\rightarrow{}^{51}V$	5.39	4.05	5.36	5.40
$^{127}Ba\rightarrow{}^{127}I$	5.20	4.82	5.25	7.76

Table 2. The log(ft) values for the ground state $1^+\rightarrow0^+$ GT β^- transition calculated by different models.

Transition	Exp.[14]	SQP	PM	SM
$^{57}Mn\rightarrow{}^{57}Fe$	5.40	6.66	5.25	4.10
$^{99}Mo\rightarrow{}^{99}Tc$	6.21	6.84	6.20	4.00

Table 3. The fixed parameter values of the PM and SM log(ft) values.

Transition	χ_{ph}	χ_{pp}
$^{51}Cr\rightarrow{}^{51}V$	1.0	0.5
$^{127}Ba\rightarrow{}^{127}I$	1.0	0.5
$^{57}Mn\rightarrow{}^{57}Fe$	1.25	1.25
$^{99}Mo\rightarrow{}^{99}Tc$	1.25	0.5

IV. CONCLUSION

The Gamow-Teller transitions in the odd mass nuclei have been searched by using two different methods within the framework of the pnQRPA approximation. Firstly, the pnQRPA procedure has been applied for the Hamiltonian containing an effective interaction term coming from the restoration. Secondly, the same procedure has been followed for schematic model (SM) Hamiltonian. Thus, the effect of the restoration on the total GT^+ transition strength has been determined by giving a comparison of the best results of both methods. The log(ft) values in Pyatov Method are in good agreement with the corresponding experimental data.

[1]. *H.A. Bethe, G.E. Brown,* J. Applegate, *J.M.Lattimer,* Nucl. Phys. A, 1979, 324, 487.

[2]. *G.M. Fuller, W.A. Fowler, M.J. Newman*, Astrophys. J. Suppl. Ser., 1980, 42, 447; *G.M.Fuller, W.A. Fowler, M.J. Newman*, Astrophys. J. Suppl. Ser., 1982, 48, 279; *G.M.Fuller, W.A. Fowler, M.J. Newman*, Astrophys. J., 1982, 252, 715; *G.M. Fuller, W.A.Fowler, M.J. Newman*, Astrophys. J., 1985, 293, 1.

[3]. *I.N.Borzov*, Nucl.Phys.A, 2006, 777,645-675.

[4]. *M. S. Yousef, V.A. Rodin, A. Faessler, and F.Simkovic*, Phys. Rev. C, 2009, 79, 014314.

[5]. *J.A. Halbleib, and R.A. Sorensen*, Nucl. Phys. A, 1967, 98, 542.

[6]. *J. Krumlinde and P. Möller*, Nucl. Phys. A, 1984, 417, 419;*P. Möller. and J. Randrup*, Nucl. Phys. A, 1990, 514, 1.

[7]. *G.F. Bertsch and S.F. Tsai*, Phys. Rep., 1975, 18, 127; *D. Cha*., Phys. Rev. C, 1983, 27, 2269; *J.Suhonen, T. Taigel and A. Faessler*, Nucl. Phys. A, 1988, 486, 91; *N.Van Giai,. Ch. Stoyanov and V.V. Voronov*, Phys. Rev. C, 1998, 57, 1204; *J.Engel, M. Bender., J. Dobaczewski, W.Nazarewicz and R. Surnam*, Phys. Rev. C, 1999, 60, 014302;*M. Bender., J. Dobaczewski, J. Engel, W. Nazarewicz*, Phys. Rev. C, 2002, 65, 954322.

[8]. *P. Sarriguren, E. Moya de Guerra, A. Escuderos and A.C. Carrizo*, Nucl. Phys. A, 1998, 635, 55.

[9]. *J. Engel, P. Vogel and M.R. Zirnbauer*, Phys. Rev. C, 1988, 37, 731; *V.A. Kuzmin and V.G. Soloviev*, Nucl. Phys. A, 1988, 486, 118; *K. Muto and H.V. Klapdor*, Phys. Lett. B, 1988, 201, 420.

[10]. *K. Muto, E. Bender and H.V. Klapdor,* Z. Phys. A, 1989, 333, 125; *M. Hirsch, A. Staudt, K. Muto and H.V. Klapdor-Kleingrothaus*, Nucl. Phys. A, 1991, 535, 62; *K. Muto, E. Bender, T. Oda and H.V. Klapdor-Kleingrothaus*, Z. Phys. A, 1992, 341, 407.

[11]. *H. Homma, E. Bender, M. Hirsch, K. Muto, H.V.Klapdor-Kleingrothaus and T. Oda*, Phys. Rev. C, 1996, 54, 2972.

[12]. *N.I. Pyatov, D.I. Salamov*, Nucleonica, 1977, 22, 127.

[13]. *Necla Çakmak,* Ph.D. Thesis, 2008, Anadolu University.

[14]. *K.Pham, et al.,* Phys.Rev.C, 1995, 51, 526

.

GROUND-STATE PROPERTIES OF AXIALLY DEFORMED Sr ISOTOPES IN SKYRME-HARTREE-FOCK-BOGOLIUBOV METHOD

A.H. YILMAZ[1], T. BAYRAM[1,2], M. DEMIRCI[1], B. ENGIN[1]

[1]*Karadeniz Technical University, Physics Department, 61080, Trabzon, TURKEY*

[2]*SinopUniversity, Physics Department, Sinop ,TURKEY*

hakany@ktu.edu.tr, tuncay42bayram@yahoo.com

Binding energies, the mean-square nuclear radii, neutron radii, quadrupole moments and deformation parameters to axially deformed Strontium isotopes were evaluated using Hartree-Fock-Bogoliubov method. Shape coexistence was also discussed. The results were compared with experimental data and some estimates obtained within some nuclear models. The calculations were performed for Sly4 set of Skyrme forces and for a wide range of the neutron numbers of Sr isotopes.

Strontium isotopes exhibit many interesting nuclear properties. These nuclei which have neutron numbers close to magic number 50 are known well deformed. It is hard to describe theoretically because their rms radii and isotope shifts behave in a manner showing the change of the slope at the neutron magic nucleus A=88. So, Sr nuclei are attractive to study both experimentally and theoretically [1-5].

The aim of this work is to analyse some ground-properties of even Sr isotopes using Skyrme-Hartree-Fock-Bogoliubov method for a wide range of neutron numbers.

A two-body Hamiltonian of a system of fermions can be expressed in terms of a set of annihilation and creation operators ($c, c^{\dagger}$):

$$H = \sum_{n_1 n_2} e_{n_1 n_2} c^{\dagger}_{n_1} c_{n_2} + \tfrac{1}{4} \sum_{n_1 n_2 n_3 n_4} \bar{v}_{n_1 n_2 n_3 n_4} c^{\dagger}_{n_1} c^{\dagger}_{n_2} c_{n_4} c_{n_3}, \qquad (1)$$

where $\bar{v}_{n_1 n_2 n_3 n_4} = \langle n_1 n_2 | V | n_3 n_4 - n_4 n_3 \rangle$ are anti-symmetrized two-body interaction matrix elements. In the Hartree-Fock-Bogoliubov (HFB) method, the ground-state wave function $|\Phi\rangle$ is defined as the quasiparticle vacuum where the quasiparticle operators ($\alpha, \alpha^{\dagger}$) are connected to the original particle operators via the linear Bogoliubov transformation:

$$\alpha_k = \sum_n \left(U^*_{nk} c_n + V^*_{nk} c^{\dagger}_n \right),$$
$$\alpha^{\dagger}_k = \sum_n \left(V_{nk} c_n + U_{nk} c^{\dagger}_n \right) \qquad (2)$$

In terms of the normal ρ and pairing κ one-body density matrices, defined as

$$\rho_{nn'} = \langle \Phi | c^{\dagger}_{n'} c_n | \Phi \rangle = (V^* V^T)_{nn'},$$

$$\kappa_{nn'} = \langle \Phi | c_{n'} c_n | \Phi \rangle = (V^* U^T)_{nn'} \qquad (3)$$

the expectation value of the Hamiltonian (1) could be expressed as an energy functional

$$E[\rho, \kappa] = \frac{\langle \Phi | H | \Phi \rangle}{\langle \Phi | \Phi \rangle}$$
$$= Tr[(e + \tfrac{1}{2}\Gamma)\rho] - \tfrac{1}{2} Tr[\Delta \kappa^*], \qquad (4)$$

where

$$\Gamma_{n_1 n_3} = \sum_{n_2 n_4} \bar{v}_{n_1 n_2 n_3 n_4} \rho_{n_4 n_2}, \quad \Delta_{n_1 n_2} = \tfrac{1}{2} \sum_{n_3 n_4} \bar{v}_{n_1 n_2 n_3 n_4} \kappa_{n_3 n_4}.$$

The HFB energy (4) has the form of local energy density functional for Skyrme forces,

$$E[\rho, \tilde{\rho}] = \int d^3 r \mathcal{H}(r), \qquad (5)$$

where

$$\mathcal{H}(r) = H(r) + \tilde{H}(r)$$

is the sum of the mean field and pairing energy densities. Variation of the energy (5) with respect to ρ and $\tilde{\rho}$ of results in Skyrme HFB equations:

$$\sum_{\sigma'} \begin{pmatrix} h(r, \sigma, \sigma') & \tilde{h}(r, \sigma, \sigma') \\ \tilde{h}(r, \sigma, \sigma') & -h(r, \sigma, \sigma') \end{pmatrix} \begin{pmatrix} U(E, r\sigma') \\ V(E, r\sigma') \end{pmatrix}$$
$$= \begin{pmatrix} E + \lambda & 0 \\ 0 & E - \lambda \end{pmatrix} \begin{pmatrix} U(E, r\sigma') \\ V(E, r\sigma') \end{pmatrix} \qquad (6)$$

Where λ is chemical potential and where local fields $h(r, \sigma, \sigma')$ and $\tilde{h}(r, \sigma, \sigma')$ can be calculated in the coordinate space by using following explicit expressions:

$$h(r, \sigma, \sigma') = -\nabla M_q \nabla + U_q$$
$$+ \tfrac{1}{2i} \textstyle\sum_{ij} \left(\nabla_i \sigma_j B_{q,ij} + B_{q,ij} \nabla_i \sigma_j \right),$$

$$\tilde{h}(r, \sigma, \sigma') = V_0 \left(1 - V_1 \left(\frac{\rho}{\rho_0} \right)^{\gamma} \right) \tilde{\rho}_q, \qquad (7)$$

where

$$M_q = \frac{\hbar^2}{2m} + \frac{1}{4}t_1\left[\left(1+\tfrac{1}{2}x_1\right)\rho - \left(x_1+\tfrac{1}{2}\right)\rho_q^2\right] + \tfrac{1}{4}t_2\left[\left(1+\tfrac{1}{2}x_2\right)\rho - \left(x_2+\tfrac{1}{2}\right)\rho_q^2\right],$$

$$B_{q,ij} = -\frac{1}{4}(t_1x_1+t_2x_2)\boldsymbol{J}_{ij} + \frac{1}{4}(t_1-t_2)\boldsymbol{J}_{q,ij} + \tfrac{1}{2}W_0\textstyle\sum_{ijk}\varepsilon_{ijk}\nabla_k(\rho+\rho_q),$$

$$U_q = t_0\left[\left(1+\tfrac{1}{2}x_0\right)\rho - \left(x_0+\tfrac{1}{2}\right)\rho_q\right] + \tfrac{1}{4}t_1\left[\left(1+\tfrac{1}{2}x_1\right)(\tau-\Delta\rho) - \left(x_1+\tfrac{1}{2}\right)\left(\tau_q-\tfrac{3}{2}\Delta\rho_q\right)\right] + \tfrac{1}{4}t_2\left[\left(1+\tfrac{1}{2}x_2\right)(\tau+\Delta\rho) + \left(x_2+\tfrac{1}{2}\right)\left(\tau_q+\tfrac{1}{2}\Delta\rho_q\right)\right] + \tfrac{1}{12}t_3\rho^\alpha\left[\left(1+\tfrac{1}{2}x_3\right)(2+\alpha)\rho - 2\left(x_3+\tfrac{1}{2}\right)\rho_q + (1-x_3)\tfrac{\alpha}{\rho}\right] - \frac{\gamma V_0 V_1}{2\rho}\left(\frac{\rho}{\rho_0}\right)^\gamma\textstyle\sum_q\tilde{\rho}_q^2 - \tfrac{1}{8}(t_1x_1+t_2x_2)\textstyle\sum_{ij}\boldsymbol{J}_{ij}^2 + \tfrac{1}{8}(t_1-t_2)\textstyle\sum_{q,ij}\boldsymbol{J}_{q,ij}^2 - \tfrac{1}{2}W_0\textstyle\sum_{ijk}\epsilon_{ijk}\nabla_k\left[\boldsymbol{J}_{ij}+\boldsymbol{J}_{q,ij}\right].$$

where index q labels the neutron (q=n) or proton (q=p) densities, while densities without index q denote the sums of proton density and neutron density. $H(\boldsymbol{r})$ and $\hat{H}(\boldsymbol{r})$ depend on the particle local density $\rho(\boldsymbol{r})$, pairing local density $\tilde{\rho}(\boldsymbol{r})$, kinetic energy density $\tau(\boldsymbol{r})$ and spin-current density $\boldsymbol{J}_{ij}(\boldsymbol{r})$. Details can be found in [6-8].

Recently, Stoitsov et al. presented a code called HFBTHO for axially deformed solution of the Skyrme HFB equations [7]. Stoitsov et al. solved the HFB equations by expanding quasiparticle wave functions on a finite basis in this code; so, the quasiparticle spectrum E_k becomes discretized. Since $E_k > 0$ and $\lambda < 0$ the lower components $V_k(\boldsymbol{r}\sigma)$ are localized functions of **r**, the density matrices

$$\rho(\boldsymbol{r}\rho,\boldsymbol{r}'\sigma') = \sum_k V_k(\boldsymbol{r}\sigma)V_k^*(\boldsymbol{r}'\sigma'),$$

$$\tilde{\rho}(\boldsymbol{r}\rho,\boldsymbol{r}'\sigma') = -\sum_k V_k(\boldsymbol{r}\sigma)U_k^*(\boldsymbol{r}'\sigma'),$$

are localized. The orthogonality relation to the single-quasiparticle HFB wave functions reads

$$\int d^3\boldsymbol{r}\sum_\sigma\left[U_k^*(\boldsymbol{r}\sigma)U_{k'}(\boldsymbol{r}\sigma) + V_k^*(\boldsymbol{r}\sigma)V_{k'}(\boldsymbol{r}\sigma)\right] = \delta_{k,k'},$$

and the norms of lower components N_k given as

$$\mathrm{N_k} = \int \mathrm{d^3\,r}\sum_\sigma|\mathrm{V_k(r\sigma)}|^2,$$

and the total number of particles defined as

$$\mathrm{N} = \int \mathrm{d^3\,r\rho(r)} = \sum_\mathrm{n}\mathrm{N_k}.$$

The best solutions of Skyrme-Hartree-Fock-Bogoliubov equations are in the coordinate space for spherical nuclei, because equation (6) reduces to a set of radial differential equations. However, for deformed nuclei, the solution of a deformed HFB equation in coordinate space is difficult and time-consuming task. Stoitsov et al. used the method proposed by Vautherin [9] to adapt the code for shorter solution time. In addition to, Stoitsov et al. treated separately the mean field and the pairing field via Hartree-Fock theory with added Lipkin-Nogami pairing. In this study this code was used.

The Strontium nuclei considered here are even nuclei with mass number A=76 up to 100. All of these isotopes are open-shell nuclei both in protons and neutrons. The number of shells taken into account is 20 and 20 for the fermionic and bosonic expansion. For solution, the basis parameter β_0 used for the calculations has been taken as 0.3.

There are number of parametrization sets for prediction of the nuclear ground state properties [10-12]. The parameter set SLy4 [12] was used in the present calculation and given in Table 1.

In Fig.1, it was shown that the binding energy per nucleon for Strontium nuclei using SLy4 parameter set in the Skyrme HFB method. Also, for comparison, empirical values, predictions of the finite-range droplet model (FRDM) [14], predictions of the extended Thomas-Fermi with Strutinsky Integral (ETF-SI) model and predictions of the relativistic mean field theory with NL-SH parameter set was showed [13]. The minimum in the binding energy per nucleon is observed at the magic neutron number N=50 in the SHFB method as well as the other nuclear models.

Table 1. SLy4 parameter set of the Skyrme forces used in this study.

Parameter	Sly4
$t_0(MeVfm^3)$	-2488.9
$t_1(MeVfm^5)$	486.82
$t_2(MeVfm^5)$	-546.40
$t_3(MeVfm^4)$	13777
x_0	0.8340
x_1	-0.3440
x_2	-1.0
x_3	1.3540
$W_0(MeVfm^5)$	123
γ	1.0

The total binding energies for Sr isotopes using SHFB with SLy4 parameter set were well produced by our calculation. The maximal error is 3 MeV for total binding energy which corresponds approximately to 0.05 MeV per particle.

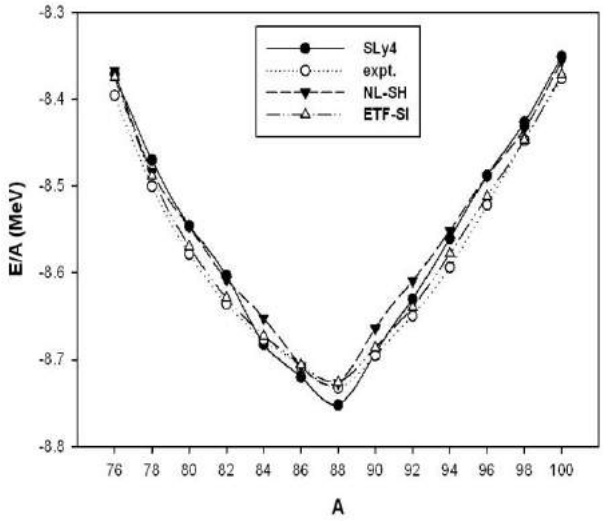

Fig.1 The binding energy per nucleon for Sr isotopes in the Skyrme HFB method with the force SLy4. The calculations from the FRDM [14], ETF-SI and relativistic mean field theory with the force NL-SH are also shown for comparison [13].

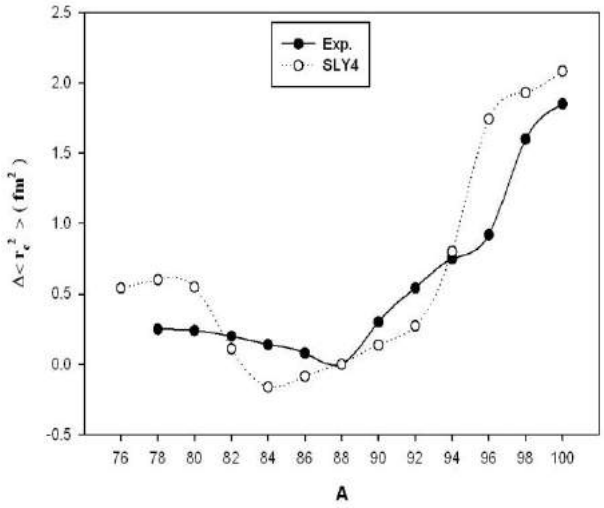

Fig.2 The isotope shifts for Sr nuclei calculated with the SLy4 parameters set. Experimental isotope shifts are also shown [15].

Isotopic shift are closely related to deformation properties and shapes. In Fig.2, the isotope shifts normalized to $< r_c^2 >_{A=88}$ for Sr isotopic chains are shown. Also, empirical data obtained from atomic laser spectroscopy [13] are shown. The predictions for isotopic shift are not totally agreement with experimental values. On the other hand, for isotopes with A>88, the agreement with empirical values is better than nuclei have A<88.

In Fig.3 values of neutron radii and rms charge radii for Sr isotopic chains are presented. General behaviour of charge radii from the lighter isotopes to the heavier ones decreases trend up to the magic isotopes. At below the magic numbers, lighter nuclei posses higher charge radii then the heavier which are closed neutron shell nucleus. This situation is agreement with kink showed in Fig.2. Adding further neutrons, the charge radii of nuclei which are heavier than the closed neutron shell starts increasing. On the other hand, also neutron radii show a kink about the neutron shell closure. However, general trend of neutron radii increases with adding neutron.

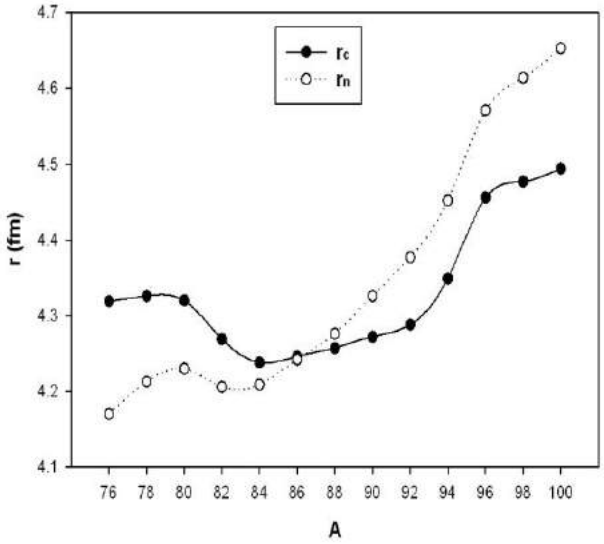

Fig. 3 The neutron and rms charge radii of Sr isotopic chains obtained in the SHFB method using Sly4 set.

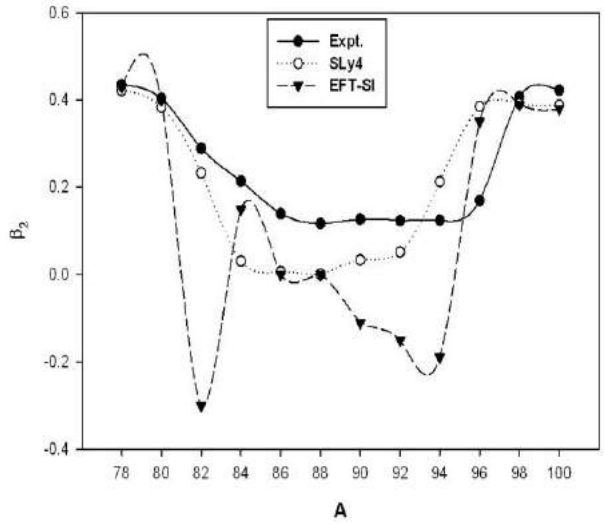

Fig.4 The quadrupole deformation β_2 for Sr isotopic chains using Sly4 parameter set. The predictions of the mass models ETF-SI and experimental values are showed for comparison.

In this work, the calculations have been performed in the Skyrme HFB method for both the prolate and oblate configurations. Results of the calculation predict deformed shapes for a large number of Sr isotopes. In Fig.4, quadrupole deformation (β_2) for the shape corresponding to the lowest energy are shown. Also predictions of finite range drop model (FRDM), predictions of ETF-SI and experimental values are shown

for comparison. As seen from the Fig.4, the predictions to the shape of Sr nuclei using axially deformed Skyrme HFB method are better than the predictions of FRDM and ETF-SI. In isotopic chain of Sr, Skyrme HFB method gives a well defined prolate shape for lighter isotopes. An addition of a few neutrons below the closed neutron shell leads to oblate shape because the shape of nuclei turn into spherical ones as nuclei approach the magic neutron number. Nuclei above this magic number (N=50) revert to the prolate shape.

In Fig.5, prolate-oblate shape coexistence of neutron-rich Sr isotopes was shown as a function of mass number. Several isotopes exhibit a second minimum beside lowest minimum. This implies shape coexistence. The prolate shape results being a few hundreds keV lower in energy than the oblate one.

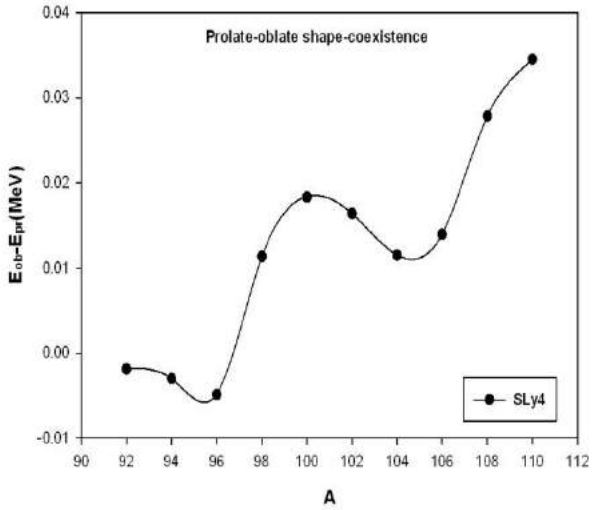

Fig.5 The prolate-oblate shape coexistence of neutron-rich Sr isotopes obtained using SHFB method.

In Table.2, calculated quadrupole values of proton, neutron and total quadrupole values for Sr nuclei are shown.

Table2.The calculated quadrupole values of Sr nuclei

	Q_p(barn)	Q_n(barn)	Q(barn)
^{74}Sr	3,579	3,127	6,707
^{76}Sr	3,718	3,567	7,286
^{78}Sr	3,693	3,739	7,433
^{80}Sr	3,442	3,513	6,935
^{82}Sr	2,070	2,176	4,246
^{84}Sr	0,249	0,328	0,577
^{86}Sr	0,062	0,076	0,138
^{88}Sr	0,006	0,006	0,012
^{90}Sr	0,270	0,435	0,704
^{92}Sr	0,405	0,721	1,126
^{94}Sr	1,908	0,932	4,840
^{96}Sr	3,752	5,702	9,454
^{98}Sr	3,844	6,119	9,964
^{100}Sr	3,873	6,347	10,220

As a result of this work, Skyrme HFB theory has been employed to obtain the ground-state properties of the isotopic chain of Sr. Region which are near the Sr nuclei are interesting because nuclei in this region have large transformations of shapes and exhibit anomalous behaviour in the isotope shifts. Using SLy4 parameters set in the Skyrme HFB method, isotopic shifts and large deformation were predicted clearly. On the other hand, Skyrme HFB method predicts prolate-oblate shape coexistence in heavy Sr nuclei. The binding energies of Sr nuclei have been described successfully in the Skyrme HFB method. The parabolic behaviour of the binding energy per nucleon was obtained well. Curve of the binding energies per nucleon are agreement with experimental curve and with the extensive mass fits of FRDM. Also, this curve is consistent with RMF theory using NL-SH parameter set. All of these reasons Skyrme HFB method provide good description of the ground state nuclear properties to isotopic chain of Sr.

[1]. [*A. Baran, W. Hohenberger,* Phys. Rev. C, 1995, 52, p. 2242-2245
[2]. *P. Bonche, H. Flocard, P. H. Heenen*, Nucl. Phys. A, 1991, 523, p. 300-312
[3]. *D. Hirata, H. Toki, I. Tanihata, P. Ring,* Phys. Lett. B, 1993, 314, p. 168-172
[4]. *P. Ring, Y. K.Gambhir, G. A. Lalazissis,* 1997, 105, p. 77-97
[5]. *P. Bonche, H. Flocard, P. H. Heenen, S. J. Krieger, M. S. Weiss,*Nucl. Phys. A, 1985, 443, p. 39-63
[6]. *P. Ring, P. Shuck,* The Nuclear Many-Body Problem, 1980, *Springer-Verlag*
[7]. *M. V. Stoitsov, J. Dobaczewski, W. Nazarewicz, P.Ring*, Comput. Phys. Comm., 2005, 167, p.43-63
[8]. *W. Greiner, J. A. Maruhn,* Nuclear Models, 1995, *Springer-Verlag*
[9]. *D. Vautherin,* 1973, Phys. Rev. C, 7, p. 296-316
[10]. *J. Bertel, P. Quentin, M. Brack, C. Guet, H.–B.Hakkansson,* Nucl. Phys. A, 1982, 386
[11]. *A. Baran, J. L. Egido, B. Nerlo-Pomorska, K.Pomorski, P. Ring, L. M. Robledo,* J. Phys. G., 1995, p. 657-668
[12]. *E. Chabanat, P. Bonche, P. Haensel, J. Meyer, R.Schaeffer,* Nucl. Phys. A, 1997, 627, p. 710-746
[13]. *G. A. Lalazissis, M. M. Sharma,* Nucl. Phys. A, 1995, 586, p. 201-218
[14]. *P. Möller, J. R. Nix, W. D. Myers, and W.J.Swiatecki,* At. Data Nucl. Data Tables, 1995, 59, p. 185-381
[15]. *F. Buchinger, E. B. Ramsay, E. Arnold, W. Neu, R.Neugart, K. Wendt, R. E. Silverans, P. Lievens, L. Vermeeren, D. Berdichevsky, R. Fleming, D.W.L.Sprung, G. Ulm,* Phys. Rev. C, 1990, 41, p. 2883-2897.

AN EXPERIMENTAL AND MONTE CARLO SIMULATION STUDY ON EQUIVALENT DOSE RATE OF TINCAL, ULEXITE AND COLEMANITE FOR 4,5 MeV MONOENERGETIC ^{241}Am/Be NEUTRON SOURCE

TURGAY KORKUT[a,♣], ABDULHALIK KARABULUT[a,b], GÖKHAN BUDAK[a,b]

[a] *Department of Physics, Faculty of Science and Art, Ağrı İbrahim Çeçen University, Ağrı, Turkey*

[b] *Atatürk University, Science Faculty, Physics Department, Erzurum, 25240, Turkey*

^{241}Am/Be radioactive sources are used as fast neutron source. Fast neutrons usually can be converted thermalized neutrons or can be absorbed with paraffin wax. ^{241}Am/Be radioactive sources release both γ-rays and neutron particles. So to shield ^{241}Am/Be radioactive sources both Pb metal and paraffin wax are used as shielding materials usually. Tincal, ulexite and colemanite are boron ores and boron can absorb thermalized neutron. Because tincal, ulexite and colemanite include B (boron), H and a lot of other elements, instead of Pb metal and paraffin wax, these boron ores may be used as shielding materials. In this study, measurements have been made to determine equivalent dose rates of tincal, ulexite and colemanite.

Boron, situated between metals and non-metals, is a semiconductor material. Turkey, the richest boron mining deposits of world, has about 64 percent of the world boron reserves. Colemanite, tincal and ulexite ($Ca_2B_6O_{11}.5H_2O$, $Na_2B_4O_7.10H_2O$, $NaCaB_5O_9.8H_2O$) are raw borates and can be used as thermalized or fast neutrons shielding. These boron compounds are used also in control bars of nuclear reactors.

Boron-bearing ores are more practical and cheaper than pure boron and so they are used to many experiments as adding to concrete. In this work colemanite, tincal and ulexite which are boron bearing materials have been used for γ-rays transmissions. There are several studies on neutron shielding properties of different materials.

For shielding fast, middle and soft neutrons, Polivka and Davis searched subjects of heavy materials which have high atomic weight, light elements like oxygen and hydrogen. They asserted that the materials contains boron must be used against these particles [1]. Yarar and Bayülken investigated neutron shield using colemanite [2].Hong et al. made laboratory tests on neutron shields for γ-ray detectors in space. In this study, Boron carbide powder encapsulated in an acrylic plastic case was used to construct the boron a shield material [3]. Hayashi et al. in 2005 investigated borohydrides as shielding materials [4]. A patent is known present that Gelena (a lead ore) and/or other lead minerals can be used for the shielding from γ-rays, and colemanite and/or other boron minerals can be used for neutron shielding. Particular purpose additives will also be used. The family of compositions according to the invention will contain by weight 65-75% of floated galena, 5-10% of colemanite and 20-25% of binding agents and additives [5]. Mollah et al. in 1992 have investigated neutron shielding properties of concretes consist of boron [6]. Kase et al. in 2003 investigated shielding characteristics of typically concrete mixtures consist of about 80 percent by weight of oxygen and silicon, with the rest of the composition comprising calcium, aluminum and lesser quantities of sodium, potassium and iron against neutron leakages [7]. Okuno have used mixture of colemanite and epoxy resin as neutron shielding material in 2005 [8]. Agosteo et al. have investigated double differential neutron distribution and neutron attenuation in concrete using 100-250 MeV proton accelerator in 2007 [9]. Adib et al. have measured neutron transmission through pyrolytic graphite crystals in 2007 [10]. And Hayashi et al. have used zirconium borohydrite and zirconium hydride for neutron attenuation process in 2009 [11]. Osborn et al. have obtained borat and polyethylene mixture for neutron shielding process [12]. Morioka et al. have developed a new neutron shielding material, has high heat resistance, based on boron-loaded resin in 2007 [13]. We used follow materials in this study:

- Samples for neutron shielding studies; colemanite, tincal and ulexite ores.
- For neutron bombardment, ^{241}Am/Be monoenergetic neutron source.
- For equivalent dose rates measurements, Canberra NP100B series BF3 neutron detector.
- For pellet sample preparation, a hydraulic press machine (SPEX P_{max} 25 tons/cm^2)
- A sieve (Retsch)

Pellet samples are prepared as in follow. The specimens (colemanite, ulexite and tincal) were dried approximately 1 hour at 300 ^{0}C in an oven. A 1-75 micrometer scaled sieve (Retsch) was used for sieving the samples to be prepared as pellets for measurement. After sieving they were mixed using a SPEX mill including 25 ml stainless-steel cup and balls. A small metallic sample holder made of aluminum was used for forming samples as pellets. The constituted pellets were pressed at 25 tons/cm^2 in a SPEX P_{max} hydraulic press along 45 seconds.

^{241}Am/Be neutron source which emits 4.5 MeV neutron particles is used in this study. Physical form of ^{241}Am/Be neutron source is compacted mixture of americium oxide with beryllium metal. Fast neutrons are produced by following nuclear reaction.

$$^{9}_{4}Be+^{4}_{2}He\rightarrow^{1}_{0}n+^{12}_{6}C$$

neutrons down to thermal energies and heavy ions. The program can also transport polarized photons (e.g., synchrotron radiation) and optical photons. Time evolution and tracking of emitted radiation from unstable residual nuclei can be performed online [14].

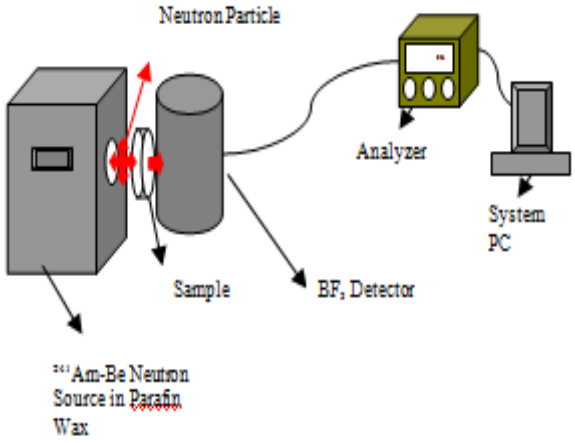

Fig.1. Experiment Design

We have used FLUKA Monte Carlo code to obtain kinetic energy losses. Firstly, chemical contents of samples have been entered MATERIAL and COMPOUND cards and then BEAM card, system geometry parameters (sample diameter and thickness as 2cm and 1,5cm. respectively) and detector properties have been written in FLUKA input file. Secondly, simulation has been started for 1000000 primary particles. Kinetic energy loss values have been read from FLUKA output file. In this paper, we have investigated neutron equivalent dose rates and kinetic energy losses for colemanite, ulexite and tincal, boron bearing ores and we have obtained information about neutron shielding capability of these materials. A plot has been obtained about equivalent dose rates as a function of measure time (Fig.2).

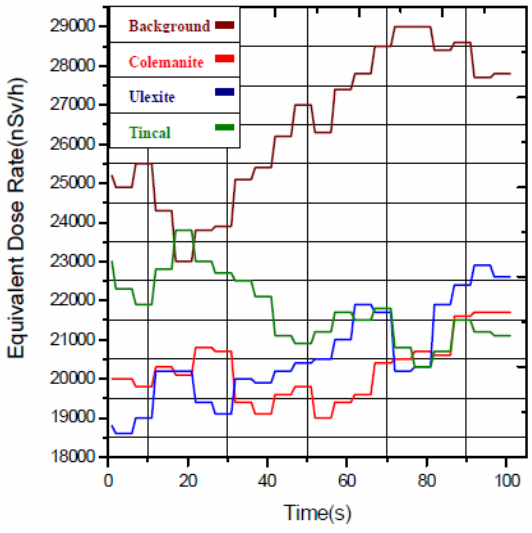

Fig.2. Equivalent Dose Rates as a Function of Measure Time

As can be seen from Fig.2 neutron dose fluence in colemanite target is slower than others. Also Fig.3 has been demonstrated kinetic energy losses while neutrons passing samples as a function of boron percentages. As can be seen from Fig.3, growing energy loss, neutrons passing in colemanite, is upwards of other samples. Besides, neutron kinetic energy loss increases with boron concentration As a result of the neutron shielding performance of the colemanite is higher than others.

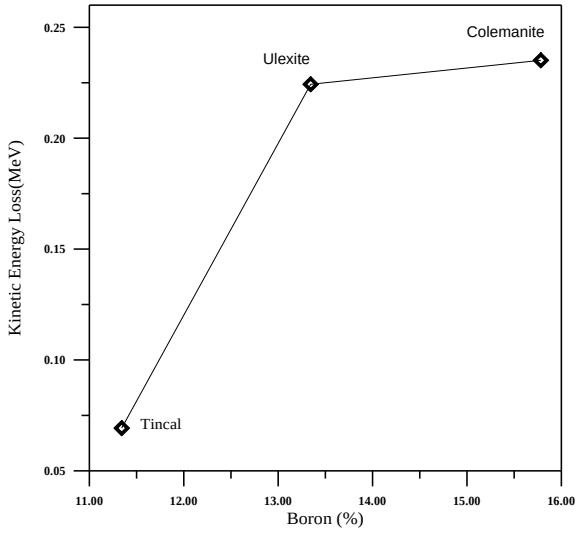

Fig.3. Kinetic Energy Losses as a Function of Boron Percentages

Alpha particles emitting from ^{241}Am have approximately 5,5 keV maximum energy. Neutron energy produced by this nuclear reaction is 4.5 MeV. Radiation characteristics of ^{241}Am-Be neutron source are shown in Table.1 (Dose rates have been taken from The Health Physics and Radiological Health Handbook, Scintra Inc., Revised Edition, 1992).

Table.1. Typical Properties of Detector*

Specifications of Canberra NP100B Neutron Detector	
Detector Type	BF3 Proportional Counter
Detector Sensitivities	0–100 mSv/h (0–10 Rem/h)
Energy Range	0.025 eV – 15 MeV
Operating Temperature Range	–10 °C to +50 °C (+14 °F to +122 °F)
Size (mm.) (Dia. x inch)	244 x 292 mm (9.6 x 11.5 in.)
Weight kg (lb)	10 kg (22 lb)
Housing	Moisture Proof Al.
Operating Humidity	0–100% no condensing
Detector Linearity	±5%
Accuracy	±10%
High Voltage Supply (internally generated)	1750–1950 V
Typical Application	Area Monitor, Boundary Monitor Accelerator Instrumentation

**http://www.canberra.com/pdf/Products/RMS_pdf/NPSeries.pdf*

Equivalent dose rates of neutron particles have been measured by Canberra NP-100B BF_3 neutron detector (Table-2) and ADM-606M model transportable rate-meter for the eight samples. The NP-100B detector provides us to detect slow and fast neutrons. Tissue equivalent dose rates of the neutron field can be measured by it. The detectors contain a proportional counter which produces

pulses resulting from neutron interactions within it. The probes contain components to moderate and attenuate neutrons. So that the net incident flux at the proportional counter is a thermal and low epithermal flux representative of the tissue equivalent dose rate and the neutron field. Due to the fact that neutrons have no charge, they can only be detected indirectly through nuclear reactions that create charged particles. The NP100B detector uses ^{10}B as the conversion target. The charged particle – alpha or proton (respectively) created in the nuclear reaction ionizes the gas. Measurement results have read on RADACS program in system PC. Experiment system is shown in Fig.1.

FLUKA is a general purpose tool for calculations of particle transport and interactions with matter, covering an extended range of applications spanning from proton and electron accelerator shielding to target design, calorimetry, activation, dosimetry, detector design, Accelerator Driven Systems, cosmic rays, neutrino physics, and radiotherapy etc. FLUKA can simulate with high accuracy the interaction and propagation in matter of about 60 different particles, including photons and electrons from 1 keV to thousands of TeV, neutrinos, muons of any energy, hadrons of energies up to 20 TeV and all the corresponding antiparticles,

Table.2. Radiation characteristics of ^{241}Am-Be neutron source*

Physical Half-Life: 432.2 years		**Specific Activity:** 127 GBq/g	
Principle Emissions	**E_{max} (keV)**	**E_{eff} (keV)**	**Dose Rate (μSv/h/GBq at 1m)**
Gamma/X-Rays	13.9 (42.7%) 59.5 (35.9%)	-	-
Alpha	5.443 (12.8%) 5.486 (85.2%)	-	85
Neutron	-	4.5 MeV	2

**http://stuarthunt.com/Downloads/RMSDS/AmBe.pdf*

As a conclusion, boron bearing ores (colemanite, ulexite and tincal etc…) has neutron attenuation and absorption capability. These materials can be use to several processes (nuclear reactors, nuclear medicine, nuclear study laboratories etc…).

[1]. *M. Polivka and H. S. Davis* ASTM STP, 1979, 169B, 26, 420-434.

[2]. *Y. Yarar and A. Bayülken* J. of Nucl. Mat., 1994, 212- 215, 1720–1720.

[3]. *J. Hong, W.W. Craig, C.J. Hailey* Nuclear Instruments and Methods in Physics Research A, 2000, 452, 192-204.

[4]. *T. Hayashi, K. Tobita, S. Nishio , K. Ikeda, Y. Nakamori, S. Orimo* Fusion Engineering and Design, 2005, 81,1285–1290.

[5]. *S. Grifoni* United States Patent,1988, Patent Number: 4,727, 257; PatentDate;February23.

[6]. *A. S. Mollah, G.U.Ahmad and S. R. Husain* Nucl. En. and Des., 1992, 135 (3), 321-25.

[7]. *K. S. Kase, W. R. Nelson, A. Fasso, J. C. Liu, X. Mao, T. M. Jenkins, J. H. Kleck* Health Physics, 2003, 84 (2), 180-7

[8]. *Okuno K. Rad.* Protec. Dos., 2005, 115(1-4), 258-61.

[9]. *S. Agosteo, M. Magistris, A. Mereghetti, M. Silari, Z. Zajacova* Nuc. Inst. and Meth. in Physics Research B, 2007, 265, 581–598.

[10]. *M. Adib, N. Habib, M. Fathaalla* Ann. of Nucl. En., 2007, Volume 33, Issue 7, Pages 627-632.

[11]. *T. Hayashi, K. Tobita, Y. Nakamori, S. Orimo* Journal of Nuclear Materials, 2009, 386– 388, 119–121.

[12]. *J.C. Osborn, T.Ersez, G. Braoudakis* Physica B, 2006, 385–386, 1321–1323.

[13]. *A. Morioka, S. Sakurai, K. Okuno, S. Sato, Y. Verzirov, A. Kaminaga, T. Nishitani, H. Tamai, Y. Kudo, S. Yoshida, M. Matsukawa* Journal of Nuclear Materials, 2007, 367–370, 1085–1089.

[14]. *A.Ferrari, P.R.Sala, A.Fasso and J. Ranft* CERN-2005- 10 INFN/TC, 2005 05/11, SLAC-R-773.

A COMPUTER PROGRAM TO CALCULATE APPROXIMATE RADIATION DOSE OF EMBRYO/FETUS FOR SOME RADIOPHARMACEUTICALS USED IN NUCLEAR MEDICINE APPLICATIONS

T. BAYRAM[1,2] , B. SONMEZ[3], A. H. YILMAZ[1]

[1]Physics Department, Karadeniz Technical University, Trabzon / TURKEY

[2]Physics Department, Sinop University, Sinop / TURKEY

[3]Nuclear Medicine Departments, Karadeniz Technical University, Trabzon / TURKEY

tuncaybayram@ktu.edu.tr, sonmezbircan@yahoo.com, hakany@ktu.edu.tr

It has been presented *fdose* computer program which calculates approximate radiation dose to embryo/fetus in some nuclear medicine applications cover all of radiopharmaceuticals include iodine isotopes. Approximate embryo/fetus radiation dose can be calculated for four cases which are early pregnant, 3-month pregnant, 6-month pregnant and 9-month pregnant using this program. On the other hand, there are some constraints to this program about some special cases. Except these cases, *fdose* program is useful. Also it provides practical solution for calculation of approximate embryo/fetus dose of nuclear medicine pregnant patients.

Many women per year expose ionizing radiation during pregnancy for medical reason (diagnostic or treatment). Ionizing radiation is known to cause harm on the human embryo and fetus. Potential adverse outcomes related to radiation exposure during pregnancy include teratogenicity, genetic damage, intrauterine death and increased risk of malignancy. The risk of each effect depends on the gestational age at the time of exposure, fetal cellular repair mechanisms, and the absorbed radiation dose level. Abnormal effect on fetus of X-radiation during gestation was evaluated by Dekaban [1, 2] and cancer mortality among atomic bomb survivors exposed was evaluated by Delongchamp et al. [3].

In nuclear medicine, patients are administered varying quantities of different radioactive materials to either diagnose or treat of diseases. In these applications, patients are exposed ionising radiation by radioactive materials. Although the doses are much higher in theraphy, the doses are usually low for diagnostic cases. Most nuclear medicine procedures do not cause large fetal doses and they lead to a fetal absorbed dose of less than 10mGy (1rad). However, some radiopharmaceuticals that are used in nuclear medicine can pose significant fetal risks [4]. Although in pregnancy it is strongly recommended to avoid diagnostic and therapeutic nuclear medicine procedures, in cases of clinical necessity or when pregnancy is not known to be the physician, especially the diagnostic procedures are to be applied.

The dose to the embryo/fetus of pregnant women from radioactive materials is variable and depends principally on factors related to maternal uptake and excretion of the radioactive material, passage of the agent across the placenta. In addition to, because shape and volume of fetus at various stages is different each other, their radiation dose value at these stages is different. In literature, these stages are named as early pregnant, 3-month pregnant, 6-month pregnant and 9-month pregnant.

In this study, embryo refers the initial stages of growth and development up to the age of 8 weeks after conception, at which time almost all of body organs have formed while fetus refers to last from the beginning of the 9th week after conception.

Knowing embryo/fetus radiation dose of pregnant woman is very important for physicians and health physicists in nuclear medicine. Russel et al. gave estimates of fetal dose from over 80 radiopharmaceuticals used in nuclear medicine, based on some standardized kinetic models and, in some cases, including knowledge of the amount of radiopharmaceutical crossover, as measured in animal or human studies [4, 5]. The aim of this study was make a useful computer program calculates approximate radiation dose of embryo/fetus at few steps using estimates of Russel et al.

In this study, for each radiopharmaceutical, radiation dose value (per MBq) of embryo/fetus which was given by Russel et al. to various stages; early pregnant, 3-month pregnant, 6-month pregnant and 9-month pregnant was used. Radiopharmaceuticals are included by *fdose* program listed in Table 1. Because we desired to use SI units, dose values of embryo/fetus given as mGy/MBq in study of Russel et al. was converted to mSv/mCi. Then *fdose* program was written in Fortran 90 language [6] and it was ran and checked on Windows XP, Windows Wista and Windows 7 Operating Systems.

Table 1. Radiopharmaceuticals included by *fdose* computer program are shown.

Radiopharmaceuticals
^{123}I Hippuran
^{123}I IMP
^{123}I MIBG
^{123}I Sodium Iodide
^{124}I Sodium Iodide
^{125}I HSA
^{125}I IMP
^{125}I MIBG
^{125}I Sodium Iodide
^{126}I Sodium Iodide
^{130}I Sodium Iodide
^{131}I Hippuran
^{131}I HSA
^{131}I MAA
^{131}I MIBG
^{131}I Sodium Iodide
^{131}I Rose Bengal

User can calculate approximate embryo/fetus radiation dose at four steps using *fdose* program. After open the program, user should select radionuclide. Then user should select radiopharmaceutical. Then gestational age should be selected and finally user should enter activity of radiopharmaceutical. Using of *fdose* program is shown in Fig.1.

In Figure 1, at first step, I-131 radionuclide was selected via entering 6. At second step, Sodium iodide compound was selected via entering 5. At third step, gestational age was selected as early pregnant via entering 1 and finally activity of I-131 Sodium iodide was selected as 5 mCi. The result of this calculation was obtained as 13.32 mSv. (This value for iodine therapy with 100 mCi is 266.40 mSv). Also, after the calculation, some suggestions compiled from literature [7] are given on screen out of *fdose* program. These are:

1. If fetal dose less than 10 milliSievert, there is no evidence supporting the increased incidence of any deleterious developmental effects on the fetus at diagnostic doses within this range.

2. If fetal dose between 10 mSv and 100 mSv, the additional risk of gross congenital malformations, mental retardation, intrauterine growth retardation and childhood cancer is believed to be low compared to the baseline risk.

3. If fetal dose exceeding 100 mSv, the lower limits (in terms of statistical confidence intervals) for threshold doses for effects such as mental retardation end diminished IQ and school performance fall within this range. Overall, exposure at levels exceeding 100 mSv could be expected to result in a dose-related increased risk for deleterious effects. For example, the lower limit (95% confidence interval) for the threshold for mental retardation is about 150 mSv, which an expectation value of about 300 mSv

Using *fdose* program, approximate fetus dose of pregnant women patients for nuclear medicine applications can be calculated easily. On the other hand, there are two constraints for this program. One of them it calculates only radiopharmaceutical including iodine isotopes. The other is that some special cases [7] to be considered which are not included by *fdose* program for the pregnant patient. These cases:

Table 2. Fetal thyroid dose [8] (mSv/mCi).

Max. thyroid uptake:	**20%**	**40%**	**60%**	**80%**	**100%**
"Fast" thyroid uptake	1.813	1.628	1.480	1.332	1.332
"Normal" thyroid uptake	2.331	2.146	2.035	1.924	1.961

"Fast" thryoid uptake meant an uptake half-time of 2.9 hours, "normal" meant a half- time of 6.1 hours.

Fetal thyroid dose: If radioiodine is administered to a woman who has passed about 10-13 weeks of gestation, the fetal thyroid will have been formed, and this tiny organ concentrates the iodine which crosses the placenta. Watson [8] calculated doses to the fetal thyroid per unit activity administered to the mother. These results are presented in Table 2.

Table 3. Fetal dose values for the hyperthyroid patient [9] (doses are in mSv/mCi administered).

Gestational Age (Month)	**I-123**	**I-124**	**I-125**	**I-131**
3	99.9	888	10730	8510
6	236.8	3700	7770	20350
9	107.3	3663	4440	9990

The hyperthyroid patient: Fetal dose has not been well established for patients whose iodine kinetics differ from the standard model for I-131 NaI. In early pregnancy (most of these exposures should occur, as the therapy will be clearly contraindicated in patients known to be pregnant), values from [9] should serve well. Estimates of [9] were converted to mSv/mCi in Table 3. These dose values are shown in Table 3.

The athyroid patient: In thyroid cancer patients, I-131 NaI is often given to patients whose thyroids have been mostly removed surgically. There may be a remnant of thyroid tissue, and/or some thyroid cancer metastases around the body, but usually a large amount of activity is given (enough to destroy all remaining thyroid tissue and the metastases). In a study involving a few athyroidic subjects [10] it was found that the kinetics could be well characterized by treating the iodine not taken up by the thyroid by the normal kinetics of urinary bladder excretion (6.1 hour half-time). Using these assumptions and assuming the other normal soft tissue uptakes occur and using Russell's results for fetal residence times it is obtained the dose estimates which are given in Table 4 [10].

Again, the dose estimates in later pregnancy are not likely to be of interest very often, as this kind of therapy should not be carried out on a pregnant woman

Table 4. Fetal dose for the athyroid patient [5]

Early pregnancy	25,16 mSv/mCi
3 months	25,16 mSv/mCi
6 months	8,325 mSv/mCi
9 months	9,99 mSv/mCi

These three cases are not included by *fdose* program. So, physician or health physicist can calculate embryo/fetus radiation dose manually using Table 2, Table 3 and Table 4 for these cases.

As a result, activity of radiopharmacetucials used in nuclear medicine applications is standardized. On the other hand, activity of radiopharmacetucial could change by virtue of various reasons. So, knowing of approximate radiation dose of embryo/fetus for different activity given to pregnant patient is very important. There is an available free computer program called *NMdoses* which is calculates radiation dose to organs and gonad for some commonly used diagnostic and therapeutic radiopharmaceuticals in nuclear medicine [11].

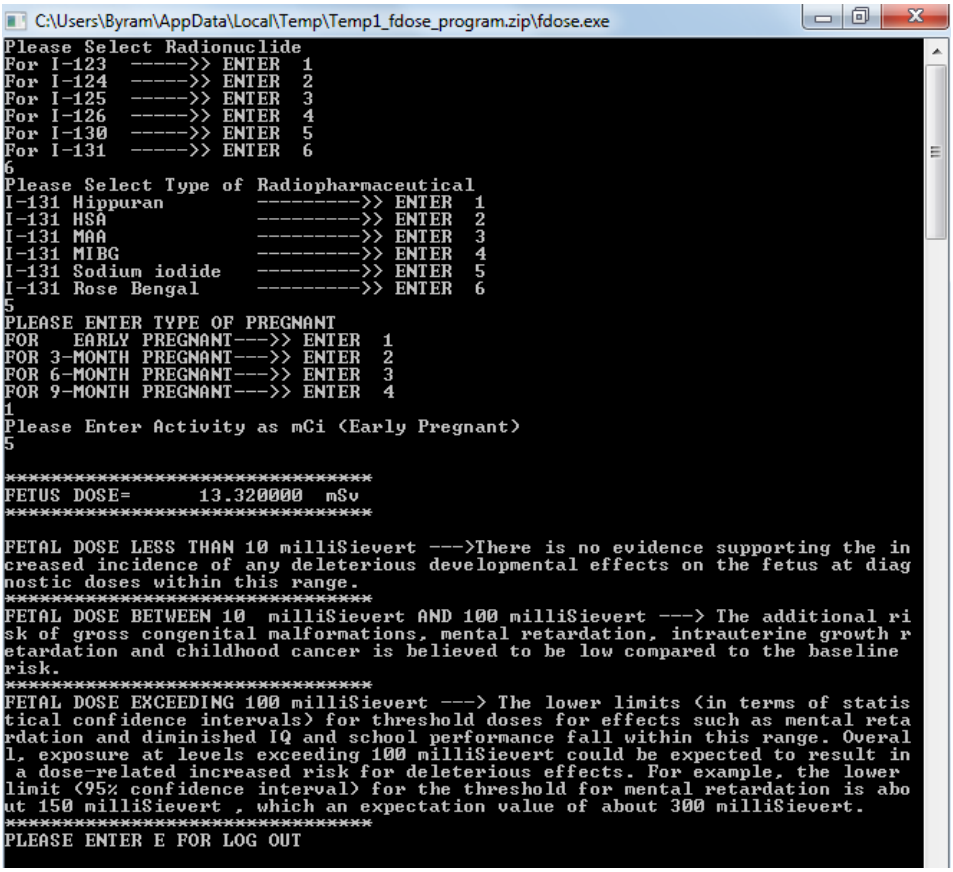

Fig.1. Example to using *fdose* program

It was adapted from [12]. On the other hand, there are not any computer program which is calculates approximate embryo/fetus dose to some nuclear medicine applications. So, except three cases mentioned before, *fdose* program is a useful and practical computer program to calculate approximate embryo/fetus radiation dose of nuclear medicine pregnant patients. Also, it could be expanded to other radiopharmaceuticals used in nuclear medicine.

ACKNOWLEDGEMENT: *fdose* program could obtain as free via e-mail from mail address given on webpage in reference [13].

[1]. *Anatole S. Dekaban*, part 1, J. Nucl. Med., 1968, 9, p.471-477.
[2]. *Anatole S. Dekaban*, part 2, J. Nucl. Med., 1968, 10, p.68-77.
[3]. *R. R. Delongchamp, K. Mabuchi, Y. Yoshimoto and L. Preston*, Radiation Research, 1997, 147, p.385-395.
[4]. ICRP Publication 84. "Pregnancy and medical Radiation". Annals of the ICRP, vol. 30, no. 1. Oxford: Pergamon Press, 1987.
[5]. *J. R. Russell, M. G. Stabin, R. B. Sparks*, Health Phys., 1997, 73, p.756-769.
[6]. *Brian D. Hahn*, in book "Introduction to Fortran 90 For Scientists and Engineers", 1996, Elsevier.
[7]. *http://www.doseinfo-radar.com/RADARHome/html, 20.03.2010*
[8]. *E. E. Watson*, Radiation Absorbed Dose to the Human Fetal Thyroid, Fifth International Radiopharmaceutical Dosimetry Symposium, Oak Ridge Associated Universities, 1992, p. 179-187.
[9]. *M. G. Stabin, E. E Watson, C. S. Marcus, R. D. Salk*, J Nucl. Med. 1991, 32, p.808-813.
[10]. *M. Rodriguez*, Master's Project, Colorado State University, 1996.
[11]. http://doseinfo-radar.aifm.it/RADAR-INT-NM.html, 31.05.2010
[12]. *Jerrold T. Bushberg, J. Anthony Seibert, Edwin M. Leidholdt Jr and John M. Boone*, in book "The Essential Physics of Medical Imaging", 2001. 2nd ed. Philadelphia, Lippincott Williams & Wilkins.
[13]. http://www.sinop.edu.tr/akademikbirimler/fakulteler/fen_edebiyat/personel/tuncay_bayram.asp

COHERENT STATES FOR A HARMONIC OSCILLATOR IN A TIME VARYING LINEAR POTENTIAL

NURİ ÜNAL
Akdeniz University, Faculty of Arts and Sciences, Department of Physics, Antalya 07058 Turkey

In this study, we construct the coherent states for the harmonic oscillator in the presence of a linear potential. In general case, the coefficient of the lineer potential are source terms and time dependent.

The coherent states were derived for the one-dimensional linear harmonic oscillator by Schrödinger [1], where the construction of the localized non-spreading wave packets was also addressed for the electrons in a Coulomb potential. The coherent states are the eigenstates of the lowering operator of the harmonic oscillator with complex eigenvalues. These eigenvalues are time dependent. The expectation values of the position and momentum operators follow the classical trajectories. They have minimum uncertainties. For these states, the probabilities are time dependent, hence, they are more useful than the stationary states in discussing the time dependent processes and the classical limit of the quantum systems. The coherent states were used in the quantum theory of electrodynamics in 1963 and recognized as the Glauber states [2]. In 1988, a radially localized electron wave packet was observed by Ten Wolde et al. [3]. Later we constructed the coherent states for the hydrogen atom by using the path integrals [4].

The forced harmonic oscillator problem (the interaction of an harmonic electric dipole with an external time dependent electric field) is discussed in standart textbooks on quantum mechanics as an example of the perturbation theory [5-9].

Examples of the forced harmonic oscillator include polyatomic molecules in varying external fields, crystals through which an electron is passing and exciting the oscillator modes [10]. Possibly, the most important applications of it is in the field of quantumelectrodynamics [11-14] and the propagator of this problem was obtained by Feynman using the path integrals techniques . Recently, Lopez and Suslov discussed the Caucy problem for the one dimensional forced oscillator [15].

The aim of this study is to derive the coherent states for the harmonic oscillator in a time dependent linear potential.

The Hamiltonian of a harmonic oscillator with mass, M, and frequency, ω_0 is given as

$$H = \frac{p^2}{2M} + \frac{(M\omega_0)^2 x^2}{2M}. \tag{1}$$

The Lagrangian of the oscillator is

$$L = p\frac{dx}{dt} - \left(\frac{p^2}{2M} + \frac{(M\omega_0)^2 x^2}{2M} \right). \tag{2}$$

Next, we introduce the new, complex, holomorphic coordinates, a, and a^*, as

$$\begin{aligned} a &= \frac{1}{\sqrt{2}}\left(\frac{ip}{\sqrt{M\omega_0}} + \sqrt{M\omega_0}\,x \right), \\ a^* &= \frac{1}{\sqrt{2}}\left(\frac{-ip}{\sqrt{M\omega_0}} + \sqrt{M\omega_0}\,x \right), \end{aligned} \tag{3}$$

and rewrite the Lagrangian in term of the new variables as

$$L = \frac{1}{2i}\left(\frac{da^*}{dt}a - a^*\frac{da}{dt} \right) - \omega_0 a^* a. \tag{4}$$

here, a, and a^*, are independent c-number variables and the phase space of the oscillator is constructed by them.

For a harmonic oscillator in an external time dependent driving force, we add the following interaction potential:

$$H_1 = j(t)a^* + j^*(t)a. \tag{5}$$

Then, the total Hamiltonian of the system is

$$H = \omega_0 a^* a + j(t)a^* + j^*(t)a.$$

The classical equations of motion are

$$\begin{aligned} \dot{a}^* &= i\omega_0 a^* + ij^*(t), \\ \dot{a} &= -i\omega_0 a - ij(t). \end{aligned} \tag{6}$$

Since a^* and a are independent variables we obtain the following solutions for Eq. (6):

$$\begin{aligned} a^*(t) &= a^*(t_b)\exp\left[i\omega_0(t-t_b)\right] \\ &+ \exp\left[i\omega_0(t-t_b\right]\times \\ &\int_{t_b}^{t} j^*(t')\exp\left[-i\omega_0(t'-t_b)\right]dt'. \end{aligned}$$

$$a(t) = a(t_a)\exp\left[-i\omega_0(t-t_a)\right] - \exp\left[-i\omega_0(t-t_a\right] \times \int_{t_a}^{t} j(t')\exp\left[i\omega_0(t'-t_a)\right]dt'.$$

As an example, we discuss a pulse in the shape of delta function such that

$$j(t) = j_0)\delta(t-t_0).$$

Then, we find the following discontinuous solutions for a^* and a:

$$a^*(t) = a^*(t_b)\exp\left[i\omega_0(t-t_b)\right]$$

for $t < t_0 < t_b$, and

$$a^*(t) = a^*(t_b)\exp\left[i\omega_0(t-t_b)\right] - ij_0\exp\left[i\omega_0(t-t_0)\right]$$

for $t_0 < t < t_b$.

$$a(t) = \lambda(0)\exp\left(-i\omega_0 t\right),$$

for $t_a < t < t_0$

$$a(t) = \lambda(0)\exp\left(-i\omega_0 t\right) - ij_0\exp\left[-i\omega_0(t-t_0)\right]$$

for $< t_a t_0 < t$.

This solutions show that a^* or a have a discontinuty at $t = t_0$. Therefore, if j_0, which corresponds to F_0/M, is real then there is a discontinuty in the momentum of the particle. To derive the quantum transition amplitudes of this system we introduce the quantum lowering and raising operators $\hat{a}$, and $\hat{a}^\dagger$ from the c-number variables a, and a^*, by the commutation relation

$$\left[\hat{a}, \hat{a}^\dagger\right] = \hbar.$$

Then, the quantum Hamiltonian is

$$\hat{H} = \hbar\omega_0\left(a^*\frac{\partial}{\partial a^*} + \frac{1}{2}\right) + j(t)a^* + \hbar j^*(t)\frac{\partial}{\partial a^*}. \tag{6}$$

In order to represent the raising and lowering operators as differential operators, we choose $\hat{a}^\dagger$ as the c-number operator, a^*. Then, the lowering operator, $\hat{a}$, is represented as

$$a = \hbar\frac{\partial}{\partial a^*}.$$

The configuration space of the particle is span by a^*, and the state function, ψ, is a functions of a^*, and t.

The Schrödinger equation is

$$i\hbar\frac{\partial\psi(a^*,t)}{\partial t} = \left[\hbar\omega_0\left(a^*\frac{\partial}{\partial a^*} + \frac{1}{2}\right) + j(t)a^* + \hbar j^*(t)\frac{\partial}{\partial a^*}\right]\psi(a^*,t) \tag{7}$$

This is a linear first order partial differential. We make he following anzatz to solve it:

$$\psi(a^*,t) = \exp\left[a^*\lambda_1(t) + \lambda_2(t) - i\omega_0 t/2\right].$$

We substitute it into the Schrödinger equation. Then we find the following equations for $\lambda_1(t)$, and $\lambda_2(t)$:

$$i\hbar\frac{\mathrm{d}\lambda_1(\mathrm{t})}{dt} = \hbar\omega_0\lambda_1(\mathrm{t}) + \mathrm{j}(\mathrm{t}),$$
$$i\frac{\mathrm{d}\lambda_2(\mathrm{t})}{dt} = \mathrm{j}^*(t)\lambda_1(\mathrm{t}).$$

We solve these coupled equations. Then, we find the coherent states for a harmonic oscillator in external field as

$$\psi_{\lambda_1(0)}(a^*,t) = \exp\left[-i\omega_0 t/2 + a^*\lambda_1(0)e^{-i\omega_0 t}\right] \exp\left[\frac{a^*e^{-i\omega_0 t}}{i\hbar}\int^t dt'\, j(t')e^{i\omega_0 t'}\right] \exp\left[-i\int^t dt'\, j^*(t')e^{i\omega_0 t'}\lambda_1(0)\right] \exp\left[-\frac{1}{\hbar}\int^t dt'\, j^*(t')e^{i\omega_0 t'}\int^{t'} dt''\, j(t'')e^{-i\omega_0 t''}\right] \tag{8}$$

For the forced harmonic oscillator with $j(t) = j_0)\delta(t-t_0)$, the functions $\lambda_1(t)$, and $\lambda_2(t)$ become discontinuos. The form of $\lambda_1(t)$ becomes as

$$\lambda_1(t) = \lambda_1(0)\exp(-i\omega_0 t)$$
$$-ij_0\begin{cases}\exp[-i\omega_0(t-t_0)] & \text{for } 0 < t_0 < t \\ 0\end{cases}$$

We solve the equation for $\lambda_2(t)$ by using the expression of $\lambda_1(t)$ and find $\lambda_2(t)$ as

$$\lambda_2(t) = \begin{cases}\lambda_2(0) - ij_0^*\lambda_1(0)\exp(-i\omega_0 t) - |j_0|^2, & \text{for } 0 < t_0 < t \\ \lambda_2(0)\end{cases}$$

Then the expression of the coherent state wave function $\psi_{\lambda_1(0)}(a^*,t)$ becomes as

$$\psi_{\lambda_1(0)}(a^*,t) = \exp[-i\omega_0 t/2 + \lambda_2(0)]\exp[a^*\lambda_1(0)e^{-i\omega_0 t}]$$

for $0 < t < t_0$ and

$$\psi_{\lambda_1(0)}(a^*,t) = \exp(-|j_0|^2)\exp[-i\omega_0 t/2 + \lambda_2(0) - ij_0^* e^{-i\omega_0 t}]\exp[a^*[\lambda_1(0) - ij_0 e^{i\omega_0 t_0}]e^{-i\omega_0 t}]$$

for $0 < t < t_0$.

This result shows that; the magnitude of the coherent state wave function decreases with the factor $\exp(-|j_0|^2)$, the phase function is changed from

$$[-i\omega_0 t/2 + \lambda_2(0)]$$

to

$$[-i\omega_0 t/2 + \lambda_2(0) - ij_0^* e^{-i\omega_0 t}],$$

and relation between the evolution function of the initial states and final states changed from

$$\exp[a^*\lambda_1(0)e^{-i\omega_0 t}] = \sum_{n=0}^{\infty}\frac{(a^*)}{\sqrt{n!}}\frac{(\lambda_1(0)e^{-i\omega_0 t})}{\sqrt{n!}},$$

to

$$\exp[a^*[\lambda_1(0) - ij_0 e^{i\omega_0 t_0}]e^{-i\omega_0 t}] = \sum_{n=0}^{\infty}\frac{(a^*)^n}{\sqrt{n!}}(e^{-i\omega_0 t}) \times \sum_{m=0}^{n}\binom{n}{k}(-ij_0 e^{i\omega_0 t_0})^k(\lambda_1(0))^{n-k}(e^{-i\omega_0 t}).$$

---

[1]. *E. Schrödinger*, Naturwissenschaften, 1926, 14, 664 .

[2]. *R. J. Glauber*, Phys. Rev. Lett., 1963 10, 84, and Phys. Rev.,1963 130, 2529 .

[3]. *A. ten Wolde, L. D. Noordam, A. Lagendijk, H. B. van Linden van den Heuvell*, Phys. Rev. Lett., 1988, 61, 2099;*N. Unal*, Phys. Rev. A, 2001 63, 052105 and Turk. J. Phys., 2000 24, 463 .

[4]. *N. Unal*, in "Fluctuating Paths and Fields", ed. by W. Janke, et. al., World Scientific, Singapore, 2001.

[5]. *N. N. Bogoliubov , D. V. Shirkov*, Introduction to the Theory of Quantized Fields, third edition, John Wiley& Sons, New York, Chichester, Brisbane, Toronto, 1980.

[6]. *K. Gottfried, T.-M. Yan*, Quantum Mechanics: Fundamentals, second edition, Springer–Verlag, Berlin, NewYork, 2003.

[7]. *B. R. Holstein*, Am. J. Phys., 1997 65, 414.

[8]. *E. Merzbacher*, Quantum Mechanics, third edition, John Wiley & Sons, New York, 1998.

[9]. *A. Messia*, Quantum Mechanics, two volumes, Dover Publications, New York, 1999.

[10]. *R.P.Feynman, A. R. Hibbs*, Quantum Mechanics and Path Integrals, McGraw–Hill, New York, 1965.

[11]. *R. P. Feynman*, The Principle of Least Action in Quantum Mechanics, Ph. D. thesis, Princeton University, 1942; reprinted in: "Feynman's Thesis – A New Approach to Quantum Theory", (L. M. Brown, Editor), World Scientific Publishers, Singapore, 2005, p. 1–69.

[12]. *R. P. Feynman*, Rev. Mod. Phys. 1948, 20, 367.

[13]. *R. P. Feynman*, Phys. Rev., 1949, 76, 749.

[14]. *R. P. Feynman*, Phys. Rev., 1949, 76, 769.

[15]. *R. M. Lopez, S. K. Suslov*, Revista Mexicana de FisicaE, 2009, 2, 196.

MOLECULAR MECHANICS AND DYNAMICS STUDY OF ELEDOISIN

G.A. AGAEVA
Institute for Physical Problems,
Baku State University, AZ-1148, Z.Khalilov Str.23,Baku, Azerbaijan
gulshen@mail.ru

The conformational behaviour of the tachykinin peptide eledoisin has been studied by molecular mechanics and dynamics methods in vacuum and in environment with water molecules. It is shown that eledoisin is observed in vacuum and in water with some flexibility of the N-terminal part of its amino acid sequence. In the middle and C-terminal parts of this molecule is saved a helical conformation in all conditions.

1. INTRODUCTION

For understanding of how biologically active peptide molecules interact with their receptors is required the knowledge of the conformational specificity and dynamics of the native molecule allowing a rational design of compounds acting selectively at the receptor level. The conformational behaviour of eledoisin and conformational dynamics of its backbone and side chains at the present article have been investigated by molecular mechanics and molecular dynamics methods. Eledoisin, an undecapeptide of mollusk origin, with the sequence pGlu-Pro-Ser-Lys-Asp-Ala-Phe-Ile-Gly-Leu-Met-NH_2, is a member of the tachykinin family of neuropeptides. It was first isolated from the posterior salivary glands of two mollusk species *Eledone muschata* and *E. aldovandi* belonging to the octopod *Cephalopoda* [1-3]. All tachykinin peptides share the same consensus C-terminal sequence, that is, Phe-Xxx-Gly-Leu-Met-NH_2. This common region, often referred as the message domain, is believed to be responsible for activating the receptor. Tachykinin peptides exhibit a wide and complex spectrum of pharmacological and physiological activities such as powerful vasodilation, hypertensive action, and stimulation of extravascular smooth muscle. The wide range of physiological activity of tachykinins has been attributed to the lack of specificity of tachykinins for a particular receptor type. Recently it is shown that eledoisin has similar activity and high level of sequence homology (73%) with β-amyloid protein fragments (Aβ 25–35) and their analogs, which play a major role in the onset and progression of Alzheimer's disease. Hence there is considerable interest in eledoisin as potential target for drug design. The first aim of the present article is the investigation of conformational properties for eledoisin, with the purpose of getting insight into basic structural requirements that determine ligand-receptor interaction by molecular mechanics method, which allow to determine a whole sets of energetically preferred conformers of peptide molecule. By some spectral methods has been found that the eledoisin display some elements of secondary structure in appropriate solution environment, though it has been suggested that they do undergo rapid conformational exchange [4-6]. There are no discernible trends in the conformation of the address segments of eledoisin. However, the tachykinin message domains are similar in each case. In general, the message domain of tachykinin peptides undergoes conformational averaging in aqueous environments. In hydrophobic environments, the message domain assumes helical conformations or exists as a series of turns in dynamic equilibrium. Although the peptides in aqueous solution exist as randomly distributed conformers, the biologically active forms of these peptides are likely to be ordered and stabilized within the lipid bilayers of the cell membrane before binding with their receptors. A molecular conformation is largely determined by its environment, so the aim of this present work is the study the differences in the conformations of the tachykinin peptides in a vacuum and in aqueous environment using a molecular dynamics method.

2. COMPUTATIONAL METHOD

Molecular mechanics (MM) study of eledoisin conformation involves multistaged extensive computations of even-increasing fraqments, with a set stable forms of each preceding step used as a starting set in the next step. Only those conformations are retained whose energies are smaller than some cut-off values. This cut-off value is usually taken as 5 kcal/mol above the lowest energy. The sequential method was used, combining all low-energy conformations of constitutive residues [7]. The conformational potential energy of a molecule is given as the sum of the independent contributions of nonbonded, electrostatic, torsional interactions and hydrogen bonds energies. The first term was described by the Lennard-Jones 6-12 potential with the parameters proposed by Scott and Scheraga. The electrostatic energy was calculated in a monopole approximation corresponding to Coulomb's law with partial charges of atoms as suggested by Scott and Scheraga. An effective dielectric constant value ε= 1 for vaccum, ε=4 for membrane environment and ε=80 for water surrounding is typically used for calculations with peptides and proteins, which create the effects of various solutions on the conformations of peptides by MM method [8]. The torsional energy was calculated using the value of internal rotation barriers given by Momany et al [9]. The hydrogen bond energy is calculated based on Morse potential.

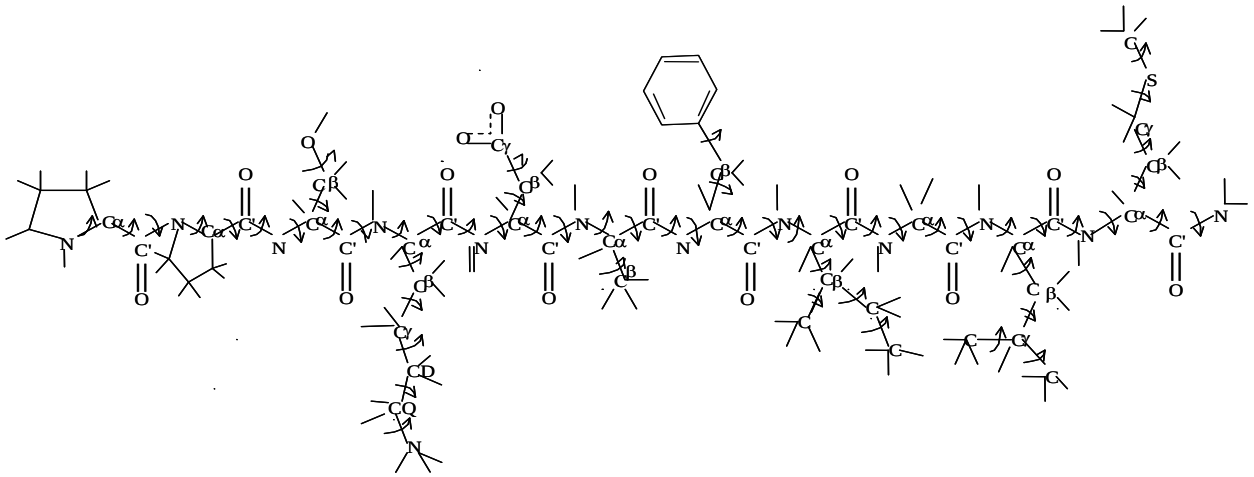

Fig.1. Atomic calculation model and variable dihedral angles of the eledoisin molecule.

Bonding lengths and angles are those given by Corey and Pauling [10] and are kept invariable; the ω angle of the peptide bond was fixed at 180°. The conformational energy was minimized using program proposed by Godjaev et al. [11]. The dihedral rotation angles were counted according to the IUPAC-IUB [12]

To understand the physical and structural properties of membrane-bound peptides and proteins and their relationship to the biological activities, molecular dynamics (MD) simulations with every improving force fields and longer time scales have been providing molecular level details of such systems. MD simulations were performed for neuropeptides in vacuum as well as in water solution using modeling package [13]. MD is widely applied to the study of biological systems, providing insight into the structure, function, and dynamics of biological molecules [14,15]. A wide range systems have been treated, from small molecules to proteins, in vacuum and in the presence of solvent [16,17]. Molecular dynamics simulations generate trajectories of atomic positions and velocities and some general thermodynamic properties. MD involves the calculation of solutions to Newton's equations of motions. Often an MD trajectory will become trapped in a local minimum and will not be able to step over high energy conformational barriers. Thus, the quality of the results from a standard MD simulation is extremely dependent on the starting conformation of the molecule. So, the low-energy structures, including the best and the worst of the calculated structures fr were used as starting conformations for molecular dynamics simulations φ, ψ and χ angles were analyzed for changes in each conformation. Runs were performed for 300 ps at 300K. The total length of the simulation depend on the system being studied and the type of information to be extracted. For example, in simulations of biological system a time step of 1 fem to second is commonly used. To ensure that information about the highest frequency in the system is±30° about a mean position during the molecular dynamics simulations. The length of the simulation (after equilibration) has to be long enough to enable the slowest modes of motion to occur. The force field parameters were those of the all atom version of AMBER by Cornell et al [18].. A harmonic force towards the center of the sphere was added to atoms when they moved out of the sphere. The nonbonded cutoff distance was 12Å. The time step was 0,5fs. The program Hyper. Chem. 7.01 [19] was used for the MD simulations.

3. RESULTS AND DISCUSSION

Three-dimensional structure of the eledoisin have been investigated basing on the fragmental analysis. An atomic calculation model and variable dihedral angles of the eledoisin molecule are presented in Fig.1. Molecular mechanics study of eledoisin has shown that its spatial structure may be described by two families of low-energy conformations with identical structure of the C-terminal heptapeptide. The C-terminal part (residues 5-11) of the eledoisin can adopt a partially helical structures, but the N-terminal part is different in each family. Only two low-energy conformations of the eledoisin are fall in the 0-3 kcal/mol energy interval. It is shown that two preferred conformations have similar C-terminal backbone form and values of the relative energy. In these conformations only Asp^5 residue is in the different backbone forms. Both conformations contain some turn at the N-terminal tripeptide, but the second conformation have β-turn structure at the Lys^4-Asp^5-Ala^6-Phe^7 segment also. These β-turns are confirmed by distance between C^α atoms of the i and i+3 residues (< 7 Å). The lowest energy structures of eledoisin exhibit the most favourable dispersion contacts and therefore may be expected to become the most preferred in a strongly polar medium, when electrostatic interactions do not play a significant role. The lowest energy α-helical structure at the C-terminal fragment is stabilized by network of hydrogen bonds. Theoretical conformational analysis of eledoisin have been indicated four families of low-energy conformations with similar C-terminal heptapeptides. This analysis has shown that eledoisin can form one global, i.e. the lowest-energy structure, which is consist one β-turn on N-terminal part on the C-terminal part α-helical segment, formed follow hydrogen bonds: $NH(Ile^8)\ldots CO(Lys^4)$, $NH(Gly^9)\ldots CO(Asp^5)$, $NH(Leu^{10})\ldots CO(Ala^6)$ and $NH(Met^{11})\ldots CO(Phe^7)$

At the second stage by MD simulation with using of the four lowest energy conformations as starting structures of eledoisin are found the significant differences in the conformations of the molecule in a vacuum and in an aqueous environment. Structural

reorganization of the global conformation of eledoisin at the molecular dynamic simulation in vacuum and in water solution are shown in Fig2. Figure 2 shows the global structure of the eledoisin as a result of the molecular simulation of aqueous environment. The MD simulations revealed the possible deviation by ±10° from the optimal values of φ, ψ, ω, χ dihedral angles in vacuum as compared to ±20° in water. MD simulations for eledoisin 300ps indicate that ψ angle for pGlu1 have a noticeable conformational flexibility. The deviations of ψ for pGlu1 by ±20° from its optimal values are allowed in all calculated structures in vacuum and water environment. The low energy changes of $\chi 1$ for pGlu1 from 182 to 88° are possible. The deviations by ±20° from minimal values are possible for χ1 angle. The rotation of the $\chi 2$ angle for Phe7 and Ile8 is considerably limited due to the effective interactions between the Phe7 and Ile8 amino acids. The mobility of the backbone and side chain of the Leu3 is more restricted as compared to preceding residues of molecules in vacuum as well as in water. Figure 3 shows the final structure, received by means of MD simulations, after computer-optimization of the lowest-energy conformation of eledoisin molecule in box with water molecules.

In contrast to water simulations, where the φ angle for Lys3 may be changed by retained, generally the bond stretching frequency of water, the trajectory has to be recorded at an interval no larger than 4 femtoseconds. MD simulations show that the molecule backbone can adopt only a limited number conformations while the side chains of the residues may populate different rotamers. A large flexibility of the pGlu1-Lys4 amino acids sequence was observed in vacuum in contrast to water simulation.

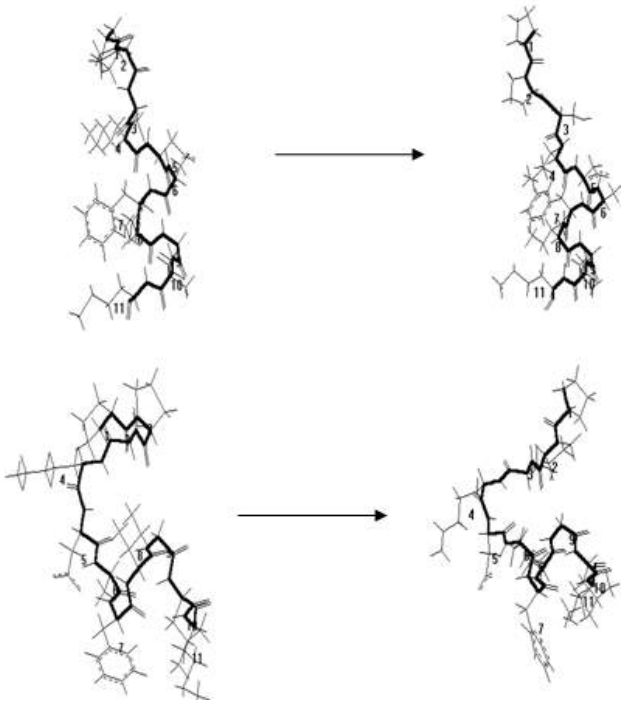

Fig.2. Conformational reorganization of the eledoisin molecule at the molecular dynamic simulation in vacuum (at the top) and in water (below).

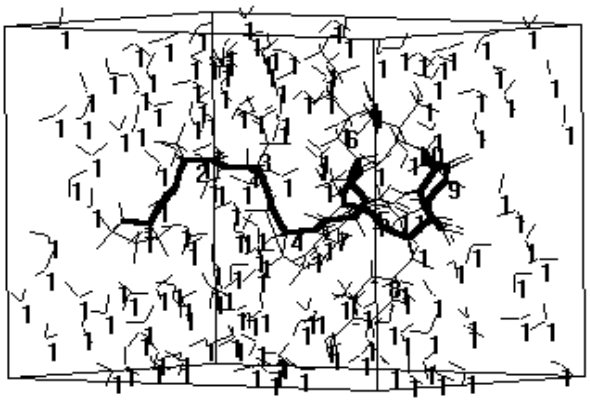

Fig.3. The final structure, received by means of MD simulations, after computer-optimization of the lowest-energy conformation of eledoisin molecule in box with water molecules.

Table 1.

The values (in degrees) of φ, ψ, ω, χ dihedral angles of two eledoisin lowest energy conformations.

Residue	Conformation	Backbone angles			Side chain angles				
		φ	ψ	ω	χ_1	χ_2	χ_3	χ_4	χ_5
pGlu[1]	I II	- -	111 117	186 187	- -	- -	- -	- -	- -
Pro[2]	I II	- -	-64 -51	180 184	- -	- -	- -	- -	- -
Ser[3]	I II	-132 -119	93 90	175 177	-61 -60	180 180	- -	- -	- -
Lys[4]	I II	-117 -120	-55 -53	182 180	180 179	180 180	180 180	180 180	180 180
Asp[5]	I II	-59 -120	-39 164	182 181	181 -59	90 90	- -	- -	- -
Ala[6]	I II	-76 -69	-37 -31	178 183	182 182	- -	- -	- -	- -
Phe[7]	I II	-64 -63	-43 -49	180 179	179 179	90 90	- -	- -	- -
Ile[8]	I II	-77 -78	-34 -31	-187 -184	-62 187	183 177	176 177	184 183	- -
Gly[9]	I II	-60 -61	-38 -38	-180 -179	- -	- -	- -	- -	- -
Leu[10]	I II	-81 -81	-64 -63	-174 -174	175 175	64 64	60 60	57 58	- -
Met[11]	I II	-93 -92	-53 -52	-182 -181	-58 -59	180 180	181 180	180 180	- -

The Asp5-Met11 heptapeptide fragment was found to be rigid in the conditions studies. Changes in intramolecular energy during simulations in water were negligible; they did not exceed 10-15 kJ/mol for molecule. At the same time, the molecule interaction energy was much higher due to the flexibility of the Lys3-Gln6 part of the peptides. Interactions between aromatic side chains of the Phe7 and Phe8 amino acids make the largest contributions to the global energy of the simulated molecule. Undoubtedly this contribution is overestimated in the vacuum approximation. The Pro4 fluctuates by ±20° from its optimal value as shown in Table1, i.e. Pro4 is very flexible in vacuum. So, the flexibility of residues in the 5th and 7th positions is limited by 10° as compared to the preceding part of molecule. This fact can be explained due to the important role of these residues in the formation of β-turn. Each angle varied about a single value, close to one of the set of possible angles calculated from molecular mechanics energy minimization.

4. CONCLUSION

We have carried out detailed analysis of the flexibility of the eledoisin molecule by employing the molecular mechanics and dynamics methods. The obtained results and discussion lead to the following conclusions: (I). molecular mechanics method and molecular dynamics simulations in vacuum as well as in aqueous solution confirm the considerable flexibility of the Arg1-Pro4 sequence of eledoisin ; (II). the α-helical conformation on Lys5- Met11 seqment of peptide was more stabilized in vacuum, with the predominant hydrogen bonds NH(Ile[8])…CO(Lys[4]), NH(Gly[9])…CO(Asp[5]), NH(Leu[10])…CO(Ala[6]) and NH(Met[11])…CO(Phe[7]), than the extended conformations; (III) the molecular dynamics simulations for eledoisin indicated that relatively high stability of the low-energy conformations resulted not only from nonvalent interactions between residues but also from hydrogen bonds networks ; (IV) the β- turn conformation at the N-terminal part were more stabilized in vacuum and provide optimal nonvalent interactions between residues. The determined structures of eledoisin may be used as the basis for the design of further peptidic selective antagonists.

[1]. *A. Anastasi, V.Erspamer,* Br.J. Pharmacol Chemother, 1962, v.19(2), p.326-336.
[2]. *V.Erspamer, A. Anastasi,* Experienta, 1962, v.15, N18, p.58-59.
[3]. *W. Jaeger,* Klin Monatsbl Augenheilkd 1988, v.192 p.163-6.
[4]. *A.De Marco, and G. Gatti,* Int. J. Pep. Pro. Res.,1975, v. 7,p.437-444.
[5]. *J.C. Wilson, K.J.Nielsen, M.J.McLeish, D.J.Craik,* Biochemistry, 1994, v..33(22), p.6802-11.
[6]. *R.C.R. Grace, I.R. Chandrashekar., S.M.Cowsik,* Biophysical, 2003, v.84, p.655-664.
[7]. *R.A.Scott, H.A.Scheraga,* J.Chem.Phys., 1966, v.45, p.2091-2111.
[8]. *F.A.Momany, McGuire, A.W.Burgess, H.A.Scheraga,* J.Phys.Chem., 1975,v.79, p.2361-2370.
[9]. *E.M.Popov,* Molec.biol.(Russian) (1985), v.19, p.1107-1118.
[10]. *E.M Popov, N.M. Godjaev, L.I.Ismailova, S.M.Musaev, R.E. Aliev, N.A. Akhmedov, I.S.Maksumov,* Bioorgan. Chem., (Russian), 1982, v.8,p. 776-791.
[11]. *N.M.Godjaev, I.S. Maksumov, L.I Ismailova,* J.Chem.Struc. (Russian), 1983, v.24, p.147-152.
[12]. IUPAC-IUB, Biochem. J. (1971) 121,577-585.
[13]. *W.F. Van Gunsteren, P.K. Weiner and A.K. Wilkinson* in Computer Simulation in Biological Systems (ESCOM Science), 1993.
[14]. *J.A. Mc Cammon and S.C.Harvey* in: Dynamics of Proteins and Nucleic Acids (Cambridge Univ. Press, New York), 1987.
[15]. *S.N. Rao and P.A. Kollman*. Prog. Natl. Acad. Sci. USA, 1987, v.17, p.6883-9.
[16]. *M. Billeter, A.E. Howard, I.D. Kuntz and P.A. Kollman*. J. Am. Chem. Soc., 1998, v.110,p. 8385-98.
[17]. *S.W. Chiu, J.A. Novontny and E. Jakobsson*. Biophysical J. , 1989, 64, №1,p. 98.
[18]. *W.D. Cornell, P.Cieplak, C.I. Bayly, I.R. Gould, K.M. Merz, et al.,* J. Am. Chem. Soc., 1995, v.117,p. 5179-88.
[19]. *N.L. Allinger, V.Yuh.* QCPE-395, Indiana Univ., 2000.

CURRENT PECULARITIES IN A LOW PRESSURE COUPLED PLASMA TOWNSEND DISCHARGE

H (YUCEL) KURT[1], S CETIN[1] and B.G. SALAMOV[1,2]
hkurt@gazi.edu.tr
[1]*Physics Department, Faculty of Arts and Sciences,*
Gazi University, Besevler, 06500 Ankara, Turkey
[2] *National Academy of Science, Institute of Physics, 1143 Baku, Azerbaijan*

The objective of this work is to contribute to that understanding current peculiarity in a Townsend-type discharge generated in a modified ionization cell with coupled short gaps between a high-resistivity semiconductor plate and two planar electrodes. It has been shown that depending on parameters of the discharge region and the external circuit, regular small-amplitude oscillations, relaxation oscillations or periodically repeating breakdown may occur in the gas-discharge region [23].

I. INTRODUCTION

Townsend discharges operate near the breakdown at such small currents that the spatial charge (and the distortion of the electric field) in the discharge gap is negligible [1,2]. The discharge parameters as well as parameters of the external electric circuit control the behaviour of the discharge current, which can exhibit growing, undamped or damped oscillations (in the last case, the oscillations relax to a stationary regime) [3–5]. The passage of the discharge current involves the formation of a space charge and the distortion of a potential distribution. As a result, the current–voltage characteristic of such a subnormal discharge on the right-hand branch of the Paschen curve decays, because the discharge operation requires a lower voltage as compared to that necessary for the discharge initiation (breakdown) [6,7]. Under these conditions, transverse instabilities can develop even at very low discharge current densities (see, e.g., [1,8-9]). Experiments show that, depending on the discharge conditions, the development of transverse instabilities can lead both to a spatially inhomogeneous stationary discharge and to an oscillatory regime accompanied by relaxation or almost sinusoidal oscillations of the whole discharge [10].

An increase in the applied dc voltage V_0 and the discharge current leads to undamped current and voltage oscillations. A further increase in the voltage and current gives rise to current filaments that frequently form regular structures, causing the device to malfunction [11].

Interest in Townsend discharge oscillations [1,12-14] has been stimulated in recent years by experiments in which a semiconductor–gas discharge system was used [15]. This is a sandwich-like device that consists of a thin plane discharge gap and a thin semiconductor cathode serving simultaneously as a ballast resistance, which is spatially distributed in the direction lateral to the current.

In this paper, coupled short gas discharge gaps are used to investigate complex dynamic behaviors of a nonequilibrium discharge in an *air*. We also present measurements of the low current density behavior of the Townsend discharges in *air*. The system studied in this work is a parallel plate, coupled discharge operated between low and moderate pressure (28-342Torr). It is shown to undergo complex oscillatory processes when the applied voltage is increased from prebreakdown to many times of the breakdown voltage. The influences of the gap spacing between electrodes on the gas discharge features are also discussed in this paper.

II. EXPERIMENTAL

As an experimental system, we apply the gas discharge system [16] that is a variant of the electronic device initially designed for the high-speed conversion of infrared images into the visible [17]. It is a planar structure the main parts of which is a semiconductor plate of a high resistivity and coupled gas discharge gap which are in the direct electrical contact with each other. The device is fed with constant voltage V_0 that has to be high enough to support the self-sustained gas discharge in the gap. In addition, the current of the discharge is controlled by a spatially homogeneous infrared light that increases the specific conductivity of the semiconductor plate σ. The most important difference between previous cell [17] (figure 1(a)) and present gas discharge setup shown in figure 1(b), is the incorporation of the semiconductor between two planar electrodes. The current–voltage characteristics (*CVC*) of the modified gas discharge cell are obtained experimentally as functions of the gas pressure p, which is varied in a sufficiently wide range (28-352 Torr). A scheme of the gas discharge cell with coupled short gaps between semiconductor plate and planar electrodes is shown in figure 1(b). In this modified cell (see figure 1(b)), the planar photosensitive *GaAs* semiconductor plate (6) is between two planar transparent electrodes which are disk of glass (3 and 3') coated with a thin layer of SnO_2 films to act as transparent conductors (4 and 4').One of the advantages of this cell compared to the previous one [16,17] (see figure 1(a)) is the exclusion of ohmic contact onthe surface of the semiconductor *GaAs* plate. Moreover, in this case we exclude the effect of contact phenomena on the shape of the *CVC* because a spatially homogeneous ohmic contact of high quality is essential for the proper operation of the system shown in figure 1(a).

The *SGD* have two main parts including a cathode and a gas layer which specifies the basic properties of the system. A gas layer is sandwiched between the glass plate and the semiconductor plate in Fig.1b (for more details, see Ref. [18]). In the experiments, a *SI GaAs* [17], an n-type high resistivity (ρ~$10^8\Omega$cm) plate oriented (100) in the plane of natural growth of the crystal, is used as a semiconducting detector. The diameter and the thickness of the *GaAs* cathode are 50 mm and 1 mm, respectively.

The surface of the *GaAs* cathode was separated from a flat anode by an insulating mica sheet with a circular aperture at its centre. Diameters of the effective electrode areas, *D* (i.e. gas discharge gap or diameters of the circular through-aperture in the insulator) are 9,12 and 15 mm.

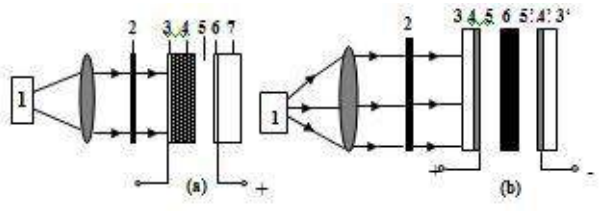

Fig 1 a) Schematic diagram of the gas discharge cell with a semiconductor *GaAs* cathode.: 1 - light source; 2 - *Si* filter; 3- semi-transparent Au-contact;4- semiconductor *GaAs* cathode; 5- gas discharge gap; 6- semi-transparent conductive SnO_2 contact; 7- flat glass disc. b) modified cell with dual short gaps between planar *GaAs* semiconductor plate and planar transparent electrodes: 1, light source; 2, Si filter; 3 and 3' flat glass disks; 4 and 4', planar transparent SnO_2 electrodes; 5 and 5', symmetrical short gas discharge gaps; 6, planar photosensitive *GaAs* semiconductor plate.

The *IR* radiation excites the photosensitive *GaAs* cathode of the cell providing control of the current density coupled discharge gap. These data were obtained for a structure with a *SI GaAs* electrode operating at room temperature.

III. RESULTS AND DISCUSSION

Figure 2 shows the *CVC* of the gas discharge cell in parallel-plane geometry with different conductivity σ of the semiconductor cathode, which was varied by its uniform illumination through the semi-transparent *Au* contact. Figure 2 also shows the complicated physical processes occurring in a modified ionization cell for weak illumination intensity L_1. At fixed physical parameters (such as the gas pressure, applied voltage and thickness of both semiconductor and discharge gap), the steady state value of electric current density is determined by ρ and the magnitude of feeding voltage V_0.

Figure 2b presents a detailed study of the time-dependence characteristics of current behavior for 150 s where the photocathode is exposed to weak illumination intensity L_1 when the discharge current slightly exceeds the critical value; the contraction occurs near one of the electrodes and evolves to the other electrode. For example in Ref [19] some experiment results with *Ar* and *Ne* are given and stepwise contraction taking place at the current increase is followed by a similar stepwise transition to the diffuse form, if the discharge current then decreases.

As it has been earlier shown [20], the surface charge also influences the physical processes in a gas-discharge system with a high ohmic electrode. Conducting properties of semi-insulating semiconductors are between those of conductors and insulators. Consequently, one should raise the question whether the accumulated surface charge affects the discharge processes. Depending on a variety of gas properties, operating parameters, boundary conditions, the discharge can exhibit pronounced filamentary character, self-organized regular-discharge patterns, or completely diffuse appearance [21]

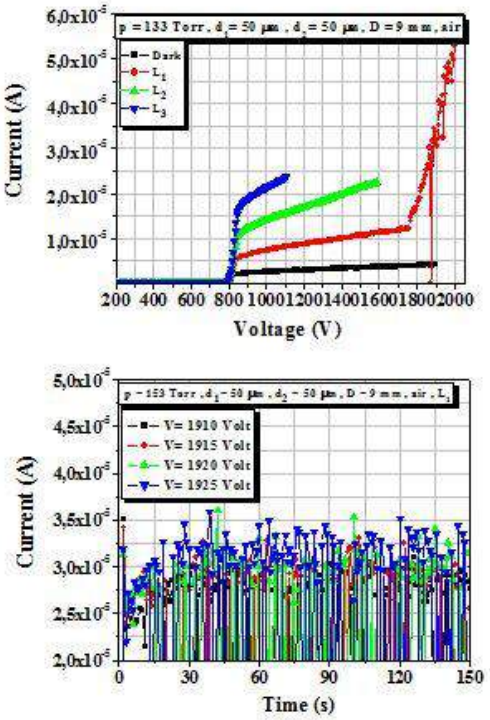

Fig 2. a) *CVC* of a modified ionization cell in darkness and under weak, moderate and maximum illumination intensity L_1, L_2 and and L_3, respectively. b) Time dependence of current oscillations in the modified cell under different feeding voltages *Vo* for weak illumination intensity L_1.

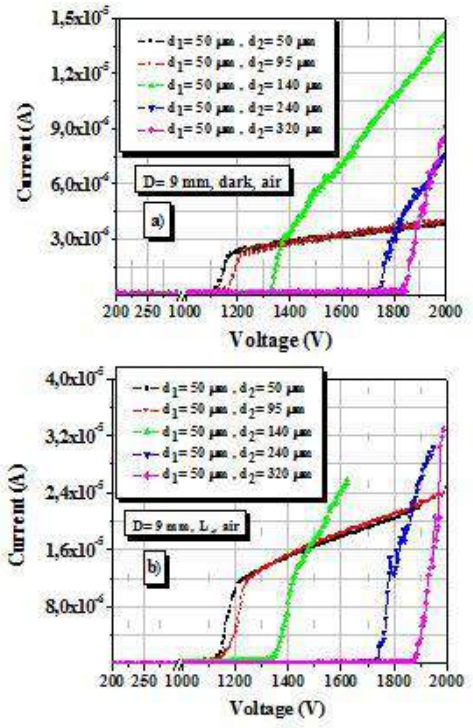

Fig 3. CVC of the modified ionization cell as a function of *d* in coupled *air* plasma a) under dark, b) under moderate illumination intensity L_2.

Figure 3 gives detailed information regarding the *CVC* of the cell with respect to electrode separation *d* when a dc voltage of a high enough magnitude is applied to the system. The experimental results in this study show that the gap spacing between electrodes can affect the discharge characteristics, including the *CVCs*, the discharge modes, etc., significantly with other parameters being constant.

Experimental study of the surface charge in a *dc* gas discharge system is very complicated, the charge on the surface of a high-ohmic electrode influences the discharge processes. Charge carriers multiplication processes in gas discharge are very sensitive to electric field [1], because the ionization coefficient depends on the field in the gap exponentially. As a result, any small effect that causes the *CVC* to drop off can induce discharge instability [3].

The physical and chemical nature of the plasma is affected by the different mechanisms available for the generation of electrons in the discharge. When gas molecules react with the surface material, producing an additional gas or surface component. Such reactions are to be expected, since reactive ions are readily created in plasma, especially in *air* [24]. During discharge or development of the same, the secondary emission, described by Townsend's second coefficient γ, changes, because now not only the surface atoms are hit by electrons and ions, but also the gas molecules on the surface. Some of the electrons emitted from the cathode can be backscattered to the cathode after taking part in the first elastic collision process. These low-energy electrons can be absorbed by the cathode or reflected from the cathode and they can also induce the emission of a 'new' electron [25].

IV. CONCLUSION

In this paper, we used the newly developed modified ionization cell with coupled short gaps to investigate the Townsend-type discharge. In the present paper, we demonstrate that under certain experimental conditions it is possible to obtain homogenous discharge. In this way, we can see that which parameter set give rise to the oscillatory regime. Space charge effects in many cases are the first nonlinear effects in gas discharges with increasing current. Instability of the Townsend discharge, resulting in oscillations and the formation of the current filaments [7], hampers the device operation. Consequently, an analysis of this instability is of practical importance [22].

ACKNOWLEDGMENT: This work is supported by the Gazi University BAP research projects 5/2009-49

[1]. *Y.P. Raizer*, Gas Discharge Physics, (Berlin, Springer 1991)
[2]. *S. C. Brown*, Basic Data of Plasma Physics:The Fundamental Data on Electrical Discharges in Gases, (New York, American Institute of Physics 1994)
[3]. *V. N Melekhin and N. Yu. Naumov*, Sov. Phys.—Tech. Phys 29, 888(1984)
[4]. *A. V Phelps, Z. L Petrovic and B. M. Jelenkovic*, Phys. Rev. E 47, 2825(1993)
[5]. *V. N. Khudik and A. Shvydky*, American Physical Society, 56th Conf. on Gaseous Electronics (San Francisco see www.plasmadynamics.com 2003)
[6]. *M.I. Dyakonov*, Sov Phys Jetp 67, 1049 (1988)
[7]. *A. A. Kudryavtseva and L. D. Tsendinb*, Technical Physics Letters 28, 1036 (2002)
[8]. *V.A. Shveigert*, Tech Phys 38, 384 (1993)
[9]. *L.D. Tsendin*, Ency Low Temperature 2, 16 (2000)
[10]. *[Z.L Petrovic*, Physical Review E 47, 806(1993)
[11]. E. *L. Gurevich, Yu. P. Raizer and H-G Purwins*, Tech. Phys 51, 180 (2006)
[12]. *E.L. Gurevich, Yu P Raizer and H-G Purwins*, Tech. Phys 51, 180(2006)
[13]. *D. D. Sijacic, Ute Ebert and I Rafatov*, Phys. Rev. E 70, 056220(2004)
[14]. *Yu. P. Raizer and E. L Gurevich and M.S.Mokrov*, Tech. Phys 51, 185(2006)
[15]. *C. Str¨umpel, Yu. A. Astrov and H.G. Purwins*, Phys.Rev E 62, 4889(2000)
[16]. *B. Salamov, Ş. Altındal, M. Özer, K. Çolakoglu and E. Bulur*, Eur. Phys. J. AP 2, 267(1998)
[17]. *B. G. Salamov, S. Buyukakkas, M. Ozer and K. Colakoglu*, Eur.Phys. J. Appl. Phys 2, 275(1998)
[18]. *H.Y. Kurt and B .G. Salamov*, J. Phys.D: Appl.Phys., 36, 1987(2003)
[19]. *Yu.B. Golubovskii and R. Sonneburg*, Sov.Phys.Tech. Phys 24, 173(1979)
[20]. *D.D. Sijacic and U. Ebert*, Phys. Rev. E 66, 066410 (2002
[21]. *U. Kogelschatz*, IEEE Trans. Plasma Sci 30, 1400 (2002)
[22]. *Yu. A. Astrov, E. Ammelt and H.G. Purwins*, Phys. Rev. Lett 78, 3129(1997)
[23]. *L. M. Portsel, A. N. Lodygin and Yu. A. Astrov*, J.Phys. D: Appl. Phys 42, 235208(2009)
[24]. *H. Kurt, E. Koc, B.G. Salamov*, IEEE Trans. Plasma Sci.38, 137(2010)
[25]. *P. Hartmann, Z. Donko, G. B.an´ o, L. Szalai and K R´ozsa,* Plasma Sources Sci. Technol 9, 183(2000)

INVESTIGATION OF INTERLAYER IMPURITY SURFACE (0001) $A_2^V B_3^{VI}$ <IMPURITY> BY SCANNING PROBE MICROSCOPY METHOD

F.K.ALESKEROV, S.Sh. KAKHRAMANOV, S.B.BAGIROV, B.Y.RZAKULIYEV

1 – Scientific Production Union "Selen" ANAS, H.Javid ave 29A, Baku, Azerbaijan.

2 – Institute of Physics Azerbaijan Academy of sciences, H. Javid ave. 33, Baku Azerbaijan

Email: kamil.qahramanov@yahoo.com

By scanning probe microscopy self-organization processes of copper and nickel antimonite impunities on interlayer vicinal (surface) (0001) $A_2^V B_3^{VI}$ <impurity> have been investigated. at is shown that forming impurity surfaces within $Te^{(1)}$-$Te^{(1)}$ $A_2^V B_3^{VI}$ <impurity> has step-layer behaviour. Height of nanoprotrusions forming in the process of vertical directed crystallization at the step edge is 10-20nm.

INTRODUCTION

Self-organization processes are understood to form ordered metal and semiconductive structures with certain density. Formation of nanofragments in interlayer space of crystals $A_2^V B_3^{VI}$ <impurity> can be served as self-organization instance [1]. The result of self-organization can be also the formation of interlayer steps. Self-organization involves interaction of systems capable of spontaneous appearance of order in space and time; structural and time order [2].

Interest to the given field of investigations is related to the necessity of various nanostructure production in sizes up to 100nm. Spontaneous ordering of nanostructures allows inclusions of narrow-band semiconductors in wide-band matrix to be obtained and thereby localized potential for charge carriers to be created [3]. Periodical structures of inclusions like these can form superlattices consisting of quantum pits, wires or points being the base for optoelectronics devices. In [2] it is shown that on vicinal surfaces Si (111) it is possible to form ordered Ge nanowises within step-layer growth.

Ordered nanoformations and steps can be created in various systems during the growth in layered quasicrystals $A_2^V B_3^{VI}$ <impurity>.

Close to the step in the bulk of quasicrystal there have been appeared deformations being characteristic of dislocations. The result obtained by author [4] leads to a number of obvious consequences for quasicrystal properties. First at rather low temperatures in equilibrium form of quasicrystals must be only some faces. Second the growth of atomic and smooth face must be taken place be generation and growth of new, layers it looks like the mechanism of atomic and smooth crystal face growth of one layer at a time. However the problem has been substantially complicated be step appearance of various height and energy behaviour. Third the phase transition in atomic and rough state must have substantial difference from such transition on crystal surface.

Explanation of appearance of periodically faceted structure is concerned with the conception of capillary phenomena on solid state surfaces [3-4]. As the atoms of solid state surface are in other surrounding than the atoms in the layer, equilibrium distance between surface atoms are different from equilibrium distance among atoms in the bulk. Therefore by microscope the crystal surface can be considered as elastostressed layer.

Bi_2Te_3 and $SbTe_3$ can be layered crystal where elastrostressed steps are taken place.

The example of scanning tunnel microscopy method is the investigation of faceting initial stage of tungsten vicinal face (110) at annealing crystal under the conditions close to thermodynamic equilibrium and mass transfer by thermodiffusion. In the first case initial nanofacets (traces of electrochemical polish) with recurrence frequency $q=(3\text{-}4)\cdot10^5 cm^{-1}$ are united forming microsteps hith distinct cutting. In the second case through conserving nanofacets the have-like structures in the form of sinusoidal corrugation has been formed. Corrugation frequency are in agreement with theoretically calculated.

Directional migration of atoms along the surface causes development of periodical wave-like or step structure on the surface of metal and semiconductive crystals.

In generation of wave –like facets irregularities may be the determing factor remaining on the crystal surface after mechanical and electro-chemical polish. Surface irregularities up to the size of atomic scale of real crystal can be presented as the set of sinusoids of Fourier series expansion. Directional migration of atoms is attended by isolation of Fourier component which defines relief period [7].

Authors [8] recording diffusion solution to describe change of surface form seen a solution as Fourier integral and derive finite expression for facet periods.

Appearance of gradation in graphite intercalation by impurities has been verified by electron-microscopic investigations. Here coexistence of steps at microstructural level is shown [9].

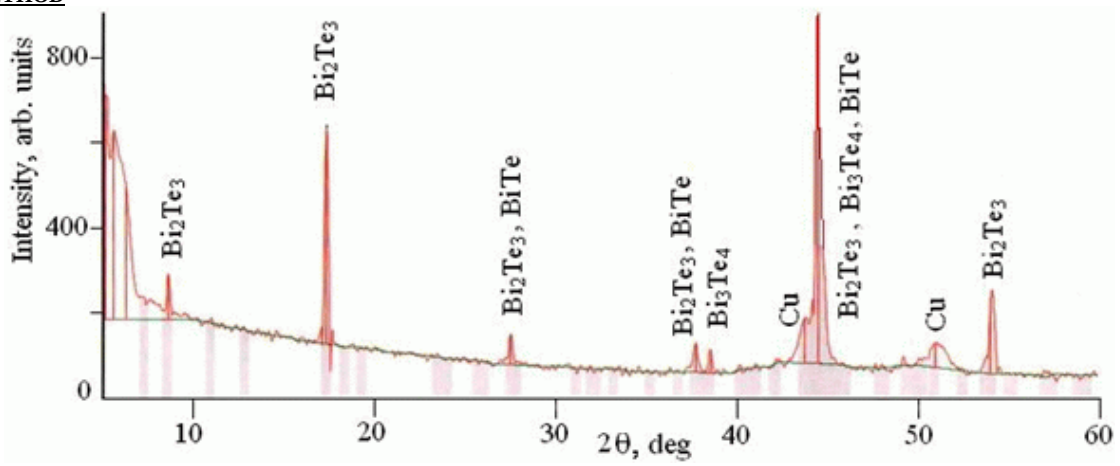

a)

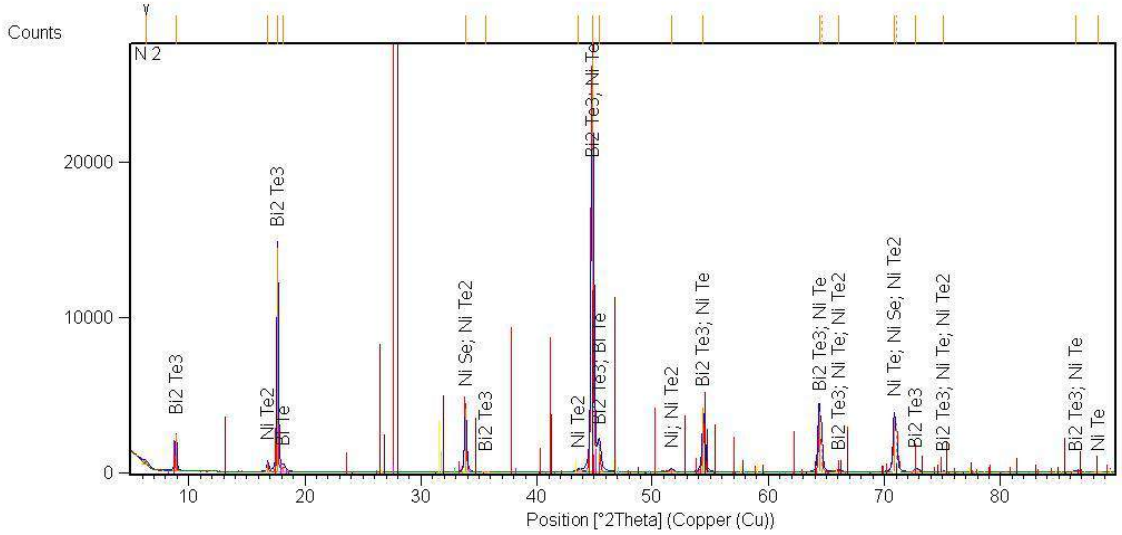

b)

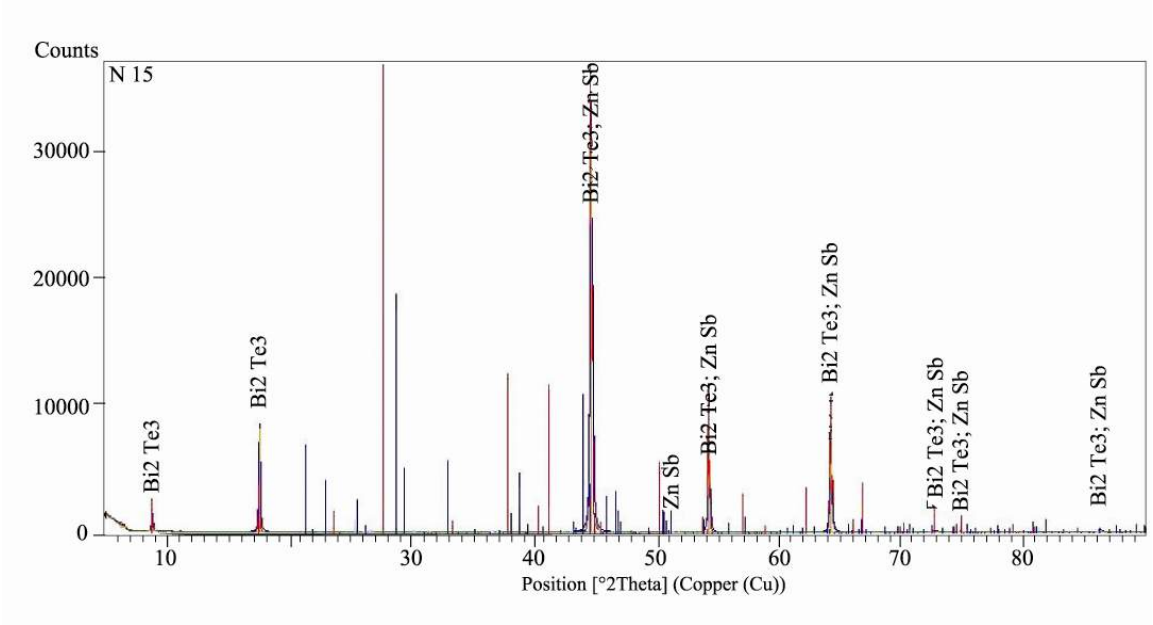

c)

Fig.1(a, b, c) X-ray diffraction patterns $A_2^V B_3^{VI}$ <impurity> spelled systems. a). Bi_2Te_3<Cu>, b) Bi_2Te_3<Ni>, c) Sb_2Te_3<ZnSb>.

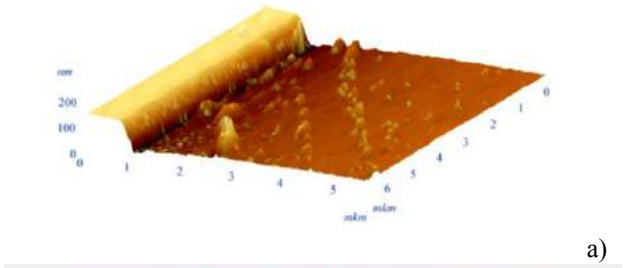

a)

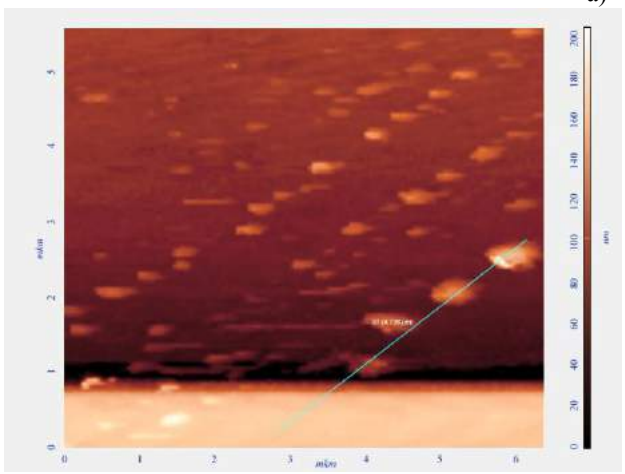

b)

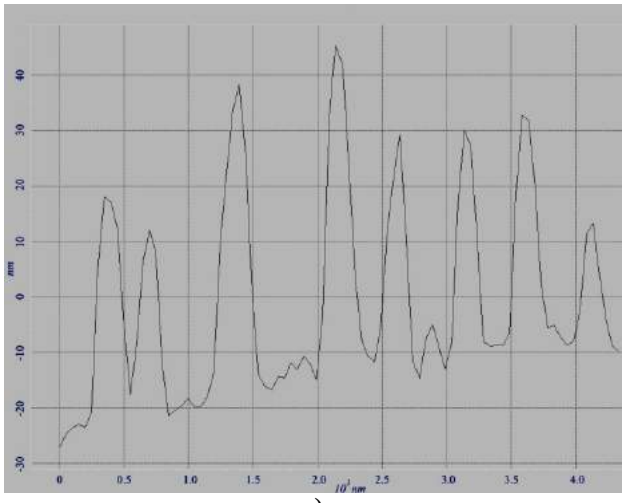

c)

Fig.2(a, b, c) SPM images of surface (0001) Bi_2Te_3<Cu> a)SPM images of Bi_2Te_3<Cu> in 3D-scale, b) Image of step and nanoprotrusions in 2D scale, c) step profile along light horizontal line on the part of Fig.2(b).

In [1, 6] there has been also studied morphology of nanofragments forming in interlayer space of Sb_2Te_3 and Bi_2Te_3 <impurity> typed layered crystals. As a result of crystallization in interlayers fractured particles and surfaces of nanometric sizes have been self-formed.

Taking into consideration above-mentioned facts we can specify a problem on revealing step interlayer structures and other nanofragments in layered crystals.

The aim of paper is to reveal interlayer steps of growth with nanofragments on base surface (0001) $A_2^V B_3^{VI}$ <Cu, Ni and ZnSb> by method of scanning prove microscopy (SPM).

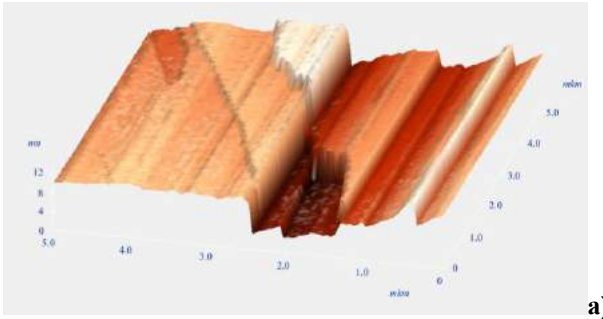

a)

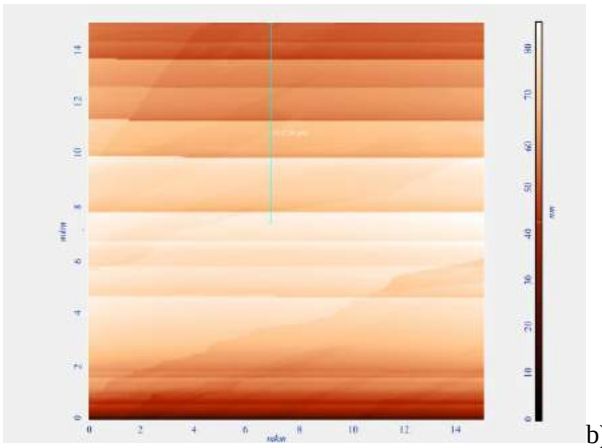

b)

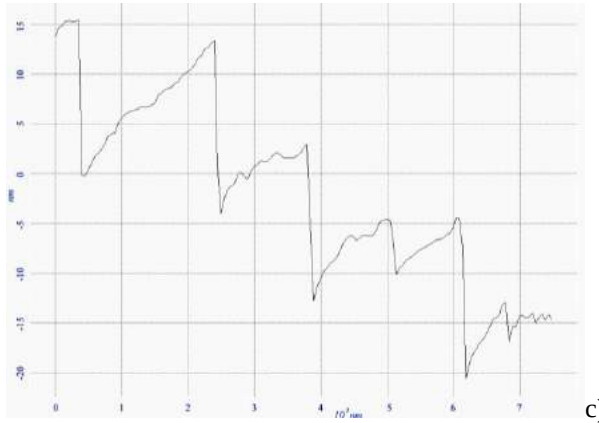

c)

Fig.3 (a, b, c) SPM images of bismuth telluride doped by Ni: a) image of steps in 3D-scale; b) image of steps in 2D- scale; c) step profile along vertical like in the middle of pattern on the part.

EXPERIMENTAL METHODS OF INVESTIGATIONS

The most convenient objects for studying processes of self-organization of "parquet" structures with step-layer growth are the crystal having rather distinct layered structure.

To analyze structural state of interlayer surface (0001) there have been investigated about 10 crystals. SPM method has become advantageous as it allows $A_2^V B_3^{VI}$ crystal surface topography and profile patterns to be investigated.

Electron-microscopic images have been taken on scanning prove microscope (SPM) of SOLVER NEXT model.

X-ray diffraction pattern investigations of surface (001) are carried on diffractometer of Philips Panalytical firm (XRD).

By investigation of surface relief we use simocontact method being the base for realizing series of other methods related to the use of cantilever resonance oscillations. Thee has been used silicon cantilever NSY 10 by operating frequency 280 kc.

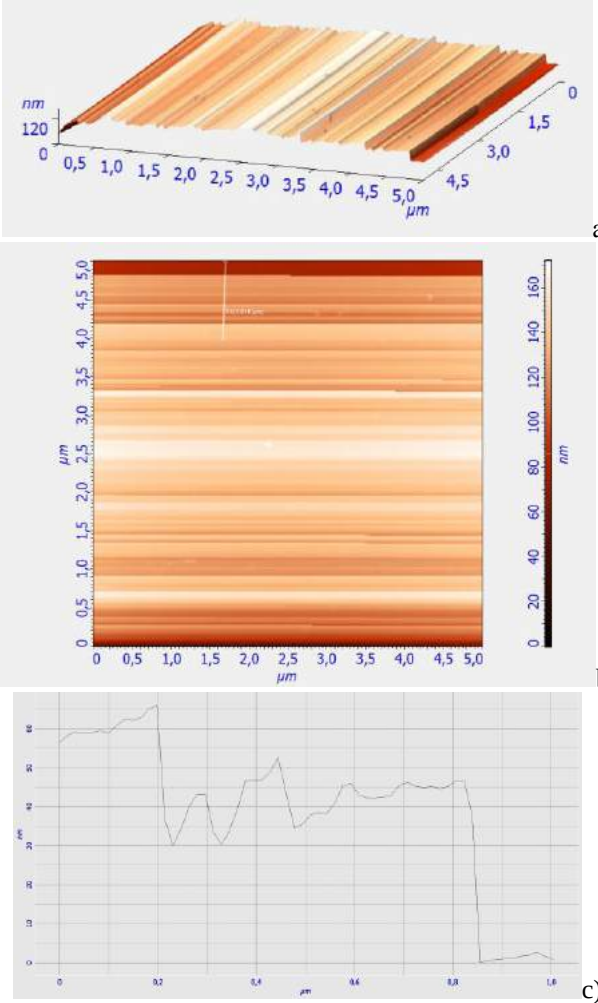

Fig.4 (a, b, c) SPM images of surface (0001) Sb_2Te_3<ZnSb>: a) images of step in 3D- scale; b) step in 2D- scale; c) surface profile along vertical like of pattern on the part b

EXPERIMENT AND RESULT DISCUSSION

X-ray diffraction pattern of doped $CuBi_2Te_3$ is given in Fig.1(a); noticed nanoparticles of BiTe, Bi_2Te_4 copper and main reflexes of Bi_2Te_3 on crystal spell surface.

In Fig.1(b) Bi_2Te_3<Ni> (Fig.1(b)) and Sb_2Te_3<ZnSb> (Fig.1(b) system experimental results are given. As it is seen copper is embedded in the layers as in the nanocontainer not interacting with stoichiometric component of Bi_2Te_3: tellurium and bismuth. X-ray diffraction peaks from copper nanoparticles are attested (Fig.1a). X-ray diffraction patterns of Bi_2Te_3<Ni> samples (Fig.(1(b)) (obtained during the process of crystal growth) shows mainly the peaks from $NiTe_2$, NiTe and Ni nanoparticles. Here the space $Te^{(1)}$-$Te^{(1)}$ Bi_2Te_3 plays the role of nanocontainer not only for Ni but the role of nanoreactor where NiTe and $NiTe_2$ nanoparticles have been formed. From Fig.1(b) it is seen that on surface (0001) Sb_2Te_3<ZnSb> nanolayers of ZnSb have been formed.

From Fig.2(a, b, c) there has been presented SPM image in scale of Bi_2Te_3<Cu>; from the figure there have been seen interlayer nanoprotrusions on the surface (0001). In Fig.2(b) there has been prescuted the same interlayer surface only in 2D scale. In Fig.2(b) there has been given the fragment of the surface along with the profile pattern 2(b) of step and nanoprotrusions along the horizontal likes on the part b. From Fig.2 there have been seen sizes of height (within (10-40nm)) and "slots" in width (200-300)nm. From Fig.2(b) there have been seen repetitions of "slot" profiles within scanning 450nm.

By SPM there have been investigated initial stages of growth of interlayer vicinal surfaces of Bi_2Te_3<Ni> and Sb_2Te_3<ZnSb> crystal. It is shown that on the surfaces grown in the direction of basic surface nanofragments under the step – layered growth have been formed. Height of steps and recesses varies from 15 to 20 nm. There have been revealed spontaneously obtained nanofragments like the processes of growth and self-organization of Ge nanostructures on Si (111) vicinal surface [2] on microscopically ordered faceted surfaces. By controlling processes of crystallization, rate of growth, introduction of impurities and annealing there have been obtained interlayer vicinal surfaces including regular series of steps (see Fig.2(b) and 3(b)).

SPM images of interlayer surfaces without electropolished are given in Fig.2 and Fig.3. The surface consist of as atomic and smooth as microheterogeneous sections not being etch figures.

Vicinal-like surface among Bi_2Te_3<Ni> layers are a system of steps in height h=15-20nm. Length of steps among the fractures is 2 μk. As a result of building impurities in steps its smooth edge does not change.

Along the step from upper and lower benches there have been seen regions with reduced concentration of nanoislands regions (See Fig.2(a, b)). In Fig.2(b) profile pattern .of Bi_2Te_3<Cu> step and impurity nanofragments distribution has been shown.

Formation of interlayer step echelons can be when impurity flow at the expense of thermodiffusion effect along the surface (0001) is taken place [8]. The same process appears to be formed in other layered crystal under the investigation.

As it is seen interlayer surface (0001) Bi_2Te_3 doped by Ni is less rough: observed nanoplates are different from Ni, NiTe and $NiTe_2$ composition (Fig.1b) and form specific structure from steps covering the whole surface (0001) Bi_2Te_3. Distribution of nanoprotrusions on interlayer surface (0001) according to [1, 6] points to fractured behavior of formed relief among the layers $Te^{(1)}$- $Te^{(1)}$ during the crystal growth.

SPM images show that nickel and copper atoms during the growth and crystallization after introduction in interlayers $Te^{(1)}$ $A_2^V B_3^{VI}$ <Cu, Ni and ZnSb> being ordered cause step gradation. By maximum concentration (0,8% wt) monolayer of particles (Cu and Ni) are embedded between the pairs of layers $A_2^V B_3^{VI}$ <impurity> (like in graphite [9]. Compounds of the first step with the concentration decrease form intercalations of higher step in the compound of the second step nanoislands is

embedded through two layers; in the compound of the third degree particles are embedded through each three layers).

In the case of $A_2^V B_3^{VI}$ matrix by unit where crystal structure is the sandwich $Te^{(1)}$- $Te^{(2)}$-Bi- $Te^{(1)}$, in which easily diffused impurity (Cu or Ni) takes among the layers positions either $Te^{(2)}$-Bi or Bi- $Te^{(1)}$ or $Te^{(1)}$- $Te^{(1)}$. Layer-sandwiches like these are built up in piles along the hexagonal axis C. Bonds within the layer are ion-covalent but between $Te^{(1)}$- $Te^{(1)}$ are week Van-der-Waals ones. These weak "slits" make chalcogenides Bi and Sb two-dimensional crystals. "Pile" of layers (sandwiches) ($T^{(1)}$-Bi-$Te^{(2)}$) are the most probable band of impurity filling. Between ($Te^{(1)}$- $Te^{(1)}$) there has been formed "gradation" by intercalation of impurities (Ni and Cu) in $A_2^V B_3^{VI}$. And the layer $Te^{(1)}$- $Te^{(1)}$ can be the band according to [9] the third step in billing. Self-intercalation results in Bi_2Te_3<Cu> can corroborate the mechanism of step formations being different in height.

Nanoobject generation (see Fig.2(a)) is taken place in places of building up at the step edge. Probably "viskers" generation close to the edge is arisen on defect boundary between initial step $A_2^V B_3^{VI}$ <Ni or Cu> and intergrown layer Ni or Cu. During the growth nanoprotrusion height at the step edge is limited by the sizes of lower bench.

By self-organization process there have been occurred interlayer slots perpendicular to steps with front along the direction [0001]. Mesa structures like these are the slots in width 200-600nm. Controlling the course of layer formation we can get systems of parallel steps with smooth not fractured edges in length up to 2 μm. In Fig.2(a) there has been prescuted image of surface (0001) Bi_2Te_3<Cu> including steps with distance among fractures more then 200nm. Such vicinal surfaces Si (111) are given in [2].

The self-organization nature of much steps appears to be similar as by epytaxy as self-organization of impurities on interlayer surface of layered crystals.

CONCLUSIONS

Morphology analysis of the surface (0001) Bi_2Te_3<Ni and Cu> and Sb_2Te_3<ZnSb> shows that nanaparticles and quasisteps can be formed among the layers with various interlayer nanofragments from: Cu, BiTe, Bi_3Te_4, $NiTe_2$, NiTe, Ni and ZnSb.

Arising steps in $A_2^V B_3^{VI}$ <Cu, Ni and ZnSb> during the process play an important role when intralayer forces contribute considerably interlayer ones. Given percularities of interlayer layered step surface can lead to specific dynamics of crystal lattice that must be manifested in physical phenomena [6, 10].

The reason of nanostep growth and nanoprotrusions lies in that the impurity atom also interact with defect on the surface (0001) flowing from accumulated layers $Te^{(2)}$-Bi and Bi-$Te^{(1)}$, interacting between each other creating elastoctressed steps with nanoislands from interacting particles.

This effect is the pecularity of self-organization during the growth of investigated layered systems leading to the formation of two- dimensional structures with steps.

[1]. *F.K.Aleskerov, S.Sh.Kakhramanov, E.M.Derun, M.Y.Pishkin, Y.Kavei*. Some pecularities of nanoobject formation in interlayer space of Bi_2Te_3 – typed crystals // Fizika, Azerbaijan, 2007, vol.XII, №4, p.41.

[2]. *K.N. Romanyuk, S.A.Tyis, B.Z.Olshanetskii*. Investigation by method of scanning tunnel microscopy of growth and self-organization Ge nanostructures on vicinal surfaces Si (111) // Physics of Solid State., 2006., vol.48, ed.9, p.1716.

[3]. *V.M.Marchenko*. Probable structures and phase transitions on crystal surfaces // Letters, JETF, vol.33, ed.8, p.397 (1981).

[4]. *V.I. Matchenko*. About steps on guazicrystal surfaces // letters, JETF, vol.56, ed.10., pp.547 (1992).

[5]. *N.A.Abdullayev*. Pecularities of layered crystal elastic properties // Physics of solid states, 2006, vol.48, ed.4, p.623.

[6]. *F.K.Aleskerov, S.Sh.Kakhramanov, M.M.Asadov, K.Sh.Kakhramanov*. Formation of impurity nanostructures on surface (0001) $Bi_2Te_{2.96}Se_{0.04}$<Ag> and Bi_2Te_3<Ni> // Condensed mediums and phase boundaries. Vol.11, №4, pp.277-279.

[7]. *V.Yu.Vityukhkin, I.V.zakurdayev*.Study of tungsten crystal surface self-organization at atom thermodifussion by method of scanning probe microscopy // FTP, 1997, vol.39, №6, p.968.

[8]. *Ya.E. Geguzin, Yu.S.Kaganavski* // Diffusion processes on crystal surface, M.(1984), p.124.

[9]. *Ch.N.P.Rao, J.Gopalakrishian* // New trends in chemistry of solid state// Novosibirsk, "Nauka", 1990, p.506.

[10]. *S.Sh. Kakhramanov*. Self-intercalation in Bi_2Te_3<Cu> // Non-organic materials. Russian, 2008, vol.44, №1, p.17-25

APPLICATION OF INDUCTIVELY COUPLED PLASMA MASS SPECTROMETRY (ICP/MS) TO DETECTION OF TRACE ELEMENTS, HEAVY METALS AND RADIOISOTOPES IN SCALP HAIR

S. ÖZTÜRK YILDIRIM [1*], Y. BENDERLİ CİHAN [2]

[1] *Physics Department, Faculty of Sciences, University, 38039 Kayseri, Turkey*

[2] *Kayseri Training & Res Hosp, Dept Radiat Oncol, 38010 Kayseri, Turkey*

* *ozturk@erciyes.edu.tr*

Trace element analysis of human hair has the potential to reveal retrospective information about an individual's nutritional status and exposure. As trace elements are incorporated into the hair during the growth process, longitudinal segments of the hair may reflect the body burden during the growth period. We have evaluated the potential of human hair to indicate exposure or nutritional status over time by analysing trace element profiles in single strands of human hair. By using inductively coupled plasma mass spectrometry (ICP-MS), we achieved profiles of 43 elements in single strands of human hair, namely, Li, Be, B, Na, Mg, Al, K, Ca, Sc, Ti, V, Cr, Mn, Fe, Co, Ni, Cu, Zn, Ga, As, Se, Rb, Sr, Rh, Pd, Ag, Cd, Sn, Sb, Cs, Ba, Ce, Pt(194), Pt(195), Pt(196), Au, Pt(198), Hg, Pb, Bi, U(234), U(235) and U(238). We have shown that trace element analysis along single strands of human hair can yield information about essential and toxic elements, and for some elements, can be correlated with seasonal changes in diet and exposure. The information obtained from the trace element profiles of human hair in this study substantiates the potential of hair as a biomarker.

1. INTRODUCTION

Multi-element determinations in biological samples have been described in the literature with focus on the analytical method development [1–22]. These papers are dealing with the analyses of blood [1–4], serum [4–12], urine [1,4,6,13– 18], hair [19,20] nails [19] bones [21] or saliva [22]. Only a few papers describe both, the method development for the determination of a large number of elements and the analysis of a statistically relevant number of real samples [2,23–26]. Rodushkin et al. [3] developed a method for the determination of 60 elements in whole blood by sector field ICP-MS. In another paper [2] of this author 50 elements were determined in blood samples of 31 non-exposed human subjects. Minoia et al. [24] determined 46 elements in urine, blood and serum by graphite furnace atomic absorption spectrometry (GF-AAS) and inductively coupled plasma optical emission spectrometry (ICP-OES). For many elements the power of detection of these two methods is not sufficient to determine elemental background concentrations. In general, lower limits of detection (LODs) are possible by inductively coupled plasma mass spectrometry (ICP-MS). To avoid spectral interferences, which are often described as the major disadvantage in ICP-MS, high-resolution sector field ICP-MS was suggested for the analysis of biological materials [2–6,11,12,16,17].

In our approach the application of a new ICP-MS instrument with the collision/reaction cell technology was used to remove spectral interferences but keeping all other unique capabilities of ICP-MS, such as low detection limits, multi-element capability and a wide linear calibration range. Compared with sector field ICP-MS it is also lower in investment costs. For the rapid and reliable routine analysis with high sample throughput collision/reaction cell ICP-MS was established for urine analysis [26].

Biomonitoring of trace elements in urine samples of healthy humans has been published for many elements at different geographical locations. Many of these papers deal with elements described as toxic or carcinogenic, such as As [24,26–28,33], Cr [24,26,29–33], Ni [24,26,30–33], Hg [24,32,33] or Pb [13,24,26,32,33]. Other publications deal with biomonitoring of essential trace elements, for example, for Se [24,26,32–34], Cu [24,26,33], Mo [24,26,33,35] or Zn [24,26,33]. For some elements (e.g., Se or Mn) other biological fluids (serum or blood) are preferred for analyses to investigate the essential trace element concentrations, however, in the case of intoxications urine is often used. For As, Cd, Cr, Cu and Hg in urine a representative population study was performed in the German Environmental Survey in 1992 [36] and this was repeated 6 years later with Pb, Cd, Hg, Au, Ir and Pt in urine [37,38]. Reference values for Cd, Hg, As in urine were derived from this survey [39]. For the US population urinary concentrations of the elements Pb, Cd, Hg, Co, U, Sb, Ba, Be, Cs, Mo, Pt, Tl, W were published in the Second National Report on Human Exposure to Environmental Chemicals [40]. Both surveys, in Germany and in the US, provide results for children. Other Reference values for youngsters in the urban area of Rome were described for Ni, Cr and V [41].

In this paper the analysis results of some hair samples from non-exposed humans are presented. The major goal of the analyses was to determine background concentrations of those elements for which only little data are available in the literature.

2. MATERIALS AND METHODS

2.1. TECHNIQUE

As the name implies, ICP-MS is a combination of an inductively coupled plasma (ICP) with a mass spectrometer (MS). Typically, the sample is introduced into the ICP by a sample introduction system consisting of a peristaltic pump and a nebuliser, which generates a fine aerosol in a spray chamber. The spray chamber separates the small droplets from the large droplets. Large droplets fall out by gravity and exit through the drain tube at the end of the spray chamber, while the small droplets pass between the outer wall and the central tube and are eventually transported into the sample injector of the plasma torch using a flow of argon gas. The aerosol is then transported to the ICP, which is a plasma ion source. This plasma is formed by the application of a high voltage spark to a tangential flow of argon gas, which causes

electrons to be stripped from their argon atoms. These electrons are caught up and accelerated into a magnetic field, formed by a radio frequency (RF) energy which is applied on a RF coil surrounding the plasma torch. This process causes a chain reaction of collision-induced ionization leading to an ICP discharge. The ICP reaches temperatures of 6,000– 8,000 K. As the aerosol transits the plasma, the droplets undergo numerous processes which include desolvation, dissociation, atomization, and ionization [42]. Ions produced by the argon ICP are principally atomic and singly charged, making it an ideal source for atomic MS. Since the ICP works at atmospheric pressure and the MS requires a vacuum, an interface typically consisting of a coaxial assembly of two cones (sampler and skimmer cone) and a series of pressured differentials to allow efficient sampling of the atmospheric pressure plasma gases while minimally perturbing the composition of the sample gases.

After passing through the sampler and skimmer cones, several electrostatic lenses or ion optics focus the ions into the MS, where the ions are separated based on their mass-to-charge (m/z) ratios. Three main mass separation principles are used in ICP-MS systems: quadrupole, magnetic sector, and time offlight (TOF). The quadrupole is the most commonly used type in ICP-MS. It comprises of two pairs of parallel cylindrical rods. The voltages applied to these rods give a dynamic hyperbolic electric field, in which any ion above or below the set mass enters an unstable trajectory and is lost from the ion beam. By varying the voltages applied to these rods, a full mass spectrum can be obtained [42]. While the quadrupole MS is used in the majority of ICP-MS instruments, some systems utilize a magnetic sector or high resolution (HR) analyzer, typically employed when higher mass resolution is required [43]. This analyzer uses a magnetic field, which is dispersive with respect to ion energy and mass and deflects different masses through different angles. The ions subsequently enter an electrostatic analyzer, which is dispersive with respecttoion energy and focuses the ions to the detector. In a TOF MS [44], a uniform electrostatic pulse is applied to all ions at the same time, causing them to be accelerated down a flight tube. Because lighter ions achieve higher velocities and arrive at the detector earlier than heavier elements, the arrival times of the ions are determined by their m/z ratios.

After passing the mass separator, the ions strike the active surface of the detector, typically an electron multiplier. Each ion which hits the channel electron multiplier generates a cascade of electrons leading to a discrete pulse. The pulses are counted and the output signal is given in counts per second.

2.2. INTERFERENCES

One of the main limitations of ICP-MS is the appearance of interferences, which can be classified into two major groups. The first group comprises the spectral interferences, which arise from other elements (isobaric interferences), polyatomic ions (e.g., oxides) with the same m/z ratio as the analyte isotope, or doubly charged ions when half of their masses are similar to the mass of the analyte isotope. Elemental isobaric interferences can usually be avoided by choosing an interference free analyte isotope when the analyte of interest is not monoisotopic. Alternatively, because of the constant nature of isotope ratios for most of the naturally occurring elements, elemental isobaric interferences can be easiliy corrected mathematically by monitoring the intensity of an isotope of the interfering element which is free from spectral interferences [42]. For the three most abundant Pt isotopes (^{194}Pt: abundance 33.0%, ^{195}Pt: 33.8%, ^{196}Pt: 25.2%), only ^{196}Pt is subject to an isobaric interference (^{196}Hg). However, this interference can be corrected online by monitoring ^{202}Hg signals. For the most abundant isotopes of Ru (^{99}Ru: 12.7%, ^{101}Ru: 17.0%, ^{102}Ru: 31.6%, ^{104}Ru, 18.7%), ^{99}Ru, ^{102}Ru, and, ^{104}Ru are subject to isobaric interferences of respectively ^{99}Tc, ^{102}Pd, and ^{104}Pd, which can also be corrected online.

Polyatomic or molecular interferences can be produced by the combination of two or more atoms and/or ions leading to a molecule ion and are usually associated with either the argon plasma, atmospheric gases, or matrix components of the solvent or the sample. These interferences can be overcome by choosing an interference free isotope, removing the matrix [45], using alternative sample introduction systems, using mathematical corrections equations [46], employing cool plasma conditions [46], using a collision or reaction cell [47], or by using a high resolution mass analyzer [48]. Elements with high masses, such as Pt, are less susceptible to molecular interferences than lower masses, such as Ru [49-50]. However, metal oxide interferences, which can occur as a result of incomplete dissociation of the sample matrix or from recombination within the plasma or the interface, can interfere with the analysis of Pt and Ru. Pt isotopes may be subject to interferences from hafnium oxides [51-52] and tungsten oxides. Ru isotopes can be subject to oxide interferences from krypton, bromine, selenium, strontium, and rubidium. Oxide formation, though, can be minimized by optimizing the gas flow rate, pump rate, and ionization conditions of the plasma. Since metal oxide formation is typically controlled, via the plasma conditions, to be less than 2% and because hafnium background concentrations in biological samples are typically lower than Pt backgrounds [53], hafniumoxides will not interfere significantly with Pt signals [54]. Prior to the development of an ICP-MS assay for Pt or Ru, however, background concentrations of the elements of potentially interfering metal oxides in the biological matrix should be investigated.

The last type of spectral interferences are the doubly charged ions, which are analyzed at half the mass of the element, since the mass spectrometer measures m/z ratios. Pt isotopes are not susceptible to interference of doubly charged ions as no element with a mass two times the mass of Pt exists.Ru isotopes, however, might be interfered by

some doubly charged ions ($[Pt]^{2þ}$, $[Hg]^{2þ}$, and $[Pb]^{2þ}$). The formation of doubly charged ions can, however, be minimized by optimizing ICP-MS parameters such as lens voltages and plasma conditions. However, because background levels of heavy metals such as Pt might vary it is advisable to monitor the signals of these elements routinely during analysis.

The second group of interferences are the nonspectral interferences which can be broadly divided into two categories: first the physical signal suppression resulting from (un)dissolved solids or organics present in the matrix. Matrix components may have an impact on the droplet formation in the nebuliser or droplet size selection in the spray chamber, which can affect the transport efficiency and thus the signal intensity (Thomas, 2002). In the case of organic matrices, the viscosity of the sample that is aspirated is modified. In addition, the solids present in the matrix might lead toa deposition of solids on the cones and subsequently result in an altered ion transmission. Furthermore, undissolved solids can clog the nebuliser and torch. A decrease in these physical effects is possible by an adapted sample pretreatment (e.g., dilution), the use of proper calibration techniques (Jarvis, Gray, & Houk, 1992) preferably combined with the use of an internal standard (IS), or by adjustment of the sample introduction system.

The second category of nonspectral interferences are the matrix interferences (Thomas, 2002) which are caused by changes in the loading of the plasma or space-charge effects and result in signal alteration. An extensive loading of the plasma may effect the ionization efficiency of the analyte ions. High concentrations of easily ionisable matrix elements, such as sodium, might result in a decreased ionization efficiency of elements with higher ionization energies and thus a decreased signal of these elements. In general, the lower the degree of ionization of the analyte in the plasma, the greater the effect of a matrix component on the ion count rate of the element will be.

Space-charge effects are frequently seen in the analysis of light elements. The magnitude of signal suppression generally increases with decreasing atomic mass of the analyte ion. This is the result ofapoor transmission ofions through the ion optics due to matrix induced space-charge effects. The high-mass matrix element will dominate the ion beam and pushes lighter elements out of the way resulting in a suppression of the signal.

It is difficult to measure and quantify nonspectral matrix interferences. Again, separation of the analytes from the matrix or dilution of samples may reduce this type of nonspectral interferences. Furthermore, internal standardization may be successful in reducing the interferences. The IS, however, must be closely matched in both mass and ionization energy because they are to behave equal to the analyte. Also, the use of matrix matched calibration standards or standard addition might correct the matrix interferences. Although the signal suppression of the
analyte will be corrected by proper calibration methods, the actual space-charge effects will not be solved. The most common approachtoreduce space-charge effects is to apply voltages to the individual ion lens components. This will steer the analyte ions through the mass analyzer while rejecting a maximum number of matrix ions [55].

2.3. COMBINATION OF ICP-MS DETECTION WITH SPECIATION TECHNIQUES

ICP-MS can be used as a Pt or Ru specific detector for several speciation technologies. ICP-MS has several advantages over other methods of detection including a wide linear dynamic range, low detection limits, potential for isotope determinations, and multi-element capability. Moreover, the signal intensities are independent of the chemical structure of the analyte incorporating Pt or Ru and hence the method does not require standards of each analyte/metabolite/adduct. ICP-MS can provide quantitative information for structurally noncorrelated metal compounds.

2.4.METHOD VALIDATION

Following development of an ICP-MS assay and before implementation into routine use, the assay needs to be validated to demonstrate that it is suitable for its intended use. Validation is required to ensure the performance of the method. As chromatography is widely used in bioanalysis, validation guidelines have already been extensively described for speciation methods (U.S. Food and Drug Administration et al., 2001). In contrast, no such guidelines are available for ICP-MS. This has led to some discrepancies concerning the definition of validation parameters in literature describing ICP-MS based bioanalytical assays. No stringent procedure is followed for the assessment of limit of detections (LODs), lower limit of quantifications (LLOQs), precision, accuracy, and linearity in the field of ICP-MS. The LOD and LLOQ for instance can be obtained by several approaches such as; signal-to-noise ratios, the standard deviation of the noise, or the standard deviation of the noise and slope of the calibration curve [56]. For reported ICP-MS assays it is not always defined which approach has been used. Furthermore, the LOD, LLOQ, and calibration range are reported either in the processed sample matrix (the final matrix entering the ICP-MS) or in the unprocessed sample matrix. The difficulty is, that the matrix in question is not always clearly defined. Another intricacy is that concentrations of compounds are commonly reported in weight per volume (w/v) instead of molar concentrations (moles/v). In case of an elemental detection technique like ICP-MS, it therefore is pivotal to report whether the metal or the metal-containing compound is used for calculation of the concentrations. Unfortunately, this is not always clear from the reported data. Because of these issues it is difficult to compare assays based on their detection limits and other validation parameters.

In our opinion, procedures followed in, for example, the FDA guidelines could, as far as applicable for ICP-MS, serve as an example for the development of a guideline for the validation of ICP-MS assays in biological matrices (U.S.Food and Drug Administration et al., 2001). Validation parameters could include assessment of the LLOQ, carry-over, linearity, specificity, accuracy, precision, cross analyte /IS interference, and stability.

2.2.5. ASSAY DEVELOPMENT

For ICP-MS analysis, biological samples cannot be analyzed directly, but require a pretreatment to reduce the matrix effects of endogenous compounds, such as cell constituents, proteins, salts, and lipids. The development of ICP-MS methods for metals in biological matrices is generally focused on the selection of an appropriate sample pretreatment and the selection of calibration

proceduresto avoid and compensate matrix effects. Additionally, instrumental modifications can be used to further optimize the assay. For the analysis of low concentrations of metal it is important to consider that, whatever sample pretreatment procedure is used, special care has to be taken to avoid contamination of samples. A careful selection of pretreatment devices and reagents should be performed. Glassware should be avoided as it may contain considerable amounts of Pt. Moreover, sample pretreatment needs to be performed in a dedicated area to prevent environmental Pt or Ru originating from, for example, pollution by car exhaust catalysts (Barefoot, 1997), from interfering with the analysis. Besides the prevention of contamination it is relevant that blanks do not contain detectable levels of analyte. Screening of background levels is, therefore, necessary. An Agilent model 7500a inductively coupled plasma mass spectrometer was used for the determination of uranium and thorium. The instrument was optimized daily before measurement and operated as recommended by the manufacturers. The conditions are given in Table 1.

Table 1. Operating conditions of ICP-MS

Inductively coupled plasma	Agilent 7500 a
Nebulizer	Babington
Spray chamber	Quartz, double pass
RF power	1260 W
Frequency	27.12 MHz
Sampling depth	7.0 mm
Plasma gas flow rate	15 L min^{-1}
Auxiliary gas flow rate	1.0 L min^{-1}
Carrier gas flow rate	1.15 L min^{-1}
Sample uptake rate	0.3 mL min^{-1}
Detector mode	Auto
Integration time	0.10 s
Number of replicates	3
Analytical masses	^{238}U, ^{232}Th
Internal standard	^{209}Bi, Be, Rh, Sc

High purity reagents were used for all preparations of the standard and sample solutions. The standard solutions used for the calibration procedures were prepared before use by dilution of the stock solution with 1 mol L^{-1} HNO_3. Stock solutions of diverse elements were prepared from the high purity compounds (99.9%, E. Merck, Darmstadt). A solution of 5 ml HNO_3 (99.9%, E. Merck) was used for accelerated samples.

A pH meter, WTW Inolab Level 3 Model glass-electrode was employed for measuring pH values in the aqueous phase. The water was purified in Millipore Synergy 185.

About ~3 g of hair were cut from the nape of the neck close to scalp, as strands ~1–3 cm long, with a pair of plastic scissors. The samples were directly stored in zip-mouthed polythene bags, duly labelled with relevant codes related to the donor's name, age, eating and drinking habits, social and general health status, all recorded and compiled on regular proforma at the time of sampling. The individual hair samples were washed with 5% (w/v) detergent solution and rinsed with plentiful distilled water to remove exogenous matter (Dombo-vari and Papp 1998). The samples were dried overnight at 50°C in an electric oven and cooled to room temperature in a desiccator containing silica gel as the desiccant. An accurately weighed portion (~1 g) of the hair sample was treated with 10.0 ml of concentrated (65%) nitric acid and heated at 80°C for 10 min. It was cooled to room temperature, followed by addition of 5.0 ml of perchloric acid with subsequent heating to a soft boil until white dense fumes evolved. Sample was cooled to room temperature and diluted to 50 ml with distilled water. The blank was prepared the same way but without the hair sample. All reagents used were of ultrahigh purity (certified >99.99%) procured from E-Merck. All statistical analyses were performed using computer program Excel X State (Microsoft Corp., Redmond, WA) and SPSS 13.0 software was used for all statistics. Data are expresssed as means ± standart deviations for our group.

3. RESULTS AND DISCUSSION

Concentrations of Cd, Cr, Cu, Mn, Mo, Ni, Pb, Se, Tl, Zn, …. were analyzed by ICP-MS in the scalp hair of male subjects from an urban area, three different quarters of Kayseri, Turkey. A questionnaire on personal data, nutritional habits, socio-economic, occupation and health status was completed by the subjects.

The main descriptive statistics of metal concentrations in scalp hair are summarized in Tables 2. Our results are in general agreement with values reported by other authors [57-68].

Our results were obtained for a relatively small group of subjects, and this fact precludes the assessment of normal ranges and firm general conclusions. Further studies need to be carried out in order to identify the greater number of analytical data in this area.

ACKNOWLEDGMENT: The authors are grateful for the financial support of the Unit of the Scientific Research Project of Erciyes University (Project no.: **EÜBAP- FBA-09-959**).

Table 2**.** Basic statistical paremeters for selected trace elements distribution (µg/g,) in the scalp hair.

Trace element	Range	Median	Mean	Std. Error	Std. Deviation	Skewness
Li	1,38-0,03	0,452	0,5625	0,16964	0,56264	0,315
Be	0,09-0,00	0,0092	0,0151	0,00782	0,02594	3,247
B	23,95-0,20	0,1959	5,8229	2,48439	8,23979	1,252
Na	42,96-0,01	0,40	4,1696	3,87945	12,86667	3,316
Mg	0,91-0,50	0,88	0,8483	0,03462	0,11482	-3,283
Al	56,22-0,17	12,90	15,9907	5,63981	18,70512	1,488
K	9,12-0,07	3,12	3,1328	0,95721	3,17469	1,127
Ca	295,00-0,00	0,00	42,9936	29,90152	99,17213	2,224
Sc	0,03-0,03	0,0272	0,0272	0,00000	0,00000	0,00000
Ti	1,00-0,16	0,54	0,5707	0,08457	0,28048	0,210
V	9,48-0,03	0,511	1,8717	0,87358	2,89733	2,104
Cr	6,99-0,19	1,19	2,4178	0,79579	2,63933	0,769
Mn	8,30-,08	1,12	1,8420	0,68033	2,25640	2,751
Fe	4,02-4,02	4,01	4,0190	0,00000	0,00000	0,00000
Co	0,15-0,01	0,171	0,0387	0,01390	0,04609	1,857
Ni	0,13-0,13	0,128	0,1287	0,00000	0,00000	0,00000
Cu	52,06-4,53	34,627	36,5976	4,41572	14,64530	-0,913
Zn	362,5-34,8	261,78	227,6433	30,09715	99,82097	-0,665
Ga	7,20-0,01	0,0054	0,6591	0,65373	2,16817	3,317
As	0,25-0,07	0,253	0,2346	0,01663	0,05514	-3,258
Se	14114,58-0,6	1066,6	2340,1155	1231,00718	4082,78893	2,834
Rb	1,76-0,00	0,0037	0,3071	0,17554	0,58221	1,960
Sr	5,40-0,00	0,1504	1,4961	0,65927	2,18656	1,268
Rh	0,00-0,00	0,0042	0,0038	0,00037	0,00124	-3,317
Pd	0,08-,01	0,0144	0,0205	0,00608	0,02017	3,317
Ag	7,78-,01	0,0549	1,8075	0,83581	2,77206	1,570
Cd	0,70-,01	0,069	0,1740	0,06293	0,20872	1,869
Sn	54,40-0,14	5,392	9,3290	4,72255	15,66292	2,805
Sb	0,02-0,02	0,015	0,0156	0,00000	0,00000	0,00000
Cs	0,15-0,00	0,0088	0,0351	0,01563	0,05183	1,588
Ba	5,17-0,08	0,079	1,2012	0,51727	1,71559	1,586
Ce	0,40-0,03	0,135	0,1806	0,03999	0,13262	0,694
Au	50,63-0,54	0,543	5,5480	4,53009	15,02460	3,260
Hg	5,93-0,21	1,315	1,7150	0,53660	1,77968	1,645
Pb	22,38-0,37	5,02	7,6008	2,10282	6,97427	1,301
Bi	0,42-0,00	0,071	0,1376	0,04624	0,15336	0,896
Pt(194)	0,02-0,2	0,021	0,0217	0,00000	0,00000	0,00000
Pt(195)	4,00-0,35	1,500	1,7015	0,33179	1,10042	0,836
Pt(196)	0,02-0,01	0,016	0,0157	0,00027	0,00090	-3,317
Pt(198)	0,28-0,01	0,029	0,0675	0,02447	0,08116	2,008
U(234)	14,97-0,00	2,940	3,9435	1,43643	4,76410	1,333
U(235)	1,14-0,14	0,655	0,6447	0,07344	0,24357	0,001
U(238)	1,37-0,1	0,022	0,3375	0,15778	0,52330	1,477

[1]. *D.E. Nixon, T.P. Moyer* Routine clinical determination of lead, arsenic, cadmium and thallium in urine and whole blood by inductively coupled plasma mass spectrometry. Spectrochim Acta Part B Atom Spectrosc 1996;51:13–25.

[2]. *I.Rodushkin, F. O¨ dman, S. Branth* Multielement analysis of whole blood by high resolution inductively coupled plasma mass spectro-metry. Fresenius' J Anal Chem 1999;364:338–46.

[3]. *I .Rodushkin, F. O¨ dman, R. Olofsson, M.D. Axelsson.* Determination of 60 elements in whole blood by sector field inductively coupled plasma mass spectrometry. J Anal At Spectrom 2000;15:937–44.

[4]. *J.M. Marchante-Gayo´n, C.S. Muniz, J.I. Garcia Alonso, A.Sanz-Medel* Multielemental trace analysis of biological materials using double focusing inductively coupled plasma mass spectrometry detection. Anal Chim Acta 1999;400:307–20.

[5]. *E. Barany, I.A. Bergdahl, A. Schu¨tz, S. Skerfving, A.Oskarsson* Inductively coupled plasma mass spectrometry for direct multi-element analysis of diluted human blood and serum. J Anal At Spectrom 1997;12:1005–9.

[6]. *B. Bocca, A. Alimonti, F. Petrucci et al.* Quantification of trace elements by sector field inductively coupled plasma mass spectro-metry in urine, serum, blood and cerebrospinal fluid of patients with Parkinson's disease. Spectrochim Acta Part A Mol Spectrosc 2004;59: 559–66.

[7]. *A. Alimonti, F. Petrucci, F. Laurenti, P. Papoff, S.Caroli* Reference values for selected trace elements in serum of term newborns from the

urban area of Rome. Clin Chim Acta 2000;292:163–73.

[8]. *C.S. Hsiung, J.D. Andrade, R. Costa, K.O. Ash.* Minimizing spectral interferences in the quantitative multielement analysis of trace elements in biological fluids by inductively coupled plasma mass spectrometry. Clin Chem 1997;43:2303–11.

[9]. *L. Yu , S.R. Koirtyohann, M.L. Rueppel , A.K. Skipor, J.J.Jacobs* Simultaneous determination of aluminium, titanium and vanadium in serum by electrothermal vaporization-inductively coupled plasma mass spectrometry. J Anal At Spectrom 1997;12:69–74.

[10]. *C. Huang, D.Beauchemin* Direct multielement analysis of human serum by ICP-MS with on-line standard addition using flow injection. J Anal At Spectrom 2003;18:951–2.

[11]. *C.S. Muniz, J.M. Marchante-Gayo´n, J.I. Garcia Alonso, Sanz-Medel*. Accurate determination of iron, copper and zinc in human serum by isotope dilution analysis using double focusing ICP-MS. J Anal At Spectrom 1999;14:1505–10.

[12]. *J. Begerow, M .Turfeld, L. Dunemann* New horizons in human biomonitoring of environmentally and occupationally relevant metals — sector field ICP-MS versus electrothermal AAS. J Anal At Spectrom 2000;15:347–52.

[13]. *P. Schramel, I. Wendler, J. Angerer* The determination of metals (antimony, bismuth, lead cadmium, mercury, palladium, platinum, tellurium, thallium, tin and tungsten) in urine samples by inductively coupled plasma mass spectrometry. Int Arch Occup Environ Health 1997;69:219–23.

[14]. *A.T. Townsend, K.A. Miller, S. McLean, S.Aldous* The determination of copper, zinc, cadmium and lead in urine by high resolution ICP-MS. J Anal At Spectrom 1998;13:1213–9.

[15]. *P. Schramel, I. Wendler* Antimony, lead, cadmium, platinum, mercury, tellurium, thallium, bismuth, tungsten, tin. In: Angerer J, Schaller KH, editors. Analyses of hazardous substances in biological materials, vol. 6. Weinheim' Wiley-VCH; 1999. p. 79–109.

[16]. *P. Schramel, Dunemann L.* Aluminum, chromium, cobalt copper, manganese, molybdenum, nickel, vanadium. In: Angerer J, Schaller KH, editors. Analyses of hazardous substances in biological materials, vol. 7. Weinheim' Wiley-VCH; 2001. p. 73–96.

[17]. *A.T. Towsend* The accurate determination of the first row transition metals in water, urine, plant, tissue and rock samples by sector field ICP-MS. J Anal At Spectrom 2000;15:307–14.

[18]. *G. Centineo, M .Montes Bayo´n, A. Sanz-Medel* Flow injection analysis with inductively coupled plasma time-of-flight mass spectrometry for the simultaneous determination of elements forming hydrides and its application to urine. J Anal At Spectrom 2000;15:1357–62.

[19]. *I. Rodushkin, D.Axelsson* Application of double focusing sector field ICP-MS for multielement characterization of human hair and nails: Part 1. Analytical methodology. Sci Total Environ 2000;250: 83–100.

[20]. *J. Yoshinaga, J. Shibata, M. Morita* Trace elements determined along single strands of hair by inductively coupled plasma mass spectrometry. Clin Chem 1993;39:1650–5.

[21]. *P. D´Haese, M.M. Couttenye, L.V. Lamberts, et al.* Aluminum, iron, lead, cadmium, copper zinc, chromium, magnesium, strontium and calcium content in bone of end-stage renal failure patients. Clin Chem 1999; 45:1548–56.

[22]. *M.A. Vaughan, A.D. Baines, D.M. Templeton* Multielement analysis of biological samples by inductively coupled plasma mass spectrometry: II. Rapid survey method for profiling trace elements in body fluids. Clin Chem 1991;37:210–5.

[23]. *E. Sabbioni, C. Minoia, R. Pietra, S. Fortaner, M. Gallorini, A.Saltelli* Trace element reference values in tissues from inhabitants of theEuropean Community: II. Examples of strategy adopted and trace element analysis of blood, lymph nodes and cerebrospinal fluid of Italian subjects. Sci Total Environ 1992;120:39-62.

[24]. *C. Minoia, E. Sabbioni, P. Apostoli, et al.* Trace element reference values in tissues from inhabitants of the European Community: I. A study of 46 elements in urine blood and serum of italian subjects. Sci Total Environ 1990;95:89-105.

[25]. *M. Rukgauer, J. Klein, J.D. Kruse-Jarres* Reference values for the trace elements copper, manganese, selenium and zinc in serum/plasma of children, adolescents and adults. J Trace Elem Med Biol 1997;11: 92-98.

[26]. *P. Heitland, H.D.Koster* Fast, simple and reliable routine determination of 23 elements in urine by ICP-MS. J Anal At Spectrom 2004;19: 1552-8.

[27]. *V. Spevackova, M. Cejchanova, M. Cerna, V. Spevacek, J. Sm´ıd, B.Benes* Population based biomonitoring in the Czech Republic: urinary arsenic. J Environ Monit 2002;4:796-8.

[28]. *A.H. Milton, Z .Hasan, A. Rahman, M. Rahman* Chronic arsenic poisoning and respiratory effects in Bangladesh. J Occup Health 2001;43:136-40.

[29]. *J.L. Chen, Y.L. Guo, P.J. Tsai, L.F.Su* Use of inhalable Cr(VI) exposures to characterize urinary chromium concentrations in plating industry workers. J Occup Health 2002;44:46-52.

[30]. *T. Eikmann, V. Makropoulus, S. Eikmann, T.Krieger* Cross-sectional epidemiological study on chromium, manganese mercury nickel, selenium excretion in urine of populations in areas with with different air pollution. Fresenius Environ Bull 1992;1:706-11.

[31]. *M. Kiilunen, J. Jarvisalo, O. Makitie, A.Aitio* Analysis, storage stability and reference values for urinary chromium and nickel. Int Arch Occup Environ Health 1987;59:43-50. [32] Herber RFM. Review of trace element concentrations in biological specimens according to the TRACY protocol. Int Arch Occup Environ Health 1999;72:279-83.

[32]. *V. Iyengar, J.Woittiez* Trace elements in human clinical specimen: evaluation of literatire data to

identify reference values. Clin Chem 1988;34:474-81.

[33]. *B. Gammelgaard, O. Jons* Determination of selenite and selenate in human urine by ion chromatography and inductively coupled plasma mass spectrometry. J Anal At Spectrom 2000;15:945-9.

[34]. *B.S. Iversen, C. Menne´, M.A. White, J. Kristiansen, J. Molin Christensen, E. Sabbioni* Inductively coupled plasma mass spectrometric determination of molybdenum in urine from a Danish population. Analyst 1998;123:81– 5.

[35]. *C.Krause, W.Babisch, K.Becker, et al.* Umwelt-Survey 1990/92 Band 1a: Studienbeschreibung und Human-Biomonitoring. Umweltbundesamt, ed., 1996.

[36]. *K. Becker, S. Kaus, C. Krause, et al.* Umwelt-Survey 1998 Band III: human-biomonitoring. Umweltbundesamt, ed., Berlin, 2002.

[37]. *K. Becker, C. Schulz, S. Kaus, M. Seiwert, B.Seifert* German Environmental Survey 1998 (GerES III): environmental pollutants in the urine of the German population. Int J Hyg Environ Health 2003; 206:15–24.

[38]. *M. Wilhelm, U. Ewers, C.Schulz* Revised and new reference values for some trace elements in blood and urine for human biomonitoring in environmental medicine. Int J Hyg Environ Health 2004;207:69– 73.

[39]. Second national report on human exposure to environmental chemicals. NCEH Pub, vol. 02-0716. Atlanta, Georgia' Department of Health and Human Services; 2003.

[40]. *A. Alimonti, F. Petrucci, M. Krachler, B. Bocca, S.Caroli* Reference values for chromium, nickel and vanadium in urine of youngsters from the urban area of Rome. J Environ Monit 2000;2:351 – 4.

[41]. *K.E. Jarvis, A.L. Gray, R.S.Houk* 1992. Handbook of inductively coupled plasma mass spectrometry. London: Blackie Academic&Professional.

[42]. *U. Giessmann, U.Greb* 1994. High resolution ICP-MS—A new concept for elemental mass spectrometry. Fresenius J Anal Chem 350:186–193.

[43]. *N.H.Bings* 2005. Plasma time-of-flight mass spectrometry as a detector for short transient signals in elemental analysis. Anal Bioanal Chem 382: 887–890.

[44]. *H.E. Evans, J.J.Giglio* 1993. Interferences in inductively coupled plasma mass spectrometry—A review. J Anal Atom Spectrom 8:18.

[45]. *R.F.J. Dams, J. Goossens, L. Moens* 1995. Spectral and non-spectral interferences in inductively coupled plasma mass-spectrometry. Mikrochim Acta 119:286.

[46]. *F. Vanhaecke, S. Saverwyns, G. de Wannemacker, L. Moens, R. Dams* 2000. Comparison of the application of higher mass resolution and cool plasma conditions to avoid spectral interferences in Cr(III)/Cr(VI) speciation by means of high-performance liquid chromatographyinductively coupled plasma mass spectrometry. Anal Chim Acta 419: 55–64.

[47]. *I. Feldmann, N. Jakubowski, C. Thomas, D.Struewer* 1999. Application of a hexapole collision and reaction cell in ICP-MS. Part II: Analytical figures of merit and first applications. Fresenius J Anal Chem 365:422–428.

[48]. *N. Nonose, M. Kubota* 2001. Non-spectral and spectral interferences in inductively coupled plasma high-resolution mass spectrometry. Part I. Optical characteristics of micro-plasmas observed just behind the sampler and the skimmer in inductively coupled plasma high resolution mass spectrometry. J Anal Atom Spectrom 16:551–559.

[49]. *C.S. Hsiung, J.D. Andrade, R. Costa, Ash KO.* 1997. Minimizing interferences in the quantitative multielement analysis of trace elements in biological fluids by inductively coupled plasma mass spectrometry. Clin Chem 43:2303–2311.

[50]. *E.E.M. Brouwers, M.M. Tibben, H. Rosing, J.H.M. Schellens, J.H. Beijnen* 2007c. Determination of ruthenium originating from the investigational anticancer drug NAMI-A in human plasma ultrafiltrate, plasma, and urine by inductively coupled plasma mass spectrometry. Rapid Commun Mass Spectrom 21:1521–1530.

[51]. *L. Lustig, S. Zang, B. Michalke, P. Schramel, W.Beck* 1997. Platinum determination in nutrient plants by inductively coupled plasma mass spectrometry with special respect to the hafnium oxide interference. Fresenius J Anal Chem 357:1157–1163.

[52]. *E. Rudolph, S. Hann, G. Stingeder, C.Reiter* 2005. Ultra-trace analysis of platinum in human tissue samples. Anal Bioanal Chem 382:1500–1506.

[53]. *I. Rodushkin, E. Engstrom, A. Stenberg, D.C.Baxter* 2004. Determination of low-abundance elements at ultra-trace levels in urine and serum by inductively coupled plasma-sector field mass spectrometry. Anal Bioanal Chem 380:247–257.

[54]. *S. Hann, G. Koellensperger, K. Kanitsar, G. Stingeder, M. Brunner, B. Erovic, M. Muller, C.Reiter* 2003a. Platinum determination by inductively coupled plasma-sector field mass spectrometry (ICP-SFMS) in different matrices relevant to human biomonitoring. Anal Bioanal Chem 376: 198–204.

[55]. *R. Thomas* 2002. A beginner's guide to ICP-MS: Part XII—A review of interferences. Spectroscopy 17:24–31.

[56]. *H. Rosing, W.Y.Man, E. Doyle, A. Bult, J.H.Beijnen* 2000. Bioanalytical liquid chromatography method validation: A review of current practices and procedures. J Liq Chrom Rel Technol 23:329–354.

[57]. *S. Caroli, Senofonte O., Violante N., For-Narelli L., Powar A.* 1992. Assessment of reference values for elements in hair of urban normal subjects. Microchem J. 46, 174.

[58]. *D.E.Ryan, J.Holybecner, D.E.* Stuart 1978. Trace elements in scalp hair of persons with multiple sclerosis and of normal individuals. Clin Chem. 24, 1996,

[59]. *A.A.E. Wibowo, R.F.M. Herber, H.A. Das , N. Ro-Eleveld, R.L. Zielhuis*, 1986. Levels of metals in hair of young children as an indicator of environmental pollution. Environ Res. 40, 346.

[60]. *H.H. Skypeck, B.J. Joseph*, 1983. Chemical Toxicology and Clinical Chemistry of Metals, edited by Brown SS, Savory J, London Academic Press, London, pp. 159-163.

[61]. *H. Merzenich, A. Hartwig, W. Ahrens, D. Bey-Ersmann, R. Schlepegrell, M. Scholze, J. Timm, K.H. Jockel*, 2001. Biomonitoring on carcinogenic metals and oxidative DNA damage in a cross-sectional study. Cancer Epidemiol Biomarkers Prev. 10, 515.

[62]. *C.P.Case, L.Ellis, J.C.Turner*, 2001. B.Fairman Development of a routine method for the determination of trace metals in whole blood by magnetic sector inductively coupled plasma mass spectrometry with particular relevance to patients with total hip and knee arthroplasty. Clin Chem. 47,275.

[63]. *J.F. Maurice, G.Wibetoe, K.E. Sjastad*, 2002. Longitudinal distribution of thallium in human scalp hair determined by isotope dilution electrothermal vaporization inductively coupled plasma mass spectrometry. J Anal At Spectrom 17, 485.

[64]. *A.Taylor*, 1986. Usefulness of measurements of trace elements in hair. Ann Clin Biochem 23, 364.

[65]. *B.Seifert, K.Becker, D.Helm, C.Krause, C.Schulz, M.Seiwert*, 2000. The German Environmental Survey 1990/1992: reference dust, drinking water and indoor air. J Expo Anal Environ Epidemiol 10, 552.

[66]. *N.Miekeley, L.M.D.Forteas, C.L.P.Da Silveira, M.B.Lima*, 2001. Elemental anomalies in hair as indicators of endocrinologic pathologies and deficiencies in calcium and bone metabolism. J Trace Elem Med Biol. 15, 46. Report WIOŚ Cracow. Poland, unpublished data, 2001.

[67]. *I.Rodushkin, M.D.Axelsson*, 2000. Application of double focusing sector field ICP-MS for multielemental characterization of human hair and nails. Part II. A study of the inhabitants of northern Sweden. Sci Total Environ. 262, 21.

QUANTUM CHEMISTRY INVESTIGATION OF THE CARNOSINE POLYMER COMPLEX WITH ZINC

S.D.DEMUKHAMEDOVA, I.N.ALIEVA, Z.I.GAJIYEV
Institute for Physical Problems, Baku State University, Azerbaijan
svetlanabest@mail.ru

The structures and electronic properties of carnosine polymeric complexes with zinc were investigated by a quantum-chemical method PM3. The total energies, heats of formation, dipole moments and energies of frontier molecular orbitals (E_{HOMO} and E_{LUMO}) were calculated and discussed.

I. INTRODUCTION

L-Carnosine is a dipeptide composed of the covalently bonded amino acids L-alanine and β-histidine, and is found in brain, heart, skin, muscle and stomach tissue [1]. Carnosine has antioxidant potential and decreases the intracellular level of reactive oxygen species. Carnosine may also act as a neurotransmitter. The biochemical behavior and biological activities of this dipeptide depend on the participation of metal cations. Carnosine forms complexes with divalent cations such as Cu^{2+}, Zn^{2+}, Co^{2+}, Ni^{2+}, Mn^{2+}, Cd^{2+}, Mg^{2+}, Ca^{2+} and Sn^{2+} [2]. The Zn(II) complex of carnosine, currently known as polaprezinc, presents a wide and very interesting pharmacological activity [3]. The interaction of zinc cations with carnosine itself is also of interest because a better understanding of the coordination mode of a simple histidinecontaining dipeptide like carnosine may help to clarify the coordination ability of the peptide linkage and the role of the N_p and N_t donor atom in the binding. The literature contains several studies on zinc(II)–carnosine complexes [4-6]. The structure tautomeric forms of carnosine, its monomer and dimer complexes with Zn(II) was studied in our early investigations [7-10]. The aim of this work is to properly characterize carnosine polymeric complexes with zinc from a theoretical point of view to help in the understanding of the properties of this very interesting molecule.

II. CALCULATION METHODS

In the present study structure of the carnosine polymeric complex with zinc was performed using the semiempirical methods of molecular mechanics MM+ and quantum chemistry method PM3. The stable conformations were determined for different number of monomeric units (n=6, 8, 10, 12, 16, 18, 20, 25). All calculations related to the study were made with the HyperChem8.06 program.

III. RESULTS AND DISCUSSION

The spatial structure and geometrical parameters of the N^1H tautomer carnosine polymeric complex with zinc were calculated by using Polak-Ribiere algorithm accurate within 0,001 kcal/mole on the base of the MM+ molecular mechanics method. The total energies, heats of formation, dipole moments and energies of frontier molecular orbitals (E_{HOMO} and E_{LUMO}) were calculated by quantum chemistry method PM3.

At first the polymeric chain with different number of repeated units (n=6, 8, 10, 12, 16, 18, 20 and 25) was constructed. Each of unit is a monomeric N^1H carnosine complex with zinc bounded at 180^0 relative one another. The three dimensional structure of complex with neutral zinc atom bounded O_{15}, N_9 and N_{13} of carnosine atoms was described in [7]. The coordination cavity consists of two five- and six-membered chelate rings bent under angle~$115^0 \div 120^0$.

Calculations showed that increasing in the length of the polymeric chain leads to the significant decrease of the total energy of the system in comparison with early calculated carnosine monomer and dimer complexes [7-10]. As followed from calculation results, adding two units to the polymeric chain step by step accompanied by energy drop about $129.5 \cdot 10^3$ kcal/mole. Electronic structure investigation carried out by a quantum-chemical method PM3 also showed that formation of the carnosine complexes with zinc lead to the strong re-distribution of the electron density and decreasing of the negative charge on the zinc atom in comparison to monomer complex approximately on 0.18 for all units with the exception of first. All other zinc atoms in polymeric chain have a charge about -0.250 (Table 1). The observed strong changing in absolute value of the partial negative charge on the zinc atom of the sixth unit (Zn 175) for all polymeric chains resulted from structure of this part of polymeric chains (Table 1, Fig.1).

On the next step the spatial and electronic structures of the polymeric chain were compared at the variation of the torsion angle between monomers. Varies structures of carnosine polymers with different initial values of torsion angles between monomers ($\tau=0^0$, 60^0, 120^0 and 180^0) are investigated in the present work. Fig.1 shows the optimized geometries of the carnosine polymeric complexes with zinc under study. As shown from Table 2 changing in the torsion angle between monomer units for each polymeric chain lead to small changing in total energy. The strong changing in nuclear, electronic energy as well as in dipole momentum was observed for all polymeric complexes (Table 2). Polymers with n=6 and n=8 more stable at $\tau=0^0$ at the same time the more stable structures at $\tau=60^0$ are formed for n=10.

Table 1. Energy parameters (kcal/mole), dipole moment (μ, debay) and partial charge on the zinc atoms in polymeric carnosine complexes

Energy	n =6	n=8	n=10	n=12	n=16	n=18	n=20	n=25
Total	-388938.6	-518455.1	-647994.7	-777686.0	-1036335.4	-1166114.1	-1295976.8	-1619561.6
Binding	-16986.9	-22720.5	-28477.2	-34385.6	-45469.1	-51464.9	-57544.7	-71672.2
Atomic	-371951.7	-495734.6	-619517.5	-743300.4	-990866.3	-1114649.2	-1238432.1	-1547889.4
Electron	-5388950.3	-7914969.9	-10580220.4	-13507770.2	-19016002.7	-22469578.8	-24907971.2	-33380642.8
Nuclear	5000011.7	7396514.8	9932225.7	12730084.1	17979667.3	21303464.8	23611994.4	31761081.2
Heat	67.8	-15.6	-122.2	-380.4	-163.6	-509.2	-938.9	-940.9
μ	99.9	125.6	160.8	184.9	273.8	295.158	368.8	420.6
Charge on the Zn atom								
Zn 29	-0.453	-0.452	-0.453	-0.455	-0.454	-0.452	-0.452	-0.453
Zn 59	-0.249	-0.250	-0.250	-0.250	-0.252	-0.249	-0.249	-0.250
Zn 88	-0.249	-0.260	-0.261	-0.258	-0.257	-0.260	-0.260	-0.260
Zn 117	-0.254	-0.254	-0.255	-0.262	-0.259	-0.252	-0.252	-0.253
Zn 135	-0.258	-0.260	-0.259	-0.267	-0.257	-0.254	-0.259	-0.262
Zn 175	-0.086	-0.107	-0.108	-0.172	-0.031	-0.123	0.107	-0.110
Zn 204		-0.260	-0.264	-0.255	-0.263	-0.258	-0.253	-0.264
Zn 233		-0.248	-0.253	-0.260	-0.258	-0.254	-0.252	-0.262
Zn 262			-0.247	-0.259	-0.258	-0.255	-0.254	-0.264
Zn 291			-0.247	-0.257	-0.258	-0.253	-0.253	-0.253
Zn320				-0.257	-0.258	-0.253	-0.253	-0.251
Zn349				-0.248	-0.258	-0.253	-0.253	-0.252
Zn 378					-0.257	-0.253	-0.253	-0.252
Zn 407					-0.256	-0.253	-0.253	-0.252
Zn 436					-0.254	-0.252	-0.253	-0.252
Zn 465					-0.244	-0.251	-0.253	-0.252
Zn 494						-0.246	-0.252	-0.252
Zn 523						-0.247	-0.250	-0.252
Zn 552							-0.246	-0.252
Zn 581							-0.246	-0.252
Zn 610								-0.251
Zn 639								-0.250
Zn 668								-0.258
Zn 697								-0.258
Zn 726								-0.248

Table 2. Energy parameters (kcal/mole), dipole moment (μ, debay) and partial charge of the zinc atoms in polymeric carnosine complexes with different torsion angles between monomeric units

Energy	n=6			n=8			n=10		
	τ=0 °	τ=60°	τ=120°	τ=0 °	τ=60°	τ=120°	τ=0°	τ=60°	τ=120°
Total	-389118.6	-389076.0	-388746.8	-518757.9	-518610.1	-518600.8	-647839.5	-648301.5	-647827.8
Binding	-17166.9	-17124.3	-16795.1	-23023.3	-22875.5	-22866.2	-28322.0	-28783.9	-28310.2
Atomic	-371951.7	-371951.7	-371951.7	-495734.6	-495734.6	-495734.6	-619517.5	-619517.5	-619517.5
Electron	-5870432.1	-5277816.9	-5247677.2	-9168068.4	-7759633.3	-7719724.5	-11562581.7	-10560259.0	-10191348.5
Nuclear	5481313.5	4888740.9	4858930.4	8649310.5	7241023.2	7201123.7	10914742.2	9911957.6	9543520.7
Heat	-112.3	-69.6	259.6	-318.4	-170.6	-161.4	33.0	-428.9	44.8
μ	26.6	106.9	131.3	69.8	117.233	158.6	64.0	159.9	215.5
Charge on the Zn atom									
Zn 29	-0.432	-0.459	-0.454	-0.455	-0.451	-0.454	-0.452	-0.454	-0.454
Zn 59	-0.228	-0.260	-0.250	-0.274	-0.258	-0.248	-0.260	-0.253	-0.252
Zn 88	-0.260	-0.250	-0.256	-0.266	-0.261	-0.250	-0.262	-0.259	-0.255
Zn 117	-0.261	-0.253	-0.257	-0.266	-0.254	-0.250	-0.261	-0.263	-0.259
Zn 146	-0.254	-0.250	-0.255	-0.253	-0.253	-0.249	-0.266	-0.248	-0.250
Zn 175	-0.250	-0.160	-0.0001	-0.266	-0.160	-0.183	-0.026	-0.263	-0.005
Zn 204				-0.260	-0.263	-0.256	-0.259	-0.264	-0.257
Zn 233				-0.233	-0.248	-0.244	-0.260	-0.257	-0.254
Zn 262							-0.257	-0.256	-0.253
Zn 291							-0.245	-0.250	-0.243

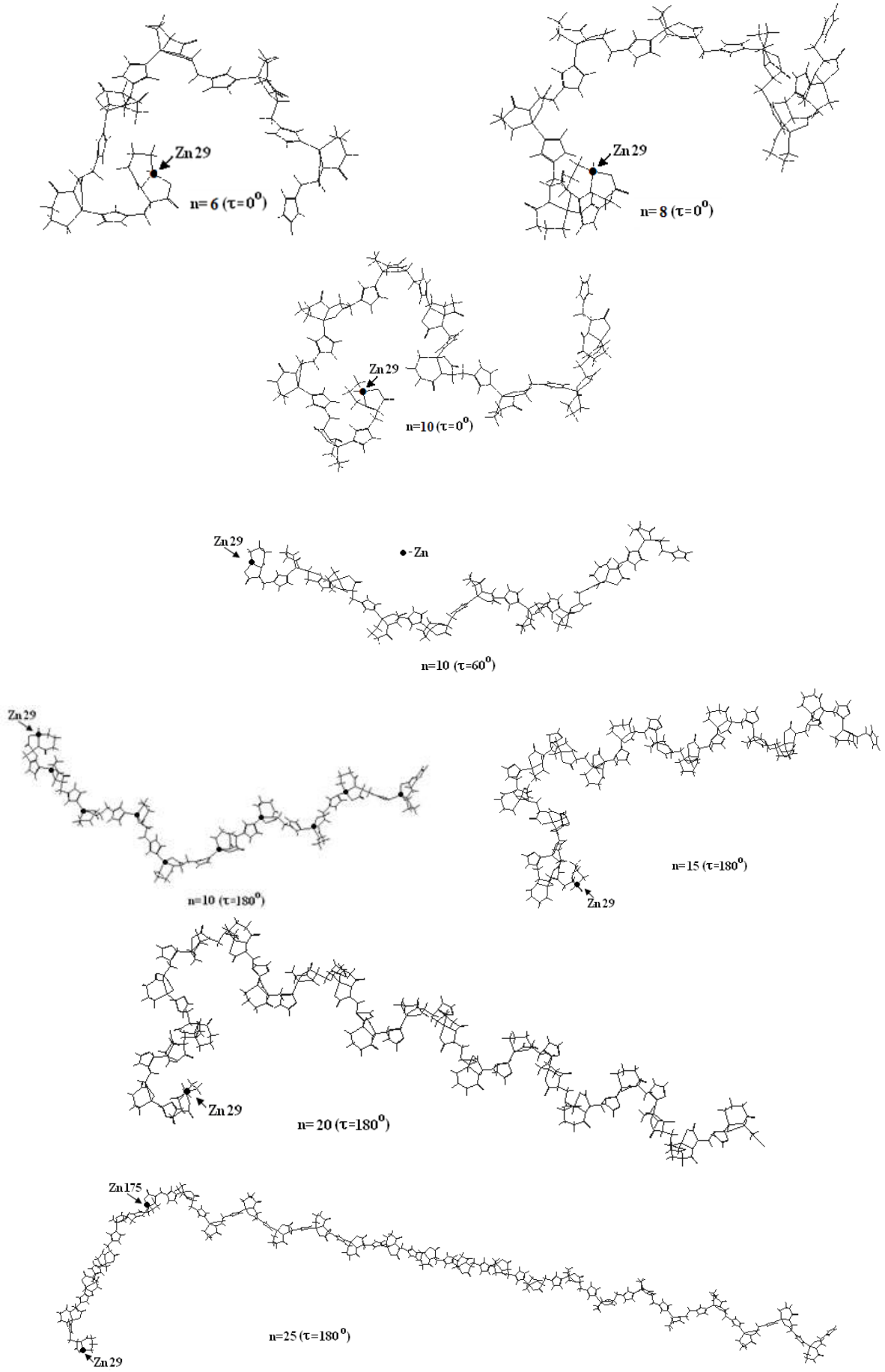

Fig.1. Model of the carnosine polymeric complex with Zn (n=6, 8, 10, 15, 20 and 25)

As shown from Table 2 the charges on the zinc atoms exception of first are identical for all monomeric units at stable conformational states of polymeric complexes for $\tau=0^0$ (n=6, 8, 10) and for $\tau=60^0$ (n=10). The charge on the zinc atom for sixth unit (Zn 175) strongly decreases at $\tau=180°$ and $\tau=120^0$ for n=6, 8, 10 and at $\tau=60°$ for n=6, 8. As seen from Fig.1 the folding and final structure of the polymeric complexes depends on the initial value of the torsion angle between monomeric units. The most stable and compact structures are formed at connection of the monomeric complexes in cis-position relative one another.

Results of our calculation open prospects of creation of new medical products on the basis of polymeric carnosine complexes and its analogues with various metals.

[1] *А.А.Болдырев* В кн.: Карнозин. Биологическое значение и возможности применения в медицине. /Из-во МГУ: Москва.-1998.- С.252-260.

[2] *E.J. Baran* Metal complexes of carnosine // Biochemistry (Moscow), 2000, v. 65, p.789-797

[3] *Т.Матсукура, Х.Танака* Применение комплекса L-карнозина с цинком в медицине. Обзор. Биохимия. 2000, т.65, вып.7, с.961-968.

[4] *A.Torreggiani, S.Bonora, G.Fini* //Biopolymers. - 2001. – 57, N 6. -P. 352.

[5] *A.Torreggiani, A.Trinchero, M.Tamba, G.Fini* // Ital.J Biochem. -2003, -52, N 2. –P.87.

[6] *A.Torreggiani , P.Taddei , Tinti A., Fini G.* // Journal of Molecular Structure. - 2002, -641, N 1. - P.61.

[7] *С.Д.Демухамедова, И.Н.Алиева, Н.М. Годжаев, Н.С. Набиев* //Journal of Qafqaz University, 2008, v.23, p.62-71.

[8] *С.Д.Демухамедова, И.Н.Алиева, Н.М. Годжаев, Н.С. Набиев* //Journal of Qafqaz University, 2009, v.25, p.114-126.

[9] *С.Д.Демухамедова, И.Н.Алиева, Н.М.Годжаев* //Application of Information and Communication Technologies, Inter.Conf., 2009, p.105-108 (http://ieeexplore.ieee.org)

[10] *С.Д.Демухамедова, И.Н.Алиева, Н.М.Годжаев* // Материалы Международной Конференции «Молекулярное моделирование», 2009, с.42

THEORETICAL MOLECULAR STRUCTURE AND VIBRATIONAL SPECTROSCOPIC INVESTIGATION OF HYDROGENATED AMORPHOUS CARBON NITRIDE FILM

CEMAL PARLAK [1] ÖZGÜR ALVER [2, 3] AND MUSTAFA ŞENYEL [2]

[1] Department of Physics, Dumlupınar University, 43100, Kütahya, Turkey

[2] Department of Physics, Science Faculty, Anadolu University, 26470, Eskişehir, Turkey

[3] Plant, Drug and Scientific Research Centre, Anadolu University, 26470, Eskişehir, Turkey

E-mail: cparlak20@gmail.com, Tel.: +90 (274) 265 20 51 / 3116, Fax: +90 (274) 265 20 56

The normal mode frequencies and corresponding vibrational assignments and structural parameters (bond lengths, bond-dihedral-torsion angles) of possible two conformers (C1 and C2) of hydrogenated amorphous carbon nitride (aH-CN_x) film have been theoretically examined by means of HF, BLYP and B3LYP density functional methods with 6-31G(d) and 6-311+G(d,p) basis sets. Theoretical results have been successfully compared against available experimental data in the literature. Regarding all the calculations, C1 form seems energetically more favorable and the lowest energy case for the optimized structures have been obtained with B3LYP/6-311+G(d,p) model.

1. INTRODUCTION

There has been increasing interest in hydrogenated amorphous carbon nitride (aH-CN_x) films which show remarkable physical and chemical properties such as extreme hardness, low friction coefficient, chemical inertness, variable optical band gap and good wear resistance [1]. Chemical analysis with X-ray photo electron, infrared and Raman spectroscopies show that majority of the incorporated nitrogen atoms are in the form of triple C≡N and overlapping C=N and C=N double bonds [2-4]. A detailed and unambiguous interpretation of the chemical structure of carbon nitrides prepared by various methods and in wide range of process parameters is not only a very difficult task but also a prerequisite for production of predetermined films for industrial applications [5].

Density functional theory calculations have provide excellent agreement with experimental vibrational frequencies of variety of organic compounds, if the calculated frequencies are scaled to compensate for the approximate treatment of electron correlation, basis set deficiencies and anharmonicity [6-9]. Separation of the overlapped bands of aH-CN_x films is very complicated due to intermolecular interactions as H-bridges which are very intensive in this region and cause the broadening of the bands [10]. Therefore, in present study, we have theoretically investigated geometric parameters (bond lengths, bond-dihedral-torsion angles) and vibrational frequencies of possible two conformers (C1 and C2) of aH-CN_x film, which is deposited by CH_4/N_2 dielectric barrier discharge plasma and reported by Majumder et al. [10], using HF, BLYP and B3LYP methods with 6-31G(d) and 6-311+G(d,p) basis sets.

2. CALCULATIONS

As seen Figure 1, there are two types of suggested conformers for deposited polymer aH-CN_x film [10]. C1 and C2 conformers were first optimized by DFT with the hybrid functionals BLYP and B3LYP and Ab-initio HF with the basis sets 6-31G(d) and 6-311+G(d,p) in the gas phase together with the keyword volume. The optimized geometric structures concerning to the minimum on the potential energy surface were provided by solving self-consistent field equation iteratively and optimizations were performed without any molecular restrictions. Calculated optimized energies, molar volumes and recommended radii for these forms are given in Table 1. Based on the optimized energy results, it is seen that B3LYP/6-311+G(d,p) level of theory provides the minimal energy case for both C1 and C2.

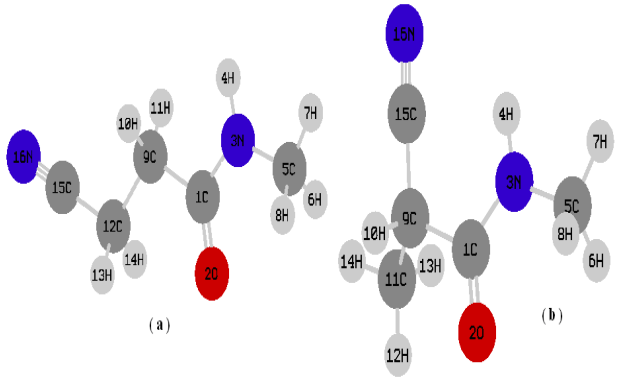

Fig. 1. The optimized molecular structures of C1 (a) and C2 (b) form at B3LYP/6-311+G(d,p) model.

Table 1. Some characteristic features of the optimized geometries of C1 and C2 conformers.

Conformer / Basis Set	6-31G(d)	6-31G(d)	6-31G(d)	6-311+G(d,p)	6-311+G(d,p)	6-311+G(d,p)
C 1	HF	BLYP	B3LYP	HF	BLYP	B3LYP
Molar volume (cm^3/mol)	92.306	81.739	90.351	86.647	92.797	91.597
Recommend a_0 (Å)	4.15	4.01	4.13	4.08	4.16	4.14
ΔG (Hartree)	-377.671465	-379.845206	-379.981330	-377.776330	-379.973579	-380.100688
C 2						
Molar volume (cm^3/mol)	93.040	89.882	103.816	95.895	73.917	66.301
Recommend a_0 (Å)	4.16	4.12	4.30	4.20	3.89	3.77
ΔG (Hartree)	-377.666860	-379.845575	-379.980859	-377.770276	-379.970576	-380.098697

Table 2. The optimized geometric parameters of C1 form.

Parameters	6-31G(d)			6-311+G(d,p)		
	HF	BLYP	B3LYP	HF	BLYP	B3LYP
R(5,6)	1.0840	1.0979	1.0949	1.0832	1.0949	1.0946
R(5,7)	1.0816	1.1042	1.0965	1.0822	1.1008	1.0907
R(5,8)	1.0805	1.1033	1.0958	1.0831	1.0988	1.0891
R(5,3)	1.4486	1.4653	1.4534	1.4502	1.4689	1.4568
R(3,4)	0.9936	1.0187	1.0101	0.9917	1.0160	1.008
R(3,1)	1.3473	1.3773	1.3639	1.3475	1.3756	1.3614
R(1,2)	1.2009	1.2387	1.2257	1.1972	1.2343	1.2213
R(1,9)	1.5212	1.5455	1.5317	1.5207	1.5430	1.5292
R(9,10)	1.0854	1.1035	1.0962	1.0859	1.0998	1.0933
R(9,11)	1.0860	1.1049	1.0975	1.0859	1.1014	1.0951
R(9,12)	1.5301	1.5524	1.5385	1.5294	1.5516	1.5374
R(12,13)	1.0817	1.1042	1.0961	1.0819	1.1008	1.0936
R(12,14)	1.0814	1.1027	1.0945	1.0819	1.0994	1.0922
R(12,15)	1.4726	1.4711	1.4645	1.4703	1.4665	1.4601
R(15,16)	1.1352	1.1735	1.1609	1.1300	1.1655	1.1533
A(6,5,7)	109.02	109.20	109.08	109.03	108.88	109.13
A(6,5,8)	108.46	109.37	109.20	108.43	109.34	108.36
A(7,5,8)	109.02	108.87	108.88	109.03	109.11	109.32
A(3,5,6)	111.68	107.13	107.36	110.94	107.82	111.84
A(3,5,7)	108.63	111.32	111.31	108.44	111.33	109.38
A(3,5,8)	109.99	110.91	110.95	110.93	110.32	108.77
A(4,3,5)	118.74	118.42	118.53	119.05	118.32	118.6
A(4,3,1)	119.11	118.59	118.59	119.14	118.37	118.63
A(3,1,2)	122.88	123.47	123.52	122.75	123.35	123.02
A(3,1,9)	115.06	114.64	114.70	115.07	114.72	114.98
A(2,1,9)	122.06	121.88	121.78	122.18	121.92	121.99
A(1,9,10)	109.39	111.60	111.20	109.00	111.44	111.07
A(1,9,11)	109.00	108.26	108.32	109.00	107.69	107.81
A(1,9,12)	111.02	110.20	110.36	111.31	110.83	110.84
A(10,9,12)	110.40	110.57	110.58	110.27	110.38	110.51
A(11,9,12)	110.20	109.27	109.54	110.27	109.33	109.55
A(9,12,13)	110.55	110.19	110.30	110.69	110.28	110.41
A(9,12,14)	110.49	108.57	109.08	110.69	109.15	109.50
A(9,12,15)	111.13	112.48	112.16	111.17	112.36	112.09
A(13,12,15)	108.76	108.98	108.92	108.55	108.69	108.65
A(14,12,15)	108.85	110.09	109.88	108.55	109.64	109.51
A(12,15,16)	179.21	179.16	179.13	179.31	179.19	179.17
D(5,3,1,9)	-177.11	-176.18	-176.50	-179.98	-175.42	-175.01
D(6,5,3,1)	70.50	-4.58	-4.089	60.35	-11.82	86.72
D(4,3,1,2)	175.32	179.28	179.55	179.98	178.77	176.88
D(3,1,9,12)	-176.38	-151.96	-156.97	-179.97	-26.87	-155.35
D(3,1,9,10)	-54.30	-28.71	-33.87	-58.13	-26.87	-32.09
D(2,1,9,11)	-118.28	-90.39	-95.88	-121.82	-88.75	-94.53
D(1,9,12,15)	-179.55	-172.51	-174.21	-179.99	-174.05	-175.06
D(1,9,12,13)	59.58	65.68	64.20	59.28	64.52	63.66
D(9,12,15,16)	0.01	-3.22	-4.77	0.14	-16.86	-13.01
D(13,12,15,16)	121.93	119.28	117.62	122.12	105.47	109.28
T(1,2,8,5)	-40.24	-82.17	-82.01	-48.34	-87.82	-27.36
T(3,4,11,9)	50.15	69.47	66.71	51.59	70.46	65.76
T(1,2,13,12)	53.02	73.06	69.22	50.36	73.43	69.56
T(9,11,16,15)	-33.32	-30.95	-31.61	-33.35	-32.08	-32.33

Table 3. The optimized geometric parameters of C2 form.

Parameters	6-31G(d)			6-311+G(d,p)		
	HF	BLYP	B3LYP	HF	BLYP	B3LYP
R(5,6)	1.0821	1.1035	1.0959	1.0828	1.0990	1.0924
R(5,7)	1.0810	1.1032	1.0956	1.0818	1.0957	1.0894
R(5,8)	1.0821	1.0978	1.0905	1.0830	1.0982	1.0917
R(5,3)	1.4496	1.4655	1.4539	1.4512	1.4706	1.4578
R(3,4)	0.9934	1.0198	1.0112	0.9921	1.0167	1.0085
R(3,1)	1.3398	1.3683	1.3559	1.3397	1.3637	1.3518
R(1,2)	1.2001	1.2358	1.2233	1.1963	1.2319	1.2191
R(1,9)	1.5368	1.5759	1.5565	1.5366	1.5725	1.5537
R(9,10)	1.0844	1.1060	1.0982	1.0846	1.1026	1.0957
R(9,11)	1.5379	1.5567	1.5438	1.5378	1.5572	1.5433
R(9,15)	1.4752	1.4724	1.4663	1.4729	1.4677	1.4620
R(15,16)	1.1355	1.1753	1.1621	1.1301	1.1669	1.1543
R(11,12)	1.0801	1.0990	1.0916	1.0807	1.0958	1.0894
R(11,13)	1.0836	1.1012	1.0941	1.0844	1.0979	1.0917
R(11,14)	1.0828	1.1005	1.0933	1.0834	1.0973	1.0909
A(6,5,7)	109.15	108.89	108.91	109.18	109.36	109.27
A(6,5,8)	108.47	109.34	109.21	108.48	108.22	108.18
A(7,5,8)	109.15	109.41	109.30	109.18	109.42	109.31
A(3,5,6)	110.83	110.91	110.94	110.78	110.85	110.90
A(3,5,7)	108.40	110.78	110.78	108.31	108.50	108.61
A(3,5,8)	110.82	107.49	107.66	110.87	110.47	110.54
A(4,3,5)	118.92	118.77	118.74	118.90	119.09	119.23
A(4,3,1)	120.20	118.63	118.86	119.97	119.32	119.54
A(3,1,2)	123.44	124.75	124.63	123.45	123.74	123.62
A(3,1,9)	118.24	116.47	116.77	118.28	117.11	117.38
A(2,1,9)	118.32	118.77	118.59	118.27	119.15	118.99
A(1,9,10)	105.39	104.87	105.02	105.25	104.63	104.82
A(1,9,11)	110.44	109.94	110.07	110.66	110.32	110.40
A(1,9,15)	113.80	113.87	113.77	113.86	113.92	113.72
A(9,15,16)	178.91	177.26	177.70	179.37	177.96	178.28
A(9,11,12)	108.84	108.12	108.25	108.92	108.53	108.58
A(9,11,13)	110.82	110.83	110.82	110.82	110.80	110.82
A(9,11,14)	110.33	110.65	110.65	110.15	110.40	110.47
A(10,9,11)	108.86	108.26	108.42	108.96	108.40	108.60
A(10,9,15)	107.10	107.60	107.44	106.88	107.37	107.23
D(5,3,1,9)	179.41	179.33	179.29	179.29	179.30	179.29
D(6,5,3,1)	60.60	117.86	117.37	59.84	63.22	62.84
D(4,3,1,2)	-179.92	179.05	178.97	-179.50	179.44	179.20
D(3,1,9,11)	125.41	130.14	130.23	124.13	126.58	127.51
D(3,1,9,15)	-0.13	3.68	3.95	-1.57	-0.06	1.09
D(1,9,15,16)	18.08	7.96	8.22	30.53	11.56	11.28
D(1,9,11,12)	54.26	50.65	51.32	54.82	51.83	52.22
D(1,9,11,13)	-65.49	-68.61	-67.96	-65.01	-67.79	-67.33
D(1,9,11,14)	174.25	170.76	171.46	174.83	171.77	172.24
D(10,9,15,16)	134.13	123.73	124.02	146.30	126.92	126.67
T(1,2,8,5)	-48.34	-1.50	-2.00	-48.86	-46.38	-46.61
T(3,4,16,15)	-0.03	3.35	3.46	-1.31	-0.94	0.08
T(1,2,10,9)	38.96	40.84	41.03	38.35	38.90	39.57
T(9,10,12,11)	-40.32	-42.05	-41.74	-39.92	-41.21	-41.10

R, A, D and T present bond distance (Å), bond angles (^{o}), dihedral angles (^{o}) and torsion angles (^{o}), respectively.
R, A, D and T present bond distance (Å), bond angles (^{o}), dihedral angles (^{o}) and torsion angles (^{o}), respectively.

After the optimization, in order to confirm the convergence to minima on the potential surface and to evaluate the zero-point vibrational energies, harmonic vibrational frequencies and corresponding IR intensities of C1 and C2 forms of aH-CN_x film were determined using analytic second derivatives with the same methods and the basis sets. The vibrational frequencies of C1 and C2 were also scaled to generate the corrected frequencies by 0.9613 for B3LYP/6-31G(d) and 0.9652 for B3LYP/6-311+G(d,p) [11, 12]. All the calculations were performed by using Gaussian 03 program [13] on a personal computer and GaussView program [14] was used for visualization of the structure.

Table 4. The approximate mode descriptions and calculated vibrational wavenumbers (cm^{-1}) of C1 form.

Mode	Approximate mode descriptions	B3LYP/ 6-31G(d)			B3LYP/ 6-311+G(d,p)		
		Cal. Freq.	Cor. Freq.	Calc. I_{IR}	Cal. Freq.	Cor. Freq.	Calc. I_{IR}
ν_1	N-H str	3624	3484	21.04	3635	3509	29.53
ν_2	CH_3 a-str	3180	3057	0.81	3141	3032	4.07
ν_3	C(9;12)-H_2 a-str	3126	3005	3.84	3103	2995	3.30
ν_4	C-H3 a-str	3105	2985	31.90	3098	2990	22.41
ν_5	C(9;12)-H_2 a-str	3096	2976	10.82	3077	2970	9.30
ν_6	C(9;12)-H_2 s-str	3078	2959	5.52	3059	2952	4.67
ν_7	C(9)-H_2 s-str	3057	2939	6.36	3039	2933	6.08
ν_8	CH_3 s-str	3051	2933	60.33	3028	2923	50.03
ν_9	C≡N str	2370	2278	12.12	2352	2270	18.93
ν_{10}	C=O str	1785	1716	215.78	1744	1683	271.43
ν_{11}	C-N-C str + N-H bend + CH_3 a-bend	1586	1525	158.32	1558	1504	206.10
ν_{12}	N-H bend + CH_3 a-bend	1530	1471	7.49	1508	1455	20.11
ν_{13}	CH_3 a-bend	1521	1462	75.08	1486	1434	35.38
ν_{14}	C(9;12)-H_2 sciss	1504	1446	12.07	1478	1427	17.01
ν_{15}	C(9;12)-H_2 sciss	1494	1436	0.96	1469	1418	0.21
ν_{16}	CH_3 s-bend	1462	1405	18.87	1447	1396	17.50
ν_{17}	C(9;12)-H_2 wag	1407	1352	12.02	1391	1342	12.89
ν_{18}	C(9;12)-H_2 twist	1340	1288	8.64	1328	1282	6.77
ν_{19}	C-C-H bend + NH bend	1303	1253	29.12	1294	1249	24.93
ν_{20}	C(9)-H_2 wag + NH bend +C-N-C str + C-C-H bend	1244	1196	92.22	1234	1191	84.18
ν_{21}	C(9;12)-H_2 twist	1196	1150	8.94	1189	1148	7.46
ν_{22}	N-H bend + CH_3 a-bend	1180	1134	39.09	1178	1137	2.31
ν_{23}	CH_3 a-bend	1161	1116	2.32	1144	1104	13.53
ν_{24}	C(9)-C(12) str + C-N str	1098	1055	4.87	1085	1047	4.11
ν_{25}	C(9;12)-H_2 rock	1045	1005	1.36	1037	1001	1.19
ν_{26}	C(9)-C(12) str + C-N str	1029	989	2.25	1016	981	3.68
ν_{27}	C(12)-C(15) str + C(1)-C(9) str	965	928	7.69	958	925	8.79
ν_{28}	C(1)-C(9) str + C-N-C bend + CH_3 a-bend	898	863	2.91	892	861	2.11
ν_{29}	C(9;12)-H_2 rock	796	765	4.54	791	763	3.35
ν_{30}	C(9)-C(12)-C(15) bend + C(1)-C(9) str + C-N-C bend	711	683	2.38	713	688	4.59
ν_{31}	C(9)-H_2-rock	624	600	4.18	622	600	1.71
ν_{32}	C-C≡N bend	528	508	5.69	525	507	2.34
ν_{33}	NH bend	455	437	81.49	448	432	77.02
ν_{34}	skelatal	408	392	8.12	402	388	6.81

3. RESULTS AND DISCUSSION

Calculated structural parameters of both conformers are given in Tables 2-3. A(12,15,16) for C1 and A(9,15,16) for C2 are around 179° and 178° which indicates that C-C≡N bond is almost linear. In view of possible internal hydrogen bondings, it is helpful to indicate that space distance between N16 and H4 was calculated as 2.67118 Å for C2 at B3LYP/6-311+G(d,p) level.

C1 and C2 conformers consist of 26 atoms, so they have 42 normal vibrational modes and belong to the point group C_1 with only identity (E) symmetry element or operation. It is difficult to determine vibrational assignments of C1 and C2 due to their low symmetry. According to the calculations, 8 normal vibrational modes of both conformations are below 400 cm^{-1}. All the theoretical vibrational modes obtained in this study are given in Tables 4-5. The assignments of the vibrational modes of C1 and C2 have been provided by animation option of the GaussView package program for the B3LYP/6-311+G(d,p) level of calculation. Regarding our calculations and previously reported infrared data [10], we have provided a reliable correspondence.

The region of 3300–3490 cm^{-1} is referred as anti-symmetric NH_2 stretching band and at 3140 cm^{-1} to 3300 cm^{-1} is H bonded NH symmetric stretching band [10]. NH stretching modes for C1 and C2 have been calculated at 3484 cm^{-1}, 3635 cm^{-1} and 3472 cm^{-1}, 3497 cm^{-1} for B3LYP/6-31G(d) and B3LYP/6-311+G(d,p), respectively. Chemical and so as to physical surrounding of NH group of both conformers are different. Henceforth, double band appearing in the region of 3300–3490 cm^{-1} could be due to this difference rather than symmetric and anti-symmetric classification.

Table 5. The approximate mode descriptions and calculated vibrational wavenumbers (cm^{-1}) of C2 form.

Mode	Approximate mode descriptions	B3LYP/ 6-31G(d)			B3LYP/ 6-311+G(d,p)		
		Cal. Freq.	Cor. Freq.	Calc. I_{IR}	Cal. Freq.	Cor. Freq.	Calc. I_{IR}
ν_1	N-H str	3612	3472	41.04	3623	3497	55.38
ν_2	C(11)H_3 a-str	3181	3058	1.27	3142	3033	3.25
ν_3	C(5)H_3 a-str	3174	3051	3.49	3136	3027	11.97
ν_4	C(11)-H_2 a-str	3149	3027	15.45	3121	3012	14.19
ν_5	C(5)H_3 a-str	3111	2991	27.56	3099	2991	16.58
ν_6	C(11)H_3 s-str + C(9)H str	3077	2958	15.80	3051	2945	14.64
ν_7	C(9)H str	3056	2938	0.90	3043	2937	0.45
ν_8	C(5)H_3 s-str	3055	2937	50.58	3042	2936	33.86
ν_9	C≡N str	2351	2260	11.64	2337	2256	17.13
ν_{10}	C=O str	1793	1724	260.43	1750	1689	329.30
ν_{11}	C-N-C str + NH bend	1598	1536	160.40	1560	1506	214.20
ν_{12}	C(5)-H_3 a-bend	1530	1471	10.34	1510	1457	9.46
ν_{13}	C(11)-H_3 a-bend	1528	1469	5.87	1502	1450	4.07
ν_{14}	C(11)-H_3 a-bend	1525	1466	8.68	1497	1445	11.25
ν_{15}	C(5)-H_3 a-bend	1521	1462	49.35	1480	1428	11.36
ν_{16}	C(5)-H_3 s-bend + NH bend	1461	1404	17.77	1458	1407	12.34
ν_{17}	C(11)-H_3 s-bend	1429	1374	3.94	1409	1360	4.28
ν_{18}	C(9)H bend	1338	1286	4.04	1324	1278	4.73
ν_{19}	C(9)H bend + N-H bend	1295	1245	5.34	1282	1237	15.44
ν_{20}	C(9)- C(1)-N a-str N-H bend +N-H bend	1277	1228	82.23	1267	1223	62.90
ν_{21}	C(5)-H_3 a-bend + C-N-C bend	1186	1140	42.05	1190	1149	0.50
ν_{22}	C(5)-H_3 a-bend	1163	1118	1.15	1152	1112	0.13
ν_{23}	C(11)-H_3 a-bend + C(1)-C(9)-C(15) str +N(3)-C(5) str	1136	1092	12.41	1130	1091	8.03
ν_{24}	C(9)-C(11) str + N(3)-C(5) str	1109	1066	2.21	1095	1057	0.43
ν_{25}	C(9)H bend + N(3)-C(5) str + C(11)-H_3 a-bend	1086	1044	0.64	1075	1038	0.91
ν_{26}	N(3)-C(5) + C(9)-C(11) str + C(9)H bend	1011	972	7.43	1000	965	5.20
ν_{27}	C-N-C bend + C-C-C str + C(5;11)-H_3 a-bend	900	865	3.62	895	864	8.16
ν_{28}	C-N-C bend + C-C-C str + C(5;11)-H_3 a-bend	828	796	2.57	827	798	4.96
ν_{29}	C-C-C bend	755	726	0.64	757	731	1.08
ν_{30}	C(9)-C(15)-N(16) bend + C-C-C bend	633	608	7.64	635	613	5.06
ν_{31}	NH bend + C(9)-C(15)-N(16) bend + C-C-C bend	569	547	21.89	560	540	3.21
ν_{32}	C-C-C str + C(9)-C(15)-N(16) bend	509	489	50.16	498	481	4.19
ν_{33}	N-H bend	497	478	11.92	471	455	59.86
ν_{34}	skeletal	404	388	9.22	395	381	6.73

The region of 2884–2965 cm^{-1} is attributed to –C-CH_3 and ≡CH bands [4]. CH, CH_2, CH_3 symmetric and anti-symmetric stretching modes have been computed for C1 at 2933-3057cm^{-1} and 2923-3032 cm^{-1} and for C2 at 2937-3058 cm^{-1} and 2936-3033cm^{-1} (Tables 4-5). Amide carbonyl groups (=C=O)NH are mainly present at 1560–1665 cm^{-1} [5]. The calculated values for carbonyl vibrations have been found as 1716 cm^{-1} (C1), 1724cm^{-1} (C2) and 1683cm^{-1} (C1), 1689cm^{-1} (C2) for 6-31G(d) and 6-311+G(d,p) with B3LYP, respectively. The absorption band observed at 1350-1480 cm^{-1} corresponds to the C–N, CH_2 or CH_3 single stretching bond [5] which is theoretically found for C1 as 1525 cm^{-1}/1504 cm^{-1} (C-N) and 1471-1288 cm^{-1}/1455-1282 cm^{-1} (CH, CH_2, CH_3) and for C2 1536 cm^{-1}/1506 cm^{-1} (C-N) and 1471-1286 cm^{-1}/1457-1278 cm^{-1} (CH, CH_2, CH_3) using 6-31G(d) / 6-311+G(d,p) with B3LYP (Tables 4-5).

Units of infrared (I_{IR}) intensity are km/mol. Freq: frequency, cal: calculated, cor: corrected, str: stretching,bend: bending, rock: rocking, sciss: scissoring, wag: wagging, twist: twisting, s: symmetric, a: anti-symmetric.

Units of infrared (I_{IR}) intensity are km/mol. Freq: frequency, cal: calculated, cor: corrected, str: stretching, bend: bending, rock: rocking, sciss: scissoring, wag: wagging, twist: twisting, s: symmetric, a: anti-symmetric.

4. CONCLUSION

Molecular geometric parameters and vibrational frequencies of C1 and C2 conformers of aH-CN_x film have been successfully completed with good results. The results obtained in this study also indicate that B3LYP/6-311+G(d,p) method is reliable and it makes easier the understanding of structural parameters, optimized energies and vibrational spectrum of aH-CN_x film.

[1]. *A. Majumdar, J. Schäfer, P. Mishra, D. Ghose, J. Meichsner, R. Hippler,* ‘‘Chemical composition and bond structure of carbon-nitride films deposited by CH_4/N_2 dielectric barrier discharge’’ Surf. Coat. Tech. 201 (2007) 6437-6444.

[2]. *A.D. Graaf, G. Dinescu, J.L. Longueville, M.C.M. Sandan, D.C. Schram, E.H.A. Dekempeneer, L.J.V. Ijzendoorn,* ‘‘Amorphous hydrogenated carbon nitride films deposited via an expanding thermal plasma at high growth rates’’ Thin Solid Films 333 (1998) 29-34.

[3]. *A. Zocco, A. Perrone, A. Luches, R. Rella, A. Klini, I. Zergioti, C. Fotakis,* ‘‘Optical characterisation of CN_x thin films deposited by reactive pulsed laser ablation’’ Thin Solid Films 349 (1999) 100-104.

[4]. *T. Heitz, B. Drevillon, C. Godet, J.E. Bouree,* ‘‘Quantitative study of C—H bonding in polymerlike amorphous carbon films using in situ infrared ellipsometry’’ Phys. Rev. B 58 (1998) 13957-13973.

[5]. *T. Szörényi, C. Fuchs, E. Fogarassy, J. Hommet, F. Le Normand,* ‘‘Chemical analysis of pulsed laser deposited a-CN_x films by comparative infrared and X-ray photoelectron spectroscopies’’ Surf. Coat. Tech. 125 (2000) 308-312.

[6]. *Ö. Alver, C. Parlak and M. Şenyel,* ‘‘FT-IR and NMR investigation of 1-Phenylpiperazine: A combined experimental and theoretical study’’ Spectrochimica Acta A, 67 (2007) 793–801.

[7]. *T. İzgi, Ö. Alver, C. Parlak, M.T. Aytekin and M. Şenyel,* ‘‘FT-IR and NMR investigation of 2-(1-Cyclohexenyl)ethylamine: A Combined experimental and theoretical study’’ Spectrochimica Acta A, 68 (2007) 55–62.

[8]. *Ö. Alver, C. Parlak and M. Şenyel,* ‘‘Theoretical and Experimental Vibrational Spectroscopic Study of 3-piperidino-propylamine’’ Journal of Molecular Structure, 923 (2009) 120-126.

[9]. *C. Parlak,* ‘‘Theoretical and experimental vibrational spectroscopic study of 4-(1-Pyrrolidinyl)piperidine’’ Journal of Molecular Structure, 966 (2010) 1–7.

[10]. *A. Majumdar, G. Scholz, R. Hippler,* ‘‘Structural characterization of amorphous hydrogenated-carbon nitride (aH-CN_x) film deposited by CH_4/N_2 dielectric barrier discharge plasma: ^{13}C, ^{1}H solid state NMR, FTIR and elemental analysis’’ Surf. Coat. Tech. 203 (2009) 2013-2016.

[11]. *A.P. Scott and L. Radom,* ‘‘Harmonic Vibrational Frequencies: An Evaluation of Hartree−Fock, Møller−Plesset, Quadratic Configuration Interaction, Density Functional Theory, and Semiempirical Scale Factors’’ J. Phys. Chem. 100 (1996) 16502-16513.

[12]. *J.B. Foresman and A. Frisch,* ‘‘Exploring Chemistry with Electronic Structure Methods’’ Second Ed., Gaussian Inc., Pittsburgh (1996).

[13]. *M.J. Frisch, G.W. Trucks, H.B. Schlegel, G.E. Scuseria, M.A. Robb, J.R. Cheeseman, J. A. Montgomery, Jr.T. Vreven, K.N. Kudin, J.C. Burant, J.M. Millam, S.S. Iyengar, J. Tomasi, V. Barone, B. Mennucci, M. Cossi, G. Scalmani, N. Rega, G.A. Petersson, H. Nakatsuji, M. Hada, M. Ehara, K. Toyota, R. Fukuda, J. Hasegawa, M. Ishida, T. Nakajima, Y. Honda, O. Kitao, H. Nakai, M. Klene, X. Li, J.E. Knox, H.P. Hratchian, J.B. Cross, C. Adamo, J. Jaramillo, R. Gomperts, R. E. Stratmann, O. Yazyev, A.J. Austin, R. Cammi, C. Pomelli, J.W. Ochterski, P.Y. Ayala, K. Morokuma, G.A. Voth, P. Salvador, J.J. Dannenberg, V.G. Zakrzewski, S. Dapprich, A.D. Daniels, M.C. Strain, O. Farkas, D.K. Malick, A.D. Rabuck, K. Raghavachari, J.B. Foresman, J.V. Ortiz, Q. Cui, A.G. Baboul, S. Clifford, J. Cioslowski, B.B. Stefanov, G. Liu, A. Liashenko, P. Piskorz, I. Komaromi, R.L. Martin, D.J. Fox, T. Keith, M.A. Al-Laham, C.Y. Peng, A. Nanayakkara, M. Challacombe, P.M.W. Gill, B. Johnson, W. Chen, M.W. Wong, C. Gonzalez, J.A. Pople,* Gaussian 03 Revision C.02, Gaussian Inc., Pittsburgh PA (2003).

[14]. *A. Frisch, A.B. Nielsen, A.J. Holder,* Gaussview Users Manual, Gaussian Inc. (2000).

RELATIVE REFLECTION EFFICIENCY OF A LiF CRYSTAL

A. BAŞTUĞ[1], A. GÜROL[2], D. DEMİR[2], P. YALÇIN[3], O. İÇELLİ[4], Y. ŞAHİN[2]

[1]*Aksaray University, Faculty of Art and Science,Department of Physics, Aksaray, Turkey*

[2]*Atatürk University, Faculty of Science,Department of Physics, Erzurum, Turkey*

[3]*Erzincan University, Faculty of Education Department of Physics,Erzincan, Turkey*

[4]*Yıldız Technical University, Faculty of Art and Science,*
Department of Physics, İstanbul, TURKEY

In this study, it' been determined the relative reflection efficiency of a LiF crystal in a WDXRF Spectrometry at 0.0387-0.2497 nm wavelenght range. For this reason, 35 mm diameter pellets of TiO, VO, Fe_2O_3, ZnO, As_2O_3, NbO, RuO_2, SnO, and $BaCl_2$ samples have been prepared by mixing with cellulose as a binder. Each pellet have been irradiated with a X-ray tube with Rh anode. High voltage and emission current has been 50 kV and 72 mA, respectively. By using the measured charactristic X-ray lines and atomic parameters it's calculated the reflection efficiency of SiLi crystal.

I. INTRODUCTION

X-ray fluorescence Spectrometry (XRF) has generally been the method of choice for the last few decades for the analysis of geologic samples, particularly for major element analyses of silicate rocks. It offers high precision (typically less than *1%* relative standard deviation (RSD) for the major elements) with minimal sample preparation and analysis times [1]. Some works were reported in the literature by using Wavelenght Dispersive XRF(WDXRF) Spectrometer in the last years [2-5]. Queralt et al. [6] evaluated macro- and microelement contents of five medicinal plants (Taraxacum officinale Weber, Eucalyptus globulus Labill, Plantago lanceolata L., Matricaria chamomilla L. and Mentha piperita L.) and their infusion by the combined use of X-ray fluorescence (WDXRF and EDXRF, bulk raw plants) and inductively coupled plasma (ICP-MS and ICP-AES, infusions) techniques. Dumlupınar et al. [7] investigated the change of inorganic elements in Drosophila melanogaster and in pulvini of bean plants at chilling temperatures. Erman et al. [8] and Erman and Gurol [9] have been determined the elemental concentrations of some insects.

The main problem in XRF analysis is to determine the intensity of the characteristic X-rays. The Sherman equation [10], later improved upon by Shriraiwa and Fujino [11], permits calculation of the theoretical X-ray fluorescence intensity emitted by an analyte in multi-element specimens. To obtain best results of the theoretical X-ray fluorescence database of atomic parameters are continuosly updated [12,13]. In practice, detected intensity of the analyte flourescent X-ray radiation is a function of theoretical intensity and instrument sensivity. The spectrometer sensivity is different for each element being determined and depends on instrument configuration and measurement conditions. For this reason, when using fundamental parameter (FP) methods, the instrument sensivity is usually determined for each element with pure element standarts (or compounds).

In WDXRF Spectrometry instrument sensivity is a function of spectrometer geometry, incident X-ray spectrum generated in X-ray tube, collimators, detection efficiency of proportional and sintilation counters as well as reflectivity of the analyzing crystal. The detection efficiency can be theoretically calculated and experimentally determined using a special procedure and the reflection efficiency of the analyzing crystal is usually determined experimentally as this parameter depends on crystal tretment; abrading, flexing and etching [14].

It's an important step to calibrate the spectrometer for measurements. For this, we need some parameters, such as fluoresce yield, photoeffect crosssections, mass-attenuation coefficients, instrument sensitivity, reflection efficiency, detector efficiency, and etc. In this study we have determined the Relative Reflection Efficiency (RRE) of a LiF (200) crystal which used widely in WDXRF spectrometers.

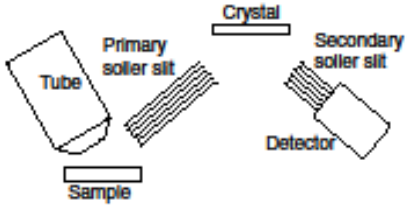

Fig. 1. A scheme of spectrometer.

II. THEORETICAL BACKGROUD

The Sherman equation for thick sample can be expressed as

$$I_{theo,i} = q_i W_i \int_{\lambda_i}^{\lambda_{edge}} \frac{\tau_i(\lambda)}{\mu(\lambda)\csc\varphi_1 + \mu(\lambda_i)\csc\varphi_2} \left(1 + S_{ij=m} W_j\right) I(\lambda) d\lambda \qquad (1)$$

where q_i is sensitivity of the analyte element *i*, if $K\alpha$ line is used then $q_i = \omega_{K,i} f_{K\alpha}(1 - 1/J_{K,i})$, where $\omega_{K,i}$ is fluorescence yield of K radiation, $f_{K\alpha}$ is weight of $K\alpha$ line within K-series, $J_{K,i}$ is the absorption edge jump ratio. If the $L\alpha_1$ or $L\beta_1$ is chosen as the analyte line, then Coster-Kronig trnsition probabilities have to be taken into consideration; $I(\lambda)$ is intensity of the primary radiation; W_i, W_j are weight fractions of the analyte element i and matrix elements j, respectively; m is the subscript for the matrix element line; $\tau_i(\lambda)$ is photoelectric absorption coefficient, μ(λ), μ(λi) are total mass attenuation

coefficients for the incident λ and fluorescent radiation λ_i, respectively;θ_1, θ_2 are angles of incidence and exit of primary and fluorescent radiation, respectively; S_{ijm} is the enhancement term for each line m of the matrix element j, which enhances the analyte element i. The enhancement term S_{ijm} is calculated from Eq. (1a).

$$S_{ijm} = 0.5\frac{\tau_j(\lambda)}{\tau_i(\lambda)}\tau_i(\lambda_{jm})\left[\ln\left(1+\frac{\mu(\lambda)}{\mu(\lambda_{jm})\sin\varphi_1}\right)\frac{\sin\varphi_1}{\mu(\lambda)}+\ln\left(1+\frac{\mu(\lambda_j)}{\mu(\lambda_{jm})\sin\varphi_2}\right)\frac{\sin\varphi_2}{\mu(\lambda_j)}\right] \quad (1a)$$

Sherman's equation gives theoretical X-ray fluorescence radiation ($I_{theo,i}$). In practice, the detected intensity of the analyte radiation depends also on instrument sensitivity. Thus, the measured intensity depends on instrumental configuration and measurement conditions. Fig. 1 presents the scheme of a WDXRF spectrometer with flat analyzing crystal. All parts of the spectrometer are enclosed in the vacuum chamber. The X-rays emited from the X-ray tube irradiate the sample and then the characteristic X-rays of matrix elements and coherent and incoherent scattered X-rays through slit is made parallel to each other. The atmosphere of analysis chamber is vacuum during the measurements. The measured X-ray fluorescence radiation can be expressed as:

$$I_i = Qi_{em}kR_{\lambda_i}\varepsilon_{sc,\lambda_i}I_{theo,i} \quad (2)$$

where Q is a factor depending on measurement geometry and sample area; i_{em} is the current of the X-ray tube; k is a coefficient depending on spectrometer geometry; R_{λ_i} is the reflection efficiency of the analyzing crystal (this parameter is a function of diffracted wavelength λ_i (Bragg angle 2θ)); $\varepsilon_{SC,\lambda_i}$ is the detection efficiency for the characteristic line of the analyte element i and it depends on thickness of thallium-doped sodium iodide crystal, transmittance of the Be window of the SC. This efficiency can be expressed by

$$\varepsilon_{sc,\lambda_i} = \exp(-\beta_{\lambda_i})\left[1-exp(-\tau_{NaI,\lambda_i}d_{NaI}\,t_{NaI})\right] \quad (3)$$

where $\beta_{\lambda_i} = \mu_{Be}d_{Be}t_{Be}$ is self-absorption coefficients of SC's window.

For calculating theoretical intensity, the X-ray tube spectral distribution and angles of incidence and exit of radiation should be known. The angle θ_2 is defined by the direction of the slit between sample and LiF crystal. The angle θ_1 can be determined using relationship (4) between wavelengths of coherent and incoherent scattered radiation. In this paper the wavelengths are in nm.

$$\lambda_{inc} - \lambda_{coh} = 0.002426(1-\cos(\theta_1+\theta_2)) \quad (4)$$

III. EXPERIMENTAL DETAILS

The experiment have been carried out by using a WDXRF Spectrometer (Rigaku ZSX100e). Ultrapure powder of TiO, VO, Fe_2O_3, ZnO, As_2O_3, RuO_2, NbO, SnO, and $BaCl_2$ have been mixed with cellulose and then pressed in the form of thick pellets of 35 mm diameter. The amounts of each compound have been such that tte analyte concentration corresponded to 25% in each pellet. These standard pellets have been used for the calibration of the spectrometer.

The WDXRF Spectrometer with 4 kW Rh X-ray tube was used for the measurements, Voltage 50 kV; emission current 72 mA; vacuum in spectrometer chamber; flat LiF (200) analysing crystal; standard slit which is a mechanism to make fluorescent X-rays generated from a sample parallel; Scintilation Counter (SC) with a thallim-doped crystal of sodium iodide 5 mm thick. The net intensities were determined for each sample by measurement of the fluorescent radiation of the element i (peak) and measurementof the continuum close to the peak. SC is only used to detect the heavy elements in the spectrometer.

IV. RESULTS AND DISCUSSION

The intensities I_i of analyte elements' $K\alpha$ X-rays in the samples; namely Ti, V, Fe, Zn, As, Nb, Ru, Sn, and Ba, have been measured. They are listed in Table 1. In addition, the theoretical intensities $I_{theo,i}$ of these lines calculated by using Eq. (1) are presented in Table 1.

The theoretical intensities $I_{theo,i}$ have been calculated by using the Eq. (1). The photoelectric absorption coefficients $\tau(\lambda)$ and μ(λ) mass attenuation coefficients have been taken from WinXCOM [15]. The absorption edge jump ratios $J_{K,i}$ are calculate by using

$$J_K = \left(\frac{J-1}{J}\right)+3.5 \quad (5)$$

ω_K and $I_{K\beta}/I_{K\alpha}$ to calculate the $f_{K\alpha}$ values are taken from Krause [16] and Scofield, respectively. The biggest problem to calculate the $I_{theo,i}$ values are predicted the X-ray tube spectra. Two important studies on this subject were carried out Pella et al. [17] and Ebel [18]. We have used The Ebel Algortihm [18] to determine the X-ray tube spectrum and it can be shown in Fig. 2. As shown this Figure, the spectrum have a continuum, Rh characteristic X-rays, Rh K and L edges, and a short-wavelenght limit as expected. To predict the spectrum is important to determine the $I_{theo,i}$ values and therefore the precise determination of elemental concentrations of sample by using the Fundemental Parameter Method (FPM) or another analysis method.

Table 1. Calculated theoretical intensity $I_{theo,i}$ and measured $K\alpha$ intensities of analytes.

	$\lambda\,(nm)$	$I_{theo,i}$(kcps)	I_i (kcps)
Ti	0.2497	$8.50.10^4$	372
V	0.2269	$1.44.10^5$	377
Fe	0.1938	$2.88.10^5$	$1.51.10^3$
Zn	0.1436	$3.96.10^5$	$3.21.10^3$
As	0.1177	$1.95.10^6$	$3.92.10^3$
Nb	0.0748	$3.21.10^6$	$5.38.10^3$
Ru	0.0645	$1.71.10^6$	$3.07.10^3$
Sn	0.0492	$1.47.10^6$	$1.17.10^3$
Ba	0.0387	$6.23.10^5$	40.4

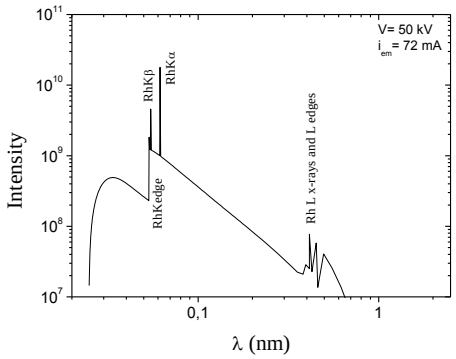

Fig. 2. X-ray tube spectrum calculated according to Ebel Algorithm [13].

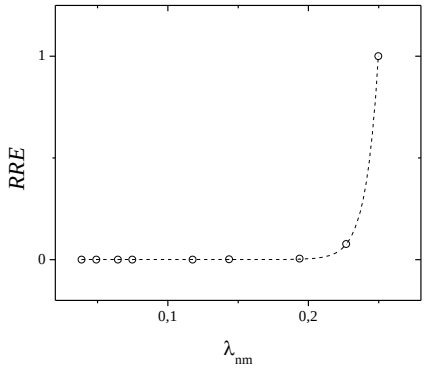

Fig. 3. Changing of RRE with λ_i.

Our precise invetigation shows that the enhancement term S_{ijm} in Eq. (1) doesn't effect the $I_{theo,i}$ values. Because, the matrix of samples consist of an analyte (Ti, V, Fe, Zn, As, Nb, Ru, Sn, or Ba) and small atomic number elements. For this reason, matrix elements have not an important effects on characteristic X-rays of analytes.

It can easily be shown that the largest values of the measured I_i and calculated $I_{theo,i}$ belobg to Nb. The reason of this is that the K absorption edge is more closer to Rh K X-rays than other elements'. It causes that the Rh K X-rays and the continuum of X-ray tube are severely absorbed by Nb atoms.

The spectrometer sensitivity Q is usually eliminated for calculation in fundamental parameter methods and in theoretical influence coefficient algorithms by replacing the absolute intensity I_i with the relative intensity R_i. The relative intensity is defined as fluorescent radiation intensity of analyte in binary, ternary or in multielement specimen to fluorescent radiation intensity of pure element or compound, e.g., oxide.

To eliminate Q, k, and i_{em} measured I_i values of each element were normalize to measured I_i values of Ti which have the largest wavelenght. Thus,it's obtained following relation for Relative Reflection Efficiency (RRE) by using Eq. (2).

$$RRE = \frac{R_{\lambda_{Ti}}}{R_{\lambda_i}} = \frac{\tau_{SC,\lambda_i} I_{theo,i} \quad I_{TiK\alpha}}{\tau_{SC,\lambda_{TiK\alpha}} I_{theo,TiK\alpha} \quad I_i} \qquad (6)$$

Clearly, RRE depends on wavelenght and the relation between them have been illustrated in Fig. (3) and this relation is

$$RRE = 8.21086 \times 10^{-4} + 5.59152 \times 10^{-13} \times e^{112.98188 \times \lambda_i} \qquad (7)$$

R-square of Eq. (7) is 0.99998. the reflection efficiencies of other analyzing crystals can be determined in the same way.

[1]. *N.W. Bower, P.E. Neifert, C.M. Lewis, G. Luedemann*, The Rigaku Journal, 1990, 7, No.1, p3-11.

[2]. *J. Christopher, M.B. Patel, S. Ahmed, and B. Basu,*. Fuel, 2001, 80, p1975-1979.

[3]. *G. van Dalen*, X-ray Spectrometry,1998, 27, p26-30.

[4]. *J. Kierzek*, B. Malozewska-Bucko, P. Bukowski, J.L Parus, A. Ciurapinski, Zaras, S., B. Kunach, and K. Wiland, Journal of Radioanalytical and Nuclear Chemistry, 1999, 240, p39- 45.

[5]. *M. Pouzar, T. Černohorský, and A. Krejčová*, Chemia Analityczna, 2003, 48, p.55-64.

[6]. *I. Queralt, M. Ovejero, M:L: Carvalho, A:F*: Marques and J.M. Llabrés, X-Ray Spectrometry, 2005, 34, p213-217.

[7]. *R. Dumlupınar, F. Demir, T. Şişman, G. Budak, G., A. Karabulut, Ö.K. Erman, E. Baydaş*, Journal of Quantitative Spectroscopy and Radiative Transfer,2006, 102, No.3, p492-498.

[8]. *Ö.K: Erman, A. Gürol and R. Dumlupınar*, R. Environmental Bulletin, 2006, 15, No.7, p.697-703.

[9]. *Ö.K. Erman and A. Gürol*, Environmental Bulletin, 2007, 16, No.12b, p.1627-1635.

[10]. *J. Sherman*, Spectrochimica Acta, 1955, 7, p.283-306.

[11]. *T. Shiraiwa, N. Fujino*, Jpn. J. Appl. Phys., 1966, 5, p.886-899.

[12]. *W.T. Elam, B. D. Ravel, J.R. Sieber*, Radiat. Phys. Chem., 2001, 63, p.121-128.

[13]. *H. Ebel, R. Svagera, M. F. Ebel, A. Shaltout, J.H. Hubbel*, X-Ray Spectrom., 2003, 32, p.442-451.

[14]. *R. Sitko and B. Zawaiska*, Spectrochimica Acta B, 2005, 60, p.95-100.

[15]. *L. Gerward, N. Guilbert, K. Bjørn Jensen, H. Levring*, Radiat. Phys. Chem., 2001, 60, p.23–24.

[16]. *M.O. Krause*, J. Phys. Chem. Ref. Data, 1979, 8, p.307.

[17]. *P.A. Pella, L. Feng, J.A. Small*, X-Ray Spectrom., 1985, 14, p.125-135.

[18]. *H. Ebel*, X-Ray Spectrom., 1999, 28, 255-266

MEASUREMENT OF *K* AND *L* X-RAY INTENSITY RATIOS FOR Nd AND Ho ELEMENTS IN AN EXTERNAL MAGNETIC FIELD

D. DEMIR, Y. ŞAHIN, A. GÜROL, P. ÖNDER, B. GÜRBULAK, S. DOĞAN
Faculty of Science, Department of Physics, Ataturk University, 25240 Erzurum, Turkey
ddemir@atauni.edu.tr, ysahin@atauni.edu.tr, ponder@atauni.edu.tr, agurol@atauni.edu.tr, gurbulak@atauni.edu.tr

K and *L* X-ray intensity ratios $K\alpha_1$/ $K\alpha_2$, $K\beta/K\alpha_2$, $L\ell/L\gamma$, $L\alpha/L\gamma$ and $L\beta/L\gamma$ for Nd and Ho are measured by using 59.54 keV incident photon energy at 110° and 130° scattering geometry by an energy dispersive x-ray fluorescence systems. The samples are located in the external magnetic field of intensities ±0.75 T. The experimental results obtained for B=0 are compared with theoretical values calculated using Scofield's tables based on the Hartree-Slater theory. The contribution to the alignment of the external magnetic field is discussed.

I. INTRODUCTION

In the photon-atom interactions, the shapes and the circulation properties of the electronic charge clouds of the atoms are rearranged. Since more than 40 years the theory of gamma and X-ray angular distribution is well established and confirmed by so many theoretical and experimental studies [1-4]. One of the most important results of these theories is that an anisotropic gamma and X-ray angular distribution may only arise if there is a non-equal population of magnetic substates. That is, if total angular momentum of the vacancy state (*J*) is greater than 1/2 it is aligned and the resulting X-ray emission is anisotropic. Thus, only those fluorescent X-rays that originate from the decay of vacancy states in *K*, L_1, L_2, M_1 and M_2 subshells with J=1/2 will be isotropically emitted. But those from L_3, M_3 and M_4 subshell with J =3/2 and from the M_5 subshell with J=5/2 will show anisotropic spatial distribution.

A study of alignment allowing the excitation between different magnetic substates of an electronic state to be distinguished is expected to provide a better test for models of the excitation process. Furthermore, alignment or orientation of an excited atomic state must be taken into account when measuring the X-ray spectra and when deriving the ion-induced X-ray production cross sections from the results of measured X-ray yield since the measured intensities of the emission of individual lines depend on the radiation polarization degree and vary with photon energy.

The atomic parameters such as the shapes and the circulation properties of the electronic charge clouds, photoionization cross section, fluorescence yield, radiation rates, vacancy transfer probabilities and spectral linewidth can change due to applied magnetic field. Demir and Şahin [5-7] investigated how the radiative transitions and the structures of the atoms in an external magnetic field are affected.

A lot of investigations on X-ray fluorescence induced by photon excitations report contradictory conclusions on the anisotropy exhibited by some *K* and *L* lines. While the strong evidence of angular dependence is reported by Kahlon *et al* [8] and Ertuğrul *et al* [9], Kumar *et al* [10] and Tartari *et al* [11] declared that all *L* X-rays emitted have an isotropic distribution. In order to clarify this discrepancy between the experimental results, we have investigated the effect of the external magnetic field on the *K* and *L* X-ray intensity ratios of Nd and Ho at 110° and 130° scattering angles. The charge cloud can be deformed with the application of magnetic field, especially for not being the spherically symmetrical states. Thus, the external magnetic field dependence of the *K* and *L* X-ray intensity ratios can be a strong evidence for the anisotropic emission of *K* and *L* shell X-rays.

II. EXPERIMENTAL

Gamma photons of 59.54 keV from a filtered point source (^{241}Am) of intensity 3.7×10^9 Bq was used for direct excitation of 99.90 % pure targets made up of Nd and Ho with the mass thickness 0.22 and 0.30 g/cm^2, respectively. The samples were placed at an angle 45° with respect to the direct beam. The scattering angle was selected as 110° and 130°. The intensities of gamma rays were measured using a Si(Li) solid state detector of a resolution of 180 eV at 5.9 keV, an active diameter of 6.2 mm, sensitive crystal depth of 5 mm and a Be window of 0.008 mm thickness. The data were collected into 16384 channels of DSA-1000 operated through Genie-2000 gamma spectroscopy software including peak searching, peak evaluation, energy/efficiency calculation mode, nuclide identification, and etc. The samples were mounted on a sample holder placed between the pole pieces of an electromagnet capable of producing the magnetic field of approximately 3 T. To check the systematic and the statistical counting errors arising from radiation emanating from the exciting source, a thin indium wire reference sample was positioned at the collimator of the Si(Li) detector. The pulse height spectrum of X-rays emitted from each sample was acquired for a period of 10 h to obtain good statistics in the evaluation of each *K* and *L* X-ray peaks. The spectra were analyzed by using Microcal Origin 7.5 Demo Version.

III. DATA ANALYSIS

The experimental *K* (or *L*) shell X-ray intensity ratio between the two considered line groups at the scattering angle can be expressed as

$$\frac{I_i}{I_j} = \frac{N_{Ki}(\theta)}{N_{Kj}(\theta)} \frac{\beta_{Kj}(\theta)}{\beta_{Ki}(\theta)} \frac{\varepsilon_{Kj}(\theta)}{\varepsilon_{Ki}(\theta)} \qquad (1)$$

where $N_{K\,i}(\theta)$ is the number of *K* X-rays detected per second in the *Ki* X-ray peak at an angle θ with the incident gamma ray beam, $\varepsilon_{K\,i}(\theta)$ is the efficiency of the detector for the detection of X-rays emitted at the angle θ and $\beta_{K\,i}(\theta)$ is the target self-absorption correction factor calculated using the equation

$$\beta_{K\,i}(\theta)=\frac{1-\exp\left[-(\mu_{inc}/\cos\theta_1+\mu_{emt}/\cos\theta_2)t\right]}{(\mu_{inc}/\cos\theta_1+\mu_{emt}/\cos\theta_2)t} \qquad (2)$$

where μ_{inc} and μ_{emt} are the attenuation coefficients (cm^2g^{-1}) of the incident photons and emitted characteristic X-rays, respectively, θ_1 and θ_2 are the angles of incident photon and emitted X-ray with the target. μ_{inc} and μ_{emt} were obtained from WinXcom the well-known program for calculating gamma and X-rays attenuation coefficients [12].

The detector efficiency ratios, $\varepsilon_{Kj}(\theta)/\varepsilon_{Ki}(\theta)$, were determined from a plot of the $I_0G\varepsilon$ factor versus energy, where I_0G is the intensity of the photons falling on the portion of target visible to the detector.

IV. RESULTS AND DISCUSSION

To investigate the sensitivity of the detection system, five pellets of Ho were prepared and measured in B=0 and B=+0.75 T for scattering angle 110°. Calculated relative standard deviation (RSD) results are given in Table 1 (a). Besides, one of the pellets was measured five times under the same experimental conditions. The relative standard deviation associated was calculated and given in Table 1 (b). The relative standard deviations of analysis results of five pellets prepared at the same conditions are higher than that of analysis results of the same pellet measured five times as shown in Tables 1 (a) and (b). For the same pellet measured five times, the relative standard deviations are very insignificant. That is, sensitivity of the detection system is very good.

The measured energies of the various *K* and *L* X-ray lines of Nd, Ho and In (reference sample) versus the magnetic field intensities at scattering angles 110° and 130° are listed in Table 2. As seen from Table 2, the energy of In $K\alpha$ line doesn't change with the angle and external magnetic field. This means that the detection system is stable. As can be seen from Table 2, the angular and magnetic field dependence of the energy of $K\alpha_2$ peaks is weaker than that of $K\alpha_1$ peaks. The energy shift is such that $L\ell > L\alpha > L\beta$ for *L* X-rays as seen from Table 2. The energy of $L\gamma$ peaks hardly any change with the angle and external magnetic field intensity, also. This result confirms that $L\gamma$ line is isotropical. Thus, $L\gamma$ transition can be selected as normalization parameter for *L* X-ray intensity ratios. The present *K* and *L* X-ray intensity ratios of Nd and Ho versus the magnetic field intensities are given together with the theoretical results [13, 14] in Table 3. It can be seen from Table 3 that our measured values for B=0 are in good agreement with the theoretical values within the experimental errors.

We applied the *t*-test to the measured values of intensity ratios for Ho. It was found that t_{expt} is 3.165 for the $L\alpha$ to $L\gamma$ intensity ratio. The critical *t* value is 1.844 at the 5 % level of significance and 8 degrees of freedom. According to the *t*-test result, the difference of the means of $L\alpha$ to $L\gamma$ intensity ratio obtained for B=0 and B=+0.75 T is significantly different than the *t*-test difference. We can say that the data collected in Table 3 shows sensitivity with respect to the magnetic field.

The isotropy of the fluorescence radiation is an analytically known constant in the special case of *s* subshell photoionization of an atom having initial orbital angular momentum *L*=0. But, the upper state alignment can cause anisotropic angular distributions when the lower energy level has spherical symmetry.

This means that the final and initial states of the atom relevant to the X-ray transition may have an aligned vacancy if the angular momenta of the states are larger than 1/2. If the state is aligned, the number of the electrons which can participate in the X-ray transition is different in the different magnetic substates and therefore the transition probability from the different magnetic substates will also be different from each other. In this case the $K\alpha_1$ (*K*-L_3) and $K\beta$ (*K*-*M*) transitions may have anisotropic angular distribution. As seen from Table 3, $K\alpha_1/K\alpha_2$ and $K\beta/K\alpha_2$ intensity ratios change with the angle and external magnetic field. The external magnetic field dependence of the measured intensity ratios for *K* X-ray confirms the symmetry change of the atomic charge distribution between the initial and final states in the external magnetic field. Thus, the external magnetic field dependence of the *K* X-ray intensity ratios is a strong evidence for the anisotropic emission of some *K* lines.

$L\ell/L\gamma$, $L\alpha/L\gamma$ and $L\beta/L\gamma$ intensity ratios change with the angle and external magnetic field as seen from Table 3. This result arise from the isotropy is changing with the changed magnetic field, especially for not being the spherically symmetrical states, since the applied magnetic field is induced to align the magnetic dipoles in the field direction. It can be seen from Table 3 that $L\ell/L\gamma$, $L\alpha/L\gamma$ and $L\beta/L\gamma$ intensity ratios for Nd and Ho decreases with the applied magnetic field intensity. This means that the transition probabilities of $L\ell$, $L\alpha$ and $L\beta$ lines decrease in the external magnetic field. As can be seen from Table 3, the angular and magnetic field dependence of the $L\ell$ peak is greater than that of $L\alpha$ peak because the $L\ell$ peak contains only one intense line (L_3-M_1) but the $L\alpha$ peak contains $L\alpha_1$ (L_3-M_5) and $L\alpha_2$ (L_3-M_4) lines.

Table 2. Measured energies of K and L X-ray lines of Nd, Ho and In versus the magnetic field intensities at scattering angles 110° and 130° (keV).

		110°					130°		
Sample	X-ray line	B=0	B=+0.75 T	B= -0.75 T	Sample	X-ray line	B=0	B=+0.75 T	B= - 0.75 T
Nd	$K\alpha_1$	47.390	47.380	47.380	Nd	$K\alpha_1$	47.375	47.365	47.365
	$K\alpha_2$	46.840	46.843	46.843		$K\alpha_2$	46.840	46.845	46.845
	$L\ell$	4.652	4.622	4.624		$L\ell$	4.612	4.582	4.582
	$L\alpha$	5.271	5.251	5.252		$L\alpha$	5.298	5.275	5.274
	$L\beta$	5.751	5.743	5.745		$L\beta$	5.779	5.764	5.762
	$L\gamma$	6.404	6.408	6.411		$L\gamma$	6.402	6.402	6.401
	In $K\alpha$	24.184	24.187	24.187		In $K\alpha$	24.185	24.183	24.180
Ho	$K\alpha_1$	47.507	47.517	47.517	Ho	$K\alpha_1$	47.515	47.505	47.505
	$K\alpha_2$	46.711	46.715	46.715		$K\alpha_2$	46.713	46.712	46.712
	$L\ell$	6.400	6.430	6.430		$L\ell$	6.356	6.386	6.386
	$L\alpha$	6.732	6.712	6.712		$L\alpha$	6.760	6.743	6.743
	$L\beta$	7.555	7.548	7.548		$L\beta$	7.573	7.560	7.562
	$L\gamma$	8.747	8.747	8.748		$L\gamma$	8.748	8.751	8.750
	In $K\alpha$	24.182	24.180	24.182		In $K\alpha$	24.184	24.187	24.187

Table 3. The K and L X-ray intensity ratios versus the magnetic field intensities at scattering angles 110° and 130°.

		110°					130°			
Sample	Int. Rat.	Experimental B=0	B=+0.75 T	B= - 0.75 T	Theory	Sample	Int. Rat.	Experimental B=0	B=+0.75 T	B= - 0.75 T	Theory
Nd	$K\alpha_1/K\alpha_2$	1.845 ± 0.028	1.715 ± 0.011	1.715 ± 0.011	1.821[a]	Nd	$K\alpha_1/K\alpha_2$	1.810 ± 0.024	1.690 ± 0.018	1.692 ± 0.019	1.821[a]
	$K\beta/K\alpha_2$	0.646 ± 0.008	0.615 ± 0.011	0.614 ± 0.010	0.649[a]		$K\beta/K\alpha_2$	0.634 ± 0.008	0.604 ± 0.011	0.602 ± 0.010	0.649[a]
	$L\ell/L\gamma$	0.392 ± 0.025	0.257 ± 0.032	0.254 ± 0.035	0.353[a]		$L\ell/L\gamma$	0.352 ± 0.032	0.222 ± 0.020	0.222 ± 0.020	0.353[a]
	$L\alpha/L\gamma$	9.252 ± 0.014	8.925 ± 0.038	8.928 ± 0.036	9.200[a]		$L\alpha/L\gamma$	9.236 ± 0.019	8.916 ± 0.033	8.914 ± 0.035	9.200[a]
	$L\beta/L\gamma$	7.107 ± 0.038	6.905 ± 0.028	6.903 ± 0.026	7.009[b]		$L\beta/L\gamma$	7.017 ± 0.035	6.795 ± 0.023	6.797 ± 0.025	7.009[b]
Ho	$K\alpha_1/K\alpha_2$	1.786 ± 0.028	1.687 ± 0.032	1.689 ± 0.031	1.779[a]	Ho	$K\alpha_1/K\alpha_2$	1.751 ± 0.019	1.632 ± 0.025	1.632 ± 0.025	1.779[a]
	$K\beta/K\alpha_2$	0.677 ± 0.018	0.646 ± 0.024	0.644 ± 0.023	0.669[a]		$K\beta/K\alpha_2$	0.665 ± 0.010	0.625 ± 0.021	0.624 ± 0.022	0.669[a]
	$L\ell/L\gamma$	0.373 ± 0.018	0.238 ± 0.015	0.234 ± 0.012	0.350[a]		$L\ell/L\gamma$	0.350 ± 0.030	0.208 ± 0.017	0.204 ± 0.015	0.350[a]
	$L\alpha/L\gamma$	8.280 ± 0.108	7.981 ± 0.051	7.980 ± 0.050	8.278[a]		$L\alpha/L\gamma$	8.137 ± 0.101	7.838 ± 0.040	7.836 ± 0.042	8.278[a]
	$L\beta/L\gamma$	6.760 ± 0.095	6.556 ± 0.075	6.555 ± 0.076	6.653[b]		$L\beta/L\gamma$	6.632 ± 0.080	6.434 ± 0.073	6.430 ± 0.071	6.653[b]

[a] Values obtained from Ref. [14]
[b] Values obtained from Ref. [13]

Also, the observed anisotropy of the $L\alpha$ peak is decreased due to interactions between the magnetic substates with opposite anisotropy and external magnetic field. The experimental results confirm that the $L\ell$ and $L\alpha$ emission originating from the L_3 subshell vacancy states with J=3/2 is anisotropic.

V. CONCLUSIONS

When the irradiated atom is placed in an external magnetic field, joint action of hyperfine interaction and the magnetic field causes the alignment of the magnetic dipoles in the field direction. Thus, both the radiation field and an external magnetic field lead to the alignment of the inner shell vacancy in ions. The magnetic field dependence of the measured intensity ratios *K* X-rays confirms the symmetry change of the atomic charge distribution between the initial and final states in the external magnetic field. Also, the magnetic field dependence of the intensity ratios *L* X-rays is a strong evidence for the anisotropic emission the $L\ell$ and $L\alpha$ emission originating from the L_3 subshell vacancy states with J=3/2.

Table 1. Comparison of the results of 1 measurement on 5 different pellets of Ho and 5 measurements on the same pellet of Ho in B=0 and B=+ 0.75 T for scattering angle 110°.

	(a) RSD (%) for 5 pellets / 1 measurement			(b) RSD (%) for 1 pellets / 5 measurements	
X-ray line	B=0	B=+ 0.75 T		B=0	B=+ 0.75 T
$L\ell$	5.5	6.0		1.2	1.4
$L\alpha$	2.6	2.9		1.4	1.5
$L\beta$	3.2	3.4		2.4	2.6
$L\gamma$	3.7	4.0		1.7	1.5
$K\alpha_2$	6.0	6.2		1.4	1.6
$K\alpha_1$	2.3	2.5		1.0	1.2
In $K\alpha$	1.5	1.9		0.7	0.9

[1]. *J.Cooper, R.N.Zare,* J.Chem.Phys., 1968,48, 942.
[2]. *S, Flügge, W. Melhorn, V. Schmidt,* Phys. Rev. Lett., 1972, 7, 29.
[3]. *S. Seven, K. Koçak,* J. Phys. B: At. Mol. Opt. Phys., 2001, 34, 2021.
[4]. *T. Papp,* Nucl. Instrum. Meth. B, 1999, 543, 300.
[5]. *D. Demir, Y. Şahin,* Nucl. Instrum. Meth. B, 2007, 254, 43.
[6]. *D. Demir, Y. Şahin*, Eur. Phys. J. D, 2007, 34, 8.
[7]. *D.Demir, Y.Şahin*, Chin.Phys.Lett.,24,2007, 668.
[8]. *K. S. Kahlon, H. S. Aulakh, N. Singh, R. Mittal, K. L. Allawadhi, B. S. Sood,* Phys. Rev. A 1991, 43, 1455.
[9]. *M. Ertuğrul, E. Büyükkasap, A. Küçükönder, H.Erdoğan,* Tr. J. Phys., 1996, 20,1.
[10]. *A. Kumar, M. L. Garg, S. Puri, D. Mehta, N.Singh*, X-Ray Spectrometry, 2001, 30, 287.
[11]. *A. Tartari, C. Baraldi, E. Casnati, A. Dare, J.E.Fernandez, S. Taioli,* J. Phys. B: At. Mol. Opt. Phys. 2003, 36, 843.
[12]. *L. Gerward, N. Guilbert, K. B. Jensen, H. Levring,* Radiat. Phys. Chem., 2001, 60, 23.
[13]. *J. H. Scofield,* At. Nucl. Data Tables, 1974, 14, 121.
[14]. *M. Ertuğrul* Nucl. Instrum. Meth. B, 1996, 111, 229

DFT STUDIES AND VIBRATIONAL SPECTRA OF 2-(2-PHENYLDIAZENYL) PROPANEDINITRILE

E AKTAN[1*], B. ÇATIKKAŞ[2], H. ESENER[1]
[1]*Department of Chemistry, Gazi University, 06500 Teknikokullar, Ankara, Turkey*
[2]*Department of Physics, Gazi University, 06500 Teknikokullar, Ankara, Turkey*
ebruaktan@gazi.edu.tr

In this study, the optimized geometries of azo and hydrazo tautomers and their bonding characteristics as well as IR, NMR and UV-Vis spectra of the 2-(2-phenyldiazenyl)propanedinitrile molecule were analyzed. Structural and vibrational calculations were carried out by using B3LYP/6-311G+(d,p) method. Vibrational assignments of the title molecule were calculated by using Scaled Quantum Mechanical (SQM) analysis. The NMR isotropic magnetic shielding tensors were calculated using the Gauge-Independent Atomic Orbital (GIAO) approach. The theoretical electronic absorption spectra were calculated using time-dependent density functional theory (TD-DFT). Calculated values were compared with corresponding experimental results.

I. INTRODUCTION

Azo dyes are used in dyeing various materials such as textile fibers, plastic materials, leather and paper. In addition to their dyeing properties they are currently used in high technology and medical areas [1-6]. Their relatively large molecular hyperpolarizing make azo dye chromophores more interesting among organic NLO molecules, and take the attention of investigators [7-10].

Azo dyes do not exist in nature and they are acquired from synthetic processes. Depending on their efficiency in dyeing, their accessible accomplishment from reasonable starting molecules, their capacity of wide range colors and their medium to high fastness characteristics, azo dyes have become the most attractive preferences.

The colors of the azo and hydrazones tautomers, dyeing efficiency and their fastness properties are different from each other. Because of this, it is eminent to know which tautomer is dominant in compounds which show azo-hydrazo tautomerism [11,12]. Semi empirical and ab-initio methods are generally used in azo-hydrozo tautomeric equation studies, besides NMR, IR, Raman, UV–Vis spectroscopy and X-ray crystallography methods [13,14]. What we tried to determine is the tautomeric form which existed assertively in solid phase with IR and Raman spectra, in solution phase with NMR and UV-Vis spectra, in the gas phase of 2–(2- phenyldiazenyl) propandinitrile compound with ab-initio methods.

The aim of the present work is to synthesis and predict structure, ^{1}H and ^{13}C NMR, vibrational and UV-Vis spectra of the 2-(2-phenyldiazenyl)propanedinitrile molecule with ab-initio methods. The calculated results will be compared with the available experimental data.

II. EXPERIMENTAL DETAILS

2.1. General

The chemicals used for the synthesis of the compounds were obtained from Sigma-Aldrich Chemical Company without further purification. The solvents used were of spectroscopic grade. The ^{1}H and ^{13}C were taken in DMSO solutions on a Bruker 300 Ultrashield spectrometer. The IR and Raman spectra were recorded with ATR objectives on a Bruker IFS/66 and FRA 106/S IR-Raman spectrometer. The electronic absorption spectra were measured on an Analytika-Jena UV-200 spectrophotometer.

2.2. Synthesis

0.83 g (0.01 mol) aniline is solved in 10 mL hydrochloric acid and 5 mL water. The solution obtained is mixed on magnetic stirrer after cooled in salt- ice bath. 0.69 g (0.01 mol) $NaNO_2$ is solved in 10 mL water and cooled in salt-ice bath. The solution obtained is gradually added to the aniline solution, taking the temperature into consideration not to be above 0° C. After the adding process is completed, the mixing process follows an hour time period. 0.66 g (0.01 mol) malonodinitrile is solved in 15 mL ethanol and the water solution of 5g sodium acetate is added in it. The mixture is cooled in salt-ice bath. The cold diazonium salt solution is added to the cooled solution, drop by drop when mixing. After this process, the mixture is calibrated to pH=5-6 with sodium acetate solution. The product prepared in this way, is mixed in room temperature and rested for 3 hours in order to complete the clasping process. At the end of this period, the diluted water of NaOH solution is added till the pH is 7. The precipitate obtained is filtered with vacuum and dried. It is crystallized from the mixture of ethanol and water.

The synthesis of 2-(2-phenyldiazenyl)propanedinitrile is shown in Scheme 1.

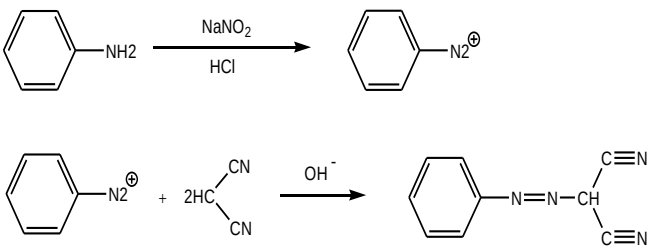

Scheme 1

III. COMPUTATIONAL DETAILS

The geometries of the azo and hydrazo tautomers have been optimised using density functional theory (DFT) approach with the hybrid functionel B3LYP [15-17] and 6-311G+(d,p) basis set.

The proton and carbon chemical shifts were calculated using GIAO-DFT method [18,19]. In the calculation stages the B3LYP functional and 6-311G++(2d,2p) basis set were employed. For the ^{1}H and ^{13}C spectra, δ_x^{ref} is equal to 31.81 and 183.73 ppm, as found on the DFT / B3LYP /6-311G++(2d,2p) geometry of the dual-reference Standard (TMS).

The Total Energy Distribution (TED) of the vibrational modes of the molecules was calculated with the Scaled Quantum Mechanics (SQM) method by using Parallel Quantum Mechanics Solutions (PQS) program [20]. The fundamental vibrational modes were characterized by their total energy distribution.

The maximum absorption wavelengths and oscillator strenghts of the dye were calculated in different solutions using time-dependent density functional theory (TD-DFT) at the 6-31+G level. The Polarizable Continuum Model (PCM) method [21] was selected for the TD-DFT calculations.

Gaussian 03 software package was used for the theoretical calculations [22].

IV. RESULTS AND DISCUSSION

2–(2-phenyldiazenyl)propandinitrile molecule presents two tautomeric forms, namely azo form and hydrazo form. The molecular structure of these tautomers are shown in Figure 1.

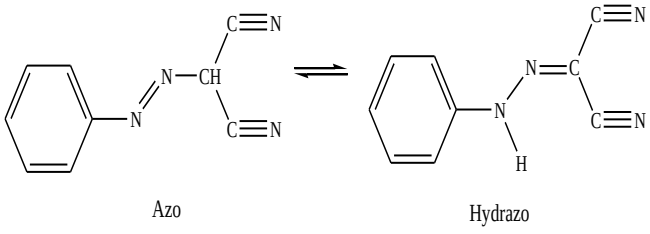

Fig. 1. Structure of azo and hydrazo tautomers

Total energy and dipole moment values of two possible tautomers are given in Table 1. As seen in Table 1, the hydrazo tautomer is the most stable form in gas phase. The results of theoretical calculations indicate that the energy difference between the two tautomers is 16.7 kcal mol^{-1} at the B3LYP/6-311+G(d,p) level.

Table 1.Total energy and dipol moment values of the tautomers

Tautomer	Total Energy (Hartree)	Dipol Moment (Debye)
Hydrazo	-565.64915628	6.4395
Azo	-565.62250564	6.2306

The optimized bond lenghts and angles for the most stable tautomer are presented in Table 2. The optimized geometry of hydrazo form was found to be completely planar at both HF and B3LYP methods. To our knowledge, calculated and experimental data on the geometric structure of the title compound is not available in the literature. Therefore, we could not compare the calculated geometrical parameters with experimental data.

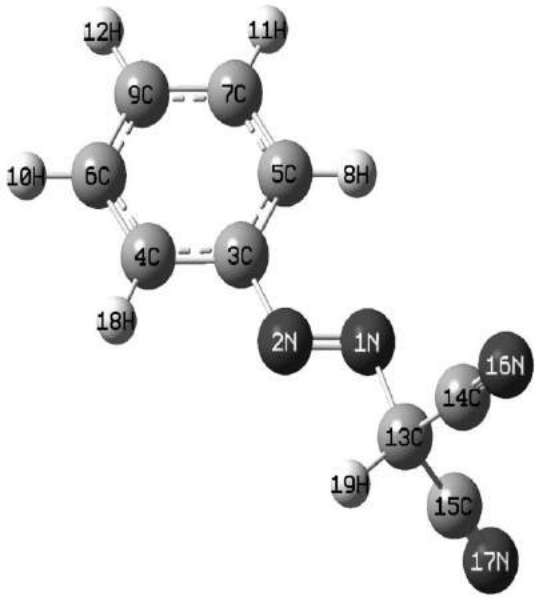

Azo

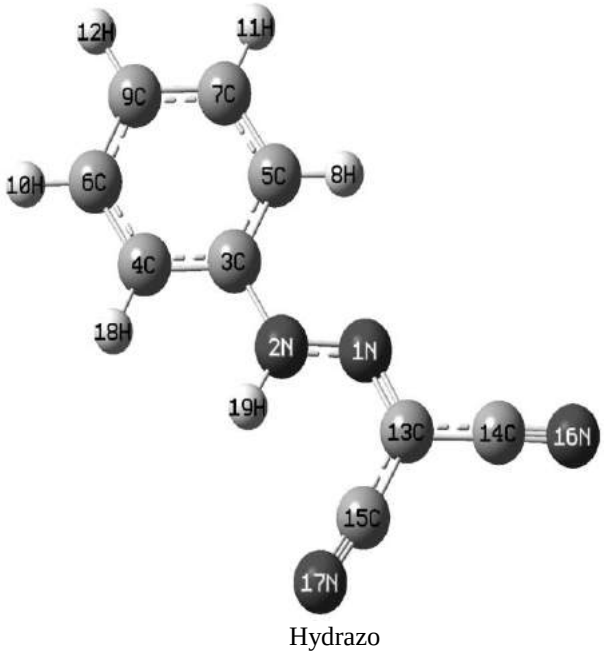

Hydrazo

Fig. 2. Azo and Hydrozo Structure

The ^{1}H and ^{13}C NMR chemical shift values were experimentally observed and compared to theoretical result (Table 3). In the ^{1}H NMR spectra in DMSO-d_6 there is a broad band at 13.0 ppm, attributed to NH proton of hydrazo tautomer. The chemical shift for NH proton was calculated at 9.53 ppm for the hydrazo form. According to these results, the title compound exists in hydrazo form in DMSO-d_6.

A medium band at 2211 and 2230 cm^{-1} in IR spectra were assigned to CN streching vibrations. The frequencies for CN groups obtained by B3LYP method are 2304 and 2336 cm-^{1}. Calculated frequencies are corrected using scale factor (0,9614) for B3LYP/6-311+G(d,p) basis set. The assignments of normal vibrations of the compound are presented in Table5.

Table 2. Optimized geometrical parameters for the tautomers (bond length/ Å, angle/degree)

Bond lengths	HF	B3LYP	Bond angles	HF	B3LYP
R(1,2)	1.302	1.241	A(2,1,13)	120.3	110.4
R(1,13)	1.312	1.501	A(1,2,3)	122.2	116.0
R(2,3)	1.412	1.421	A(2,3,4)	117.7	115.0
R(2,19)	1.021	1.000	A(4,3,5)	120.7	120.7
R(3,4)	1.398	1.398	A(3,4,18)	120.2	118.7
R(3,5)	1.397	1.403	A(4,6,9)	120.3	119.7
R(4,6)	1.391	1.392	A(4,6,10)	119.4	120.0
R(4,18)	1.085	1.083	A(5,7,9)	120.9	120.4
R(5,7)	1.391	1.387	A(9,7,11)	120.0	119.9
R(5,8)	1.082	1.082	A(1,13,14)	118.5	120.0
R(6,9)	1.394	1.393	A(1,13,15)	121.8	120.0
R(6,10)	1.084	1.083	A(14,13,15)	119.7	120.0
R(7,9)	1.395	1.400	Torsion angles	HF	B3LYP
R(7,11)	1.084	1.084	D(13,1,2,3)	180.0	-180.0
R(9,12)	1.083	1.084	D(13,1,2,19)	0.0	0.0
R(13,14)	1.425	1.469	D(2,1,13,14)	180.0	180.0
R(13,15)	1.429	1.469	D(1,2,3,4)	180.0	-180.0
R(14,16)	1.156	1.151	D(1,2,3,5)	0.0	0.0
R(15,17)	1.157	1.151	D(2,3,4,6)	180.0	-180.0

On the basis of calculated results, assignments off all the fundamental vibrational frequencies were made. Our average percentage error for total 51 fundamental vibrations is 3.50. RMS (root-mean-square) and mean deviations are 5.56 cm-1 and 2.84 cm-1, respectively. These results are well compared with the RMS error values (RMS: 12.0) presented for 30 organic molecules for their 663 vibrational frequencies [24].

The electronic absorption spectra of the title compound were measured in various solvents in the concentration range from 10^{-6} to 10^{-8} M (Table 4). Experimental λ_{max} values were compared with calculated λ_{max} values. The λ_{max} values of the hydrazo tautomes are closer to the experimental results.

Table 3. Comparison of calculated and experimental values of ^{1}H and ^{13}C NMR chemical shifts (ppm) relative to TMS

^{1}H-NMR			^{13}C-NMR		
Atom	Exp.	Calc.	Atom	Exp.	Calc.
H19	13.0, NH,(s, 1H, b)	9.53	C3	141.9	147.8
H8	7.48, Ar CH, (d,2H)	8.18	C7	130.0	137.4
H18		7.25	C6	130.0	135.8
H11	7.42, Ar CH, (t,2H)	7.85	C9	126.3	132.4
H10		7.73	C5	116.9	120.5
H12	7.22, Ar CH, (t,1H)	7.58	C4	116.9	120.3
			C14	114.9	117.3
			C15	110.4	113.3
			C13	85.0	90.8

Table 4. Experimental and calculated λ_{max} (nm) values of dye

		Chloroform	Methanol	Acetonitrile	DMSO
Exp.	λ_{max}	362	360	355	368
Hydrazo	λ_{max}	369	367	368	371
	f	0.6688	0.6566	0.6581	0.6807
Azo	λ_{max}	294	294	295	297
	f	0.5537	0.5332	0.5368	0.5517

V. CONCLUSIONS

We have reported the optimized molecular structure, experimental and calculated vibrational, NMR and UV-Vis spectra of the 2-(2-phenyldiazenyl)propanedinitrile. The hydrazo structure of the title compound (rather than the tautomeric azo structure) was assessed by experimental and ab-initio calculations in solid, solution and gas phase .

Table 5. Fundamental vibrations of compound: comparison between the HF, DFT, SQM and experimental results.

		HF/B3LYP			DFT/B3LYP			Experimental		SQM	TED(5%<)
		$n_{har.}$	Şiddet		$n_{har.}$	Şiddet					
			IR	Raman		IR	Raman	IR	Raman		
υ_1	A"	34	0.1	1.0	37	0.0	0.9		41	37	τ(CCNH)(27)+τ(CCNN)(26)+τ(CCNN)(25)
υ_2	A"	66	0.9	0.1	67	1.4	0.0		62	66	τ(CNNC)(43)+τ(NCCC)(21)+τ(CCCC)(14)
υ_3	A'	82	1.5	1.4	75	1.0	3.1		73	74	δ(NNC)(27)+δ(CCN)(41)
υ_4	A'	135	8.6	8.6	118	7.8	12.5		113	116	δ(NCC)(12)+δ(CCC)(63)
υ_5	A"	194	7.4	0.8	176	4.5	0.8		172	172	τ(NCCC)(65)+τ(NNCC)(34)
υ_6	A'	218	3.8	4.0	198	2.5	5.2	190		195	δ(CCN)(51)+δ(CNN)(9)
υ_7	A"	280	0.8	3.8	265	0.0	3.2		257	259	τ(CNNC)(21)+τ(CCCN)(15)+τ(CCNN)(12)+τ(CCCC)(15)
υ_8	A"	356	0.4	2.4	325	26.0	0.7		317	319	τ(NCCC)(75)+τ(CCNN)(33)
υ_9	A'	361	35.4	1.6	328	0.3	2.3	320		321	δ(NNC)(35)+ν(NC)(20)+δ(CCC)(8)
υ_{10}	A"	452	0.0	0.1	414	0.0	0.0		406	405	τ(CCCC)(48)+τ(CCCH)(21)
υ_{11}	A'	456	4.9	1.5	419	3.0	6.4	409		412	δ(CCN)(27)+δ(NNC)(13)
υ_{12}	A"	538	11.4	4.5	488	3.4	3.5	485	475	483	τ(NCCN)(28)+τ(CCCN)(22)+τ(CCCH)(12)
υ_{13}	A"	560	15.6	2.5	511	13.1	1.0		500	501	τ(CCCC)(29)+τ(CCNN)(21)+τ(CCCH)(25)
υ_{14}	A'	594	34.5	3.2	579	2.5	10.6	565		569	δ(CCN)(46)+δ(CNN)(7)+ν(CC)(8)
υ_{15}	A'	623	3.5	7.4	602	1.0	10.0	590	584	591	ν(CC)(32)+δ(NCC)(10)+ρ_w(NCNC)(13)
υ_{16}	A"	650	3.3	1.0	609	16.8	6.6		602	599	τ(NCCN)(86)+τ(CCNN)(29)+ρ_S(NCNC)(13)
υ_{17}	A'	662	11.0	12.5	619	19.3	19.8	605		606	ν(CC)(7)+δ(NNC)(51)
υ_{18}	A'	675	1.7	6.0	633	1.3	7.3	619	616	619	δ(CCC)(53)+δ(CCH)(5)
υ_{19}	A"	743	3.2	13.0	686	1.4	1.4		682	672	τ(CCNN)(17)+τ(NCCN)(31)+τ(CNNH)(20)
υ_{20}	A"	761	45.5	4.5	703	61.6	1.3		689	689	τ(NCCN)(16)+τ(CCCC)(10)+τ(CNNH)(21)
υ_{21}	A"	840	81.9	5.3	765	62.8	3.4		753	748	τ(NCCH)(12)+τ(CCCH)(60)
υ_{22}	A'	855	19.2	3.0	807	6.9	22.4	787	785	790	ν(CC)(26)+ν(CN)(13)+δ(CCC)(13)
υ_{23}	A"	930	0.1	1.0	839	0.1	0.3		819	821	τ(NCCH)(20)+τ(CCCH)(67)
υ_{24}	A'	949	12.4	13.2	894	12.5	11.5	883	879	877	ν(CC)(32)+ν(CN)(7)+δ(NNC)(25)+δ(CNH)(7)
υ_{25}	A"	1011	7.2	0.0	916	5.0	0.0		879	896	τ(HCCH)(51)+τ(CCCH)(26)
υ_{26}	A"	1078	0.2	82.3	984	0.0	0.0		965	962	τ(HCCH)(54)+τ(CCCH)(19)
υ_{27}	A"	1097	0.0	0.0	1006	0.2	0.7		989	984	τ(CCCH)(70)
υ_{28}	A'	1114	0.3	0.9	1013	0.1	115.7	998		991	δ(CCC)(44)+ν(CC)(23)
υ_{29}	A'	1117	0.8	21.6	1045	1.7	25.9	1027	1023	1022	δ(CCH)(25)+ν(CC)(50)
υ_{30}	A'	1175	14.0	9.6	1107	8.5	0.9		1076	1081	δ(CCH)(35)+ν(CC)(42)
υ_{31}	A'	1201	3.0	22.8	1184	0.5	23.2	1159	1155	1155	δ(CCH)(76)+ν(CC)(16)
υ_{32}	A'	1285	7.8	82.8	1194	2.6	231.2	1171	1170	1165	δ(CCH)(68)+ν(CC)(10)
υ_{33}	A'	1295	19.1	73.2	1217	5.9	137.1	1197	1191	1190	ν(CN)(18)+ν(NN)(13)+ν(CC)(27)+δ(CCH)(5)

Vibrational modes: ν, stretching; δ, bending; τ, torsion; ρs, scissoring; ρw, wagging. IR intensities are in kM/mol, Raman activity are in A^4/AMU.

Table 5. Fundamental vibrations of compound: comparison between the HF, DFT, SQM and experimental results (continued)

		HF/B3LYP			DFT/B3LYP			Experimental		SQM	TED(5%<)
		$n_{har.}$	Şiddet		$n_{har.}$	Şiddet					
			IR	Raman		IR	Raman	IR	Raman		
υ_{34}	A'	1323	24.4	9.9	1262	18.6	52.7		1246	1235	ν(CC)(44)+δ(NNC)(10)+δ(CCN)(13)
υ_{35}	A'	1365	32.4	119.9	1317	246.8	691.9	1287	1279	1289	δ(NNH)(9)+ν(NN)(49)+ν(CN)(13)
υ_{36}	A'	1419	1000.3	15.5	1342	2.5	250.1		1318	1312	ν(benzen)(68)+δ(CCH)(15)
υ_{37}	A'	1467	14.9	11.9	1358	2.8	8.6		1329	1325	δ(CCH)(62)+ν(CC)(14)
υ_{38}	A'	1597	20.5	44.0	1475	69.6	159.2	1445	1443	1441	δ(CCH)(40)+ν(CC)(28)+ν(CN)(11)
υ_{39}	A'	1647	263.2	22.5	1507	341.7	253.3	1477	1468	1475	ν(CN)(51)+ν(NN)(7)
υ_{40}	A'	1682	210.0	891.5	1526	14.1	303.8	1489		1489	ν(benzen)(36)+δ(CCH)(44)
υ_{41}	A'	1739	546.7	197.6	1591	389.2	14.6		1536	1560	δ(NNH)(42)+ν(CC)(13)+ν(CN)(8)+ν(NN)(9)
υ_{42}	A'	1786	15.2	419.6	1638	11.2	881.1	1597	1603	1602	ν(CC)(61)
υ_{43}	A'	1796	173.7	72.7	1645	68.3	87.2		1603	1613	δ(NNH)(11)+δ(CNH)(16)+ν(CC)(39)
υ_{44}	A'	2577	48.2	349.1	2304	42.4	497.8	2211	2211	2255	ν(CN)(87)
υ_{45}	A'	2594	70.4	615.7	2336	73.6	1117.8	2230	2231	2285	ν(CN)(85)
υ_{46}	A'	3318	9.6	33.5	3161	5.8	36.8	3066	3059	3096	ν(CH)(98)
υ_{47}	A'	3332	0.1	82.2	3176	0.2	82.1			3110	ν(CH)(98)
υ_{48}	A'	3343	17.2	81.7	3185	11.0	112.0			3119	ν(CH)(93)
υ_{49}	A'	3357	16.9	223.7	3197	12.6	282.8		3131	3131	ν(CH)(95)
υ_{50}	A'	3379	0.5	67.7	3214	0.4	64.2			3148	ν(CH)(99)
υ_{51}	A'	3773	39.7	161.6	3441	21.8	193.3		3192	3370	ν(NH)(100)

Vibrational modes: ν, stretching; δ, bending; τ, torsion; ρs, scissoring; ρw, wagging. IR intensities are in kM/mol, Raman activity are in A^4/AMU.

[1]. *H. Zollinger,* Color chemistry: synthesis, properties and applications of organic dyes and pigments. 3rd reviseded. Weinheim,Germany: Wiley-VCH;2003.
[2]. *A.D. Towns,* Dyes Pigments 1999,42,3.
[3]. *G.J. Hallas,* J Soc Dyers Colour 1979,95,285.
[4]. *G. Griffits,* Rev Prog Color 1981,11,37.
[5]. *M. Matsuoka,* Infrared absorbing dyes, Plenum Press, New York and London, 1990, 1-4.
[6]. *K.Taniike, T. Matsumoto, T.Sato ,Y. Ozaki, K. Nakashima, K. Iriyama,* J Phys Chem. 1996,100, 15508.
[7]. *K.A. Bello, J. Griffiths* Chem Commun. 1986,1639.
[8]. *S.K. Yesodha, C.K. Sadashiva Pillai, N. Tsutsumi*, Prog. Polym. Sci. (2004,29,45.
[9]. *Y. Cui, M. Wang, L. Chen and G. Qian,* Dyes Pigments 2004,62, 43.
[10]. *Y. Cui, M. Wang, L. Chen and G. Qian,* Dyes Pigments, 2005,65, 61.
[11]. *P. Gregory,* Dyes Pigments 1986,7,45.
[12]. *N. Ertan,* Dyes and Pigments 2000,44,41. In the IR spectra , a band at 3192 cm^{-1} is assigned to NH group. This result suggest that the title molecule is predominantly in hydrazo form in solid state. In the solid state the frequency shifts to lower values [23].
[13]. *K. Cheon, Y.S. Park, P.M. Kazmeier, E. Buncel,* Dyes and Pigments, 2002,53,3.
[14]. *S.J. Cho, A.A. Mohamed, S.A.K. Elroby* Int J of Quant Chem. 2007,107, 63.
[15]. *A.D., Becke,* J.Chem. Phys. 1993, 98(7,8), 5648.
[16]. *A.D., Becke,* J.Chem. Phys. 1992, 96(3,4), 2155.
[17]. *C.,Lee, W., Yang, R. G., Parr*, Physical ReviewB,37(1,3),785.
[18]. *R. Dichfield,* Mol. Phys. 1974,27,789.
[19]. *K. Wolinski, J.F. Hilton, P. Pulay,* J. Am. Chem. Soc. 1990,112,8251.
[20]. *SQM version 1.0,* Parallel Quantum Solutions, 2013 Green Acres Road, Suite A, Fayetteville, AR
[21]. *M. Cossi, V. Barone,* J. Chem. Phys. 2001,115,4708.
[22]. *Gaussian03,* Revision D.01,Gaussian, Inc. Wallingford,CT,2004.
[23]. *A. Suwaiyan, M.A. Morsy* Spectrochim Acta A 1997, 53,575.
[24]. *G.Rauhut, P. Pulay,* J. Phys. Chem. 1995, 99, 3096.

CHEMICAL EFFECTS IN THE Kα OF X-RAY EMISSION SPECTRA OF CU AND NI

E. BAYDAŞ[a], E. ÖZ[b], F.G. ARAS[b], M. BÜYÜKYILDIZ[c]

[a]*Atatürk University Faculty of Sciences, Department of Physics, Erzurum, Turkey*

[b]*Gazi University, Institute of Science and Technology, Department of Advanced Technologies, Ankara,Turkey*

[c]*Ağrı İbrahim Çeçen University, Faculty of Education, Ağrı, Turkey*

e-mail: elifbaydas@atauni.edu.tr

Chemical shifts and full widths at half maximum intensity (FWHM) of Kα x-ray emission lines and differences of full widths at half maximum intensity (ΔFHWM) using metallic element as reference for these emission lines were measured for the following Cu and Ni compounds: Cu, Cu_2O, CuCl, CuCl .$2H_2O$, CuF_2, $CuF_2.3H_2O$, CuBr, $CuBr_2$ and Ni, Cl_2NiO_8, $NiCl_2$, $NiCl_2.H_2O$, NiF_2, $NiF_2.4H_2O$. The measurements were performed with a wavelength-dispersive X-ray fluorescence spectrometry (WDXRF). It was found that the calculated results for Cu and Ni compounds are strongly correlated with the oxidation state. At the same time chemical shift for F compounds is generally more than that for Cl compounds.

I. INTRODUCTION

High resolution X-ray fluorescence (XRF) spectroscopy is a powerful method to investigate the elemental chemical state in unknown compounds and the electronic structure of materials. Since the pioneer work of Parratt nearly 70 years before (Kα lines from Ca (Z=20) to Ni (Z=28) [1], sulphur $K\alpha_{1,2}$ lines [2], Kα satellite lines from S (Z=16) to Pd (Z=46) [3,4], and Ag L lines [5], this spectroscopy has been developed rapidly and is now still receiving attention from some researchers [6]. X-Ray emission spectra are known [7-9] to be influenced by the chemical combination of x-ray emitting atoms with different ligands. The effects of the chemical combination, however, are not large and a theoretical interpretation of these effects has not been established completely. Therefore, chemical effects have rarely been utilized in the characterization of materials. X-ray emission and absorption processes have been used in a large number of analytical techniques for investigations of many kinds of materials. Since the early days of x-ray spectrometry, the Kβ/ Kα x-ray intensity ratio and x-ray fluorescence cross-sections for elements has been extensively studied [10-12]. In our earlier studies we investigated chemical effects [13-16] using a Si(Li) detector with resolution 160 eV at 5.9 keV. Chemical shift research has been done on high-resolution spectrometers. Lee et al. [17] examined energy shifts of K x-ray lines for different chemical compounds of Ru, Pr, and Yb. Zhenlin et al. [18] measured high-resolution Pd Lα x-ray fluorescence spectra of several Pd compounds. The Kα and Kβ x-ray emission spectra of Cu has been studied in many previous investigations [19, 20]. Katare et al. [21] measured K-absorption spectral studies of some copper (II) mixed-ligand complexes. The possibility of chemical state analysis with a wavelength-dispersive x ray spectrometer system for particle-induced x ray emission using a light ion microbeam were discussed by Kawatsura et al [22]. Kawai et al. [23] observed L x-ray line shape of copper (II) compounds and their covalence. Chemical shift and lineshape of high-resolutions Ni Kα x-ray fluorescence spectra were measured by Konishi et al [24].

The aim of this paper was to study the chemical shifts and full widths at half maximum intensity (FWHM) of Kα the x-ray emission line in Cu and Ni compounds.

II. EXPERIMENTAL

Chemical shifts and full widths at half maximum intensity (FWHM) of Kα x-ray emission lines of Kα x-ray emission line was measured for the following Cu and Ni compounds: Cu, Cu_2O, CuCl, CuCl .$2H_2O$, CuF_2, $CuF_2.3H_2O$, CuBr, $CuBr_2$ and Ni, Cl_2NiO_8, $NiCl_2$, $NiCl_2.H_2O$, NiF_2, $NiF_2.4H_2O$. The measurements were performed with a wavelength-dispersive x-ray fluorescence spectrometry (WDXRF). Powder samples were put on the top of sample cup and mylar film was put on the top of powder samples . Metal (Cu, Ni) was measured as received.

The experiments were carried out using a Rigaku ZSX100e Wavelength-Dispersive X-ray Fluorescence Spectrometer. The x-ray tube for primary excitation was a rhodium anode x-ray tube with a typical input power of 50kV and 50 mA. Vacuum atmosphere were employed in this system. LiF1 (200) crystal and scintillation counter (SC) were used according to the range of wavelength of sample. Scintillation counter was scanned from 5^0 to 118^0. The abscissa axis of a chart is displayed in the 2-theta angle. Spectra were scanned 0.001 degrees. In this studied, the abscissa axis is changed from the 2-theta angle to the energy.

For Cu Kα spectrum, one channel was a 0.01000 keV step from 7.71740 to 8.39600 keV. For Ni Kα spectrum, one channel was a 0.01000 keV step from 7.37830 to 7.54940 keV. The strongest x-ray signal was obtained from metal (Cu and Ni). The strongest x-ray signal were obtained from pure metals, the intensity of which was deliberately made low by adjusting the input power of the x-ray tube, because the spectrometry response was different when the count rate was too high Each compound was measurement at least five times to check the reproducibility. A spectrum of chrome metal was measured just before and after the five fold measurement of each compound to calibrate the spectrometer energy. The spectrometer was evacuated

down to 13.0 Pa and the spectrometer temperature was stabilized at 36.5 °C.

The five-point Savitzky-Golay smoothing method was iteratively processed five times [25]. The peak position was determined at the centre point of the 9/10 intensity of the smoothed lineshape as illustrated in Fig.1. It was known that the standard deviation of the peak position determined using the 9/10 intensity was less than that determined using the peak top.

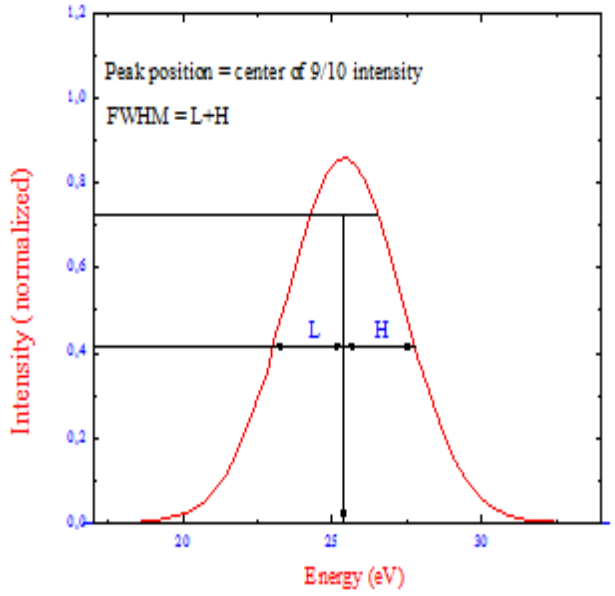

Fig. 1. FWHM and peak positiondeterminedfrom 9/10 intensity.

The measured lines can be simulated, with quite a good approximation, by Voight functions. These are the convolution of a Lorentzian function with a Gaussian function, the first one describing the emission line and the second one, the response of the spectrometer. If the resolution of the spectrometer is large as compared to the natural line width, the Gaussian function will predominate. For this reason, the spectra measured with the conventional spectrometer were fitted by Gaussian function, whereas for the ones measured with high resolution Voight functions were used.

The chemical shift was the difference between the centre point of the 9/10 peak intensity of a compound and that of Cu and Ni metal measured before and after the measurement of the compound. Spectral smoothing was important for reducing the standard deviation of these parameters. Full widths at half maximum intensity (FWHM) were determined by fitting a Voight function having a constant background to the experimental data.

Chemical shifts (ΔE) are defined by E_{metal} - $E_{compund}$ where E_{metal} is the central energy of the peak of relevant metal element and $E_{compound}$ is the central energy of the peak of relevant compound. Differences of full widths at half maximum intensity (ΔFHWM) are defined by $FWHM_{metal}$ - $FWHM_{compound}$ where $FWHM_{metal}$ is the full widths at half maximum intensity of relevant metal element and $FWHM_{compound}$ is the full widths at half maximum intensity of relevant compound.

In the present work, the errors stated correspond to the counting statistics and to the fitting procedure. Ni and Cu metal was taken as a reference in determining the chemical shifts.The uncertainties in the chemical shifts are approximately ± 1.10^{-5} eV. The uncertainties in FHWM are approximately ± 0.001 eV or less.

III. RESULT AND DISCUSSION

Chemical shifts and full widths at half maximum intensity (FWHM) of Kα x-ray emission line were measured for the following Cu and Ni compounds: Cu, Cu_2O, CuCl, CuCl .$2H_2O$, CuF_2, $CuF_2.3H_2O$, CuBr, $CuBr_2$ and Ni, Cl_2NiO_8, $NiCl_2$, $NiCl_2.H_2O$, NiF_2, $NiF_2.4H_2O$. For measured Cu and Ni compounds, oxidation number and local crystal structure is given in Table 1.

Table1.Measured nickel and cupper compounds, oxidation number and local crystal structure.

Compounds	Oxidation number	Local crystal structure	Latttice energy [27] (kjmol^{-1})
Ni metal	0		
Cl_2NiO_8	2		
$NiCl_2$	2	O_h	2753
$NiCl_2.H_2O$	2	O_h	
NiF_2	2	O_h	2845
$NiF_2.4H_2O$	2	O_h	
Cu metal	0	-	
Cu_2O	1		3273
CuCl	1		921
$CuCl_2$	2	O_h	2774
CuBr	1		879
$CuBr_2$	2		2711
CrF_2	2	O_h	3046
$CuF_2.3H_2O$	2		

Peak energies, chemical shifts (ΔE), full widths at half maximum intensity (FWHM) and difference of full widths at half maximum intensity (ΔFWHM) for Kα x-ray emission lines are given in Table 2.

Measured and fitted Kα lines by Voight function for Ni and Cu compounds were given in Fig. 2.

For Cu and Ni compounds, chemical shifts and difference of full widths at half maximum intensity (ΔFWHM) of Kα x-ray emission line were given in Fig. 3-4.

The individual characteristics of the structure of molecules, complexes, and crystals mainly affect the energy position of the Ki line. In actuality, an atom in a molecule or crystal differs from the free atom. Participation of the atom in a chemical bond leads to a change in its electron density, and the valence electron

density is changed to an especially high degree. The electron density decreases or increases depending on the type of bonding with adjacent atoms in a molecule or crystal. The energies of the inner levels depend strongly on the resulting electron density at the atom; accordingly, the parameters of any inner line may be used to identify the chemical state of atoms in molecules or crystals.

The structure of these molecular orbital will be determined both by the nature of the partner atoms in the bond and by the symmetry of the molecule which includes the emitting atom. Within the molecule, the inner levels have an atom-like character and correspond to the inner 1s levels of the atoms forming the molecule, the outer levels correspond to the system of molecular orbital characteristic for the given molecule.

Table 2. Peak energies, chemical shifts (ΔE), full widths at half maximum intensity (FWHM) and difference of full widths at half maximum intensity (ΔFWHM) with respect to metal element for Kα x-ray emission line

Compounds	Kα line energy (eV)	ΔE (eV)	Kα for FWHM (eV)	Kα for ΔFWHM (eV)
Ni metal	7468.89	0	43.07	0
Cl_2NiO_8	7469.88	0.90	43.93	0.86
$NiCl_2$	7469.59	0.70	42.41	-0.66
$NiCl_2.H_2O$	7468.14	-0.75	43.21	1.43
NiF_2	7468.09	-0.80	43.10	0.03
$NiF_2.4H_2O$	7469.74	0.85	43.05	-0.02
Cu metal	8037.22	0	48.89	0
CuBr	8036.85	0.37	48.49	0.40
$CuBr_2$	8036.83	0.39	48.54	0.35
CuCl	8037.64	0.42	48.66	-0.23
$CuCl_2.2H_20$	8037.66	0.44	48.95	0.06
CuF_2	8037.69	0.47	49.04	0.15
$CuF_2.3H_2O$	8037.71	0.49	48.91	0.02
Cu_2O	8037.42	0.20	49.19	0.30

Electron density and quantum states are influenced by the environment of the atom with consequent wavelength shifts, or so-called chemical shifts, of the emitted lines. Chemical shifts are small and detectable only if the spectral line widths are sufficiently small and if an instrument is available with sufficient spectral resolution. For x-rays the line shift is at most a few electronvolts. In spectrometers with high resolution, such as WDXRF systems, most spectral shifts are easily detectable. The structure of x-ray emission lines has been extensively studied over a long period. The $K\alpha_{1,2}$ diagram lines of the 3d elements are of special interest because of their asymmetric shape. According to both classical and quantum theories of radiation, an emission line has a Lorentzian shape [26].

All the compounds are assumed to have tetrahedral (T_d) or octahedral (O_h) symmetry in which the central metal atom is surrounded by four or six ligand atoms, respectively. In the T_d symmetry are, in general larger than those in the O_h symmetry. In the T_d symmetry the chemical bonding is more covalent than in the O_h symmetry and the bond length in former is shorter than that in the latter. Both effects increase the interaction between the central metal atom and ligands in Td symmetry. In this work, many Cu and Ni compounds have O_h symmetry. The results obtained are summarized as follows:

1) Halogens compounds are more sensitive for the chemical states than the other compounds. Particularly, F compounds are more sensitive than the other halogens compounds. Because electronegativity of F is higher than that of other halogens and the chemical shift is strongly correlated to electronegativity. The halogens all have seven electrons in their outer shell and they either gain an electron by forming an ionic bond or form a covalent bond, in order to complete their octet. Fluorine is always univalent. Since it is the most electronegative element it always has the oxidation number (–1). Interaction between ligands and central atom has changed by changing electronegativity. Energy levels are strongly affected from this interaction. It is observed that this interaction plays an important role for the Kα x-ray transition. F compounds show higher chemical shifts than Cl compounds. For Cu Kα line, $CuF_2.3H_2O$ and CuF_2 compounds show higher chemical shifts than $CuCl_2.2H_2O$, CuCl, CuBr and $CuBr_2$ compounds. For Ni Kα line, NiF_2 compounds show higher chemical shifts than $NiCl_2$ compound.

2) Energy shifts related to the oxidation state of Cu and Ni are observed. As seen in Fig. 4, the chemical shifts in energies for Kα line of $CuBr_2$ with divalance are higher than CuBr with monovalance. The chemical shifts in energy of $CuCl_2.2H_2O$ with divalance are higher than CuCl with monovalances.

3) On the other hand, for Cu_2O lattice energy is 3273 kj mol^{-1}, CuCl lattice energy is 921 kj mol^{-1}, $CuCl_2$ lattice energy is 2774 kj mol^{-1}, CuBr lattice energy is 879 kj mol^{-1} , $CuBr_2$ lattice energy is 2711 kj mol^{-1} , CuF_2 lattice energy is 3046 kj mol^{-1} $CoSO_4$ lattice energy is 3038 kj mol^{-1}, $NiCl_2$ lattice energy is 2753 kj mol^{-1},NiF_2 lattice energy is 2845 kj mol^{-1}, Therefore, in the Cu_2O, $CuCl_2.2H_2O$, $CuBr_2$, $CuF_2.3H_2O$, CuF_2 , NiF_2 compounds of the bond length is shorter than that in the CuCl, CuBr, $NiCl_2$ compounds of the bond length is shorter than that in the CuBr and this effect increases the interaction between the central atom and ligands [27].

4) The FWHM values for all the compounds investigated are given in Fig. 3, 4. When the oxidation state increase, the line become more end more narrow and the width decrease. In all the divalent compounds the line is very sharp and the width of this line is very small. For example; $CuF_2.3H_2O$, CuF_2 , $CuCl_2.2H_2O$

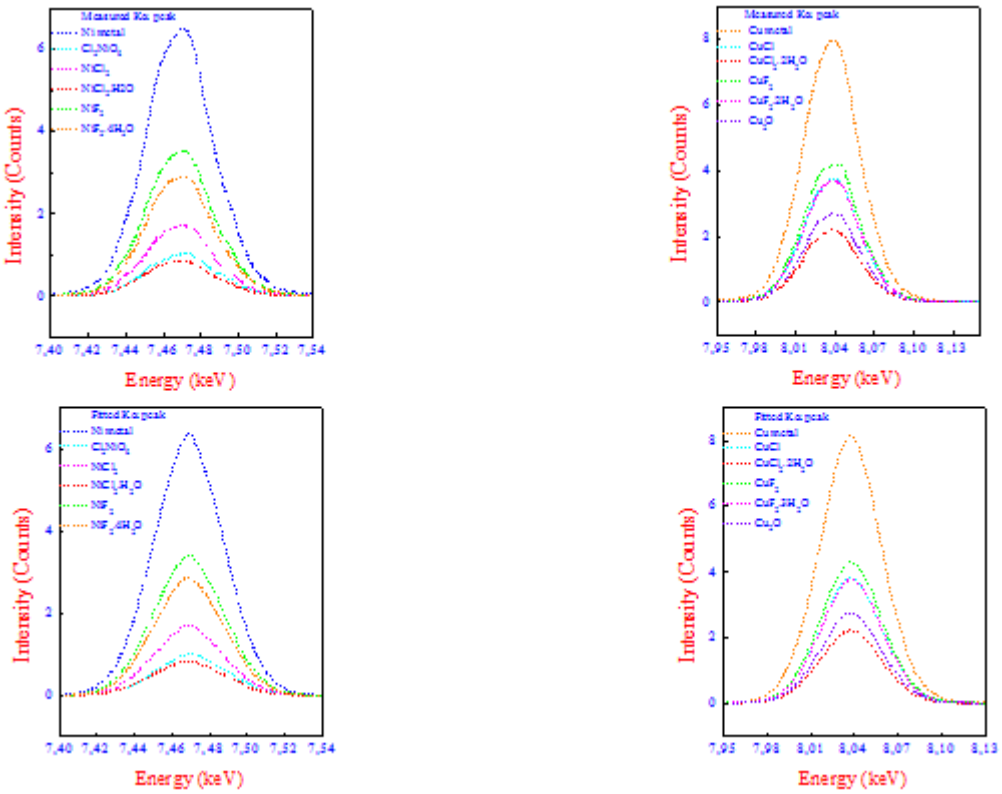

Fig. 2. Measured and fitted Kα lines by Voight function for Ni and Cu compounds.

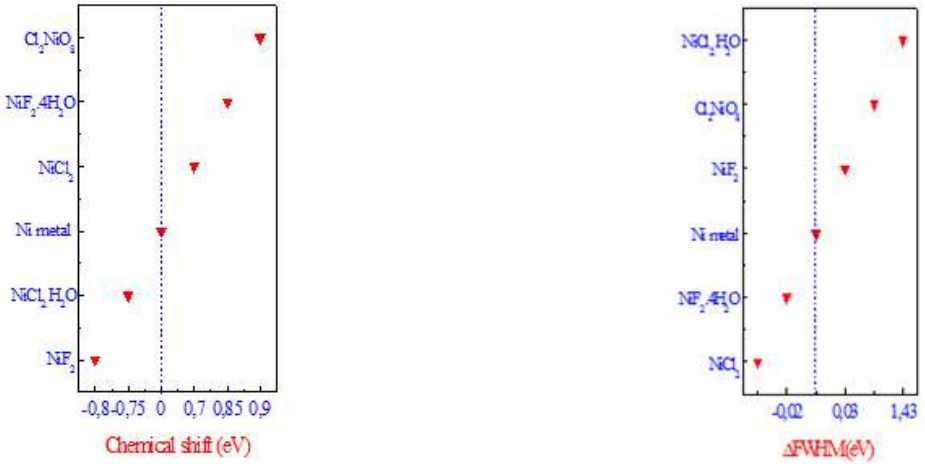

Fig. 3. Chemical shift and ΔFWHM (eV) for Kα lines of Ni compounds.

Fig. 4. Chemical shift and ΔFWHM (eV) for Kα lines of Cu compounds.

[1]. *L.G. Parratti*, Phys. Rev. 1933, 44, p.695-702.
[2]. *L.G. Parratti*, Phys. Rev. 1936, 49, p.14-16.
[3]. *L.G. Parratti*, Phys. Rev. 1936, 50, p.1-15.
[4]. *C. H. Shaw, L.G. Parratti*, Phys. Rev. 1936, 50, p. 1006-1012.
[5]. *L.G. Parratti*, Phys. Rev. 1938, 54, p.99-114.
[6]. *C.Bonnelle, C. Monde* (Eds), Advances in X-Ray Spectrometry, Pergamon Pres, Oxford, 1982.
[7]. *K. Tsutsumi, H. Nakamori, K. Ichikawa*, Phys. Rev. B 1976, 13, p.929-933**.**
[8]. *K. Tsutsumi, H. Nakamori*, J. Phys. Soc. Jpn. 1968, 25, p.1418.
[9]. *O. I. Sumbaev*, Sov.Phys. JETP (Engl. Transl.) 1970, 30, p.927.
[10]. *Ö. Söğüt, E. Büyükkasap, A. Küçükönder, and M. Ertuğrul,* Appl. Spect. Rev. 1997,32, p.167.
[11]. *A. Küçükönder, Y. Şahin, E. Büyükkasap, and A. I. Kopya*, J. Phys. B 1993, 26, p.101- 105.
[12]. *A. Küçükönder, Y. Şahin, and E. Büyükkasap*, J. Phys. Chem. Article. 1993, 170, p.125-132.
[13]. *E. Baydas, Y. Şahin, and E. Büyükkasap*, J. Quant. Spectrosc. Ra. 2003, 77, p. 87-93.
[14]. *E. Baydas, Ö. Söğüt, Y. Şahin, ve E. Büyükkasap*, Spectrochim. Acta Part B 2002, 57 p. 375-380.
[15]. *E. Baydaş*, Instrum. Sci and Technol. 2005, 33, p.461-471.
[16]. *E. Baydas, Y. Şahin, and E. Büyükkasap*, J. of Radioanal. and Nucl.Chem 2003, 256, p. 27-30.
[17]. *P.L. Lee, F. Boehm and P. Vogel*, Phys. Rev. A 1974, 9, 2, p.614-621.
[18]. *Z. Liu K. Yuge and J.Kawai*, Spectrochim. Acta Part B 2004, 59, p.93.
[19]. *G. Hölzer, J. Hörtwig*, *J. Wolf*, M, Fritsch, and E. Förster, Phys.Rev. A 1995, 51, p.283-296.
[20]. *R.K. Katare, S.K. Joshi, B.D. Shrivastava, R.N. Patel, K.B. Pandeya, and A. Mishra*, X-Ray Spectrom. 2002, 31, p.327-331.
[21]. *R.K. Katare, S.K. Joshi, B.D. Shrivastava, R.N. Patel, K.B. Pandeya, and A. Mishra*, X-Ray Spectrom. 2000, 29, p.187-191.
[22]. *K. Kawatsura, N. Takeshima, K. Takahiro, Y.Mokuno, Y. Horino, A. Kinomura, A.Chayahara, N. Tsubouchi, T. Sekioka, M. Terasawa*, Nucl. Instrum. and Meth. Phys. Res. B 2001, 181, p. 128-133.
[23]. *J. Kawai, K. Nakajima, K. Maeda, and Y. Gohshi*, Adv. X-Ray Anal. 1992, 35, p.1107.
[24]. *T. Konishi, J. Kawai, M. Fujiwara, T. Kurisaki, H.Wakita and Y. Gohshi*, X- Ray Spectrom. 1999, 28, p. 470-477.
[25]. *A. Savitzky, M.J.E. Golay*, Anal. Chem. 1964, 36, p.1627-1639.
[26]. *T. Mukoyama*, X-Ray Spectrom. 2000, 29, p.413-417.
[27]. *R. C. Weast*, Ph.D. Handbook of Chem. and Phys. 66th Ed. 1986.

TEMPERATURE DEPENDENCE OF NMR T1 RELAXATIONS OF CROWN ETHER DERIVATIVES

NİL ERTEKİN BİNBAY, ALİ YILMAZ, M.ZAFER KOYLU
Department of Physics, Faculty of Science, Dicle University
Diyarbakir, Turkey

T_1 spin-lattice relaxation times has been measured for different temperatures varied between 20 ^oC and 45 ^oC with 5 ^oC steps for following two crown ether derivatives; ligand1 (N,N'-Dibenzil-7,16-diaza-1,4,10,13-tetraoksa-2,3,11,12-dibenzosiklooktadeka-2,11-dien); ligand2 (N,N'-DiDodesil–7,16-diaza–1,4,10,13-tetraoksa–2,3-benzosiklooktadek–2-ene). Experiments carried out with Avance Bruker 400 Mhz NMR spectrometer for ^1H nucleus. The aim of this work is to explain dynamical behaviour of these molecules in solution, and also to see how this dynamical behaviour changes with temperature. It has been observed that T_1 increase with increasing temperature for both ligands. The analysis of the experimental data suggests that, dipolar interaction is the main mechanism for T_1 relaxation.

Crown ethers are ringed poliethers, were invented by Pedersen in 1967 [1][2]. The importance of Crown ethers has been increasing since they have found themselves a wide application area, such as chemistry, metallurgy, atomic industry and medical industry. Crown ethers also are widely used as models for molecular recognition. They have broad significance, especially in biological chemistry; enzyme-substrate selectivity nucleic acid-protein interactions and DNA base pairing..

NMR relaxation times in solutions of crown ethers have extensively been studied in order to understand molecular dynamics of the molecules [3][4][5][6][7][8][9].

In this work, T_1 spin-lattice relaxation times in solutions of two crown ether derivatives; N,N'-Dibenzil-7,16-diaza-1,4,10,13-tetraoksa-2,3,11,12 dibenzosiklooktadeka-2,11-dien (ligand 1) and N,N'-DiDodesil–7,16-diaza–1,4,10,13-tetraoksa–2,3-benzosiklooktadek–2-ene (ligand 2); have been measured for different temperatures varied between 20 ^oC and 45 ^oC with 5 ^oC steps

These ligands are synthesized at Chemistry Department of our Faculty. The samples were prepared by solving 10 mg of each Ligands in 10 ml of CDCl3. The prepared samples were are replaced in 5mm NMR tubes under vacuum conditions. Then T_1 measurements were carried out at 20, 25, 30, 35, 40, 45 ^0C for each ligand with 400 MHz AVANCE BRUKER NMR spectrometer. The Inversion Recovery (IR) pulse technique was used and the delay times had been changed between 0,01- 14 s. At least 15 minutes had been waited between every temperature change to get a stabilized sample temperature in probe..

The open forms of each ligand can be seen at Figures 1 and 2, and also 400 MHz ^1H NMR spectrums of these ligands are given in Figure 3 and 4.

The measured T_1 Relaxation times of each ligands are given in table 1 and table 2.

There are several mechanisms causing T_1 relaxation. One of them is called as dipolar relaxation. In dipolar relaxation, relaxation is caused by spin-spin interaction modulated by molecular motions such as molecular tumbling. The T_1 formula for dipolar relaxation is given as follows[10][11]:

$$\frac{1}{T_1} = \frac{3}{10}\frac{\gamma^4\hbar^2}{b^6}\left(\frac{\tau_c}{1+\omega^2\tau_c^2} + \frac{4\tau_c}{1+4\omega^2\tau_c^2}\right) \quad (1)$$

Where "b" represents the distance between two interacted spin. This formula was used to calculate the correlation times for the first peaks of both ligands (Ar-H). In our situation b value is equal to $1{,}39.10^{-8}$ m. Calculated correlation times are given in table.3.

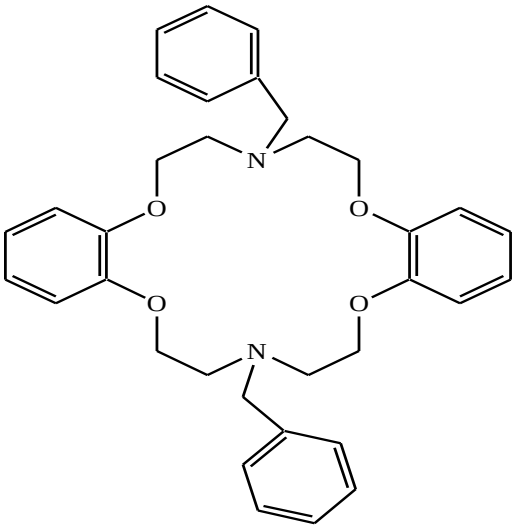

Fig.1. Ligand 1 N,N'-Dibenzil-7,16-diaza-1,4,10,13-tetraoksa-2,3,11,12-dibenzosiklooktadeka-2,11-dien

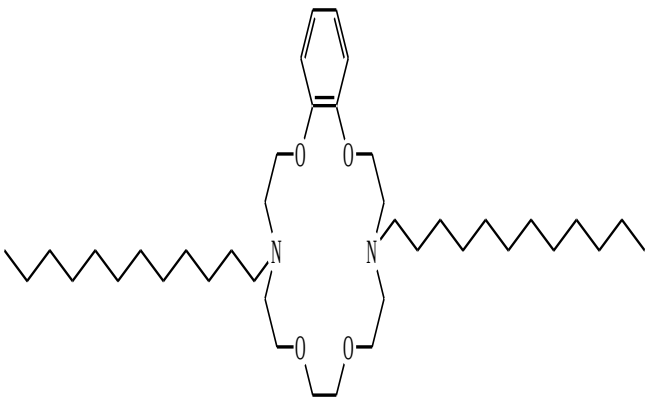

Fig.2. Ligand 2 N,N'-DiDodesil-7,16-diaza-1,4,10,13-tetraoksa-2,3-benzosiklooktadek-2-ene'

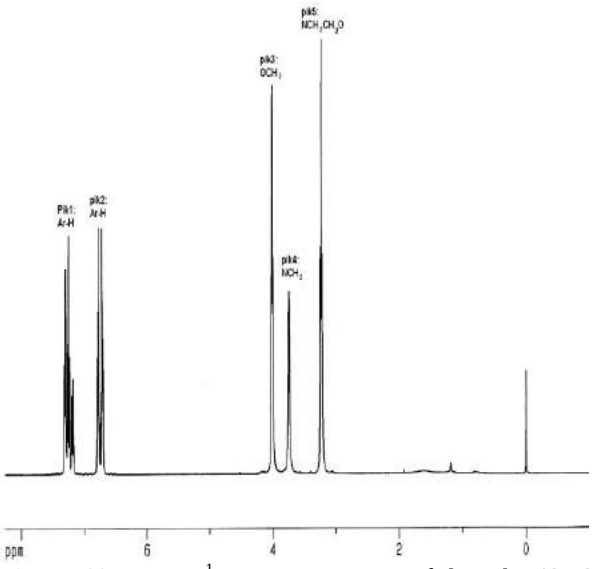

Fig.3. 400 MHz ^{1}H-NMR spectrum of ligand1 ($CDCl_3$). Peak1:Ar-H; peak2:Ar-H; peak3:OCH_2; peak4:NCH_2; peak5:$N\underline{CH_2}CH_2O$

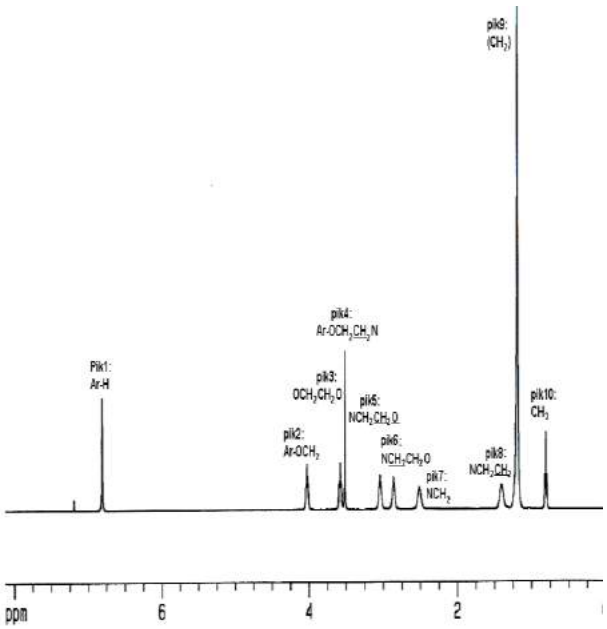

Fig.4. 400 MHz ^{1}H-NMR spectrum of ligand2 ($CDCl_3$). Peak1:Ar-H; peak2:Ar-OCH_2; peak3:OCH_2CH_2O; peak4:Ar-$OCH_2\underline{CH_2}N$; peak5:$NCH_2\underline{CH_2O}$; peak6:$N\underline{CH_2}CH_2O$; peak7:NCH_2; peak8:$NCH_2\underline{CH_2}$; peak9:(CH_2); peak10:CH_3

.

Table.1 The temperature dependence of first ligand's peaks**.**

	T_1 (s)					
T(K)	**293**	**298**	**303**	**308**	**313**	**318**
peak1	2,435	2,524	2,650	2,812	3,089	3,283
peak2	1,606	1,243	1,300	1,353	1,998	2,103
peak3	0,4180	0,4500	0,4710	0,4982	0,5247	0,546
peak4	0,4459	0,4750	0,505	0,5311	0,5622	0,588
peak5	0,3728	0,3970	0,4162	0,4355	0,4576	0,475

Table.2 The temperature dependence of second ligand's peaks.

	T_1 (s)					
T (K)	**293**	**298**	**303**	**308**	**313**	**318**
peak1	1,379	1,395	1,447	1,547	1,698	1,703
peak2	0,4047	0,4285	0,4643	0,4881	0,5067	0,5231
peak3	0,4345	0,4547	0,4914	0,5060	0,5253	0,5517
peak4	0,4495	0,4696	0,4933	0,5234	0,5506	0,5813
peak5	0,3307	0,3443	0,3644	0,3803	0,3926	0,4054
peak6	0,3477	0,3612	0,3789	0,3941	0,3977	0,4237
peak7	0,3762	0,3894	0,4096	0,4243	0,4254	0,4721
peak8	0,5121	0,5300	0,5431	0,5765	0,5149	0,6562
peak9	1,170	1,235	1,309	1,416	1,528	1,622
peak10	3,608	3,861	3,946	4,145	4,231	4,973

Table.3 Calculated correlation times for first peaks of both ligands

T (K)	Ligand1 peak1. τ values (s)	Ligand1 peak1. τ Values (s)
293	$0{,}6935 .10^{-12}$	$1{,}2246 .10^{-12}$
298	$0{,}6691 .10^{-12}$	$1{,}2106 .10^{-12}$
303	$0{,}6373 .10^{-12}$	$1{,}1671 .10^{-12}$
308	$0{,}6001 .10^{-12}$	$1{,}0916 .10^{-12}$
313	$0{,}5462 .10^{-12}$	$0{,}9946 .10^{-12}$
318	$0{,}5144 .10^{-12}$	$0{,}9902 .10^{-12}$

As it is seen from Table.3, the correlation times decreases with temperature. This situation is consistent with the dipolar relaxation theory. And also the orders of the τ values are consistent with the literature[12][13[[14][15]. So the analysis of the experimental data is suggests that; T1 in these solutions is dominantly caused by the dipolar relaxation mechanism.

[1]. *C. J.Pedersen*, J. Am. Chem. Soc., **1967**, 29, 7017.

[2]. *C. J. Pedersen* J. Am. Chem. Soc., **1967**, 29, 2495.

[3]. *A.G. Marshall, P. G. Schmidt, B.D.Sykes*, Effect of Internal Rotation on Nuclear Magnetic Relaxation Times for Macromolecules, Biochemistry 1972, 11, 21.

[4]. *P.S. Hubbard*, Theory of Nuclear Magnetic Relaxation by Spin-Rotational Interactions in Liquids, Physical Review, 1963, 131

[5]. *L.Y. Echegoyen, L.M.V. Martinez-Diaz, J. D. Mendoze, T. J. Torres* Org. Chem., 1991 56, 4193

[6]. *L.Echegoyen, A.Kaifer, H.Durst, R.A.Schultz, D.M.Dishong, M.G.Deepa, G.W. Gokel*, J. Am. Chem. Soc. , 1984, 106, 5100

[7]. *A.Kaifer, H.Durst, L.Echegoyen, D.M.Dishong, M. G. Deepa, G. W.Gokel*, J. Org. Chem., 1982, 47, 3195

[8]. *J.M. Lehn, J. P.Kintzinger*, J. Am. Chem. Soc. 1974, 96, 3313

[9]. *A. I. Popov*, Pure Appl. Chem. **1979**, 51, 101

[10]. *T.L.James*, Nuclear Magnetic Resonance in Biochemistry, Academic Pres, NewYork, 1975

[11]. *C.P.Slıchter*, Principles of Magnetik Resonance, New York, U.S.A., 1996

[12]. *G.W.Buchanan, A.Moghimi, C.I.Ratcliffe*, Can. J. Chem. 1996, 74, 1437-1446

[13]. *D.W.G. Smith, J.G. Powles*, Proton spin-lattice relaxation in liquid water and liquid ammonia, 1966, 451-463

[14]. *A.Yılmaz, M.Z.Köylü, H. Budak*, Estimation of τ value in proton NMR relaxation times of dibenzo diaza 18-crown-6 ether derivative in solution , Chemical Physics Letters, 2006, 427, 346-349

[15]. *R. E. Taylor, A. D. Bacher, C.Dybowski*, 1H NMR Relaxation in Urea, Journal of Molecular Structure, 2007, 846, 147-152

X-RAY FLUORESCENCE IN SOME MEDIUM-Z ELEMENTS EXCITED BY 59.5 KEV PHOTONS

I. HAN[1,*], M. ŞAHİN[2], L. DEMİR[3], E. NARMANLI[3]

[1]*Ağrı İbrahim Çeçen University, Faculty of Arts and Sciences, Department of Physics, 04100 Ağrı, Turkey*

[2]*Rize University, Faculty of Arts and Sciences, Department of Physics, Rize, Turkey*

[3]*Atatürk University, Faculty of Arts and Sciences, Department of Physics, 25240 Erzurum, Turkey*

** ibrahimhan25@hotmail.com*

K X-ray fluorescence parameters ($K\alpha_1$, $K\alpha_2$, $K\beta_1'$, $K\beta_2'$, $K\alpha$ and Kβ X-rays fluorescence cross sections and ω_K average K shell fluorescence yields) for selected ten elements in the atomic range $42 \le Z \le 66$ have been experimentally determined at photon excitation energy of 59.5 keV. K X-rays emitted from the samples have been counted by a Si(Li) detector. The $K\alpha_1$, $K\alpha_2$, $K\beta_1'$, $K\beta_2'$ spectra for investigated elements have been derived from the measured K shell X-ray spectra by peak fitting process. Experimental results of K X-ray fluorescence parameters have been compared with theory. In general there is an agreement within the standard uncertainties of the experimental and theoretical values.

I. INTRODUCTION

X-ray fluorescence (XRF) spectrometry is used world-wide. The most established technique is energy dispersive X-ray fluorescence (EDXRF) for quantitative analysis because EDXRF is relatively inexpensive and requires less technical effort to run the system. EDXRF is very useful for determination XRF parameters such as fluorescence cross sections, fluorescence yields, intensity ratios and vacancy transfer probabilities. Accurate values of these parameters are required in several fields such as atomic, molecular and radiation physics, material science, environmental science, agriculture, forensic science, dosimetric computations for health physics, cancer therapy, elemental analysis, basic studies of nuclear physics etc.

A vacancy in the inner shell of an atom is produced by various methods; photoionization is one of them. In this method, the incident gamma photon ejects the bound electron to the continuum state, creating a vacancy in the inner shell. This vacancy is filled through radiative or nonradiative processes. In the radiative process, the electron from the higher shell fills the inner shell vacancy, emitting X-ray photons. The number of X-ray photons emitted per vacancy is known as fluorescence yield.

In the recent years, theoretical values of ω_K were obtained in the region $44 \le Z \le 54$ [1, 2]. Bambynek et al. [3] have fitted their collection of selected most reliable experimental values of ω_K in the $13 \le Z \le 92$ range in a review article. K shell photoelectric cross sections for intermediate elements at 37 and 74 keV energies have been measured [4]. Krause [5] compiled ω_K adopted values for elements $54 \le Z \le 110$. Chen et al. [6] used a Dirac–Hartree–Slater approach to calculate the ω_K values of elements in the $18 \le Z \le 96$ range. Kumar et al. [7] measured K shell photoelectric cross sections for intermediate elements at 26 keV energies. K shell photoelectric cross sections for Tb, Ho, Er and Pt at 84.26 keV have been determined [8]. The Kα and Kβ X-ray fluorescence cross sections for some elements with $73 \le Z \le 82$ have been studied [9]. The Kα and Kβ X-ray fluorescence cross sections for ten elements at eight excitation energies ranging from 8 to 47 keV have been measured by Singh et al. [10]. Rao et al. [11] have determined K X-ray fluorescence cross sections for some light elements in the energy range 20–60 keV. Hubbell et al. [12] have collected more recent experimental values of ω_K. Horakeri et al. [14,15] determined K shell fluorescence yields using a simple method for some elements in $62 \le Z \le 83$ at 123.6 and 320 keV energies. Durak and Sahin [16] measured K shell fluorescence yields for Cs, Sm, Eu, Ho, Ta, W, Hg and Pb. Karabulut et al. [17] have measured Kα and Kβ X-ray fluorescence cross sections in the atomic region $26 \le Z \le 42$ excited by 59.5 keV photons and Kα and Kβ fluorescence cross sections for elements in the range $44 \le Z \le 68$ at 59.5 keV have been studied by Budak et al. [18]. Simsek et al. [19] measured K shell fluorescence cross sections and K shell fluorescence yields for 21 elements in the atomic range $64 \le Z \le 71$ by using a Si(Li) detector and 59.5 keV photons. The Kα, Kβ, and total K X-rays fluorescence cross sections, as well as the average fluorescence yields for six elements with $16 \le Z \le 23$ at 5.96 keV have been measured [20].

II. EXPERIMENTAL

The geometry and the shielding arrangement of the experimental set-up employed in the present work are as shown in Fig. 1.

The samples were excited with an Am-241 radioisotope source. The Am-241 (100mCi) radioisotope source emits monoenergetic (59.5 keV) γ-rays.

The γ-rays of 26.4, 33.2, 43.4 keV and the characteristic L series of Np coming from Am-241 are completely (approx. 99.99%) filtered out with their help of graded filter of Pb, Fe and Al of thickness 0.1 mm, 0.1 mm and 1 mm, respectively, because even a small fraction of these radiations would produce sizable interference due to their large interaction cross sections with K-shell electrons. Spectroscopically pure samples ($99.9^{o}/_{o}$) of thickness ranging from 0.1 to 0.3 g/cm^2 have

been used for the measurement. The K X-ray spectrums from various samples were recorded with a Si(Li) detector (full-width at half-maximum (FWHM)=160 eV at 5.9 keV, active diameter=3.91mm, active area=12mm^2, sensitivity depth=3mm, Be window thickness=0.025 mm) coupled to a computerized multi-channel analyzer. The detector has been shielded with Pb, Fe and Al metals. The Pb shield was been used to avoid direct exposure of the detector to radiation of source. The Fe and Al shields located inside of Pb shields were been used to hinder the Pb L X-rays and Fe K X-rays, respectively. The spectrums were accumulated in time intervals ranging from 4 to 10h and the spectrums for each target were recorded separately in order to obtain sufficient statistical accuracy. A typical K-shell X-ray spectrum of Ce is shown in Fig. 2.

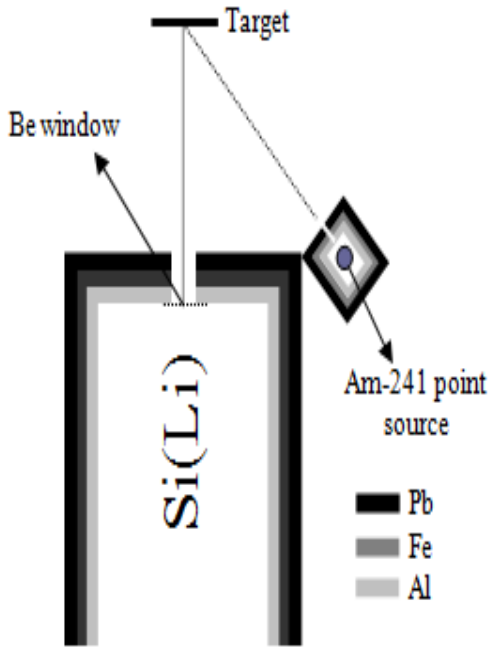

Fig.1. Experimental setup.

The spectra were analyzed by using Microcal Origin 7.0 software program with least-squares fit method. The FWHM of all the peaks is allowed to vary independently in the fitting procedure. The uncertainty in the area of the K X-ray peak was evaluated by weighted method. The net peak areas were separated by fitting the measured spectra with multi-Gaussian function plus polynomial backgrounds. Due to the overlap of the $K\alpha_1$ and $K\alpha_2$ lines in the lighter elements XRF spectra, it was necessary to fix the positions of the Gaussian components of the fit to their respective known energies.

When an electron was excited by exciter such as photons, electrons, protons or heavy ions vacancy occurs in K shell, K shell vacancy to be filled either the Kα (K–$L_{1,2,3}$) from the L shell electron transition or Kβ (K– $M_{2,3}$ $N_{2,3}$) from the M and N shells electron transition. The fluorescent K X-rays which consisting of X-ray lines from the filling of vacancies in the K shell were described in Table 1.

K X-ray fluorescence cross sections and fluorescence yields are important parameters in qualitative and quantitative element analysis using XRF technique, atomic and molecular physics,

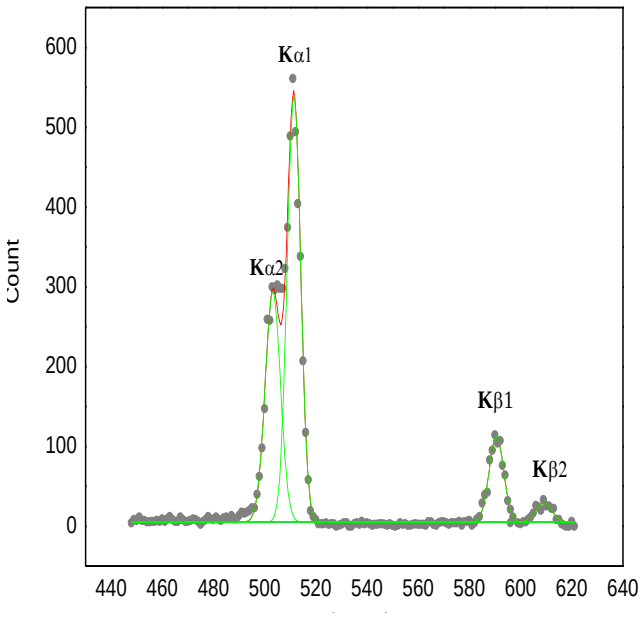

Fig. 2 Typical K X-ray spectra of Ce with Am-241 exciter.

Table 1. The K X rays transitions

$K\alpha$	$K\alpha_1 = L_3 - K$	$K\beta$	$K\beta_1'$	$K\beta_1 = M_3 - K$
	$K\alpha_2 = L_2 - K$			$K\beta_3 = M_2 - K$
	$K\alpha_3 = L_1 - K$			$K\beta_5 = M_{4,5} - K$
			$K\beta_2'$	$K\beta_2 = N_{2,3} - K$
				$K\beta_4 = N_{4,5} - K$

The theoretical fluorescence cross sections (σ_{Ki}) for K X-ray transitions are calculated using the fundamental parameter equation:

$$\sigma_{Ki} = \sigma_K(E)\omega_K F_{Ki} \quad i = \alpha_1, \alpha_2, \beta_1' \text{ and } \beta_2' \qquad (1)$$

where $\sigma_K(E)$ is the K-shell photoionization cross section for the given elements at the excitation energy E [21] and ω_K is the fluorescence yield of the K-shell line [12]. The values of F_{Ki} are the fractional ratio of the K_i X-rays, and are defined as:

$$F_{K\alpha} = (1 + I_{K\beta}/I_{K\alpha})^{-1}$$

$$F_{K\alpha_1} = I_{K\alpha_1}/(I_{K\alpha} + I_{K\beta})$$

$$F_{K\alpha_2} = (I_{K\alpha_2}/I_{K\alpha})F_{K\alpha_1} \qquad (2)$$

$$F_{K\beta} = (1 + I_{K\alpha}/I_{K\beta})^{-1}$$

$$F_{K\beta_1'} = (I_{K\beta_1'}/I_{K\alpha_1})F_{K\alpha_1}$$

$$F_{K\beta_2'} = (I_{K\beta_2'}/I_{K\alpha_1})F_{K\alpha_1}$$

where $I_{K\beta}/I_{K\alpha}$ is the Kβ-to-Kα X-ray intensity ratio [22].

The experimental K_i X-ray fluorescence cross sections are evaluated using the relation:

$$\sigma_{Ki} = I_{Ki}\left[I_o G \varepsilon_{Ki} T_{Ki} t\right]^{-1} \quad (3)$$

where I_{Ki} is the net number of counts under the corresponding photo-peak, the product I_0G is the intensity of the exciting radiation falling on the area of the target samples visible to the detector, ε_{Ki}, is the detector efficiency for K_i X-rays, t is the area mass of the sample in g/cm^2 and T_{Ki} is the self-absorption correction factor for the incident photons and emitted K X-ray photons and calculated using the relation:

$$T_{Ki} = \frac{1-\exp\left[-\left(\mu_i/\cos\theta_1 + \mu_e/\cos\theta_2\right)t\right]}{(\mu_i/\cos\theta_1 + \mu_e/\cos\theta_2)t} \quad (4)$$

where μ_i and μ_e are the attenuation coefficients (cm^2/g) of incident photons and emitted characteristic X-rays, respectively. The values of μ_i and μ_e are taken from the tables of [23]. The angles of incident photons and emitted X-rays with respect to the normal at the surface of the sample are θ_1 and θ_2 in the present setup.

Table 2. Experimental and theoretical values of K_i X-ray fluorescence cross sections (barns/atom) and fluorescence yields for investigated elements.

Element	$\sigma_{K\alpha_1}$		$\sigma_{K\alpha_2}$		$\sigma_{K\beta_1}$		$\sigma_{K\beta_2}$		$\sigma_{K\alpha}$		$\sigma_{K\beta}$		ω_K	
	Exp	Theo	Exp	Theo	Exp	Theo	Exp	Theo	Exp	Theo	Exp	Theo	Exp	Theo
Mo	258±9	241	128±7	126	38±4	45	5±1	6	386±11	367	43±4	51	0.767±0.010	0.762
Ag	375±12	390	213±10	207	105±7	101	13±2	13	588±15	597	118±7	114	0.831±0.009	0.822
In	476±14	461	253±11	246	112±8	122	24±3	24	729±17	707	136±8	146	0.851±0.014	0.866
Sb	551±17	539	260±11	289	151±9	146	35±4	35	811±20	828	186±9	181	0.868±0.017	0.863
I	641±20	623	311±12	336	158±9	172	46±5	46	952±23	959	204±10	218	0.882±0.016	0.874
La	825±16	810	412±14	441	245±10	231	59±6	59	1237±21	1251	304±11	290	0.905±0.018	0.906
Ce	883±24	858	424±14	468	271±15	256	65±6	65	1307±27	1326	336±16	321	0.910±0.018	0.910
Nd	951±25	971	556±16	533	288±16	284	81±7	81	1507±29	1504	369±17	365	0.918±0.019	0.927
Eu	1181±27	1141	603±16	632	336±17	342	92±6	92	1784±31	1773	428±18	434	0.939±0.019	0.934
Dy	1320±32	1322	766±15	741	416±20	404	94±7	94	2086±35	2063	510±21	498	0.938±0.025	0.948

In this study, the effective incident photon flux $I_0G\varepsilon_{Ki}$, which contain terms related to the incident photon flux, geometrical factor and the efficiency of the X-ray detector, was determined by measuring t, T and the K X-ray intensities from thin samples of Zr, Nb, Cd, Sn, Ba, Pr, Sm, Gd, Ho and Er and using theoretical σ_{Ki} values in Eq. (3).

The ω_K fluorescence yield of an atomic K shell is defined as the probability that a vacancy in that K shell is filled through a radiative transition. Thus, for a sample containing many atoms, the fluorescence yield of K shell is equal to the number of photons emitted when vacancies in the shell are filled divided by the number of primary vacancies in the K shell. The K-shell fluorescence yields for the present elements were derived from the measured K_i X-ray fluorescence cross sections using the relationship;

$$\omega_K = \frac{\sigma_{Ki}}{\sigma_K(E)} \quad (5)$$

where σ_{Ki} is the K_i X-ray fluorescence cross section and $\sigma_K(E)$ is the total K-shell photoionization cross section.

III. RESULTS AND DISCUSSION

Experimental and theoretical values of K X-ray fluorescence parameters for Mo, Ag, In, Sb, La, Ce, Nd, Eu, Gd and Dy at 59.54 keV incident photon energies are listed in Table 2. For comparison, the experimental results with the theoretical values of K X-ray fluorescence parameters were plotted as a function of the atomic number, as shown in Figure 3. It is evident from Table 2 and Figure 3 that the experimental values for all elements are in general, agreement with theoretical values within experimental error. The present agreement between the theoretical and the experimental values leads to the conclusion that these present data will benefit using radioisotope XRF technique in applied fields such as radiation transport in matter, absorbed dose and radiation-effect determinations, trace elemental analysis. The overall error in the measured experimental K X-rays fluorescence cross sections is estimated to be 10-11%, which arises due to the uncertainties in various parameters

required to evaluate the experimental values of cross sections using Eq. (3). The uncertainty in each parameter was described in Table 3.

K X-rays fluorescence cross sections can be calculated theoretically by using photoelectric cross sections, fluorescence yields, and fractional emission rates. Uncertainties in these tabulated quantities largely reflect the error in the K X-rays fluorescence cross sections. For this reason, most users prefer the experimental values of the cross sections whenever large discrepancies are observed between theoretical and experimental results. For quantitative analytical applications, it is necessary to know the different relative intensities of the photons which contribute to the fluorescence.

Due to the agreement between the experimental and theoretical K X-ray fluorescence parameters, the radioisotope XRF technique can be used with confidence for EDXRF element analysis.

Table 3. Uncertainties in the quantities used to determine K X-ray fluorescence parameters.

Quantity	Nature of uncertainty	Uncertainty(%)
I_{Ki}	Statistical and other possible errors in area evaluation	6
$I_0 G\varepsilon$	Errors in different parameters used to evaluate $I_0 G\varepsilon$	8
T	Error in the absorption coefficients at incident and emitted photon energies	2
t	Thickness of target	1

Also, for the overlapped peaks, net peak areas are determined using peak fitting procedures. With the result that, the present agreement between the theoretical and the experimental values is seen that the peak fitting processes are useful in XRF technique for the elemental analysis and can be used to separate mixed peaks.

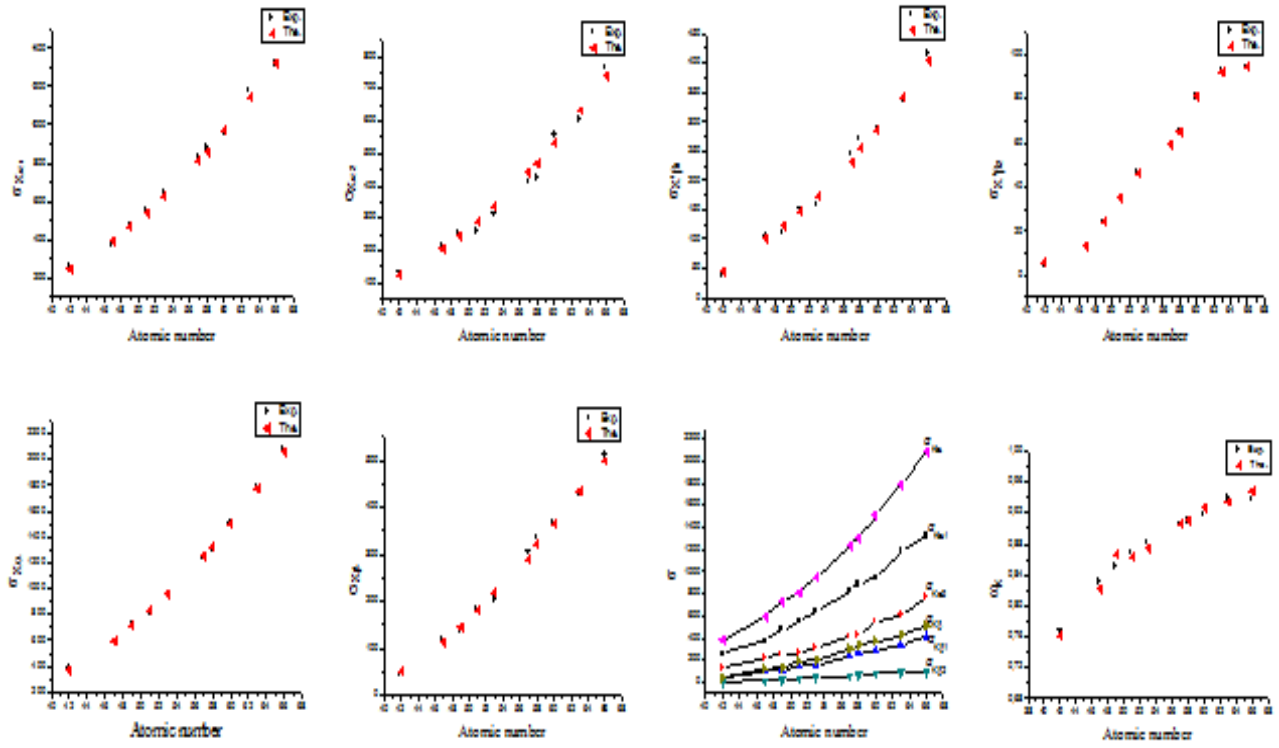

Fig.3 The K X-ray fluorescence parameters versus atomic number.

[1] *E.J. McGuire* 1970a, Phys. Rev. A, 185, 1.

[2] *E.J. McGuire* 1970b, Phys. Rev. A 2, 273.

[3] *W.B.Bambynek, R.W.Crasemann, H.U.Fink, H.Freund, C.D. Mark*, Swift RE, Price PV. Rao 1972, Rev. Mod. Phys. 44, 716.

[4] *K.L.Allawadhi, B.S. Sood* 1975, Phys. Rev. A 11, 1928.

[5] *M.O.Krause* J. Phys. Chem. Ref. Data 1979, 8,307.

[6] *M.H.Chen, B. Crasemann, H. Mark* 1980, Phys. Rev. A 21, 436.

[7] *S. Kumar, N. Singh, K.L. Allawadhi, B.S. Sood* 1986, Phys. Rev. A 34, 1571.

[8] *R.S.Prakhya, K.Parthasaradhi, V.Lakshmina-rayana, K.L. Narasimham, K.V. Ramanaiah, S.B.Reddy* 1986, Phys. Rev. A 33, 2440.

[9] *N.S. Saleh, K.A. Al-Saleh*, Appl. Radi. and Isotop. 1987, 11, 975.

[10] *S. Singh, R. Rani, D. Mehta, N. Singh, P.C.Mangal, P.N. Trehan*. 1990, X-Ray Spectrom. 19, 155.

[11] *D.V. Rao, R. Cesareo, G.E. Gigante*, 1993, X-Ray Spectrom. 22, 406.

[12] *J.H. Hubbell, P.N. Trehan, N. Singh, B. Chand, D.Mehta, M.L. Garg, R.R. Garg, S. Singh*, S Puri, 1994, J. Phys. Chem. Ref. Data 23, 339.
[13] *M. Ertugrul, O. Simsek, O. Dogan, U. Turgut*. 1996, J. Radioanal. Nuc. Chem. 213, 37.
[14] *L.D. Horakeri, B. Hanumaiah, S.R. Thontadarya*, 1997, X-Ray Spectrom. 26, 69.
[15] *L.D. Horakeri, B. Hanumaiah, S.R. Thontadarya*, 1998, X-Ray Spectrom. 27, 344.
[16] *R. Durak, Y. Sahin*, 1998, Phys. Rev. A 57, 2578.
[17] *A. Karabulut, G. Budak, L. Demir, Y. Sahin*, 1999, Nucl. Instrum. Methods Phys. Res. B 155, 369.
[18] *G. Budak, A. Karabulut, L. Demir, Y. Sahin*, 1999, Phys. Rev. A 60, 2015.
[19] *O. Simsek, S. Yilmaz, D. Karagoz, M. Ertugrul*, 2002, J. Radioanal. Nuc. Chem. 253, 143.
[20] *M. Sahin, L. Demir, G. Budak*, 2005, Appl. Radi. and Isotop. 63, 141.
[21] *J.H. Scofield*, 1973, Lawrence Livermore National Laboratory, Report UCRL 51326.
[22] *J.H. Scofield*, At. Data Nucl. Data Tables 1974, 14, 121.
[23] *J.H. Hubbell, S.M. Seltzer*, 1997, Gaithersburg, MD: National Institute of Standards and Technology, NISTIR 5632.

ASSOCIATION CONSTANTS OF DIAZA 18-CROWN ETHER-6 DERIVATIVES –Na^+ COMPLEX DETERMINED BY PROTON NMR T_1 MEASUREMENTS

ALİ YILMAZ, M.ZAFER KOYLU, NİL ERTEKİN BİNBAY

Department of Physics, Faculty of Science, Dicle University, Diyarbakir, Turkey

In this work, the association constants of three crown ether derivatives were determined by using proton T1 relaxivies of certain peaks.

INTRODUCTION

The NMR technique is widely used for studying the complexation of crown ethers with alkali cations in solution [1-12]. However, the methods used for determination of association constants involve complex formulas and time consuming experimental steps. On the other hand, proton relaxivity of ion or a complex is defined as the relaxation arte increase per unit concentration of the ion or complex [13-15]. Then the concentration of an ion is calculated if the relevant relaxivity and and relaxation rate increase are known [15,16]. This phenomena can be utilised for determination of association constants of crown ethers complexed with Na^+.

In this work, association constants of three diaza 18-crown-6 ethers derivatives complexes were determined through proton relaxivities of Na^+ ions. For this purpose, the samples were prepared by solving 10 mg of each ligand in 10 ml of $CDCl_3$, and they were are then replaced in 5mm NMR tubes under vacuum conditions. The concentrations of crown ethers were kept constant (2.5 mM) for each ligand, while concentration of the added $NaClO_4$ was increased from 0.066mM to 12mM. The experiments were carried out on a BRUKER AVANCE-NMR spectrometer operating at 400 MHz. The inversion recovery pulse sequence (180^o-delay time-90^o) was used for T_1 measurements. The relaxation times for the different peaks of each ligand were measured for versus increasing amount of $NaClO_4$. The relaxation rate ($1/T_1$) was fitted versus sodium concentration. The ligands used are given in Figure 1.

The relaxivity were determined from the following expression:

$$R_i = \frac{(1/T_1)_t - (1/T_{1i})_k}{C_t - C_i} \qquad (1)$$

Where k denotes ligand number. $(1/T_1)_t$ denotes relaxation time of the sample in k=1,2 and 3 which added sodium(C_t) is fully bound to crown ether. In 1:1 complex, the C_t is equal to concentration of crown ether [13-15].

C_i and $(1/T_{1i})_k$ denote initial sodium concentration and relevant relaxation rates, respectively. In the present case , C_t and C_i were 2.5mM and 0.625mM, respectively. Free (Na_f) and bound (Na_b) ions were then determined from following equation [14,15].

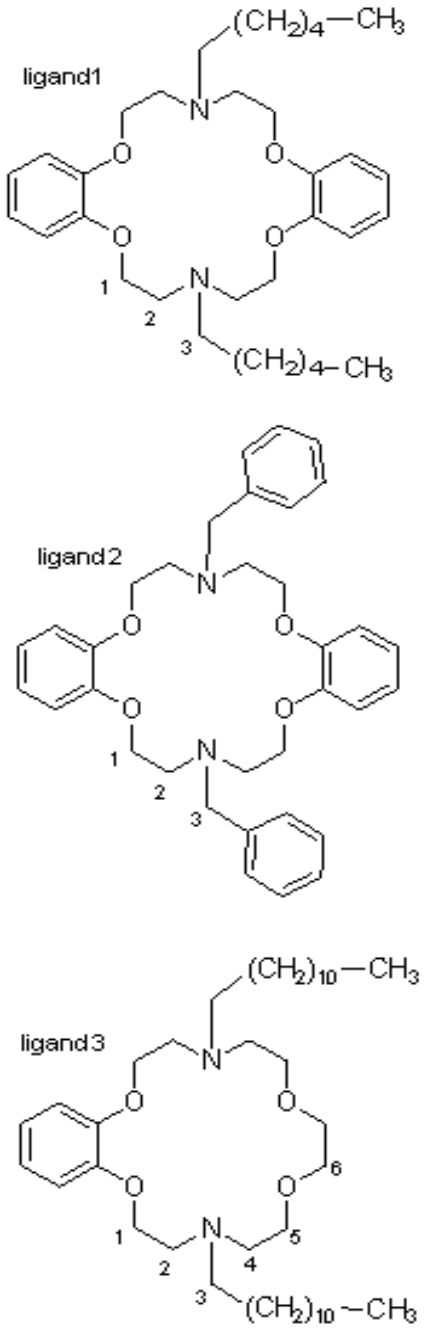

Fig.1. Ligand(1):.N,N'-Dihegzil-7,16-diaza-1,4,10,13-tetraoksa-2,3,11,12 dibenzosiklooktadeka-2,11-dien. Ligand (2):.N,N'-DiDodesil-7,16-diaza-1,4,10,13-tetraoksa-2,3-enzosiklooktadek-2-ene. Ligand (3): N,N'-Dibenzil-7,16-diaza-1,4,10,13-tetraoksa-2,3,11,12-dibenzosiklooktadeka-2,11-dien

$$Na_b = \frac{(1/T_1) - (1/T_{1i})}{R_i} \quad (2)$$

where $(1/T_1)$ denote a relaxation time on the increasing curve. $1/T_1$ was selected for a concentration of 1.245 mM. Association constant of the ligands were determined from the following equation by using relevant concentrations and relaxation rates[16]:

$$K = \frac{[N_a]_b}{[N_a]_f [Crown]_f} \quad (3)$$

RESULTS AND DISCUSSION

The plots of relaxation rates versus concentration total sodium are shown in figures 2-4. It is seen that the relaxation rates become flat after a certain concentration. Such a behaviour has already been reported in earlier works, and attributed to contribution of chemical shift anisotropy to the relaxation [4].

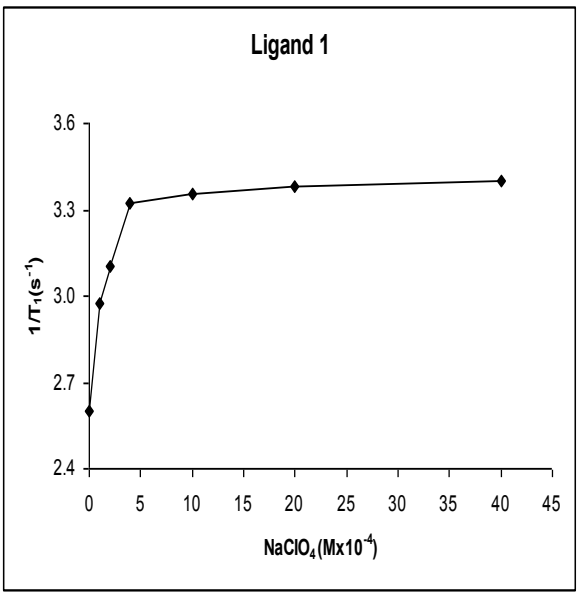

Fig. 2. Spin-lattice relaxation rates versus concentration of Na+ ions for ligand 1

Table 1 Relaxation times (T_1) of protons (H_1 for **1**-**2** and H_2 for **3**) of the macrocyclics upon complexation with $NaClO_4$ concentrations

.

parameters	Ligand 1	Ligand 2	Ligand 3
R $(mM)^{-1}s^{-1}$	183	150	323
$Na_{b\ (mM)}$	0.710	1,14	1.1.
$Na_{f\ (mM)}$	0.535	0.11	0.15
C_f	1,790	1 .28	1.40
K_a	741	7882	5238

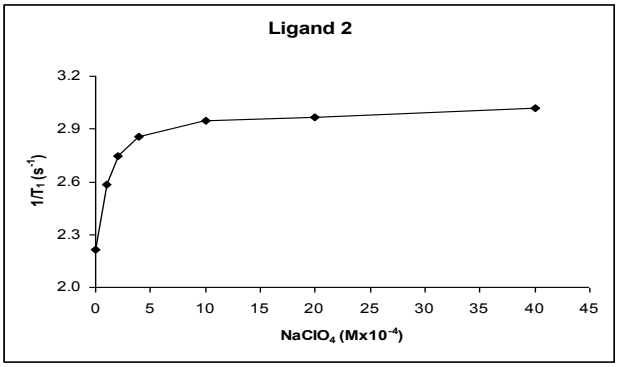

Fig.3 Spin-lattice relaxation rates versus concentration of Na+ ions for ligand 2

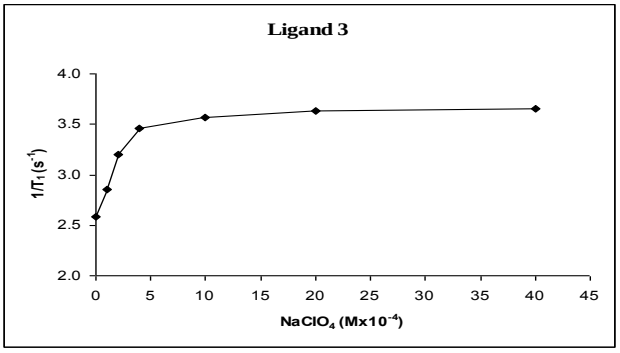

*Fig.4.*Spin-lattice relaxation rates versus concentration of Na+ ions for ligand 3

All parameters calculated from Eqs.1-3 are given in Table 1. The association constants derived by relaxivity are consistent with other methods [9-11]. The present method has a superiority to others since it is simple, and directly related to relaxation measurements.

In conclusion, present data suggest that association constants of crown ethers can be calculated by relaxometrik methods.

[1]. Kaifer, A.; Durst, H. D.; Echegoyen, L.; A.Dishong, D. M.; Schultz, R. A.; Gokel, G. W. Dynamics of Sodium Cation Complexation by Carbon-and Nitrogen- Pivot Lariat Ethers. *J. Org. Chem*, 1982,47,3195-3197

[2]. Echegoyen, L.; Kaifer, A.; Durst, H. D.; Gokel, G. W. Times.*J. Org. Chem.* 1984, 49, 688.

[3]. Echegoyen, L.; Kaifer, A.; Durst, H.; Schultz, R. A.; Dishong, D. M.; Goli, D. M.; Gokel, G. W. Dynamics of Crown and Lariat Ether Cation Complexation Assessed by ^{13}C NMR Relaxation Times. *J Am. Chem. Soc.* 1984, 106, 5100.

[4]. Özkan, E.; Erk, Ç. Determination of the complexing constants by the aid of ^{13}C Dipole-

Dipole relaxation time measurements. *Spectrosc. Let.* 1986, 19, 693.

[5]. Kleinpeter, E.; Stoss, S.; Gabler, M.; Schroth, W. The Stereochemistry of Crown Ethers. *Mag. Reson. Chem.* 1989, 27, 676.

[6]. Li, Y; Echegoyen, L, Enantiometric Recognition of Organic Ammonium Salts by Chiral Dialkyl-Substituded Triazole-18-crown-6 Ligands. *J. Org. Chem.* 1991, 56,4193-4196.

[7]. Li, Y; Echegoyen, L, Enantiometic Recognition between Chiral Triazole-18-crown-6 Ligandsand Ammonium Cations Assessed by ^{13}C and ^{1}H NMR Relaxation Times *J. Org. Chem.* 1994, 59,6539-6542

[8]. Starke, I.; Koch, A.; Uhlemann, E.; Kleinpeter, E. Nuclear Magnetic Resonance Studies and Molecular Modelling of The Solution Stuructureof Dibenzo Crown Ethers and Their Complexes. *J. Mol. Struct.* 1995, 351, 165.

[9]. Bang,E.; Jung J.W.;Lee W, Lee D.W.; Lee W, Chiral Recognition of (18-crown-6)-Tetracarboxylic acid as a Chiral Selector Determined by NMR Spectroscopy. *J. Chem.Soc.,Perkin Trans. 2*,2001,1685-1692

[10]. Kleinpeter, E.; Grotjahn M.; Klika, D.K.; Drexler,H.J.; Holdt, H.J. Conformational and Complexional Study of Some Melaonitrile Mixed Oxadithia Crown ethers by NMR Spectroscopy and Molecular Modelling. *J. Chem.Soc.,Perkin Trans. 2*,2001 ,988-993.

[11]. Erk, Ç.; Zeidler, M. D. ^{13}C NMR Relaxation Time Measurements of Macrocyclic ether complexes. Part XII: The Association Constants of Benzo[15]crown-4 with $NaClO_4$. H_2O . *J. Chemphys* .2004, 115-120

[12]. Köylü, M. Z.; Demirel, N.; Doğanel-Polat, F.; Yilmaz, A.; Hoşgoren, H.; Balci, M. The Effect of Benzo Substitution on Complexation of Diaza 18-Crown-6 Ethers Derivatives With $NaClO_4$ *J. Incl. Phenom. Macroc.* 2005, 52, 51.

[13]. Nakatsuji,Y.; Nakahara, Y.; Muramatsu,A.; Kida,T.; Akashi,M.; Novel C_2-Symmetric Chiral 18-crown-6 Derivativeswith Two Aromatic Sidearms as Chiral NMR Discriminating Agents. *J.tetlet* .2005,4331-4333

[14]. Barnhart; J. L; Berk, R.N. Influence of paramagnetic ions and pH on proton NMR relaxation of biologic fluids. *Invest Radiol* 1986 21(2):132-6

[15]. A.Yılmaz, Birol Otludil, M.Sabri Batun, Yavuz Ensari, Renata Longo and L.Dalla Palma,, , Determination of iron and iron binding capacity by NMR .*Physics in Medicine and Biology* 37. 1589-1596,1992.

[16]. Yilmaz, A; Yurdakoc, M; Isik, B. Influence of transition metal ions on NMR proton T1 relaxation times of serum, blood and red cells *Biol Trace Elem Res* 1999, 67(2):187.

[17]. Mildvan, A.S.; Cohn, M; Magnetic Resonance Studies of the Interaction of the Manganous Ion with Bovine Serum Albumin,*Biochemistry* 1963, 5, 911

CONFORMATIONAL AND VIBRATIONAL STUDY OF 4-AMINOHIPPURIC ACID

S. HAMAN BAYARI[1], HACI ÖZIŞIK[2], SEMRAN SAĞLAM[3]

[1]Faculty of Education, Department of Physics Education, Hacettepe University, Beytepe, Ankara, Turkey
bayari@hacettepe.edu.tr
[2]Aksaray University, Faculty of Science and Letters, Department of Physics, Aksaray, Turkey
hacioz@aksaray.edu.tr
[3]Gazi University, Faculty of Science and Letters, Department of Physics, Teknikokullar, Ankara, Turkey
semran@gazi.edu.tr

The molecular vibrations of 4-aminohippuric acid (PAH) were investigated in polycrystalline sample by Fourier Transform Infrared Spectroscopy. The quantum chemical calculations based on Density Functional Theory (DFT) are used to determine the geometrical, energetic and vibrational characteristics of the molecule. Three different geometries were found to be energy minima. The conformational stability, vibrational frequencies and corresponding normal mode analysis for conformers of PAH were investigated using the 6-311++G(2d,2p) basis set by the B3LYP method. A complete assignment of the fundamentals was proposed based on the total energy distribution (TED) calculation.

I. INTRODUCTION

4-aminohippuric acid or p-Aminohippuric acid (PAH**)** (2-[(4-Aminobenzoyl) amino] acetic acid) is the glycine amide of 4-aminobenzoic acid. it is involved in sulfate transport in human neutrophils [1]. Its sodium salt is used as a diagnostic aid to measure effective renal plasma flow (ERPF) and excretory capacity.

The X-ray crystal structure of PAH [2, 3] and the coordination chemistry with metal ions of PAH have been studied [4-6].

A detailed spectroscopic and harmonic vibrational frequency calculations for PAH is not reported and analyzed in the literature so far. In this paper, we present the Fourier transform infrared (FT-IR) study of PAH and report, harmonic frequencies and normal mode assignments of its minimum energetic structure, employing the density functional (DFT) method with the 6-311++G(2d,2p) basis set by the B3LYP method [7]. The conformational stabilities and optimized geometrical parameters have been carried out using same method.

The complete assignments were performed on the basis of the total energy distribution (TED) of the vibrational modes, calculated with scaled quantum mechanics (SQM) method [8].

II. EXPERIMENTAL

The FT-IR spectra of PAH was recorded in the 4000–400 cm^{-1} region on a Perkin Elmer Spectrum 100 spectrophotometer using KBr pellet.

III. CALCULATIONS

All quantum chemical calculations were performed using the Linux workstations using the Gaussian 03 suite of programs [9]. To study different conformations of the molecule, potential energy scans (PES) were performed DFT/B3LYP/6-311++G(2d,2p) levels of theory. Torsional angles τ_1 (N4, C13, C14, O2) and τ_2 (H16, O1, C14, C13) was varied in steps of 10^o (Fig. 1). Geometries at the energy minimum points were fully optimized.

This was followed by harmonic frequency calculations at the same level of theory and confirmed by the absence of DFT calculated imaginary (negative) frequencies. In the fitting processes performed to correct overestimations at the calculated harmonic wave numbers, we applied scaling procedures (scale factor 0.98). SQM calculations were carried out using SQM v.1.0.

IV. RESULTS AND DISCUSSION

a. Molecular parameters and conformation

Three stables conformations are obtained (Fig 1). From the relative stability of possible conformations, it is found that conformer **I** more stable than the others in the gas phase (Table 1). Conformational energy profiles are given in Fig. 2. As shown in Fig. 2, two minima were found for dihedral τ_1. When rotating the dihedral τ_2, were also found two minima **I**, is equivalent **I** for τ_1 and The energy difference between conformers **I** and **II**, $\Delta E_{I,II}$ is 2.47 kcal/mol, the, $\Delta E_{II,III}$ is 4.55 kcal/mol.

The angle τ_1 [O2 C14 C13 N4] is equivalent in **I** and **III** structures. However its geometry is different. The calculated geometric parameters (Table 2) of the structure **I** are closer to corresponding X-ray structure [3] than the structure **II** and **III**.

The benzene ring is planar in the experimental structure. The dihedral angle between this plane and the carboxyl (COOH) plane is 54.8^o and between the plane and the plane of the amino group (NH_2), 34^o. In most stable structure (I) these angles 51.73^o and 26.12^o, respectively.Experimental data of the isolated molecule in gas phase has not been reported. Thus, our present computed values (structure **I**) were compared with the crystal data in the solid phase determined by X-ray [3]. As is seen from Table 3, the calculated bond distances agree well with experimental values. The C-C lengths of benzene ring are c.a. 1.39 Å [5] in the crystal structure. In the optimized structure **I**, this bond length was also calculated as c.a. 1.39 Å.

The calculated lengths of O1-C14, O2=C14 and O3-C12 bands are 1.348, 1.197 and 1.226 Å, respectively. Small differences are observed. This is due to H -bonding in the experimental structure.

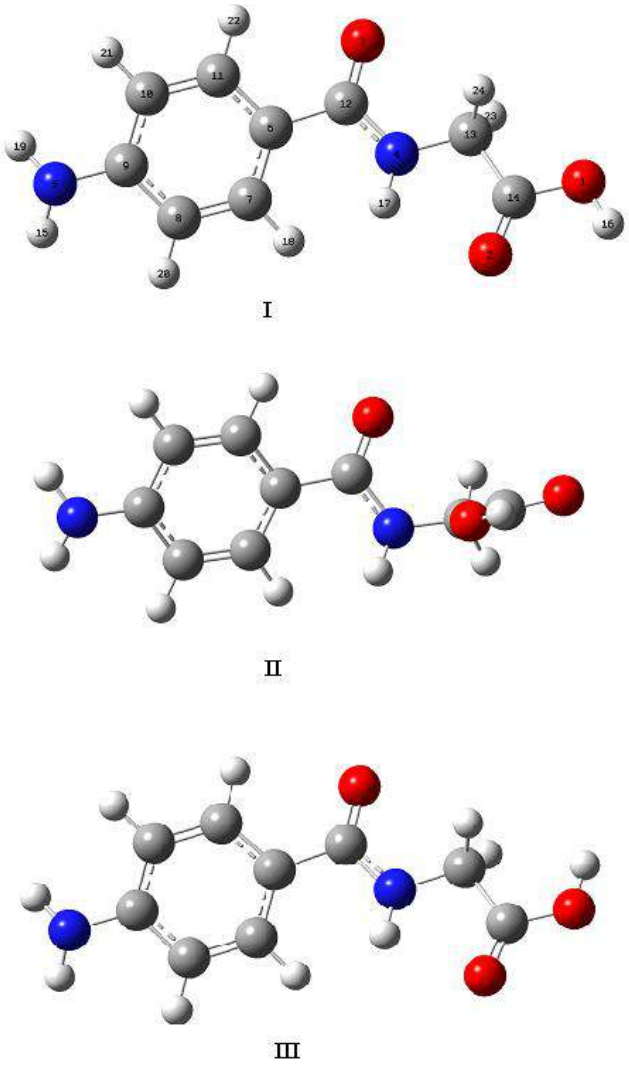

Fig. 1. Optimized structures of the tree most stable conformers of PAH.

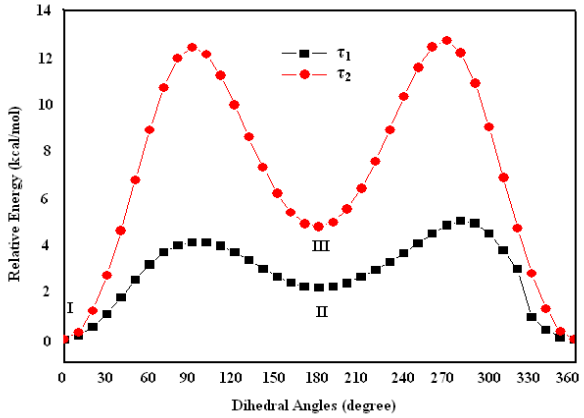

Fig. 2. Conformational energy profile for the rotation around the τ_1 (N4, C13, C14, O2) and τ_2 (H16, O1, C14, C13) angles of PAH

b. Infrared spectrum

The experimental and calculated (DFT/B3LYP) IR spectra (non-scale) of most stable conformer of PAH are given in Fig.3a and b, respectively. The observed wave numbers, infrared intensities and proposed assignments are summarized in Table 3. The agreement between scaled and experimental wave numbers can be considered acceptable. There are differences between theory and experiment for the relative intensities of some bands (Fig. 3). This is consistent with previous studies [10].

Table 1. DFT (B3LYP)/6-311++G(2d,2p) Energies, Relative Stabilities (ΔE) and Dipole Moments of 4-aminohippuric acid (PAH) Conformers

Conformer	Energy		ΔE Kcal/mol	Dipole Moment (Debye)
	Hartree	kcal/mol		
I	-684.422667	-429482.0682837	0	3.0363
II	-684.418727	-429479.5954048	2.47	6.0856
III	-684.415416	-429477.5180267	4.55	2.6464

Table 2. Selected Bond lengths (Å), bond angels (°) and dihedral angels (°) of PAH conformers

Bond lengths (Å)	X-ray[3]	B3LYP 6-31++G(2d,2p)		
		I	II	III
N(5)-H(15)	0.9076	1.0051	1.0065	1.0064
N(5)-H(19)	0.9325	1.0061	1.0065	1.0064
N(4)-H(17)	0.8651	0.9875	1.0047	1.0067
O(3)=C(12)	1.2430	1.2262	1.2228	1.227
O(2)=C(14)	1.1945	1.1970	1.2027	1.1994
O(1)-C(14)	1.3272	1.3476	1.3512	1.3529
O(1)-H(16)	0.9486	0.958	0.9682	0.9646
C(6)-C(12)	1.4736	1.4822	1.4908	1.4907
C(10)-C(11)	1.3719	1.3812	1.3820	1.3820
C(6)-C(11)	1.3906	1.3983	1.3985	1.3985
Bond angles(°)				
H(15)-N(5)-H(19)	115.86	112.76	112.78	112.89
O(1)-C(14)-O(2)	124.58	123.23	123.17	120.51
C(13)-N(4)-H(17)	113.90	114.23	117.43	115.82
O(3)=C(12)-C(6)	120.42	122.25	122.26	122.37
Dihedrals				
D(4,13,14,2)	3	-3	-173	-2
D(16,1,14,13)	-176	179	-180	0

As seen in Table 3, three peaks observed for PAH in the 3300–4000 cm^{-1} range experimentally. The peak at 3342 cm^{-1} had been assigned as N–H stretching in hippuric acid [11]. According to calculations, the experimental bands at 3475 cm^{-1} and 3343 cm^{-1} in the IR spectrum corresponds to the NH_2 asymmetric and symmetric stretching vibration, respectively. We observed a strong band at 3384 cm^{-1} and assigned to the NH stretching vibration. Because of the formation of the hydrogen bond, the symmetric NH_2 vibration will be lowered much more than the asymmetric NH_2 vibration.

In addition, the NH_2 group has scissoring, rocking, wagging and torsional modes of vibration.

The NH_2 scissoring frequency is found at 1665 cm^{-1} by B3LYP method and corresponding strong FT-IR band observed at 1600 cm^{-1}. The other modes are given in Table 3.

The aromatic C-H stretching bands occur in the range of 3100-3000 cm^{-1} [12]. The bands observed in the region 3075–3030 cm^{-1} is assigned to the CH stretching vibrations of benzene ring in PAH. The C-H in-plane and out of plane deformation vibrations of PAH are given in Table 3.

Table 3. Experimental and DFT-calculated harmonic wave numbers (cm^{-1}) and intensities for most stable PAH conformer (I).

	T.E.D (%)	Cal	Int.	Scale	Obs.
1	τ_{ring} (53)+τ_{CCNH2}(24)+ τ_{CCOH} (10)+τ_{NCCO}(10)	19	0.2	18	
2	t_{COOH}(36)+τ_{CCNH}(22) +τ_{CCCO}(19)	46	0.2	45	
3	τ_{CCNH}(32)+τ_{NCCC}(28) +τ_{CNCH2}(17)+δ_{NCC}(6)	60	6.2	58	
4	δ_{CCN}(36)+τ_{CCCN}(7) +τ_{CCNH}(7)+τ_{CCCO}(5) +δ_{CNH}(5)	69	3.7	67	
5	τ_{CCCC}(19)+δ_{CH2}(11) +τ_{CNCO}(16)+τ_{CCOH} (11) +τ_{CNH2}(10)	101	2.1	98	
6	δ_{CH2}(25)+δ_{CNC}(20)	156	4.2	152	
7	τ_{CCCN}(22)+τ_{CNCH}(19) +τ_{CCNH}(15)+τ_{CCOH}(10)	200	15.2	196	
8	δ_{CCC}(23)+δ_{CCN}(21)+ $\delta_{C\text{-}COOH}$(19)+ν_{CN}(18)	251	0.6	245	
9	τ_{CCCN}(29)+τ_{CCCC}(21) +τ_{CNCO}(12)	288	12.4	282	
10	$^{COOH}\delta_{C=O}$(50)+δ_{NCO}(23) +δ_{CCC}(12)	311	2.2	304	
11	twist NH_2(96)	329	16.4	322	
12	δ_{CCN} (58)+ ν_{CC}(10)	380	1.6	372	
13	γ_{ring} (27)+γ_{NH} (19) +δ_{CCO} (13)+γ_{CH}(10)	414	8.6	405	
14	γ_{ring}(34)+δ_{CCO} (19)+ γ_{CH} (12)+δ_{CCN}(10)	427	12.4	418	
15	γ_{NH}(58)+τ_{CNOH}(14) +τ_{CNHH}(10)	465	31.0	455	469vw
16	γ_{NH2} (29)+γ_{CH} (22)	501	223.3	490	509mw
17	γ_{OH}(69)+γ_{CH2}(15) +γ_{NH}(10)	518	8.1	507	
18	NH_2wag(35)+δ_{CH2}(19)+ δ_{NCC}(11)+δ_{COH}(10)	544	91.0	533	550m
19	NH_2wag(29)+γ_{CH}(18) +γ_{NH}(15)	549	181.4	538	
20	δ_{CCO}(26)+$\delta_{O=C\text{-}O}$(15) +γ_{NH2}(12)+$\delta_{NC=O}$(12) +δ_{CCC}(10)	621	14.4	608	588w
21	δ_{COO}(31)+$\delta_{CC=O}$(15) +γ_{NH2}(13)+δ_{CCC}(10)	638	13.5	625	624mw
22	δ_{OH}(72)+δ_{CH2}(15)	652	98.0	638	
23	δ_{CCC}(61)	655	0.9	641	669m
24	γ_{CH}(25)+τ_{CCCC}(19)+ τ_{CNCO}(12)+τ_{CCCO}(10)	708	12.4	693	702mw
25	τ_{CCCC}(34)+τ_{CCCN}(16) +τ_{CCCH}(12)	779	28.3	763	771m
26	γ_{CH}(35)+ν_{CN}(13)+ $\delta_{NC=O}$(11)+τ_{CCOH}(10)	819	0.2	802	795vw
27	γ_{CH} (55)+τ_{NCCH}(13)	822	2.1	805	
28	ν_{CC}(31)+ν_{CN}(13)	853	16.6	835	841m
29	γ_{CH}(46)+τ_{CCCC}(23)	859	19.6	841	855w
30	ν_{CC}(23)+δ_{CCN}(15) +δ_{NCO}(11)	942	29.9	923	884mw
31	γ_{CH}(80)	961	0.1	941	955w
32	γ_{CH}(82)	995	0.9	975	963w
33	δ_{CH2}(54)$_{rock}$+τ_{CCNH}(23)	101	2.7	996	997m
34	δ_{CCC}(33)+ν_{CC}(32) +δ_{CH}(31)	1029	0.3	1008	1012w
35	rock$_{NH2}$(39)+ν_{CC}(27) +ν_{CN}(15)	1077	4.8	1055	1037vw
36	ν_{CN}(33)+δ_{NH2}(19) +ν_{CO}(11)	1095	49.1	1073	1085w
37	δ_{CH}(45)+ν_{CC}(20) +δ_{NH}(12)	1154	65.1	1130	1136mw
38	ν_{CO}(28)+δ_{COH}(18) +ν_{CN}(17)	1165	253.9	1141	
39	ν_{CN}(38)+ν_{CO}(15) +δ_{OH}(12)+ν_{CC}(10) +δ_{CH2}(10)	1187	146.0	1163	
40	δ_{CH}(48)+ ν_{CC}(15) + ν_{CN}(10)	1214	30.0	1189	1184vs
41	t_{CH2}(85)	124	1.1	1216	
42	δ_{NH}(34)+ν_{CC}(27) +ν_{CN}(14)+δ_{COH}(11)	1265	87.0	1239	1257mw
43	ν_{CNH2}(47)+ν_{CC}(18) +δ_{CH}(10)	1311	81.3	1284	
44	δ_{OH} (38)+δ_{CH2}(26) +ν_{CO}(10)	1324	17.2	1297	1300m
45	ν_{CC}(54)+δ_{CH}(26) + δ_{OH} (11)	1336	1.6	1309	1317m
46	δ_{CH}(46)+ν_{CC}(21) +δ_{NH}(12)	1364	0.2	1336	1347w
47	δ_{CH2}(56)+δ_{OH}(31)	141	297.9	1388	1399w
48	δ_{CH}(37)+ν_{CC}(32)	146	5.6	1437	1411m
49	δ_{CH2}(53)+δ_{CNH}(21)	149	31.3	1461	1439w
50	δ_{NH}(42)+$\nu_{C=N}$(15)	1524	427	1493	1451vw
51	δ_{CH}(41)+ν_{CC}(24) +δ_{NH}(12)	1557	33.6	1525	1516s
52	ν_{CC}(62)+δ_{CH}(19)	160	19.2	1573	1556sh
53	ν_{CC}(49)+δ_{CH}(23) +δ_{NH2}(11)	1647	140.7	1614	1560s
54	δ_{NH2}(65)+ν_{CC}(18)	166	190.1	1631	1600vs
55	$\nu_{C=O}$(72)carbonyl	169	271.1	1664	1647s
56	$\nu_{C=O}$(79)carboxyl +δ_{COH}(7)	1801	235.7	1764	1745vs
57	ν_{CH2}(100)	303	30.2	2978	2932mw
58	ν_{CH2}(100)	306	5.4	2998	2975w
59	ν_{CH}(100)	316	14.8	3100	
60	ν_{CH}(100)	316	15.8	3102	3022w
61	ν_{CH}(99)	318	9.8	3119	3044w
62	ν_{CH}(96)	320	2.6	3141	3072w
63	ν_{sNH2}(100)	358	38.0	3508	3384s
64	ν_{NH}(100)	362	56.6	3555	3343w
65	ν_{aNH2}(100)	367	20.6	3604	3475m
66	ν_{OH}(100)	376	93.0	3687	

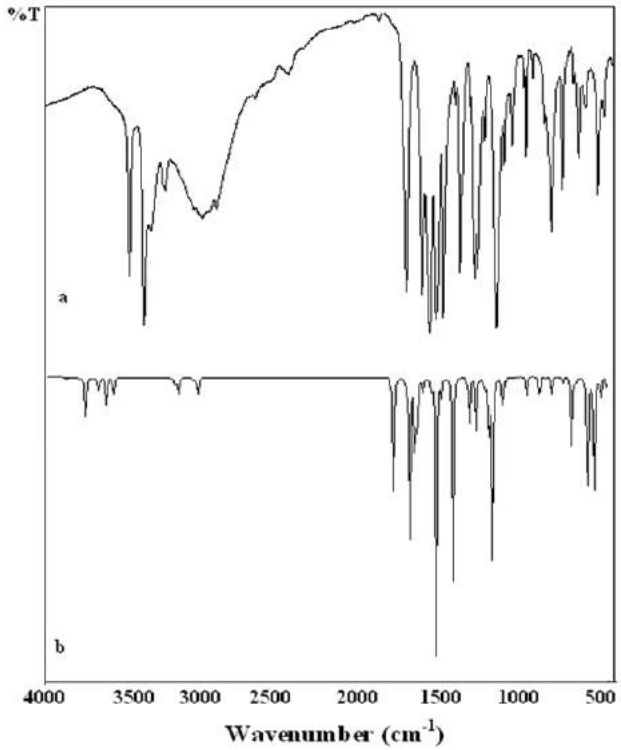

Fig. 3. FTIR spectrum of solid PAH in a KBr disk (a) and calculated spectrum (b)

Carboxylic acids contain a carbonyl group and a hydroxyl group. The O-H stretching mode is not observed in the IR spectrum because this wave number is attributed to hydrogen bonding between COOH groups in the three dimensionally hydrogen-bonded structures. This mode is calculated to be 3762 cm^{-1}. The strong absorption band at 1745 cm^{-1} is assigned to the C=O carboxyl stretching mode. The C-O stretching bond is calculated at 1165 cm^{-1}. This mode is coupled with the in-plane O-H bending mode. The in plane and out-of-plane O-H bending mode is calculated at 652 and 518 cm^{-1}, respectively.

The ketone carbonyl stretch appears at 1715 cm^{-1} [12]. The C=O stretching wave number is lowered by conjugation with the benzene ring. A strong band observed in the IR spectrum at 1647 cm^{-1} is assigned to this mode.

The methylene CH_2 group stretching vibrations fall between 2800 and 3000 cm^{-1} (Table 3). The acid containing -CH_2COOH group show a band at 1411 cm^{-1} due to the CH_2 deformation frequency [12]. A weak infrared band at 1399 cm^{-1} is assigned to CH_2 scissors mode. The twisting and wagging vibrations of the methylene group occur in the region 1300-1200 cm^{-1}.

The observed bands at 1556, 1560 and 1516 cm^{-1} in the experimental IR spectrum (Fig. 3a) are assigned to ν(CC) stretching vibration. They are not pure CC stretching mode. The other vibrational modes of PAH and assignments are given in Table 3.

V.CONCLUSIONS

The infrared spectrum of 4-aminohippuric acid (PAH) was recorded in the solid state. Geometry optimization has been performed for the possible conformers of PAH using GAUSSIAN 03 package. The computed structural parameters of most stable PAH conformer was found to correlate well with the experimental values determined by X-ray.

Based on the comparison between calculated and experimental results and the comparison with related molecules, assignments of fundamental vibrational modes were made.

[1] *L. Simchowitz, A.O. Davis,* J. Gen. Physiol. 94 (1989) 95-124.

[2] *C. Chakrabarti, J.K. Dattagupt*a, Zeitschrift Für Kristallographie 207:11 (1993) 53-58.

[3] *A.J. Dobson, R.E. Gerkin,* Acta Crystallogr C. 55:2 (1999) 206-208.

[4] *G. Micera, L. Naldini, L. Strinna Erre, M.A.Zoroddu, F. Cariati*, Inorg. Chim. Acta 97 (1985) 183-187.

[5] *M.S. Refat, S.M. Teleb, S.A. Sadeek, H.M.Khater, S.M. El-Megharbel*, Journal Of The Korean Chemical Society 49:3 (2005) 261-268.

[6] *P. Sgarabotto, F. Bisceglie, G. Pelosi, L. Abdel-Rahman*, Polyhedron 18:19 (1999) 2505-2510.

[7] *C. Lee, W. Yang, R.G. Parr,* Phys Rev B 37 (1988) 785.

[8] *J. Baker, A.A. Jarzecki, P. Pulay*, J. Phys. Chem. A 102 (1998) 1412.

[9] *M.J. Frisch, G.W. Trucks, H.B. Schlegel et al.*, Gaussian 03, Revision B.04, Gaussian, Inc., Pittsburgh, Pa, 2003.

[10] *M.D. Halls, H.B. Schlegel*, J Chem Phys 109:24 (1998) 10587–10593.

[11] *M. Karabacak, M.Cinar, M. Kurt*, Spectrochimica Acta Part A 74 (2009) 1197–1203.

[12] *N.B. Colthup, L.H. Daly, S.E. Wiberley*, Introduction to Infrared and Raman Spectroscopy, Academic Press, London, 1990.

FTIR SPECTROSCOPIC STUDY OF M(CYCLOHEXANETHIOL)$_2$Ni(CN)$_4$.(1,4-DIOXANE) CLATHRATE (M = Co, Ni And Cd)

ZEKI KARTAL[1], ELVAN SAYIN[2]

[1] *Physics Department, Faculty of Arts and Sciences, Dumlupmar University, Kütahya, TÜRKİYE*

[1] *zkartal@dumlupinar.edu.tr*

[2] *higgsbozonu@mynet.com*

In this study, clathrate of Cyclohexanethiol-tetracyanonickel-dioxane, given by the formula M(Cyclohexanethiol)$_2$Ni(CN)$_4$.(l,4-dioxane) (M = Co, Ni and Cd), is obtained for the first time through chemical methods. The similarities of the observed spectra indicate that the obtained clathrate of Cyclohexanethiol-tetracyanonickel-dioxane is a new example of Hofmann-type clathrates. In our study, the Hofmann-type clathrates formed by bounding electrons of sulphur-donor atoms of the thiol group of Cyclohexanethiol ligand to transition metal atoms consist of the corrugated $|M–Ni(CN)_4|_\infty$ polymeric layers which are held in parallel through the van der Walls interactions (-M- Cyclohexanethiol...Cyclohexanethiol-M-).

I. INTRODUCTION

In various studies, Hofmann-type clathrates, given by the general formula $ML_2Ni(CN)_4.G$, were produced. Here M is a transition metal atom, L a ligand molecule or half of a bidentate ligand molecule, and G a guest molecule [1]. The clathrates are of interest because of their inclusion behavior and use as catalysts, anti-oxidants and stabilizing agents [2]. Infrared spectroscopy is one of the best method for the investigation of the guest-host interactions in Hofmann-type clathrates.

In this study we used Cyclohexanethiol molecule (abbreviation CHT) as a ligand for the first time and 1.4-dioxane (abbreviation D) as a guest (G) molecule to produce new Hofmann-type clathrates with the formula $M(CHT)_2Ni(CN)_4.G$, where M is a transition metal atom (M = Co, Ni and Cd).

II. EXPERIMENTAL

All chemicals, namely CHT ($C_6H_{11}SH$, Fluka, 99%), $CoC1_2.6\ H_2O$ (Fluka, 99%), $NiCl_2.6\ H_2O$ (Fluka, 98%), $CdCl_2.2H_2O$ (Fluka, 96%), $K_2[Ni(CN)_4]$.aq (Fluka, 98%) and D ($C_4H_8O_2$, Fluka, 98%) were used without further purification. First 1 mmol of $K_2Ni(CN)_4$ was disolved in water. 2 mmol of CHT were added to this solution. Then 5 mmol of D was added to the mixture. After that, a solution of 1 mmol MCl_2 (M = Co, Ni and Cd) in water was added to the mixtures, and was stirred for 5 days.

The clathrates prepared were filtered, washed with pure water, ethanol and diethyl ether, and kept in a desiccator containing D vapor. The FTIR spectra of the clathrates were recorded at room temperature with a Perkin-Elmer BX FT-IR Spectrometer having a resolution of 4 cm^{-1}.

The clathrates were analyzed for metals with Perkin-Elmer optima 4300 DV ICP-OES and for C, H and N amounts with CHNS-932 (LECO) elemental analyzer. The results of elemental analyses are given in Table 1. According to elemental analysis results there is one guest molecule D in a unit cell of the all clathrates.

I. RESULTS AND DISCUSSION

The FTIR spectrum of liquid CHT and $M(CHT)_2Ni(CN)_4.D$ (M = Co, Ni and Cd) clathrates is illustrated in Fig 1. The FTIR spectral features of the clathrates $M(CHT)_2Ni(CN)_4.D$ (M = Co, Ni and Cd) are found to be similar to each other. The similar spectral features of the clathrates suggest that they have similar analogous structural features [3].

The FTIR spectral datas obtained can be interpreted by considering the vibrations of ligand CHT molecules, the $Ni(CN)_4^{-2}$ ion units and guest D molecules.

Table1. Elemental analysis of the $M(CHT)_2Ni(CN)_4.D$ (M = Co, Ni and Cd) clathrates.

Abbreviations of clathrates and M_r (g)	Elemental analysis, Found (%)/ (Calculated) (%)					
	C	H	N	Co	Ni	Cd
$Co(C_6H_{11}SH)_2Ni(CN)_4.C_4H_8O_2$ Co-CHT-Ni-D, M_r = 542.24	44.07 (44.30)	5.56 (5.95)	10.46 (10.33)	10.43 (10.87)	10.66 (10.82)	- (-)
$Ni(C_6H_{11}SH)_2Ni(CN)_4.C_4H_8O_2$ Ni-CHT-Ni-D, M_r = 541.99	43.97 (44.32)	5.57 (5.95)	10.06 (10.34)	- (-)	21.24 (21.66)	- (-)
$Cd(C_6H_{11}SH)_2Ni(CN)_4.C_4H_8O_2$ Cd-CHT-Ni-D, M_r = 595.72	40.06 (40.32)	5.05 (5.41)	9.62 (9.40)	- (-)	9.94 (9.85)	18.13 (18.87)

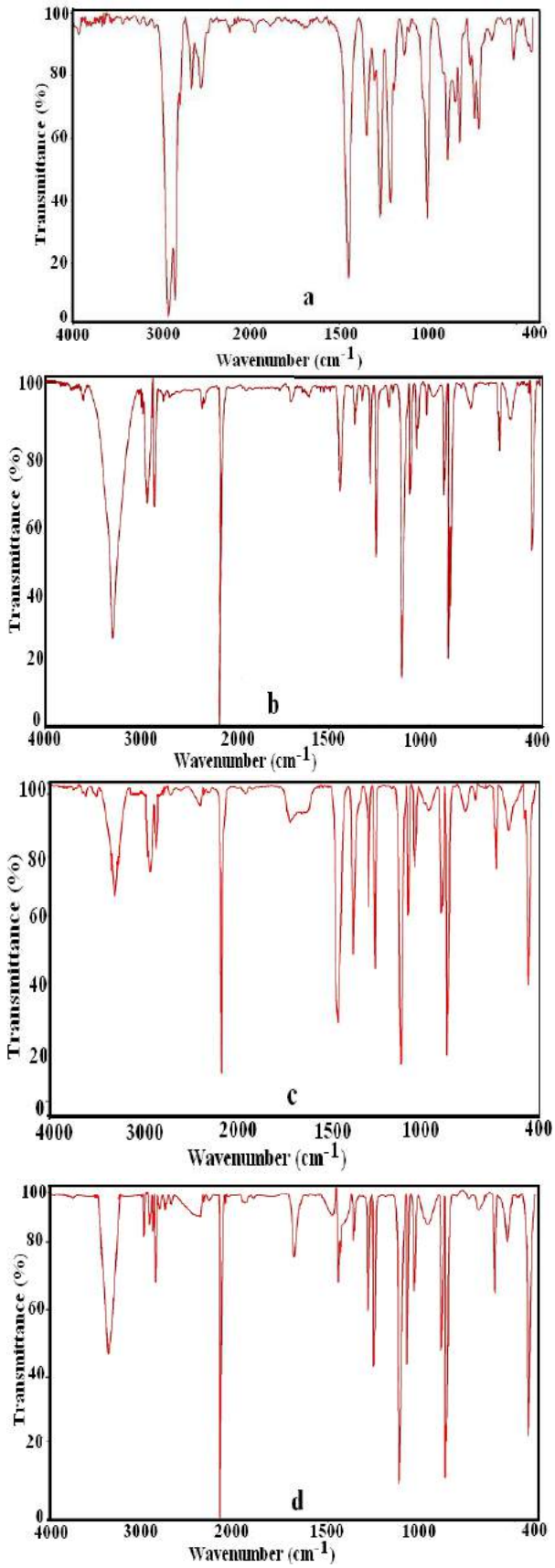

Fig. 1. The FT-IR spectra of the liquid CHT (a), the Co(CHT)$_2$Ni(CN)$_4$.D (b), the Ni(CHT)$_2$Ni(CN)$_4$.D (c) and the Cd(CHT)$_2$Ni(CN)$_4$.D (d) clathrates.

CHT vibrations

In organic chemistry, a **thiol** is a compound that contains the functional group composed of a sulfur-hydrogen bond (-SH). This functional group is referred to either as a *thiol group* or a *sulfhydryl group*. More traditionally, thiols are often referred to as **mercaptans.** The term mercaptan is derived from the Latin **mercurium captans** (capturing mercury) because the thiolate group bonds so strongly with mercury compounds [4]. The molecular structure of the CHT is shown in Fig. 2. The CHT molecule contains a **thiol** group having sulfur atom which can donate electrons. Hence, it expect that the binding takes place with the sulfur atom of the thiol groups. There are various vibrational (Raman and infrared) and other studies reported for the CHT molecule [5-13].

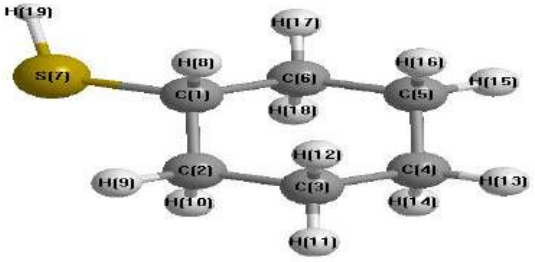

Fig. 2. The molecular structure of the CHT.

The thiols decompose on burning producing toxic gases including sulfur dioxide, it reacts with strong oxidants, reducing agents and metals. The thiols are used in commercial industry, such as liquid petroleum gas tankers and bulk handling systems; the use of an oxidizing catalyst is used to destroy the odor. A copper-based oxidation catalyst neutralizes the volatile thiols and transforms them into an inert product. The CHT is colorless liquid with a strong, offensive odor. The CHT is used as starting material for manufacture of biologically active compounds such as inhibitors of prostaglandin and leukotriene; canine COX-2 inhib-itors; phosphodiesterase inhibitors, …etc [11].

The CHT has two C_s conformations, having the (–SH) group in the equatorial (e-form) and axial (a-form) positions respectively [6, 7]. The e-form is more stable than a-form [7]. It has 51 normal vibrations, among which 3 vibrations are only Raman active, 18 vibrations are IR active and 19 vibrations are both Raman and IR active [7]. These normal modes are observed in the liquid phase spectrum of the CHT molecule [5, 7 and 8, 9]. The frequencies of for the bulk CHT vibrations in clathrates are assigned on the basis of the work of Sheppard, Takeoka and Varsanyi [5, 7 and 14]. The tentative assignments and wavenumbers of the infrared bands for the CHT molecule observed in the FTIR spectra of the clathrates together with the vibrational wavenumbers of bulk the CHT are given in Table 2.

According to the spectral data, the liquid CHT is a combination of equatorial (e-form) and axial (a-form) positions. The observed small frequency shifts are due to the changes of the surround of the CHT molecule and the pairing of the internal vibration of the CHT molecule with the vibrations of (M–S) bond. Such small frequency shifts were also reported in other studies [15, 16].

Table 2. The IR wavenumbers (cm^{-1}) of CHT in the M-CHT-Ni-D (M = Co, Ni and Cd) clathrates along with bulk CHT.

Assignment[a]	CHT	Co-CHT-Ni-D	Ni-CHT-Ni-D	Cd-CHT-Ni-D
$\nu_a(CH_2)$	2930 s	2929 m	2924 m	2934 w
$\nu_s(CH_2)$	2853 s	2856 m	2855 m	2860 m
ν(S-H)	2553 m	n. o.	n. o.	n. o.
$\delta(CH_2)$	1447 s	1450 m	1453 s	1452 m
	1351 w	1357 w	n. o.	n. o.
	1341 m	1338 vw	1340 sh	1335 vw
	1301 m	1295 m	1294 m	1293 m
	1224	?	?	?
	1204	1197 w	1197 vw	1203 vw
	1184	1175 vw	1169 vw	1172 vw
	1128	Obs.	Obs.	Obs.
ν(C-S)	1030	1048 w	1049 m	1045 m
δ(S-H)	1019 m	n. o.	n. o.	n. o.
ν(C-S)	1000 s	996 w	1004 w	1001 w
$\delta(CH_2)$, e	927 w	n. o.	937 vw	n. o.
δ(C-SH)	916 m	n. o.	n. o.	n. o.
δ(S-H)	904 w	n. o.	n. o.	n. o.
ν(C-C-C), e	885 s	897 m	898 m	899 m
$\delta(CH_2)$	839 m	n. o.	n. o.	n. o.
Ring breat. e	819 m	814 w	830 vw	831 vw
ν(C-S),e Fr.[b]	722 m	738 w	722 w	722 w
δ(C-C-C), a	634 w	635 vw	621 w	621 vw
δ(C-C-C), a	561 vw	555 w		
δ(C-C-C), e	524 w	505 vw	504 w	
δ(C-C-C), a	471 w	478 vw	461 w	461 w
δ(C-C-C), e	410w	Obs.	Obs.	Obs.

ν_a, asymmetric stretching; ν_s, symmetric stretching; ν, stretching; δ, in-plane bending; e, equatorial form; a, axial form; s, strong; m, medium; w, weak; vw, very weak; sh, shoulder; n.o., not observed; Obs., Obscured.

[a] Taken from References [5, 7 and 14].

[b] The corrected wavenumber for Fermi resonance according to Ref. [17].

In general, the bulk CHT vibration bands in the FTIR spectrum correlate very well with those in the FTIR spectrum of $M(CHT)_2Ni(CN)_4$.D clathrates. However, a few remarkable changes occurred on bound of CHT to the transition metal atoms. Firstly, the ν(S-H) band which appears at 2553 cm^{-1} in the FTIR spectrum of bulk CHT is completely missing in the FTIR spectrum of $M(CHT)_2Ni(CN)_4$.D clathrates.

In the FTIR spectrum of $M(CHT)_2Ni(CN)_4$.D clathrates, no band is found to correlate with this band in the FTIR spectrum of bulk CHT, which confirms that the S-H bond of the CHT is broken on the bound to the transition metal atoms (Co, Ni and Cd). This result indicat that the CHT molecule is bounds to the transition metal atoms dissociative as a cyclohexoanethiolate anion. If this is a true case, the δ(S-H) and δ(C-SH) modes should also disappear in the FTIR spectrum of $M(CHT)_2Ni(CN)_4$.D clathrates [11, 12]. This situation is shown clearly in the Table 2 and in the Fig. 1. The resulting cyclohexoanethiolate anions were found to bind to the transition metal atom via their sulfur atoms. Similar situations were observed and reported in the other studies with aliphatic and aromatic thiols [11, 12]. Another remarkable change in the FTIR spectrum of $M(CHT)_2Ni(CN)_4$.D clathrates on bound of the CHT with the transition metal atom is the high frequencies shift of the ν(C-S) bands. There is agreement in the literature that the doublet at 735 cm^{-1} and 709 cm^{-1} caused by Fermi

resonance between the ν(C-S) stretching and combination band at 711 (= 284 + 427) cm^{-1} of the equatorial chair conformers of the liquid CHT vibrations [8-11]. A Fermi resonance is the shifting and splitting of the energies and intensities of absorption bands in a vibrational (IR or Raman) spectrum. It is a consequence of quantum mechanical mixing. The method of Langseth and Lord to correct Fermi resonance was used to obtain the unperturbed ν(C-S) frequency in the liquid CHT [17]. The corrected frequency value of the ν(C-S) is 722 ± 1.46 cm^{-1}. The ν(C-S) bands at 722 cm^{-1}, 1000 cm^{-1} and 1030 cm^{-1} for the bulk CHT molecule shifted to high frequency region around 4–19 cm^{-1} in the clathrates.

The FTIR spectral data for the CHT in the clathrates are consistent with all the vibrational features the ν(C-S) group of a coordinated ligand. The ν(C-S) stretching frequency should increase due to the consecutive effects and coordination. Hence, the (C-S) bonds should become stronger. This shift shows that CHT molecule is connected directly to transition metals atoms through the sulfur atom of the (C-S) group. There are various frequency shifts to higher or lower frequencies in the FTIR spectrum of the M(CHT)$_2$Ni(CN)$_4$.D clathrates. All of these frequency shifts are sensitive to connect directly transition metals atoms to CHT ligand molecule. The reason is that the bonding of the (C-S-M) makes difficult the C–S deformation motion for the C-S and the other groups. Similar shifts were observed in Şenyel's and Kartal's study with various ligand molecules [18-22].

It is obvious that the observed FTIR peaks observed between 3613 and 3100 cm^{-1} result from the presence of water molecules in the M(CHT)$_2$Ni(CN)$_4$.D clathrates [23].

The non covalent Ni–π binding force among the Ni ions with aromatic systems of the CHT ligand molecules is very important in stabilizing the polymeric layers of the Hofmann-type complexes and Hofmann-type clathrates [22, 24].

Ni(CN)$_4$ group vibrations

The structure of unit cell of $[Ni(CN)_4]^{2-}$ ions is shown in Figure 3. The FT-IR wavenumbers of Ni(CN)$_4$ anions in our investigated clatrates are given in Table 3 and refer to the work of McCullough and et al [25]. The diagnostic wavenumbers of the (CN) and (Ni-CN) modes are found to be similar those of Hofmann-type complexes [15, 16 and 18-22, 24].

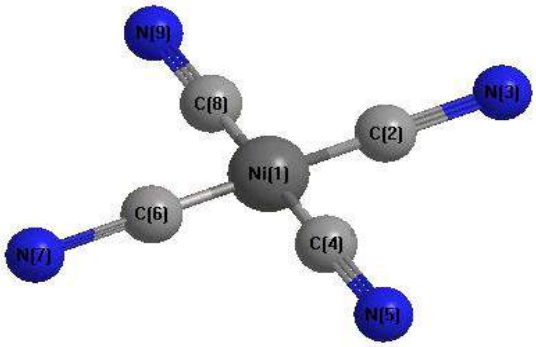

Fig. 3. Unit cell of $[Ni(CN)_4]^{2-}$ ions.

As the stretched vibrations of the CN group of the $K_2[Ni(CN)_4]$ were observed at 2122 cm^{-1} region, the band ν(CN) E_u for the clathrates of M-CHT-Ni-D shifted to a higher frequency range at around 32-39 cm^{-1}. The stretched of (Ni-CN) E_u mode of the $K_2[Ni(CN)_4]$ were observed at 539 cm^{-1} region, the band of ν(Ni-CN) E_u modes, for the clathrates of M-CHT-Ni-D shifted to a higher frequency range at around 5-12 cm^{-1}. The same higher frequency shift range at around 9–23 cm^{-1} appeared also in the in plane bending of δ(Ni-CN) E_u mode, of the $K_2[Ni(CN)_4]$ were observed at 416 cm^{-1} region for clathrates. On the other hand the out of plane bending of (Ni-CN) A_{2u} mode, of the $K_2[Ni(CN)_4]$ were observed at 474 cm^{-1} region, the band of π(Ni-CN) A_{2u} modes, for the clathrates of M-CHT-Ni-D shifted to a lower frequency range at around 13-21 cm^{-1}. The all shifts show that both bands are connected to the transition metal atoms (M = Co, Ni and Cd).

Table 3. The IR wavenumbers (cm^{-1}) of the $Ni(CN)_4^{-2}$ group in the M(PhCOCl)$_2$Ni(CN)$_4$ (M = Co, Ni and Cd) complexes.

Assignment[a]	$K_2[Ni(CN)_4]$[a]	Co-CHT-Ni-D	Ni-CHT-Ni-D	Cd-CHT-Ni-D
ν(CN), E_u	2122	2154 s	2161 s	2157 s
Hot band	2118	2116 sh	2124 sh	2116 w
ν(Ni-CN), E_u	539	551 w	544 w	546 m
π(Ni-CN), A_{2u}	474	453 w	460 w	461 w
δ(Ni-CN), E_u	416	431 s	439 s	425 s

s, strong; m, medium; w, weak; sh, shoulder; ν, stretching; π, out-of-plane bending; δ, in plane bending.
[a] Taken from Ref. [25].

Such frequency shifts were observed and explained as the mechanical coupling of the internal modes of Ni(CN)$_4$ with the metal M-NC (M = Co, Ni and Cd) vibrations. The characteristic frequencies of Ni(CN)$_4$ group are found to be similar to those of the Hofmann-type complexes and clathrates suggesting that coordination around Ni atom is square and that $\left|\text{M-Ni(CN)}_4\right|_\infty$ layers have been conserved [18-22, 24]. Therefore, $[Ni(CN)_4]^{2-}$ anions and $[M\text{-}(CHT)_2]^{2+}$ cations come together in square planar sheet constitution. These polymeric layers are held in parallel by Van der Waals interactions between CHT molecules. The α type cavity occurs in these clathrates. The cavities have volume depending on the type of transition metals. The CHT molecules are located below and above the plane. Nickel atoms are surrounded by four carbon atoms of cyanide groups and, M, atoms are also surrounded by four nitrogen atoms of the cyanide groups and at the same time two sulfur atoms of thiol group of the CHT molecules are bonded to the metal atoms in the regular square plane.

Guest D-Molecules vibrations

The assignment and the frequencies of the vibrational bands arising from the enclathrated D observed in the spectrum of M(CHT)$_2$Ni(CN)$_4$.D are given in Table 4. The wavenumbers of D in the liquid phase found by Sopková and Bubanec are also given in Table 4 for comparetion [26]. The vibrational studies show that the D

molecule has a chair conformation with a centre of symmetry *(C_{2h})* in the gas and liquid phases [27]. In some of our clathrates, several D bands are split into doublets. This results indicate that the host ($M(CHT)_2Ni(CN)_4$)-guest (D) interaction is strong (i. e, crystal field effecs). Similar observations have also been seen for Hofmann-type D clathrates [28, 21] and Hofmann-T_d-type D clathrates [29]. The FTIR spectrum shows that the D molecule is centro-symmetric and is thus most likely in a chair conformation (Table 4). Similar observations have been observed for metal halide complexes [30], for Hofmann-type D clathrates [31] and Hofmann-T_d-type D clathrates [29, 21].

The explanation given above indicates that the clathrates obtained in this study are new examples of Hofmann-type clathrates. These clathrates can be used as molecular sieves for the chemical purification and separation of isomers.

Table 4. The IR vibrationaI wavenumber (cm^{-1}) of 1,4-dioxane in $M(CHT)_2Ni(CN)_4$.D clathrates.

Assignment[a]	Liquid D	Co-CHT-Ni-D	Ni-CHT-Ni-D	Cd-CHT-Ni-D
$\nu_{11}(a_u)$, $\nu_{28}(b_u)$	2961 vs	2953 m	2950 m	2933 m
$\nu_{12}(a_u)$, $\nu_{29}(b_u)$	2854 vs	2855 m	2856 m	2860 m
$\nu_{30}(b_u)$	1453 s	1456 m	1452 m	1452 m
$\nu_{14}(a_u)$	1366 s	1376 s	1372 m	1373 m
$\nu_{32}(b_u)$	1289 s	1293 m	1291 m	1293 m
$\nu_{15}(a_u)$	1255 s	1258 s	1259 m	1260 m
$\nu_{16}(a_u)$	1122 vs	1120 vs	1120 vs	1120 vs
$\nu_{17}(a_u)$	1084 s	1083 m 1079 m	1083 m 1080 m	1081 m
$\nu_{33}(b_u)$	1048 s	1049 m 1042 m	1049 m 1044 m	1045 m
$\nu_{18}(a_u)$	874 s	876 s 865 s	875 s 866 s	873 s 866 s
$\nu_{35}(b_u)$	614 s	622 m 611 m	621 m 611 m	613m

s, strong; m, medium; w, weak; vs, very strong; sh, shoulder.
[a] Taken from Ref. [26].

ACKNOWLEDGEMENT

This work was supported in the part by the Dumlupınar University for the technical and financial with the project number 46. The author thanks the Anadolu University Plant Drug and Scientific Research Centre (AÜBIBAM) for providing technical support.

[1]. *T. Iwamoto*, in: Inclusion Compounds, Vol. I, Chapter 2 (Eds. J. L. Atwood, J. E. D. Davies, and D. D. MacNicol). Academic Press, London 1984, p. 29.
[2]. *M. Hagan*, Clathrate Inclusion Compounds. Reinhold Publishing Corporation, Chapman & Hall Ltd., New York 1962, p. 5.
[3]. *E. Kasap, A. Özbay and S. Özçelik*, Spectroscopy Letters, 30 (1997) 491.
[4]. *T. W. Graham Solomons*, Organic Chemistry, John Wiley & Sons, Inc., New York, 1996 (Special Topic L).
[5]. *N. Sheppard*, Trans. Faraday Soc. 46 (1950) 429.
[6]. *G. Chiurdoglu, J. Ressi and M. Vander Stichelen Rogier*, Chemistry and Industry, (1961) 1874.
[7]. *Y. Takeoka*, Journal of Molecular Spectroscopy, 30 Issues 1 (1965) 29.
[8]. *D. W. Scott and G. A. Crowder*, J. Chem. Phys. 46 (1967) 1054.
[9]. *D. W. Scott and M. Z. El-Sabban*, Journal of Molecular Spectroscopy, 30 Issues 1-3, (1969) 317.
[10]. *R. Fausto, J. J. C. Teixeira-Dias and P. R. Carey*, Journal of Molecular Structure 159, Issues 1-2 (1987) 137.
[11]. *C. K. Kwon, M. S. Kim and K. Kim*, Journal of Raman Spectroscopy, 20 (1989) 575.
[12]. *S. M. Kane, J. L. Gland*, Surface Science 468 (2000) 101.
[13]. *Mohamed A. Metwally and Bakr F. Abdel-Wahab*, A C G publications *Org. Commun*. 2:4 (2009) 84.
[14]. *G. Varsanyi*, Vibrational Spectra of Benzene Derivatives, Academic Press, New York, 1969.
[15]. *Z. Kartal, A. Ölmez*, Z. Naturforsch. 60a (2005) 537.
[16]. *Z. Kartal*, Journal of Molecular Structure, 938 (2009) 70.
[17]. *A. Langseth, R. C. Lord, Kgl. Dnaske Videnskab*, Mat-fys Medd. 15 (1938) 6.
[18]. *M. Şenyel*, Bull. Pure App. Sci. 20D (2) (2001).
[19]. *Z. Kartal, and A. Ölmez*, Z. Naturforsch. 60a, (2005) 537.
[20]. *Z. Kartal and Ş. Şentürk*, Z. Naturforsch. 60a, (2005) 285.
[21]. *Z. Kartal*, Z. Naturforsch. 60a, (2005) 469.
[22]. *Z. Kartal*, J. Mol. Struct., 938, (2009) 70.
[23]. *K. Nakamoto*, Infrared and Raman Spectra of Inorganic and Coordination Compounds, Part B, John Wiley & Sons, Inc, New York, 1963 (Section III).
[24]. *G. S. Kürkçüoğlu, O. Z. Yeşilel, İ. Kavlak and O. Büyükgüngör*, J. Mol. Struct. 920 (2009) 220.
[25]. *R. L. McCullough, L. H. Jones, G. A. Crosby*, Spectrochimica Acta, 16 (1960) 929.
[26]. A. Sopková and J. Bubanec, J. Therm. AnaL.12, (1977) 97.
[27]. *O. H. Ellestas and P. Klæboe*, Spectrochim. Acta 27A (1960) 1025.
[28]. *B. Dempster and H. Uslu*, Spectrochim. Acta 34A (1978) 71.
[29]. *T. Zengin, Z. Kantarcı and E. Kasap*, J. Mol. Struct. 81 (1999) 482.
[30]. *G. W. Fowles, O. A. Rice, and R. A. Walton*, Spectrochim. Acta 26A (1970) 143.
[31]. *E. Kendi and O. Ülkü*, Z. Kristallogr. 144 (1976) 91.

CHEMICAL STATE ANALYSIS ON $K_{\alpha 1,2}$ AND $K_{\beta 1,3}$ X-RAY EMISSION LINES OF THE 3d TRANSITION METALS USING WDXRF SYSTEM

S. PORIKLI[*], Y. Ö. YEŞİLBAĞ[*], Y. KURUCU[**]

[*] *Department of Physics, Faculty of Sciences, Erzincan University, 24030, Erzincan, Turkiye, sporikli@gmail.com*

** *Department of Physics, Faculty of Sciences, Ataturk University, 25240, Erzurum, Turkiye, ykurucu@atauni.edu.tr*

The *K* series x-ray lines of 3d transition elements V, Cr, Mn, Fe, Co, Ni, Cu and Zn were measured using a wavelength-dispersive x-ray fluorescence spectrometer (WDXRF). The measurements were performed using a ZSX-100e sequential spectrometer equipped with a Rh x-ray tube operated. The asymmetry, peak energy,, full width of half maximum (FWHM) and relative intensity ratio values were extracted from the measured spectra. An accurate analytical representation of each line is obtained by a fit to a Lorentz function. The peak energy and line width changes due to the changes in the chemical states are reported. Possible origins for the observed Z dependent trends are discussed.

I. INTRODUCTION

The structure of the x-ray diagram emission lines of the transition elements has been the subject of numerous experimental and theoretical studies [1-6]. This was motivated by their asymmetric shapes, indicating large contributions process other than the main single electron bound-bound diagram transitions which dominate corresponding symmetric emission lines of higher *Z* atoms. The asymmetry of the transition elements $21 \leq Z \leq 31$ lines has also been observed and measured [7-9], and with some success has been explained as the result of the interaction between the 3*d* and 2*p* electrons. Such an interaction splits each of the $2p_{3/2}$ and $2p_{1/2}$ electronic levels [10], resulting in two and possibly more closely associated emission lines. The width of the Kα1 [K-L3] and the Kα2 [K-L2] x-ray emission lines of this elements were measured by Parratt [11] and Allison [12-13]. The results of most of these experiments were tabulated by Blokhin [14] and the subject was reviewed by Parratt [6] and by Sevier [15].

The Kα1,2 line shapes were previously shown [16-17] to be well described by the many-body conduction band excitation theory of Doiach and Šunjić [18], and almost as well, by shake up processes [19]. Shake up from the 3*d* shell was also shown to account reasonably well for the measured Kβ1,3 line shape, although a complete quantitative fit was not reported and possible contributions from other shells were not investigated [20-21].

This paper present and discusses the measured spectra. Spectra of *K* x-rays emitted from a V, Cr, Mn, Fe, Co, Ni, Cu and Zn target were measured in high resolution wave dispersive x-ray spectrometer (WDXRF). After the measurement, characteristic quantitative such as peak energy, indices of asymmetry, FWHM are determined and finally, the relative intensity ratios Kβ1,3/Kα1,2 are delivered from the fits. The measured spectra were described in terms of a background function (a straight line) and peaks having Lorentz profiles. The Microcal Orgin 7.5 was used for peak resolving and background subtraction of *K* x-rays

.

II. MATERIAL AND METHODS

2.1. Sample preparation:

The experiments were carried out using high purity V, Cr, Mn, Fe, Co, Ni, Cu and Zn elements (in powder form). For powdered samples, particle size effects have a strong influence on the quantitative analysis of infinitely thick specimens. Even for specimens of intermediate thickness, in which category the specimens analyzed in the present study fall, these effects can be significant. Therefore, in order to circumvent particle size effects all samples were grounded and sieved through a -400 mesh (<37 μm) sieve. The powder was palletized to a uniform thickness of 7-12 mg cm^{-2} by a hydraulic press using 10 ton in^{-2} pressure. The diameter of the pellet was 13 mm.

2.2. Measurements:

Wavelength-dispersive x-ray fluorescence spectrometry was used for analysis of the semi-qualitative method. The measurements were performed using a ZSX 100e sequential spectrometer equipped with a Rh x-ray tube operated. Rigaku has improved their semi-quantitative software package further with the introduction of SQX. It is capable of automatically correcting for all matrix effects, including line overlaps. SQX can also correct for secondary excitation effect by photoelectrons (light and ultra-light elements), varying atmospheres, impurities and different sample sizes.

To investigate the spectrometer sensitivity in measuring of intensity and energy shift, one sample at same conditions was measured for 10 times. Because of the use of instruments such as sieve weight and hydraulic press, errors are caused in the results of analysis. These errors were called manual and instrumental errors. 10 samples were prepared and measured for same conditions to determine these errors.

The measured emission lines were registered with about 1000 steps and measuring times between 100 and 200 s at each point. The total counts in collected at a single point at the peak varied between 200 and 50 000 counts. In the measurements of the absolute peak position, it was found advantageous to choose these three parameters (steps, time and total counts) differently.

III. RESULTS AND DISCUSSION

Two example of the fitted spectra (Kα1,2, Kβ1,3) are shown in Figure 1. Measured numbers of counts are shown as solid black circles, while the red line represents the overall fit. The background is shown as a blue line.

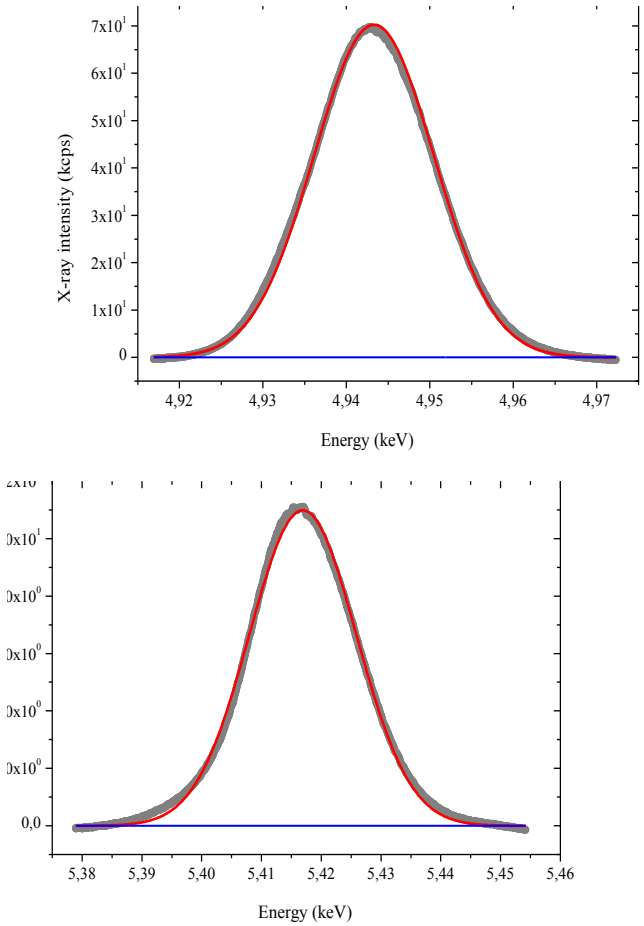

Fig. 1 Solid circles: Measured spectrum of V $K\alpha_{1,2}$ and $K\beta_{1,3}$ x-rays. Lines: Overall fitting function (red) and background (blue).

A frequently used and convenient (but not very accurate) quantification of the line shape is by its full width at half maximum (FWHM) and index of asymmetry. In both the classical and quantum theory the natural line shape of an emission line in the frequency or energy scale is a Lorentzian [22]. This is observed in practice for a large number of Kα emission lines and in classical theory, they are highly symmetric. By contrast, the experimentally observed Kα and Kβ emission lines of the 3d transition metals are pronouncedly asymmetric. The index of asymmetry is defined as the ratio of the half height on the low and high energy sides of the peak [23]. In our measurements the FWHM and index of asymmetry were determined from the background corrected Lorentzian fits. In Table 1, the index of asymmetry for Kα1,2 and Kβ1,3 are presented. As can be seen from Table 1, the line shapes of Kα1,2 and Kβ1,3 are not symmetric.

From the analysis of single crystal detector wave dispersive x-ray spectra, the energies of the Kα1,2 and Kβ1,3 lines were determined. The measured Kα1,2 and Kβ1,3 line widths and asymmetries are shown in Table 1 and are also plotted as function of atomic numbers in Fig. 2-5. The FWHM of the Kα1,2 and Kβ1,3 peak increases monotonically from V to Cu.

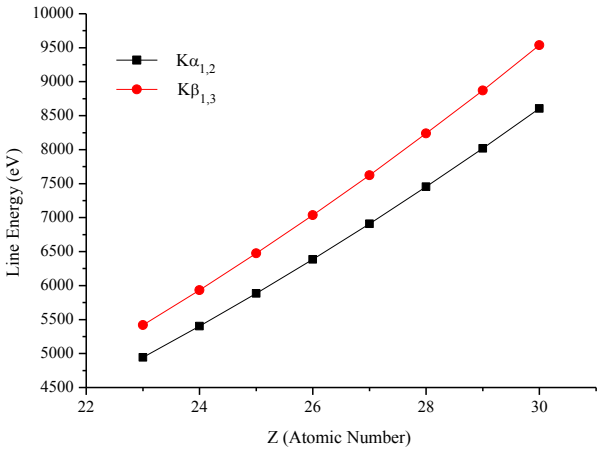

Fig. 2 Line energy of the 3d elements as a function of the atomic number.

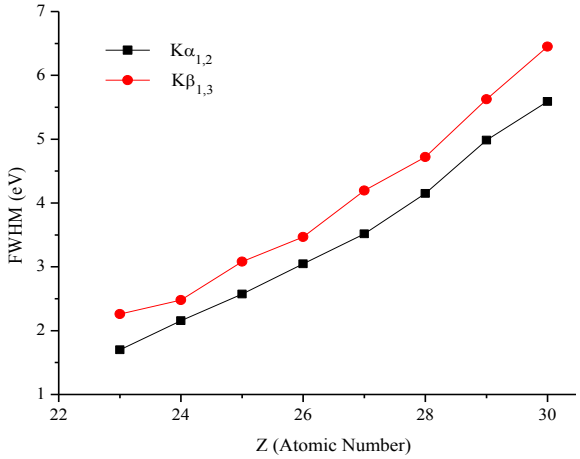

Fig. 3 FWHM of the Kα1,2 and Kβ1,3 lines plotted as a function of the atomic number.

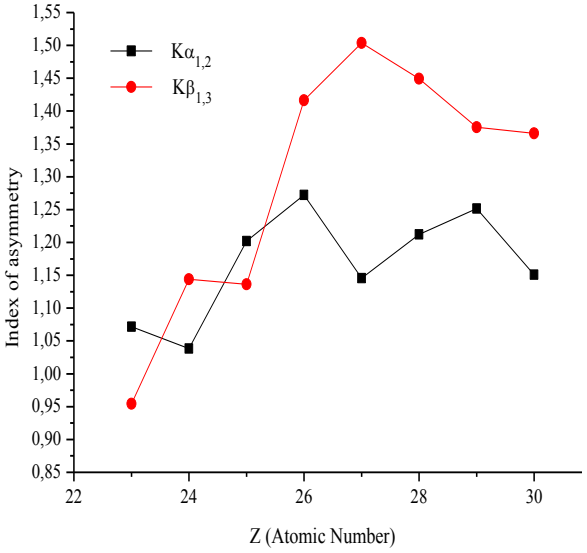

Fig. 4 Asymmetry index of the Kα1,2 and Kβ1,3 lines plotted as a function of the atomic number.

Table 1 Positions (E), widths FWHM, Asymmetry Index and Relative intensity of the $K\alpha_{1,2}$ and $K\beta_{1,3}$ lines.

Atomic Number	E (eV)	E (eV)	FWHM (eV)	FWHM (eV)	Asymmetry Index	Asymmetry Index	Relative Intensity	Relative Intensity
	$K\alpha_{1,2}$	$K\beta_{1,3}$	$K\alpha_{1,2}$	$K\beta_{1,3}$	$K\alpha_{1,2}$	$K\beta_{1,3}$	$I(K\alpha_{1,2})$	$I(K\beta_{1,3})$
23	4942,75	5417,45	1,700	2,259	1,07181	0,95420	1,26955	0,24981
24	5401,90	5932,30	2,155	2,480	1,03842	1,14416	1,98670	0,41289
25	5883,83	6474,10	2,574	3,082	1,20192	1,13636	3,61991	0,72870
26	6384,81	7036,43	3,048	3,466	1,27226	1,41643	5,15060	1,08931
27	6909,24	7623,65	3,517	4,195	1,14548	1,50376	8,10557	1,58179
28	7453,20	8238,20	4,150	4,720	1,21212	1,44928	11,38842	2,27548
29	8019,22	8871,86	4,985	5,624	1,25156	1,37552	15,75283	3,24485
30	8605,56	9536,24	5,592	6,449	1,15075	1,36612	19,10754	4,03461

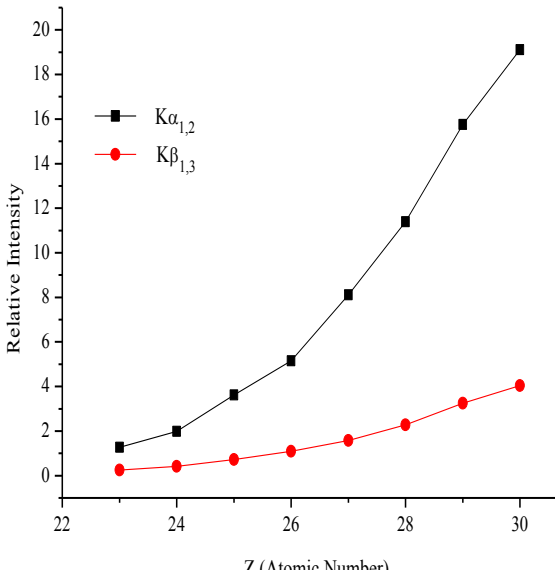

Fig. 5 Relative intensity of the Kα1,2 and Kβ1,3 lines plotted as a function of the atomic number.

The spread of the data is large, probably due to high sensitivity of the width of instrumental function [24]. A broad instrumental function should result in a systematically too low asymmetry. It is clear from the results that the asymmetry is generally larger for the Kβ1,3 peak. Kβ1,3 lines emitted after the transition of valance electrons are more sensitive to the chemical environment. Thus the asymmetry of the Kβ1,3 x-ray emission lines are usually much more pronounced than the Kα1,2 emission lines, which are expected to be less affected by the chemical environment effect. This is particularly true for Fe to Cu, which have the highest asymmetry among the 3d transition elements.

Despite the large spread, a general trend for the *Z* dependence of the index can be observed. In addition, Kβ1,3/Kα1,2 relative intensity ratios depend sensitively on the atomic structure. Thus they have been widely used also for critical evaluation of atomic structure model calculations.

The errors of the energies, presented in Table 1, originate mainly from the limited precision of our measurements, determined from repetitive measurements of pure targets, which were prepared and placed in the sample chamber in a similar way.

The precision of the Kα1,2 and Kβ1,3 lines was determined as 0.2 eV, whereas maximum deviation of a single measurement from the average value was 0.5 eV. The overall errors given in Table 1 incorporate also fitting errors. The experimental uncertainties in the values were determined taking into account multiple measurements and multiple fits of each spectrum. They are always <0.05 eV for the FWHM. The errors for the index of asymmetry are <0.05 eV for Kα1,2 and Kβ1,3.

IV. CONCLUSION

We have presented and discussed the essential features of the Kα1,2 and Kβ1,3 emission lines of 3d transition elements. The observed spectral features, namely asymmetry indices, FWHM, energy separation and relative intensity ratio between Kα1,2 and Kβ1,3 lines, show interesting correlations with atomic number.

The FWHM and asymmetry index values for 3d and 4d transition elements have therefore been also confirmed by our experiments [25,26]. To avoid complications, the measuring conditions (tube voltage and current, slit widths) remained the same for both runs. As a possible explanation for these fairly small changes of these elements, unique electronic structure of the atoms in this range, which have partly or fully populated 4s shell and an open 3d shell, giving rise to complicated transition structures in the x-ray emission process. Tsutsami [5] proposed that the anomalous widths and asymmetric line shape results from an exchange interaction between electrons of the incomplete 3d shell and lose of 2p shell, left open by the x-ray emission process.

---

[1]. *A.Meisel, G.Leonhadrt, and R.Szargan,* X-Ray Spectra and Chemical Binding (Springer, New York, 1989).

[2]. *J.Edamoto,* Rep. Res. Inst. Tohoku Univ. A2, 561 (1950).

[3]. *H. Sørum*, J. Phys. F 17, 417 (1987).

[4]. *J. Finster, G.Leonhardt, and A.Meisel*, Phys., (Paris) 32, C4-218 (1971).

[5]. *K.Tsutsumi and H.Nakamori*, X-Ray Spectra and Electronic Structure of Matter, edited by A. Faessler and G.Wiech (Fotodruck Frank OHG, München, 1973).

[6]. *L.G.Parratt*, Rev. Mod. Phys., 31, 616 (1959).

[7]. *L.G Parratt*, Rev. Mod. Phys., 50, 1 (1936).

[8]. *J.A.Bearden and C. H. Shaw*, Phys. Rev. 48, 18 (1935).

[9]. *T.Snyder*, Phys. Rev. 59, 689 (1941).

[10]. *E. E. Wainstein*, C. R. (Dokl.) Acad. Sci. URSS 40, 102 (1943).

[11]. *L.G.Parratt*, Phys. Rev. 44, 695 (1933).

[12]. *S.K.Allison*, Phys. Rev. 44, 63 (1933).

[13]. *S.K.Allison and J.H.Williams*, Phys. Rev. 35, 1476 (1930).

[14]. *M.A.Blokhin*, The Physics of X-Rays, 2nd edition (State Pub. House of Tech.- Theor. Lit., Moscow, (1957), p. 404 (English translation by U.S. AEC Officeof Technical Inf.).

[15]. *K.D.Sevier*, Low Energy Electron Spectroscopy (Wiley, New York, 1972), p.220.

[16]. *M.Deutsch and M.Hart*, Phys. Rev. B 26, 5558 (1982).

[17]. *N.Maskil and M.Deutsch*, Phys. Rev. A 37, 2947 (1988).

[18]. *S.Doniach and M.Šunjić*, J. Phys. C 3, 285 (1970).

[19]. *W.C.Sauder, J.R.Huddle, J.D.Wilson and R.E.LaVilla*, Phys. Lett. 63A, 131 (1977).

[20]. *R.E.LaVilla*, Phys. Rev. A19, 717 (1979).

[21]. *J.Bremer and H.Sørum, J.Wolf, and E.Förster*, J. Appl. Crystallogr. 26, 539 (1993).

[22]. *B. Agarwal*, X-Ray Spectroscopy (Springer Verlag, Berlin, 1979).

[23]. *V. Pessa, E. Suoninen and T. Valkonen*, Phys. Fenn. 8, 71 (1973).

[24]. *G. Hölzer, M. Fritsch, M. Deutsch, J. Hartwig and E. Förster*, Phys. Rev. A, 56, 6 (1997).

[25]. *S. Porikli and Y. Kurucu*, Instr. Science and Tech., 36, 4 (2008).

[26]. *S. Porikli, İ. Han, P. Yalçın and Y. Kurucu*,Article in Prss. (2010).

CONTENT

OPTIC, LASER, LUMINESCENT MATERIALS. SOLAR, OPTICAL AND MATRIX ELEMENTS, OPTICAL AND ELECTRONIC DEVICES

NUCLEAR PHYSICS

ATOMIC AND MOLECULAR PHYSICS